AeroBest 2021

International Conference on Multidisciplinary Design Optimization of Aerospace Systems

Proceedings

21–23 July 2021

Lisboa, Portugal

André C. Marta & Afzal Suleman (editors)

Preface

This new ECCOMAS Thematic Conference focuses on the multidisciplinary design optimization of aerospace systems, both aircraft and spacecraft. Given the complexity of aerospace design problems and the ever demanding requirements that must fulfilled, the 21st-century aerospace design must necessarily tackle the physical multidisciplinarity present. The current advances in algorithms and computing power make possible the design optimization of single components up to complex systems. Not surprisingly, there is a growing acceptance of multidisciplinary design and optimization in the Aerospace industry, thanks to algorithms and tool developments, capable of tackling robust and reliability-based designs.

The goal of AeroBest is to discuss the latest developments in multidisciplinary design, analysis, and optimization of aerospace systems, covering both manned and unmanned aircraft and spacecraft.

The conference scope encompasses design optimization and inverse problems applied to Aerospace systems, with focus on aircraft and spacecraft. Aerospace design spans from discipline-level conceptual and preliminary design studies up to system level studies of complete aircraft or spacecraft. Multidisciplinary analysis and optimization of conventional and novel configurations is sought. This includes the coupling of disciplines, such as acoustics, aerodynamics, heat and mass transfer, dynamics and control, performance and structural mechanics. The discussion of architectures of discipline coupling is also within the scope of the conference. Focus on numerical optimization algorithms (deterministic or heuristic), discipline analysis models (high-fidelity, low-fidelity and surrogate models) and sensitivity analysis techniques is also desired. The nature of the coupled design problems includes size, shape and topology optimization, using deterministic, reliability-based or robust design optimization approaches.

This first edition, AeroBest 2021, had been previously planned to be held at Instituto Superior Técnico of the University of Lisbon but, given the on-going Covid-19 pandemic, it had to be run online. Nevertheless, we hope all participants made the most of it, to whom we leave a final word of appreciation for making this conference possible.

André C. Marta
(Conference Chair)

Afzal Suleman
(Conference Chair)

Image: MDO Lab, University of Michigan

Scientific Committee

André C. Marta, Instituto Superior Técnico, Portugal

Joaquim R. R. A. Martins, University of Michigan, USA

Joseph Morlier, ISAE-SUPAERO / ICA, France

Jacques F. Périaux, CIMNE / UPC Barcelona, Spain

Hélder C. Rodrigues, Instituto Superior Técnico, Portugal

Carlos A. M. Soares, Instituto Superior Técnico, Portugal

Afzal Suleman, University of Victoria, Canada

Sponsors

Mechanical Engineering Institute (*Instituto de Engenharia Mecânica*)

Portuguese Society for Theoretical, Applied and Computational Mechanics (*Associação Portuguesa de Mecânica Teórica, Aplicada e Computacional*)

European Community on Computational Methods in Applied Sciences

Secretariat

✉ IDMEC

Instituto Superior Técnico

Av. Rovisco Pais, 1

1049-001 Lisboa, Portugal

📞 (+351) 218 417 351

@ aerobest2021@idmec.tecnico.ulisboa.pt

🌐 https://aerobest2021.idmec.tecnico.ulisboa.pt/

Keynote Lecturers

From 2007 to 2010, he was selected by TEKES governmental Finnish Organization as Distinguished Professor at the Mathematical Information Technology Department at the University of Jyvaskyla, Finland. In 2010, he received a UNESCO Chair position on Numerical Methods in Engineering at CIMNE/UPC Barcelona, Spain. Dr. Périaux has built during the last two decades many scientific and technological cooperations, in Europe, USA, Australia and China. His research interests include Evolutionary Algorithms, Game Strategies and Multidisciplinary Design Optimization (MDO). Dr. Jacques Périaux career started at Dassault Aviation (France), where he held the roles of Head of the Numerical Analysis Group in the Département d'Aérodynamique Théorique, High Scientific Adviser of the Advanced Studies Division, and later chair the Pôle Scientifique Dassault Aviation / University Pierre et Marie Curie.

Joaquim R. R. A. Martins is a Professor of Aerospace Engineering at the University of Michigan, where he heads the MDO Lab. He is a Fellow of the American Institute of Aeronautics and Astronautics and a Fellow of the Royal Aeronautical Society. His research involves the development and application of MDO methodologies to the design of aircraft configurations, with a focus on high-fidelity simulations that take advantage of high-performance parallel computing. Before joining the University of Michigan faculty in 2009, he was an Associate Professor at the University of Toronto, where from 2002 he held a Tier II Canada Research Chair in MDO. Prof. Martins received his undergraduate degree in Aeronautical Engineering from Imperial College, London, with a British Aerospace Award. He obtained both his M.Sc. and Ph.D. degrees from Stanford University, where he was awarded the Ballhaus prize for best thesis in Aeronautics. He has served as Associate Editor for the AIAA Journal, Optimization and Engineering, and Structural and Multidisciplinary Optimization. He is currently an Associate Editor for the Journal of Aircraft.

Prof. Jonathan Cooper holds the Airbus Royal Academy of Engineering Sir George White Chair of Aerospace Engineering at the University of Bristol. He has an international reputation for research in aeroelasticity, loads and structural dynamics, having published over 400 technical papers in leading journals and conferences, with 4 written paper prizes, and is the co-author of the Wiley textbook, Introduction to Aircraft Aeroelasticity and Loads. Over the past 30 years he has worked closely with industry to develop solutions that enable aircraft designs to be more fuel efficient and environmentally friendly through exploitation of the interactions between the airflow and aircraft structures. His Airbus sponsored chair is one of only 7 in the UK. Prof. Cooper is a Fellow of the Royal Academy of Engineering, a Fellow of the Royal Aeronautical Society (RAeS), a Fellow of the American Institute of Aeronautics and Astronautics (AIAA) and has been a Chartered Engineer for over 25 years. He has currently just finished a two year term as President of the Royal Aeronautical Society.

Programme Overview

UTC time		
Day 1 – 21 July 2021		
13:00 - 13:10	Opening Ceremony	
13:10 - 13:55	Keynote Lecture I	
	Prof. Jacques Périaux, CIMNE/UPC Barcelona	
13:55 - 14:00	Break	
14:00 - 15:00	Session 1A	Session 1B
15:00 - 15:20	Break	
15:20 - 17:20	Session 2A	Session 2B

Day 2 – 22 July 2021		
13:00 - 13:50	Keynote Lecture II	
	Prof. Joaquim Martins, University of Michigan	
13:50 - 14:00	Break	
14:00 - 15:20	Session 3A	Session 3B
15:20 - 15:40	Break	
15:40 - 17:20	Session 4A	Session 4B

Day 3 – 23 July 2021		
13:00 - 13:50	Keynote Lecture III	
	Prof. Jonathan Cooper, University of Bristol	
13:50 - 14:00	Break	
14:00 - 15:00	Session 5A	Session 5B
15:00 - 15:20	Break	
15:20 - 17:00	Session 6A	Session 6B
17:00 - 17:10	Conference Closure	

Conference Program

Day 1 – 21 July 2021

Keynote Lecture I – Jacques Périaux, CIMNE/UPC Barcelona

Session 1A – Aerospace Design and Integrated Systems – UAV

Session 1B – Discipline Analysis Models – Acoustics & Propulsion, Energy and Heat Transfer

Session 2A – MDO – Approximation and Surrogate Models

Session 2B – Design Optimization – Topology Optimization

Day 2 – 22 July 2021

Keynote Lecture II – Joaquim R. R. A. Martins, University of Michigan

Session 3A – Aerospace Design and Integration Systems – VSTOL

Session 3B – Systems Engineering and Integration

Session 4A – Design Optimization – Shape and Size Optimization

Session 4B – Discipline Analysis and Models – Materials and Structures

Day 3 – 23 July 2021

Keynote Lecture III – Jonathan Cooper, University of Bristol

Session 5A – Aerospace Design and Integr. Sys. – Sailplanes, Ultralight and Flexible Aircraft & Reusable Spacecraft

Session 5B – Design Optimization – Optimization Algorithms & Sensitivity Analysis Methods

Session 6A – MDO – Design under Uncertainty & Decomposition Architectures

Session 6B – Discipline Analysis Models – Aerodynamics

HYBRIDIZED EVOLUTIONARY OPTIMIZATION WITH GAME STRATEGIES FOR MULTI OBJECTIVE / MULTIDISCIPLINARY DESIGN: APPLICATIONS TO AERONAUTICS AND AEROSPACE

Yongbin Chen, Xiao Hu, Jacques Périaux, Zhili Tang, Peng Wu, Lianhe Zhang

International Center for Numerical Methods in Engineering (CIMNE)/UPC Barcelona, Spain
periaux@cimne.upc.edu, http://www.cimne.com

Abstract. *Drag reduction by laminarization, an innovative technology in aerodynamics design, remains a challenge to significantly improve the aerodynamic performance of aircraft and spacecraft. In this lecture, two complex physical flows modeling are considered: (1) the multi design optimization of transonic NLF airfoils/wings and (2) the multidisciplinary design integration of a supersonic combustion ramjet engine (SCRAMJET) in an air breathing hypersonic vehicle, involving aerodynamics, thermodynamics and propulsion disciplines. Both associated complex physical modeling are non-differentiable and strongly suggest the use of evolutionary computing for MO/MDO problems. The two above applications consider multi-objective design optimization (MO) solutions, the trade-offs decisions of which must be taken by the designer.*

Referring to the well-known Game Theory foundations [1], there are three main game strategies to capture solutions of multi objective optimization problems: Pareto solutions (cooperative game), Nash equilibrium solution (competitive game), and Stackelberg equilibrium solution (hierarchical game). Game strategies are hybridized with Evolutionary Algorithms (introduced in the late 60' by John Holland [2] in the context of adaptation in Natural and Artificial Systems). Their implementation with additional speed ups (variable fidelity, games coalition,..) provides a reliable "core software" used to solve complex problems in Aerodynamics and Aerospace.

Hybridized methods are successfully implemented to optimize 2-D /3D aerodynamic shapes of NLF airfoils/wings (maximization of laminar region and reduction of shock intensity with active devices; (Mach=0.729, angle of attack=2.31 deg and Re=1.6×10^7); and the shapes of an hypersonic air breathing vehicle with an idealized supersonic combustor (SCRAMJET) (fore body and after body; Euler flow, Mach=8; angle of attack = 0 deg; flight altitude=30km). Numerical results [3,4] are presented and discussed; they illustrate the potential of the approach for optimizing aerodynamical configurations operating around complex physical flows. It is concluded that the hybridization of games strategies with Evolutionary Algorithms (EAs) [5] is a computationally efficient design tool which can be used in 3-D industrial design environments with large HPC facilities.

Keywords: Natural Laminar Flow (NLF) wing; Transition prediction, Shock wave control technology; Scramjet combustor, Hypersonic air breathing vehicle; Variable-fidelity hierarchical optimization; Pareto, Nash, Stackelberg Games, Evolutionary Algorithms (EAs); Variable fidelity

Yongbin Chen, Xiao Hu, Jacques Périaux, Zhili Tang, Peng Wu, Lianhe Zhang

REFERENCES

[1] O. Morgenstern and J. V. Neumann. *Theory of games and economic behavior.* `http://hdl.handle.net/2042/28548`, 1953.

[2] J. Holland. *Adaptation in natural and artificial systems.* The University of Michigan Press, Michigan, 1975.

[3] Z. Tang, X. Hu, and J. Priaux. Multi-level hybridized optimization methods coupling local search deterministic and global search evolutionary algorithms. *Arch. of Computational Methods in Engineering*, pages –, 2019. doi:10.1007/s11831-019-09336-w.

[4] Z. L. Tang, Y. B. Chen, L. Zhang, and J. Priaux. Solving the two objective evolutionary shape optimization of a natural laminar airfoil and shock control bump with game strategies. *Arch. Computat. Methods Eng.*, 29:119–141, 2019.

[5] J. Périaux, F. Gonzalez, and D. S. C. Lee. *Evolutionary Optimization and Game Strategies for Advanced Design: applications to Aeronautics.* ISCA, Springer, 2015.

THE CONCEPT OF SELF-DEPLOYABLE HELIUM-FILLED AEROSTATS BASED ON TENSEGRITY STRUCTURES

Lech Knap[1], Andrzej Świercz[2], Cezary Graczykowski[2*], Jan Holnicki-Szulc[2]

1: Institute of Vehicles and Construction Machinery
Warsaw University of Technology
Narbutta 84, 02-524 Warsaw, Poland
Lech.Knap@pw.edu.edu, http://www.simr.pw.edu.pl

2: Institute of Fundamental Technological Research
Polish Academy of Sciences
Pawinskiego 5B, 02-106 Warsaw, Poland
{aswiercz, cgraczyk, holnicki}@ippt.pan.pl, http://www.ippt.pan.pl

Abstract *In this contribution, the authors propose a concept of novel type of an ultra-light helium-filled aerostat. The internal construction of the proposed aerostat is based on a self-deployable tensegrity structure equipped with prestressed tensioned elements of controllable lengths. Such construction enables convenient transportation of the aerostat and its fast deployment at the required operational point at the atmosphere. The controllable tensegrity structure can be used for simultaneous changes of the aerostat volume and external shape during the flight. This enables modification of buoyancy and drag forces and obtaining a desired vertical and horizontal motion as well as a desired flight path. The authors propose a method of numerical modelling of self-deployable helium-filled aerostats based on the finite element method as well as CFD and FSI models presenting behaviour of aerostat during typical operational conditions. The presented results show the interaction of the internal tensegrity structure and aerostat envelope and positively verify the feasibility of the proposed concept of tensegrity-based aerostats.*

Keywords: tensegrity structure, internal construction, helium-filled aerostat, numerical modelling

Lech Knap, Andrzej Świercz, Cezary Graczykowski, Jan Holnicki-Szulc

1. INTRODUCTION

Airships and balloons were the first vehicles built by men but for many years their applications have been very limited due to intensive development of aviation. Specified military application of airships included reconnaissance missions, combat of submarines and ocean surveillance [1-2], while the attempts of their civil use were interrupted for many years by well-known crash of the Hindenburg airship in 1937 [3]. However, recent technological changes have caused renaissance of airship applications. At the beginning of the century many new-generation helium-filled airships with the ability to undertake long-term and low-energy flights have been constructed and initially used for low-cost missions aimed at exploration of stratosphere and mesosphere [4-6]. Currently constructed airships provide telecommunication systems in rarely populated areas, serve as remote monitoring or surveillance systems and research pseudo-satellites [7-10]. The most well-known examples of airships are Zephyr S [11], Russian concept Berkut [12], Lockheed Martin's ISIS [13] and French Stratobus [14].

Significant effort in the design of airships is focused on the reduction of the self-weight, which largely influences the load capacity and the possibility of carrying payloads. The first technological challenge in construction of airships is development of ultra-light envelopes of thickness of several micrometers, which are helium-tight and maintain elastic properties at wide range of temperatures [15]. The second important technological problem is design of skeletal structure which supports airship envelope and provides its appropriate shape and resistance to aerodynamic forces. The related challenge is designing connections of the internal skeletal structure and airship envelope and attachment of the cargo to this fragile structure.

In this paper the authors propose construction of the aerostat based on deployable tensegrity structure equipped with elements of controllable lengths. Such construction enables convenient transport of the aerostat with the use of a balloon or an aircraft to the operational altitude and its automatic deployment at certain location at the atmosphere. The tensegrity structure provides very low mass of the aerostat, adequate strength to support the aerostat envelope during strong wind gusts and possibility of transferring point loads resulting from carried cargo. On the other hand, application of tensegrity structure equipped with controllable elements enables convenient change of the aerostat volume and shape during the flight. The change of volume is used to control the actual buoyancy force and resulting vertical motion of the aerostat ("V-mobility"). In turn, the change of aerostat shape can be used for changing the influence of lateral wind gusts or controlling horizontal stability or positioning during the mission ("H-stability").

The paper is organized as follows. The second section describes general construction of aerostats based on the tensegrity structures and details of the proposed design. The third section shows FEM-based strength analysis of the aerostat including distributions of internal forces caused by pressure differences. The fourth section presents CFD analysis of the flow around aerostat and simplified FSI analysis revealing an interaction of the flow and the tensegrity-supported aerostat envelope. Finally, the fifth section concludes the conducted research.

2. CONSTRUCTION OF TENSEGRITY-BASED AEROSTATS

The simplest proposed tensegrity-based aerostat utilizes skeletal structure in the form of tensegrity prism which is composed of three struts and nine tendons (Fig.1a). While the selected nodes (1a) of the tensegrity structure are permanently integrated with the aerostat envelope, the

Lech Knap, Andrzej Świercz, Cezary Graczykowski, Jan Holnicki-Szulc

other nodes (1b) are linked in slidable fashion to avoid excessive internal forces in both substructures. In considered case three vertical tendons (denoted as (1e), green-coloured) are highly elastic, while the length of three horizontal stiff tendons (denoted as (1e), blue-coloured) can be controlled. The proposed structure is distinguished from the classic tensegrity structure by highly elastic tendons (1e) with a much lower Young's modulus than Young's modulus for the other elements. A structural stability of the structure is ensured by the red-coloured bars (1d). The aerostat based on such a tensegrity structure can be cylindrical-shaped with two hemispheres located at the lateral sides (Fig.1b). Symmetric shortening of the stiff tendons of controllable lengths implies change of the radius along the cylinder, decease of volume of the aerostat and causes that its shape becomes slender. In turn, asymmetric shortening of the tendons causes asymmetric deformation of the aerostat and changes it resistance to winds in axial direction.
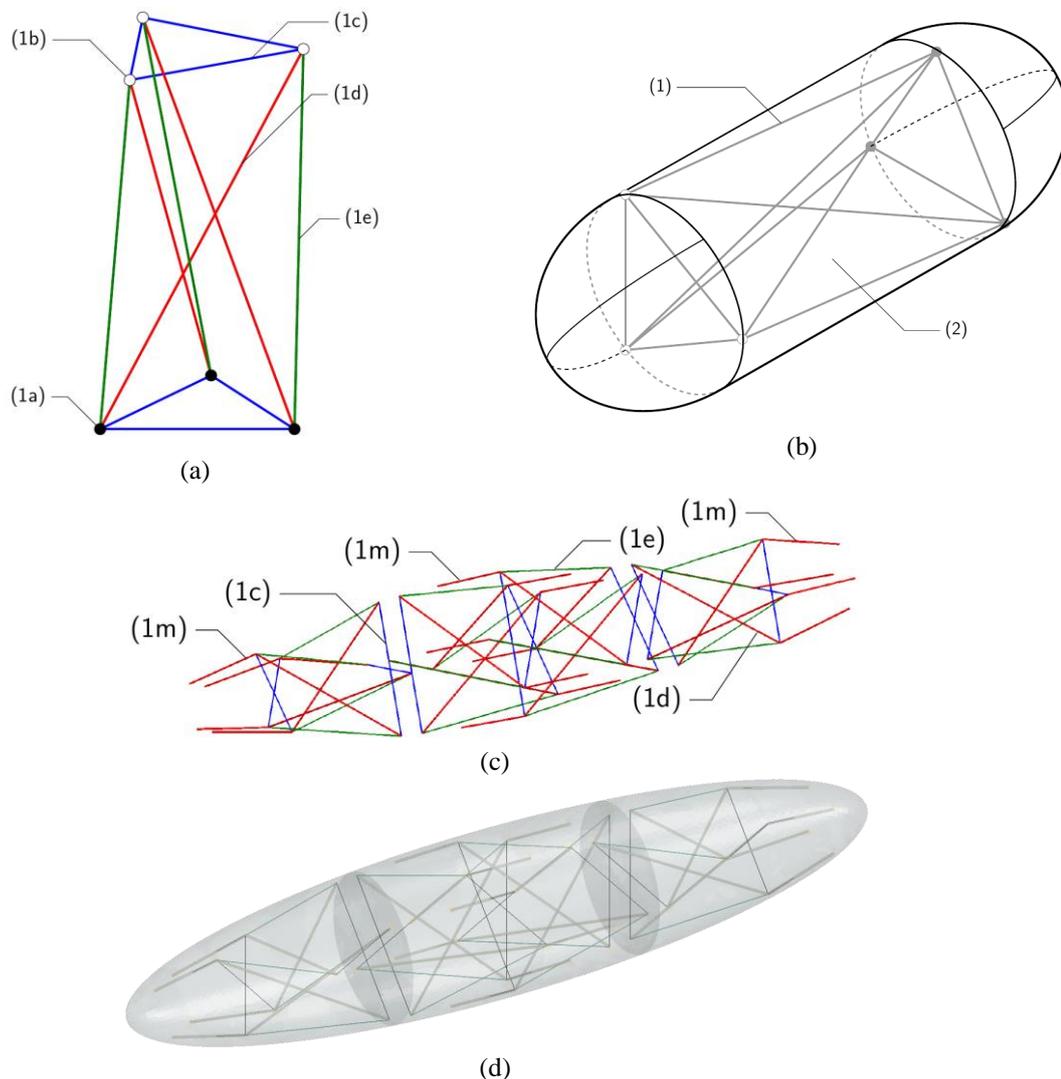
Figure 1. (a) A single module of foldable tensegrity structure; (b) a single-chambered tensegrity-based aerostat; (c) a four-module tensegrity structure; (d) a tree-chamber aerostat with four modules of tensegrity structure.

Lech Knap, Andrzej Świercz, Cezary Graczykowski, Jan Holnicki-Szulc

The more complex tensegrity-based ellipsoid-shaped aerostat, considered in further part of this paper is composed of four modules of tensegrity structure. Each unit is based on two squares rotated by 45 degrees (Fig.1c-d). Contrary to the previous case, stiff tendons (1c) are arranged into crosses instead of peripherally. The struts, highly elastic and controllable tendons are shown in Fig.1c. Additionally, the set of movable joints of each unit tensegrity structure is slidingly connected to guide rails (1m) which are bounded to the aerostat envelope.

In this case the shape of the aerostat is based on ellipsoid with a circular cross-section in the vertical plane. The considered aerostat is 10 metres long and 2 m wide and it is divided into three chambers with the use of two internal diaphragms. Similarly, as in the case of single-chambered aerostat, the shortening of the tendons causes decrease of aerostat radius and reduction of its volume. Nevertheless, the application of four modules of the tensegrity structure provides wide possibilities of change of the aerostat shape (two modules are placed in the middle chamber). In the proposed solution, shape of the arbitrary section of the aerostat can be significantly modified, which causes that aerostat can be precisely adjusted to wind gusts in both axial and lateral directions (the process of "adaptive morphing").

The above process of changing the length of tendons can be efficiently conducted using controllable retractors, such as rotary electric motors or linear actuators, serving for contraction or elongation of stiff tendons (1c). Let us note that shortening of tendons of tensegrity structure leads to substantial redistribution of internal forces in the entire tensegrity structure and affects deformations and stresses generated in the aerostat envelope.

3. STRENGTH ANALYSIS OF TENSEGRITY-BASED AEROSTAT

This section presents the results of FEM-based strength analysis aimed at finding distributions of internal forces in skeletal structure and envelope of the aerostat caused by pressure differences at various altitudes. A numerical model of the aerostat presented in Fig.1d was created using Abaqus package. The mesh of the envelope and nodes of the tensegrity structure are illustrated in Fig.2.
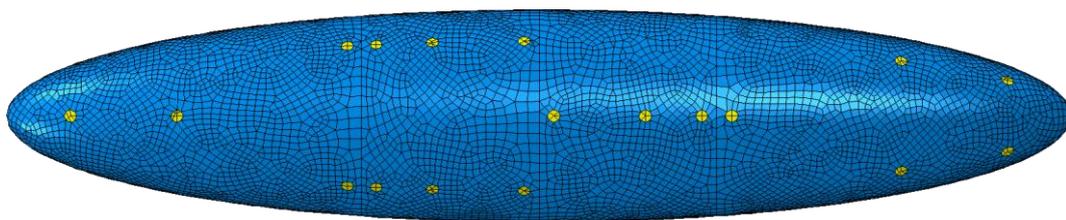
Figure 2. A numerical model of a three-chamber aerostat with four internal modules of tensegrity structure.

The envelope and diaphragms are modelled by means of 3-node and 4-node membrane finite elements. However, in the locations of connection with non-movable tensegrity joints and guide rails, the stiffening plates (yellow-coloured in Fig.2) are applied and modelled by shell finite elements. The internal structure is modelled by truss elements (highly elastic tendons), beam elements (bars and guide rails) and connectors (stiff tendons, retractors and sliding connections). The connector element-type is applied to define interaction between two points and it is useful for control of tendon lengths by means of retractors. The total number of finite

Lech Knap, Andrzej Świercz, Cezary Graczykowski, Jan Holnicki-Szulc

elements in the model is equal to 13 811. For computations, the following material data was assumed:

- envelope and diaphragms: thickness 50 µm, density 1390 kg/m^3 and Young's modulus 0.43 GPa;
- bars, guide rails (both pipe cross-section, diameter of 12 mm and thickness of 1 mm) and stiffening plates (thickness of 1 mm) are made of carbon fibre with density of 1580 kg/m^3 and Young modulus of 87.0 GPa;
- highly elastic tendons (rubber-like material): circular cross-section with diameter of 3.6mm, density of 900 kg/m^3 and Young modulus of 0.05 GPa;
- stiff tendons: circular cross-section with diameter of 3 mm, density of 7850 kg/m^3 and Young's modulus of 210 GPa.

The total mass of the aerostat (including payload) is equal to 15.172 kg. A structural strength assessment of the aerostat was performed for three altitudes: h_2=5 km, h_1=3.725 km and h_s=2 km. Firstly, to reach the altitude of h_2, helium mass of 2.537 kg was inflated into the aerostat. Then, aerostat was partially deflated and helium was compressed in an additional tank (of 0.095 kg to lower the altitude). Finally, all stiff tendons were uniformly shortened to achieve the altitude of h_s=2 km. Outer atmospheric pressure in the numerical model is applied outwardly to the aerostat envelope and linearly varies from ground level to the target altitude. The quasi-static calculations were based on NASA's atmosphere model available on the web site https://www.grc.nasa.gov/www/K-12/airplane/atmosmet.html.

(a)

(b)

(c)
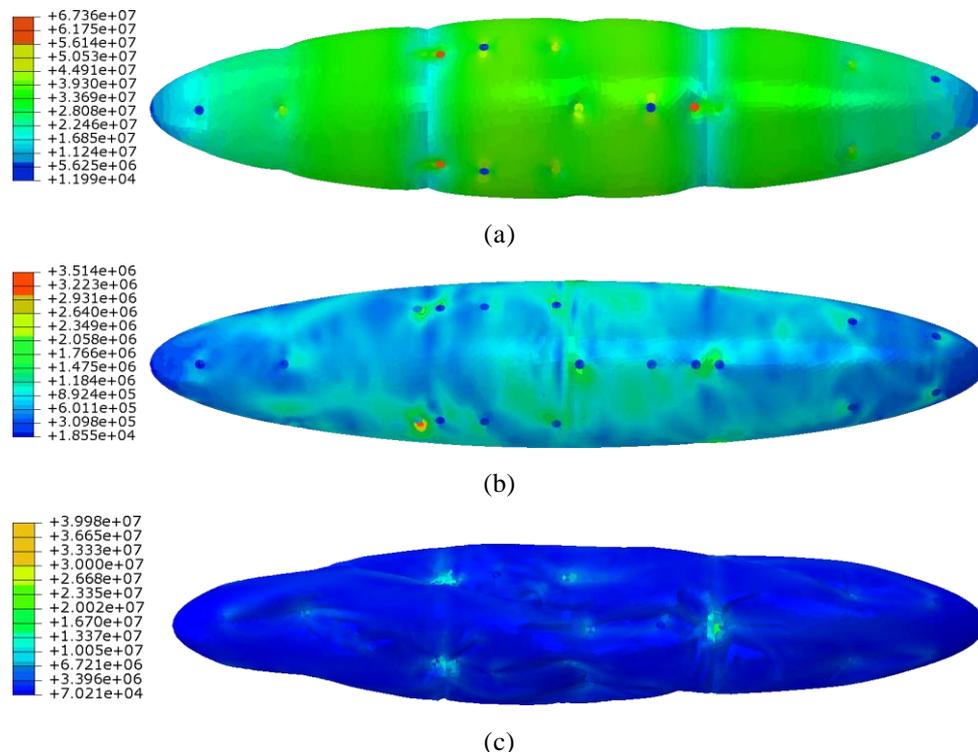
Figure 3. The equivalent von Misses stresses in the envelope at altitude of (a) h_2=5 km, (b) h_1=3.725 km and (c) h_s=2 km.

Lech Knap, Andrzej Świercz, Cezary Graczykowski, Jan Holnicki-Szulc

The obtained results are presented in Fig.3 and Fig.4. In Fig.3 equivalent Mises stresses in the envelope computed for the aforementioned altitudes are presented. The highest level of the equivalent Mises stresses is reached for the altitude of h_2=5 km – about 50MPa in the membrane and 67MPa in the stiffening plates. While the aerostat descents to the altitude h_1=3.725 km (as a results of partial helium compressing), the equivalent Mises stresses are also decreasing. When the aerostat continues its descent by shortening tendons, the stresses level in the bar members sharply increases to 240 MPa , as illustrated in Fig.4 (longitudinal stresses), but they do not exceed the yield stresses limit.

(a)

(b)

(c)
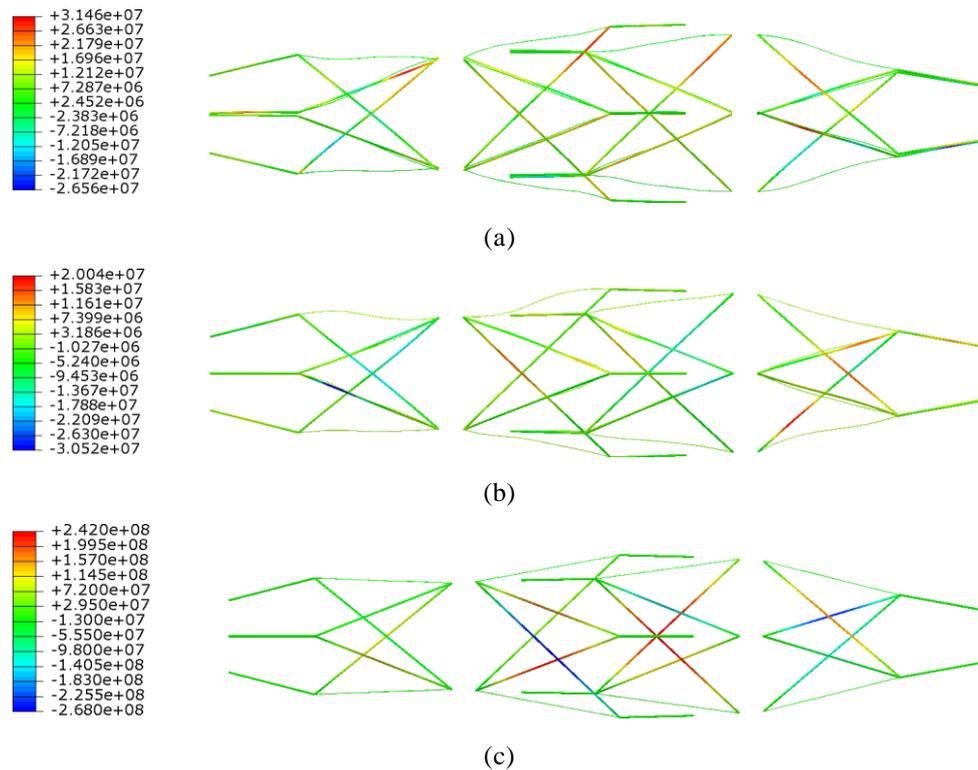
Figure 4. Longitudinal stresses in tensegrity structure elements at altitude of (a) h_2=5 km, (b) h_1=3.725 km, (c) h_s=2 km.

4. CFD AND FSI ANALYSIS OF TENSEGRITY-BASED AEROSTAT

The section presents CFD analysis of the flow around aerostat in vertical and horizontal direction as well as simplified FSI analysis revealing interaction of the vertical flow and envelope of the aerostat supported by the tensegrity structure.

4.1. CFD analysis

The simulations of the flow around the aerostat were aimed at determination of the flow profiles, computation of pressures exerted at certain points of aerostat envelope and calculation of total forces exerted on the aerostat. The analysis was conducted using ANSYS Fluent and was performed for both lateral and axial direction of the flow (Fig.5a-b and Fig.5c-d, respectively). The results of the conducted analyses were used to determine change of the drag

Lech Knap, Andrzej Świercz, Cezary Graczykowski, Jan Holnicki-Szulc
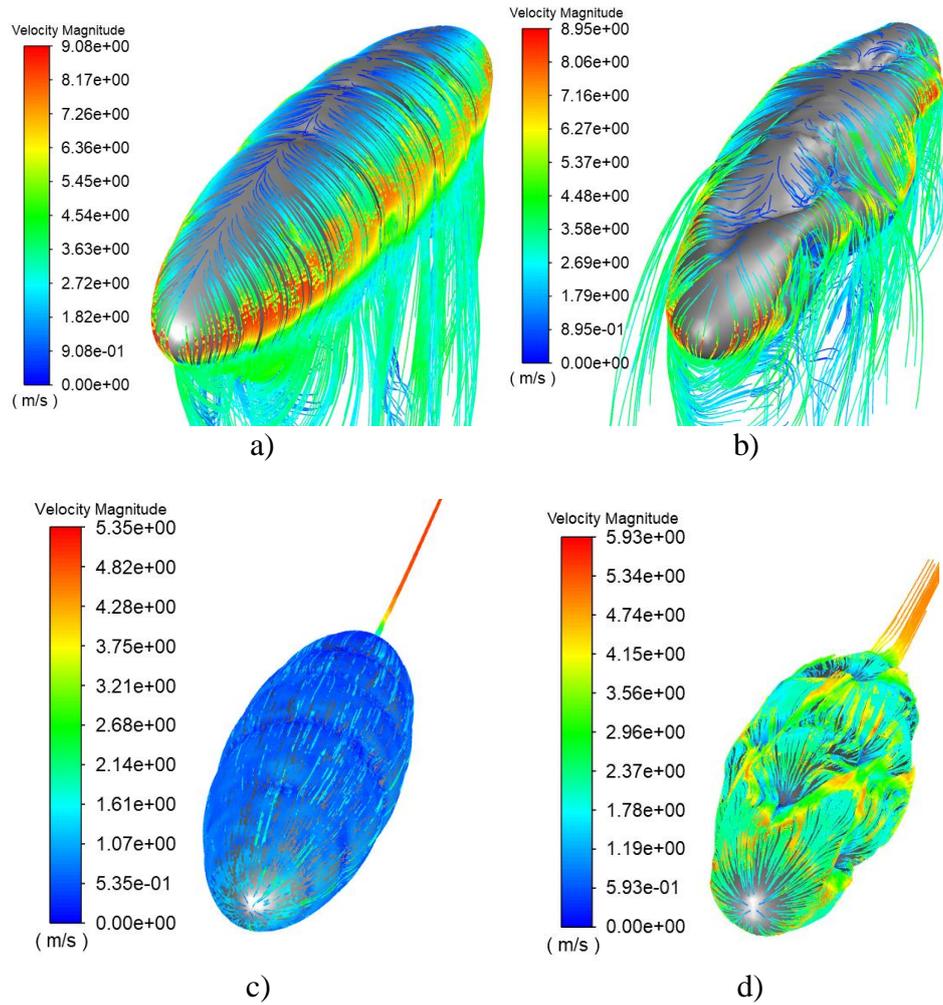
Figure 5. Pathlines of the air flows computed for the vertical and horizontal aerostat velocity of: 5 m/s and altitude a) and c) h_2 , b) and d) h_s.
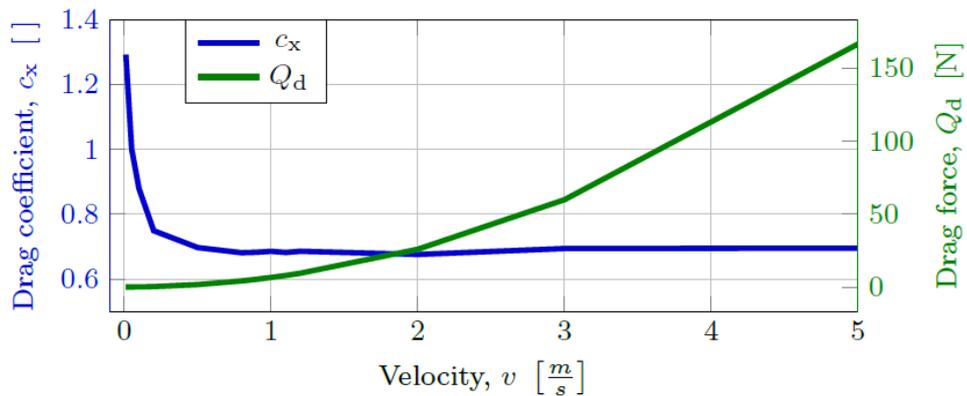
Figure 6. Example of numerically determined dependencies of the drag coefficient c_x and the drag force Q_d for vertical velocities at the altitude h_2

force Q_d and drag coefficient c_x in terms of velocity of the flow (Fig.6). In Fig.7 we have shown change of coefficient c_x for various forms of the aerostat, which depend on the applied method of control. The particular forms correspond to: form 1 - aerostat maximally inflated with helium, form 2 - nominal volume V_0, form 3 - shortening of tendons (3a - in all chambers, 3b - in the middle chamber, 3c - in the outermost chambers). The change of drag coefficient corresponding to lateral flow was further used in analytical model of vertical motion of the aerostat. In turn, the change of drag coefficient corresponding to axial flow was further used in a model of horizontal motion of the aerostat.
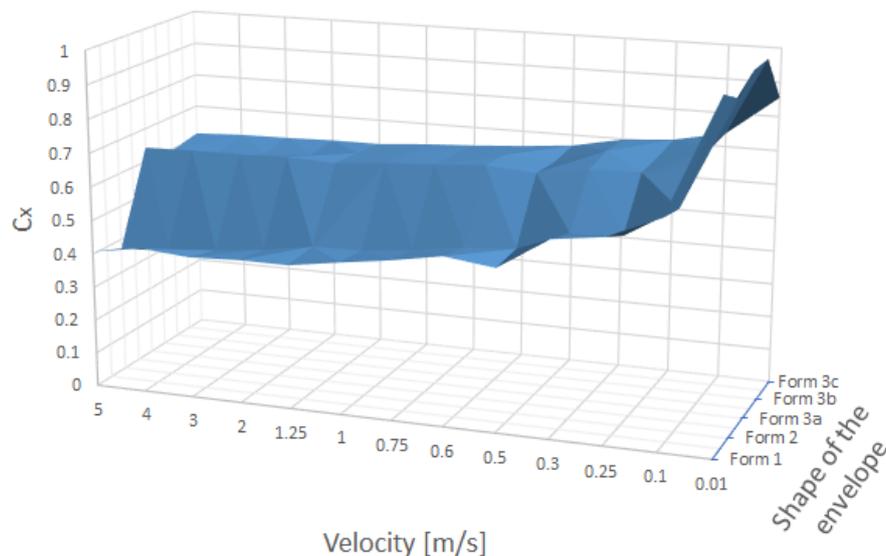
Figure 7. Numerically determined dependence of the coefficient c_x on vertical velocity for different forms of the aerostat

4.2. FSI analysis

The presented study is focused on investigation of the interaction of tensegrity structure and envelope of helium-filled aerostat so the air flow analysis is limited to steady-state conditions. The cases considered in this subsection are focused on the air flow with two speeds applied in the Z-direction (V-mobility). In the first case, the wind velocity increases up to 1.2 m/s (mean velocity during ascend of the aerostat) whereas in the second scenario the air speed reaches 5 m/s (an excessive air flow). In both cases, after time $t_0=2.5s$ the air velocities remain constant. The assumed air density corresponds to the air at ground level, i.e. $\rho_a=1.225$ kg/m^3.

A computational domain has dimensions: 80 m (Z-direction) by 30 m, (Y-direction) by 14 m (X-direction) and is presented in Fig.8a, whereas the air speed loads are shown in Fig.8b. The velocity boundary condition is applied to the top surface of the cuboid domain. On the bottom surface, the air pressure is expected to be zero and air flows by sidewalls of the computational domain are not permitted. The distances between aerostat semi-axes and computational domain boundary are equal: 10 m (to the top surface along Z-direction), 7 m (along X-direction) and 15 m (Y-direction).

Lech Knap, Andrzej Świercz, Cezary Graczykowski, Jan Holnicki-Szulc

The response of the aerostat is computed utilizing coupled Eulerian-Lagrangian technique with uniform mass scaling applied to the aerostat structure (Lagrangian domain). An air flow (Eulerian domain) interacts with the aerostat membrane by means of defined Eulerian-Lagrangian contact. Due to applied mass scaling, the natural time scale of this dynamic process is perturbated. This, however, can be neglected since only the steady-state deformation of the aerostat, obtained after sufficiently long time of exposure to the gust load, has to be considered.

(a)   (b)
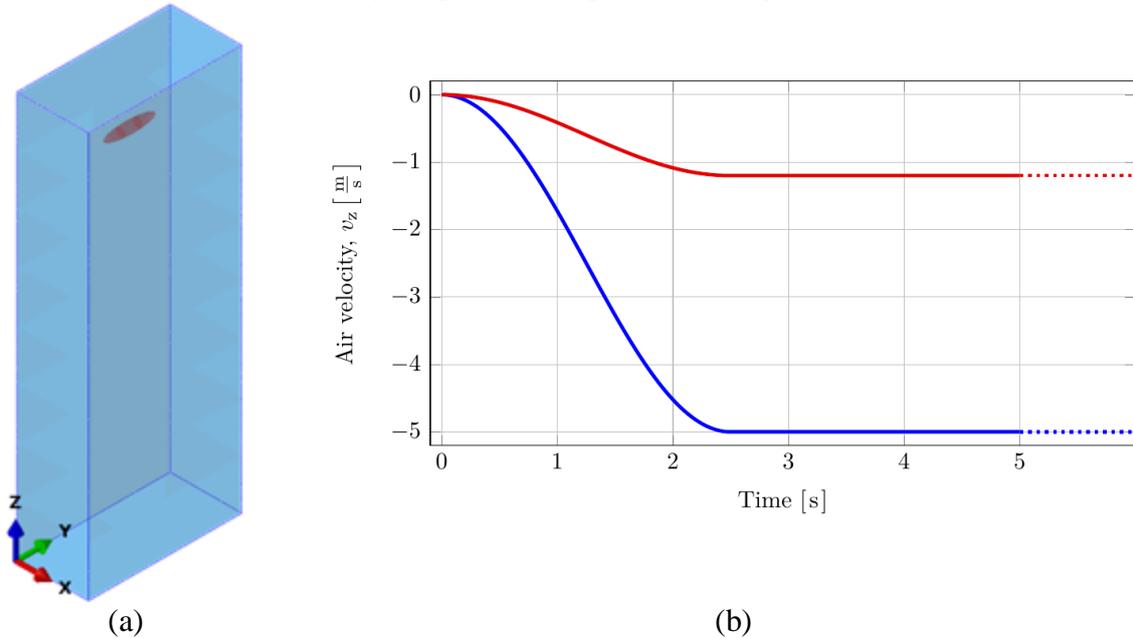
Figure 8. (a) Computational domain with the initial configuration of the aerostat, (b) velocity functions applied for the air gust loads.

(a)   (b)
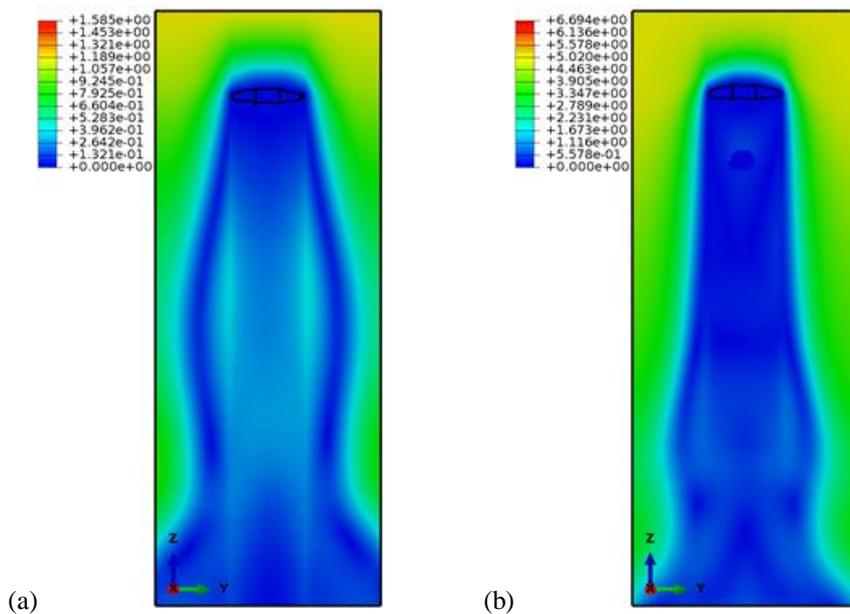
Figure 9. Velocity contour plot of the air flow subjected to air wind load: (a) 1 m/s, (b) 5m/s.

Lech Knap, Andrzej Świercz, Cezary Graczykowski, Jan Holnicki-Szulc

The aerostat membrane deformation and equivalent von Mises stresses computed for the wind speed 5m/s are shown in Fig.10a. The obtained numerical results show that the mean value of helium pressures reach 20 Pa and 400 Pa in middle chamber and lateral chambers, respectively. The equivalent von Mises stresses locally reach significant values only in stiffening plates (see Fig.10a) and the supporting structure (see Fig.10b). However, they do not exceed tensile strength for carbon fibre which is above 1 GPa. Moreover, the aerostat shape becomes one-side slightly curved. This modified aerostat shape also has influence for the air flow, which is illustrated in Fig.9 for both wind load cases.
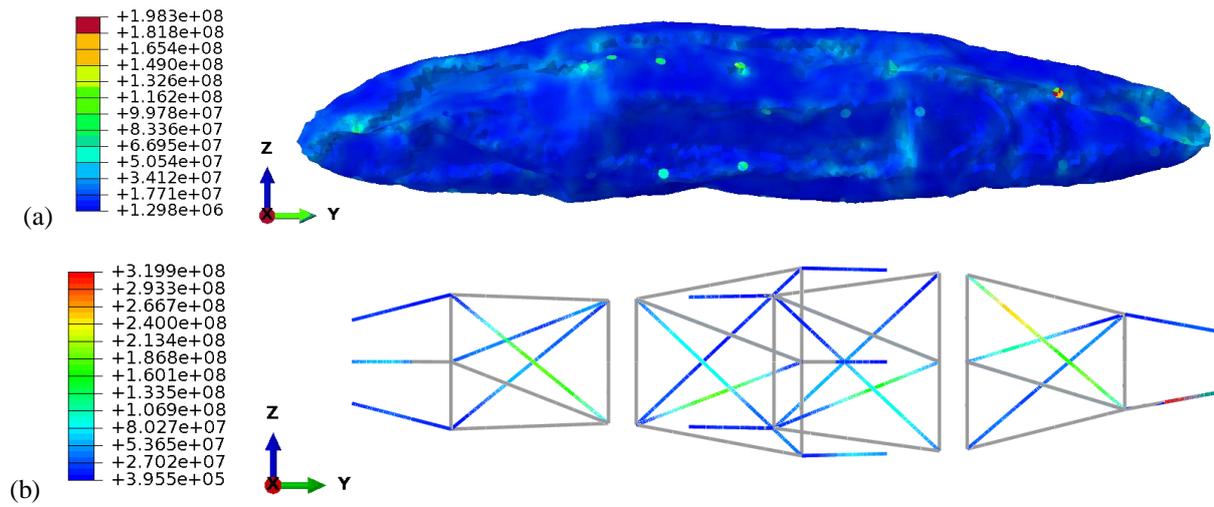
Figure 10. Equivalent von Mises stresses (Pa) in the aerostat membrane (a) and supporting structure (b) caused by the air wind loads with the speed of 5 m/s.

5. CONCLUSIONS

The conducted numerical simulations prove the feasibility of the proposed concept of tensegrity based aerostat. In particular, the strength analysis has shown low values of stresses generated in aerostat envelope and skeletal structure as a result of pressure difference during quasi-static process of aerostat vertical movement. The stresses generated as a result of shortening of the active tendons of tensegrity structure appeared to be significantly larger, but below the strength limit of the applied material. This indicates that control of the aerostat shape and resulting control of its motion can be successfully executed by the proposed methods of tendons shortening. Moreover, the conducted CFD and FSI analyses have shown large values of stresses generated in carbon fiber bars of the tensegrity structure under the wind flow. This indicates that for larger aerostats further optimization of topology and mechanical properties of the applied tensegrity structures is required and have to be developed in the next stage of the conducted research.

Lech Knap, Andrzej Świercz, Cezary Graczykowski, Jan Holnicki-Szulc

ACKNOWLEDGMENTS

REFERENCES

[1] Brayan T, Rava G., British airships 1905-1930, Osprey Publishing, New York, 2009.

[2] Ege L. Baloons and Airships. Blandford Press, London, 1974.

[3] Freedman A. Zeppelin Fictions and the British Home Front, Journal of Modern Literature, Vol. 27, No. 3, Writing Life/Writing Fiction, pp. 47-62, Winter, 2004.

[4] Ghanmi A., Sokri A., Airships for military logistics heavy lift, Defence R&D Canada.

[5] Centre for Operational Research and Analysis, DRDC CORA TM 2010-011, 2010.

[6] Future Aerostat and Airship Investment Decisions Drive Oversight and Coordination Needs, Report to the Subcommittee on Emerging Threats and Capabilities, Committee on Armed Services, U.S. Senate, GAO, 2012.

[7] Saleh S., Weiliang HE., New design simulation for a high-altitude dual-balloon system to extend lifetime and improve floating performance, Chinese Journal of Aeronautics, Vol 31, No 5, pp. 1109-1118, 2018.

[8] Araripe d'Oliveira F., Lourenço de Melo F. C., Devezas T. C. High-Altitude Platforms – Present Situation and Technology Trends, J. Aerosp. Technol. Manag., São José dos Campos, Vol.8, No 3, pp.249-262, 2016.

[9] Lee M, Smith S, Androulakakis S (2009) The high altitude lighter-than-air airship efforts at the US Army Space and Missile Defense Command/Army Forces Strategic Command. Proceedings of the 18th AIAA Lighter-Than-Air Systems Technology Conference; Seatle, USA.

[10] K. Eguchi, Y. Yokomaku and M. Mori, "Overview of Stratospheric Platform Airship R&D Program in Japan", in AIAA 14th LTA TCCE, Acron, OH, July 2000.

[11] Airbus, Zephyr S set to break aircraft world endurance record [accessed 30 Jun 2021], https://www.airbus.com/newsroom/press-releases/en/2018/07/Zephyr-S-set-to-break-aircraft-world-endurance-record.html.

[12] Augur RosAeroSystems, High Altitude Airship "Berkut"; [accessed 30 Jun 2021], http://rosaerosystems.com/projects/obj687.

[13] ElectronicsWeekly.Com Airship set to become the ultimate eye in the sky; [accessed 30 Jun 2021], https://www.electronicsweekly.com/news/business/information-technology/airship-set-to-become-the-ultimate-eye-in-the-sky-2011-08

[14] Tales, What's up with Stratobus? [accessed 30 Jun 2021], https://www.thalesgroup.com/en/worldwide/space/news/whats-stratobus

[15] Mizuta E., Akita D., Fuke H., et al, Development of a 2,5 um Plyethylene Film for the Hihgh Altitude Ballon, Trans JSASS Space tech Japan, Vol 7, No 26, 2009.

ADAPTIVE MORPHING OF TENSEGRITY-BASED HELIUM-FILLED AEROSTATS

Lech Knap[1], Andrzej Świercz[2*], Cezary Graczykowski[2], Jan Holnicki-Szulc[2]

1: Institute of Vehicles and Construction Machinery
Warsaw University of Technology
Narbutta 84, 02-524 Warsaw, Poland
Lech.Knap@pw.edu.pl, http://www.simr.pw.edu.pl

2: Institute of Fundamental Technological Research
Polish Academy of Sciences
Pawinskiego 5B, 02-106 Warsaw, Poland
{aswiercz, cgraczyk, holnicki}@ ippt.pan.pl, http://www.ippt.pan.pl

Abstract *In this contribution the authors propose and investigate the concept of adaptive morphing for recently introduced tensegrity-based helium-filled aerostats. The proposed aerostat is based on an ultra-light tensegrity structure equipped with prestressed tensioned elements of controllable lengths. Such internal structure allows for adaptive morphing of the aerostat defined as simultaneous controllable modifications of aerostat volume and external shape during the flight. The controlled volume changes enable influencing buoyancy forces acting on the envelope and obtaining desired vertical motion of the aerostat during the ascending and descending process ("vertical mobility"). In turn, the controlled changes of external shape of the aerostat can be used either for lowering the aerodynamic drag forces and reducing energy usage needed to maintain stable horizontal position or to follow the desired path of aerostat horizontal motion ("horizontal stability"). The authors effectively apply the previously introduced mechanical FEM model of the tensegrity-based aerostat and dynamic model of the aerostat's vertical and horizontal motion to conduct simulations of the process of adaptive morphing and maintain a proper position in the atmosphere. The obtained results positively verify the idea of adaptive morphing and its efficiency in controlling vertical and horizontal motion of the aerostat.*

Keywords: tensegrity structure, helium-filled aerostat, adaptive morphing, vertical mobility, horizontal stability

Lech Knap, Andrzej Swiercz, Cezary Graczykowski, Jan Holnicki-Szulc

1. INTRODUCTION

The airships and balloons were the first vehicles built by men and although their use was originally widespread, they have been superseded for many years by aircrafts. In recent years it has been observed a renewed interest in aerostats, mainly due to their ability to carry out long missions at much lower costs than aircrafts [1]. Currently constructed airships successfully fulfil various purposes, e.g. provide communication in hardly reachable areas (including ensuring the possibility of using 4G / 5G technology), serve as reconnaissance and surveillance systems, military communication centres or research pseudo-satellites [2]. For example, stratospheric airships offer adequate operational flexibility, which allow to provide locally broadband telecommunications and connectivity in areas of natural disasters or areas with a low level of ground infrastructure in much faster and easier way [3]. Simultaneously, the total costs (mainly consisting of fuel and service) for cargo transport or for exploration of stratosphere, mesosphere – and even space observation – are much lower than in case of using airplanes or satellites [1,4-5].

Although air vehicles are more and more used, their wider application is still limited by a number of design problems. These mainly include adequate structural strength, which must be ensured at the lowest possible weight. Increase of the structure self-weight causes that the possible payload diminishes. Therefore, the significant effort in design and construction of the airships is oriented towards reduction of the self-weight by reducing mass of internal structure and mass of the envelope. The main technological challenge is to develop ultra-light envelopes (range 2.8-24 μm), which are impermeable to helium, resistant to UV radiation and maintain elastic properties at temperatures reaching -70°C [6-7]. The problem is to ensure that the internal structure is sufficiently stiff to provide the adequate shape and volume necessary for the airship to fly with a designed payload and under the load exerted by the wind flow.

Currently, many research works are devoted to solving problem of predicting the movement of airships in both the vertical and the horizontal direction [8-9], as well as to analyse the changes in volume resulting from heating of the envelope by the sun and heat exchange with the environment [10-11].

In this article the authors propose and investigate the concept of adaptive morphing for recently introduced tensegrity-based helium-filled aerostats. The proposed aerostat is based on an ultra-light tensegrity structure equipped with prestressed tensioned elements of controllable lengths. Such internal structure allows for adaptive morphing of the aerostat defined as simultaneous controllable modifications of aerostat volume and external shape during the flight. The controlled volume changes enable influencing buoyancy forces acting on the envelope and obtaining desired vertical motion of the aerostat during the ascending and descending process ("vertical mobility"). Additionally, the controlled changes of the altitude can be used to maintain horizontal position in appropriate weather conditions.

The proposed internal structure of the aerostat is based on the use of tensegrity type construction. Such a construction allows to obtain a relatively low mass of the internal structure but also provides adequate strength of the aerostat. An additional advantage of such a structure is the possibility to control its selected elements (e.g. shortening of tendons or elongation of struts), which enables to obtain various shapes of the envelope stretched on the structure. In this way it is possible to control the aerostat balloon volume within a certain range. With an appropriate configuration of the tensegrity structure, the aerostat can be assembled and transported using different means of transport e.g., a rocket or an aircraft. In this way the adaptive aerostat can be delivered quickly to a chosen point of the atmosphere and disassembled.

Lech Knap, Andrzej Swiercz, Cezary Graczykowski, Jan Holnicki-Szulc

2. CONCEPT OF THE ADAPTIVE AEROSTAT

An example of application of supporting lightweight truss structure with modifiable lengths of selected members used to reinforce the helium-filled aerostat is demonstrated in a simplified form in Fig.1. For the clarity of the presented approach, the further discussed vertical mobility problem is presented using 2D model.
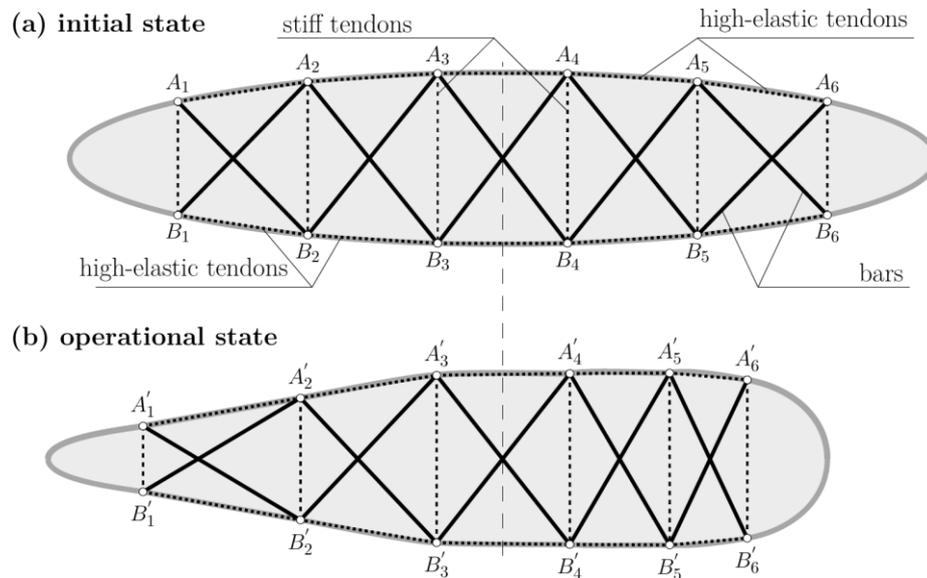
Figure 1. Aerostat reinforced by the lightweight truss supporting structure: (a) initial state with designed element lengths; (b) operational state – after possible modification of controllable members lengths.

The internal truss structure is composed of 5 sections and each section consists of 3 types of elements: rigid bars (diagonal members), high-elastic tendons (top and bottom members) and stiff tendons (vertical members). The nodal points of the initial supporting structure are denoted by A_i (top members) and B_i (bottom members), see Fig.1a. Lengths modifications are introduced by a set of controllable actuators (electric motors) installed on stiff tendons. Assuming the possibility of elongation and shortening of those members (stiff tendons), the aerostat volume and shape modifications are available. In Fig.1b, the nodal points of the supporting structure in an operational configuration are denoted by A'_i and B'_i. However, in the full 3D configuration the lengths modifications of vertical members affect the aerostat volume with the square exponent, while modifications of the horizontal ones affect it only linearly. The modifications of the aerostat shape can be used for volume corrections which affect the vertical and horizontal mobility (V-Mobility, H-stability).

3. MATHEMATICAL MODEL OF AEROSTAT MOTION

The numerical analyses presented in this paper consist of two parts. In the first part, we consider the motion of the aerostat and methods of controlling vertical and horizontal motion without the use of propulsion (horizontal motion of the aerostat under the influence of wind). For this purpose, a numerical model of the aerostat has been built to study the aerostat control and kinematics under atmospheric conditions (pressure, air density, temperature, gravity, wind direction and wind speed). The atmospheric conditions were approximated by an atmospheric

Lech Knap, Andrzej Swiercz, Cezary Graczykowski, Jan Holnicki-Szulc

model according to NASA[i]. The data concerning wind directions and speeds at various altitudes were taken from FlyMeteo[ii] and are shown in Fig.2 in two views. The first view (Fig.2a) uses dual axes (one for wind speed, another one for wind direction), whereas the second view (Fig.2b) is oriented according to the directions of the World. Each pair of measurement data is aligned along the radial direction. An exemplary data for the highest altitude (about 16 km) is highlighted by the line *A–A'*.
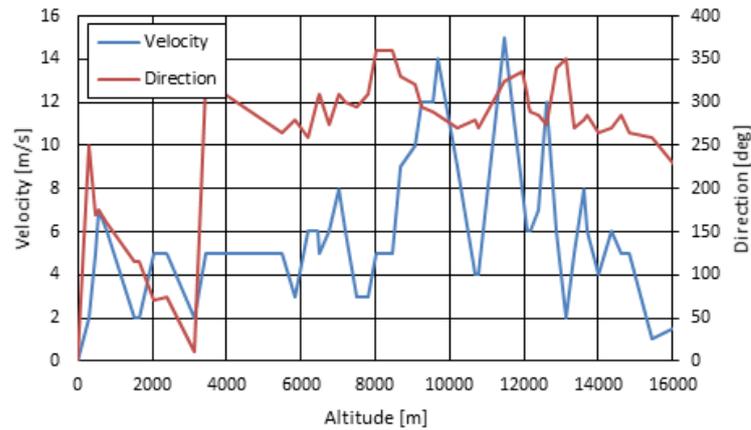
(a) Atmospheric data in the linear view.
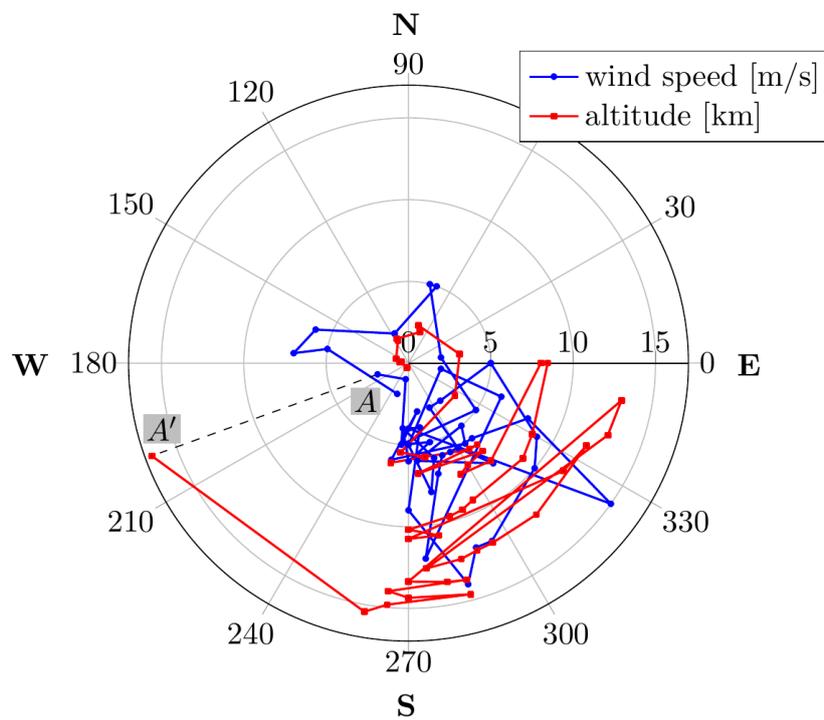
(b) Atmospheric data in the polar view.

Figure 2. Distribution of wind speed and direction for a sample location Praha-Libus (Czech Republic).

---

[i] Glenn Research Center. Earth Atmosphere Model Metric Units, (accesed on 21 June, 2021) https://www.grc.nasa.gov/www/K-12/airplane/atmosmet.html.

[ii] FlyMeteo, Wieter Pilot (accessed on 21 June, 2021), https://flymeteo.org/sounding/diag_p.php?p10&index=11520&termin=2021_06_20_00.

Lech Knap, Andrzej Swiercz, Cezary Graczykowski, Jan Holnicki-Szulc

The motion of the aerostat in the atmosphere is described by the following system of equations:

$$m_t \frac{d^2 x}{dt^2} = -Q_{dh} \cos \alpha \qquad (1)$$

$$m_t \frac{d^2 y}{dt^2} = -Q_{dh} \sin \alpha \qquad (2)$$

$$m_t \frac{d^2 h}{dt^2} = -Q_g + Q_b - Q_{dv} \qquad (3)$$

where:

- x, y – spatial variables describing the movement of the aerostat in a horizontal plane (x – east, y – north),
- h – a spatial variable describing the movement of the aerostat in a vertical direction,
- α – an angle between the aerodynamic force exerted on the aerostat and the direction related with spatial variable x,
- m_t – total mass of the aerostat,
- Q_{dh} – aerodynamic force exerted by the wind in the horizontal direction,
- Q_{dv} – aerodynamic drag force in the vertical direction,
- Q_b – buoyancy force of the aerostat,
- Q_g – aerostat weight.

Mentioned above forces are determined as follows:
- the weight of the aerostat:

$$Q_g(h) = m_t g(h) \qquad (4)$$

where: $g(h)$ describes the value of the gravity in function of the altitude h,

- the buoyancy force of the aerostat:

$$Q_b(m_h, \varepsilon_t, h) = \rho_a(h) \, g(h) V(m_h, \varepsilon_t, h) \qquad (5)$$

where: $\rho_a(h)$ describes the air density at the altitude h, while $V(m_h, \varepsilon_t, h)$ describes the balloon volume as a function of the helium mass m_h in the aerostat balloon and $\varepsilon_t = \frac{l_t - l_t^0}{l_t^t}$ denotes the elongation of the stiff tendons with the actual length l_t and the initial length l_t^0.

- the aerodynamic drag force in the vertical direction:

$$Q_{dv}(m_h, \varepsilon_t, h) = \text{sgn}(v_v) \, c_x(v_v, h) \, \rho_a(h) A_v(m_h, \varepsilon_t, h) \frac{v_v^2}{2} \qquad (6)$$

where: v_v denotes the vertical speed of the aerostat, $A_v(m_h, \varepsilon_t, h)$ is the cross-sectional area of the aerostat in the vertical direction, $c_x(v_v, h)$ is the drag coefficient in the vertical direction,

- the aerodynamic drag force in the horizontal direction:

$$Q_{dh}(m_h, \varepsilon_t, h) = sgn(v_h) \, c_x(v_h, h) \, \rho_a(h) A_h(m_h, \varepsilon_t, h) \frac{v_h^2}{2} \qquad (7)$$

Lech Knap, Andrzej Swiercz, Cezary Graczykowski, Jan Holnicki-Szulc

where: v_h denotes the horizontal speed of the aerostat, $A_h(m_h, \varepsilon_t, h)$ is the cross-sectional area of the aerostat in the horizontal direction, $c_x(v_v, h)$ is the drag coefficient in the horizontal direction.

In order to determine the value of the above forces it is necessary to know the volume occupied by the helium filling the aerostat balloon. The volume of helium depends on the mass of helium m_h inside the balloon, the properties of the envelope material and the atmospheric pressure outside the balloon.

In the case when the balloon volume V is smaller than the design value V_0 (with the balloon filled but without the imposing tensile stresses into the envelope), the pressure in the balloon p will be close to the atmospheric pressure p_a. If the balloon is fully inflated, the stretching of the balloon envelope has to be taken into account when determining the pressure value in the balloon. In addition, the control of the balloon volume below the volume V_0 can be conducted by changing the lengths of the tensegrity structure members (i.e. stiff tendons). Therefore, the volume V of the aerostat can be determined based on the system of equations:

$$V = \begin{cases} \dfrac{m_h R T_a(h)}{p_a(h)} & \text{for } V \le V_0 \text{ and } \varepsilon_t = 0 \\[2mm] \dfrac{V_0}{2k}\left(k - p_a(h) + \sqrt{\Delta}\right) & \text{for } V > V_0 \text{ and } \varepsilon_t = 0 \\[2mm] \hat{V}(\varepsilon_t, m_h, h) & \text{for } \varepsilon_t \ne 0 \end{cases} \tag{8}$$

The second relationship in Eq.(8) contains Δ which is a determinant of the equation:

$$\frac{k}{V_0}V^2 + (p_a - k)V - m_h R T_a = 0 \tag{9}$$

The above equation has one physical solution and results from the combination of the ideal gas law applied for helium inside the aerostat:

$$pV = m_h R T_a \tag{10}$$

and the equation defining the relationship between pressure p and the volume of the aerostat balloon V with the use of coefficient k defining elastic properties of the material of the aerostat envelope:

$$p - p_a(h) = k\left(\frac{V - V_0}{V_0}\right) \tag{11}$$

The value of the coefficient k can be determined numerically using simulation of the aerostat inflation based on Finite Element Method. Similarly, the relation between shortening of the tendons and volume of the aerostat can be obtained using corresponding FEM simulation of aerostat compression. The final dependence between mass of helium and aerostat volume, defined by Eq.8b, is presented in Fig.3a, whereas final dependence between tendons length reduction and aerostat volume, defined by Eq.8c, is shown in Fig.3b.

Lech Knap, Andrzej Swiercz, Cezary Graczykowski, Jan Holnicki-Szulc

(a) Volume controlled by helium mass

(b) Volume controlled by tendons
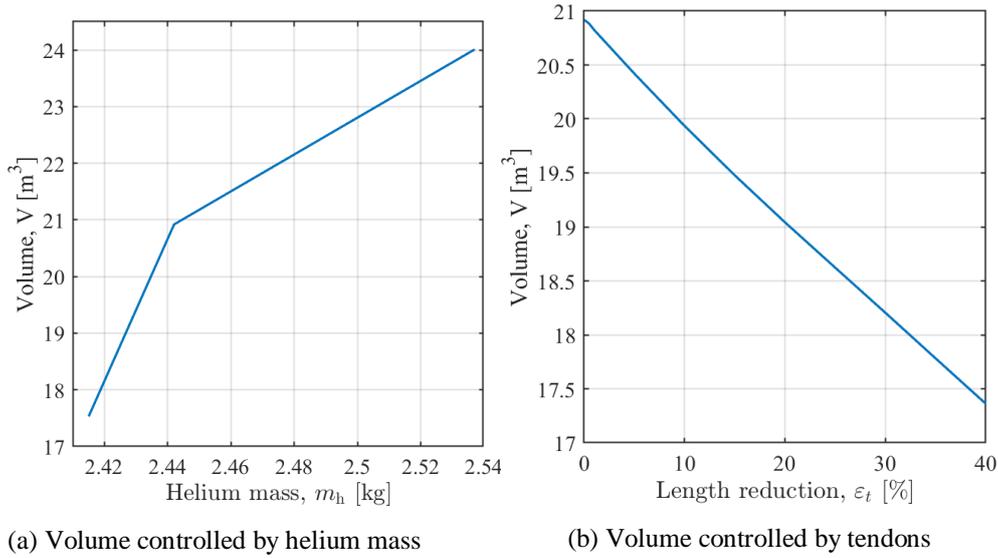
Figure 3. Aerostat volume changes.

4. NUMERICAL SIMULATIONS

As mentioned in the Introduction, it is assumed that the aerostat can be transported to a selected point in the atmosphere in a folded position. Next, the aerostat can then be unfolded and filled with helium. Therefore, in the numerical model the simultaneous processes of filling the envelope and at the same time the free fall of the aerostat is taken into account. The analyses of the numerical results show that the process of unfolding the aerostat must be carried out as quickly as possible in order to prevent its deployment at high speed.

Using the mathematical model described above, it is possible to analyse the movement of the airship for different scenarios and two types of control:

- controlling the mass of helium, and
- controlling the length of tendons in the aerostat structure.

For example, it is possible to consider the scenario in which the mission in performed in such a way that aerostat position at the mission end is close to the position at the mission start. In such a case, the corresponding dynamic optimization problem is aimed at finding functions describing change of helium mass in time m_h^{opt} and tendons shortening in time $\varepsilon_t^{opt}(t)$, which minimize the difference between final horizontal position of the aerostat at arbitrary time instant t_{end} and its desired horizontal position (x_0, y_0):

$$\left\{ m_h^{opt}(t), \varepsilon_t^{opt}(t) \right\} = \arg \min \left[\sqrt{[x(m_h(t), \varepsilon_t(t), t_{end}) - \mathrm{x}_0]^2 + [y(m_h(t), \varepsilon_t(t), t_{end}) - \mathrm{y}_0]^2} \right]$$
(12)

Solution of the above problem can be obtained by searching for the altitudes with winds of appropriate directions and using either helium mass control or tendons control in order to modify actual operational altitude of the aerostat, catch the suitable winds and use them for aerostat motion towards desired final position. Consequently, the following scenarios will be considered:

a) **Scenario 1** – this scenario corresponds to the execution of a sample standard mission consisting of steps:
- Step 1 – ascending from $h_1 = 0$ m to $h_2 = 5$ km,

Lech Knap, Andrzej Swiercz, Cezary Graczykowski, Jan Holnicki-Szulc

- Step 2 – maintaining the aerostat altitude at the level $h_2 = 5$ km,
- Step 3 – descending to altitude $h_3 = 3.8$ km at which volume $V = V_0$. In this step the decrease of the height takes place by decreasing the amount of helium in the aerostat balloon.
- Step 4 – maintaining the aerostat altitude at the level h_3,
- Step 5a – reducing the length of the stiff tendons by 34.4% and descending to the altitude $h_4 = 2$ km,
- Step 5b – maintaining the aerostat altitude at the level h_4,
- Step 6 – aerostat descending and landing at the level $h_1 = 0$ m.

b) **Scenario 2** – this scenario corresponds to an almost identical mission as in Scenario 1, except that in Step 1 the aerostat is disembarked at an altitude h_2 and in Steps 5a and 5b the altitude is maintained in the range of 3.1-3.3 km so that it is possible to return to the initial position in the horizontal plane, but at h_0 level, due to wind effects.

In both scenarios, the control of the balloon volume and the ascending velocity is carried out both by the mass of helium control and the tendons length control. The control of vertical mobility is realized by tendons length control in the range of 2-3.8 km of the altitude, while outside this range by helium mass control. Tendon control outside this range is problematic because at a given helium mass it can lead to the formation of significant overpressures in the balloon which can lead to damage to the aerostat envelope. However, such a solution allows to operate between operational altitudes (e.g. 2-3.8 km) using only tendons and without changing the helium mass. Thus, it is possible to provide easier control of the aerostat altitude within the mentioned range. Additionally, volume change can be realized quickly which is difficult in the case of helium mass control.

In the Fig.4, the changes in the aerostat vertical motion control signals are presented. However, instead of the changes in the length of the tendons, the recalculated value of the decrease in the aerostat volume resulting from the assumed change in the length of the tendons is shown (maximum 39% for Scenario 1 and 11% for Scenario 2). The figure also presents a plot of the helium mass change in the aerostat balloon.
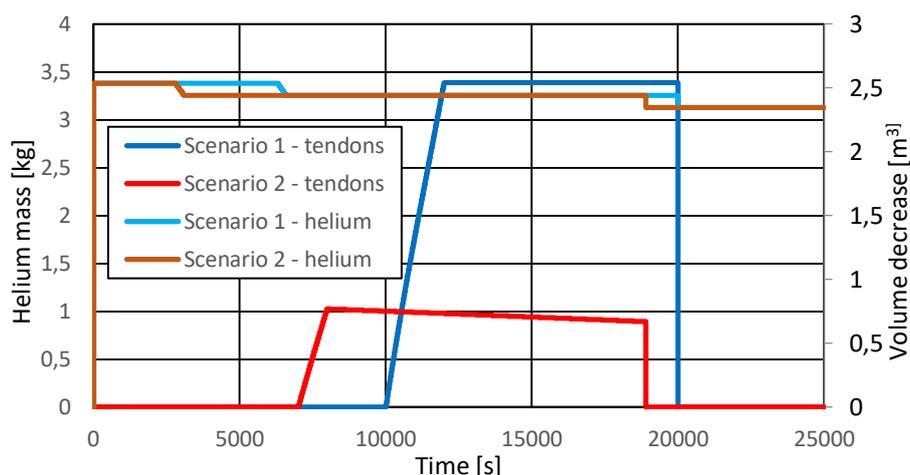
Figure 4. Variation of helium mass and balloon volume changes due to tendons control signals

Changes in control signals are accompanied by changes in the volume of the aerostat, which correspond to a change in balloon volume and therefore in the value of the buoyancy forces as well as ascending and descending velocities. The initial helium mass allows the aerostat to reach an altitude of 5 km in both scenarios - cf. Fig.5. Subsequently, the first decrease in helium mass

causes that the aerostat descends to an altitude of about 3.78 km. The next step of control consists of changing the length of the tendons. In the case of the maximum allowable shortening of the tendons, it is possible to reduce the height of the aerostat to an altitude of 2 km in Scenario 1. In Scenario 2, a different strategy of controlling the length of the tendons is adopted, which is aimed at obtaining a starting position in the horizontal plane. Therefore, it is necessary to search for altitudes at which the direction of the wind allows to return to the starting position without additional propulsion (cf. Fig.2). This is achieved by keeping the aerostat altitude in the range 3.1-3.3 km for some time. In Fig.6 the course of changes in the distance of the aerostat from the initial position is shown, while in Fig.7 its components in horizontal plane are presented. At the end of both scenarios, the second decrease in helium mass which leads to the landing of the aerostat and the end of the scenarios (Fig.4).
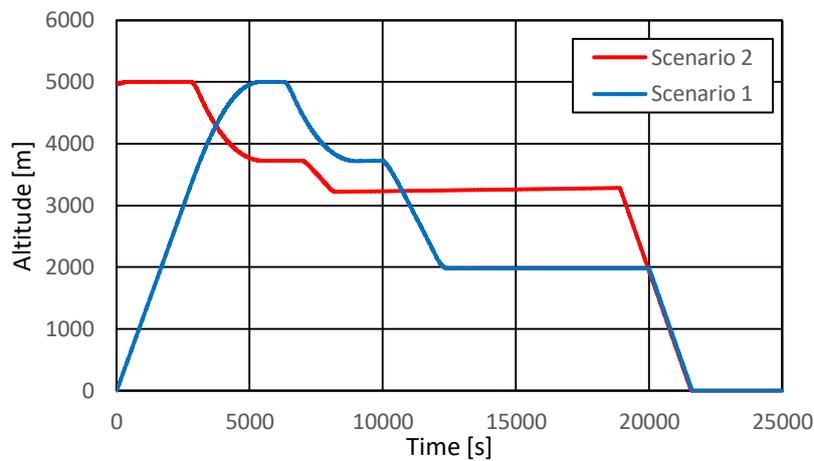
Figure 5. Change in aerostat altitude in Scenario 1 and 2.
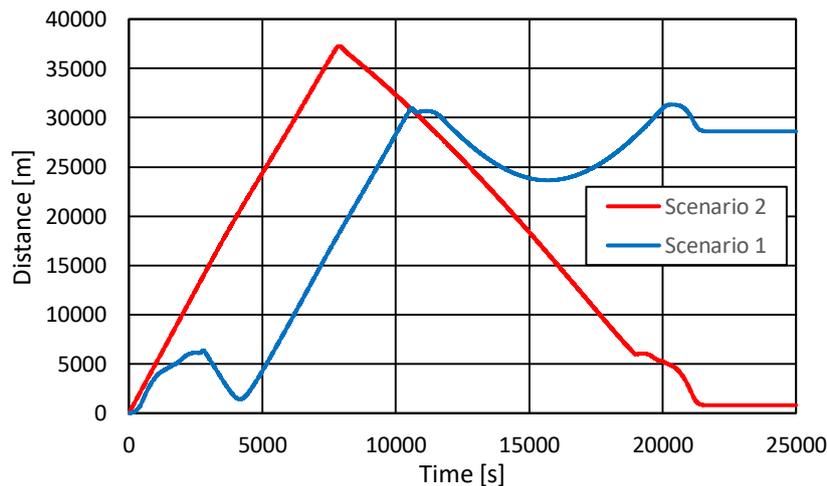
Fig. 6. Change in aerostat distance from initial horizontal position.

Lech Knap, Andrzej Swiercz, Cezary Graczykowski, Jan Holnicki-Szulc
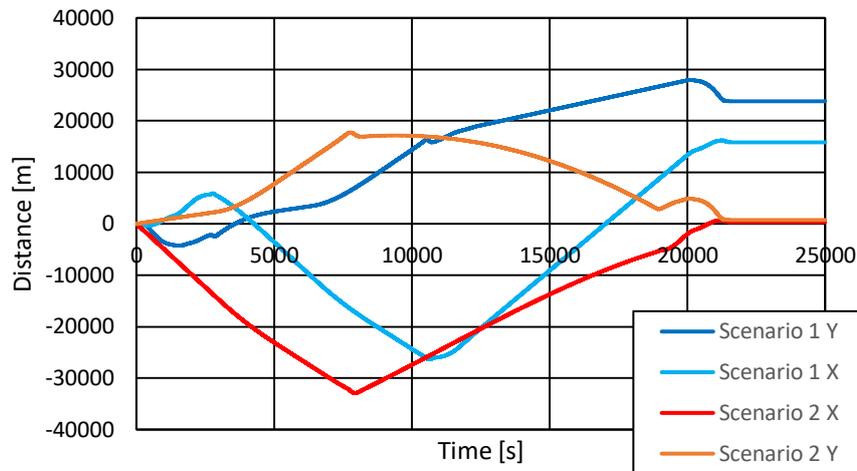
Figure 7. Change in aerostat distance components (direction X and Y) from initial horizontal position.

The obtained results indicate that in favourable atmospheric conditions it is possible to use the presented method of controlling the aerostat volume based on changing the length of the tensegrity structure tendons on which the balloon envelope is extracted. This approach enables both to control the change of the aerostat altitude and to maintain a certain horizontal position (circling around desired position) of the aerostat under favourable atmospheric conditions.

The durability of the aerostat envelope greatly depends on the gauge pressures inside the balloon. If the gauge pressure is too high during changes in helium mass or changes in tendon length, damage of the envelope may occur. Figure 8 shows the changes in the balloon gauge pressure (compared to atmospheric pressure at a given altitude) in both scenarios. Changes in helium mass and tendons lengths were limited in order to avoid obtaining a gauge pressure higher than 2150 Pa. Higher pressure can cause overloading of internal tensegrity structure and its damage. Also, attention should be paid to the fact that keeping a low value of a gauge pressure is favourable because it allows to increase resistance to wind gusts and the resulting undesirable changes in volume of the aerostat.
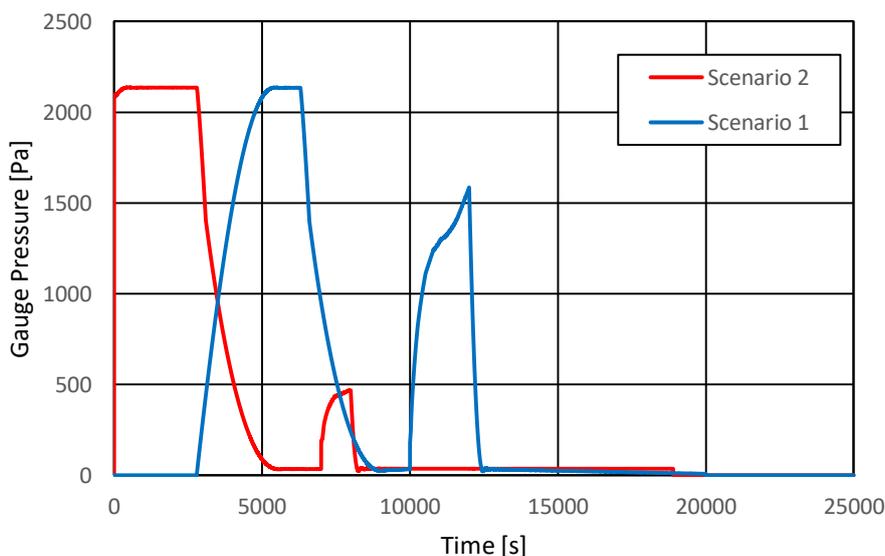
Figure 8. Change in the gauge pressure in the aerostat balloon.

5. FINITE ELEMENT STRENGTH ANALYSIS

The results of the numerical simulation based on above model of aerostat motion allow indicating the time instants in the aerostat motion where the structure is the most loaded. This is particularly visible in Step 2 at height h_2 where the gauge pressure has the highest value. In addition, the control of tendons length can also cause an increase in gauge pressure, what is visible in Step 5. Therefore, this section will present the results of the finite element analysis of the aerostat structure corresponding to the mentioned critical time instants.

For this purpose, a numerical model of the aerostat was created using Abaqus software. The ellipsoid-shaped aerostat has a length of 10 m (along the major axis) with circular cross-section (with respect to the vertical plane) and with the largest diameter of 2 m. It was assumed that the envelope is made of polyethylene (E=0.43 GPa) and has thickness of 50 µm. The supporting internal structure of the aerostat is composed of four separate modules of tensegrity structures. Each module is made of:

- carbon fibre bars (a pipe cross-section with outer diameter of 12 mm and wall thickness of 1mm),
- stiff tendons (circular cross-section with diameter of 3 mm, E=210 GPa) made of steel, and
- highly-elastic tendons (circular cross-section with diameter of 3.6 mm, E=0.05 GPa) made of a gum-like material.

For control of the stiff tendon lengths, the electric motors (retractors) are utilized and placed in each crossing of stiff tendons, as presented in Fig.9.
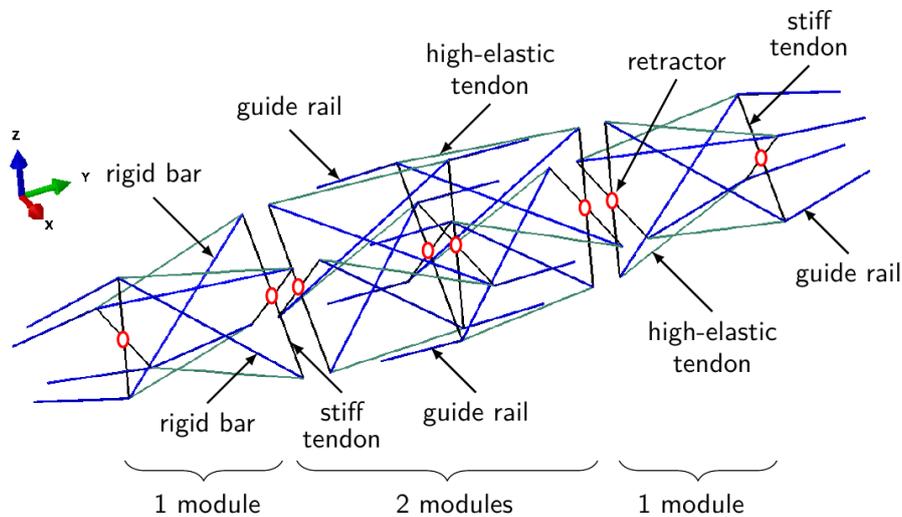
Figure 9. A scheme of the supporting structure.

Lech Knap, Andrzej Swiercz, Cezary Graczykowski, Jan Holnicki-Szulc
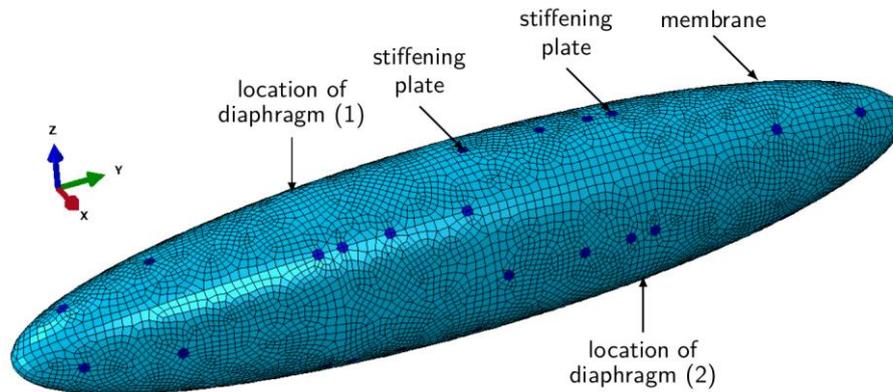
Figure 10. The supporting structure scheme of the aerostat.

The numerical model consisting of 13 811 finite elements (i.e. shell elements, membrane elements, truss elements and connectors) is shown in Fig.10. Total mass of the aerostat (including payload and helium) is equal to 17.709 kg. Each aerostat chamber was inflated proportionally and subjected to internal and external loadings (i.e. pressure, temperature) corresponding to the altitude of h_2=5 km. The model atmosphere was applied according to NASA's model.

Three aerostat loading cases are analysed as far as structural integrity is concerned:

i.   an initial state with prestressed internal structure (σ_0 =2 MPa in high-elastic tendons) – aerostat ready for ascending (Step 1 valid for Scenario 1),

ii. the highest altitude of aerostat of 5 km (Step 2 valid for both scenarios), and

iii. the altitude of 2 km with partially released mass of helium and uniformly shortened tendons (about 34.4%) – Step 5b (valid for Scenario 1).

The computed stress distributions under aforementioned load conditions are presented in Fig.11. For the envelope, the equivalent von Mises stresses and for the internal structure, and the longitudinal stresses are visualised. In the initial state – case (i), small stress values are revealed in the envelope and in the internal structure. This is caused by initial stresses σ_0 introduced into the highly-elastic tendons. In the case (ii) – at the altitude of 5 km, the equivalent von Mises stresses in the envelope reach the level of 40 MPa, however in the stiffening plate they are much larger and reach about 65 MPa. In this state, the maximal longitudinal stresses in the tensegrity elements have the highest values of ca. 30 MPa.

A different stress distribution is revealed in the case (iii) when a small amount of helium is released and stiff tendons are shortened. The equivalent von Mises stresses in the envelope locally reach the values of ca. 20 MPa (in the stiffened plates about 40 MPa), whereas the internal structure is heavily loaded. The bars of the tensegrity structures are relatively slender and therefore can buckle. In order to ensure the integrity of the structure, it is important to apply appropriate structural material (e.g. carbon fibre) or increase its bending stiffness which, on the other hand, adversely influences the structural mass.

For comparison purposes, the total displacements corresponding to above discussed states are presented in Fig.12. Interestingly, for the considered cases the relatively small radial displacements of the envelope causes the largest state of stress in the envelope. However, the largest displacement for both internal structure and the envelope were obtained for the case (iii).

Lech Knap, Andrzej Swiercz, Cezary Graczykowski, Jan Holnicki-Szulc
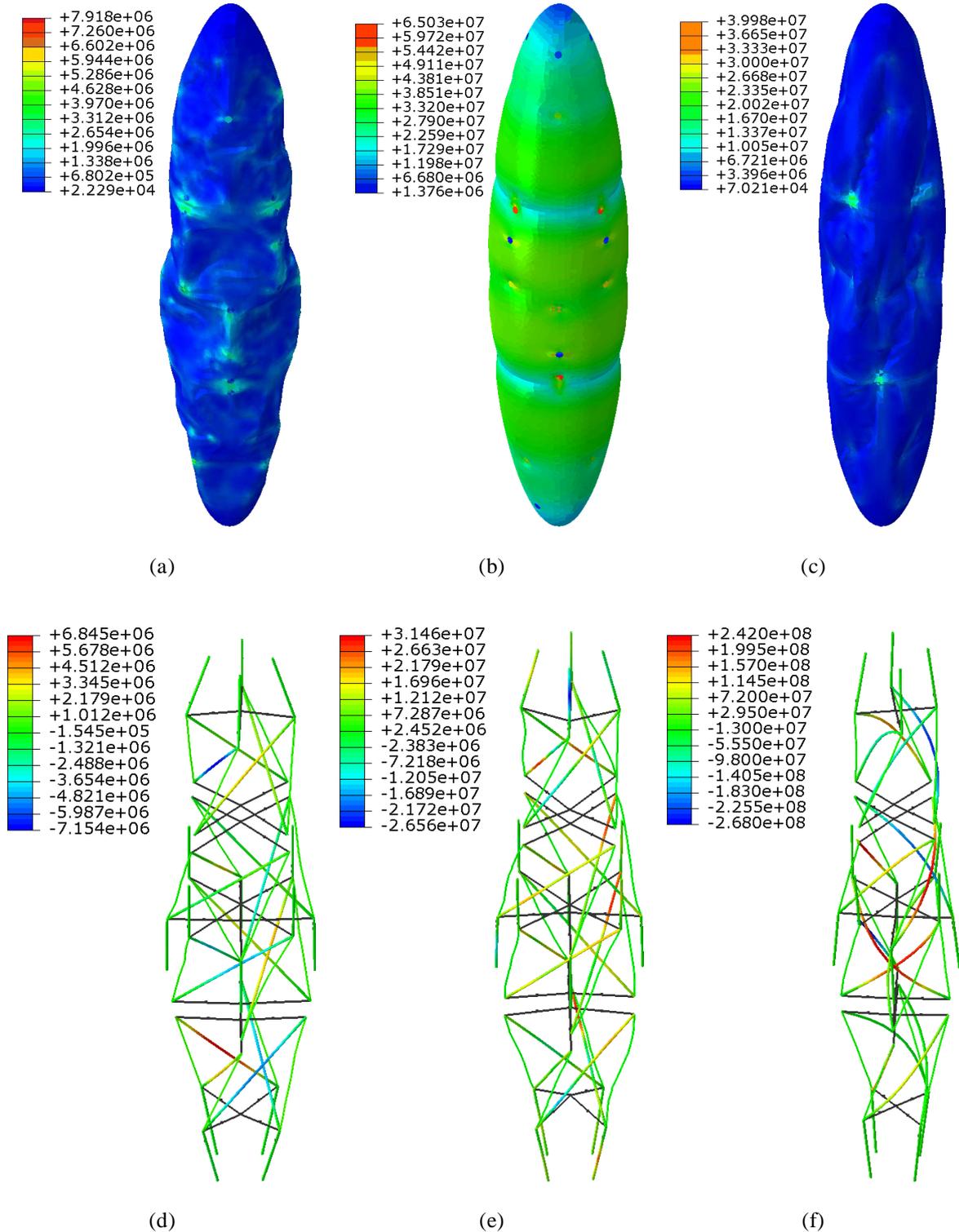
Figure 11. Distribution of stresses in the envelope (a)-(c) and internal structure (d)-(f) computed for: case (i) – first column, case (ii) – second column and case (iii) – third column
(no data in the greyed members – stiff tendons – modelled by connectors).

Lech Knap, Andrzej Swiercz, Cezary Graczykowski, Jan Holnicki-Szulc
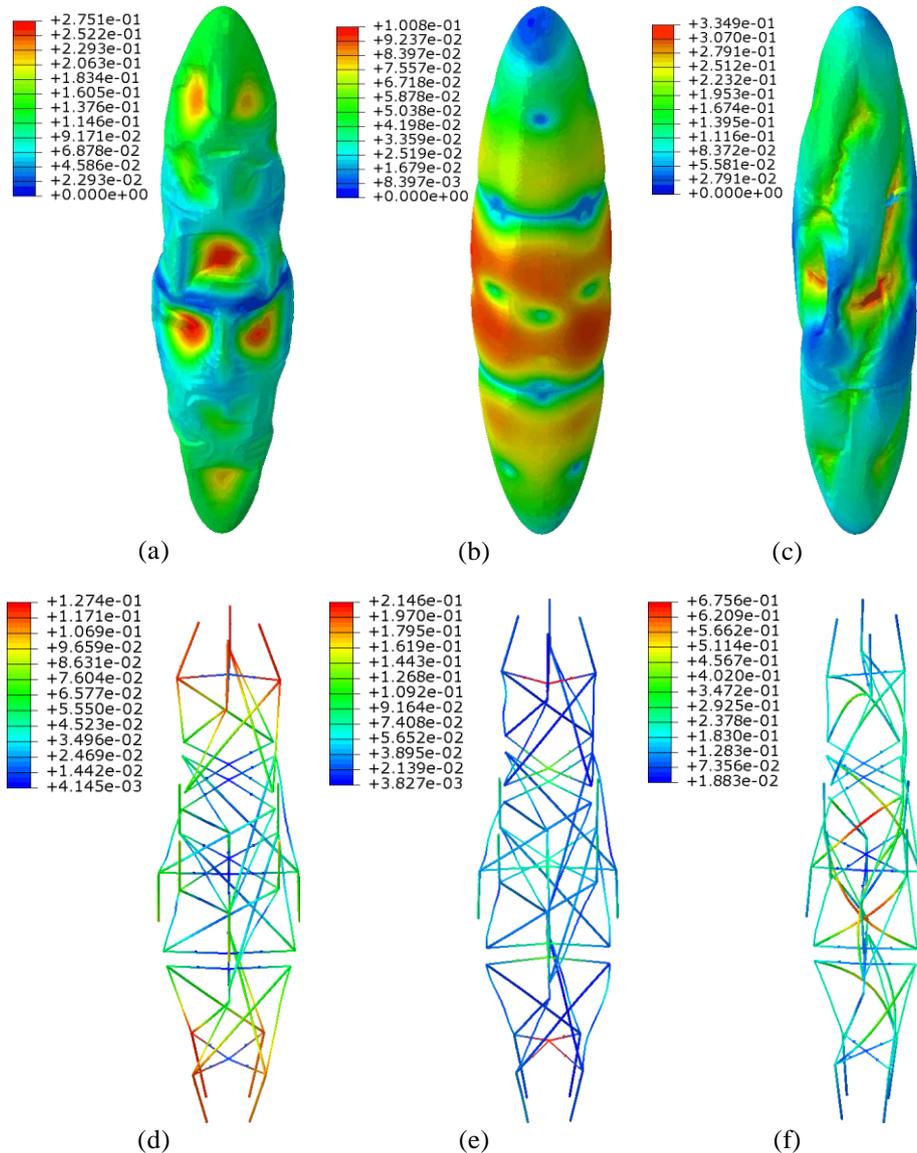
Figure 12. A map of total displacements in the envelope (a)-(c) and internal structure (d)-(f) computed for: case (i) – first column, case (ii) – second column and case (iii) – third column.

6. CONCLUSIONS

In this study, the aerostat internally supported by the tensegrity structure was presented and its hypothetical mission was analysed. The mission was considered in two scenarios. In the first one the aerostat starts form the ground level, whereas in the second one the aerostat is disembarked at initial non-zero altitude. The presented numerical model enables comparative analysis of both scenarios. It shows that it is possible to use internal tensegrity structure and apply tendons length control in order to ensure required aerostat altitude as well as to maintain horizontal position during favourable weather conditions. This type of control can significantly reduce the usage of energy during long aerostat missions. Moreover, it allows to adjust the altitude and horizontal position by limiting the amount of helium required during the aerostat operational range. On the other hand, the results of numerical analysis have shown that for a given distribution of wind speeds, a required

internal pressure can cause threats to envelope strength. Therefore, the structural strength analysis was also performed in order to ensure the aerostat structure integrity can be assured during the considered missions.

ACKNOWLEDGMENTS

REFERENCES

[1] Recent Development Efforts for. Military Airships, The Congress of the United States, Congressional Budget Office (CBO), November 2011, https://fas.org/irp/program/collect/cbo-airship.pdf

[2] Saleh S., Weiliang HE., New design simulation for a high-altitude dual-balloon system to extend lifetime and improve floating performance, Chinese Journal of Aeronautics, Vol 31, No 5, pp. 1109-111, 2018.

[3] Loon.com. The Stratosphere: High Altitude, Higher Ambitions, https://loon.com/resources/content-library. [accessed on 21 June, 2021]

[4] Ghanmi A., Sokri A., Airships for military logistics heavy lift, Defence R&D Canada, Centre for Operational Research and Analysis, DRDC CORA TM 2010-011, 2010, https://cradpdf.drdc-rddc.gc.ca/PDFS/unc92/p532881.pdf.

[5] Future Aerostat and Airship Investment Decisions Drive Oversight and Coordination Needs, Report to the Subcommittee on Emerging Threats and Capabilities, Committee on Armed Services, U.S. Senate, GAO, 2012.

[6] Mizuta E., Akita D., Fuke H., IIjima I., Izutsu N., Kato Y., Kawada J., Matsuzaka Y., Nameki M., Nonaka N., Ohta S., Saito Y., Seo M., Takada A,. Tamura K., Toriumi M., Yamada K., Yamagami T., Yoshida T., Ichimura K., Kobayashi T., Development of a 2,5 um Plyethylene Film for the Hihgh Altitude Ballon, Trans JSASS Space tech Japan, Vol 7, No 26, 2009.

[7] H. Fuke, D. Akita, I. Iijima, N. Izutsu, Y. Kato, J. Kawada, Y. Matsuzaka, E. Mizuta, M. Namiki, N. Nonaka, S. Ohta, Y. Saito, M. Seo, A. Takada, K. Tamura, M. Toriumi, K. Yamada, T. Yamagami, T. Yoshida (2010), A new balloon base in Japan: Advances in Space Research, Vol. 45 (4), pp. 490-497

[8] Kumar B. S., Nagendra N., Ojha D. K., Peter G. S., Vasudevan R., Anand D., Kulkarni P. M., Reddy V. A., Development of Ultra-Thin Polyethylene Balloons for High Altitude Research upto Mesosphere. Journal of Astronomical Instrumentation. 03. 10.1142/S2251171714400029. 2014

[9] Gai M., Guglieri G., Lattanzi M. G., Lombardi A., Mana M., Masserano L., Musso I., Navone P., A Scientific Mission Based on a High Altitude Stratospheric Balloon, International Journal of Aerospace Sciences 2014, 3(1): 18-29

[10] Kayhan Ö., Hastaoglu M. A., Modeling of Stratospheric Balloon Using Transport Phenomena and Gas Compress–Release System, Journal of Thermophysics and Heat Transfer, Vol 28, No 3. 2014

[11] Saleh S., Weiliang HE., New design simulation for a high-altitude dual-balloon system to extend lifetime and improve floating performance, Chinese Journal of Aeronautics, Vol 31, No 5, 2018, pp. 1109-1118.

DESIGN OF A SOLAR UAV FOR NIGHT SURVEILLANCE OPERATIONS

Rúben D.A. Santos[1*], Anuj Regmi[2] and Pedro V. Gamboa[1]

1: Center for Mechanical and Aerospace Science and Technologies (C-MAST-UBI)
Faculty of Engineering
Universidade da Beira Interior
6200-001 Covilhã
ruben.almeida.santos@ubi.pt, pgamboa@ubi.pt, http://www.ubi.pt

2: Department of Electrical and Computer Engineering
Faculty of Engineering
University of Porto
4200-465 Porto
anuj@fe.up.pt, https://sigarra.up.pt/feup

Abstract. *Since the beginning of human flight, one of the most desirable and difficult goals has been to make an airplane to stay aloft for very long periods of time. One of the solutions to this problem is to harvest solar power during flight to increase the flight time and ideally achieve perpetual flight. A solar plane has the advantage of not having to be refueled or recharged every start of the mission, instead it collects solar energy during day-time for flight and to recharge the battery for night flight. This process reduces the need for daily ground operations.*

This paper presents a methodology to design a solar Unmanned Aerial Vehicle (UAV) capable of flying for long periods of time which may be dedicated to performing night surveillance operations. The developed methodology builds on previous works by Noth by adding the possibility of analyzing several wing and tail airfoils as well as computing the respective aerodynamic characteristics to have more reliable results. It also includes a second phase where a more detailed analysis is performed to provide more reliable results for a given mission profile defined by a high-altitude daytime segment and a low altitude night flight.

A test case is presented to demonstrate the methodology. This test case represents a fixed wing UAV that flies at a latitude of 30ºN to monitor the night activity of nocturnal animals over a period of several days in a row. At this latitude, the winter solstice has 10.2 hours of daylight and 13.8 hours of night time. Since the solar UAV will have an endurance of at least 24 hours at the winter solstice, the aircraft is able to fly every day of the year. The design of a solar UAV capable of flying several days is a challenging, complex, and multidisciplinary problem. This work shows that even for a very light payload mass a relatively large wing aircraft is needed due to the very low wing loading required for high flight efficiency and flight overnight. Also, parameters such as battery energy density, solar panel area ratio, structural mass, mission profile, and mission location and time of the year have important effects on the final design size and mass.

Keywords: Aircraft design, Solar UAV, Design methodology, Perpetual flight

Rúben D.A. Santos, Anuj Regmi and Pedro V. Gamboa

1 INTRODUCTION

Since the beginning of flight one of the most difficult objectives has been to greatly increase the endurance of a given airplane. One of the solutions to this problem is to harvest solar energy and store it in the airplane while flying during the day and then use the stored energy during the night.

When compared to internal combustion engines, the electric motor is more efficient, emits less noise and is friendly to the environment. It can use energy harvested while flying without the help of another airplane, while in the case of an internal combustion engine the refueling process usually needs to be done with the help of a tanker airplane. The big disadvantage of the electric motor is the energy storage solution that is very low in density when compared to fossil fuels. Despite this disadvantage, a solar airplane can perform specific missions that are very hard or even impossible to other airplanes, for example wild-life monitoring, communications relaying and weather monitoring for very long periods of time. Other advantage of solar airplanes is that since they can stay airborne for very long periods of time, the ground operations are greatly reduced since the airplane only needs to land at the end of the mission or if there is a critical problem to continue the mission (for example a failure of a critical system).

The use of electric motors is not new. The first electric powered flight occurred in France in 1884 where a hydrogen filled dirigible with electric motors won a 10 km race around Villacoulbay and Medon [1]. At that time, the only opponent was the steam engine. With the arrival of the internal combustion engine the development of the electric flight almost stopped [1]. Only later in 1974 the first solar powered flight took place at Camp Irwin, California, with Sunrise I, designed by Boucher from Astro Flight Inc. Its first flight took 20 minutes at an altitude of 100 m, and the maximum time of flight during the winter was between three to four hours. It had a wingspan of 9.76 m and a mass of 12.25 kg, with 4096 solar cells and a power output of 450 W [1]. Other important landmark close to this date was Fred Millitky's airplane called Solaris that made three flights of 150 seconds reaching 50 m of altitude [2]. Four years later in 1978 the first manned solar airplane, Solar One, made by David Wiliams and Fred To was launched with the intend to cross the English Channel [3]. The airplane used a nickel-cadmium battery to store the energy. Other manned solar airplanes like the Solar Riser and Gossamer Penguin also marked important stages in solar flight. More recently we have the example of Solar Impulse 2 that made a fly around the world in seventeen stages during sixteen and a half months in 2015 [4].

With the interest in solar flight increasing the development of high altitude high endurance airplanes started. The first one to be built was the Pathfinder that made its first flight in 1993 at Dryden. It had a 30 m wingspan and 254 kg of mass, and it became a part of NASA's Environmental Research Aircraft Sensor Technology (ERAST) program. In 1995 it reached a record altitude of 15392 m, and two years later set the record to 21802 m. Following Pathfinder, new versions were made: Pathfinder Plus with a larger wingspan and new systems, Centurion that was built as a technology demonstrator and later the Helios airplanes. Other companies also started to develop their own solar airplanes like Zephyr that holds the current records of endurance and altitude. The latest version, Zephyr S, has a 28 m wingspan and a maximum takeoff mass of around 75 kg. In the Summer of 2008 it flew non-stop for almost 26 days [4].

Other companies are also testing their own prototypes in order to build the full-scale

versions. For example, Phasa 35 with a more conventional configuration with a rectangular wing and a conventional tail, and the more unconventional UAVOS solar airplane ApusDuo that uses a tandem configuration [5].

There is also a big academic interest in solar airplanes. For example, the AtlantikSolar [6] holds the current endurance record for airplanes under 50 kg of 81 hours, and André Noths' airplane Sky-Sailor [7] was designed for a mission in Mars.

Regarding the design process, very little information is available in the literature. It is a complex matter and the designers of most developed airplanes do not make the used design process publicly available, or the publications that present such process do not validate them. For example, following the Sunrise airplane design Boucher published in 1979 a description of the performance and hardware of the airplane but did not describe the design methodology [8]. In 1978, Gedeon presented the idea of the feasibility of solar airplanes [9]. Schoeberl published his work on propulsion and aerodynamics [10, 11], while Colozza presented the implementations of the solar cells [12].

The first paper presenting the design process is from Irving in 1974 for a manned airplane [13], allowing the mass of several components to vary with wingspan and power. Bailey also introduced in 1992 separate mass models for the motor, controller, gearbox, propeller, and fuel cell [14]. Hall and Hall developed a very accurate method to predict the airframe mass of a solar aircraft taking into account all elements of the structure but it proved to be very complex [15]. Many authors also simplify the mass model of the airplane by making it proportional only to the wing surface as shown in [16] but this rapidly decreases the range where the model is valid. Other great source of information comes from academic students, from their design process and construction of prototypes to validate those methodologies. For example, students from Israel built the SunSailor and presented the design methodology in 2006 [17]. Also, a consortium of Portuguese universities developed in 2014 a solar UAV for civilian applications with an endurance of 8 hours [18].

This paper describes a methodology for sizing solar airplanes. This methodology is divided into two main phases. The first one is based on André Noth's work for Sky-Sailor solar unmanned aerial vehicle (UAV), extending it to include the analysis of several combinations of airfoils for the wing and tail section of the airplane and the calculation of the aerodynamic characteristics for that specific combination. It also includes a second phase where a more detailed analysis is performed to analyze the design in more detail and to assess the airplane's viability for the required mission.

A test design case for a fixed wing UAV that flies at a latitude of 30°N aimed at performing night surveillance missions over a period of several days is presented. Since the airplane will have an endurance of at least 24 hours at the winter solstice the airplane should be able to fly every day of the year.

2 METHODOLOGY

The design methodology presented can be divided into two main phases. The first phase takes specific parameters, for example the average power to weight ratio, weight per unit area of certain components and the provided airfoils' polars, and outputs possible solutions for a perpetual flight airplane, providing the initial values for a more detailed analysis. The second phase, more detailed than the first one, takes as inputs the characteristics of all the components on the airplane, that are selected taking into account the output from

the first phase, in order to check the viability for the airplane to perform a 24-hour flight without landing and with enough energy to be able to fly through the next day.

2.1 Conceptual methodology

The first phase is based on the work of André Noth [7] for the unmanned aircraft vehicle (UAV) named Sky-Sailor.

Before starting the calculations, it is necessary to create a database that contains a large amount of components that can be used on this type of airplanes, for example data of motors, maximum power point tracking (MPPT) devices, batteries and electronic speed controllers (ESC). It is also advisable to have a collection of airfoils to be analyzed for the wing and tail sections of the airplane. Note that this phase does not restrict the use of a single combination of airfoils for the wing and tail sections, but since there are a large number of airfoils available it is possible to analyze a large set of combinations to try and find the most efficient ones.

After having the database complete it is possible to calculate the specific properties of each component or group of components, such as the power to weight ratio for the propulsion group (including ESC, motor and propeller) and MPPT, the weight per unit area of the solar cells, and the energy per unit mass of the batteries. It is also necessary to have an estimative of the avionics and payload mass and systems' power consumption, since the airplane has to be designed around those systems. Some mass penalty factors are added in this phase to account for the encapsulation and the amount of energy of the battery, as well as a safety factor and an efficiency factor for the solar cells.

Next a solar module that can estimate the average Sun energy during a complete day for a specific latitude and day of the year was also added. This module is explained in more detail in Section 2.1.1

Following this step, it is necessary to find a way of estimating the airframe mass. Again, following Noth's method, Eq.(1) is used. A collection of similar airplanes to the one being designed are used to calculate coefficients k_{af}, x_1 and x_2. One problem with this airframe mass prediction method is that it is almost impossible to have a very small mass error for a relatively large range of aircraft sizes, rendering the equation only fit for a small group of airplanes at a time.

$$m_{af} = k_{af} b^{x_1} AR^{x_2} \tag{1}$$

Phase 1 starts by selecting a given configuration of airfoils, wingspan and aspect ratio. Next it passes through the aerodynamic module where all the aerodynamic coefficients of the airplane are calculated and interpolated from polars imported from XFOIL [19] (as explained in Section 2.1.2). This process has the advantage of having more precise values for the lift, drag and moment coefficients of the wing, tail and consequently the airplane itself, but it has the disadvantage of being highly dependent on the convergence of the aerodynamic analysis in XFOIL.

With the coefficients of the airplane calculated the phases passes through a module presented in Noth [7] to calculate the power, velocity, and mass of each component of the airplane. Since the aerodynamic coefficients are interpolated among different flight conditions, it is important to make it an iterative process with the Reynolds number, which tries to match the Reynolds number with the velocity obtained from Noth's module. When the Reynolds number is converged, the next configuration of airfoils, wingspan and aspect ratio is analyzed.

Rúben D.A. Santos, Anuj Regmi and Pedro V. Gamboa

After all configurations have been analyzed, it is possible to calculate further performance values as it is demonstrated in Section 2.1.3.

This process is summarized in Fig.1.
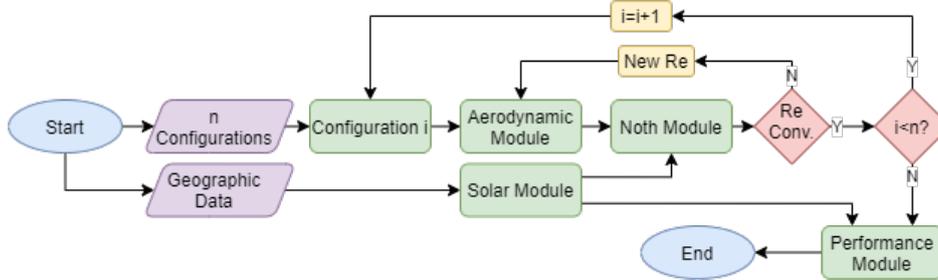
Figure 1: Phase 1 flowchart.

This phase is very important in the early stage of the project since it can give an idea of the size, mass, and power consumption of the airplane. Nevertheless, it is important to note that in most cases the program gives optimistic results, but on the other hand it is a very fast way to analyze a large number of configurations in a short time. It was also added the ability of the airplane to store gravitational energy by climbing during the day and gliding through the night, this process is very useful to lower the number of batteries cells needed for a given scenario.

With the output from this phase, it is possible to start selecting the correct components for the airplane, for example a suitable motor, ESC and MPPT.

2.1.1 Solar module

This module exists to better estimate the average Sun energy that the airplane is able to harvest for a given latitude and day of the year.

First the time of sunlight, t_D, is calculated for a given day with Eq.(2).

$$t_D = 3600 \left[12 + \frac{N_{h_{max}} - N_{h_{min}}}{2} \sin \left(\frac{2\pi}{365} (n_D - 79) \right) \right] \tag{2}$$

where $N_{h_{max}}$ and $N_{h_{min}}$ represent the maximum and minimum hours of sunlight during the year, and n_D is the day to consider.

Then the declination of the Sun, δ_{Sun}, is calculated with Eq.(3).

$$\delta_{Sun} = - \arcsin(0.39779 \cos(0.01720(n_D + 10) + 0.03341 \sin(0.01720(n_D - 2)))) \tag{3}$$

Lastly, the cosine of the solar zenith, $\cos(\theta_{Sun})$, for a given time of the day is calculated with Eq.(4).

$$\cos(\theta_{Sun}) = \sin \left(\frac{\pi}{180} Lat \right) \sin(\delta_{Sun}) + \left(\frac{\pi}{180} Lat \right) \cos(\delta_{Sun}) \cos(h_D) \tag{4}$$

where Lat is the latitude that must be taken into account and h_D the angular hour.

Since for this first design phase it is necessary to average the Sun energy, $E_{D_{av}}$, the average of the cosine of the solar zenith is calculated giving Eq.(5).

$$E_{D_{av}} = avg(\cos(\theta_{Sun}))I_{Sun_{max}}t_D \tag{5}$$

The maximum Sun irradiance, $I_{Sun_{max}}$, is assumed to be approximately 1100 W/m^2.

Rúben D.A. Santos, Anuj Regmi and Pedro V. Gamboa

2.1.2 Aerodynamics module

Inside this module the aerodynamic coefficients for the airplane are calculated. Since the target is to maximize the airplane endurance, then ${C_{L_{AC}}}^{3/2}/C_{D_{AC}}$ should be maximized, where $C_{L_{AC}}$ and $C_{D_{AC}}$ are the total aircraft lift and drag coefficients, respectively. First the lift, drag, pitching moment coefficients of the wing (C_{L_W}, C_{D_W}, C_{M_W}) are interpolated by the polars imported from XFOIL for a given Reynolds number, where the three dimensional coefficients are calculated using the lift line method. Following this step the lift coefficient of the equivalent horizontal tail, C_{L_H}, is calculated iteratively by the equilibrium of moments around the center of gravity of the airplane, as demonstrated in Eq.(6). The concept of an equivalent horizontal tail allows a V-tail to be used.

$$C_{L_H} = \frac{S_W}{S_H(l_{tail} - \bar{x}_{CG} c_W)} \left[C_{M_W} + C_{M_H} \frac{c_H S_H}{c_W S_W} + C_{L_W} c_W \left(\bar{x}_{CG} - \frac{1}{4} \right) \right] \qquad (6)$$

where S_W and S_H are the wing and tail areas, l_{tail} is the distance from the leading edge of the wing to the leading edge of the tail, $\bar{x}_{CG}$ is the relative position of the center of gravity on the wing and c_W and c_H are the chords of the wing and tail, respectively.

From this coefficient it is now possible to interpolate the drag coefficient of the tail, C_{D_H}. Then, lift and drag coefficient of the airplane are computed with Eq.(7) and Eq.(8), respectively, where e is the Oswald coefficient and AR_W is the wing aspect ratio. Note that for the drag coefficient an extra coefficient named $C_{D_{other}}$, is added which contains an estimative of other sources of drag, for example the fuselage.

$$C_{L_{AC}} = \quad C_{L_W} + C_{L_H} \frac{S_H}{S_W} \qquad (7)$$

$$C_{D_{AC}} = \quad C_{D_W} + \frac{C_{L_W}^2}{e\pi AR_W} + C_{D_H} \frac{S_H}{S_W} + C_{D_{other}} \qquad (8)$$

It is also important to leave enough margin for the cruise speed to be at least 1.2 times the stall speed, so the airplane does not fly close to stall conditions. For this, the lift coefficient of the wing during cruise is compared against the maximum lift coefficient, $C_{L_{W_{max}}}$ to fulfill Eq.(9).

$$\frac{C_{L_{W_{max}}}}{C_{L_W}} > 1.2^2 \qquad (9)$$

With this condition verified, the values of lift and drag coefficients are introduced in Noth's method.

2.1.3 Performance module

This is the final module in phase 1, and it calculates extra values of performance that might be important to choose the correct airfoils depending on the priorities of the design, or initial values for the more detailed analysis presented in Section 2.2.

Inside this module parameters such as takeoff and landing distances, time to climb, best climb rate and fraction of battery used during climb are calculated. For the takeoff and landing, the best angle of attack of the airplane is chosen in such a way that the distances are minimized, whilst for the climb section of the flight the condition that minimizes the overall used energy is selected.

2.2   Preliminary methodology

In this part of the methodology, a more detailed analysis is performed for a given configuration, verifying the viability of the mission from the day and time of takeoff covering the next 24 hours. A second phase, Phase 2, is created. In this analysis it is also possible to have a mission profile with a climb during the day and descent during the night to save battery weight by using stored potential energy.

First it is necessary to choose the correct systems' components based on the results obtained in Section 2.1. The correct characteristics of those components must be gathered from manufacturer datasheets. For example, for the motor it is necessary to have the speed constant, *Kv*, maximum current and mass; for the ESC, the maximum current and mass; for the battery, the cells configuration and mass; for the MPPT, the total mass and quantity needed based on the maximum power of the solar cells; and for the solar cells, the efficiency, mass and area of the wing covered with them. It is also important to have a more correct value for the payload and avionics mass and power consumption. These components may change along with the iterative process since it is almost impossible to find components that perfectly respect the requirements given by Phase 1, or due to compatibility issues.

Another factor that is of great importance is the airframe mass, since it is very complicated to have a perfectly correct model through Eq.(32), a new model is used. This new model is created by designing a simple representative structure. Since the initial values from the previous section should not be far from the optimal values, the geometry adopted from Phase 1 can be used. Once the structure is designed, a simple structural analysis can be made to check the mass of materials to be used. Next with the mass values divided into four main components (wing, tail, tail-boom and fuselage), the final mass can be extrapolated for other sizes close to the original. Although this process is more complex than the one used in the previous section it should be more reliable for a larger set of configurations which use a similar structure. Also note that a penalty factor should be used for possible corrections to the final structure and for components that might not be considered. For example, one might not consider the mass of ailerons but then it is necessary to consider a higher penalty factor, so the mass of the structure is not under-estimated.

This phase is also able to analyze several scenarios where a different sized propeller is used on the same airplane. This is of great importance since one of the objectives is to maximize the efficiency of the systems. For that, a database of several propellers with the size, power coefficient, C_P, and advance ratio, *J*, is created.

To start the analysis for a given airplane, first the stall speeds for day and night cruise altitudes must be calculated. This is required not only to have the actual stall speed for the design but also to have a starting point to find the best velocities for cruise flight.

Following this step, the aerodynamic characteristics of the airplane for several cruise speeds are calculated, similarly to what is done in Section 2.1.2, and the respective propulsion characteristics, described in Section 2.2.1, for a given required power obtained from the aerodynamics module. After this, the angle of attack of the tail with respect to the angle of attack of the wing is fixed and it is also possible to retrieve the flight characteristics for the most efficient cruise speed at night (cruise velocity that uses the less amount of energy). The same process is done for the day cruise, but this time the relative angles between the tail and wing are fixed, this is done so that the night flight is more efficient,

where the flight is only done using energy from the batteries. Despite the day flight being sacrificed, the final design results in a smaller mass of batteries needed.

Since the mission might have a climb and descend during the whole day, the energy used during the flight phases is calculated, among other properties, as it is described in Section 2.2.2 and 2.2.3.

With the main part of the mission analyzed, comprising climb, cruise during the day, descent and cruise during the night, it is necessary to assess whether the airplane can even flight through the first day of the mission. For that, the properties of the takeoff (described in Section 2.2.4), climb to cruise altitude and with the rest if the normal mission until the end of the day are calculated.

The airplane is then classified as viable if the usable energy inside the batteries never runs out and if the energy inside the battery at the end of the first day is equal to the energy at the end of the second day. The energy inside the battery as well as the solar energy are calculated throughout the day in very small time-steps. By doing this, it is possible to see where the airplane is lacking energy contrary to the first approach in Section 2.1 where the average energies are used. Also note that for the airplane to be able to fly through out all year, this verification should be true for the day with less sunlight possible (winter solstice) and for the highest possible latitude of the mission.

Additionally, there are some other performance parameters that are calculated such as landing distance, top speed for the night and day altitudes, and minimum time from cruising altitude to the landing altitude.

A summary of how this part of the method works can be seen in Fig.2.
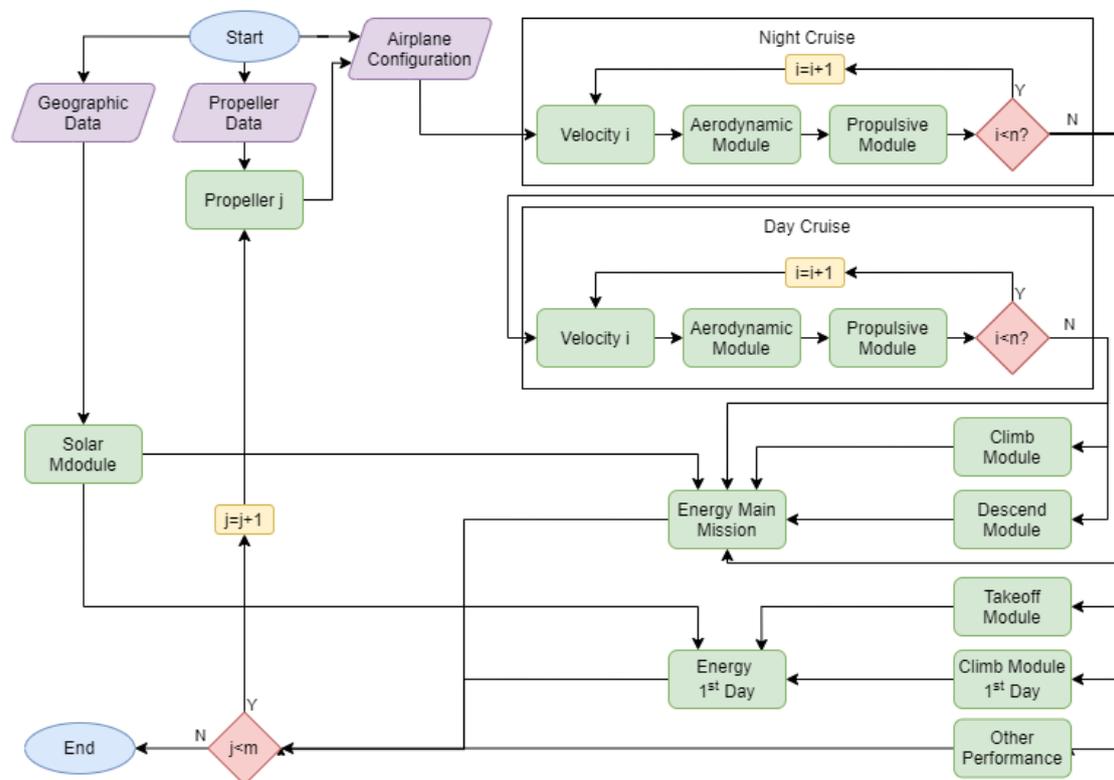
Figure 2: Phase 2 flowchart.

Rúben D.A. Santos, Anuj Regmi and Pedro V. Gamboa

2.2.1 Propulsion module

In this module the objective is to determine the power usage by the motor during a certain phase of the mission. To achieve this objective, it is required to know the motor and propeller characteristics, possible current and voltage limits as well as the aerodynamic drag that the propulsion system must overcome.

The iterative calculation in this module starts by giving an arbitrary initial value for the throttle setting and current that is being supplied to the motor. After that the motor power coefficient, $C_{P_{mot}}$, is calculated (Eq.(16)), alongside the advance ratio of the propeller in Eq.(18). Knowing the propeller advance ratio, it is possible to calculate the power coefficient of the propeller for that given case. Next the two power coefficients are compared. If the coefficients are not equal the current that is being supplied to the motor is iterated until they match. Then, the propeller power is compared to the power required to fly the airplane at the given condition. If they are not equal, the throttle setting is iterated until they are. The propulsion model is summarized in the following equations.

$$U = U_{max}f \tag{10}$$

$$U_i = U - IR \tag{11}$$

$$N = U_i Kv \tag{12}$$

$$I_{eff} = I - I_0 \tag{13}$$

$$P_{ele} = UI \tag{14}$$

$$P_{mot} = U_i I_{eff} \tag{15}$$

$$C_{P_{mot}} = \frac{P_{mot}}{\rho D_{prop}^5 (N/60)^3} \tag{16}$$

$$J_{factor} = 1 - \frac{0.329 S_c}{D_{prop}} \tag{17}$$

$$J = J_{factor} \frac{U}{D_{prop}(N/60)} \tag{18}$$

where U_{max} is the maximum voltage of the battery, f is the throttle setting, R is the internal resistance of the motor, U_i is the induced voltage on the motor, N is the rotational speed of the motor in rpm, I_0 is the idle current of the motor, I_{eff} is the effective current of the motor, P_{ele} is the power the motor is consuming, P_{mot} is the output power of the motor, S_c is the cross section of the fuselage behind the propeller, D_{prop} is the propeller diameter and J_{factor} is a correction factor for the propeller advance ratio.

This process continues until the point where the coefficients and powers are the same, providing not only the throttle setting and current that is being supplied to the motor but also the power that the motor is consuming and the power efficiency of these two components (propeller and motor) as it is shown in Eq.(19) to Eq.(24).

Rúben D.A. Santos, Anuj Regmi and Pedro V. Gamboa

$$Re_f = \frac{\rho U l_{fus}}{\mu} \tag{19}$$

$$c_f = \frac{0.455}{(log_{10} Re_f)^{2.58} (1 + 0.144\frac{U}{a})^{0.65}} \tag{20}$$

$$\eta_f = 1 - 1.558\rho c_f \frac{S_{wet}}{1.225 D_{prop}^2} \tag{21}$$

$$\eta_{eff_{plr}} = \eta_{prop}\eta_f \tag{22}$$

$$P_{prop} = P_{mot}\eta_{eff} \tag{23}$$

$$\eta_{overall} = \frac{P_{prop}}{P_{ele}} \tag{24}$$

where Re_f is the fuselage Reynolds number, l_{fus} is the fuselage lenght, c_f is the friction coefficient, η_f is the correction of the propeller efficiency due to friction forces of the airflow, S_{wet} is the wet area behind the propeller, $\eta_{eff_{prop}}$ is the effective efficiency of the propeller, P_{prop} is the propeller output power and $\eta_{overall}$ is the overall efficiency of the motor and propeller.

2.2.2 Climb module

To calculate the climb properties, it is important to have the motor and propeller characteristics, alongside the aerodynamic parameters of the airplane, to be able to calculate not only the energy consumption during the climb but also the average rate of climb.

To calculate these two values the climb is divided into several altitude steps and possible speeds the airplane must acquire to save the largest amount of energy. Next with the geometry of the airplane fixed by the process mention above and for a set of altitude and speed, the propulsion power and aerodynamic drag are calculated with a process similar to what is described in Section 2.2.1 and Section 2.1.2, respectively. With the propulsive power, drag, speed and mass of the airplane it is possible to calculate the rate of climb, for a given altitude and speed of the aircraft (Eq.(25)).

$$RC = \frac{P_{prop} - D_{AC}U}{m_{AC}g} \tag{25}$$

where D_{AC} is the total drag of the airplane, m_{AC} is the total mass of the airplane and RC is the rate of climb.

This process is repeated for all the altitude steps from the lower one until the target altitude and for every speed step from 20% above stall speed until a maximum one. In the end for each altitude step, the airplane speed that uses the least amount of power during the whole climb is chosen. Consequently, it is possible to calculate the total climb time, t_{climb}, and average rate of the climb, RC_{avg}, with Eq.(26) and Eq.(27).

$$t_{climb} = \sum_{i=1}^{n} \frac{\Delta h}{RC_i} \tag{26}$$

$$RC_{avg} = \frac{h_{end} - h_{start}}{t_{climb}} \tag{27}$$

where Δh is the altitude step, h_{start} and h_{end} are the initial and final altitudes of the climb respectively.

Rúben D.A. Santos, Anuj Regmi and Pedro V. Gamboa

2.2.3 Descent module

For this module, the objective is again to calculate the energy used by the airplane. Unlike the climb module presented above the descent module has a fixed rate of descent, since generally the cruise during the day and night will use more energy than a descent with a given time. This happens because during a descent the airplane does not need to produce the same amount of trust that it needs for level flight.

Given a fixed time for the descent and the intervals of altitudes, the rate of descent, *DR*, can be easily calculated with Eq.(28). Then, the altitude range is divided into small steps, and it is assumed that the airplane will have a constant equivalent speed during the descent.

$$DR = \frac{\Delta h}{\Delta t} \tag{28}$$

For each combination of equivalent speed and altitude the aerodynamic characteristics (mainly the lift and drag forces) of the airplane are calculated, similarly to what is done in the other modules. Next the propulsion power is calculated and, since the rate of descent is fixed, it is now possible to calculate the energy consumed during this phase of the flight.

At the end of this module the equivalent speed that the airplane should have during the descent is selected to use the least amount of energy possible.

2.2.4 Takeoff module

This last module calculates the distance needed for takeoff, the energy used and the best angle of attack the airplane should have to takeoff in the shortest distance. First, the lift-off speed that is 20% above stall speed is calculated. Next the interval of speeds from 0 to lift-off speed is divided into small steps so it is possible to calculate the time taken in every velocity step as well as the energy used by the airplane in every step.

To achieve this, for every velocity step the maximum power the motor can generate with a propulsion function similar to that in Section 2.2.1 is calculated. Next, the aerodynamic characteristics for this given speed are calculated for several angles of attack of the wing.

With these two parameters it is possible to calculate the acceleration of the airplane, a_{TO}, in this instant (Eq.(29)), and consequently the time that the airplane takes to overcome this velocity step, t_{TO_i}, can also be calculated using Eq.(30).

This process is repeated until the lift-off velocity is reached and all angles of attack are analyzed. In the end, the angle of attack that minimizes the takeoff distance, s_{TO}, (the angle of attack is fixed during the whole run because the airplane is still on the ground) is selected. As output, the energy that the airplane needs to takeoff is also calculated. It is however very important to note that the use of flaps for example is not considered, so if the real airplane uses flaps the takeoff distance can be reduced even further.

$$a_{TO} = \frac{T - D_{AC}}{m_{AC}} \tag{29}$$

$$t_{TO_i} = \frac{\Delta U}{a_{TO}} \tag{30}$$

$$s_{TO} = \sum_{i=1}^{n} t_{TO_i} U_i \tag{31}$$

3 PRACTICAL EXAMPLE

A design example for a night surveillance solar UAV capable of continuous flight for several days is presented next. This UAV's mission requirements are: Day cruise altitude of 3000m; Night cruise altitude of 500 m; Descent time from day to night cruise no longer than 8 hours; Climb time from night to day cruise no longer than 2 hours and 30 minutes; Fly throughout the whole year at 30ºN latitude; Takeoff is performed with the help of a trolley, detachable from the airplane; Landing is performed by belly landing; Sunpower E60 or C60 solar cells must be used; MaxAmp batteries must be used; Must be as small as possible.

The characteristics of the carried payload must be specified, since the airplane must be designed around the payload system, as presented in Section 3.1. Then, the conceptual design presented in Section 3.2 can start, where the initial sizing and wing and tail airfoils are determined. Lastly the preliminary design is described in Section 3.3.

3.1 Payload

The payload consists of a combination of two cameras, one optical camera and one thermal camera. The optical camera should be used when there is still enough light to have a clear image of the ground or to map the ground for the night surveillance, while the thermal camera will be used for night operations. From preliminary tests, where photographs have been taken from various distances, it was determined that the image from the camera should have no less than 100 pixels per square meter on the ground in order to distinguish objects or animals. Having this pixel density as a requirement, the Raspberry Pi HQ camera with a Arducam 35 mm lens and 8º of field of view (FoV) was chosen, as for the thermal camera the FLIR Boson with a 36 mm and 12º HFoV lens was chosen.

3.2 Conceptual design

Before starting the sizing, it is necessary to define the global characteristics of the airplane from airplanes with similar missions. One of the solar airplanes with a similar mission is Zephyr S, that has the current endurance record. Despite the difference in operational altitude, the missions are similar.

Regarding the airplane layout, a pull propeller arrangement was selected since it increases the overall propulsion efficiency. A rectangular wing and a V shaped tail were adopted. The wing is rectangular because of its sizing and fabrication inherent simplicity owing to its constant cross-section geometry. The V-tail, also with constant chord, is better when compared with a conventional tail (inverted T) since the number of parts and mass are lower [20] and also because they produce less interference drag. It also allows for the tail to be outside the wing wake and allows for ground clearance when landing. These two elements of the airplane would use a skin on frame with a transparent film acting as skin. Since the covering film used will be transparent the impact on the solar panels' efficiency is low [21]. This type of structure is also known to be lighter than a monocoque type of structure.

Rúben D.A. Santos, Anuj Regmi and Pedro V. Gamboa

3.2.1 Data

As presented in Section 2.1, the first step should be to gather a large amount of data from several components to calculate the specific parameters for each part of the airplane. The coefficients of mass in Noths' method for the MPPT, ESC and motor were obtained using a linear regression of mass per unit power. The database created includes 12 MPPT, 2045 motors and 34 ESC of several brands. The propeller mass model used is the same as Noth's. For the batteries, a similar approach was used to obtain the specific energy equation. Regarding the solar cells, the data was obtained directly from the datasheet of the manufacturer. Thus

$$m_{MPPT} = 0.0006128 P_{MPPT}, \quad R^2 = 0.868$$
$$m_{mot} = 0.0002048 P_{mot}, \qquad R^2 = 0.867$$
$$m_{ESC} = 0.0000568 P_{ESC}, \qquad R^2 = 0.967$$
$$m_{bat} = 0.0054975 E_{bat}, \qquad R^2 = 0.991$$

where m_{MPPT}, m_{mot}, m_{ESC}, m_{MPPT} are the masses of the MPPT, motor, ESC and battery, respectively; P_{MPPT}, P_{mot}, P_{ESC} are the powers of the MPPT, motor and ESC, respectively; and E_{bat} is the energy of the battery.

The airframe mass equation was created using several airplanes with similar missions with its coefficients being obtained with the least square method. The airframe mass model is given in Eq.(32) and is represented in Fig.3 together with the airplanes used to build the model. For the airplanes with unknown airframe mass, its value was assumed as 40% of the total mass.

$$m_{af} = 0.23707 b_W^{1.60524} AR_W^{-0.16748} \tag{32}$$
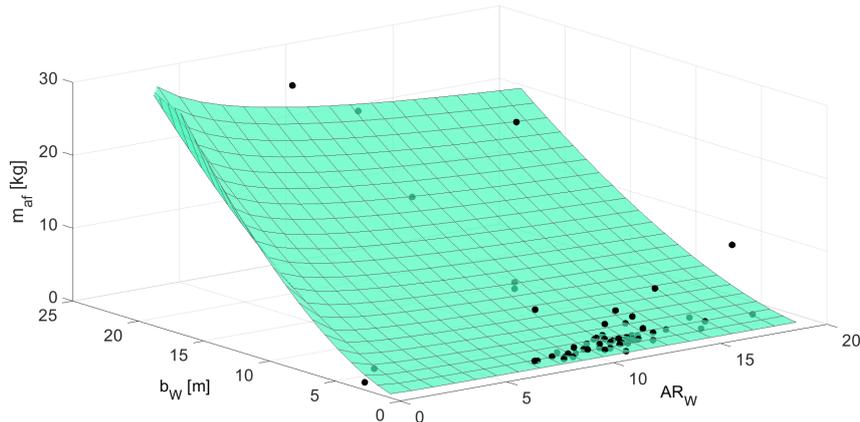
Figure 3: Representation of the used airplanes and the regression obtained for the airframe mass as a function of wingspan and aspect ratio.

As it can be seen in Fig.3 most airplanes have a very low wingspan because the majority of the airplanes with similar layouts are small scale prototypes, so the number of solar airplanes with large wingspan is very small. This fact is important for the preliminary design presented in Section 3.3.

In the aerodynamics module, 75 different airfoils were gathered and analyzed using XFOIL in the range of Reynolds numbers between 10,000 and 2,000,000.

Rúben D.A. Santos, Anuj Regmi and Pedro V. Gamboa

3.2.2 Phase 1 results

For Phase 1 it is necessary to first define the intervals of wing aspect ratio and wingspan. According to Isaienko *et al.* [5], the airplane should have a very high aspect ratio. Therefore, wingspan values ranging from 10 to 25 m and aspect ratio values ranging from 10 to 20 were adopted.

The analysis in Phase 1 was divided into two main steps to better select the wing and tail airfoils without analyzing all possible combinations (71 airfoils for the wing and 75 airfoils for the tail). In the first analysis the five airfoils for the wing that have the best $C_l^{3/2}/C_d$ for a Reynolds number of 400,000 were selected. These airfoils were used on the wing, and each one was analyzed with all airfoils of the tail (75 airfoils on the tail giving a total of 375 possible combinations). The airfoils used on the wing were: DAE-51, NACA 63-412, SD7032-099-88, USA35bModified and WE3.55-9.3.

In order to choose the best airfoil for the tail the following criteria was used: minimum total mass of the airplane, more than one viable airplane configuration, minimum required power and reduced amount of noise in the results (since the aerodynamic coefficients are interpolated from the airfoils aerodynamic coefficient curves, a large amount of noise in the data may indicate a large number of non-converged points in the polars). From this analysis, the following best airfoils were obtained for the tail: A18 inverted, E193 inverted, HS ACC2021 inverted, S4110 inverted and WE3.55-9.3 inverted.

Next, a similar approach was used to obtain the best airfoils for the wing. In this case all seventy-one non-symmetrical airfoils were combined with the five tail airfoils giving a total of 355 possible combinations. Again, the main criteria for choosing the best airfoil were minimum total mass, having more than one viable airplane configuration, minimum required power and reduced amount of noise in the results. After this filtering process, other criteria were applied: the airfoil thickness, since a thinner airfoil will result in a heavier wing for a given applied wing bending moment, and the airfoil camber, since the wing is to use skin on frame and a larger camber would make the adhesion of the film onto the ribs more difficult.

Having applied these criteria to the airfoils' selection, the best airplane has a wingspan of 10 m (for the smallest airplane possible), an aspect ratio of 20, WE3.55-9.3 and E193 inverted as the airfoils of the wing and tail, respectively, an equivalent vertical tail volume coefficient of 0.03, an equivalent horizontal tail volume coefficient of 0.70, a l_{tail} of one third of the wingspan and a total mass of 19.8 kg. It is important to note that, according to Noth [7], this approach benefits higher values of aspect ratio. The solutions for this combination of airfoils with respect to the total mass can be seen in Fig.4.

3.3 Preliminary design

In this second more detailed phase, it is necessary to select some components starting with the values obtained from the previous phase. But first it is necessary to understand the correlation between some components of the airplane, for example the change in size and mass of the airplane with the solar panel area to wing area ratio and with the battery energy per unit mass. Fig.5 shows the effect of these two parameters on the wingspan and total airplane mass. It is possible to see that both the wingspan and total mass of the airplane, for a given aspect ratio, decrease with the increase of the area of solar cells and with batteries with higher specific energy. Because of this, and since the airplane should

Rúben D.A. Santos, Anuj Regmi and Pedro V. Gamboa
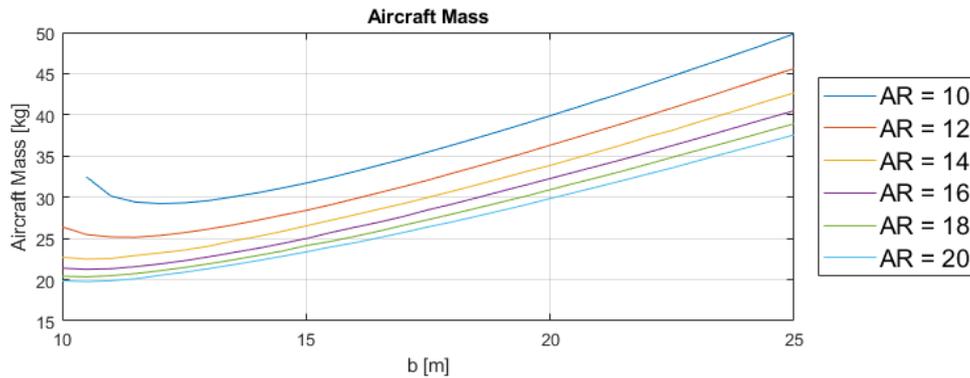
Figure 4: Total mass of the airplane for several wingspan and aspect ratio values.

be as small as possible, a solar area ratio of 0.9 is used. The remaining 10% of the wing area cannot be covered with solar cells because of aileron control hinges and excessive surface curvature at the leading edge.
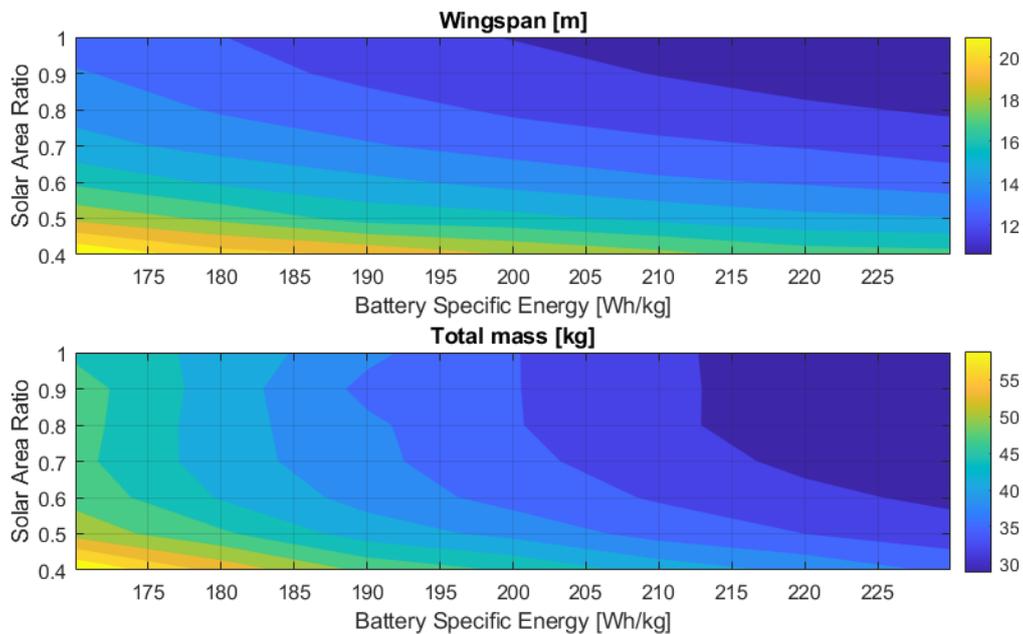
Figure 5: Wingspan and total airplane mass as functions of solar panel area ratio and battery specific energy.

Another factor to take into account is the need for a high propeller diameter and a low propeller blade count to maximize the propeller efficiency. So, a motor with a low *Kv* should be used and the LiPo battery should have six cells in series to provide a maximum nominal voltage output of 22.2 V, which offers a good compromise between low maximum voltage supplied to the motor and high enough voltage to have less losses through Joule effect on the other systems.

The process of selecting the components is iterative since it is very hard to find the exact components that are obtained from the previous phase. The considered components and sizes for the final airplane are shown later in Section 3.3.1.

Also, the mass model needs to be updated, as it is described in Section 2.1. To accomplish this a very simple structure was simulated using finite element analysis to

Rúben D.A. Santos, Anuj Regmi and Pedro V. Gamboa

estimate the airframe mass. This provides a better estimate for the airframe mass without being overly complex. The new model separates the airplane into four main parts: wing, tail, fuselage, and tail-boom. Next, for the wing and tail correlations between the size of the ribs, spar, leading edge cap and skin with the wingspan and wing chord are found. The tail-boom's mass is assumed to be a function of wingspan only, based on its estimated size. The mass of the fuselage is correlated with the mass of the wing, since a larger airplane will, in principle, need heavier and larger avionics. The whole iteration process should be accompanied by a structural analysis and if possible real tests of the structure, in such a way that not only the airframe mass model converges to a more precise value but also to help select more suitable components. This process is illustrated in Fig.6.
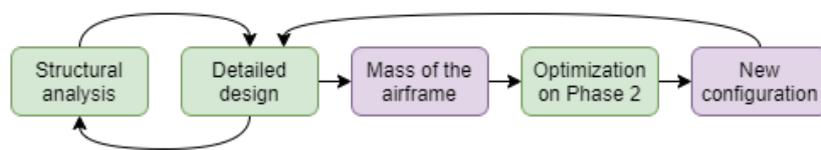
Figure 6: Iterative process flowchart.

3.3.1 Phase 2 results

Before the start the iteration process a more detailed analysis of the avionics and payload was made. The payload has 0.400 kg and consumes 27 W, and the avionics (including communications and control components), 3.5 kg and use 29 W of power.

The airplane has a wingspan of 19.5 m and an aspect ratio of 17, with a total mass of 101.183 kg. The propulsion group consists of a 50 in x 23 in two-bladed propeller; a Hacker Q100-7L motor with 3.2 kg of mass, a *Kv* of 99 rpm/V, *R* of 8.5 mΩ and a maximum current above 300 A; a Jeti model SPIN Pro 300 opto ESC with 0.2 kg that is capable of supplying 220 A. Note that a use of a gearbox was considered but the extra mass and the power limitations of existing gearboxes heavily restricts the power and efficiency of the propulsion system. The use of several motors was also considered, but again the mass of this system would greatly increase. As for the power system, the battery pack would be made of twenty cells in parallel of 6S cells from MaxAmp with a total mass of 50.551 kg; it also uses 1222 solar cells. In addition to these main components, an emergency power system of 0.3 kg with just enough energy to bring the airplane to the ground in case of motor, propeller or main power system failure was included.

The developed tool allows to perform design trade-offs to better understand the design influence of key design parameters. Thus, a study was performed to obtain the effect of the airframe mass, difference in altitude during the night cruise, the flight latitude, and the time of the year on the airplane wingspan and total mass. Figure 7a and Fig.7b illustrate these effects. For this airplane, it is possible to see that the day of the year and latitude have the most impact on wingspan and total airplane mass. While the airframe mass and the altitude during night cruise mostly impacts the final mass.

Regarding the mission itself, the airplane would takeoff at 6 am, climb to the day cruise altitude and do the mission as planned. During the day cruise the airplane would use 637 W to feed all systems while at night during cruise it would only need 516 W. Both cruise phases have an overall propulsive efficiency of 64% with the selected components. The

Rúben D.A. Santos, Anuj Regmi and Pedro V. Gamboa
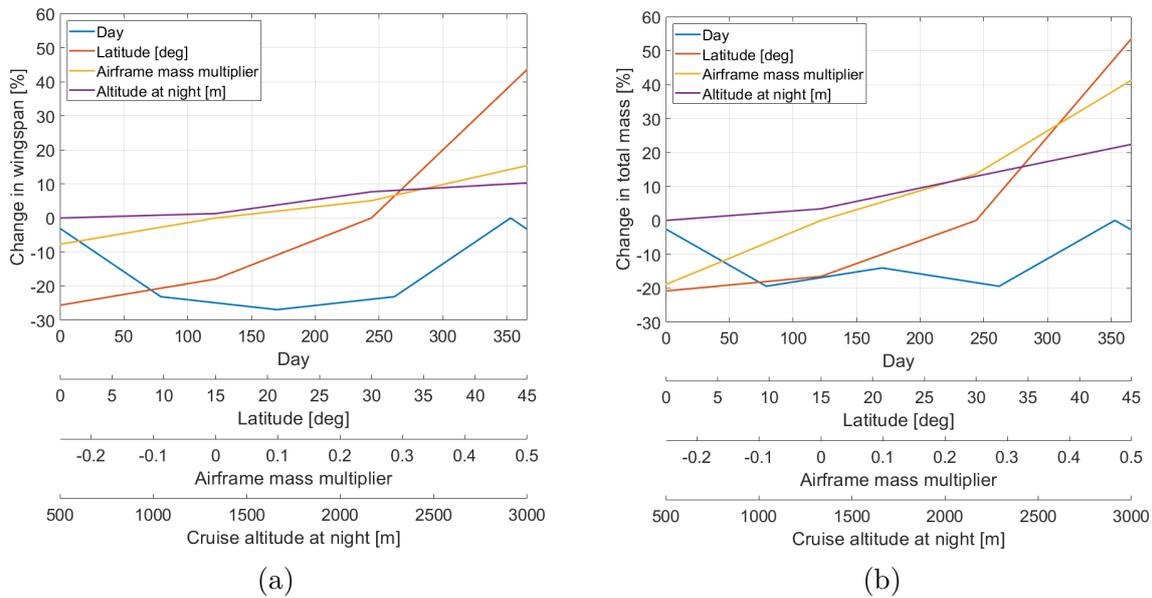
Figure 7: Percentual change in wingspan, (a), and in total airplane mass, (b), with day, latitude, airframe mass and altitude at night during cruise.

battery energy balance is illustrated in Fig.8 for the full 24-hour period.

In Fig.8 the top graph shows the usable energy inside the battery. Here the minimum energy inside the battery occurs during the day. That happens not only because the airplane is climbing, using more power than in cruise, but also because the airplane cannot harvest enough sunlight to offset the power being used. In the second graph shows that the harvested power reaches its maximum at 2,140 W. The third graph shows the power being used by the airplane at any given time, while the fourth graph shows the power flux from the batteries throughout the day, where a negative value means energy exiting the battery. Note that at the beginning of the mission there is a power spike on consumption due to the takeoff. The last graph illustrates the excess power that the airplane could harvest should there not be limited battery capacity. Ideally this value would always be zero, but since the number of solar and battery cells is discrete it is not possible. Note that this excess power can be used to make unexpected maneuvers, like climbing above mission altitude for example. Figure 9, depicts the final layout of the airplane.

4 CONCLUSION

In this paper a methodology to design a solar airplane is presented. The methodology is divided into two main phases. The first one tackles the conceptual design, where the initial airplane sizing and the best combination of airfoils for the wing and tail are obtained as starting points for a more detailed analysis. This phase builds on Noths' work by adding the capability to calculate the aerodynamic coefficients of the wing, tail and consequently the airplane itself by interpolating the aerodynamic polars of the airfoils. It enables the investigation of the defined design space to obtain an initial good design. The second phase gives room to a more detailed design where specific characteristics of the airplane components are considered, as well as the energy balance throughout the day. A new model for the airframe mass is also created to provide a better estimate of the airplane mass during the analysis.

Rúben D.A. Santos, Anuj Regmi and Pedro V. Gamboa
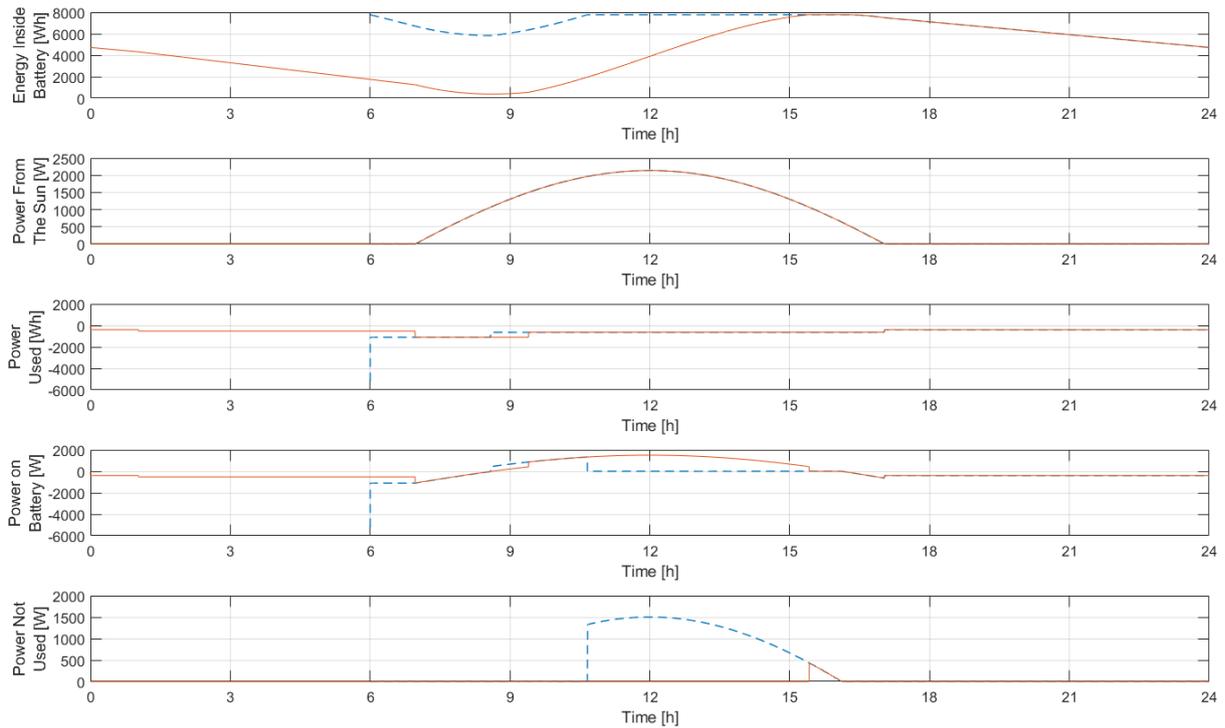
Figure 8: Energy and power flow during the first day (blue dashed line) and the following 24-hour periods (orange line).
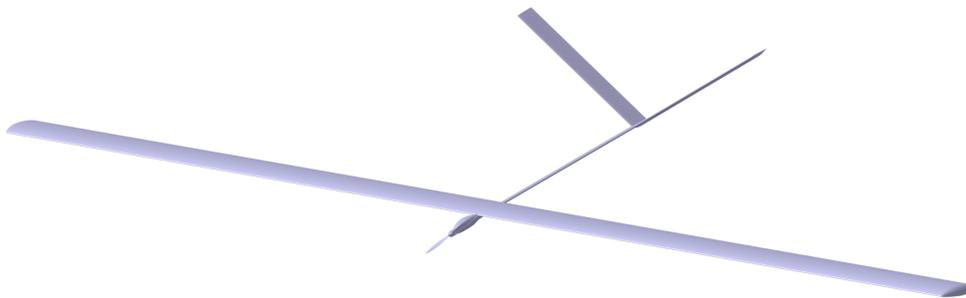
Figure 9: Final layout of the airplane.

With the developed design methodology, a solar UAV capable of perpetual flight was designed for a nighttime surveillance mission. The design passed through two developed phases and reached the main values of aspect ratio 17, wing area 22.4 m^2, total mass 101.183 kg and intalled power 2,140 W for a paylad mass of 0.400 kg. The final airplane's size and mass obtained in Phase 2 are far from the ones obtained in Phase 1. This happened because the mass model for the airframe in Phase 1 included a very large portion of small airplanes. One possible solution to this situation is to use only the larger airplanes in the mass model but the number of data points would rapidly decrease since most existing airplanes have very small wingspan (because they are mostly prototypes or sometimes proof of concept airplanes) or they have a complete different geometry, like the Helios family. This mass model is known to work only in a very narrow region so an error to the mass model was expected. In Phase 2 this problem is almost solved with the complete new model that accounts for every part of the airplane structure in some detail.

Designing a solar UAV is a complex multidisciplinary problem because the mass and

Rúben D.A. Santos, Anuj Regmi and Pedro V. Gamboa

power consumption of all components and the mission time greatly impacts the size of the airplane. Also, even for a very small payload a very large aircraft is needed to fly all year at a latitude of 30º. At this latitude, the day and night have, respectively, 10.2 and 13.8 hours in the winter solstice, with the addition that the sun rays are very inclined relative to the airplane's vertical axis. Also choosing the correct technology for the batteries (due to their energy density and cycle lifespan) and solar panel area ratio have large impacts on the size or even on the viability of the mission.

As a further development, a new structural analysis should be made in order to try and find a better airframe mass model. Validation of this tool could be achieved by, manufacturing structural parts to ensure the correct mass is being estimated, possibly finding better model coefficients for Phase 1. Another solution would be to integrate Phase 1 into Phase 2 making it possible to analyze several airplane configurations in greater detail.

ACKNOWLEDGEMENTS

REFERENCES

[1] R. Boucher. History of solar flight. In *20th joint propulsion conference*, page 1429, 1984.

[2] H. Bruß. *Solar-Modellflug: Grundlagen, Entwicklung, Praxis.* Verlag für Technik und Handwerk, 1991.

[3] D. Howe. The design of the aeroplane. *The Aeronautical Journal*, 106(1062):459–459, 2002.

[4] Airbus Zephyr Solar High Altitude Pseudo-Satellite flies for longer than any other aircraft during its successful maiden flight. Avaiable online: https://www.airbus.com/newsroom/press-releases/en/2018/08/Airbus-Zephyr-Solar-High-Altitude-Pseudo-Satellite-flies-for-longer-than-any-other-aircraft.html (accessed on 23 June 2021).

[5] V. Isaienko, V. Kharchenko, M. Matiychyk, and I. Lukmanova. Analysis of layout and justification of design parameters of a demonstration aircraft based on solar cells. In *E3S Web of Conferences*, volume 164, page 13007. EDP Sciences, 2020.

[6] P. Oettershagen, A. Melzer, T. Mantel, K. Rudin, T. Stastny, B. Wawrzacz, T. Hinzmann, S. Leutenegger, K. Alexis, and R. Siegwart. Design of small hand-launched solar-powered UAVs: From concept study to a multi-day world endurance record flight. *Journal of Field Robotics*, 34(7):1352–1377, 2017.

[7] A. Noth. *Design of solar powered airplanes for continous flight.* PhD thesis, ETH Zurich, 2008.

Rúben D.A. Santos, Anuj Regmi and Pedro V. Gamboa

[8] R. Boucher. Project sunrise-a flight demonstration of astro flight model 7404 solar powered remotely piloted vehicle. In *15th Joint Propulsion Conference, AIAA-79-1264, Las Vegas, Nevada*, 1976.

[9] J. Gedeon. Some thoughts on the feasibility of a solar-powered plane. *Technical Soaring*, 6(1):11–18, 1980.

[10] E. Schoberl. Solar-powered aircraft design. *Technical Soaring*, 15(2):38–47, 1989.

[11] E. Schoeberl. Possibilities and requirements for long endurance high flying solar powered platforms. *Technical Soaring*, 23(3):66–70, 1999.

[12] A. J. Colozza, D. A. Scheiman, and D. J. Brinker. Gaas/ge solar powered aircraft. *SAE Transactions*, 108:49–54, 1999. ISSN 0096736X, 25771531. URL http://www.jstor.org/stable/44729381.

[13] F. Irving and D. Morgan. The feasibility of an aircraft propelled by solar energy. In *2nd International Symposium on the Technology and Science of Low Speed and Motorless Flight*, page 1042, 1974.

[14] M. Bailey and M. Bower. High altitude solar power platform. [aircraft design analysis]. 1992.

[15] D. W. Hall and S. A. Hall. Structural sizing of a solar powered aircraft. Technical report, NASA, 1984.

[16] S. A. Brandt and F. T. Gilliam. Design analysis methodology for solar-powered aircraft. *Journal of Aircraft*, 32(4):703–709, 1995.

[17] A. Weider, H. Levy, I. Regev, L. Ankri, T. Goldenberg, Y. Ehrlich, A. Vladimirsky, Z. Yosef, and M. Cohen. Sunsailor: solar powered UAV. *Technion IIT, Haifa, Israel*, 2006.

[18] A. C. Marta and P. V. Gamboa. Long endurance electric UAV for civilian surveillance missions. *29th Congress of the International Council of the Aeronautical Sciences, St. Petersburg, Russia*, page 19, 2014.

[19] M. Drela. Xfoil: An analysis and design system for low reynolds number airfoils. In *Low Reynolds number aerodynamics*, pages 1–12. Springer, 1989.

[20] J. Gundlach. *Designing unmanned aircraft systems: a comprehensive approach.* American Institute of Aeronautics and Astronautics, 2012.

[21] J. C. C. Sousa. Solar system for a long endurance electric UAV. Master's thesis, Universidade da Beira Interior, 2015.

SURROGATE MODELLING OF PROPELLER NOISE IN UNSTEADY LOAD CONDITIONS

Pedro M. Neto[1*] and Pedro V. Gamboa[1]

1: Centre for Mechanical and Aerospace Science and Technologies (C-MAST-UBI)
Faculdade de Engenharia
Universidade da Beira Interior
6200-001 Covilhã
pedro.matos.neto@ubi.pt, pgamboa@ubi.pt, http://www.ubi.pt

Abstract. *This paper presents the formulation and implementation of a numerical propeller noise analysis tool. The tool is capable of estimating the noise produced by a propeller under different inflow conditions and is designed to be used in propeller geometry optimization problems where the inflow conditions, observer position and velocity and the range of propeller geometric characteristics are specified. The code uses Latin Hypercube Sampling to select a space-filling set of propellers; Then, the overall sound pressure level (OASPL) for these samples is calculated using a formulation of the Ffowcs-Williams and Hawkings (FW-H) equation with loading data from a modified Blade Element Momentum (BEM) theory; A Kriging model is then produced and made available to the user for direct analysis or further implementation in optimization problems. Validation cases are presented for all modules of the tool and a study case with a propeller operating in a push configuration is analysed.*

Keywords: Propeller noise, Unsteady load, Disturbed airflow, Blade Element Momentum Theory, Farassat 1A, Surrogate models

Pedro M. Neto and Pedro V. Gamboa

1 INTRODUCTION

The recent development of electric technologies has been a catalyst to the electrification of air transport. In addition, unmanned aerial vehicles (UAVs) have been growing in popularity and will be used in a broad spectrum of missions. Urban air mobility has also been the focus of several organizations' research and is thought to play an important role on the future of urban mobility [1]. These rapidly expanding technologies require the usage of propellers to generate thrust hence the importance of the study of propellers for the future of aviation. Tightening noise regulations and the possibility of operation near urban areas have lead to interest in the study of propeller noise generation.

The noise generated by a propeller can be split in two main components: broadband noise and harmonic/rotational noise [2]. Broadband noise consists of noise generated by stochastic sources such as unsteady pressure disturbances caused by turbulence. This component does not contribute significantly to the total noise of aircraft propellers in flight and can be disregarded [3]. Rotational noise is comprised of two main components: thickness noise and loading noise. Thickness noise is generated by the displacement of air caused by the movement of the propeller blades and loading noise is generated by the forces applied on the fluid by the propeller blade.

Current propeller noise models are based on the Ffowcs Williams and Hawkings (FW-H) equation [4]. This equation was derived from the Navier-Stokes equations and comprises three different noise sources: a quadrupole source in the volume surrounding the noise emitting body and monopole and dipole sources on the surface of the noise emitting body. Farassat's Formulation 1A is a widely used solution of the FW-H equation that neglects the quadrupole volume sources [5]. These sources do not represent a significant contribution to propeller noise at subsonic speeds [6]. Farassat's formulations of the FW-H equation have been implemented in programs such as the Aicraft Noise Prediction Program (ANOPP, [7]), the Dunn-Farassat-Padula Advanced Turboprop Prediction program (DFP-ATP, [8]), WOPWOP, [9] and PSU-WOPWOP, [10].

One of the required parameters to solve the FW-H equation is blade loading. Blade element momentum (BEM) theory is one of the simplest and most commonly used tools to estimate propeller performance. The first developments of propeller theory started in the 19th century [11] however, it was not until 1935 that the current BEM theory in its classic form was developed [12]. This theory remains popular due to its simplicity and effectiveness at describing the complex propeller-fluid interaction. Corrections to the classic BEM theory have also been developed and implemented with success in programs such as AeroDyn [13].

Optimization problems usually require running a computationally expensive engineering function repeatedly with different input parameters. Surrogate models are used to emulate the expensive engineering model's behaviour without the slow, expensive computational work and, therefore, reduce optimization time and costs. The Kriging model, originally developed for geostatistics applications [14] has seen widespread use and is usually preferred for most generic applications [15–17]. Other surrogate modelling techniques such as Polinomials and Radial Basis Functions (Gaussian, Multiquadric, Thinplate, Spline, Cubic and Linear) have also showed great robustness [16]. The adequacy of a surrogate to a certain engineering problem depends on the data set noise, number of samples, number of variables and linearity of the problem.

The efficacy of a surrogate is highly dependent on the quality of the samples of the

Pedro M. Neto and Pedro V. Gamboa

expensive engineering function which are used to train the surrogate. Several methods have been developed to generate an evenly distributed efficient sampling plan in the design space. The most common method is Latin Hypercube Sampling (LHS) known for its conceptual simplicity and space filling qualities when optimised [15, 17]. Adaptive sampling plans [18] are an alternative to LHS that use space-filling criteria to dynamically update the sampling plan and the surrogate. The Expected Improvement (EI) criteria selects the next sampling location that is expected to improve the surrogate model the most [15].

The objective of this paper is to describe the creation of a tool capable of predicting the noise generated by different innovative configurations and designs in a quick and accurate way. This tool also has the capability to predict the noise generated when the propeller operates in disturbed airflow caused, for example, by the wing in a push configuration. Such consideration is important since an innovative aircraft design often deviates from the traditional fuselage or wing mounted pull propeller. This tool's ability to be easily implemented in aircraft optimization problems, where propeller noise is a design criterium, is also a fundamental aspect.

This paper briefly describes the theoretical formulation of the tool and its implementation in a python computer code. Some validation test cases of the different modules are also presented. To conclude, the analysis of a case study with a propeller operating in a push configuration is presented.

2 THEORETICAL FORMULATION

2.1 The Farassat 1A formulation

Farassat's 1A formulation as presented by Brentner [9] (Eq. 1) is used to calculate acoustic pressure calculation in a given observer position and time instant:

$$p'(\vec{x}, t) = p'_T(\vec{x}, t) + p'_L(\vec{x}, t)$$

$$4\pi p'_T(\vec{x}, t) = \frac{1}{c} \int_{f=0} \left[\frac{\rho \dot{v}_n}{r(1 - M_r)^2} \right]_{ret} dS + \int_{f=0} \left[\frac{\rho v_n (r\dot{\vec{M}}\hat{r} + cM_r - cM^2)}{r^2(1 - M_r)^3} \right]_{ret} dS$$

$$4\pi p'_L(\vec{x}, t) = \frac{1}{c} \int_{f=0} \left[\frac{\dot{\vec{l}}\hat{r}}{r(1 - M_r)^2} \right]_{ret} dS + \int_{f=0} \left[\frac{l_r - \vec{l}\vec{M}}{r^2(1 - M_r)^2} \right]_{ret} dS \tag{1}$$

$$+ \frac{1}{c} \int_{f=0} \left[\frac{l_r(r\dot{\vec{M}}\hat{r} + cM_r - cM^2)}{r^2(1 - M_r)^3} \right]_{ret} dS$$

where p'_T and p'_L denote, respectively, the acoustic pressure generated due to thickness and loading; v, M, l and r denote, respectively, the surface velocity, local Mach number, pressure loading and distance to the observer. Subscripts n and r denote that the property must be evaluated in the normal direction to the surface and in the observer direction, respectively. The terms in square brackets must be evaluated in the retarded time. All integrals are calculated at the surface (f=0).

Since this expression requires detailed pressure data on the source's surface, prior computationally expensive simulations are required. To overcome this, compact formulations

Pedro M. Neto and Pedro V. Gamboa

can be developed where the distributed pressure load is simplified to a distributed radial-wise load [19]. The compact approach was applied to the loading term of Eq. 1:

$$
4\pi p'_L(\vec{x}, t) = \frac{1}{c} \int \left[\frac{\dot{\vec{L}}\hat{r}}{r(1 - M_r)^2} \right]_{ret} dy + \int \left[\frac{L_r - \vec{L}\vec{M}}{r^2(1 - M_r)^2} \right]_{ret} dy
$$
$$
+ \frac{1}{c} \int \left[\frac{L_r(r\dot{\vec{M}}\hat{r} + cM_r - cM^2)}{r^2(1 - M_r)^3} \right]_{ret} dy
$$

(2)

where L and y denote the radial-wise distributed load and the radial position coordinate, respectively.

The acoustic pressure must be measured in a range of points from which the overall sound pressure level (OASPL) is calculated [20, 21]:

$$
OASPL = 20 \log_{10} \left(\frac{RMS(p')}{p_{ref}} \right)
$$

(3)

where RMS is the root mean square of the acoustic pressure, p', and p_{ref} is the reference pressure of $10^{-5}\ Pa$.

2.2 Blade Element Momentum (BEM) theory

This model divides a propeller blade in a set of independent blade elements which are analysed independently as discrete wings. It is assumed that the flow in a given element is two-dimensional and therefore there is no interaction between the flow of adjacent elements. The effective flow velocity at the element is the sum of the incoming flow velocity, which includes the induction effects caused by the blade element, and the blade element velocity. The theory was initially developed with the assumption of perfectly axial flow. This condition may be relaxed if the proper corrections are applied [13]. In this present work, modified BEM theory is applied to non-uniform inflow conditions. Skewed flow corrections are also applied locally at each element.

The velocity triangle from Fig. 1 is used to determine the local relative velocity, U, and respective inflow angle, ϕ. The two components of the induced velocity are denoted v_a and v_t for the axial and tangent directions, respectively. The components caused by movement of the propeller in the incoming airflow are $U_a = u_a$ and $U_t = \omega r - u_t$ for the axial and tangent directions, respectively, where u_a and u_t are components of the incoming airflow and ωr is caused by the rotation of the blade element.

The axial and tangential induction factors are calculated, respectively, with Eqs. 4 and 5.

$$
a_a = \frac{v_a}{U_a}
$$

(4)

$$
a_t = \frac{v_t}{U_t}
$$

(5)

The local relative air velocity and inflow angle can therefore be calculated by:

$$
U = \sqrt{(U_a(1 + a_a))^2 + (U_t(1 - a_t))^2}
$$

(6)

$$
\phi = \arctan \left(\frac{U_n(1 + a_a)}{U_t(1 - a_t)} \right)
$$

(7)

Pedro M. Neto and Pedro V. Gamboa
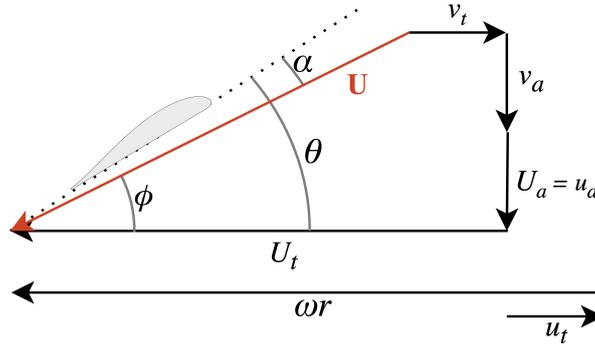
Figure 1: Velocity triangle at an arbitrary blade element.

The local angle of attack, α, is:

$$\alpha = \phi - \theta \tag{8}$$

where θ is the local incidence angle.

With the local angle of attack and Reynolds number, the lift and drag aerodynamic coefficients, C_l and C_d can be sourced. These coefficients are then projected in the axial and tangential directions:

$$C_a = C_l \cos\phi - C_d \sin\phi \tag{9}$$

$$C_t = C_l \sin\phi + C_d \cos\phi \tag{10}$$

A correction factor is implemented to account for blade tip vortices [12]:

$$F = \frac{2}{\pi} \arccos\!\left(e^{-\frac{B}{2}\frac{R-r}{r\sin\phi}}\right) \tag{11}$$

where R is the propeller radius and r the local radius. This correction factor, along with the local solidity ratio, $\sigma = (Bc)/(2\pi r)$, are used to calculate the induction coefficients:

$$a_a = \left(\frac{4F\sin^2\phi}{\sigma C_a} - 1\right) \tag{12}$$

$$a_t = \left(\frac{4F\sin\phi\cos\phi}{\sigma C_t} + 1\right) \tag{13}$$

In other to include skewed flow effects the same correction used in AeroDyn [13] was used:

$$a_{a_{skew}} = a_a \left(1 + \frac{15\pi}{32}\frac{r}{R}\tan\frac{\chi}{2}\cos\psi\right) \tag{14}$$

where ψ is the azimuth angle measured from the most downwind position and χ is the wake skew angle.

2.3 Surrogate model

The computational time required to solve the previous models thousands of times for every propeller-inflow combination is considerably high. In order to feasibly apply the methodology to real engineering situations, the creation of a more time efficient surrogate is fundamental.

The construction of a surrogate model comprises of three different stages [15]. First, a set of sample locations must be generated; Secondly, the surrogate model is constructed from the sampled values of the engineering model on the sample locations previously selected; The last stage is the validation of the surrogate against the original model.

2.3.1 Latin Hypercube Sampling (LHS)

Latin Hypercube Sampling originates from the concept of Latin Squares which are a square grid of any dimension where only one point in each row and column is marked. This characteristic is called stratification and is a fundamental concept for a good sampling plan.

To construct a Latin Hypercube, the design space is divided into a series of bins of equal space. Then, a point is placed in each bin so that the projection of two given points along an axis does not coincide. This method yields a random stratified sampling plan but it does not guarantee an evenly filled design space. One way to overcome this drawback is the usage of a quality criterion to evaluate the sampling plan and implement an optimization routine to seek an optimal Latin Hypercube [15, 22].

2.3.2 Kriging

The Kriging model, formulated by Matheron [14] based on the work of Krige [23], is widely used in engineering optimization applications.

$$\psi^{(i)} = \exp\left(-\sum_{j=1}^{k} \theta_j |x_j^{(i)} - x_j|^{p_j}\right) \tag{15}$$

This method uses the basis function in Eq. 15 which is similar to the Gaussian basis function differing in the fact that Kriging allows different widths of the basis function, θ, and exponents, p, to every variable. The building of a Kriging model involves selecting the set of values for θ and p that provides the best estimate of the engineering function. This is done by maximizing the concentrated ln-likelihood function [15] which depends on the parameters θ and p:

$$\ln(L) \approx -\frac{n}{2}\ln(\hat{\sigma}^2) - \frac{1}{2}|[\Psi]| \tag{16}$$

Due to being easy to compute and non-differentiable, the recommended way to optimize this function is through a global search model such as a genetic algorithm.

Once the ordinary Kriging model is built, estimates can be made at previously unsampled locations in the design space:

$$\hat{y}(x) = \hat{\mu} + [\psi]^T [\Psi]^{-1}(\{y\} - \{1\}\hat{\mu}) \tag{17}$$

2.3.3 Testing the surrogate

When possible, a fresh space-filling set of data with around 25% of the size of the training data should be used to evaluate the accuracy of the surrogate [24]. Different metrics like the Root Mean Square Error (RMSE) or the correlation coefficient (r^2) are commonly used [15].

$$RMSE = \sqrt{\frac{1}{n}\sum_{i=0}^{n}(y^{(i)} - \hat{y}^{(i)})^2} \tag{18}$$

Pedro M. Neto and Pedro V. Gamboa

$$r^2 = \left(\frac{n \sum_{i=0}^{n}(y^{(i)}\hat{y}^{(i)}) - \sum_{i=0}^{n} y^{(i)} \sum_{i=0}^{n} \hat{y}^{(i)}}{\sqrt{\left[n \sum_{i=0}^{n} y^{(i)2} - (\sum_{i=0}^{n} y^{(i)})^2 \right] \left[n \sum_{i=0}^{n} \hat{y}^{(i)2} - (\sum_{i=0}^{n} \hat{y}^{(i)})^2 \right]}} \right)^2 \qquad (19)$$

3 CODE DESCRIPTION

The code was designed to be as modular as possible in order to facilitate future improvements and is structured as presented in Fig.2. The four variables to be studied are: the number of blades, propeller radius, blade chord and blade incidence angle.

The user must provide the flow conditions in the propeller plane in the form of a velocity profile table. In addition, air density, dynamic viscosity and the speed of sound must be specified. The observer position and velocity relative to the propeller are also required. A base propeller design must be introduced by selecting the number of blades and a series of sections which are defined by their radial position, chord, incidence and airfoil.

In addition to the operating thrust, the design space for each propeller geometry variable must also be specified. For the number of blades, a range of acceptable solutions must be declared; For the chord and radius, the range for a multiplier factor by which the values of the base propeller are multiplied must be set; For the blade incidence angle, a range of increment angles, which can be negative to decrease blade incidence, must be set.

Once the space filling sampling plan is generated, the overall sound pressure level for each propeller at the determined flow and thrust conditions is calculated. For the purpose of acoustic pressure calculation, propeller blades are divided in a set of 20 radial-wise and 40 chordwise evenly spaced elements. This was found to be the best compromise between accuracy and computational requirements and is in line with previous works [25, 26].

The aerodynamic coefficients are either calculated in-code by an open-source python XFOIL port or imported from an external source. Due to the possibility of encountering extreme angles of attack, these polars are extended to 360 degrees using Viterna's method [27].

Evenly spaced observation times are selected during an entire rotation of the propeller. It was found that results converged at 128 samples per rotation which is considerably lower than the 512 points suggested by Brentner [26]. It is important to use a number of base two in this process to ensure optimal Fast Fourier Transform (FFT) performance when required in the validation process.

The number of sampling points required for the sampling plan was found to be highly dependent on the range of the variables. The user is responsible for tuning this value such that the surrogate testing metrics are satisfactory. A quality surrogate should have a value of normalized RMSE of up to 10% and a value of correlation coefficient greater than 0.9 [15].

4 MODEL VALIDATION

In order to validate de tool, results from all modules were compared to results available in the literature. Validation cases are presented for thrust in axial conditions, thrust in unsteady load conditions and propeller noise.

Pedro M. Neto and Pedro V. Gamboa
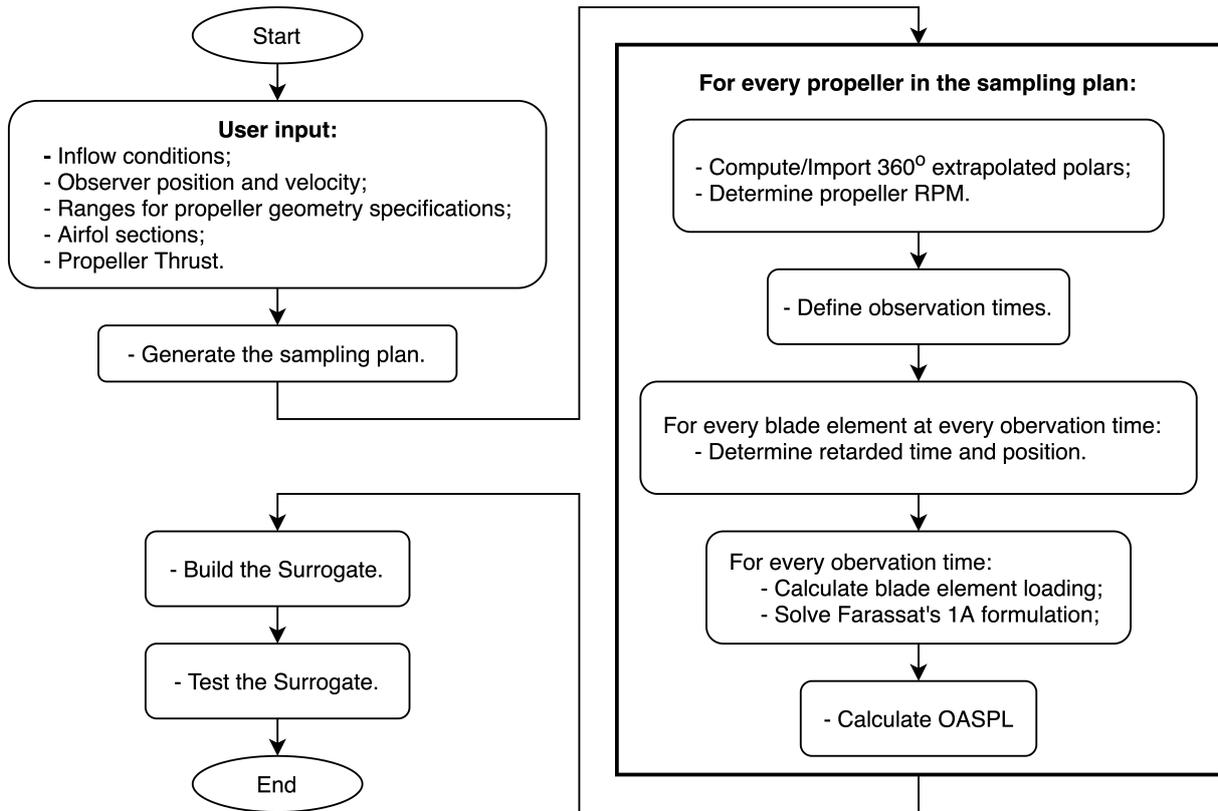
Figure 2: Code structure.

4.1 Axial flow thrust

For the axial flow blade loading case, thrust comparisons were made with experimental results available in the literature and JBLADE [28–30]. A detailed description of two of the propellers tested can be seen in Fig.3. The two bladed propeller from Fig. 3a uses the NACA 4415 airfoil and the three bladed propeller from Fig. 3b uses the RAF 6 airfoil.

(a) Validation case 1 [31].

(b) Validation case 2 [32].
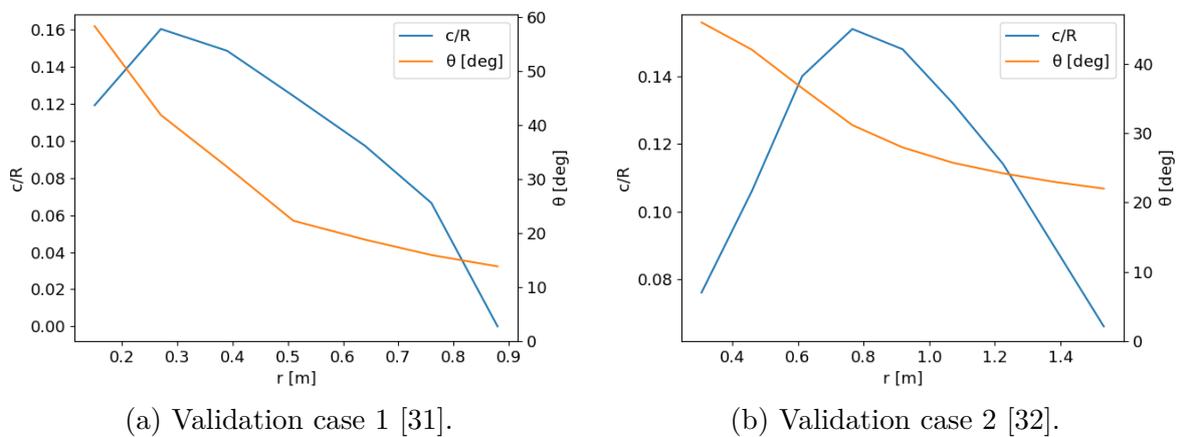
Figure 3: Propeller geometry used in the axial thrust validation cases.

The results for the thrust coefficient against the advance ratio are presented in Fig.4. The operating conditions of the propellers are the same as the original references [31, 32].

Pedro M. Neto and Pedro V. Gamboa

(a) Validation case 1 [31].　　　　　　(b) Validation case 2 [32].
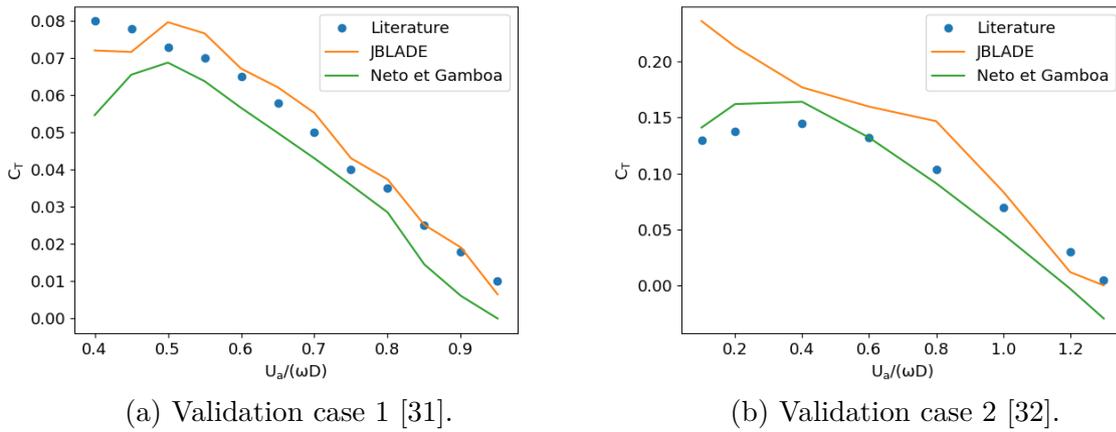
Figure 4: Thrust coefficient against advance ratio.

The results correlate well with the literature and JBLADE analysis. In some cases, such as validation case 1, there is a tendency to under predict the thrust coefficient at lower advance ratios which suggests that the extended polar method used may not be modelling the high angle of attack aerodynamic coefficients adequately in all situations.

4.2　Thrust in unsteady load conditions

This operation condition was checked using experimental data of propellers operating in yaw available in the literature.

The thrust coefficient while operating at a 15 degree angle of yaw was compared to experiments [33]. The detailed geometry description of the NACA 44- series airfoil, two bladed propeller is shown in Fig.5.
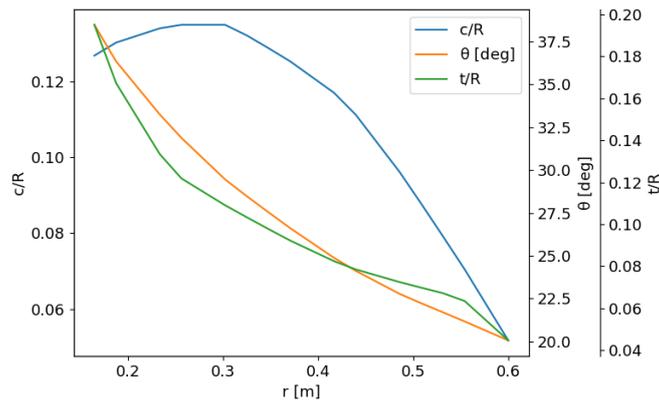
Figure 5: Propeller geometry used in the first unsteady load validation case.

The experimental and numerical values of C_T against $U_a/(nD)$ are plotted in Fig.6. The overall trend of the numerical results is coherent with the experiment, however, a certain degree of over prediction at low advance ratios and under prediction at high advance ratios occurs. Since this phenomenon also occurred in the second case of axial flow validation (Fig.4b), it is believed to be a limitation of this implementation of BEM theory and not a result of the non-axial flow conditions.

Pedro M. Neto and Pedro V. Gamboa
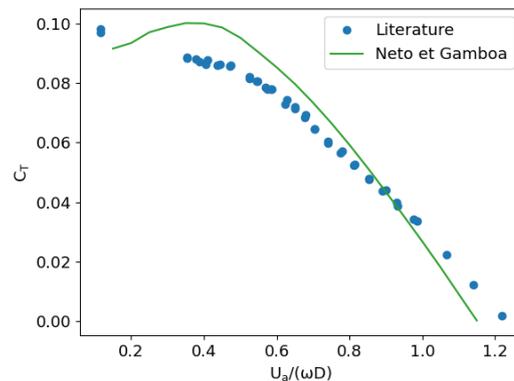
Figure 6: Thrust coefficient against advance ratio.

4.3 Propeller noise

The last step to ensure the validity of the model is to compare results from the noise prediction module.

Firstly, noise predictions were compared to experimental measurements and predictions from ANOPP [34]. Since detailed geometry of the two bladed 80 inch propeller was not made available, it was decided to use the dimensionless geometry from the Hamilton-Standard 1C1-0 propeller show in Fig.7.
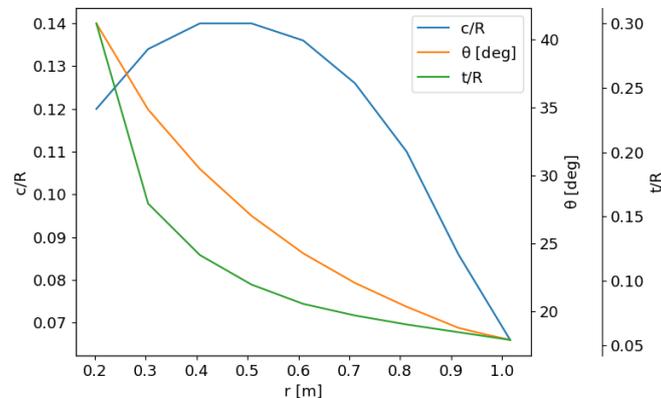
Figure 7: Propeller geometry used in the first noise validation case [32].

The three different test conditions considered are described in Tab.1. For each test condition, noise measurements were made at a 4 m distance from the propeller hub in the propeller plane and ahead of the propeller, at a 60 degree angle from its axis.

Table 1: Conditions for test cases [34].

Case	ω [rpm]	U_a [m/s]	Incidence at .75R [deg]
1	2400	77.2	22.3
2	2700	77.0	22.0
3	2700	77.2	21.2

The results, shown in Tab.2, are similar to the measured in the experiment and pre-

Pedro M. Neto and Pedro V. Gamboa

dicted by the more advanced noise prediction code in ANOPP. It must be noted that a certain degree of discrepancy is to be expected since the propeller geometry that was used does not represent the real geometry of the propeller from the experiments. In Case 1, where the predicted OASPL differs the most from the literature, the predicted thrust is also 10% greater than the measurements which would increase loading noise and, therefore, the overall sound pressure level.

Table 2: Comparison of OSAPL prediction to ANOPP and experimental values [34].

Case	Experimental [dB]	ANOPP [dB]	Neto et Gamboa [dB]
1 (in-plane)	113.1	113.8	117.6
2 (in-plane)	123.6	123.2	120.4
3 (in-plane)	122.7	122.5	120.1
1 (out-of-plane)	108.5	108.1	115.1
2 (out-of-plane)	115.6	116.3	117.4
3 (out-of-plane)	115.7	116.2	117.2

Comparisons of the directivity of the noise produced with experimental data [35] were also made. The directivity of the blade passing frequency (BPF) of an APC 13 X 6.5E propeller is compared in Fig.8 where 0 degrees coincides with the axial direction ahead of the propeller and 180 degrees coincides with the axial direction behind the propeller.

(a) Experimental results [35].

(b) Numerical results.
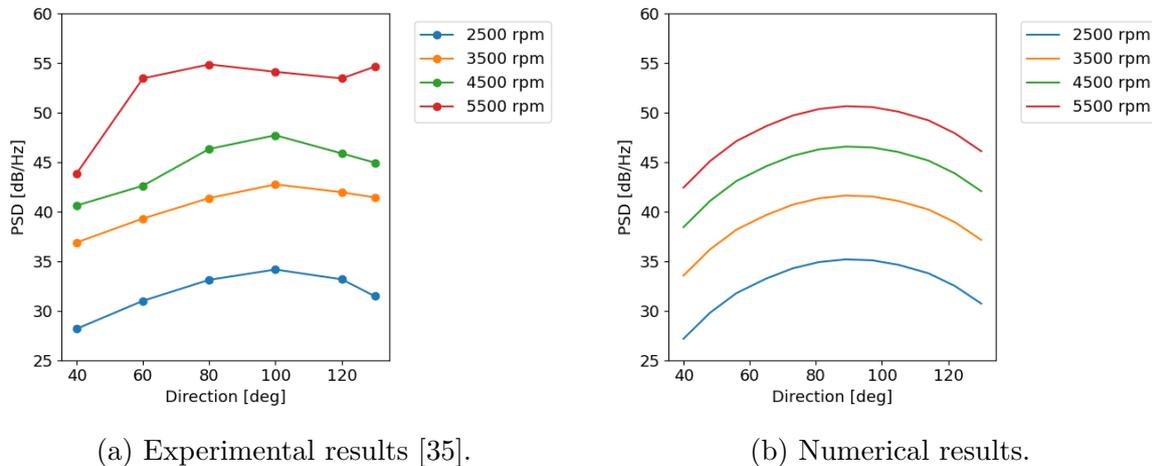
Figure 8: Directivity of power spectral density (PSD) of the APC 13 X 6.5E propeller at BPF.

Overall, there is an agreement between the numerical model and the experimental measurements. For the three lower propeller angular velocities, numerical values tend to be up to 3 dB/Hz lower than numerical values. However, at 5500 rpm, the measurements differ considerably from the numerical prediction. This may be a result of experimental errors, since at 5500 rpm the behaviour of the PSD directivity is much different than other angular velocities.

Overall, it can be said that the model is capable of making good predictions and follows the experiments both in absolute value and overall behaviour. It should also be noted that the model shows promising results for both small and large aircraft propellers.

5 CASE STUDY

In order to illustrate the general behaviour of the noise emitted by an aircraft propeller under different conditions and the impact of changing certain design elements, a case study was created. In this case, the base propeller uses the blade geometry from the Navy planform 3790, represented in Fig.9. All simulations were performed at sea level in horizontal flight at 75 m/s. Noise measurements were taken from an observer 15 m directly below the propeller hub.
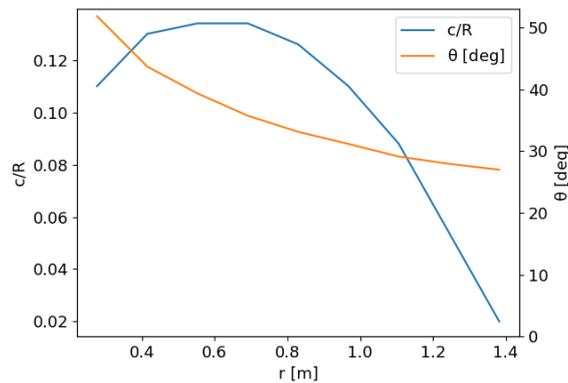
Figure 9: Propeller geometry used in the test case [32].

In order to compare the OASPL produced in free stream and disturbed airflow, calculations were made at different thrust levels using a 3 bladed propeller at 75 m/s. For the disturbed airflow case, the velocity profile 0.5 m behind the trailing edge of a NACA 23013 airfoil with 1.84 m chord at a 0 degree angle of attack was simulated in Ansys Fluent using the k-omega turbulence model.

From Fig.10 it can be concluded that the OASPL emitted by a propeller is influenced by the inflow velocity profile and generally increases when thrust is increased. Previous work has determined that at a given rotational velocity, both thrust and noise tend to increase when the propeller operates in a wake [36, 37]. However, results are seldom presented at constant thrust conditions.
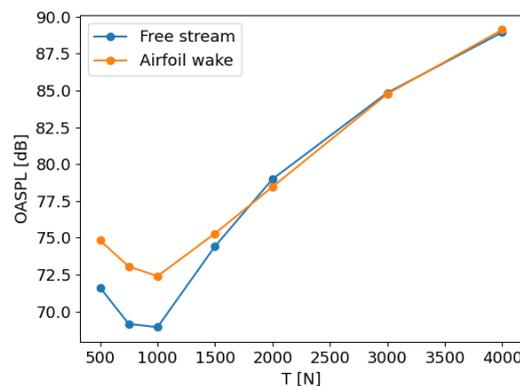
Figure 10: OASPL at different thrust levels in a wake and free stream.

Pedro M. Neto and Pedro V. Gamboa

5.1 Building and Using the Surrogate

Having concluded that the OASPL tends to increase when operating in a wake, a surrogate was built for a propeller operating in the wake conditions described above at 1500 N of thrust. The boundaries for the design space are represented in Tab.3.

Table 3: Design space used in the surrogate.

Variable	Lower boundary	Upper boundary
Number of blades	2	6
Chord ratio	0.5	2
Radius ratio	0.5	2
Twist increment [deg]	-10	10

In order to better understand the model and the surrogate, the process was initiated with a simple study where different surrogates were generated using a range of LHS of different sizes. These surrogates were then tested against a set of 50 space filling samples gathered from the original model. The results, as presented in Fig.11, show that although there is a clear trend of model refinement as the number of points increases, there is some degree of volatility in the evaluation parameters. This is a direct result of the nature of the process of generating the LHS. Since every LHS is unique and random, it is possible for a sampling plan to be "lucky" and hit more relevant points in the engineering function while a different sampling plan with the same number of points might be "unlucky" and hit less relevant points in the engineering function. With the increase in the number of points, in addition to the increased overall fidelity, the influence of "luck" decreases and the volatility also decreases.

(a) Correlation coefficient.   (b) Normalized RMSE.
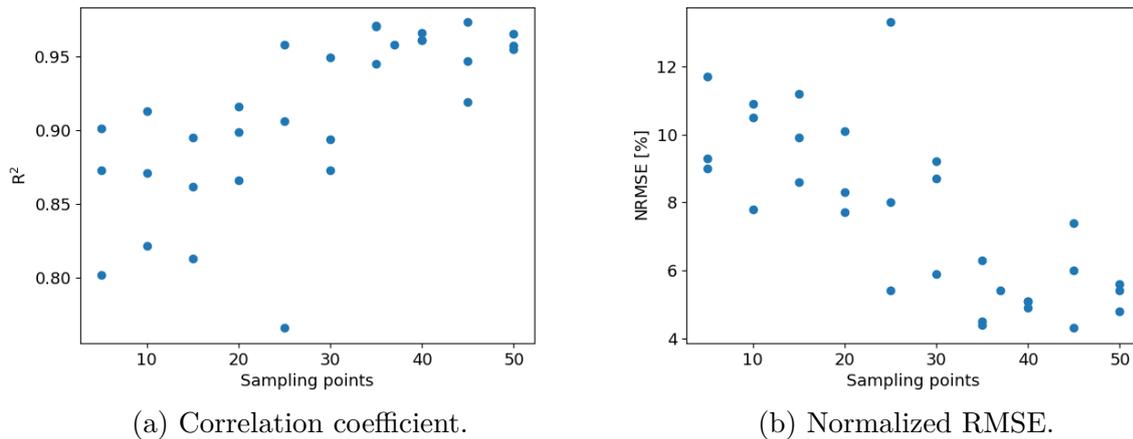
Figure 11: OASPL at different design specifications.

The strategy used was to select a number of points that would ensure the surrogate would meet the threshold criteria of normalised RMSE up to 10% and a correlation coefficient greater than 0.9 [15] most of the time, hence the decision to use 50 sample points in the final surrogate. The typical validation process with a space filling set of samples of the engineering function with 25% the number of points used in the surrogate was still kept to ensure the surrogate met the threshold and was not "unlucky".

The surrogate was built using 50 sample points and was deemed representative of the engineering function due to having a correlation coefficient of 0.99 and a normalised RMSE of 4.1%. The quality of this surrogate was evaluated using 12 samples of the original function from a space filling LHC.

In Fig.12, the OASPL at different design specifications for a two bladed propeller is represented. It can be observed that this propeller base geometry in these operating conditions tends to favour lower blade radius. Smaller blade chords are also generally favoured. These conclusions favour an overall reduction in the volume of the propeller blades which indicates that under these conditions, thickness noise is the main source of acoustic pressure. Overall, blade incidence did not significantly influence the results. The base propeller's incidence was favoured at small blade radii and higher blade incidence was favoured at higher blade radii. The favouring of the increase in incidence at high propeller radii can be explained by the reduction in propeller rotational velocity and, therefore a reduction in propeller thickness noise which is prevalent due to the increased amount of air displaced by the larger blades.
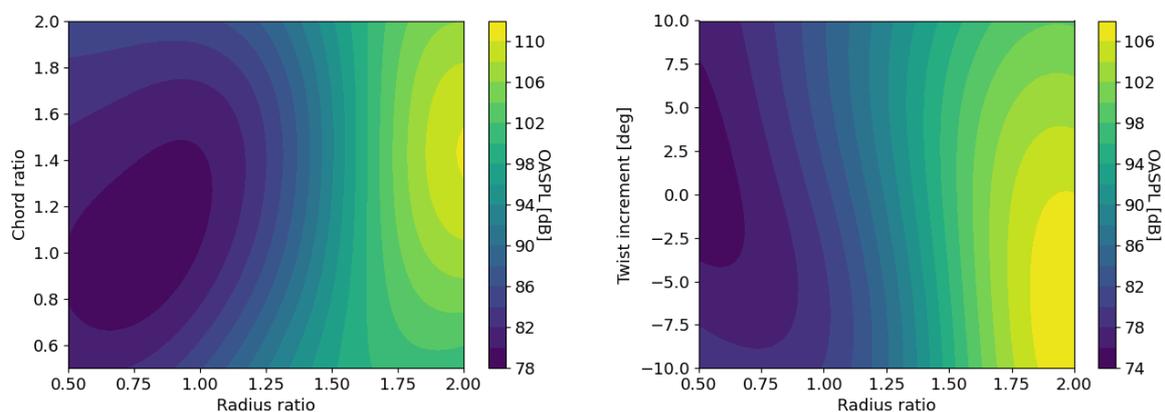
(a) Twist increment = 0; 2 blades. (b) Chord ratio = 1; 2 blades.

Figure 12: OASPL at different design specifications.

In Fig.13, the OASPL for different numbers of blades at different blade radii is compared. For larger radii, an increase in the number of blades leads to a considerable reduction in noise which is a direct result of the decrease in blade loading and, therefore the decrease in loading noise. For smaller blade radii, this is not always the case indicating that at a certain point, the loading noise decrease caused by the increasing number of blades is offset by the increase in thickness noise caused by the increase in the volume of air displaced by the propeller.

6 COMPUTING TIME COMPARISON

In order to determine if the construction of a surrogate is a good approach to this problem, a comparison of the processing times for the case study was performed.

Using the times from Tab.4, Fig.14 was created. Since computing a point using the surrogate is essentially instantaneous, using the surrogate is always more computationally efficient if the number of desired points is greater than the number of points used to build and validate the surrogate. In this case, if the model were to be used in a parametric
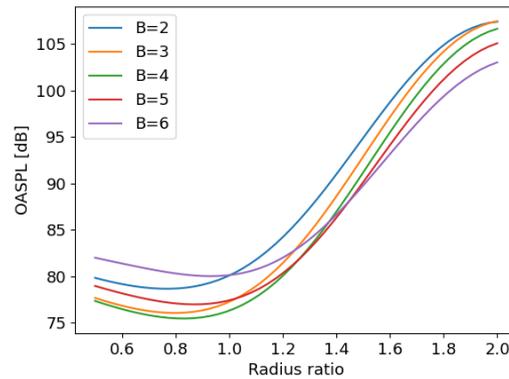
Figure 13: OASPL at different blade counts and blade radii. Twist increment $= 0$; Chord ratio $= 1$.

Table 4: Computing time required at different stages.

Step	Computing time [s]
Compute OASPL directly at a point	187.5
Train and validate the surrogate	4.9
Compute OASPL with the surrogate at a point	0.004

study or optimization study, the number of points required would most likely be greater than 62 and, therefore, using the surrogate would be the most efficient approach.
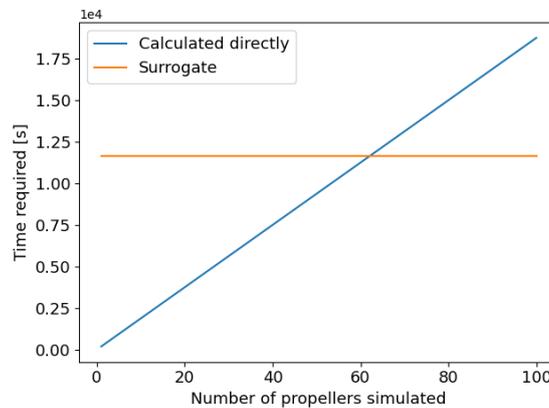
Figure 14: Required compute time for different numbers of simulated propellers.

7 CONCLUSIONS

A tool for the quick and accurate prediction of the aeroacoustic noise generated by a propeller has been developed using the FW-H equation, BEM theory and a Kriging surrogate. This tool was validated against experimental and numerical data available in the literature with promising results and was later used in a case study to showcase the tool's capabilities.

In the case study, it is observed that under the tests' conditions, the OASPL generated by a propeller is typically larger for a propeller operating in the wake of an airfoil. It is

also observed that a decrease in propeller radius and reasonable increase in the number of blades will result in the reduction of the noise generated by the propeller.

In future work, the integration of this tool in an aircraft preliminary analysis code and its usage in aircraft optimization problems could be valuable. In addition, the creation of a parallel model to evaluate the performance impact of the geometry changes caused by the noise reduction code is of great interest.

RESOURCES

The computer code, including the script used in section 5, is made available in a github repository: https://github.com/Pedr0Neto/propeller-noise-predictor [38].

REFERENCES

[1] D. P. Thipphavong, R. Apaza, B. Barmore, V. Battiste, B. Burian, Q. Dao, M. Feary, S. Go, K. H. Goodrich, J. Homola, et al. Urban air mobility airspace integration concepts and considerations. In *2018 Aviation Technology, Integration, and Operations Conference*, page 3676, 2018.

[2] K. S. Brentner and F. Farassat. Modeling aerodynamically generated sound of helicopter rotors. *Progress in Aerospace Sciences*, 39(2-3):83–120, 2003.

[3] W. Dobrzynski, H. Heller, J. Powers, and J. Densmore. Dfvlr/faa propeller noise tests in the german-dutch wind tunnel dnw. *DFVLR-IB*, 129(86):3, 1986.

[4] J. F. Williams and D. L. Hawkings. Sound generation by turbulence and surfaces in arbitrary motion. *Philosophical Transactions for the Royal Society of London. Series A, Mathematical and Physical Sciences*, pages 321–342, 1969.

[5] F. Farassat. Derivation of formulations 1 and 1a of farassat. Technical report, 2007.

[6] D. B. Hanson and M. R. Fink. The importance of quadrupole sources in prediction of transonic tip speed propeller noise. *Journal of Sound and Vibration*, 62(1):19–38, 1979.

[7] W. E. Zorumski and D. S. Weir. Aircraft noise prediction program theoretical manual: Propeller aerodynamics and noise. *Unknown*, 1986.

[8] F. Farassat, S. Padula, and M. Dunn. Advanced turboprop noise prediction based on recent theoretical results. *Journal of Sound and Vibration*, 119(1):53–79, 1987.

[9] K. S. Brentner. Prediction of helicopter rotor discrete frequency noise: A computer program incorporating realistic blade motions and advanced acoustic formulation. *Unknow*, 1986.

[10] K. S. Brentner, G. A. Bres, G. Perez, and H. E. Jones. Maneuvering rotorcraft noise prediction: A new code for a new problem. 2002.

[11] W. J. M. Rankine. On the mechanical principles of the action of propellers. *Transactions of the Institution of Naval Architects*, 6, 1865.

[12] H. Glauert. Airplane propellers. In *Aerodynamic theory*, pages 169–360. Springer, 1935.

[13] P. J. Moriarty and A. C. Hansen. Aerodyn theory manual. Technical report, National Renewable Energy Lab., Golden, CO (US), 2005.

[14] G. Matheron. Principles of geostatistics. *Economic geology*, 58(8):1246–1266, 1963.

[15] A. Forrester, A. Sobester, and A. Keane. *Engineering design via surrogate modelling: a practical guide*. John Wiley & Sons, 2008.

[16] M. R. Kianifar and F. Campean. Performance evaluation of metamodelling methods for engineering problems: towards a practitioner guide. *Structural and Multidisciplinary Optimization*, 61(1):159–186, 2020.

[17] R. Yondo, E. Andrés, and E. Valero. A review on design of experiments and surrogate models in aircraft real-time and many-query aerodynamic analyses. *Progress in Aerospace Sciences*, 96:23–61, 2018.

[18] N. Bartoli, T. Lefebvre, S. Dubreuil, R. Olivanti, R. Priem, N. Bons, J. R. Martins, and J. Morlier. Adaptive modeling strategy for constrained global optimization with application to aerodynamic wing design. *Aerospace Science and technology*, 90:85–102, 2019.

[19] F. Farassat. Linear acoustic formulas for calculation of rotating blade noise. *AIAA journal*, 19(9):1122–1130, 1981.

[20] L. L. Beranek et al. *Acoustics*. 1954.

[21] C. H. Hansen. Fundamentals of acoustics. *Occupational Exposure to Noise: Evaluation, Prevention and Control. World Health Organization*, pages 23–52, 2001.

[22] M. D. Morris and T. J. Mitchell. Exploratory designs for computational experiments. *Journal of statistical planning and inference*, 43(3):381–402, 1995.

[23] D. G. Krige. A statistical approach to some basic mine valuation problems on the witwatersrand. *Journal of the Southern African Institute of Mining and Metallurgy*, 52(6):119–139, 1951.

[24] J. Friedman, T. Hastie, R. Tibshirani, et al. *The elements of statistical learning*, volume 1. Springer series in statistics New York, 2001.

[25] M. O. Hansen. Aerodynamics and design of horizontal-axis wind turbines. In *Wind Energy Engineering*, pages 161–184. Elsevier, 2017.

[26] K. S. Brentner, C. L. Burley, and M. A. Marcolini. Sensitivity of acoustic predictions to variation of input parameters. *Journal of the American Helicopter Society*, 39(3): 43–52, 1994.

[27] L. A. Viterna and R. D. Corrigan. Fixed pitch rotor performance of large horizontal axis wind turbines. In *NASA Lewis Research Center: Energy Production and Conversion Workshop, Cleveland, OH, United States January*, volume 1, 1982.

[28] J. Páscoa, J. Morgado, and M. Silvestre. Validation of new formulations for propeller analysis. 2015.

[29] M. A. Silvestre, J. P. Morgado, and J. Pascoa. Jblade: a propeller design and analysis code. In *2013 International Powered Lift Conference*, page 4220, 2013.

[30] J. P. S. Morgado. *Development of an open source software tool for propeller design in the MAAT project.* PhD thesis, University of Beira Interior, 2016.

[31] C. N. Adkins and R. H. Liebeck. Design of optimum propellers. *Journal of Propulsion and Power*, 10(5):676–682, 1994.

[32] T. Theodorsen, G. W. Stickle, and M. Brevoort. Characteristics of six propellers including the high-speed range. *Annual Report-National Advisory Committee for Aeronautics*, 401, 1937.

[33] H. B. Freeman. *The effect of small angles of Yaw and Pitch on the characteristics of airplane propellers.* National Advisory Committee for Aeronautics, 1931.

[34] D. WEIR and J. POWERS. Comparisons of predicted propeller noise with windtunnel and flyoverdata. In *25th AIAA Aerospace Sciences Meeting*, page 527, 1987.

[35] H. Wang, B. Zang, A. Celik, D. Rezgui, and M. Azarpeyvand. An experimental investigation of propeller noise in forward flow. In *25th AIAA/CEAS Aeroacoustics Conference*, page 2620, 2019.

[36] T. Sinnige, D. Ragni, A. M. Malgoezar, G. Eitelberg, and L. L. Veldhuis. Apian-inf: an aerodynamic and aeroacoustic investigation of pylon-interaction effects for pusher propellers. *CEAS Aeronautical Journal*, 9(2):291–306, 2018.

[37] Y. Yauwenas, J. R. Fischer, D. Moreau, and C. J. Doolan. The effect of inflow disturbance on drone propeller noise. In *25th AIAA/CEAS Aeroacoustics Conference*, page 2663, 2019.

[38] P. Neto. Propeller noise predictor, June 2021. URL `https://doi.org/10.5281/zenodo.5040385`.

APPLICATION OF THERMAL ENGINEERING SYSTEMS COMPUTATIONAL MODELS IN AIRCRAFT PASSENGER VIRTUAL CABIN

Eusébio Z. E. Conceição[1]*, João M. Gomes[2], Mª Manuela J. R. Lúcio[1] and Hazim B. Awbi[3]

1: Faculdade de Ciências e Tecnologia
Universidade do Algarve,
Campus de Gambelas, 8005-139 Faro, Portugal
econcei@ualg.pt, maria.manuela.lucio@gmail, http://www.ualg.pt

2: CINTAL
Campus de Gambelas, 8005-139 Faro, Portugal
jgomes@ualg.pt http://www.ualg.pt

3: School of Built Environment,
University of Reading, Reading, RG6 6AW, United Kingdom
h.b.awbi@reading.ac.uk.com http://www.reading.ac.uk/

Abstract. *This numerical work presents a design of an indoor environment and comfort evaluation, namely the thermal comfort and the air quality, in aircraft passenger cabin simulated through a virtual chamber similar to a real experimental chamber. This work presents and applies a numerical model, that considers the coupling of the CFD (Computational Fluids Dynamics) and HTR (Human Thermo-Physiology Response) numerical models. The coupling system, itself, generates the occupation presence and transfers the inputs/output between the CFD and HTR numerical models. The input of the compartment, using the Computational Aid Design, the location of the occupants and the external environmental variables are introduced in the software, while the occupants' geometry is generated by empirical equations, based on the height and width dimensions. The study is made in a virtual chamber occupied by twenty-four virtual occupants and twenty-four seats and equipped with a ceiling-mounted air distribution system. The inlet airflow is located above the head level, while the outlet airflow is located in the aircraft passenger cabin central area at the ceiling level. In the present study, the thermal comfort level (using the Predicted Mean Vote and the Percentage of People Dissatisfied indexes), the air quality level (using the carbon dioxide concentration in the respiration area), the Draught Risk (using the Predicted percentage of dissatisfied people), ventilation effectiveness for heat removal and effectiveness for contaminant removal and the ADI (Air Distribution Index), that each occupant is subjected, are calculated. Four Cases studies, defined for different mean internal air temperature, with an external air temperature of -50ºC, were developed. In accordance with the obtained results the thermal comfort level and the air quality are acceptable and ADI index is highest for the highest internal air temperature.*

Keywords: CFD, Human Thermo-physiology, Thermal comfort, Air Quality, ADI

Eusébio Z. E. Conceição, João M. Gomes, Mª Manuela J. R. Lúcio and Hazim B. Awbi

1. INTRODUCTION

A ceiling-mounted air distribution system (see Awbi [1]), used as inlet, applied in a aircraft passenger cabin with an exhaustion system, is located in the aircraft passenger cabin central area at the ceiling level.

The Air Distribution Index (ADI) is function of the thermal comfort number and the air quality number. This index was been developed in Awbi [1], for uniform thermal environment, and includes the thermal comfort, the indoor air quality and the effectiveness for heat removal and the effectiveness for contaminant removal. The ADI for non-uniform thermal environments was developed by Conceição et al [2]. The Air Distribution Turbulence Index (ADTI), more recently, have been developed in Conceição and Awbi [3]. This new index is used to consider simultaneously the thermal comfort, the indoor air quality, the Draught Risk and the effectiveness for heat removal, contaminant removal and room air removal.

To evaluate the thermal comfort level, they are used the Predicted Percentage of Dissatisfied people (PPD) and the Predicted Mean Vote (PMV) indexes, developed by Fanger [4] and presented in ISO 7730 [5]. Some applications can be analyzed, as example, in Conceição et al. [6], in application of the PMV Index in the control of Heating, Ventilating and Air-Conditioning (HVAC) system, in Conceição et al. [7], in the development of a control temperature, in Conceição et al. [8], in the application of adaptive thermal comfort models and in Conceição et al. [9], in experimental studies using the airflow around occupants in vehicles.

In the indoor air quality level evaluation, it is used the carbon dioxide concentration, release by the occupants, as indicator of the indoor air quality in occupied spaces (ASHRAE 62.1 [10] and Awbi [1]). Others works applied in this area can be analyzed in Conceição et al. [11], Conceição et al. [12] and Conceição et al. [13].

In the occupant local thermal discomfort evaluation, it is used the Draught Risk (DR). The DR, presented in ISO 7730 [5] and developed in Fanger et al. [14], is function of the air temperature, air velocity and air turbulence intensity (see applications in Conceição et al. [3]).

In the assessment of ADI are used three software: building thermal response (BTR) model, human thermal response (HTR) model and a Computational Fluid Dynamics (CFD) model.

The BTR software model simulates the building thermal behavior response and calculates numerically the internal temperature and surrounding virtual chamber surfaces temperatures (see Conceição and Lúcio [16]). The software application can be seen in Conceição et al. [17], Conceição and Lúcio [18], Conceição and Lúcio [16], Conceição and Lúcio [19] and Conceição and Lúcio [20].

The HTR numerical model simulates the human thermo-physiology and evaluates the human thermal comfort level and the tissue, blood and clothing temperatures (see Conceição et al. [16]). Some applications of this numerical model can be analyzed in Conceição et al. [21], [22] and [23].

More information of others numerical models, related with human thermal response can be seen in the works of Tang et al. [24] and Ozeki [25]. Tang et al. [24] simulates the local skin temperature in older people and Ozeki [25] evaluates the thermal comfort level of occupants subjected to solar radiation.

To simulate the airflow and evaluate the air quality, air temperature, air velocity, air turbulence intensity and carbon dioxide concentration the CFD was used. CFD is a differential numerical model and its applications can be seen in Conceição et al. [26].

Eusébio Z. E. Conceição, João M. Gomes, Mª Manuela J. R. Lúcio and Hazim B. Awbi

Other studies related with CFD techniques can be found in Takabayashi [27] and Nilsson and Holmér [28].

Temperature, humidity, air pressure, noise, vibration, among others influence the cabin comfort. Cui et al. [29] conducted a field study on 10 aircrafts, which consisted of measuring parameters and carrying out questionnaires to passengers to evaluate the thermal comfort in airplanes cabins. Fan and Zhou [30] presents an overview of thermal comfort in aircraft cabin, focusing on aspects such as the application of thermal comfort models, types of ventilation systems used and energy savings. In a comparative study about the performance of three ventilation systems in sections of the cabins of two airplanes, You et al. [31] concluded that the personalized ventilation system presents the best results regarding the thermal comfort of the passengers.

In this study, the HVAC system performance, based in an exhaust system, located in the aircraft passenger cabin central area at the ceiling level, and an inlet system, based on a ceiling-mounted air distribution system, is analysed. The influence of this HVAC system, using the ADI, in the occupant thermal comfort, indoor air quality and draught Risk levels are analysed.

2. NUMERICAL MODEL

The numerical model presented in this work considers the:

- Aircraft passenger cabin thermal response numerical models, used to evaluate the aircraft passenger cabin surface temperature around the passengers. This model calculates the air temperature inside the spaces, in the inner bodies, in the glazed surfaces and in the opaque surfaces. This numerical model is based on mass and energy integral equations and works in transient conditions, considers the convection, conduction, radiation and other phenomena.
- Integral HTR numerical model, used to evaluate the passengers' temperature distribution and thermal comfort levels. The passenger thermal response calculates the body temperature, the clothing temperature, the skin water vapour and the clothing water vapour. This numerical model is based on mass and energy integral equations and works in transient conditions, considers the convection, conduction, radiation and other phenomena.
- Differential CFD numerical model, used to evaluate the environment variables around the passengers and the internal air quality. The differential CFD numerical model evaluates the environmental thermal variables inside the spaces and around the passengers, namely, the air temperature; air velocity, carbon dioxide concentration, DR and other variables. This numerical model is based on Navier-Stokes differential equations in Cartesian coordinates and works in steady-state conditions and in non-isothermal conditions.

The space geometry with complex topology is developed using a Computer Aided-Design system, while the passengers' geometry is done using a geometric equations methodology. In the CFD, the geometry is based on volume elements, while the geometry in the HTR numerical model is based on surfaces. In both cases, the virtual passenger is divided into twenty-four elements.

3. NUMERICAL METHODOLOGY

This study is made in an aircraft passenger virtual cabin, simulated by a virtual chamber,

Eusébio Z. E. Conceição, João M. Gomes, Mª Manuela J. R. Lúcio and Hazim B. Awbi

with dimensions of $4.50 \times 2.55 \times 2.50$ m^3. The virtual chamber, occupied with twenty-four virtual manikins, is equipped with:
- Twenty-four seats;
- One exhaust system, located in the aircraft passenger cabin central area at the ceiling level;
- One inlet system based on a ceiling-mounted air distribution system (see Fig. 1).

In this simulation the following conditions are used:
- The renovation airflow is 35 m^3/h/passenger;
- The activity level is 1.2 met;
- The clothing level is 1 clo (typical winter insulation clothing);
- The external air temperature is -50ºC;
- The inlet air velocity is 3.9 m/s.

In this study four Case studies are analysed. The inlet air temperature is the following:
- Case A, 10.6 ºC;
- Case B, 12.6 ºC;
- Case C, 14.7 ºC;
- Case D, 16.8 ºC.

The mean internal air temperature is the following:
- Case A, 18 ºC;
- Case B, 20 ºC;
- Case C, 22 ºC;
- Case D, 24 ºC;

In this simulation, the air temperatures around the aircraft passenger cabin are evaluated through the aircraft passenger cabin thermal response, the air temperatures around the passengers are evaluated through the HTR and the airflow around the passengers is evaluated using the CFD.

Eusébio Z. E. Conceição, João M. Gomes, Mª Manuela J. R. Lúcio and Hazim B. Awbi
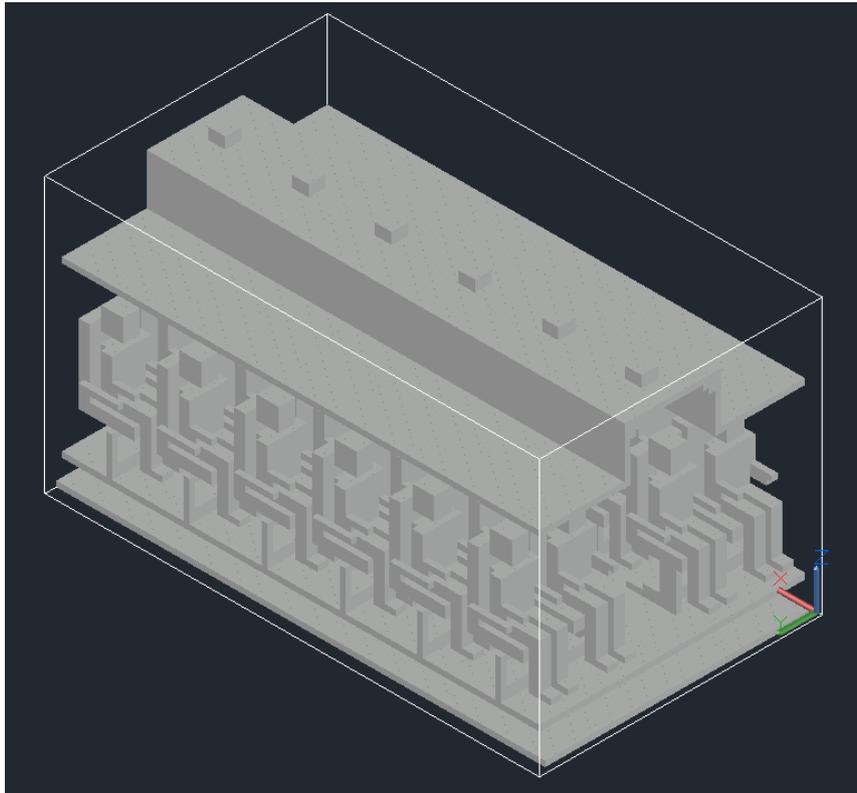
a)
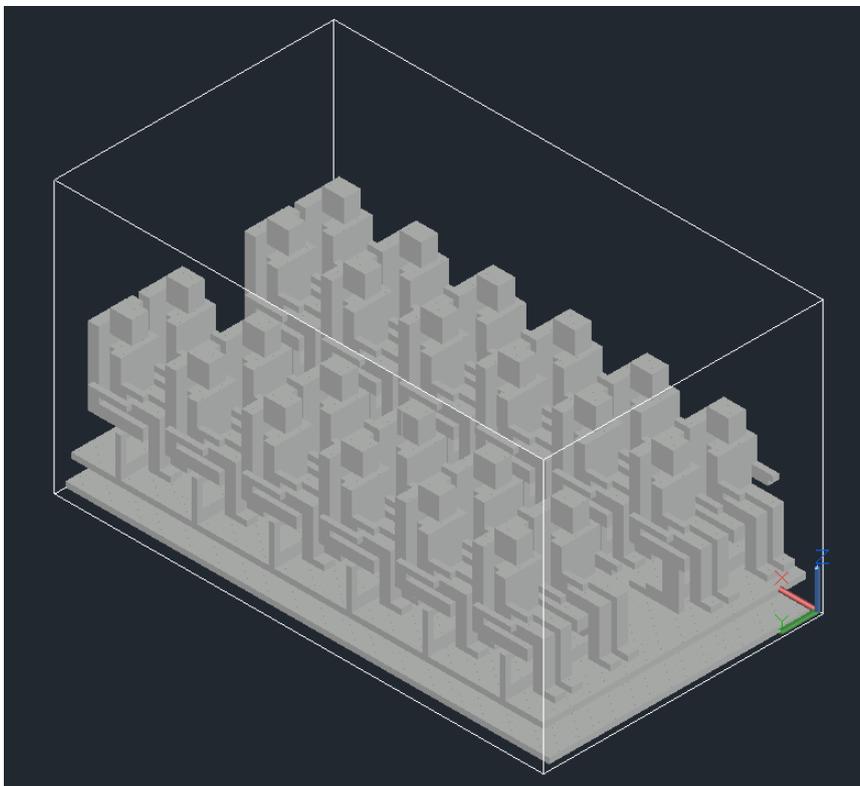
b)

Fig.1. Geometry used in the CFD of the aircraft passenger cabin.

Eusébio Z. E. Conceição, João M. Gomes, Mª Manuela J. R. Lúcio and Hazim B. Awbi

4. RESULTS

In this section, they are obtained the results of the air velocity, air temperature and DR that each occupant are subjected around the human body and of the performance of the HVAC system.

In Fig. 2, the distribution of air velocity around the occupants for the Cases A, B, C and D are presented. The distribution of air temperature around the occupants for the Cases A, B, C and D are presented in Fig. 3, while in Fig. 4 the distribution of air temperature around the occupants for the Cases A, B, C and D are showed.

The air velocity around the occupants sections is not strongly influenced by the mean value of the internal temperature and the inlet air temperature. In general, the air velocity in the upper bodies sections are slightly higher than in the lower bodies sections.

The air temperature around the occupants sections is relatively uniform. The air temperature around the occupants sections increase slightly when the internal mean air temperature and the inlet air temperature increase.

Finally, the DR around the occupants' sections decreases when the internal mean air temperature and the inlet air temperature increase. The DR is slightly highest in the head than in the other human bodies section. In accordance with the international standards, the DR levels are acceptable. For an internal mean air temperature of 18 and 20 ºC, Cases A and B, the DR level is according to the Category C of the international standards, while for an internal mean air temperature of 22 and 24 ºC, Cases C and D, the DR level is according to the Category B of the international standards.

In Tables 1, 2, 3 and 4 are presented ADI values for, respectively, the mean value of the Cases A, B, C and D. In these tables, N represents the Number of occupants; Tm (ºC) represents the Body mean temperature; ETC (%) represents the Effectiveness for heat removal; PPD (%) represents the Predicted Percentage of dissatisfied People; NTC represents the Thermal Comfort Number; C (mg/m3) represents the carbon dioxide concentration in the respiration area; EIAQ represents the Effectiveness for contaminant removal; PDIAQ represents the Predicted Dissatisfied people related with the Indoor Air Quality; NIAQ represents the Air Quality Number; and ADI represents the Air Distribution Index.

Eusébio Z. E. Conceição, João M. Gomes, Mª Manuela J. R. Lúcio and Hazim B. Awbi
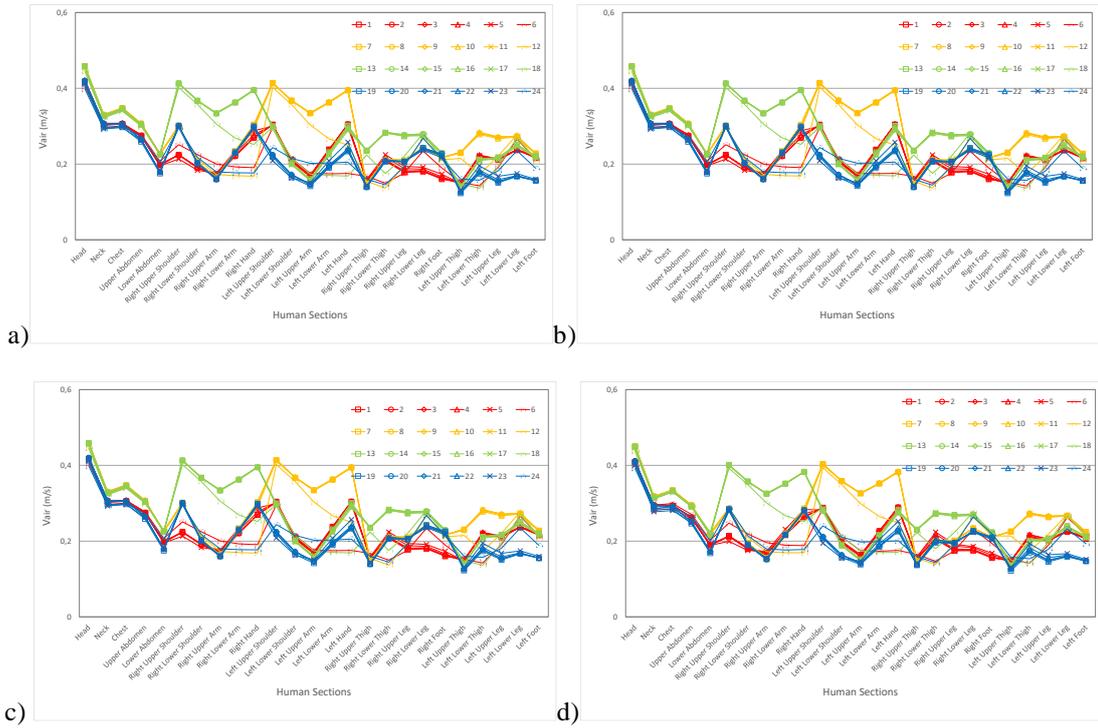
Fig.2. Distribution of air velocity around the occupants for the Cases A, B, C and D.
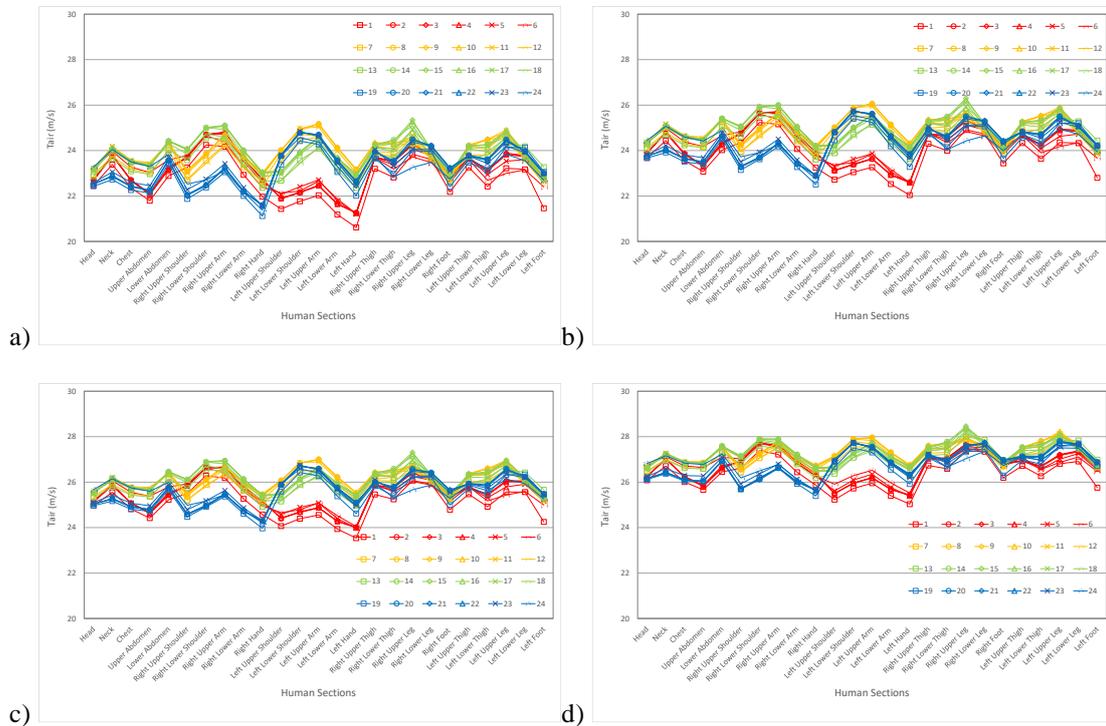
Fig.3. Distribution of air temperature around the occupants for the Cases A, B, C and D.

Eusébio Z. E. Conceição, João M. Gomes, Mª Manuela J. R. Lúcio and Hazim B. Awbi
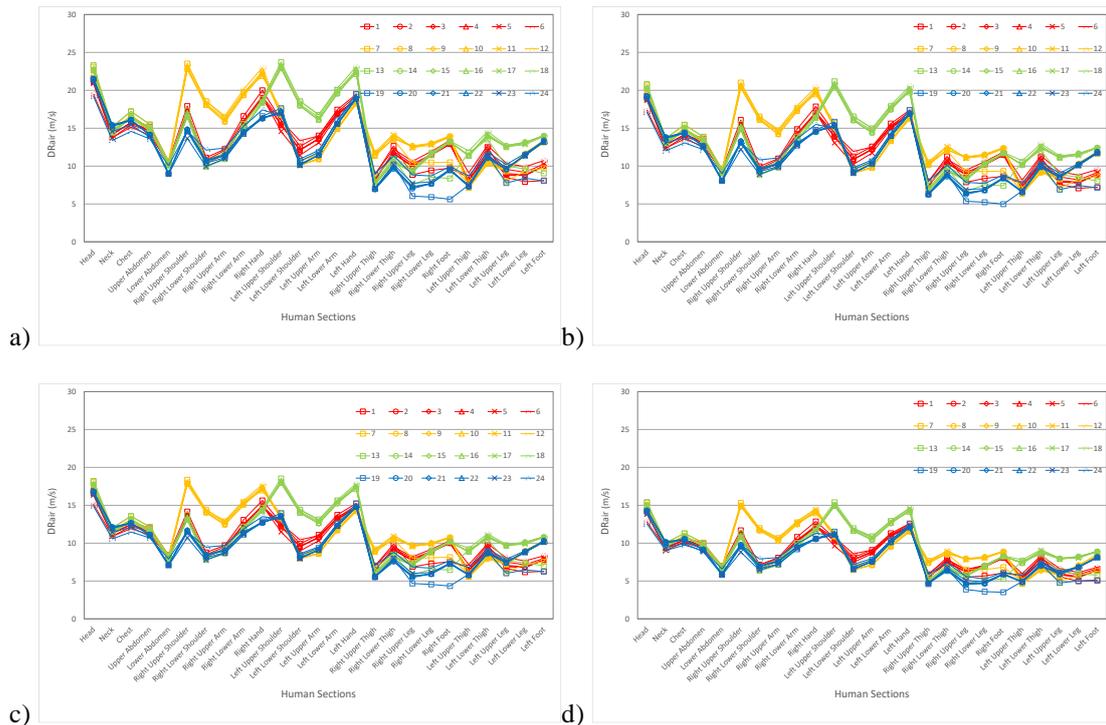
Fig.3. Distribution of DR around the occupants for the Cases A, B, C and D.

The PPD decreases when the mean air temperature and the inlet air temperature increase. In Case A, the thermal comfort is not in accordance with the international standards, however, the PPD values are near the acceptable values. The Case B is in accordance with the category C, by negative PMV values, of the international standards, and the Cases C and D are in accordance to the category A, by negative PMV values, of the international standards.

The thermal comfort number increases when the internal mean air temperature and the inlet air temperature increase.

The carbon dioxide concertation in the breathing area is slightly constant for the Cases A, B, C and D. However, the carbon dioxide concentration is acceptable in accordance to the international standards.

Table 1. ADI for the Case A.

N	Mean
T_m (ºC)	23,4
E_{TC} (%)	73,0
PPD (%)	18,9
N_{TC}	3,9
C (mg/m³)	1098,9
E_{IAQ}	97,1
PD_{IAQ}	14,9
N_{IAQ}	6,5
ADI	5,0

Eusébio Z. E. Conceição, João M. Gomes, Mª Manuela J. R. Lúcio and Hazim B. Awbi

Table 2. ADI for the Case B.

N	Mean
T_m (ºC)	24,5
E_{TC} (%)	75,1
PPD (%)	10,2
N_{TC}	7,4
C (mg/m³)	1100,4
E_{IAQ}	97,1
PD_{IAQ}	14,9
N_{IAQ}	6,5
ADI	6,9

Table 3. ADI for the Case C.

N	Mean
T_m (ºC)	25,7
E_{TC} (%)	77,6
PPD (%)	5,6
N_{TC}	13,8
C (mg/m³)	1100,4
E_{IAQ}	97,1
PD_{IAQ}	14,9
N_{IAQ}	6,5
ADI	9,5

Table 4. ADI for the Case D.

N	Mean
T_m (ºC)	26,9
E_{TC} (%)	80,0
PPD (%)	5,6
N_{TC}	14,3
C (mg/m³)	1100,1
E_{IAQ}	98,1
PD_{IAQ}	14,9
N_{IAQ}	6,6
ADI	9,7

The indoor air quality number is constant for all Cases studied.

Finally, the ADI value increases when the internal mean air temperature and the inlet air temperature increase. This increase is associated with the increase of the thermal comfort number.

Eusébio Z. E. Conceição, João M. Gomes, Mª Manuela J. R. Lúcio and Hazim B. Awbi

12. CONCLUSIONS

In this study was made an application of thermal engineering systems computational models in an aircraft passenger virtual cabin.

In accordance with the obtained results, the air temperature around the occupants' sections increases slightly when the internal mean air temperature and the inlet air temperature increase and the DR around the occupants' sections decreases when the internal mean air temperature and the inlet air temperature increase. The air velocity, air temperature and DR around the occupants' sections are relatively uniform and the air velocity and DR in the upper bodies sections are slightly higher than in the lower bodies sections.

In accordance with the international standards, the DR levels are acceptable. For an internal mean air temperature of 18 and 20 ºC, Cases A and B, the DR levels are in accordance with the Category C of the international standards, while for an internal mean air temperature of 22 and 24 ºC, Cases C and D, the DR levels are in accordance with the Category B of the international standards.

The PPD decreases and the indoor air quality is quite constant, when the mean air temperature and the inlet air temperature increase.

In the thermal comfort level, the Case B is in accordance with the category C, by negative PMV values, and the Cases C and D are in accordance to the category A, by negative PMV values, of the international standards. The indoor air quality is also acceptable in accordance to the international standards.

The thermal comfort number increases and the indoor air quality number is constant, when the internal mean air temperature and the inlet air temperature increase. The ADI value increases when the internal mean air temperature and the inlet air temperature increase.

Thus, in accordance with the obtained results, the developed HVAC system for the Cases C and D, guarantees acceptable thermal comfort and internal air quality for the occupants. In both situations, the DR are also acceptable in accordance to the Category B of the international standards.

ACKNOWLEDGMENTS

REFERENCES

[1] *Awbi, H.B. Ventilation of Buildings; Routledge: London, UK, 2004.* 2004.

[2] E.Z.E. Conceição, M.M.J.R. Lúcio and H.B. Awbi, "Comfort and airflow evaluation in spaces equipped with mixing ventilation and cold radiant floor". Build. Simul. 6, 51–67 (2013). https://doi.org/10.1007/s12273-012-0093-4."

[3] E.Z.E. Conceição and H.B. Awbi "Evaluation of Integral Effect of Thermal Comfort , Air Quality and Draught Risk for Desks Equipped with Personalized" *Energies 14, no. 11: 3235. 2021. https://doi.org/10.3390/en14113235*.

[4] P. O. Fanger, "Thermal comfort: Analysis and applications in environmental engineering," *Appl. Ergon.*, vol. 3, no. 3, p. 181, 1972, doi: 10.1016/s0003-6870(72)80074-7.

[5] *ISO 7730: Ergonomics of the Thermal Environments—Analytical Determination and*

Eusébio Z. E. Conceição, João M. Gomes, Mª Manuela J. R. Lúcio and Hazim B. Awbi

Inter-pretation of Thermal Comfort Using Calculation of the PMV and PPD Indices and Local Thermal Comfort Criteria. Geneva, Switzerland: International Standard Organization.

[6] E. Z. E. Conceição, J. M. M. Gomes, and A. E. Ruano, "Application of HVAC Systems with Control Based on PMV Index in University Buildings with Complex Topology," *IFAC-PapersOnLine*, vol. 51, no. 10, pp. 20–25, 2018, doi: 10.1016/j.ifacol.2018.06.230.

[7] E. Z. E. Conceição, M. M. J. R. Lúcio, A. E. B. Ruano, and E. M. Crispim, "Development of a temperature control model used in HVAC systems in school spaces in Mediterranean climate," *Build. Environ.*, vol. 44, no. 5, 2009, doi: 10.1016/j.buildenv.2008.06.015.

[8] E. Z. E. Conceição, A. R. L. Nunes, J. M. M. Gomes, and M. J. R. Lúcio, "Application of a school building thermal response numerical model in the evolution of the adaptive thermal comfort level in the Mediterranean environment," *Int. J. Vent.*, vol. 9, no. 3, 2010, doi: 10.1080/14733315.2010.11683887.

[9] E. Z. E. Conceição, M. C. G. Silva, and D. X. Viegas, "Airflow around a passenger seated in a bus," *HVAC R Res.*, vol. 3, no. 4, 1997, doi: 10.1080/10789669.1997.10391380.

[10] ANSI/ASHRAE Standard 62-1: Ventilation for Acceptable Indoor Air Quality, American Society of Heating, Refrigerating and Air-Conditioning Engineers." Atlanta, GA, USA.

[11] E. Z. E. Conceição, J. P. Farinho, and M. M. J. R. Lúcio, "Evaluation of indoor air quality in classrooms equipped with cross-flow ventilation," *Int. J. Vent.*, 2012, doi: 10.1080/14733315.2012.11683970.

[12] E. Z. E. Conceição, M.M.J.R. Lúcio, V. Vicente, and V. Rosão, "Evaluation of local thermal discomfort in a classroom equipped with crossed ventilation," *Int. J. Vent.*, vol. 7, no. 3, pp. 267–277.

[13] E. Z. E. Conceição, M. C. G. Silva, and D. X. Viegas, "Air quality inside the passenger compartment of a bus," *J. Expo. Anal. Environ. Epidemiol.*, vol. 7, no. 4, 1997.

[14] P. O. Fanger, A. K. Melikov, H. Hanzawa, and J. Ring, "Air turbulence and sensation of draught," *Energy Build.*, 1988, doi: 10.1016/0378-7788(88)90053-9.

[15] E. Z. E. Conceição and M.M.J.R. Lúcio, "Numerical Simulation of the Application of Solar Radiant Systems, Internal Airflow and Occupants' Presence in the Improvement of Comfort in Winter Conditions," *Buildings*, vol. 6, no. 3, p. 38, Sep. 2016, doi: 10.3390/buildings6030038.

[16] E. Z. E. Conceição and M. M. J. R. Lúcio, "Numerical simulation of passive and active solar strategies in buildings with complex topology," *Build. Simul.*, vol. 3, no. 3, pp. 245–261, Sep. 2010, doi: 10.1007/s12273-010-0010-7.

[17] E. Z. E. Conceição, M. C. G. Da Silva, J. C. S. André, and D. X. Viegas, "Thermal behaviour simulation of the passenger compartment of vehicles," *Int. J. Veh. Des.*, vol. 24, no. 4, 2000, doi: 10.1504/IJVD.2000.005199.

[18] E. Z. E. Conceição and M. M. J. R. Lúcio, "Numerical study of the thermal efficiency of a school building with complex topology for different orientations," *Indoor Built Environ.*, vol. 18, no. 1, pp. 41–51, Feb. 2009, doi: 10.1177/1420326X08099550.

[19] E. Z. E. Conceição and M. M. J. R. Lúcio, "Numerical study of the influence of opaque external trees with py-ramidal shape on the thermal behaviour of a school building in summer conditions," *Indoor Built Environ.*, vol. 19, no. 6, pp. 657–667.

Eusébio Z. E. Conceição, João M. Gomes, Mª Manuela J. R. Lúcio and Hazim B. Awbi

[20] E. Z. E. Conceição and M. M. J. R. Lúcio, "Numerical study of thermal response of school buildings in summer conditions," in *HB 2006 - Healthy Buildings: Creating a Healthy Indoor Environment for People, Proceedings*, 2006, vol. 3.

[21] E. Z. E. Conceição, S. P. Rosa, A. L. V. Custódio, R. L. Andrade, M. J. P. A. Meira, and M. M. J. R. Lúcio, "Study of airflow around occupants seated in desks equipped with upper and lower air terminal devices for slightly warm environments," *HVAC R Res.*, vol. 16, no. 4, pp. 401–412, 2010, doi: 10.1080/10789669.2010.10390912.

[22] E. Z. E. Conceição and M. M. J. R. Lúcio, "Evaluation of thermal comfort conditions in a localized radiant system placed in front and behind two students seated nearby warmed curtains," *Build. Environ.*, vol. 45, no. 10, pp. 2100–2110, Oct. 2010, doi: 10.1016/j.buildenv.2010.03.006.

[23] E. Z. E. Conceição, M. M. J. R. Lúcio, and M. C. Lopes, "Application of an indoor greenhouse in the energy and thermal comfort performance in a kindergarten school building in the South of Portugal in winter conditions," *WSEAS Trans. Environ. Dev.*, vol. 4, no. 8, pp. 644–654, Aug. 2008.

[24] Y. Tang, H. Yu, Z. Wang, M. Luo, and C. Li, "Validation of the Stolwijk and Tanabe Human Thermoregulation Models for Predicting Local Skin Temperatures of Older People under Thermal Transient Conditions," *Energies*, 2020, doi: 10.3390/en13246524.

[25] Ozeki; Yoshiichi & Takabayashi; Toru & Tanabe; Shin-ichi., "Numerical Comfort Simulator for Thermal Environment (Part 1) A Comprehensive Combined Analysis Method with Multi-Node Thermoregulation Model, Radiation Model and CFD for Evaluation of Thermal Comfort. SAE Technical Papers. 10.4271/2002-01-0515." SAE Technical Papers, doi: 10.4271/2002-01-0515.

[26] J. R. Conceição, E.Z.; Vicente, V.D.; Manuela, M.; Lucio, "Airflow Inside School Building Office Compartments with Moderate Environments. HVAC&R Res. 2008, 14, 195–207.," 2008.

[27] S.-I. Takabayashi, T.; Ozeki, Y.; Tanabe, "Numerical Comfort Simulator for Thermal Environment (Part 2) An Application of Simulator for the Evaluation of Solar Reduction Glass in a Vehicle Model. SAE Tech. Paper 2002.," *SAE Tech. Pap.*, 2002.

[28] H. O. Nilsson and I. Holmer, "Comfort climate evaluation with thermal manikin methods and computer simulation models. Indoor Air 2003, 13, 28–37. No Title," *Indoor Air*, pp. 28–37, 2003.

[29] Cui, W., Q. Ouyang and Y. Zhu, 2014, Field study of thermal environment spatial distribution and passenger local thermal comfort in aircraft cabin. *Building and Environment* 80: 213-220.

[30] Fan, J. and Q. Zhou, 2019, A review about thermal comfort in aircraft. *Journal of Thermal Science* 28(2): 169-183.

[31] You, R., C. Lin, D. Wei and Q. Chen, 2019, Evaluating the commercial airliner cabin environment with different air distribution systems. *Indoor Air* 29: 840–853.

SURROGATE-BASED MULTIDISCIPLINARY DESIGN OPTIMIZATION OF AN UAM-VTOL AIRCRAFT FOR ENERGY MINIMIZATION

Catarina Ribeiro[1], Frederico Afonso[1], Martin Sohst[2] and Afzal Suleman[1,2]

1: IDMEC
Instituto Superior Técnico
Universidade de Lisboa
Av. Rovisco Pais, 1049-001, Lisboa, Portugal
{catarina.fonseca.ribeiro,frederico.afonso,suleman}@tecnico.ulisboa.pt,
https://www.idmec.tecnico.ulisboa.pt/

2: Department of Mechanical Engineering
University of Victoria
Victoria, BC, V8P 5C2 Canada
{msohst,suleman}@uvic.ca, https://www.uvic.ca/

Abstract. *This work aims at evaluating surrogate based Multidisciplinary Design Optimization (MDO) strategies for designing an Urban Air Mobility (UAM) Vertical Take-Off and Landing (VTOL) aircraft. During the conceptual stages, it is important to have a vast exploration of the design space, using models for several disciplines that need to be considered regarding the mission requirements. Surrogate models are a potentially good approach to rapidly explore the design space. Therefore, in this work, a comparison between the results of a MDO using real functions and the surrogate models of these functions is provided. Three major strategies for the aircraft optimization are carried out: an optimization using the real, analytical functions and their derivatives with the adjoint method; a surrogate-based optimization where Kriging-based surrogate models for both the objective function and constraints are built, using the Surrogate Modeling Toolbox (SMT); and an optimization based on adaptive sampling using the Watson and Barnes (WB2) infill criteria. To compare these MDO strategies, an energy minimization problem is established for the VTOL aircraft as a case study in OpenMDAO, where aerodynamics and structures are modeled using the low-fidelity models provided in the OpenAeroStruct (OAS) framework. Initially, only two design variables are considered. Then, more design variables are added to the problem, and therefore increasing the complexity of the optimization problem.*

Keywords: Multidisciplinary design optimization, surrogate models, adaptive sampling, aircraft design, aerostructural

Catarina Ribeiro, Frederico Afonso, Martin Sohst and Afzal Suleman

1 INTRODUCTION

Over the last years, there has been a significant increase in the research of Urban Air Mobility (UAM), with the number of applications also growing [1]. New problems have to be solved in order to turn UAM into a reality, as the society also demands a cleaner and more sustainable aviation, capable of responding to the requisites of transportation in urban scenarios. As these demands grow, the necessity for developing tools that consider different requirements from different disciplines also increases. Hence, Multidisciplinary Analysis and Optimization (MDAO) [2] is a tool that can be very useful in early design stages of a new aircraft [3], where usually there is a great exploration of possible concepts. Using MDAO allows a designer to integrate multiple disciplines (e.g. aerodynamics, structures, propulsion, emissions, performance, among others) with the objective of considering the influence of a discipline on the others, so that in the end, the obtained solution is one that satisfies a compromise between all the disciplines taken into account. As the complexity of the problem increases, by the increment in disciplines considered, or the higher fidelity models used, the computational burden of this optimization can become too demanding.

There are some possible approaches to mitigate this computational burden, such as using the adjoint method [4] or surrogate models [5]. The former approach is a numerical method that provides efficiently the sensitivities to the optimizer, even though the analysis code needs to be prepared to solve the adjoint equations. In the latter approach, computational models that mimic the real functions are used to reduce the optimization time, however at the cost of building expensive databases. However, the size of these databases can be reduced when considering adaptive sampling techniques [6–8], which recur to statistical information to accelerate the optimization process.

This work aims at comparing three optimization strategies, used to solve an aircraft design problem: (i) optimization using the real functions with sensitivities computed by means of the adjoint method; (ii) optimization using the surrogate models of the previous functions; and (iii) optimization using adaptive sampling with the Watson and Barnes (WB2) infill criteria [9]. The aircraft design problem consists in minimizing the mission energy consumption of a Vertical Take-Off and Landing (VTOL) aircraft for UAM. The physical models are defined using a low-fidelity tool, the OpenAeroStruct (OAS) [10] and the optimization problem is defined using the OpenMDAO framework [11]. The surrogate models are built using the open-source Surrogate Modeling Toolbox (SMT) [12].

2 METHODS AND TOOLS

Even though the main objective of this work is to provide a comparison between the three optimization strategies mentioned before, it is also a goal to re-design the Flexcraft concept [13] at the conceptual level such that it would be enabled with VTOL capability to improve its versatility. To this end, the design sequence illustrated in Fig.1 was followed.

Revised Mission Requirements → Concept Generation and Selection → Initial Sizing → Baseline Definition → Optimization

Figure 1: Design sequence flowchart.

A brief description of each of these stages is presented next with a higher focus on the optimization.

Catarina Ribeiro, Frederico Afonso, Martin Sohst and Afzal Suleman

2.1 Revised Mission Requirements

The Flexcraft concept consists of a modular hybrid-electric Short Take-Off and Landing (STOL) aircraft composed by a lifting system capable of carrying several different multi-mission fuselage pods [13]. All the essential systems to flight are integrated in the lifting system, which includes the flight control system, avionics, control surfaces, batteries, fuel and the propulsive system composed by four propeller-driven electric motors and one turbo-generator.

Vertical Take-Off and Landing (VTOL) capability would be an interesting addition to this concept such that a higher versatility for UAM applications would be enabled. To accomplish this capability, a compromise in the top-level requirements for the design mission was required with consequences in both range and payload. The former was reduced from 1000 km to 800 km, while the latter was decreased from 900 kg to 500 kg. In what concerns the mission profile, depicted in Fig.2, the differences to the original design mission are in the segments related to the vertical flight and transition to forward flight. The aircraft takes-off and climbs vertically up to 15.24 m. Then it hovers for 60 s before transition to climb. After cruising for 800 km at 110 m s^{-1}, the aircraft starts descending to the landing site where it transits to vertical flight and hovers for 60 s before landing vertically.
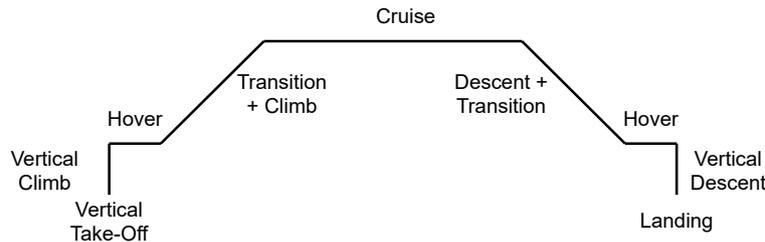
Figure 2: Mission profile.

Regarding the hybrid-electric strategy, a series architecture [14] was chosen which consists in four propeller-driven electric motors connected to batteries and a turbo-generator by means of a power distribution module. In this configuration, an internal combustion engine burns fuel and rotates an AC generator. The power generated can be used to charge the batteries and to be delivered to the AC electric motors that drive the propellers. The series configuration allows for a separation of power and thrust generation and also to have different flight modes, i.e, to have flight phases where only the electric energy of the batteries is used to propel the aircraft, and other phases where only the Internal Combustion Engine (ICE) is the provider of the necessary energy. This way, the vertical climb, hover, transition and vertical descent are driven using the batteries and the forward flight phases are carried out using only fuel energy. Therefore, the ICE and generator can be sized for cruise, which allows the system to be working at a steady state in most of the mission, and so it is working at its optimal Specific Fuel Consumption (SFC) point. However, this system implies an increase of the propulsive system weight and its complexity.

Catarina Ribeiro, Frederico Afonso, Martin Sohst and Afzal Suleman

2.2 Concept Generation and Selection

The idea was to maintain the geometry as close as possible to the original Flexcraft concept, which consists of a main wing with four mounted four propeller driven engines and an inverted U-tail connected with booms. To that end, several concepts were conceived and qualitatively compared in light of aerodynamics, weight and structures, stability and control, manufacturing complexity and noise. An Analytical Hierarchy Process (AHP) [15] based on the previous subjects was used to select the best concept, which is the one illustrated in Fig.3. The main difference of this aircraft concept to the original one is the tilt capacity of the four propeller-driven electric motors.
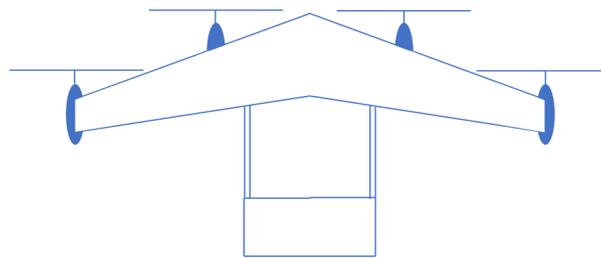
Figure 3: Selected aircraft concept.

2.3 Initial Sizing

With a concept for the general configuration of the aircraft chosen and considering a Maximum Take-Off Mass (MTOM) of 3500 kg from the Flexcraft project as a first guess, now some of the general dimensions can be defined. This is done using the design point equations, for both vertical and forward flight. A more detailed explanation of the design point analysis can be found in [16]. Stall speed was found to constrain the wing area (28.18 m^2) and the cruise speed limited the power required for forward flight (535 kW). Regarding the vertical flight design point: the power (890 kW) was constrained by the vertical climb condition; while the rotor area (57.23 m^2) was defined by the maximum allowable disc loading, 600 N m^{-2}, which is a typical value for a tilt rotor aircraft [17].

2.4 Baseline Definition

Based on the initial sizing, the baseline aircraft to be used for the optimization process can be defined. For that purpose the methodology described in [16] was followed to re-design the wing and stabilizers, besides refining the weights estimation and stability. The fuselage was kept the same as the one from the Flexcraft project and the power requirements considered were those estimated in the initial sizing. In the end, the main aircraft parameters estimated and considered for the baseline model are summarized in Tab.1.

2.5 Optimization

The baseline aircraft was then modelled in the OAS [10, 18] considering two disciplines, aerodynamics and structures. For the former, OAS uses a Vortex Lattice Method (VLM) with both compressibility (Prandtl-Glauert) and viscous (flat-plate) corrections. The Finite Element Method (FEM) is used for the latter, where an equivalent beam model is built based on inertial information of the cross-sectional areas throughout the aircraft.

Catarina Ribeiro, Frederico Afonso, Martin Sohst and Afzal Suleman

Table 1: Aircraft main parameters.

Parameter	Nomenclature	Value	Units
Maximum Take-Off Mass	MTOM	3530.56	kg
Disk area	A_R	57.23	m^2
Vertical flight required power	P_{VF}	890	kW
Forward flight required power	P_{FF}	535	kW
Wing area	S_w	28.18	m^2
Wing span	b_w	15	m
Wing mean aerodynamic chord	$\bar{c_w}$	1.994	m
Wing root chord	$c_{w,root}$	2.684	m
Wing tip chord	$c_{w,tip}$	1.074	m
Wing taper ratio	λ_w	0.4	—
Wing sweep angle	Λ_w	20	°
Wing dihedral angle	Γ_w	2	°
Horizontal tail area	S_{ht}	7.44	m^2
Horizontal tail span	b_{ht}	4	m
Horizontal tail chord	c_{ht}	1.86	m
Horizontal tail taper ratio	λ_{ht}	1	—
Horizontal tail sweep angle	Λ_{ht}	0	°
Horizontal tail dihedral angle	Γ_{ht}	0	°
Vertical tail area	S_{vt}	(×2) 2.28	m^2
Vertical tail span	b_{vt}	2	m
Vertical tail chord	c_{vt}	1.14	m
Vertical tail taper ratio	λ_{vt}	1	—
Vertical tail sweep angle	Λ_{vt}	35	°
Vertical tail dihedral angle	Γ_{vt}	0	°
Fuselage length	l_f	6.2	m
Fuselage width	l_w	1.6	m

After setting up these models, an optimization problem was defined in the OpenMDAO framework [11] using a Multidisciplinary Design Optimization (MDO) architecture. To formulate the optimization problem, the objective function, design variables and constraints have to be defined alongside the MDO architecture employed.

2.5.1 Objective Function

With the range fixed (800 km), one main objective is to minimize the fuel consumption. Also, since VTOL phases play a major role in the required power, which influences the weight of the rotors and batteries, this power should also be considered. In order to deal with these different possible objectives, an energetic objective function is used, combining the energy spent during both cruise and VTOL operations. This way the total energy is given by:

$$E = m_{fuel} \times E_f^* + P_{vc} \times t_{vc} + P_{hover} \times t_{hover} + E_{tr} \tag{1}$$

where m_{fuel} is the mass of necessary fuel to complete the cruise phase, calculated with the Breguet equation; E_f^* is the specific energy density of the fuel, assumed to be equal

Catarina Ribeiro, Frederico Afonso, Martin Sohst and Afzal Suleman

to 43.28 MJ kg^{-1}; P_{vc} and P_{hover} are the power needed for the vertical climb and hover phases, respectively, which are calculated using the design point equations; t_{vc} and t_{hover} are the times of the vertical climb and hover phases, respectively; and E_{tr} is the energy needed for the transition phase, which is assumed to be constant (1.13×10^7).

2.5.2 Design variables

Different case studies are made, using different design variables (DV). Here all the DV used are presented. The wing planform is defined using a linear distribution for the chord, by controlling the chord at the root, $c_{w,root}$, and the chord at the tip $c_{w,tip}$. The same happens for the horizontal tail planform, using $c_{ht,root}$ and $c_{ht,tip}$. The wingbox structure is defined by the thickness of the spars and the skins. Using the OAS model for the wingbox, the rear and front spar thicknesses, $t_{w,spar}$, are considered to be the same, as well as the upper and lower skin thicknesses, $t_{w,skin}$. A constant thickness is considered along the span for both the spars and the skins. This consideration was taken because of manufacturing restrictions. Once again, the same happens for the horizontal tail, thus adding two more design variables, $t_{ht,spar}$ and $t_{ht,skin}$. The angle of attack at cruise condition, α, is also used as design variable in one of the case studies. The upper and lower boundaries of these DV are listed in Tab.2 alongside the values of the baseline aircraft.

Table 2: Upper and lower boundaries of the design variables.

Design Variable	Baseline	Lower Boundary	Upper Boundary	Units
$c_{w,root}$	2.684	1.5	3.5	m
$c_{w,tip}$	1.074	0.5	2.0	m
$c_{ht,root}$	1.86	1.15	2.5	m
$c_{ht,tip}$	1.86	1.15	2.5	m
$t_{w,spar}$	0.0038	0.001	0.01	m
$t_{w,skin}$	0.0038	0.001	0.01	m
$t_{ht,spar}$	0.00255	0.0005	0.01	m
$t_{ht,skin}$	0.00255	0.0005	0.01	m
α	-0.8	-1.5	0.5	°

2.5.3 Constraints

To ensure a longitudinally stable aircraft, the static margin [16], K_n, will have to be between 5 and 20 % of the mean aerodynamic chord. Additionally, in order to have a trimmed flight during cruise two constraints are added: the pitching moment coefficient, C_M, is set to zero; and the lift must be equal to the total weight. To ensure structural integrity two load cases are considered: the vertical climb, and a pull-up of 3.8g. The four critical points on the wingbox, explained in [18], must satisfy the Von-Mises failure criterion at these load cases. During the pull-up manoeuvre considered, an additional constraint is imposed, so that the lift is equal to the total weight multiplying by the pull-up load factor, $n = 3.8g$. Finally, a constraint regarding the volume of the necessary fuel is employed. This, ensures that the volume occupied by the fuel is smaller than the available volume inside the wingbox structure of the wing, where it will be stored.

Catarina Ribeiro, Frederico Afonso, Martin Sohst and Afzal Suleman

2.5.4   MDO architecture

The architecture sets the structure of how the MDAO problem is going to be solved, i.e. it defines the sequence of the optimization [2]. In this work, a Multi-Discipline Feasible (MDF) [2] architecture is used, which ensures that at the end of each optimization iteration the two disciplines used, aerodynamics and structures, are coupled. The eXtended Design Structure Matrix (XDSM) diagram [19] of this architecture for the current problem is depicted in Fig.4.
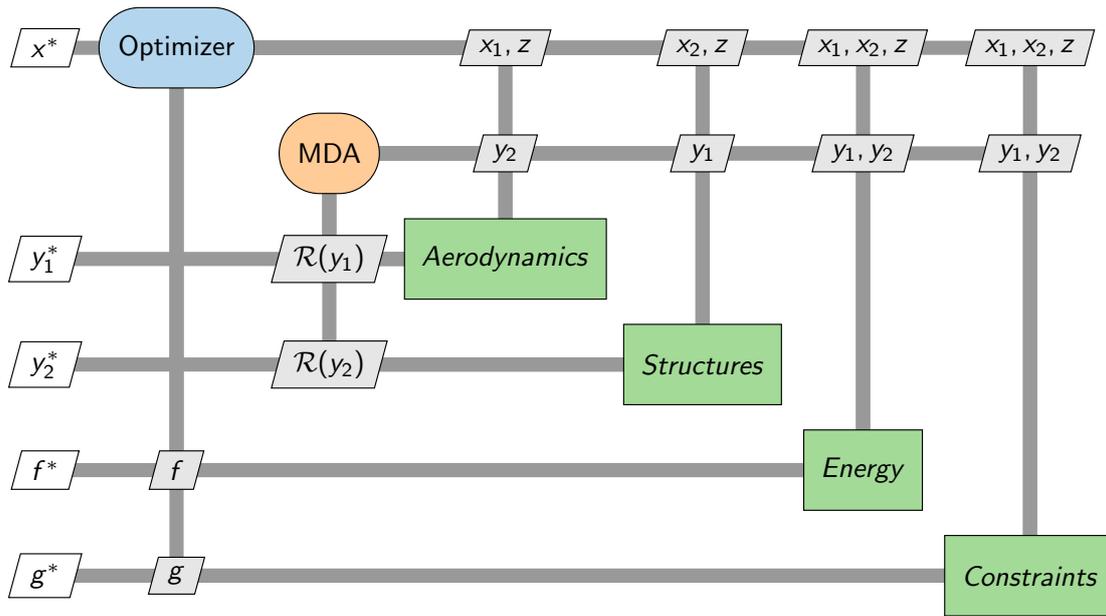
Figure 4: XDSM diagram [19] of the MDF architecture applied to the current problem using a Non-Linear Block Gauss-Seidel (NLBGS) solver for the Multidisciplinary Design Analysis (MDA).

In Fig.4, x is the set of design variables which is divided in global variables z (i.e. those that are common to both disciplines, $c_{w,root}, c_{w,tip}, c_{ht,root}$, and $c_{ht,tip}$) and variables associated only to aerodynamics x_1 (α) or structures x_2 ($t_{w,spar}, t_{w,skin}, t_{ht,spar}$, and $t_{ht,skin}$). The state variables y_1 and y_2 correspond to the set of outputs from the aerodynamics and structures disciplines, respectively, that are used not only to ensure an aerostructural equilibrium, but also to compute the objective function f (Eq.(1)) and constraints g. In each iteration of the optimization, each discipline analysis is done and the Multidisciplinary Design Analysis (MDA) solver ensures the convergence between the two disciplines, i.e. that the residuals $\mathcal{R}(y_1)$ and $\mathcal{R}(y_2)$ are zero and an aerostructural equilibrium is reached. In this work, the MDA solver used is the Non-Linear Block Gauss-Seidel (NLBGS) with Aitken relaxation. After the MDA is converged, the objective function and constraints are calculated with the variables that result from the MDA and the point to be evaluated at the next optimization iteration is defined.

This MDAO problem using the MDF architecture was solved considering the three approaches earlier mentioned and briefly described next.

Catarina Ribeiro, Frederico Afonso, Martin Sohst and Afzal Suleman

Optimization with Real Functions and the Adjoint Method Before building the surrogate models, and solving the optimization problem using these approximated functions, the problem is solved using the real functions and their analytical derivatives given by the adjoint method. As some of the functions were manually implemented, they also needed to provide sensitivities by means of the adjoint method. This was done prior to the optimization via computation of the partial derivatives implemented in the code, which are subsequently integrated using the chain rule to obtain the total derivatives. A gradient-based algorithm, namely the Sequential Least SQuares Programming (SLSQP), was used to optimize the baseline aircraft. Summarily, the optimization cycle when using the real functions is described by the flowchart of Fig.5.
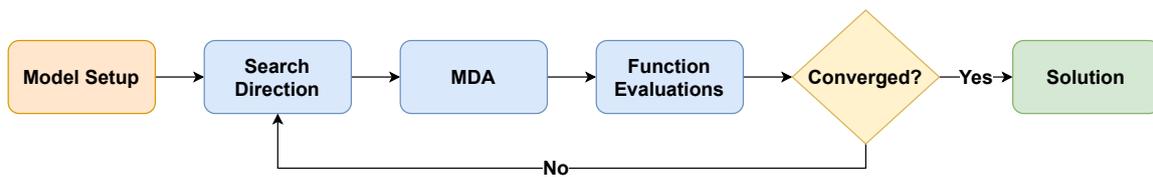
Figure 5: Optimization cycle when using the real functions.

Surrogate Based Optimization In the surrogate based offline approach metamodels of the objective and constraint functions are built based on a predefined number of function evaluations. The optimization itself is then performed in the aforementioned metamodels. The surrogate models are generated in the Surrogate Modeling Toolbox (SMT) [12] using a constant regression and Gaussian correlation. As shown in Fig.6, firstly the Design of Experiments (DOE) using the Latin Hypercube Sampling (LHS) technique is generated and the surrogate models, for the objective functions and constraints, are built. The quality of the surrogate models is then assessed and if deemed insufficient more samples are added, otherwise these models are used for the optimization process. The gradient-based algorithm (SLSQP) is used to solve this problem, however now the gradient information is provided by the Kriging methodology, and therefore, fewer evaluations are conducted in the real functions. The final solution is then evaluated with the real model to check if there are any major discrepancies.
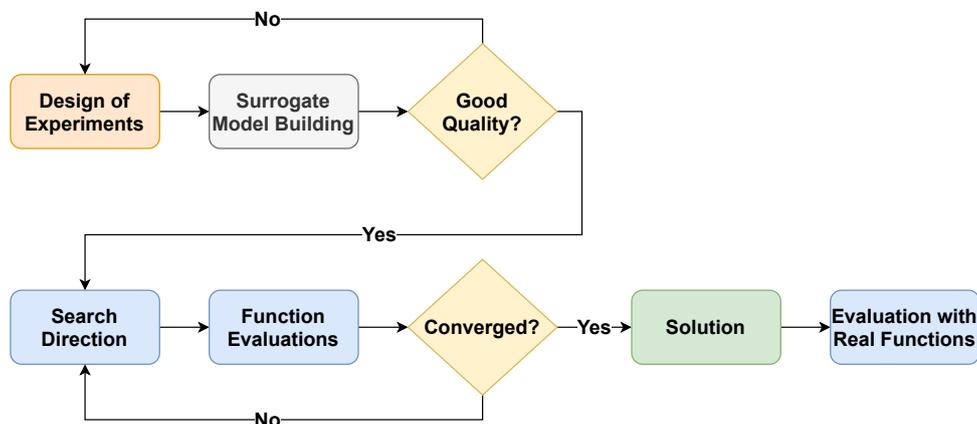
Figure 6: Optimization cycle when using the surrogate models.

Catarina Ribeiro, Frederico Afonso, Martin Sohst and Afzal Suleman

Surrogate Based Optimization with Adaptive Sampling   In the adaptive, or on-line, sampling approach, instead of minimizing the metamodel of the objective function, the WB2 infill criterion function [9] is employed. The constraints used in the problem correspond to the surrogate models of the constraints. As shown in Fig.7, an initial DOE is generated and the initial surrogate models are built. Subsequently, the infill criterion function is defined, using the objective function (total energy) surrogate model including its uncertainty. At this point, the objective function for the optimizer to minimize becomes the infill criterion function itself. The optimization problem is solved using a genetic algorithm, and the solution obtained is then evaluated with the real model and a new sample point is added to the DOE. The surrogate models, and consequently the infill criterion function, are then updated and the process starts over again until the maximum number of evaluations or convergence is achieved.
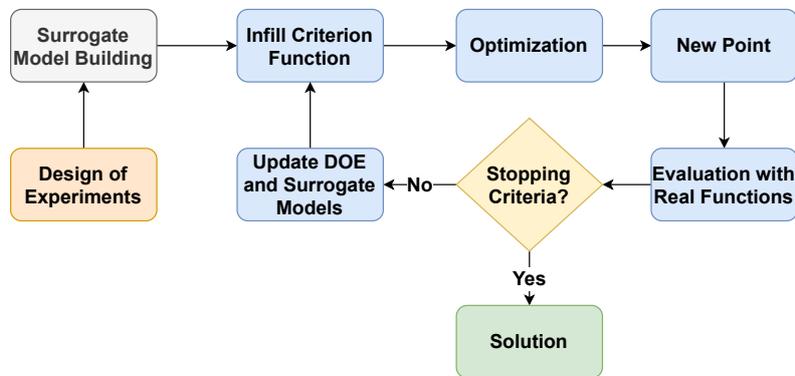
Figure 7: Optimization cycle when using surrogate models and adaptive sampling.

3   RESULTS

The baseline aircraft defined in the conceptual design phase and modelled in OAS (see Tab.1) is the starting point of the three optimization approaches followed here. Based on the previously established values for the design variables (see Tab.2) the main performance parameters shown in Tab.3 were calculated in the OAS framework.

Table 3: Baseline performance.

Wing structural mass [kg]	Horizontal tail structural mass [kg]	Fuel mass [kg]	Total mass [kg]	L/D [-]	Total energy [MJ]
408.35	37.68	407.07	3524.10	13.36	17937.11

To compare the different strategies five case studies of the problem are carried out: 2.1, 2.2 and 2.3 correspond to the first, second and third case studies with 2 design variables, respectively; 4 and 8 are the case studies with 4 and 8 design variables, respectively. A map of these case studies can be found in Tab.4.

3.1   Quality of the surrogate models

Before carrying out the optimization, using the three different approaches explained before, a study on the quality of the surrogate models for each case is done. The goal is to find out how many points are needed to have a surrogate model that is able to adequately

Catarina Ribeiro, Frederico Afonso, Martin Sohst and Afzal Suleman

Table 4: Design variables used in each case study.

Case study	α	$c_{w,root}$	$c_{w,tip}$	$t_{w,spar}$	$t_{w,skin}$	$c_{ht,root}$	$c_{ht,tip}$	$t_{ht,spar}$	$t_{ht,skin}$
2.1		x			x				
2.2			x	x					
2.3	x	x							
4		x	x	x	x				
8		x	x	x	x	x	x	x	x

mimic the real function behaviour. Surrogate models of both the objective function and constraints are tested using a different set of test points for each case study. However, only the results of the average relative error of the objective function, the total energy, are presented here.

The objective function surrogate model in each case presents very low values of the average relative error even with a small number of sample points. However there are some constraints that show a significantly higher relative error, sometimes reaching values around 300%. This happens when the constraints show a non-linear behaviour, which explains the need for more sample points such that the surrogates can better represent the real behaviour of the function. Nevertheless, with an increase of the number of sample points, the relative error tends to decrease and converge to a value near 0%.

The number of sample points needed to have a relative error smaller than 5% is: 35 for case study 2.1; 10 for case 2.2; 25 for case 2.3; 40 for case 4; and more than 300 for case 8.

3.2 Optimization results

For each case study, the optimization problem is solved using three different approaches previously mentioned: (i) using the real functions, implemented on OAS and using the adjoint method; (ii) using the surrogate models of these real functions; (iii) using an adaptive sampling with the WB2 criterion. For the first two strategies, the optimization algorithm is the SLSQP, while for the last approach the GA is used, where an adequate population size and number of generations is chosen. The relatively cheap real function evaluation enabled a more thorough metamodel exploration, meaning the best possible surrogate fit was used in the optimization. It should be noted that this approach is not possible in general, as high fidelity evaluations commonly are costly.

3.2.1 Case 2.1

The results for case 2.1 obtained with the three strategies mentioned before are presented in Tab.5.

All the three solutions present very similar results, with differences between them smaller than 1%. This way the results obtained with the surrogate models are validated. It is worth to notice that the performance parameters, that correspond to strategies where the surrogate models are used, are the real function evaluations with the obtained design variables.

In the second approach, the optimization results shown correspond to the ones when the surrogate models are built using 50 sample points. When the adaptive sampling is

Catarina Ribeiro, Frederico Afonso, Martin Sohst and Afzal Suleman

(a) Case 2.1

(b) Case 2.2

(c) Case 2.3

(d) Case 4

(e) Case 8
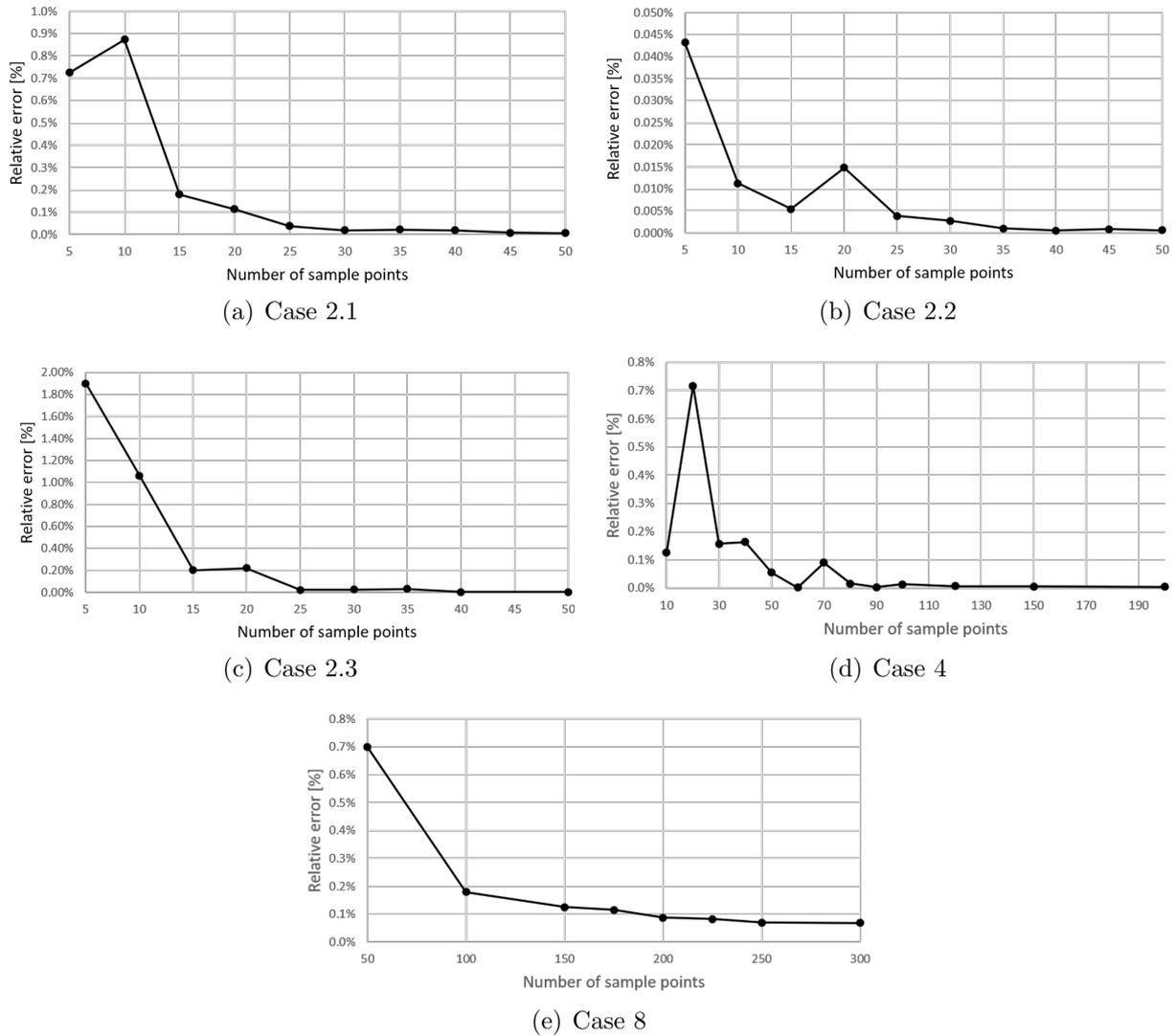
Figure 8: Average relative error of the objective function surrogate model for each case.

Table 5: Results of the different solutions of case 2.1.

	$c_{w,root}$ [m]	$t_{w,skin}$ [m]	Wing structural mass [kg]	Fuel mass [kg]	Total mass [kg]	L/D [-]	Total energy [MJ]
Baseline	2.684	0.0038	408.35	407.07	3524.10	13.36	17937.11
Real functions	2.739	0.00155	228.68 -44.00 %	378.10 -7.12 %	3315.47 -5.92 %	13.54 1.35 %	16433.35 -8.38 %
Surrogate search	2.739	0.00154	228.26 -44.10 %	378.02 -7.14 %	3314.96 -5.93 %	13.54 1.38 %	16429.71 -8.40 %
Adaptive sampling	2.739	0.00157	230.06 -43.66 %	378.42 -7.04 %	3317.16 -5.87 %	13.54 1.38 %	16446.95 -8.31 %

used, the starting sampling plans to build the surrogate models are composed by: 5 sample points in the case of the objective function, 20 sample points for the constraints with a linear behaviour, and 50 sample points for the constraints with non-linear behaviour. The number of points added to the sampling plans is 50. However, the best solution is found

Catarina Ribeiro, Frederico Afonso, Martin Sohst and Afzal Suleman

after the third iteration, i.e. after adding only three points. To assure the best possible solution, the full number of iterations was utilized, as the solution is not known prior.

In terms of computational cost, the number of iterations, function and gradient evaluations associated with each approach are presented in Tab.6.

Table 6: Computational cost of the four methods for case 2.1.

	Real functions	Surrogate search	Adaptive sampling
Iterations	6	11	50
Function evaluations	6	1+50	50+50
Gradient evaluations	6	0	0

The benefits of using the surrogate models, in terms of computational cost (Tab.6), are not verified in this case, since the optimization using the real functions when using the SLSQP algorithm with the gradient information obtained from the adjoint method takes only 6 iterations to find the optimum, which corresponds to 6 function and gradient evaluations. On the other hand, the second approach takes the 50 real function evaluations to build the surrogate models plus an additional one for the converged result. The adaptive sampling approach takes the 50 initial sample evaluations and the additional 50 infill point evaluations. Therefore, the adjoint method for this case is by far the best choice given the much lower number of function evaluations.

3.2.2 Case 2.2

The different solutions obtained in this case are presented in Tab.7.

Table 7: Results of the different solutions of Case 2.2.

	$c_{w,tip}$ [m]	$t_{w,spar}$ [m]	Wing structural mass [kg]	Fuel mass [kg]	Total mass [kg]	L/D [-]	Total energy [MJ]
Baseline	1.074	0.0038	408.35	412.76	3529.79	13.19	17937.11
Real functions	1.340	0.00108	363.58 -10.96 %	397.75 -3.64 %	3470.01 -1.69 %	13.47 2.18 %	17286.07 -3.63 %
Surrogate search	1.347	0.00100	362.06 -11.34 %	397.39 -3.73 %	3468.13 -1.75 %	13.48 2.20 %	17270.45 -3.72 %
Adaptive sampling	1.341	0.00111	364.38 -10.77 %	397.76 -3.63 %	3470.82 -1.67 %	13.47 2.18 %	17286.72 -3.63 %

The results from the different approaches are, once again, very similar to each other, with differences smaller than 1%.

For the surrogate search approach 10 initial sample points are used to build the models. With the adaptive sampling approach, the number of sample points of the starting sampling plan is: 5 for the total energy and 20 for the constraints. Since in the previous case the best solution was achieved within few iterations, the maximum iterations were reduced to 25 to allow for further exploration with manageable costs.

In terms of computational cost, a comparison between the different approaches is presented in Tab.8.

Catarina Ribeiro, Frederico Afonso, Martin Sohst and Afzal Suleman

Table 8: Computational cost of the different approaches for Case 2.2.

	Real functions	Surrogate search	Adaptive sampling
Iterations	8	3	25
Function evaluations	10	1+10	25+20
Gradient evaluations	8	0	0

Similarly to the previous case, the adjoint method optimization presents low computational costs, having only 10 real function evaluations, while the optimization using the surrogate models needs 10 real functions evaluations to build models plus the additional final evaluation. The adaptive sampling approach is the most costly, needing the 20 real function evaluations to build the total energy and the constraints initial surrogate models, plus 25 real functions evaluations throughout the process. However, the best found result is obtained after 6 iterations. In this case, the computational costs of the first two approaches are very similar.

3.2.3 Case 2.3

The different solutions obtained with the used approaches are presented in Tab.9 for this case.

Table 9: Results of the different solutions of Case 2.3.

	$c_{w,root}$ [m]	α [m]	Wing structural mass [kg]	Fuel mass [kg]	Total mass [kg]	L/D [-]	Total energy [MJ]
Baseline	2.684	-0.8	408.35	407.07	3524.10	13.36	17937.11
Real functions	2.500	-0.455	388.29 -4.91 %	360.28 -11.49 %	3457.25 -1.90 %	14,91 11.59 %	15664.39 -12.67 %
Surrogate search	2.500	-0.454	388.29 -4.91 %	360.23 -11.51 %	3457.20 -1.90 %	14.91 11.61 %	15662.03 -12.68 %
Adaptive sampling	2.512	-0.465	389.57 -4.60 %	361.54 -11.18 %	3459.79 -1.82 %	14.87 11.30 %	15719.06 -12.37 %

The results are, once more, very consistent between each other, with differences smaller than 1% again. The number of sample points used to build the surrogate models that lead to the optimal solution in the second approach, is 10. On the other hand, the number of sample points used to build the initial sampling plans in the last approach are: 5 for the total energy function, 25 for every constraint except the pitching moment coefficient, and 40 for this latter constraint to achieve low prediction errors. The maximum number of iterations is set to 25.

In terms of computational costs (shown in Tab.10), the real functions optimization approach presents a lower number of real function evaluations, 4 for the objective function and 4 for the gradients. The surrogate based optimization requires the 10 initial real functions evaluations to build the surrogate models and the final confirmation one. As for the adaptive sampling it takes the 40 real functions evaluations to build the metamodel, plus 25 real functions evaluations during the process.

The gradient-based optimization with the adjoint method shows again an efficient

Catarina Ribeiro, Frederico Afonso, Martin Sohst and Afzal Suleman

Table 10: Computational cost of the three methods for case 2.3.

	Real functions	Surrogate search	Adaptive sampling
Iterations	4	3	25
Function evaluations	4	1+10	25 +40
Gradient evaluations	4	0	0

convergence towards the optimum, followed by the surrogate based search. The adaptive sampling requires the highest computational time, as the termination is caused by the maximum number of iterations, although the best sample is identified in the 6$^{\text{th}}$ iteration.

3.2.4 Case 4

In the four-dimensional case the three solutions obtained with each optimization approach are presented in Tab.11.

Table 11: Results of the different solutions obtained in case study 4.

	$c_{w,tip}$ [m]	$c_{w,root}$ [m]	$t_{w,spar}$ [m]	$t_{w,skin}$ [m]	Wing structural mass [kg]	Fuel mass [kg]	Total mass [kg]	L/D [-]	Total energy [MJ]
Baseline	1.074	2.684	0.0038	0.0038	408.35	407.07	3524.10	13.36	17937.11
Real functions	0.972	2.812	0.00196	0.00171	191.99 -52.98 %	375.72 -7.70 %	3275.66 -7.05 %	13.46 0.75 %	16329.59 -7.69 %
Surrogate search	0.982	2.818	0.00155	0.00186	194.64 -52.33 %	376.78 -7.44 %	3280.10 -6.92 %	13.44 0.60 %	16375.18 -7.43 %
Adaptive sampling	0.959	2.825	0.00245	0.00178	210.41 -48.47 %	378.99 -6.90 %	3298.08 -6.41 %	13.43 0.52 %	16471.23 -6.89 %

For the gradient based surrogate search, the DoE contains 50 samples. The number of initial sample points for the adaptive surrogate approach are: 10 for the objective function, 30 for every constraint except two failure criteria of the wing for the pull-up manoeuvre, which have 40 initial samples. The maximum number of iterations is 50. In this case, contrarily to what happened in the two dimensional cases, the 50 additional points show different results in almost every iteration, which suggests that a convergence is not reached yet and a better solution can be found. Also, the number of infeasible points increased, showing that there are still some errors in the surrogate models, even though their accuracy seems high, with an average relative error lower than 3%.

The differences between the solutions are with less than 1 %, thus not very significant. The best solution is found with the adjoint based optimization. As stated before, the solution found with the last approach may correspond to a local minimum. Continuing the process might result in identification of the global optimum region. The limited number of points added is explained by the time constraints.

In the gradient based surrogate approach, the optimizer may have reached a local minimum since the predicted derivatives may contain errors and therefore divert the search towards a local solution.

With 21 funtion and 14 gradient evaluations the adjoint approach is in terms of computational costs the most efficient procedure. The gradient based surrogate strategy requires 50 samples to accomplish sufficient accuracy for identifying a valid minimum. With the

Catarina Ribeiro, Frederico Afonso, Martin Sohst and Afzal Suleman

Table 12: Computational cost of the different optimization approaches for case 4.

	Real functions	Surrogate search	Adaptive sampling
Iterations	14	21	50
Function evaluations	21	1+50	50+40
Gradient evaluations	14	0	0

adaptive technique besides the initial 40 samples the maximum number of iterations (50) are performed to assure an appropriate feasible design. However, the best determined solution is obtained after 29 iterations.

3.2.5 Case 8

The values of the design variables of the different solutions found are presented in Tab.13 and the corresponding performance parameters are presented in Tab.14.

Table 13: Design variables values of the different solutions obtained in case study 8.

	$c_{w,tip}$ [m]	$c_{w,root}$ [m]	$t_{w,spar}$ [m]	$t_{w,skin}$ [m]	$c_{ht,tip}$ [m]	$c_{ht,root}$ [m]	$t_{ht,spar}$ [m]	$t_{ht,skin}$ [m]
Baseline	1.074	2.684	0.0038	0.0038	1.86	1.86	0.00255	0.00255
Real functions	1.230	2.511	0.00199	0.00222	1.15	1.15	0.0005	0.00168
Surrogate search	1.205	2.533	0.0028	0.00203	1.15	1.15	0.0005	0.00089
Adaptive sampling	1.253	2.488	0.00986	0.00132	1.155	1.161	0.00348	0.00054

Table 14: Performance parameters of the different solutions obtained in case study 8.

	Wing structural mass [kg]	Horizontal tail mass [kg]	Fuel mass [kg]	Total mass [kg]	L/D [-]	Total energy [MJ]
Baseline	408.35	37.68	407.07	3524.10	13.36	17937.11
Real functions	232.82 -42.99 %	7.85 -79.17 %	349.93 -14.04 %	3261.61 -7.45 %	14.45 8.19 %	15213.01 -14.00 %
Surrogate search	237.67 -41.80 %	7.12 -81.12 %	349.70 -14.09 %	3265.48 -7.34 %	14.48 8.41 %	15203.15 -14.06 %
Adaptive sampling	362.52 -11.22 %	13.14 -65.14 %	362.80 -10.87 %	3409.45 -3.25 %	14.58 9.14 %	15772.57 -10.84 %

The differences between the solutions obtained with the first two approaches are very small. However, the difference of the solution found with the last approach is higher than on the previous cases. This suggests that in the last approach the global minimum was not found. This might have happened because either the number of individuals or the

Catarina Ribeiro, Frederico Afonso, Martin Sohst and Afzal Suleman

number of added points is too low and so some areas of the design space might not be considered.

In terms of computational cost, the surrogate models present a higher cost once again, with the number of real function evaluations in the first approach being only 15, while in the second approach 200 real function evaluations are necessary to build sufficient surrogate models of the objective and constraint functions. For the adaptive sampling strategy 300 initial samples are generated and 200 are added throughout the process. The best configurations is already found in the first iteration and a further improvement could not be achieved regardless of the additional infill points.

Table 15: Computational cost of the different optimization approaches for Case 8.

	Real functions	Surrogate search	Adaptive sampling
Iterations	14	19	200
Function evaluations	15	200	200+300
Gradient evaluations	14	0	0

In this high dimensional case the apparent advantage of the adjoint method compared with the other approaches is distinct, where a significant lower number of evaluations are necessary to reach an optimal solution. Further, one can observe that with the adjoint method the number of evaluations is not increasing substantially with the increase of the number of design variables throughout the cases, contrary to the surrogate based approaches, where more and more samples are needed for building the metamodels.

3.3 Optimal solution

The optimum found for minimizing the total energy for the defined mission corresponds to the solution determined with the surrogate model strategy for Case 8. The proposed configuration presents a wing structural mass that is around 42 % lighter than the baseline, a reduction of around 81 % in the horizontal stabilizer structural mass and a reduction of about 14 % of the fuel mass. This leads to an overall mass that is around 7 % smaller than the baseline. The lift-to-drag ratio of this configuration is almost 8.5 % higher than the baseline. The solution shows a significant reduction of the total energy needed, 14.06 %. The baseline and the optimal solution are illustrated in Fig.9.

Baseline
Optimal solution
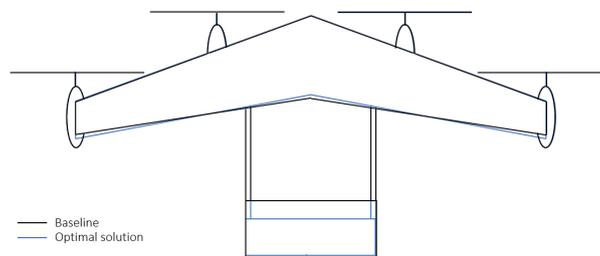
Figure 9: Baseline and optimal solution general configurations

Examining the different cases and the design variables considered for each of them, one can also draw conclusions regarding the influence of each design variable. Case 2.2 shows the high influence of α, considered in the L/D of the Breguet range equation. The cases 2.1 and 2.3 are point optimizations of case 4, where all four former variables are

combined in the optimization statement. As expected, the highest benefit is achieved with the largest number of DVs considered, meaning a full adaptation of the wing and horizontal stabilizer. Evan though in Case 4 the optimizer was able to minimize the objective function, it was not possible to achieve as good results as the one for Case 2.1, which comprises two of the same design variables. Based on this outcome one can believe that there is some kind of multi-modality in the design space, which could have been surpassed if a different gradient based algorithm and a multi-start approach have been employed. Given the fact that with the adaptive sampling technique it was not possible to identify this region, it is expected to be a shallow multi-modality.

4 CONCLUSIONS

The presented work addresses the optimization of a UAM-VTOL regarding its mission energy consumption. The number of constrains, including structural, aerodynamic and stability topics, poses a complex challenge. Different strategies for finding an improved configuration based on an initial configuration are investigated, namely adjoint method and surrogate based approaches.

Comparing the surrogate model based optimizations with an adjoint based optimization of the real functions shows lower computational cost for the latter strategy. At times the optimization results in a slightly worse solution. However, this difference is marginal and does not justify the significant higher costs. This means, that for the problem at hand, the surrogate models do not present a relevant advantage over the real functions, which are already simple, since the physical models are of low-fidelity. To improve the performance of the adaptive sampling strategy, a lower number of initial samples together with a finer tuned setup could be more target-oriented towards lower computational costs.

This can also be explained because the analytical partial derivatives of each function, computed by means of the adjoint method, were possible to give as an input to the optimizer. If for instance the derivatives were more complex or not available, the real functions approach may not have been the better strategy.

The design of the wing is also very similar to the baseline used, which can lead to the quick optimization process using the real functions. This can either be happening because the optimization is too constrained, since the number of design variables is relatively small, or because the baseline is already a good design. Based on the case studies conducted a possible conclusion is that the design space is of multi-modal nature, although shallow, since the adaptive sampling was not able to capture it.

ACKNOWLEDGEMENTS

REFERENCES

[1] S. Rajendran and S. Srinivas. Air taxi service for urban mobility: A critical review of recent developments, future challenges, and opportunities. *Transportation Research Part E: Logistics and Transportation Review*, 143, 2020. doi:10.1016/j.tre.2020.102090.

Catarina Ribeiro, Frederico Afonso, Martin Sohst and Afzal Suleman

[2] J. R. R. A. Martins and A. B. Lambe. Multidisciplinary design optimization: A survey of architectures. *AIAA Journal*, 51(9):2049–2075, 2013. doi:10.2514/1.J051895.

[3] A. Papageorgiou, M. Tarkian, K. Amadori, and J. Ölvander. Multidisciplinary design optimization of aerial vehicles: A review of recent advancements. *International Journal of Aerospace Engineering*, 2018:1–21, 2018. doi:10.1155/2018/4258020.

[4] G. K. Kenway, C. A. Mader, P. He, and J. R. Martins. Effective adjoint approaches for computational fluid dynamics. *Progress in Aerospace Sciences*, 110:100542, 2019. doi:10.1016/j.paerosci.2019.05.002.

[5] R. Yondo, E. Andrés, and E. Valero. A review on design of experiments and surrogate models in aircraft real-time and many-query aerodynamic analyses. *Progress in Aerospace Sciences*, 96:23–61, 2018. doi: 10.1016/j.paerosci.2017.11.003.

[6] A. J. Booker, J. E. Dennis Jr., P. D. Frank, D. B. Serafini, V. Torczon, and M. W. Trosset. A rigorous framework for optimization of expensive functions by surrogates. *Structural and Multidisciplinary Optimization*, 17:1–13, 1999. doi:10.1007/BF01197708.

[7] D. R. Jones and M. Schonlau. Efficient Global Optimization of Expensive Black-Box Functions. *Journal of Global Optimization*, 13:455–492, 1998. doi:10.1023/A:1008306431147.

[8] M. J. Sasena, P. Papalambros, and P. Goovaerts. Exploration of metamodeling sampling criteria for constrained global optimization. *Engineering Optimization*, 34 (3):263–278, 2002. doi:10.1080/03052150211751.

[9] A. G. Watson and R. J. Barnes. Infill sampling criteria to locate extremes. *Mathematical Geology*, 27:589–608, 1995. doi:10.1007/BF02093902.

[10] J. P. Jasa, J. T. Hwang, and J. R. R. A. Martins. Open-source coupled aerostructural optimization using python. *Structural and Multidisciplinary Optimization*, 57:1815–1827, 2018. doi:10.1007/s00158-018-1912-8.

[11] J. S. Gray, J. T. Hwang, J. R. R. A. Martins, K. T. Moore, and B. A. Naylor. OpenMDAO: An Open-Source Framework for Multidisciplinary Design, Analysis, and Optimization. *Structural and Multidisciplinary Optimization*, 59:1075–1104, 2019. doi:10.1007/s00158-019-02211-z.

[12] M. A. Bouhlel, J. T. Hwang, N. Bartoli, R. Lafage, J. Morlier, and J. R. Martins. A python surrogate modeling framework with derivatives. *Advances in Engineering Software*, 135, 2019. 10.1016/j.advengsoft.2019.03.005.

[13] Flexcraft Consortium. Flexcraft - Flexible Aircraft. `https://flexcraft.pt/en/home_en/`, 2020. Accessed on July 2021.

[14] B. J. Brelje and J. R. Martins. Electric, hybrid, and turboelectric fixed-wing aircraft: A review of concepts, models, and design approaches. *Progress in Aerospace Sciences*, 104:1–19, 2019. doi:10.1016/j.paerosci.2018.06.004.

Catarina Ribeiro, Frederico Afonso, Martin Sohst and Afzal Suleman

[15] T. L. Saaty. *The Analytic Hierarchy Process: Planning, Priority Setting, Resource Allocation.* McGraw-Hil, 1980.

[16] D. P. Raymer. *Aircraft Design: A Conceptual Approach.* American Institute of Aeronautics and Astronautics, Inc., 4th edition, 2006. ISBN: 1563478293.

[17] M. D. Maisel, D. J. Giulianetti, and D. C. Dugan. *The history of the XV-15 tilt rotor research aircraft: from concept to flight.* Number 17 in Monographs in Aerospace History. National Aeronautics and Space Administration, Office of Policy and Plans, NASA History Division, Washington, D.C., USA, 2000.

[18] S. S. Chauhan and J. R. R. A. Martins. Low-fidelity aerostructural optimization of aircraft wings with a simplified wingbox model using openaerostruct. In H. C. Rodrigues, J. Herskovits, C. M. M. Soares, A. L. Araújo, J. M. Guedes, J. O. Folgado, F. Moleiro, and J. F. A. Madeira, editors, *EngOpt 2018 Proceedings of the 6th International Conference on Engineering Optimization*, pages 418–431, Cham, 2019. Springer International Publishing. ISBN 978-3-319-97773-7. doi:10.1007/978-3-319-97773-7_38.

[19] A. B. Lambe and J. R. R. A. Martins. Extensions to the design structure matrix for the description of multidisciplinary design, analysis, and optimization processes. *Struct Multidisc Optim*, 46, 2012. doi:10.1007/s00158-012-0763-y.

MULTI-FIDELITY GAUSSIAN PROCESS MODEL FOR CFD AND WIND TUNNEL DATA FUSION

Rubén Conde Arenzana[1], Andrés F. López-Lopera[1], Sylvain Mouton[2], Nathalie Bartoli[1] and Thierry Lefebvre[1]

1: ONERA/DTIS, Université de Toulouse, F-31055 Toulouse, France
2: ONERA/DS, F-31410 Mauzac, France

Abstract. *In aerodynamic design, both Computational Fluid Dynamics (CFD) simulations and wind tunnel (WT) experiments deliver datasets that are complementary in terms of uncertainties and density of information. In many situations it is desirable to use methods that combine all available information while accounting for the strengths of both sources. In this paper, we combine the sources in a multi-fidelity Gaussian process (GP) model to foretell the aerodynamic forces and moments. The resulting model accounts for input-dependent error measurements in both experimental and simulated data. To validate the model, we construct a proper multi-source aerodynamic database containing CFD and WT data. This database is based on the NASA Common Reference Model. The CFD simulations are based on Reynolds-averaged Navier-Stokes (RANS) equations. We demonstrate in numerical settings that the suggested multi-fidelity GP framework outperforms the single-fidelity one in terms of prediction accuracy at the highest level of fidelity (i.e. WT data). The resulting model also allows to reconstruct common aerodynamic profiles (e.g. representations of longitudinal forces) with uncertainties.*

Keywords: CFD, wind tunnel tests, multi-fidelity databases, error measurements, surrogate models, Gaussian processes

R. Conde Arenzana, A. F. López-Lopera, S. Mouton, N. Bartoli and T. Lefebvre

1 INTRODUCTION

Nowadays, aerodynamic data for aerospace vehicles are obtained from different sources such as in-flight tests, wind tunnel (WT) experiments and several types of numerical simulations [1–4]. All those sources provide information about the same flying aircraft, but with different characteristics in terms of accuracy, cost, cycle-time and availability [2]. In principle, data collected from flight testing are the most representative of the reality, but are limited in scope by cost and safety issues. They are also unavailable during most of the design phase, although data from a previous similar aircraft can actually be useful. On the other hand, numerical simulations, in particular Computational Fluid Dynamics (CFD), can be exploited even in early design phases, especially if one bears in mind their significant advances during the last decades [3]. However, their accuracy is still limited by issues such as turbulence modelling and discretization errors, and their ability to produce thousands of flight conditions is also limited by available computational power. Finally, WT testing lies somewhat in between.

Although these sources of data were sometimes seen as competitors in the past, the growing consensus today is that they can be used in a complementary manner for the foreseeable future [2]. Indeed, their characteristics and the aerodynamic data they generate are very different, and, in many instances, complementary. For example, flow simulations are able to provide a complete mapping of the local pressure on the aircraft surface, but generally for a limited number of flow conditions due to the high recurring computational cost involved for each new simulation. Quite the opposite is observed in WT data: the number of pressure measurements is limited by the available room in the model, but any new flow condition is easily obtained by changing the tunnel conditions. In this context, appropriate data fusion methods are needed to consider these datasets in a unified framework aiming at fully leveraging the knowledge gathered by the different sources.

For aerodynamic data fusion, due to the cost of experimental tests including both in-flight and WT tests, many of the previous works focus on simplistic models (e.g. such the vortex lattice model, VLM), and/or CFD simulations [5–7]. It is often assumed that Reynolds-averaged Navier-Stokes (RANS) simulations accurately describe aerodynamic phenomena at a tractable computational cost (in the order of minutes or hours depending on the mesh resolution and machine capacity). On the other hand, since VLM-based frameworks are faster but less accurate, they can provide complementary information that may reinforce aerodynamic databases [5, 6]. As a result, it is possible to meet the desired requirements in terms of reliability but with the advantage of achieving a non-negligible reduction of resources. There are only a few works that exploit WT tests as another source data [see, e.g., 8–12], however they commonly consider a low amount of data (less than 100 points).

Efforts in this direction have been made [6, 8–10], and in particular, surrogate models based on Gaussian processes (GPs) are drawing attention in the aerodynamic community due to its versatility and its ability to quantify uncertainties [11–17]. For example, in [11], a multi-task GP regression model (also known as co-Kriging) has been proposed, accounting for both CFD simulations (Euler and RANS equations) and a notional WT database. In [14], a multi-fidelity GP framework based on the auto-regressive model proposed by [18] has been further investigated for (Bayesian) optimization purposes. As shown by [11, 14], GPs provide promising results that can be exploited for decision tasks when considering multiple aerodynamic data sources. In fusing such datasets, uncertainty quantification is

R. Conde Arenzana, A. F. López-Lopera, S. Mouton, N. Bartoli and T. Lefebvre

Figure 1: Large Reference Model (LRM) used in the S1-WT at ONERA.

playing a key role. Quantifying and propagating uncertainties is a difficult topic, both in CFD modeling [see, e.g., 9] and in WT experiments [see, e.g., 19].

Our contributions here are threefold. We first provide a large aerodynamic database that features the implementation of WT data and CFD simulations based on RANS equations. Second, we set up simplified uncertainty models of the CFD and WT data, aiming at defining realistic values for the input varying uncertainties of force coefficients. Finally, we further investigate a multi-fidelity GP framework that exploits both WT and CFD data, while accounting for input-varying uncertainties (heteroscedastic case). The suggested model is based on the auto-regressive GP scheme proposed by [18].

This paper is organized as follows: Section 2 presents the construction of the multi-source database, explaining how WT and CFD data are collected. Section 3 delves into the WT and CFD uncertainty models. The heteroscedastic multi-fidelity GP model is detailed in Section 4. The results are discussed in Section 5. Lastly, Section 6 summarizes the conclusions and potential future works that could complement this study.

2 CONSTRUCTION OF THE MULTI-SOURCE DATABASE

The construction of a proper database is an essential component to develop a data-driven aerodynamic model. In addition, different data acquisition schemes can lead to different features in terms of reliability and lead time, which are usually inversely related. For this purpose, a multi-source aerodynamic database based on the NASA Common Reference Model (CRM) [20] is proposed. One of the main contributions here is the use of WT data provided by ONERA which will be considered as the high-fidelity data. Figure 1 shows one of the models used in the WT experiments. The low-fidelity data are obtained from numerical CFD simulations based on RANS equations. Further details are given in Sections 2.1 and 2.2.

The aerodynamic database contains three inputs: the Mach number (M), the Reynolds number (Re), and the angle of attack (α [deg]). Figure 2 shows pairwise histograms for those input parameters. The outputs are the drag coefficient (C_x), the lift coefficient (C_z), and the pitch moment coefficient (C_M). 4D scatter plots of those coefficients are shown in Fig.3. Section 2.3 describes the methodology considered to construct the design of experiments (DoE) used to run the simulations and to choose the experimental points that will be taken into account to train the model.

R. Conde Arenzana, A. F. López-Lopera, S. Mouton, N. Bartoli and T. Lefebvre
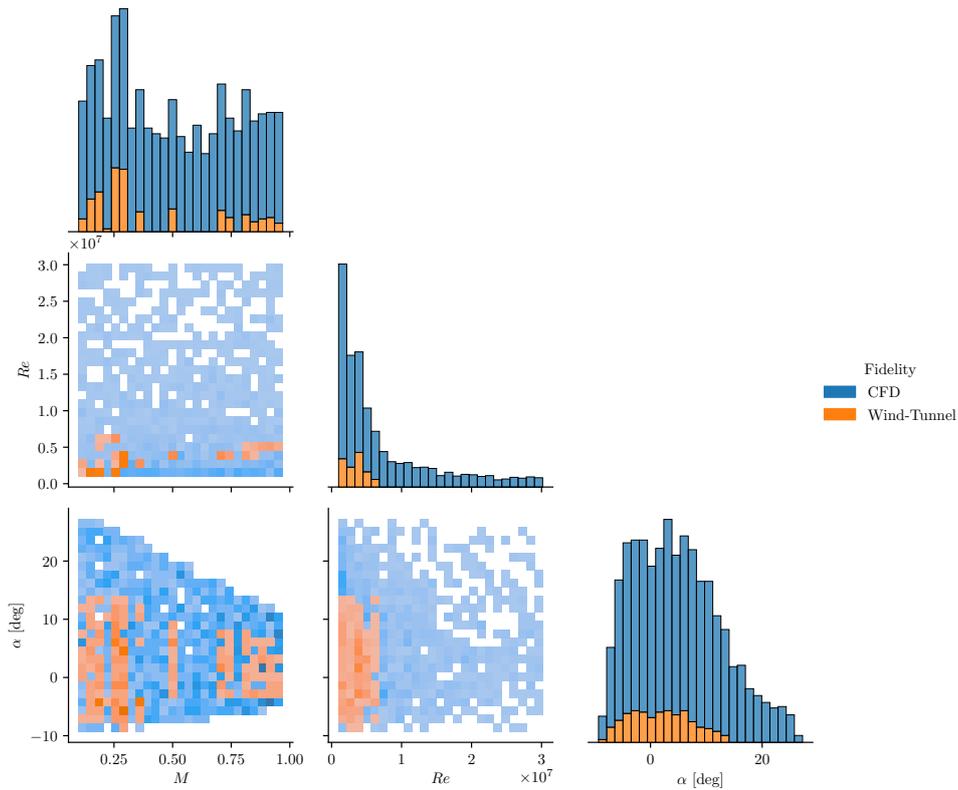
Figure 2: Pairwise histograms of the aerodynamic inputs α, Re and M. Results are shown for both (orange) WT and (blue) CFD data. The panels in the diagonal show 1D marginal histograms, while the other ones show 2D histograms of pairs of inputs. For the 2D illustrations, darker pixels represent a bigger concentration of points.
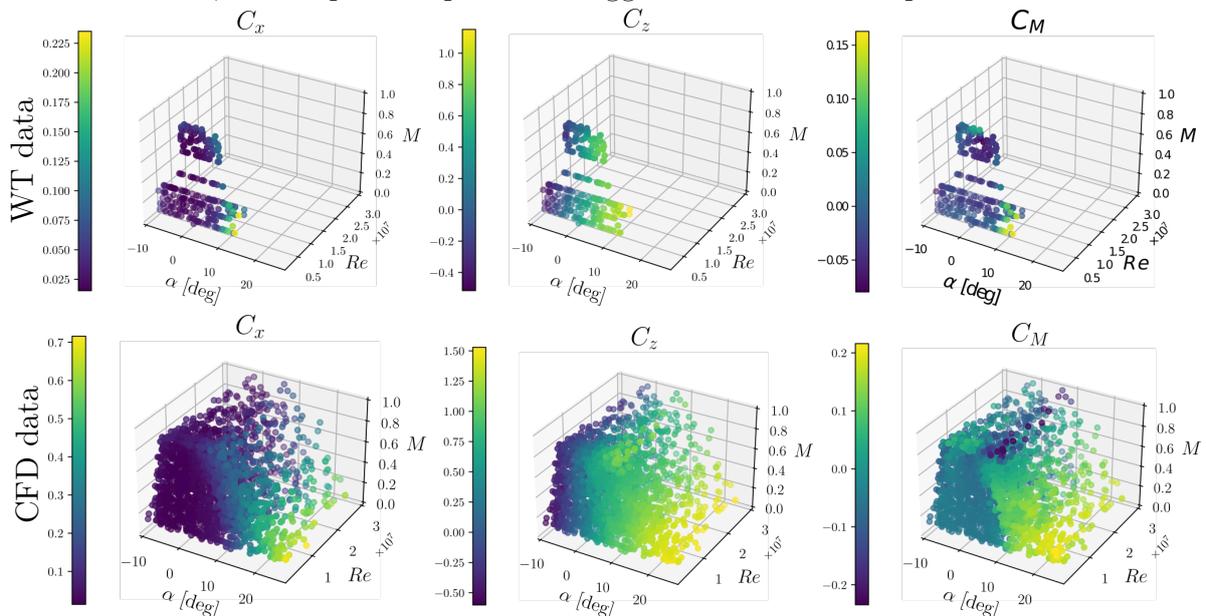
Figure 3: 4D scatter plots for the multi-fidelity database generated in Section 2. 3D axes correspond to the aerodynamic input parameters (α, Re and M), and the colorbar shows the magnitude of the output coefficient (either C_x, C_z or C_M). Results are shown for both (top) WT and (bottom) CFD data.

R. Conde Arenzana, A. F. López-Lopera, S. Mouton, N. Bartoli and T. Lefebvre

2.1 Wind tunnel (WT) data

Experimental testing is performed in two different ONERA WT centers: the F1-WT, which focuses on high Re values and $M \in [0.05, 0.36]$ [21]; and the S1MA-WT, which focuses on transonic speeds [22] (see Fig.1). The CRM shape is used to build two Large Reference Models (LRMs): the first one for S1-WT with a wing span of 3.5m (scale 1/16.835) and the second one for F1-WT with a wing span of 3m (scale 1/19.5). Aeroelastic deformations are considered in the design to produce a shape under load that is comparable to previous CRM tests in NTF [23] and ETW [24]. In the database construction, we use the wing-body configuration without tail planes to be consistent with the CFD model. The boundary layer transition is forced on the wing and fuselage. The WT models are equipped with hundreds of pressure taps, but for the present study only the aerodynamic forces measured by internal balances are considered. The measurements are corrected from the effect of the WT walls thanks to potential flow theory [25], which has been recently verified to work well even under transonic conditions [26]. They are also corrected from support effect, using CFD for the S1 database [27], and by performing a dummy sting test for the F1 database. The extent of WT data is limited by the operating envelope of the WT and some other experimental considerations, such as the avoidance of excessive loads on the model support or force balance.

By collecting data from experimental tests performed in the past with the aforementioned configuration, we construct a WT database composed by 5473 samples. Due to the cost of WT tests, in further developments (e.g. in the construction of the DoE, Section 2.3), we use historical WT events instead of performing new tests.

2.2 Numerical CFD data

The RANS equations are the most widespread way to model turbulent flows, and even though if its calculation is usually related to long-time computations, the use of a coarse grid allows the extraction of a large set of points in a suitable time. RANS simulations here are carried out with the elsA software developed at ONERA [28]. In our study, we use a mesh, namely "L1", composed of 63.9×10^3 cells (approximately), which can be retrieved in the DPW5 website.[1] The one equation Spalart-Allmaras turbulence model is used, resulting in computations that are similar to the ones performed in [29]. With this configuration, seven simulations (executed in parallel) are obtained in about 35 min on a Intel$^{®}$ Xeon$^{®}$ E5-2680 v4, 14 cores, 2.4 GHz.

2.3 Design of experiments (DoE) via Latin hypercube sampling

For the construction of a DoE that properly covers the input domain, we consider a nested construction based on a maximin Latin hypercube sampling (LHS). The nested assumption is contemplated to count on an efficient implementation of the surrogate model described in Section 4. We must note that standard LHS are usually defined for hypercube domains [30]. However, this is not our case since we need to account for physical constraints. For example, experiments with simultaneously high values of M and α will lead to high-speed deep stall situations that are far outside of the flight envelope of this aircraft, and are therefore not interesting to include in the database.

---

[1]Drag Prediction Workshop 5 : `https://aiaa-dpw.larc.nasa.gov/Workshop5/workshop5.html`

R. Conde Arenzana, A. F. López-Lopera, S. Mouton, N. Bartoli and T. Lefebvre

| (a) Original input space | (b) Transformed input space |
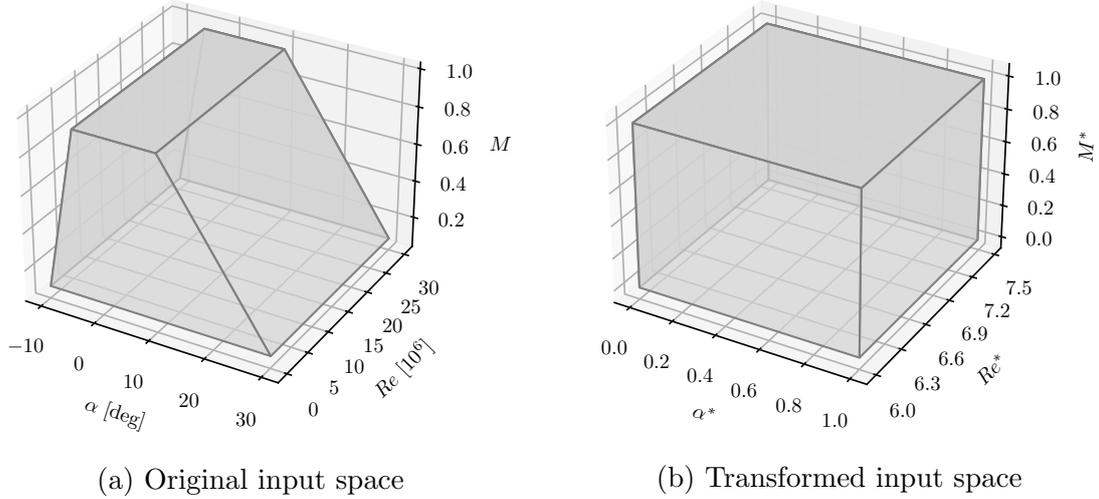
Figure 4: Aerodynamic input space used for the construction of the DoE via LHS.

By considering the different physical constraints based on [31] and on expert knowledge, it is possible to define the input space in Fig.4a with maximal ranges defined in Tab.1. Such space can be transformed into a cube (see Fig.4b) by using the parametric transformation given by

$$M^* = \frac{M - 0.1}{0.87}, \qquad \alpha^* = \frac{\alpha + 10 - 5M}{40 - 25M^*}, \qquad Re^* = \log_{10}(Re) \qquad (1)$$

With this new parametrization (M^*, α^*, Re^*), we can then propose an optimal nested DoE via LHS. To do so, we use the dedicated LHS function `NestedLHS` from the Python toolbox SMT [32], based on the enhanced stochastic evolutionary algorithm proposed in [33]. This function returns an optimal DoE per each level of fidelity while preserving a nested construction. After defining the nested DoE, we then map the generated design points into the original input space using the expressions below:

$$M = 0.1 + 0.87M^*, \qquad \alpha = -10 + 40\alpha^* + 5M^* - 25\alpha^*M^*, \qquad Re = 10^{Re^*} \qquad (2)$$

In our study, we generate a nested DoE with 250 and 1949 design points for the WT and CFD databases, respectively (see Fig.2). We must note that, to benefit from WT tests performed in the past, we match the resulting DoE of the highest fidelity level with respect to the WT database described in Section 2.1. This procedure is based on a nearest-neighbor scheme where a generated design point is replaced by the nearest WT input configuration. Although such procedure breaks down the Latin hypercube's properties, the resulting DoE still covers the input space properly (see Fig.2).

2.4 Database overview

As shown in Tab.1, CFD data are taken in a parametric space larger than the one of WT data. This is chosen with the aim of stretching out the study to the entire flight envelope of the aircraft. This is meant to illustrate the complementary nature of the two datasets in hands, one being more accurate but covering only a limited domain of the parametric space, and the other one being used to expand that knowledge, especially in terms of α and Re values.

R. Conde Arenzana, A. F. López-Lopera, S. Mouton, N. Bartoli and T. Lefebvre

Table 1: Parameters of the CRM aerodynamic database. For each data source, the ranges of the inputs are shown along with the number of samples that are part of the database.

	Wind Tunnel	elsA CFD
Mach Number (M)	[0.01, 0.95]	[0.01, 0.97]
Reynolds Number (Re) [1×10^6]	[0.77, 6.60]	[0.1, 30.0]
Angle of Attack (α) [deg]	[-9.3, 20.5]	[-10.0, 30.0]
Number of samples	250	1949

The capabilities of the RANS simulations are here pushed to their limits, and sometimes beyond, with cases that do not converge properly, especially at high AoA (see Section 3.2). This kind of data would probably be of little use to actually design the aircraft, but are regarded as sufficient for the purpose of demonstrating the data fusion process.

3   ERROR PROPAGATION ANALYSIS

In assembling data, it is helpful, and sometimes necessary, to know the uncertainty of samples. We now present how the experimental and numerical uncertainties are modelled.

3.1   WT data

A full analysis of experimental uncertainties is not immediately available for the WT tests. Indeed, such analysis has always been a complex subject [see, e.g., 19, 34]. Nevertheless, in the framework of this work, a simplified uncertainty model of the experimental dataset is set up to define realistic values for the uncertainties of C_x, C_z and C_M. This analysis does not consider uncertainties in Mach number, and ignores or overly simplifies a number of sources such as the manufacturing accuracy of the model. Some sources of uncertainty (e.g. on wall corrections) are given by an expert estimate that is appropriate for most of the database, but whose validity is more doubtful beyond stall for example. In spite of its deficiencies, this uncertainty model is regarded as rich enough for using it in the data fusion process that is the topic of the present work.

To be consistent with the surrogate model described in Section 4, all the aerodynamic parameters considered here are regarded as random Gaussian variables. We denote $\tau_{\mathcal{X}}^2$ as the variance parameter of the variable $\mathcal{X}$. In Appendix 8, we provide further details about the uncertainty model.

As an example, the drag coefficient is obtained from balance and dynamic pressure measurement as $C_x = \dfrac{A \cos \alpha + N \sin \alpha}{q S_{\text{ref}}}$, where A and N are the axial and normal aerodynamic forces in model axes (respectively), q is the dynamic pressure, S_{ref} and L_{ref} are the reference length and surface area (respectively) of the model. Consequently, the variance of the error on C_x is given by

$$\tau_{C_x}^2 = \left(\frac{\cos \alpha}{q S_{\text{ref}}}\right)^2 \tau_A^2 + \left(\frac{\sin \alpha}{q S_{\text{ref}}}\right)^2 \tau_N^2 + C_x^2 \left(\frac{\tau_q}{q}\right)^2 + C_z^2 \tau_\alpha^2. \tag{3}$$

From Eq.(3), we observe that $\tau_{C_x}^2$ varies with α. Moreover, as detailed in Appendix 8, τ_q^2 and τ_α^2 also depend on the values of M and C_z, which itself also depends on M, Re and α. This implies that the resulting variances $\tau_{C_x}^2$, $\tau_{C_z}^2$ and $\tau_{C_M}^2$ are input-varying as

R. Conde Arenzana, A. F. López-Lopera, S. Mouton, N. Bartoli and T. Lefebvre
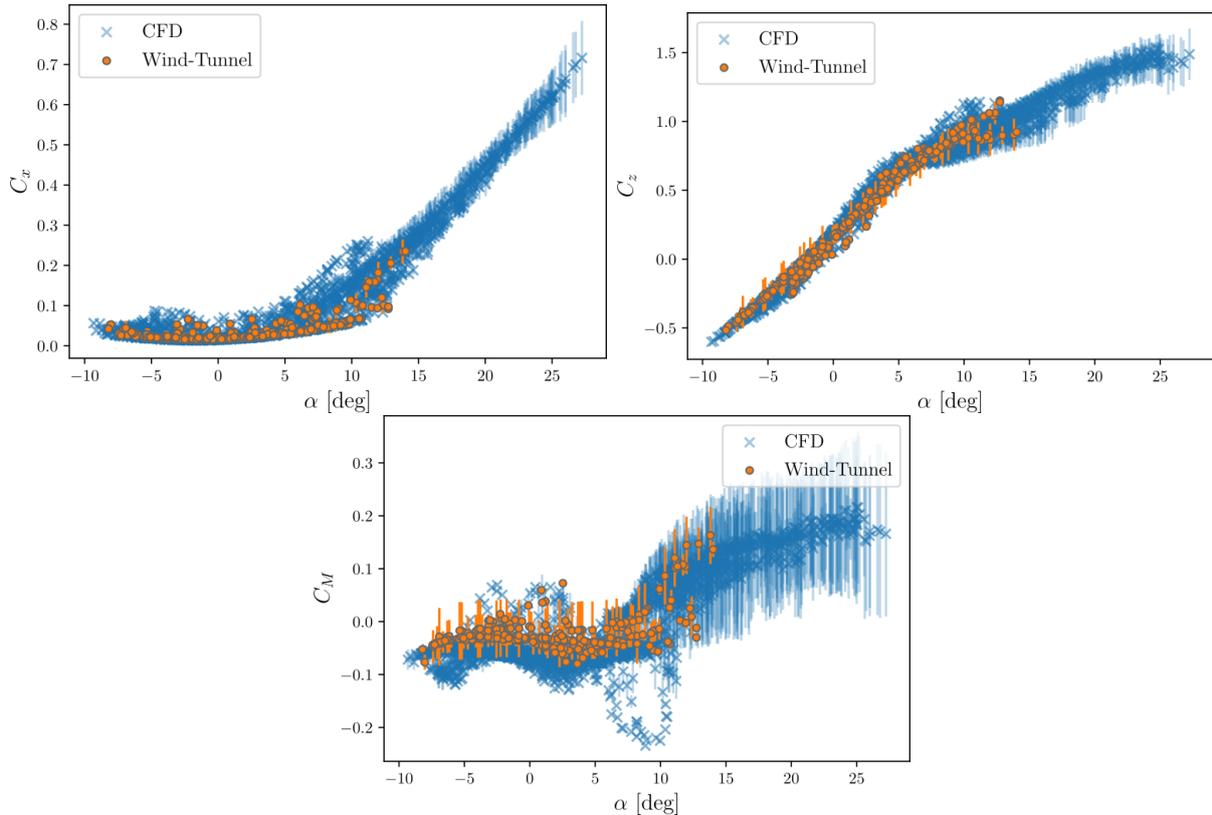
Figure 5: 1D profiles of the force coefficients C_x, C_z and C_M with respect to α [deg]. Panels show: the WT data (orange points), CFD data (blue crosses) and the associated one standard-deviation error intervals (vertical bars). To improve the visibility, four standard-deviation error intervals (orange bars) are displayed for the WT data.

we illustrate in Fig.5. There, panels show 1D profiles of the C_x, C_z, C_M as functions of α. One of the driving factors for this matter of fact is that the force balance is chosen to withstand the maximum forces expected during the test, which makes it oversized for the lowest forces to measure, which occur when the dynamic pressure q is low. In Appendix 8, we also write the expressions of variance of the errors for C_z and C_M.

3.2 CFD simulations

Defining uncertainty on the outcome of CFD simulations is even more difficult than for experiments, since both physical modeling, discretization, and solution errors play a role [35]. In particular, the uncertainty associated with turbulence modelling is an active field of research [36]. A practical solution being not available for the simulations dealt with in the present work, it is decided to use the convergence history of the force coefficient as an indication of simulation uncertainty. For that purpose, the standard deviation of the force coefficients over the last 300 iterations is used. Figure 6 shows an example of an improperly converged CFD simulation (properly converged CFD results are shown in Appendix 7), where the flow solver exhibits limit-cycle oscillations, due to the massive flow separation on the wing upper surface. This is of course a crude approximation of simulation uncertainty, and certainly not a good practice as underlined by [37]. This is contemplated however to demonstrate the ability of the GPs to handle this kind of uncertainty, until better estimates are available.

R. Conde Arenzana, A. F. López-Lopera, S. Mouton, N. Bartoli and T. Lefebvre
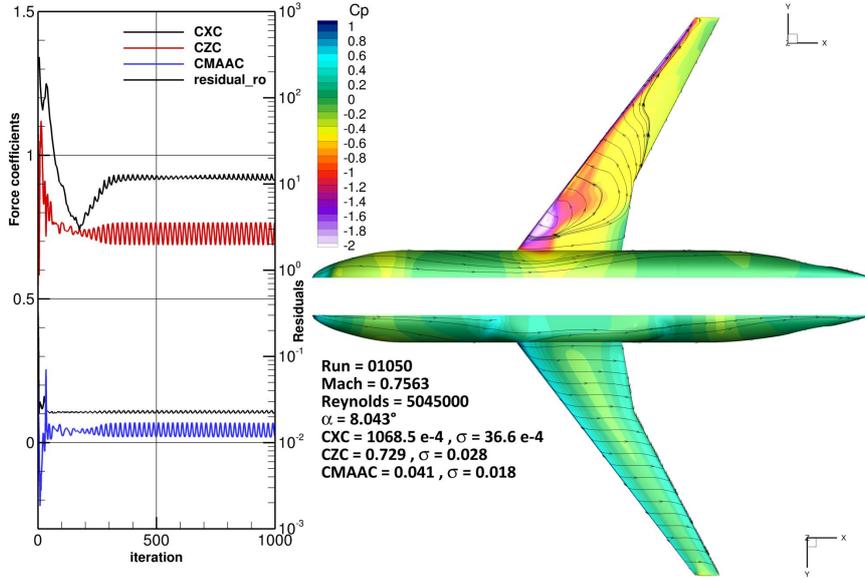
Figure 6: Example of a CFD simulation from the database constructed in Section 2, at $M = 0.7563$, $Re = 0.1 \times 10^6$ and $\alpha = 8.043$ [deg], where limit-cycle oscillations are encountered. On the left panel, convergence plots (solid lines) after 1000 iterations are shown for C_x (CXC, in black), C_z (CZC, in red) and C_M (CMAAC, in blue). On the right panel, the pressure coefficient distribution is depicted for the CRM model.

4 MULTI-FIDELITY GAUSSIAN PROCESS MODEL

In this paper, we study a multi-fidelity surrogate model based on Gaussian processes (GPs). More precisely, we consider the framework proposed by [18]. To account for the error measurements proposed in Section 3, we adapt the GP model in [18] for the case of input-varying additive Gaussian noises (heteroscedastic case).

4.1 Gaussian processes

A GP is a collection of random variables, where the resulting joint distribution of those variables is Gaussian [38]. Let $\{Y(\boldsymbol{x}), \boldsymbol{x} \in \mathcal{D}\}$ be a GP in $\mathbb{R}$ with compact input space $\mathcal{D} \subset \mathbb{R}^d$, e.g. $\mathcal{D} = [0,1]^d$. Then, Y is completely defined by its mean function $m : \mathcal{D} \to \mathbb{R}$ and covariance function (kernel) $k : \mathcal{D} \times \mathcal{D} \to \mathbb{R}$, i.e.

$$Y \sim \mathcal{GP}(m, k).$$

For ease of notation, we focus on centered GPs, i.e. $m(\cdot) = 0$, but equations can be generalized for non-centered cases [see, e.g., 38]. An example of a valid (stationary) covariance function is the squared exponential (SE) kernel given by

$$k(\boldsymbol{x}, \boldsymbol{x}') = \sigma^2 \exp\left(-\sum_{i=1}^{d} \theta_i (x_i - x_i')^2\right), \tag{4}$$

with $\boldsymbol{x}, \boldsymbol{x}' \in \mathcal{D}$, $\boldsymbol{x} = (x_1, \ldots, x_d)$, $\boldsymbol{x} = (x_1', \ldots, x_d')$, σ^2 the variance parameter and $\theta_1, \ldots, \theta_d$ the inverse length-scale parameters.

In regression tasks, we aim at fitting a GP to a training dataset $D = (\boldsymbol{x}_i, f(\boldsymbol{x}_i))_{1 \leq i \leq n}$, which relies in the computation of the conditional distribution given by

$$Y | \{Y(\boldsymbol{x}_1) = f(\boldsymbol{x}_1), \ldots, Y(\boldsymbol{x}_n) = f(\boldsymbol{x}_n)\} \sim \mathcal{GP}(\mu_n, c_n), \tag{5}$$

where the conditional mean function is given by $\mu_n(\boldsymbol{x}) = \boldsymbol{k}_n^\top(\boldsymbol{x})\boldsymbol{K}_n^{-1}\boldsymbol{y}_n$, with an observation vector $\boldsymbol{y}_n = [y_1 := f(\boldsymbol{x}_1), \ldots, y_n := f(\boldsymbol{x}_n)]^\top$; the conditional covariance function is given by $c_n(\boldsymbol{x}, \boldsymbol{x}') = k(\boldsymbol{x}, \boldsymbol{x}') - \boldsymbol{k}_n^\top(\boldsymbol{x})\boldsymbol{K}_n^{-1}\boldsymbol{k}_n(\boldsymbol{x}')$, with a cross-covariance vector $\boldsymbol{k}_n^\top(\boldsymbol{x}) = (k(\boldsymbol{x}, \boldsymbol{x}_i))_{1 \leq i \leq n}$ and a covariance matrix $\boldsymbol{K}_n = (k(\boldsymbol{x}_i, \boldsymbol{x}_j))_{1 \leq i,j \leq n}$. The conditional process in Eq.(5) is then used as a surrogate model to approximate the target function f. We must note that the kernel $k := k_{\sigma, \theta_1, \ldots, \theta_d}$ is parametrized by $\sigma, \theta_1, \ldots, \theta_d$ (also known as hyperparameters) that can be estimated via maximum likelihood [38].

4.2 Extension to the multi-fidelity framework

Since the aerodynamic database considers only two data sources (WT and CFD data), here we focus on a multi-fidelity GP framework with two levels of fidelity. The extension to more than two levels of fidelity can be obtained recursively as it is shown by [18, 39]. We denote Y_e and Y_s as the processes related to the WT *experiments* and CFD *simulations*, respectively. As suggested by [18], we consider the auto-regressive model given by

$$Y_e(\boldsymbol{x}) = \rho(\boldsymbol{x})Y_s(\boldsymbol{x}) + \nu(\boldsymbol{x}), \tag{6}$$

where $\rho : \mathcal{D} \to \mathbb{R}$ is a scale factor between Y_s and Y_e, and $\nu : \mathcal{D} \to \mathbb{R}$ the discrepancy function tasked with capturing the differences between both fidelity levels beyond scaling. The scale factor ρ can be a scalar parameter as suggested in [40]. As proposed in [18], we assume $\rho(\boldsymbol{x}) = \sum_{i=1}^q g_i(\boldsymbol{x})\beta_i$ where $g_1, \ldots, g_q$ are regression functions (e.g. constant, linear, quadratic), and $\beta_1, \ldots, \beta_q$ are their corresponding weights. We must note that predictors of the latter weights are obtained by best linear unbiased estimators [18, 38].

Let Y_s and ν be two independent (centered) GPs given by $Y_s \sim \mathcal{GP}(0, k_s)$ and $\nu \sim \mathcal{GP}(0, k_\nu)$ with covariance functions k_s and k_ν. Due to the linearity of Eq.(6), we can show that Y_e is also (centered) GP-distributed with covariance function given by

$$k_e(\boldsymbol{x}_i, \boldsymbol{x}_j) := \text{cov}\{Y_e(\boldsymbol{x}_i), Y_e(\boldsymbol{x}_j)\} = \rho(\boldsymbol{x}_i)\rho(\boldsymbol{x}_j)k_s(\boldsymbol{x}_i, \boldsymbol{x}_j) + k_\nu(\boldsymbol{x}_i, \boldsymbol{x}_j). \tag{7}$$

According to our aerodynamic application, we aim at predicting profiles of Y_e using both WT data $(\boldsymbol{x}_{e,i}, y_{e,i})_{1 \leq i \leq n_e}$ and CFD simulations $(\boldsymbol{x}_{s,i}, y_{s,i})_{1 \leq i \leq n_s}$. Therefore, we need to compute the conditional distribution of $Y_e | \{Y_s(\boldsymbol{x}_{s,1}) = y_{s,1}, \ldots, Y_s(\boldsymbol{x}_{s,n_s}) = y_{s,n_s}, Y_e(\boldsymbol{x}_{e,1}) = y_{e,1}, \ldots, Y_e(\boldsymbol{x}_{e,n_e}) = y_{e,n_e}\}$ which is also GP-distributed [18]. Note that this construction allows to exploit CFD data in order to improve the predictability of the GP model Y_e. We refer to [18] for a further discussion about the predictive formulas of the multi-fidelity GP framework.

In further developments, in order to benefit from efficient computations due to the nested structure of the aerodynamic databases in Section 2, i.e. $(\boldsymbol{x}_{e,i})_{1 \leq i \leq n_e} \subseteq (\boldsymbol{x}_{s,j})_{1 \leq j \leq n_s}$, we consider the recursive GP formulation proposed in [41].

4.3 Consideration of input-varying noisy observations

To account for additive input-varying noisy observations, we can consider the system:

$$Y_s^{\text{noise}}(\boldsymbol{x}_i) = Y_s(\boldsymbol{x}_i) + \varepsilon_{s,i}, \tag{8}$$

$$Y_e^{\text{noise}}(\boldsymbol{x}_j) = \rho(\boldsymbol{x}_j)Y_s(\boldsymbol{x}_j) + \nu(\boldsymbol{x}_j) + \varepsilon_{e,j}, \tag{9}$$

where $\varepsilon_{s,i} \sim \mathcal{N}(0, \tau_{s,i}^2)$ and $\varepsilon_{e,j} \sim \mathcal{N}(0, \tau_{e,j}^2)$, for all $i = 1, \ldots, n_s$ and $j = 1, \ldots, n_e$. Here we assume that the additive Gaussian noises are independent and identically distributed,

and that they are independent of Y_s and ν. Then we have that Y_s^{noise} and Y_e^{noise} are (centered) GP-distributed with covariance functions given by

$$\widetilde{k}_s(\boldsymbol{x}_i, \boldsymbol{x}_j) = k_s(\boldsymbol{x}_i, \boldsymbol{x}_j) + \tau_{s,i}^2 \delta_{\boldsymbol{x}_i}(\boldsymbol{x}_j), \tag{10}$$

$$\widetilde{k}_e(\boldsymbol{x}_i, \boldsymbol{x}_j) = \rho(\boldsymbol{x}_i)\rho(\boldsymbol{x}_j)k_s(\boldsymbol{x}_i, \boldsymbol{x}_j) + k_\nu(\boldsymbol{x}_i, \boldsymbol{x}_j) + \tau_{e,i}^2 \delta_{\boldsymbol{x}_i}(\boldsymbol{x}_j), \tag{11}$$

with $\tau_{s,i}^2$ and $\tau_{e,i}^2$ the noise variances at the input $\boldsymbol{x}_i$, and $\delta_{\boldsymbol{x}_i}(\boldsymbol{x}_j)$ the Dirac delta function that is equal to one if $\boldsymbol{x}_i = \boldsymbol{x}_j$, and zero otherwise. Equation (11) follows a similar structure than the one in Eq.(7) but with one additional terms $\tau_{e,i}^2 \delta_{\boldsymbol{x}_i}(\boldsymbol{x}_j)$ that models the input-varying noises. Since Y_s^{noise} and Y_e^{noise} are GP-distributed, we can establish the formulas for computing the conditional Gaussian distribution $Y_e | \{Y_s(\boldsymbol{x}_{s,1}) + \varepsilon_{s,1} = y_{s,1}, \ldots, Y_s(\boldsymbol{x}_{s,n_s}) + \varepsilon_{s,n_s} = y_{s,n_s}, Y_e(\boldsymbol{x}_{e,1}) + \varepsilon_{e,1} = y_{e,1}, \ldots, Y_e(\boldsymbol{x}_{e,n_e}) + \varepsilon_{e,n_e} = y_{e,n_e}\}$. Those formulas follow the same structure as the ones for the noise-free case but replacing $k_s(\boldsymbol{x}, \boldsymbol{x}')$ to $\widetilde{k}_s(\boldsymbol{x}, \boldsymbol{x}')$ and $k_e(\boldsymbol{x}, \boldsymbol{x}')$ to $\widetilde{k}_e(\boldsymbol{x}, \boldsymbol{x}')$. Since the Gaussian noises are mutually independent, independent of Y_s and ν, then the cross-covariance terms will remain unchangeable:

$$\begin{aligned}
\text{cov}\left\{Y_e^{\text{noise}}(\boldsymbol{x}_i), Y_s^{\text{noise}}(\boldsymbol{x}_j)\right\} &= \text{cov}\left\{\rho(\boldsymbol{x}_i)Y_s(\boldsymbol{x}_i) + \nu(\boldsymbol{x}_i) + \varepsilon_{e,i}, \ Y_s(\boldsymbol{x}_j) + \varepsilon_{s,j}\right\} \\
&= \text{cov}\left\{\rho(\boldsymbol{x}_i)Y_s(\boldsymbol{x}_i) + \nu(\boldsymbol{x}_i), \ Y_s(\boldsymbol{x}_j)\right\} \\
&= \text{cov}\left\{Y_e(\boldsymbol{x}_i), Y_s(\boldsymbol{x}_j)\right\}.
\end{aligned}$$

In our application, the noise variances $\varepsilon_{s,1}, \ldots, \varepsilon_{s,n_s}$ and $\varepsilon_{e,1}, \ldots, \varepsilon_{e,n_e}$ are known and they are defined in Section 3. However, we must note that they can also be estimated via sensible estimators [42] or via maximum likelihood [43]. In those cases, we need to account for repetitions of observation, i.e., for a fixed set of aerodynamic inputs $\boldsymbol{x}$, we have to execute n_{e,r_e} times the same WT test and keep the outcomes $Y_e^{(1)}(\boldsymbol{x}), \ldots, Y_e^{(n_{e,r_e})}(\boldsymbol{x})$. Taking into account the cost (in both time and resources) of experimental WT tests, we can easily conclude that the approaches in [42, 43] become expensive. This drawback is mitigated by considering directly the error propagation analysis described in Section 3.

4.4 1D numerical illustration

Python codes of the resulting heteroscedastic GP framework described in Section 4.3 are available in the *Surrogate Modeling Toolbox* (SMT) [32], an open-source toolbox developed by ONERA, ISAE-SUPAERO, University of Michigan and NASA Glenn.

Figure 7 shows 1D predictions under heteroscedastic assumptions either considering an independent GP model for each level of fidelity or the multi-fidelity GP framework.[2] We consider the one dimensional "benchmark" problem proposed in [44] and used in some other works related to multi-fidelity surrogate models [14, 45]. The target functions are:

$$f_s(x) = (6x - 2)^2 \sin(2[6x - 2]), \quad \text{(low-fidelity function)}$$

and

$$f_e(x) = 0.5f_s(x) + 10(x - 0.5) - 5, \quad \text{(high-fidelity function)}$$

for $x \in [0, 1]$. As a nested DoE, we proposed 12 and 4 equidistant low-fidelity and high-fidelity design points, respectively. For illustration, the associated error measurements

---

[2]The example in Fig. 7 can be reproduced using the Python-based Jupyter notebook available in SMT: `https://github.com/SMTorg/smt/blob/master/tutorial/SMT_MFK_Noise.ipynb`

R. Conde Arenzana, A. F. López-Lopera, S. Mouton, N. Bartoli and T. Lefebvre
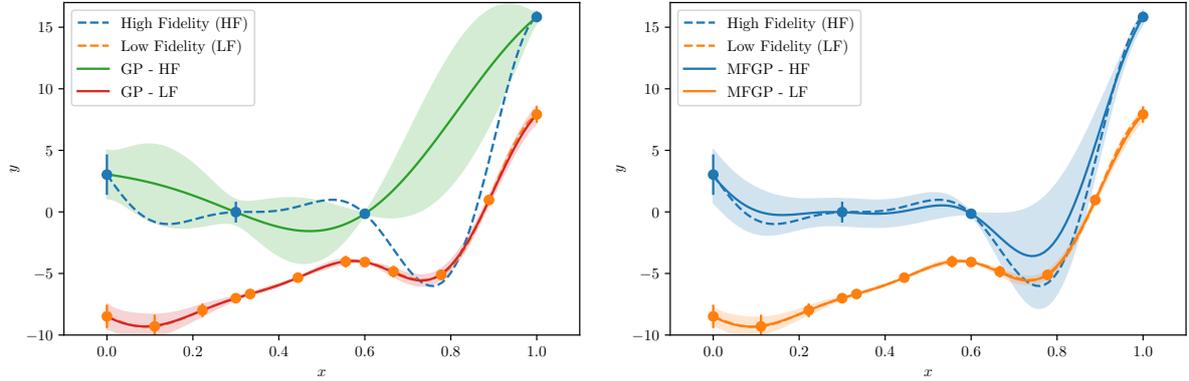
Figure 7: Predictions considering (left) an independent GP per level of fidelity or (right) a multi-fidelity GP (MFGP). Both schemes account for the input-varying noise variances described in Section 4.4. Each panel shows: the target low-fidelity and high-fidelity functions (in orange and blue dashed lines, respectively), the design points (dots) with the corresponding 3 standard-deviation error bars, the resulting predictions (solid lines) and 3 standard-deviation confidence intervals (light areas) provided by the GP frameworks.

are manually fixed and are given by

$$\tau_s^2 = (10^{-1}, 3.5 \times 10^{-2}, 10^{-3}, 3 \times 10^{-8}, 2.5 \times 10^{-2}, 2.5 \times 10^{-2},$$
$$2 \times 10^{-2}, 1.5 \times 10^{-2}, 10^{-1}, 5 \times 10^{-3}, 2.5 \times 10^{-6}, 5 \times 10^{-2}),$$

and $\tau_e^2 = (3 \times 10^{-1}, 8 \times 10^{-2}, 2 \times 10^{-3}, 2 \times 10^{-2})$.

For the GP models, we consider SE kernels (see Eq.(4)), with covariance parameters estimated via maximum likelihood.[3] In Fig.7, we observe that the noise variance of both independent GPs and the multi-fidelity GP properly cover the error measurements (vertical bars) at the design points (dots), however, prediction at the high-fidelity level f_e is significantly improved by considering the multi-fidelity GP framework, with a better approximation where data are scarce (e.g. around $x = 0.8$).

5 RESULTS

5.1 Assessment of the multi-fidelity GP model

We here assess the performance of the multi-fidelity GP model considering different percentage of training WT data. The training data are randomly chosen from the nested database generated in Section 2. We test three different GP models for each coefficient (C_x, C_z and C_M): two independent single-fidelity GPs exploiting data either from CFD simulations (namely GP-CFD) or WT experiments (namely GP-WT), and a multi-fidelity GP (MFGP) that exploits both data sources. All the models are trained using the 100% of the CFD dataset (1949 data points). For the models accounting for WT data (250 data points), we consider different WT training dataset, i.e. 10%, 30%, 50%, 70% and 90%. Matérn 5/2 kernels are considered as covariance functions for the GP priors:

$$k(\boldsymbol{x}, \boldsymbol{x}') = \sigma^2 \prod_{i=1}^{3} \left(1 + \sqrt{5}\theta_i |x_i - x_i'| + \frac{5}{3}\theta_i^2 (x_i - x_i')^2 \right) \exp\left(-\sqrt{5}\theta_i |x_i - x_i'| \right),$$

---

[3]We considered as initial covariance parameters $\sigma_e^2 = \sigma_s^2 = 1$, $\theta_e = 0.1$ and $\theta_s = 0.5$.

R. Conde Arenzana, A. F. López-Lopera, S. Mouton, N. Bartoli and T. Lefebvre
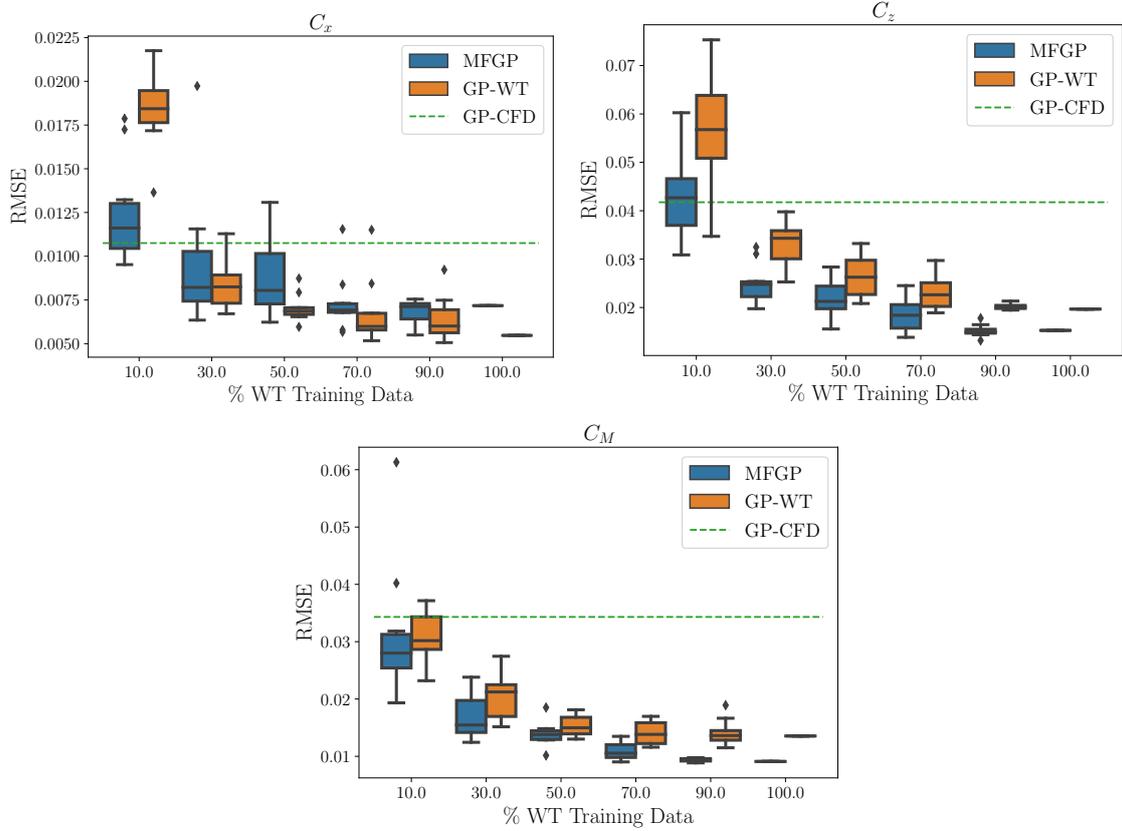
Figure 8: RMSE results for three different GP models for each coefficient (C_x, C_z and C_M): two independent single-fidelity GPs exploiting data either from CFD simulations (GP-CDF, green line) or WT experiments (GP-WT, orange), and a multi-fidelity GP that exploits both data sources (MFGP, blue). All the models are trained using the 100% of the CFD data (1949 data points). For the models accounting for WT data (250 data points), we consider different WT training dataset. Boxplots are computed over ten different random replicates.

with $\boldsymbol{x} = (x_1, x_2, x_3)$.[4] The hyperparameters $(\sigma, \theta_1, \theta_2, \theta_3)$ are estimated via maximum likelihood. As mean functions of the priors, we assume linear trends for all the forces coefficients, i.e. $m_{\text{linear}}(\boldsymbol{x}) = a_0 + a_1\boldsymbol{x}$, except for C_x where we consider a quadratic trend $m_{\text{quadratic}}(\boldsymbol{x}) = a_0 + a_1\boldsymbol{x} + a_2\boldsymbol{x}^2$. The coefficients a_0, a_1, a_2 are obtained via best linear unbiased estimation within a universal GP framework [38]. Those trends are defined according to expert knowledge. For the testing step, the predictions of the resulting models are assessed on a validation WT database containing a thousand test points. The test WT DoE is constructed via LHS as discussed in Section 2.3.

Figure 8 shows the root mean square error (RMSE)[5] results for ten different random replicates. The RMSE values obtained when considering 100% of the WT data for training the GP models are also displayed. From C_z and C_M profiles, we observe that the MFGP outperformed the RMSE results of the single-fidelity implementations GP-CFD and GP-

---

[4]Other types of kernels (e.g. SE kernels) were tested but the Matérn 5/2 class resulted in more accurate results.

[5]RMSE $= \sqrt{\frac{1}{n_{\text{test}}} \sum_{i=1}^{n_{\text{test}}} (y_i - \mu_i)^2}$ with $y_1, \ldots, ny_{n_{\text{test}}}$ the test observations and $\mu_1, \ldots, \mu_{n_{\text{test}}}$ the corresponding GP predictions.

R. Conde Arenzana, A. F. López-Lopera, S. Mouton, N. Bartoli and T. Lefebvre
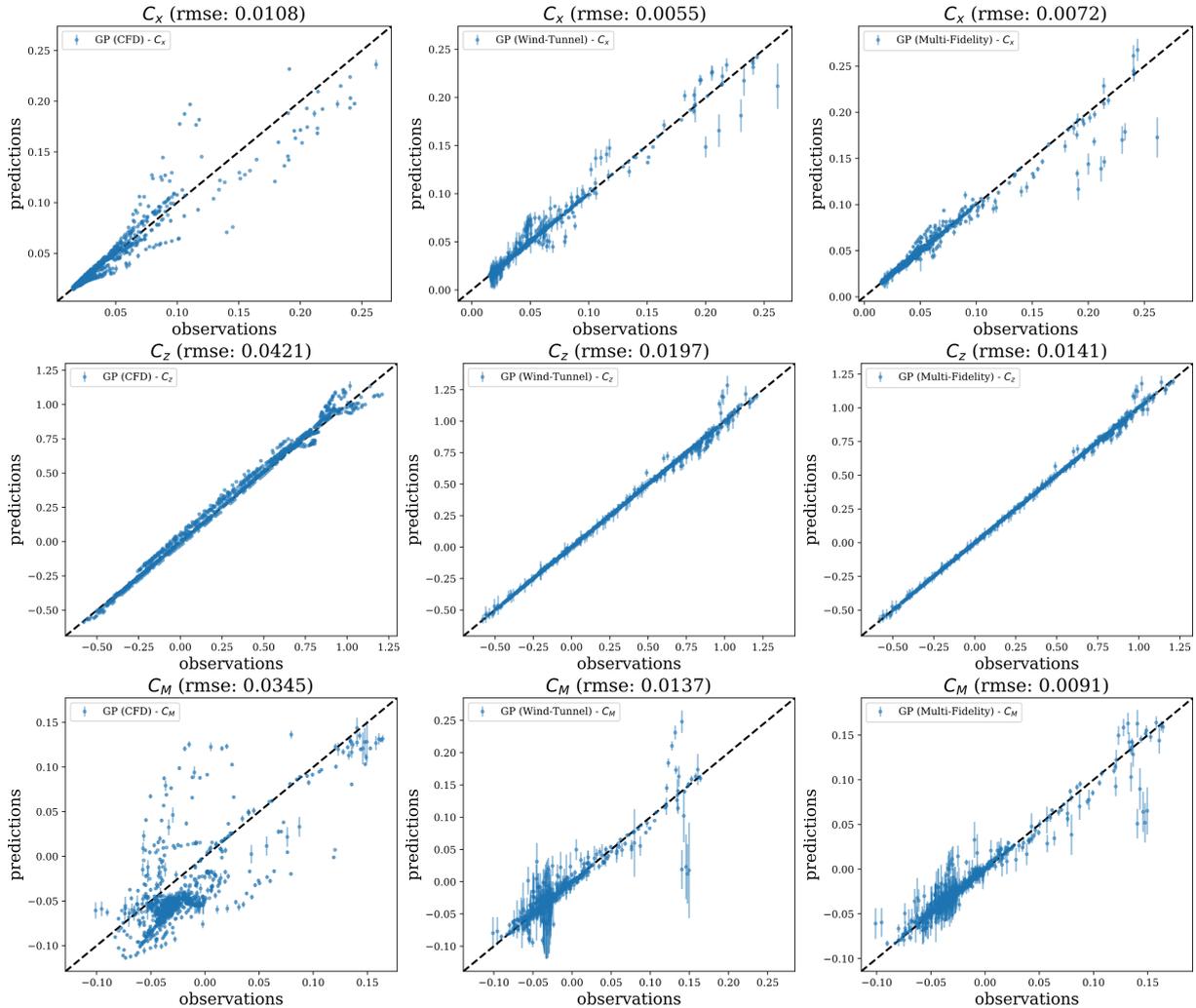
Figure 9: Scatter plots of the test data vs predictions obtained by two independent GPs exploiting data from CFD simulations (left) or WT tests (middle), and a multi-fidelity GP that exploits both types of data (right). Results are shown for C_x (top), C_z (middle) and C_M (bottom). The vertical bars represent the one standard-deviation conditional predictive errors led by the models. RMSE indicators are shown on top of each panel.

WT, leading to significant improvements when WT training sets are small (e.g. using less than 30% of the WT data). For the C_x coefficient, although we note smaller RMSE values when considering only 10% of the WT data, the quality of predictions provided by the MFGP is degraded when the number of WT data points increases. This drawback is produced due to WT data are scarce for $C_x > 0.2$, and therefore, predictions rely mostly on the biased CFD simulations. This bias is observed in Fig.5, and is also reflected by the Pearson correlation coefficient. By computing the Pearson coefficient only over the C_x observations associated to the 250 design points shared by both WT and CFD data, and for $C_x > 0.2$, it results in a value of 0.863 (compared to 0.934 for the case where $C_x \leq 0.2$). To mitigate this issue, we can add additional WT data with $C_x > 0.2$ aiming at better learning the discrepancy function ν.

In Fig.9, we show scatter plots of the test data vs predictions obtained by the proposed GP models accounting for the 100% of WT data. Observe that clearer improvements are

R. Conde Arenzana, A. F. López-Lopera, S. Mouton, N. Bartoli and T. Lefebvre
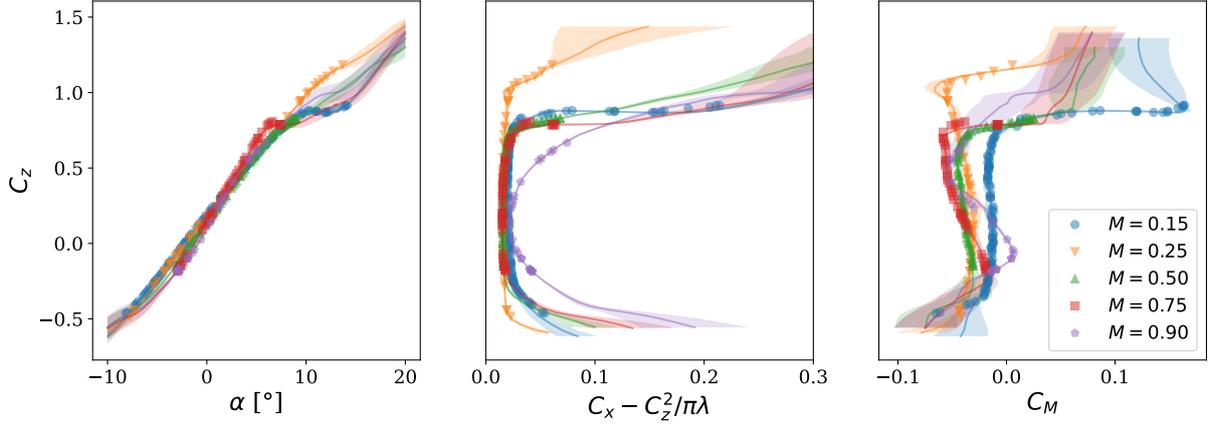
Figure 10: Multi-fidelity GP predictions of common polar of longitudinal forces used in the analysis of WT experiments. For $Re = 7 \times 10^6$ and different values of M, each panel shows: the nearest available test points (dots), the conditional GP mean functions (solid lines) and one standard-deviation predictive confidence intervals (light areas). Confidence intervals are considered for the horizontal-axes except for the plot with respect to α where uncertainty is displayed vertically.

obtained for high-values of the lift coefficient C_z. For C_x and C_M, we note that significant mispredictions are obtained for high values. Due to data are scarce for $C_x > 0.2$ and $C_M > 0.15$, and the high variability of the C_M (see Fig.3 and Fig.5), we can conclude that the MFGP model could not learn such behaviours from the training dataset. Note also that those mispredictions are also encountered when considering either the GP-CFD or GP-WT. As pointed out in the results from Fig.8, this drawback can be mitigated by considering additional training points for $C_x > 0.2$ and $C_M > 0.15$. The poor predictions of the GP-CFD models are justified by the existing bias between the CFD and WT data.

5.2 Representation of longitudinal forces

As discussed in Section 4, one of the main benefits of considering (multi-fidelity) GP models relies in the associated confidence intervals of predictions. Next, we show how those confidence intervals can be exploited in the analysis of WT experiments, more precisely, in the construction of polar representation of longitudinal forces. In Fig.10, for a fixed Reynolds number $Re = 7 \times 10^6$ and for different values of Mach number M, we show the profiles of C_z with respect to α, $C_x - C_z^2/(\pi\lambda)$, with $\lambda = 9$ the LRM model wing aspect ratio,[6] and C_M. Confidence intervals are considered for the horizontal-axes except for the profile with respect to α where the uncertainty is displayed for the vertical-axe. We observe that the resulting multi-fidelity GP model commonly leads to reasonable aerodynamic profiles, where higher uncertainties are obtained in regions where data are not available. We must note that those uncertainties can be reduced by adding new WT training points on those regions. This may motivate the proposition of adaptive DoE aiming at reducing uncertainty in multi-fidelity GP models [46, 47]. We do not consider such improvement in this paper but it can be considered in further developments.

---

[6]Since $C_z^2/(\pi\lambda)$ is a crude estimate of lift-induced drag (from Prandtl lifting-line theory), then the term $C_x - C_z^2/(\pi\lambda)$ is an estimate of the drag other than lift induced, sometimes called profile drag.

R. Conde Arenzana, A. F. López-Lopera, S. Mouton, N. Bartoli and T. Lefebvre

6 CONCLUSION

In this paper, several contributions were addressed in the field of aerodynamic data fusion. First, we constructed a large multi-source aerodynamic database based on the NASA Common Research Model. The database contains 250 and 1949 data points, from wind-tunnel tests and CFD simulations (respectively), covering the entire flight envelope of the model. Second, we set up a simplified uncertainty model of the experimental WT data aiming at defining realistic values for the input varying uncertainties of force coefficients. Finally, we adapted a multi-fidelity Gaussian process (GP) framework to account for input-varying additive noises (heteroscedastic case) in all the levels of fidelity. We demonstrated, in both a synthetic example and a real-world application, that the resulting multi-fidelity GP outperformed single-fidelity ones in terms of predictive capability.

The work presented in this paper can be improved in different ways. A further investigation may be contemplated with the increase in the number of inputs and outputs. We may consider the slideslip angle as an input to allow the prediction of the lateral aerodynamic forces and moments of the aircraft. We can also consider additional data sources, such as numerical simulation based on VLM or Euler equations. Those sources will be considered as lower or intermediate fidelity levels in the multi-fidelity GP framework. Finally, to improve the predictability of the GP model, and looking for uncertainty reduction, adaptive design of experiments can be further investigated accounting for multi-fidelity schemes.

ACKNOWLEDGMENTS

REFERENCES

[1] F. Stoliker. Introduction to flight test engineering. AGARDograph AG-300, pages 1–456. RTO/NATO, 2005. ISBN 92-837-1126-2.

[2] M. Malik and D. Bushnell. Role of computational fluid dynamics and wind tunnels in aeronautics R and D. NASA/TP–2012-217602, pages 1–63, 2012.

[3] F. Johnson, E. Tinoco, and N. Yu. 30 years of development and application of CFD at Boeing commercial airplanes, Seattle. *Computers & Fluids*, 34:1115–1151, 2005.

[4] J. Slotnick, A. Khodadoust, J. Alonso, D. Darmofal, W. Gropp, E. Lurie, and D. Mavripilis. CFD vision 2030 study: A path to revolutionary computational aerosciences. NASA/CR-2014-218178, pages 1–51. NASA, 2014.

[5] D. Singh, A. Antoniadis, P. Tsoutsanis, H. Shin, A. Tsourdos, S. Mathekga, and K. Jenkins. A multi-fidelity approach for aerodynamic performance computations of formation flight. *Aerospace*, 5:66, 2018.

R. Conde Arenzana, A. F. López-Lopera, S. Mouton, N. Bartoli and T. Lefebvre

[6] Z. Zhang, N. Bartoli, A. Jungo, W. Lammen, E. Baalbergen, and M. Voskuijl. Data fusion and aerodynamic surrogate modeling for handling qualities analysis. HAL preprint, 2020.

[7] J. Kou and W. Zhang. Multi-fidelity modeling framework for nonlinear unsteady aerodynamics of airfoils. *Applied Mathematical Modelling*, 76, 2019.

[8] Y. Kuya, K. Takeda, X. Zhang, and A. Forrester. Multifidelity surrogate modeling of experimental and computational aerodynamic data sets. *AIAA Journal*, 49:289–298, 2011.

[9] J. Mukhopadhaya, B. Whitehead, J. Quindlen, and J. Alonso. Multi-fidelity modeling of probabilistic aerodynamic databases for use in aerospace engineering. *arXiv: Fluid Dynamics*, 2019.

[10] L. He, W. Qian, T. Zhao, and Q. Wang. Multi-fidelity aerodynamic data fusion with a deep neural network modeling method. *7th European Conference for Aeronautics and Space Sciences (EUCASS)*, 22, 2020.

[11] A. Feldstein, D. Lazzara, N. Princen, and K. Willcox. Multifidelity data fusion: Application to blended-wing-body multidisciplinary analysis under uncertainty. *AIAA Journal*, 58(2):889–906, 2020.

[12] N. Nigam, S. Mohseni, J. Valverde, S. Voronin, J. Mukhopadhaya, and J. Alonso. Toolset for creation of multi-fidelity probabilistic aerodynamic databases. pages 1–20, 2021.

[13] A. Bertram and R. Zimmermann. Theoretical investigations of the new coKriging method for variable-fidelity surrogate modeling: Well-posedness and maximum likelihood training. *Advances in Computational Mathematics*, 44, 2018.

[14] M. Meliani, N. Bartoli, T. Lefebvre, M. Bouhlel, J. Martins, and J. Morlier. Multifidelity efficient global optimization: Methodology and application to airfoil shape design. In *AIAA Aviation Forum*, pages 1–18. 2019.

[15] M. Bouhlel, N. Bartoli, J. Morlier, and A. Otsmane. Improving Kriging surrogates of high-dimensional design models by partial least squares dimension reduction. *Structural and Multidisciplinary Optimization*, 53:935–, 2016.

[16] B. Peherstorfer, K. Willcox, and M. Gunzburger. Survey of multifidelity methods in uncertainty propagation, inference, and optimization. *SIAM Review*, 60:550–591, 2018.

[17] D. Khatamsaz and D. Allaire. A comparison of reification and coKriging for sequential multi-information source fusion. pages 1–14, 2021.

[18] L. Le Gratiet. *Multi-Fidelity Gaussian Process Regression for Computer Experiments*. Theses, Université Paris-Diderot - Paris VII, 2013.

[19] AGARD Advisory Report No. 304. Quality assessment for wind tunnel testing. pages 1–81. NATO, 1994.

R. Conde Arenzana, A. F. López-Lopera, S. Mouton, N. Bartoli and T. Lefebvre

[20] J. Vassberg, M. Dehaan, M. Rivers, and R. Wahls. Development of a common research model for applied CFD validation studies. pages 1–22, 2008.

[21] J. Carrara and A. Masson. Three years of operation of the ONERA pressurized subsonic wind tunnel. In *12th Congress of the International Council of the Aeronautical Sciences*, pages 778–792, Munich, Germany, 1980. ICAS.

[22] A. Cartieri, D. Hue, A. Chanzy, and O. Atinault. Experimental investigations on common research model at ONERA-S1MA–Drag prediction workshop numerical results. *Journal of Aircraft*, 55, 2017.

[23] M. Rivers and A. Dittberner. Experimental investigation of the NASA common research model. In *28th AIAA Applied Aerodynamics Conference*, pages 1–29, 2010.

[24] M. Rivers, J. Quest, and R. Rudnik. Comparison of the NASA common research model European transonic wind tunnel test data to NASA national transonic facility test data. *CEAS Aeronautical Journal*, 9:307–317, 2018.

[25] X. Vaucheret. Recent calculation progress on wall interferences in industrial wind tunnels. *La Recherche Aérospatiale*, pages 45–47, 1988.

[26] J. Hantrais-Gervois and J. Piat. A methodology to derive wind tunnel wall corrections from RANS simulations. In *Advanced Wind Tunnel Boundary Simulation*, pages 1–24. ST0/NATO, 2018.

[27] A. Cartieri and D. Hue. Using RANS computations to calculate support interference effects on the common research model. In *Advanced Wind Tunnel Boundary Simulation*, pages 1–18. ST0/NATO, 2018.

[28] L. Cambier, S. Heib, and S. Plot. The ONERA elsA CFD software: Input from research and feedback from industry. *Mechanics & Industry*, 14:159–174, 2013.

[29] D. Hue. 5th drag prediction workshop: Computational fluid dynamics studies carried out at ONERA. *Journal of Aircraft*, 51(4):1295–1310, 2014.

[30] M. Mckay, R. Beckman, and W. Conover. A comparison of three methods for selecting vales of input variables in the analysis of output from a computer code. *Technometrics*, 21:239–245, 1979.

[31] A. Da Ronch, M. Panzeri, M. Bari, R. d'Ippolito, and M. Franciolini. Adaptive design of experiments for efficient and accurate estimation of aerodynamic loads. In *6th Symposium on Collaboration in Aircraft Design*, 2016.

[32] M. Bouhlel, J. Hwang, N. Bartoli, R. Lafage, J. Morlier, and J. Martins. A Python surrogate modeling framework with derivatives. *Advances in Engineering Software*, page 102662, 2019. URL https://github.com/SMTorg/smt.

[33] R. Jin, W. Chen, and A. Sudjianto. An efficient algorithm for constructing optimal design of computer experiments. *Journal of Statistical Planning and Inference*, 134: 268–287, 2005.

R. Conde Arenzana, A. F. López-Lopera, S. Mouton, N. Bartoli and T. Lefebvre

[34] J. Walter, W. Lawrence, D. Elder, and M. Treece. Development of an uncertainty model for the national transonic facility. In *27th AIAA Aerodynamic Measurement Technology and Ground Testing Conference*, pages 1–18, 2012.

[35] W. Oberkampf and F. Blottner. Issues in computational fluid dynamics code verification and validation. *AIAA Journal*, 36(5):687–695, 1998.

[36] A. Mishra, J. Mukhopadhaya, G. Iaccarino, and J. Alonso. Uncertainty estimation module for turbulence model predictions in SU2. *AIAA Journal*, 57(3):1066–1077, 2019.

[37] P. Spalart and V. Venkatakrishnan. On the role and challenges of CFD in the aerospace industry. *Aeronautical Journal*, 120(1223):209–232, 2016.

[38] C. Rasmussen and C. Williams. *Gaussian Processes for Machine Learning (Adaptive Computation and Machine Learning)*. The MIT Press, Cambridge, MA, 2005.

[39] L. Le Gratiet. Bayesian analysis of hierarchical multifidelity codes. *SIAM/ASA Journal on Uncertainty Quantification*, 1(1):244–269, 2013.

[40] M. Kennedy and A. O'Hagan. Predicting the output from a complex computer code when fast approximations are available. *Biometrika*, 87(1):1–13, 2000.

[41] L. Le Gratiet and J. Garnier. Recursive co-Kriging model for design of computer experiments with multiple levels of fidelity. *International Journal for Uncertainty Quantification*, 4(5):365–386, 2014.

[42] B. Ankenman, B. Nelson, and J. Staum. Stochastic Kriging for simulation metamodeling. *Operations Research*, 58:371–382, 2010.

[43] M. Binois, R. B. Gramacy, and M. Ludkovski. Practical heteroscedastic Gaussian process modeling for large simulation experiments. *Journal of Computational and Graphical Statistics*, 27(4):808–821, 2018.

[44] A. Forrester, A. Sobester, and A. Keane. Multi-fidelity optimization via surrogate modelling. *Proceedings of the Royal Society A*, 463:3251–3269, 2007.

[45] J. Bailly and D. Bailly. Multifidelity aerodynamic optimization of a helicopter rotor blade. *AIAA Journal*, 57:1–12, 2019.

[46] R. Jin, W. Chen, and A. Sudjianto. On sequential sampling for global metamodeling in engineering design. 28th Design Automation Conference, pages 539–548, 2002.

[47] V. Picheny, D. Ginsbourger, O. Roustant, R. Haftka, and N. Kim. Adaptive designs of experiments for accurate approximation of a target region. *Journal of Mechanical Design*, 132(7):071008, 2010.

APPENDIX

7   ADDITIONAL CFD SIMULATION

In this appendix, we show two additional CFD results: an example where elsA has properly converged after 1000 iterations, and another example where limit-cycle oscillations are encountered (see Fig.11).
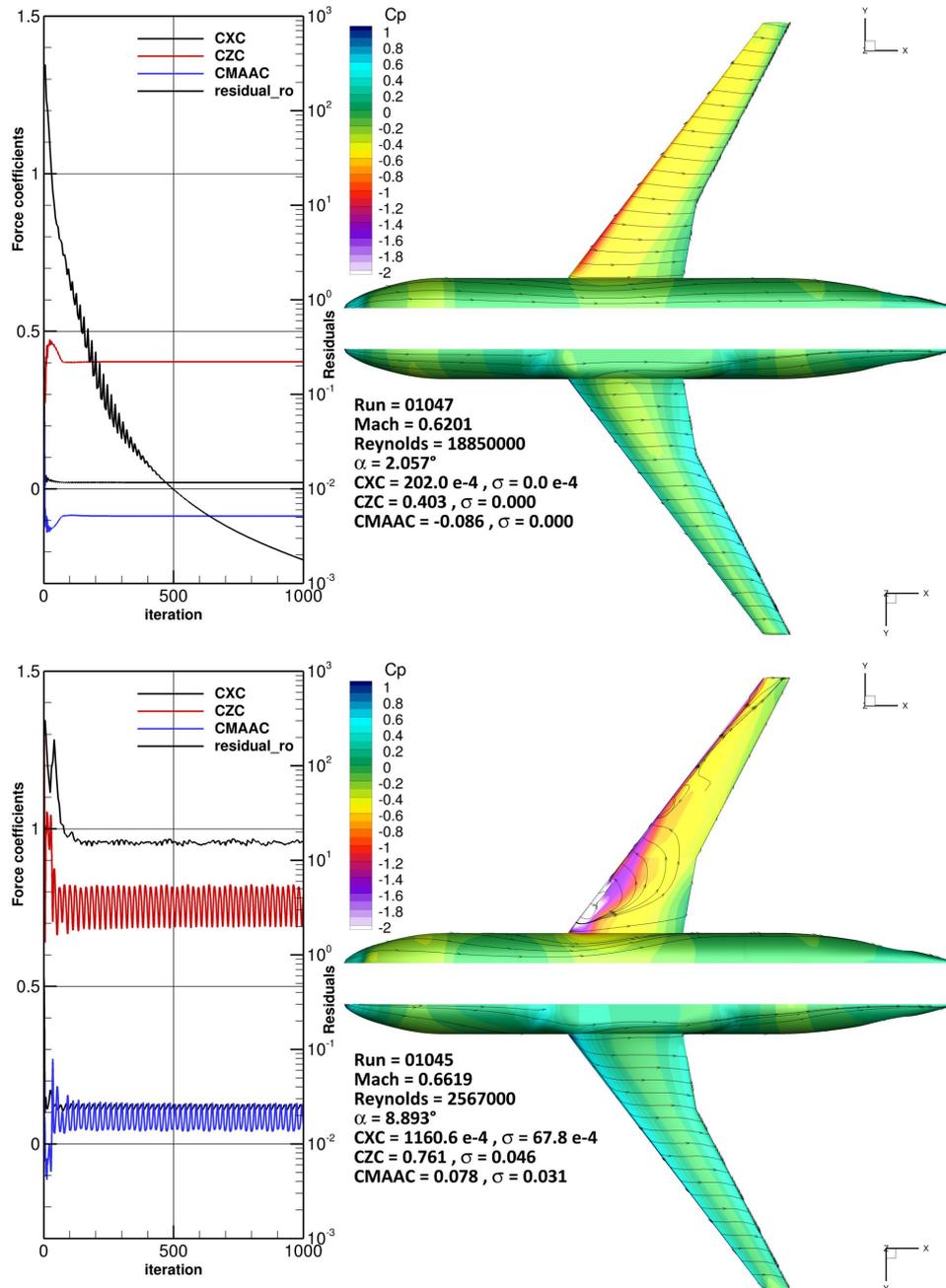
Figure 11: Examples of CFD simulations from the database constructed in Section 2. The panel description is the same as the one in Fig.6.

R. Conde Arenzana, A. F. López-Lopera, S. Mouton, N. Bartoli and T. Lefebvre

8 EXPERIMENTAL UNCERTAINTY

In this appendix, we give some complementary information required in Section 3. More precisely, we provide further details about the estimation of error associated to the angle of attack α, the aerodynamic forces, and the dynamic pressure. According to the structure of the database constructed in Section 2, a zero sideslip angle is considered.

Experimental error in aerodynamic forces in model axes. The measurement of the aerodynamic forces is carried out in the body axes by an internal strain-gauge balance. Each force component is considered to be affected by an uncertainty equal to $c = 0.5 \times 10^{-3}$ of the balance capacity on this component, independently of the other components:

$$\tau_A = c A_{\text{capa}}, \qquad \tau_N = c N_{\text{capa}}, \qquad \tau_{M_A} = c M_{A,\text{capa}}.$$

We neglect uncertainties associated to the positioning of the balance axes with respect to the model axes, and to the calculation of the weight of the model, that is subtracted from raw balance readings to deduce aerodynamic forces.

Error measurements associated to the angle of attack. Since the slideslip angle is zero, α is given by

$$\alpha = \theta + \gamma_a + \Delta\alpha, \tag{12}$$

where θ [deg] is the pitch angle of the model, γ_a [deg] is the mean upwash angle of the flow in the wind tunnel, and $\Delta\alpha$ [deg] is a corrective term associated to the wall and support effects. Assuming that θ, γ_a and $\Delta\alpha$ are independent Gaussian random variables, the variance parameter for α is given by

$$\tau_\alpha^2 = \tau_\theta^2 + \tau_{\gamma_a}^2 + \tau_{\Delta\alpha}^2, \tag{13}$$

where τ_θ^2, $\tau_{\gamma_a}^2$ and $\tau_{\Delta\alpha}^2$ are the corresponding noise variance parameters for θ, γ_a and $\Delta\alpha$, respectively. τ_θ^2 is deduced from uncertainty analysis of the pitch angle sensor. $\tau_{\gamma_a}^2$ results from an uncertainty analysis of the procedure used to determine upwash angle, namely the model inversion method, which implies again the pitch angle sensor, and the force balance. $\tau_{\Delta\alpha}^2$ is computed by considering that most of the wall correction in angle of attack stems from lift-induced effect. Therefore, $\tau_{\Delta\alpha}$ is made proportional to the lift coefficient.

Experimental error in dynamic pressure. The dynamic pressure is derived from the value of the total pressure p_i and the static pressure p. These values are themselves deduced from measurements made on reference pressure taps of the wind tunnel, using tunnel calibration laws. Finally, wall and support corrections results in a blockage correction Δq. Finally the dynamic pressure q reads:

$$q = \frac{\gamma}{\gamma - 1} p \left(\left(\frac{p_i}{p} \right)^{\frac{\gamma-1}{\gamma}} - 1 \right) + \Delta q$$

Hence, defining $\lambda = 1 + \frac{\gamma-1}{2} M^2$, the uncertainty on q can be written as:

$$\tau_q^2 = \left(\frac{\gamma}{2} M^2 + \lambda(\lambda^{-\frac{\gamma}{\gamma-1}} - 1) \right)^2 \tau_{p_i}^2 + \left(1 - \frac{M^2}{2} \right)^2 \tau_p^2 + \tau_{\Delta q}^2.$$

R. Conde Arenzana, A. F. López-Lopera, S. Mouton, N. Bartoli and T. Lefebvre

Note that the two first terms result from the propagation of the errors in pressure measurements. The last term is added to account for uncertainties in the tunnel calibration and the wall corrections. Variances $\tau_{p_i}^2$ and τ_p^2 are evaluated thanks to an uncertainty analysis of the pressure sensors involved in the measurements of the reference total and static pressures, and confirmed by considering redundancy in the measurements. $\tau_{\Delta q}$ was chosen to be proportional to q.

Experimental error in force coefficients in wind axes. The expression of the variance of the error on the drag coefficient C_x was already provided in Section 3. Reminding that A and N are the axial and normal aerodynamic forces in model axes (respectively), the lift coefficient is expressed as $C_z = \dfrac{-A \sin\alpha + N \cos\alpha}{q S_{\text{ref}}}$. Consequently, the variance of the error is given by:

$$\tau_{C_z}^2 = \left(\frac{\sin\alpha}{q S_{\text{ref}}}\right)^2 \tau_A^2 + \left(\frac{\cos\alpha}{q S_{\text{ref}}}\right)^2 \tau_N^2 + C_z^2 \left(\frac{\tau_q}{q}\right)^2 + C_x^2 \tau_\alpha^2.$$

The pitching moment coefficient equals to $C_M = \dfrac{M_A}{q S_{\text{ref}} L_{\text{ref}}}$, where M_A is the aerodynamic pitching force. Then the variance of the error is equal to:

$$\tau_{C_M}^2 = \left(\frac{1}{q S_{\text{ref}} L_{\text{ref}}}\right)^2 \tau_{M_A}^2 + C_M^2 \left(\frac{\tau_q}{q}\right)^2.$$

EFFICIENT GLOBAL MULTIDISCIPLINARY DESIGN OPTIMIZATION TO SUPPORT AIRCRAFT CONCEPTUAL DESIGN

Daigo Maruyama[1]*, Florian Schültke[2], Eike Stumpf[2] and Ali Elham[1]

1: Chair of Overall Aircraft Design
Institute of Aircraft Design and Lightweight Structures (IFL)
Technical University of Braunschweig
Hermann-Blenk-Straße 35, D-38108 Braunschweig
{d.maruyama, a.elham}@tu-braunschweig.de

2: The Institute of Aerospace Systems (ILR)
RWTH Aachen University
Wüllnerstraße 7, 52062 Aachen
{florian.schueltke, eike.stumpf}@ilr.rwth-aachen.de

Abstract *This paper presents an efficient global optimization (EGO) framework which is integrated into the UNICADO software to perform multidisciplinary design optimization (MDO). The EGO framework is based on surrogate modelling to efficiently predict cost functions and the constraints by the TALRs (Top-Level Aircraft Requirements). The MDO architecture is the multidisciplinary feasible (MDF) composed by the developed EGO framework and the multidisciplinary analysis (MDA) module available in the UNICADO workflow. The developed toolbox was demonstrated by using a test case using a short-range reference aircraft CSR-01as a conceptual aircraft design problem to perform its usability of efficiently exploiting the global optimum solution. The EGO framework was further developed by introducing an extended Gaussian process (GP) model to handle various conceivable application problems such as multi-fidelity analyses, cases of a large number of geometrical design variables, complicate cost functions, and an online EGO framework for further efficiency by offline database by treating the conventional EGO framework as an online process. It was demonstrated in this paper by using test functions that the extended GP model can provide more efficiency in finding the global optimum than the conventional EGO framework.*

Keywords: Efficient Global Optimization, Multidisciplinary Design Optimization, Gaussian Processes, Neural Networks, Adaptive Sampling, Multidisciplinary Feasible Architecture

1. INTRODUCTION

The conceptual aircraft design has been used for years to develop new aircraft configurations or evaluate new technologies in existing aircraft configurations. For this reason, there are many conceptual aircraft design environments worldwide, especially in universities, which are now all more or less at the same level. The UNICADO[i] project aims to develop and establish a university conceptual aircraft design environment to bundle the design and disciplinary competencies of German universities and make them usable in the long term. The fundamental goal is to exploit synergy potentials and shift the focus of research and teaching from code development to actual design work. The design environment will be validated together with industry and large-scale research. Please refer [1] for more details on the objective of the UNICADO project.

---

[i] UNICADO: Development and Establishment of a University Conceptual Aircraft Design and Optimization Environment – project is funded by the German government in "Luftfahrtforschungsprogramm VI-I"

Daigo Maruyama, Florian Schültke, Eike Stumpf and Ali Elham

The UNICADO software with its architecture and underlying models is based on MICADO [2,3] of RWTH Aachen University. UNICADO consists of several modules, one for each aircraft design discipline, integrated into a global framework. The modular structure of the design environment makes it possible, on the one hand, to quickly incorporate own competencies into the conceptual aircraft design and, on the other hand, to take disruptive technologies into account and investigate their influence on the overall system. Besides, this allows easy extensibility with regard to Multidisciplinary Design Optimization (MDO).

The objective of this paper is to present an efficient global optimization (EGO) framework which is integrated into the UNICADO workflow. One of the goals of development of the EGO framework is effective use of statistical inference methods (also often called machine learning techniques). Dimensionality reduction and surrogate modelling are powerful techniques to achieve literally efficient optimization and widely used in engineering problems [4,5,6,7,8,9,10]. Since the EGO framework needs to be applied to the MDO process, it is summarized in a perspective of the MDO architectures [11] by focusing on which variables are required to be assisted by surrogate models. Then the MDO architecture as the developed EGO framework integrated into the UNICADO software is applied to a test case. As the test case, the CeRAS[ii] short-range reference aircraft CSR-01 is used, which data is publicly available. Detail of the CSR-01 can be found in [12]. The problem setting of the EGO using this test case is a conceptual design as minimizing a cost function composed by the MDA process available in the UNICATO toolbox. Apart from the cost function from our setting, the required aircraft performance by the TLARs (top-level aircraft requirements) needs to be satisfied so that the problem setting is a framework of constrained optimization problems. Details of the description including the architecture and the EGO framework are presented in Section 2. Section 3 introduces an extended EGO framework by introducing an extended Gaussian process (GP) model to overcome conceivable applications such as complex aircraft models governed by a large number of geometrical design variables, integration of multi-fidelity models in the discipline analyses, and use of offline database to further assist the EGO framework which is considered an online process. The extended GP model provide a solution for these conceivable applications in the MDO process. Section 4 concludes the works.

2. APPLICATIONS OF EGMDO TO AN UNICADO TEST CASE

In this section, an MDO architecture which can also explain the developed EGO framework is presented with optimization formulation. The EGO framework is explained to connect to an extended Gaussian process (GP) model in Section 3 which can be replaced by the conventional GP model used in the application test case.

2.1. Optimization formulation and MDO Architecture

The MDO architecture used in this work is the multidisciplinary feasible (MDF) architecture [11]. The UNICADO software equips a module of multidisciplinary analysis (MDA). The MDF architecture inherently contains a process of Multidisciplinary Analysis (MDA). The process of MDA can be modelled as a blackbox whose input is design variables x and output is converged coupling variables. The converged coupling variables as the output can compose a scalar cost function f. The process of defining the input design variables and the cost function is a problem setting of optimization formulation. Once the problem setting is done, a generalized formulation of the optimization problem based on the MDF architecture can be described as follows:

[ii] CeRAS: Central Reference Aircraft data System – http://ceras.ilr.rwth-aachen.de

Daigo Maruyama, Florian Schültke, Eike Stumpf and Ali Elham

$$
\begin{aligned}
Minimize \quad & \tilde{f}(\boldsymbol{x}) \\
w.r.t. \quad & \boldsymbol{x} \\
subject\ to \quad & \tilde{\boldsymbol{g}}(\boldsymbol{x}) = 0 \\
& \tilde{\boldsymbol{h}}(\boldsymbol{x}) \le 0
\end{aligned}
\tag{1}
$$

where $\boldsymbol{g}$ is a set of functions of equality constraints and $\boldsymbol{h}$ is that of inequality ones which are basically determined by the TLARs. The converged coupling variables are omitted. The tilde on all the functions indicates approximation. In the EGO framework, the functions to be evaluated with respect to the input design variables $\boldsymbol{x}$ are approximated by techniques of statistical inference (machine learning techniques). Models for the approximation are called surrogate models. In practice, these functions are outputted by running the MDA module. Figure 1 shows the architecture of the MDF-based EGO framework. This architecture simply describes integration of a conventional EGO framework including adaptive sampling techniques into the MDF architecture. The DOE means design of experiments as generating initial sample points on the input space $\boldsymbol{x}$. The function $\boldsymbol{c}$ in Fig. 1 represents a set of $\boldsymbol{g}$ and $\boldsymbol{h}$. Once the optimization is finished with obtaining $\tilde{f}(\hat{\boldsymbol{x}})$, where the hat indicates *optimized* in this paper, the EGO framework is required to re-evaluate all the functions by the MDA module as $f(\hat{\boldsymbol{x}}), g(\hat{\boldsymbol{x}}), h(\hat{\boldsymbol{x}})$. Especially the constraints are important if the optimum solution truly satisfies TLARs.
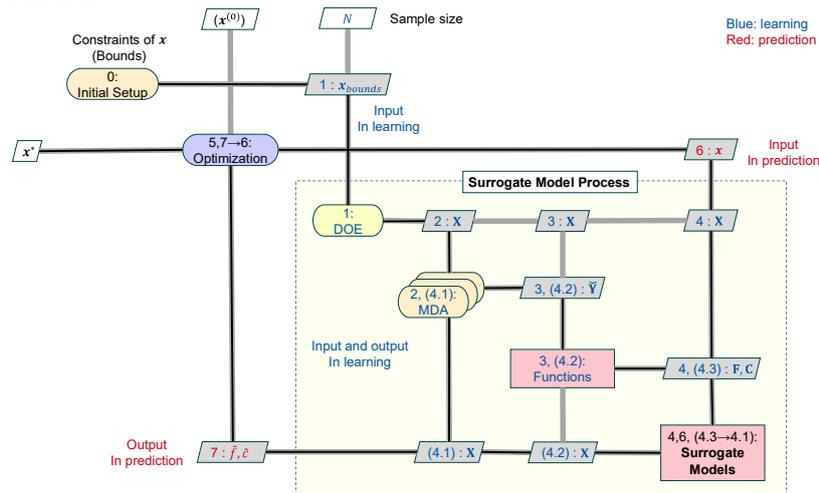
Figure 1. A MDF architecture with an EGO framework.

2.2. Efficient Global Optimization (EGO)

The objective of the efficient global optimization (EGO) is defined to find the global optimum design variable with as minimum computational costs as possible. The minimum computational costs can correspond to realizing as a small number of the MDA process (with convergence of the discipline analyses) as possible under the following conditions:

Assumption 1   The computational cost of the MDA process is the most time-consuming part and not negligible.

Assumption 2   The computational costs of the learning and prediction processes of the surrogate models are negligible.

Assumption 2 is basically a required property to be the optimization framework as EGO. Since the surrogate models are modelled as functions $\tilde{f}(\boldsymbol{x}), \tilde{g}(\boldsymbol{x}), \tilde{h}(\boldsymbol{x})$ by Eq. (1), any supervised learning techniques on machine learning approaches can be applicable.

In general, the functions $\tilde{f}, \tilde{g}, \tilde{h}$ as surrogate models are determined by using sample datasets of the input $\boldsymbol{x}$ generated by the DoE and the corresponding output $\boldsymbol{y}$. This is the learning process

Daigo Maruyama, Florian Schültke, Eike Stumpf and Ali Elham

in *Assumption 2*. The prediction process is to output corresponding y for arbitrary input x by using the functions $\tilde{f}, \tilde{g}, \tilde{h}$ determined by the learning process. The functions can be regarded as blackboxes. This is a schematic expression of the supervised learning methods. More generally the output y is predicted as a probability by a Bayesian perspective. Considering probabilistic models provide us with more benefits on EGO strategies.

The expected improvement (EI) [4,13,14] is one of the most widely used techniques in EGO strategies in general. Optimization methods using the EI are in general called Bayesian optimization [13,14]. These methods are based on using the information of the probabilities derived by Bayesian approaches. Therefore, the usability of the surrogate models is dependent on if the models are Bayesian models.

Gaussian processes (GPs) are one of the most promising models in the Bayesian models. There are mainly two reasons behind that. One is that the probability of the output can be analytically obtained. The other one is that only week assumption on definition of the model is required. The former one is a very important property. Only limited models as the supervised learning methods possess this property such as GPs and some special cases in Bayesian linear regression models. For example, neural networks (NNs) with the Bayesian approaches (Bayesian NNs) are computationally hard to compute the probability. Even approximation methods to compute the probability require additional optimization processes, which is computationally not efficient compared to the GPs. The pros and cons of GPs of NNs are summarized in Table 1. Note that the GPs have another disadvantage that multiple output is inherently impossible even though the NNs are possible. This property is not that important compared with the other properties in Table 1 in the EGO framework. It is also noted that there are some techniques to extend the GP models available for multiple output.

Thus, GPs are the first candidate as the surrogate models as far as the models satisfy the second bullet of the conditions due to its property to execute the adaptive sampling efficiently. Equation 2 represent the GP model used in this work:

$$p(\mathbf{y}|\mathbf{x}, \boldsymbol{\theta}) = \mathcal{N}\left(\mathbf{y} \middle| \underbrace{\widehat{\boldsymbol{\mu}}}_{trend}, \boldsymbol{\Sigma}(\mathbf{x}, \boldsymbol{\theta})\right) \tag{2}$$

where p represents a probability in general. Especially since the output y is a continuous value, p represents a probability density function (pdf) here. Therefore $p(\mathbf{y}|\mathbf{x}, \boldsymbol{\theta})$ is interpreted as a conditional probability of $\mathbf{y}$ when $\mathbf{x}, \boldsymbol{\theta}$ are given, where $\mathbf{x}$ and $\mathbf{y}$ are an arbitrary set of the input x and the output y as $\mathbf{x} = (x_1, x_2, \cdots)$ and $\mathbf{y} = (y_1, y_2, \cdots)$, respectively. $\mathcal{N}$ represents Gaussian distribution in general whose distribution is determined by its mean and covariance. $\boldsymbol{\Sigma}$ is a covariance matrix whose component is represented by a kernel function of a pair of the input x and parametrized by $\boldsymbol{\theta}$, which is called hyperparameter. The kernel function is therefore represented as $k(x, x', \boldsymbol{\theta})$ in general, where x' is another input from the set $\mathbf{x}$. $\widehat{\boldsymbol{\mu}}$ named as *trend* in Eq. (2) is a fixed constant vector determined only by the initial sample dataset as $\widehat{\boldsymbol{\mu}} = \mathbf{1}\widehat{Y}$, where $\widehat{Y}$ is the mean of the output sample dataset $\mathbf{Y}$. The model is equivalent to a normal GP model $p(\mathbf{y}|\mathbf{x}, \boldsymbol{\theta}) = \mathcal{N}(\mathbf{y}|\mathbf{0}, \boldsymbol{\Sigma}(\mathbf{x}, \boldsymbol{\theta}))$ after pre-processing of the dataset from $\mathbf{Y}$ to $\mathbf{Y} - \mathbf{1}\widehat{Y}$. More details of the GP models including the extended GP models in Section 3, and their learning and prediction processes, are summarized in Appendix. Note that all the parameters $x, \boldsymbol{\theta}$ except for y is treated as deterministic. Only y is stochastic as it can be represented as $p(y)$. The kernel function $k(x, x', \theta)$ in all the application problems in this paper is a Gaussian kernel as $k(x, x', \theta) = \sigma^2 \exp(-\theta' \|x - x'\|^2)$.

Thus, the next step is to determine the hyperparameters $\boldsymbol{\theta}$ by using a dataset $\mathcal{D} = (\mathbf{X}, \mathbf{Y})$ by the maximum likelihood estimation (MLE). After this step, prediction of the output y_{prd} when

Daigo Maruyama, Florian Schültke, Eike Stumpf and Ali Elham

arbitrary input $\boldsymbol{x}_{prd}$ becomes available as a probability $p\big(y_{prd}\big|\boldsymbol{x}_{prd},\mathcal{D}\big)$. The probability is represented as follows:

$$p(y|\boldsymbol{x},\mathcal{D}) = \mathcal{N}\left(y\,\bigg|\,\underbrace{\mu_N(\boldsymbol{x})}_{regression}\,,\,\underbrace{\sigma_N{}^2(\boldsymbol{x})}_{uncertaity}\right) \tag{3}$$

where $\mu_N(\boldsymbol{x})$ and $\sigma_N{}^2(\boldsymbol{x})$ are mean and variance of the Gaussian distribution. In this paper, $\mu_N(\boldsymbol{x})$ and $\sigma_N{}^2(\boldsymbol{x})$ are just named as *regression* and *uncertainty*, respectively, for simplicity of the discussion later. As insisted in the above, if the model is not a Bayesian model such as NNs, only the regression model $\mu_N(\boldsymbol{x})$ is obtained ($\sigma_N{}^2(\boldsymbol{x})$ as the updated trend can be also obtained but it contains only the noise information. Please see Appendix). Thus, all the information is available to search for the next candidate location $\boldsymbol{x}$ to add a new sample point as the adaptive sampling techniques. The expected improvement (EI) [4,13,14] is one of the most promising indicators for the adaptice sampling techniques for the puropose of finding the global optimum location $\boldsymbol{x}$. It is represented as follows by considering the standerdized prorability of Eq. (2) by the minimum (or maximum) in the current sample datase **Y**:

$$EI(\boldsymbol{x};\mu_N,\sigma_N,y_{min}) = \big(y_{min} - \mu_N(\boldsymbol{x})\big)\mathrm{cdf}\big(p_{std}(\boldsymbol{x})\big) + \sigma_N(\boldsymbol{x})\mathrm{pdf}\big(p_{std}(\boldsymbol{x})\big)$$
$$where,\ p_{std}(\boldsymbol{x}) = \tfrac{y_{min}-\mu_N(\boldsymbol{x})}{\sigma_N(\boldsymbol{x})} \tag{4}$$

Note that when the objective is finding the maximum, the equation can be easily reformulated by using y_{max} instead of y_{min}. Thus, the EI on arbitrary input $\boldsymbol{x}$ is determined by μ_N, σ_N and y_{min}. A new sample location $\boldsymbol{x}_{new}$ is indicated by $\boldsymbol{x}_{new} = \max_{\boldsymbol{x}} EI(\boldsymbol{x};\mu_N,\sigma_N,y_{min})$. There are other indicators in the adaptive sampling techniques dependent on purposes, which are called acquisition functions [13,14]. For example, the constrained EI [4] which is a combination of the EI and the probability of improvement (PI) [4, 13,14] is expected to be useful to deal with constraint optimization problems. In this paper overall, the EI is used for more focusing on finding the global optimum.

Table 1. Pros and cons (trade-off) on surrogate models (supervised learning techniques) – comparison of Gaussian Processes (GPs) and neural networks (NNs). Pros are in bold.

	Adaptive sampling	Learning process	Function approximation
Gaussian Process	**Very cheap**	Intractable when the sample size is large	Universal
Neural Networks	Expensive	**Much less sensitive than the GPs**	**Universal (including non-smooth functions and non-stationary processes when multi layers)**

2.3. Results

The problem definition (formulations) of the conceptual design optimization is determined to satisfy TLAR [12], which results in eight inequality and two equality constraints in the formulations (Eq. (1)). The optimization algorithm used for global search under constraints is differential evolution. The baseline aircraft configuration is the CSR-01 [12]. The cost function and design variables are chosen as mission fuel weight, wing loading, and thrust-to-weight ratio, respectively. The initial condition is summarized in Table 3 with the optimization result.

We set 30 sample points by the DoE and 10 additional infill points by the adaptive sampling strategy. The Sobol sequence as a quasi Monte Carlo sampling method is used for the DoE. The output values (mission fuel weight and other 10 output values) at each sample point are

Daigo Maruyama, Florian Schültke, Eike Stumpf and Ali Elham

computed by the MDA module in the UNICADO software and the module is run in parallel on the initial DoE sample points. Based on the reference values of the CSR-01 [12], The design space of wing loading and thrust-to-weight ratio as the input design variables are set to be from 600 to 650 and from 0.30 to 0.34, respectively. This user-definition of the design range is due to the fact that the MDA process is aborted because of violated input design variables, especially when the thrust-to-weight ratio is below 0.3 despite of the satisfaction of the TLARs.

Eventually one of the 30 initial sample points, and two of the 10 adaptive sample points were aborted due to its violated values of the input design variables. Figures 2 and 3 show the surrogate models of each function with depicting the sample points. Two surrogate models for the cost function are presented in Fig. 2. This is for comparison of how efficiently the adaptive sampling technique works. Eventually a global optimum is obtained by in this EGO framework. The results are compared with the initial conditions in Table 3. It is usually not desirable to have the global optimum around the edge of the surrogate models since the prediction accuracy of the extrapolation is worse than the interpolation in general. The reason of the definition of the design spaces is as mentioned in the above. However, the adaptive sampling technique could cover this problem by making the predictions around the optimum location the interpolation by effectively adding new sample points. After the optimization the cost functions and the functions for constraints were re-evaluated by the MDA module on the optimized input design variables. TALRs are all satisfied. It is noted that the difference between $f(\hat{x})$ and $\tilde{f}(\hat{x})$ was around 0.26 [kg] where the prediction order in the design space is decades to a hundred kg.

The designed point is optimum with respect to the mission fuel with satisfying the TLARs. However, as it can be observed from Fig. 3, the optimum solution is quite critical in terms of the take-off filed length and the max operating altitude compared with those in the initial condition. The formulation in Eq. (1) is not taking into account other factors such as robustness of the output values with respect to the input variables. Therefore, it can be evaluated that the EGO framework itself successfully worked on this test case. It is noted that the scikit-learn module was used for the GP models in this test application.

Table 2. Design variables and cost function at initial and optimized conditions.

	Wing Loading [kg]	Thrust-to-weight ratio [kg/m^2]	Mission fuel weight [kg]
Initial	631.2500	0.3218750	6045.517
Optimized	633.5872	0.3001961	5973.523
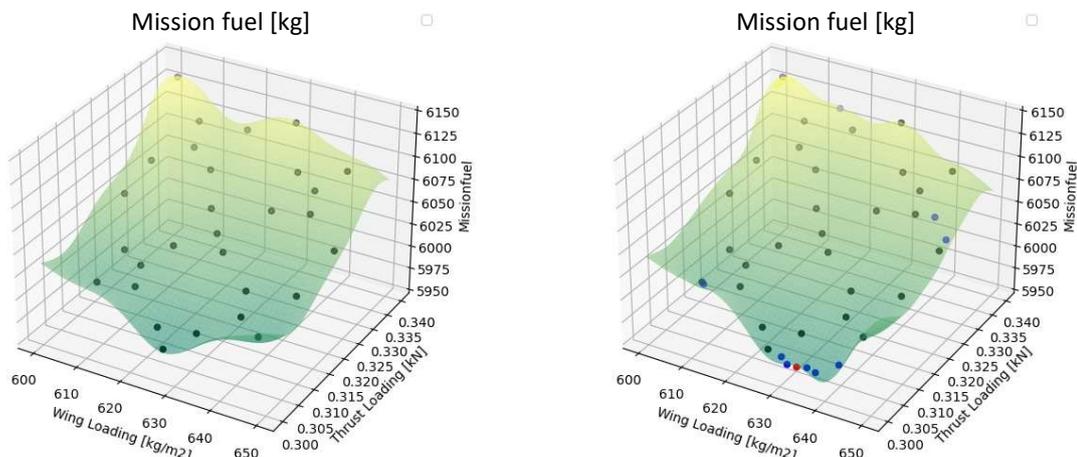
Figure 2. Surrogate models of the cost function (mission fuel weight, the unit is kg), left: generated by initial DoE sample, right: generated by initial DoE sample with adaptive sample points (bule points). The red point in the right figure is the optimum point with true output (the cost function re-evaluated by the MDA module).

Daigo Maruyama, Florian Schültke, Eike Stumpf and Ali Elham
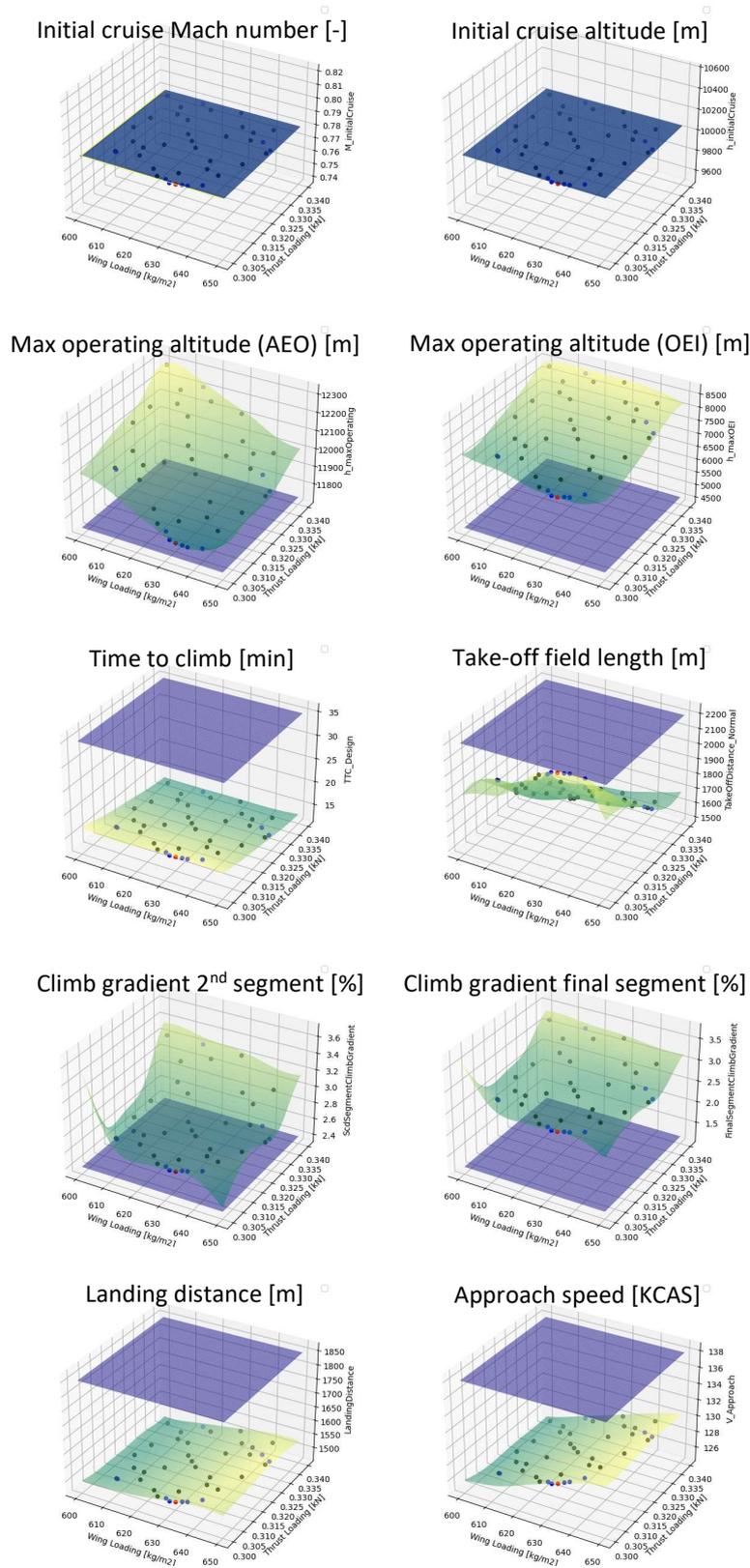
Figure 3. Surrogate models (green contour colors constructed by the initial DoE sample with the adaptive sample points) of each output value for design requirements by TLAS. The blue planes are the values of the constraints by TLAS. The red point for each output value is the output value on the optimum point with true output (the cost function re-evaluated by the MDA module).

Daigo Maruyama, Florian Schültke, Eike Stumpf and Ali Elham

3. EXTENSION OF THE EGO FRAMEWORK

The EGO framework using the GPs is not versatile in some problem settings. In this section, an extended GP model is presented to support the efficiency of the conventional EGO design process used in the previous sections by taking topics of further applications of MDO using the EGO framework.

The applications of the EGO framework are to be extended to more complex problems. The application of the previous section is a conceptual aircraft design with respect to the wing loading and the thrust-to-weight ratio. This application problem can be modelled as two-dimensional input variables and one-dimensional output value in a modelling viewpoint of the EGO framework. Thus, in the first sub-section, conceivable applications for further extension of the EGO framework are mentioned. Then, the problems that confront on the efficiency and accuracy of the EGO framework are introduced. The solutions are presented in the next sub-section with methodologies introduction. A global perspective of the methodologies for implementation is summarized in Appendix. Different from the case of the previous section, the extended GP model was created by basic libraries.

3.1. Problem Setting and Extensibility of EGO Framework

The EGO framework required to be improved for further application cases in MDO. The conceivable application cases are as follows:

Case 1.   A large number of the input (design) variables
         A)   Use of other datasets in offline processes
Case 2.   Using multi-fidelity models in the discipline analyses
Case 3.   Evaluating complicated cost functions / functions for constraints

Case 1 is natural for further applications due to especially increase of geometrical design variables. Extensibility as a strategy to be derived to solve this issue is also mentioned as a *Case 1.A* (use of offline database). It has to be noted at first that some dimensionality-reduction techniques (unsupervised learning techniques in the machine learning) are considered [5,6,7,9] for cases where the input variables are either not uniformly generated like using the DoE for some reasons or for cases where the input variables compose manifold structures in the space based on a purpose (e.g. the purpose is the cost function). The active subspace method [5,6] can be one of the useful methods for the latter situation. These dimensionality-reduction techniques can be independently applied to the discussion in this section as a pre-processing of the entire EGO framework since the techniques can be modelled as a mapping of the input variables $x \to x'$, where x' is a new coordinate system on the manifold. Therefore, this process is not discussed in this paper. In practice it is very important especially to consider *Case 1*.

The problem of *Case 1* affects the efficiency of the GPs because the sample size N incrase along with the increase of the dimensionality D of the input space. This fact does not satisfy *Assumption 2* in Subsection 2.2 that the learning and the prediction processes are negligible in the entire MDO process. Particularly the learning process becomes intractable [15] since the computational cost is cubic proportional to the sample size N as $O(N^3)$ since the process contains the inverse matrix calculation whose size is $N \times N$. Especially, it is time-consuming to search for the optimal solution of the hyperparameter $\boldsymbol{\theta}$ in a high-dimensional space when using heuristic optimization methods (e.g. when using the kernel function $k(\boldsymbol{x}, \boldsymbol{x}', \boldsymbol{\theta}) = \sigma^2 \exp\left(-\sum_{i=1}^{D} \theta_i' \left\| x^{(i)} - x'^{(i)} \right\|^2\right)$). When the gradient-enhanced GP models are uses, the increase of the time becomes remarkable as $O(N^3(1+D)^3)$. Several approximation methods to approximate the hyperparameter $\boldsymbol{\theta}$ have been developed so far [15,16,17,18,19]. Here other approaches based on the objectives of the EGO framework are

introduced to overcome the problems of *Case 1*.

Case 2 is a case of using multiple datasets, each of which is obtained by a different fidelity of a common model analysis. For example there are two datasets where one is a low-fidelity dataset and the other one is a high-fidelity dataset. In practice, the sample size of the low-fidelity dataset tends to be larger than that of the high-fidelity one. The multi-fidelity models aim at further efficiency by reducing the sample size of the high-fidelity analysis model. They are widely used nowadays to assist the efficiency of the entire EGO framework [4,8,20,21]. The co-Kriging method [4,20] is an example of the multi-fidelity models for EGO frameworks.

Case 3 is about the performance accuracy of the surrogate model (the supervised learning technique) itself in the prediction process. In Subection 2.2 by using Table 1, the pros and cons of GPs and NNs are briefly summarized in a practical application aspect. Here for *Case 3*, the strong points of both will be reconfirmed. We use one dataset shown in [22] to consider *Case 3*. This dataset represents characteristics of the pitching moment of a trajectory of a space plane on a wide range of Mach numbers. The authors applied a GP model with non-stationary kernel functions to predict these characteristics since GP models with stationary kernel functions as conventional GP models do not properly achieve good performance accuracy.

Considering the respective properties of various supervised learning techniques and the objectives of EGO, the methods that can handle the problems of all the cases (from *Case* 1 to *Case 3*) are summarized in one perspective.

3.2. An Extended Gaussian Process and Preliminary Results

The basic concept as common for all is that all the disadvantages of GPs shown in Table 1 are compensated by NNs. This concept is that of the extended GP model. A GP model where its trend is substituted by arbitrary regression model such as NNs is an example of the extended GP model. Details of the theory of the extended GPs is summarized in Appendix. The essentially-same model is used in [23] as complementary Bayesian optimization processes assisted by a NN model, which are compared with adjoint-based optimization.

When $\hat{\boldsymbol{\mu}} = \mathbf{f}.(\mathbf{x})$ in Eq. (2), the trend is uniquely defined as a function of arbitrary input $\boldsymbol{x}$ as $\hat{\mu} = f(\boldsymbol{x})$, where $\mathbf{f}.(\mathbf{x})$ is a vector composed of the common function f to each element of the input vector $\mathbf{x}$. Any regression models (including GPs with using their regression parts $\mu_N(\boldsymbol{x})$ in Eq. (3)) are applicable to the function $f(\boldsymbol{x})$. NNs are the first candidate from the viewpoints of the function approximation and efficiency of the learning process compared with the GPs (see Table 1). The performance of the NNs about the function approximation can be seen in Fig. 4, which also shows one solution in terms of *Case 3*. Figure 4 shows three figures: the GP model by Eq. (2) ($\hat{\boldsymbol{\mu}} = \mathbf{0}$), a NN model, and the extended GP model with its trend as the NN model in the middle figure. It is known that GP models are universal for function approximation as well as NN models but not for non-smooth functions and non-stationary processes like the case of Fig. 4 whereas NN models are able by increasing the number of the layers. On the other hand, the uncertainty of NN models cannot be analytically obtained whereas GP models can as shown in the left figure in Fig. 4 even though the performance prediction of the regression part is not acceptable. The right figure in Fig. 4 is the result obtained by applying the extended GP model to the same dataset, which shows the advantages of both GPs and NNs. Since the uncertainty information is available, the EI can be computed by Eq. (3) to proceed the adaptive sampling technique. The new input locations are indicated in the figures.

This approach is also used to solve the problem of *Case 1*. We can split the whole dataset into two subsets. One is used for the learning of a NN model. The other one is for the

Daigo Maruyama, Florian Schültke, Eike Stumpf and Ali Elham
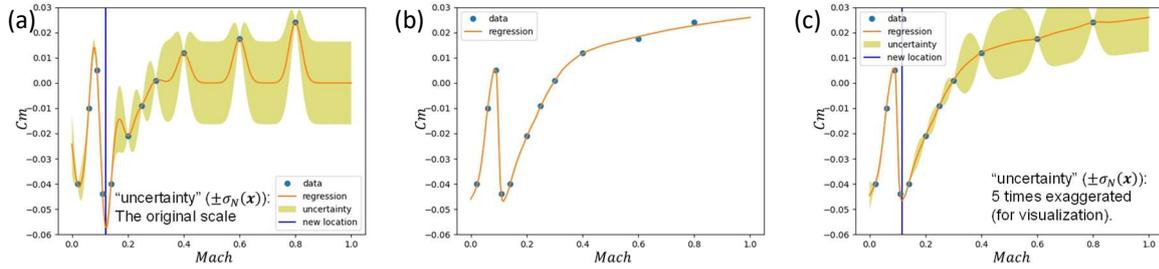
Figure 4. The conventional GP model, a NN model, and the extended GP model with its trend by the NN model in (b) ($\pm\sigma_N(\boldsymbol{x})$ of the figure (c) is scaled to 5 times for visualization), the data points is from [22].

learning of the extended GP model with the NN model by the other subset as its trend. The objective is to ease the computational burden of the learning process of GP models in general due to its complexity of $O(N^3)$. By using the subset whose sample size is N' ($N' < N$), the cost is reduced to $O(N'^3)$. The process where a dataset is split into two datasets enables us to consider offline/online processes to efficiently construct GP models. Note that the uncertainty information of the subset used to by the offline process is discarded. Otherwise, the co-Kriging model [4,20] could be applied by taking $\hat{\rho} = 1$ (see Eq. (6) later).

The benefit of this approach is tested by a comparison of two test cases using a common test function. Figure 5 shows a result of the conventional EGO approach shown in the Section 2 (where $\hat{\boldsymbol{\mu}} = \mathbf{0}$ in Eq. (2)). This is a basic approach of EGO frameworks (also known as the Bayesian optimization). The initial sample size N is $N = 4$. Please refer [4,20] for the information of the sample datasets and the reference function. As can be seen in Fig. 5, $N = 7$ to 9 of sample size is required to predict the global optimum. On the other hand, Fig. 6 is a result of using the extended GP model with the fixed trend that was learned by a subset of the whole data. The fix trend can be any regression models which possess on the regression information. In this case, the fixed trend in Fig. 6 is the regression part of the GP model in Fig. 5 of when $N = 4$. It can be confirmed that the trend shown in the red broken lines in all the figures in Fig. 6 are the regression in Fig. 5(a) shown in the green line. The extended GP model is constructed based on this trend information and the EGO process (the
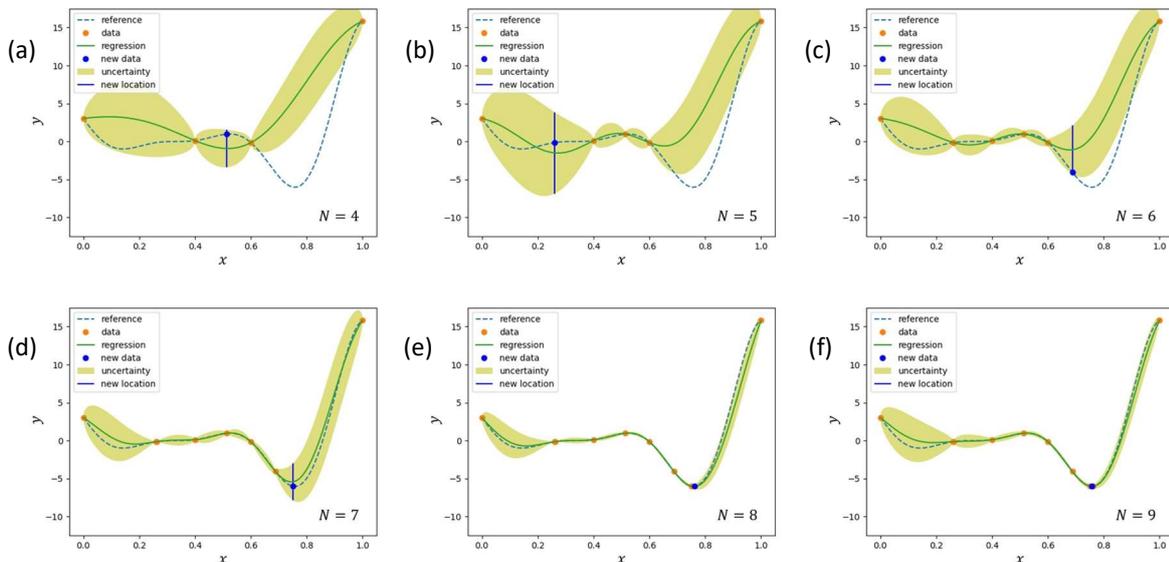
Figure 5. The conventional GP model (the trend is fixed at 0), from (a) to (f) corresponds to the 1st to the 6th iteration ($\pm\sigma_N(\boldsymbol{x})$ is scaled to 5 times for visualization).

Daigo Maruyama, Florian Schültke, Eike Stumpf and Ali Elham
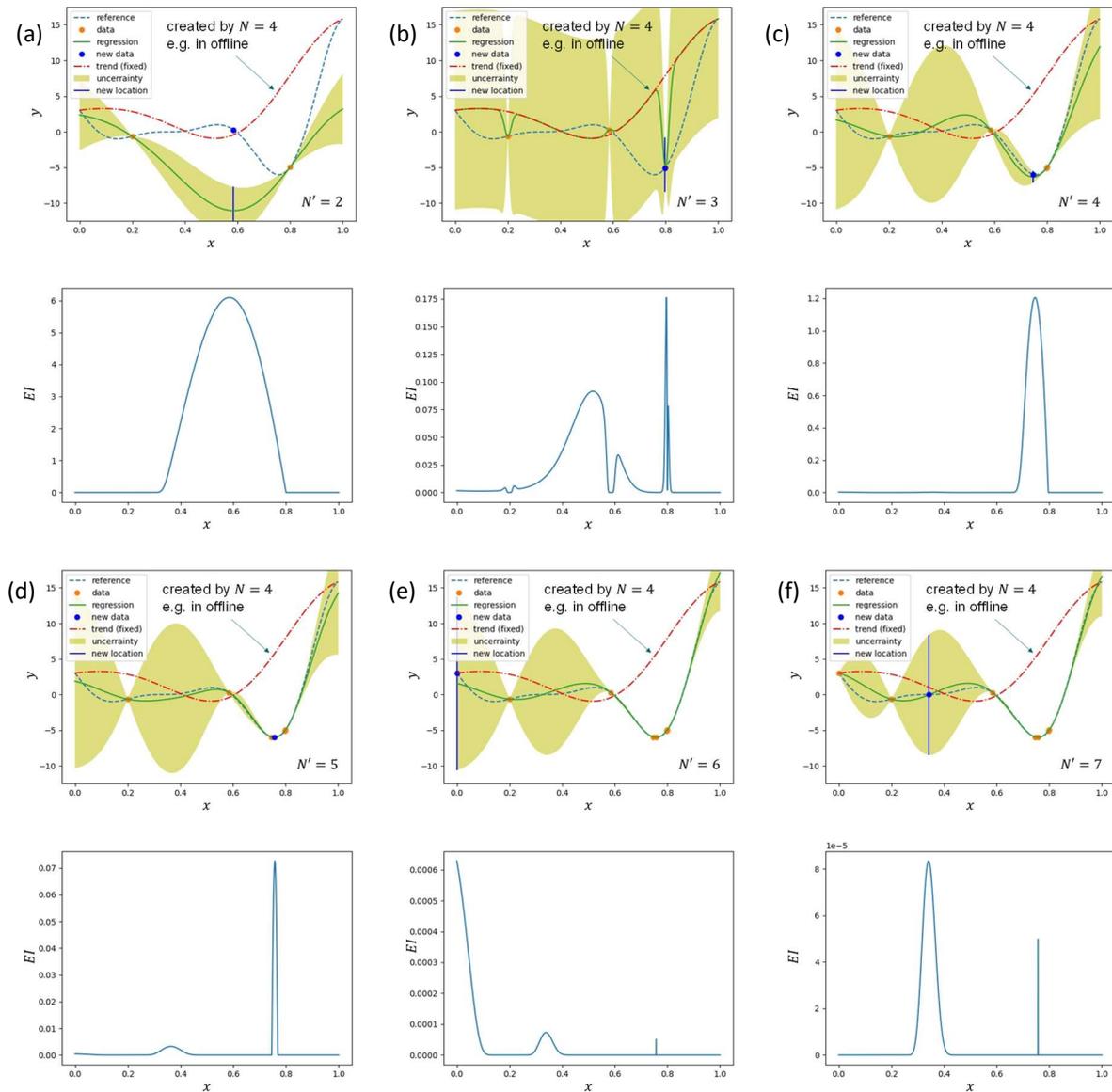
Figure 6. The extended GP model with the fixed trend generated by a subset of the whole dataset (to imitate an offline/online process), and the respective EI, from (a) to (f) corresponds to the 1st to the 6th iteration ($\pm \sigma_N(x)$ is scaled to 5 times for visualization).

Bayesian optimization) was conducted with $N' = 2$, where N' is assumed to be a subset of the whole sample points whose size is $4 + 2 = 6$. It has to be emphasized that the practical sample size used in the extended GP model is only $N' = 2$. After adding sample points one by one as usual based on the EI, the global optimum is being predicted when the sample size of the subset $N' = 3$ to 5. This indicates that to find the global optimum, it is able to avoid the full sample size which causes rapid increase of the computational burden due to the property of GP models $O(N'^3)$ in the learning process. Note that the sample locations of Fig. 6 might look intentional since one of the newly added two sample points of the subset is close to the global minimum. However, all the six sample points are now equally distributed from 0 to 1 of x. This is imitating sample points by the DoE. The actual sample points are $\mathbf{X} = \{0, 0.2, 0.4, 0.6, 0.8, 1\}$. It is also noted that commonly in this section, the uncertainty depicted as a band in many figures are scaled to make it visible. However, to

Daigo Maruyama, Florian Schültke, Eike Stumpf and Ali Elham

the scale ratio is fixed for each application. Therefore, sometimes the error band is too small to be visible.

Finally, to overcome the problem of *Case 2*, using multi-fidelity dataset, the extended GP model is edited to be more generalized here. It can be regarded then as a generalized approach of the co-Kriging when the low-fidelity dataset is modelled as regression models (not possessing the uncertainty information). The idea is that now the trend needs to be also statistically tuned by the learning process. Equation (2) is modified by changing the constant trend $\hat{\boldsymbol{\mu}}$ to unknown trend $\boldsymbol{\mu}$ (but $\boldsymbol{\mu}$ will not treated as stochastic):

$$p(\mathbf{y}|\mathbf{x}, \boldsymbol{\theta}, \boldsymbol{\mu}) = \mathcal{N}\big(\mathbf{y}\big|\boldsymbol{\mu}, \Sigma(\mathbf{x}, \boldsymbol{\theta})\big) \tag{5}$$

$\boldsymbol{\mu}$ is now included in the conditional statement. Therefore $\boldsymbol{\mu}$ can be determined by the MLE together with $\boldsymbol{\theta}$. However, we need strong assumption on the trend $\boldsymbol{\mu}$. One example of the assumption is that trend function $f(\mathbf{x})$, which is a regression model obtained by using the low-fidelity dataset, is linearly varied as $\boldsymbol{\mu} = \rho \mathbf{f}.(\mathbf{x})$, where ρ is a scalar parameter. Equation (5) can be redescribed as follows:

$$p(\mathbf{y}|\mathbf{x}, \boldsymbol{\theta}, \rho) = \mathcal{N}\big(\mathbf{y}\big|\rho \mathbf{f}.(\mathbf{x}), \Sigma(\mathbf{x}, \boldsymbol{\theta})\big) \tag{6}$$

Now ρ is added into the conditional statement instead of $\boldsymbol{\mu}$ and it is determined by the MLE together with $\boldsymbol{\theta}$ as $\hat{\rho}$. When ρ is treated as a fixed parameter $\hat{\rho}$, the model becomes equivalent to the previous approaches (by $\hat{\rho} = 1$).

An application example of multi-fidelity analyses of using the more generalized extended GP model in Eq. (6) is shown in Fig. 7. This test case is the same example as those in [4,20]. The co-Kriging model in [4,20] can be roughly regarded as a model of Eq. (6) when the trend is stochastic (by a GP model). In this paper we would like to emphasize two things. One is that if the uncertainty of GP models is not used, other regression models such as NNs can be also candidates. The other is that the model efficiency is harmed by the sample size N as $O(N'^3)$. These properties in the extended GP models are expected to be useful when considering cases of combination of *Case 1.A* and *Case 2*. For instance, a fuge ammont of sample data obtained by a low-fidelity analysis is stocked as a offline database and the EGO framework using the extended GP models for find the global optimum by running several iterations of high-fidelity analysis using the adaptive sampling technique to achieve as small number of the high-fidelity analysis as possible. The sample size N of the offline database is exptected to be large and the uncertainty information is expected to be less important due to the reduction of the amount of the uncertainty informaiton with the increase of teh sample size N, which is guaranteed by the Bayesian theorem. Therefore, the trend can be subsistuted for a regression model.

Thus, a powerful regression model such as NNs is efficiently applied to the low-fidelity dataset as the trend, and the uncertainty of the GP model obtained by the high-fidelity dataset is fully used for the purpose of finding the global optimum efficiently. It has to be noted that if GP models are sufficient to approximate the characteristics of the low-fidelity dataset and the uncertainty information is used, the co-Kriging is useful.

Figure 7 shows the result of when the extended GP model by Eq. (6) was applied to the test case [4,20]. It can be observed in the middle-upper figure in Fig. 7 that the regression part of the extended GP model by using two datasets: a low-fidelity dataset ($N_{low} = 11$) and a high-fidelity dataset ($N_{high} = 4$), fits to the reference function. This is the same result as [4,20]. Here, the low-fidelity dataset and the regression model $\mathbf{f}.(\mathbf{x})$ in Eq. (6) are shown in the left-upper side of Fig. 7. The high-fidelity dataset is shown in the left-lower side of Fig. 7. Both figures contain the reference function, which is depicted by a light blue dotted line. The test-case is basically the same as that in [4,20] but a small noise ϵ is additionally added

Daigo Maruyama, Florian Schültke, Eike Stumpf and Ali Elham

on the low-fidelity data ($\mathcal{N}(\epsilon|0, 0.2^2)$). In the middle figures in Fig. 7, the information of where to add a new sample point is indicated. The middle-lower figure shows $EI(\boldsymbol{x})$ by Eq. (4). Not only the model could fit to the reference data well, but also the model could detect a proper input location $\boldsymbol{x}$ to enhance the model for the purpose of finding the global minimum. The figures of right side in Fig. 7 show the updated model after adding the new sample point. The quality of the model around the global minimum location $\boldsymbol{x}$ is slightly improved (the model created by the initial multi-fidelity datasets was already good) and $EI(\boldsymbol{x})$ indicated again around the global minimum. Since the initial datasets were already sufficient to fit accurately to the locations around the global minimum, another example which has a lower sample size of the high-fidelity analysis data is presented with Fig. 8.

Figure 8 is a result of using the same technique but using a fewer sample size $N_{high} = 2$ of the high-fidelity data. N_{low} is the same as $N_{low} = 11$ and so as to the trend. It can be more obviously observed that the low-fidelity dataset can assist not only to fit to the reference function around the global minimum location but also contributing function $EI(\boldsymbol{x})$ for exploiting a new location to further improve the function around the optimum. In a practical application viewpoint, the global minimum can be found only by running four times high-fidelity analyses ($N_{high} = 4$). As a comparison, the conventional GP model shown in Fig. 5 started with $N_{high} = 4$ as the initial sampling and required eventually $N_{high} = 7$. Note that the two sample points of the high-fidelity dataset was intentionally selected to avoid nearby the global minimum. The sample data is $\mathbf{X}_{high} = \{0.2, 0.9\}$.

All the methods described as the extended GP model to solve the problems of *Cases 1-3* basically share common properties due to the one perspective mentioned in the beginning of this section (please see Appendix for more details). Therefore, we can also regard the multi-fidelity approaches can contribute to reduce the sample size used for the learning process of the GP models as shown by the comparison of Figs 5 and 8. A common property of the extended GP models is that the uncertainty $\sigma_N{}^2(\boldsymbol{x})$ in Eq. (2) tends to small due to the assistance of the trend (please see the scaling for the visualization especially in Fig. 7). The assistance by the trend might cause some difficulties on precision of the computations.
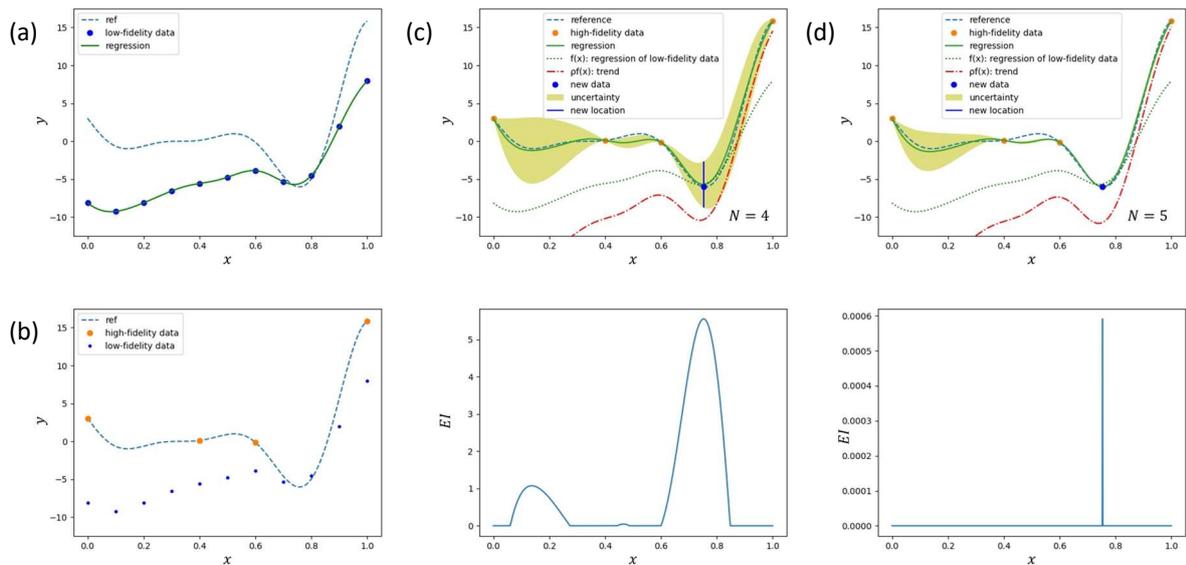
Figure 7. The and the dataset, and the extended GP model with a scalable fixed trend generated by a low-fidelity dataset initiated with four sample points of high-fidelity dataset, and the respective EI: (a) the low-fidelity dataset with the generated regression model used as the trend, (b) the high-fidelity dataset, (c) and (d) corresponds to the 1st to the 2nd iteration ($\pm\sigma_N(\boldsymbol{x})$ is commonly scaled to 5×10^4 times for visualization).

Daigo Maruyama, Florian Schültke, Eike Stumpf and Ali Elham
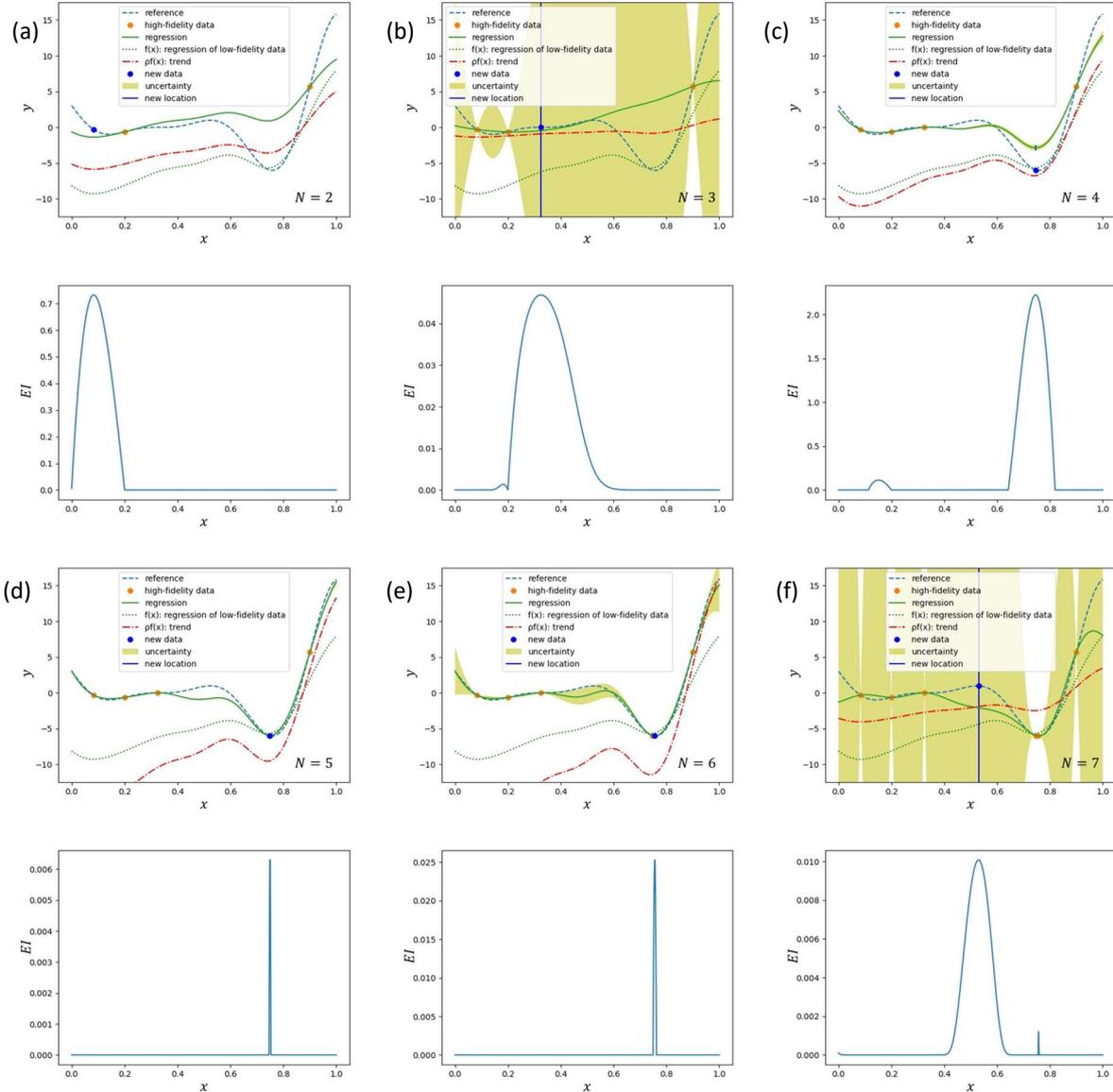
Figure 8. The extended GP model with a scalable fixed trend generated by a low-fidelity dataset initiated with two sample points of high-fidelity dataset, and the respective EI, from (a) to (f) corresponds to the 1st to the 6th iteration ($\pm \sigma_N(x)$ is commonly scaled to 10^2 times for visualization).

During the update of the GP models by adding sample points, the trend function $\rho f(\mathbf{x})$ varies when ρ is treated as a parameter like the multi-fidelity model applications. For example, when the trend model (not the regression $\mu_N(\mathbf{x})$ as *posterior* in Eq. (3) after the learning but the $\mu(\mathbf{x})$ as *prior* before the learning) can model the sample points very well, the GP model is obliged to work on compensating small-orders differences. Variations of GP models (and Kriging models) are summarized in Appendix.

4. CONCLUSIONS

An efficient global optimization (EGO) framework for multidisciplinary design optimization (MDO) was proposed with conceptual aircraft design test case as a preliminary result. The objective of the framework is to assist the UNICADO software. The UNICADO software provide a multidisciplinary analysis (MDA) module to facilitate the EGO framework. The

multidisciplinary feasible (MDF) architecture enables to concatenate the EGO framework and the MDA module as a backbox. Then, development of the EGO framework for the purpose of MDO was conducted. A conventional EGO approach based on the Bayesian optimization was developed and applied to a short-range reference aircraft called CSR-01 by satisfying the TLARs using a constrained evolutional algorithm as the optimizer. The mission fuel as the cost function was efficiently minimized by Gaussian process models which were used also to handle the constraints by TLARs. The design variables are the wing loading and the thrust-to-weight ratio, which are modelled as prediction strategies on a two-dimensional input space in an EGO perspective.

Further extension of the EGO framework for future applications was then conducted. An extended Gaussian process model was proposed to overcome conceivable three issues: A large sample size is required due to increase of the number of design variables. Multi-fidelity discipline analysis models are used to speed-up the MDA process. Complicated cost function prediction may be needed. The extended Gaussian process model enables to offer solutions of these issues by combining the pros of the Gaussian process models and neural network models. The model can provide further efficiency of the EGO framework in general by concatenating the online optimization process using design of experiments and offline database. Preliminary results of all the issues were presented by using one dimensional test functions.

APPENDIX

Introduction of a generic perspective of the extended GP model including the conventional GP models by explaining the uncertainty information which is the key feature in the EGO framework is described here for implementation of the framework.

First of all, it is not limited on the topics of the Bayesian approaches to consider the output y as a probability $p(y)$. We now consider a single output y for a given multiple input x. In general in regression models $f(x, w)$ in the supervised learning methods, the sample data has a stochastic variable ϵ on the regression model as $f(x, w) + \epsilon$ to represent noise. Therefore, the data is assumed to be generated by a probability distribution. The parameter w is determined by the learning process using given sample datasets $\mathcal{D} = (\mathbf{X}, \mathbf{Y})$. Most of cases, it is justified to define an isotropic Gaussian distribution on the stochastic noise as $\mathcal{N}(\epsilon|0, \lambda^2)$, where λ is a deterministic parameter. Therefore, the probability distribution of the output y is represented as follows:

$$p(y|x, w, \lambda) = \mathcal{N}\left(y \middle| f(x, w), \underbrace{\lambda^2}_{noise}\right)$$

$$p(\mathbf{y}|\mathbf{x}, w, \lambda) = \mathcal{N}\left(\mathbf{y} \middle| \mathbf{f}.(\mathbf{x}, w), \underbrace{\lambda^2 \mathbf{I}}_{noise}\right) \qquad (A.1a)$$

In that sense, the GP models are considered to be models of a multivariate Gaussian distribution with zero mean a covariance matrix $\mathbf{\Sigma}$, each component of which is composed by a kernel function $k(x, x', \boldsymbol{\theta})$, where $\boldsymbol{\theta}$ is a vector of all the hyperparameters in the kernel function:

$$p(\mathbf{y}|\mathbf{x}, \boldsymbol{\theta}) = \mathcal{N}\left(\mathbf{y} \middle| \mathbf{0}, \mathbf{\Sigma}(\mathbf{x}, \boldsymbol{\theta})\right) \qquad (A.2a)$$

The notation of all the parameters is the same as Eq. (2). Equations (A.1) and (A.2) are in a relationship of dual representation in a Bayesian perspective on some special conditions where the regression model $f(x, w)$ is a linear regression model as $w^{\mathrm{T}} \boldsymbol{\phi}(x)$ in Eq. (A.1) and only the model parameter w is treated as stochastic, λ is as deterministic. The probabilistic model of a linear regression model in general is expressed as a special case when $f(x, w) = w^{\mathrm{T}} \boldsymbol{\phi}(x)$ and $\mathbf{f}.(\mathbf{x}, w) = \mathbf{\Phi}(\mathbf{x})w$ in Eq. (A.1). The likelihood function of the probabilistic model by Eq. (A.1)

Daigo Maruyama, Florian Schültke, Eike Stumpf and Ali Elham

when the data $\mathcal{D} = (\mathbf{X}, \mathbf{Y})$ is given is then:

$$p(\mathbf{Y}|\mathbf{X}, \boldsymbol{w}, \lambda) = p(\mathcal{D}|\boldsymbol{w}, \lambda) = \prod_{i=1}^{N} \mathcal{N}(y_i|f(\boldsymbol{x}_i, \boldsymbol{w}), \lambda^2) \tag{A.3}$$

In this stage, $\widehat{w}$ and $\hat{\sigma}$ can be determined by MLE as $\widehat{w}, \hat{\lambda} = \max\limits_{w,\sigma} p(\mathbf{Y}|\mathbf{X}, \boldsymbol{w}, \lambda)$ so that the surrogate models without the probability information such as NNs are obtained in this stage by $y = f(\boldsymbol{x}, \widehat{w})$. If the regression model is a linear regression model as $f(\boldsymbol{x}, \boldsymbol{w}) = \boldsymbol{w}^{\mathrm{T}} \boldsymbol{\phi}(\boldsymbol{x})$, $\widehat{w}$, $\hat{\lambda}$ by MLE can be analytically obtained.

We extend the models in the above equations to the Bayesian approaches by treating the model parameter $\boldsymbol{w}$ as stochastic as $p(\boldsymbol{w})$. Not like the model parameter $\boldsymbol{w}$, the noise parameter λ is treated as deterministic like $\lambda = \hat{\lambda}$. Therefore, for simplicity of the notations, the noise parameter as the conditional part is omitted, e.g. the likelihood function $p(\mathcal{D}|\boldsymbol{w}, \lambda)$ in Eq. (A.3) is expressed as $p(\mathcal{D}|\boldsymbol{w})$ unless otherwise noted. The goal is to obtain the predictive distribution $p(\mathbf{y}|\mathbf{x}, \mathcal{D})$ when $\mathcal{D} = (\mathbf{X}, \mathbf{Y})$ is given, which literally means the probability of the corresponding output $\mathbf{y}$ when arbitrary set of the input $\mathbf{x}$ and the data $\mathcal{D}$ is given, as the prediction process. The predictive distribution $p(\mathbf{y}|\mathbf{x}, \mathcal{D})$ is introduced by the sum and product rules of probability using the probabilistic model by Eq. (A.1) and a posterior $p(\boldsymbol{w}|\mathcal{D})$:

$$p(\mathbf{y}|\mathbf{x}, \mathcal{D}) = \int \underbrace{p(\mathbf{y}|\mathbf{x}, \boldsymbol{w})}_{probabilistic\ model} \underbrace{p(\boldsymbol{w}|\mathcal{D})}_{posterior} d\boldsymbol{w} \tag{A.4}$$

The posterior $p(\boldsymbol{w}|\mathcal{D})$ is the probability distribution of the parameter $\boldsymbol{w}$ when the data $\mathcal{D}$ is given. can be obtained the likelihood function $p(\mathcal{D}|\boldsymbol{w})$ and a prior $p(\boldsymbol{w})$ which can be defined by us:

$$p(\boldsymbol{w}|\mathcal{D}) = \frac{p(\mathcal{D}|\boldsymbol{w})p(\boldsymbol{w})}{p(\mathcal{D})} \tag{A.5}$$

The prior is a probability distribution of the parameter $\boldsymbol{w}$ which is not dependent on the data $\mathcal{D}$. The $p(\mathcal{D})$ can be implicitly determined to satisfy the constraint of probability that $\int p(\boldsymbol{w}|\mathcal{D})d\boldsymbol{w} = 1$. Computation of the predictive distribution in Eq. (A.5) is troublesome in general. However, under the assumption/condition that the parameter $\boldsymbol{w}$ is stochastic and its prior is a Gaussian distribution, and the noise parameter λ is deterministic, the predictive distribution of the output y is analytically obtained. Further assumptions are set that the probbilistic model is a Gaussian distribution with a linear regression model (it is Eq. (A.1) with $f(\boldsymbol{x}, \boldsymbol{w}) = \boldsymbol{w}^{\mathrm{T}}\boldsymbol{\phi}(\boldsymbol{x})$) and that the posterior is a Gaussian distribution derived by taking the conjugate prior [24] into accont, the predictive distribution (as the *posterior* in the GP representation) is also represented by a closed-form represented by a multivariate Gaussian distirubution as follows:

$$p(\mathbf{y}|\mathbf{x}, \mathcal{D}) = \mathcal{N}\left(\mathbf{y} \,\middle|\, \underbrace{\boldsymbol{\Phi}(\mathbf{x})\boldsymbol{m}_{\mathcal{D}}}_{regression}, \underbrace{\overbrace{\hat{\lambda}^2 \mathbf{I}}^{noise} + \overbrace{\boldsymbol{\Phi}(\mathbf{x})\boldsymbol{S}_{\mathcal{D}}\boldsymbol{\Phi}(\mathbf{x})^{\mathrm{T}}}^{model\ uncertainty}}_{uncertainty} \right) \tag{A.6a}$$

where, $\boldsymbol{m}_{\mathcal{D}}$ and $\boldsymbol{S}_{\mathcal{D}}$ are the mean and the covariance of the posterior $p(\boldsymbol{w}|\mathcal{D})$ as $p(\boldsymbol{w}|\mathcal{D}) = \mathcal{N}\left(\boldsymbol{w}\middle|\boldsymbol{m}_{\mathcal{D}}(\mathbf{X}, \mathbf{Y}), \boldsymbol{S}_{\mathcal{D}}(\mathbf{X})\right)$. They are functions of the data $\mathcal{D}$. Equation (A.6a) is the predictive distribution after the posterior $p(\boldsymbol{w}|\mathcal{D})$ is integrated out, and this can be the surrogate model as a special case of Bayesian linear regression models. This corresponds to Eq. (3) the form of a set of the input $\boldsymbol{x}$ and the output y as $p(\mathbf{y}|\mathbf{x}, \mathcal{D}) = \mathcal{N}(\mathbf{y}|\boldsymbol{\mu}_N.(\mathbf{x}), \boldsymbol{\Sigma}_N(\mathbf{x}))$. The noise parameter λ is not integrated out since it is a deterministic parameter. The covariance in Eq. (A.6a) is composed of two terms. The first one represents the noise on the data as shown in Eq. (A.1). The second one does the uncertainty associated with the parameter $\boldsymbol{w}$. This uncertainty as the second term is named *model uncertainty* here. The uncertainty in the main context first defined in Eq. (3) is

Daigo Maruyama, Florian Schültke, Eike Stumpf and Ali Elham

a mix of these two terms. Practically it is no problems to treat $\sigma_N{}^2(x)$ in Eq. (3) like the model uncertainty since the noise term is constant over $\mathbf{x}$ (see also Fig. A.1).

A basic idea of GP models starts from the fact that the predictive distribution of the output $\mathbf{y}$ behaves as a multivariate Gaussian distribution as Eq. (A.6a) even though the probabilistic model that we defined as Eq. (1) is an isotropic Gaussian distribution (). Therefore, we take the same predictive distribution as Eq. (A.6a) as a *prior* before the data $\mathcal{D}$ is given, which will be the same starting point of the point estimate approach in Eq. (A.1) (The MLE is conducted on w and λ for Eq. (A.1) and $\boldsymbol{\theta}$ on for Eq. (A.6a)).

$$p(\mathbf{y}|\mathbf{x}) = \mathcal{N}\left(\mathbf{y}\,\middle|\,\underbrace{\boldsymbol{\Phi}(\mathbf{x})\boldsymbol{m}_0}_{trend},\ \underbrace{\overbrace{\lambda^2\mathbf{I}}^{noise} + \overbrace{\boldsymbol{\Phi}(\mathbf{x})\boldsymbol{S}_0\boldsymbol{\Phi}(\mathbf{x})^{\mathrm{T}}}^{model\ uncertainty}}_{uncertainty}\right) \quad (A.7a)$$

where $p(w)$ is a prior as $p(w) = \mathcal{N}(w|m_0, S_0)$, which is not a function of the data $\mathcal{D}$. The parameters m_0 and S_0 are omitted to be displayed in the conditional statement. Then when the prior $p(w)$ is set as a Gaussian distribution as $p(w) = \mathcal{N}(w|\mathbf{0}, \sigma_w{}^2\mathbf{I})$ $(m_0 = \mathbf{0}, S_0 = \sigma_w{}^2\mathbf{I})$, Eq. (A.7a) is represented as:

$$p(\mathbf{y}|\mathbf{x}) = \mathcal{N}\left(\mathbf{y}\,\middle|\,\underbrace{\mathbf{0}}_{trend},\ \underbrace{\lambda^2\mathbf{I} + \sigma_w{}^2\boldsymbol{\Phi}(\mathbf{x})\boldsymbol{\Phi}(\mathbf{x})^{\mathrm{T}}}_{\Sigma(\mathbf{x},\boldsymbol{\theta})}\right) \quad (A.7b)$$

where, the covariance of Eq. (7b) can be now represented by a covariance matrix $\Sigma(\mathbf{x}, \boldsymbol{\theta})$ composed by arbitrary kernel function $k(x, x', \boldsymbol{\theta})$ by our problem settings. Then Equation (A.7b) becomes the GP model represented by Eq. (A.2a). Equations (A.7) and (A.6) corresponds to Eqs. (3) $(p(\mathbf{y}|\mathbf{x}, \mathcal{D}) = \mathcal{N}(\mathbf{y}|\boldsymbol{\mu}_N.(\mathbf{x}), \Sigma_N(\mathbf{x}))$ for a set as $\mathbf{x}, \mathbf{y}$) and (2), respectively.

The kernel function $k(x, x', \boldsymbol{\theta})$ can be designed by considering the covariance term of Eq. (A.7b) since it is obvious that the second term can become a Gram matrix $\mathbf{K}$ even by its definition $\mathbf{K} \equiv \boldsymbol{\Phi}(\mathbf{x})\boldsymbol{\Phi}(\mathbf{x})^{\mathrm{T}}$:

$$\Sigma(\mathbf{x}, \boldsymbol{\theta}) = \Sigma(\mathbf{x}, \lambda, \boldsymbol{\theta}') = \quad (A.8)$$

$$= \lambda^2 \begin{pmatrix} 1 & \cdots & 0 \\ \vdots & \ddots & \vdots \\ 0 & \cdots & 1 \end{pmatrix} + \begin{pmatrix} k_1(x_1, x_1, \boldsymbol{\theta}') & \cdots & k_1(x_1, x_N, \boldsymbol{\theta}') \\ \vdots & \ddots & \vdots \\ k_1(x_N, x_1, \boldsymbol{\theta}') & \cdots & k_1(x_N, x_N, \boldsymbol{\theta}') \end{pmatrix}$$

$$= \begin{pmatrix} k_1(x_1, x_1, \lambda) & \cdots & k_1(x_1, x_N, \lambda) \\ \vdots & \ddots & \vdots \\ k_1(x_N, x_1, \lambda) & \cdots & k_1(x_N, x_N, \lambda) \end{pmatrix} + \begin{pmatrix} k_2(x_1, x_1, \boldsymbol{\theta}') & \cdots & k_2(x_1, x_N, \boldsymbol{\theta}') \\ \vdots & \ddots & \vdots \\ k_2(x_N, x_1, \boldsymbol{\theta}') & \cdots & k_2(x_N, x_N, \boldsymbol{\theta}') \end{pmatrix}$$

$$= \begin{pmatrix} k(x_1, x_1, \boldsymbol{\theta}) & \cdots & k(x_1, x_N, \boldsymbol{\theta}) \\ \vdots & \ddots & \vdots \\ k(x_N, x_1, \boldsymbol{\theta}) & \cdots & k(x_N, x_N, \boldsymbol{\theta}) \end{pmatrix} \quad where, \quad \begin{cases} \boldsymbol{\theta} = (\lambda, \boldsymbol{\theta}') \\ k_1(x, x', \lambda) = \begin{cases} \lambda^2\ if\ x = x' \\ 0\ else \end{cases} \end{cases}$$

where, $k_1(x, x', \boldsymbol{\theta})$ can be arbitrary kernel function. Due to the fact that the sum of kernel functions is a kernel function, the presence of the noise can be control by our definition of the kernel function. Therefore, the noise parameter λ can be included as hyperparameters $\boldsymbol{\theta}$ (e.g. $\boldsymbol{\theta} \equiv (\boldsymbol{\theta}, \lambda)$) in general which are tuned by MLE. The hyperparameter $\boldsymbol{\theta}$ is treated as deterministic even though the GP models themselves are Bayesian approaches. It is because directly the predictive distribution (by Eq. (7)) after the Bayesian approach is modelled to determine that distribution. When the kernel k_1 is not included in the kernel function k, the model implicitly does not take noise into account, which bring that the GP model pass through all the sample points. Then only the model uncertainty shown in Eqs. (A.6a) and (A.7a) remains. Now all the hyperparameters defined in kernel functions are summarized by $\boldsymbol{\theta}$. Figure A.1 shows comparison of the GP models by different kernel functions to represent the component of

Daigo Maruyama, Florian Schültke, Eike Stumpf and Ali Elham

the noise and the model uncertainty. It can be observed that in the left figure the difference of the error band is remarkable by the location x while it is not in the right figure. This is because the noise is more dominant than the model uncertainty in the right figure. Since no noise is assumed in the definition of the kernel function in the left figure, the mean value $\mu_N(x)$ as a regression model passes through all the sample points. Due to this practical aspect, the λ is sometimes called regularization parameter.
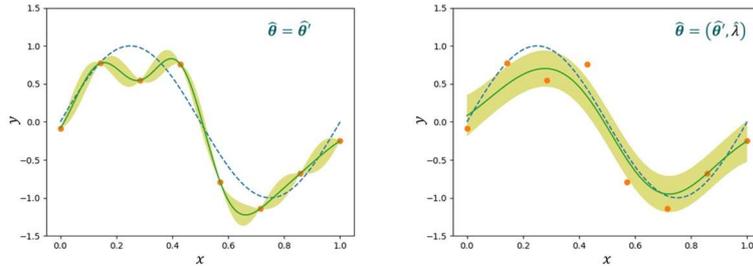
Figure A.1. GP models using a common sample dataset but using different kernel functions, left: a kernel function composed only by k_2, right: a kernel function composed by $k_1 + k_2$ in Eq. (A.8) The green lines show $\mu_N(x)$ and the error bands do $\pm\sigma_N(x)$ in Eq. (2).

When we have strong brief on the prior $p(w)$, we can set a different prior, which is for example, a proper m_0 that can make the mean $\Phi(x)m_0$ in Eq. (7a) a (mean) vector μ. Dependent on our assumption on the vector μ, some variations of GPs are introduced.

Example 1. $\mu = 0$ or $\overline{Y}$, or $\mu(x) = f.(x)$ – *simple Kriging*
Example 2. $\mu(\mu) = 1\mu$ (μ is a scalar parameter) – *Ordinary Kriging*
Example 3. $\mu(x; a) = f.(x, a)$ (regression model in general: a is a vector parameter)
        A) $\mu(x; a) = \Phi(x)a$ (linear regression model in general) *Universal Kriging*

The correspondences of methods in Kriging are also noted here. The examples can be also summarized as *regression Kriging* essentially. The methods introduced in Sections 2 and 3 are when $\mu = \overline{Y}$ and when $\mu = f.(x)$ in Eq. (2), respectively. The parameters μ in Example 2 or a in *Example 3* can be determined by the MLE with the hyperparameters θ at the same time. Especially the parameters of *Example 2* and the cases of linear regression model as *Example 3.A* have closed-forms expressed by θ, which result in that the parameter optimization in the MLE is only in the space θ. The closed-forms are the solution of the generalized least squares:

$$\hat{c}(\theta) = (C^T\Sigma(X,\theta)^{-1}C)^{-1}C^T\Sigma(X,\theta)^{-1}Y \tag{A.9}$$

where $c = \mu$ and $C = 1$ for *Example 2*, and $c = a$ and $C = \Phi(X)$ for *Example 3.A*. When the regression model $f.(x, a)$ in *Example 3* is not a linear regression model, all the parameters a, θ need to be searched in a wider input space composed by a and θ in the MLE process. The optimization in the MLE process tend not to be stable due to multimodal of the likelihood function. A prior distribution on the parameter a as $p(a)$ is better to be used if we have it.
    The method basically used for multi-fidelity models shown in Section 3 is then:

Example 4. $\mu = \rho\mu'$ (where μ' corresponds the μ in *Examples 1-3*)

It is our definition if the parameter ρ is known or deterministically learned by the MLE. Finally the probabilistic model of the extended GP by using a generalized trend μ and the learning and the prediction processes when a dataset $\mathcal{D} = (X, Y)$ is given are summarized. The generalized probabilistic model is shown Eq. (5). The trend vector μ can be a function of the avobe-mentioned *Examples 1-4*. For, example, combination of 3 and 4 leads $\mu = \mu(\rho, a) = \rho f.(x; a)$.
    To learn all the parameters deterministically, the likelihood function is first described when

Daigo Maruyama, Florian Schültke, Eike Stumpf and Ali Elham

the data $\mathcal{D} = (\mathbf{X}, \mathbf{Y})$ is given:

$$p(\mathbf{Y}|\mathbf{X}, \boldsymbol{\theta}, \boldsymbol{\mu}) = \mathcal{N}\big(\mathbf{Y}\big|\boldsymbol{\mu}, \boldsymbol{\Sigma}(\mathbf{X}, \boldsymbol{\theta})\big) \tag{A.10}$$

The error function $(-\ln p(\mathbf{Y}|\mathbf{X}, \boldsymbol{\theta}, \boldsymbol{\mu})$ with omitting constant values with respect to the parameters $\boldsymbol{\theta}, \boldsymbol{\mu})$ can be represented as follows:

$$E(\boldsymbol{\theta}, \boldsymbol{\mu}; \mathcal{D}) = \ln|\boldsymbol{\Sigma}(\mathbf{X}, \boldsymbol{\theta})| + (\mathbf{Y} - \boldsymbol{\mu})^{\mathrm{T}}\boldsymbol{\Sigma}(\mathbf{X}, \boldsymbol{\theta})^{-1}(\mathbf{Y} - \boldsymbol{\mu}) \tag{A.11}$$

where the data $\mathcal{D} = (\mathbf{X}, \mathbf{Y})$ are constant. $\hat{\boldsymbol{\theta}}, \hat{\boldsymbol{\mu}}$ are obtained by the MLE to determine the probability distribution by Eq. (5):

$$\hat{\boldsymbol{\theta}}, \hat{\boldsymbol{\mu}} = \min_{\boldsymbol{\theta}, \boldsymbol{\mu}} E(\boldsymbol{\theta}, \boldsymbol{\mu}; \mathcal{D}) \tag{A.12}$$

where $\boldsymbol{\mu}$ should be reformulated by user's purposes to represent by a constant value, a function of the input, and combination of them with limited parameters such as the scaling parameter ρ as the candidates shown in the above. Dependent on user's definition of the kernel function k, the error function $E(\boldsymbol{\theta}, \boldsymbol{\mu}; \mathcal{D})$ should be simplified for practical implementation. It should be noted that due to increase of the number of the parameters and differences of their properties, constraints/priors are recommended to be set on the parameters to avoid the multi-modal in the larger parameter space than that of only the $\boldsymbol{\theta}$.

Once all the parameters are determined, the predictive distribution, as a posterior updated by the data $\mathcal{D} = (\mathbf{X}, \mathbf{Y})$ from Eq. (A.7a) to Eq. (A.6a), can be computed by the generalized formulations of conditional Gaussian distributions [24]:

$$p(\mathbf{y}|\mathbf{x}, \mathcal{D}) = \mathcal{N}\left(\mathbf{y}\left|\underbrace{\boldsymbol{\Phi}(\mathbf{x})\boldsymbol{m}_{\mathcal{D}}}_{\boldsymbol{\mu}_{a|b}}, \underbrace{\lambda^2\mathbf{I} + \boldsymbol{\Phi}(\mathbf{x})\boldsymbol{S}_{\mathcal{D}}\boldsymbol{\Phi}(\mathbf{x})^{\mathrm{T}}}_{\boldsymbol{\Sigma}_{a|b}}\right.\right)$$
$$\begin{cases} \boldsymbol{\mu}_{a|b} = \boldsymbol{\mu}_a + \boldsymbol{\Sigma}_{ab}\boldsymbol{\Sigma}_{bb}^{-1}(\mathbf{y}_b - \boldsymbol{\mu}_b) \\ \boldsymbol{\Sigma}_{a|b} = \boldsymbol{\Sigma}_{aa} - \boldsymbol{\Sigma}_{ab}\boldsymbol{\Sigma}_{bb}^{-1}\boldsymbol{\Sigma}_{ba} \end{cases} \tag{A.6b}$$

where a and b are a set of new predictions and data used for the learning, respectively. $\boldsymbol{\mu}$ and $\boldsymbol{\Sigma}$ are $\boldsymbol{\mu} = \hat{\boldsymbol{\mu}}$ and $\boldsymbol{\Sigma} = \boldsymbol{\Sigma}(\hat{\boldsymbol{\theta}})$, respectively, where notation of new prediction $(\mathbf{x}, \mathbf{y})$ and the data $\mathcal{D} = (\mathbf{X}, \mathbf{Y})$ are omitted for simplicity, $\mathbf{y}_b$ in Eq. (A.6b) corresponds to $\mathbf{Y}$. When the size of the prediction dataset a in Eq. (A.6b) is one, the generalized expression of Eq. (A.6b) for a single set of a new prediction $(\boldsymbol{x}, y)$ becomes to be equal to Eq. (3). Note that Equation (A.6b) can be regarded as a dual representation form of Eq. (A.6a) (from a Bayesian linear regression model to a GP model by using kernel). The expected improvement (EI) generally represented by Eq. (4) can be then commonly used by the information of Eq. (A.6b) to execute the adaptive sampling techniques. The discussion until here can be applied to gradient-enhanced GPs. Hierarchical trends can be also applied since the extended GP model can simply be regarded as another GP model on the trend of $\mathbf{Y} - \boldsymbol{\mu}$.

REFERENCES

[1] F. Schueltke and E. Stumpf, "UNICADO: Aufbau und Etablierung einer universitären Flugzeugvorentwurfsumgebung,"Deutscher Luft- und Raumfahrtkongress, 2020.

[2] K. Risse et al. "An Integrated Environment for Preliminary Aircraft Design and Optimization," AIAA paper, AIAA-2012-1675, 2012.

[3] K. Risse. "Preliminary Overall Aircraft Design with Hybrid Laminar Flow Control". PhD thesis. RWTH Aachen University, 2016. DOI: 10.18154/RWTH-2017-00974.

[4] Forrester, A. I. J, Sobester, A., and Keane, A. J., *Engineering Design via Surrogate*

Modelling: A Practical Guide, Wiley, 2008.

[5] Lukaczyk, T., Palacios, F., and Alonso, J.J, "Active Subspaces for Shape Optimization", AIAA SciTech Forum, AIAA-2014-1171, 2014.

[6] Constantine, P.G., Dow, E., and Wang, Q., "Active subspace methods in theory and practice: applications to kriging surfaces", *SIAM Journal on Scientific Computing*, Vol. 36, No. 4, 2014, pp. 1500-1524.

[7] Diez, M., Serani, A., Campana, E. F., Volpi, S., and Stern, F., "Design-Space Dimensionality Reduction for Single- and Multi-Disciplinary Shape Optimization," AIAA paper, 2016-4295, 2016.

[8] Garland, N., Le Riche, R., Richet, Y., and Durrande, N., "Multi-fidelity for MDO using Gaussian Processes," In book: Aerospace System Analysis and Optimization in Uncertainty (pp.295-320), 2020.

[9] Maruyama, D., Liu D., and Görtz S., "An efficient aerodynamic shape optimization framework for robust design of airfoils using surrogate models," in: Proceedings of ECCOMAS Congress 2016, 2016.

[10] Ripepi, M., Verveld, M. J., Karcher, N. W., Franz, T., Abu-Zurayk, M., Görtz, S., and Kier, T. M., "Reduced-order models for aerodynamic applications, loads and MDO", CEAS Aeronautical Journal, 9, pages171–193, 2018.

[11] Martins, J.R.R.A. and Lambe, A.B., "Multidisciplinary Design Optimization: A Survey of Architectures", *AIAA Journal*, Vol. 51, No. 9, pp. 2049-2075, 2013.

[12] K. Risse et al. "Central Reference Aircraft data System (CeRAS) for research community". *CEAS Aeronautical Journal* 7.1, 2016, pp. 121–133.

[13] Brochu, E., Cora, V., M., and Nando de Freitas, A Tutorial on Bayesian Optimization of Expensive Cost Functions, with application to active user modeling and hierarchical reinforcement learning, arXiv:1012.2599v1 [cs.LG], 2010.

[14] Snoek, H. Larochelle, and R. Adams. Practical Bayesian optimization of machine learning algorithms. *In Advances in Neural Information Processing Systems 25*, pages 2960–2968, 2012.

[15] Rasmussen, C.E. and Williams, C.K.I., *Gaussian Processes for Machine Learning*. MIT Press, 2006.

[16] Snelson, E. and Ghahramani, Z., "Sparce Gaussian processes using pseudo-inputs," In Proceedings of Advanced Neural Information Processing Systems, pp. 1257-1264, 2005.

[17] Hensman, J., Fusi, N., and van Lawrence, N.D, "Gaussian processes for big data," In Uncertainty in Artificial Intelligence, pp. 282-290, 2013.

[18] Wilson, A. and Nickisch, H., "Kernel interpolation for scalable structured Gaussian processes (KISS-GP)," In International Conference on Machine Learning, pp. 1775-1784, 2015.

[19] Maruyama, D., Görtz, S. and Coggon, S., "Efficient Surrogate Model Construction for Large Data Sets Using Bayesian Learning", UNCECOMP 2019, 2019.

[20] Forrester, A. I. J, Sobester, A., and Keane, A. J., "Multi-Fidelity Optimization via Surrogate Modelling," Proceedings of the Royal Society A, 463(2088), 3251-3269, 2007.

[21] Yamazaki, W., and Mavriplis, D. J., "Derivative-Enhanced Variable Fidelity Surrogate Modeling for Aerodynamic Functions," *AIAA journal*, 51(1):126-137, 2013.

[22] Dofour, R., de Muelenaere, J., and Elham, A., "Trajectory driven multidisciplinary design optimization of a sub-orbital spaceplane using non-stationary Gaussian process," *Structural and Multidisciplinary Optimization*, Vol. 52, No. 4, 2015, pp. 755‑771,

[23] Renganathan, S. A., Maulik, R., and Ahuja, J., "Enhanced data efficiency using deep neural networks and Gaussian processes for aerodynamic design optimization," *Aerospace Science and Technology*, Vol. 111, 106522, 2021.

[24] Bishop, C.M., *Pattern Recognition and Machine Learning*, Springer, 2006.

DEVELOPMENT OF MDO FORMULATIONS BASED ON DISCIPLINARY SURROGATE MODELS BY GAUSSIAN PROCESSES

S. Dubreuil[1*], N. Bartoli[1], G. Berthelin[1], O. Chandre Vila[2], C. Gogu[2], T. Lefebvre[1], J. Morlier[2] and M. Salaün[2]

1: ONERA/DTIS
Université de Toulouse
Toulouse, France
{sylvain.dubreuil,nathalie.bartoli,gaspard.berthelin,thierry.lefebvre}@onera.fr

2: ICA, ISAE-SUPAERO, MINES ALBI, UPS, INSA, CNRS
Université de Toulouse
Toulouse, France
{oriol.chandre-vila,joseph.morlier,michel.salaun}@isae-supaero.fr
{christian.gogu}@gmail.com

Abstract. *Surrogate based optimization is now well established in the field of derivative free optimization. Among the various possible approaches, this study focuses on Bayesian optimization using Gaussian process interpolation as surrogate models. From the pioneering work on unconstrained optimization based on the expected improvement to the latest developments of enrichment criteria to deal with nonlinear constrained problems, the Bayesian framework has been extensively studied and used in many application fields. During the last few years a collaboration between the authors led to the publication of several contributions aiming at the development and the evaluation of MDO formulations based on disciplinary Gaussian process surrogate models. In these formulations each disciplinary solver is modeled by Gaussian processes that are coupled to solve the MDA. Hence, the formulation is uncoupled as only the disciplinary surrogate models are coupled and not the actual disciplinary solvers. It is proposed here to focus on two challenges raised by this formulation, to which the authors contributed in the past. The first one concerns the extension and application of the Bayesian framework to the case in which the objective function is not modelled by a Gaussian random field. To make progress with respect to this issue, an original representation of this random field using an adaptive discretization strategy has been proposed leading to the Efficient Global Multidisciplinary Optimization (EGMDO) formulation. The second one concerns the resolution of the interdisciplinary coupling in the case of large vector valued coupling variables. As an example, static aeroelasticity which couples a CFD solver and a FEM solver is studied. Some proposals, based on model order reduction (e.g. Proper Orthogonal Decomposition) and Gaussian process interpolation, have been evaluated by the authors. Objective of this paper is thus to sum up these various contributions while presenting the potential benefits and remaining challenges of these MDO formulation to the MDO researchers community.*

Keywords: Multidisciplinary Design and Optimization, Bayesian Optimization, Gaussian Process Interpolation, Model Order Reduction

S. Dubreuil, N. Bartoli, G. Berthelin, O. Chandre Vila, C. Gogu, T. Lefebvre, J. Morlier and M. Salaün

1 INTRODUCTION

Multidisciplinary Design and Optimization (MDO) is an attractive approach for aeronautic industry compared to the sequential optimization of each discipline involved in the design of a complex system (such as an aircraft). Indeed, by taking into account the interactions between disciplines, MDO allows to solve both the performance optimization and the consistency constraints between disciplines. Formally, this approach deals with the optimization of complex systems involving several disciplinary solvers coupled together in a non linear system of equations called Multidisciplinary Design Analysis (MDA). On the counterpart, the main drawbacks of this approach are the difficulty to set up the disciplinary coupling (non intrusive coupling between various numerical solvers) and the numerical cost due to the resolution of the MDA's non linear system of equations. Hence many studies have been focused on the development of MDO formulations in order to ease the implementation of the MDO and to reduce its computational cost. As representative examples one can cite the Multidisciplinary Feasible approach (MDF) and the Individual Discipline Feasible approach (IDF) [1]. These two approaches solve the exact MDO problem, MDF consists in solving the MDA by a non intrusive coupling of the disciplinary solvers at each iteration of the optimization algorithm, and thus uncouples the resolution of the optimization problem and the resolution of the MDA non linear system. It offers the advantage to reach a physically relevant solution at each step of the optimization phase, but leads to an important numerical cost as the MDA has to be solved at each iteration of the optimization process. Contrarily, the IDF approach uncouples the disciplinary solvers but couples the resolution of the optimization problem and the resolution of the MDA *i.e.* the optimization algorithm handling both the design variables and the coupling variables. Several other formulations have been proposed in the literature in order to solve the MDO problem in an efficient way. A review of some of these approaches can be found in [2]. It should be noted that the majority of these approaches only solve an approximation of the original MDO formulations.

In the following we are mainly interested in derivative free optimization (DFO), thus the gradient based approaches and coupled adjoined based developments will not be discussed here. Regarding the DFO approaches this paper will focus on Bayesian approaches. Indeed, since the pioneer work of [3] leading to the Efficient Global Optimization algorithm (EGO), the Bayesian framework has been regularly used and improved in many different optimization contexts. As an example in MDO Xu et al. [4] used the EGO as optimizer in the MDF, IDF and simultaneous analysis and design (SAND) MDO formulations and compared the results with gradient based and genetic optimization algorithms. A similar approach is also applied in [5] to a mixed discrete-continuous MDO problem. Another application of Bayesian optimization to costly MDO problem is presented in [6]. However these studies use the Bayesian framework with a minimal adaptation to the MDO context and mainly substitute classical gradient based optimizers by Bayesian ones. This remark was the starting point of several developments made by the authors to further increase the coupling between MDO and the Bayesian framework in the last years. The ambition of the present paper is thus to introduce these developments and to illustrate the advantages and constraints of a Bayesian approach in a multidisciplinary context.

The starting point of Bayesian optimization is the approximation of the objective function by a stochastic process, generally a Gaussian process. Then, this approximation is sequentially enriched to increase its accuracy in promising areas for optimization. This

S. Dubreuil, N. Bartoli, G. Berthelin, O. Chandre Vila, C. Gogu, T. Lefebvre, J. Morlier and M. Salaün

strategy relies on the exploitation of the stochastic character of the approximation. Several criteria have been proposed in the literature to find these promising areas, the most famous one being probably the Expected Improvement. Thus a light coupling between MDO and Bayesian optimization consists in applying the previous strategy directly to the MDO formulation. Although this approach can be efficient it does not exploit the partitioned architecture of the MDA and our motivation is to take advantage of this partitioning to further improve the efficiency of the approach in a multidisciplinary context.

As a consequence, the basic idea that drove the development of an Efficient Global Multidisciplinary Design and Optimization (EGMDO) algorithm during the last 5 years was to replace each disciplinary solver involved in the MDA by a disciplinary Gaussian process (GP) surrogate model. This simple idea is illustrated in Fig. 1 on an MDO problem involving two disciplines.
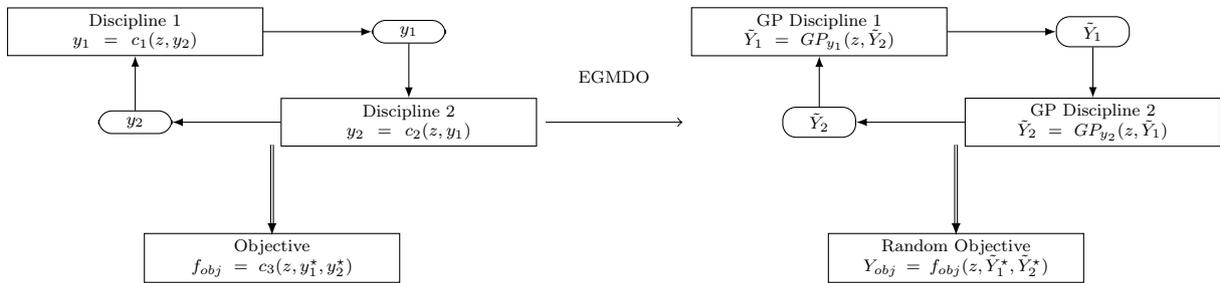
Figure 1: Illustration of an MDO problem involving two coupled disciplines and an objective function. On the left, the disciplines are given by some costly black-boxes. On the right, the disciplines have been replaced by some surrogate models (Gaussian Processes denoted by GPs).

Besides the apparent simplicity of this formulation, it raises several questions about the disciplinary surrogate model construction and their exploitation in a Bayesian framework. It is proposed here to focus on the two following topics:

1. How to sample the disciplinary surrogate models with respect to the coupling variables? In the case of scalar coupling variables this difficulty is generally solved by an expert judgement able to define appropriate variation bounds for each coupling variable. However in the case of large vector valued coupling variables, such as in the case of high fidelity aeroelastic coupling for example, this question is challenging and will be discussed in Section 3.

2. How to deal with the error introduced by the use of GP disciplinary surrogate models? Simplest answer is to construct disciplinary surrogate model *as accurate as possible* and to neglect the error introduced in the optimization process (as for example in [7], [8], [9] and [10]). Even if this approach can lead to satisfactory results it is obvious that its numerical cost can be far from optimal and that the accuracy at the minimum is hazardous.

   Following the path of Bayesian optimization we proposed to sequentially enrich the disciplinary GPs with respect to their accuracy in promising areas for optimization. As a consequence the first step is to model the objective function as a stochastic process. In our context this objective function cannot be modelled by a GP as the

S. Dubreuil, N. Bartoli, G. Berthelin, O. Chandre Vila, C. Gogu, T. Lefebvre, J. Morlier and M. Salaün

non linear coupling between the disciplinary GP leads to a non Gaussian model for the objective function. However this difficulty can be tackled by propagating the uncertainties introduced by the disciplinary GPs through the MDA. Section 2 described the proposed strategy to, propagate these uncertainties, model the objective function as a non Gaussian random process, and enrich the disciplinary GPs.

2 EFFICIENT GLOBAL MULDISCIPLINARY DESIGN AND OPTIMIZATION

2.1 Problem definition

First of all let us define the MDO problem that is of interest in the following:
Find the optimal design variables $z^\star \in \mathcal{Z}$ such that

$$z^\star = \arg \min_{z \in \mathcal{Z}} f_{obj}(z, y^\star_{c^{(obj)}}(z)) \tag{1}$$

where f_{obj} is the objective function to minimize which depends on the design variables z and on some (possibly all) of the converged coupling variables denoted by $y^\star_{c^{(obj)}}(z)$. The design variables z belong to a design space $\mathcal{Z} \subset \mathbb{R}^n$. The converged coupling variables are denoted by $y^\star(z) = \{y^\star_i(z), i = 1, \cdots, n_d\}$ and $c^{(obj)}$ is a set of indexes used to identify the coupling variables involved in the computation of the objective function. We wrote $y^\star(z)$ as the solution of the non linear system of n_d equations, called MDA,

$$y_i = f_i(z, y_{c^{(i)}}), \ i = 1, \cdots, n_d \quad \forall z \in \mathcal{Z} \tag{2}$$

where $y_{c^{(i)}}$ is the vector of the coupling variables for the discipline i and n_d is the number of disciplines. The set of indexes denoted by $c^{(i)}$ identifies the coupling variables *i.e.* $\#(c^{(i)}) \leq (n_d - 1)$ and $i \notin c^{(i)}$. Finally, f_i is the solver of discipline i. Let us note that, with the previously introduced notations, disciplines i and j are said to have a feedback loop (or coupling) if $i \in c^{(j)}$ and $j \in c^{(i)}$. In the following, it is assumed that Eq. (2) contains at least one feedback coupling. It is also assumed that Eq. (2) has a unique solution for any point of the design space.

As stand in the introduction, the idea of the proposed approach is to take advantage of the partitioned formulation of the MDA to construct disciplinary GPs. Hence the following notations are introduced to denote the disciplinary GPs. The GP that is used to approximate the disciplinary solver f_i is build from a Design of Experiments (denoted by DoE_{f_i}) sampled over the space $\mathcal{Z} \times C^{(i)}$ where $C^{(i)}$ denoted the space of the coupling variables $y_{c^{(i)}}$ for the discipline i. The idea of GP approximation is then to condition a prior GP on DoE_{f_i} and to estimate the parameters of this GP (by maximum likelihood in this work). In the following, random quantities will be denoted by upper case letters. This leads to the following stochastic approximation,

$$\tilde{Y}_i(z, y_{c^{(i)}}) = \mu_{f_i}(z, y_{c^{(i)}}) + \epsilon_i(z, y_{c^{(i)}}) \tag{3}$$

where $\mu_{f_i}(z, y_{c^{(i)}})$ is the mean function of the GP and $\epsilon_i(z, y_{c^{(i)}})$ is a zero mean GP whose covariance function is the one of the prior GP conditioned on DoE_{f_i}. Thus for a given couple $(z^{(0)}, y^{(0)}_{c^{(i)}}) \in \mathbb{R}^n \times C^{(i)}$ that does not belong to DoE_{f_i}, the obtained approximation reads,

$$\tilde{Y}_i(z^{(0)}, y^{(0)}_{c^{(i)}}) = \mu_{f_i}(z^{(0)}, y^{(0)}_{c^{(i)}}) + \sigma_{f_i}(z^{(0)}, y^{(0)}_{c^{(i)}})\xi_i \tag{4}$$

S. Dubreuil, N. Bartoli, G. Berthelin, O. Chandre Vila, C. Gogu, T. Lefebvre, J. Morlier and M. Salaün

where $\mu_{f_i}(z^{(0)}, y_{c^{(i)}}^{(0)})$ is the mean value, $\sigma_{f_i}(z^{(0)}, y_{c^{(i)}}^{(0)})$ is the standard deviation and ξ_i is a standard Gaussian random variable. It should be noted that the expressions of ϵ_i, μ_{f_i} and σ_{f_i} are fully specified by the kind of Gaussian process approximation used. For conciseness we choose here to not detail the theory of Gaussian process interpolation and refer the reader to [11] instead.

In practice one can note that the construction of disciplinary GP assumed that it is possible to sample the disciplinary solver f_i over the space $\mathcal{Z} \times C^{(i)}$. If it is easy to define the range of variation for $\mathcal{Z}$ it could be much more challenging for $C^{(i)}$. In this section it is assumed that an expert judgement defines the range of variation of the coupling variables.

Once each disciplinary GP has been constructed independently one can form the following stochastic non linear system of n_d equations,

$$\tilde{Y}_i(z, \tilde{Y}_{c^{(i)}}) = \mu_{f_i}(z, \tilde{Y}_{c^{(i)}}) + \epsilon_i(z, \tilde{Y}_{c^{(i)}}), \ i = 1, \cdots, n_d \quad \forall z \in \mathcal{Z} \tag{5}$$

where $\tilde{Y}_{c^{(i)}}$ stands for the random vector of coupling variables affecting the discipline i. We define the solution of this random non linear system of equations as the joined probability distribution of the random vector of the converged coupling variables $\tilde{Y}^\star(z) = \left\{ \tilde{Y}_i^\star(z), \ i = 1, \cdots, n_d \right\}$ such that,

$$\tilde{Y}_i^\star(z, \tilde{Y}_{c^{(i)}}^\star(z)) = \mu_{f_i}(z, \tilde{Y}_{c^{(i)}}^\star(z)) + \epsilon_i(z, \tilde{Y}_{c^{(i)}}^\star(z)), \ i = 1, \cdots, n_d \quad \forall z \in \mathcal{Z} \tag{6}$$

Let us underline here that the joined probability density function of $\tilde{Y}^\star(z)$ is not Gaussian as the MDA is a non linear system. However samples of $\tilde{Y}^\star(z)$ can be obtained by drawing various realizations of the GP surrogate models and solving the MDA for each draw.

Random MDA has been previously studied and several approaches have been proposed to approximate solution of such a system (see for example [12], [13], [14], and [15]). The next section details the proposed method in our context.

2.2 Coupling of disciplinary GPs and uncertainty propagation

Objective of this part is to solve the stochastic non linear system of equations given by Eq. (5) in order to get the probability distribution of the objective function defined by,

$$Y_{obj}(z, \tilde{Y}_{c^{(obj)}}^\star(z)) = f_{obj}(z, \tilde{Y}_{c^{(obj)}}^\star(z)), \ \forall z \in \mathcal{Z} \tag{7}$$

In order to simplify this resolution we proposed in [15] to use a specific GP model for each disciplinary solver. Indeed, the GP model given by Eq. (3) involved a zero mean GP ϵ_i with a complex correlation structure. Dealing with the simulation of such a stochastic process is not straightforward as it needs to be represented by a finite number of random variables to be exploitable (by Karhunen-Loève decomposition for example). Instead, we propose to simplify the disciplinary GP model by a perfectly dependent stochastic process that shares the same pointwise variance as the initial one and that reads,

$$\tilde{Y}_i'(z) = \mu_{f_i}(z, y_{c^{(i)}}) + \sigma_i(z, y_{c^{(i)}})\xi_i$$

where the variance is computed regarding Eq. (5) by $\forall z, y_{c^{(i)}} \in \mathcal{Z} \times \mathbb{R}^{\#c^{(i)}}$, $\sigma_i(z, y_{c^{(i)}})\xi_i = \epsilon_i(z, y_{c^{(i)}})$, with ξ_i a standard Gaussian random variable.

S. Dubreuil, N. Bartoli, G. Berthelin, O. Chandre Vila, C. Gogu, T. Lefebvre, J. Morlier and M. Salaün

The huge advantage of this approach is that each disciplinary GP is now described by a single Gaussian random variable ξ_i. As a consequence it is proposed to solve the system,

$$\tilde{Y}_i'^{\star}(z, \tilde{Y}_{c^{(i)}}'^{\star}) = \mu_{f_i}(z, \tilde{Y}_{c^{(i)}}'^{\star}) + \sigma_i(z, \tilde{Y}_{c^{(i)}}'^{\star})\xi_i, \ i = 1, \cdots, n_d \tag{8}$$

whose solution is denoted by the random vector $\tilde{Y}'^{\star}(z) = \left\{\tilde{Y}_1'^{\star}(z), \cdots, \tilde{Y}_{n_d}'^{\star}(z)\right\}$. As the variances of the simplified disciplinary GP involved in Eq. (8) and the ones of the disciplinary GP involved in Eq. (5) are equal, we assume that the probability distribution of $\tilde{Y}'^{\star}(z)$ is a correct approximation of the one of $\tilde{Y}^{\star}(z)$. It should be noted that the accuracy of this approximation has been numerically checked in [15]. Moreover, from a numerical point of view, Eq. (8) is much more simple to solve than Eq. (5) as it only involves n_d independent standard Gaussian random variables denoted by the vector $\Xi = \{\xi_i, \ i = 1, \cdots, n_d\}$ in the following.

Once the problem is described by n_d independent Gaussian random variables, it is easy to simulate a sample of the random vector $\tilde{Y}'^{\star}(z)$ by solving Eq. (8) for various draws of the simplified disciplinary GP. It should be noted that any non linear solver can be used for this task and that the numerical cost of this operation is negligible as it only involves analytical simplified GP.

Using this sample, it is straightforward to obtain a sample of $Y_{obj}(z, \tilde{Y}_{c^{(obj)}}^{\star}(z))$ by evaluations of Eq. (8) and Eq. (7). At this step it is proposed to construct a representation of this random variable by a Polynomial Chaos Expansion (PCE). This choice can seem arbitrary but offers many advantages for setting up the Bayesian optimization framework presented in the next section. Hence, the objective function is approximated by

$$\hat{Y}_{obj}(z, \Xi) = \sum_{j=1}^{P} a_j^{(obj)}(z)H_j(\Xi) \quad \forall z \in \mathcal{Z} \tag{9}$$

where $H_j, \ j = 1, \cdots, P$ are the n_d-variate Hermite polynomials, P is the number of selected polynomial terms and $a_j^{(obj)}(z), \ j = 1, \cdots, P$ are the coefficients of the expansion to be determined. The retained truncation strategy consists in keeping all the polynomials with a degree less or equal to d, thus $P = \frac{(n_d+d)!}{n_d!d!}$. Computation of these coefficients can be obtained by various approaches. In the following the regression approach introduced in [16] is retained. It should be noted that this method is easy to set up in the context of the study as a large number of samples of $Y_{obj}(z, \tilde{Y}_{c^{(obj)}}^{\star}(z))$ can be obtained at a very low numerical cost as explained previously.

A PCE representation of $Y_{obj}(z, \Xi)$ can thus be obtained for any point $z \in \mathcal{Z}$ by Eq. (9). The variation of $Y_{obj}(z, \Xi)$ is representative of the uncertainty introduced by the use of the disciplinary GPs, hence if the disciplinary GPs are not accurate for a given $z^{(0)}$ the variation of $Y_{obj}(z^{(0)}, \Xi)$ is expected to be important and if the disciplinary GPs are accurate for a given $z^{(1)}$ the variation of $Y_{obj}(z^{(1)}, \Xi)$ is expected to be low. As one is able to evaluate the variation of $Y_{obj}(z, \Xi)$, thanks to the PCE representation, for any point $z \in \mathcal{Z}$, the next step is to enrich the disciplinary GP until the variation of $Y_{obj}(z, \Xi)$ is null at the minimum value. The difficulties are then to propose an enrichment criterion that focuses on the interesting areas and to deal with a non Gaussian representation of $Y_{obj}(z, \Xi)$.

S. Dubreuil, N. Bartoli, G. Berthelin, O. Chandre Vila, C. Gogu, T. Lefebvre, J. Morlier and M. Salaün

2.3 A non Gaussian model for $Y_{obj}(z, \Xi)$ and its enrichment

The previous section introduces a *discrete* representation of the stochastic process $Y_{obj}(z, \Xi)$ thanks to the PCE representation given by Eq. (9). This representation allows to compute approximations of $Y_{obj}(z, \Xi)$ for different values of z by an uncertainty quantification step. In the following it is assumed that the uncertainty quantification by PCE has been performed on a DoE denoted by $\text{DoE}_{UQ} = \left\{ z^{(i)}, \ i = 1, \cdots, n_{UQ} \right\}$. The obtained PCE formed the following random vector

$$\hat{\mathbf{Y}}_{obj}(\Xi) = \left\{ \hat{Y}_{obj}(z^{(i)}, \Xi), \ i = 1, \cdots, n_{UQ} \right\}$$

The random vector $\hat{\mathbf{Y}}_{obj}$ is a discretization of the random field $\hat{Y}_{obj}(z, \Xi)$. As shown in [12] the Karhunen Loève expansion of this random vector can be easily obtained thanks to the coefficients of the polynomial chaos expansion and reads,

$$\hat{\mathbf{Y}}_{obj}(\Xi) = \mu_{\hat{\mathbf{Y}}_{obj}} + \sum_{k=1}^{n_{UQ}} \left(\sum_{j=2}^{P} \mathbf{a}_j^t \hat{\varphi}_k \phi_j(\Xi) \right) \hat{\varphi}_k \qquad (10)$$

where $\mathbf{a}_j = \left\{ a_j^{(obj)}(z^{(1)}), \cdots, a_j^{(obj)}(z^{(n_{UQ})}) \right\}$, $j = 2, \cdots, P$, $\mu_{\hat{\mathbf{Y}}_{obj}} = \mathbf{a}_1$ and $\hat{\varphi}_k$ are the n_{UQ} eigenvectors of the covariance matrix $\mathbf{K}_{\hat{\mathbf{Y}}} = \sum_{i=2}^{P} \mathbf{a}_i \mathbf{a}_i^t$.

In order to set up a Bayesian optimization framework it is now necessary to introduce a *continuous* representation of the random field $\hat{Y}_{obj}(z, \Xi)$, with respect to z. For that purpose we propose in [17] to approximate the random field $\hat{Y}_{obj}(z, \Xi)$ by Gaussian process interpolation of the mean value and of the eigenvectors based on the vectors $\mu_{\hat{\mathbf{Y}}_{obj}}$ and $\hat{\varphi}_k$ respectively. This leads to the following representation of the random field,

$$\hat{Y}_{obj}(z, \Xi) \approx \tilde{Y}_{obj}(z, \Xi, \eta) = \tilde{\mu}_{\hat{\mathbf{Y}}_{obj}}(z, \eta_0) + \sum_{k=1}^{n_{UQ}} \left(\sum_{j=2}^{P} \mathbf{a}_i^t \hat{\varphi}_k \phi_j(\Xi) \right) \tilde{\varphi}_k(z, \eta_k), \ \forall z \in \mathcal{Z} \quad (11)$$

where $\tilde{\mu}_{\hat{\mathbf{Y}}_{obj}}(z, \eta_0)$ and $\tilde{\varphi}_k(z, \eta_k)$ are respectively the GP interpolation of the mean vector $\mu_{\hat{\mathbf{Y}}_{obj}}$ and of the eigenvectors $\hat{\varphi}_k$. The term $\eta = [\eta_0, \cdots, \eta_k, \cdots, \eta_{n_{UQ}}]^t$ is a random vector of $n_{UQ} + 1$ independent normal random variables modeling the uncertainty associated with these GP interpolations.

Even if the representation given by Eq. (10) can look complex it is actually quiet easy to implement and, more importantly, it is a very efficient tool to set up our Bayesian optimization framework. Indeed, one can note that it contains all the uncertainties due to the proposed approximations. More precisely, the vector Ξ models the uncertainty stemming from the use of disciplinary GPs to approximate the costly disciplinary solvers and the vector η models the uncertainty due to the interpolation of the mean and eigenvectors of the KL decomposition used to obtain a continuous representation of the objective function random field.

Using this continuous representation it is now possible to define an enrichment criterion. The one use in this work is the classical Expected Improvement (EI) defined by, $\forall z \in \mathcal{Z}$

$$\text{EI}(z) = \mathbb{E} \left[\left(\hat{Y}_{min}^{(obj)}(\Xi) | z \in \text{DoE}_{UQ} - \tilde{Y}_{obj}(z, \Xi, \eta) \right) \mathbb{1}_{\tilde{Y}_{obj}(z, \Xi, \eta) \leqslant \hat{Y}_{min}^{(obj)}(\Xi) | z \in \text{DoE}_{UQ}} \right] \qquad (12)$$

S. Dubreuil, N. Bartoli, G. Berthelin, O. Chandre Vila, C. Gogu, T. Lefebvre, J. Morlier and M. Salaün

where
$$\mathbb{1}_{\tilde{Y}_{obj}(z,\Xi,\eta) \leqslant \hat{Y}_{min}^{(obj)}(\Xi)|z \in \mathrm{DoE}_{UQ}} = 0 \text{ if } \tilde{Y}_{obj}(z,\Xi,\eta) > \hat{Y}_{min}^{(obj)}(\Xi)|z \in \mathrm{DoE}_{UQ} \text{ and}$$
$$\mathbb{1}_{\tilde{Y}_{obj}(z,\Xi,\eta) \leqslant \hat{Y}_{min}^{(obj)}(\Xi)|z \in \mathrm{DoE}_{UQ}} = 1 \text{ if } \tilde{Y}_{obj}(z,\Xi,\eta) \leqslant \hat{Y}_{min}^{(obj)}(\Xi)|z \in \mathrm{DoE}_{UQ}.$$
One can note that $\mathrm{EI}(z)$ is positive for $z \notin \mathrm{DoE}_{UQ}$ and that $\mathrm{EI}(z) = 0$ if $z \in \mathrm{DoE}_{UQ}$. The point $z^{(new)}$ where the uncertainty quantification by PCE should be performed is thus solution of the optimization problem,

$$z^{(new)} = \arg \max_{z \in \mathcal{Z}} (\mathrm{EI}(z)) \qquad (13)$$

It should be noted that the EI defined by Eq. (12) is different from the one proposed in [3] in the context of optimization of black-box functions. In particular, as the approximation Eq. (11) is not a Gaussian process, the EI defined by Eq. (12) can not be computed analytically and will be estimated by MC sampling (see [17] for details about estimation and optimization of the EI).

The point $z^{(new)} \in \mathcal{Z}$ that solves Eq. (13) is the one where the uncertainty should be reduced to improve our knowledge on the minimum of the deterministic objective function. There are two ways to reduce this uncertainty, first one is to compute the PCE representation $\hat{Y}_{obj}(z^{(new)}, \Xi)$ which cancels the uncertainty due to the continuous representation of the random field and modelled by the random vector η. Second one is then to enrich the disciplinary GP in order to reduce the uncertainty modelled by the vector Ξ. As this second step is not always necessary to discriminate a candidate $z^{(new)}$ it is proposed in [18] a two step enrichment, one at the continuous level (with respect to η) and one at the discrete level (with respect to Ξ) to further reduce the number of calls to the disciplinary solvers. The details of this enrichment strategy can be found in [18] and will not be detailed here as these technical details are not necessary for the global understanding of the proposed method. It should also be noted that two slightly different versions of the enrichment procedure are available in [19] and [18].

2.4 Application example

The EGMDO strategy described in the previous section has been applied to different test cases in [19] and in [18] including overall aircraft design problem.

In the following it is proposed to detail and comment an analytical example studied in [18] as this one offers a robustness study and several comparisons with other MDO algorithms. This test case is derived from the one proposed by Sellar et al. [20]. The proposed test case is unconstrained and counts one local and one global minima. It it defined by the following set of equations,

$$f_{obj}(z, y^{\star}_{c^{(obj)}}) = z_1 + z_3^2 + y_1^{\star} + \exp(-y_2^{\star}) + 10\cos(z_2)$$

where $z = \{z_1, z_2, z_3\}$, $c^{(obj)} = \{1, 2\}$ and $y^{\star} = \{y_1^{\star}, y_2^{\star}\}$ is solution of the following MDA, $\forall z \in \mathcal{Z}$,

$$y_1 = f_1(z, y_2) = z_1 + z_2^2 + z_3 - 0.2y_2$$
$$y_2 = f_2(z, y_1) = \sqrt{y_1} + z_1 + z_2$$

Design space is defined by $\mathcal{Z} = [0, 10] \times [-10, 10] \times [0, 10]$. Reference solution is obtained by using MDF approach with SLSQP optimization algorithm and leads to $z^{\star} \approx \{0, 2.634, 0\}$, $f_{obj}(z^{\star}) \approx -2.808$. Figure 2 presents the variation of f_{obj} in the plane (z_2, z_3) with $z_1 = 0$.

S. Dubreuil, N. Bartoli, G. Berthelin, O. Chandre Vila, C. Gogu, T. Lefebvre, J. Morlier and M. Salaün

It should be noted that the local minimum is located at $z^{lm} \approx \{0, -2.595, 0\}$ and leads to $f_{obj}(z^{lm}) \approx -0.809$.
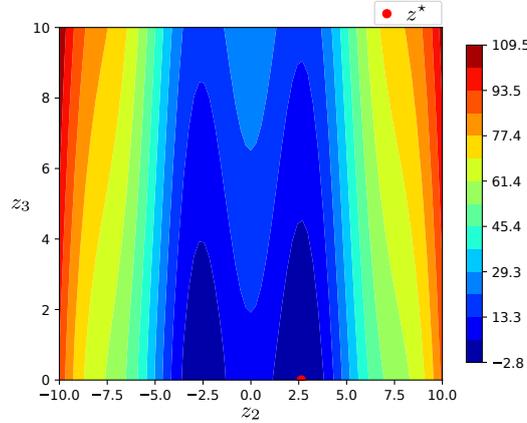
Figure 2: Application problem. Variation of f_{obj} in the plan (z_2, z_3) with $z_1 = 0$ and location of the global minimum $z^\star$.

In order to set up the proposed approach, the initial guesses for the coupling variables spaces are the following, $C^{(1)} = [-5, 24]$ and $C^{(2)} = [1, 50]$. It should be noted that choosing the initial guesses for the coupling variables spaces is one of the drawback of the proposed approach. However, in a realistic case one can rely on expert judgment to get a first approximation and, more importantly, the proposed enrichment strategy is designed to enrich these coupling spaces in promising areas without any limitation. As a consequence the boundaries of the coupling variables spaces might evolve during the iterations of the EGMDO algorithm and thus a poor initial choice for these boundaries might lead to some extra iterations but should not be detrimental to the global convergence.

The initial disciplinary DoEs, DoE_{f_1} and DoE_{f_2}, count 5 points, respectively sampled by Latin Hypercube Sampling (LHS) over $\mathcal{Z} \times C^{(1)}$ and $\mathcal{Z} \times C^{(2)}$. Initial disciplinary GPs are then constructed using these DoEs and constant mean function and Gaussian covariance function are used. According to the proposed method the objective function is represented by a random field over $\mathcal{Z}$. The initial DoE_{UQ}, used to discretized this random field, counts 20 points sampled by LHS over $\mathcal{Z}$. Hence, uncertainty propagation by PCE is carried out at 20 points, PCE of degree 3 is retained and computation of the PCE coefficients is obtained by regression over 100 points. It should be noted that the regression sample of size 100 is obtained by solving non linear systems given by Eq. (8) only involving disciplinary GPs and thus having a negligible numerical cost.

At this initial stage, the approximation given by Eq. (11) is used to compute the approximation of the random variable modeling the position of the minimum (denoted by $\hat{Z}^\star$) and the random variable modeling the value of the minimum (denoted by $\hat{Y}_{min}^{(obj)}$). Figure 3 presents the results where histograms are obtained by 100 MC simulations using the model defined by Eq. (11).

Figure 3 shows that at initialization, the position of the global minimum (Fig. 3 i)) as well as its value (Fig. 3 ii)) are poorly predicted by the model given by Eq. (11). Indeed the mean value of the random position of the minimum $\hat{Z}^\star$ is far from the reference one and its variance is quite large and consequently the random minimum value of the objective

S. Dubreuil, N. Bartoli, G. Berthelin, O. Chandre Vila, C. Gogu, T. Lefebvre, J. Morlier and M. Salaün
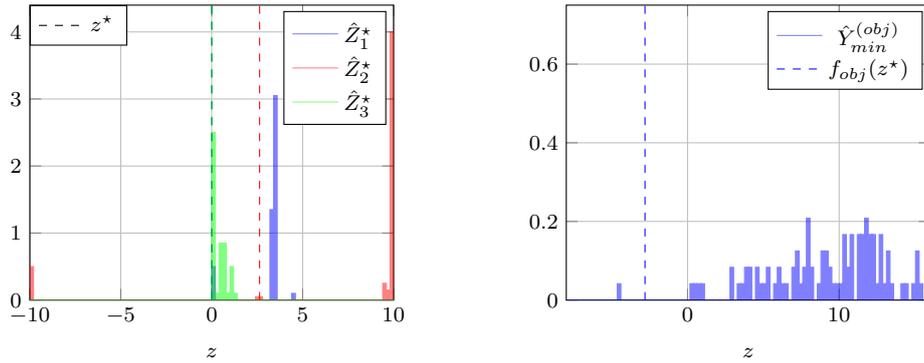
i) 3 components of $\hat{Z}^\star$ and the reference ones $z^\star \approx \{0, 2.634, 0\}$ ii) Objective value $\hat{Y}_{min}^{(obj)}$ and the reference one $f_{obj}(z^\star) \approx -2.808$

Figure 3: Application example. i) Histograms of the minimum value position $\hat{Z}^\star$ ii) Histogram of the minimum value $\hat{Y}_{min}^{(obj)}$ at initialization of the EGMDO algorithm.

function $\hat{Y}_{min}^{(obj)}$ presents a large variation. The objective of the proposed approach is to increase the accuracy of the model given by Eq. (11) by improving the disciplinary GPs only where the minimum is likely to be.

On this example the number of enrichment steps is set to $n_{max} = 10$. During these 10 iterations, 6 points are added to the disciplinary GPs which leads to a number of disciplinary solver evaluations equal to $5 + 6 = 11$.

Figure 4 presents the evolution of the maximum value of the EI defined by Eq. (12) with respect to the enrichment steps. As expected the maximum value of the EI is globally decreasing during iterations. Hence the uncertainty about the minimum value and position of the minimum of f_{obj} is reduced by the enrichment strategy.
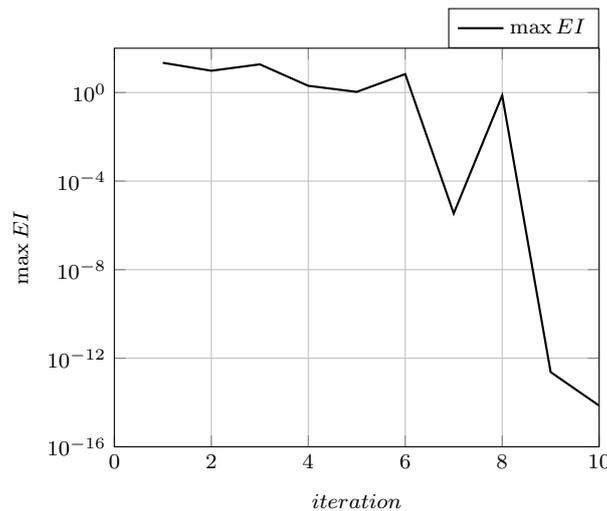
Figure 4: Application example. Evolution of the maximum value of the EI defined by Eq. (12) with respect to the number of iterations of the proposed EGMDO algorithm.

Figure 5 illustrates this uncertainty reduction and presents the histograms of $\hat{Z}^\star$ and $\hat{Y}_{min}^{(obj)}$ obtained after the 10 enrichment steps. Histograms are still obtained by 100 MC simulations using the model defined by Eq. (11).

Compared to Fig. 3 one can note in Fig. 5 that the proposed algorithm reaches its
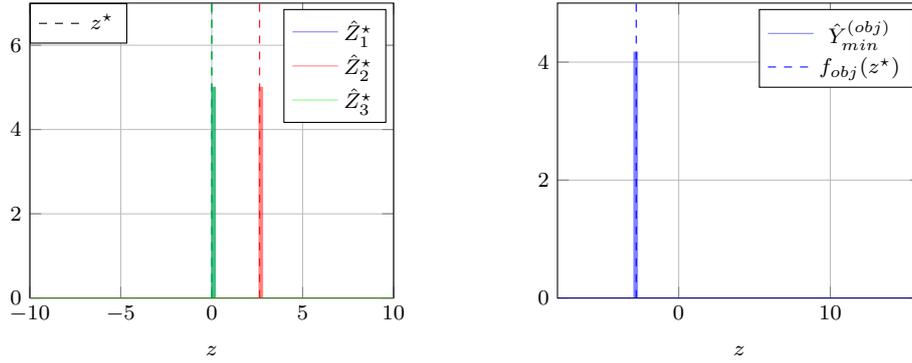
S. Dubreuil, N. Bartoli, G. Berthelin, O. Chandre Vila, C. Gogu, T. Lefebvre, J. Morlier and M. Salaün

i) 3 components of $\hat{Z}^\star$ and the reference ones $z^\star \approx \{0, 2.634, 0\}$

ii) Objective value $\hat{Y}_{min}^{(obj)}$ and the reference one $f_{obj}(z^\star) \approx -2.808$

Figure 5: Application example. i) Histograms of the minimum value position $\hat{Z}^\star$ ii) Histogram of the minimum value $\hat{Y}_{min}^{(obj)}$ after 10 enrichment steps.

objective after 10 iterations as the random minimum position $\hat{Z}^\star$ is almost multi-Dirac distributed and the three modes are in perfect agreement with the reference values. Concerning the random minimum value $\hat{Y}_{min}^{(obj)}$ the obtained probability distribution is also very close to a Dirac in perfect agreement with the reference value.

Some comparisons with classical MDO formulations are now provided. More precisely the MDF and IDF formulations are used in conjunction with the following optimization algorithm:

- A gradient based algorithm namely SLSQP Sequential Least SQuares Programming [21] where gradient is estimated by finite differences,

- A gradient free algorithm namely COBYLA Constrained Optimization BY Linear Approximation [22],

- A surrogate based algorithm namely EGO Efficient Global Optimization [3] using either the Expected Improvement criterion (EI) or an alternative criterion denoted by WB2s (see [6] for the definition of WB2s criterion).

Resolution with SLSQP and COBYLA has been implemented using the python package scipy [23], resolution with EGO used an in house python implementation [6]. For each of these formulations 100 runs are performed with different starting points for SLSQP and COBYLA and different initial DoE for EGO (initial DoE of size 12 for the MDF-EGO and of size 20 for the IDF-EGO) and different DoE_{f_1}, DoE_{f_2}, DoE_{UQ} for EGMDO. Table 1 presents the number of runs that converged towards the global optimum (line n_{con}) and the mean number of disciplinary solver evaluations over the n_{con} runs that converged (line n_{eval}).

Results provided by Table 1 allow to draw several conclusions:

- As expected, the number of evaluations of the disciplinary solvers is lower using the IDF approach than the MDF approach.

- Classical local optimization algorithms (gradient based SLSQP or gradient free COBYLA) have a poor convergence rate (between 56% and 70%) using either the MDF or the IDF formulation.

S. Dubreuil, N. Bartoli, G. Berthelin, O. Chandre Vila, C. Gogu, T. Lefebvre, J. Morlier and M. Salaün

	MDF-SLSQP	MDF-COBYLA	MDF-EGO-EI	MDF-EGO-WB2s	EGMDO
$n_{con}(\%)$	57	66	96	100	88
n_{eval}	197	638	296	212	13
	IDF-SLSQP	IDF-COBYLA	IDF-EGO-EI	IDF-EGO-WB2s	
$n_{con}(\%)$	56	70	99	100	
n_{eval}	68	206	63	44	

Table 1: Application example, comparative study. Results obtained with MDF and IDF formulations with 3 different optimizers (SLSQP, COBYLA, EGO with two criteria EI and WB2s). Number of converged runs and mean number of disciplinary solver evaluations are reported for each formulation over 100 runs. Results obtained by the proposed EGMDO approach are provided in the last column.

- Global surrogate based optimizer EGO reaches the best results in terms of convergence rate (between 96% and 100%). It is notable that both MDF and IDF formulations in conjunction with the WB2s criterion converge to the global optimum for every run.

- The best result is obtained using IDF formulation with EGO-WB2s as optimizer. This approach converges to the global optimum for every case with a mean number of disciplinary solver evaluations equals to 44 which is the lowest value on this comparison.

- Concerning the result obtained with the proposed EGMDO approach, one can note that the convergence rate of 88% is better than the one obtained using local optimizers but lower than the one obtained by EGO. However the mean number of disciplinary solver evaluations is only 13 for the EGMDO approach, compared to 44 for the IDF-EGO-WB2s. As a conclusion these results should be seen as promising for the new EGMDO approach as, even if it does not reach a 100% convergence rate, the benefit in terms of disciplinary solver evaluations is important.

2.5 Conclusions

This first section has briefly presented the EGMDO method that has been developed by the authors over the last five years. This approach can be summarized by the following few points:

- Construct disciplinary surrogate models by GP for each disciplinary solver involved in the MDA.

- Propagate the uncertainty stemming from the disciplinary GP. This step has been studied by the authors in [15] in which a PCE representation of the objective function was proposed.

- Construct a continuous representation of the non Gaussian random field modelling the objective function. Such a continuous model has been introduced by the authors in [17].

- Exploit this model to enrich the disciplinary GP until the global minimum of the objective function is reached with a given accuracy. This enrichment strategy has been proposed in [19] and in [18].

S. Dubreuil, N. Bartoli, G. Berthelin, O. Chandre Vila, C. Gogu, T. Lefebvre, J. Morlier and M. Salaün

The first results obtained by this approach are promising and it is clear for the authors that many improvements can be achieved in the different steps of the proposed algorithm. However the proposed approach is dedicated to low dimensional coupling variables as each one is modelled by a disciplinary GP. In the following we proposed an extension dedicated to the large vector valued coupling variables, which opens the gate to the resolution of high fidelity MDA by a Bayesian approach as it will be presented in the last part of the next section.

3 HANDLING LARGE VECTOR VALUED COUPLING VARIABLES: THE EXAMPLE OF AEROELASTICITY

In the following we are interested in the partitioned resolution of non linear system of equations involving the resolution of partial differential equation by numerical methods such as the finite element method and/or the finite volume method. Compared to the previous section the new difficulty here comes from the dimension of the coupling variables. Indeed, in the *strong* coupling case, the disciplinary solvers exchange high dimensional information such as pressure or displacement fields expressed on different meshes. Sharing this high dimensional information creates some difficulties in terms of sharing information between meshes and different approaches [24] are available to set up the partitioned approach. This difficulty will not be discussed any further in the present paper and coupling will be set up using interpolation by radial basis function as presented in [25].

Even if the approach detailed in the following can be set up for any MDA involving vector valued coupling variables it is proposed to focus on static aeroelasticity of a wing. More precisely it is assumed that the structural model is linear elastic and solved by a finite element method and that the aerodynamic model is a potential fluid model solved by the vortex lattice (VLM) method. Hence this illustrative MDA problem reads:

Find the displacement field $U(z, \Gamma)$ and the circulation vector $\Gamma(z, U)$ over a wing that solve,

$$\begin{cases} U(z, \Gamma) &= f_1(z, \Gamma) \\ \Gamma(z, U) &= f_2(z, U) \end{cases} \tag{14}$$

where f_1 and f_2 are respectively the finite element and the VLM solvers. In Eq. (14) it is assumed that the interpolation operators discussed previously are *hidden* in f_1 and f_2, thus the coupling variables of the problem are $U \in \mathbb{R}^{n_s}$, n_s being the dimension of the finite element discretization (number of degrees of freedom), and $\Gamma \in \mathbb{R}^{n_a}$, n_a being the size of the VLM mesh (number of panels).

As an illustration, Fig. 6 presents the type of numerical models that are used for our numerical experiments. These models, while not state of the art, are representative of the complexity of the models used in overall aircraft design MDO problems and allow to set up and assess the performance of the proposed approach efficiently. Note that we plan to increase the complexity of these models in the future.

In order to apply the EGMDO strategy developed in the previous section it is proposed to use model order reduction and interpolation by GP in different ways introduced in the following.

3.1 Model order reduction of converged multidisciplinary analysis

The first idea to introduce high fidelity coupling in the EGMDO algorithm is to use reduced order model of the disciplinary solution of the MDA. Hence it is proposed to use

S. Dubreuil, N. Bartoli, G. Berthelin, O. Chandre Vila, C. Gogu, T. Lefebvre, J. Morlier and M. Salaün

i)   ii)
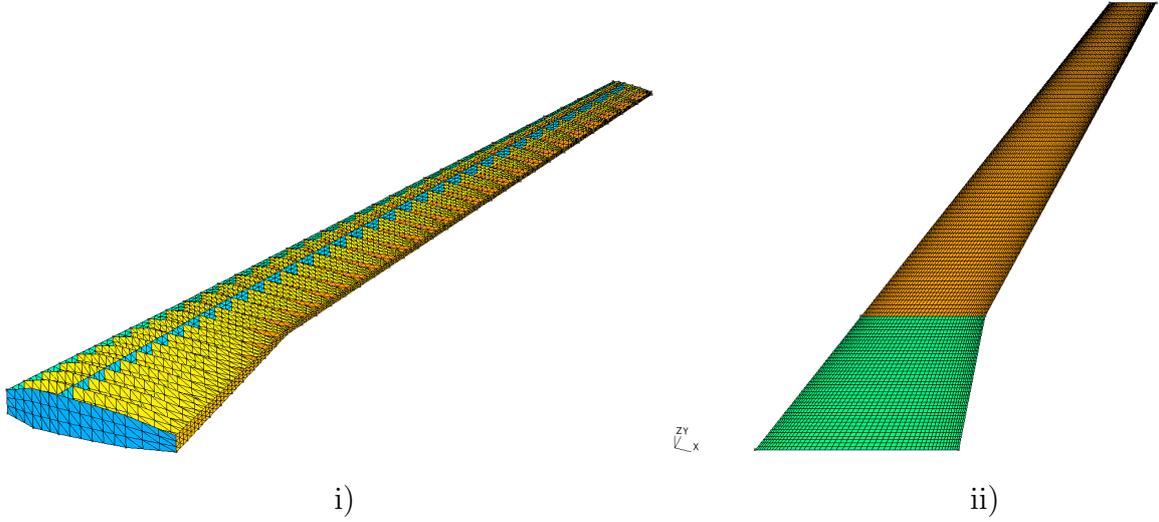
Figure 6: i) Finite element model of the structural part of the wing (skin, spars, ribs). ii) VLM mesh of the wing.

disciplinary surrogate models of the form,

$$\hat{U}(z) = \sum_{i=1}^{N_U} \hat{u}_i(z) U_i \tag{15}$$

and

$$\hat{\Gamma}(z) = \sum_{i=1}^{N_\Gamma} \hat{\gamma}_i(z) \Gamma_i \tag{16}$$

where the bases U_i, $i = 1, \cdots, N_U$ and Γ_i, $i = 1, \cdots, N_\Gamma$ are constructed by snapshot Proper Orthogonal Decomposition (POD) and $\hat{u}_i$, $i = 1, \cdots, N_U$ and $\hat{\gamma}_i$, $i = 1, \cdots, N_\Gamma$ are GP interpolations of the POD coefficients. These surrogates models are known as POD+I (POD+Interpolation) in the literature ([26] or [27] among others). The use of GP interpolation for the coefficients of the reduced order model, as in [28] for example, allows to quantify the uncertainty associated to the interpolation and thus to set up the EGMDO algorithm. However it should be noted that the error associated to the POD approximation is neglected. Hence, it is important to control this error, in a so called offline phase, before the use and the enrichment of the disciplinary surrogate models. In the following we present an application of this first strategy.

In this application the design space $\mathcal{Z}$ is of dimension 6 and made by 4 thicknesses of different wingbox parts, the span and the chord. These 6 variables define the vector z. Then a DoE is created by sampling over $\mathcal{Z}$. In order to ensure a prescribed level of accuracy of the reduced order model built from this DoE, a greedy procedure presented in [29] is used. This construction needs the evaluation of 15 MDA using the actual disciplinary solvers. Solving this MDA using Gauss Seidel algorithm needs around 10 evaluations of each disciplinary solver to achieve convergence. Thus the number of disciplinary solver evaluations to construct the initial disciplinary surrogate models given by Eq. (15) and Eq. (16) is around $10 \times 15 = 150$.

Once these disciplinary surrogate models are constructed it is straightforward to set up the proposed EGMDO algorithm. Indeed, given Eq. (15) and Eq. (16), let us denote $\mu_{\hat{u}_i(z)}$,

S. Dubreuil, N. Bartoli, G. Berthelin, O. Chandre Vila, C. Gogu, T. Lefebvre, J. Morlier and M. Salaün

$\mu_{\hat{\gamma}_i(z)}$ and $\sigma_{\hat{u}_i(z)}$, $\sigma_{\hat{\gamma}_i(z)}$ the mean and standard deviation of the GP used to interpolate the coefficients of the reduced order model, then the disciplinary surrogate models are Gaussian random variables (by linear combination of independent Gaussian variables) whose mean and standard deviation are given by,

$$\begin{cases} \mu_{\hat{U}} = \sum_{i=1}^{N_U} \mu_{\hat{u}_i(z)} U_i \\ \sigma_{\hat{U}}^2 = \sum_{i=1}^{N_U} \sigma_{\hat{u}_i(z)}^2 U_i^2 \end{cases} \tag{17}$$

and

$$\begin{cases} \mu_{\hat{\Gamma}} = \sum_{i=1}^{N_\Gamma} \mu_{\hat{\gamma}_i(z)} \Gamma_i \\ \sigma_{\hat{\Gamma}}^2 = \sum_{i=1}^{N_\Gamma} \sigma_{\hat{\gamma}_i(z)}^2 \Gamma_i^2 \end{cases} \tag{18}$$

where $(U_i^2)_j = ((U_i)_j)^2$, $j = 1, \cdots, n_s$ and $(\Gamma_i^2)_j = ((\Gamma_i)_j)^2$, $j = 1, \cdots, n_a$. These disciplinary surrogate models allow to quantify the uncertainty introduced by the interpolation on the whole solution vectors. As an example, Fig. 7 i) presents the exact displacement field for a given z as well as the mean $\mu_{\hat{U}}$, one can see that the approximation slightly underestimates the exact value. Figure 7 ii) presents the exact value of the displacement field and a 99% confidence interval constructed from $\sigma_{\hat{U}}^2$, it is interesting to note that the exact value bounded by this confidence interval meaning that the uncertainty propagation is, in that case, relevant.

<div align="center">i)   ii)</div>
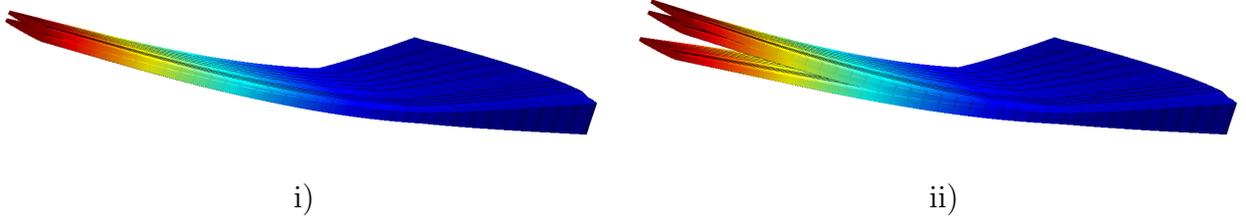
Figure 7: i) Mean value and exact value of the displacement field (the approximation slightly underestimates the exact value). ii) Exact value of the displacement field and 99% confidence interval.

It should be noted that the computation of the PCE of an objective function that depends on $\hat{U}$ and $\hat{\Gamma}$ is parametrized by $N_U + N_\Gamma$ independent standard Gaussian variables denoted by the random vector Ξ in the previous section.

This first solution to deal with large vector valued coupling variables has the following characteristics:

- The disciplinary surrogate models only depend on the design variables z contrarily to the one introduced in the first section which depends on both the design variables and the coupling variables. This offers the advantage to be easy to implement but requires a higher computational budget as the training of these POD+I surrogate models is done on a DoE of converged MDA.

- In this approach the MDA is seen as a black box and the approximation is done on the output of this black box (the displacement field and the circulation vector that

solve Eq. (14) in that particular case). This allows to easily set up the proposed EGMDO algorithm but does not take advantage of the partitioned MDA which was our primary objective.

Hence, in order to further increase the coupling between MDO and the Bayesian framework it is proposed in the next section to extend the concept of disciplinary surrogate models that depends on both the design and the coupling variables to the case of vector valued coupling variables.

3.2 Coupling of disciplinary reduced order model

3.2.1 Proposed formulation

In order to take advantage of the partitioned MDA (i.e. the possibility to run simulations of the disciplinary solvers independently) it is proposed in this section to study the construction of POD+I disciplinary surrogate models of the form,

$$
\begin{aligned}
\hat{U}(z, \hat{\gamma}_j, j = 1, \cdots, N_\Gamma) &= \sum_{i=1}^{N_U} \hat{u}_i(z, \hat{\gamma}_j, j = 1, \cdots, N_\Gamma) U_i \\
\hat{\Gamma}(z, \hat{u}_i, i = 1, \cdots, N_U) &= \sum_{j=1}^{N_\Gamma} \hat{\gamma}_j(z, \hat{u}_i, i = 1, \cdots, N_U) \Gamma_j
\end{aligned}
\tag{19}
$$

Compared to the disciplinary surrogate models given by Eq. (15) and Eq. (16) it should be noted that the ones in Eq. (19) not only depend on the design variables z but also on the coupling variables $\hat{\gamma}_j, j = 1, \cdots, N_\Gamma$ and $\hat{u}_i, i = 1, \cdots, N_U$ respectively. Hence, Eq. (19) is the *high dimensional* equivalent of the stochastic non linear system of equations given in the first section by Eq. (5). As in the first section it is proposed to model the GPs $\hat{u}_i(z, \hat{\gamma}_j, j = 1, \cdots, N_\Gamma)$ and $\hat{\gamma}_j(z, \hat{u}_i, i = 1, \cdots, N_U)$ by perfectly dependent GPs leading to a stochastic system of equations of dimension $N_U + N_\Gamma$. Following the notation introduced in the first section the random vector used to sample these GPs is denoted by $\Xi = \{\Xi_U, \Xi_\Gamma\}$, where $\Xi_U = \{\xi_i, i = 1, \cdots, N_U\}$ and $\Xi_\Gamma = \{\xi_i, i = 1, \cdots, N_\Gamma\}$ where ξ_i are $N_U + N_\Gamma$ independent standard Gaussian variables.

This formulation relies on the capability to construct the disciplinary surrogate models. In that case, this means the construction of POD+I surrogate models over the space of the design variables and the coupling variables. Contrarily to the scalar coupling variables case, the sampling over the coupling variables space is more challenging in the large vector valued coupling variables context.

3.2.2 Construction of the disciplinary surrogate models and exploitation

The simplest strategy to sample over the coupling variables space and manage to construct a disciplinary surrogate model is to use the deterministic non linear solver as sampler. First, a sample of p design variables z_i, $i = 1, \ldots, p$ over the space $\mathcal{Z}$ is generated using an appropriate DoE method, Latin Hypercube Sampling (LHS) for example. Then, the exact MDA associated to each design sample is computed using the MDA solver (or unconverged ones as proposed by [27]). For each design z_i, a certain number of iterations is needed. All those solver solutions are used as snapshots to build disciplinary POD bases $U_i, i = 1, \cdots, N_U$ and $\Gamma_j, j = 1, \cdots, N_\Gamma$. Using these bases it is possible to obtain a sample of the POD coefficients by projection of the already computed disciplinary solver solutions.

S. Dubreuil, N. Bartoli, G. Berthelin, O. Chandre Vila, C. Gogu, T. Lefebvre, J. Morlier and M. Salaün

This first strategy is relatively simple to set up and has been applied by the authors in [30] to the study of the static aeroelasticity of a wing. In this first test case the design variable is one dimensional (the angle of attack has been retained for the illustration) and the quantity of interest is the lift-to-drag ratio of the wing. Following the proposed strategy this quantity of interest is approximated by a PCE with respect to the vector Ξ (as in Eq. (9)). For this illustration the initial DoE is created by the resolution of 5 MDA (for z in $[1, 10]$) leading to 50 evaluations of each disciplinary solver (Gauss Seidel algorithm is used and around 10 iterations are necessary to reach the convergence). The disciplinary surrogate models are constructed from these 50 solutions leading to $N_U = 4$ and $N_\Gamma = 3$ (see [30] for the numerical details of the POD implementation). Hence the stochastic dimension of the problem is 7. Figure 8 presents a sample of the lift-to-drag ratio (denoted by Y_{QoI}) as well as its PCE approximation (denoted by $\hat{Y}_{QoI}$). One can note that the PCE approximation is accurate enough to represent the uncertainty introduced by the disciplinary surrogate models. It is also notable that due the non linearity of the MDA the quantity of interest is not Gaussian.
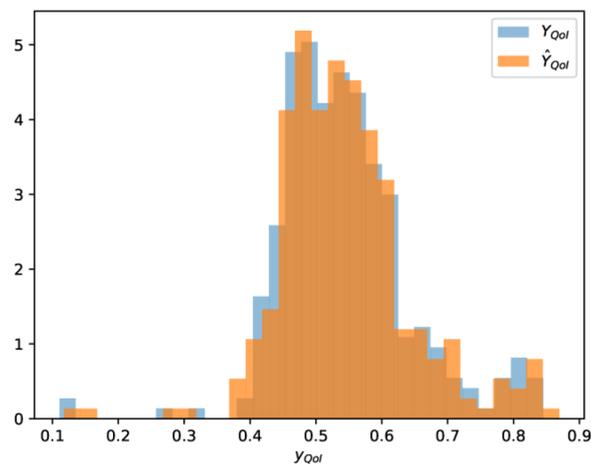
Figure 8: Illustration of the lift-to-drag ratio variation and its PCE approximation.

It is also proposed to perform a sensitivity analysis of the quantity of interest in order to decide which disciplinary solver to enrich. This PCE based sensitivity analysis approximates the Sobol indices which quantify the respective contribution of each disciplinary surrogate models to the variance of the quantity of interest. In the case study in [30] the conclusion of the sensitivity analysis was that the surrogate model $\hat{\Gamma}$ should be enriched. It should be noted that this enrichment only involves a single resolution of the VLM solver (to be compared to the first strategy in which a whole MDA is performed at each enrichment). Figure 9 presents the results after this enrichment as well as the reference obtained by solving the MDA with the disciplinary solvers.

This figure illustrates how the uncertainty of the quantity of interest can be reduced by the enrichment of the relevant disciplinary surrogate model. One can also note that the variation of the quantity of interest is centered on the reference value. Hence it should be possible to further reduce the uncertainty of the quantity of interest by successive disciplinary enrichment. This strategy of uncertainty reduction can be seen as a Bayesian way of solving the MDA.

Even if this approach offers some interesting results it appears that it suffers from sev-

S. Dubreuil, N. Bartoli, G. Berthelin, O. Chandre Vila, C. Gogu, T. Lefebvre, J. Morlier and M. Salaün
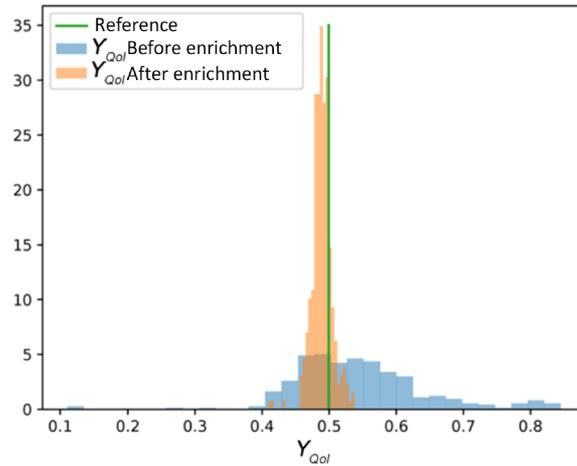
Figure 9: Illustration of the lift-to-drag ratio variation after the enrichment of the disciplinary surrogate model $\hat{\Gamma}$.

eral numerical issues during the creation of the initial DoE and during the enrichment step. We recall that the initial DoE is obtained by the resolution of MDA at various points of the design space, which is not efficient for the exploration of the coupling variables spaces and creates some numerical instabilities in the construction of the GPs. Indeed, during one MDA resolution, the design variables are constant (equal to z_i) and the coupling variables follow a convergence path to the exact MDA. Hence the samples are clustered around the MDA solutions and it is well known that a cluster of points leads to numerical issues in the determination of the GP.

As a consequence we recently investigated the possibility to sample a DoE without resolving MDA. This new sampling strategy is presented in [31] and it is based on an iterative process in which some random variations in the design variables are introduced. It should be noted that this sampling problematic has been also study recently by [32] in which a sample scheme based on physical considerations is proposed. Contrarily the method we proposed assumed very little knowledge regarding the physics of the coupling variables.

Using this new sampling strategy it is possible to enrich the disciplinary surrogate models on problems of higher complexity. As an example, we present in [31] a test case based on the aerolasticity study of the previous wing (Fig. 6) that counts 8 design variables, namely the angle of attack, the speed, and 6 thicknesses of the different structural components of the wing. The initial DoE used to create the disciplinary surrogate models counts 50 solutions of the structural solver and 60 solutions of the disciplinary solvers. The POD construction leads to $N_U = 11$ and $N_\Gamma = 5$.

In order to evaluate the accuracy of the proposed enrichment strategy at a point z that does not belong to the DoE it is proposed to study the dispersion of the relative error between the solution of the MDA using the mean values of the disciplinary surrogate models and the one using a sample of realisations of the disciplinary surrogate models. Figure 10 presents the evolution of this relative error (denoted by $\hat{q}$) after 2 enrichment steps. According to the result of the sensitivity analysis the first model to be enriched is the structural one, followed by an enrichment of the aerodynamic surrogate model.

One can see on this figure that the proposed strategy leads to an important reduction

S. Dubreuil, N. Bartoli, G. Berthelin, O. Chandre Vila, C. Gogu, T. Lefebvre, J. Morlier and M. Salaün
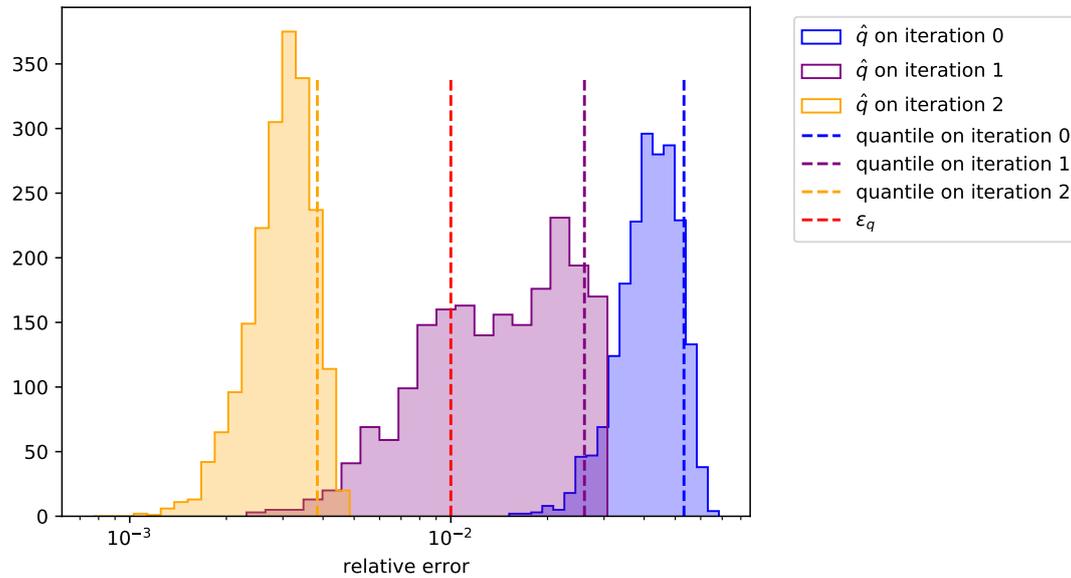
Figure 10: Evolution of the relative error of the MDA solution at a new design point after 2 enrichment steps, the 90% quantiles of the relative error distribution are also given.

of the relative error $\hat{q}$ meaning that the dispersion of the MDA solution tends towards 0. Moreover Fig. 10 also presents the 90% quantile of the relative error distribution. It is interesting to note that this quantile is lower than 1% after the second enrichment, in practice this can be used as a criterion to stop the enrichment procedure. Details of the enrichment procedure as well as others examples and robustness study can be found in [31].

Finally it is interesting to compare the strategy based on the coupling of disciplinary GPs and successive enrichment presented in Section 3.2 with the direct approximations of converged solution presented in Section 3.1. For this comparison the previous 8 parameter test case is used and the accuracy of both approaches are evaluated. This comparison is made on a test set of 100 points randomly sampled in the design space. For both approaches the numerical cost *i.e.* the number of disciplinary solver calls, is almost equal. The direct approximations are constructed from a DoE of 30 converged MDA leading to 121 calls to the disciplinary solvers whereas the coupling of disciplinary GPs needs 128 calls to the disciplinary solvers. Figure 11 presents the relative errors on the norm of U and Γ between the reference results and the results obtained by the two approximations approaches.

This figure clearly illustrates that the adaptive construction of disciplinary surrogate models leads to better results than the direct approximations of converged MDA solution. It should be noted that a comparison at iso relative error level is also performed in [31] showing that the same accuracy level can be reached by the direct approximation method but a higher numerical cost. These results illustrate that by taking into account the interaction between disciplines in the disciplinary surrogate models' construction it is possible to significantly reduce the numerical cost of the approximations construction. However it should also be noted that this coupling strategy involves a higher dimension of the input spaces of the surrogates, which remains a challenge in surrogate model development.

S. Dubreuil, N. Bartoli, G. Berthelin, O. Chandre Vila, C. Gogu, T. Lefebvre, J. Morlier and M. Salaün
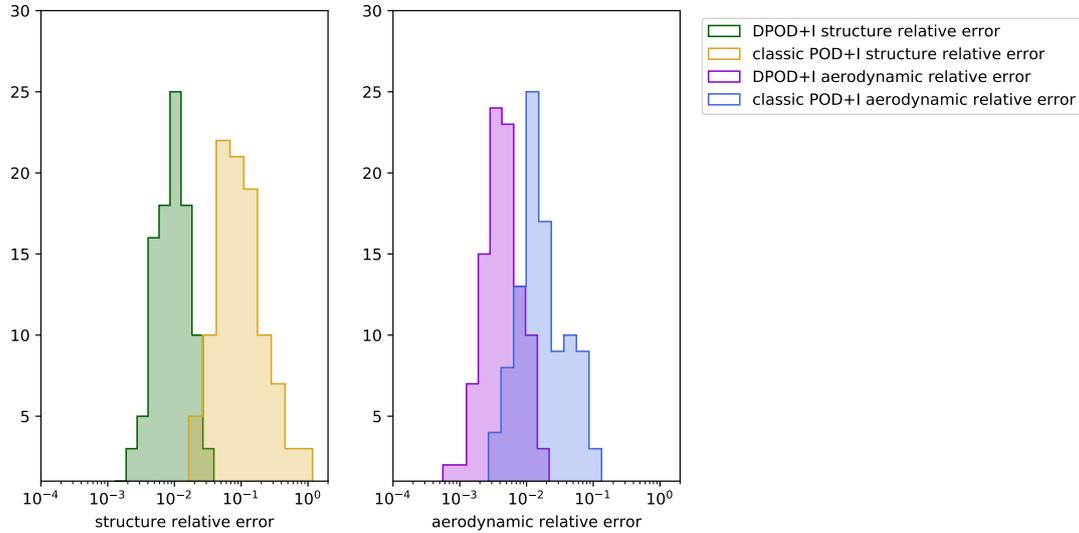
Figure 11: Comparison of the accuracy of direct approximations of converged solutions (denoted by classic POD+I) with approximations from the coupling of disciplinary GPs (denoted by DPOD+I). Relative error on a test set of 100 points.

4 CONCLUSION

The objective of this study was to highlight some recent developments in the field of Multidisciplinary Design Analysis and Optimization within the Bayesian framework. With respect to this objective Section 2 presents the contribution of the authors to an Efficient Global Multidisciplinary Design and Optimization formulation. The originality of this formulation lies in the approximation of the objective function by a non Gaussian random field obtained from the uncertainty propagation of the disciplinary GPs to the objective function. This random field model of the objective function allows to follow the path of Bayesian optimization by enrichment of the disciplinary GPs based on an Expected Improvement criterion. Some promising results have been reached with this formulation in terms of the number of disciplinary solver evaluations to converge towards the global minimum of MDO problems. However many improvements with respect to the robustness of the approach and to the different approximation choices could be achieved in the future.

Section 3 focuses of the case of MDA with vector valued coupling variables and illustrates this context by the study of a high fidelity coupling for static aeroelasticity. As a first attempt to extend the concept of Bayesian framework to that case, two formulations based on model order reduction by POD and GP interpolation have been studied. Once again it is shown that a careful uncertainty propagation stemming from the randomness of the disciplinary surrogate models offers valuable information. This information can further be used to perform a sensitivity analysis and to enrich the relevant disciplinary surrogate model leading to a Bayesian way of solving the deterministic MDA. With respect to the proposed approach to this problem it is also clear that improvements can be obtained by working on the model order reduction method for example.

As a general conclusion on this work it appears that increasing the coupling between MDO and the Bayesian framework can help to tackle some challenges of MDO. Nevertheless, as illustrated throughout the paper, the construction and coupling of disciplinary GP

S. Dubreuil, N. Bartoli, G. Berthelin, O. Chandre Vila, C. Gogu, T. Lefebvre, J. Morlier and M. Salaün

brings their own new issues. Fortunately in the future we might be able to benefit from the numerous developments in both MDO and Bayesian optimization to further improve the proposed methods.

ACKNOWLEDGEMENTS

REFERENCES

[1] E. Cramer, J. Dennis, Jr., P. Frank, R. Lewis, and G. Shubin. Problem formulation for multidisciplinary optimization. *SIAM Journal on Optimization*, 4(4):754–776, 1994. doi:10.1137/0804044. URL `https://doi.org/10.1137/0804044`.

[2] J. R. R. A. Martins and A. B. Lambe. Multidisciplinary Design Optimization: A Survey of Architectures. *AIAA Journal*, 51(9):2049–2075, 2013. ISSN 0001-1452. doi:10.2514/1.J051895. URL `http://dx.doi.org/10.2514/1.J051895`.

[3] D. R. Jones, M. Schonlau, and W. J. Welch. Efficient global optimization of expensive black-box functions. *Journal of Global Optimization*, 13(4):455–492, 1998. ISSN 1573-2916. doi:10.1023/A:1008306431147. URL `http://dx.doi.org/10.1023/A:1008306431147`.

[4] C.-Z. Xu, Z.-H. Han, k.-s. Zhang, and W. Song. Surrogate-based optimization method applied to multidisciplinary design optimization architectures. In *31st Congress of the International Council of the Aeronautical Sciences (ICAS 2018)*, 09 2018.

[5] R. Shi, L. Liu, T. Long, Y. Wu, and G. G. Wang. Multidisciplinary modeling and surrogate assisted optimization for satellite constellation systems. *Structural and Multidisciplinary Optimization*, 58(5):2173–2188, Nov 2018. ISSN 1615-1488. doi:10.1007/s00158-018-2032-1. URL `https://doi.org/10.1007/s00158-018-2032-1`.

[6] N. Bartoli, T. Lefebvre, S. Dubreuil, R. Olivanti, R. Priem, N. Bons, J. Martins, and J. Morlier. Adaptive modeling strategy for constrained global optimization with application to aerodynamic wing design. *Aerospace Science and Technology*, 90:85 – 102, 2019. ISSN 1270-9638. doi:https://doi.org/10.1016/j.ast.2019.03.041. URL `http://www.sciencedirect.com/science/article/pii/S1270963818306011`.

[7] R. M. Paiva, A. R. D. Carvalho, C. Crawford, and A. Suleman. Comparison of surrogate models in a multidisciplinary optimization framework for wing design. *AIAA Journal*, 48(5):995–1006, 2010. doi:10.2514/1.45790. URL `https://doi.org/10.2514/1.45790`.

[8] X. Wang, M. Li, Y. Liu, W. Sun, X. Song, and J. Zhang. Surrogate based multidisciplinary design optimization of lithium-ion battery thermal management system in electric vehicles. *Structural and Multidisciplinary Optimization*, 56(6): 1555–1570, Dec 2017. ISSN 1615-1488. doi:10.1007/s00158-017-1733-1. URL `https://doi.org/10.1007/s00158-017-1733-1`.

S. Dubreuil, N. Bartoli, G. Berthelin, O. Chandre Vila, C. Gogu, T. Lefebvre, J. Morlier and M. Salaün

[9] X. Chen, P. Wang, and D. Zhang. Surrogate-based multidisciplinary design optimization of an autonomous underwater vehicle hull. In *2017 16th International Symposium on Distributed Computing and Applications to Business, Engineering and Science (DCABES)*, pages 191–194, Oct 2017. doi:10.1109/DCABES.2017.48.

[10] M. Zhang, W. Gou, L. Li, F. Yang, and Z. Yue. Multidisciplinary design and multi-objective optimization on guide fins of twin-web disk using kriging surrogate model. *Structural and Multidisciplinary Optimization*, 55(1):361–373, 2017.

[11] C. E. Rasmussen and C. K. I. Williams. *Gaussian processes for machine learning.* Adaptive computation and machine learning. MIT Press, Cambridge, Mass, 2006. ISBN 978-0-262-18253-9.

[12] M. Arnst, R. Ghanem, E. Phipps, and J. Red-Horse. Dimension reduction in stochastic modeling of coupled problems. *International Journal for Numerical Methods in Engineering*, 92(11):940–968, 2012. ISSN 1097-0207. doi:10.1002/nme.4364. URL `http://dx.doi.org/10.1002/nme.4364`.

[13] S. Sankararaman and S. Mahadevan. Likelihood-Based Approach to Multidisciplinary Analysis Under Uncertainty. *Journal of Mechanical Design*, 134(3):031008 12 pages, 2012.

[14] Z. Jiang, W. Li, D. W. Apley, and W. Chen. A spatial-random-process based multidisciplinary system uncertainty propagation approach with model uncertainty. *Journal of Mechanical Design*, 137(10):101402, 2015.

[15] S. Dubreuil, N. Bartoli, C. Gogu, and T. Lefebvre. Propagation of modeling uncertainty by polynomial chaos expansion in muldisciplinary analysis. *Journal of Mechanical Design*, 138(11):111411, 2016. doi:10.1115/1.4034110.

[16] M. Berveiller, B. Sudret, and M. Lemaire. Stochastic finite elements: a non-intrusive approach by regression. *European Journal of Computational Mechanics*, 15(1-3):81 – 92, 2006.

[17] S. Dubreuil, N. Bartoli, C. Gogu, T. Lefebvre, and J. M. Colomer. Extreme value oriented random field discretization based on an hybrid polynomial chaos expansion - kriging approach. *Computer Methods in Applied Mechanics and Engineering*, 332:540 – 571, 2018. ISSN 0045-7825. doi:https://doi.org/10.1016/j.cma.2018.01.009. URL `http://www.sciencedirect.com/science/article/pii/S0045782517302736`.

[18] S. Dubreuil, N. Bartoli, C. Gogu, and T. Lefebvre. Towards an efficient global multidisciplinary design optimization algorithm. *Structural and Multidisciplinary Optimization*, 62(4):1739–1765, 2020.

[19] S. Dubreuil, N. Bartoli, T. Lefebvre, and C. Gogu. Efficient global multidisciplinary optimization based on surrogate models. In *2018 Multidisciplinary Analysis and Optimization Conference*, page 3745, 2018.

[20] R. S. Sellar, S. M. Batill, and J. E. Renaud. Response surface based, concurrent subspace optimization for multidisciplinary system design. In *34th AIAA Aerospace Sciences Meeting and Exhibit*, pages 96–0714, 1996.

S. Dubreuil, N. Bartoli, G. Berthelin, O. Chandre Vila, C. Gogu, T. Lefebvre, J. Morlier and M. Salaün

[21] D. Kraft. A software package for sequential quadratic programming. Technical Report DFVLR-FB–88-28, DLR German Aerospace Center – Institute for Flight Mechanics, Koln, Germany, 1988.

[22] M. J. D. Powell. Direct search algorithms for optimization calculations. *Acta Numerica*, 7:287–336, 001 1998. doi:10.1017/S0962492900002841.

[23] E. Jones, T. Oliphant, P. Peterson, et al. SciPy: Open source scientific tools for Python, 2001–. URL `http://www.scipy.org/`.

[24] A. de Boer, A. van Zuijlen, and H. Bijl. Review of coupling methods for non-matching meshes. *Computer Methods in Applied Mechanics and Engineering*, 196(8):1515 – 1525, 2007. ISSN 0045-7825. doi:https://doi.org/10.1016/j.cma.2006.03.017. URL `http://www.sciencedirect.com/science/article/pii/S0045782506002817`. Domain Decomposition Methods: recent advances and new challenges in engineering.

[25] T. C. Rendall and C. B. Allen. Unified fluid–structure interpolation and mesh motion using radial basis functions. *International journal for numerical methods in engineering*, 74(10):1519–1559, 2008.

[26] J. Hesthaven and S. Ubbiali. Non-intrusive reduced order modeling of nonlinear problems using neural networks. *J. Comput. Phys.*, 363:55–78, 2018.

[27] R. Coelho, P. Breitkopf, C. Knopf-Lenoir, and P. Villon. Bi-level model reduction for coupled problems: Application to a 3d wing. *Structural and Multidisciplinary Optimization*, 39, 01 2010. doi:10.1007/s00158-008-0335-3.

[28] M. Xiao, P. Breitkopf, R. Coelho, C. Knopf-Lenoir, M. Sidorkiewicz, and P. Villon. Model reduction by cpod and kriging. *IntJStruc Multidisc Optim*, 41:555–574, 01 2009.

[29] A. Paul-Dubois-Taine and D. Amsallem. An adaptive and efficient greedy procedure for the optimal training of parametric reduced-order models. *International Journal for Numerical Methods in Engineering*, 102(5):1262–1292, 2015.

[30] S. Dubreuil, N. Bartoli, C. Gogu, and T. Lefebvre. *Reduction of Uncertainties in Multidisciplinary Analysis Based on a Polynomial Chaos Sensitivity Study*, chapter 4, pages 113–142. John Wiley & Sons, Ltd, 2021. ISBN 9781119817635. doi:https://doi.org/10.1002/9781119817635.ch4. URL `https://onlinelibrary.wiley.com/doi/abs/10.1002/9781119817635.ch4`.

[31] G. Berthelin, S. Dubreuil, M. Salaün, N. Bartoli, and C. Gogu. Disciplinary Proper Orthogonal Decomposition and Interpolation for the resolution of parametrized Multidisciplinary Analysis. working paper or preprint, June 2021. URL `https://hal.archives-ouvertes.fr/hal-03274761`.

[32] W. Scholten and D. Hartl. Uncoupled method for static aeroelastic analysis. *Journal of Fluids and Structures*, 101:103221, 2021. ISSN 0889-9746. doi:https://doi.org/10.1016/j.jfluidstructs.2021.103221. URL `https://www.sciencedirect.com/science/article/pii/S0889974621000049`.

PROPELLER BLADE OPTIMIZATION FOR UNMANNED AIR VEHICLES DESIGN APPLICATION

Tenon Charly Kone[1]*, Sebastian Ghinet[1], Anant Grewal[1] and Viresh Wickramasinghe[1]

National Research Council Canada,
Flight Research Laboratory
1200 Montreal Road, Ottawa, ON, K1A 0R6, Canada
TenonCharly.Kone@nrc-cnrc.gc.ca, https://nrc.canada.ca
Sebastian.Ghinet@nrc-cnrc.gc.ca, https://nrc.canada.ca
Anant.Grewal@nrc-cnrc.gc.ca, https://nrc.canada.ca
Viresh.Wickramasinghe@nrc-cnrc.gc.ca, https://nrc.canada.ca

Abstract *Due to their impact on vehicle performance, energy efficiency and noise, propeller design is important in aircraft design in general and in unmanned aerial systems (UAS) in particular. The design of appropriate propeller configuration with optimum number of blades, allows for improvements in aerodynamic performance while decreasing the UAS energy dependence and thus reducing the CO_2 emissions. Recent advances in numerical simulation has resulted in the implementation of multidisciplinary optimization for complex shape propeller blade designs a feasible and affordable option. However, the numerical simulation linked to the optimization of complex systems such as propeller blades is known as a task of considerable computational time and complexity. In addition, the cost associated with the required commercial software contribute to the increase in design costs. As a result metamodel techniques using open source algorithms as a mean to explore and support the initial design concepts have become standard practice as they reduce the computational time required and decrease the total design cost.*

This paper proposes an optimization approach based on metamodels. The approach adopted is to combine several open source codes such as Salomé for the design and development of the mesh, OpenFoam for aerodynamic modelling and finally Dakota for the generation of new design parameters and the optimization of the aerodynamic performance. Improved aerodynamic performance was demonstrated numerically for an optimized propeller blade configuration as compared to a baseline geometry configuration.

Keywords: multidisciplinary design, propeller blade, optimization, aerospace, metamodel

T. C. Kone, S. Ghinet, A. Grewal and V. Wickramasinghe

1. INTRODUCTION

Large-scale deployment of commercial Unmanned Aerial Systems (UAS) promises to revolutionize the aerospace and wider transportation market. Hundreds of vehicle concepts are detailed in the public domain, with the majority leveraging electric or hybrid propulsion and vertical take-off and landing (VTOL) capabilities to provide convenient personal transportation or improved cargo delivery services. However, many technological, operational and regulatory barriers remain unresolved, thus preventing the realization of this future transport vision. For example, if nothing is done, the growing number of UAS will contribute significantly to global warming through an increase in their carbon footprint. The aeronautical industries must therefore comply with various government policies to reduce CO_2 emissions throughout the world. One of the solutions proposed in the literature is an appropriate design of main components in order to increase the aerodynamic performance of UAS which will de facto lead to a reduction in energy consumption. Thus, the optimization of the propeller blades as well as their number becomes one of the avenues envisioned.

In the literature, much research has been published concerning the optimization of the aerodynamic performance of propeller blades. Some studies are based on the traditional theory of blade elements as a model for aerodynamic analysis [1]. Other subsequent studies used more advanced models [2, 3], notably the vortex network method [4, 5]. The blade element momentum theory (BEM) is the most common method used for the preliminary design of propellers and their performance analysis. It is used either as the basic aerodynamic model [6] or is combined with another analysis tool such as computational fluid dynamics (CFD) model [7–11]. Because of their high computational cost, CFD simulations are usually used only for analyzing or validating final design results and are less frequently used during the optimization process as in this study. However, with the expansion of high performance computing (HPC) it is more and more common to use CFD simulations in the optimization of aerodynamic performance. The application of CFD approach coupled with the methods of optimizing the aerodynamic performance of unmanned aerial systems is recent. Therefore the literature review cannot be exhaustive. Haider et al. [12] used the coupling of CFD with polynomial response surface methods to optimize the blades of an unmanned helicopter for agriculture application. To obtain an optimal blade more powerful than that of the baseline, the angle of torsion was optimized by varying the pitch angles at the root and at the tip, by changing the length of the chord of the tip and by keeping the length of the root cord unchanged. Qing et al. [13] designed a rotor aerodynamic shape for improving performance of an unmanned helicopter. The method they used was based on coupling the CFD to an optimization method on the blades of an unmanned helicopter with a NACA8H12 baseline profile. By comparing the numerical data, the airfoil optimized has better lift-drag ratio compared to the original. Yeong et al. [14] studied the propeller design of micro quadrotor aircraft by using STAR-CCM+ CFD method, and optimized the aerodynamic performance of the aircraft through the shear stress transfer K-Omega (SST K-Omega) turbulence model. Sankar et al. [15] used N-S equation and free wake method to solve the flow field of a rotor, and obtained a better simulation result with a relatively small computational cost. In view of this review of the literature, each optimization approach stand out by the choice of optimization parameters and the use of commercial software which would increase the design cost.

The main objective of the present study was to develop and propose propeller blade shapes that maximize aerodynamic thrust while minimizing engine torque for improved aerodynamic performance. Moreover, the proposed solution had to be optimized not only for aerodynamic performance but also for low fabrication costs. The challenge was therefore to select a concept which, through multivariable optimization at a lower cost, would produce improved

T. C. Kone, S. Ghinet, A. Grewal and V. Wickramasinghe

aerodynamic performance and quickly reach a level of technological readiness level for integration into UAS. The methodology was based on the building of a Kriging-type metamodel with a Latin Hypercube Sampling (LHS) method from the optimization design parameters of the propeller blades. Additionally, the optimum blade design was developed using the multi-objective genetic algorithm (MOGA) [16, 17] of open source software Dakota [18]. The CFD-RANS approach of the Multi-References frame (MRF) solver of OpenFoam [19] has been used to evaluate the objective functions such as thrust and motor torque.

The combination of the LHS method using CFD allowed for the development of an accurate, fast, and appropriate stochastic aerodynamic efficiency characterization approach. The widespread popularity of LHS has led to technical developments in various fields, such as improved space filling [20, 21], optimization of projective properties [22] and aerodynamic optimization [23]. The complexity of the shape of the propeller blades made it impossible to establish an exact, simple, and independent relationship between design parameters, thrust and torque. Because of the complexity, the traditional regression approach would no longer be suitable and it has been necessary to turn to other approaches such as the Kriging metamodel. Originally developed by Daniel G. Krige [24], its application to the approximation of functions arising from physical problems was introduced by Sacks et al. [25]. Kriging has been interpreted as a mixture of a polynomial response surface and a radial basis function approximation. The purpose of the trend function, the polynomial response surface, has been to roughly approximate the model. The difference or error between the prediction of the trend function and the true value of the sampled data points was computed. The Kriging model became one of the most appropriate and precise [26] means to solve the optimization problem in this paper. With the advancement of numerical technology, the application of model Kriging is spreading in mechanical engineering and related fields [27–31] and in the aircraft industry [23-33]. In addition, the Kriging model is attractive for its interpolation characteristic, providing accurate predictions [26] and reducing the time for expensive analysis. When there is a high nonlinearity in a large number of factors, the modelling of the polynomial regression becomes insufficient while the modelling by Kriging is an alternative choice despite the additional complexity [26].

2. MATERIALS

The baseline geometry (Fig. 1a) was set to $N = 3$ identical propeller blades with constant angular spacing of $360/N$ degrees mounted around a motor shaft of diameter $D_e = 4.3\ in$ and length $L_e = 10.5\ in$ with a parabolic shaped hub (Fig. 2). The blade was constructed using NACA 6412 type profiles (Fig. 1b). Each profile section was characterized by its radial position r non-dimensionalised by the radius $R = D/2$ of the rotor (r/R), by its chord b non-dimensionalised by the diameter $D = 15\ in$ of the rotor (b/D), its thickness h non-dimensionalised by the chord b of the profile (h/b) and its blade angle β. The evolution curves of these geometric characteristics of the propeller blade as a function of the dimensionless radial position are shown in the Fig. 1c according at Ref. [34].

T. C. Kone, S. Ghinet, A. Grewal and V. Wickramasinghe
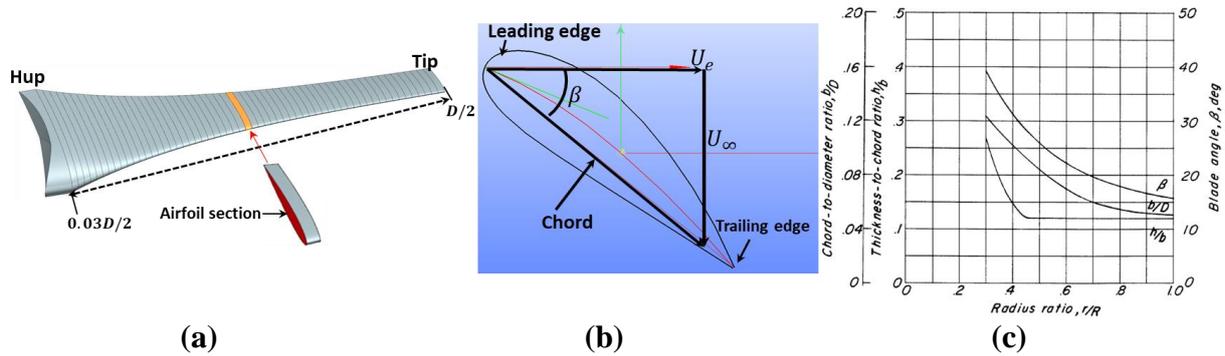
Figure 1: The baseline geometry of the propeller blades: (a) A view of 40 profiles forming the blade, (b) NACA 6412 profile and (c) Characteristics of the propeller blade as a function of the dimensionless radial position [34]

The propellers was ducted by a shroud of profiled section (Fig. 2c), the characteristics of which are given in Ref. [34]. The length of the shrouded profile chord b_{sh} was $10.31\ in$, the shrouded propeller had a tip clearance $e = 0.04\ in$ and the struts supporting the shroud were not considered in this study (Figs. 2b and 2c). The shroud's axis of revolution coincides with the axis of rotation of the propellers. The angle of attack was zero throughout this study.
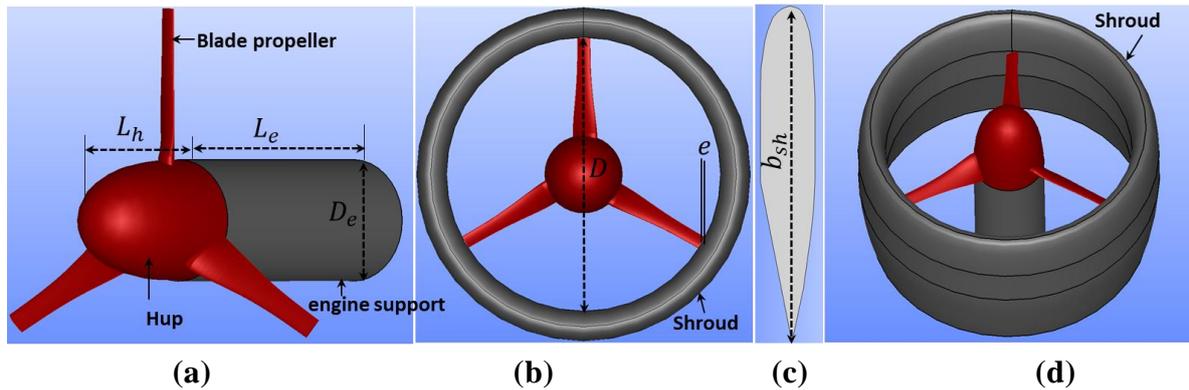
Figure 2: Baseline rotor geometry: (a) geometry without shroud, (b) View in the plane perpendicular to the axis of rotation of the rotor geometry with shroud, (c) Shroud profile and (c) 3D-view of study rotor.

3. OPTIMIZATION PROBLEM

The objective of this study was to improve the aerodynamic performance of a propeller blade by modifying its shape using an optimization approach. Thus this section will focus on the definition of the geometric parameters of the blade which were used as design or optimization variables. Additionally, the objective functions as well as the optimization problem were defined.

3.1. Optimization variables

During our recent investigations, it was noted that the number of propeller blades N, the blade angle $\beta_{75\%}$ at 75% of the rotor radius (that is to say at $r/R = 0.75$) and the blade skew were design parameters of the propeller blade that could have a significant influence on the aerodynamic performance of the rotor according to preliminary investigations. The blade skew was defined in the plane perpendicular to the rotation axis of the rotor. It was characterized by the angular position θ_s with respect to the radial of the mid-chord point of the profile considered. For this study, the blade skew was defined using a polynomial function of degree n. This polynomial function is defined by the knowledge of n + 1 blade skew angle θ_{si} were $0 \leq i \leq n$. Once the polynomial skew curve of the blade has been defined, the centre of each blade

T. C. Kone, S. Ghinet, A. Grewal and V. Wickramasinghe

profile is repositioned on this curve. The baseline geometry was defined by a configuration with all blade skew angles equal to 0 (i.e $\theta_{si} = 0$). For illustration, let us consider 3 blade skew angles $\theta_{s0} = 0^o$ at $r = 0.3R$, $\theta_{s1} = -30^o$ at $r = 0.65R$ and $\theta_{s2} = 30^o$ at R. The geometry of the corresponding propeller blade is shown in the Fig. 3b.

(a)　　　　　　**(b)**
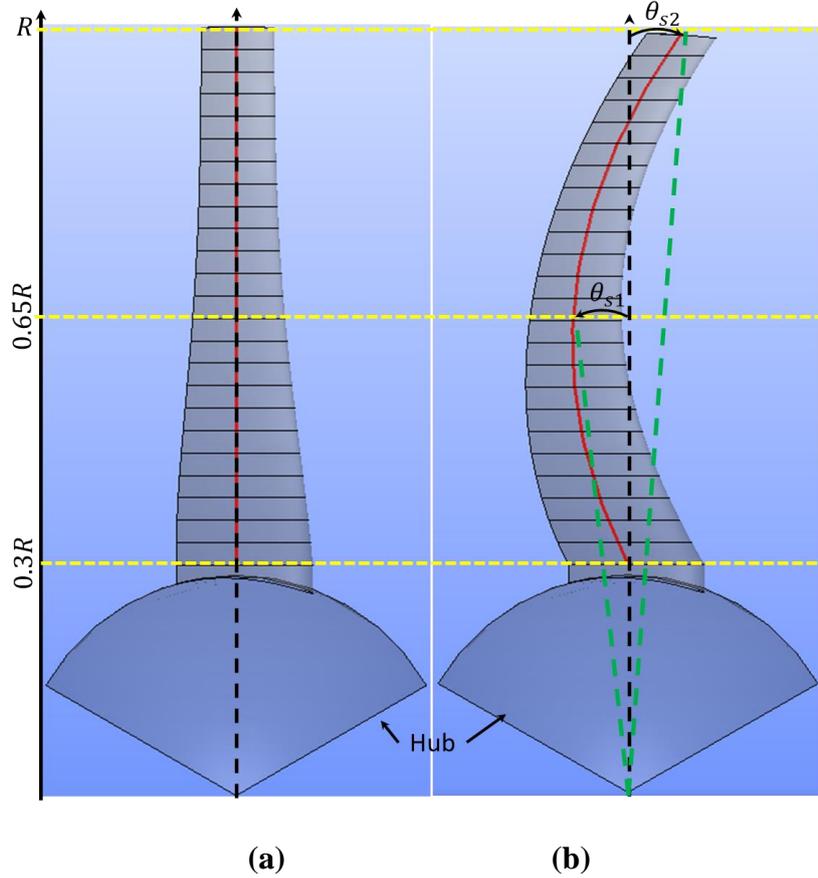
Figure 3: Deformation of the propeller blade as a function of the skew in the plane perpendicular to the axis of the rotor. (a) Base geometry without skew and (b) with skew.

Thus, the optimization variable vector was given by:

$$\boldsymbol{x} = (\boldsymbol{N}, \boldsymbol{\beta_{75\%}}, \boldsymbol{\theta_{s0}}, \dots, \boldsymbol{\theta_{sn}}) \tag{1}$$

3.2. Objective functions

The aerodynamic performance was characterized by the thrust T and the motor torque Q. The thrust was defined as the set of forces exerted by the rotor on the fluid. Thus, in this study it was the total force of the N propeller blades, the hub, the motor support and the shroud. As for the engine torque, it was defined as the component along the axis of rotation of the rotor of the moment of the rotating surfaces such as the propeller blades and the hub. For a rotation speed Ω given in rpm and a forward given velocity U_∞, the aerodynamic performance is defined as the ratio:

$$\boldsymbol{\eta} = \frac{\boldsymbol{TU_\infty}}{2\pi Q\Omega/60} \tag{2}$$

According to Eq. (2), having a more aerodynamically efficient rotor amounts to obtaining

a large thrust for a low motor torque. Therefore, the objective functions of this study have been the thrust and motor torque.

3.3. Definition of the optimization problem

The optimization parameters being defined as well as the objective functions, it remains to define the optimization problem. Assuming that all the other geometric design parameters in the study remain constant, and the rotor operating point is given by the forward velocity U_∞, characterized by the advance ratio $J = U_\infty/(D\Omega/60)$, the multi-objective optimization problem is defined as finding the design parameters x which maximize the thrust T while minimizing the motor torque Q and is given by:

$$
\begin{cases}
\underset{x}{\textbf{maximized}}\ \boldsymbol{T(x)} \\
\underset{x}{\textbf{minimized}}\ \boldsymbol{Q\ (x)} \\
\boldsymbol{J, \Omega\ constant} \\
\boldsymbol{N, integer} \\
\boldsymbol{\beta_{75\%_{min}} \leq \beta_{75\%} \leq \beta_{75\%_{max}}} \\
\boldsymbol{\theta_{si_{min}} \leq \theta_{si} \leq \theta_{si_{max}}},\ \text{were}\ \boldsymbol{1 \leq i \leq n} \\
\boldsymbol{\theta_{s0} = 0^o}
\end{cases}
\tag{3}
$$

4. METHODOLOGY

The solution of the optimization problem was carried out in 4 stages: *(i)* spatial discretization of the geometry space (sampling); *(ii)* prediction of the objective functions by a numerical CFD model of each sample; *(iii)* building the response surface called a metamodel from the results of the CFD; *(iv)* determining the optimum metamodel; and finally, (*v*) once one or more optimum is found, a CFD calculation is performed to verify the accuracy of the metamodel. If the result is satisfactory, the process stops. Otherwise the optimization returns to step (*i*) by refining the discretization and / or by injecting into the sample the optimums found and repeating steps (*ii*) to (*v*). This process is iterated until one or several satisfactory optimums are found. Each of these steps will be presented in this section.

4.1. Sampling

The design space is defined by the knowledge of the lower and upper bounds of each optimization variable of the problem to be solved. Once this space is defined, it is explored by a discretization according to the optimization variables, a process known as sampling. Several sampling techniques exist in the literature, but very often the Latin Hypercube (LHS) sampling is employed for complex optimization problems as is the present case where the geometry under study is a propeller blade of an unmanned aerial system . LHS is based on a statistical method to generate a quasi-random sample of optimization parameter values from a multidimensional distribution. For this study 4 optimization variables were used. The number of blades N could take only the integer values 3, 4 and 5. The blade angle of the propeller at 0.75R varied between 17° and 30° ($17^o \leq \beta_{75\%} \leq 30^o$). Two variables θ_{s1} at 0.65R and θ_{s2} at R to define the curve of the propeller blade skew with $-30^o \leq \theta_{s1}, \theta_{s2} \leq 30^o$. The angle θ_{s0} at 0.3R has been set to zero so that there was no deformation at the propeller blade hub. Initially, 50 LHS were used for the first round of optimization (first cycle). Then a second cycle was required by doubling

T. C. Kone, S. Ghinet, A. Grewal and V. Wickramasinghe

samples to 100 LHS. The 2D projection of design space samples is shown in Fig.4. The black dots represented the first 50 LHS and the red dots represent the additional 50 LHS points for the second round.
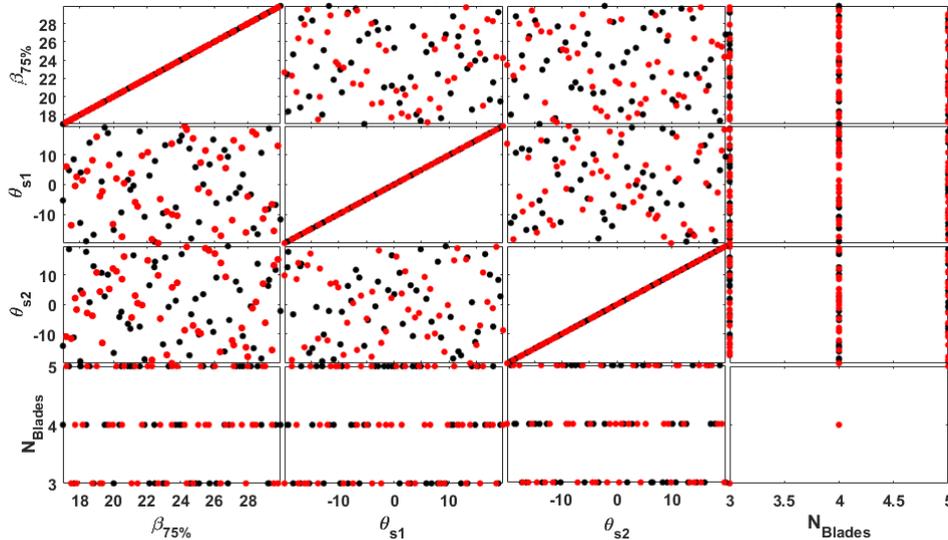
Figure 4: 2D projection of the samples in the base of the optimization parameters.

4.2. The CFD Model

Each LHS point of the variable space should be evaluated to obtain the objective functions. It was necessary to define the CFD model for the various calculations. All CFD calculations were performed on a Compute Canada server using 32 processors per case. Each case took an average of 18 hours to converge.

4.2.1 CFD Model geometry

Each Latin Hypercube sampling geometry comprised N identical propeller blades, the motor support, the hub and the shroud had a symmetry of revolution as described in section 2 and illustrated in Fig.2. To facilitate the setup, the geometry under study was placed in a cylinder of a diameter of $1.5D$, a length of $1.25D$ and sharing the same axis as the rotor. The volume of air thus defined was called the rotation volume. The volume of rotation was also channelled in a cylindrical channel of diameter $4D$, length $12D$ and with the same axis. The rotation volume is located in the center of the channel. The volume of the channel excluding the rotation volume is called the tunnel. The set of study volumes thus defined were axisymmetric. By design, the study geometry could be reduced to $1/N$ of the total volume (Fig. 5). Fig.5c, illustrates the CFD model used for each design point. As for the periodic model of the rotating volume, it is represented in Fig. 5b while the rotor comprising the propeller blade, the hub, the motor support and the shroud has been shown in Fig. 1a. Only the geometry of the propeller blade was modified during the optimization process. In order, to run all the sample points without intervening, a python script, which is executable on Salome, was developed to design the CFD model geometry. The only variables in the script are the optimization variables. The script is able to automatically identify and define the boundary surfaces like interfaces, periodic faces, wall surfaces as well as the Inlet and Outlet faces of the CFD model. The periodic faces had a rotation symmetry of an angle equal to $360^o/N$ and the same axis of revolution as the rotor. As a result, the faces Periodic_r bound the rotating volume, while the faces Periodic_t bound the tunnel. As for the interfaces, they are defined as the common surfaces of the rotation volume and of the tunnel (Figs. b and c). Two categories of wall faces were defined in this study. The

wall surfaces which were in rotational movement were called the rotating wall and included the propeller blade and the hub. The remaining wall faces were stationary and included the motor support and the shroud in the rotating volume as well as the lateral surface of the tunnel. These faces were called stationary walls.

(a)   **(b)**   **(c)**
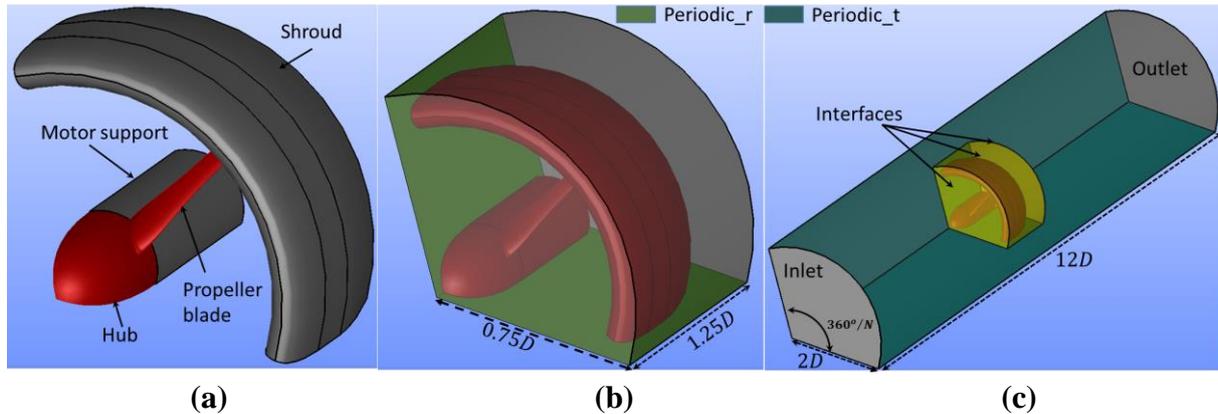
Figure 5: CFD study geometry: (a) $1/N$ th of the rotor, (b) $1/N$ th rotation volume and (c) CFD model

4.2.2 Mesh

The volume of each Latin Hypercupe sample study geometry was discretized into a finite volume. Salome's Netgen 1D-2D-3D algorithm was used to create a tetrahedral 3D mesh. As for the boundary faces, a triangular 2D mesh was used using the 1D-2D algorithm of Salome. The mesh is characterized by the minimum (Minsize) and maximum (Maxsize) sizes of the mesh edges. Since the objective functions are evaluated using the boundary faces as propeller blade, hub, support motor and shroud, the minimum size was imposed on these boundary faces. The recent versions of Salome (9.3 to 9.6) have a mesh optimizer that allows for the definition of a higher quality mesh for the OpenFoam software. This optimizer was used for this study. Moreover, a python script executable on Salome has been developed to automatically create the mesh of each geometry under study. The script also allowed for the exporting of the mesh in a universal format convertible by OpenFoam. The modeling of the boundary layer by wall functions was thus used to accelerate the CFD modeling. In our recent investigations on the quality of the near-wall mesh, a minimum size ($minSize$) of about 0.035 m was necessary to have a $y^+ = u_* y/\nu$ (with u_* was the friction velocity near wall and y was the size of the first cell near the walls) below 35. This was sufficient for RANS calculations using wall functions. Therefore $minSize = 0.035\ in$ was imposed while a $maxSize = 0.2\ in$ was used in the rotating volume. The cell size in the tunnel was defined using the following parameters: $maxSize = 0.2\ in$ and $maxSize = 2.0\ in$. By applying these cell sizes to the baseline geometry, we obtained an average of 13.2 million elements in the rotating volume, including 57,618 elements on the propeller blade including the hub. The Fig. 6a shows an illustration of the mesh in the rotating volume. A close up of the propeller blade tip is illustrated in Fig. 6b. The quality of the mesh on the propeller blade has been shown in Fig. 6c.

T. C. Kone, S. Ghinet, A. Grewal and V. Wickramasinghe

Figure 6: Illustration of the mesh. (a) in the rotating volume, (b) at the blade tip and (c) on the propeller blade.

4.2.3 CFD setup and boundary conditions

An incompressible solution using the OpenFoam RANS method was computed using air at $20^o C$ and 1 atm. For modelling the rotation, the multi-rotational frames (MRF) approach of the OpenFoam MRFSimpleFoam solver 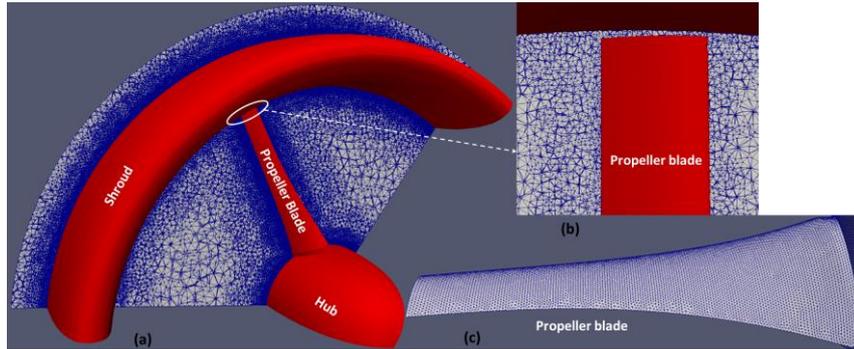was chosen. The boundary conditions used on the boundary faces described in the previous section are given in Table 1. For all CFD calculations, a uniform inlet velocity of $U_\infty = 30.226 \, m/s$ corresponding to the advance ratio J = 0.596, was applied at the Inlet tunnel. Pressure boundary conditions were used on the outlet tunnel. The conditions of zero relative velocity was imposed on the rotating wall while the no-slip conditions have been imposed on the other rotational walls. A sliding condition was imposed on the lateral boundary face of the tunnel. The rotating volume without the fixed walls (shroud and motor support) rotated at a rotational velocity of 8000 rpm. The kOmega-SST turbulence model was used with a turbulence intensity of 5% imposed at the inlet to the tunnel. Wall functions were used on all walls.

Table 1: OpenFoam boundary conditions dictionary of velocity U and pressure p used.

	Inlet	Outlet	Rotating walls	Stationary walls	Interfaces	Periodic faces
U	FixedValue	inletoutlet	FixedValue	Slip/ no slip	CyclcAMI	CyclcAMI
p	Zerogradient	FixedValue	Zerogradient	Zerogradient	CyclcAMI	CyclcAMI

4.3. Metamodel

Once all the objective functions of all the geometries of the LHS were evaluated by the OpenFoam CFD, the metamodel was then constructed using the Dakota software with the Kriging approach. The Kriging metamodel is a superposition of a regression model $P(x)^T\beta$ and a random error model $\varepsilon(x)$ of zero mean and σ^2 covariance which is used to correct the regression model portion. Therefore, the prediction $\hat{Y}$ of the objective functions by the Kriging model are given by:

$$\hat{Y} = P(x)^T\beta + \varepsilon(x) \tag{4}$$

with $P(x) = [p_1(x), ..., p_m(x)]^T$ the matrix of design or optimization variables x in the polynomial basis linked to the regression function. $\beta = [\beta_0, \beta_1, ..., \beta_p, \beta_{12}, ..\beta_{ij}, ..., \beta_{ii}]$ (with $i \neq j \, and \, i,j = 1, ..., N_p$ and N_p is the parameters design number) is the vector coefficient in the polynomial basis. The random part $\varepsilon(x)$ is defined by the knowledge of its covariance between two calculation points. This covariance between the arbitrary points x_i and x_j two

design parameters from LHS is given by:

$$cov\left(\varepsilon(x_i), \varepsilon(x_j)\right) = \sigma^2 r(x_i, x_j) \tag{5}$$

with $r(x_i, x_j) = exp\left(\sum_{k=1}^{N_p} \theta_k |x_{i_k} - x_{j_k}|^2\right)$ the Gaussian correlation function, $1 \leq i, j \leq N_s$, N_s the LHS number, N_p design parameter number, $\theta_k = 1/2L_k^2$ the correlation parameter and L_k the correlation length.

If $\in$ characterizes the error vector of the regression model and $R_{ij} = r(x_i, x_j)$ the correlation matrix, then the interpolation by the Kriging model of a design point x of the design space is given by:

$$\hat{Y}(x) = P(x)^T\beta + r(x)^T R^{-1} \in \tag{6}$$

where $r(x) = r(x, x_j)$ and x_j, the design variable of the jth design of the sampling space.

This Kriging metamodel was implemented in Dakota and had as input data the optimization variables and the objective functions simulated by OpenFoam of all the geometries from the LHS. For this study $m = 2$ object functions (the torque and the thrust) were used with $N_s = 100$ LHS and $N_p = 4$ design parameters.

4.4. Optimization

Once the metamodel (Eq. 6) had been built, the next step was to find the design parameters which maximized the thrust while minimizing the motor torque using the Kriging metamodel (response surface). The Dakota multi-objective genetic algorithm (MOGA) was used in this investigation. Finally the CFD calculations were carried out for the validation of the optimum geometries proposed by the metamodel.

5. RESULTS

The objective of this study was to find propeller blade shape geometries which would increase the aerodynamic performance (Eq. 2) of an unmanned aerial system rotor. The optimization problem linked to this objective was presented in section 3 (Eq. 3). The resolution methodology used is that presented in section 4. Following two cycles of the optimization process, several potential geometry solutions were found by the optimization model. The solutions resulting from the optimization are presented here and compared with regard to their respective aerodynamic performance versus the baseline geometry.

5.1. Solutions

The objective functions (the thrust as a function of the torque), are presented in Fig. 7. These potential solutions are represented by the blue circles as a result of the optimization problem obtained on the Kriging metamodel. The black circles represent the thrust as a function of the torque of the 100 LHS obtained using CFD. To find the best solution among the potential solutions, a filter has been created to retain only the solutions whose aerodynamic performance (Eq. 2) was above 70% superior to the aerodynamic performance of the baseline geometry ($\eta = 66.3\%$). Three resulting best solutions have been found and have been represented as the green squares in the Fig. 7. The design parameters of these 3 solutions and the two objective functions, the thrust (T) and torque (Q) obtained with Kriging metamodel and with CFD calculation have been grouped together in the Table 2. The reliability of the metamodel was evaluated by the relative error ($er_{.f_i} = |f_{i_{CFD}} - f_{i_{model}}|/|f_{i_{CFD}}|$ with $i = 1, 2$) between the predictions of the Kriging metamodel and the results of the CFD calculation of the two objective functions $f_1 = $

T. C. Kone, S. Ghinet, A. Grewal and V. Wickramasinghe

T and $f_2 = Q$. The relative torque errors $er._Q$ of the 3 solutions were observed to be relatively small. The larger value obtained with solution 1 was 0.6%. The model was more accurate with solution 2 whose relative error was 0.001%. The model was observed to be accurate as well in predicting the thrust. The maximum relative error for the thrust calculation $er._T$ was 0.8 % obtained with solution 3, while the lowest error value was obtained with solution 2 and was 0.04%. These low values of the relative errors show the reliability of the Kriging metamodel in the prediction of thrust and torque.
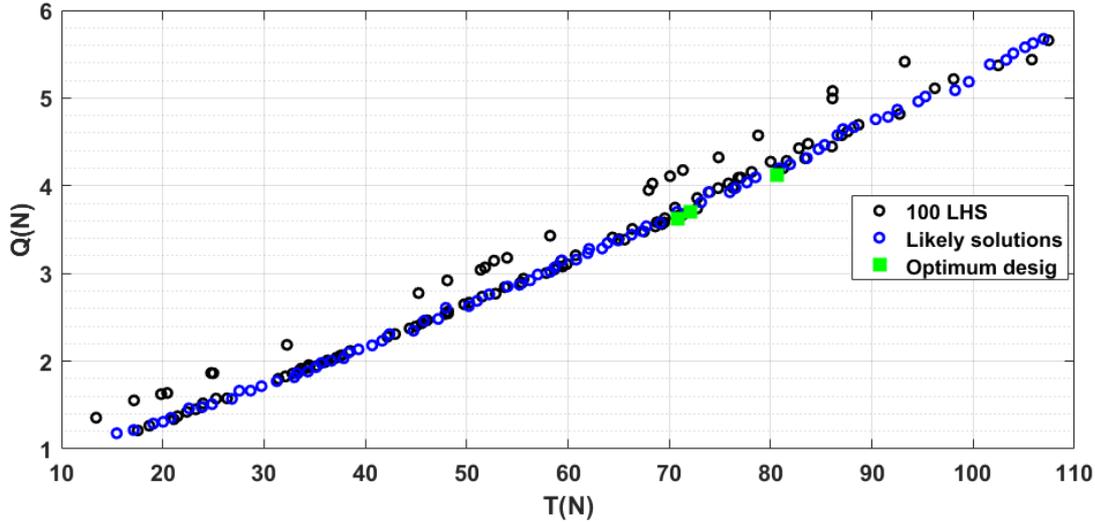
Figure 7: The thrust (T) in Naccording to the torque (Q) in .N.m of 100 HLS calculated with the CFD in black circles, the possible solutions with the optimization in blue circles and the proposed 3 solutions shown with the green squares.

Table 2: Design parameters of the optimization problem and the predictions of the Torque and the Thrust for the Kriging metamodel and using CFD calculation.

	Design parameters				Model		CFD		error	
Sol.	$\beta_{75\%}(°)$	$\theta_{s1}(°)$	$\theta_{s2}(°)$	N	$Q(N.m)$	$T(N)$	$Q(N.m)$	$T(N)$	$er._Q$ (%)	$er._T$ (%)
1	24.92	−10.61	−17.45	3	3.62	70.79	3.64	70.54	0.6	0.35
2	25.01	−16.65	−11.47	3	3.71	72.12	3.71	72.09	0.001	0.04
3	26.11	−11.31	17.69	3	4.12	80.67	4.13	79.99	0.24	0.8

This reliability of the Kriging metamodel was demonstrated as well for the aerodynamic performance η_{model} of the three solutions. The results of the predictions using the Kriging model and using the CFD performance calculation (η_{CFD}) have been compiled in the Table 3. The relation error $er._\eta = |\eta_{CFD} - \eta_{model}|/\eta_{CFD}$ is demonstrated to remain low with a maximum value at 1% for solutions 1 and 3. The Kriging model is even more precise for solution 2 with a relative error at 0.14%.

In conclusion the Kriging metamodel built with 100 LHS is reliable in predicting the aerodynamic performance of the propeller blade of an unmanned aerial system rotor.

Table 3: Aerodynamic performance of the three solutions predicted using the Kriging metamodel and calculated using CFD.

Sol.	$\eta_{model}(\%)$	$\eta_{CFD}(\%)$	$er._\eta$ (%)
1	70.5	69.8	1
2	70.2	70.1	0.14
3	70.6	69.9	1

T. C. Kone, S. Ghinet, A. Grewal and V. Wickramasinghe

The geometries of the shapes of the propeller blades of the 3 solutions numbered 1 to 3 shown in the plane perpendicular to the axis of rotation of the rotor are illustrated in the Fig. 8. The number 0 in the figure represents the baseline geometry. The shapes of the 3 solutions were different and the mid-chord points of their 25 profiles are all on the skew curves defined by the parameters θ_{s1} and θ_{s2} given in Table 2. As for the baseline geometry, the mid-chord points coincide with the radial axis.
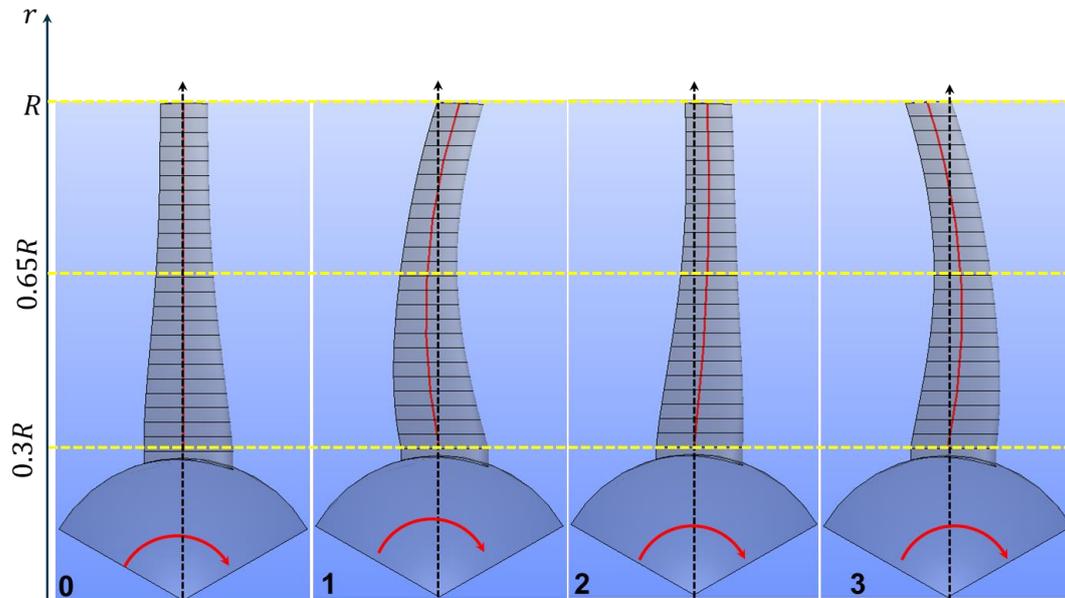
Figure 8: Propeller blade shape optimizer: (0) baseline geometry, (1) solution 1, solution 2 and (3) solution 3.

5.1. Comparison

This section presents the validation results for the CFD model as well as the comparisons between the aerodynamic performance of the 3 solutions and the baseline geometry. The aerodynamic performance of the rotor of the unmanned aerial system as a function of the advance ratio J of the 3 optimized solutions and of the baseline geometry, all obtained using the CFD model compared to the experimental results are presented in Fig. 9. Only the measurements at $J = 0.595$ were available.

At the advance ratio $J = 0.595$, the aerodynamic performance calculated using the CFD model was in agreement with the testing results with a relative error of 0.35%. This showed that the CFD model used in the optimization process was reliable. An improvement in the aerodynamic performance has been achieved with the optimized geometries. A relative gain on average of 6% was obtained with the 3 optimized rotors. The relative gain was calculated using the expression $|\eta_{baseline} - \eta_i|/\eta_{baseline}$ with $\eta_{baseline}$ the aerodynamic performance of the baseline geometry and η_i that of solution i. The best aerodynamic performance was obtained with solution 2. However, the operation at $J = 0.595$ was not the optimum operating point of the 3 solutions unlike the case for the baseline geometry. The optimal operating points were approximately at $J = 0.615\%$ for solutions 1 and 2 resulting in an aerodynamic performance of 69.9% for solution 1 and 70.3% for solution 2. As for solution 3, the optimum operating point was in the vicinity of $J = 0.655$ with a resulting aerodynamic performance of 70.4% (Fig. 9).

T. C. Kone, S. Ghinet, A. Grewal and V. Wickramasinghe
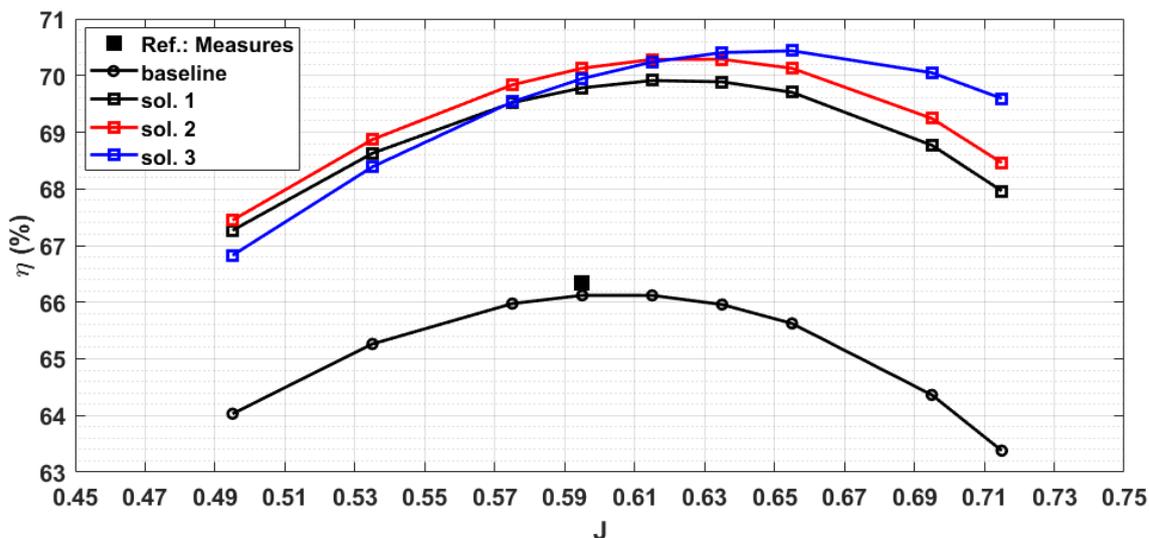
Figure 9: Aerodynamic performance according to the advance ratio. The measurements at J = 0.565: black square, the basiline geometry: the black curve with circles, solution 1: the black curve with squares, solution 2: the red curve with squares and solution 3: the blue curve with squares.

6. CONCLUSIONS

This study presented a reliable methodology for optimizing the aerodynamic performance of an Unmanned Aerial System (UAS) propeller blade. The Kriging metamodel approach with Latin Hypercube Samples (LHS) was employed. The torque and thrust required to build the Kriging metamodel were calculated using an OpenFoam CFD model. The optimization has carried out using four design parameters of the propeller blade. A Dakota multi-objective optimization algorithm was used to find the shape of the propeller blades that maximized the thrust while minimizing the torque for a better aerodynamic performance. Three distinct optimum geometries were found and shown to improve the aerodynamic performance of the UAS rotor by approximately 6% when compared to the baseline geometry.

Despite the encouraging results of this study, several points remain to be explored. Notably an increase in design parameters including for example the sweep angle of the propeller blade and the diameter of the rotor will developed and investigated in subsequent studies. However, this work lays the foundations for a multidisciplinary optimization of aerodynamic and aeroacoustic performance.

7. REFERENCES

[1]   J. P. Mendoza. *Propeller design by numerical optimization*. In Business aircraft meeting, 29 March - 1April 1977, Wichita, KS.

[2]   L. Chang and G. Stefko. Application of an optimization method to high performance propeller designs. In 20th joint propulsion conference, 11–13 June 1984, Cincinnati, OH,

[3]   M. H. Rizk and W. H. Jou. Propeller design by optimization. *AIAA Journal,* 1(24): 1554–1556, 1984.

[4]   J. Cho and S. C. Lee. Propeller blade shape optimization for efficiency improvement. *Compute Fluids*, 27: 407–419, 1998.

[5]   C. Burger, R. J. Hartfield and J. Burkalter. Propeller performance optimization using vortex lattice method and genetic algorithm. In: 44th AIAA aerospace sciences meeting and exhibit, 9–12 January 2006, pp.12818–12831, Reno, NV.

[6]   O. Gur A. and Rosen. Optimization of propeller based propulsion system. *Journal Aircraft*, 46: 95–106, 2009.

[7]   X. Zhao, J. Wang, W. Fu, et al. Aerodynamic propeller design using optimization method and genetic algorithm generation. In: Proceedings of 2010 Asia-Pacific international symposium on aerospace technology, Xi'an, China, 13–15 September 2010, pp.1019–1022. Northwestern Polytechnical University.

[8]   J. Sodja, D. Stadler and T. Kosel. Computational fluid dynamics analysis of an optimized load-distribution propeller. *Journal Aircraft*, 49: 955–961, 2012.

[9]   G. Droandi and G. Gibertini. Aerodynamic shape optimisation of a proprotor and its validation by means of CFD and experiments. *Aeronaut Journal*, 119: 1223–1251, 2015.

[10] H. Kwon, S. Yi, S. Choi and K. Kim. Design of efficient propellers using variable-fidelity aerodynamic analysis and multilevel optimization. *Journal Propulsion Power*, 31(4): 1057–1072, 2015.

[11] J. Morgado, M. Abdollahzadeh, M. A. R.Silvestre, and J. C. Pascoa. High altitude propeller design and analysis. *Aerospace Science Technology*, 45: 398-407, 2015.

[12] B. A. Haider, C. H. Sohn, Y. S. Won and Y. M. Koo, Aerodynamic performance optimization for the rotor design of a hovering agricultural unmanned helicopter. *Journal of Mechanical Science and Technology* 31 (9): 4221-4226, 2017

[13] Qing Wang, Qijun Zhao. Rotor aerodynamic shape design for improving performance of an unmanned helicopter, *Aerospace Science and Technology*, 87: 478–487, 2019.

[14] S. P. Yeong and S. S. Dol. Aerodynamic Optimization of Micro Aerial Vehicle. *J. Appl. Fluid Mech*, 9: 2111–2121, 2016.

[15] Z. Yang, L. N. Sankar, M. J. Smith and O. Bauchau. Recent Improvements to a Hybrid Method for Rotors in Forward Flight. *Journal Aircraft,* 39(5): 804–812, 2002.

[16] K. Deb. *Multi-Objective Optimization Using Evolutionary Algorithms*, John Wiley & Sons, Hoboken, NJ07030, USA, 2001.

[17] M. Kurdi, P. Beran, B. Stanford and S. Snyder. Optimal Actuation of Nonlinear Resonant Systems, *J. Struct. Multidisc. Optimal.* , 41 (1): 65-86, 2009.

[18] Dakota. *A Multilevel Parallel Object-Oriented Framework for Design Optimization, Parameter Estimation, Uncertainty Quantification, and Sensitivity Analysis*. Version 6.13 User's Manual, SAND2020-12495 Unlimited Release, 2020.

[19] OpenFoam. https://cfd.direct/openfoam/user-guide/

[20] K. Burrage, P. Burrage, D. Donovan, and B. Thompson. Populations of models, experimental designs and coverage of parameter space by Latin hypercube and orthogonal sampling, *Procedia Computer Science*, 51, 1762–1771, 2015.

[21] T. M. Cioppa and T. W. Lucas. Efficient nearly orthogonal and space-filling Latin hypercubes, *Technometrics*, 49(1), 45-55, 2007.

[22] V. R. Joseph and Y. Hung. Orthogonal-maximin Latin hypercube designs, *Statistica Sinica*, 1: 171-186, 2008.

[23] Kone T. C. *Etude numérique de l'identification des sources acoustiques d'une pale de ventilateur* (Numerical study of the identification of the acoustic sources of a fan blade), thesis, Universte de Sherbrooke, QC, Canada, 2016.

[24] D. G. Krige. *A statistical approach to some mine valuation and allied problems on the Witwatersrand*, University of the Witwatersrand, Dissertation, 1951.

[25] J. Sacks, W. J. Welch, T. J. Mitchell and H. P. Wynn. Design and Analysis of Computer Experiments. *In Statistical Science 4-4*, S. 409-435, 1989.

[26] T. W. Simpson, J. D. Poplinski, P. N. Koch and J. K. Allen. Metamodels for computer-based engineering design: survey and recommendations, *Engineering With Computers*,

17(2): 129-150, 2001.

[27] G. Rennen. Subset selection from large datasets for kriging modeling, *Structural and Multidisciplinary Optimization*, 38(6): 545–569, 2009.

[28] G. Pistone and G. Vicario. Comparing and generating Latin hypercube designs in Kriging models, *AStA Advances in Statistical Analysis*, 94(4): 353–366, 2010.

[29] O. Sen, N. J. Gaul, K. K. Choi, G. Jacobs and H. S. Udaykumar. Evaluation of kriging based surrogate models constructed from mesoscale computations of shock interaction with particles, *Journal of Computational Physics*, 336: 235–260, 2017.

[30] S. Dubreuil, N. Bartoli, C. Gogu, T. Lefebvre, and J. M. Colomer. Extreme value oriented random field discretization based on an hybrid polynomial chaos expansion - Kriging approach, *Computer Methods in Applied Mechanics and Engineering*, 332: 540–571 2018.

[31] A. Cousin, H. Maatouk, and D. Rullière. Kriging of financial term-structures, *European Journal of Operational Research*, 255(2), 631–648, 2016.

[32] R. Mukesh, K. Lingadurai and U. Selvakumar. Airfoil Shape Optimization based on Surrogate Model. *J. Inst. Eng. India Ser. C* 99, 1-8 2018.

[33] J.-C. Jouhaud , P. Sagaut and B. Labeyrie. A Kriging Approach for CFD/Wind-Tunnel Data Comparison, *J. Fluids Eng*. 128(4): 847-855, 2006.

[34] Kalman J. Grunwald and Kenneth W. Goodson, Isolated shrouded-Propeller Configuration for Angles of Attack from -10º to 110º, NASA TN D-995,1962.

A MULTIFIDELITY AERODYNAMIC SURROGATE MODEL IMPLEMENTATION FOR OPTIMIZATION OF A NONPLANAR LIFTING SURFACE

Berkay Pirlepeli[1], Melike Nikbay[2] and Konstantinos Kontis[3]

1: Faculty of Computer and Informatics Engineering
Istanbul Technical University
34467
pirlepeli18@itu.edu.tr, http://www.itu.edu.tr

2: Professor of Aerospace Engineering
Faculty of Aeronautics and Astronautics
Istanbul Technical University
34467
nikbay@itu.edu.tr, http://www.itu.edu.tr

3: Professor of Aerospace Engineering
School of Engineering
University of Glasgow
James Watt South Building
Glasgow, G12 8qq
kostas.kontis@glasgow.ac.uk, https://www.gla.ac.uk

Abstract. *As the requirements for green aviation technologies emerge, improving aerodynamic and structural performance of the lifting surfaces is beneficial to reduce costs and environmental pollution. Novel wing shapes such as non-planar lifting system configurations promise a significant improvement of aerodynamic efficiency by reducing lift-induced drag and consequently increasing aerodynamic efficiency for low-speed flight conditions in aircraft design. In this study, an optimal design study for a non-planar wing based on the planar SACCON configuration has been performed using a multi-fidelity surrogate model. To investigate the design space thoroughly and capture the sensitivities of the design variables, aerodynamic analyses are conducted with a low fidelity vortex lattice method on a large set of samples which are generated by the Latin Hypercube Sampling method. High fidelity prediction of the induced drag is obtained with Reynolds Averaged Navier Stokes (RANS) equations by using OpenFOAM solver. As the number of optimization parameters is high and RANS simulations are computationally expensive, a remedy for the optimization process is needed. Thus, a co-Kriging aerodynamic surrogate model is generated with low fidelity and high fidelity analyses by reducing the number of high fidelity CFD analyses efficiently.*

Keywords: non-planar wings, induced drag, multifidelity, co-Kriging, surrogate model, SACCON

Berkay Pirlepeli[1], Melike Nikbay[2] and Konstantinos Kontis[3]

1 INTRODUCTION

The aviation industry forecasts a fast growth in the next decade as a consequence of which global fuel consumption is also expected to increase significantly in accordance with this trend. Increasing fuel consumption causes environmental impacts on the ecosystem and economic impacts on the aviation industry. As the requirements for green aviation technologies emerge, improving the aerodynamic and structural performance of air vehicles is beneficial to reduce costs and environmental pollution. The main technology necessary for reduction of aviation fuel consumption is through increasing the aerodynamic efficiency of air vehicles. As one of the aerodynamic design techniques, nonplanar wingtip devices increase aerodynamic efficiency of conventional planar lifting surfaces by reducing induced drag forces around wings [1].

The pressure gradient at the wingtip of a planar lifting surface generates a vortex induced drag force on the surface as a result of which aerodynamic efficiency decreases. In literature, a variety of nonplanar wingtip devices have been proposed to improve aerodynamic efficiency of wings by reducing the induced drag. Considering aerodynamic and geometric properties of nonplanar wing systems, Kroo [2] determined four main categories; multiple-wing designs, closed lifting systems, tip devices, and nonlinear aerodynamic concepts. Fig.1 shows different types of nonplanar wing configurations with their span efficiencies for fixed total lift and span. Span efficiency which is defined by the ratio of the induced drag of a planar wing to that of a nonplanar wing is an indicator for theoretical aerodynamic efficiency for a nonplanar wing configuration.
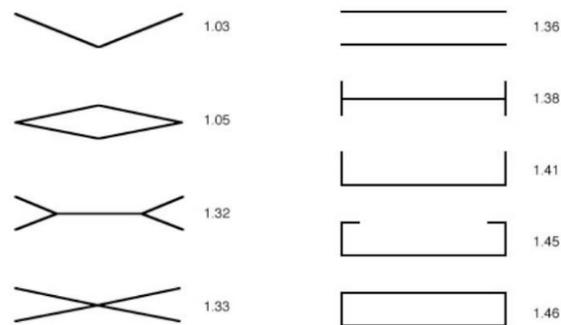
Figure 1: Theoretical span efficiency of nonplanar wing configurations. [2]

Experimental work of Whitcomb concluded that a winglet device compared to a planar wing provides a 9 percent increase in aerodynamic efficiency with 20 percent reduction in the induced drag at high subsonic speeds [3]. Andrews and Perez [4] investigated the performance of box-wing and traditional wing designs, and it was concluded that box-wing configurations were better than conventional planar wing designs in terms of aerodynamic performance. An aerostructural optimization was performed by Jansen et al. [5] for nonplanar wing systems coupling the panel method and the FEM method. The work concluded that enclosed surfaces such as box-wing or joined wing were optimum designs if wing systems were examined only aerodynamically. According to the work of Suresha et al. [6], C-wings were more efficient compared to planar wings in terms of aerodynamic performance for a certain range of angle of attacks.

In this study, firstly, a modified version of the SACCON configuration; a planar blended

Berkay Pirlepeli[1], Melike Nikbay[2] and Konstantinos Kontis[3]

wing–body with 53° low leading edge sweep configuration is selected as a baseline model. An aerodynamic optimization is carried out by adding nonplanar wingtip features to the baseline main wing geometry for a fixed span of the nonplanar wing. To overcome the computational burden during optimization procedure, a multi-fidelity surrogate model based on the co-Kriging method is employed by using a low-fidelity VLM solver and also a high-fidelity Reynolds Averaged Navier Stokes (RANS) solver.

2 MODEL DESCRIPTION

2.1 Geometry Description and Flow Conditions

The baseline planar wing geometry is based on the SACCON configuration with 53° sweep angle [7]. The baseline wing is composed of three parts which are the fuselage, the mid-section and the tip-section as shown in Fig.2. The dimensions of the planar wing is given in Tab.1. In the root section, a NACA 64012 airfoil is used and NACA 64008 airfoils are used along the span.
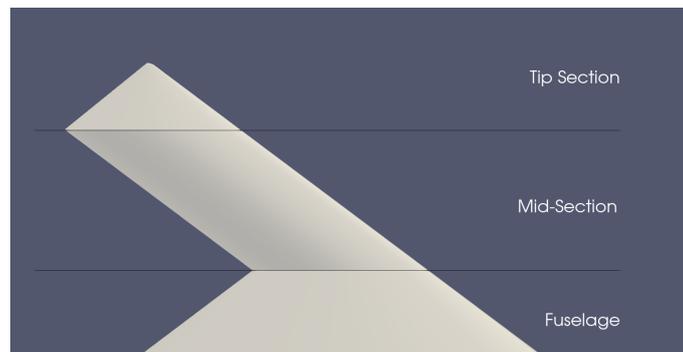
Figure 2: Planar wing configuration.

Table 1: Planar wing dimensions

Semi span	0.769 [m]
Root Chord	1.0608 [m]
Cref	0.479 [m]
Xcg	0.514 [m]

The nonplanar wing configuration has two additional sections, first and second sections, compared to the baseline planar wing geometry (Fig.3). The fuselage and the midsection of the nonplanar wing have the same dimensions with the baseline geometry. The parametric nonplanar wing model is generated with a parametric vehicle design generation tool, OpenVSP which is developed by NASA Langley Research Center [8]. The design variables are shown in Tab.2 and in Fig.4. The first section shown in Fig.4, ensures a smooth transition between the tip section and the second section.

The current study is carried out at a single design point for the flow conditions shown in Tab.3. As the Mach number is very low in the subsonic range, the incompressible flow assumption is made.

Berkay Pirlepeli[1], Melike Nikbay[2] and Konstantinos Kontis[3]
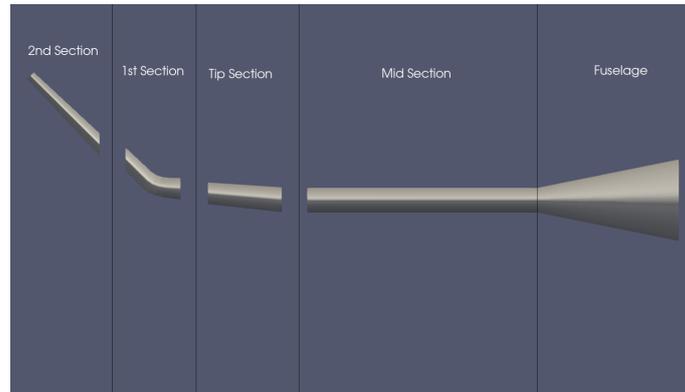
Figure 3: Nonplanar wing configuration.

Table 2: Design Parameters

Parameter	Description
h	2nd section span
c_0	tip section tip chord length
c_0	2nd section tip chord length
d_0	tip section dihedral angle
d_1	2nd section dihedral angle
Λ_0	1st section sweep angle
Λ_1	2nd section sweep angle
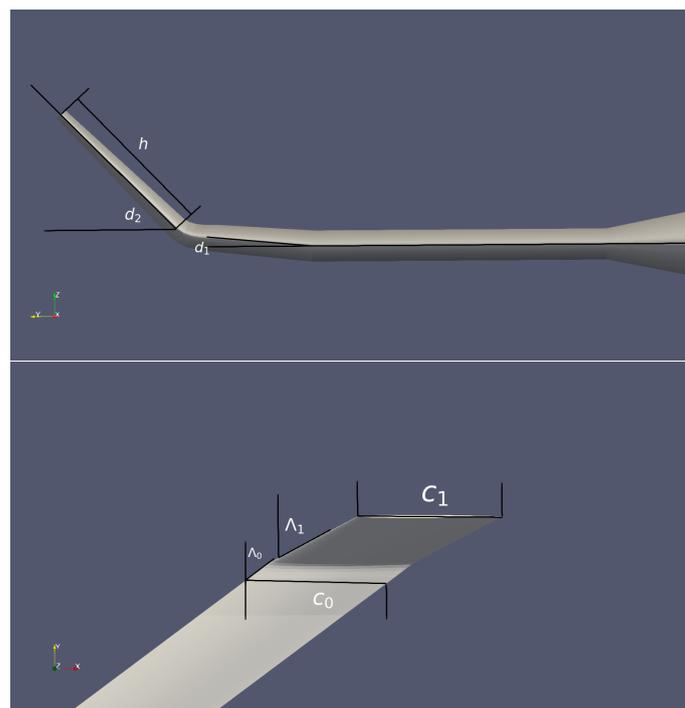
Figure 4: Nonplanar wing design parameters.

Berkay Pirlepeli[1], Melike Nikbay[2] and Konstantinos Kontis[3]

Table 3: Flow conditions

Mach	0.145	
Altitude	0	[m]
Dynamic Pressure	1488.68	$[\frac{kg}{ms^2}]$
Reynolds Number	1.5E-06	

2.2 Numerical Flow Model

In this study, aerodynamic performances of variable wing designs are evaluated using two different computational flow solvers with different fidelities. The low fidelity aerodynamic analysis methods are suitable to explore the design parameters space within the feasible design space determined by the constraints. Here, low fidelity analyses are conducted using a linear vortex lattice method (VLM) solver called VSPAERO developed by David Kinney at NASA Ames Research Center. This method assumes that the flow is incompressible, inviscid and the thickness of the geometry is neglected. The grid is generated on the reduced planform geometry which is obtained from the 3D model.

For high fidelity analysis, a steady, incompressible Reynolds Averaged Navier-Stokes (RANS) solver, simpleFOAM [9], is used to predict aerodynamic performance of the nonplanar wing. The solver uses the Semi-Implicit Method for Pressure-Linked Equations (SIMPLE) algorithm [10] to solve the continuity and momentum equations given in Eq.(1) where u is the velocity vector, p is the pressure, S_u are the source terms and R is the stress tensor [9].

$$\nabla.\mathbf{u} = 0 \tag{1}$$
$$\nabla(\mathbf{u} \otimes \mathbf{u}) - \nabla\mathbf{R} = -\nabla p + \mathbf{S}_u$$

The incompressibility assumption is pursued in the simulations since the flow is low speed subsonic. The hexagonal cell dominated numerical grid is generated using Snappy-hexmesh. To capture flow fields accurately, sensitive areas such as the boundary layer and wing tip have finer cell sizes. The turbulence fluctuations are modeled with the Spalart Allmaras (SA) turbulence model which is a one-equation model Eq.(2) that solves the transport equation for kinematic eddy turbulent viscosity $\tilde{\nu}$ which is computed from Eq.(3) . The SA model is a relatively computationally cheaper model and it provides accurate results for wall bounded applications for solving the transport equation without calculating a length scale for eddy viscosity. The function f_{v1} is calculated by Eq.(4) and χ is given by Eq.(5). The constants are $\sigma = 2/3$; $C_{b1} = 0.1355$; $C_{b2} = 0.622$; $\kappa = 0.41$; $C_{w1} = C_{b1}/\kappa^2 + (1 + C_{b2})/\sigma$; $C_{w2} = 0.3$; $C_{w3} = 2$; $C_{v1} = 7.1$; $C_{t1} = 1$; $C_{t2} = 2$; $C_{t3} = 1.1$; $C_{t4} = 2$ [11].

$$\frac{D}{Dt}(\tilde{\nu}) = \nabla(D_{\tilde{\nu}}\tilde{\nu}) + \frac{C_{b2}}{\sigma_{\nu_t}}|\nabla\tilde{\nu}|^2 + C_{b1}\tilde{S}\tilde{\nu}(1 - f_{t2}) - \left(C_{w1}f_w - \frac{C_{b1}}{\kappa^2}f_{t2}\right)\frac{\tilde{\nu}^2}{\tilde{d}^2} + S_{\tilde{\nu}} \tag{2}$$

Berkay Pirlepeli[1], Melike Nikbay[2] and Konstantinos Kontis[3]

$$\nu_t = \tilde{\nu} f_{v1} \tag{3}$$

$$f_{v1} = \frac{\chi^3}{\chi^3 + C_{v1}^3} \tag{4}$$

$$\chi = \frac{\tilde{\nu}}{\nu} \tag{5}$$

2.3 Surrogate Model and Multi-fidelity Optimization

To gather information about the design space and support selection of the design points to generate a surrogate model, a space filling design process is performed using the Latin Hypercube sampling technique (LHS). This technique divides the range of the each design variable into a number of samples and then generates randomly selected samples such that each sample will reside in one of the divided zone inside the range of the design variables [12].

The global sensitivity of the design parameters on the response functions is determined with the correlation matrix. Partial correlation coefficients are calculated to find the design parameters with strong linear relationship with the response functions. Given a multivariate data set $X = X_1, ..., X_n$ where n is number of variables and response Y, partial correlation coefficients measures relationship between X_k, while removing the effect of other variables X_i where $i = \{1, .., k-1, k+1, ..., n\}$. The partial correlation is a simple correlation of the residuals e_{X_k} and e_Y where e_{X_k} is the difference between X_k^j and the linear regression of X_k and X_i, e_Y is the difference between Y^j and the linear regression of Y and X_i where j denotes number of sample.

The surrogate model generation process is composed of four steps. Since the high fidelity analysis requires more computational resource, an initial sample set with low number of samples, is selected with the LHS method. The number of initial sample set is incremented such that the stratification of the design space in the initial set is maintained. This second set is used for low fidelity analysis. After evaluation of response functions, the data generated is used to create a multi-fidelity co-Kriging surrogate model.

The co-Kriging method combines the data with different fidelity, cheap and expensive, to generate a better model to represent the response functions [13]. Since the high fidelity analysis requires more computational resource, low number of randomly generated design points sets are evaluated using high fidelity simulations and these results are used to correct the high number of low fidelity results during the surrogate model generation process.

The co-kriging model is constructed using the formulation in [14]. Given multiple data sets X_e, y_e where y_e is high fidelity response at X_e and X_c, y_c where y_c is high fidelity response at X_c, the high fidelity model is approximated as :

$$Z_e(\mathbf{x}) = \rho Z_c(\mathbf{x}) + Z_d(\mathbf{x}) \tag{6}$$

where Z_e and Z_c are Gaussian process obtained from high fidelity and low fidelity data sets, ρ is a scalar factor and Z_d is Gaussian process of difference of two terms. the co-variance matrices have the form:

$$\text{cov}\left\{\mathbf{y}_c(\mathbf{X}_c), \mathbf{y}_c(\mathbf{X}_c)\right\} = \hat{\sigma}_c^2 \psi_c(\mathbf{X}_c, \mathbf{X}_c) \tag{7}$$

$$\text{cov}\left\{\mathbf{y}_e\mathbf{X}_e, \mathbf{y}_c\mathbf{X}_c\right\} = \rho\hat{\sigma}_c^2 \psi_c(\mathbf{X}_c, \mathbf{X}_e) \tag{8}$$

$$\text{cov}\left\{\mathbf{y}_e(\mathbf{X}_e), \mathbf{y}_e(\mathbf{X}_e)\right\} = \rho^2\hat{\sigma}_c^2 \psi_c(\mathbf{X}_e, \mathbf{x}^{n+1}) + \sigma_d^2\psi_d(\mathbf{X}_e, \mathbf{x}^{n+1}) \tag{9}$$

Berkay Pirlepeli[1], Melike Nikbay[2] and Konstantinos Kontis[3]

and the co-variance matrix is obtained as:

$$\mathbf{C} = \begin{pmatrix} \text{cov} \{\mathbf{y}_c(\mathbf{X}_c), \mathbf{y}_c(\mathbf{X}_c)\} & \text{cov} \{\mathbf{y}_e(\mathbf{X}_e), \mathbf{y}_c(\mathbf{X}_c)\} \\ \text{cov} \{\mathbf{y}_e(\mathbf{X}_e), \mathbf{y}_c(\mathbf{X}_c)\} & \text{cov} \{\mathbf{y}_e(\mathbf{X}_e), \mathbf{y}_e(\mathbf{X}_e)\} \end{pmatrix} \tag{10}$$

The correlations ψ_c and ψ_d is dependent on hyper-parameters ; $\theta_c, theta_d, p_c, p_d$. these hyper-parameters are determined using maximum likelihood estimation.

the new design point evaluated using the equation:

$$\hat{f}_e(\mathbf{x}) = \hat{\mu} + \mathbf{c}\mathbf{C}^{-1}(\mathbf{y} - \hat{\mu}) \tag{11}$$

where:

$$c = \begin{pmatrix} \hat{\rho}\hat{\sigma}_c^2\psi_c(\mathbf{X}_c, \mathbf{x}^{n+1}) \\ \hat{\rho}^2\hat{\sigma}_c^2\psi_c(\mathbf{X}_e, \mathbf{x}^{n+1}) + \hat{\sigma}_d^2\psi_d(\mathbf{X}_e, \mathbf{x}^{n+1}) \end{pmatrix} \tag{12}$$

and $\hat{\mu} = \frac{\mathbf{1}\mathbf{C}^{-1}\mathbf{y}}{\mathbf{1}\mathbf{C}^{-1}\mathbf{1}}$.

The constrained optimization problem is solved by using a gradient based method, Fletcher-Reeves conjugate gradient method [15]. Since the method is first order, it requires gradient of the response functions. Starting from an initial guess for x, the method finds new search direction s_n using the numerical gradient information $\nabla_x f(x_n)$ and β_n as shown in Eq.(13) and Eq.(14) proposed by [15]. The step size is calculated minimizing the function in Eq.(15). Lastly, the new design parameters are obtained with step size and direction Eq.(16) until process is converged.

$$\triangle x_n = -\nabla_x f(x_n)$$
$$s_n = \triangle x_n + \beta_n s_{n-1} \tag{13}$$

$$\beta_n = \frac{\triangle x_n^T \triangle x_n}{\triangle x_{n-1}^T \triangle x_{n-1}} \tag{14}$$

$$\alpha_n = argmin_\alpha f(x_n + \alpha s_n) \tag{15}$$

$$x_{n+1} = x_n + \alpha_n s_n \tag{16}$$

3 RESULTS

3.1 Planar Wing Aerodynamic Analysis

The aerodynamic performance of the planar wing is analyzed by conducting the low fidelity VLM and high fidelity RANS simulations at the design point given in Tab.3 for different angle of attacks. The results, obtained with two different methods VLM and RANS, are compared in terms of lift coefficient (C_L), drag coefficient (C_D), pitch moment (C_{My}) and lift to drag ratio (L/D) shown in Fig.5. The nonlinear stall region in Fig.5a can be seen in RANS simulation results for high angle of attacks while the VLM results increase linearly with angle of attack. Since the VLM is inviscid, viscous drag is predicted calculating the wetted area of the geometry which leads to under-prediction of the total drag which can be seen in Fig.5b. The maximum lift to drag ratio is obtained around 4 degrees of angle of attack which will be used as the single design point during the sensitivity study and optimization. The numerical grid and the z component of the velocity at a slice on the wing can be seen in Fig.6

Berkay Pirlepeli[1], Melike Nikbay[2] and Konstantinos Kontis[3]

(a) Lift Coefficient vs Angle of Attack

(b) Drag Coefficient vs Angle of Attack

(c) Pitch moment coefficient vs Angle of Attack

(d) Lift/Drag vs Angle of Attack
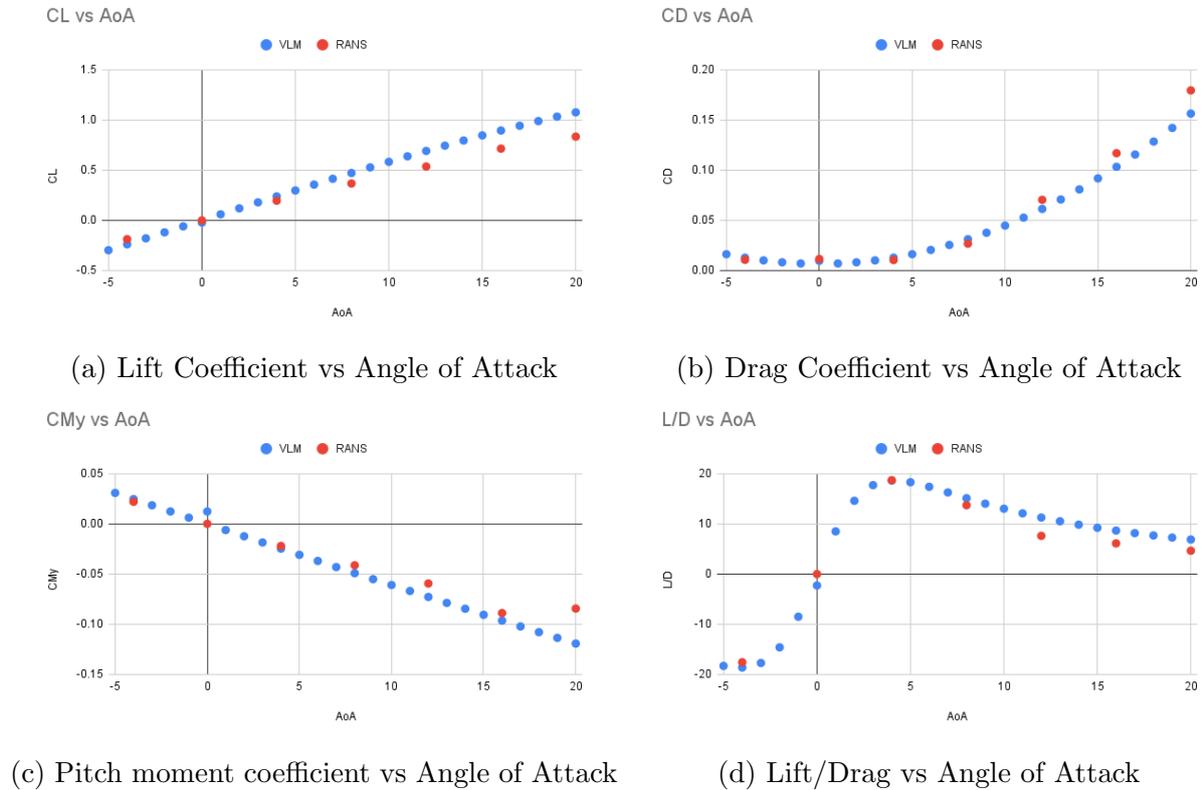
Figure 5: VLM and RANS Comparison
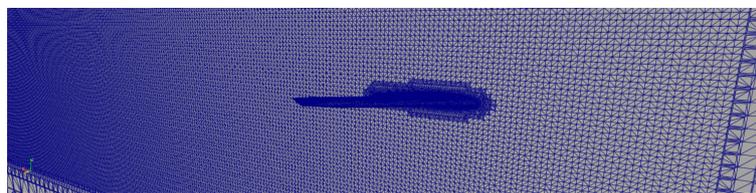
(a) Surface and domain mesh
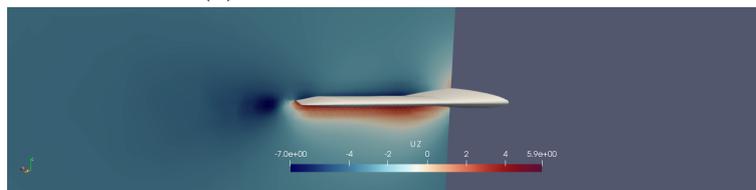
(b) Z component of velocity at 4 degree angle of attack

Figure 6: Numerical grid and velocity contours at 4 degrees of angle of attack

3.2 Sensitivity Study for a Nonplanar Wing

In order to get the information on how the changes in the design parameters affect the response functions, sensitivity information of the design variables is evaluated using randomly selected design points. The list of design variables with their upper bound, lower bound and initial values is given in Tab.4. Design space is sampled uniformly with LHS method and the generated points can be seen in Fig.7. A sample set of 280 points is evaluated using VLM simulations to get the aerodynamic performance of the parametric nonplanar wing shown in Fig.3.

Berkay Pirlepeli[1], Melike Nikbay[2] and Konstantinos Kontis[3]

Table 4: Design Parameters

Parameter	Description	Interval	Initial Value
h	2nd section span	[0.0,0.2]	0.1
c_0	tip section tip chord length	[0.1,1]	0.479
c_0	2nd section tip chord length	[0.1,1]	0.479
d_0	tip section dihedral angle	[0,10]	5
d_1	2nd section dihedral angle	[0,180]	90
Λ_0	1st section sweep angle	[40,60]	53
Λ_1	2nd section sweep angle	[40,60]	53
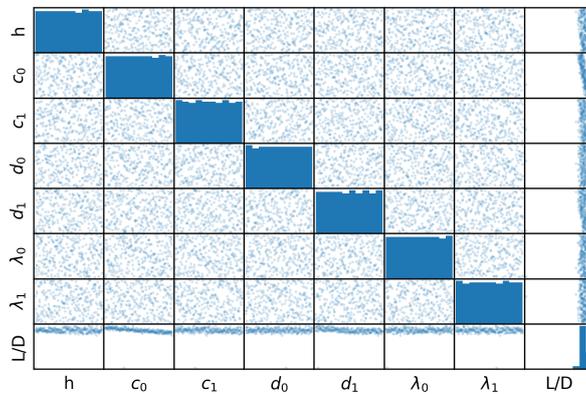
Figure 7: Scatter matrix plot of design variables and L/D

To identify the most important design variables for the nonplanar wing, a partial correlation matrix is generated. As it is seen in Fig.8, the most influential parameters, for both L/D and C_{My}, are c_0, c_1, d_1 and Λ_0. The dihedral of the tip section and the sweep of the second section are discarded from the design variables during the optimization process.

(a)   (b)
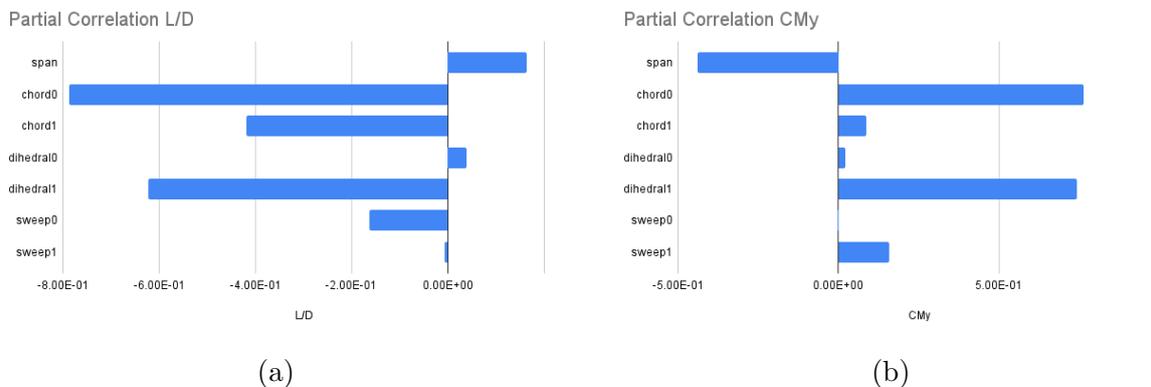
Figure 8: Partial Correlation Coefficients

Berkay Pirlepeli[1], Melike Nikbay[2] and Konstantinos Kontis[3]

3.3 Nonplanar Wing Multi-fidelity Surrogate Based Optimization

Five most influential variables are selected for the optimization process. The optimization formulation is shown in Eq.(17).

$$
\begin{aligned}
\text{minimize} \quad & f(\text{s}) = L/D(\text{s}) \\
\text{subject to} \quad & g_2(\text{s}) = C_{My} \leq C_{My_{ref}} \\
& g_3(\text{s}) = -C_L \leq -C_{L_{baseline}} \\
\text{w.r.t.} \quad & \text{s} = \{h, c_0, c_1, d_1, \Lambda_0\}
\end{aligned}
\tag{17}
$$

Here, 30 samples are generated for high fidelity flow analysis. The sample set with 30 points is incremented with randomly selected 280 design point such that stratification of the initial sample set is maintained. A total 310 design point is evaluated with low fidelity analysis. The surrogate model for L/D were cross validated with ten percent of the results with the errors reported in Tab.5.

Table 5: Surrogate model error for L/D

Quality metric	Value
Root mean squared	1.22984
Mean absolute value of residuals	0.335806
Max absolute value of residuals	3.5859

The baseline wing and the optimized nonplanar wing geometries are seen in figure 9. Next, Tab.6 shows the obtained aerodynamic coefficients for the baseline planar and the optimized nonplanar wings. Approximately 10 percent increase in the lift over drag ratio, compared to the original planar wing is obtained, using only aerodynamic analysis. Fig.10 show component of velocity in z-direction and pressures on a slice normal to x-direction on the baseline planar wing and optimized nonplanar wing . The optimized wingtip extension reduces the pressure gradient at the wingtip compared to the planar wing as shown in the Fig.11. The reduced pressure gradient at the tip of the wing improves the aerodynamic efficiency decreasing induced drag.

Table 6: Comparison of the results

	L/D	C_{My}	C_D
Baseline	18.70	-0.01896	0.010468
Optimized	20.47	-0.01483	0.0095153
Improvement[%]	9.5	-21.8	-9.1

Berkay Pirlepeli[1], Melike Nikbay[2] and Konstantinos Kontis[3]

Table 7: Optimized parameters

Parameter	Initial	Final
h	0.1	0.165
c_0	0.479	0.700
c_1	0.479	0.290
d_1	90	171
Λ_0	53	44.5
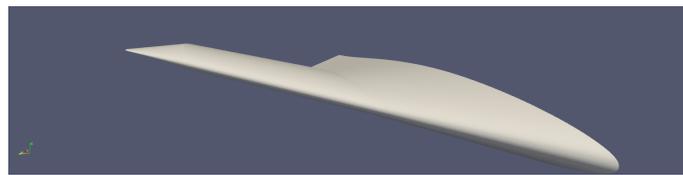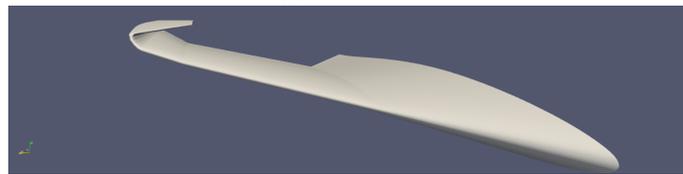
(a) Baseline

(b) Optimized

Figure 9: Baseline and Optimized geometries.
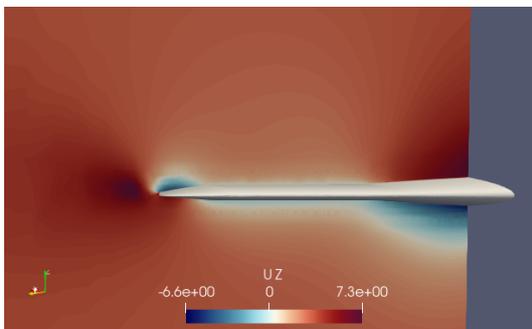
(a) Baseline
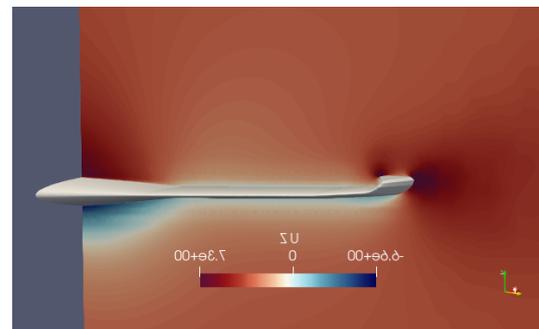
(b) Optimized

Figure 10: Baseline and optimized wing, z component of velocity

Berkay Pirlepeli[1], Melike Nikbay[2] and Konstantinos Kontis[3]

(a) Baseline   (b) Optimized
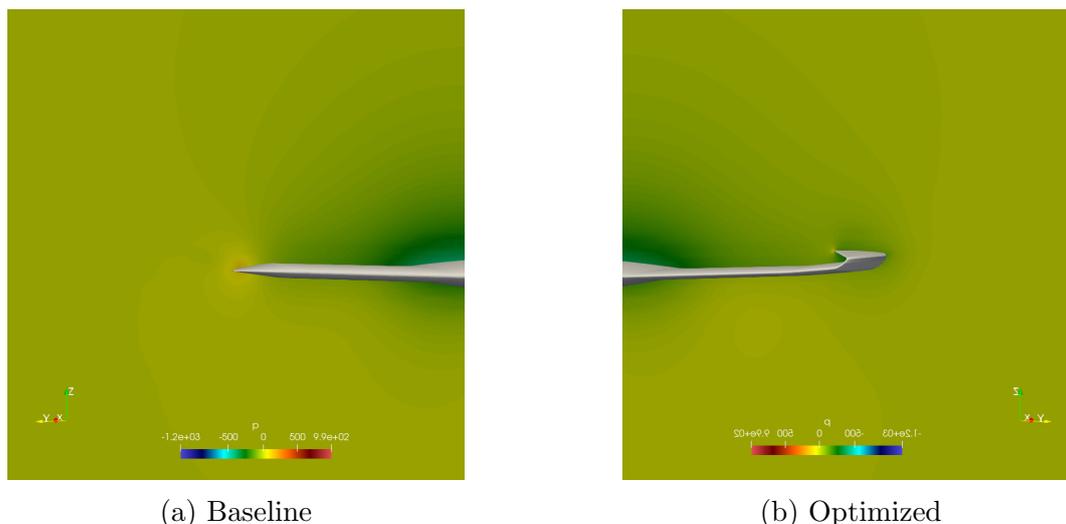
Figure 11: Pressure on a slice normal to the x-direction

4   CONCLUSIONS

In this work, a nonplanar wing extension is designed on a low sweep angle lambda wing based on the SACCON geometry. In the first part the baseline geometry performance is evaluated using both high and low fidelity solvers. After the sensitivity analysis, the initial of design parameter space dimension is reduced eliminating the less important 2 parameters. Lastly a multifidelity surrogate based optimization is performed. A new design with higher aerodynamic efficiency is obtained. The optimized wing configuration has converged to a C-wing type nonplanar wing reducing the velocity gradient on the wingtip the aerodynamic efficiency increased by approximately %10 compared to the planar wing.

In the future work, a multidisciplinary optimization study planned to extend the contraints of the optimization including aero-structural and aero-elastic interactions.

REFERENCES

[1] I. Kroo. Drag due to lift: Concepts for prediction and reduction. *Annual Review of Fluid Mechanics*, 33(1):587–617, 2001. doi:10.1146/annurev.fluid.33.1.587. URL https://doi.org/10.1146/annurev.fluid.33.1.587.

[2] I. Kroo. Nonplanar wing concepts for increased aircraft efficiency. In *VKI lecture series on Innovative Configurations and Advanced Concepts for Future Civil Aircraft*, 2005.

[3] R. T. Whitcomb. A design approach and selected wind-tunnel results high subsonic speeds for wing-tip mounted winglets. Technical report, NASA, 1976.

[4] R. P. S.A. Andrews. Comparison of box-wing and conventional aircraft mission performance using multidisciplinary analysis and optimization. *Aerospace Science and Technology*, 2018.

[5] J. R. R. A. M. P. W. Jansen R. E. Perez. Aerostructural optimization of nonplanar lifting surfaces. *Journal of Aircraft 47*, 5:1490–1503, 2010.

Berkay Pirlepeli[1], Melike Nikbay[2] and Konstantinos Kontis[3]

[6] K. R. C. Suresh, V. Paramaguru. Aerodynamic performance analysis of a non-planar c-wing using cfd. *Aerospace Science and Technology*, 40:56–61, 2015.

[7] A. S. Thomas D.Loeser, Dan D.Vicroy. Saccon static wind tunnel tests at dnw-nwb and 14×22 nasa larc. *28th AIAA Applied Aerodynamics Conference*, 2010.

[8] *OpenVSP, OpenVSP is a parametric aircraft geometry tool*, 2021. URL `http://openvsp.org/`.

[9] *OpenFOAM, The Open Source CFD Toolbox, User Guide*, 2021. URL `https://nav.dl.sourceforge.net/project/openfoam/v2106/UserGuide.pdf`.

[10] L. S. Caretto, A. D. Gosman, S. V. Patankar, and D. B. Spalding. Two calculation procedures for steady, three-dimensional flows with recirculation. In H. Cabannes and R. Temam, editors, *Proceedings of the Third International Conference on Numerical Methods in Fluid Mechanics*, pages 60–68, Berlin, Heidelberg, 1973. Springer Berlin Heidelberg. ISBN 978-3-540-38392-5.

[11] S. R. A. P. R. Spalart. One-equation turbulence model for aerodynamic flows. *Recherche Aerospatiale*, 1:5–21, 1994.

[12] M. D. McKay, R. J. Beckman, and W. J. Conover. A comparison of three methods for selecting values of input variables in the analysis of output from a computer code. *Technometrics*, 21(2):239–245, 1979. ISSN 00401706. URL `http://www.jstor.org/stable/1268522`.

[13] A. K. J. Alexander I J Forrester, András Sóbester. Engineering design via surrogate modelling. *Journal of Aircraft 47*, 2008.

[14] A. Forrester, A. Sobester, and A. Keane. Multi-fidelity optimization via surrogate modelling. *Proc. R. Soc. A*, 463:3251–3269, 12 2007. doi:10.1098/rspa.2007.1900.

[15] R. Fletcher and C. M. Reeves. Function minimization by conjugate gradients. *The Computer Journal*, 7(2):149–154, 01 1964. ISSN 0010-4620. doi:10.1093/comjnl/7.2.149. URL `https://doi.org/10.1093/comjnl/7.2.149`.

P.N. Mishra and A. Gogulapati

TOPOLOGY OPTIMIZATION OF FULLY COUPLED AEROTHERMOELASTIC SYSTEM

Pankil N. Mishra[1] and Abhijit Gogulapati[2]

1: Ph.D. Candidate
Department of Aerospace Engineering
Indian Institute of Technology Bombay
IIT Bombay, Powai, Mumbai 400 076, Maharashtra, India
pankilmishra@iitb.ac.in

2: Assistant Professor
Department of Aerospace Engineering
Indian Institute of Technology Bombay
IIT Bombay, Powai, Mumbai 400 076, Maharashtra, India
abhijit@aero.iitb.ac.in

Abstract. *Topology optimization of a coupled aerothermoelastic system is of interest here. The aerothermoelastic system is a simplified model of the panel in a hypersonic flow. The aerothermal loads are computed using a combination of piston theory and Eckert's reference enthalpy approaches. A thermal buckling metric is developed which is used as the objective function for the optimization study. The topology optimization is performed using the Solid Isotropic Material with Penalization (SIMP) model. Results are shown for various types of admissible design domain with thermal boundary conditions on different surfaces of the panel.*

Keywords: Topology optimization, aerothermoelastic system, coupled aerothermal loads, SIMP, fluid-thermal-structural interaction

Pankil N. Mishra and Abhijit Gogulapati

1 INTRODUCTION

A study of compliant aerospace structures subjected to the simultaneous application of aerodynamic pressure and thermal loads is a critical consideration in the design and development of hypersonic vehicles that operate in extreme environments. Numerous studies [1–3] have highlighted that the feedback between the aerothermal loads and the structural response, referred to as fluid-thermal-structural interactions (FTSI) or aerothermoelasticity, cannot be neglected when determining the static and dynamic response of structures in such settings.

Here, feedback refers to the situation in which aerothermal loads drive the structural response, which in turn leads to a modification of both pressure and heat flux acting on the surface. In particular, the coupling between the structural response and flow induced heat flux introduces a path dependency to the evolution of the structural response that cannot be adequately captured by ignoring this coupling. In this context, one-way coupling refers to the situation in which the aerothermal loads drive the structural response; however, the impact of structural response on aerodynamic pressure or heat flux or both is ignored. Two-way coupling refers to the fully coupled scenario described previously.

Topology Optimization (TO) techniques, which integrate seamlessly with finite element modeling and analysis, offer mathematically rigorous search strategies to determine mass or stress minimized structures for specific applications [4, 5]. Their application to structures in multi-disciplinary environments has also been explored [6–9]. Despite the large body of published work on aerothermoelasticity and TO, the application of TO to aerothermoelastic systems has received limited attention [10–14].

Effort towards the development of an optimization framework in which a transient adjoint sensitivity analysis approach was used to identify optimal configuration of a fully coupled aerothermoelastic system is described in [10]. The aerothermoelastic solver was obtained by coupling finite element based structural, compressible flow, and transient thermal solver in a monolithic manner. The author however notes that additional work is required before meaningful results can be obtained. A density approach based on SIMP (Solid Isotropic Material with Penalization) methodology was used to optimize panels for buckling metric and heated panels for the flutter metric in [11]. The linear piston theory was used to couple the aerodynamic pressure and panel response. The structural response was determined using a linear finite element model. The temperature conditions on the top and bottom surface of the panel were prescribed, i.e. interactions between the thermal loads and structural response were ignored. It concluded that flutter and thermal buckling were competing objectives. A similar study was carried out by applying Level-set methodology of topology optimization on the aerothermoelastic model in [12]. This study included only static aeroelastic loads and a flutter constraint. An evolutionary topology optimization study with stress minimization as the objective was conducted in [13]. In this study, the coupling involved updating the boundary layer velocities due to the structural deformations. The effect of material degradation due to temperature was also incorporated. The aerodynamic and thermal loads were determined using the supersonic panel method and conjugate heat analysis, respectively. Reference [14] describes a preliminary effort towards the optimization of steady state aerothermoelastic response using gradient based approach. The aerothermoelastic response was computed by coupling a flexible supersonic wedge to a fluid solver.

It is evident from the review of literature above that TO of fully coupled aerothermoe-

lastic systems remain unexplored. Note that such a study has not been considered prior to this work. The specific objectives of the current study are to investigate the following in the context of a coupled aero-structural heating problem:

1. TO for improvement of the thermal buckling metric.

2. Impact of constraints and admissible design domain on optimal topology for heated structures.

The remainder of the paper is organized as follows: section 2 talks about the panel configuration, finite element solvers and various models required to carry out the topology optimization, section 3 gives an insight into the methodology used for topology optimization, section 4 consists of the topology optimization results for various case studies and their discussion and section 5 gives the conclusions from the present study.

2 CONFIGURATION AND MODELLING

The structural system is a panel with length L and thickness h, as shown in Fig.1. The panel is assumed to be infinitely long in the third dimension. The L/h ratio is fixed as 25 to complete the study in a computationally feasible manner and to observe the changes in the internal topology of the panel. The panel geometric and material properties are provided in Tab.1. The top surface is subjected to a hypersonic flow conditions mentioned in Tab.2.
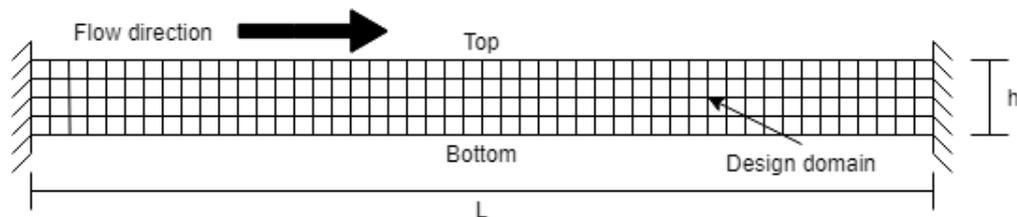
Figure 1: Panel geometry

Table 1: Panel geometric and material properties

Property	Value
Length	0.125 m
Thickness	0.005 m
Young's Modulus	103 GPa
Density	4520 kg/m^3
Poisson's Ratio	0.30
Coefficient of thermal expansion	4.7x10^{-6} /deg C
Conductivity	7.1 W/m-K
Specific heat	463.0 J/kg-K

The aerothermoelastic response is obtained by coupling finite element based structural and thermal solvers with pressure and heat loads computed using piston theory and Eckert's reference enthalpy approaches, respectively. The description of various models is provided in the following subsections.

Pankil N. Mishra and Abhijit Gogulapati

Table 2: Flow conditions

Property	Value
Free-stream Mach No. (M_∞)	7.0
Altitude	30.0 km
Free-stream Pressure (P_∞)	1090 Pa
Free-stream Temperature (T_∞)	227 K
Upstream Transition to Turbulence	1.0 m

2.1 Aerodynamic Pressure Model

The aerodynamic pressure p_a at a point along the top surface of the panel is calculated using the third order piston theory given by:

$$
\begin{aligned}
p_a =& 2 \cdot \frac{q_\infty}{M_\infty} \cdot \left[\left(\frac{1}{U_\infty} \cdot \frac{\partial w}{\partial t} + \frac{\partial w}{\partial x} \right) + M_\infty \cdot \frac{\gamma + 1}{4} \cdot \left(\frac{1}{U_\infty} \cdot \frac{\partial w}{\partial t} + \frac{\partial w}{\partial x} \right)^2 \right. \\
&+ \left. M_\infty \cdot \frac{\gamma + 1}{12} \cdot \left(\frac{1}{U_\infty} \cdot \frac{\partial w}{\partial t} + \frac{\partial w}{\partial x} \right)^3 \right]
\end{aligned}
\tag{1}
$$

where, q_∞ is the dynamic pressure, w is the panel displacement in transverse direction, x is the free-stream direction along the flow as shown in Fig.1 and t is time. Note that the undeformed configuration of the panel is parallel to the free-stream flow.

2.2 Aerodynamic Heating Model

The thermal loads generated due to the flow over the panel's top surface are estimated using the Eckert's reference enthalpy method [15]. The Eckert's reference enthalpy is calculated using Eq.(2), where H_e, H_w and H_{aw} are enthalpy at the edge of boundary layer, the wall and the adiabatic wall condition, respectively.

$$
H^* = H_e + 0.50 \cdot (H_w - H_e) + 0.22 \cdot (H_{aw} - H_e)
\tag{2}
$$

The calculation of the reference enthalpy is an iterative procedure. Note that the coupling between panel deformation and thermal load is incorporated by updating the edge-of-boundary-layer pressure using piston theory, mentioned in section 2.1.

The thermal load associated with the aerodynamic flow is determined from the Eq.(3), where U_e is the velocity of the flow at the edge-of-boundary-layer, St^* is the Stanton number and ρ^* is the density of the flow at the reference condition.

$$
Q_{aero} = St^* \cdot \rho^* \cdot U_e \cdot (H_{aw} - H_w)
\tag{3}
$$

2.3 Finite Element Models

In-house finite element code has been developed for the present case study. The panel is discretized using bi-linear Q4 finite elements for both the structural (two displacement degrees of freedom per node) and thermal (one temperature degree of freedom per node) solver discussed below. Note that consistent matrices are used wherever required and the finite element mesh is identical for both the solvers. More information about the finite element procedure and analysis is available in [16].

2.3.1 Thermal Solver

The temperature of the panel is determined by using the finite element formulation of the heat transfer governing equation, mentioned below:

$$\mathbf{C_T} \cdot \dot{\mathbf{T}} + \mathbf{K_T} \cdot \mathbf{T} = \mathbf{R_T} \tag{4}$$

where, $\mathbf{C_T}, \mathbf{K_T}$ and $\mathbf{R_T}$ are the global heat capacity, thermal conductivity matrices and thermal load vector, respectively. The transient thermal analysis is performed using Eq.(5), a *Backward difference* scheme. The thermal load vector $\mathbf{R_{Tn}}$ is computed based on thermal boundary conditions specified for the panel. Note that a staggered scheme is used with respect to the calculation of thermal heat load vector in Eq.(5).

$$\left(\frac{\mathbf{C_T}}{\mathbf{\Delta t_{AT}}} + \mathbf{K_T} \right) \cdot \mathbf{T_{n+1}} = \frac{\mathbf{C_T}}{\mathbf{\Delta t_{AT}}} \cdot \mathbf{T_n} + \mathbf{R_{Tn}} \tag{5}$$

where, $\mathbf{\Delta t_{AT}}$ is the thermal time-step. The thermal boundary condition along the top surface includes aerodynamic heat load calculated using section 3 and radiation heat load using Eq.(6). The thermal radiation is calculated by assuming the upper surface as non-black, diffuse and enclosed by the environment. The environment temperature is assumed to be constant at 300 K. Adiabatic boundary conditions are assumed for remaining surfaces of the panel, unless stated otherwise.

$$Q_{rad} = \sigma \cdot \epsilon \cdot (T_w^4 - T_{env}^4) \tag{6}$$

2.3.2 Structural Solver

The temperature of an element T_e, is calculated using the average of 4 nodal temperatures extracted from the vector $\mathbf{T}$ at a given time step. The element temperature is assumed to be spatially uniform within each finite element e. The elastic stress generated within each element, due to thermal expansion is given by:

$$\sigma_{0_e} = \frac{-\alpha \cdot (T_e - T_{ref}) \cdot E_e}{1 - \nu} \cdot \begin{bmatrix} 1 \\ 1 \\ 0 \end{bmatrix} \tag{7}$$

where, α, ν and E_e are the coefficient of thermal expansion, the Poisson's ratio and the elastic modulus of the element, respectively. They are assumed to be independent of the temperature.

Note that the stresses produced due to the thermally induced displacements in the panel are not considered in the current study. Thus, the geometric stress stiffness matrix $\mathbf{K_\sigma}$ of the structure is then obtained using:

$$\mathbf{K_\sigma} = \sum_{e=i}^{N} \mathbf{G_e^T} \cdot \mathbf{S_e(\sigma)} \cdot \mathbf{G_e} \cdot \mathbf{V_e} \tag{8}$$

where, $\mathbf{G_e}$, $\mathbf{V_e}$ and $\mathbf{S_e}$ are the shape differentiation matrix, volume of the element and matrix reordering of the element stress $\boldsymbol{\sigma_{0_e}}$, respectively.

Pankil N. Mishra and Abhijit Gogulapati

2.4 Thermal Buckling Metric

The stability of the panel in terms of thermal buckling is obtained from the eigen-problem defined below:

$$\{(\mathbf{K} + \mathbf{K}_{\boldsymbol{\sigma}}) - \lambda_{\mathbf{b}} \cdot \mathbf{I}\} \cdot \boldsymbol{\phi_b} = \mathbf{0} \tag{9}$$

where, $\mathbf{K}$ is the linear stiffness matrix and terms in parentheses comprise of a net stiffness matrix $\mathbf{K_{net}}$. The eigenvector $\boldsymbol{\phi_b}$ is associated with the bth eigenvalue λ_b of the net stiffness matrix.

Thermal buckling means loss of stability of an equilibrium configuration due to thermal loads. In mathematical terms, $\mathbf{K_{net}}$ becomes singular i.e. the lowest eigenvalue λ^* obtained from Eq.(10) becomes zero.

$$\lambda^* = min(\lambda_b) \tag{10}$$

2.5 Solid Isotropic Material with Penalization (SIMP)

The discreteness inherent in the topology optimization problem is avoided by using a solid-void interpolation scheme. In density based SIMP method, the design domain is discretized into finite elements. Each element is assigned a relative density x_e, which is a continuous design variable, allowed to vary between 0 (void) to 1 (solid).

The aim is to determine an optimal solid-void distribution of given material over the admissible design domain. The material property relations used in the current study based on the SIMP model are discussed below, where the lower bound on the design variable is changed from 0 to x_{min}. The elastic modulus E_e of an element is obtained using:

$$E_e = x_e \cdot E_0 \tag{11}$$

where, E_0 is the elastic modulus for fully solid material. Similarly, the global mass matrix $\mathbf{M}$ and heat capacity matrix $\mathbf{C_T}$ of the panel are computed using Eq.(12) and Eq.(13), respectively.

$$\mathbf{M} = \sum_{\boldsymbol{e}}(x_e \cdot \mathbf{M_e}) \tag{12}$$

$$\mathbf{C_T} = \sum_{\boldsymbol{e}}(x_e \cdot \mathbf{C_{Te}}) \tag{13}$$

where, $\mathbf{M_e}$ and $\mathbf{C_{Te}}$ are the element mass matrix and element heat capacity matrix for fully solid material. The global thermal conductivity matrix $\mathbf{K_T}$ of the panel is obtained using:

$$\mathbf{K_T} = \sum_{\boldsymbol{e}}(x_e^3 \cdot \mathbf{K_{Te}}) \tag{14}$$

where, $\mathbf{K_{Te}}$ is the element thermal conductivity matrix for the fully solid material. The linear stiffness matrix $\mathbf{K}$ of the panel is assembled using:

$$\mathbf{K} = \sum_{\boldsymbol{e}}(\frac{x_{min} + (1 - x_{min}) \cdot x_e^3}{1 - \nu^2} \cdot \mathbf{K_e}) \tag{15}$$

Pankil N. Mishra and Abhijit Gogulapati

where, $\mathbf{K_e}$ is the element stiffness matrix for the fully solid material, computed using a unit depth of the structure in the third dimension.

3 SENSITIVITY ANALYSIS

The design derivatives needed for the topology optimization problem are calculated analytically. The thermal buckling metric λ^* is used as the objective function for the topology optimization problem discussed in the next section. The adjoint-based sensitivity analysis is presented below.

The linear stiffness matrix $\mathbf{K}$ is dependent directly on the element densities $\mathbf{x}$ while the geometric stress stiffness matrix is dependent on the nodal temperatures and element stresses as well. The total derivative of $\mathbf{K}_\sigma$ matrix is:

$$\frac{d\mathbf{K}_\sigma}{d\mathbf{x}} = \frac{\partial \mathbf{K}_\sigma}{\partial \mathbf{x}} + \frac{\partial \mathbf{K}_\sigma}{\partial \mathbf{T_x}} \cdot \frac{\partial \mathbf{T_x}}{\partial \mathbf{x}} \tag{16}$$

The direct dependency on $\mathbf{x}$ and on the unknown nodal temperatures $\mathbf{T_x}$ comes from the computation of $\boldsymbol{\sigma_{0_e}}$ in Eq.(7). The nodal temperatures at the $(n+1)^{th}$ time step are the unknown nodal temperatures $\mathbf{T_x}$ while the temperature calculated at the previous n^{th} time step are the known nodal temperatures $\mathbf{T_c}$. The derivative of Eq.(5) is:

$$\left(\frac{1}{\mathbf{\Delta t_{AT}}} \cdot \frac{\partial \mathbf{C_T}}{\partial \mathbf{x}} + \frac{\partial \mathbf{K_T}}{\partial \mathbf{x}} \right) \cdot \mathbf{T_x} + \left(\frac{\mathbf{C_T}}{\mathbf{\Delta t_{AT}}} + \mathbf{K_T} \right) \cdot \frac{\partial \mathbf{T_x}}{\partial \mathbf{x}} = \frac{1}{\mathbf{\Delta t_{AT}}} \cdot \frac{\partial \mathbf{C_T}}{\partial \mathbf{x}} \cdot \mathbf{T_c} + \frac{\partial \mathbf{R_{T_n}}}{\partial \mathbf{x}} \tag{17}$$

For the current study, the last term $\frac{\partial \mathbf{R_{T_n}}}{\partial \mathbf{x}}$ becomes zero because the thermal load vector at n^{th} time step is calculated using known nodal temperatures $\mathbf{T_c}$. Thus, the derivatives of the thermal buckling metric are:

$$\frac{d\lambda^*}{d\mathbf{x}} = \frac{(\boldsymbol{\phi_b})^T \cdot \left(\frac{\partial \mathbf{K}}{\partial \mathbf{x}} + \frac{\partial \mathbf{K}_\sigma}{\partial \mathbf{x}} + \frac{\partial \mathbf{K}_\sigma}{\partial \mathbf{T_x}} \cdot \frac{\partial \mathbf{T_x}}{\partial \mathbf{x}} \right) \cdot (\boldsymbol{\phi_b})}{(\boldsymbol{\phi_b})^T \cdot \mathbf{I} \cdot (\boldsymbol{\phi_b})}$$
$$+ (\boldsymbol{\beta_T})^T \cdot \left(\left(\frac{1}{\mathbf{\Delta t_{AT}}} \cdot \frac{\partial \mathbf{C_T}}{\partial \mathbf{x}} + \frac{\partial \mathbf{K_T}}{\partial \mathbf{x}} \right) \cdot \mathbf{T_x} + \left(\frac{\mathbf{C_T}}{\mathbf{\Delta t_{AT}}} + \mathbf{K_T} \right) \cdot \frac{\partial \mathbf{T_x}}{\partial \mathbf{x}} - \frac{1}{\mathbf{\Delta t_{AT}}} \cdot \frac{\partial \mathbf{C_T}}{\partial \mathbf{x}} \cdot \mathbf{T_c} \right) \tag{18}$$

The standard formulation for the derivative of an eigenvalue is used to compute the first term in Eq.(18). The second term is represents the multidisciplinary nature of the problem, where $(\boldsymbol{\beta_T})^T$ is an adjoint vector multiplied with an Eq.(17) that is exactly equal to zero. The adjoint vector $(\boldsymbol{\beta_T})^T$ is computed by collecting the terms that pre-multiply $\frac{\partial T_x}{\partial x}$:

$$\left(\frac{\mathbf{C_T}}{\mathbf{\Delta t_{AT}}} + \mathbf{K_T} \right) \cdot \boldsymbol{\beta_T} = \frac{(\boldsymbol{\phi_b})^T \cdot \frac{\partial \mathbf{K}_\sigma}{\partial \mathbf{T_x}} \cdot (\boldsymbol{\phi_b})}{(\boldsymbol{\phi_b})^T \cdot I \cdot (\boldsymbol{\phi_b})} \tag{19}$$

The design derivatives of the thermal buckling metric are finally obtained by substituting the adjoint vector $\boldsymbol{\beta_T}$ obtained from Eq.(19) into Eq.(18):

$$\frac{d\lambda^*}{d\mathbf{x}} = \frac{(\boldsymbol{\phi_b})^T \cdot \left(\frac{\partial \mathbf{K}}{\partial \mathbf{x}} + \frac{\partial \mathbf{K}_\sigma}{\partial \mathbf{x}} \right) \cdot (\boldsymbol{\phi_b})}{(\boldsymbol{\phi_b})^T \cdot \mathbf{I} \cdot (\boldsymbol{\phi_b})} + (\boldsymbol{\beta_T})^T \cdot \left(\frac{\partial \mathbf{C_T}}{\partial \mathbf{x}} \cdot \left(\frac{\mathbf{T_x} - \mathbf{T_c}}{\mathbf{\Delta t_{AT}}} \right) + \frac{\partial \mathbf{K_T}}{\partial \mathbf{x}} \cdot \mathbf{T_x} \right) \tag{20}$$

4 TOPOLOGY OPTIMIZATION METHODOLOGY

The analysis module consists of the computational models described in section 2. The analysis terminates either due to thermal buckling or due to completion of the stipulated simulation time, N_s seconds. The objective of the topology optimization problem is to maximize the thermal buckling metric λ^* obtained at the termination of the analysis module. Hypothetically, in simple terms the objective is to obtain a topology which never buckles for the given boundary conditions. The method of moving asymptotes (MMA) [17] is used as the optimizer to solve the topology optimization problem. The optimizer searches the design space using the sensitivity analysis performed in the 3.

Generally, a spatial filter is used on the design gradients to restrict the topology optimization. However, for a coupled and multi-modal design space the degradation in the gradient accuracy is detrimental for the optimization process. Thus, a density filter [18, 19] is used for the current study. Equation 21 is used to obtain the element densities $\mathbf{x}$ from the design variables $\tilde{\mathbf{x}}$ using the density filter $\mathbf{H}$.

$$\mathbf{x} = \mathbf{H} \cdot \tilde{\mathbf{x}} \tag{21}$$

The current study is inspired based on the work carried out in [11]. The mathematical formulation of the topology optimization problem considered here is shown below:

$$
\begin{aligned}
\text{Maximize} \quad & \lambda^* \\
\text{w.r.t.} \quad & \tilde{\mathbf{x}} \\
\text{subject to} \quad & \mathbf{v^T} \cdot \mathbf{x} \leq \mathbf{V}^* \\
& \tilde{\mathbf{x}_e} \in [\mathbf{x_{min}}, \mathbf{1}] \quad \mathbf{e} = \mathbf{1}, \ldots, \mathbf{N_e}
\end{aligned} \tag{22}
$$

where, V^* is the volume constraint on the element densities $\mathbf{x}$. A particular surface is considered as solid by prescribing certain portion of panel near that surface as solid (i.e. $x_e = 1.0$). Here, elements lying in the upper 10%, lower 5% and side 5% of the panel shown in Fig.1 are selected for the top, bottom and side surfaces, respectively.

A continuation method implemented in [11] is also used here. It leads the optimizer towards a topology consisting of either solid or void element. The initial radius is 15% of the panel thickness, which reduces by 2.5% each time the iterations converge within the specified tolerance. The optimization algorithm terminates either due to maximum number of iterations N_I or when the filter radius value equals to 1.0

5 RESULTS AND DISCUSSION

The MMA algorithm used here to solve the problem in Eq.(22) has a parameter *move*, which restricts the step size of the design variables. For each unique design domain and the boundary conditions applied on it, various case studies were solved for a range of *move* parameter values. Out of those many results did not converge properly due to very small or too large value of *move* parameter. Case study with optimal results are presented here.

The value of various parameters related to the topology optimization problem are given in Tab.3. Note that the flow is over the undeformed (flat) panel which means that effect of pressure load is not considered since the focus is on thermal-structural coupling.

The results presented below consist of two types of figure. Topology formation of the panel starting from iteration 0 and then after every 70 iterations till termination of the

Pankil N. Mishra and Abhijit Gogulapati

Table 3: Common parameters

Parameter	Value
Number of elements	1600
Max. number of iterations, N_I	700
Min. change	0.001
Volume fraction, V^*	0.350
Simulation time, N_s	3.0 seconds
Thermal time-step, Δt_{AT}	0.1 seconds
Reference temperature, T_{ref}	300 K

algorithm is presented in the first type. Objective function value and volume of the design domain with respect to the iterations is shown in another.

5.1 Case Study

The topology optimization problem Eq.(22) is solved for the following three types of design domain:

1. The top surface of the panel is fixed as solid - Case Study **A**

2. The top and bottom surface of the panel are fixed as solid - Case Study **B**

3. The top, bottom and side surface of the panel are fixed as solid - Case Study **C**

5.1.1 Case Study A

The top surface of the panel is fixed as solid while the rest constitutes the admissible design domain. There is only one type of problem in this case study:

1. Thermal load only on top surface - Case Study **A-I**

Thus, the thermal loads due to aerodynamic heating are considered on the top surface while adiabatic boundary conditions are assumed for rest of the surfaces. The topology formation of the panel for the case study A-I is shown in Fig.2. The convergence metrics for the optimization and the volume of the design domain are shown in Fig.3.

5.1.2 Case Study B

The top and bottom surfaces of the panel are fixed as solid while the rest constitutes the admissible design domain. This case study is divided into two type of problems:

1. Thermal load only on top surface - Case Study **B-I**

2. Thermal load only on top and bottom surfaces - Case Study **B-II**

Adiabatic boundary conditions are assumed on the remaining surfaces. The thermal load on the bottom surface in the case study B-II is an approximate cooling load meant to represent effect of the convective cooling. The topology formation of the panel for the case study B-I and B-II are shown in Fig.4 and Fig.6, respectively. The convergence metrics for the optimization and the volume of the design domain for case study B-I are shown in Fig.5.

Pankil N. Mishra and Abhijit Gogulapati
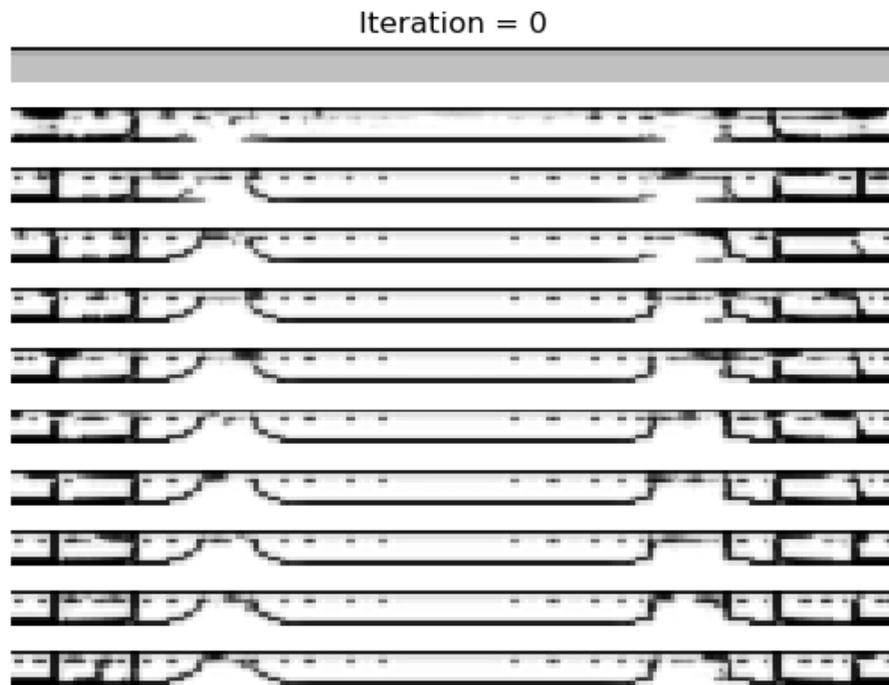
Figure 2: Topology formation for case study **A-I**

Figure 3: Objective function *(top)* and volume of design domain *(bottom)* for case study **A-I**

Figure 4: Topology formation for case study **B-I**

Figure 5: Objective function *(top)* and volume of design domain *(bottom)* for case study **B-I**

Figure 6: Topology formation for case study **B-II**

5.1.3 Case Study C

The top, bottom and side surfaces of the panel are fixed as solid while the rest constitutes the admissible design domain. Note that uncontrolled periodicity can be achieved using this type of design domain. This case study is divided into three type of problems:

1. Thermal load only on top surface - Case Study **C-I**

2. Thermal load only on top and bottom surfaces - Case Study **C-II**

3. Thermal load on top, bottom and side surfaces - Case Study **C-III**

In the above case studies, adiabatic boundary conditions are assumed on the remaining surfaces, if any. Similar to the case study B-II, cooling load of same magnitude is applied in the case study C-II and C-III. In addition to this, cooling load is also applied on both the side surfaces of the panel. The topology formation of the panel for the case study C-I, C-II and C-III are shown in Fig.7, Fig.9 and Fig.10, respectively. The convergence metrics for the optimization and the volume of the design domain for case study C-I are shown in Fig.8.

5.2 Discussion

Only the thermal stresses are considered in the present topology optimization problem. For all the case studies, the optimal topology is asymmetric due to the thermal loads and

Pankil N. Mishra and Abhijit Gogulapati
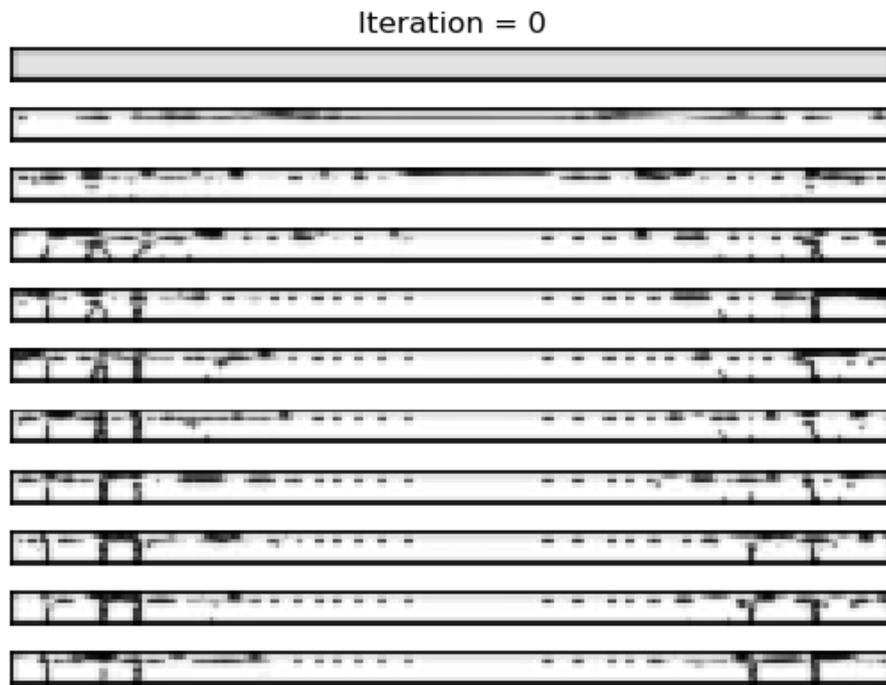
Figure 7: Topology formation for case study **C-I**
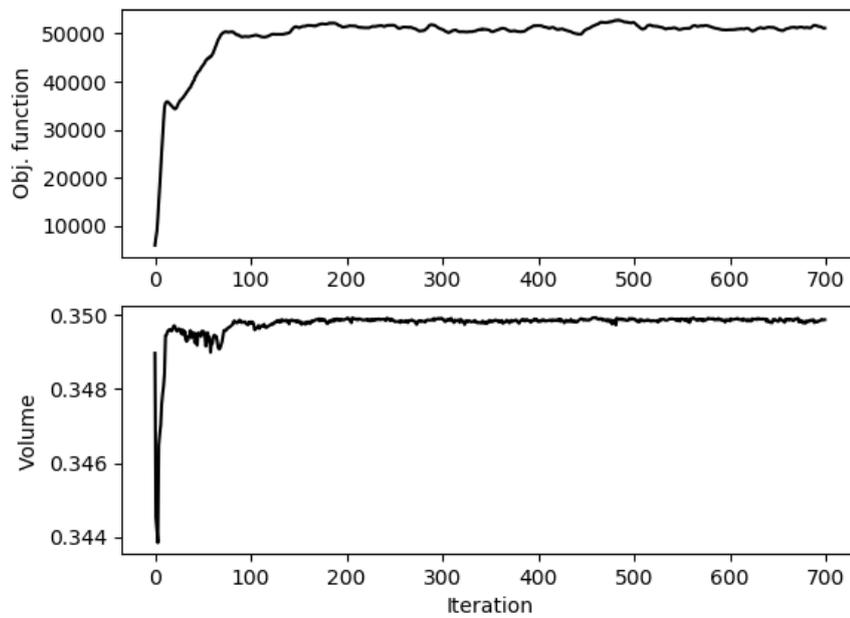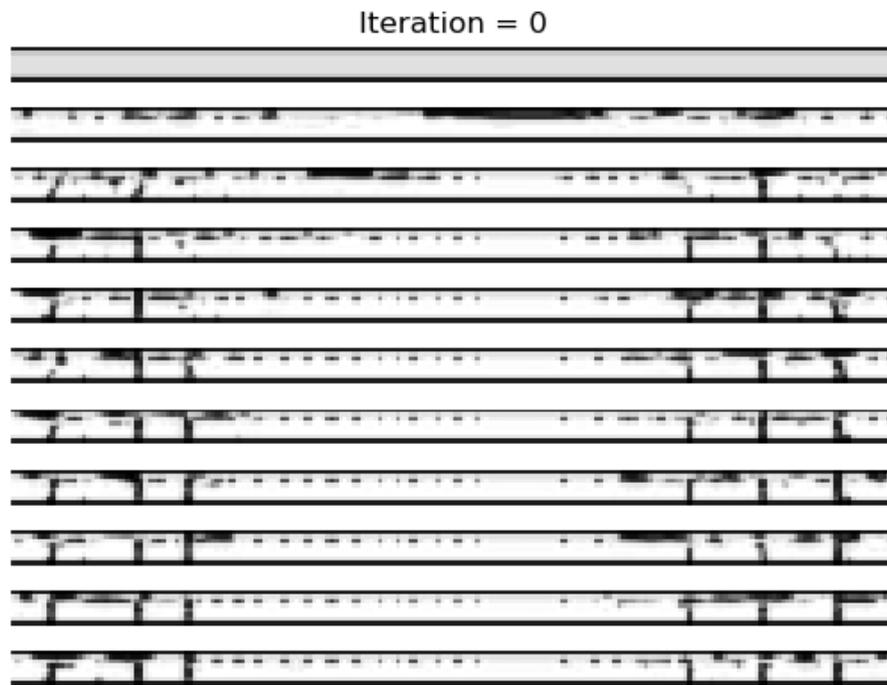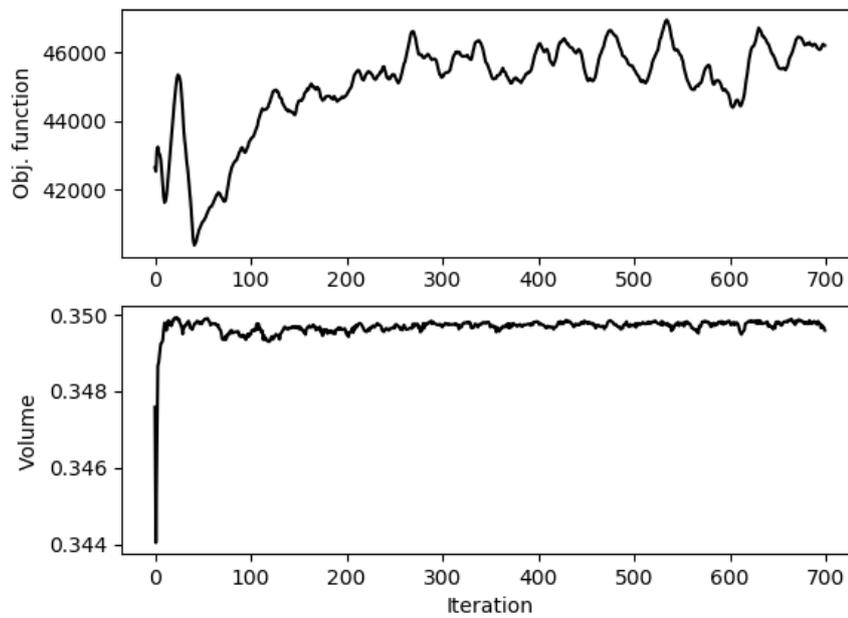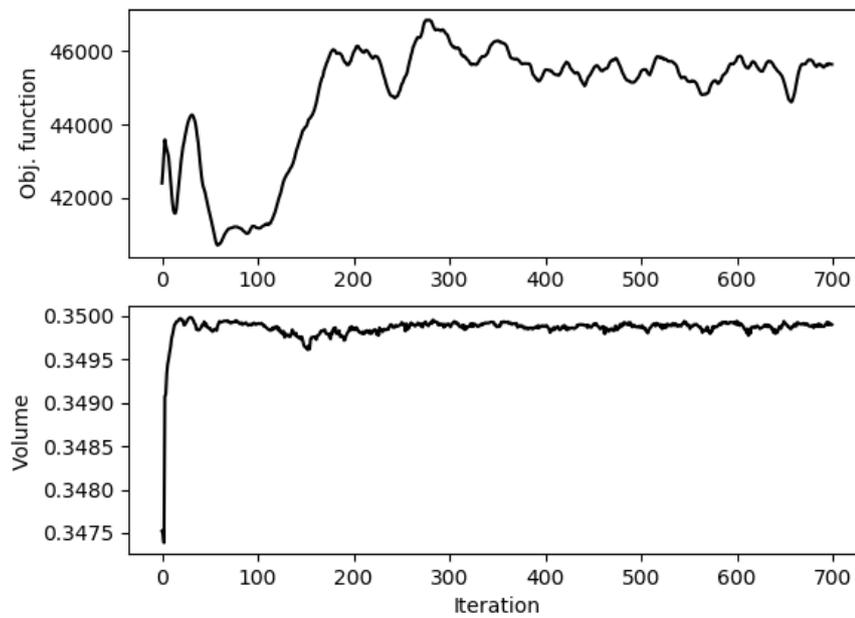

Figure 8: Objective function *(top)* and volume of design domain *(bottom)* for case study **C-I**
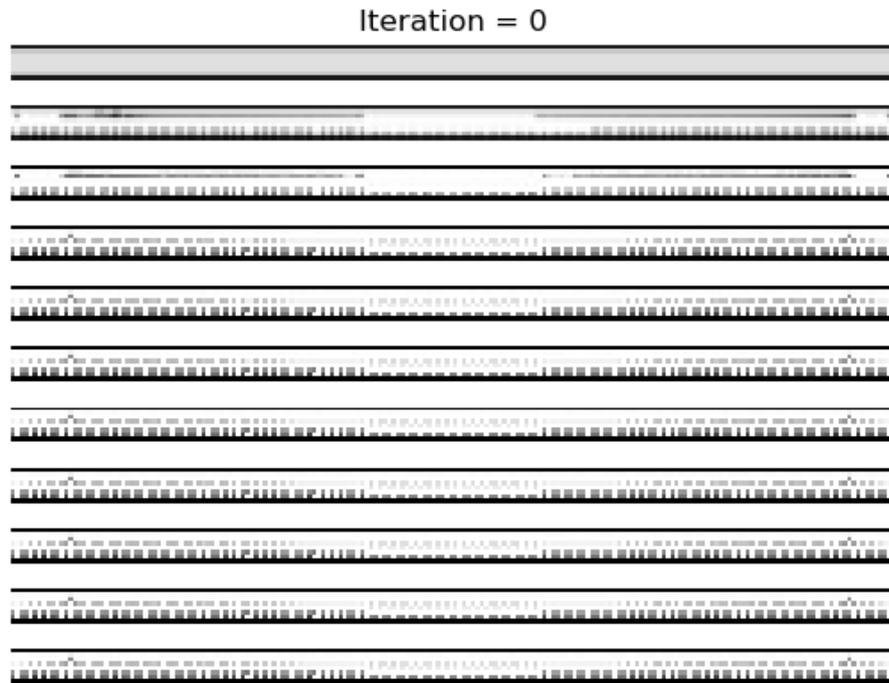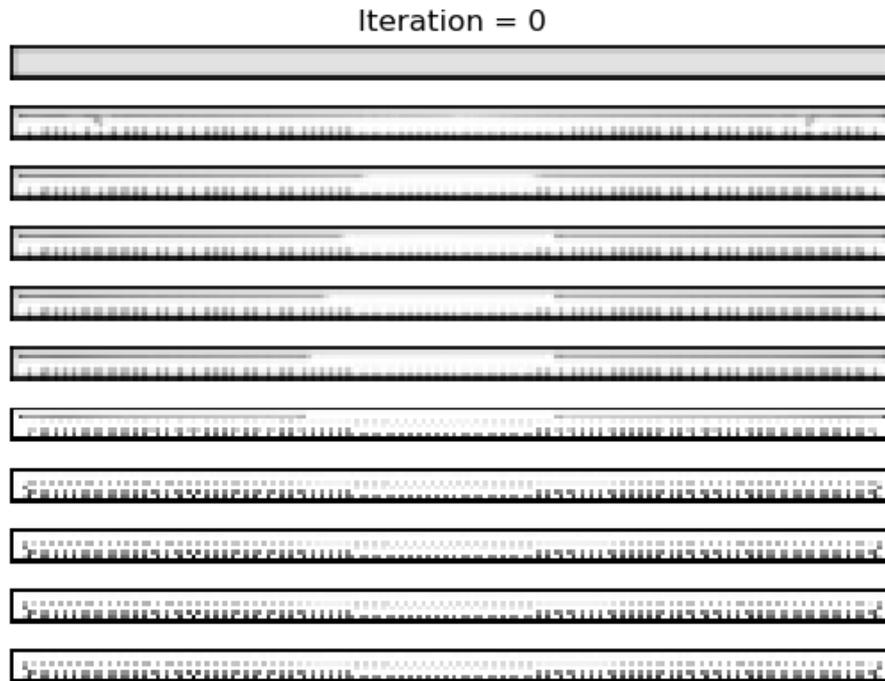
Figure 9: Topology formation for case study **C-II**

the biasing effect of the flow over the top surface. Traditionally, the structural designers attach stringers on flat panel sheet to increase its stiffness-to-weight and strength-to-weight ratio.

The material has been removed from middle and allocated to the highly stressed panel ends in the optimal topology from the case study A-I, B-I and C-I as shown in Fig.2, Fig.4 and Fig.7, respectively. An interesting point to note is that, though the bottom surface is not fixed as solid in case study A-I shown in Fig.2, the optimizer has retained the bottom surface in the middle portion of the panel which connects the two inverted hat sections formed at either ends. There is a formation of T-section, C-section and S-section type of stringers to increase the buckling strength of the panel. However, for case study B-I and C-I the formation of hat section is absent. Instead there is formation of I-section type stringers at extreme ends of the panel. This happens due to the constraint on bottom surface to remain solid, which results in less available material for the formation of topology as compared to case study A-I.

The addition of cooling heat load in the case study B-II, C-II and C-III makes a significant impact on the optimal topology shown in Fig.6, Fig.9 and Fig.10, respectively. The cooling heat load on the bottom and side surface leads to a larger temperature difference in the panel. The major feature in all the three case study is the removal of the material from just below the top surface, where the aerodynamic heat load is applied. Mathematically, this is an optimal solution as the optimizer disconnects the top and bottom surface, which heavily reduces the conductive heat transfer from the top surface to rest of the panel. The bottom surface is made stiff by the formation of stringers on it,
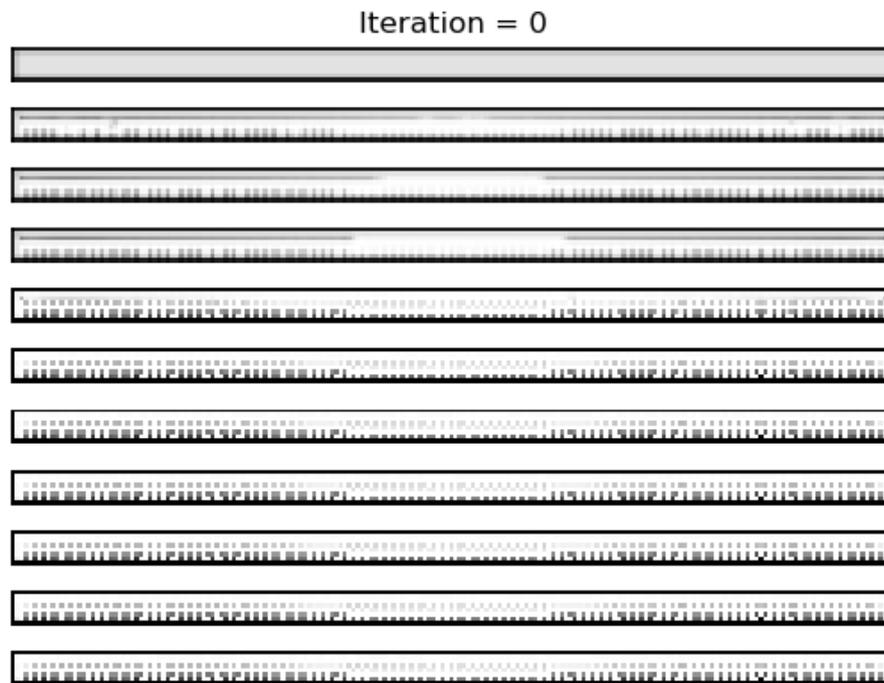
Figure 10: Topology formation for case study **C-III**

excluding the middle portion, while the top surface gets heated due to the flow. This is due to the objective function formulation, where the buckling metric is computed for the whole panel and due to the heat conduction from top surface to bottom surface. Thus resulting in such a topology, which is not a practical solution from design perspective, however it is a feasible optimal solution for the problem in Eq.(22).

6   CONCLUSIONS

Topology optimization of a 2D panel heated by the flow is described. The optimization is performed using a series of problem statements to investigate the impact of constraints and admissible design space on the optimization process and final topology. In all cases, the top surface is assumed to be heated by a hypersonic flow. Case studies in which the bottom surface is actively cooled are also considered.

The convective heating case considered in the current study introduces differential spatial heating into the system. To this end the admissible domain has a significant impact on the final topologies obtained.

The investigations revealed the following insights:

- The inclusion of cooling on the bottom surface has a significant impact on the final configuration.

- Relaxation of the bottom and side surfaces as solid materials produces configurations that resemble thin panels stiffened using hat type structures.

- Retaining the bottom surface as a solid material promotes removal of the material internally thereby creating 'hollow' structures in which the top and bottom surfaces are disconnected from each other. In such cases, selective stiffening of the bottom surface was observed to maximize the buckling metric whereas all allowable material was removed from the top surface to minimize the effect of heating.

- The MMA algorithm has an ad-hoc parameter, *move*. It was selected based on a trial and error approach for the current study. A mathematically robust selection criteria for *move* parameter is required.

REFERENCES

[1] J. J. McNamara and P. P. Friedmann. Aeroelastic and aerothermoelastic analysis in hypersonic flow: past, present, and future. *AIAA journal*, 49(6):1089–1122, 2011.

[2] A. J. Culler and J. J. McNamara. Studies on fluid-thermal-structural coupling for aerothermoelasticity in hypersonic flow. *AIAA journal*, 48(8):1721–1738, 2010.

[3] A. Gogulapati, K. R. Brouwer, X. Wang, R. Murthy, J. J. McNamara, and M. P. Mignolet. Full and reduced order aerothermoelastic modeling of built-up aerospace panels in high-speed flows. In *58th AIAA/ASCE/AHS/ASC Structures, Structural Dynamics, and Materials Conference*, page 0180, 2017.

[4] M. P. Bendsoe and O. Sigmund. *Topology optimization: theory, methods, and applications.* Springer Science & Business Media, 2013.

[5] O. Sigmund and K. Maute. Topology optimization approaches. *Structural and Multidisciplinary Optimization*, 48(6):1031–1055, 2013.

[6] F. Feppon, G. Allaire, C. Dapogny, and P. Jolivet. Topology optimization of thermal fluid–structure systems using body-fitted meshes and parallel computing. *Journal of Computational Physics*, 417:109574, 2020.

[7] J. D. Deaton and R. V. Grandhi. A survey of structural and multidisciplinary continuum topology optimization: post 2000. *Structural and Multidisciplinary Optimization*, 49(1):1–38, 2014.

[8] X. Wang, S. Xu, S. Zhou, W. Xu, M. Leary, P. Choong, M. Qian, M. Brandt, and Y. M. Xie. Topological design and additive manufacturing of porous metals for bone scaffolds and orthopaedic implants: A review. *Biomaterials*, 83:127–141, 2016.

[9] J. Liu, A. T. Gaynor, S. Chen, Z. Kang, K. Suresh, A. Takezawa, L. Li, J. Kato, J. Tang, C. C. Wang, et al. Current and future trends in topology optimization for additive manufacturing. *Structural and Multidisciplinary Optimization*, 57(6): 2457–2483, 2018.

[10] M. A. Howard. Finite element modeling and optimization of high-speed aerothermoelastic systems. *Ph. D. Thesis*, 2010.

[11] B. Stanford and P. Beran. Aerothermoelastic topology optimization with flutter and buckling metrics. *Structural and Multidisciplinary Optimization*, 48(1):149–171, 2013.

Pankil N. Mishra and Abhijit Gogulapati

[12] P. D. Dunning, B. Stanford, and H. A. Kim. Level-set topology optimization with aeroelastic constraints. In *56th AIAA/ASCE/AHS/ASC Structures, Structural Dynamics, and Materials Conference*, page 1128, 2015.

[13] D. J. Munk, D. Verstraete, and G. A. Vio. Effect of fluid-thermal–structural interactions on the topology optimization of a hypersonic transport aircraft wing. *Journal of Fluids and Structures*, 75:45–76, 2017.

[14] L. J. Smith, L. J. Halim, G. Kennedy, and M. J. Smith. A high-fidelity coupling framework for aerothermoelastic analysis and adjoint-based gradient evaluation. In *AIAA Scitech 2021 Forum*, page 0407, 2021.

[15] E. Eckert. Engineering relations for heat transfer and friction in high-velocity laminar and turbulent boundary-layer flow over surfaces with constant pressure and temperature. *Transactions of the ASME*, 78(6):1273–1283, 1956.

[16] R. D. Cook et al. *Concepts and applications of finite element analysis*. John wiley & sons, 2007.

[17] K. Svanberg. The method of moving asymptotes—a new method for structural optimization. *International journal for numerical methods in engineering*, 24(2):359–373, 1987.

[18] T. E. Bruns and D. A. Tortorelli. Topology optimization of non-linear elastic structures and compliant mechanisms. *Computer methods in applied mechanics and engineering*, 190(26-27):3443–3459, 2001.

[19] T. Bruns. A reevaluation of the simp method with filtering and an alternative formulation for solid–void topology optimization. *Structural and Multidisciplinary Optimization*, 30(6):428–436, 2005.

AEROSTRUCTURAL TOPOLOGY OPTIMIZATION USING HIGH FIDELITY MODELING

Pedro Gomes[1] and Rafael Palacios[1*]

1: Department of Aeronautics
Faculty of Engineering
Imperial College London
Exhibition Rd, South Kensington, London SW7 2BX
r.palacios@imperial.ac.uk

Abstract. *We investigate the use of topology optimization to design the aeroelastic response of a very flexible wing. A Reynolds-averaged Navier-Stokes finite volume solver is coupled to a geometrically nonlinear finite element structural solver to simulate the large displacement fluid-structure-interaction. A gradient-based approach is used with derivatives obtained via a coupled adjoint solver based on algorithmic differentiation. In the example problem, the optimization uses strong coupling effects and the internal topology of the wing to allow mass reduction while maintaining the lift. We propose a method to accelerate the convergence of the optimization to discrete topologies, which partially mitigates the computational expense of high-fidelity modelling approaches.*

Keywords: Topology optimization, Fluid-structure-interaction, MDO, Discrete adjoint, Multiphysics

Pedro Gomes and Rafael Palacios

1 INTRODUCTION

Topology optimization has been successfully applied to aircraft structures for more than one decade. So far, industrial applications have used the decoupled approach where a particular component is designed in isolation and for fixed loads [1–3]. On the other hand, some research in topology optimization using fully coupled simulation of the fluid-structure interaction (FSI) can also be found in the literature, where the components targeted for optimization are larger (for example, wing boxes [4–6] or spars and ribs [7, 8]) the latter resulting in structures more amenable to manufacturing by current methods. By and large, these larger applications have focused on structural objectives (e.g. weight and compliance) and used other variables (such as angle of attack or twist distribution) to maintain trim. Of course, reducing mass also reduces drag since less lift needs to be produced, and this effect is even more significant if compliance is limited (due to its relation with the applied force). Another shared characteristic of these larger examples is the use of medium fidelity fluid models, namely vortex lattice methods or the Euler equations in earlier examples [7], and of linear elasticity for the structure. The main motivation for this is the high computational cost of using higher fidelity models such as the RANS equations. Lower fidelity models can result in unfeasible designs. In previous work [9], we have found that in the presence of large deformations, the surface irregularities in the deformed configuration (that topology optimization tends to produce), may have a significant impact on drag even under subsonic conditions. Furthermore, a geometrically nonlinear structural model is also required to account for those irregularities, and it allows buckling to be implicitly taken in account during the optimization. Other aerodynamically richer applications have been studied, showing that structural topology can be used to radically alter the aerostructural characteristics of the system. For example, to produce load alleviation or augmentation (passive or active) or specific flutter characteristics [10–15]. However, small scale models were used for these applications. In effect, aerodynamic-driven problems create additional challenges for topology optimization which ultimately increase the cost of the optimizations.

For density-based methods, the main challenge is that aerodynamic objectives do not benefit naturally from a discrete material distribution. In fact, even when lower fidelity models are used, the distributed nature of aerodynamic loads makes the resulting topologies highly sensitive to the resolution of the grid, since it is more efficient to support this type of load with a large number of small support structures. Note that this mesh sensitivity aspect also affects level-set approaches [6]. Taking viscous effects in consideration increases the challenge due to their close dependency on superficial irregularities. Furthermore, as deformations increase, so does the influence of topology on aerodynamic quantities since, for example, the structure is able to adapt passively to different operating conditions. It is important, therefore, to understand the structural mechanisms that appear in optimizations to produce certain aerodynamic effects (for example augmenting load). For they are likely to develop when multiple operating points are considered (regardless of whether this is desired or not). Simultaneously, it is also relevant to propose methods to accelerate the convergence of this type of computationally expensive problem.

Here, these aspects are demonstrated by a flexible wing where, by optimizing its internal topology, the same aerodynamic performance can be maintained by an overall more flexible, hence lighter, structure. The work is carried within the SU2 open-source suite which has been well described in the literature, both in terms of methods [16, 17], and

Pedro Gomes and Rafael Palacios

recent improvements [18] that contributed to the feasibility of this work. The most relevant of which are succinctly described in section 2. To alleviate the aforementioned discrete-topology challenges, a two-material topology is sought (similarly to what was done in [15]), therefore the entire structure is solid, and guarantees that the outer layer is never left without support. Such a structure, built from a combination of flexible and stiff material, may also be easier to manufacture in certain conditions, than one with hollow regions. For example, if additive manufacturing techniques are used, auxiliary support structures are not needed since the two materials support each other. The focus of the example in section 3, is on static characteristics and large deformations, but using high fidelity models, which previous work showed to be important.

2 METHODOLOGY

A partitioned approach is used to solve the FSI problem. In particular, a Newton-Krylov method is used to solve the RANS equations on the fluid side, Newton iterations are used for the nonlinear structural equations, and the fluid mesh is deformed based on a pseudo-elasticity problem [9, 19]. The transfer of fluid loads and structural displacements is based on isoparametric interpolation. Gradient-based methods are used for numerical optimization, since these are the only cost efficient alternative for general large scale optimization problems. The gradients of functions (objective and constraints), are obtained using an algorithmic differentiation (AD) -based coupled discrete adjoint solver [17, 20]. Similarly to the primal problem, a Krylov approach is used on the fluid side and a block Gauss-Seidel (BGS) method is used for coupling the fluid and structural problems. The open-source suite SU2 [16, 18] is used for primal and adjoint computations, by and large the methods and their implementation are described in the references above. Therefore they are presented briefly, and the emphasis of this section will be on the key methodological improvements developed in SU2 for this work, namely the Krylov approaches.

2.1 Fluid problem

In the fluid domain the flow is governed by the continuity, Navier-Stokes, and energy conservation equations. Because we deal with steady state problems, grid velocities are zero and the equations can be written as

$$\frac{\partial \mathbf{w}}{\partial t} + \nabla \cdot \mathbf{F^c}(\mathbf{w}) = \nabla \cdot \mathbf{F^d}(\mathbf{w}) + \mathbf{Q}(\mathbf{w}), \tag{1}$$

where $\mathbf{w} = (\rho, \rho\mathbf{v}, \rho E)$ is the vector of conservative variables. The convective and diffusive fluxes, and the volumetric sources are defined, respectively, as

$$\mathbf{F^c}(\mathbf{w}) = \begin{pmatrix} \rho\mathbf{v} \\ \rho\mathbf{v} \otimes \mathbf{v} \\ \rho E\mathbf{v} \end{pmatrix}, \tag{2}$$

$$\mathbf{F^d}(\mathbf{w}) = \begin{pmatrix} \mathbf{0} \\ \overline{\overline{\boldsymbol{\tau}}} \\ \kappa\nabla T \end{pmatrix}, \tag{3}$$

$$\mathbf{Q}(\mathbf{w}) = \begin{pmatrix} 0 \\ -\nabla p \\ \nabla \cdot (\overline{\overline{\boldsymbol{\tau}}} \cdot \mathbf{v} - p\mathbf{v}) \end{pmatrix}, \tag{4}$$

Pedro Gomes and Rafael Palacios

where ρ is the density, $\mathbf{v}$ the flow velocities in a Cartesian coordinate system, p the pressure, E the total energy per unit mass, $\overline{\overline{\boldsymbol{\tau}}}$ the stress tensor, κ the thermal conductivity and T the temperature. A Newtonian fluid is considered to compute the viscous stress tensor, and bulk viscosity effects are ignored. Furthermore, under the Boussinesq hypothesis turbulence is modeled as increased viscosity. In this work we use the Spalart-Allmaras turbulence model [21] in the "noft2" variant. Pressure and temperature are related with the conservative variables via the ideal gas equation of state. Equation (1) is integrated in space using the finite volume method (FVM) on a median-dual grid, resulting in a semi-discrete integral equation for each volume Ω_i of the form [16]

$$\int_{\Omega_i} \frac{\partial \mathbf{w}}{\partial t} d\Omega + \mathbf{R}_i(\mathbf{w}) = \mathbf{0}, \tag{5}$$

where the residual $\mathbf{R}_i$ is obtained by summing the discretized fluxes for all faces of the control volume and integrating the volumetric sources. To obtain a steady state solution, equation (5) can be marched implicitly in pseudo time (τ), that is, the new solution $\mathbf{w}^*$ is obtained by solving

$$\left(\frac{|\Omega_i|}{\Delta \tau_i} \delta_{ij} + \frac{\partial \tilde{\mathbf{R}}_i}{\partial \mathbf{w}} \right) (\mathbf{w}^* - \mathbf{w}) = -\mathbf{R}_i, \tag{6}$$

where the continuous temporal derivative has been replaced by a backward-Euler approximation and the tilde indicates that the linearization of the residual is approximate. In the context of second order upwind schemes, the most common approximation is to consider only the influence of direct neighbors, which simplifies the computation of the Jacobian matrix and reduces its density (especially for medial-dual discretizations). However, this simplification can have the adverse effect of reducing the robustness of the solution method, which is highly relevant for numerical optimization to avoid divergence of intermediate designs. Moreover, adequate convergence of the primal problem has been shown to improve the convergence of the adjoint (e.g. [22]). Newton-Krylov (NK) methods can be implemented in a matrix-free manner by obtaining Jacobian-vector products using finite differences, or the forward mode of AD, or the complex-step method. The accuracy of the Jacobian is then only limited by the differentiation strategy. In the current implementation in SU2, a finite difference-based NK method (based on [23]) is used for the flow equation, while turbulence is solved by the quasi-Newton approach in a segregated manner. The linear preconditioner used for the NK approach is the ILU(0) factorization of the approximate Jacobian matrix. Currently this is the bottleneck of the implementation (in terms of maximum CFL number) and also the reason why it is not yet profitable to couple flow and turbulence variables. In what follows, we represent this fluid solution process by the fixed-point iteration

$$\mathbf{w} = \mathcal{F}(\mathbf{w}, \mathbf{u}), \tag{7}$$

where $\mathbf{u}$ are the structural displacements, responsible for the deformation of the fluid mesh. For the purposes of the fixed-point representation, the turbulence variables are considered to be part of $\mathbf{w}$.

2.2 Solid mechanics

The deformed state of a solid domain (Ω) is governed by the point-wise equilibrium of linear momentum and of tractions on its surface (Γ), that is,

$$\rho(\ddot{\mathbf{u}} - \mathbf{f}) - \nabla \cdot \overline{\overline{\boldsymbol{\sigma}}} = \mathbf{0} \quad \text{in } \Omega \tag{8}$$

$$\overline{\overline{\boldsymbol{\sigma}}}\mathbf{n} - \boldsymbol{\lambda} = \mathbf{0} \quad \text{on } \Gamma \tag{9}$$

where ρ is the density, $\ddot{\mathbf{u}}$ the acceleration with respect to an inertial frame, $\mathbf{f}$ the inertial body forces, $\overline{\overline{\boldsymbol{\sigma}}}$ the Cauchy stress tensor, $\mathbf{n}$ the outward surface unit normal, and $\boldsymbol{\lambda}$ the external tractions (i.e. fluid forces). To solve equation (8) for the structural displacements via the finite element method (FEM), its weak form is first established by applying the principle of virtual work (see [24]),

$$\int_{\Omega_c} \delta\mathbf{u} \cdot \rho(\ddot{\mathbf{u}} - \mathbf{f}) \, d\Omega + \int_{\Omega_r} \delta\overline{\overline{\boldsymbol{E}}} : \overline{\overline{\boldsymbol{S}}} \, d\Omega - \int_{\Gamma_c} \delta\mathbf{u} \cdot \boldsymbol{\lambda} \, d\Gamma = 0 \tag{10}$$

where $\delta\overline{\overline{\boldsymbol{E}}}$ is the variation of the Green-Lagrange strain tensor with respect to $\delta\mathbf{u}$, $\overline{\overline{\boldsymbol{S}}}$ is the second Piola-Kirchhoff stress tensor, Ω_r refers to the reference (undeformed) configuration of the structure, and Ω_c and Γ_c to the current configuration of the structure and its surface, respectively. For hyperelastic materials the relation between stress and strain is given by the strain energy density function Ψ, as $\overline{\overline{\boldsymbol{S}}} = \frac{\partial\Psi}{\partial\overline{\overline{\boldsymbol{E}}}}$. In particular, for a neo-Hookean material with Lamé constants μ and λ, it is given as

$$\Psi = \frac{\mu}{2}\left(\text{tr}\overline{\overline{\boldsymbol{C}}} - 3\right) - \mu \ln J + \frac{\lambda}{2}(\ln J)^2 \tag{11}$$

where J is the determinant of the deformation gradient. Equation (10) is linearized around the current state of deformation before being discretized (linear isoparametric elements are used in SU2 [25]). The solution is then found iteratively via the Newton-Raphson method, where systems with the tangent stiffness matrix are solved using the direct sparse solver PaStiX [26]. This process is also formulated as a fixed-point iteration, namely

$$\mathbf{u} = \mathcal{S}(\mathbf{u}, \boldsymbol{\lambda}(\mathbf{w})) = \mathcal{S}(\mathbf{u}, \mathbf{w}), \tag{12}$$

noting that the tractions are computed based on the fluid variables. The coupled problem is solved by a BGS approach by alternating between fluid (7) and structural (12) iterations. Both displacements and fluid traction are interpolated using an isoparametric approach. A fixed relaxation factor $(0.6 - 0.8)$ is applied to the transferred displacements to improve stability.

2.3 Coupled discrete adjoint sensitivities

For a given function of interest J, of the solution variables $\mathbf{x} = (\mathbf{w}, \mathbf{u})$, and of the parameters of the problem $\boldsymbol{\alpha}$ (undeformed mesh coordinates, local material properties, etc.), where it is $\mathbf{x} = \mathbf{x}(\boldsymbol{\alpha})$ via the solution of the FSI problem. The total derivatives of J with respect to $\boldsymbol{\alpha}$ can be obtained via the discrete adjoint method as [17, 20]

$$d_\alpha J = J_\alpha + \boldsymbol{\lambda}^{\text{T}} \mathcal{P}_\alpha, \tag{13}$$

Pedro Gomes and Rafael Palacios

where $\mathcal{P} = (\mathcal{F}, \mathcal{S})$ is the fixed point iterator of the coupled problem, and subscripts denote partial derivatives. The adjoint variables $\boldsymbol{\lambda}$ are obtained by solving

$$\boldsymbol{\lambda}^{\mathrm{T}} = J_x + \boldsymbol{\lambda}^{\mathrm{T}}\mathcal{P}_x. \tag{14}$$

Similarly to the primal problem, the solution of the coupled adjoint problem with $\boldsymbol{\lambda} = (\overline{\mathbf{w}}, \overline{\mathbf{u}})$, can be obtained by a BGS method with inner iterations on the fluid and structural adjoint sub-problems, by first noting that due to the partitioned approach (14) is equivalent to

$$\begin{aligned}
\overline{\mathbf{w}} &= (J_w^{\mathrm{T}} + \mathcal{S}_w^{\mathrm{T}}\overline{\mathbf{u}}) + \mathcal{F}_w^{\mathrm{T}}\overline{\mathbf{w}} \\
\overline{\mathbf{u}} &= (J_u^{\mathrm{T}} + \mathcal{F}_u^{\mathrm{T}}\overline{\mathbf{w}}) + \mathcal{S}_u^{\mathrm{T}}\overline{\mathbf{u}}
\end{aligned} \tag{15}$$

due to the block nature of $\mathcal{P}_x$. The over-bar denotes the adjoints of the associated primal solution variable. Note that each sub-problem is equivalent to the general fixed-point (14), but with a contribution to the right-hand-side due to the coupling between fluid and structure. For efficiency, those contributions are only computed once per coupling iteration In particular, the product with $\mathcal{F}_u$ involves the mesh deformation operation. This fixed-point format naturally fits the reverse mode of AD, and more importantly, it allows a generic treatment of any type of solver [17] by differentiating its *entire* primal fixed-point iteration, that is, the program (or code path) used to obtain a new solution iterate.

There are, however, some drawbacks to this strategy. Effectively this fixed-point is a right-preconditioned version of the more conventional left-preconditioned adjoint fixed-point approach [27]. Consequently, the preconditioner is applied to the adjoint variables, instead of to the residual of the adjoint linear system. This implies that the preconditioner is effectively the transposed (by AD) solution method of the recorded primal iteration, e.g. a quasi-Newton strategy. When this embedded preconditioner consists in the solution of a linear system by a Krylov solver, it is then necessary (in general) to converge such iterative processes to higher accuracy than in the primal solver, for the preconditioner is applied to a vector that does not converge to zero. Furthermore, it is well known that fixed-point approaches (either left- or right-preconditioned) may suffer from stability issues [22, 28, 29], even when the primal problem shows sufficient convergence. Krylov adjoint approaches are a common way to both accelerate convergence and improve stability and can be seen as the dual of Newton-Krylov methods for the primal (nonlinear) equations [29]. To cast (14) as a linear system, note that it can be written as

$$(\mathcal{P}_x^{\mathrm{T}} - \mathbf{I})\boldsymbol{\lambda} = -J_x^{\mathrm{T}}, \tag{16}$$

which can be solved by any matrix-free method, for example GMRES. However, because the adjoint preconditioner is embedded and not easily extricable from $\mathcal{P}$, applying a Krylov method to (16) is only efficient (i.e. results in a speed up) if the action of $\mathcal{P}_x$ on a vector is guaranteed to be linear, otherwise GMRES may not minimize the adjoint residuals. Nevertheless, we have still found that using a fixed number $(20 - 30)$ of ILU smoothing steps with suitable relaxation $(0.4 - 0.7)$ (i.e. a Richardson iteration), together with GMRES, is highly effective for fluid problems (compared with the fixed-point approach). The structural adjoint problem can be solved by the fixed-point method without issues,

Pedro Gomes and Rafael Palacios

its preconditioner (effectively the inverse of the tangent stiffness matrix) is very close to the inverse of the Jacobian $\mathcal{S}_u$, and thus around five iterations are typically sufficient.

2.4 Density-based topology optimization

The well known density-based approach with continuous variables is used in this work. It consists in specifying a design density at discrete locations of the solid domain, the element centroids in this case, and making the local elasticity modulus a function of it. Here, the modified SIMP formulation is used to relate the elasticity modulus with the design variable as

$$E(\rho) = E_{\min} + (E_0 - E_{\min})\rho^p \quad 0 \le \rho \le 1, \tag{17}$$

where $E_{\min}$ is greater than zero (even for solid-void problems to avoid a singular stiffness matrix), and E_0 is the reference value of the elasticity modulus. To avoid checker-boarding in the solution, a discrete filtering operation [30] is applied to the design density variables (ρ) exposed to the optimizer. This results in physical densities ($\tilde{\rho}$) considered for each finite element given by

$$\tilde{\rho}_i = \sum_{j \in \mathcal{N}(i)} w_{ij}\rho_j \quad / \sum_{j \in \mathcal{N}(i)} w_{ij}, \tag{18}$$

where $w_{ij} = (R - ||\mathbf{x}_i - \mathbf{x}_j||)\Omega_j$ and $\mathcal{N}$ is the set of elements within radius R of element i. This conical filter kernel is less numerically challenging than other strategies that introduce steep gradients (as they approach discontinuous functions), however, it invariably results in regions of intermediate density.

This type of topology optimization problem is characterized by a large number of design variables and relatively few constraints (excluding simple bound constraints), that from a physics point of view, do not need to be imposed strictly. Therefore, the exterior penalty method is herein used to impose constraints, that is, problems of the form

$$
\begin{aligned}
\min_{\boldsymbol{\alpha}} \ & f(\boldsymbol{\alpha}) \\
\text{subject to}: \ & g_i(\boldsymbol{\alpha}) = 0 \\
& h_j(\boldsymbol{\alpha}) \le 0
\end{aligned}
\tag{19}
$$

become $\min_{\boldsymbol{\alpha}} \hat{f}(\boldsymbol{\alpha})$ with

$$\hat{f}(\boldsymbol{\alpha}) = f(\boldsymbol{\alpha}) + \sum_{i=1}^{N_g} a_i g_i(\boldsymbol{\alpha})^2 + \sum_{j=1}^{N_h} b_j h_j^+(\boldsymbol{\alpha})^2, \tag{20}$$

where $h^+ = \max(0, h)$. The penalized objective function can then be minimized using an unconstrained (but bounded) optimization method. The penalty parameters (a_i and b_j) need to be gradually increased (usually by multiplying the previous value by a fixed factor r) until a predetermined small constraint tolerance is met. This creates the need for outer iterations since updating the parameters within unconstrained (inner) iterations leads to bad approximations of the Hessian matrix. Although these outer iterations force an undesired reversion to steepest descent, they are also needed to update topology optimization parameters. However, in the example in this paper this type of parameter update was not necessary. Before the constraint tolerance is met, loose convergence

criteria are used for the unconstrained optimizer (e.g. 40 inner iterations). The objective function is shifted and scaled by representative minimum value and range respectively, the constraints are shifted by their bounds and scaled by a reference value (the reciprocal of the bound unless otherwise specified). Doing so allows the same constraint tolerance (≈ 0.01) to be used, the penalty parameters to be initialized equally ($a_i^0, b_i^0 \in [1, 10]$), and also updated with the same factor ($r \in [1.4, 4]$).

The unconstrained optimizer used in this work is the L-BFGS-B [31] implementation available with SciPy [32]. This choice was made based on initial comparisons with the MMA method [33]. Later, the constrained optimizer IPOPT [34] was also tested, based on promising results in the literature [35], however, it performed worse than L-BFGS-B in our studies. Recently, other researchers have also found that current versions of IPOPT have difficulties with topology optimization problems [36]. One computationally advantageous aspect of the exterior penalty approach, not explored in this work, is that it may reduce the cost of evaluating gradients. For example, it may be possible to differentiate the penalized function at the same cost of differentiating one of the constraints or objectives, and as a result, only one adjoint problem needs to be solved per primal simulation (e.g. operating point) instead of one per function.

3 RESULTS

The purpose of this example is to study the feasibility of using the internal topology of a wing to alter its aerodynamic performance. In effect, this is a proof of concept for a new design strategy for wings built using additive manufacturing techniques. Specifically, in this example the internal material distribution will be used to obtain a more flexible wing (and thus presumably lighter) that produces the same lift at the same angle of attack as a rigid baseline design. This is effectively a load augmentation problem. Shape optimization is first used to produce a minimum-drag design with small deformations, this is described in section 3.1. Topology optimization is then used on this design, which should show the impact of load augmentation on aerodynamic performance. Previous work with 2-D models already showed the potential of using the internal layout to passively adapt to different operating conditions [9]. However, to study feasibility in 3-D and the physical mechanisms developed during the optimization, only one operating point is considered here.

3.1 Baseline rigid design

A baseline design is obtained by optimizing the shape of a solid wing with uniform material properties for minimum drag, with constraints on lift, pitching moment, and minimum thickness (over multiple spanwise sections). The initial geometry, shown in Fig. 1a, is generated by *lofting* two symmetric 4-digit NACA profiles. The root profile has 0.25 m chord and 9% thickness, whereas the tip has 0.175 m chord and 7.2% thickness. The wing span is 1 m, the 25% chord-line is swept back 5 degrees, and a linear twist distribution of -3 degrees is used. Fig. 1a also shows the FFD box used to parameterize the shape. Out of the 98 control points, 97 are allowed to move in the vertical direction (± 30 mm), the bottom right point of the root section (right side of the page) is fixed. Chord and translation (chord-wise displacement) are defined for each of the 7 spanwise sections of the FFD box by controlling the horizontal coordinates of the 14 control points in each section. The tip section is not allowed to translate, this helps maintaining the quality

Pedro Gomes and Rafael Palacios
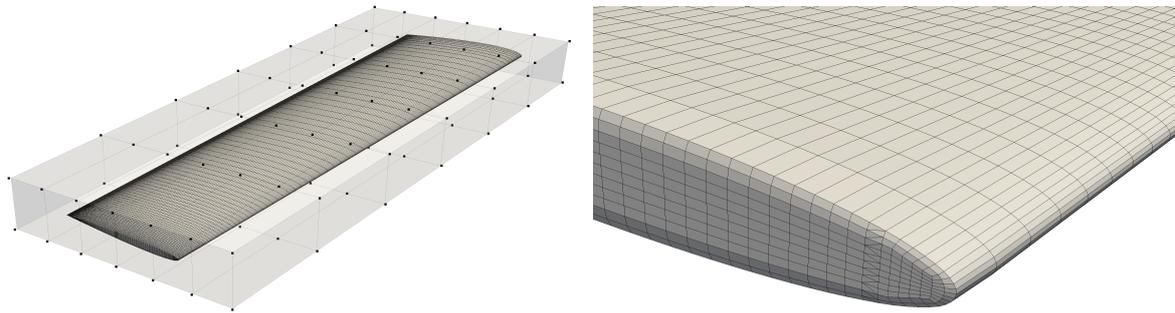
(a) Initial wing geometry and FFD box.   (b) Structural mesh near wing tip.

Figure 1: Details of initial geometry for shape optimization.

of the mesh. The bounds for these two variables are ($\pm 60\,\text{mm}$) at the root and decrease linearly to ($\pm 20\,\text{mm}$) at the tip. There are 110 variables in total. A single operating point was considered, namely Mach 0.6 at sea-level and $273.15\,\text{K}$ (the Reynolds number is $3.7\,\text{M}$ for the root chord). Convective fluxes are computed using Roe's scheme with 1% entropy correction, the second order reconstruction of flow variables uses Green-Gauss gradients and Venkatakrishnan and Wang's limiter. The Spalart-Allmaras turbulence model is used with first order convective fluxes. The fluid and structural grid are composed mostly by hexaedra and have 4.1 million nodes and $220\,000$ nodes, respectively. The radius of the farfield boundary is 25 span lengths, Fig. 1b shows a detail of the structural grid near the wing tip. The solid material is modelled as hyperelastic with Poisson's ratio of 0.35 and Young's modulus of $75\,\text{GPa}$, which results in small deformations (comparable to the thickness).

At 4 degrees AoA the initial geometry has lift, drag, and pitching moment coefficients of 0.295, 0.0103, and -0.0429 respectively. To obtain a baseline for topology optimization, drag was minimized with lower bounds of 0.29 on lift and -0.06 on pitching moment coefficients. A geometric constraint was also included to prevent the maximum thickness of the thinnest spanwise section from decreasing. The SLSQP implementation from SciPy was used to solve the optimization problem, all constraints and variables were scaled by their bounds and the objective (drag) by its initial value.

Fig. 2 shows a comparison of the planforms and spanwise sections at the root, mid-span, and tip of the initial and optimized geometries. All constraints are active on the optimized design and the drag coefficient was reduced to 0.00829. The design achieves this by reducing the loading on tip sections and increasing it in the first half of the span. The sections towards the tip are significantly cambered, which requires the root sections to operate with more incidence to counteract the effect of camber on pitching moment, as shown by the pressure contours in Fig. 3. Due to this camber (and moment) distribution, lift decreases if a more flexible material is considered in the simulation, note that the aerodynamic forces act to twist the wing, which reduces incidence and thus lift. Of course, the AoA can be increased to counteract this effect (up to the point of static divergence), here however, topology optimization is used to obtain a two-material structure that, although more flexible, is able to compensate the twisting action of the aerodynamic forces. The optimized geometry was re-meshed before proceeding to optimize the internal topology.
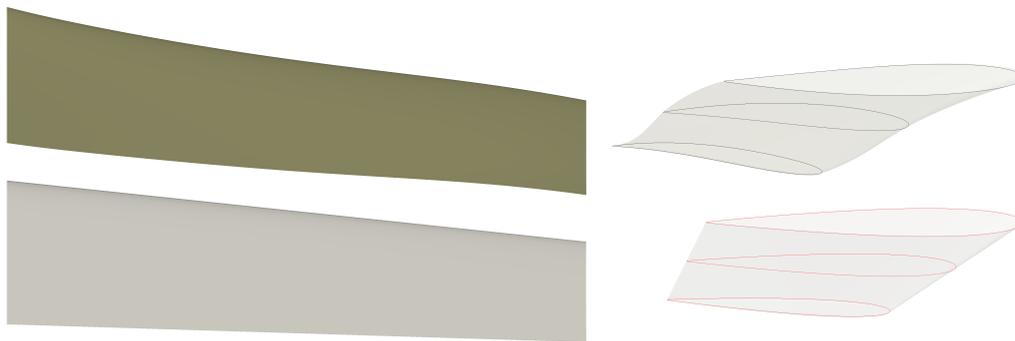
Figure 2: Comparison of initial (bottom) and optimized (top) wing.
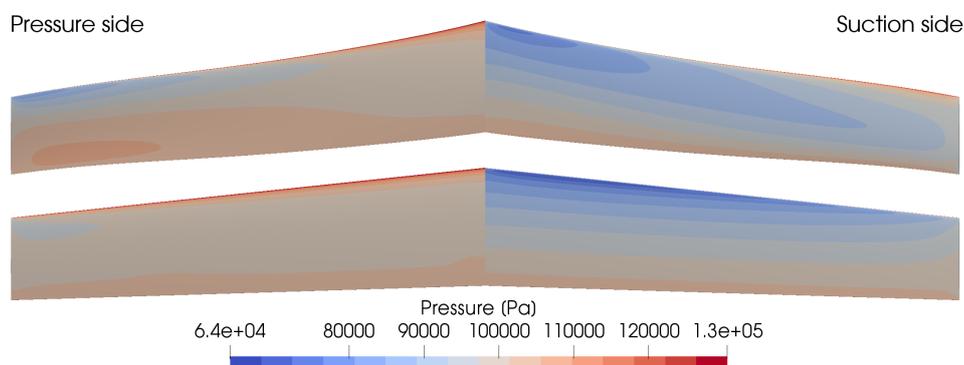
Figure 3: Pressure contours on initial (bottom) and optimized (top) designs.

3.2 Topology optimization

For topology optimization the soft and stiff materials were considered to have elasticity modulus of 1.5 and 30 GPa, respectively. It is not relevant for the purpose of this study if such materials exist, these values were simply chosen based on expected deformation at 50% material fraction (comparable to the chord). The structural elements are stretched (see Fig. 1b), because using a smaller size in the spanwise direction would result in an impractical number of elements. This presents a challenge for density filtering strategies, since setting the filter radius based on the longest element size would span the entire thickness of the wing. To avoid this, the neighborhood search ($\mathcal{N}$ in (18)) was constrained to consider only neighbors of neighbors, on a 2-D grid this would limit the filter to the equivalent of a 13-point stencil. The filter radius was then set as 1.5 times the largest element size (in the spanwise direction), and the linear weight function (18) was used. Finally, a fixed SIMP exponent of 3 is used throughout the investigation.

Due to the reasons described above, with a material with elasticity modulus of 22.3 GPa the lift coefficient drops to 0.24. Then, a first objective is to recover the target value of 0.29, using the minimum amount of stiff material. Note that a density of zero corresponds to the softer material and a density of one to the stiffer material, therefore minimizing the fraction of the latter is equivalent (in formulation) to minimizing mass in a classical "solid-void" problem. Note that it is not possible to do so "simply" by stiffening the structure, since the stiffer material is still 60% more flexible than the one used for the baseline rigid design. Of course, some structural constraint has to be introduced (the softer material is too flexible), although maximum stress would be most appropriate, it is less

challenging (numerically) to limit compliance. Moreover, given the challenges associated with aerodynamic-driven topology optimization (described in the previous section), it was judged as beneficial to divide the optimization in several steps, also as a way to make the trade-offs between goals more evident. These steps are discussed next, the starting point for each step are the results from the previous, unless noted otherwise. While this may lead to some loss of performance, such incremental strategies are necessary to understand the challenges of new problems, especially those with large design spaces.

3.2.1 Recovering lift

The first step was to recover lift, which also serves as evidence for the feasibility of the optimization problem. To that end the exterior penalty algorithm (20) was used with a single equality constraint with fixed penalty factor of 32. Note that this method would start by recovering lift even if other goals were included because this constraint is not respected. Fig. 4a shows the surface view of the resulting topology after the 11 L-BFGS-B iterations required to meet the constraint, starting with uniform fraction of 0.9. By removing stiff material close to the leading edge, the incidence on spanwise sections close to the root negates the pitch-down moment of the tip sections. In fact, in the deformed configuration the incidence on tip sections is slightly larger compared with the baseline rigid wing, as shown in Fig. 4b. In part this is also necessary to compensate the smaller projected area that results from larger displacements (because the structural model accounts for geometric non-linearity).

(a) Material distribution to meet lift constraint.

(b) Spanwise distribution of twist.
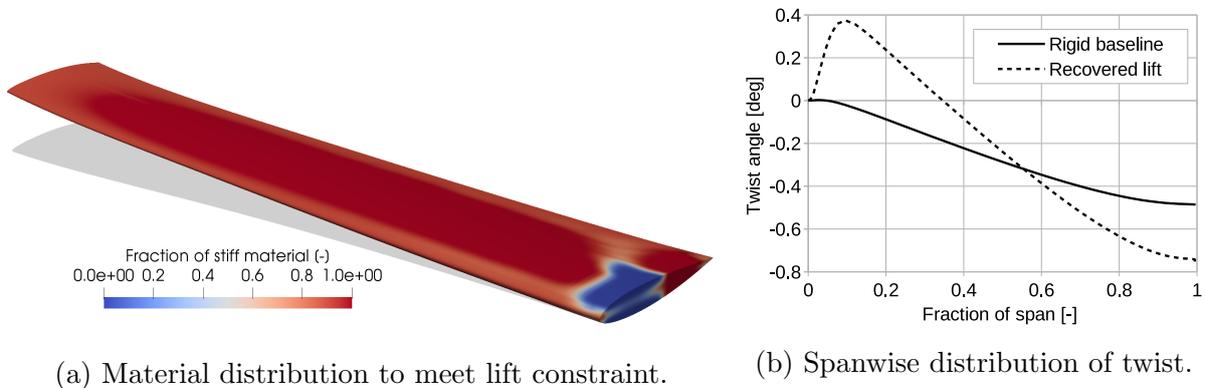
Figure 4: Results of recovering lift.

3.2.2 Determining a suitable bound for the fraction of stiff material

In the previous step there was no incentive to use a minimal amount of stiff material. That is introduced in this step alongside an upper bound on compliance of 75 J (the compliance after the initial step is 44.8 J). Although it is known that minimizing mass for a given compliance may give rise to structures that are close to a stability limit, this formulation helps determining a suitable target for the stiff fraction (which can then be constrained instead of outright minimized). The penalty factors for the two constraints were fixed at 8 and the objective (stiff fraction) was not scaled since its initial value (resulting from the previous step) was close to one. Fig. 5 shows the resulting topology after 55 L-BFGS-B iterations. Mass fractions below 0.5 were made transparent to reveal

the internal structure, which is mostly composed of the softer material. On the figure, the spanwise slices are taken from 0.25 to 0.55 span in increments of 0.075. The main mechanism to maintain lift remains the same and the stiffer material was removed from less strained areas, e.g. close to the wing tip. The stiff fraction was reduced to 0.33, which made the compliance constraint active. However, the material distribution is not discrete, mainly for two reasons: first, due to the relatively small number of iterations (for a topology problem); and second, due to the lift constraint, which requires material to be removed from a high strain region (the root). Note that this constraint is responsible for the main load applied to the structure (and thus in part for its compliance) and this contradiction between the two constraints makes the problem more difficult to solve.
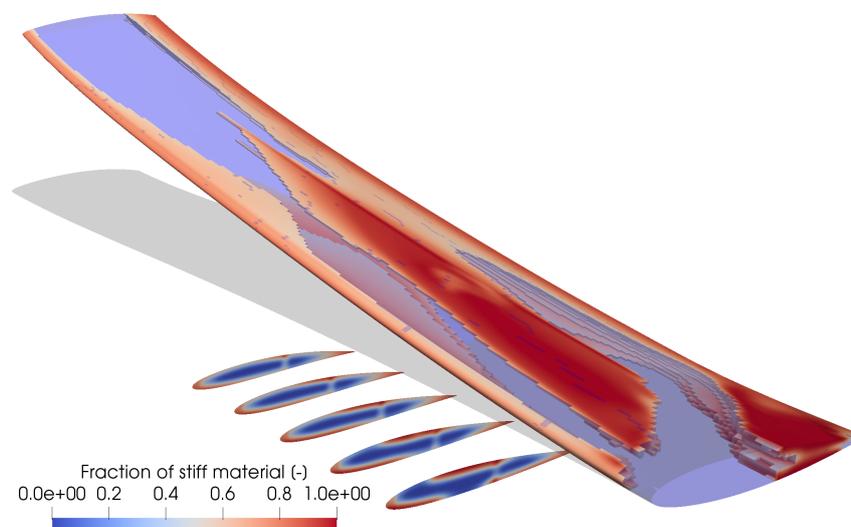
Figure 5: Material distribution after minimizing stiff fraction.

3.2.3 Lift-constrained compliance minimization

To avoid the contradiction between constraints (described above), the roles of compliance and stiff fraction were switched from 3.2.2, i.e. compliance should be minimized under the 0.29 lift coefficient constraint and a maximum stiff fraction of 0.4 (if this value was known, e.g. from experience, the previous step would have been necessary). The initial penalty factors were again set to 8 but increased by 50% (up to 64) every 30 L-BFGS-B iterations for constraints that did not meet a 0.5% tolerance. Note that constraints are scaled by their bounds and the objective by initial value. Fig. 6 shows the resulting topology after 225 iterations, which has compliance of 38.1 J, lift coefficient of 0.286, and stiff fraction of 0.403. The material distribution is significantly more discrete than before, but not as much as desired. Although the type of filter used (linear weight) will never produce a discrete result, only 50% of the variables are at their bounds (0 or 1), it should be possible, therefore, to improve this result.

3.2.4 Improving the discreteness of the material distribution

Ideally a topology optimization problem should benefit from a discrete solution due to the way it is posed and parameterized. However, in this problem (and others like it), the

Pedro Gomes and Rafael Palacios
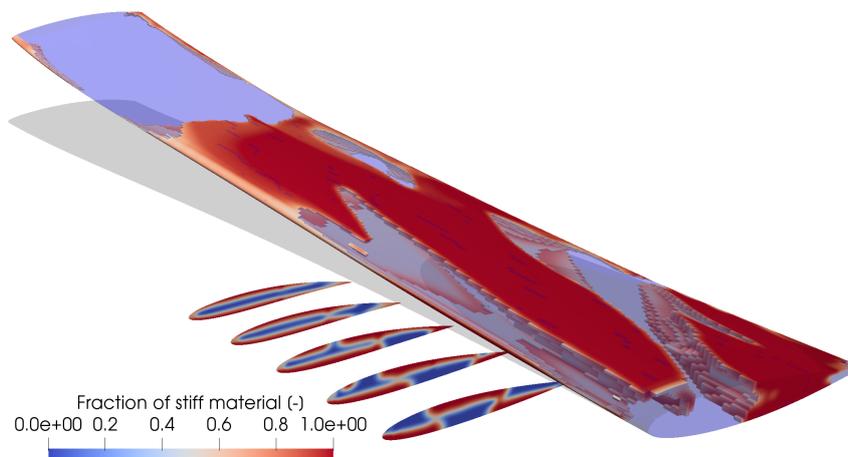
Figure 6: Material distribution after minimizing compliance.

requirement on lift makes this difficult to achieve, since the structure is both responsible for creating the load and resisting it. It is worth showing that posing the problem as a compliance (and lift) -constrained mass minimization is not beneficial. To that end the roles of stiff fraction and compliance were switched (again). The penalty factors were fixed at 64 and the bound on compliance set to 40 J to direct the optimization towards the current local optimum (i.e. the result of the previous step).

Fig. 7 shows the resulting topology after 180 iterations. The stiff material fraction is reduced to 0.336 with lift coefficient of 0.285 and compliance of 40.2 J. However, it is clear that conventional formulations do not produce a discrete result for this problem. Along with reducing the size of areas with intermediate material fraction (note the larger gaps from Fig. 6 to Fig. 7), i.e. moving the boundaries, the optimization also removed stiff material from areas that were already completely stiff (note the change near the leading edge at 60 to 70% span on the same two figures). A plausible explanation for this is that, to support a distributed load, it is better to distribute the stiff material than to concentrate it to produce stiff regions. In the literature, authors have used explicit penalization of non-discreteness metrics for problems that do not converge naturally to discrete solutions (see e.g. [37]). It is known that such strategies need to be managed with care (e.g. ramped), to avoid fast convergence to locally optimal solutions before any topological features begin to develop. However, ramping strategies have the downside of increasing the computational cost of the optimization, which is already significant for this problem due to high-fidelity modelling. Moreover, even for topology problems that naturally converge to discrete solutions, most of the objective function reduction takes place in the first iterations, where the main features of the topology develop. The remainder of the iterations serve mostly to refine those features, and in general, do not contribute substantially towards improving the objective function. For example, note how in this problem the lift constraint can be met by a wide range of topologies (from mostly soft to mostly stiff). Based on these observations it is tempting to propose an early termination of the optimization, followed by a post-processing operation to force the discreteness of the result (for example considering all values above a certain threshold to be completely stiff, and vice versa). Though this may be viable for more linear problems, in the presence of strong FSI it is likely that some constraints will no longer be respected after the post-processing.

Pedro Gomes and Rafael Palacios
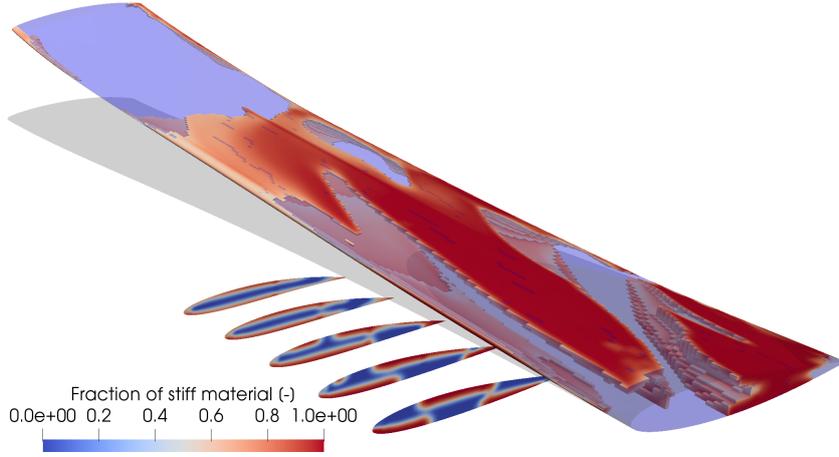
Figure 7: Material distribution after minimizing stiff fraction for a lower compliance constraint.

Therefore, to address the challenges of high computational cost and of obtaining discrete topologies, the solution proposed here is as follows. After obtaining a feasible solution (e.g. either 3.2.3 or the one in this section), the discreteness of the solution is improved by explicitly targeting (minimizing) a non-discreteness metric (d), namely

$$d = 4\frac{\boldsymbol{\rho} \cdot (1 - \boldsymbol{\rho})}{N}, \tag{21}$$

where $\boldsymbol{\rho}$ are the filtered densities (material fractions in this case) and N the number of design variables. The reduction of computational cost is achieved by simulating only the structure under fixed fluid loads (obtained from the last FSI simulation). To ensure those loads are appropriate throughout the entire process, a deformation target is introduced for the surface (Γ) nodes, that is,

$$\epsilon_\Gamma = \frac{||\mathbf{u}_\Gamma - \mathbf{u}_\Gamma^*||^2}{N_\Gamma}. \tag{22}$$

This error metric is both minimized (as a secondary objective) and constrained to a small value (10^{-7} in this case). Despite the similar formulation, this step has a very different role than the inverse-design approach of previous work [9], here the initial topology is nearly discrete, and thus only requires some incremental refinement. Conversely the inverse approach does not use initialization and therefore produces substantially different material layouts.

On the result from stiff fraction minimization for compliance of $40\,\mathrm{J}$ the discreteness metric is 0.3. This is reduced to 0.2 over the course of 1000 (inexpensive) iterations, after which the error metric is $4 \cdot 10^{-8}$ and the stiff fraction 0.339. To ensure that the final solution would be as discrete as the type of filter allows, the weight of the non-discreteness metric was progressively increased up to 500. In the end 75% of the variables were within 2% of their bounds. Furthermore, evaluating (21) for the design variables (i.e. unfiltered fractions) yields 0.008. As expected, the lift constraint is not respected by this solution, for which the value is 0.272. To restore it to the target 0.29 the discretized solution was used as starting conditions for an optimization with coupled FSI simulations,

where non-discreteness is also minimized. After 25 iterations both this metric and the stiff fraction were maintained, lift was restored but compliance increased to 42.2 J. The resulting material distribution is shown in Fig. 8 and Fig. 9.
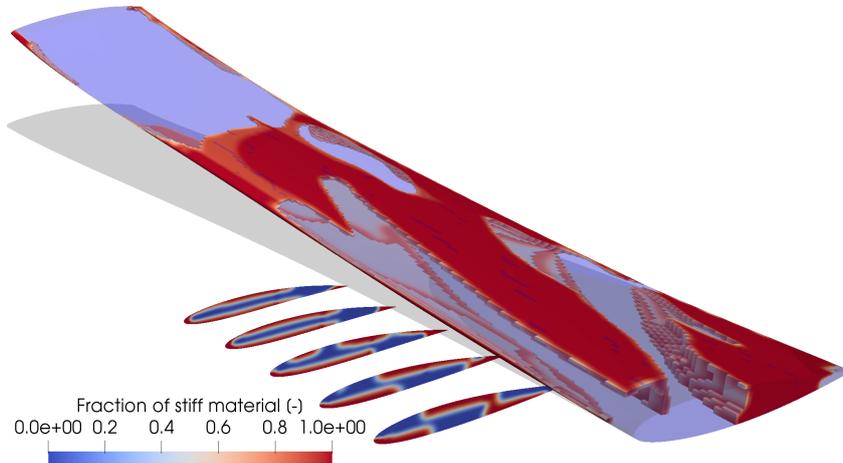
Figure 8: Material distribution after improving discreteness.
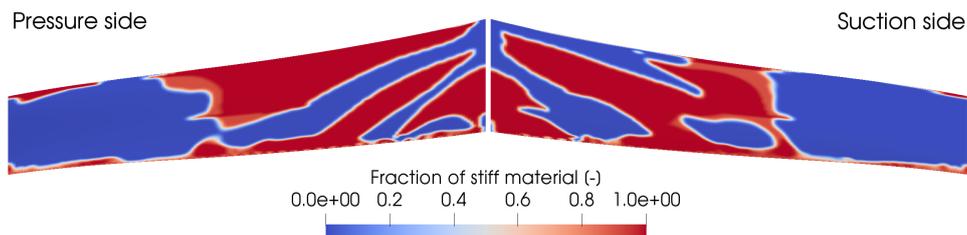
Figure 9: Material distribution after improving discreteness.

3.2.5   Discussion

The optimization process in the subsections so far can be summarized in the following steps.

1. Determining the feasibility of the aerodynamic goals, e.g. meeting lift ($O(10)$ iterations).

2. Approximately solving the optimization for suitable structural targets ($O(100)$ iterations). This may include determining those targets via different formulations of the problem (as done here).

3. Accelerating convergence to a discrete solution considering only the structure and fixed loads (equivalent to $O(10)$ iterations).

4. Correcting the aerodynamic goals for the discrete solution ($O(10)$ iterations).

The main part of the optimization takes place in step 2, with steps 3 and 4 constituting a post processing operation. Moreover, note that step 1 may be dispensed if the

aerodynamic targets are guaranteed by other variables (e.g. shape or AoA). The drag coefficient for the design that only meets the lift constraint is 0.00917 (step 1). Some of the increase with respect to the baseline is due to re-meshing, most however, is due to the larger deformation which reduces the projected area of the wing, and thus requires the loading to be increased past the optimum found by shape optimization. This is expected to become worse with larger deformations at smaller fractions of stiff material. It is worth noting that single-point optimum shapes for flexible wings tend to result in flat deformed shapes (i.e. straight line from root to tip), which should be expected since for a given span this maximizes the projected area (after deformation). For the designs with smaller stiff fraction (after 3.2.1), the drag coefficient increases to 0.011 and in the final discrete solution (that meets the lift constraint more strictly) it is 0.0115. This is a significant increase that is not entirely justified by larger deformations. Recall that the lift-generation mechanism used by the topology optimization is to allow the mid span to pitch-up to both reduce and compensate the effects of higher pitch-down moments near the tip. In addition, to reduce the stiff fraction with limited compliance requires material to be removed from low strain regions, note how past 60% span the design uses almost no stiff material. Consequently, this allows those areas to deform more, that is, incidence is reduced due to the pitch-down moments. This reduces the lift generated by those sections of the wing, in turn requiring the inboard sections to produce even more lift to compensate (drag increases as the spanwise distribution of lift moves away from the optimized baseline). This effect is visible in Fig. 10a and Fig. 10b, where the deformation of the final design is compared with the one from section 3.2.1, and it explains the vestigial areas of stiff material near the tip of the wing, whose placement at the leading and trailing edges maximizes torsional stiffness.
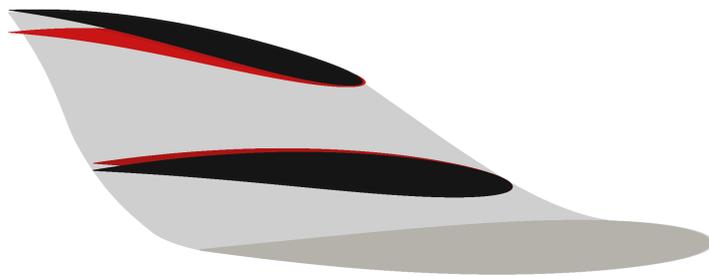
(a) Deformation at mid-span and tip, of the final design (dark colors, reduced by 20%), and the design obtained to meet the lift constraint.
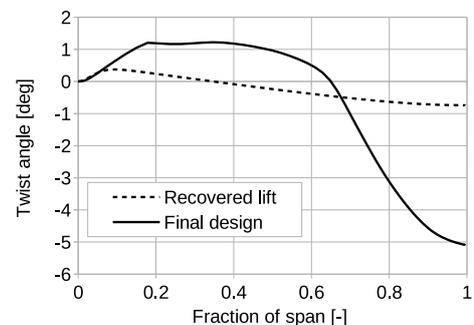
(b) Spanwise distribution of twist.

Figure 10: Comparison of deformed configurations, between recovering lift and final design.

Note finally that these reinforced areas (discussed above) are not connected to the larger areas of stiff material, in effect, this reduces the coupling between the two (note the rapid change of twist after 0.6 span in Fig. 10b). Moreover, although the final design deforms more in torsion and bending, the corresponding moments are lower. These interruptions of the main load paths (i.e. stiff material portions) are necessary for the aerodynamic goals but raise structural concerns. In particular they cause the soft material to be more strained than its stiff counterpart, due to being compressed and sheared between floating regions of stiff material that are not connected to the root. Figure 11 shows the von Mises

Pedro Gomes and Rafael Palacios

stresses divided by the local elasticity modulus. It would important, therefore, to include stress constraints in future work.
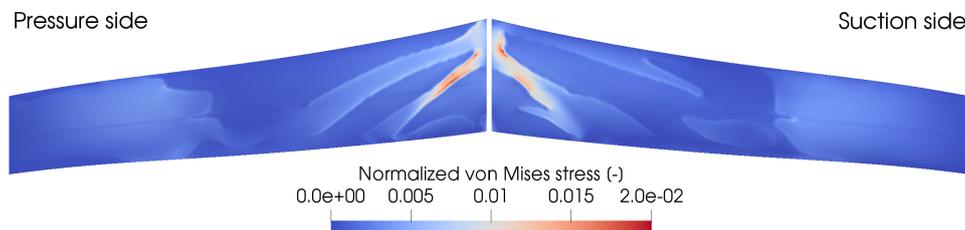
Figure 11: Von Mises stress normalized by local elasticity modulus.

4 FINAL REMARKS

This work aimed to explore the merits and challenges of applying a technique (topology optimization) that is well established for purely structural applications, to problems where the structure is largely responsible for the aerodynamic performance. This was done by restricting the example problem to a single operating point and only topology variables. To fully access the challenges of topology optimization in state-of-the-art wing design methods, many other aspects would have to be considered (shape optimization, multiple operating points, off-design performance, composite materials, manufacturability, cost, etc.). Nevertheless, this use of topology optimization appears to have merit, to the extent that the topological features can be traced back to aerodynamic effects. Furthermore, such features develop in a similar number of iterations as they would for purely structural problems. However, as a consequence of the limited means the optimization was given to realize its goals, the aerodynamic performance of the final design was reduced. Better performance could be expected, for example, from simply allowing the angle of attack to change, thereby allowing the inboard sections to operate at higher incidence without having to compromise the stiffness of the structure so severely by removing stiff material near the root. However, in so doing, the (desired) load augmentation characteristic of the problem would be lost. Ideal performance, on the other hand, can only be expected from a simultaneous optimization of shape and topology, which proved challenging for this type problem. In particular, the exterior penalty approach is much less suited for shape optimization than SLSQP, especially if the design space is augmented with three orders of magnitude more design variables (conversely SLSQP is not adequate for large scale optimization problems due to its dense approximation of the Hessian matrix).

One of the challenges in this type of topology optimization is the higher computational cost of using high-fidelity models, when approximately 10 times more iterations are required than for shape optimization. The greatest challenge, however, is that aerodynamic goals do not benefit from an optimally stiff structure, and thus the optimization will not converge to a discrete solution, unless that goal is explicitly introduced. Of course, level-set topology optimization methods (which were not explored in this work) guarantee that the solution will be discrete. However, a further contributor to the discreteness challenge is that loads are distributed over a large surface, whose smoothness is important for aerodynamic performance. Since it is more efficient to maintain that smoothness with a large number of small supports, than with a few highly rigid connections, the mesh size required to resolve those features may render 3-D application impractical. In that respect density-

based methods may have some advantage due to their connection with homogenization theory. In any case, the solutions proposed in this work address both the high computational cost and the discrete-solution challenges. Notwithstanding, comparing level-set approaches with density-based methods for the type of problem studied here should be the subject of future work. For that it will be important to study the interaction between shape and topology optimization, whether by proposing efficient sequential approaches or by using an optimization method that can consider both sets of variables simultaneously.

ACKNOWLEDGEMENTS

REFERENCES

[1] L. Krog, A. Tucker, M. Kemp, and R. Boyd. Topology Optimisation of Aircraft Wing Box Ribs, September 2004.

[2] T. W. Chin and G. Kennedy. Large-Scale Compliance-Minimization and Buckling Topology Optimization of the Undeformed Common Research Model Wing. In *57th AIAA/ASCE/AHS/ASC Structures, Structural Dynamics, and Materials Conference*, January 2016.

[3] J. H. Zhu, W. H. Zhang, and L. Xia. Topology Optimization in Aircraft and Aerospace Structures Design. *Archives of Computational Methods in Engineering*, 23(4):595–622, 2016.

[4] K. A. James, G. J. Kennedy, and J. R. Martins. Concurrent aerostructural topology optimization of a wing box. *Computers and Structures*, 134:1–17, 2014.

[5] P. D. Dunning, B. K. Stanford, and H. A. Kim. Coupled aerostructural topology optimization using a level set method for 3D aircraft wings. *Structural and Multidisciplinary Optimization*, 51(5):1113–1132, 2015.

[6] S. Kambampati, S. Townsend, and H. A. Kim. Coupled Aerostructural Level Set Topology Optimization of Aircraft Wing Boxes. *AIAA Journal*, 58(8):3614–3624, 2020.

[7] K. Maute, M. Nikbay, and C. Farhat. Conceptual layout of aeroelastic wing structures by topology optimization. In *43rd AIAA/ASME/ASCE/AHS/ASC Structures, Structural Dynamics, and Materials Conference*, Denver, Colorado, Apr 2002.

[8] K. Maute and M. Allen. Conceptual design of aeroelastic structures by topology optimization. *Structural and Multidisciplinary Optimization*, 27(1-2):27–42, 2004.

[9] P. Gomes and R. Palacios. Aerodynamic-driven topology optimization of compliant airfoils. *Structural and Multidisciplinary Optimization*, 62(4):2117–2130, 2020.

[10] K. K. Maute and G. W. Reich. Integrated Multidisciplinary Topology Optimization Approach to Adaptive Wing Design. *Journal of Aircraft*, 43(1):253–263, 2006.

[11] B. Stanford and P. Ifju. Aeroelastic topology optimization of membrane structures for micro air vehicles. *Structural and Multidisciplinary Optimization*, 38(3):301–316, 2009.

[12] B. Stanford and P. Beran. Optimal Structural Topology of a Platelike Wing for Subsonic Aeroelastic Stability. *Journal of Aircraft*, 48(4):1193–1203, 2011.

[13] B. Stanford, P. Beran, and M. Kobayashi. Simultaneous Topology Optimization of Membrane Wings and Their Compliant Flapping Mechanisms. *AIAA Journal*, 51 (6):1431–1441, 2013.

[14] S. Townsend, R. Picelli, B. Stanford, and H. A. Kim. Structural Optimization of Platelike Aircraft Wings Under Flutter and Divergence Constraints. *AIAA Journal*, 56(8):3307–3319, 2018.

[15] B. Stanford. Topology Optimization of Low-Speed Aeroelastic Wind Tunnel Models. In *AIAA Scitech 2021 Forum*. American Institute of Aeronautics and Astronautics, January 2021.

[16] T. D. Economon, F. Palacios, S. R. Copeland, T. W. Lukaczyk, and J. J. Alonso. SU2: An Open-Source Suite for Multiphysics Simulation and Design. *AIAA Journal*, 54(3):828–846, 2016.

[17] O. Burghardt, N. R. Gauger, P. Gomes, R. Palacios, T. Kattmann, and T. D. Economon. Coupled Discrete Adjoints for Multiphysics in SU2. In *AIAA AVIATION 2020 FORUM*, volume 1 PartF. American Institute of Aeronautics and Astronautics, June 2020.

[18] P. Gomes, T. D. Economon, and R. Palacios. Sustainable High-Performance Optimizations in SU2. In *AIAA Scitech 2021 Forum*. American Institute of Aeronautics and Astronautics, Jan 2021.

[19] R. Sanchez, T. Albring, R. Palacios, N. R. Gauger, T. D. Economon, and J. J. Alonso. Coupled adjoint-based sensitivities in large-displacement fluid-structure interaction using algorithmic differentiation. *International Journal for Numerical Methods in Engineering*, 113(7):1081–1107, 2018.

[20] T. A. Albring, M. Sagebaum, and N. R. Gauger. Efficient aerodynamic design using the discrete adjoint method in SU2. In *17th AIAA/ISSMO multidisciplinary analysis and optimization conference*, Washington, D.C., June 2016.

[21] P. R. Spalart and S. R. Allmaras. One-Equation Turbulence Model for Aerodynamic Flows. *Recherche Aerospatiale*, (1):5–21, 1994.

[22] S. Xu, D. Radford, M. Meyer, and J.-D. Müller. Stabilisation of discrete steady adjoint solvers. *Journal of Computational Physics*, 299:175–195, 2015.

[23] L. Wang, B. Diskin, E. J. Nielsen, and Y. Liu. Improvements in Iterative Convergence of FUN3D Solutions. In *AIAA Scitech 2021 Forum*. American Institute of Aeronautics and Astronautics, January 2021.

Pedro Gomes and Rafael Palacios

[24] J. Bonet and R. D. Wood. *Nonlinear continuum mechanics for finite element analysis, 2nd edition*. Cambridge University Press, 2008. ISBN 9780511755446.

[25] R. Sanchez, R. Palacios, T. D. Economon, H. L. Kline, J. J. Alonso, and F. Palacios. Towards a Fluid-Structure Interaction Solver for Problems with Large Deformations Within the Open-Source SU2 Suite. In *57th AIAA/ASCE/AHS/ASC Structures, Structural Dynamics, and Materials Conference*, January 2016.

[26] P. Hénon, P. Ramet, and J. Roman. PaStiX: A High-Performance Parallel Direct Solver for Sparse Symmetric Definite Systems. *Parallel Computing*, 28(2):301–321, 2002.

[27] M. B. Giles, M. C. Duta, J.-D. Muller, and N. A. Pierce. Algorithm Developments for Discrete Adjoint Methods. *AIAA Journal*, 41(2):198–205, 2003.

[28] M. S. Campobasso and M. B. Giles. Effects of Flow Instabilities on the Linear Analysis of Turbomachinery Aeroelasticity. *Journal of Propulsion and Power*, 19(2): 250–259, 2003.

[29] G. K. Kenway, C. A. Mader, P. He, and J. R. Martins. Effective adjoint approaches for computational fluid dynamics. *Progress in Aerospace Sciences*, 110, 2019.

[30] T. E. Bruns and D. A. Tortorelli. Topology optimization of non-linear elastic structures and compliant mechanisms. *Computer Methods in Applied Mechanics and Engineering*, 190(26-27):3443–3459, 2001.

[31] C. Zhu, R. H. Byrd, P. Lu, and J. Nocedal. Algorithm 778: L-BFGS-B: Fortran subroutines for large-scale bound-constrained optimization. *ACM Transactions on Mathematical Software*, 23(4):550–560, 1997.

[32] E. Jones, T. Oliphant, P. Peterson, et al. SciPy: Open source scientific tools for Python, 2001–. URL `http://www.scipy.org/`. [Online; accessed 08/06/2021].

[33] K. Svanberg. The method of moving asymptotes—a new method for structural optimization. *International Journal for Numerical Methods in Engineering*, 24(2):359–373, 1987.

[34] A. Wächter and L. T. Biegler. On the implementation of an interior-point filter line-search algorithm for large-scale nonlinear programming. *Mathematical Programming*, 106(1):25–57, 2006.

[35] S. Rojas-Labanda and M. Stolpe. Benchmarking optimization solvers for structural topology optimization. *Structural and Multidisciplinary Optimization*, 52(3):527–547, 2015.

[36] G. Kennedy and Y. Fu. Topology Optimization Benchmark Problems for Assessing the Performance of Optimization Algorithms. In *AIAA Scitech 2021 Forum*. American Institute of Aeronautics and Astronautics, January 2021.

[37] T.-Y. Chen and S.-C. Wu. Multiobjective optimal topology design of structures. *Computational Mechanics*, 21(6):483–492, 1998.

TOWARDS MANUFACTURED LATTICE STRUCTURES: A COMPARISON BETWEEN LAYOUT AND TOPOLOGY OPTIMIZATION

Enrico Stragiotti[1], François-Xavier Irisarri[1], Cédric Julien[1] and Joseph Morlier[2]

1: ONERA - The French Aerospace Lab
DMAS - Département matériaux et structures
92320 Châtillon, France
{enrico.stragiotti, francois-xavier.irisarri, cedric.julien}@onera.fr

2: ICA - Institut Clément Ader
ISAE - SUPAERO
31400 Toulouse, France
joseph.morlier@isae-supaero.fr

Abstract. *The repetitive nature of cellular lattice structures brings various interesting features among which fast assembly and repair time, reduced tooling, and manufacturing costs are major advantages. Additionally, as the mechanical performances of the structure are heavily influenced by the topology and materials of the cell, the designers can optimize the cell to tailor the structure for various scenarios. In this paper, we discuss and compare two relevant structural optimization methods for lattice structures: topology optimization and layout optimization. In the first part of the article, we presented an innovative cellular topology optimization formulation that minimizes the structural mass taking into account the internal stresses. The cellular implementation is based on the full-scale method called variable linking. In the second part, a qualitative comparison of topology and layout optimization is carried out, analysing the strength and the weakness of the two methods when applied to a lattice structure context.*

Keywords: Lattice Structures, Topology Optimization, Layout Optimization, Stress-Constrained Optimization, Structural Optimization

Enrico Stragiotti, François-Xavier Irisarri, Cédric Julien and Joseph Morlier

1 INTRODUCTION

The reduction of weight and the minimization of environmental cost are some of the major subjects on which every aerospace company is focusing at this moment. One of the fields that could significantly contribute to achieving this goal is structural optimization. The efficient use of the material in complex components helps to achieve enhanced mechanical performances, failure-safe behaviour, and minimum weight. The general aim of our study is to develop an optimization methodology for cellular lattice structures. The repetitive nature of such structures brings various interesting features among which fast assembly and repair time, reduced tooling, and manufacturing costs are major advantages. Additionally, as the mechanical performances of the structure are heavily influenced by the topology and materials of the cell, the designers can optimize the cell to tailor the structure for various scenarios. For instance, cellular lattice structures have been shown to be interesting candidates for innovative wing structures [1–3].

In this paper, we discuss and compare two relevant structural optimization methods for lattice structures: topology optimization [4, 5] and layout optimization [6, 7]. Topology optimization considers the design domain as a continuum, in which each location may or may not have a material assigned to it, while layout optimization is applied to a ground structure, a discrete environment. The latter is an algorithm that identifies the optimal section sizes and connectivity of the members of a truss. To benchmark the two algorithms, a stress-constrained multi-scale optimization is set up, in which the objective is to minimize the volume of the structure. The performances, shape, and manufacturability of the optimized results are compared.

The literature of cellular structure optimization is mainly divided into full-scale and multi-scale approaches [8]. This paper focuses on cellular structures for which there is no clear scale separation between the repeating pattern and the full structure. Thus, we are from now on only considering full-scale approaches. Compared to multi-scale approaches, full-scale approaches are less covered in the literature.

While full-scale approaches have been already applied to compliance minimization [8] and mechanism design [9] problems, there are, to the authors' knowledge, no published studies on stress-constrained volume minimization full-scale optimization.

This paper is structured in the following way: in Section 2 we present the stress-based volume minimization topology optimization problem [10] and its extension to cellular structures using the variable linking method [9, 11]. Cellular and non-cellular approaches are compared. In Section 3, layout optimization is compared in a qualitative way to topology optimization in the full-scale optimization framework. Concluding remarks are given in Section 4.

2 STRESS-BASED CELLULAR TOPOLOGY OPTIMIZATION

2.1 Stress-based Topology Optimization

Let Ω be a rectangular domain of dimensions X and Y, containing respectively N_x and N_y linear 4-nodes elements. Following the classic topology optimization theory, a density variable ρ is linked to every element of the structure. The density variable can span between zero and one and represents void or full material, respectively. The classic objective function for a topology optimization problem is the minimization of the compliance [5]. Instead of finding the stiffest structure with a fixed volume fraction, we decided in

Enrico Stragiotti, François-Xavier Irisarri, Cédric Julien and Joseph Morlier

this paper to reformulate the compliance minimization problem and search for the lowest volume structure with a local strength constraint.

Three main difficulties may arise in solving this problem:

1. The stress constraints are defined only for the elements where $\rho_i > 0$, thus the set of constraints changes during the optimization. This class of problems are called mathematical programs with vanishing constraints (MPVCs) [12] and are known for being difficult to solve.

2. Is it known in the literature [13, 14] that MPVCs often suffer from *singular minima*: firstly observed on truss structure optimization [15], they are inaccessible to standard gradient-based optimizer, and they represent the *minima* of the optimization. This problem is often solved using a technique called *relaxation*.

3. The stress is a local measure, and thus a large set of constraints is generated when a reasonably fine mesh is used (one element, one constraint). This problem is often solved using a technique called *aggregation*.

The implementation of this paper is based on the use of a lower bound Kreisselmeier-Steinhauser (KS) function [16] to apply relaxation and aggregation at the same time [10]. One could formulate the normalized local stress constraint as:

$$g_j = \frac{\sigma_{VM,j}}{\sigma_l} - 1 \leq 0, \quad \forall j \in \Omega_{mat}(\boldsymbol{\rho}), \tag{1}$$

where $\Omega_{mat}(\boldsymbol{\rho})$ represents the design-dependent set of elements with a non-zero density, $\sigma_{VM,i}$ represents the equivalent von Mises stress for the element i, and σ_l is the maximum allowable equivalent von Mises stress. In this formulation all the stresses are evaluated using the microscopic stress formulation and assuming that there is no direct correlation between stress and density [17]. Indeed, the use of the macroscopic stress in volume minimization optimization problems creates all-void design [18]. The original set of constraints is reformulated into an equivalent design-independent set of constraints [19]:

$$\bar{g}_i = \bar{\bar{\rho}}_i g_i = \bar{\bar{\rho}}_i \left(\frac{\sigma_{VM,i}}{\sigma_l} - 1 \right) \leq 0, \quad \forall i \in \Omega. \tag{2}$$

Following the work developed by Verbart [10], the lower bound Kreisselmeier-Steinhauser function is used to approximate the local relaxed stress constraint maximum:

$$G_{KS}^l = \frac{1}{P} \ln \left(\frac{1}{N_e} \sum e^{P\bar{g}_i} \right) \quad \text{with } N_e = \text{ number of elements } e \in \Omega. \tag{3}$$

Its main advantage over other different formulations is that it uses a single hyperparameter P to control the aggregation and the relaxation of the constraints.

The optimization problem is then written as:

$$(\mathbb{P}_1): \quad \min_{\boldsymbol{\rho}} \quad V = \frac{1}{V_0} \sum_{i \in \Omega} \bar{\bar{\rho}}_i v_i$$

$$\text{s.t.} \quad G_{KS}^l = \frac{1}{P} \ln \left(\frac{1}{N_e} \sum_{i \in \Omega} e^{P\bar{g}_i} \right) \leq 0 \tag{4}$$

$$\boldsymbol{KU} = \boldsymbol{F}$$

$$0 \leq \rho_i \leq 1,$$

Enrico Stragiotti, François-Xavier Irisarri, Cédric Julien and Joseph Morlier

where v_i represents the volume of the i-th element and the objective function V is the volume fraction occupied in the volume $V_0 = \sum v_i$. $\boldsymbol{\rho} = [\rho_1, \rho_2, \ldots, \rho_{Ne}]^T$ represents the design variable of the optimization, while $\overline{\widetilde{\boldsymbol{\rho}}} = [\overline{\widetilde{\rho}}_1, \overline{\widetilde{\rho}}_2, \ldots, \overline{\widetilde{\rho}}_{Ne}]^T$ represents the physical density, obtained after filtering and projection of $\boldsymbol{\rho}$. $\boldsymbol{K}\boldsymbol{U} = \boldsymbol{F}$ is the state equation of the problem and define the elastic response of the structure to an external load $\boldsymbol{F} = [f_1, f_2, \ldots, f_{Ne}]^T$. The global stiffness matrix $\boldsymbol{K}$ is assembled from the element stiffness matrix $\boldsymbol{K} = \sum_{i \in \Omega} \boldsymbol{K}_{e,i}$ and $\boldsymbol{K}_{e,i} = E_i \boldsymbol{K}_{e,0}$ where $\boldsymbol{K}_{e,0}$ represents the stiffness matrix relative to the chosen type of element and $E_i(\overline{\widetilde{\rho}}_i)$ the Young's modulus of the element. In this paper, we use the Solid Isotropic Material Interpolation with Penalization (SIMP) [20] approach to calculate $E_i(\overline{\widetilde{\rho}}_i)$. It is governed by the equation:

$$E_i = E_{\min} + \overline{\widetilde{\rho}}_i^p (E_0 - E_{\min}), \tag{5}$$

where the parameter p penalizes the intermediate densities and pushes the result to a black and white result. E_0 is the young's modulus of the full material and $E_{\min}$ is a small value that avoid the global stiffness matrix $\boldsymbol{K}$ from being singular when $\overline{\widetilde{\rho}}_i = 0$. In this paper we set $E_0 = 1$, $E_{\min} = 10^{-9}$ and $p = 3$.

To solve the problems linked to the mesh discretization, such as the mesh dependence or the chequerboard problem, a standard linear spatial filter based on the 2D convolution operator [21] is used. The weight function $w(d)$ is defined as:

$$w(d_j) = R - d_j, \quad j \in \mathbb{N}_{i,R}, \tag{6}$$

where $\mathbb{N}_{i,R}$ represent the set of elements lying within a circle of radius R centred on the i-th element. d_i is the distance of the j-th element to the centre of the filter. The filtered values of the design variable calculated as:

$$\widetilde{\rho}_i = \frac{\sum_{j \in \mathbb{N}_{i,R}} w(d_j) v_j \rho_j}{\sum_{j \in \mathbb{N}_{i,R}} w(d_j) v_j}. \tag{7}$$

The derivative of the filtered densities $\widetilde{\boldsymbol{\rho}}$ with respect to the design variables $\boldsymbol{\rho}$ is:

$$\frac{\partial \widetilde{\rho}_i}{\partial \rho_j} = \frac{w(d_j) v_j}{\sum_{j \in \mathbb{N}_{i,R}} w(d_j) v_j}. \tag{8}$$

As the filtering phase usually produces a large quantity of grey element, a smooth projection technique based on the *tanh* function is implemented [22]:

$$\overline{\widetilde{\rho}}_j = \frac{\tanh(\beta\eta) + \tanh(\beta(\widetilde{\rho}_j - \eta))}{\tanh(\beta\eta) + \tanh(\beta(1 - \eta))}, \tag{9}$$

where β is a parameter that define the slope of this approximation function and η is the threshold value. It is important to note that this type of projection is not volume conservative for all values of η. In order to stay conservative we decided to have a volume-increasing filter, and a value of $\eta = 0.4$ is chosen in this work [23]. The sensitivity of the physical densities $\overline{\widetilde{\boldsymbol{\rho}}}$ with respect to the filtered $\widetilde{\boldsymbol{\rho}}$ can be written as:

$$\frac{\partial \overline{\widetilde{\rho}}_j}{\partial \widetilde{\rho}_j} = \beta \frac{1 - \tanh^2(\beta(\widetilde{\rho}_j - \eta))}{\tanh(\beta\eta) + \tanh(\beta(1 - \eta))}. \tag{10}$$

Enrico Stragiotti, François-Xavier Irisarri, Cédric Julien and Joseph Morlier

Using the chain rule is possible to write:

$$\frac{\partial f}{\partial \rho_i} = \sum_{j \in \mathbb{N}_{i,R}} \frac{\partial f}{\partial \overline{\widetilde{\rho}}_j} \frac{\partial \overline{\widetilde{\rho}}_j}{\partial \widetilde{\rho}_j} \frac{\partial \widetilde{\rho}_j}{\partial \rho_i}, \tag{11}$$

where f represent a generic function.

Using the adjoint method the sensitivity analysis of $\mathbb{P}_1$ with respect to the physical densities $\overline{\widetilde{\boldsymbol{\rho}}}$ become:

$$\frac{\partial V}{\partial \overline{\widetilde{\rho}}_i} = \frac{v_i}{V_0}, \tag{12}$$

$$G_{KS}^l = g(\overline{\widetilde{\boldsymbol{\rho}}}, \boldsymbol{U}(\overline{\widetilde{\boldsymbol{\rho}}})) \iff \frac{dg}{d\overline{\widetilde{\rho}}_i} = \frac{\partial g}{\partial \overline{\widetilde{\rho}}_i} + \frac{\partial g}{\partial \boldsymbol{U}}^T \frac{d\boldsymbol{U}}{d\overline{\widetilde{\rho}}_i} \tag{13}$$

$$\frac{\partial g}{\partial \boldsymbol{U}} = \frac{\frac{\rho_i}{\sigma_l \sigma_i} e^{P\bar{g}_i}}{\sum_i e^{P\bar{g}_i}} |\boldsymbol{S_i}|_g \boldsymbol{U} \tag{14}$$

$$\frac{dg}{d\overline{\widetilde{\rho}}_i} = \left(\frac{\sigma_{VM,j}}{\sigma_l} - 1 \right) \frac{e^{P\bar{g}_j}}{\sum_k e^{P\bar{g}_k}} - \boldsymbol{\lambda} \left(-P \overline{\widetilde{\rho}}_i^{P-1} \boldsymbol{K}_{e,i} \right) \boldsymbol{U}, \tag{15}$$

where $\boldsymbol{\lambda}$ is the adjoint vector that solves the adjoint system $\boldsymbol{K\lambda} = \partial g/\partial \boldsymbol{U}$ and $|\boldsymbol{S_i}|_g$ represents the matrix that links local to global coordinates (in the same way we linked $\boldsymbol{K}_{e,i}$ to $\boldsymbol{K}$).

2.2 Cellular approach — Variable linking scheme

The cellular approach is implemented using a variable linking scheme on a structured grid [11]. The design variables $\boldsymbol{\kappa} = [\kappa_1, \kappa_2, \ldots, \kappa_{n_e}]^T$ where $n_e = n_x \times n_y$ is the number of elements are defined in a design cell Ω_c. $\boldsymbol{\kappa}$ is defined on every finite element of Ω_c and linked to the density $\boldsymbol{\rho}$ over the entire structure Ω (see Figure 1). Following the nomenclature of Wu [8], this method can be described as a full-scale approach with repeated pattern.
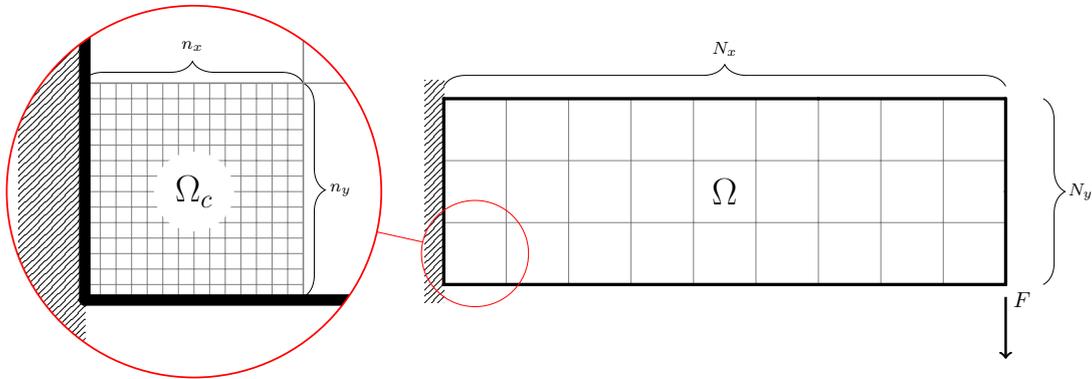

Figure 1: Design domain and boundary condition for a cantilever beam using a variable linking scheme. The design variables $\boldsymbol{\kappa}$ inside the domain Ω_c are linked to the structure Ω to evaluate the state equation.

Enrico Stragiotti, François-Xavier Irisarri, Cédric Julien and Joseph Morlier

A common way to implement this approach is by defining a mapping matrix $\boldsymbol{G}$ [9] and retrieving the optimization densities by using the following relation $\boldsymbol{\rho} = \boldsymbol{G}\boldsymbol{\kappa}$. $\boldsymbol{G}$ is a sparse $N_e \times n_e$ matrix where, if the design variable κ_j is linked to the optimization variable ρ_i, then $\boldsymbol{G}(i,j) = 1$. Problem $\mathbb{P}_1$ is then reformulated as follows:

$$
\begin{aligned}
(\mathbb{P}_1^*): \quad \min_{\boldsymbol{\kappa}} \quad & V = \frac{1}{V_0} \sum_{k \in \Omega_c} \kappa_k v_k \\
\text{s.t.} \quad & G_{KS}^l = \frac{1}{P} \ln\left(\frac{1}{N} \sum_{i \in \Omega} e^{P\bar{g}_i} \right) \leq 0 \\
& \boldsymbol{KU} = \boldsymbol{F} \\
& 0 \leq \kappa_k \leq 1 \\
& \boldsymbol{\rho} = \boldsymbol{G}\boldsymbol{\kappa}.
\end{aligned}
\tag{16}
$$

where Ω_c represents the design cell (see Figure 1).

The sensitivity of the objective function and the constraints with respect to the design variables are calculated as [9]:

$$
\frac{\partial f}{\partial \kappa_k} = \boldsymbol{G}^T \frac{\partial f}{\partial \overline{\bar{\rho}}_i}.
\tag{17}
$$

The full sensitivities can then be calculated combining Equation 11, 12, 15 and 17. Derivatives are smooth and then suitable for gradient descent optimization algorithms.

2.3 Numerical results and discussion

The cantilever beam, together with the L-shape domain, represents one of the standard load cases used to assess the performance of a stress-constrained topology optimization [10]. The mesh used to discretize the full structure is made up by 400×200 linear 4-nodes
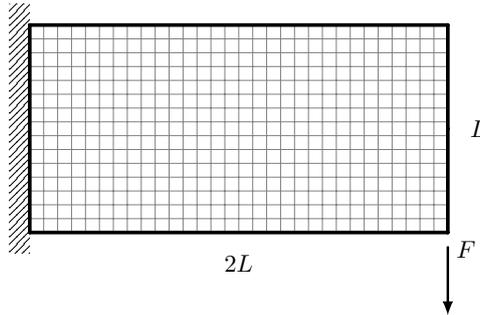
Figure 2: Cantilever beam load case. The domain is discretized into 400×200 linear quadratic elements.

elements (see Figure 2). The punctual load is distributed over 10 elements to avoid stress concentrations.

Problem 16 is solved for four different numbers of design cells (1×1, 2×1, 4×2, and 8×4 cells). It is important to note that the full structure mesh is the same for all the cases, while the design space Ω_c shrinks down as more and more cells are added.

The optimizing algorithm chosen is the Method of Moving Asymptotes (MMA) [24]. The parameter called *movelimit* is set to 0.1. The other algorithm's parameters are set to their default value. More information on the implementation of the *movelimit*

Enrico Stragiotti, François-Xavier Irisarri, Cédric Julien and Joseph Morlier

(a) 1×1 cell
V = 10.52%

(b) 1×1 cell
$\sigma_{\max} = 0.350$

(c) Compliance min.
V = 10.52%

(d) 2×1 cells
V = 14.41%

(e) 2×1 cells
$\sigma_{\max} = 0.383$

(f) Compliance min.
V = 14.41%

(g) 4×2 cells
V = 24.25%

(h) 4×2 cells
$\sigma_{\max} = 0.379$

(i) Compliance min.
V = 24.25%

(j) 8×4 cells
V = 27.57%

(k) 8×4 cells
$\sigma_{\max} = 0.396$

(l) Compliance min.
V = 27.57%

Figure 3: Topology optimization results. The first column presents the volume minimization density results. The central subfigures present the equivalent von Mises stress of the four load cases for the elements with a physical density $\widetilde{\overline{\rho}} > 0.5$. The last column presents the density of the results of the compliance minimization. The volume used as a constraint is the same found by the volume minimization.

Enrico Stragiotti, François-Xavier Irisarri, Cédric Julien and Joseph Morlier

parameter can be found on the original paper by Verbart [10]. A continuation scheme for the aggressiveness of the projection parameter β is set to increase by one every 200 iterations, the number of max iteration is set to 3000, the stoppi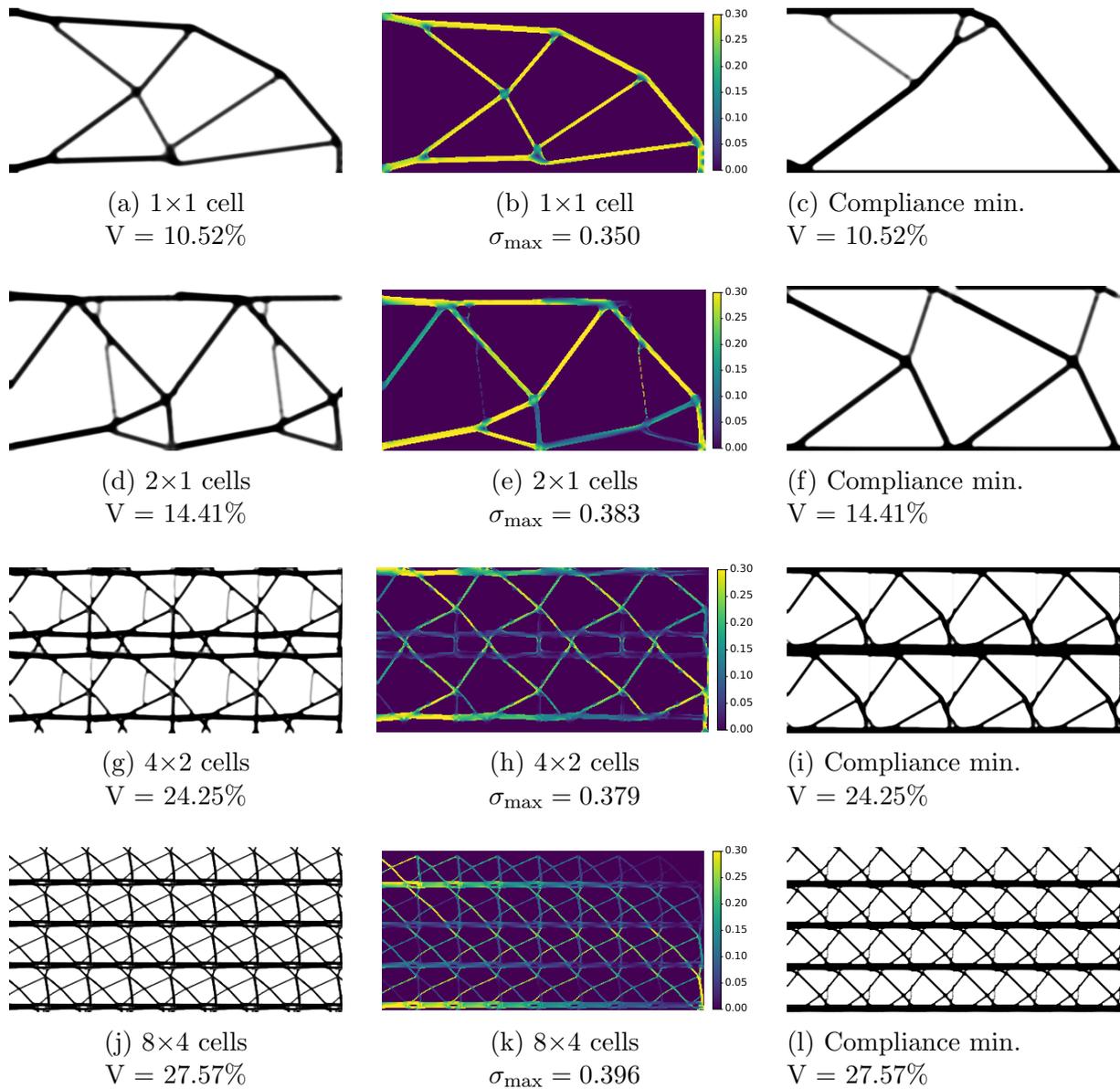ng criteria is calculated as $\|r_k\|_2/\sqrt{N_e}$ on the physical densities $\widetilde{\widetilde{\rho}}$ [23], and it is set to 10^{-4}. The aggregation parameter P is set to 32.

The isotropic material used for the optimization has been modelled with $E = 1$, $\nu = 0.3$ and the maximum allowable stress is set to $\sigma_L = 0.3$.

To evaluate the quality of the solutions, we evaluate the Measure of Non-Discreteness [25], where results near-zero mean a completely black and white design.

$$M_{nd} = \frac{\sum_e 4\overline{\widetilde{\rho}}_e(1 - \overline{\widetilde{\rho}}_e)}{n} \times 100\%. \tag{18}$$

Our optimization take into account only the linear behaviour of the structure.

Mesh size	Cells	Design Space	Volume	Max stress	M_{nd}
	1x1	400x200	10.52%	0.350	4.45%
400x200	2x1	200x200	14.41%	0.383	5.56%
	4x2	100x100	24.25%	0.379	10.22%
	8x4	50x50	27.57%	0.396	10.24%

Table 1: Numeric results of the variable linking approach applied to a topology optimization problem with stress constraints for increasing number of cells.

Looking at Table 1 and at Figure 3, we can summarize the results as:

- A first important remark is that the constraint function G_{KS}^l is always lower than the actual $\bar{g}$. As a consequence, the maximal von Mises stress is always greater than the actual allowable of 0.3. This is a known problem of this formulation [10].

- The optimized volume fraction increases with the number of cells, for a fixed maximal allowable stress (see Figure 4a). As the structure is divided into additional cells, the design space shrinks, constraining *de facto* our problem even more. This is a known drawback of cellular structures [8, 9].

- Classic volume minimization with stress constraints formulations tends to create full-stressed structures (see Figures 3a and b). When the linking variable approach is used, cells become less stressed, with the presence of elements that do not participate in the structural integrity of the cantilever. However, cellular structures are naturally more robust as they show structural redundancies and multiples stress paths. This opens up to the design of damage-tolerant structures [9].

- It is interesting to note that if the cells are stacked all one over the others, and we calculate the maximum stresses, one would find a full-stressed cell (see Figure 4b).

To assess the advantages of the volume minimization formulation, we compare the obtained results with those of compliance minimization. The compliance problem is formulated to accept a maximum volume fraction constraint, and we set that to the very same value found by the volume minimization. By doing so, it is possible to compare

maximum stresses and the compliance of the two linked formulations. Stress and compliance columns of Table 2 show the differences between the volume and the compliance minimization formulations. Figure 4a presents the general trend of the two different optimizations.

Volume	Cells	Volume minimization		Compliance minimization	
		Compliance	Max stress	Compliance	Max stress
10.52%	1x1	430.23 (1.19)	0.350 (1.0)	361.57 (1.0)	0.769 (2.19)
14.41%	2x1	412.52 (1.28)	0.383 (1.0)	320.89 (1.0)	0.783 (2.04)
24.25%	4x2	376.18 (1.34)	0.379 (1.0)	280.57 (1.0)	0.601 (1.58)
27.57%	8x4	369.50 (1.18)	0.396 (1.0)	312.52 (1.0)	1.470 (3.71)

Table 2: Comparison of the results obtained with the volume and the compliance minimization formulations. In the parenthesis, the results are normalized with respect to the maximum stress of the volume formulation and the compliance of the compliance formulation for a fixed volume fraction.

(a)   (b)
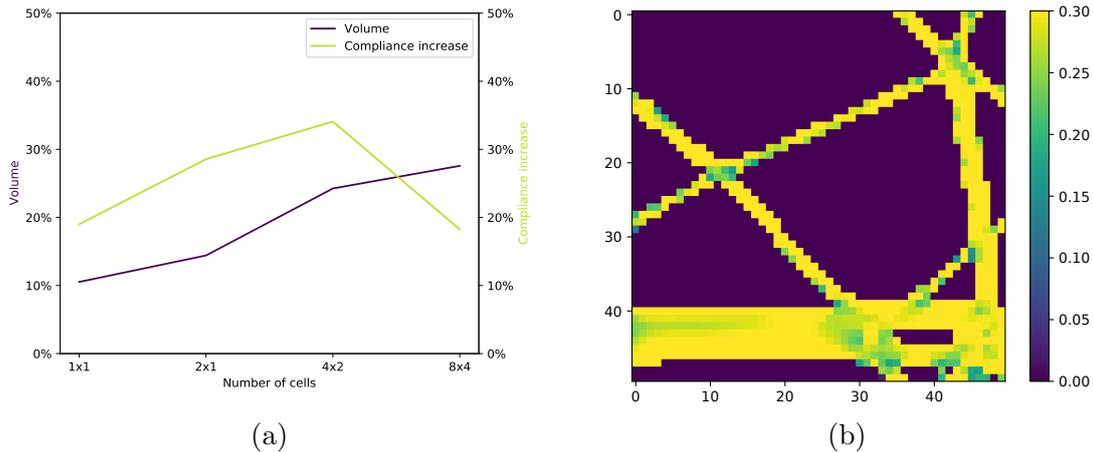
Figure 4: Figure 4a shows the trends of the optimization for the volume minimization formulation. The objective function is increasing with the number of cells. Figure 4b shows the 50×50 full-stressed cell, obtained superposing the maximum stress of all the cells inside Ω.

3 COMPARISON BETWEEN TOPOLOGY AND LAYOUT OPTIMIZATION

3.1 Cellular Layout Optimization

Layout optimization is a structural optimization algorithm that finds a near-optimal truss structure with respect to a given load case. Instead of working with a continuous domain as topology optimization does, layout optimization optimizes the sections and the connectivity of the members of a discrete ground structure [6]. The ground structure is defined as the full set of members that connect a grid of M points. For each member, we define a section a and a length l. As all the joints in the ground structure are treated as pin-joints, all the straight members face only tension or compression load.

Enrico Stragiotti, François-Xavier Irisarri, Cédric Julien and Joseph Morlier

Compared to the SIMP-based topology optimization described in Section 2, layout optimization seems appealing for the following reasons:

1. Looking at the pioneering works of Cramer [2] on ultralight structures as an example, we observe that the volume fraction of the cells is very low. The Ultem 100 and 200, the materials used by the authors to manufacture the cells, have a density of 1.42 g cm^{-3}. As the density of the cell structure is $5.566 \cdot 10^{-3}$ g cm^{-3}, we find a volume fraction of about 0.438%. It is known that such a low volume fraction on a regular, or even adaptive [26], mesh increases exponentially the number of elements required to correctly discretize the members in a topology optimization framework.

2. Even if the freedom of the design space offered by the continuum meshes used by topology optimization is higher, it is known that at these volume fractions and, especially if buckling constraints and manufacturing consideration are taken into account, the optimal topology is a truss structure [27]. Thus, for manufacturing easiness, one would prefer to directly work on a discrete ground structure. In addition to that, truss structures design naturally relies on constraints on maximum allowable stress, buckling, and maximum slenderness, which are all known for being difficult to implement on topology optimization.

3. Topology optimization needs massive computational resources to operate on large scale optimization [28], while layout optimization has been proven to work efficiently and fast for large aerospace applications [3].

The layout optimization problem is formulated as:

$$(\mathbb{P}_2): \quad \min_{\boldsymbol{a}} \quad V = \boldsymbol{l}^T \boldsymbol{a}$$
$$\text{s.t.} \quad \boldsymbol{B} \boldsymbol{q} = \boldsymbol{f}$$
$$-\sigma^- \boldsymbol{a} \leq \boldsymbol{q} \leq \sigma^+ \boldsymbol{a} \quad (19)$$
$$\boldsymbol{a} \geq 0,$$

where V represent the structural volume evaluated as the product of the member lengths $\boldsymbol{l} = [l_1, l_2, \ldots, l_N]^T$ and the design variables of the problem, the member sections $\boldsymbol{a} = [a_1, a_2, \ldots, a_N]^T$. $\boldsymbol{B}$ is a $2M \times N$ matrix containing the direction cosines of j-th member with respect to the i-th degree of freedom to calculate the nodal force equilibrium. M is the number of nodes and $N = M(M-1)/2$ the number of members of a fully connected ground structure. $\boldsymbol{q} = [q_1, q_2, \ldots, q_N]^T$ is a vector containing the internal member forces caused by the external load $\boldsymbol{f} = [f_1, f_2, \ldots, f_M]^T$. σ^- and σ^+ are the compressive and tensile maximum allowable stress of the material, respectively. The resolution of Problem 19 produces complex structures made up of a multitude of small members that tends to the shapes of Michell structures [7, 29]. While it is known that these structures are nearly optimal, one would want to limit the complexity of the structure. Substituting $\boldsymbol{l}$ with $\tilde{\boldsymbol{l}} = [l_1 + s, l_2 + s, \ldots, l_N + s]^T$, one would penalize the appearance of small members [30]. $\tilde{\boldsymbol{l}}$ is called augmented member length and s is the joint cost. This approach mimics the mesh-independency regularization filter of topology optimization [5].

As formulated, Problem 19 represents a linear programming (LP) problem that can be efficiently solved by modern algorithms. In this work, we used the python library CVXPY [31].

Enrico Stragiotti, François-Xavier Irisarri, Cédric Julien and Joseph Morlier

The cellular approach of layout optimization is formulated following the same steps used for the topology optimization. The only implementation difference is that one should note that two contiguous cells share multiples members. So we added to the formulation an equality constraint between the upper and lower, and the right and left members of the cells (see Figure 5a). The problem is still linear after that reformulation.
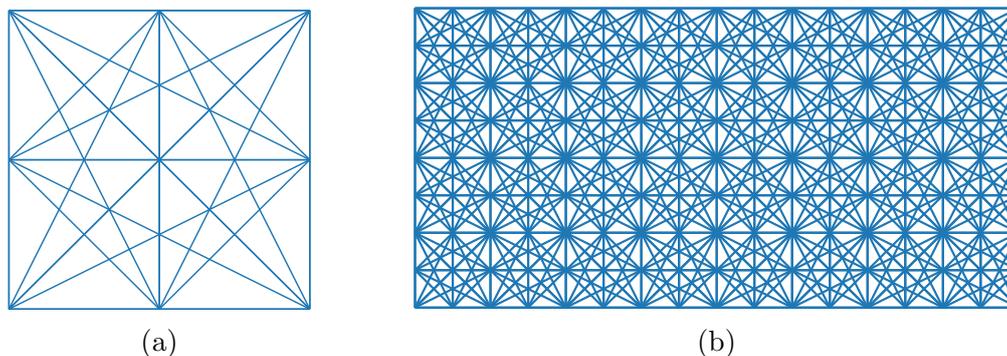

(a)   (b)

Figure 5: Figure 5a shows a 3-nodes cell of a ground structure made by the set of the 36 members that connect the nine points. Figure 5b present the 17×9 nodes ground structure made by 8×4 linked 3×3 cells.

3.2   Numerical results and topology optimization comparison

The python implementation of Problem 19 is based on the 98-lines code provided by He [32]. The code has been extended by the authors to perform variable linking. The cantilever beam load case is used once again to assess the performance of the optimization algorithm. The analysis is performed on a fixed ground structure made up by 17×9 points, with a total of 11628 candidate members for the 1×1 case, 6444 for the 2×1 case, 2300 for the 4×2 case, and 996 for the 8×4 case (see Figure 5a and 5b). The maximum allowable stress is set to $\sigma_L = 0.3$ for tension and compression. The results of the optimization are presented in Figure 6. We can summarize them as:

- Layout optimization presents the same trends of topology optimization concerning mechanical properties with respect to the number of cells. This is due to the restriction of the design space of the optimizer with the increase in the number of cells. It's interesting to note that changing the number of cells and thus the connectivity of the initial ground structure, not only the number of design variable, but the total number of members decrease as well.

- We find once again a full-stress design for the non-cellular case (see Figure 6b). The same considerations made for the full-stressed cell found in topology optimization hold for layout optimization as well.

- A direct comparison of the two formulations is non-trivial. In its most simple and diffused formulation, the mechanics of the material used for layout optimization follows the plastic design formulation. This means that the strain in the elastic region is considered negligible, and constant stress σ_y is therefore assumed for all non-zero strains. It is known that in stress-based topology optimization modifying Young's modulus E influences the solution found. Layout optimization and the

Enrico Stragiotti, François-Xavier Irisarri, Cédric Julien and Joseph Morlier

(a) 1×1 cell
V = 12446.12

(b) 1×1 cell.

(c) 2×1 cells
V = 18598.48

(d) 2×1 cells.

(e) 4×2 cells
V = 27916.67

(f) 4×2 cells.
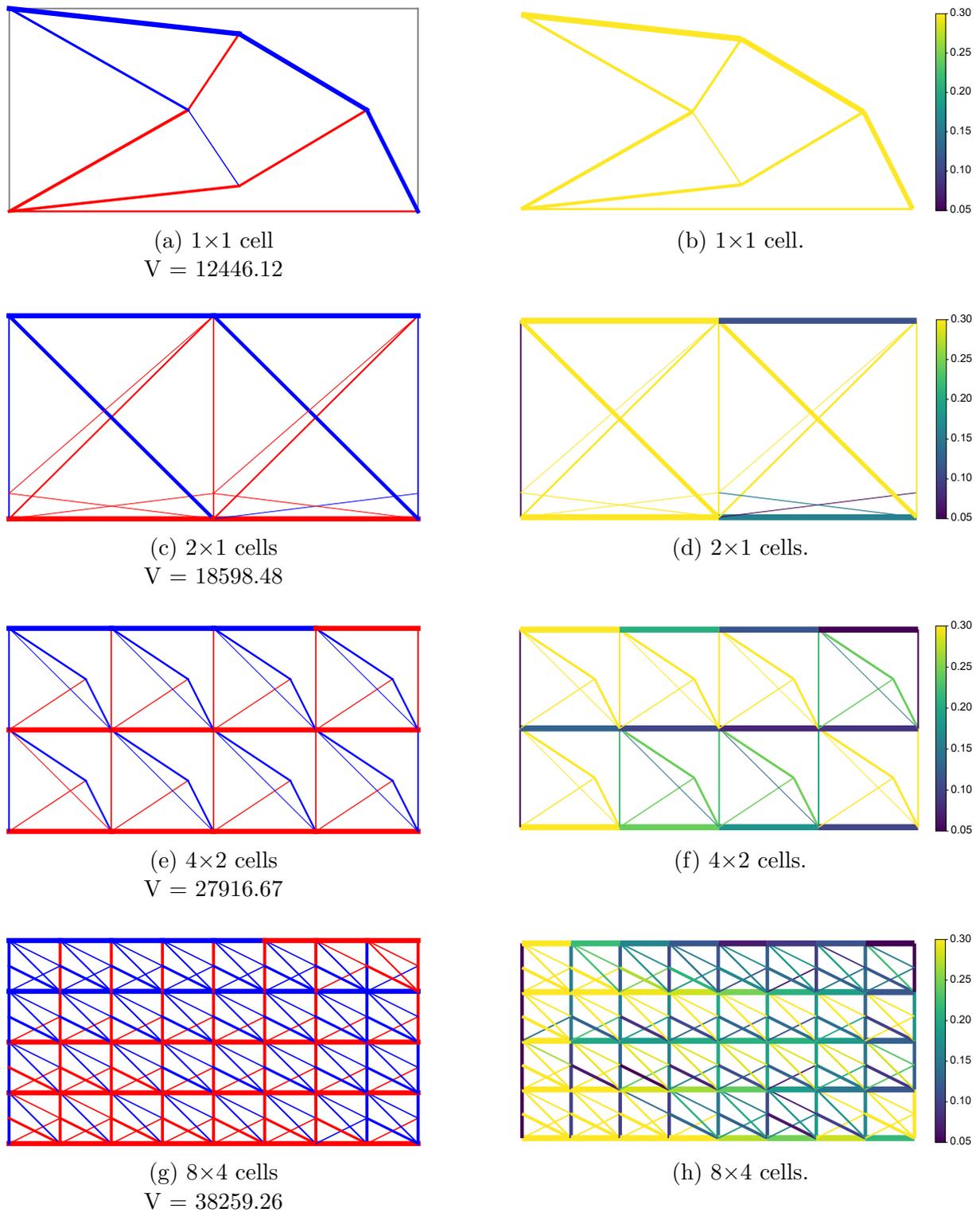
(g) 8×4 cells
V = 38259.26

(h) 8×4 cells.

Figure 6: Layout optimization results. The colour of the member represents the load state, with red used for compression and blue for tension. The optimal section of the members is proportional to the thickness of the segments.

Enrico Stragiotti, François-Xavier Irisarri, Cédric Julien and Joseph Morlier

plastic material formulation, instead, aren't influenced by this parameter at all. It is thus difficult to compare the two formulations from a quantitative point of view.

- The topology of the optimal lattice structure could be constrained by the initial ground structure if the latter is too coarse.

- Compared to topology optimization, the computational time of layout optimization for a comparable number of design variables is between three and four orders of magnitude inferior. The lack of FEA and the simpler problem formulation reduce the iteration cost and the iteration number.

4   CONCLUDING REMARKS

In the first part of the article, we presented an innovative cellular topology optimization formulation that minimizes the structural mass of a 2D structure taking into account the internal stresses. The cellular implementation is based on the full-scale method called *variable linking*. The optimized structures are easier to manufacture and assemble and naturally damage tolerant, at the cost of a higher structural volume and compliance. In the second part, a qualitative comparison of topology and layout optimization applied to a cellular structure is carried out, analysing the strength and the weakness of the two methods.

The results obtained by the two methods exhibit the same general trends. The calculation cost of layout optimization is significantly lower than for topology optimization. Nonetheless, the plastic formulation in the layout optimization problem does not account for the material stiffness. With pin-jointed trusses and no material elastic behaviour, the obtained result is questionable from a mechanical point of view.

To do a proper quantitative comparison there is the need to add the material elastic behaviour to the layout optimization. A promising way to do that is to add what is known in the literature as a stress-strain compatibility [3]. Formulated in that way, the problem becomes non-linear, but the resulting structures will have a more meaningful mechanical behaviour.

REFERENCES

[1] B. Jenett, S. Calisch, D. Cellucci, N. Cramer, N. Gershenfeld, S. Swei, and K. C. Cheung. Digital Morphing Wing: Active Wing Shaping Concept Using Composite Lattice-Based Cellular Structures. *Soft Robotics*, 4(1):33–48, Mar. 2017. doi:10.1089/soro.2016.0032.

[2] N. B. Cramer, D. W. Cellucci, O. B. Formoso, C. E. Gregg, B. E. Jenett, J. H. Kim, M. Lendraitis, S. S. Swei, G. T. Trinh, K. V. Trinh, and K. C. Cheung. Elastic shape morphing of ultralight structures by programmable assembly. *Smart Materials and Structures*, 28(5):055006, Apr. 2019. doi:10.1088/1361-665X/ab0ea2.

[3] M. M. J. Opgenoord and K. E. Willcox. Design for additive manufacturing: cellular structures in early-stage aerospace design. *Structural and Multidisciplinary Optimization*, 60(2):411–428, Aug. 2019. doi:10.1007/s00158-019-02305-8.

[4] M. P. Bendsøe. Optimal shape design as a material distribution problem. *Structural optimization*, 1(4):193–202, Dec. 1989. doi:10.1007/BF01650949.

Enrico Stragiotti, François-Xavier Irisarri, Cédric Julien and Joseph Morlier

[5] M. P. Bendsøe and O. Sigmund. *Topology Optimization.* Springer Berlin Heidelberg, Berlin, Heidelberg, 2004. doi:10.1007/978-3-662-05086-6.

[6] W. S. Dorn, R. E. Gomory, and H. Greenberg. Automatic design of optimal structures. *J. Mécanique*, 1964.

[7] M. Gilbert and A. Tyas. Layout optimization of large-scale pin-jointed frames. *Engineering Computations*, 20(8):1044–1064, Dec. 2003. doi:10.1108/02644400310503017.

[8] J. Wu, O. Sigmund, and J. P. Groen. Topology optimization of multi-scale structures: a review. *Structural and Multidisciplinary Optimization*, Mar. 2021. doi:10.1007/s00158-021-02881-8.

[9] K. Wu, O. Sigmund, and J. Du. Design of metamaterial mechanisms using robust topology optimization and variable linking scheme. *Structural and Multidisciplinary Optimization*, 63(4):1975–1988, Apr. 2021. doi:10.1007/s00158-020-02791-1.

[10] A. Verbart, M. Langelaar, and F. v. Keulen. A unified aggregation and relaxation approach for stress-constrained topology optimization. *Structural and Multidisciplinary Optimization*, 55(2):663–679, Feb. 2017. doi:10.1007/s00158-016-1524-0.

[11] W. Zhang and S. Sun. Scale-related topology optimization of cellular materials and structures. *International Journal for Numerical Methods in Engineering*, 68(9):993–1011, 2006. doi:10.1002/nme.1743.

[12] W. Achtziger and C. Kanzow. Mathematical programs with vanishing constraints: optimality conditions and constraint qualifications. *Mathematical Programming*, 114 (1):69–99, July 2008. doi:10.1007/s10107-006-0083-3.

[13] G. Rozvany. On design-dependent constraints and singular topologies. *Structural and Multidisciplinary Optimization*, 21(2):164–172, Apr. 2001. doi:10.1007/s001580050181.

[14] M. Stolpe. *On Models and Methods for Global Optimization of Structural Topology.* PhD thesis, KTH, 2003.

[15] G. Sved and Z. Ginos. Structural optimization under multiple loading. *International Journal of Mechanical Sciences*, 10(10):803–805, Oct. 1968. doi:10.1016/0020-7403(68)90021-0.

[16] G. Kreisselmeier and R. Steinhauser. Systematic Control Design by Optimizing a Vector Performance Index. *IFAC Proceedings Volumes*, 12(7):113–117, Sept. 1979. doi:10.1016/S1474-6670(17)65584-8.

[17] P. Duysinx and M. P. Bendsøe. Topology optimization of continuum structures with local stress constraints. *International Journal for Numerical Methods in Engineering*, 43(8):1453–1478, 1998. doi:10.1002/(SICI)1097-0207(19981230)43:8<1453::AID-NME480>3.0.CO;2-2.

[18] C. Le, J. Norato, T. Bruns, C. Ha, and D. Tortorelli. Stress-based topology optimization for continua. *Structural and Multidisciplinary Optimization*, 41(4):605–620, Apr. 2010. doi:10.1007/s00158-009-0440-y.

[19] G. Cheng and Z. Jiang. Study on Topology Optimization with Stress Constraints. *Engineering Optimization*, 20(2):129–148, Nov. 1992. doi:10.1080/03052159208941276.

[20] M. P. Bendsøe and O. Sigmund. Material interpolation schemes in topology optimization. *Archive of Applied Mechanics*, 69(9):635–654, Nov. 1999. doi:10.1007/s004190050248.

[21] E. Andreassen, A. Clausen, M. Schevenels, B. S. Lazarov, and O. Sigmund. Efficient topology optimization in MATLAB using 88 lines of code. *Structural and Multidisciplinary Optimization*, 43(1):1–16, Jan. 2011. doi:10.1007/s00158-010-0594-7.

[22] F. Wang, B. S. Lazarov, and O. Sigmund. On projection methods, convergence and robust formulations in topology optimization. *Structural and Multidisciplinary Optimization*, 43(6):767–784, June 2011. doi:10.1007/s00158-010-0602-y.

[23] F. Ferrari and O. Sigmund. A new generation 99 line Matlab code for compliance Topology Optimization and its extension to 3D. *arXiv:2005.05436 [cs, math]*, July 2020.

[24] K. Svanberg. The method of moving asymptotes—a new method for structural optimization. *International Journal for Numerical Methods in Engineering*, 24(2):359–373, 1987. doi:https://doi.org/10.1002/nme.1620240207.

[25] O. Sigmund. Morphology-based black and white filters for topology optimization. *Structural and Multidisciplinary Optimization*, 33(4):401–424, Apr. 2007. doi:10.1007/s00158-006-0087-x.

[26] K. Ejlebjerg Jensen. Anisotropic Mesh Adaptation and Topology Optimization in Three Dimensions. *Journal of Mechanical Design*, 138(6), June 2016. doi:10.1115/1.4032266.

[27] O. Sigmund, N. Aage, and E. Andreassen. On the (non-)optimality of Michell structures. *Structural and Multidisciplinary Optimization*, 54(2):361–373, Aug. 2016. doi:10.1007/s00158-016-1420-7.

[28] N. Aage, E. Andreassen, B. S. Lazarov, and O. Sigmund. Giga-voxel computational morphogenesis for structural design. *Nature*, 550(7674):84–86, Oct. 2017. doi:10.1038/nature23911. Number: 7674 Publisher: Nature Publishing Group.

[29] A. G. M. Michell. The limits of economy of material in frame-structures. *The London, Edinburgh, and Dublin Philosophical Magazine and Journal of Science*, 8 (47):589–597, Nov. 1904. doi:10.1080/14786440409463229.

[30] E. Parkes. Joints in optimum frameworks. *International Journal of Solids and Structures*, 11(9):1017–1022, Sept. 1975. doi:10.1016/0020-7683(75)90044-X.

Enrico Stragiotti, François-Xavier Irisarri, Cédric Julien and Joseph Morlier

[31] S. Diamond and S. Boyd. CVXPY: A Python-Embedded Modeling Language for Convex Optimization, 2016.

[32] L. He, M. Gilbert, and X. Song. A Python script for adaptive layout optimization of trusses. *Structural and Multidisciplinary Optimization*, 60(2):835–847, Aug. 2019. doi:10.1007/s00158-019-02226-6.

TOPOLOGY OPTIMIZATION OF A SMALL UAV FUSELAGE FOR ADDITIVE MANUFACTURING

Ricardo Costa[1], Frederico Afonso[1], José Chaves Pereira[1], Hugo Policarpo[1,2] and João Lourenço[1,3]

1: IDMEC
Instituto Superior Técnico
Universidade de Lisboa
Av. Rovisco Pais, 1049-001, Lisboa, Portugal
{ricardo.teixeira.costa, frederico.afonso, jose.chaves, hugo.policarpo}@tecnico.ulisboa.pt,
https://tecnico.ulisboa.pt/pt/

2: CINAV
Escola Naval, Instituto Universitário Militar
Base Naval de Lisboa - Alfeite
2810-001, Almada, Portugal

3: Althima - Engineering Software Solutions, Lda
Rua Dr. Ferreira Alves, 750 4405-936,Vila Nova de Gaia, Portugal
jlourenco@althima.com

Abstract. *Applications of Additive Manufacturing (AM) combined with Topology Optimization (TO) has grown over the past years for a multitude of engineering fields. One example is the design of tailored structures for Unmanned Aerial Vehicles (UAVs). TO is a powerful computational tool to devise these structures since it is able to provide a lightweight design that can handle the most critical aerodynamic loads in the flight envelope. The resulting design can be then post-processed for manufacturing, using an AM technology such as Fused Deposition Modeling (FDM). In this work, the aim is to topologically optimize the internal structure of the fuselage of a small UAV. For this purpose, the critical aerodynamic loads obtained from Computational Fluid Dynamic (CFD) simulations for the boundaries of the flight envelope will be considered. Furthermore, all the required onboard instrumentation, wiring and propulsive system must be accommodated inside the fuselage creating holes in the structure and increasing design complexity.*

Keywords: Topology Optimization; Additive Manufacturing; Computational Fluid Dynamics; Aircraft Design; Unmanned Aerial Vehicle

Ricardo Costa, Frederico Afonso, José Chaves Pereira, Hugo Policarpo and João Lourenço

1 INTRODUCTION

The computational capabilities at the user's disposal have undergone an exponential growth in recent years, which, combined with the development of software geared towards topology optimization processes, allows these technological advances to be applied to the production of the most diverse products and systems, in several engineering fields, including aeronautics [1]. When both numerical and manufacturing issues are properly addressed, topology optimization for additive manufacturing can be a powerful tool [2]. This process have already been explored for some components of Unmanned Aerial Vehicles (UAVs) [3].

Taking advantage of this greater ease of carrying out a development project, in this case, an aircraft, the present paper reports the process of studying and conceptually designing an UAV. In its development process several analysis techniques and additive manufacturing technology are applied, coupled with topology optimization, which allows to fully exploit the advantages inherent to this type of manufacturing technology. By considering the critical aerodynamic loads obtained from CFD analyses performed based on the boundaries of the flight envelope, and taking into account the mass and allocation of the aircraft internal components, the topology optimization process aims to simplify and optimize the fuselage structure of this UAV under study. With a reduction in the material needed for its manufacturing, not only a more environmentally feasible result is obtained, but it also reduces costs and allows improving the performance of the aircraft, by reducing its mass and, consequently, increasing its endurance.

Common to the development of any type of aircraft is the need to define requirements and constraints for its sizing and design. Many of these stem from the purpose for which the aircraft is intended. In this case, it is intended to create an UAV capable of flying over and supervising motorsport races on a racetrack. The need for greater visual coverage of the track, hitherto guaranteed only by fixed cameras distributed along the track and by the eyes of the track marshalls themselves, becomes, in certain circumstances, quite noticeable, and the current solution does not cover all the angles of vision necessary to clarify some dubious situations, in case of accident or unsportsmanlike practices.

Therefore, a set of UAVs that could fly over the racetrack, with a pre-defined route, covering all sectors and maintaining constant coverage of the activity on the track, could be part of the solution to the aforementioned problem.

2 METHODS AND TOOLS

Behind the development of any product or component is a reason that led to its production. In this case, the desire to explore the capabilities of using topological optimization, coupled with additive manufacturing, applied to the development of an UAV. Now, although this is the motto for the beginning of the project, by itself is not enough to move forward to the development of the aircraft, it is necessary a reason to guide its production, an applicability that justifies its need. Therefore, it was decided to idealize a solution to supervise motor sports competitions, an UAV that had the ability to fly over a circuit, in a set of equal aircraft, each responsible for a certain sector of the track.

Ricardo Costa, Frederico Afonso, José Chaves Pereira, Hugo Policarpo and João Lourenço

2.1 Requirements and Initial Sizing

The function for which the aircraft will be designed, demands certain requirements that served as constraints for the conceptual development of it. Among them are the need to carry a high-resolution camera, with a wide-angle lens, that allows to cover the largest possible runway area without losing image quality when approaching for incident observation, so as to reduce as much as possible the number of UAVs needed to visually cover the entire track. It is also necessary to integrate an autopilot system, so that the trajectory of the aircraft can be defined in advance and does not require constant monitoring by a pilot for each of them. Other requirements relate to the choice of a geometry that benefits a greater endurance, as well as its versatility when being launched and transported. Therefore, a flying wing configuration was chosen, as it has a high lift area and low drag values [4]. On the other hand, it requires greater care with the internal layout of the UAV, in order to control the longitudinal position of the center of gravity, and the longitudinal control of this type of aircraft is more demanding [5]. However, its flight path will be simple and repeatable, so the autopilot should have no problem maintaining stability, provided the aircraft is well designed.

In terms of wingspan restrictions, these are related to the goal that the UAV can be hand launched by anyone. The average arm length of an adult is around 60 to 80 cm, so this was the measure selected for the half-span of the aircraft.

The initial sizing of an aircraft is one of the first steps in the aircraft development process [6, 7]. To this end, a prior choice had to be made of the internal components to be used, in order to allow a more correct prediction of the size of the fuselage and to calculate the mass of all of them, and with that, to begin the process of sizing the wings. In order to estimate a target for the UAV structure mass value, a survey of the masses of aircraft with similar configurations and wingspan was done.

The whole process below follows the normal phases of an aircraft development, according to Corke's textbook [6], with only minor adaptations taking into account the type of propulsion system and the use for which the UAV is intended.

2.2 Conceptual Design

Once the mass balance of the internal components and structure of the UAV was completed, it was then possible to calculate the Maximum Take Off Weight (MTOW) which, together with other selected flight parameters, such as cruise speed, flight altitude and corresponding air characteristics at this same altitude, allowed proceeding with the determination of the wing area and required power, using semi-empirical equations. The selection of wing loading (W/S) and power-to-weight ratio (P/W) plays a key role in the design of any aircraft, including UAVs. These two parameters not only guide flight performance, but also help determine the dimensions of the aircraft for a given set of aerodynamic and weight properties.

In order to calculate their value, and thus find the Design Point that will drive the beginning of the aircraft design, some restrictive equations were selected, each corresponding to a different flight phase or event. Right from the start, since this is an aircraft with the purpose of performing long duration and surveillance flights, the constraints of the cruise and endurance flight conditions would have to be taken into account. Additionally, the cruise flight conditions for maximum speed, climb and stall speed condition were also considered.

Ricardo Costa, Frederico Afonso, José Chaves Pereira, Hugo Policarpo and João Lourenço

By obtaining the Design Point, it becomes possible to calculate the wing area (S) and the power (P) required to execute any phase of flight. With this data and the imposed wingspan (b) limitation, the geometric parameters of the wings are obtained.

2.3   Preliminary Design

2.3.1   Wing Profile Selection

Once the aircraft sizing and configuration are complete, it is time to proceed with the selection of the wing profile to be used in the wings. Due to the fact that this is a flying wing, with no horizontal stabilizer to assist in longitudinal stability, it is of utmost importance that the moment coefficient is as close to zero as possible. Based on this requirement, and based on studies done and published [8, 9], an initial selection of some possible profiles to be used was made.

The choice of the program that allowed performing aerodynamic studies on those same profiles, from which resulted the selection of one of them, fell on an open source software named XFLR5 [10]. This software uses XFoil [11] to provide the aerodynamic coefficients of an airfoil.

In preparing the analyses made on the various profiles, a refinement was made to the number of points that constitute them, in order to obtain better and more realistic results. The analysis parameters were also introduced, such as the Reynolds number (Re), related to the aircraft flight speed, the wing chord and air characteristics at the flight altitude, and the range of attack angles at which the profiles are to be subjected to analysis. Regarding the chord used, this was the average chord, calculated earlier in the initial sizing process.

Several aspects were taken into account to select the most suitable airfoil based on the obtained graphs, such as the curves C_l/C_d as a function of the angle of attack α, C_l as a function of α, C_d as a function of α and C_m as a function of α, where C_l represents the lift coefficient, C_d the drag coefficient and C_m the moment coefficient.

As far as the C_l/C_d ratio is concerned, we want higher values, but also a wide range of angles of attack in which the value remains high. A more efficient profile has a higher lift-to-drag ratio. As for the drag coefficient (C_d), it is intended to be as low as possible, since it is directly related to the drag force present in the profile and in the aircraft, and consequently to the power required to keep the aircraft in level flight. As for the lift coefficient (C_l), we want its maximum value ($C_{l_{max}}$) to be as high as possible before entering in stall, which should not be too abrupt. Finally, the moment coefficient (C_m) is wanted as close as possible to zero and negative in the operational range of the aircraft.

Based on the analysis of the graphs of the parameters obtained, the selection of the profile that presented the most satisfactory results was made.

2.3.2   Wing Configuration

After selecting the airfoil to be used, it was time to configure the wing. In terms of sizing, this was subject to requirements imposed by aspects such as the accommodation capacity of the servo motors and the possibility of performing take-offs by hand launching, which entails minimum or maximum values for dimensions such as wing thickness and wingspan.

Being an aircraft with the purpose of performing flights of considerable duration, privileging the endurance, there is a natural demand for obtaining a low aerodynamic resistance

induced by lift. Based on this requirement, even though an elliptical shape would be more efficient from an aerodynamic perspective, its construction process would be difficult and expensive [6]. Therefore, the best compromise between aerodynamic efficiency and ease of construction led to the adoption of a trapezoidal wing.

Before moving on to the aerodynamic analysis of the wing, a number of parameters had to be defined. Starting with an intrinsic characteristic of trapezoidal wings, the taper ratio (λ), which is the ratio between the chords at the wing tip (c_{tip}) and root (c_{root}), brings about some effects, namely changing the distribution of lift on the wing, allowing it to become more elliptical. Another aspect that changes with the introduction of tapering is the position of the center of mass of each wing, tending to move closer to the fuselage, since there is less area and less material in the outer region of the wing. Consequently, the bending moment at the wing root will have less magnitude, enabling a reduction in structural weight. Ideal values for the taper ratio, in order to minimize the induced air drag and bring the lift distribution as close as possible to the elliptical distribution, can be consulted in the references [6, 12].

The wing sweep angle (Λ) was another parameter taken into account and studied for a better wing configuration. The lateral stability of the aircraft tends to increase with the introduction of sweep angle [13]. On the other hand, the stall speed tends to increase with the sweep angle, and for very high values, the efficiency of the wing (C_L/C_D) decreases, as well as the maximum lift coefficient. More information about the importance of the sweep angle and the most appropriate values for UAV's without tail can be found in the reference [14].

Besides λ and Λ, also the dihedral angle (Γ) of the wing was analyzed. Low dynamic lateral stability is a problem that characterizes tailless aircraft, and this can be countered by introducing a positive dihedral on the wing. Values indicated for the type of aircraft under study can be consulted in the reference [15].

Finally, the last parameter to take into account for a complete wing configuration is the aspect ratio (AR), which is the ratio between the wingspan squared and the wing area. If on the one hand high values lead to a greater aerodynamic efficiency, since the induced drag reduces with increasing AR, on the other hand these wings are usually associated to large wingspans that result in larger bending moments, which in turn require structural reinforcement. In the reference [16] small UAVs are analyzed, and the most appropriate range of AR values can be consulted.

After defining the above parameters, an aerodynamic analysis on the complete aircraft is performed. First, a 2D analysis should be run for the wing and fuselage profiles, with a Reynolds number range that goes from the lowest Reynolds number verified at the wing tip, where the chord is the smallest, to the maximum value allowed by XFLR5. This range aims to encompass any values experienced in the model.

The full aircraft is then modelled in XFLR5 considering not only its dimensions but also its mass and weight distribution, a point that will be the subject of analysis in sub-chapter 2.3.3. The flow parameters, velocity (V), density (ρ), kinematic viscosity (ν) were also defined. The Lifting Line Theory [17], proposed by Prandtl (1921), which consists of the superposition of horseshoe vortices along the wingspan is the method used. It has some limitations, namely the impossibility of application to multiple surfaces or asymmetric flows. Still, it already takes viscosity into account when calculating the model friction. A polar type was selected with constant speed, in this case the cruise speed, and inertial

Ricardo Costa, Frederico Afonso, José Chaves Pereira, Hugo Policarpo and João Lourenço

properties and reference dimensions from the aircraft configuration were introduced. It should also be noted that the study should be carried out for a range of angles of attack that encompasses all flight conditions to which the UAV is subjected.

This aerodynamic analysis provides important data about the aircraft, such as the angle of attack for cruise condition, which can be obtained by consulting the graph of C_L vs. α, having previously calculated the lift coefficient for level flight ($C_{L_{eq}}$). Having access to the α value, all the other coefficients for cruise condition can be consulted. Other relevant data that can be taken from the results of this analysis are the angle at which the aircraft stalls, in this case for its cruise speed, and the stall speed (Eq.1) for α_{trim}, which allows to impose limits and a safety margin when programming the autopilot.

$$V_s = \sqrt{\frac{2W}{S\rho\, C_{L_{max}}}} \qquad (1)$$

2.3.3 Static Stability Analysis

To ensure airworthiness of the proposed aircraft it is necessary to evaluate its static and dynamic stability. However, since at the early design stages only static stability is usually considered, for this work only a static stability analysis was performed on the full aircraft. This analysis was done in the XFLR5 by assessing the longitudinal stability and static margin. Longitudinal stability can be assessed by the sign of the slope C_{M_α}. If this is negative, it means that with increasing angle of attack the aircraft will experience an increasingly negative pitch moment (C_M), counteracting the unwanted increase in angle of attack and leading to stability [13]. Thus, a negative value of C_M for $\alpha = 0$ is a requirement for longitudinal stability. The static margin (K_n) plays an important role in the longitudinal stability of the aircraft. With this in mind, it is important to ensure that its value is positive. Static margin values between 0.02 and 0.08 are advised for tail-less aircraft [18]. Its value can be calculated with the following expression,

$$K_n = \frac{x_n - x_{CG}}{\bar{c}} \;, \qquad (2)$$

where the values of x_n and x_{CG} correspond to the distance from the aircraft nose to its neutral point and center of gravity (CG), respectively, in the longitudinal direction (x).

First, an initial distribution of the components inside the fuselage is made, which will be redefined after obtaining the first estimate of the static margin. Then, analyzing the graph of the moment coefficient as a function of the angle of attack, the coordinates of the neutral point, which coincides with the aerodynamic center, is taken, since it is tail-less aircraft, by determining the position of the CG for which C_M is independent of α. Having found this value, one proceeds to the reposition of the internal components in order to obtain a x_{CG} coordinate that leads to a static margin within the advised range.

Directional stability should also be analyzed given the unconventional nature of the chosen design. Directional motion in an aircraft corresponds to a rotation about the vertical axis. In a flight situation, the forces that induce a yaw motion in the aircraft are lateral forces produced by the fuselage and wings, thanks to a lateral skid vector that makes a slip angle β with the longitudinal axis [6]. To ensure directional stability, the yaw moment coefficient C_{n_β} of the aircraft has to be positive [6].

Ricardo Costa, Frederico Afonso, José Chaves Pereira, Hugo Policarpo and João Lourenço

2.3.4 Flight Envelope

The last step before starting the CFD analyses, to obtain the aerodynamic loads to be used in the topology optimization, is to define the flight envelope, from which the limit load factors will be taken. Based on these factors the lift coefficients can be obtained, and their corresponding angles of attack, through the XFLR5 graphs. This flight envelope consists of a diagram of the load factor (n) to which the aircraft is subjected, as a function of the speed (V) at which it travels. The load factor is measured in multiples of the gravity acceleration (g).

The flight envelope, without gust loads, is limited by aerodynamics, through the $C_{L_{max}}$ and the stall curve, by structural limit loads, in the form of maximum and minimum load factors, and by the dynamic pressure limit, which is expressed through maximum or terminal velocity (V_{dive}) [19, 20].

In order to define the maximum and minimum load factors that can be expected for the UAV, the STANAG 4703 standard is used [21], intended for the certification of fixed-wing UAVs with a maximum takeoff weight not exceeding $150kg$. According to this standard, for aircraft subject to symmetrical maneuvering, the maximum load factor shall be equal to or greater than 3.8g for positive loads and less than or equal to -1.5g for negative loads.

In addition to being dependent on flight operating conditions and maneuvers, the loads applied to the aircraft are also strongly related to external factors. The atmosphere behaves as a dynamic system, and gusts occur during flight. These imply a variation in the angle of attack and consequently in the value of the lift coefficient, so the load factor will also vary. For this reason, their effects on the loads experienced by the aircraft must also be included. For simplicity, gusts are often assumed to be symmetrical and vertical, so that the increment due to the gust load can be calculated directly.

The gust speed is extremely difficult to predict accurately, and is obtained from statistical flight data, taking into account the altitude range and flight conditions [19]. In the case under study, since it is a small aircraft, the values of gusts that it should support, depending on the flight altitude, are present in the FAR 23 regulation [22]. Once the increment in load factors from gusts that the aircraft may suffer is calculated, the flight envelope must be updated and contain new maximums and minimums for what the aircraft should withstand.

2.4 CFD Analyses

Computational Fluid Dynamics (CFD) can be seen as the use of numerical methods for the analyses of fluid flows. In the context of this article, the use of this resource aims to obtain the aerodynamic loads to which the aircraft will be subjected, and then use them in the topology optimization process. The software used in this process is Star-CCM+ [23], a commercial simulation software based on CFD, which allows high fidelity analyses of the aerodynamic characteristics of the UAV.

2.4.1 Validation

Before starting the study of the UAV, CFD analyses were performed on a NACA0012 airfoil, in order to validate the results obtained with the software and to justify the procedures for the CFD analysis of the UAV, both regarding mesh generation and the turbulence and transition models selected. To accomplish this purpose, wind tunnel data

Ricardo Costa, Frederico Afonso, José Chaves Pereira, Hugo Policarpo and João Lourenço

from NASA for the same airfoil is used as a term of comparison. The report presenting this experimental data is available in [24].

In order to faithfully reproduce the tests performed in the wind tunnel, the CFD analysis was performed in two dimensions, in a plane that aims to replicate the center section of the wing used in the experimental tests. The selection of this plane is due to the fact that it is at this section that the pressure tapping points along the chord are found, and with which it was possible to obtain the graphs of pressure coefficient as a function of the chord percentage of the profile, which served as a term of comparison and validation for the analyses performed in CFD. The dimensions of the control area are equal to the length and height of the test volume of the wind tunnel where NASA performed the tests, as well as the remaining test parameters, such as the stagnation pressure, temperature, fluid velocity entering the test section, Reynolds number and angle of attack of the profile.

The Reynolds-Averaged Navier-Stokes (RANS) equations, which give an approximate time-averaged solution to the Navier-Stokes equations [25], are used for this work. These equations require a turbulence model to be solved. The choice fell on the $k - \omega$ model, a suitable model for low Reynolds number [26], where the boundary layer is relatively thick and the viscous sub-layer can be resolved. This is automatically coupled, by the software, to the turbulence model $k - \omega \, SST$ [27, 28].

In addition to a turbulence model, it is also necessary to select a transition model. The function of this is to predict the location of the transition from laminar to turbulent flow, if it exists, and whether it is a natural transition or a bypass transition, that is, a transition in which some of the steps of the natural transition process do not occur, due to external disturbances. In this case, the model used was $\gamma - Re_{\theta}$, compatible with unstructured meshes and built on local variables [29].

The boundary conditions were chosen in order to try to replicate the wind tunnel test conditions as much as possible. Therefore, a uniform inlet velocity was imposed, a zero pressure difference at the outlet compared to the stagnation pressure, a wall condition on the profile surface and a symmetry condition on the upper and lower surfaces of the test plane, in order to avoid the formation of boundary layer, since the tunnel where NASA performed the tests has a grid system that sucks the airflow close to the wall, in order to prevent the formation of boundary layer, and thus, reduce the wall effect as much as possible [30].

Next began the generation of the 2D, unstructured, hybrid mesh that is a mesh where each cell is a block, which leads to unlimited geometric flexibility and allows the most efficient use of computational resources for complex flows [31]. This type of mesh is more advantageous when dealing with more complex geometries. The term hybrid mesh, on the other hand, is due to the use of more than one type of element, regular and irregular polygons. In order to better predict the flow behavior in the boundary layer near the solid wall, an unstructured mesh was generated with a mix of non-regular pentagons and hexagons in the generality of the test domain, and quadrilaterals in the region around the profile, called prism layer. Areas of further refinement were also created, one of rectangular shape around the entire profile and another in the wake region.

Once the mesh creation was finished, the convergence study was started. Between each analysis, a refinement ratio (r) was used, applied to all the mesh creation parameters. The

Ricardo Costa, Frederico Afonso, José Chaves Pereira, Hugo Policarpo and João Lourenço

formula used to calculate this refinement ratio is the following [28]

$$r = \left(\frac{N_1}{N_2}\right)^{\frac{1}{d}}, \tag{3}$$

where N_k is the number of mesh cells k and d is the number of dimensions of the problem under analysis. In this case, k takes the value of 1 for the most refined mesh and 2 for the least refined one, out of the two under study at each refinement, while d takes the value of 2, since the validation analyses were performed in two dimensions.

As mentioned above, in order to better capture the flow behavior in the boundary layer, prism layers were applied. The parameter that defines the thickness of the first prism layer and, consequently, how coarse or refined the mesh next to the profile is $y+$. This has not been defined directly, but rather through factors that are intrinsically linked to it, such as the total number of prism layers, the total thickness of these layers and the growth rate of these layers. The value of $y+$ must be carefully defined, because, depending on the turbulence and transition model chosen, it must be within a range of values (between 0 and 5) [32] that allows the correct application of the models.

In line with the primary objective of the validation analyses, the final step consists in comparing the parameters obtained through the CFD software used and those provided by NASA. In this case, this comparison was made through the C_p curves as a function of the chordwise percentage. The main objective of this comparison is the validation not only of the adopted models, but also of the chosen parameters and the mesh generation performed.

2.4.2   UAV CFD Analyses

Once the validation studies of turbulence and transition models, the parameterization of the analyses and the creation of the mesh are completed, the conditions are met to begin the study of the UAV.

The UAV wet surface is symmetric, so the analyses can be performed with only half of the aircraft, by using a symmetry condition in the longitudinal central plane.

The geometry and corresponding control volume were obtained using the geometric modeling program SolidWorks [33], where a parallelepiped was created from which half the aircraft was subtracted, thus remaining with a positive mold of the aircraft, corresponding to the wet surface of the aircraft. Regarding the dimensions of the domain, it was taken into account that this is an analysis with subsonic flow, so the disturbance waves propagate in all directions, which implies larger dimensions of the domain, so that the selected boundary conditions do not negatively influence the results [34, 35].

The dimensions of the domain can be found in Fig.1, where c corresponds to the maximum chord of the aircraft (365 mm) and b corresponds to the total wingspan with the fuselage (1410 mm).

Once the geometry is imported and the control volume is defined, it remains to define the boundary conditions and generate the surface and volume mesh, as the turbulence and transition models are the ones tested in the validation tests. For the inlet was assigned the condition of constant speed and equal to the cruise speed of the aircraft, 16.6667 m/s, to the outlet was assigned constant pressure equal to the reference pressure, in this case the atmospheric pressure (101325 Pa), to the side faces was assigned symmetry condition, on

Ricardo Costa, Frederico Afonso, José Chaves Pereira, Hugo Policarpo and João Lourenço
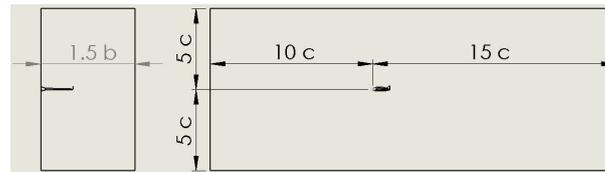

Figure 1: Domain dimensions as a function of the maximum chord (c) and wingspan (b)

the right side for representing only half of the aircraft and on the left side for simulating free flight condition without walls to delimit the domain. Finally, the UAV surface is considered a wall, being the interface between the solid and the fluid, and the upper and lower faces of the domain are considered inlet and outlet, respectively, for negative angles of attack, and vice-versa for positive angles of attack.

Similar to the procedure adopted in the validation studies, also in the case of the UAV a mesh convergence was performed in order to obtain a satisfactory set of parameters for mesh generation.

In this mesh convergence process three meshes with different refinements were generated. The first to be created was the coarsest and least computationally demanding. From there we went on to more refined meshes, having used the same method previously mentioned for the validation studies, the application of a refinement ratio (r) applied to all parameters of the generated mesh, between each of the cases.

Once the mesh convergence study was completed, a final mesh was obtained that was subsequently used in all the analyses performed on the UAV, for different angles of attack. This method was possible to be applied by keeping the geometry unchanged for all angles of attack and varying only the flow incidence angle. Thus it became feasible to always use the same mesh, speeding up the process.

After having generated the final mesh to be used in the analyses to remove the aerodynamic loads, it was time to proceed to three analyses with different angles of attack. These were intended to serve as starting points to perform a linear regression from the end points of C_L as a function of α.. The need to elaborate this linear regression is due to the fact that the results obtained with Star-CCM+ may diverge from those obtained with XFLR5. In the case under study, some of the reasons that may lead to this difference are the non-use of winglets in the XFLR5 analyses, or the differences in the fuselage profile, which was generated in XFLR5 for the XFLR5 studies, and in SolidWorks for the model applied in the Star-CCM+ tests. Since the reliable geometry corresponding to the final UAV is that generated in SolidWorks, the results obtained through Star-CCM+ were the ones accepted as being the most realistic and reliable. Therefore, with the linear regression it becomes possible to achieve the value of the new angles of attack for the cruise and extreme conditions of the flight envelope previously presented, that is, the cases of +3.8g and -1.5g.

The UAV analyses were all started in steady state, but in order to achieve satisfactory convergence for the lift coefficient, it was decided to change one of the physical parameters of the analysis and switch to non-steady state. The non-convergence in steady state can be related to some location of the flow where there is no stationarity, and thus, the solution do not converge. The location of these points responsible for the phenomenon, in the UAV under development, should be at the point where the transition from laminar to turbulent regime takes place, on the upper surface of the fuselage and at certain points located along the wingspan.

Ricardo Costa, Frederico Afonso, José Chaves Pereira, Hugo Policarpo and João Lourenço

After performing the three simulations, for cruise conditions and load factors of -1.5g and +3.8g, according to the data obtained from XFLR5, we proceeded to linear regression and to the calculation of the new angles of attack to be used in the final analyses, which are in line with the values obtained in Star-CCM+.

Similarly to what was done in the analyses for the linear regression, it was also chosen in these final analyses to start the process in steady state and, in order to obtain the convergence of the parameters, move to unsteady state when the residuals of the steady state analysis stabilize.

Once the analyses were finished and having convergence in all parameters, a comparison was made between the values obtained with the CFD software and those obtained with the XFLR5, as well as calculated the new estimate of the maximum flight time. The pressure distributions, resulting from the final analyses, were subsequently used to import the aerodynamic loads in the topological optimization analyses performed.

2.5   Topology Optimization

Topology optimization is a mathematical and computational method that allows, through the distribution of material in a structure without prior topology, or with freedom in it, to maximize the performance of the system of which it is part [36]. The optimization is done taking into account an allowed design space and the boundary conditions and loads to which the structure is subjected. The application of this method leads to the introduction of cavities in the structure, which, without compromising its stiffness and strength, allow weight reduction and savings in the amount of material used.

The CAD model imported into the software responsible for the topology optimization, HyperWorks [37], was created using the geometric modeling software SolidWorks. This was the same that was used to do the subtraction process that originated the enclosure with the wet surface used in the CFD analyses .It was created based on the constraints imposed by the internal components and according to the measurements obtained in the initial design and configuration of the wing. In Fig.2 a view of this same model is depicted, with a certain degree of transparency, to give an idea of the internal configuration of the fuselage and wings of the UAV.
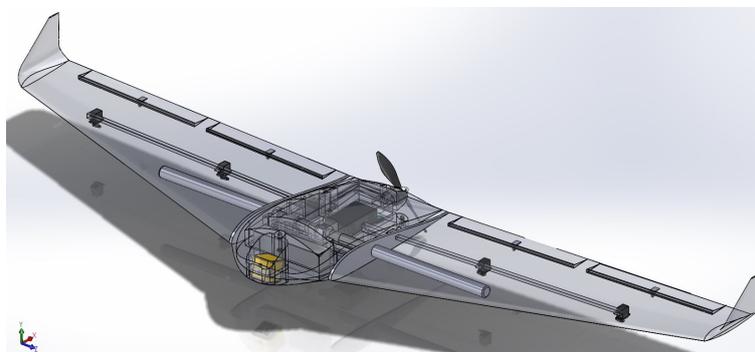

Figure 2: CAD obtained with SolidWorks

Once the geometry has been imported, a mesh that is refined enough to provide a correct discretization and accurately describe the shape of the aircraft must be generated. This can have different degrees of refinement, depending on the area where it is applied, i.e. whether it is a part that is intended to be optimized or not. In order to make

Ricardo Costa, Frederico Afonso, José Chaves Pereira, Hugo Policarpo and João Lourenço

this distinction, and thus save some computational power, it is important to divide the geometry into different components, i.e. to delineate the zones of the reference domain that are intended to be optimized, as well as those that are intended to be solid or empty domains.

Once the geometry has been introduced, the separation into different regions made, and the mesh generated, the loads that will give rise to the optimization process can then be applied. These are applied at isolated points or distributed over the nodes of a given surface of the generated mesh. In this case study, the masses of the internal components were applied, the materials and respective characteristics of the various UAV components were defined, and the aerodynamic loads from the CFD analyses were imported. It is also necessary to fix nodes of the geometry, so that the forces can be applied, otherwise there would be no constraints and the geometry would have total freedom of movement when applying the loads. In this case, it was chosen to fix the fuselage nodes that are in contact with the carbon spar, for being the element with the highest stiffness of the assembly, and those that are in contact with the fitting pins of the side profiles located between the fuselage and the wings.

The last step to take before initializing the structural analysis and subsequent topology optimization, is to create groups with selected contact surfaces, in order to transmit forces and displacements between the different components that constitute the complete geometry under study.

Then, the setup for the optimization is done, in which various constraining parameters can be entered, based on which the analysis will run. In the context of the UAV development project in question, the goal of the topology optimization is to reduce the percentage of material, a percentage that is relative to the volume occupied by the aircraft. Therefore, minimum mass and maximum stress limit values, which the aircraft should not exceed and to which its components should not be subjected, should be introduced. These maximum stress values must be taken from studies performed on the materials in use, in order to obtain their mechanical properties.

After the software runs the optimization, the user has the ability to visualize the shape of the structure obtained in the process of optimal material distribution and, with this, try to reproduce the shape achieved with the aid of CAD software, for example.

3 RESULTS

This chapter presents the results that have been obtained in the various phases of the UAV conceptual development project, as well as the analyses and information to be retained from them. As such, in order to make its reading and interpretation easier and more direct, its structure will be the same as the previous chapter, starting from the topic of the Conceptual Design, so that the results can be easily associated with the phase of the project in which they are inserted.

3.1 Conceptual Design

In the conceptual design phase, the MTOW was calculated by surveying the masses of the internal components and an estimate of the airframe weight, based on comparison with alternatives of similar size and configuration. From the sum of all these masses, a MTOW value of 10.9293N was obtained. The values of the remaining parameters used to calculate the Design Point, by applying the constraints mentioned in Sec. 2.2, are

Ricardo Costa, Frederico Afonso, José Chaves Pereira, Hugo Policarpo and João Lourenço

presented in Tab.1. From the analysis of the Design Point graph, a $P/W = 3.74325\,W/N$ constrained by the climb stage and a $W/S = 44.3064\,N/m^2$ limited by stall speed were obtained. Using these values, together with the MTOW, a wing area of $0.2467\,m^2$ was obtained.

Table 1: Parameters and properties considered in the initial design.

Parameters and Properties	Dimension
MTOW $[N]$	10.9293
Cruise altitude (h_{cr}) $[m]$	$[20, 30]$
Air density (ρ_{cr}) $[kg/m^3]$	1.225
Air temperature (T_{cr}) $[^{\circ}C]$	20
Cruising Speed (V_{cr}) $[m/s]$	16.667
Viscosity (μ_{cr}) $[Pa \cdot s]$	0.000018134

3.2 Preliminary Design

3.2.1 Wing Profile Selection

This sub-section will not present the graphics resulting from the analyses performed on the various profiles in hypothesis, since they do not add relevant information to the analysis of the article. Instead, the justifications for the choice of the MH 81 profile as the profile to be used in the UAV wings will be presented.

Starting with the analysis of the graph of C_l/C_d as a function of α, there were four profiles that stood out, these being the EH 3. 0/12, the S 5020, the MH 81 and the MH 83, the first two for presenting the highest peaks of the ratio value, and the last two for, although not reaching such high peaks, registering a high value in a wide range of angles of attack and for having the highest values of C_l/C_d for $\alpha = 0°$, the value intended to be obtained for level flight.

Moving on to the analysis of the graph of C_d as a function of α, the four profiles that stood out in the curve of C_l/C_d vs. α show similar values for C_{d_0}, however, for angles of attack greater than 12°, profiles MH 81 and MH 83 show values of the aerodynamic drag coefficient considerably lower than all others.

According to the graph of C_l as a function of α, the profiles that stand out positively are the MH 81 and the MH 83, with respect to the loss region. Both present values of $C_{l_{max}}$ much higher than the others, which means that they will present lower loss velocities, with the MH 81 profile having a slightly softer loss behavior than the MH 83, the latter leading to a more abrupt loss.

Finally, studying the graph of the moment coefficient (C_m) as a function of the angle of attack, and taking into account that this is wanted as close as possible to zero and negative in the operational range of the aircraft, MH 83 profile is excluded because it is quite high in modulus compared to the other profiles. On the positive side, the S 5020 profile stands out for having the lowest value of C_{m_0} and for maintaining the lowest values in modulus until approximately 6°.

After presenting all the considerations that were taken into account for the selection of the profile, the choice fell on the MH 81, for being the one that demonstrated a more

Ricardo Costa, Frederico Afonso, José Chaves Pereira, Hugo Policarpo and João Lourenço

homogeneous behavior, standing out in a positive way regarding the lift coefficient and the stall behavior, and presenting a rather neutral behavior in the remaining evaluations.

3.2.2 Wing Configuration

Using the value of the wing area defined in the previous sub-section, together with the constraint of a wingspan of 1200 mm and the selection of some parameters stated in the Sec. 2.3.2, according to the references present therein and for a flying wing aircraft, the parameters summarized in Tab.2 were obtained. Note that the values shown in Tab.2, relate only to the wings, not taking into account the fuselage, which was created in XFLR5, due to the impossibility of uploading the one generated in SolidWorks. From the analyses performed on the complete aircraft in XFLR5, with the characteristics listed above, resulted the data presented in Tab.3. With all this information, is already possible to define the stall speed, using Eq.1, which is $7.22 m/s$.

Table 2: Wing configuration parameters.

Parameter	Dimension
Wing Span (b) [mm]	1200
Root chord (c_{root}) [mm]	293.66
Tip chord (c_{tip}) [mm]	117.46
Mean chord (c_{mean}) [mm]	218.15
Taper ratio (λ)	0.4
Sweep angle (Λ) [°]	15
Aspect ratio (AR)	5.839

Table 3: Data regarding the aircraft study in XFLR5.

Data	Value	Data	Value	Data	Value
$C_{L_{max}}$	1.260	$C_{L_{cr}}$	0.237	C_{D_0}	0.0138
$C_{D_{cr}}$	0.015	$C_{M_{cr}}$	-0.0532	C_{M_0}	-0.0494
$(C_L/C_D)_{max}$	19.788	$(C_L/C_D)_{cr}$	15.70	$(C_L^{3/2}/C_D)_{max}$	14.465
$(C_L^{3/2}/C_D)_{cr}$	7.65	α_{cr} [°]	0.23	$\alpha_{C_{L_{max}}}$ [°]	15
C_{L_α} [/°]	0.0648				

3.2.3 Static Stability Analysis

As mentioned earlier, the aircraft under study was subjected to a static stability analysis. This can be divided into longitudinal and directional, and it is necessary to meet some requirements in order to be considered as verifying both.

Regarding longitudinal stability, a negative C_{M_α} and a value of C_{M_0} of -0.0494 were estimated, i.e., ensuring longitudinal stability. A rearrangement of the internal components in the fuselage was also performed in order to move the CG of the UAV and obtain a static margin of 0.077, situated within the desired value range of 0.02 to 0.08.

Ricardo Costa, Frederico Afonso, José Chaves Pereira, Hugo Policarpo and João Lourenço

Turning now to the directional stability analysis, the yaw coefficient was calculated, with previously obtained data, such as $C_{L_{cruise}}$, AR, Λ and $x/\bar{c}$, where $\bar{c}$ is the mean chord and x is the distance between the center of gravity and the aerodynamic center. Upon completion of the calculation, a yaw coefficient value of 0.0013 was obtained, meeting the requirement that it must be positive.

3.2.4 Flight Envelope

Following the methodology presented in chapter 2.3.4, the flight envelope obtained was as present in Fig.3 in black dashed lines, where the dive speed is $25.0m/s$, the cruise speed is $16.667m/s$ and the stall speed is $7.223m/s$. Going by the information contained in the STANAG 4703 standard, the maximum load factor for positive loads is +3.8g and for negative loads is -1.5g.

By introducing the increments, in the load factor, caused by gusts in the situations of high angle of attack, level flight at cruising speed, and diving situation with terminal speed, the new flight envelope is the comprised by the black solid lines shown in Fig.3. The maximum load factor for positive and negative loads, became, respectively, 9.5765 and -7.5765, this when not considered any design factor that multiplies this value, introducing a safety margin.
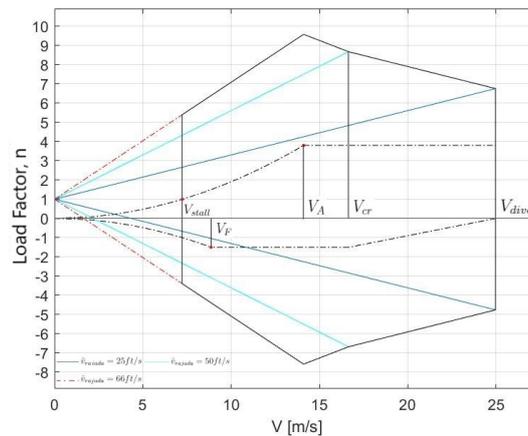
Figure 3: Flight envelope and gust-induced load factors

3.3 CFD Analyses

3.3.1 Validation

The first validation analyses were intended to perform a mesh convergence, which was successful and achieved with only two refinements, verifying relative errors in lift and drag coefficients below 5%.

In all three cases, for an angle of attack equal to $-4°$ (Fig.4a), $0°$ (Fig.4b) and $4°$ (Fig.4c), the curves from the analyses carried out, follow the curves generated by the data acquired from the NASA study almost perfectly. Small visible deviations can be justified with errors associated with CFD analyses, which do not represent at 100% the test conditions experienced in the wind tunnel used by NASA. These differences in the value of C_p along the chord are more visible in the case of analyses with angle of attack equal to $-4°$ and $4°$, more sensitive to slight changes in the flow parameters, since , being

a symmetrical profile, at 0° theoretically there is no lift creation or pressure difference between the lower and upper surfaces, being this analysis less susceptible to errors. Even so, these verified deviations take the form of curve displacements and not peaks at certain points, so they must be associated with disparities in the test parameters and not with domain discretization or model applicability errors. This suggests that the analyses provide reliable data and are worthy of validating the adopted process.
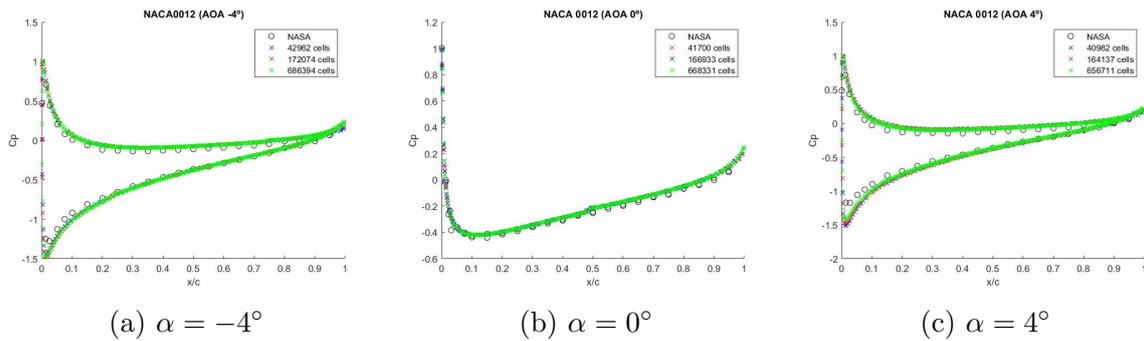

(a) $\alpha = -4°$ (b) $\alpha = 0°$ (c) $\alpha = 4°$

Figure 4: Pressure coefficient as a function of chord percentage for (a) $\alpha = -4°$, (b) $\alpha = 0°$ and (c) $\alpha = 4°$.

3.3.2 UAV CFD Analyses

Similar to the procedure adopted in the studies for validation, a mesh convergence was also performed in the case of the UAV. In this process three meshes with different refinements were generated, from the coarsest to the most refined, with refinement ratios of 1.5. In Fig.5a, Fig.5b and Fig.5c are close-ups of the meshes generated in the plane of symmetry of the aircraft, for the entire domain, where the regions of localized refinement can be seen, around the UAV and in the region of the wake generated by it.

Tab.4 contains the data analyzed in the mesh convergence process for the UAV.

Table 4: Mesh convergence data for UAV.

Mesh Type	Number of Cells	C_L [-]	Relative Error [%]	C_D [drag counts]	Relative Error [%]
Coarse	722130	0.0880	6.0	103.44	60.6
Intermediate	2095696	0.0809	2.5	69.78	8.3
Refined	7159918	0.0830	-	64.41	-

The criterion for acceptance of convergence was the 5% relative error, also used in the validation process. This criterion was met in the case of the lift coefficient, however, for the drag coefficient it was not possible to achieve. This result was to be expected, partly because it is notoriously more demanding to achieve convergence for drag. Therefore, it was decided to accept the 8.333%, since to decrease this value would already require a great deal of refinement and available computational power.

The mesh was then given as converged and accepted. It was therefore this mesh with 7159918 elements that was subsequently used in all the analyses done on the UAV, for different angles of attack.

Ricardo Costa, Frederico Afonso, José Chaves Pereira, Hugo Policarpo and João Lourenço

(a) Less refined convergence mesh

(b) Intermediate convergence mesh

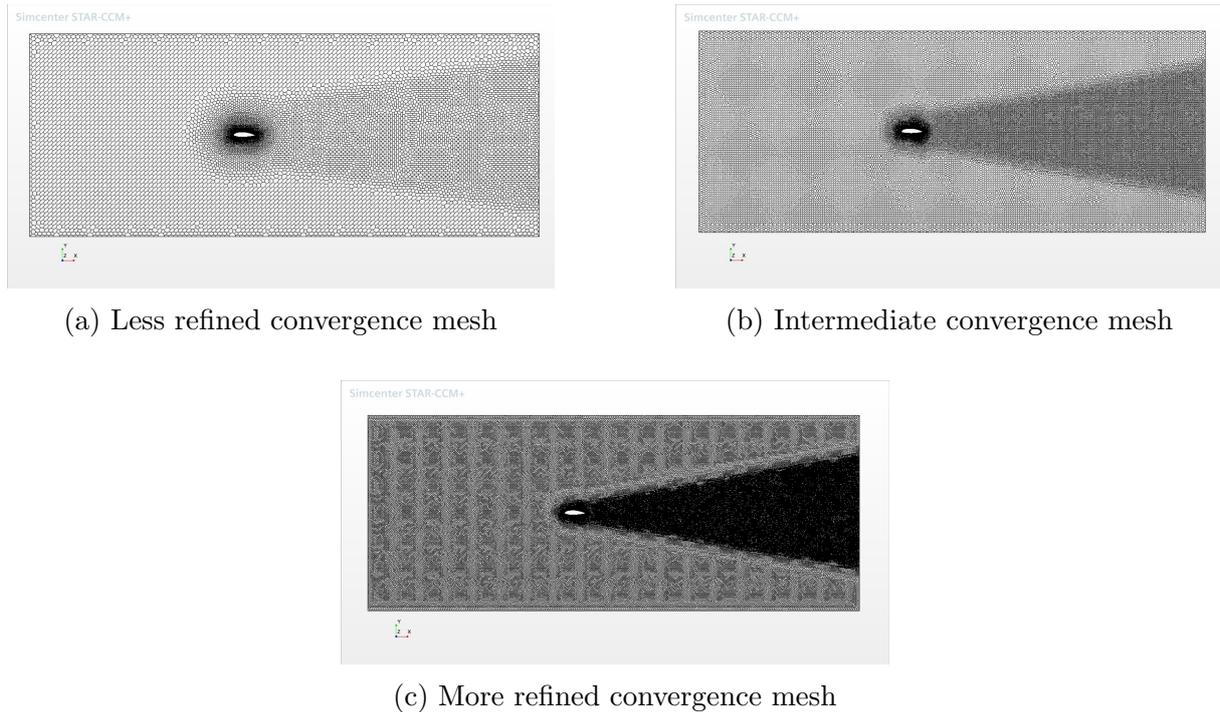(c) More refined convergence mesh

Figure 5: Different mesh refinements for UAV's mesh convergence

During the analyses performed for mesh convergence, it was found that the results obtained from Star-CCM+ were quite disparate from those calculated with XFLR5. As a way to combat this discrepancy in the C_L and C_D values, a linear regression was performed to obtain the new angle of attack values that would lead to C_L values similar to those needed to perform simulations taking into account the +3.8g and -1.5g load factors. Note that these were the load factor values used for limit situations, as they already correspond to angles of attack relatively close to those of stall, so before the aircraft reaches the load factors calculated taking gusts into account, it would go into stall. That is, the aerodynamic limits would be reached before the structural limits could be reached.

Table 5: Comparison of the results obtained with XFLR5 and Star-CCM+.

Flight Condition	Software	α [°]	C_L	Diff [%]	C_D	Diff [%]
-1.5 G	XFLR5	-7.3	-0.355	3.27	0.0512	7.91
	Star-CCM+	-6.893	-0.367		0.055596	
Cruise	XFLR5	0.23	0.237	0.42	0.0156	0.29
	Star-CCM+	1.078	0.236		0.015555	
+3.8 G	XFLR5	8.75	0.900	4.76	0.0597	0.69
	Star-CCM+	9.548	0.945		0.060112	

Consulting the values of the relative differences obtained, could be concluded that the linear regression performed previously, with the objective of finding the new angles of attack that would lead to the values of C_L corresponding to the loads in question, was successfully performed, because the magnitude of the differences between both programs is quite low. These were therefore the final analyses from which the aerodynamic loads to be applied in the topological optimization were taken.

4   CONCLUDING REMARKS

Following standard aircraft development methodology, the design and study of an UAV for motorsport surveillance in a racetrack environment was carried out. This methodology had to undergo minor adjustments, given the unusual geometry of the aircraft in question, yet the main steps were followed.

In an initial phase, the MTOW of the aircraft as calculated, through a careful choice of materials and components for the aircraft, followed by the Design Point, which allowed to proceed to a preliminary design of the UAV. With the aid of CAD software, this concept aircraft was designed, taking into account the design constraints, the dimensions obtained previously, the selected geometry and the component distribution resulting from a stability analysis.

With the geometry designed, the CFD analyses process was started, in order to obtain the aerodynamic loads to be used in the subsequent topology optimization.

It's important to note that the topology optimization process is still in progress, so the results are not available yet for presentation in the present version of this paper. As soon as they are available, it will be done an update with the results and conclusions taken from them.

ACKNOWLEDGEMENTS

REFERENCES

[1] J.-H. Zhu, W.-H. Zhang, and L. Xia. Topology optimization in aircraft and aerospace structures design. *Archives of Computational Methods in Engineering*, 23:595–622, 2016. doi:10.1007/s11831-015-9151-2.

[2] L. Meng, W. Zhang, D. Quan, G. Shi, L. Tang, Y. Hou, P. Breitkopf, J. Zhu, and T. Gao. From topology optimization design to additive manufacturing: Today's success and tomorrow's roadmap. *Archives of Computational Methods in Engineering*, 27:805–830, 2020. doi:10.1007/s11831-019-09331-1.

[3] H. Klippstein, A. D. D. C. Sanchez, H. Hassanin, Y. Zweiri, and L. Seneviratne. Fused Deposition Modeling for Unmanned Aerial Vehicles (UAVs): A Review. *Advanced Engineering Materials*, 20(2):1700552, 2018. doi:10.1002/adem.201700552.

[4] R. Karimi Kelayeh and M. H. Djavareshkian. Aerodynamic investigation of twist angle variation based on wing smarting for a flying wing. *Chinese Journal of Aeronautics*, 34(2):201–216, 2021. doi:10.1016/j.cja.2020.06.022.

[5] L. Wang, N. Zhang, T. Yue, H. Liu, J. Zhu, and X. Jia. Three-axis coupled flight control law design for flying wing aircraft using eigenstructure assignment method. *Chinese Journal of Aeronautics*, 33(10):2510–2526, 2020. doi:10.1016/j.cja.2020.03.016.

[6] T. C. Cork. *Design of Aircraft*. Prentice Hall, Upper Saddle River, NJ, USA, 2003. ISBN 0-13-089234-3.

[7] D. P. Raymer. *Aircraft Design: A Conceptual Approach.* AIAA Education Series, 5th edition, 2012. ISBN 9781600869112.

[8] P. Edi, N. Yusoff, and A. Ahmad-Yazid. The design improvement of airfoil for flying wing uav. *WSEAS Transactions on Applied and Theoretical Mechanics*, 3:809–818, 09 2008.

[9] A. Alsahlani and T. Rahulan. Aerofoil design for unmanned high-altitude aft-swept flying wings. *Journal of Aerospace Technology and Management*, 9:335–345, 08 2017. doi:10.5028/jatm.v9i3.838.

[10] General description. URL `http://www.xflr5.tech/xflr5.htm`.

[11] URL `https://web.mit.edu/drela/Public/web/xfoil/`.

[12] A. Lennon. *Basics of R C Model Aircraft Design: Practical Techniques for Building Better Models.* Air Age Media Inc., East Ridge, TN, USA, 1996. ISBN 0911295402.

[13] M. H. Sadraey. *Aircraft Design : A Systems Engineering Approach.* John Wiley & Sons, Ltd, Chichester, UK, 2013. ISBN 978-1-119-95340-1.

[14] J. Hall, K. Mohseni, D. Lawrence, and P. Geuzaine. Investigation of variable wing-sweep for applications in micro air vehicles. 4:6–9, 09 2005. doi:10.2514/6.2005-7171.

[15] A. Suleman. Aircraft Design - Wing Design, Course Notes, 2019.

[16] A. J. Keane, A. Sóbester, and J. P. Scanlan. *Small Unmanned Fixed-wing Aircraft Design: A Practical Approach.* John Wiley & Sons, Ltd, Chichester, UK, 2017. ISBN 9781119406303.

[17] J. D. Anderson. *Fundamentals of Aerodynamics.* McGraw-Hill, 5th edition, 2010. ISBN 0073398101.

[18] Z. Chen, M. Zhang, Y. Chen, W. Sang, Z. Tan, D. Li, and B. Zhang. Assessment on critical technologies for conceptual design of blended-wing-body civil aircraft. *Chinese Journal of Aeronautics*, 32(8):1797–1827, 2019. doi:10.1016/j.cja.2019.06.006.

[19] T. H. G. Megson. *Aircraft Structures for Engineering Students.* Butterworth-Heinemann, Oxford, UK, 4th edition, 2007. ISBN 978-0-7506-6739-5.

[20] F. Perini. Structural design, manufacturing and testing of a new wing for the csir's modular uas in composite materials. Master's thesis, University of Bologna, 2012.

[21] NATO. *STANAG 4703 Light Unmanned Aircraft Systems Airworthiness Requirements.* NSO, 2nd edition, 2016.

[22] *Part 23 - Small Airplane Certification Process Study, Recommendations For General Aviation For The Next 20 Years.* Federal Aviation Administration, July 2009.

[23] Star-ccm. URL `https://www.plm.automation.siemens.com/global/pt/products/simcenter/STAR-CCM.html`.

[24] C. L. Ladson, A. S. Hill, and W. G. Johnson. Pressure distributions from high reynolds number transonic tests of an naca 0012 airfoil in the langley 0.3-meter transonic cryogenic tunnel. Technical Report 100526, NASA, December 1987.

[25] J. H. Ferziger and M. Peric. *Computarional Methods for Fluid Dynamics*. Springer, Germany, 2002. ISBN 978-3-642-56026-2.

[26] A. Tomboulides, S. Aithal, P. Fischer, E. Merzari, A. Obabko, and D. Shaver. A novel numerical treatment of the near-wall regions in the k class of rans models. *International Journal of Heat and Fluid Flow*, 72:186–199, 2018. doi:10.1016/j.ijheatfluidflow.2018.05.017.

[27] Y. You, F. Seibold, S. Wang, B. Weigand, and U. Gross. Urans of turbulent flow and heat transfer in divergent swirl tubes using the k- sst turbulence model with curvature correction. *International Journal of Heat and Mass Transfer*, 159:120088, 2020. doi:10.1016/j.ijheatmasstransfer.2020.120088.

[28] T. Rocha. Numerical and experimental study of wing tip endplates of a formula student car. Master's thesis, Instituto Superior Técnico, 2020.

[29] F. Menter, R. Langtry, S. Likki, Y. Suzen, P. Huang, and S. Völker. A correlation-based transition model using local variables—part i: Model formulation. *ASME J. Turbomach*, 128, 07 2006. doi:10.1115/1.2184352.

[30] C. L. Ladson and E. J. Ray. Evolution, calibration, and operational characteristics of the two-dimensional test section of the langley 0.3-meter transonic cryogenic tunnel. 1987.

[31] J. Tu, G. H. Yeoh, and C. Liu. *Computarional Methods for Fluid Dynamics*. Butterworth-Heinemann, Oxford, UK, 2013. ISBN 9780080982779.

[32] M. Ariff, S. M. Salim, and S. Cheah. Wall y+ approach for dealing with turbulent flows over a surface mounted cube: Part 2 - high reynolds number. 01 2009.

[33] 3d cad design software. URL `https://www.solidworks.com/`.

[34] F. Goetten, D. F. Finger, M. Marino, C. Bil, M. Havermann, and C. Braun. A review of guidelines and best practices for subsonic aerodynamic simulations using rans cfd. In *Asia Pacific International Symposium on Aerospace Technology*, Gold Coast, Qld, Australia, 2019. URL `https://search.informit.org/doi/10.3316/informit.938995657936656`.

[35] B. Gossant. Chapter 4 - solid propellant combustion and internal ballistics of motors. In A. Davenas, editor, *Solid Rocket Propulsion Technology*, pages 111–191. Pergamon, Amsterdam, 1993. doi:10.1016/B978-0-08-040999-3.50009-6.

[36] O. Sigmund and K. Maute. Topology optimization approaches. *Structural and Multidisciplinary Optimization*, 48:1031–1055, 2013. doi:10.1007/s00158-013-0978-6.

[37] Altair hyperworks™. URL `https://www.altair.com/hyperworks/`.

A DAMAGE-BASED FRAMEWORK TO IMPROVE THE STRENGTH OF STRAIN DRIVEN GENERATIVE DESIGNS

Gonzalez Marco, Miguel[1]*, Saucedo Mora, Luis[2], Garcia Modet, Hugo[3], Sanz Gomez, Miguel Angel[4] and Montans Leal, Francisco Javier[5]

GAMOSINOS: Grupo Avanzado de MOdelado y SImulación NO-lineal de Sólidos
Escuela Tecnica Superior de Ingenieria Aeronáutica y del Espacio
Universidad Politécnica de Madrid
28040
miguel.gonzalez.marco@alumnos.upm.es
luis.saucedo@upm.es
hugo.garcia.modet@alumnos.upm.es
miguelangel.sanz@upm.es
fco.montans@upm.es

Abstract. *This dissertation aims to achieve a damaged-based framework of the study of generative design pieces by optimizing the structural behavior in strain. By putting the piece through a virtual traction test, the objective is to achieve the breakage point which will give the necessary information to enhance the structural properties of weak areas in strain behavior. This will change the form of the design reinforcing these zones, so if done iterative, it will give a full-optimized piece against traction, reinforced in those areas which could be critical in a real-case scenario.*

Keywords: Topological Optimization, Tension test, damage, Generative design, structures, aerospace

Miguel González Marco, Hugo García Modet, Luis Saucedo Mora, Miguel Angel Sanz Gómez, Francisco Javier Montans Leal

1   INTRODUCTION

The scope of this work is to develop an accurate model which can be able to represent the behaviour of a metamaterial and automatically generate a structure optimised to the loads.

Having successfully developed the generative design model, the scope of this damaged-based model is to enhance the strain behaviour of the designed piece. So, in order to reach a full understanding of the project, a brief introduction of how the generative model works is going to be given. Having obtained a full-working topological optimization module, the damage model is going to be explained and how these programs are implemented.

2   TOPOLOGICAL OPTIMIZATION

The general formulation that is commonly used to solve the topological optimization problem is:

$$F = F(u(\rho), \rho) = \int_{\Omega} f(u(\rho), \rho)\mathrm{d}V$$
$$G_i(u(\rho), \rho) \leq 0, i = 1, ..., M$$
$$\rho(x) = 0, 1; \forall x \in \Omega$$

This equation represents the minimization of an objective function F, subject to M different constraints G_i(2.2). The material distribution is described by the design variables, commonly represented as densities, ρ. These densities can be equal to 0(void) or 1(solid material) at any point in the design domain Ω.

The previous framework of study has been the topological optimization with Young modulus updates. The specific mathematical statement to this approach is:

$$c = \int_{\Omega} \frac{1}{2}\sigma : \epsilon\mathrm{d}\Omega$$
$$K(\rho)U = F$$
$$G_j(u(\rho), \rho) \leq 0, j = 1, ..., M$$
$$0 \leq E_i \leq E_{max}, i = 1, ..., N$$

In this expression, the objective function is the structural compliance c, G_j represents additional constraints, E_i are the design variables which represents the Young modulus of each element i, and E_{max} is the maximum Young modulus value, necessary to achieve the convergence of the method.

This equation geometrically optimizes the piece using the input loads and the imposed constraints obtaining an optimized piece with different layers of Young modulus within the body. This result slightly deviates from the reality of the construction of a metamaterial, being almost impossible to build a piece with so many layers of Young modulus. One of the results obtained from this thesis is the adaptation of the topology optimization to the input materials, minimizing the energy while reducing the Young modulus spectrum.

3   DAMAGE-BASED MODEL

The damage model came as a way to develop the generative design, trying to improve the strain behaviour of the piece. The idea behind the project was to reach the breakage
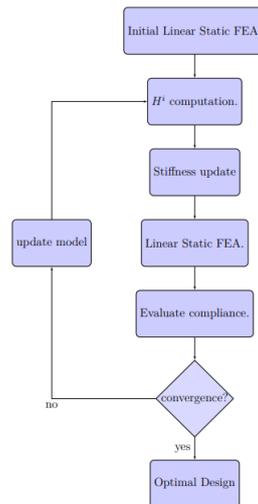
Miguel González Marco, Hugo García Modet, Luis Saucedo Mora, Miguel Angel Sanz Gómez, Francisco Javier Montans Leal

Figure 2.1: Optimization Flow Chart.

Figure 1: Flowchart of Topological Optimization

point of the optimized piece and save the last state of the mesh to restart the optimization and enhance the weakest zones of the piece. The main difficulty of this project is that the specimen is a metamaterial so there are different properties within the whole piece.

This idea is complementary to the topology optimization and is based on the idea of the experiment of traction. Extracting the eigenvalues of each element, computing the energy associated to that element and equalizing this expression to the experimental energy obtained from a real experiment of traction the young modulus is updated. A further explanation will be given.

Basing the explanation in the flowchart attached below the damage model is composed of three different functions. The main function is called tractionfunction and is composed of another function called damagecore that, at the same time, has two functions called scalenormalizer and damagecore.

Starting with the working procedures, the main iterative value is the imposed displacement which represent the control value of the traction experiment. After fixating this parameter in each iteration, a FEM analysis is made to extract the value of the reaction forces in the embedment. This value may be wrong, so a conditional loop is made to relax the forces and, if the force of one step is very similar – a tolerance error is defined – to the force of the next step, this value is assumed to be correct, and the next iteration starts.

This procedure is going to be made all the necessary times until one of the general stop conditions is fulfilled. If the reaction forces are zero, or the next force of the force-displacement graphic is less than a control parameter defined outside the program called "invslope", it is assumed that the piece has broken, and the program stops.

The stop condition of the combined program is that if the last reaction force of the k iteration is similar to the k + 1 iteration – defining this similarity outside the program – the piece is assumed to be the same as the previous step and the solution has converged.

The FEM analysis is combined with the young modulus update to calculate the value of the reaction forces, so this FEM analysis and the damage model are combined in each iteration of the program.

After stopping, the last young modulus mesh is stored and given to the optimization program which will again generate a piece, this time reinforced in the specific areas where
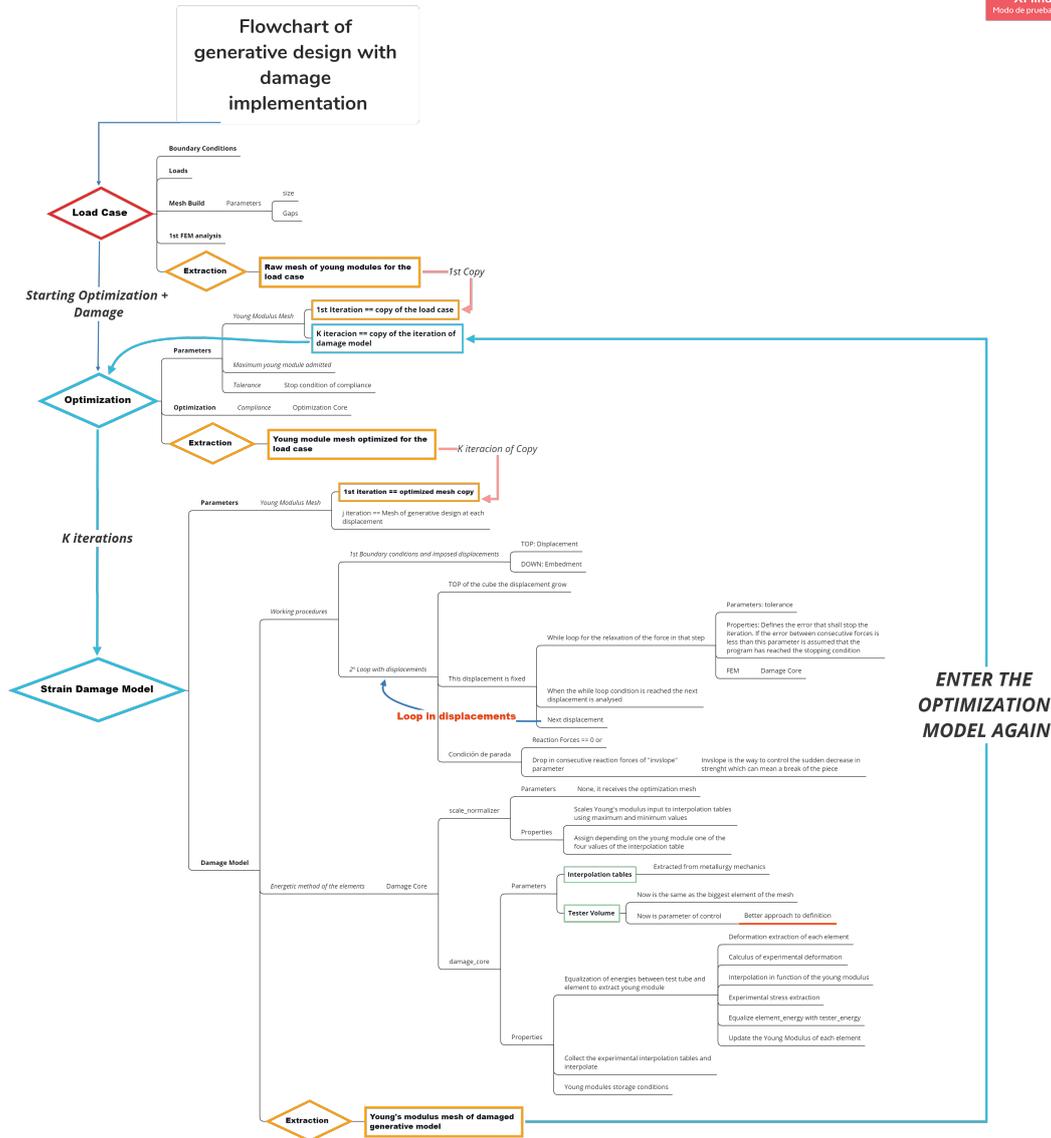
Miguel González Marco, Hugo García Modet, Luis Saucedo Mora, Miguel Angel Sanz Gómez, Francisco Javier Montans Leal

Figure 2: Flowchart of Generative Design and Damage-Based Model

is breaking.

4 RESULTS

The results extracted from this process are attached below as "Complete process of the algorithm". There are four steps of optimization, having represented three of them. The first one is the initial, the second one is an intermediate process and the third one is the final state of the piece.

Having shown how the optimization of the piece evolves, the stress-strain curves of each step of optimization are going to be presented as "Stress - Strain Curves in the algorithm steps".

Miguel González Marco, Hugo García Modet, Luis Saucedo Mora, Miguel Angel Sanz Gómez, Francisco Javier Montans Leal
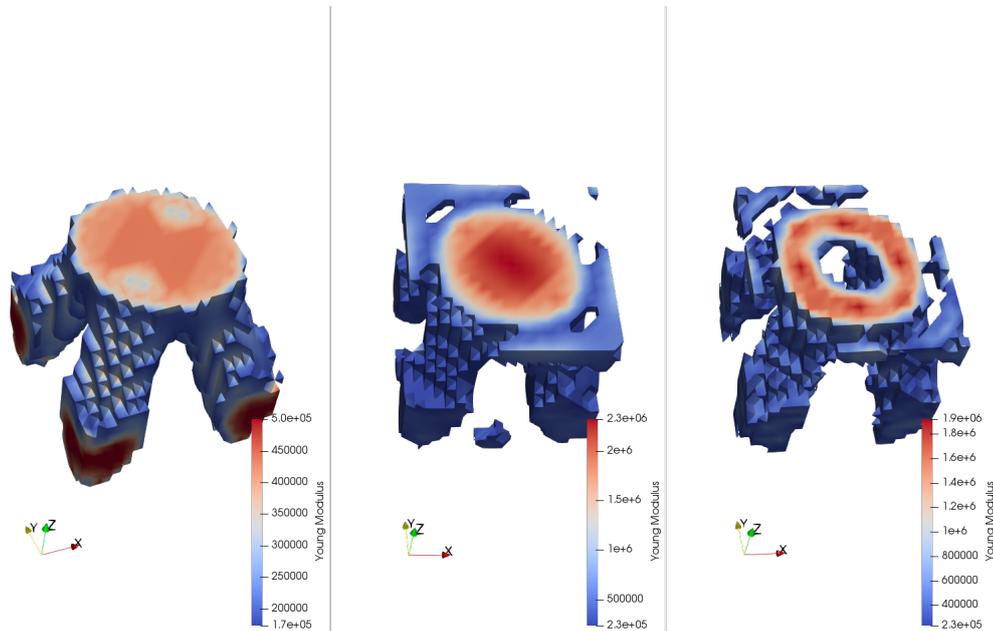
Figure 3: Complete process of the algorithm

(a) State 1

(b) State 2

(c) State 3
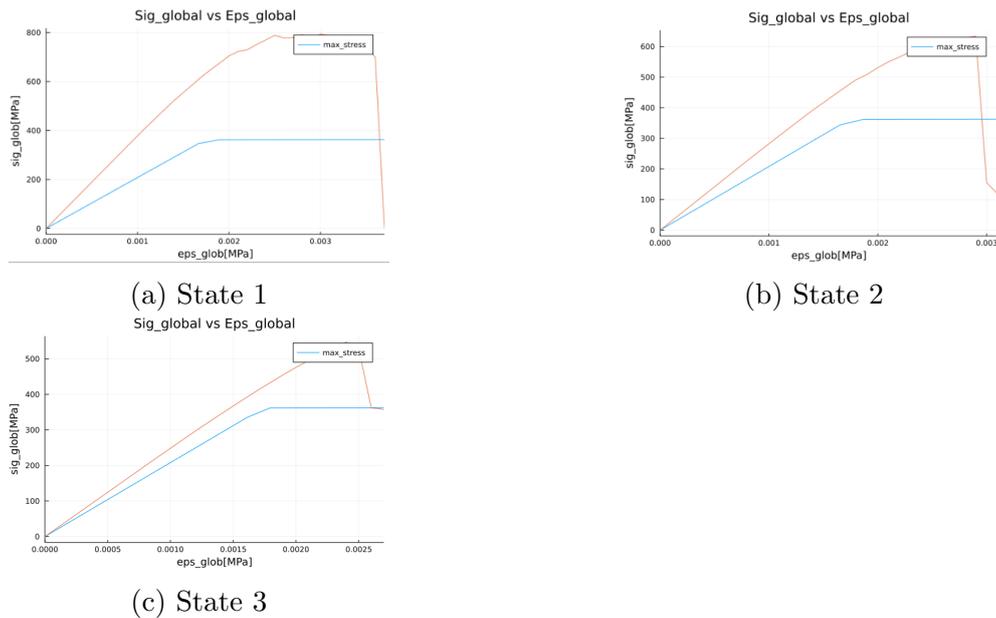
Figure 4: Stress - Strain Curves in the algorithm steps

5 CONCLUSIONS

The program is showing interesting results related to the optimization. The scope of the topology optimization is to minimize energy, and as it can be seen from the Stress-Strain curves, the objective is being fulfilled after each iteration decreasing the area under the curve. Also, the program is behaving anti-naturally intuitive because the total stiffness is decreasing after each iteration, but the Young Modulus in critical zones is increased from the beginning. This is because the main part of the damage algorithm is based on real materials such as 2024-T3 steel, with real dimensions of experiment like the volume parameter. So, after each iteration the minimization of the energy is being produced geo-

Miguel González Marco, Hugo García Modet, Luis Saucedo Mora, Miguel Angel Sanz Gómez, Francisco Javier Montans Leal

metrically (topological optimization) and with the correspondent input materials, reaching a strain optimized piece with a lowered spectrum of Young modulus. Making it possible to build with additive fabrication.

The negative aspects are mainly the out-layers produced within the process. These are being investigated now and the line of work is currently to apply machine learning techniques to extract these points and obtain a clean usable model.

6 REFERENCES

For more information about the FEM models, the stress-strain behavioural curves and the topological optimization.[1–3]

REFERENCES

[1] M. Bendsoe and N. Kikuchi. *Generating Optimal Topologies in Structural Design Using a Homogenization Method. Computer Methods in Applied Mechanics and Engineering.* Springer, 2th edition, 1988. ISBN 9783642076985.

[2] G. Dieter. *Mechanical Metallurgy (Materials Science Engineering) by Dieter.* Mc Graw Hill, 1986. ISBN B013PRHMDC.

[3] E. W. V. C. y Roberto Mıngue. *Mecanica computacional en la ingenieria con aplicaciones en Matlab.* PhD thesis, Universidad de Castilla La Mancha, Escuela Técnica Superior de Ingenieros de Caminos, Canales y Puertos, 2010.

MULTIDISCIPLINARY DESIGN OPTIMIZATION FOR THE NEXT GENERATION OF AIRCRAFT

Joaquim R. R. A. Martins

University of Michigan, USA
jrram@umich.edu, https://mdolab.engin.umich.edu/

Abstract. *Despite the progress in high-fidelity numerical simulations enabled by high-performance computing, challenges have remained in the use of these simulations for design optimization. This talk focuses on the developments that made it possible to perform high-fidelity design optimization of aircraft configurations. The challenges addressed include handling a large number of design variables, robust and efficient large-scale simulations, effective geometry and mesh handling, and efficient discipline coupling. To tackle these issues, we combine gradient-based optimization algorithms with adjoint gradient computation and develop an adaptive coupled Newton-Krylov approach to solve the coupled numerical simulations efficiently and robustly. The applications focus on aircraft design, including unconventional configurations. We first tackle wing design by coupling computational fluid dynamics to structural finite-element solvers and simultaneously optimizing the aerodynamic shape and structural sizing. The methods we developed to tackle this problem are generalized in the OpenMDAO framework, an open-source framework for multidisciplinary analysis and optimization. This and other open-source tools developed in this work open the door to further advances in algorithms and their application to aircraft design and beyond.*

Keywords: High-fidelity design optimization, Adjoint gradient, Coupled numerical simulations, OpenMDAO framework

PRELIMINARY DESIGN OF THE PROPULSION SYSTEM OF A FIXED-WING TILT-ROTOR QUADCOPTER CLASS I MINI UNMANNED AIRCRAFT

Pedro Mendes, Luís Félix, Tiago Oliveira, and Vasco Franco

Centro de Investigação da Academia da Força Aérea
Academia da Força Aérea
Instituto Universitário Militar
2715-311 Pêro Pinheiro
{pdmendes, lffelix, tmoliveira, vhfranco}@academiafa.edu.pt http://www.academiafa.edu.pt

Abstract *This paper presents the preliminary design of the propulsion system of a fixed wing quadcopter Tilt-Rotor Unmanned Aircraft (TRUA) with Vertical Take-Off and Landing, following the conceptual design made in a previous work. It is also a goal to determine if the TRUA configuration is more efficient than using a fixed-wing quadcopter with an extra motor for forward flight (Quad+1). Initially, the most appropriate components of the propulsion system (motors, controllers and batteries) are selected, based on thrust requirements. A sample of eight propellers is selected, for which two comparison methods are applied: one theoretical (Blade Element Theory) and another experimental (wind tunnel). From these, the HP (propellers with best performance in forward flight which can deliver the required thrust in vertical flight), and VP (propellers with best performance in vertical flight) are selected. From the performance data obtained in the wind tunnel tests, two comparisons are made for five different arrangements – the first based in the efficiency of the arrangements and the second based in the endurance of the aircraft with different arrangements considering weight limitations. It is shown that if the TRUA solution is to be used, the most efficient arrangement is B2 – different front and rear propellers asymmetrically distanced longitudinally from the CG. It is concluded that the Quad+1 solution is more efficient and simpler to integrate and control than the TRUA solution. It is also concluded that if the weight available for the power and energy supply system is less than 8.93 kg, the endurance may be higher with the TRUA solution, if a light and robust tilting system is attained.*

Keywords: Tilt Rotor, Propellers, Blade Element Theory, Aircraft Design, Unmanned Aircraft, Vertical Take-Off and Landing

Pedro Mendes, Luís Félix, Tiago Oliveira, and Vasco Franco

1. INTRODUCTION

The use of Unmanned Aircraft Systems (UAS) in civil society and in the military is growing. The spectrum of possible uses of these systems is also increasing, as there are increasingly more UAS both under development and available on the market [1].

The UAS study at the Air Force Academy Research Center (CIAFA) has been going on for several years, during which its efficiency, usefulness and versatility in dull, dirty and dangerous missions have been systematically demonstrated - including a set of missions of general interest to society, such as fire monitoring and maritime space surveillance.

At the start date of this project, the CIAFA did not have any UAS platform with Vertical Take-Off and Landing (VTOL) capability. In a first step to increase the operational versatility of the CIAFA, Ferreira [2] developed in 2019 the conceptual design of a class I mini fixed-wing Tilt-Rotor Unmanned Aircraft (TRUA) with the following operational requirements:

- Maximum Take Off Weight (MTOW): 15 kg
- Configuration: TRUA (Fixed-wing quadcopter with tiltable frontal propellers – the rear propellers stop in position during fixed-wing flight)
- Cruise velocity: 20 m/s
- Cruise altitude Above Medium Sea Level (AMSL): 305 m
- Maximum velocity > 25 m/s

The focus of this work is to perform the preliminary design of its propulsion system. This involves the selection of the components which constitute it and to assess the most efficient arrangement of the motor-propeller pairs. It is also a goal to determine if the TRUA configuration is more efficient than using a fixed-wing quadcopter with an extra motor for forward flight (Quad+1).

In this paper, a systematic methodology for the characterization and selection of components of a propulsive system is proposed, for TRUA aircraft with up to 15 kg MTOW. This methodology allows, during the preliminary design of a new aircraft, to select the most adequate propulsive system configuration according to the shown flight profile. This methodology was applied to an aircraft built at CIAFA. The results obtained in each stage of the proposed methodology are detailed below.

2. REQUIRED THRUST ESTIMATION

Before selecting the components of the propulsion system, the required thrust for both cruise and vertical stages of flight is estimated. Although when referring to propeller-based aircraft propulsion systems the most usual approach is to estimate the required power (not the required thrust), since the required power P_R depends on the velocity of the flow approaching the powerplant [3] (see Equation 1), it is impractical to estimate the power required for vertical flight at hovering conditions. For this reason, the selection process is based on thrust requirements instead of power requirements.

$$P_R = V \cdot D \qquad (1)$$

In order to estimate the required thrust for both vertical and horizontal flights, the drag produced by the aircraft is estimated both by using algebraic empirical expressions [4] and CFD simulations (using *SOLIDWORKS Flow Simulation*), from which the most conservative values are considered. Figure 1 illustrates the free body diagrams for the relevant stages of flight. A detailed description of the methods used to estimate the drag can be found in [5] and the main results are shown in Table 1. The required thrust for each flight

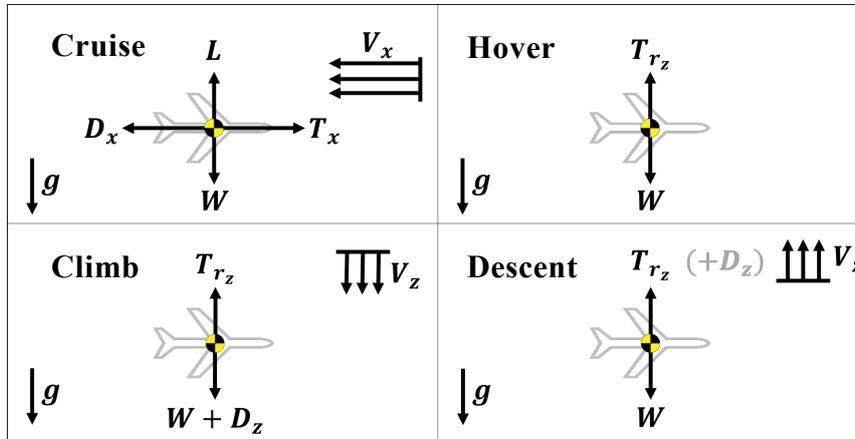stage is then assumed to be equal to the estimated drag ($T_R = D$).

Figure 1 - Free body diagram for relevant flight stages

Table 1 - Estimated Drag

Flight Stage (configuration)	Estimated Drag
Cruise (TRUA)	$D_{x_{TRUA}} = 12.04\ N$
Cruise (Quad+1)	$D_{x_{QUAD}} = 14.08\ N$
Vertical flight	$D_z(\text{N}) = 1.0231\ V^2$

3. PROPELLER SELECTION

3.1. Propulsion system components

The appropriate propulsion system for any aircraft depends on several factors, among which the design cruise speed and altitude [4]. For medium and small UA, such as the one designed in this project, the propulsion is generally carried out by some form of propeller-based system [6]. In a prior stage of this project, the motors, Electronic Speed Controllers (ESCs) and batteries were selected, respectively: the *T-Motor P-60 KV170* [7] motor ; the *T-Motor FLAME 60A HV* ESC [8]; and the *Tattu 22 000 mAh 6S* batteries (two packs, connected in series).

3.2. Propeller performance and propeller selection

During vertical flight, the flow velocity is small when compared to cruise flight. The efficiency of a fixed pitch propeller is optimal only within a short velocity envelope. A propeller optimized for forward flight has a poor performance in vertical flight and vice versa. To address this deficiency in performance, variable pitch propellers are used in some aircraft. Such type of propellers does not exist on the market for aircraft with the dimensions of the one in this project (based both on consulted bibliography [6] and carried out research). It would be possible to develop new propellers, but that would be unattainable within the available time frame of this project. The propellers used in this UA project have therefore fixed pitch.

Different propulsion arrangements can be achieved by combining propellers optimized only for vertical flight (from here on mentioned as "VP"), or propellers optimized for forward

flight which deliver the required thrust for vertical flight with reasonable efficiency (from here on mentioned as "HP"). Both extensively using VP during forward flight, or shortly (but intensively) using HP in vertical flight conditions can be inefficient, and therefore an optimized point must be reached.

In order to compare the proposed arrangements, the HP and VP propellers must be selected between a set of available propellers. The operation of the aircraft in project requires each propeller to be able to lift more than ¼ of its weight at around 70% of the available thrust (when in vertical stage of flight), and to deliver at least ½ of the required thrust for cruise flight at $20 \, m \, s^{-1}$. These factors depend not only on the propeller but also on the power output that the motor is able to deliver.

3.3. Selection of the sample for comparison

In order to select the propeller sample for testing with the chosen motor, the first approach is to make iterative simulations using the online calculator *eCalc*, which has calculators for both multicopter [9] and fixed wing [10] configurations. According to simulations made with the current project's specifications and selected motors, it would only be reasonable to fly vertically with propellers larger than 17 inches in diameter (since with smaller propellers the amount of required throttle at hovering flight would be superior to 80%, potentially making the aircraft uncontrollable [9]). For cruise flight, on two motors, it is predictable only to be possible to fly with propellers with 15 inches or more in diameter (for smaller propellers to be able to output the required thrust, the rotational speed would have to be greater than what is achievable with the selected motors [10]).

Propellers larger than 22 inches in diameter would be impractical, given the expected dimensions of the aircraft and because an increase in diameter would result in a decrease of efficiency for both horizontal and vertical stages of flight (according to simulations performed in *eCalc*). The available propellers at the CIAFA range from 12x6 to 22x6.6, allowing to test the desired range in a meaningful and representative way. Between these, the following are chosen for the test sample: 17x8, 17x10, 18x8, 18x10, 20x8, 20x10, 20x6 and 22x6.6.

4. OBTAINING PROPELLER PERFORMANCE DATA

In order to select the most appropriate HP and VP, two comparisons are made to the propellers in the selected sample: a theoretical comparison with a method based on the Blade Element Theory (BET), and an experimental method with wind tunnel testing.

This comparison could be made only with the experimental method, since it provides accurate performance data of the actual propellers with the selected motors. Using the BET method aims at understanding if such method is an appropriate approach when selecting propellers, when a wind tunnel is not available.

4.1. Blade Element Theory Method

The concept of the BET is to divide the blade of the propeller into several blade elements, analyze each element and integrate the results along the blade's length, accounting for all elements. Thrust, torque, and efficiency can be estimated with this method. The BET analysis of the propeller sample is solved numerically, through spreadsheets, and follows a method adapted from Gudmundsson [3].

Firstly, the geometrical properties of each propeller are obtained and measured: the airfoil of the inner half of the blades is assumed to be Eppler E63 and the outer half is assumed to

Pedro Mendes, Luís Félix, Tiago Oliveira, and Vasco Franco

be Clark-Y, based on a reference from the propeller manufacturer *APC* [11]; the torsion of the tip of the blade is measured, the torsion at 75% of the blade radius is obtained from the geometric pitch, and a linear variation of the torsion along the radius of the blade is assumed; finally, the chord variation along the radius of the blade is measured using a caliper rule. These properties are inserted in the spreadsheets: one for each propeller at each transverse and rotational velocities.

The higher is the number of elements considered, the more accurate are the results. The number of elements (ε) is therefore set to $\varepsilon = 40$ (twice the number of elements recommended by Gudmundsson [3]). The results for all propellers are shown in Table 2 at cruise velocity and in Table 3 at climbing velocity.

In Table 2, the selected rotational velocity is 6700 RPM, since according to the eCalc calculator it is the regime for highest efficiency of the *P60* motors.

Table 2 - BET results for 20 m/s @ 701.6 $rad\ s^{-1}$ (6700RPM)

Propeller	T	Q	P_R	P_{eff}	η
	N	N·m	W	W	
17x8	18.90	0.65	458.54	378.09	0.82
17x10	28.51	0.89	624.89	570.11	0.91
18x8	22.24	0.78	547.59	444.72	0.81
18x10	35.53	1.12	785.58	710.68	0.90
20x6	10.40	0.72	501.97	208.00	0.41
20x8	30.95	1.11	777.19	618.94	0.80
20x10	54.91	1.72	1208.68	1098.24	0.91
22x6.6	26.59	1.32	928.83	531.89	0.57

The propeller thrust output values from Table 2 vary between each other but are still greater than the required thrust for cruise flight. The rotational velocity at cruise velocity is therefore smaller than 701.6 $rad\ s^{-1}$ for all propellers. The propellers with geometric pitch $P_D = 10\ in$, in addition to having the best efficiency, are the ones with the highest thrust output values. Thus, it is expected that they have the best performance at the recommended regime for cruise flight. These are, therefore, the most likely choices for HP. However, since these propellers also must work for vertical flight in some of the proposed configurations, the chosen HP is the one which has the most available thrust and efficiency at $V = 5\ m\ s^{-1}$. In Table 3, the rotational velocity of each propeller is set to Ω_{75}, the rotational velocity that at 5 m/s results in an angle of attack (α) of 4.5º in the blade at 75% of the radius, which was found to be the α correspondent to the highest L/D for Reynolds ranging between 150 000 and 300 000 and the Clark-Y airfoil (the airfoil considered at 75% of the radius). This is assumed to be the condition of highest efficiency at each velocity, since the highest amount of thrust is produced near 75% of the radius of the blades.

Table 3 - BET results for 5 m/s at each respective Ω_{75}

Propeller	Ω_{75}	T	Q	P_R	P_{eff}	η
	$rad\ s^{-1}$	N	N·m	W	W	
17x8	259.2	4.321	0.102	29.62	21.61	0.7296
17x10	184.2	1.491	0.056	11.87	7.455	0.6281
18x8	269.2	6.168	0.143	42.51	30.84	0.7255
18x10	189.1	2.262	0.079	16.97	11.31	0.6665
20x6	545.3	57.143	0.649	368.4	285.72	0.7756
20x8	292.1	11.159	0.236	74.64	55.80	0.7475
20x10	199.9	4.639	0.143	32.14	23.195	0.7217
22x6.6	495.6	69.62	0.863	445.4	348.10	0.7815

The results in Table 3 indicate that the propeller with greatest efficiency and available thrust at $V = 5\ m\ s^{-1}$ is the 22x6.6 propeller. It is predictably the propeller with best performance during climb and hovering, and therefore is selected for VP. However, since the thrust for the propellers with $P_D = 10\ in$ is smaller than what is required for vertical flight, no conclusions can be taken for the choice of the HP solely based on the values from this table. In order to estimate the required Ω for each propeller to deliver the required thrust, since it cannot be obtained directly from the BET, a simulation is performed using *eCalc*. For each propeller, the corresponding estimated Ω for hover thrust is obtained. From these values, another BET calculation is performed, which results are expressed in Table 4.

Table 4 - BET results for estimated hovering Ω

Propeller	Ω	T	Q	P_R	P_{eff}	η
	$rad\ s^{-1}$	N	N·m	W	W	
17x10	571.7	34.857	0.420	240.11	174.29	0.7259
18x10	519.7	36.281	0.459	238.54	181.41	0.7605
20x10	435.9	36.799	0.528	230.16	184.00	0.7994

According to Table 4, the propeller with $P_D = 10\ in$ with highest efficiency and lowest required power, at estimated required thrust for hovering, is the 20x10 propeller. This propeller is therefore the chosen HP.

4.2. Wind tunnel experimental method

Having compared the sample propellers theoretically, follows the wind tunnel experimental tests, which main objective is to extract performance data from combining the selected motors with the sample propellers. Propellers 17x8 and 17x10 are not considered, since their expected performance is the worst both at vertical and horizontal flight, according to BET, and do not physically fit the motor mount.

Each propeller is tested at two flow velocities: $V = 0\ m\ s^{-1}$ (simulating hover conditions) and $V = 20\ m\ s^{-1}$ (simulating cruise flight conditions). In each test, data is acquired for a full range of rotational velocities, starting at minimum Ω delivered by the motor, with steps of $\Omega = 26.18\ rad\ s^{-1}$ (250 RPM) until maximum rotational velocity (at full throttle). The test setup is shown in Figure 2.

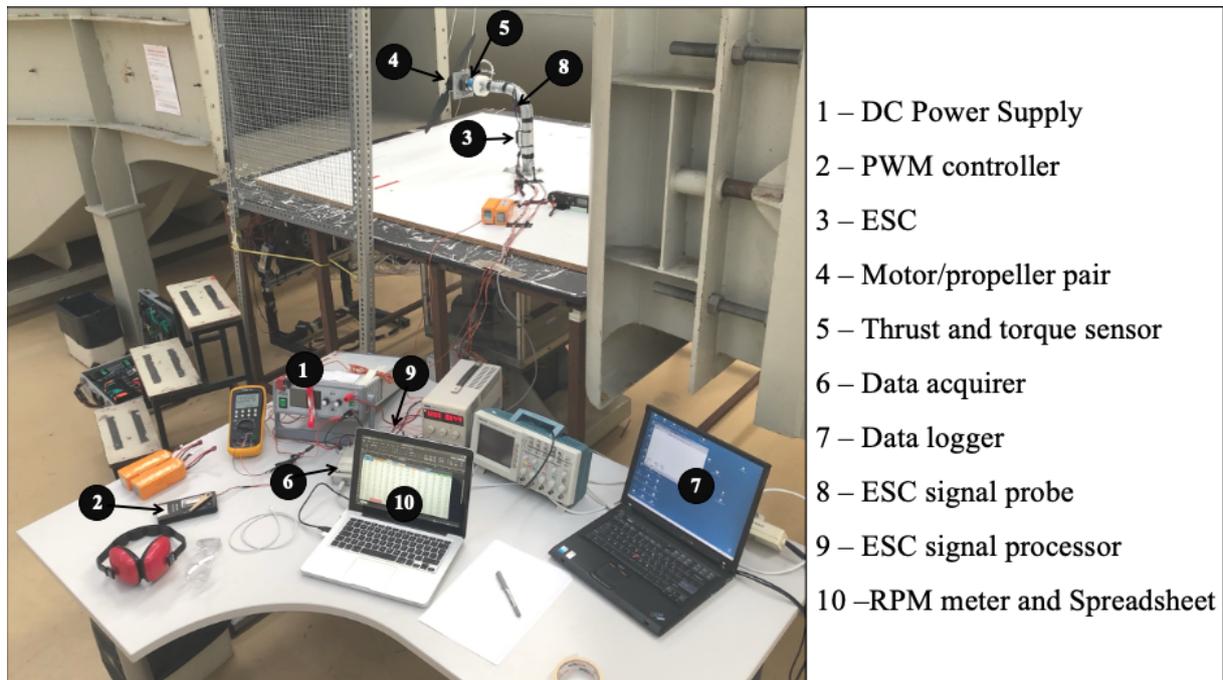Pedro Mendes, Luís Félix, Tiago Oliveira, and Vasco Franco

Figure 2 - Wind tunnel test setup

Testing is made with a DC power supply delivering 48 V, which corresponds to the mean voltage of a 12S battery pack. The voltage and current values are obtained through the power supply's display. The resulting thrust and torque values are obtained from the display of the computer connected to the data logger. All values are inserted manually in a spreadsheet, for each rotational velocity.

From the values registered in the spreadsheet, the mechanical power required (P_R) and electrical power required (P_e) are obtained, respectively, by equation (1) and equation (2):

$$P_e = U \cdot I \tag{2}$$

where U = voltage and I = current.

The efficiency of the propeller/motor pair is obtained by equation 3 [3]:

$$\eta = \frac{P_R}{P_e} \tag{3}$$

Since P_R is dependent on the incoming flow velocity, η can not be obtained for the tests made with $V = 0\ m\ s^{-1}$. For these conditions, T is graphically compared to P_e. Higher T for the same P_e means higher efficiency.

4.3. Wind tunnel performance results

Figure 3 gives the output thrust at each Ω. It can be noted that the propeller which delivers the most thrust for each Ω is the 20x10, followed by the 18x10. The 20x10 is also the propeller with the most available thrust of the sample. Two horizontal lines represent the required thrust for cruise forward flight both for TRUA and Quad+1 configurations.

Pedro Mendes, Luís Félix, Tiago Oliveira, and Vasco Franco
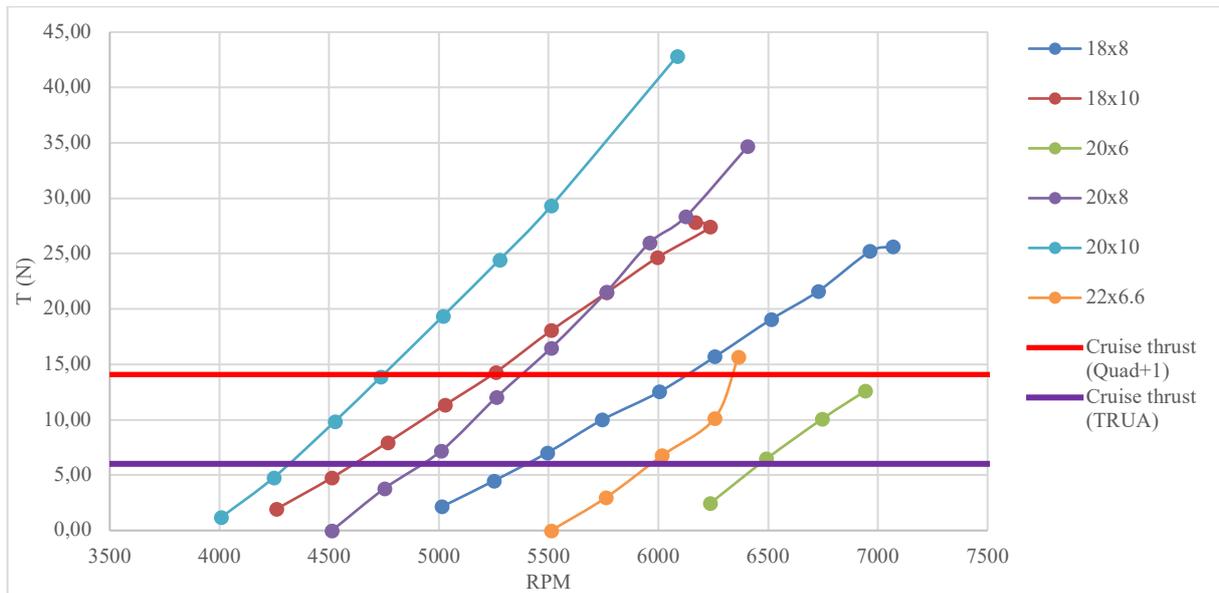
Figure 3 – T/Ω at $V = 20\ m/s$

Figure 4 gives the η of each propeller for each thrust output. There is no significant variation in the efficiency of each propeller, apart from 22x6.6 and 20x6, which have significantly lower efficiencies at $V = 20\ m\ s^{-1}$.
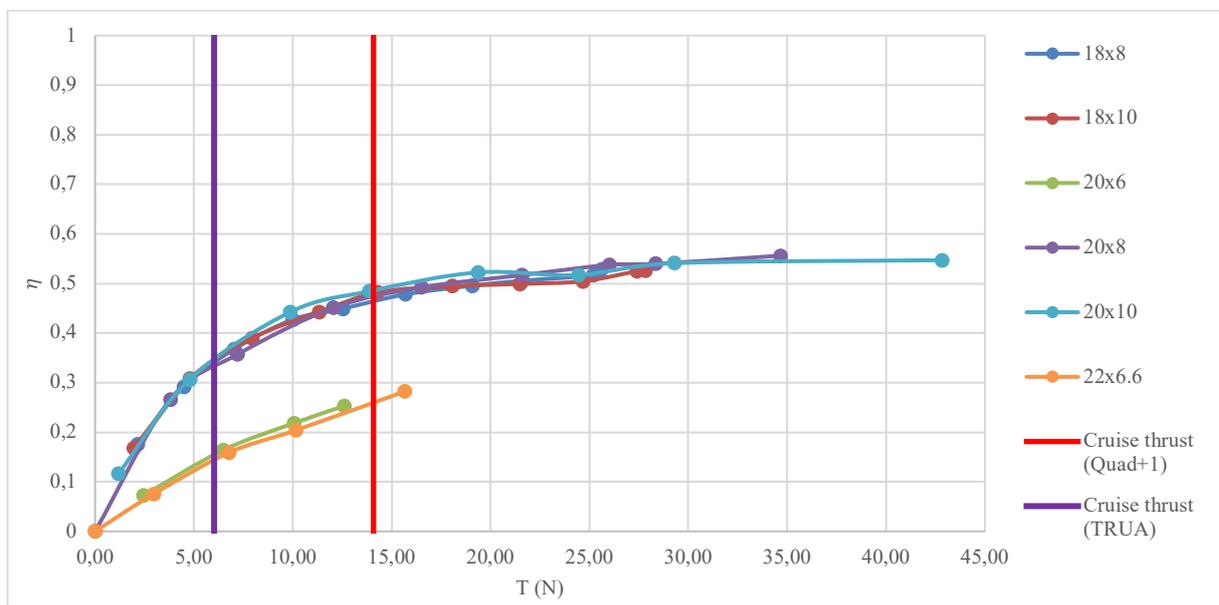
Figure 4 – Efficiency vs thrust at $V = 20\ m/s$

An initial observation of the data obtained from testing at $V = 20\ m\ s^{-1}$ indicates that the HP choice can be either 18x10, 20x8 or 20x10 and that all propellers have a higher forward flight efficiency with a Quad+1 configuration.

Table 5 shows interpolated values for these three propellers at cruise flight required thrust, for each propeller in TRUA configuration ($T = 6.02\ N$). Table 6 shows the same values, for the propeller in Quad+1 configuration (T=14.08 N). The propeller from the sample with the

Pedro Mendes, Luís Félix, Tiago Oliveira, and Vasco Franco

highest (although far from optimum) efficiency at theses regimes is the 20x10. The final choice of the HP depends on the performance of these propellers at vertical flight conditions.

Table 5 – Propeller performance at $V = 20\ m/s$ and $T = 6.02\ N$ (TRUA)

Propeller	Ω (RPM)	P_e	P_{eff}	η
18x10	4615	354.74	121.86	0.3435
20x8	4919	363.94	123.27	0.3387
20x10	4319	344.75	123.14	0.3572

Table 6 - Propeller performance at V=20 m/s and ($T = 14.08\ N$) (Quad+1)

Propeller	Ω (RPM)	P_e	P_{eff}	η
18x10	5239	606.33	285.02	0.4701
20x8	5375	609.55	288.33	0.4730
20x10	4737	594.55	288.01	0.4844

Figure 5 relates the available thrust with the rotational velocity (T/Ω) for vertical flight tests. From this graph it can be noted that the propellers which output the most thrust, for any given Ω, are the 22x6.6 and 20x10.
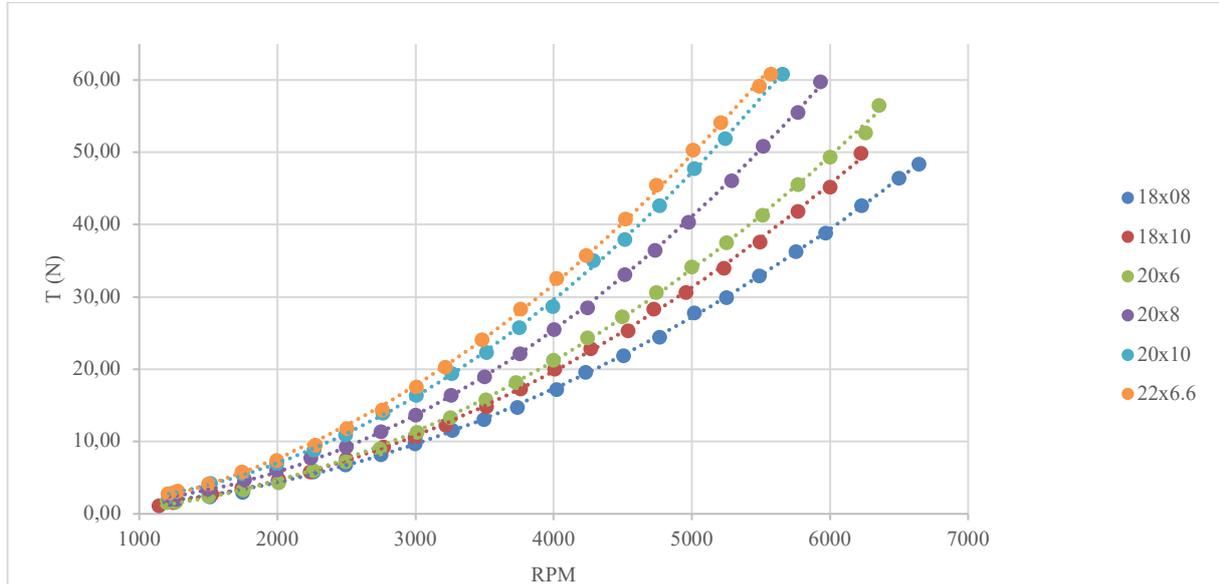
Figure 5 - T/Ω at $V = 0\ m/s$

Figure 6 compares the output thrust with the electrical power required. With the purpose of easing the distinction between values, a fifth-degree polynomial regression is added to the values of each propeller (dashed lines). The thrust output vs electrical power input is ordered (from highest to lowest): 22x6.6, 20x6, 20x8, 20x10, 18x8, 18x10. Therefore, the propeller selected for vertical flight is 22x6.6. Taking into consideration the wind tunnel test data for horizontal flight, the propeller selected for the tilt rotors is 20x10, because it has the best performance at horizontal flight, and from the sample of propellers suitable for horizontal

Pedro Mendes, Luís Félix, Tiago Oliveira, and Vasco Franco

flight is also the one the presents best performance at vertical flight.
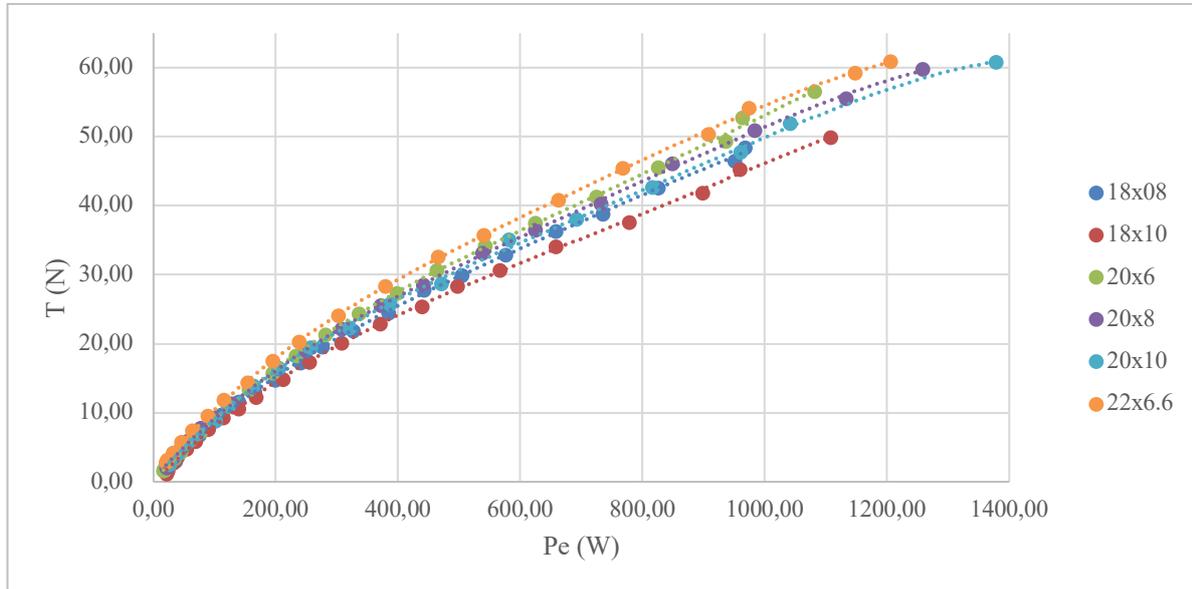
Figure 6 - T/P_e at $V = 0\ m/s$

Since the chosen HP is subject to operating in both lower and higher than cruise velocities, wind tunnel data is also obtained for $V = 15\ m\ s^{-1}$ and $V = 24\ m\ s^{-1}$. A comparison is made in Figure 7. For each rotational velocity, the available thrust decreases with an increase in flow velocity.
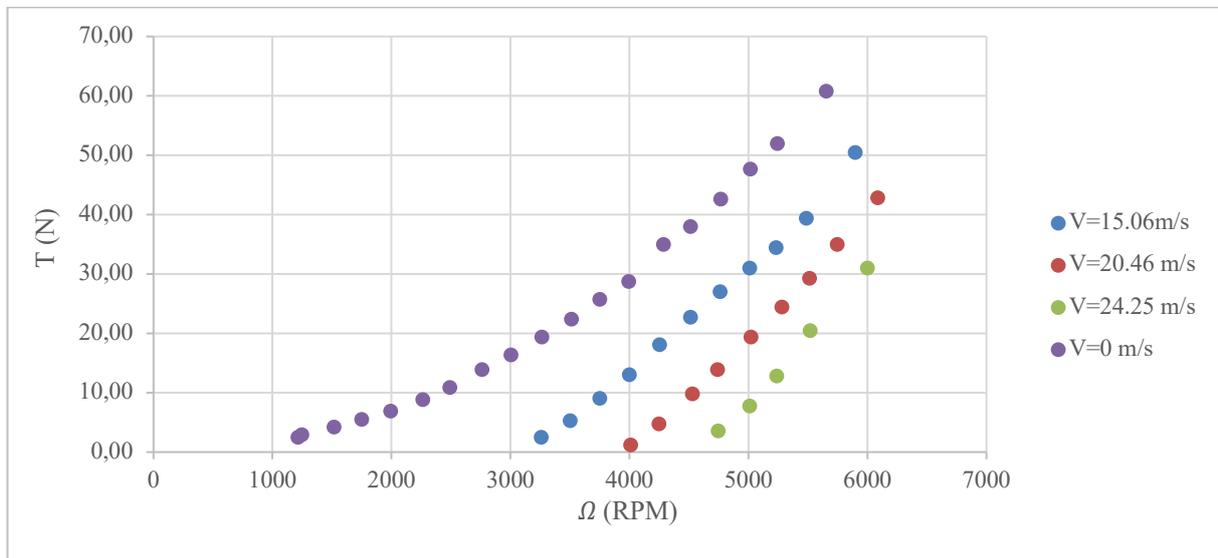

Figure 7 - Propeller 20x10 thrust output under various flow velocities

The propellers used in the aircraft result from comparing the arrangements, each with a different combination of VP and HP. The subsequent step is to combine the performance data from the selected propellers in order to compare the different arrangements.

4.4. Automated BET method

One of the greatest setbacks of using the BET through spreadsheets is the highly repetitive and exhaustive workload (the need to manually obtain C_L and C_D values for each element using a computational tool such as *XFLR5*). Another main constraint is the requirement of firstly selecting the rotational velocity of each propeller before performing the actual analysis. This can either be achieved by an exhaustive iterative process (picking alternating higher and lower rotational velocities and performing their respective analysis until the required thrust value is achieved), or a less exhaustive process, if a calculator such as *eCalc* is used (which immediately outputs an approximated value for the required rotational velocity).

In an endeavor to suppress these setbacks, Fernandes [12], as part of his *TUDelft*'s MSc Aerospace Engineering internship at the PAF, developed an automated application of the BET implementation method using *ParaPy*.

Firstly, Fernandes [12] modeled the 20x6 propeller with CAD, which then he used to obtain the geometries of the blade element airfoils. Then, implemented in *Python* an algorithm similar to the one used in the BET spreadsheet, which directly imported C_L and C_D values of each element from XFoil and output the totals for thrust, torque and power of the propeller.

Fernandes [12] concluded, based mainly on inconsistent results caused by limitations in the *X-Foil* panel code, that the BET *ParaPy* application should only be used to get rough estimates of the thrust generated by a propeller and should not be preferred to CFD simulations or wind tunnel tests.

4.5. BET as a method for propeller selection

Comparing the results from the BET analyses and the wind tunnel tests at $V = 20 \; m \; s^{-1}$ and $\Omega = 6700 \; RPM$ reveals that most propellers do not reach such rotational velocities with the selected motor. As shown in Table 7, the values obtained in wind tunnel tests for the propellers which reach this Ω are similar in terms of thrust, but torque values are at least 25.3% higher than BET estimates. However, due to lack of test data it is not possible to confirm this trend.

Table 7 - Comparison between BET and wind tunnel values at $V = 20 \; m/s$ and $\Omega = 6700 \; RPM$

Propeller	BET		Tunnel		Discrepancy (Tun-BET)/BET	
	$T(N)$	$Q(N \cdot m)$	$T(N)$	$Q(N \cdot m)$	T	Q
18x8	22.24	0.78	21.61	1.05	-2.91 %	25.7 %
18x10	35.53	1.12	n/a	n/a		
20x6	10.40	0.72	10.06	1.12	-3.37 %	35.7 %
20x8	30.95	1.11	n/a	n/a		
20x10	54.91	1.72	n/a	n/a		
22x6.6	26.59	1.32	n/a	n/a		

Comparing the BET results with the wind tunnel values at low flow velocities shows that the BET results are not precise. Table 8 compares the BET predicted values from Table 3 and Table 4 with the values from the wind tunnel tests for the corresponding T. Since the velocities are different, it is expected that there is a discrepancy (which should follow a

Pedro Mendes, Luís Félix, Tiago Oliveira, and Vasco Franco

similar tendency line). However, the discrepancy of the obtained values is somewhat random, which suggests that there are significant errors on the estimates.

Table 8 - Discrepancy between BET and wind tunnel values at low flow velocities

Propeller	T	BET ($V = 5\ m/s$)		Tunnel ($V = 0\ m/s$)		Discrepancy (Tun-BET)/BET	
		$rads^{-1}$	$Q(N \cdot m)$	$rads^{-1}$	$Q(N \cdot m)$	$rads^{-1}$ (%)	Q (%)
18x8	6.168	269.2	0.143	247.6	0.167	-9%	14%
18x10	2.262	189.1	0.079	149.2	0.0765	-27%	-3%
	36.281	519.7	0.459	524.9	1.05	1%	56%
20x6	57.143	545.3	0.649	615.7	1.46	11%	55%
20x8	11.159	292.1	0.236	284.0	0.316	-3%	25%
20x10	4.639	199.9	0.143	167.0	0.120	-20%	-20%
	36.799	435.9	0.528	476.4	1.13	8%	53%
22x6.6	69.62	495.6	0.863	445.7	1.01	-11%	14%

Although the resulting selected propellers being equal in both methods, it is shown that BET estimated values are not precise enough when compared with wind tunnel testing. This means that the BET method can be used to compare and select from a given propeller sample but is not able to preview a given propeller performance accurately.

In sum, if a wind tunnel is available, it is preferable to perform testing to the propeller sample through it. If not, it is recommended to use a tool such as *eCalc* to compare the propellers and determine the estimated efficiencies through it, albeit not being as precise as having the wind tunnel test results.

5. SELECTING THE PROPELLER ARRANGEMENT

Having selected both the HP and VP, an analytical comparison between the proposed motor-propeller arrangements mentioned in Table 9 follows. Firstly, an infinite energy comparison is made, which does not consider the weight of each device. This comparison allows to know effectively which configuration is the most efficient. Then, a limited energy comparison is made, which estimates the maximum weight of propulsion and energy system for which configuration B2 allows higher endurance than configuration C.

The following assumptions are made:
-   Propellers in vertical flight have the same behavior as when at $0\ m\ s^{-1}$;
-   Propellers in cruise flight have the same behavior as when at $20\ m\ s^{-1}$;
-   The wind tunnel test atmospheric conditions are valid for these comparisons.

5.1. Proposed arrangements

The TRUA with four equal propellers is from now on mentioned as "Arrangement A". The TRUA with two sets of different propellers, either equally distanced longitudinally from the CG or asymmetrically distanced (in order to compensate for different propulsive forces and efficiencies) is from now on mentioned as "Arrangement B".

For comparison purposes, an "Arrangement C", (Quad+1) is also considered. The different sets of each arrangement are explained in the table below.

Table 9 – Proposed arrangements

Arrangement	Propellers		Equal (F/R) distance from the CG	Front Tilt	Fifth propeller
	Front	Rear			
A1	HP	HP	Yes	Yes	-
A2	VP	VP	Yes	Yes	-
B1	HP	VP	Yes	Yes	-
B2	HP	VP	No	Yes	-
C	VP	VP	Yes	No	HP

Having established the possible combinations of propeller sets, the selection of the propulsion system arrangement is dependent on the payload requirements, available energy and the actual performance of the motor-propeller pairs.

5.2. Efficiency comparison for a typical flight plan

Efficiency energy comparison assumes a typical flight plan with the following characteristics:

- Climbing to cruise altitude takes 60 seconds and is made with constant $T_{R_{z\,climb}} = 172.72\ N$;
- Cruise flight time is 1200 seconds (20 minutes), with constant $T_{R_{xab}} = 12.04\ N$ or $T_{R_{xc}} = 14.08\ N$, for arrangements A/B and C respectively;
- Descending to land from cruise altitude takes 90 seconds with constant $T_{R_{z\,descend}} = W = 147.15\ N$.

For each flight stage, the required electrical power is obtained by quadratic polynomial regressions of the values obtained experimentally. The lowest R^2 resulted from the regression of the electrical power values in order to the thrust produced by the 20x10 propeller and is equal to $R^2 = 0.9970$. The regressions are therefore considered valid for the approximations made below.

The load asymmetry which leads to minimal electrical power required during climb (with the above-mentioned assumptions) is 45% of the thrust on the front motors and 55% on the rear motors. As can be seen in Table 10, for the total required thrust, $T_{r_{z\,climb}} = 172.72\ N$, the total electrical power required is lower with asymmetric load (3027.73 W) when compared to an even load distribution among the motors (3042.56 W).

Table 10 - Load distribution optimization

	B1(50/50)		B2 (45/55)	
	Thrust (N)	Power (W)	Thrust (N)	Power (W)
Forward (each motor)	43.18	813.56	38.86	696.52
Rearward (each motor)	43.18	707.72	47.50	817.35
Total (all four motors)	172.72	**3042.56**	172.72	**3027.73**

As shown in Table 11, the most efficient TRUA configuration is B2 – different propellers and differential load distribution (20x10 at the front, carrying 45% of the load during vertical flight, and 22x6.6 at the rear, carrying 55% of the load). It is also noticed that arrangement C is the overall most efficient. It uses the most efficient configuration for vertical flight stages and, although the single propeller produces more thrust for forward

Pedro Mendes, Luís Félix, Tiago Oliveira, and Vasco Franco

flight, since the motor-propeller efficiency is higher for higher loads (see figures 3 and 4), the overall electric power required for this flight stage is lower.

Table 11 - Infinite energy comparison

		Flight stage					Total Energy
		Climb (60 s)		Cruise (1200 s)	Descent (90 s)		
		Forward motor (ea.)	Rear motor (ea.)	Horizontal flight motors (total)	Forward motor (ea.)	Rear motor (ea.)	(Wh)
A1	T (N)	43.18	43.18	12.04	36.79	36.79	355.64
	P (W)	813.56	813.56	691.96	643.04	643.04	
A2	T (N)	43.18	43.18	12.04	36.79	36.79	678.31
	P (W)	707.72	707.72	1703.82	558.08	558.08	
B1	T (N)	43.18	43.18	12.04	36.79	36.79	347.86
	P (W)	813.56	707.72	691.96	643.04	558.08	
B2	T (N)	38.86	47.50	12.04	29.43	44.15	347.53
	P (W)	696.52	817.35	691.96	467.82	731.62	
C	T (N)	43.18	43.18	14.08	36.79	36.79	295.39
	P (W)	707.72	707.72	541.18	558.08	558.08	

5.3. Limited energy comparison

Similarly to the infinite energy comparison, a limited energy comparison is made. This study considers the available mass, limited by the initially stated MTOW. The goal is to find the minimum power and energy supply system (propulsion system and batteries) weight so configuration C outperforms configuration B2 in terms of endurance. The powerplant weight is considered fixed for each configuration.

The estimated weight of the structural and propulsion components is shown in Table 12 and Table 13. This estimative is made based on values displayed below. The mass of the propulsion system of configuration C is higher by $0.5955\,kg$, since it considers an additional motor.

Table 12 - Weight of each motor assembly (estimate)

Propulsion	Mass (kg)	Weight (N)
Motor	0.3750	3.679
ESC	0.0735	0.721
Propeller	0.0470	0.461
Cabling	0.1000	0.981
TOTAL	0.5955	5.842

Pedro Mendes, Luís Félix, Tiago Oliveira, and Vasco Franco

Table 13 - Structural weight (estimate)

Structural	Mass (kg)	Weight (N)
Fuselage	1.9880	19.502
Wing	1.8250	17.903
Tail	0.4500	4.415
Electronics	0.4000	3.924
TOTAL	4.6630	45.744

Instead of defining a whole typical flight plan, the cruise flight time is left variable and is used to compare the different configurations. A reference battery energy density of $200\,Wh/kg$ is used and the available energy is obtained by multiplying the battery mass with this energy density (see Table 14). The objective is to find the minimum weight of the power plant from which configuration C offers higher endurance than configuration B2. It is concluded that if the power and energy supply system weights less than 8.93 kg, configuration B2 offers higher endurance than configuration C. Table 15 reflects the estimated endurance for each configuration at the turnaround point.

Table 14 - Available energy (estimate)

		A and B	C	
MASS	MTOW	15	15	kg
	STRUCTURAL +PAYLOAD	6.08	6.08	
	PROPULSION	2.38	2.98	
AVAILABLE MASS FOR BATTERIES		6.54	5.95	
ENERGY	SPECIFIC	200	200	Wh/kg
	AVAILABLE	1308.23	1189.13	Wh

Table 15 - Endurance estimate with 8.93 kg power and energy supply system

Configuration	Endurance (s)
A1	6021.24
A2	2513.89
B1	6060.59
B2	6063.40
C	6063.40

6. TILTING SYSTEM

In order to verify the energy consumption and the tilting concept, a prototype of the aircraft was manufactured (Figure 8). A tilting system was designed (Figure 9) and manufactured with addictive manufacturing in PLA. The mechanical actuation of this system is made with a servomotor.

Testing the tilting system in a flight test (Figure 10) revealed an intense resonance effect at a certain RPM regime which resulted in damage to the tilting system. Another two different tilting system versions were designed and manufactured. However, not even using a heavier solution – a linear bearing which removed all gaps (except in the tilting direction) – prevented such phenomenon to occur. Eventually, adding two functional tilting systems to the aircraft would result in adding more weight than if Quad+1 configuration was selected.

A detailed description of the methods used to manufacture the prototype, the tilting systems and the tests that were made is available in [5].

Figure 8 - Assembled prototype
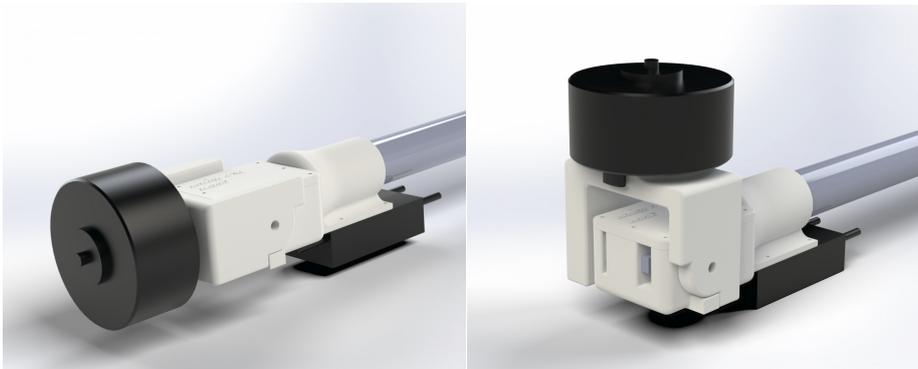
Figure 9 -Tilting system v.1 (CAD) - Horizontal (left) and vertical (right) positions

Figure 10 - Testing the prototype in flight

Pedro Mendes, Luís Félix, Tiago Oliveira, and Vasco Franco

If a TRUA solution is to be applied, one must keep in mind that the tilting system should be robust yet light enough, so that its weight does not surpass the weight of an additional motor for forward flight.

7. CONCLUSIONS

It was the focus of the present work to perform the preliminary design of the propulsion system of a TRUA, which conceptual design was previously carried out at the CIAFA. This involved the selection of the components which constitute it and to assess the most efficient arrangement of the motor-propeller pairs. It was also a goal to determine if the TRUA configuration is more efficient than using a fixed-wing quadcopter with an extra motor for forward flight (Quad+1). It was also proposed a methodology which allows, during the preliminary design of a new aircraft, to select the most adequate propulsive system configuration according to the shown flight profile. This methodology was applied to an aircraft built at CIAFA. The results obtained in each phase of the proposed methodology were presented in detail.

Based on drag estimations made previously, the required thrust values for the various flight stages were obtained, which allowed to compare a set of propellers for vertical and horizontal flight, using two comparison methods were: one theoretical (BET) and another experimental (wind tunnel). From these, the HP (propellers with best performance in forward flight which can deliver the required thrust in vertical flight) and VP (propellers with best performance in vertical flight) were selected: 20x10 and 22x6.6, respectively. Although resulting in the same VP and HP propellers, the performance values from the BET method do not converge with the wind tunnel performance data.

The data gathered in wind tunnel tests allowed to perform two comparative studies for five different arrangements – the first based in the efficiency of the arrangements and the second based in the endurance of the aircraft with different arrangements considering weight limitations.

It is shown that if the TRUA solution is to be used, the most efficient arrangement is B2 – different front and rear propellers asymmetrically distanced longitudinally from the CG.

On the one hand, it can be concluded that the Quad+1 solution is more efficient and simpler to integrate and control than the TRUA solution. On the other hand, if the weight available for the power and energy supply system is less than 8.93 kg, the endurance may be higher with the TRUA solution, if a light and robust tilting system is attained. Therefore, the main conclusion is that a TRUA configuration is only beneficial for low autonomy UA and if there are weight restrictions for the propulsive and power system.

It is concluded that the BET methodology, although being appropriate to compare the overall performance of propellers from a sample, is not sufficiently precise to infer their actual performance and energy consumption values. Therefore, resources such as *eCalc* or wind tunnel tests should be used instead, if available.

REFERENCES

[1] R. Austin, Unmanned Aircraft Systems –UAVS Design, Development and Deployment, New Jersey: John Wiley & Sons, Ltd, 2010.

[2] F. Ferreira, "Projeto Conceptual de uma Aeronave de Asa Fixa com Descolagem Vertical (Dissertação para obtenção do Grau de Mestre em Aeronáutica Militar, Especialidade Piloto Aviador)," Academia da Força Aérea, Sintra, 2019.

Pedro Mendes, Luís Félix, Tiago Oliveira, and Vasco Franco

[3]   S. Gudmundsson, "The Anatomy of the Propeller," in *General Aviation Aircraft Design*, S. Gudmundsson, Ed., Butterworth-Heinemann, 2014, pp. 581-659.

[4]   T. Corke, Design of Aircraft, New Jersey: Pearson Education, Inc., 2003.

[5]   P. Mendes, *Design of a Fixed-Wing Tilt-Rotor Quadcopter Class I Mini Unmanned Aircraft: Propulsion System Design and Prototype Manufacturing,* Sintra: Academia da Força Aérea, 2021.

[6]   A. J. Keane, A. Sobester and J. P. Scanlan, Small Unmanned Fixed-Wing Aircraft Design. A Practical Approach, New Jersey: John Wiley & Sons, Inc., 2017.

[7]   T-Motor, "P60 Without Pin KV170," [Online]. Available: https://store-en.tmotor.com/goods.php?id=931. [Accessed 10 Oct 2020].

[8]   T-Motor, "FLAME 60A HV," [Online]. Available: https://store-en.tmotor.com/goods.php?id=370. [Accessed 10 Oct 2020].

[9]   eCalc, "xcopterCalc - Multicopter Calculator," [Online]. Available: https://www.ecalc.ch/xcoptercalc.php?lang=en. [Accessed 15 Oct 2020].

[10] eCalc, "propCalc - Propeller Calculator," [Online]. Available: https://www.ecalc.ch/. [Accessed 15 Oct 2020].

[11] APC Propellers, "Engineering Design Process Used to Develop APC Propellers," [Online]. Available: https://www.apcprop.com/technical-information/engineering/#airfoil. [Accessed 10 Dec 2020].

[12] F. M. Fernandes, *Internship Report - MSc Aerospace Engineering - Flight Performance and Propulsion,* Delft: TUDelft, 2021.

[13] EERE Publication and Product Library, *Determining Electric Motor Load and Efficiency,* USDOE Office of Energy Efficiency and Renewable Energy (EERE), 1997.

[14] A. Harrington and C. Kroninger, *Characterization of Small DC Brushed and Brushless Motors,* Aberdeen: Army Research Laboratory, 2013.

[15] "T-Motor," [Online]. Available: store-en.tmotor.com. [Accessed 10 Oct 2020].

DESIGN OF A HYDROGEN POWERED SMALL ELECTRIC FIXED-WING UAV WITH VTOL CAPABILITY

Bernardo M. Alves[1*], Vasco L. Coelho[1], Pedro A. Silva[1], André C. Marta[2], Frederico J. Afonso[2], Paulo J. Sá[1], Luís F. Félix[1] and João V. Caetano[1]

1: Centro de Investigação da Academia da Força Aérea
Academia da Força Aérea
Instituto Universitário Militar
Granja do Marquês, 2715-021 Pêro Pinheiro, Portugal
{bmalves, vlcoelho, paasiva, pjsa, lffelix, jvcaetano}@academiafa.edu.pt,
http://www.academiafa.edu.pt

2: IDMEC
Instituto Superior Técnico
Universidade de Lisboa
Av. Rovisco Pais 1, 1049-001 Lisboa, Portugal
{andre.marta, frederico.afonso}@tecnico.ulisboa.pt, http://www.tecnico.ulisboa.pt

Abstract. *Most electric small UAVs require large batteries, which lead to increased weight and low endurance. With the current development of new energy sources and emerging technologies, the present work aims to design a fixed-wing UAV with vertical take-off and landing (VTOL) capability using a fuel cell-based propulsion system. The design requirements made by the Portuguese Air Force include a maximum take-off mass of 25 kg and a minimum flight time of two hours. To accomplish these, a conceptual design framework was developed, supported by fast estimates for the disciplines of aerodynamics, structures, propulsion and controls, and a multi-objective optimisation approach led to the initial UAV configuration and sizing. The different discipline models were coupled and multidisciplinary optimisation was conducted to find the UAV optimal design. This process led to a 22 kg aircraft, having a maximum endurance over 3 hours with a 7.2L hydrogen tank, assisted with batteries for VTOL and climb. The results obtained suggest that the application of the hydrogen-powered fuel cell system meets the requirements set, while also proving to be a feasible alternative to conventional solutions.*

Keywords: Fuel cell, Green aircraft, MDO, Multi-objective optimisation, Multi-rotor, Pusher configuration

B. M. Alves, V. L. Coelho, P. A. Silva, A. C. Marta, F. J. Afonso, P. J. Sá, L. F. Félix and J. V. Caetano

1 INTRODUCTION

Aircraft design is a branch of aerospace engineering which takes a set of mission requirements and develops a viable solution that bests satisfies them. To do so, it must incorporate knowledge from the different disciplines, namely, aerodynamics, structures, propulsion and control [1].

Despite being an iterative process, the design can be divided into three primary stages: conceptual, preliminary and detailed. It starts with a market study, the analysis of different configurations and trade-off studies between design and requirements are taken into account in the conceptual stage. Then, the configuration selected is fixed and the in-depth design and disciplinary studies of the major components, mostly resorting to computational simulations, take place in the preliminary stage. Finally, in the detailed stage, the structure is fully defined and a prototype is built, where the tooling and construction methods are defined alongside tests of major structural components, ending on a full-scale model to perform flight tests and validate the results [2].

Many energy sources have been tried in aircraft design, being hydrogen a topic of recent research and development progress, despite having already been exhaustively studied as an alternative energy source to fossil fuels for several decades [3].

In the context of seeking innovation in the aeronautical sector, the Air Force Academy Research Centre (CIAFA) started a project to design a class-I fixed-wing small Unmanned Aerial Vehicle (UAV) capable of performing Vertical Take-off and Landing (VTOL) and having a fuel cell as the primary source of energy. The proposed major performance and operational requirements are presented in Tab.1.

Table 1: Performance and operational requirements.

Payload	MTOW	Endurance	Cruise speed	Stall speed	Max TO altitude	Ceiling
2 kg	≤ 25 kg	≥ 2 h	35-45 kts	≤ 25 kts	3000 m	4500 m

This work focuses on the initial steps of the design process, where the goal is to search for a feasible solution and assess its performance. To that end, different possible configurations were studied and the most adequate selected, followed by a market research on similar UAV and adequate propulsion system components (Sec.2), to estimate some of the design parameters. The UAV main mission profile is presented (Sec.3) before the conceptual design methodology is laid down (Sec.4). Then, the initial design point is discussed (Sec.5), followed by optimal trade-off studies (Sec.6). The resulting conceptual design is described (Sec.7), culminating in the current preliminary design progress (Sec.8).

2 CONCEPT GENERATION

2.1 Configuration Selection

A market study was conducted on configurations and methodologies currently used to produce an UAV capable of performing endurance-focused missions, whilst being capable of VTOL, for the expected MTOW category. The main focus was to investigate the advantages and disadvantages of the various configurations available for fixed wing configuration: a) Tail sitter [4] is a simple design, light, less prone to mechanical failures and easy to transport. However, it has low tolerance to lateral wind in VTOL mode and can be difficult to control during landing (Fig.1a); b) Lift+cruise [5] is the most common

B. M. Alves, V. L. Coelho, P. A. Silva, A. C. Marta, F. J. Afonso, P. J. Sá, L. F. Félix and J. V. Caetano

configuration. The fact that the propulsion system is divided in forward and vertical modes offers greater efficiency for each mode. The downside is the increase in parasite drag and a higher overall dead weight (Fig.1b); c) Tilt rotor [5, 6] has rotors that tilt for vertical or horizontal propulsion. It exhibits good control and stability but has higher structural complexity and reduced propeller efficiency since they are designed to perform both VTOL and horizontal flight (Fig.1c); d) Transwing [7] offers great control and response during VTOL mode and, since the fuselage stays parallel to the ground, the image gathering devices can be always operational. The disadvantages are related with the high complexity of the design: shortage of time and little information regarding the wing root joint mechanism are the main ones (Fig.1d).

| (a) Tail sitter [4] | (b) Lift + cruise [5] | (c) Tilt rotor [6] | (d) Transwing [7] |
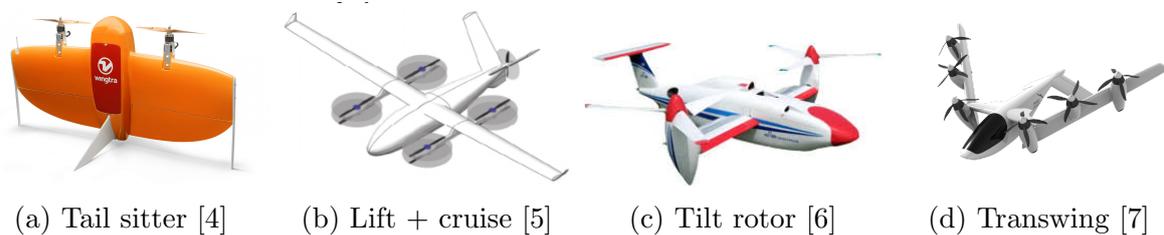
Figure 1: Possible UAV configurations.

To select the appropriate aircraft configuration for the project needs, an Analytic Hierarchy Process (AHP) was carried out [8]. This process stipulates a set of criteria which are compared among themselves. In this work, the design team defined four main groups: operation, manufacturing, maintenance and innovation. In the operation criterion, the parameters taken into account were aerodynamics, stability and control, endurance, propulsion efficiency, flexibility and redundancy. Regarding the construction criterion, the parameters cost and feasibility were considered. In the maintenance criterion, the parameters were cost, interior access, reliability and transport. Finally, in the innovation criterion, the importance of using new technologies in the design was evaluated, when compared to the requirements and the knowledge available at CIAFA.

A numerical scale ranging from 1 (same importance) to 9 (extremely important) was used to quantitatively compare the different criteria among the different configurations, resulting into matrix arrangements. Firstly applied to the four main categories, secondly, to the several parameters within each main category and finally to the four design concepts to each sub-category. Figure 2 represents, in a multi-level pie chart, the process done with each component weight compared to the others. The inner layer has the four main categories, the middle layer has the subcategories with the color pattern of the corresponding main category, and the external layer represents each configuration classification. The final results are presented on the right, with the lift+cruise configuration proving to be the most suitable for the project requirements.

2.2 Configuration Refinement

Following the choice of a lift+cruise configuration, the tail type as well as the placement of the VTOL and forward mode propulsive systems were defined.

With regard to the placement of the VTOL propulsive system, there were two main solutions identified during the market study: either a design based on a single fuselage with added booms to support the VTOL system, or a design that uses a twin boom

B. M. Alves, V. L. Coelho, P. A. Silva, A. C. Marta, F. J. Afonso, P. J. Sá, L. F. Félix and J. V. Caetano
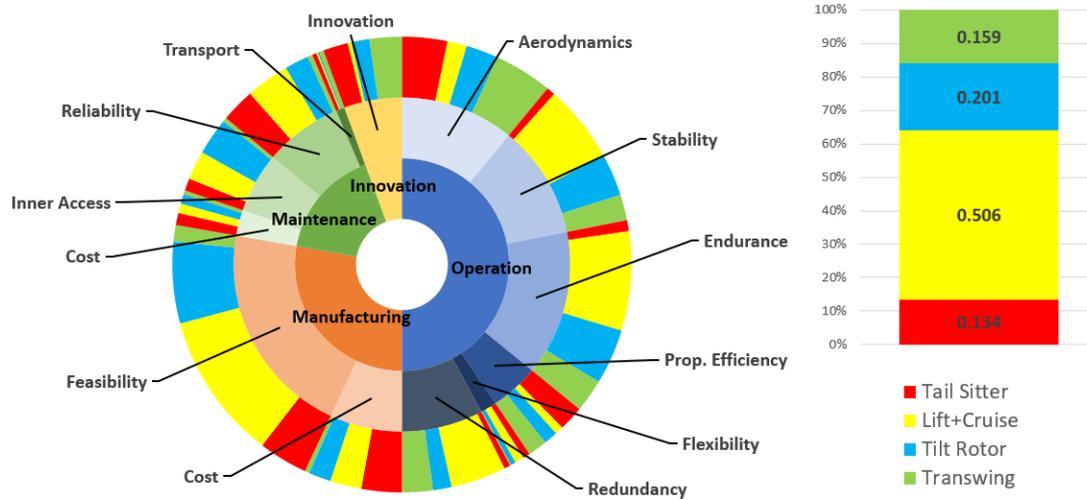
Figure 2: Representation of the Analytic Hierarchy Process for the configuration selection.

configuration where the tail and the propulsive system are both applied [9]. The design team opted for the double boom configuration to reduce the overall weight, since there is no need to create additional structures for VTOL system, and to provide additional structural rigidity [10]. A double boom also gives more freedom for the placement of the forward mode propulsive system, making possible either tractor or pusher configurations.

In terms of tail type, among the various double boom arrangements analyzed, the design team decided that the inverted V-tail had the best characteristics for the project, namely: it is free from the influence of the propeller and wing wakes; it has less surface area, making the least parasite drag possible and becoming less heavy; and it provides good stability in the presence of cross-wind. It is also the most common configuration in UAVs, being the UAV Factory Penguin B or the Ogassa OGS 42 some examples found during the market study (Tab.2). The main drawback of an inverted V-tail is the coupling between longitudinal and lateral modes, making the aircraft control more complex.

Regarding the propulsion for forward flight, there are two configurations possible, tractor or pusher, as illustrated in Fig.3. Since the twin-boom configuration was already

(a) Tractor

(b) Pusher

Figure 3: Forward propulsion system configurations [11].

adopted, the pusher configuration was selected, which is also the most common for this type of UAVs. The pusher configuration provides beneficial payload integration options [9] and better visibility for the gimbal module [11]. In addition, since the propeller wake will not interact with the fuselage, wing or tail, it reduces the overall friction coefficient and, consequently, the UAV total drag [2]. This configuration has two major drawbacks: worse propeller efficiency and displacement of the centre of gravity towards the rear, which in turn implies a longer tail in order to maintain stability and control [2].

B. M. Alves, V. L. Coelho, P. A. Silva, A. C. Marta, F. J. Afonso, P. J. Sá, L. F. Félix and J. V. Caetano

2.3 Market Research

With the lift+cruise configuration chosen, a market research of UAVs with similar configuration was done, including UAVs with VTOL capability and UAVs with fuel cell as primary energy source, as summarised in Tab.2.

Table 2: Market study of similar UAVs.

VTOL UAV	MTOW	Propulsion sys.	Structural weight	Empty weight
Ogassa OGS42V	36 kg	hybrid	-	22.0 kg
MMC Griflion M8	12 kg	electric	5.5 kg	-
Alti Transition	18 kg	hybrid	5.8 kg	11.8 kg
UAV fuel cell powered	MTOW	Fuel type	Structural weight	Endurance
Sparkle Eagle Plus - VTOL	21 kg	hydrogen	12.5 kg	5 h
Top Engineering Falcon-V	18 kg	hydrogen	6.5 kg	3 h

Other studies were carried out to estimate initial parameters used during the conceptual phase. Regarding the VTOL motor, based on an MTOW of 25 kg, a configuration with 4 electric motors providing sufficient power at 80% of their maximum rating, the power-to-weight ratio was estimated based on components available at T-Motor manufacturer [12] as summarised in Tab.3. For the forward mode motor, another power-to-weight ratio value

Table 3: Market study of VTOL motors.

Motor	Power @80%	Weight	Power to weight ratio
P80IIIPin KV100	2335.0 W	0.649 kg	3.598 kW/kg
V605 KV210	1827.5 W	0.310 kg	5.895 kW/kg
V505 KV260	1451.2 W	0.215 kg	6.750 kW/kg
V602 KV180	1147.4 W	0.300 kg	3.825 kW/kg

was assumed and based on MTOW, cruise speed, required thrust and on the reference [13], motors capable of producing around 1500 W of continuous power were analysed. The market research includes motors from T-motor [12] and Hacker [14] manufacturers, as presented in Tab.4. These studies allowed for the estimation of the power-to-weight ratio,

Table 4: Market study of motors for forward flight mode.

Motor	Rated Power	Weight	Power-to-weight ratio
Hacker A60-5S V4	1591 W	0.595 kg	2.674 kW/kg
Hacker A60-5XS V4	1870 W	0.480 kg	3.896 kW/kg
T-Motor AT4125 long shaft	1554 W	0.355 kg	4.378 kW/kg

for both VTOL and forward motors, that will be used further as initial data estimates during the conceptual design Tab.6.

2.4 Fuel Cell System

The main focus of the project is the design of a small fixed-wing UAV with a fuel cell as a primary source of energy. A fuel cell is an electrochemical equipment that directly converts chemical energy from a supplied fuel into electrical energy. Its primary parts consist of two layers, the anode and the cathode, where the oxidation and reduction

B. M. Alves, V. L. Coelho, P. A. Silva, A. C. Marta, F. J. Afonso, P. J. Sá, L. F. Félix and J. V. Caetano

occurs, respectively. Between the layers, there is an electrolyte material that works as a barrier, allowing ions to flow, while forcing the electrons to move out of the electrolyte, thus generating electricity [15].

There are different fuel cell types, depending on the the electrolyte material, being the Polymer Electrolyte Membrane Fuel Cell (PEMFC) the most common in UAVs [16]. This uses a polymer membrane as an electrolyte material and runs on hydrogen, as schematically shown in Fig.4.
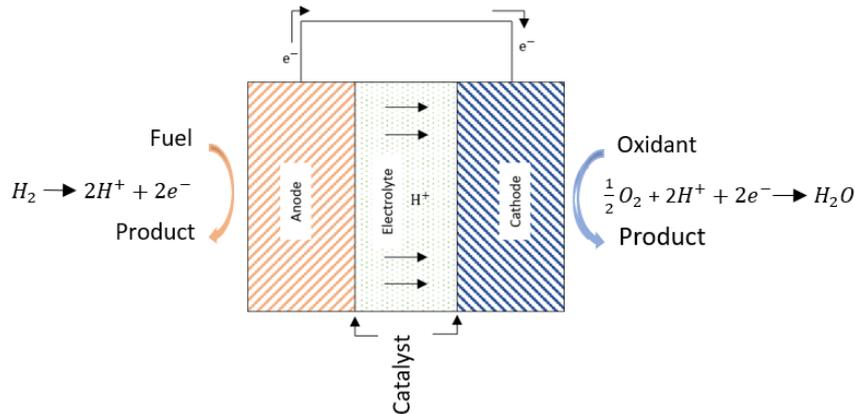
Figure 4: Schematic of $H_2 - O_2$ PEMFC (adapted from [17]).

A market research was done to evaluate the characteristics of different fuel cells to be used as a starting point in the conceptual design. This led to the identification of two models from Intelligent Energy [18] that meet the project requirements, as listed in Tab.5: a single IE-Soar™ 800W cell or two IE-Soar™ 650W cells mounted in parallel.

Table 5: Market research of fuel cells.

Fuel cell model	IE-Soar 800 W	IE-Soar 650 W (x2)
Rated Power [W]	800	1300
Mass [kg]	0.930	1.620
Power-to-weight ratio [W/Kg]	860.2	802.5

Hydrogen can be stored in different forms depending on the fuel cell operation - compressed gas, liquid, chemical or physical absorption [19]. Compressed hydrogen is the most common in UAVs applications, where it is kept at high pressure (35 to 70 MPa) on cylindrical fuel tanks made of composite materials [16]. The tanks present a considerable mass when compared to the quantity of hydrogen they store, as attested in Fig.5 that shows the hydrogen to tank mass ratio of different tank capacities from different suppliers.

3 MISSION PROFILE

The stated requirements and target performance criteria are based on typical mission scenarios. The main mission profile of the developed UAV, set by the design team, starts with a vertical take-off, followed by a vertical climb at 2 m/s (1-2). This phase is pursued by hover (2) coupled with an acceleration in forward mode (2-3), for a total of 45s, to transition from VTOL to forward fight. A climb phase succeeds, divided into two parts: first a high-gradient climb with 2.5 m/s vertical speed to overcome possible high altitude

B. M. Alves, V. L. Coelho, P. A. Silva, A. C. Marta, F. J. Afonso, P. J. Sá, L. F. Félix and J. V. Caetano
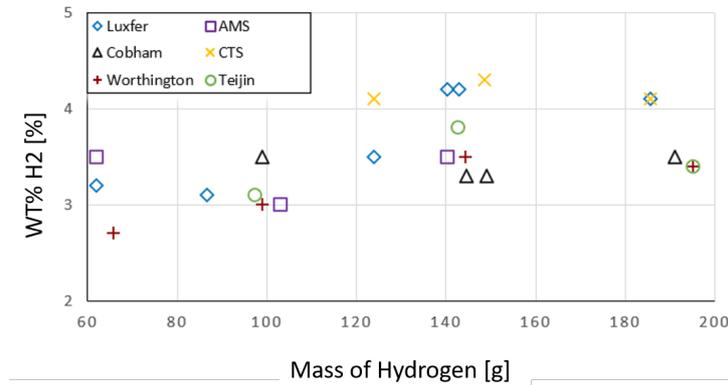
Figure 5: Hydrogen to tank mass ratio of different tank capacities (adapted from [20])

obstacles (3-4), then a low-gradient climb to allow a higher speed closer to cruise speed (4-5). Subsequently, two cruise phases occurs (5-6 and 7-8), encompassing the main mission - loiter - in between (6-7). These cruise segments will be set between 35 and 45 knots according to requirements. As cruise ends, the UAV initiates the descent (8-9), until it starts the landing circuit for 5 minutes (9-10). When ready to land, the UAV starts the hover phase to do the transition (10), followed by the vertical descent at 1 m/s (10-11). The described mission profile is sketched in Fig. 6.
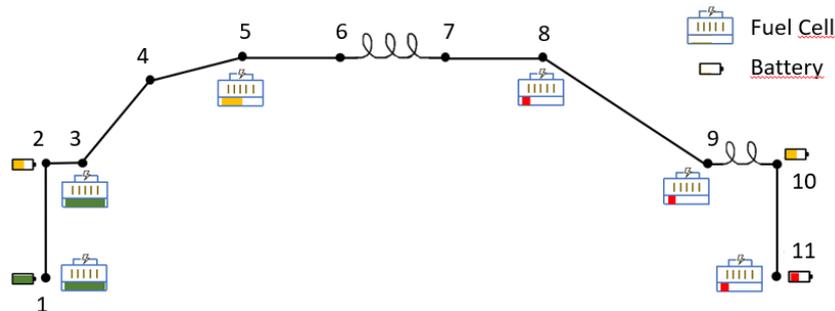
Figure 6: Main mission profile.

A strategy for operating each segment was sought: the fuel cell used in forward flight mode is sized to produce enough power during level flight; an additional battery is sized to be used in the vertical climb and vertical descent phases.

4   CONCEPTUAL DESIGN METHODOLOGY AND INITIAL DATA

The design methodology consisted of using a numerical tool developed by the authors together with a multi-objective optimisation algorithm to perform trade-off studies that assess the impact of some design decisions on the overall project.

A flowchart of the developed numerical tool developed is represented in Fig.7. The methodology and design process is based on Gundlach [9] with some additional considerations from other authors.

For the conceptual design, some initial parameters of the UAV must be set, encompassing different areas, based on available state-of-the-art data. The market studies conducted form the basis for some of the values considered regarding the airframe but also motors, propellers and fuel tanks. Avionics data is based on a similar CIAFA aircraft. Special care was taken when estimating C_{D_0} since the presence of the VTOL propulsion system

B. M. Alves, V. L. Coelho, P. A. Silva, A. C. Marta, F. J. Afonso, P. J. Sá, L. F. Félix and J. V. Caetano
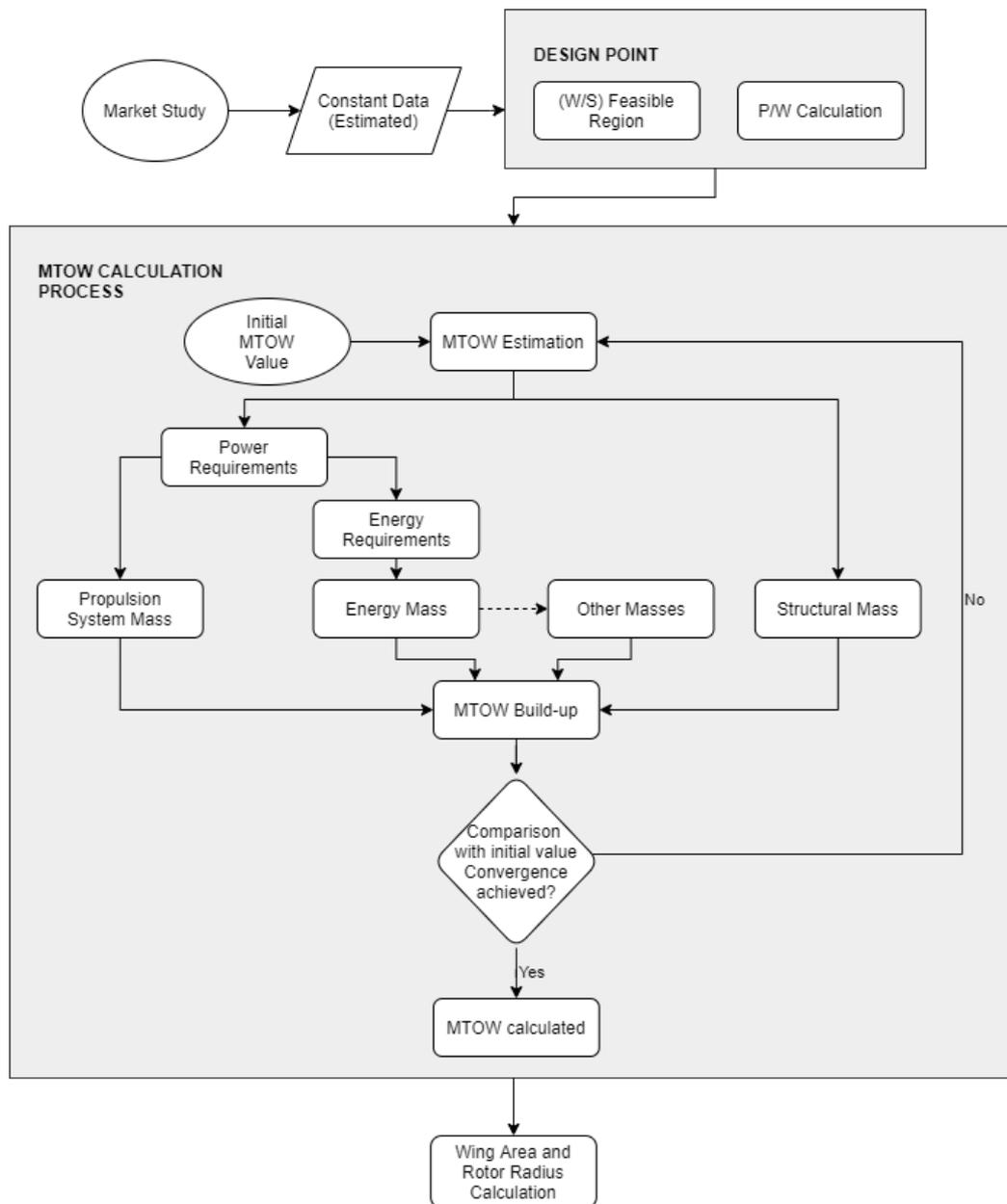
Figure 7: UAV conceptual design methodology.

increases drag at horizontal flight. Table 6 summarises all the UAV initial parameter values. Some of them will be used at the design point phase while others during the weight build-up (Sec.5)

5 DESIGN POINT AND WEIGHT BUILD-UP

With the initial data defined, the design point is found for forward flight (power loading as a function of wing loading) and for vertical flight (power loading vs disk loading).

The wing loading is subjected to a set of constrains imposed by design proposal, those being the stall condition and the maximum ceiling. The power loading for each forward flight segment of the mission profile is computed through a simple performance equation

B. M. Alves, V. L. Coelho, P. A. Silva, A. C. Marta, F. J. Afonso, P. J. Sá, L. F. Félix and J. V. Caetano

Table 6: UAV initial parameter values.

Parameter	Value	Parameter	Value
Airplane base drag coefficient - C_{D_0}	0.04	Forward motors power-to-mass ratio	3.5
Oswald efficiency factor - e	0.75	VTOL motors power-to-mass ratio	4.5
Maximum lift coefficient - $C_{L_{max}}$	1.3	Batteries safety factor	0.3
Structural factor	0.35	Batteries specific energy density	160 Wh/kg
Propeller efficiency - η_{pr}	0.65	Electric system efficiency	0.85
Induced power factor - k_i	1.2	Hydrogen-to-tank mass ratio	0.035
Rotor solidity - σ	0.10	Hydrogen low heating value	120 MJ/kg
Rotor profile drag coefficient - $C_{d_{0(rotor)}}$	0.012	Avionics power requirement	80 W
Fuel cell efficiency	0.4-0-5	Avionics and cabling mass	2.5 kg

considering the rate of climb (ROC) [2], applicable for climb and level flight,

$$\left(\frac{P}{W}\right)_{min} = \frac{1}{\eta_p}\left[ROC + \frac{\rho V^3 C_{D_0}}{2\left(\frac{W}{S}\right)} + \frac{2K\left(\frac{W}{S}\right)}{\rho V}\right] , \tag{1}$$

which considers the base drag coefficient and the induced power factor,

$$K = \frac{1}{\pi \, AR \, e} . \tag{2}$$

For the vertical flight stages, that include vertical climb, hover and vertical descent, a disk loading value is defined. Each flight condition has its own power loading equation [21], using the momentum theory for hover and vertical climb (V_y representing the vertical climb speed),

$$\left(\frac{P}{W}\right)_{hover} = k_i\sqrt{\frac{DL}{2\rho}} + \frac{\rho V_{tip}^3}{DL}\left(\frac{\sigma C_{d_{0_{rotor}}}}{8}\right) \text{ and} \tag{3}$$

$$\left(\frac{P}{W}\right)_{vertical\ climb} = V_y - \frac{k_i}{2}\left(V_y - \sqrt{V_y^2 + \frac{2DL}{\rho}}\right) + \frac{\rho V_{tip}^3}{DL}\left(\frac{\sigma C_{d_{0_{rotor}}}}{8}\right) , \tag{4}$$

and, due to the low descent velocity, experimental curve-fitting expression for the vertical descent segment, considering the descent speed lower than twice the induced velocity at the rotor plane,

$$\left(\frac{P}{W}\right)_{vertical\ descent} = V_y + v_{i,d}\ k_i + \frac{\rho V_{tip}^3}{DL}\left(\frac{\sigma C_{d_{0_{rotor}}}}{8}\right) , \tag{5}$$

with

$$v_{i,d} = v_h\left[k_i - 1.125\left(\frac{V_y}{v_h}\right) - 1.372\left(\frac{V_y}{v_h}\right)^2 - 1.718\left(\frac{V_y}{v_h}\right)^3 - 0.655\left(\frac{V_y}{v_h}\right)^4\right] . \tag{6}$$

The aircraft weight can be divided into four main contributions: structural (related to airframe), propulsion systems (accounts for the weight of the motors, ESCs and propellers/rotors), energy part (includes the batteries and hydrogen weight) and other weights (includes some fixed weight components such as avionics, cabling, servos, payload, fuel cell system, and a variable weight such as the hydrogen tank since its size depends on the

B. M. Alves, V. L. Coelho, P. A. Silva, A. C. Marta, F. J. Afonso, P. J. Sá, L. F. Félix and J. V. Caetano

hydrogen mass required). Referring to Fig.7, the MTOW calculation process required an initial estimate for each of these.

The structural weight is simply defined as as fraction of the MTOW because of the lack of information at the conceptual phase that does not allow an estimate of the airframe weight based on the aircraft dimensions.

The propulsion weight is obtained through a ratio between the power output of the electric motor and its weight. The motors are selected based on the required maximum output power, computed from the power loading equations at the design point multiplied by the initial MTOW estimate. The forward and VTOL motors have different properties, as such power-to-weight ratios and power requirements. A safety factor of 15 % is applied to the maximum power requirement (for both flight operation modes) to account for estimates inaccuracies and additional power requirement due to sudden events like wind gusts.

The energy weight calculations are based on the power requirements and duration of each flight phase, being the power consumption of the avionics also considered. As mentioned previously, vertical flight segments are purely powered by battery while horizontal flight has hydrogen as its energy source. Additionally, the fuel cell maximum output cannot provide enough power for certain segments (climb), so the additional battery is considered for those cases. With this in mind, some hydrogen is accounted to recharge that battery to account for additional peak power demand. Moreover, a safety margin is considered for the battery and additional hydrogen to serve as reserve. The battery and hydrogen mass is determined by applying the specific energy density of Li-Po batteries and the low heating value of hydrogen. The total hydrogen mass is then used to compute the mass of the tank needed to store it.

The total weight is then build up by summing the group estimates together, and compared with the previous estimate. A correction is applied based on the difference between the two and the process is repeated until a stopping criteria is met: either the absolute difference is less than one gram or the number of iterations exceeds 50.

Knowing the converged MTOW, the wing area and rotor area (and consequently rotor radius) are determined with the wing loading and disk loading, respectively.

6 OPTIMAL TRADE-OFF STUDIES

To assess the impact of some early design decisions on the overall UAV design, two main objectives were considered: MTOW and endurance. The multi-objective constrained optimisation problem was posed in the standard form

$$
\begin{aligned}
\text{minimise} \quad & f_m(\boldsymbol{x}), & m &= 1, 2 \\
\text{subject to} \quad & g_j(\boldsymbol{x}) \leq 0, & j &= 1, ..., J \\
& x_i^L \leq x_i \leq x_i^U, & i &= 1, ..., n \,,
\end{aligned}
\tag{7}
$$

where six design variables were considered, as listed in Tab.7.

The objective function can be written in vector form as

$$
\boldsymbol{f}(\boldsymbol{x}) = [MTOM(\boldsymbol{x}), -Endurance(\boldsymbol{x})]^T
\tag{8}
$$

and the inequality constraints as

B. M. Alves, V. L. Coelho, P. A. Silva, A. C. Marta, F. J. Afonso, P. J. Sá, L. F. Félix and J. V. Caetano

Table 7: Design variables for the multi-objective optimisation problem.

Design var.	Description	Lower bound	Upper bound	Units
x_1	Disk loading, W/A	100	350	N/m^2
x_2	Wing loading, W/S	100	250	N/m^2
x_3	Wing aspect ratio	5	12	-
x_4	Loiter time	2	∞	h
x_5	Stall speed	26	32	kts
x_6	Operational speed	30	45	kts

$$\boldsymbol{g}(\boldsymbol{x}) = \begin{Bmatrix} MTOM(\boldsymbol{x}) - 25 \\ -E(\boldsymbol{x}) + 2.5 \\ b(\boldsymbol{x}) - 4.0 \\ P_{\text{Con. Mode}} - P_{\text{nominal}} \\ m_{\text{fuel}} - m_{\text{Tank}} \\ V_{\text{stall}} - V_{\text{Op}} + 8 \end{Bmatrix} \begin{bmatrix} kg \\ h \\ m \\ W \\ g \\ kts \end{bmatrix} \leq 0 \,, \tag{9}$$

where $g_1(\boldsymbol{x})$ sets the maximum MTOW; $g_2(\boldsymbol{x})$ sets the minimum endurance; $g_3(\boldsymbol{x})$ constraints the maximum wingspan; $g_4(\boldsymbol{x})$ imposes that the required power at all times must be less than the fuel cell nominal power when flying in forward flight mode; $g_5(\boldsymbol{x})$ forces the total amount of hydrogen needed to be within the tank capacity; and $g_6(\boldsymbol{x})$ establishes that minimum operational speed should be at least 8 kts higher than the stall speed.

With the problem defined in Eq.(7), the *Pymoo* open-source optimisation framework was used [22]. The Non-Dominated Sorting Genetic Algorithm (NSGA-ii) was selected for its multi-objective handling, which sorts the individuals in the population by rank. The objective function vector is evaluated using the numerical tool developed by the authors (Fig.7). The stopping criteria is defined with design variable ($x_{tol} = 10^{-4}$), objective ($f_{tol} = 10^{-3}$) and constraint violation ($x_{cv} = 10^{-6}$) tolerances. In case the algorithm is not able to meet these, a maximum of 150 generations are run.

Several trade-off studies were performed running the *Pymoo* framework with the numerical analysis tool (Fig.7), using the parameters defined in Tab.6.

Considering the first four design variables in Tab.7, all constraints but $g_5(\boldsymbol{x})$, and a fuel cell with a nominal power of 800 W, the optimisation problem is solved and the Pareto-front (with rank 1 or non-dominated solutions) obtained is shown in Fig.8.

Three optimal solutions were selected for comparison purposes: one corresponding to the lightest UAV (MTOW=19.2 kg); an intermediate solution (MTOW=19.7 kg); and the heaviest solution (MTOW=20.4 kg). The mass of hydrogen varies between 120 and 130 g. The maximum required power to be supplied by the fuel cell corresponding to each solutions is represented in Fig.9, which shows that there is always an excess of power as imposed by the constraint g_4. Nevertheless, the power margin in each solution is small, being largest for the lightest solution.

Due to the uncertainty in estimating some key parameters needed to assess the power required, particularly the aircraft base drag coefficient C_{D_0}, solutions with larger power margins were searched. To do so, instead of using a ratio to estimate the fuel tank mass based on the fuel mass, two distinct tanks were chosen: a large tank with dry mass of 4.3 kg and a capacity for 185 g of H_2; and a small one of 3.3 kg with 148 g hydrogen capacity.

B. M. Alves, V. L. Coelho, P. A. Silva, A. C. Marta, F. J. Afonso, P. J. Sá, L. F. Félix and J. V. Caetano
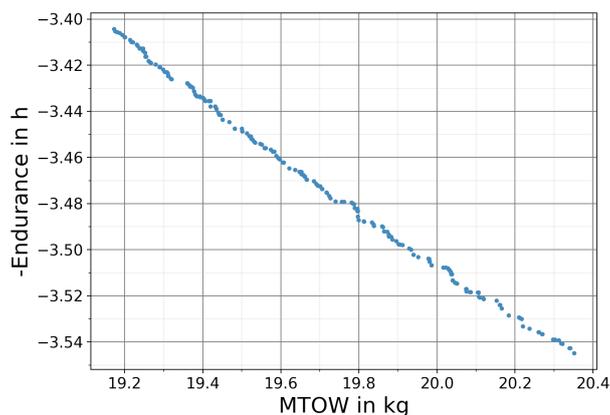
Figure 8: Optimal trade-off solutions
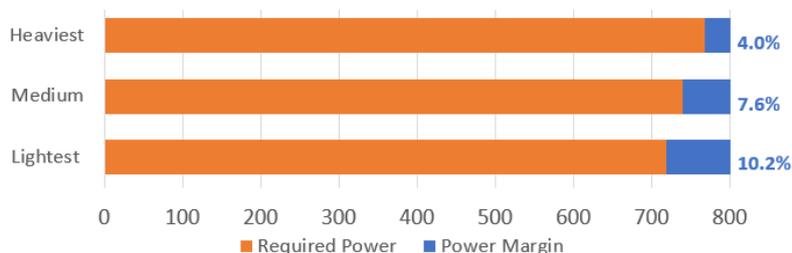
Figure 9: Maximum required power in level flight.

The small tank and the 800 W fuel cell are used in one problem formulation and the large tank with a 1300 W is used in another. For the lightest configuration, two additional design variables were added to the optimisation problem, stall speed and operational speed (x_5 and x_6 in Tab.7) and the constraint g_5 added to guarantee that the mass of hydrogen can be held in the tank, Eq.(9). For the heavier configuration, the constraint g_5 was added as well, with $m_{\text{tank}} = 175\,\text{g}$, Eq.(9) but no additional design variables were considered. After comparing the two different set of solutions, it was concluded that, if the wingspan constraint is to be satisfied, then any solution in the obtained Pareto-front of the heavier configuration will have a larger MTOW and smaller Endurance when compared to any other optimal solution of the smaller configuration.

7 FINAL CONCEPTUAL DESIGN

With the smaller configuration, a Pareto-front was obtained with the different optimal trade-off solutions. Because the fuel mass is small compared to the total UAV mass (200 g compared to 19 kg), there is no reason for flying without the hydrogen tank completely full. The selected final design corresponds to the lighter configuration with 800 W fuel cell and the hydrogen tank fully topped off at the start of the mission.

After analysing all estimates made by the analysis tool, a market search was conducted to select appropriate motors, propellers and batteries. The general characteristics of the final configuration are summarised in Tab.8.

As expected, the total UAV weight increased when the ratios were replaced by the actual components since all the batteries and motors had to be rounded up to the nearest commercially available component. The propulsion system mass is comprised of four V605 KV210 motors coupled to 22x7.4 propellers to power the VTOL and hover segments, and

B. M. Alves, V. L. Coelho, P. A. Silva, A. C. Marta, F. J. Afonso, P. J. Sá, L. F. Félix and J. V. Caetano

Table 8: General characteristics of the UAV final configuration.

Description	Value	Description	Value
Stall Speed	28 kts	Op. Speed	36 kts
Wingspan	4 m	Propulsion sys. mass	2.60 kg
Wing area	1.372 m^2	Energy sys. mass	7.23 kg
Payload	0.9 kg	Structural mass	7.56 kg
Endurance	3h20min	MTOW	21.6 kg

one AT 5220-A 20 25-CC motor with a 19x10 propeller to power the forward flight. The energy system includes: two Li-Po 6S batteries, one coupled to the fuel cell system and another used solely to power the VTOL and hover segments; a 7.2 L hydrogen tank and a single fuel cell with 800W nominal power.

8 PRELIMINARY DESIGN PROGRESS

In order to have a more refined design than the one presented in the conceptual phase, the wing, tail and fuselage preliminary design is conducted. The methodology followed is based on Corke and Sadrey, with considerations from other authors regarding design for UAVs [1, 9, 23].

The wing structure is divided into three panels: one rectangular in the middle and two tapered ones at the tips. To meet the maximum lift coefficient estimated previously, SG6042 airfoils are chosen, which also have good aerodynamic efficient at cruise conditions.

The fuselage is shaped around the hydrogen tank and it is sized to accommodate all the necessary components, distributed along its length.

The tail arm length of the inverted V-tail is based on the total aircraft length and the symmetric NACA 0008 airfoil is selected for the stabilizers, that generate a downward force at cruise.

Figure 10 represents the initial CAD model of the design with the preliminary considerations stated before.

Figure 10: CAD model of the UAV following considerations from preliminary design.

B. M. Alves, V. L. Coelho, P. A. Silva, A. C. Marta, F. J. Afonso, P. J. Sá, L. F. Félix and J. V. Caetano

9   CONCLUSIONS

During the conceptual and preliminary design of the UAV, some challenges were found using hydrogen as energy source: the fuel cell efficiency is highly dependent on its power output level; the maximum available power is too small for some flight stages, such as VTOL or hover; and the tank empty weight represents a very large portion of the MTOW.

Market studies were done to define initial parameter values that were used by the developed numerical analysis tool to perform the initial sizing. It followed a multi-objective optimisation to compare different optimal trade-off solutions with respect to MTOW and Endurance.

After selecting the most suitable solution, the estimates computed served as guidance in the choice of some key components commercially available, such as motors and batteries. With more realistic values for MTOW and power consumption during flight, the analysis tool was re-executed and the general UAV characteristics were obtained for the conceptual design. Some progress has been made in preliminary design, having produced a CAD model that represents the final design in some detail.

Future work include further analyses with higher fidelity computational methods to complete the preliminary and the detailed design. The project end goal is to build and fly the proposed concept for validation and refinement purposes.

REFERENCES

[1] T. C. Corke. *Design of Aircraft*. Pearson Education, 2002. ISBN 0130892343.

[2] D. P. Raymer. *Aircraft Design: A Conceptual Approach*. AIAA Education Series, 5th edition, 2012. ISBN 9781600869112.

[3] R. M. Dell and N. J. Bridger. Hydrogen — the ultimate fuel. *Applied Energy*, 1(4): 279–292, 1975. doi:10.1016/0306-2619(75)90029-X.

[4] Wingtra. Tailsitters vs. quadplanes – why a VTOL tailsitter is the best surveying drone for your mapping missions. `https://wingtra.com/`, November 2018.

[5] D. F. Finger, C. Braun, and C. Bil. A review of configuration design for distributed propulsion transitioning VTOL aircraft. In *Asia-Pacific International Symposium on Aerospace Technology (APISAT)*, Seoul, Korea, Oct. 2017.

[6] S. Park, J. Bae, Y. Kim, and S. Kim. Fault tolerant flight control system for the tilt-rotor uav. *Journal of the Franklin Institute*, 350(9):2535–2559, 2013. ISSN 0016-0032. doi:https://doi.org/10.1016/j.jfranklin.2013.01.014. URL `https://www.sciencedirect.com/science/article/pii/S0016003213000318`.

[7] sUAS News. Transwing – a revolutionary VTOL. `https://www.suasnews.com/2019/03/transwing-a-revolutionary-vtol/`, Mar. 2019.

[8] T. L. Saaty and L. G. Vargas. *Models, Methods, Concepts & Applications of the Analytic Hierarchy Process*. International Series in Operations Research & Management Science. Springer, 2nd edition, 2012. ISBN 9781461435976.

B. M. Alves, V. L. Coelho, P. A. Silva, A. C. Marta, F. J. Afonso, P. J. Sá, L. F. Félix and J. V. Caetano

[9] J. Gundlach. *Designing Unmanned Aircraft Systems: A Comprehensive Approach.* American Institute of Aeronautics and Astronautics, 2nd edition, 2014. ISBN 9781624102615.

[10] L. M. Parada. Conceptual and preliminary design of a long endurance electric UAV. Master's thesis, Instituto Superior Técnico, Universidade de Lisboa, Portugal, 2016.

[11] S. Gudmundsson. *General Aviation Aircraft Design: Applied Methods and Procedures.* Elsevier, 2014. ISBN 9780123973085.

[12] T-Motor. T-motor website. `https://store-en.tmotor.com/`, 2021.

[13] N. Gavrilovic, D. Vincekovic, and J.-M. Moschetta. A long range fuel cell/soaring UAV system for crossing the Atlantic ocean. In 11th *International Micro Air Vehicle Competition and Conference*, Madrid, Spain, Sept. 2019.

[14] Hacker Motor GmbH. Hacker motor gmbh website. `https://www.hacker-motor-shop.com/`, 2021.

[15] M. F. Omar Z.Sharaf. An overview of fuel cell technology: Fundamentals and applications. *Renewable and Sustainable Energy Reviews*, 21:810–853, 2014. doi:10.1016/j.rser.2014.01.012.

[16] N. S. Brun. Preliminary design of a fuel cell - battery hybrid propulsion system for a small VTOL UAV. Master's thesis, Faculty of Science and Technology, University of Stavanger, Norway, 2018.

[17] S. M. Haile. Materials for fuel cells. *Materials Today*, 6(3):24–29, 2003.

[18] Intelligent Energy. Intelligent energy website. `https://www.intelligent-energy.com/our-products/uavs/`, 2021.

[19] J. Z. Zhang, J. Li, Y. Li, and Y. Zhao. *Hydrogen Generation, Storage, and Utilization.* John Wiley & Sons, 2014. ISBN 9781118140635.

[20] Intelligent Energy. *Guide to Cylinder Options for UAV Applications.* Leicestershire, UK, 2020.

[21] J. G. Leishman. *Principles of Helicopter Aerodynamics.* Cambridge Aerospace Series. Cambridge University Press, 2nd edition, 2016. ISBN 9781107013353.

[22] J. Blank and K. Deb. Pymoo: Multi-objective optimization in Python. *IEEE Access*, 8, 2020. doi:10.1109/ACCESS.2020.2990567.

[23] M. H. Sadrey. *Aircraft Design - A Systems Engineering Approach.* Aerospace Series. John Wiley & Sons, 2013. ISBN 9781119953401.

DESIGN AND OPTIMIZATION OF A 3D PRINTED PROPELLER FOR A VTOL UAV

H. Rocha[1], P. Alves[1], A. Rodrigues[1], M. Silvestre[1]

1: C-MAST—Center for Mechanical and Aerospace Science and Technologies
Department of Aerospace Sciences
University of Beira Interior
Rua Marquês d'Ávila e Bolama, 6201-001 Covilhã, Portugal
hugo.rocha;ferreira.alves;andre.filipe.rodrigues;mars@ubi.pt

Abstract. *Propeller design and optimization is widely present in aircraft development. Generally, UAV propeller optimization lays in minimizing the consumed electrical power for certain flight condition. In the field of eVTOL aircraft, one type of mission segment in which the importance of propeller optimization is highlighted is in hovering flight. This is especially relevant to surveillance and monitoring UAVs. In this work, promoted by Tekever, an inverse design method was implemented in order to obtain an optimum propeller for an eVTOL UAV, with the objective to minimize the electric power consumption of the propulsion system in hovering flight. The algorithm, based on vortex theory, considered a Prandtl's root correction, which is usually not present in optimum propeller design algorithms. Two propellers were obtained using the method, one considering the Prandtl's root correction, and another without considering it. The propellers were then 3D printed and tested in a wind tunnel. The experimental results were also compared to results obtained with a Blade Element Momentum analysis code. The results suggest that the consideration of the Prandt'ls root correction in the inverse design of the propeller rendered a more optimized propeller, with a higher efficiency. This indicates that the corrections made to the Blade Element Momentum analysis models, such as 3D and stall delay corrections, might also be necessary to implement in Inverse Design methods, in order to obtain correctly optimized propellers.*

Keywords: Propeller, performance, inverse design, optimization, 3D printing, wind tunnel

H. Rocha, P. Alves, A. Rodrigues and M. Silvestre

1 INTRODUCTION

UAV propeller optimization is usually based on the minimization of the power required by the propulsion system for a prescribed thrust and/or freestream velocity. Other variables to the problem that can be prescribed are the diameter of the propeller, the rotation velocity, or even qualities related to the structural integrity of the blade.

In the recent field of eVTOL aircrafts, one kind of mission segment where this type of optimization is used is in hovering, where the objective is usually to maximize the time in this mission segment (minimizing the consumed power of the propulsion system, at least in that operating point). This is especially useful, for example, in surveillance or monitoring UAVs.

To analyze and design optimum propellers, there are several tools at one's disposal, from high fidelity time-dependent Computational Fluid Dynamics (CFD) approaches to Blade Element and Blade Element Momentum theories. However, this type of CFD approach is highly time-cost prohibitive, especially if it is intended to analyze a large number of different propellers. Blade Element Momentum (BEM) theory has been shown to have good agreement with experimental results for propellers, depending on some of the propeller and flow characteristics [1–5].

The work surrounding rotary wing devices optimization and BEM theory dates back to the 19th-century works of Rankine and Froude [1]. BEMT was later developed by Glauert, in which they provide a method for analysis of arbitrary propeller designs [6]. However, it was only in 1979 that Larrabee presented a procedure for optimum propeller design, based on Betz's condition for minimum energy loss [7]. Since then, this method has been validated in many pieces of literature and it has been subject to numerous improvements, allowing for quite accurate results for various operational ranges and loading types ([2, 8–11], as brief examples).

This work is part of the Hyprop project, promoted by Tekever, and its objective is to minimize the required electrical power of the propeller-electric motor hovering system of an eVTOL UAV. Since the electric motor is already chosen, the problem of minimizing the consumed power by the system lies solely on the propeller definition and its impact on the electric power consumption. This can be translated to finding the propeller blade design, namely its diameter, chord and used airfoils, with respective chord and pitch, along its radius. A vortex theory optimization algorithm was used to obtain the optimum propeller design at a determined rotation velocity. Afterward, the design was 3D printed and tested in a wind tunnel. The experimental results were then compared to ones obtained with Blade Element Momentum models.

2 METHODOLOGY

2.1 Optimum propeller design model

The optimum propeller design theory presented here is based on the one developed by Traub in [9] and the one presented by Phillips in [12]. In Traub's work, a simplified method of propeller analysis based on vortex theory is carried out. In vortex theory, the induced angle of attack is obtained, instead of the axial and tangential induction factors (which is usually the procedure in the BEM method). Fig.1 depicts some of the blade element geometric variables and aerodynamic variables.

According to Betz, the losses in the wake of a propeller are minimized if the displace-

H. Rocha, P. Alves, A. Rodrigues and M. Silvestre
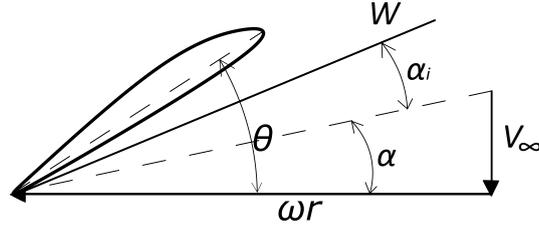
Figure 1: Blade element and some geometric and aerodynamic nomenclature.

ment velocity is constant which means that the wake moves aft as a rigid helical screw [13]. Traub [9] provides the following relation for the induced angle of attack, $\alpha_i(r)$ and the wake vortex sheet displacement velocity, w_0:

$$\alpha_i(r) = \frac{\cos(\phi_\infty(r))}{\sin(\phi_\infty(r)) + \frac{2\omega r}{w_0 \cos(\phi_\infty(r)])}} \tag{1}$$

where r is the radial position of the element, ω the angular velocity of the propeller, w_0 the wake vortex sheet displacement velocity, and $\phi(r)$ is the angle of the resulting flow at r without the induced effects, which is obtained by:

$$\phi_\infty(r) = \arctan(\frac{V_\infty}{\omega r}) \tag{2}$$

where V_∞ is the freestream velocity. w_0 must be iterated in order to meet a prescribed thrust or power requirement, which is shown in subsection 2.6.

Based on the Betz condition, Goldstein's vortex theory states that the vortex sheet trailing from a rotating propeller blade can be assumed to lie along a helical surface of constant pitch, and that the induced velocity can be assumed to be normal to the resultant velocity of the propeller [14]. From this and with the Kutta-Joukowski theorem, Phillips [12] obtains the following relation:

$$\frac{Bc(r)}{16r}C_l(r) - F(r)\frac{\pi}{2}\tan(\alpha_i(r))\sin(\alpha_i(r) + \phi_\infty(r)) = 0 \tag{3}$$

In Eq.(3), B is the number of blades, $c(r)$ is the chord of the element, $C_l(r)$ is the element lift coefficient, and $F(r)$ is the element Prandtl's correction (which will be discussed in the next subsection).

By using small-angle approximations in Eq.(3), meaning $\tan(\alpha_i(r))$ and $\sin(\alpha_i(r))$ are approximately equal to $\alpha_i(r)$ and $\cos(\alpha_i(r)) \approx 1$, Eq.(3) can be solved for the radial position's chord:

$$c(r) = F(r)\frac{\pi}{2}\alpha_i(r)\frac{16r}{BC_l(r)}[\sin(\phi_\infty(r)) + \alpha_i(r)\cos(\phi_\infty(r))] \tag{4}$$

Finally, the element pitch, θ, can be obtained through:

$$\theta(r) = \alpha(r) + \alpha_i(r) + \phi_\infty \tag{5}$$

Now, the differential thrust and torque components can be integrated over the span of the propeller blade, in order to obtain the thrust and torque of the propeller. The differential thrust and torque components are obtained through:

$$\frac{dT}{dr}(r) = r^2 c(r) \frac{\cos^2(\alpha_i(r))}{\cos^2(\phi_\infty(r))} [C_l(r) \cos(\alpha_i(r) + \phi_\infty(r)) - C_d(r) \sin(\alpha_i(r) + \phi_\infty(r))] \quad (6)$$

$$\frac{dQ}{dr}(r) = r^3 c(r) \frac{\cos^2(\alpha_i(r))}{\cos^2(\phi_\infty(r))} [C_l(r) \sin(\alpha_i(r) + \phi_\infty(r)) + C_d(r) \cos(\alpha_i(r) + \phi_\infty(r))] \quad (7)$$

where ρ is the air density and $C_d(r)$ is the airfoil drag coefficient of the element. The thrust and torque are obtained by:

$$T = \frac{B\rho\omega^2}{2} \int_{r_{root}}^{R} \frac{dT}{dr} dr \quad (8)$$

$$Q = \frac{B\rho\omega^2}{2} \int_{r_{root}}^{R} \frac{dQ}{dr} dr \quad (9)$$

The shaft power can simply be obtained by:

$$P = \omega Q \quad (10)$$

In order to compare different operating conditions, it is standard to use non-dimensional propeller coefficients.

$$C_T = \frac{T}{\rho n^2 D^4} \quad (11)$$

$$C_Q = \frac{Q}{\rho n^2 D^5} \quad (12)$$

$$C_P = \frac{P}{\rho n^3 D^5} = 2\pi C_Q \quad (13)$$

$$J = \frac{V_\infty}{nD} \quad (14)$$

$$\eta = J \frac{C_T}{C_P} \quad (15)$$

In the equations above, C_T is the thrust coefficient, C_Q the torque coefficient, C_P the power coefficient, J the advance ratio, n is the rotation rate of the propeller in rotations per second, D is the propeller diameter, and η is the propeller efficiency.

2.2 Electric motor and propeller coupling model

The coupling between the propeller and the electrical model is a simple one, which uses the commonly known motor parameters, namely K_v, the motor constant in $rad/s/V$, its resistance R, and the zero-load current I_0. This will allow to estimate the electrical power expended by the motor, which is the optimization variable in this work.

From the propeller torque, the electrical current can be obtained through Eq.(16):

H. Rocha, P. Alves, A. Rodrigues and M. Silvestre

$$I = QK_v + I_0 \tag{16}$$

The electrical potential difference can be calculated by:

$$U = \frac{\omega}{K_v} + IR \tag{17}$$

The electrical power expended by the motor can be obtained through Ohm's law:

$$P_{elec} = IV \tag{18}$$

2.3 Blade aerodynamic characteristics

As was seen in Subsection 2.1 and like all BEM models, it is necessary to consider the blade's airfoil aerodynamics for the implementation of the algorithm. Usually, the value of interest for optimum propeller design is the C_l that maximizes C_l/C_d.

The accuracy of the BEM and optimum propeller design models is extremely dependent on the correct estimation of the local aerodynamic coefficients [3]. Yet, small-scale propellers operating on low Reynolds numbers have a performance that is difficult to predict [15].

The aerodynamic characteristics of the airfoils can be obtained through wind tunnel testing, CFD, or using simpler analysis schemes, like panel methods. Since one part of this work consists in comparing the performance of a number of different airfoils, it was chosen to use XFLR5 [16] to obtain the $C_l(\alpha)$ and $C_d(\alpha)$ curves for the various airfoils. This has the great advantage of expeditiously testing several airfoils, at different Reynolds and Mach numbers.

2.4 Corrections to the model

The basic BEM formulation carries some limitations. For example, in BEMT, the blade is discretized into several blade elements, which operate independently from each other, considering a "quasi 2-D flow" [3]. However, several authors have shown spanwise flows to exist, which are not accounted for in the basic BEM formulation [3, 17].

In response to these limitations, some correction models have been developed, either for propeller or wind turbine analysis, for tip and hub losses, stall delay and rotational effects [5, 9, 18, 19]. However, as [17] points out, these are difficult to generalize for a wide range of propellers and operating conditions, often being somewhat empirical.

In this work, because of the non-linear iterative method of the optimization model, only three types of corrections are made, which are described in the next subsections.

2.4.1 Prandtl's tip and root correction

Prandtl estimated the tip losses of a propeller due to the fact that it is not a disk, but rather a set of finite rotating wings. Because of pressure equalization, a flow circulation appears between the different pressure sides of the propeller blade, creating blade tip vortices, resulting in a local lift reduction. This correction is largely used in BEM implementations since Glauert's methodology was laid out. However, in the last decade, some modifications to it were developed, like the one by Shen [5]. Most notably, in BEM

analysis algorithms, a root (or hub) correction is often considered. However, its consideration in Inverse Design algorithms is not common. Therefore, this work will consider both the case considering just the Prandtl's tip correction and the case considering both tip and root correction. Therefore, the Prandtl's correction factor F(r) is composed by $F_{tip}(r)$ and $F_{root}(r)$. $F_{tip}(r)$ is given by [9]:

$$F_{tip}(r) = \frac{2}{\pi} \arccos e^{-\frac{B(1-r/R)}{2\sin\theta_{tip}}} \tag{19}$$

where θ_{tip} is the value of θ at $r = R$, R being the radius of the propeller. $F_{root}(r)$, is obtained through [20]:

$$F_{root}(r) = \frac{2}{\pi} \arccos e^{-\frac{B}{2}\frac{r/R-r_{root}/R}{(r_{root}/R)\sin\theta}} \tag{20}$$

$F(r)$ is equal to $F_{tip}(r)$ if only the Prandtl's tip correction is considered, or the product $F_{tip}(r)F_{root}(r)$ if both corrections are considered.

2.4.2 Compressibility correction

Not all elements of the blade are subjected to the same aerodynamic conditions. The elements at larger radii are subjected to higher velocities, and therefore higher Mach, M values. Considering a C_l curve for an airfoil tested at $M = 0$, a higher Mach value translates to an increase of the lift curve slope. This effect is also present in the C_d curve, and for small C_l, an increase in M translates to an increase in C_d. These relations can be obtained through Prandtl-Meyer's correction [12], which is a "compressibility correction to incompressible data" [21]:

$$C_{l_M} = \frac{C_{l_{M=0}}}{\sqrt{1-M^2}} \tag{21}$$

$$C_{d_M} = \frac{C_{d_{M=0}}}{\sqrt{1-M^2}} \tag{22}$$

in which M is obtained through:

$$M(r) = \frac{W(r)}{a} = \frac{\omega r \cos(\alpha_i(r))}{\cos(\phi_\infty(r))a} \tag{23}$$

where a is the velocity of sound of the freestream air.

This correction is quite accurate in the linear part of the C_l curve, which can be observed in Fig.2. After stall is reached, the difference between the predicted value using the correction and the result from XFLR5 starts to differ quite much. This was not considered a major drawback, since the maximum efficiency of the section always laid in the linear portion of the airfoil polar.

2.4.3 Reynolds number correction

Small diameter UAV propellers usually operate in Reynolds numbers between 3×10^4 and 3×10^5 [22]. As mentioned in Subsection 2.3, propellers operating at this Re range have a performance that is difficult to predict. This can be due to several characteristics, like stall aerodynamics [15], and due to the fact that laminar separation and transition to

H. Rocha, P. Alves, A. Rodrigues and M. Silvestre
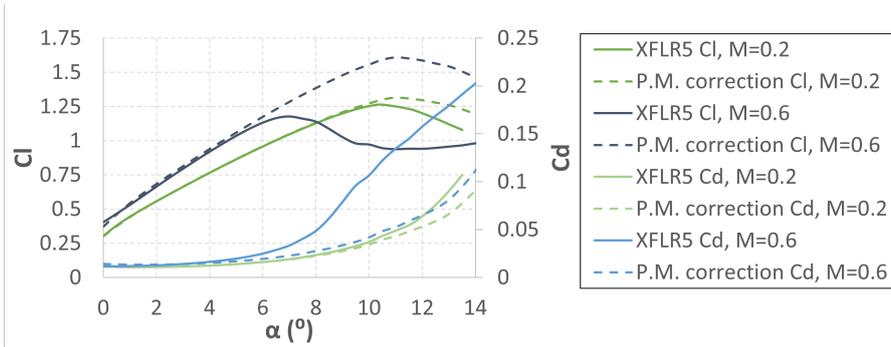
Figure 2: Prandtl-Meyer correction applied to S 9000 airfoil compared with XFLR5 results.

turbulent flow affect the performance of the propeller in low Reynolds numbers [23]. Moreover, there are Reynolds-related effects on these propellers that are not usually present on larger and higher-power ones [3].

In order to account for the variation of Reynolds number in the operating conditions, the following relation [24] is applied to C_d :

$$C_{d_{Re}}(r) = C_{d_{Re\,ref}}(r) \left(\frac{Re_{ref}}{Re} \right)^{Re_{exp}} \tag{24}$$

and the Reynolds number is obtained by:

$$Re(r) = \frac{W(r)\rho c(r)}{\mu} = \frac{\omega r \cos\left(\alpha_i(r)\right)\rho c(r)}{\cos\left(\phi_\infty(r)\right)\mu} \tag{25}$$

where μ is the freestream dynamic viscosity.

The value of Re_{exp} must be well studied, in order to correctly predict the drag coefficient. One can use a surface fitting tool to obtain its best value.

2.5 Airfoil selection

In this work, two predefined airfoils are considered: one at the root/hub of the blade; and another at the tip of the blade. The intermediate sections are interpolations of the root and tip airfoils. One of the most important characteristics to aim for when choosing airfoils for propellers is a high C_l/C_d value, if possible for a high C_l. For small-scale propellers with considerable rotation rates, another relevant characteristic is the effect of the Mach number at a low Re range.

To estimate the Reynolds and Mach range of the propeller in order to correctly assess the suitability of the airfoils, an optimization was done considering the NACA 4415 airfoil, at different rpm values. It was assessed that for the root part of the blade Re and M varied approximately between 6×10^4 and 1.1×10^5 and between 0.05 and 0.1, respectively, while for the tip region the Re range was from 1.2×10^5 to 1.7×10^5 and the M from 0.3 to 0.65.

The airfoils considered for this work are presented in Tab.1 and were analyzed in XFOIL.

After this, another consideration was made. Looking at Tab.1, the airfoils can be divided into groups of thin and thick airfoils. For the assessments made in this work, it

H. Rocha, P. Alves, A. Rodrigues and M. Silvestre

Table 1: Studied airfoils for the root and tip of the propeller blade.

Airfoil name	Max. camber (%)	Thickness (%)
Clark Y	3.43	11.71
NACA 4309	4.00	9.00
NACA 4415	4.00	15.00
NACA 4512	4.00	12.00
NACA 4521	4.00	21.01
NACA 5515	5.00	15.00
NACA 5521	5.00	21.01
RG 15	1.76	8.93
S 3016-95-87	2.09	9.52
S 9000	2.37	9.01
SD 7080	2.48	9.16

can be assumed that an airfoil is thick when its relative thickness is above 11%, although usually it is considered above 12% [25].

Thick airfoils are considered a better choice for the root part of the blade since they, in principle, can provide higher structural strength and blade stiffness comparing to thinner airfoil sections. Moreover, thicker airfoils have smoother stall characteristics, entering stall at higher angles of attack, which progresses from the trailing edge to the leading edge [25], while sometimes allowing for higher maximum C_l values [26]. This is especially relevant to the inner parts of the blade, since higher angles of attack and lower Re might be experienced in that region of the blade.

On the other hand, thin airfoils are greater contenders for the tip region since they have higher critical Mach values, and therefore their C_d will not increase as much with M, contrary to what happens with thicker airfoils [26]. More so, considering that, for the same Re, a thinner airfoil might have a lower maximum C_l/C_d [25], the optimization algorithm will balance this by increasing the chord value, which, in turn, increases the Reynolds number. This has the advantage of increasing the airfoil efficiency - increasing C_l/C_d [25].

From the assessment made to the Re and M ranges, it is safe to assume that for the tip region of the blade the most relevant analysis to refer is the effect of Mach, while for the root region the most relevant analysis to make is the effect of the Reynolds number in the airfoil performance. Therefore, the thin airfoils were analyzed at $Re = 1.45 \times 10^5$, with $M = 0.2$ and $M = 0.6$, while the thick airfoils were analyzed at $M = 0$, for $Re = 6 \times 10^4$ and $Re = 1.1 \times 10^5$. Some of these results are presented in Fig.3.

It can be observed in Fig.3a that the S 9000 airfoil presents the highest value of C_l/C_d. NACA 4309 also presents a high value of C_l/C_d, at a higher value of C_l. However, this maximum is present close to stall stall, which is not a stable condition for the airfoil to operate at (evidenced by the non converged results in the vicinity of the maximum). S 9000 also seems to maintain good performance with higher Mach values, due to the lower thickness, as expected, but probably also because of the position of maximum camber, located slightly more aft than the rest of the airfoils (42.25% comparing to, for example, 29.83% for the NACA 4309 or 38.24% for the S 3016-95-87. Therefore, the S 9000 airfoil was selected for the tip of the propeller.

H. Rocha, P. Alves, A. Rodrigues and M. Silvestre
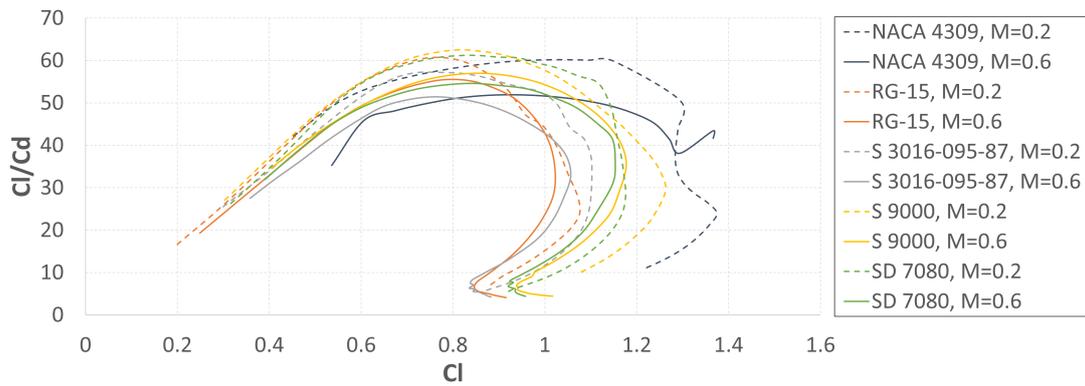
(a) C_l/C_d versus C_l for different M, for the thin airfoils.
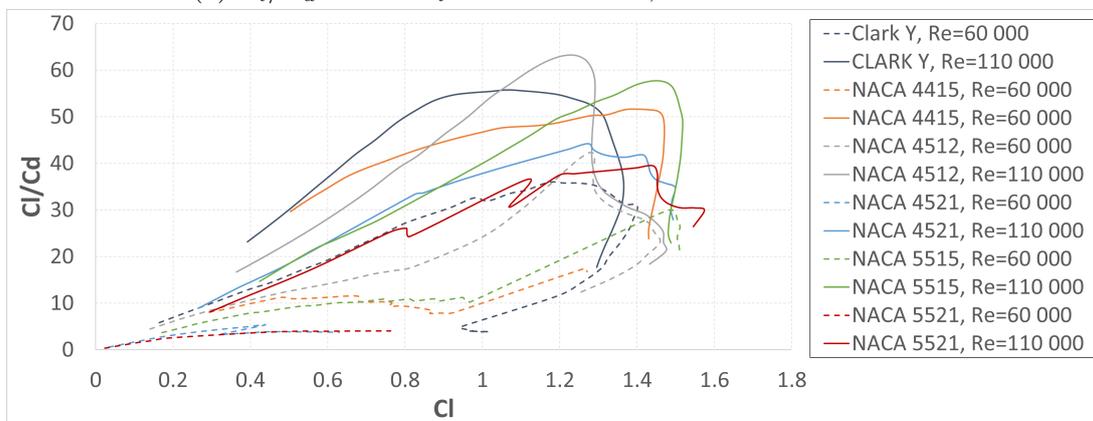
(b) C_l/C_d versus C_l for different Re, for the thick airfoils.

Figure 3: XFLR5 results for the airfoils enumerated in Tab.1.

Figure 3b presents somewhat worse results for all airfoils, especially at the lowest Re number. At this very low value of Reynolds number, the flow might have some trouble remaining attached to the airfoil after the point of maximum thickness. This is even more prevalent in higher camber airfoils, like NACA 5521. Observing the results, the three best performing airfoils for this Re range are the Clark Y, NACA 4512 and NACA 5515. Although the NACA 5515 seems to behave poorer than the other two, the stall behaviour is somewhat smoother. Furthermore, its value of C_l corresponding to maximum C_l/C_d is higher than the others, while the difference between $(C_l/C_d)_{max}$ is close to 10%. Since this airfoil also has a bigger relative thickness and therefore can provide additional structural stiffness, the airfoil NACA 5515 was chosen for the root section of the propeller.

2.6 Optimization algorithm

The optimization algorithm is implemented with the following steps:

1. The various inputs are obtained, namely the electric motor characteristics, the air properties, the propeller diameter and number of blades, the specified thrust, the number of elements used for calculation, and the tip and root airfoils and their respective polar curves;

2. The elements are distributed with a sinusoidal function throughout the blade, using

H. Rocha, P. Alves, A. Rodrigues and M. Silvestre

the:

$$r = r_1 + \frac{1}{2}(R - r_1)\left(1 + \sin\left(\frac{i-1}{N-1}\pi - \frac{\pi}{2}\right)\right) \tag{26}$$

where N is the number of elements the blade is discretized in;

3. An initial value for the initial rpm is selected and the optimization process for the selected rpm is started;

4. Some value for w_0 is considered. In this work, $30m/s$ worked correctly, although a more formal way to obtain this value might be implemented;

5. $\phi_\infty(r)$ is obtained through Eq.(2);

6. α_i is obtained through Eq.(1);

7. M is calculated by Eq.(23);

8. The C_l and C_d curves are obtained for the element. The polars are obtained through weighted interpolation of the root and tip C_l and C_d curves based on the distance to them. This is done to drastically reduce the amount of XFOIL analyses needed, and it is a good approximation since the polar curve of an interpolated airfoil is quite close to the interpolation of the polar curves of its two "parent" airfoils [27];

9. From the element polar curves, the value of C_l which maximizes C_l/C_d is obtained and considered;

10. The $C_l(r)$ is corrected through Eq.(21);

11. From the polar curves and the $C_l(r)$, the value of $\alpha(r)$ is obtained;

12. $\theta(r)$ is obtained through Eq.(5);

13. $F(r)$ is obtained through the process elucidated in 2.4.1;

14. The chord $c(r)$ is calculated by Eq.(4);

15. $Re(r)$ is obtained through Eq.(25);

16. From the $\alpha(r)$ and the element polar curve, $C_d(r)$ is obtained, and corrected by Eq.(24);

17. $\frac{dT}{dr}(r)$ and $\frac{dQ}{dr}(r)$ are obtained through Eq.(6) and Eq.(7) respectively;

18. After all variables for all the elements are obtained, the thrust and shaft power are obtained by Eq.(8) and Eq.(10);

19. The prescribed value for either thrust or power is compared to the according one which was obtained through the model. If the difference is sufficiently small, then

H. Rocha, P. Alves, A. Rodrigues and M. Silvestre

convergence has been reached. If not, the value w_0 for the next iteration is calculated. In this work, this was done in an oscillation damping manner, similar to [2, 5], with the following relation (considering a prescribed thrust value):

$$w_{0_{i+1}} = \gamma \frac{w_{0_i}}{\sqrt{\frac{T_i}{T_{specified}}}} + (1 - \gamma)w_{0_i} \tag{27}$$

If, instead, power is prescribed, T_i and $T_{specified}$ are replaced with P_i and $P_{specified}$ respectively. The relaxation term γ was set to 0.3;

20. If convergence is reached, the value of P_{elec} is obtained through Eq.(18);

21. A new value of rpm is set and steps 4-20 are repeated;

22. After all values of $P_{elec}(rpm)$ are obtained, they are compared, and the minimum P_{elec} and its respective rotation rate are obtained. The $c(r)$ and $\theta(r)$ distribution for the respective rotation rate data are output.

2.7 3D modeling and 3D printing

In order to 3D print the propellers, some modifications were made to the theoretical optimum design. Since a chord of 0 is not practically possible, a value of chord that allowed the propeller to withstand its centrifugal force was considered for the root of the P.R.T.C configuration, and the chord at the tip of both propellers was set at the minimum to possibly 3D print, $0.4mm$. Because of that minimum, the trailing edge was also ensured to have $0.4mm$ of thickness. The last 90% of the propeller's sections were increased in thickness and decreased in chord length, to also accommodate this 3D printing limitation.

The propeller sections were also positioned such that all their centroids of area lined exactly in a radial axis. This was made to minimize the twisting caused by the aerodynamic forces.

The propellers were printed with a diameter of 15 in, since the wind tunnel testing area does not allow for the full-size propellers to be tested.

2.8 Wind tunnel experimental setup

The experimental setup is fully documented and explained in [28]. For sake of brevity, only some of its aspects are presented here. The propeller thrust balance is a T-shape pendulum configuration, which pivots around the axis defined by two flexural pivots, and is constrained by a load cell outside the tunnel. It was designed to ensure that the thrust vector is located at the center of the test section. The load cell is kept in tension by a pre-load weight placed on its opposite side, in order to counter slipping which might occur at negative thrust conditions.

The used thrust load cell is the FN3148, manufactured by *FGP Sensors & Instrumentation*, and has a maximum capacity of 100N. Torque is measured by two torque transducers, the RTS-100 and RTS-200, manufactured by *Transducer Techniques*. All load cells are connected to a high-precision strain gauge converter.

The propeller rotation rate is measured with a Fairchild Semiconductor QRD1114 photo-reflector, with a fixed measuring time interval of $0.75s$.

The freestream velocity is measured by means of a differential pressure transducer, an MPXA4115A absolute pressure transducer, made by *Freescale Semiconductor*, and a

H. Rocha, P. Alves, A. Rodrigues and M. Silvestre

LM335 thermocouple, made by *National Instruments*. One static pressure probe is placed at the tunnel settling section and another at the entrance of the test volume, which can be observed in Fig.4.
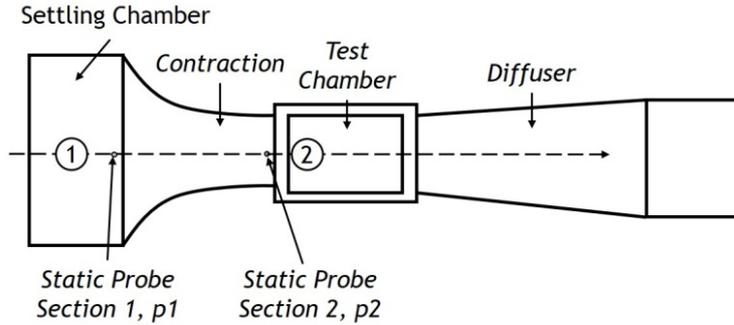
Figure 4: Scheme of the wind tunnel and location of the static pressure ports.

3 RESULTS AND DISCUSSION

In this section, the various results regarding the optimization problem are laid out. Firstly, a comparison between other optimum propeller design methods is presented. Secondly, some stipulations to the design are made before the optimization is executed. Finally, the optimization, wind tunnel testing, and BEM code results are presented.

3.1 Comparison with Adkins and QMil

The optimum propeller inverse design methodology presented in this work was compared to the one developed by Adkins [8] and to QMil, a freely available inverse design software [29]. Figure 5 shows the results for the Adkins propeller, whose characteristics and design inputs are presented in [8].

Observing Fig.5, the algorithm closely follows the results of the Adkins propeller. If Re and M corrections are in place, the chord between r/R $\approx$ 0.5 and 1 is slightly larger, but still showing the same trend. This might be because the Adkins methodology does not consider the corrections described in Section 2.4. On the other hand, θ is closelly predicted among the several methodologies. The comparison was made without considering Prandtl's root correction, since the other optimum propeller design models also do not consider it.

3.2 Propeller diameter definition

In order to reduce one of the optimization variables, the diameter was prescribed *a priori*. From the actuator disk theory, the relationship between thrust and power for hovering flight is:

$$P = \sqrt{\frac{T^3}{0.5\rho\pi D^2}} \tag{28}$$

From Eq.(28) it can be deduced that, for a given thrust, the bigger the diameter of the propeller the lower the minimum necessary shaft power is. However, there are some limiting factors to the value. As the diameter increases, the tip speed increases

H. Rocha, P. Alves, A. Rodrigues and M. Silvestre

(a) c/R *versus* r/R.

(b) θ *versus* r/R.
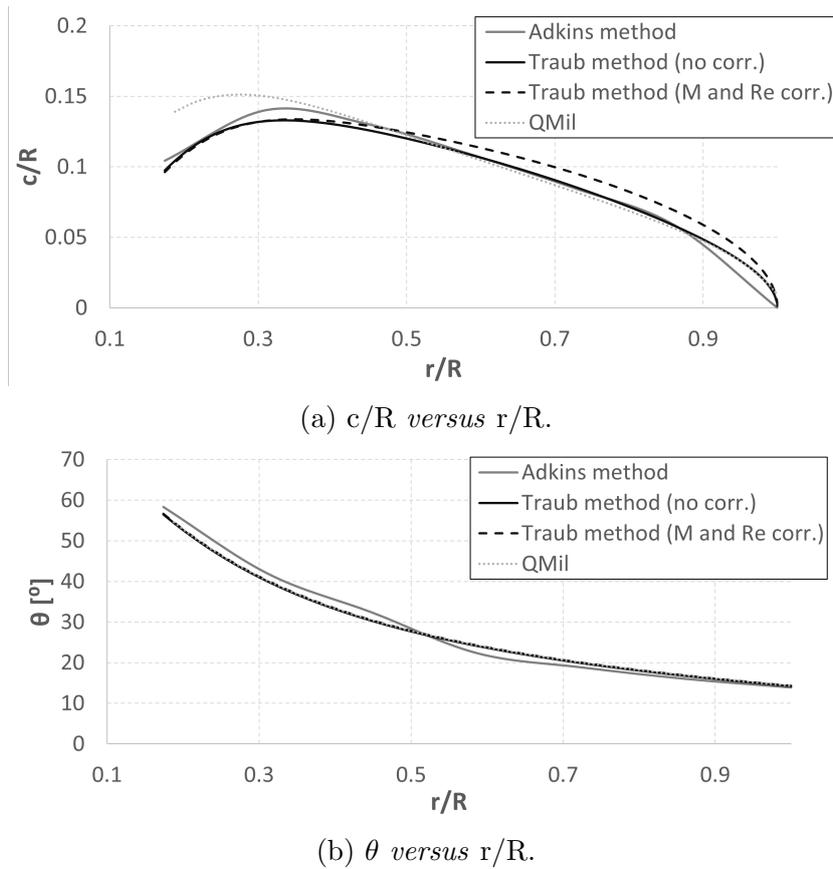
Figure 5: Optimization results for various optimum propeller inverse design methodologies.

linearly (for the same rotational speed), which might increase compressibility effects in the outer radius of the blades and possibly posing a problem increased losses and actual required shaft power, but also requires stronger blades in order to withstand the centrifugal inertial forces. Furthermore, propeller vortex noise - a source of power consumption of the propeller - increases drastically with the local velocity at 70% of radius [30].

Considering a simplified case with a constant airfoil throughout the blade, a simple parametric study was done, varying the rotation rate between 4000 *rpm* and 9000 *rpm* and the diameter of the propeller between 18 *in* and 22 *in*. As predicted by the actuator disk theory, the bigger diameter allowed for a slightly lower minimum power output by the electric motor. Since 22 *in* exceeded a geometric constraint for the aircraft configuration, the value of 21 *in* was chosen for the propeller diameter.

3.3 Optimization results

Following the airfoil selection, the optimization algorithm described in section 2.6 was used to optimize the propeller chord and pitch distribution for the rotation rate which minimizes the electrical power required by the motor, for a prescribed thrust of 65 *N*. Two geometries were obtained: one considering Prandtl's tip and root correction, and other considering just the tip correction. For concision, P.R.T.C. will from now on refer to the propeller considering both Prandtl's corrections, and P.T.C. to the one considering only the tip correction. Figure 6 shows the results of P_{elec} *versus rpm* for the different

correction consideration. Each point corresponds to an optimum design, at that *rpm* value, for the same prescribed thrust. The global minimum power required by the electric motor for the P.T.C. configuration is 1143.0 W and occurs at 7350 rpm, while for the P.R.T.C. one is 1153.7 at 7400 rpm.
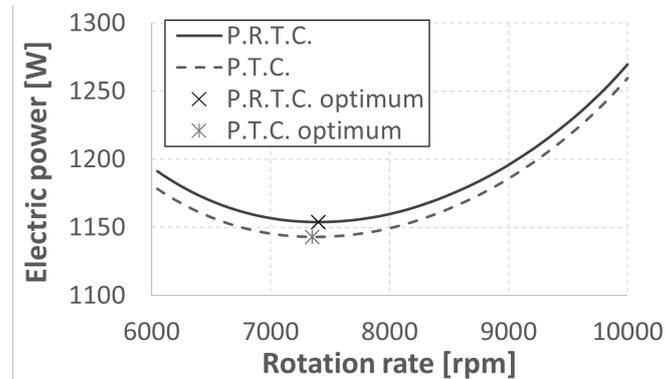
Figure 6: P_{elec} *versus* rotation rate for the different correction considerations.

Table 2 and Fig.7 show the results for the geometry of the propellers for their respective optimum rotation rates (7400 *rpm* for the P.R.T.C. and 7350 *rpm* for P.T.C). It is noted that Prandtl's root correction to the results acts the same way as the tip correction in an inverse design problem: the chord at the corrected region tends to zero.

Table 2: Optimization results.

P.R.T.C.			P.T.C.		
r/R	c/R	θ	r/R	c/R	θ
0.15	0.00	28.98	0.15	0.21	28.97
0.19	0.10	24.62	0.19	0.17	24.61
0.23	0.12	21.19	0.23	0.14	21.19
0.29	0.11	17.63	0.29	0.11	17.80
0.36	0.09	14.77	0.36	0.09	14.77
0.45	0.08	12.91	0.45	0.08	12.91
0.53	0.07	11.14	0.53	0.07	11.14
0.67	0.07	9.30	0.67	0.07	9.30
0.75	0.06	8.46	0.75	0.06	8.46
0.89	0.05	7.03	0.89	0.05	7.03
0.97	0.03	6.53	0.97	0.03	6.53
1.00	0.00	6.22	1.00	0.00	6.22

3.4 Wind tunnel results and comparison with a BEM analysis code

Some of the wind tunnel results are present in Fig.8, along with results obtained using a BEM analysis code, based on the methodology developed by Traub [9]. Tests were done between 3000 *rpm* and 5000 *rpm*, with varying advance ratios, and some static thrust cases, i.e. $V_\infty = 0$, were also carried out. However, only the results for the 5000 *rpm* are shown here, allowing for an adequate comparison between the two propeller configurations.
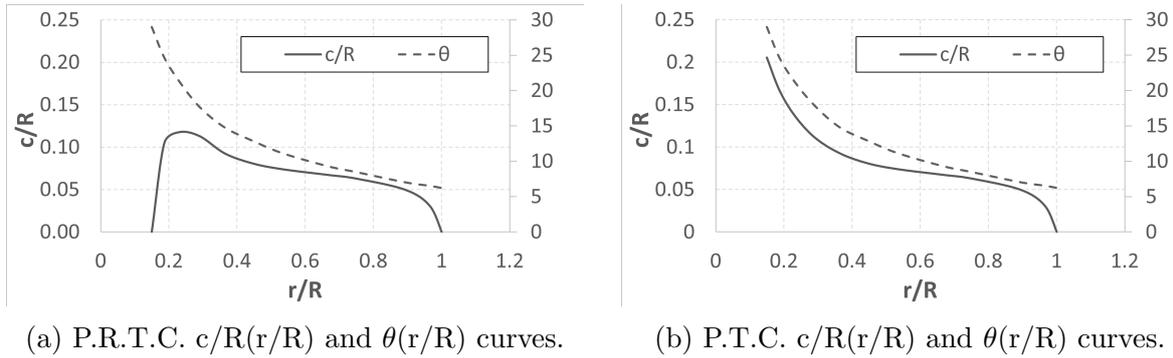
(a) P.R.T.C. c/R(r/R) and θ(r/R) curves.

(b) P.T.C. c/R(r/R) and θ(r/R) curves.

Figure 7: Propeller optimization results for their respective optimum points.

There were some limitations to the testing and, consequently, to the results. One of the main issues was that, even though the propeller was tested as a $\approx 71.4\%$ diameter model, dynamic similarity was not obtained, and, therefore, these tests do not represent the propeller results for its design point. On the other hand, dynamic similarity was not possible to achieve, because of the lack of strength and stiffness of the blades: to achieve dynamic similarity with $V_\infty = 0$, a much higher rotation rate was needed, and at that point, a great amount of vibration was present. Moreover, due to the low stiffness, low rotation velocities coupled with higher freestream velocities resulted in bending and, therefore, poor results.

The results show that the propeller which was designed considering Prandtl's root correction seems to have a higher efficiency than the other configuration (Fig.8c). The static thrust case results are somewhat inconclusive. At 3000 rpm, the P.T.R.C. presents a higher value of T/P_{shaft}, 0.1599 N/W, compared to 0.1467 N/W of the P.T.C. configuration, while at 4000 rpm the P.T.C. propeller has a higher value of T/P_{shaft}, 0.1304 N/W compared to 0.1217 N/W. BEM results predict that the parameter T/P_{shaft} is always around 20% higher in the P.R.T.C. propeller in between 4000 rpm and 8000 rpm.

The BEM code seems to correctly predict the power coefficient, while underestimating the thrust coefficient and, therefore, also underestimating the efficiency (see Eq.(15)). There might be several sources for this issue: even though Snel's 3D correction was implemented [31], which increases the airfoil lift coefficient due to rotation, it is still an empirical model, which is often fine-tuned to match with certain measurements [18, 32], which was not done in this case; as said before, propellers operating at low Re have a performance which is sometimes difficult to predict [15]; it is possible that, due to bending stemming from the low blade stiffness, the resulting pitch at some portions of the blade changes throughout the tests, which would significantly affect the resulting aerodynamic forces, an effect which cannot be correctly predicted in such a simple BEM code. Another possibility is that, from previous 3D printed propeller testing done in this wind tunnel [33], it was observed that, when the 3D printed surface is not smooth finished, the sensitivity of the results to the Re number is low.

4   CONCLUSIONS

The applied inverse design method presented in this work has some advantages: it uses the actual polar data results for the airfoils, either from wind tunnel, CFD, or other methods, without considering simplified airfoil models; the method allows for the

H. Rocha, P. Alves, A. Rodrigues and M. Silvestre
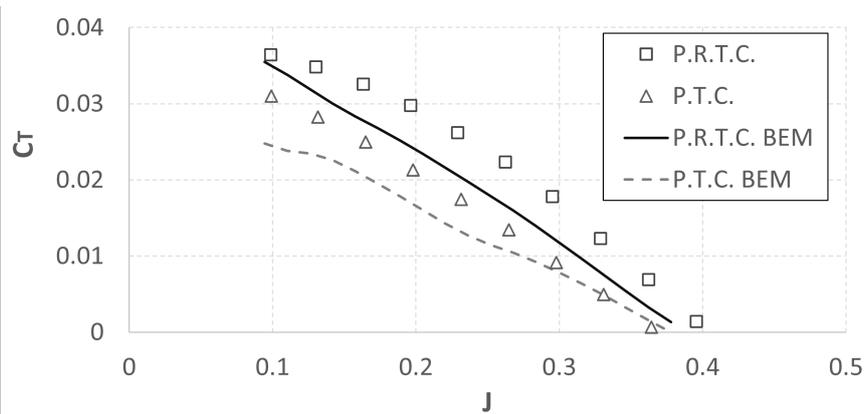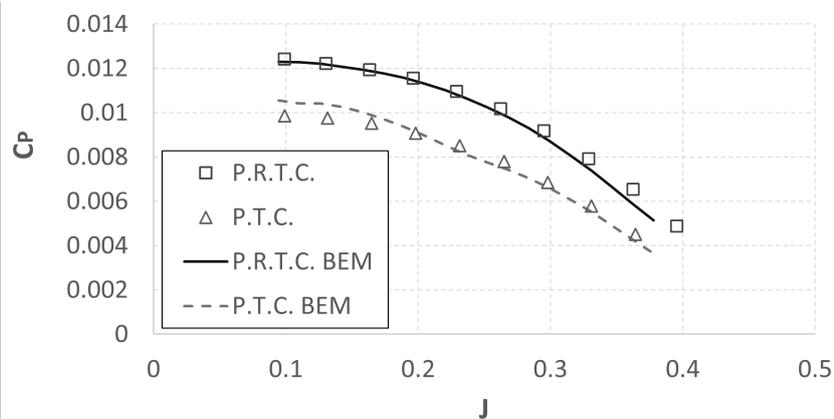
(a) $C_T(J)$ results.

(b) $C_P(J)$ results.
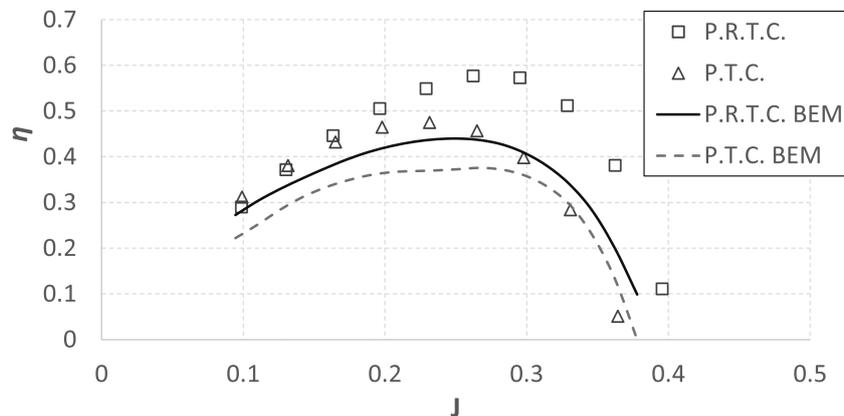
(c) $\eta(J)$ results.

Figure 8: Wind tunnel results for 5000 rpm, for both configurations.

specification of different airfoils along the radius of the blade. The method was developed to consider a Prandtl's root (or hub) correction, in addition to the already well-established Prandtl's tip correction, allowing for two different optimum propeller configurations: one considering both corrections, another just considering the tip correction.

Preliminary results seem to suggest that the Prandtl's root correction is as necessary to a correct inverse design model as to a direct analysis one, resulting in a more optimized propeller. This might suggest that the corrections already validated and highly used in

BEM methods should also be considered in propeller inverse design, to obtain a correctly optimized propeller.

Wind tunnel tests suggest that, for the reduced scale propellers, the material used in the 3D printing of these propellers might not be suitable, since they have a high aspect ratio and considerable small chord, which resulted in very low stiffness. In turn, the low stiffness of the blades limited the rotational rates which could be run in the wind tunnel.

4.1 Future work

For future work, it will be necessary to test the different propellers with dynamic similarity to the full size propellers. Therefore, it will be necessary to 3D print propellers with a much higher stiffness. This can be done by using a different material or by modifying the optimization algorithm to output the $C_l(r)$ and $\theta(r)$ of the blade, with the chord distribution along the blade radius as an input. This way, a higher chord can be considered, increasing the blade stiffness.

More airfoils should be evaluated. This process could also be automatized, being a part of the optimization algorithm.

A more accurate Mach correction will be implemented, which will more accurately predict the maximum efficiency point at different Mach values.

The resulting propellers will be tested for the same thrust, so that the optimization result can be properly compared between the propellers.

ACKNOWLEDGEMENTS

REFERENCES

[1] E. V. Loureiro, N. L. Oliveira, P. H. Hallak, F. de Souza Bastos, L. M. Rocha, R. G. P. Delmonte, and A. C. de Castro Lemonge. Evaluation of low fidelity and cfd methods for the aerodynamic performance of a small propeller. *Aerospace Science and Technology*, 108, 2021.

[2] J. P. S. Morgado. *Development of an open source software tool for propeller design in the MAAT project.* PhD thesis, Universidade da Beira Interior (Portugal), 2016.

[3] M. H. McCrink and J. W. Gregory. Blade element momentum modeling of low-reynolds electric propulsion systems. *Journal of Aircraft*, 54(1):163–176, 2017.

[4] J. Carroll and D. Marcum. Comparison of a blade element momentum model to 3d cfd simulations for small scale propellers. *SAE International Journal of Aerospace*, 6(2013-01-2270):721–726, 2013.

[5] D. Marten, G. Pechlivanoglou, C. Nayeri, and C. Paschereit. Integration of a wt blade design tool in xfoil/xflr5. 01 2010.

[6] H. Glauert. *The elements of aerofoil and airscrew theory.* Cambridge University Press, 1983.

[7] E. E. Larrabee. Practical design of minimum induced loss propellers. *SAE Transactions*, pages 2053–2062, 1979.

[8] C. N. Adkins and R. H. Liebeck. Design of optimum propellers. *Journal of Propulsion and Power*, 10(5):676–682, 1994.

[9] L. Traub. Simplified propeller analysis and design including effects of stall. *The Aeronautical Journal*, 120(1227):796–818, 2016.

[10] B. D. Rutkay. *A process for the design and manufacture of propellers for small unmanned aerial vehicles.* PhD thesis, Carleton University, 2014.

[11] M. Hepperle. Inverse aerodynamic design procedure for propellers having a prescribed chord-length distribution. *Journal of aircraft*, 47(6):1867–1872, 2010.

[12] W. F. Phillips. *Mechanics of flight.* John Wiley & Sons, 2004.

[13] A. Betz. with appendix by prandtl. *L.," Screw propellers with Minimum Energy Loss," Göttingen Reports*, pages 193–213, 1919.

[14] S. Goldstein. On the vortex theory of screw propellers. *Proceedings of the Royal Society of London. Series A, Containing Papers of a Mathematical and Physical Character*, 123(792):440–465, 1929.

[15] D. Uhlig and M. Selig. Post stall propeller behavior at low reynolds numbers. In *46th AIAA Aerospace Sciences Meeting and Exhibit*, page 407, 2008.

[16] M. Drela. Xfoil: An analysis and design system for low reynolds number airfoils. In *Low Reynolds number aerodynamics*, pages 1–12. Springer, 1989.

[17] H. Dumitrescu and V. Cardos. A stall-delay model for rotating blades. In *PAMM: Proceedings in Applied Mathematics and Mechanics*, volume 7. Wiley Online Library, 2007.

[18] C. Lindenburg. Investigation into rotor blade aerodynamics. *Energy research Centre of the Netherlands (ECN) Wind Energy publication, ECN-C–03-025*, 2003.

[19] J. Morgado, M. Silvestre, and J. Páscoa. Validation of new formulations for propeller analysis. *Journal of Propulsion and Power*, 31(1):467–477, 2015.

[20] S. Schmitz and D. C. Maniaci. Analytical method to determine a tip loss factor for highly-loaded wind turbines. Technical report, Sandia National Lab.(SNL-NM), Albuquerque, NM (United States), 2016.

[21] J. D. Anderson Jr. *Fundamentals of aerodynamics.* McGraw-Hill Education, 2010.

[22] M. Merchant and L. S. Miller. Propeller performance measurement for low reynolds number uav applications. In *44th AIAA Aerospace Sciences Meeting and Exhibit*, page 1127, 2006.

[23] K. Wang, Z. Zhou, X. Zhu, and X. Xu. Aerodynamic design of multi-propeller/wing integration at low reynolds numbers. *Aerospace Science and Technology*, 84:1–17, 2019.

[24] J. Hernandez and A. Crespo. Aerodynamic calculation of the performance of horizontal axis wind turbines and comparison with experimental results. *Wind Engineering*, pages 177–187, 1987.

[25] V. Brederode. *Fundamentos de Aerodinâmica Incompressível*. Instituto Superior Técnico - IDMEC, 1997.

[26] D. Scholz and S. Ciornei. Mach number, relative thickness, sweep and lift coefficient of the wing–an empirical investigation of parameters and equations. *Hamburg: HAW Hamburg University of Applied Sciences, DLRK. Paper*, 2005.

[27] M. Drela. Xfoil 6.9 theory document, 2001. URL `http://web.mit.edu/aeroutil_v1.0/xfoil_doc.txt`.

[28] M. Silvestre, J. Morgado, P. Alves, P. Santos, P. Gamboa, and J. Páscoa. Propeller performance measurements at low reynolds numbers. *International Journal of Mechanics*, 9:154–166, 2015.

[29] M. Drela. Qmil (version 1.22), 2007.

[30] D. Kurtz and J. Marte. A review of aerodynamic noise from propellers, rotors, and lift fans. 1970.

[31] H. Snel, R. Houwink, and J. Bosschers. Sectional prediction of lift coefficients on rotating wind turbine blades in stall. 1994.

[32] R. MacNeill and D. Verstraete. Blade element momentum theory extended to model low reynolds number propeller performance. *The Aeronautical Journal*, 121(1240): 835–857, 2017.

[33] P. Alves, A. Rodrigues, and M. Silvestre. Assessment of low cost fdm 3d printing in low reynolds number propeller prototyping. 2021 AIAA Propulsion & Energy Forum, August 2021.

MODELING AND OPTIMIZATION OF AN OBSTACLE DETECTION SYSTEM FOR SMALL FIXED-WING UAV

N. M. P. Alturas [*] and A. C. Marta

IDMEC
Instituto Superior Técnico
Universidade de Lisboa
Av. Rovisco Pais 1, 1049-001 Lisboa, Portugal
{nuno.alturas,andre.marta}@tecnico.ulisboa.pt, https://www.idmec.tecnico.ulisboa.pt/

Abstract. *A solution for the enhancement of safety during the flight of small fixed-wing UAVs, regarding the detection of obstacles during flight, is presented. This was achieved by making a market study on available sensors to find the most suitable to equip a UAV and by modeling them, so that these models could be integrated into collision detection and avoidance simulations. Different tracking filters and sensor fusion techniques were studied, where the Converted Measurement Kalman Filter and the Weighted Filter technique were found to be the best to implement. In the simulations, the Potential Fields avoidance method was chosen for being computationally inexpensive and for providing feasible solutions in real time. Several parametric studies were conducted to test the performance of the selected sensors and to assess how their different parameters affect the success of the obstacle avoidance. An optimization study was also conducted, using a global optimizer, to find the orientation of sensors, for different sets of sensors, that results in the best performance for a set of randomly generated collision scenarios with both stationary and moving obstacles. Relatively simple detection configurations were found that still provide high collision avoidance success rate.*

Keywords: Potential Fields, Genetic Algorithm, Kalman Filter, Unbiased Conversion, Sensor Fusion

N. M. P. Alturas and A. C. Marta

1 INTRODUCTION

Like many other technologies, Unmanned Aircraft Vehicles (UAVs) were initially developed for military purposes and have since made their way into the civil domain. Nowadays, UAV applications include, but are not limited to, photography and video, precision agriculture, inspections, monitoring and deliveries. The market continues to grow and projections show that non-military UAV production will total 14.3 billion dollars in 2028, while totaling 4.9 billion dollars in 2019 [1].

UAV classification is important to differentiate existing systems, since each category has different legal regulations, and also commercial and operational purposes. Considering the classification of UAVs [2], our work is specifically aimed at fixed-wing mini UAVs (maximum take-off weight < 25 kg, range < 10 km, endurance < 2h and flight altitude < 120 m), which accounts for the majority of the market share for their versatility and low-cost, but lack efficient and robust safety systems. A representative example of such UAV category is the Tekever AR4 shown in Fig.1, that has a maximum take-off weight of 4 kg, an endurance of 2 hours and a maximum speed of 15 m/s [3].

Figure 1: Tekever AR4 UAV [3].

For the UAVs to perform the missions previously described efficiently, autonomous and Beyond Visual Line of Sight (BVLOS) flight is essential, which is already foreseen by the European law. To that end, for a safe flight to be possible, a robust and reliable Obstacle Sense and Collision Avoidance (S&A) system is needed.

There are already numerous proposals for avoidance algorithms and sensor layouts, but most are limited to multi-rotor UAVs. Adapting these systems to fixed-wing UAV characteristics and keeping the cost low continues to be a challenge. Among the many vision based applications [4], obstacle detection has been developed significantly. The hardware solutions range from simple monocular cameras, either to complement GPS data [5] or even in GPS deprived environments [6]. Better performance is obtained using binocular vision [7] or RGB-D cameras (with depth sensor) [8] at an expense of higher on-board computational power. Much simpler solutions have been proposed with low cost ultrasonic and infrared range finders, but they are limited to low-speed and high-maneuverability multi-rotor UAVs due to their limited sensing range [9]. Advanced solutions often include sensor fusion, where data is gathered from multiple sources. There are many possible combinations of sensors but some representative examples include merging monocular cameras with RADAR [10], and ADS-B with a thermal camera [11]. It should be noted that the latter poses significant limitations since it cannot detect non-ADS-B-equipped aircraft under adverse meteorological conditions.

Therefore, the main goal of this work is to improve the safety of low-cost fixed-wing mini UAVs regarding the detection of obstacles during their flight. It is part of an extensive two-stage sense and avoidance system, being focused on the former.

N. M. P. Alturas and A. C. Marta

2 SENSORS BENCHMARK

A thorough study was conducted on the various types of sensors available on the market that could be integrated into our representative UAV. After this analysis, one sensor of each type was picked to be compared in terms of range and field of view (FOV), so that their attributes and flaws could be better showcased. The chosen sensors for this comparison were the uAvionix pingRX ADS-B [12], the Lightware LW20/C laser rangefinder [13], the Aerotenna μSharp Patch RADAR [14], the Intel D435 stereo camera [15] and the MaxBotix MB1242 sonar [16]. Their corresponding sensed areas on the horizontal plane are represented in Fig.2, except for the ADS-B sensor since it is omnidirectional and its range depends on the power of the other aircraft emitted signal. The sonar FOV is almost invisible as a result of its small range (two orders of magnitude below the RADAR range).
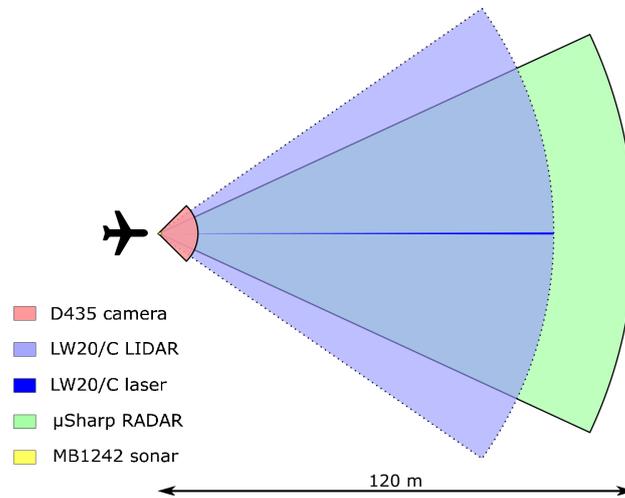
Figure 2: Comparison of several sensor ranges and FOVs.

It is important to note that the LIDAR is based on the laser rangefinder, being its multidirectionality obtained from coupling a scanning actuator. In Fig.2, an arbitrary but typical 70° horizontal FOV was chosen and, because of this, the limits of the sensed area were dotted. The LW20/C's laser area, when the scanning mode is not activated, is represented in dark blue, where its 0.3°beam divergence can be observed.

The camera sensed area is associated with its depth image sensors. The infra-red and color cameras have their own range and FOV but these are more applicable to complement other sensors as they do not provide depth data.

Based on this comparison, the ultrasound and stereo vision sensors were not modeled in Sec. 3 due to their very limited range, as identifying obstacles when they are only at a distance of 10 m or 0.765 m generally do not result in successful avoidance maneuvers when the UAV is traveling at a maximum cruise speed of 15 m/s. The ADS-B was also excluded for being a cooperative sensor, meaning it would require other vehicles to be equipped with similar equipment to allow the UAV to detect them, which is outside the scope of this work.

N. M. P. Alturas and A. C. Marta

3 SENSORS MODELS

A sensor model is an abstraction of the actual sensing process that describes the information a sensor can provide, how this information is limited by the environment and how it can be enhanced by data obtained from other sensors.

For the developed simulations, different sensors were modeled to compare their behavior and find the combination that produce the best S&A results. The sensors are characterized by their range, FOV, accuracy and data acquisition frequency. The values used for these parameters are from the sensors presented in Sec. 2, which were obtained from their technical manuals or inferred from available data, and are summarized in Tab.1. Since our simulations were restricted to the horizontal plane of motion, the vertical FOV is not relevant.

Table 1: Characteristics of the different sensors used in simulations.

	Laser rangefinder	LIDAR	RADAR
Range (m)	100	100	120
Horizontal FOV (°)	0.3	variable	50
Accuracy (m)	0.2	0.2	0.22
Max. frequency (Hz)	388	388	90

3.1 LIDAR/Laser Rangefinder

Fayad and Cherfaoui [17] presented an approach to solve the problem of tracking partially hidden objects by a single layer laser scanner to be used in driving situations. In their proposed method, if an object is totally visible, it is considered that its half was detected and the remaining of the obstacle is reconstructed assuming symmetry, where the center of symmetry is the medium point of the segment connecting the first and last point of the cluster. In our simulations, the obstacles were modeled as circles, so this distance corresponds to the diameter of the obstacle.

That same reference [17] also provides a solution to the errors caused by the higher distance between consecutive points in farther obstacles which results in smaller detected dimensions, as seen in Fig.3, where the modeled obstacle is considerably smaller than the real obstacle. To solve this problem, the measured diameter is passed through the time
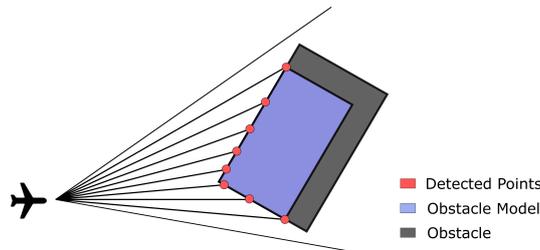
Figure 3: Obstacle reconstruction using a LIDAR.

filter

$$D_k = D_{k-1} + G(D_{meas} - D_{k-1})\,, \tag{1}$$

where G $(0 < G < 1)$ is the filter gain, D_k is the filtered diameter at instant t_k, D_{k-1}

is the filtered diameter at instant t_{k-1}, and D_{meas} is the measured dimension at instant t_k. The gain needs to be carefully selected as it impacts the speed of the variation of the dimensions. A small gain corresponds to a slow variation and it is preferable for noisy environments but not suitable for high relative speed objects. The gain can be determined by

$$G = 1 - \sqrt[n]{1 - p}, \tag{2}$$

where p corresponds to a fraction that represents the desired accuracy of the dimensions and n corresponds to the number of filter cycles required to get an accuracy of p.

Regarding the tracking phase, classical Kalman filters [18] were used, where the motion of detected obstacles is considered to be two-dimensional, linear and constant between consecutive scans. This simplification describes the state of the targets with an acceptable error, considering a high scanning frequency. This model assumes a LIDAR that only scans horizontally, but if the rangefinder was to be attached to a gimbal with two degrees of freedom, it would have to be extended to include the third dimension.

3.2 RADAR

To evaluate the system performance, the RADAR sensor was modeled in the context of the Sense and Avoid system. So, this model addresses the angular accuracy, update rate, range and FOV, rather than being a lower-level model that would deal with signal and environment modeling.

Assuming the RADAR sensor outputs the range, bearing and elevation of the detected obstacles, the state estimation becomes more complex than the estimation used in the LIDAR model, as these outputs are polar whereas the intruder dynamics are best expressed in rectangular coordinates. The chosen RADAR model was the converted measurement Kalman filter (CMKF) due to its simple implementation [19]. The following equations reflect a 2-D model, as used in the simulations presented, but it can easily be extended to 3-D.

The unbiased conversion [20] was used, as the standard conversion method gives biased inconsistent estimates for certain levels of cross-range measurement error owing to the nonlinear transformation of the noisy bearing. Using the unbiased conversion, modeling the measurement errors as Gaussian white noise, the compensation of the bias is multiplicative and the conversion is given by

$$\begin{aligned}
x_m^u &= \lambda_\alpha^{-1} r_m \cos(\alpha_m) \tag{3} \\
y_m^u &= \lambda_\alpha^{-1} r_m \sin(\alpha_m), \tag{4}
\end{aligned}$$

where (x_m^u, y_m^u) are the measurements converted to the Cartesian frame, r_m is the measured range, α_m is the measured azimuth and λ_α is the bias compensation factor expressed as

$$\lambda_\alpha = e^{-\sigma_\alpha^2/2}, \tag{5}$$

where σ_α is the standard deviation of the noise in the azimuth measurements.

The covariance matrix used in the Kalman Filter is given by

$$\mathbf{R}_u = \begin{bmatrix} var(x_m^u | r_m, \alpha_m) & cov(x_m^u, y_m^u | r_m, \alpha_m) \\ cov(x_m^u, y_m^u | r_m, \alpha_m) & var(y_m^u | r_m, \alpha_m) \end{bmatrix}, \tag{6}$$

with the details of the computation of these variances found in reference [20].

N. M. P. Alturas and A. C. Marta

4   MULTISENSOR DATA FUSION

When the sensing system is composed of multiple sensors, the input data provided by the sensors needs to be merged in some way. In this work, the weighted filter method [21] was used.

A weight is evaluated for each sensor, which is related to its reliability. The UAV needs to be equipped with reference data sensors, which provide information about the UAV state. IMUs and optical flow sensors are examples of reference data sensors used to evaluate the reliability of the main sensor data and help to decide between those sensors, based on the rationale that changes in distance to obstacles correspond to analogous changes in the UAV position. If the obstacles are stationary, then these variations should coincide. If the obstacles are moving, that information becomes corrupted, but it is unlikely that that motion corresponds better to randomly wrong measurements. The weights are then computed by comparing all possible sensor combinations of main data and reference data using a differential norm.

The obstacle distance measurement corresponding to the sensor with the lowest weight is selected in the current time instance of the sensing process, while the remaining are rejected based on the idea that they are corrupted. However, if the computed weights have a low variation, the sensor values are fused according to their weights.

5   OBSTACLE DETECTION AND AVOIDANCE ALGORITHMS

The collision detection and avoidance algorithm used in the subsequent simulations is based on the work developed in reference [22]. Each detected obstacle has several safety zones associated with it, which play a role in the obstacle detection phase as well as in the collision avoidance phase.

The obstacles were modeled as circles and, as such, the collision radius (R_c) defines the occurrence of collision if it is trespassed. The safety radius (R_s) defines the minimum distance that should be maintained between the UAV and the obstacle to take into account possible deviations and uncertainties that could happen during the detection and path prediction phases. The action radius (R_a) is the distance from which the replanned paths begins to depart from the original path given by the global planner. Lastly, the detection radius (R_d) represents the distance from which an obstacle is considered by this algorithm. The R_s should be similar to the UAV size; the R_a should be comparable to the R_s and the R_d corresponds to the range of the sensors used. A representation of the described safety zones is displayed in Fig.4.
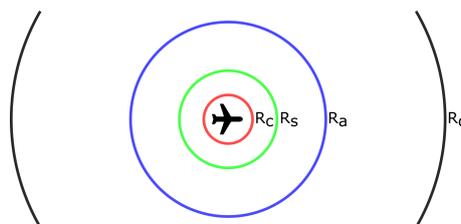
Figure 4: Representation of the safety zones around an obstacle.

N. M. P. Alturas and A. C. Marta

5.1 Geometric Collision Detection Method

The chosen collision detection method computes straight projections of the obstacles, considering future distances between the obstacles and the UAV [23]. As such, the resulting collision detection method consists of computing the closest point of approach (CPA) between the UAV and the target, assuming that both will maintain constant velocities and rectilinear paths. If the CPA distance is smaller than the safety radius R_s, an evasive maneuver must be performed, otherwise the obstacle is not considered a threat to the UAV.

In case of multiple collisions being detected, the obstacles are sorted by their time for collision t_{CPA}, so that the obstacles associated with possible earlier collisions are avoided first.

5.2 Potential Fields Method

To solve the local path planning problem, the Potential Fields approach is used, where the waypoints and obstacles are considered charged particles [24]. Considering this analogy, the waypoints generate an attractive field, the obstacles a repulsive field and the sum of all forces is used to generate the direction of motion.

The attractive potential is given by

$$\mathbf{f}_{at} = \alpha_{PF}\frac{P_c - P}{||P_c - P||} + (1 - \alpha_{PF})\frac{P_n - P_c}{||P_n - P_c||}, \tag{7}$$

where the first term is responsible for guiding the UAV to the nearest point of the global path and the second term is responsible for guiding the UAV to the next defined waypoint. P is the the UAV position, P_c is the closest point of the global path and P_n is the position of the next waypoint. The parameter α_{PF} is responsible for giving more or less predominance to each term. An example of a global path to a waypoint and its corresponding attractive potential field is represented in Fig.5 for $\alpha_{PF} = 0.7$.
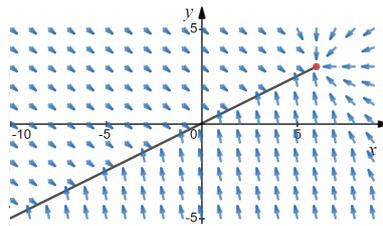
Figure 5: Attractive field for a linear path.

Using a simple repulsive potential to avoid obstacles is not feasible since that would lead to irregular motion around the obstacle. Instead, the potential associated to the obstacle is described by

$$\mathbf{f}_{rep} = \begin{cases} \infty\frac{\mathbf{d}_0}{||\mathbf{d}_0||} & \text{if } ||\mathbf{d}_0|| \leq R_c \\ S_m\mathbf{s} & \text{if } R_c < ||\mathbf{d}_0|| \leq R_s \\ S_m\frac{R_a - ||\mathbf{d}_0||}{R_a - R_s}\mathbf{s} & \text{if } R_s < ||\mathbf{d}_0|| \leq R_a \\ 0 & \text{if } ||\mathbf{d}_0|| \geq R_a \vee \theta \leq \theta_c \end{cases}. \tag{8}$$

This way, the field is different according to the distance between the obstacle and the UAV. If the UAV is in the collision zone, the field will be repulsive ($\mathbf{d}_0$ is the vector

pointing from the obstacle to the UAV) with infinite intensity. If it is in the safety zone, the field will have the direction of $\mathbf{s}$, a swirling term that makes the UAV maneuver in the correct direction, and the intensity of S_m, a constant to be defined depending on the velocity of the UAV. In the action zone, the field is similar to the previous one but with the addition of a gradient term that ensures the intensity of the field decreases linearly with the distance of the UAV to the obstacle until becoming null for $||\mathbf{d}_0|| = R_a$. Lastly, outside the action zone, the obstacle has no influence in the motion of the UAV, thus the field intensity is null. To avoid the UAV being trapped around the obstacle, the generated field needs to become zero once the obstacle is overcome. To achieve this, the angle θ between the desired direction of motion and the direction of the obstacle is also computed and the field becomes null if θ is smaller than a defined cut-off angle θ_c. A potential field associated with an obstacle is displayed in Fig.6 for $R_c = 2$, $R_s = 3$ and $R_a = 6$.
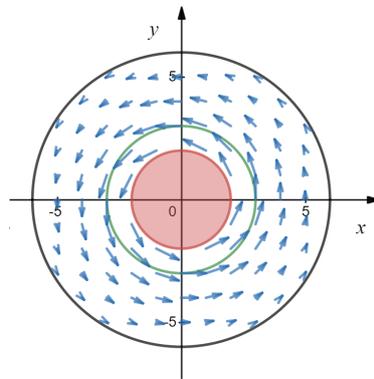
Figure 6: Repulsive field for an obstacle.

6 UAV MODEL DEFINITION

Since the S&A simulations were performed in a two-dimensional environment, the most important performance parameters to define are the UAV speed (V) and the maximum yaw rate that defines the angular velocity (ω) of its turns. Considering the Tekever AR4 described in Sec.1, the UAV speed considered varied between 8 m/s and 15 m/s. The faster it moves, the larger its yaw rate capability needs to be so that the obstacles can be effectively avoided. To prove this concept, a series of simulations were performed where the UAV was set in a head-on collision course with a moving obstacle with a 2 m radius and a safety radius of 2 m that moves with opposite velocity of the UAV. The UAV was equipped with a RADAR with 50° FOV and 120 m range. For each speed, the maximum yaw rate was decreased until the UAV could not perform the avoidance maneuver without breaching the safety zone R_s. The results are presented in Fig.7, where a linear dependency can be recognized.

To check the roll angles corresponding to the speeds and yaw rates obtained, the avoidance maneuver is approximated to a coordinate turn [25], where the turning is made at a constant vertical angular velocity with null lateral force. Considering no wind, the sideslip angle is almost null and the angle of attack and climb angle are very small, being the speed and angular velocity related by $tan(\phi) = \frac{\omega V}{g}$, where ϕ is the roll angle and g is the gravitational acceleration. Some of the obtained values are displayed in Tab.2. The roll angles obtained are acceptable considering the urgency of the maneuvers needed to

N. M. P. Alturas and A. C. Marta
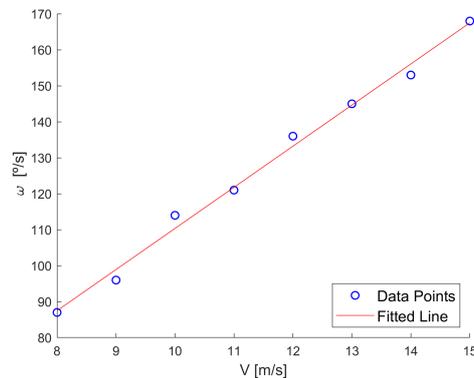
Figure 7: Minimum yaw rate capability to avoid obstacle safely for different speeds.

Table 2: Roll angles for each maneuver considering a coordinate turn.

V (m/s)	Yaw rate (°/s)	Roll Angle (°)
8	87	51.1
10	114	63.8
12	136	71.0
15	168	77.4

avoid obstacles. Since, for the highest speed of 15 m/s, the corresponding roll angle is high but achievable nonetheless, the maximum UAV yaw rate was set to 168°/s for the subsequent simulations.

As described in Sec. 3, using polar measurements and a Cartesian state space leads to inaccuracies when tracking the obstacles with a Kalman filter. To test the measurement error covariance matrix described in that section, the UAV was put in a head-on collision course, where the UAV is moving at 8 m/s and the obstacle is moving at 10 m/s. The UAV was equipped with a RADAR with the specifications of the Aerotenna μSharp Patch (100 m range, 50° FOV and 0.22 m accuracy). The noise was divided into a radial and an angular component, where both components were modeled as a zero-mean Gaussian noise, with the corresponding variance chosen so that 99.73% of the set would be within the accuracy range. The angular accuracy was considered at half the sensor range (50 m). To perform this test, one hundred simulations were performed for the unbiased conversion matrix, the standard conversion matrix and the identity matrix (as a control group), then, the average position errors were computed for both Cartesian coordinates. The root mean square (RMS) deviation for the three matrices for both spatial coordinates is listed in Tab.3. Only the first 250 scans were considered in the computations, so that the points where the obstacle is not detected anymore do not influence this metric, as the avoidance maneuver starts after this point. From Tab.3, one can conclude that using the standard conversion or the unbiased conversion result in very similar results. This may be due to the particular conditions of our study, where the sensor range and the noise variance are not very high. Despite the similar results, the unbiased conversion matrix was selected for all subsequent simulations.

N. M. P. Alturas and A. C. Marta

Table 3: Root mean square deviations for each of the used matrices.

RMS (m)	x axis	y axis
Standard conversion matrix	0.0165	0.0013
Unbiased conversion matrix	0.0163	0.0016
Identity matrix	0.5993	0.0009

7 SENSOR PARAMETRIC STUDIES

The response of the UAV to imminent collisions, when equipped with sensors with different parameters, is studied to verify whether the chosen sensors perform acceptably.

To study how the sensor range influences the response of the UAV to detected obstacles, the UAV was set in a head-on collision course with an obstacle animated with an incoming speed of 10 m/s with a radius of 2 m and a safety radius of 4 m. The UAV is traveling at 8 m/s and it is equipped with a RADAR sensor pointing forward with 50° FOV, though the type of sensor does not affect the results significantly. In Fig.8, the different collision avoidance trajectories with varying sensor ranges are presented. The obstacle
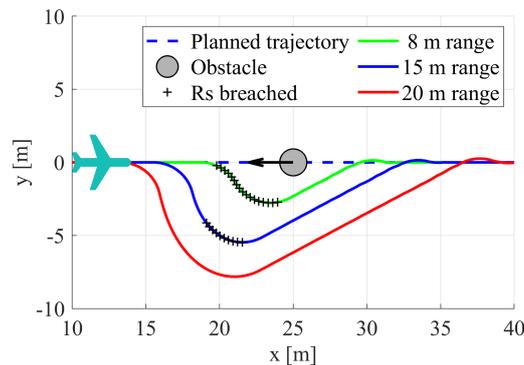
Figure 8: Avoidance trajectories for different RADAR ranges for head-on collision threat.

is always properly tracked and avoided, which results in similar tight maneuvers. If the UAV is equipped with a RADAR with a range of 8 m, it is already inside the action radius of the obstacle when the obstacle is detected. Then, it immediately initiates the avoidance maneuver but cannot avoid breaching the safety radius of the obstacle. For this particular scenario, sensing ranges greater than 20 m result in identical collision avoidance trajectories.

To test the effect of the FOV of the sensor on the avoidance capabilities of the UAV, the UAV was set in a 60° angled collision course with an obstacle moving at a speed of 12 m/s, while being equipped with a LIDAR that performs a measurement every half degree with a range of 100 m. The LIDAR gain from Eq.(2) also needs to be defined. For the sensor to reach 99% of the real dimensions, p is set to 0.99 and, to get this precision before the obstacle transverses 10% of the 100 m range, the filter needs to perform 20 iterations (n), considering the LIDAR is working at a 50 Hz frequency and assuming the obstacles can move at the same speed of the UAV, which results in a maximum relative speed of 30 m/s. Knowing n and p, the minimum gain to be used can be computed using

said equation, it being 0.2057. The responses of the UAV for different FOVs, when it is moving at a speed of 8 m/s, is displayed in Fig.9. For FOVs greater than 66°, the obstacle
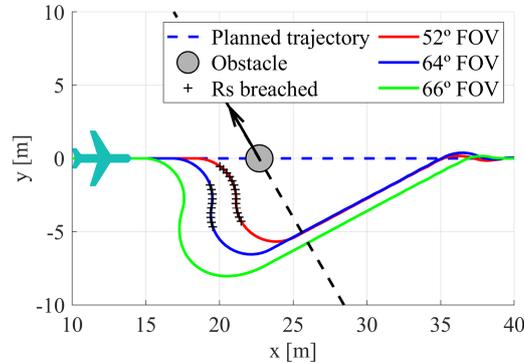
Figure 9: Avoidance trajectories for different LIDAR FOVs for angled collision threat.

is properly tracked in advance, which results in a proper safe maneuver. For a FOV of 52°, the obstacle is detected when it is already dangerously close to the UAV so the UAV breaches the safety radius for several points, despite avoiding a collision. Finally, for smaller FOVs, the UAV cannot avoid the collision because the available actuation time is simply too short for the evasion maneuver to be executed. This also covers the case of a fixed laser rangefinder (0° FOV) as the UAV detects the obstacle only when it is directly in front of it, which causes a quick breach of the safety radius. Because of the singular nature of this case, the obstacle velocity can only be tracked with a radial component and so, the obstacle is tracked as being in a head-on collision course with a small velocity.

The obstacles were avoided by the UAVs with different sensors, but the success of the maneuver depends on the approach angle of the obstacle.

Another important parameter studied, but not shown due to its length, was the approximation (relative) velocity between the UAV and the obstacle. As expected, to guarantee the S&A success, the required sensor range and/or FOV needs to be increased as the UAV speed increases, so that the detection occurs earlier, allowing an evasion time that is still smaller than the sensed collision time.

8 OPTIMAL SENSING SYSTEM

A study was made to determine the optimal sensor configuration, for four different sensor sets. To that end, fifty collision-leading scenarios were randomly generated, where the UAV speed randomly varied in the range [8,15] m/s and the obstacle parameters were randomly picked from Tab.4. Three examples of such scenarios can be seen in Fig.10.

Table 4: Data for randomly generated imminent collision scenarios.

# fixed obst.	# moving obst.	obst.radius	obst.speed	obst.direction
{0,1,2}	{0,1,2}	[0.5, 2] m	[5, 15] m/s	[0, 90] °

Then, a function $f(\beta)$, to be minimized dependent on the sensor orientation β was

N. M. P. Alturas and A. C. Marta

(a) Scenario #2   (b) Scenario #17   (c) Scenario #49
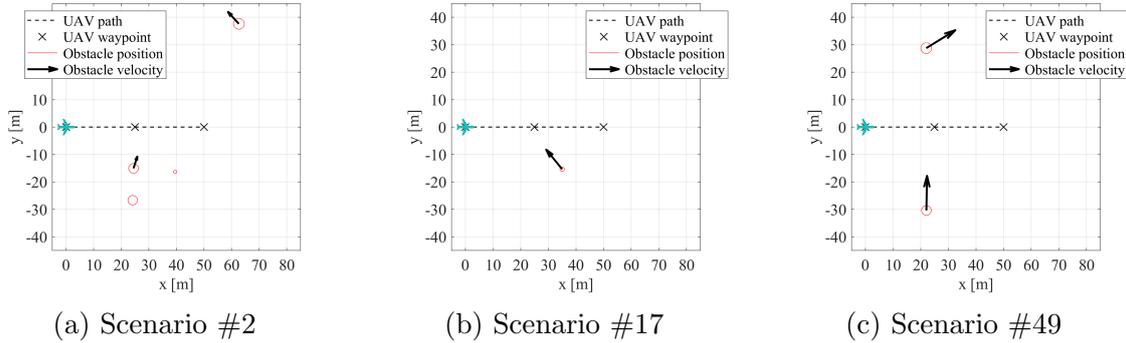
Figure 10: Examples of randomly generated collision-leading scenarios.

defined as

$$
f(\beta) = \sum_j \sum_i \left(-d_{min}(i) + \phi_1 |\max(R_s(i) - d_{min}(i), 0)|^2 + \phi_2 |\max(R_c(i) - d_{min}(i), 0)|^2 \right),
$$

(9)

where the first term drives the evasion maneuver to maximize the minimum distance d_{min} between the UAV and the obstacle i, the second term represents the penalty when the minimum distance violates the safety radius R_s $(d_{min} \leq R_s)$, and the last term represents the penalty when the minimum distance violates the obstacle collision radius R_c $(d_{min} \leq R_c)$. The metric accumulates not only for every obstacle i in each scenario but also for all scenarios j. The weights used were $\phi_1 = 10$ and $\phi_2 = 50$ to penalize more the collision cases than the close-call cases.

The metric defined in Eq.(9) is multi-modal and relatively noisy, as illustrated in Fig.11 for the particular sensor solution case using a pair of laser rangefinders with a 100 m range, symmetrically pointing forward with an angle β with respect to the UAV longitudinal axis.
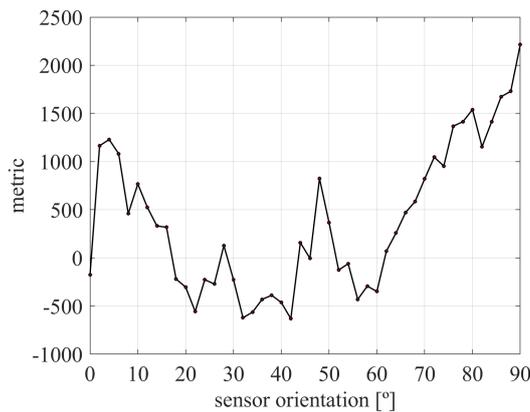
Figure 11: S&A metric as function of sensor orientation.

Given the identified nature of the S&A metric function, the Genetic Algorithm (GA) [26] was used to find its minimum. This is a gradient-free, population-based method, which, instead of working with a single solution candidate, deals with a set of solutions that are updated simultaneously from iteration to iteration, which increases the likelihood

of finding the global optimum. The problem was posed in standard form as

$$
\begin{aligned}
\text{Minimize} \quad & f(\beta) \\
\text{w.r.t.} \quad & \beta \\
\text{subject to} \quad & \beta_{min} < \beta < \beta_{max}\,,
\end{aligned}
\tag{10}
$$

where β_{min} and β_{max} are the lower and upper bounds of β, respectively, to be defined for each particular case.

Before performing the simulations, several optimization parameters needed to be defined: the initial population was set to be created with a uniform distribution; the crossover function was set to create 80% of the population in each generation; because the variables are bounded, the mutation function randomly generates directions that are adaptive with respect to the last successful or unsuccessful generation, where the chosen direction and step length satisfy the set bounds. The convergence criteria were set such that the global minimum was found in a timely but accurate manner: a function convergence of 10^{-3} was used with 10 stall generations, and a maximum of 50 generations prescribed. The population size was set to 30 individuals. These parameters were chosen following best practices [27].

8.1 Two Laser Rangefinder Solution

For a set of two laser sensors, the orientation of each sensor was bounded between $0°$ and $70°$ from the longitudinal axis, in the horizontal plane and, to simplify the problem, the two lasers were considered to have a symmetrical orientation, resulting in just one design variable. A sensing range of 100 m was adopted.

The GA optimization algorithm terminated after 18 generations due to average change in the fitness value less than the specified tolerance, corresponding to 536 function evaluations. The optimal sensor orientation was $39.3°$, which corresponds well with one of the approximate minimum shown in the preliminary study in Fig.11. The optimal two laser rangefinder sensor configuration is illustrated Fig.12.
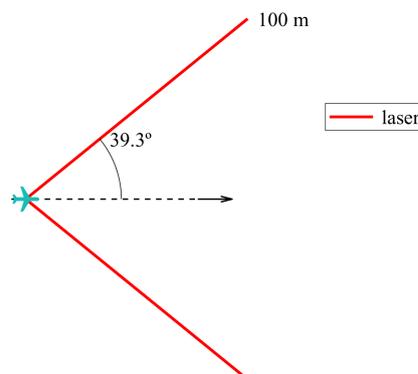
Figure 12: Optimal orientation for two laser rangefinder configuration.

A comparison of performance between the optimal orientation and a single laser pointing forward is presented in Tab.5, where a failure corresponds to a collision with an obstacle and a close call happens if the UAV breaches the safety radius of an obstacle. The optimal configuration results in just two collisions in all 50 scenarios. However, in

N. M. P. Alturas and A. C. Marta

52% of the scenarios, the safety radius of obstacles was breached because a UAV equipped only with two laser rangefinders is not capable of properly tracking the moving obstacles when collisions are imminent. Even though the optimal solution holds the same success

Table 5: Performance comparison for different orientations of two laser rangefinders.

Orientation	Metric	Failure	Close call	Success rate
0°	-176.5	2/50	36/50	96%
39.3°	-958.2	2/50	26/50	96%

rate (96%) as when only one laser rangefinder pointing forward is used, there is a considerable decrease of close calls, meaning that the likelihood of collisions in a real-scenario is significantly reduced. This is expected as more obstacles approaching from an angle can be detected ahead of the collision.

8.2 Two RADAR Solution

Like in the previous study, the two RADAR sensors were considered to be symmetrical about the UAV longitudinal axis, so that only one variable needed to be optimized. Given the previous findings, the orientation variable range was set between 0° and 70°. Each RADAR had a range of 120 m, an accuracy of 0.22 m and a FOV of 20°.

The expected result of this simulation would be a sensor orientation close to 10°, which would yield the same result as if the UAV were equipped with a single RADAR with double (40°) FOV. The optimizer halted after 14 generations due to average change in the fitness value less than the specified tolerance, corresponding to 424 function evaluations. The optimal RADAR orientation was 29.6°, as illustrated in Fig.13.
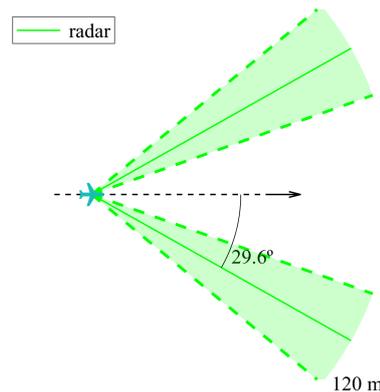
Figure 13: Optimal orientation for two RADAR configuration.

Table 6 compares the performance between the optimal orientation, a 10° orientation and a single RADAR pointing forward. Some failures that occur when the UAV is equipped with one RADAR pointing forward do not happen for the optimal solution because the obstacles that approached the UAV from a steep angle could now be detected, whereas they were undetectable by a single pointing forward RADAR solution.

The optimal solution did not have overlapping FOVs, which would increase the accuracy of the measurements through the data fusion algorithm. Given the set of scenarios

Table 6: Performance comparison for different orientations of two RADARs.

Orientation	Metric	Failure	Close call	Success rate
0°	2117.4	12/50	22/50	76%
10°	810.2	10/50	15/50	80%
29.6°	257.4	8/50	15/50	84%

used, having a wider effective FOV revealed to be a more favorable solution than the juxtapositioning, that would correspond to an orientation of 10°.

Compared to the previous case of laser sensors, these simulations demonstrated that the smaller accuracy of RADARs have a high impact on the obstacle tracking precision. Despite their wider FOV, this led to worse overall performance in terms of collisions but better performance in terms of close calls. It is fair to state that the RADAR accuracy is the more important parameter for precise collision avoidance but the RADAR FOV is more important for obstacle detection.

8.3 Two Laser Rangefinder and one RADAR Solution

This case involved three sensors: two laser rangefinders symmetrical about the UAV longitudinal axis, whose orientations were bonded between 0° and 70°; and one fixed RADAR pointing forward. Each sensor type had the same characteristics as the ones simulated in the previous two cases.

The optimizer converged in 11 generations, after 340 function evaluations. The optimal laser orientation was 38.3°, as illustrated in Fig.14. Again, the obtained optimal solution did not involve overlapping sensors.
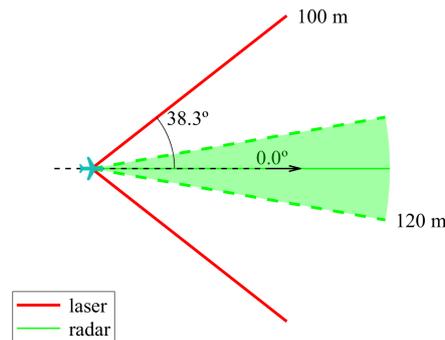
Figure 14: Optimal orientation for two laser rangefinder and one RADAR configuration.

In Tab.7, the optimal solution is compared in terms of S&A performance to the solutions that would result from a UAV being equipped with only one type of sensor, it being two symmetrical laser rangefinders with an orientation of 38.3° or a RADAR pointing forward.

Comparing the performance of each type of sensors separately, the pointing forward RADAR, perhaps due to its narrow FOV (20°), performed much poorly, with as many as 24% collisions, whereas the two lasers pointing sideways (@ 38.3% orientation) led to 8% collisions.

N. M. P. Alturas and A. C. Marta

Table 7: Performance comparison for optimal solutions using two lasers and one RADAR.

Sensors	Metric	Failure	Close call	Success rate
2 lasers @ 38.3°	-163.2	4/50	27/50	92%
1 RADAR @ 0°	2117.4	12/50	22/50	76%
2 lasers + 1 RADAR	-954.1	2/50	19/50	96%

As expected, it was the combined 2 lasers + 1 RADAR configuration that held considerably the best results, proving that multiple sensors are required to properly detect not only head-on but also angled approaching obstacles. Using this combination led to just 4% collisions and also the lowest instances of closed calls to obstacles.

8.4 Two RADAR and one Laser Rangefinder Solution

The last case consisted of two RADARs symmetrical about the UAV longitudinal axis and one fixed laser rangefinder pointing forward, under the same previous assumptions.

Coincidentally, this case converged in the same iterations as the previous case (11 generations with 340 function evaluations) The optimal RADAR orientation was 30.5°, as illustrated in Fig.15, which meant no sensor overlapping.
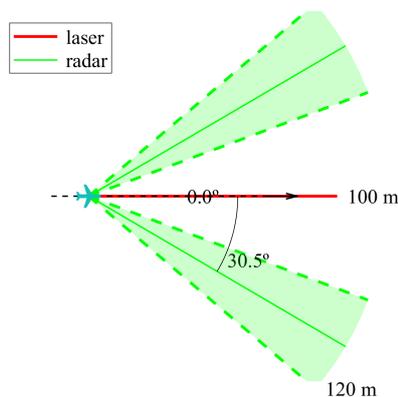
Figure 15: Optimal orientation for two RADARs and one laser rangefinder configuration.

Similarly to the previous case, the optimal solution is compared to the solutions of a UAV equipped with only one type of sensor, as summarized in Tab.8.

Table 8: Performance comparison for optimal solutions using two RADARs and one laser.

Sensors	Metric	Failure	Close call	Success rate
2 RADARs @ 30.5°	314.8	8/50	17/50	84%
1 laser @ 0°	-176.5	2/50	36/50	96%
2 RADARs + 1 laser	-1719.3	2/50	14/50	96%

Analyzing each type of sensors separately, the pointing forward laser led the fewer collisions but considerable more close calls compared to the two RADARs pointing 30.5% sideways. It was the combination of 2 RADARs + 1 laser that led to both lower failure and fewer close calls, due to the improved capability for obstacle detection.

8.5 Performance Comparison of the Different Sensor Sets

The performance of the four sensor configurations studied in this work, at optimal orientations, are summarized in Tab.9.

Table 9: Comparison of the optimal performance for the four different sensor sets studied.

Sensors	Metric	Failure	Close call	Success rate
2 lasers @ 39.3°	-958.2	2/50	26/50	96%
2 lasers @ 38.3°+ 1 RADAR @ 0°	-954.1	2/50	19/50	96%
2 RADARs @ 29.6°	257.4	8/50	15/50	84%
2 RADARs @ 30.5°+ 1 laser @ 0°	-1719.3	2/50	14/50	96%

For the set of scenarios tested, the laser rangefinder demonstrated better performance than the RADAR if only one sensor type is to be used. However, this is tightly dependent on the sensor characteristics, such as range, FOV and accuracy.

Among the four configurations tested, it was the two RADAR and 1 laser rangefinder that not only produced the least collisions but also led to the least close calls. Unexpectedly, the combination of different type of sensors revealed more advantageous. From these findings, it is expected that increasing even more the number of sensors would lead to even better performance, thought at a higher hardware cost.

9 CONCLUSIONS

This work focused on the first stage of the S&A phase, responsible for the acquisition of the necessary information that allows the vehicle to detect threatening situations. Our goal was to study simple, and yet effective, safety enhancing obstacle detection solutions for fixed-wing mini UAVs.

A selection of sensors in terms of range, FOV, accuracy and cost, led to the conclusion that laser/LIDARs and RADARs are the most adequate to this particular application, in detriment of ultrasound, and stereo vision and ADS-B sensors. Simulation models were developed for each of the relevant sensors, that were then integrated into an avoidance system. For laser rangefinders and LIDARs, classic Kalman filters were sufficient to guarantee adequate tracking, but for the RADARs, a Converted Measurement Kalman Filter with unbiased conversion was required. At a decision level, the weighted filter technique was selected for the data fusion from different redundant sensors due to its simplicity and effectiveness.

Having modeled the sensors, several parametric studies were made, where the impact of the range and field of view of the vehicle in the avoidance of obstacles from predetermined scenarios was made clear. From these simulations, the specifications of the studied sensors were verified as more than acceptable for avoiding obstacles at the considered speed range.

Additionally, some optimization studies were conducted to determine the best orientation of the sensors on the UAV for different sets of sensors. The optimization process was accomplished by using a genetic algorithm to minimize a metric related to the minimum distance to the obstacles, with penalties in case of safety radius breach and collisions. It is clear that the required range depends on the relative speed towards the obstacles. Provided that the sensor ranges are sufficiently large, their FOV becomes the most relevant parameter so that the UAV surroundings can be properly scanned for obstacles.

Overall, the developed sensor configurations provided very satisfactory performance for obstacle detection for fixed-wing mini UAVs in the simulated environment.

The best sensor configuration will always depend on the UAV performance and the minimum acceptable obstacle S&A success rate. UAVs with high maneuverability or low speeds do not require very advanced sensing systems but if the allowed S&A failure rate is to be kept very low, then the opposite is holds.

Future work includes the study of other possible combination of sensors and the implementation and validation of the simulated optimal solutions in both terrestrial and aerial test vehicles.

REFERENCES

[1] P. Finnegan. *2019 World Civil Unmanned Aerial Systems Market Profile & Forecast*. Teal Group Corporation, Aug. 2019.

[2] K. Dalamagkidis. Classification of UAVs. In K. P. Valavanis and G. J. Vachtsevanos, editors, *Handbook of Unmanned Aerial Vehicles*, pages 83–91. Springer Netherlands, 2015. doi:10.1007/978-90-481-9707-1_94.

[3] TEKEVER AR4. `http://uas.tekever.com/ar4-evo//`. Accessed: 24-11-2020.

[4] C. Kanellakis and G. Nikolakopoulos. Survey on computer vision for uavs: Current developments and trends. *J Intell Robot Syst*, 87:141—168, 2017. doi:10.1007/s10846-017-0483-z.

[5] L. Jian and L. Xiao-min. Vision-based navigation and obstacle detection for uav. In *2011 International Conference on Electronics, Communications and Control (ICECC)*, pages 1771–1774, 2011. doi:10.1109/ICECC.2011.6066586.

[6] S. Saha, A. Natraj, and S. Waharte. A real-time monocular vision-based frontal obstacle detection and avoidance for low cost uavs in gps denied environment. In *2014 IEEE International Conference on Aerospace Electronics and Remote Sensing Technology*, pages 189–195, 2014. doi:10.1109/ICARES.2014.7024382.

[7] Z. Chen, X. Luo, and B. Dai. Design of obstacle avoidance system for micro-uav based on binocular vision. In *2017 International Conference on Industrial Informatics - Computing Technology, Intelligent Technology, Industrial Information Integration (ICIICII)*, pages 67–70, 2017. doi:10.1109/ICIICII.2017.87.

[8] M. Odelga, P. Stegagno, and H. H. Bülthoff. Obstacle detection, tracking and avoidance for a teleoperated uav. In *2016 IEEE International Conference on Robotics and Automation (ICRA)*, pages 2984–2990, 2016. doi:10.1109/ICRA.2016.7487464.

[9] N. Gageik, P. Benz, and S. Montenegro. Obstacle detection and collision avoidance for a UAV with complementary low-cost sensors. *IEEE Access*, 3:599–609, 2015. doi:10.1109/ACCESS.2015.2432455.

[10] H. Yu, F. Zhang, P. Huang, C. Wang, and L. Yuanhao. Autonomous obstacle avoidance for uav based on fusion of radar and monocular camera. In *2020 IEEE/RSJ International Conference on Intelligent Robots and Systems (IROS)*, pages 5954–5961, 2020. doi:10.1109/IROS45743.2020.9341432.

[11] A. Carrio, Y. Lin, S. Saripalli, and P. Campoy. Obstacle detection system for small uavs using ads-b and thermal imaging. *J Intell Robot Syst*, 88:583—595, 2017. doi:10.1007/s10846-017-0529-2.

[12] *PING-RX ADS-B Dual Receiver*. uAvionix, 2019.

[13] *LW20 / SF20 LiDAR sensor Product manual*. Lightware, 2018. Rev 9.

[14] *μSharp Patch Collision Avoidance Radar*. Aerotenna, 2018.

[15] *Intel RealSenseTM D400 Series (DS5) Product Family*. Intel, 2018. Rev 001.

[16] *MB1242 Datasheet*. MaxBotix, 2012.

[17] F. Fayad and V. Cherfaoui. Tracking objects using a laser scanner in driving situation based on modeling target shape. In *2007 IEEE Intelligent Vehicles Symposium*, pages 44–49, June 2007. doi:10.1109/IVS.2007.4290089.

[18] M. S. Grewal, A. P. Andrews, and C. G. Bartone. Kalman filtering. pages 355–417. Wiley Telecom, 2020.

[19] D. Lerro and Y. Bar-Shalom. Tracking with debiased consistent converted measurements versus EKF. *IEEE Transactions on Aerospace and Electronic Systems*, 29(3): 1015–1022, July 1993. doi:10.1109/7.220948.

[20] M. Longbin, S. Xiaoquan, Z. Yiyu, S. Z. Kang, and Y. Bar-Shalom. Unbiased converted measurements for tracking. *IEEE Transactions on Aerospace and Electronic Systems*, 34(3):1023–1027, 1998. doi:10.1109/7.705921.

[21] N. Gageik, P. Benz, and S. Montenegro. Obstacle detection and collision avoidance for a UAV with complementary low-cost sensors. *IEEE Access*, 3:599–609, May 2015. doi:10.1109/ACCESS.2015.2432455.

[22] J. Alves. Path planning and collision avoidance algorithms for small RPAS. Master's thesis, Instituto Superior Técnico, June 2017.

[23] B. Albaker and N. Rahim. Unmanned aircraft collision detection and resolution: Concept and survey. In *5th IEEE Conference on Industrial Electronics and Applications*, pages 248–253, June 2010. doi:10.1109/ICIEA.2010.5516808.

[24] A. Alexopoulos, A. Kandil, P. Orzechowski, and E. Badreddin. A comparative study of collision avoidance techniques for unmanned aerial vehicles. In *2013 IEEE International Conference on Systems, Man, and Cybernetics*, page 1969–1974, Oct. 2013. doi:10.1109/SMC.2013.338.

[25] B. Etkin and L. D. Reid. *Dynamics of flight*, volume 2. Wiley New York, 3rd edition, 1959.

[26] M. J. Kochenderfer and T. A. Wheeler. *Algorithms for Optimization*. MIT Press, 2019. ISBN 9780262039420.

[27] Mathworks ®. Global optimization toolbox ™: User's guide (r2020b). `https://www.mathworks.com/help/pdf_doc/gads/gads.pdf`, 2020. Accessed: 29-12-2020.

GLOBAL MODEL OF AIRCRAFT DESIGN: FROM PERFORMANCE REQUIREMENTS TOWARDS ARCHITECTURES OPTIMIZATION

Carlos GARCIA-RUBIO[1*], Kittinan THANISSARANON[1*], Jean-Charles CHAUDEMAR[2], Nathalie BARTOLI[3] and Thierry LEFEBVRE[3]

1: ISAE-SUPAERO, Université de Toulouse
Toulouse, France
{Carlos.Garcia-Rubio,Kittinan.Thanissaranon}@student.isae-supaero.fr

2: ISAE-SUPAERO, Université de Toulouse
Toulouse, France
jean-charles.chaudemar@isae-supaero.fr

3: ONERA/DTIS, Université de Toulouse
Toulouse, France
{Nathalie.Bartoli,Thierry.Lefebvre}@onera.fr

Abstract. *Systems engineering is a transdisciplinary approach that seeks the successful realisation of a system. In order to reach that, it is necessary to satisfy a series of needs and stakeholders, which have to be defined as a group of requirements to be fulfilled. Design approaches such as MDAO, MBSE, and MBSA have been created to help better designing aircraft in different aspects. However, there has never been an aircraft design method which combines all the mentioned design approaches and that, nowadays, has an increasing interest in the industry. Therefore, the paper aim is to produce aircraft design tools and methodology which link all the three design approaches together by using a surveillance UAV as a study case. As a part of the MDAO-MBSE global project, a MDAO model has been developed using a web application (WhatsOpt) and a MDAO platform (OpenMDAO) on Python, while the tool considered to develop the MBSE model is Eclipse Papyrus, a powerful tool that allows to use XML for export their models. Some promising results show the coupling between MDAO and MBSE based on XML file exchange.*

Keywords: MBSE, MDAO, SysML, XML

C. Garcia-Rubio, K. Thanissaranon, J.-C. Chaudemar, N. Bartoli and T. Lefebvre

1   INTRODUCTION

Aircraft design is a complex process that involves several fields of study. Currently, there are different aircraft design approaches which help engineers designing aircraft more effectively. Approaches which are widely and separately used are MDAO (Multidisciplinary Design Analysis and Optimization process), MBSE (Model-Based Systems Engineering), and MBSA (Model-Based Safety Assessment). MDAO focuses on optimizing and obtaining design parameters to achieve certain design objectives. MBSE focuses on the traceability of design requirements and the consistency of information throughout all engineering processes. Finally, MBSA focuses on the safety analysis of a system.

Up to today, there has not been work which combines all the three design approaches together to effectively design an aircraft. Given that, the goal of this study is to identify and obtain a framework which includes MDAO, MBSE, and MBSA to optimally design an aircraft while meeting all the safety objectives by using a surveillance UAV as a studying subject. Given that, this project was initially divided into two parts: MDAO-MBSE part and MBSA-MBSE part. This reports focuses on the MDAO-MBSE part. Firstly, a brief explanation of MDAO and MBSE is provided along with the study-subject UAV and the developed MDAO model from the work earlier. Then, the investigation method used for developing MBSE models is given. The investigation method includes requirements implementation on MBSE, MDAO implementation on Eclipse Papyrus, and MDAO-MBSE connection. After that, the result and analysis obtained from the investigation method are explained. Finally, the conclusion of the project along with the perspectives for future work are provided.

2   MDAO AND MBSE MODELS AND CONTEXT

2.1   MDAO and XDSM

Since designing an aircraft involves several disciplines such as aerodynamics, structure, propulsion, and performance, any design changes in one discipline certainly will affect other disciplines. MDAO allows the possibility to obtain the optimized value of the desired parameters in order to minimize some quantities of interest such as fuel consumption or weight with respect to some constraints. MDAO models are usually displayed in a graphical representation known as eXtended Design Structure Matrix (XDSM). Figure 1 shows an example of an XDSM of a system that has four disciplines.

While green rectangle represents each discipline, grey parallelogram represents response variables which are being transferred and calculated among the disciplines. White parallelogram represents design variables which are initially introduced to the system. Finally, the round rectangular shape represents driver which distributes variables and performs the optimization calculation.

C. Garcia-Rubio, K. Thanissaranon, J.-C. Chaudemar, N. Bartoli and T. Lefebvre
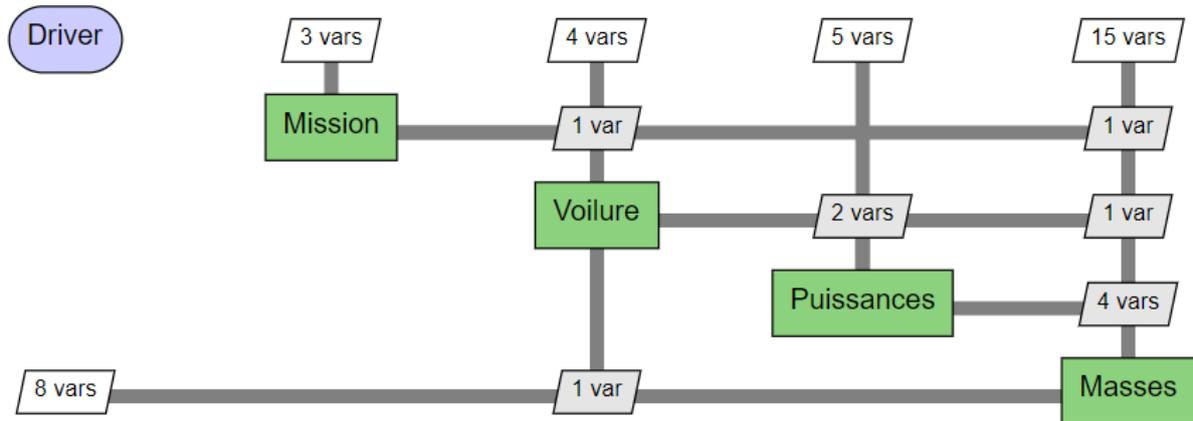
Figure 1: MDAO Mock-up model [1].

Within this project, there are two tools that were used to obtain the MDAO model of a UAV. The first tool is OpenMDAO [2]. It is an opensource platform on Python that is capable of performing an optimization calculation. The second tool is WhatsOpt [3]. It is a web-based tool that allows users to graphically construct an XDSM [4] representation, which can be exported directly from a web browser to the computer as Python files. The exported files are to be further coded on Python along with the previously mentioned OpenMDAO platform.

2.2 MBSE

The more complex a system is, the more difficult to trace down the design requirements and also to ensure that the information is consistent among each design process. The MBSE approach replaces the previous document-based approach.

Initially, MBSE used to propose methods close to software engineering to visualize the design of a system using UML (Unified Modeling Language). Then, due to the absence of specific MBSE concepts, SysML (System Modeling Language), an extension of the UML, was developed [5]. SysML provides nine different kinds of diagrams displaying different perspectives of a system. Within the scope of this project, Requirements diagram and Block Definition Diagram (BDD) were mainly used.

Apart from allowing the visualization of relationship among each requirement, Requirements diagram also enables the traceability of requirements to other elements in the system (i.e., BDD) [6]. The main elements in the diagram includes Requirement and Requirements relationship. Requirement is basically a block that has two string attributes: "id" and "text" to tag and accommodate a requirement respectively. Requirements relationships show the relationships between each requirement for example: "Derive" and "Refine". While "Derive" emphasizes that a requirement is further expanded, "Refine" means a requirement is further clarified.

BDD provides the capability to visualize the structural architecture of a system. The important elements that were used within the scope of this project are Block, Port and ItemFlow. A Block contains Property which is practically its attribute. Port can be used on each Block to specify the Property being exchanged among the Blocks. Lastly, ItemFlow specifies the path of the Property exchange between Ports.

Within this project, Eclipse Papyrus with SysML 1.6 was used to house the MBSE

models. It is an opensource tool that supports UML/SysML modeling with the capability to have a semantic variation to customize diagrams and Object Constraint Language (OCL) to implement a consistency validation process.

Study case

To develop a framework that includes the MDAO, MBSE, and MBSA model, a study subject was needed. Inspired by Delair's DT26 [7], missions and certain parameters of the study subject were referred to.

2.3   Context and key issues

Initially, the MDAO model was first developed. Starting with a simple UAV design developed by ONERA [1] as seen in Fig. 1, there are 4 main disciplines: Mission, Voilure, Puissances, and Masses. With the given model, the Voilure discipline was redesigned and renamed to be called Aero. Then the Fuselage and the Empennage disciplines were also added as seen in Fig. 2.
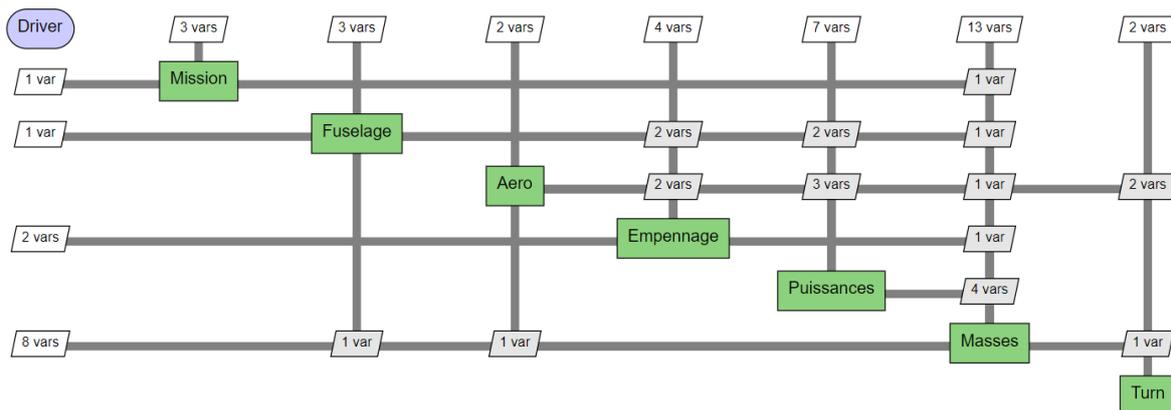
Figure 2: Final MDAO model from last year research.

Each discipline has inputs, outputs, and equations that calculate different design parameters. Section below briefly explains each discipline. Note that the detailed explanation was thoroughly explained in previous reports [8], [9].

Mission

The Mission discipline calculates the vit_max from the defined vit_eco and vit_vent. Then it uses the simple velocity equation to calculate the duree_crois.

Fuselage

The Fuselage discipline calculates the area_fus by assuming that the shape of the fuselage is a cylinder. Then with the assumption of skin friction drag as a majority of drag, Cx_fus is calculated by combining drag from the laminar and turbulent area. Finally, masse_fuselage is calculated from the mass approximation equation [10].

C. Garcia-Rubio, K. Thanissaranon, J.-C. Chaudemar, N. Bartoli and T. Lefebvre

Aero

The Aero discipline calculates the wing parameter such as chord, surface, and Cz using the OpenAeroStruct library and constraint inputs like vit_eco and wing_span.

Empennage

The Empennage discipline calculates S_HT and S_VT from the tail volume equation [11] with the tail volume constant [11]. Also, masse_empenn is calculated from the mass approximation equation [10].

Puissances

The Puissances discipline calculates the puissance_crois_eco and puissance_crois_max from Cx_fus, area_fus, Cx, Cz and surface with the basic drag coefficient and velocity equation.

Masses

The Masses discipline calculates the mass of motor and turbine according to the power needed. It also calculates the empennage mass from the calculated surface area using the historical data. Finally, it combines mass of every component and obtains mtow.

Turn

The Turn discipline calculates the bank angle and the turn radius from the aircraft parameters such as vit_eco, mtow, and surface using the steady turn assumption. The importance of this discipline is that the operating range is constrained by regulations and requirements.

2.4 Aims and objectives

Recall the aim of this project to successfully connect the MDAO and MBSE models together. This means the realization of a design framework which optimizes system parameters (MDAO) while ensuring the consistency and fulfilling all requirements (MBSE).

Since the MDAO part was well established, the steps to be further achieved are to obtain the MBSE part and to identify the connection between MDAO and MBSE. Given that the following objectives were planned.

1. To identify all related UAV's stakeholders and requirements

2. To document all the requirements onto MBSE

3. To establish a connection between MBSE and MDAO

4. To establish information transferring method between MDAO and MBSE

C. Garcia-Rubio, K. Thanissaranon, J.-C. Chaudemar, N. Bartoli and T. Lefebvre

3   INVESTIGATION METHOD

The principal objective of this project is to be able to link the requirements of the surveillance UAV defined in the early stages of any system design (and refined in MBSE) with the design model and its optimization in MDAO as it has been explained. In order to achieve this connection, three steps should be performed: 1) definition of the system requirements and its refining in MBSE, 2) preparation for implementing the MDAO model in Eclipse Papyrus (MBSE) and, 3) the connection between models using XML language.

3.1   Requirements implementation in MBSE

The requirements definition is a process done previously to the architecture design. It gathers all the needs from the stakeholders and transforms them into specific, measurable, achievable and traceable requirements which must be fulfilled by the system after its development.

The first step is, thus, the identification of the different stakeholders involved on the design and use of the UAV and its interest and priority in the system development as it can be seen in Table 1. This will allow to define all the needs and technical requirements of the system which are displayed in [12].

Table 1: Stakeholders list.

ID	Stakeholder	Interest	Flexibility/Priority
STH.01	Shareholders	Profit/Funding	Mandatory / Medium
STH.02	Manufacturer	Design/Performance/Cost/Delay	Mandatory / High
STH.03	Operator	Quality/Performance/Design	Mandatory / High
STH.04	Customer	Quality/Delay/Services	Mandatory / High
STH.05	G.F	Regulation/Employment	Not applicable / Low
STH.05.1	D.G.A	Legislation/Safety	Mandatory / High
STH.06	Local community	Employment/environmental issues	Optional / Medium
STH.07	Environmental association	Pollution/Regulation	Optional / Medium

Profile definition and Requirement diagram in SysML

Once all the requirements are defined, the next step is to introduce them in the MBSE model. In order to do so, Eclipse Papyrus allows to gathered all of them in the Requirement diagram available in the SysML package. This diagram represents the requirements in blocks which contains a descriptive text of them and an identifying id. However, Papyrus and SysML give the possibility of refining this diagram in two different ways.

The first one is creating a stereotyping profile in Papyrus. The creation method of the profile is explained in [12] and it is displayed in Fig. 3. It allows to introduce more information in the requirement block, such as the type (performance, operational context, functional, design or safety requirement), the source (if the requirement was found in any special documentation), the stakeholder's involved and a verified attribute.

The second way is to connect the requirements using the diagram in SysML. Requirement diagram has some features that help to establish links between the requirements, which are generally used to clarify their hierarchy, as it can be seen in Fig. 4. For this project, three different types of link are used: *refine*, used when the client requirement add information more concrete than the one contained in the supplier requirement; *derive*,

C. Garcia-Rubio, K. Thanissaranon, J.-C. Chaudemar, N. Bartoli and T. Lefebvre

which conveys that the requirement at the client end is derived from the requirement at the supplier end (e.g. when the client requirement imposes a constraint in a subsystem derived from a system specified in the supplier); and *copy*, when the text in the client is a read-only copy of the text in the supplier.
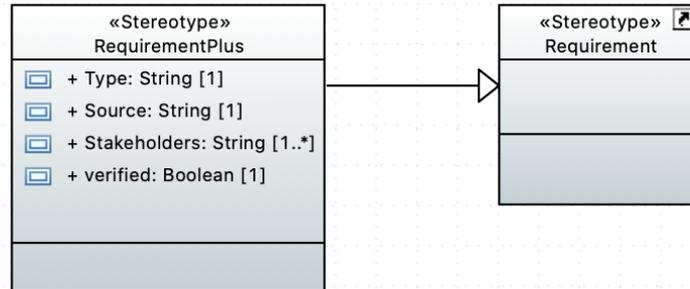
Figure 3: Requirements profile.

Finally, all the requirements have been organised in different packages that represent their type, so it is easier to access the diagram. Moreover, for the MDAO connection, the requirements that will be fulfill by the MDAO process are more related, obviously, to the design and performance package, which is decomposed in three other packages (Mission, landing and take-off performance). SysML also generates automatically requirement tables with all the refined information.
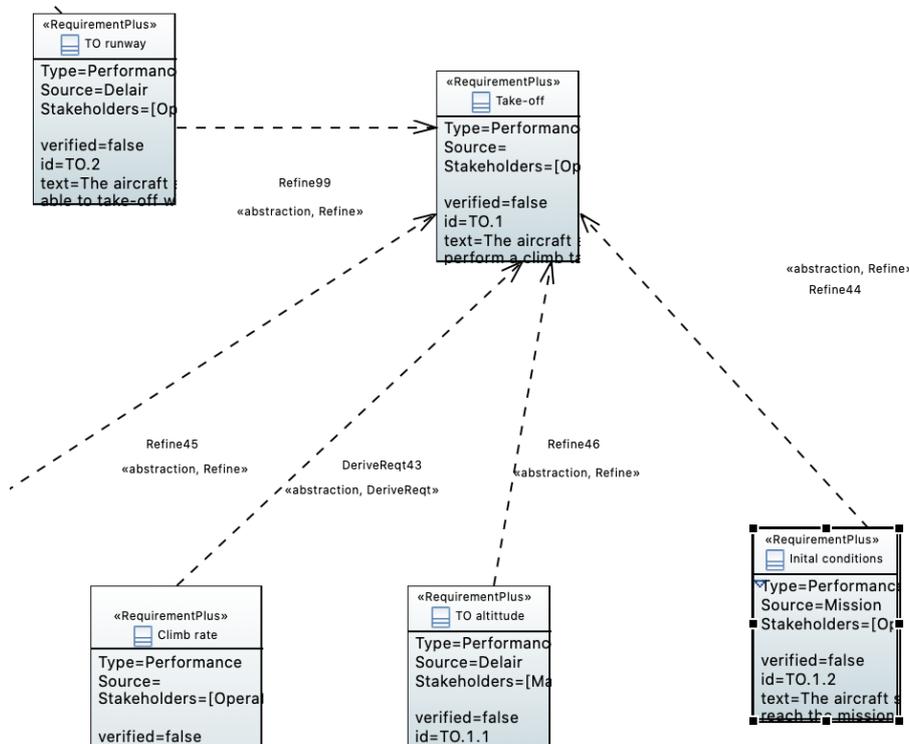
Figure 4: Requirements diagram with refine and derive connections.

C. Garcia-Rubio, K. Thanissaranon, J.-C. Chaudemar, N. Bartoli and T. Lefebvre

Requirement connection with MDAO

Defining a connection between the requirements and the MDAO model is the main reason for starting this research process and, thereby, it is the last objective to accomplish. The great interest in this connection is due to the reduction in the time effort of the design process as, nowadays, there is no optimized process to link the requirements that may be take into account or be satisfied in the analysis and optimization design. Thus, these parts are performed independently and a connection will lead to a more efficient process.

Although this connection can only been established once the MDAO model has been implemented in Papyrus, it is important to highlight in this section that the Requirement diagram has a type of link called *satisfied*, which refers to a block defined in the BDD (Block Definition Diagram) from SysML, that is identified as the party responsible for fulfilling the requirement. As it will be explained later, the MDAO model will be reproduced in the MBSE using this BDD diagram. By doing it, the disciplines from MDAO are defined as blocks, which can be linked with those requirements they will be in charge of by using the *satisfied* connection. In this way, it is possible to fulfill all the design and performance requirements identified prior to the design process. An example can be seen in Fig. 5, where the discipline Mission satisfies the cruise speed limit that have been taken into account in the MDAO model.
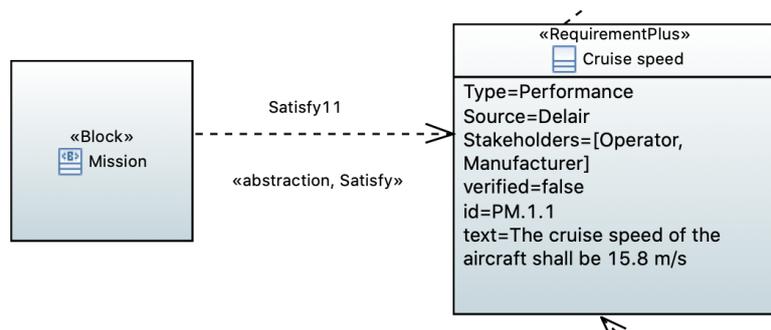
Figure 5: Satisfy connection between block and requirement.

3.2 MDAO implementation on Eclipse Papyrus

The MDAO representation on MBSE was thought to be necessary because it would allow the developed MDAO to exist right inside MBSE model. This allows the previously developed requirements diagram to be directly connected to the (representation of) MDAO model. To represent the MDAO model on Papyrus (MBSE platform), BDD was used. As Block is a representation of Discipline, Property (Attribute) within each Block represents variables. Furthermore, Port and ItemFlow were used to represent the variables exchange among disciplines. However, the basic BDD of SysML alone is not capable of wholly representing the MDAO model. Given that, a profile was created to further extend the BDD.

Profile definition

Initially, the meta-class Class is extended by a stereotype called Discipline as seen in the top left of Fig. 6. This is to have each discipline in the MDAO model to exist in the BDD.

C. Garcia-Rubio, K. Thanissaranon, J.-C. Chaudemar, N. Bartoli and T. Lefebvre

Secondly, the meta-class Property of a Block is extended by a stereotype called "DisciplineVariable" as seen in the middle of Fig. 6. The DisciplineVariable stereotype has two attributes to better represent the MDAO variables. The two attributes are "Description" and "Unit". While "Description" was thought to be used for referencing purpose, "Unit" will directly represent each variable's unit. With this extension, each variable can be represented with a Block's Property.

Thirdly, the meta-class Port is extended by a stereotype called "Artefact". This extension of Port has two attributes: "direction" and "VariableTransfered". The "direction" attribute has a specially defined Enumeration Type called "Direction" to specify whether the Port receives (input) or sends (output) DisciplineVariable. The VariableTransfered specifies which DisciplineVariable going through a Port. Note that the "Association" relation was used to specify that the VariableTransfered attribute refers to the DisciplineVariable stereotype. With this extension, the variables exchange in the MDAO model can be represented.
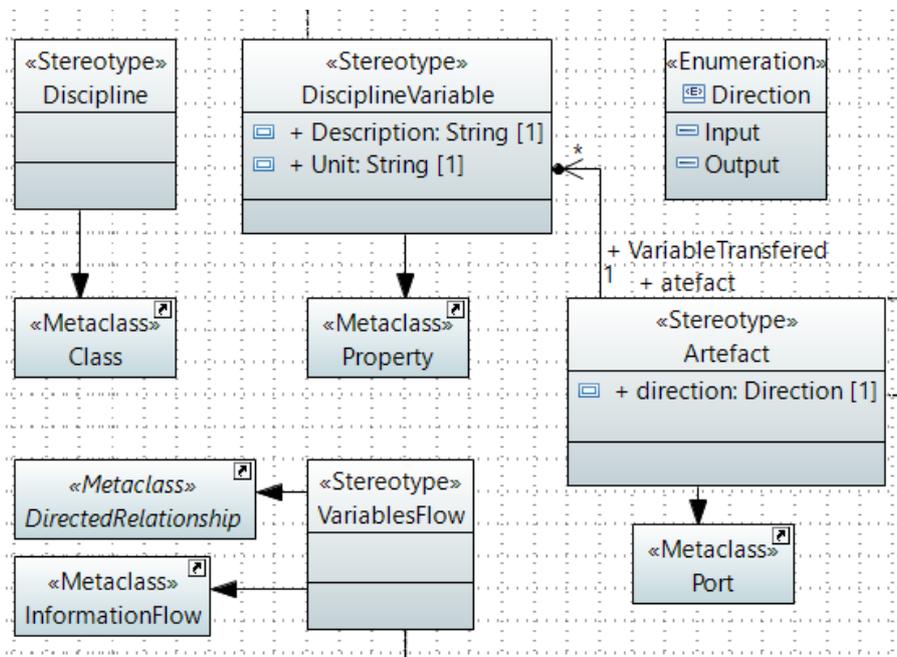
Figure 6: Profile diagram.

Lastly, the meta-class DirectedRelationship and InformationFlow were extended by a stereotype called VariablesFlow. Basically, this was done so that the ItemFlow entity in the BDD can have more than one variable and to accommodate some constraints as it is mentioned in the following section.

OCL constraint language

As it is defined in the OMG documentation [13], Object Constraint Language (OCL) is a formal language used to describe expressions on UML models and, thus, it can be extended to SysML models (as in Papyrus SysML packages stereotypes UML meta-classes). The OCL constraints can be applied to any kind of meta-class, Stereotype, operation, guard, message, action or attribute, which will be the Context of the constraint defined [14], [15].

C. Garcia-Rubio, K. Thanissaranon, J.-C. Chaudemar, N. Bartoli and T. Lefebvre

OCL can be used for several purposes, but for this project the common use is for specifying invariants for the Stereotypes created in the profile and for specifying target (sets) for messages. Whenever a specific OCL constraint is defined, it imposes a boolean condition stated by the invariant contained in it and affects only the Context. Papyrus incorporates a tool for performing the OCL validation and if any condition is not satisfied, this validation will give an error.

The main idea is to use OCL as a validation method to implement the MDAO models to Papyrus. As it is explained later, the BDD diagram used to duplicate the MDAO model in MBSE can use the profile previously defined and, consequently, any OCL constraint contained in it. Therefore, any MDAO model can be implemented in Papyrus and use this profile and, moreover, any modification on an existing one will not affect the OCL validation (as long as all the invariants are still satisfied). This provides a versatile profile capable of being adapted to any model and with a validation process already incorporated.

The OCL constraints added to the profile are used to validate the BDD diagram consistency with the MDAO model and, additionally, they provide a guide for building this diagram that will be of help to establish the connection between MBSE and MDAO when using XML. Six OCL constraints were added to the model, the three first ones have *Artefact* as Context and the last three, *VariablesFlow*:

- *PortType*: verifies that the port is typed with the classifier (the *Discipline* block) of the variables contained in it.

- *PortVariableName* (represented in Fig. 7 and *PortVariableType*: check that the variables contained in a port of a Discipline are also contained in the Discipline with the same name and type.

- *FlowInput*: used to verify that the set of variables in a *VariableFlow* sent between ports is exactly the same as the set of variables in the Input port.

- *FlowOutput*: check that the set of variables in a *VariableFlow* is included in the set of variables of the Output port. The reason for not declaring same sets as done with the Input port is that all the variables sent from a Discipline, which may share variables with more than one Discipline, are contained in the same Output port.

- *InputOutput*: similar to the previous one, but between the Input and the Output port connected with a *VariableFlow*.
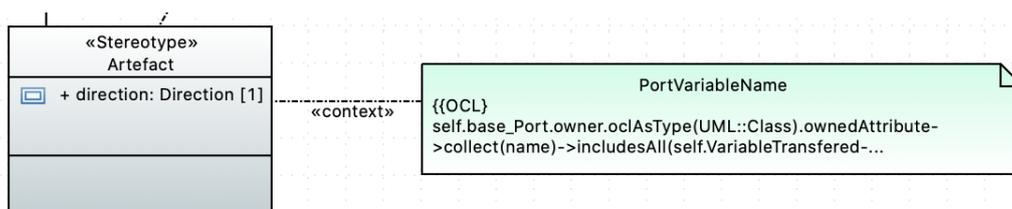
Figure 7: OCL constraint (*PortVariableName*).

All these constraints will be taken into account for building the BDD diagram and the XML file that will be explained in the last part of the investigation methods. Nevertheless, more constraints can be added to improve the profile and the validation process,

C. Garcia-Rubio, K. Thanissaranon, J.-C. Chaudemar, N. Bartoli and T. Lefebvre

or even constraints coming from the requirements for the computation of the value of some discipline variables (e.g. a limit value that cannot be exceeded for a special kind of variable). It is necessary to remark that Papyrus gave some problems when trying to define the OCL constraints in the SysML diagrams. Consequently, for the last example, the constraint should be apply on the discipline variable stereotype from the profile and referring to its default value, such as follows:

```
if self.base_Property.defaultValue.oclIsTypeOf(UML::LiteralReal) then
self.base_Property.defaultValue.oclAsType(UML::LiteralReal).value<20.0
else
true
endif
```

Listing 1: OCL constraint for discipline variable value

The constraint in List 1 is applied to every discipline variable whose default value has been defined as a LiteralReal and checks that the value given is lower than 20. This is a general example, but there are several ways to delimit the number of variables to which the constraint is applied.

Finally, although it is not really necessary for the model, it would be useful to add an OCL constraint in the requirement stereotype from the requirement profile in order to verify that all the design and performance requirements are satisfied by at least one Discipline block from the BDD. However, in this project some problems with this process in Papyrus made impossible to perform the validation.

Block Definition Diagram

Once the profile with the OCL constraints is completely defined, it is possible to build the Block Definition Diagram (BDD), which is going to be the representation of the MDAO model in Papyrus (MBSE model). However, so far in this section, this implementation is done independently, which means that the BDD is totally built in Papyrus tool, just using a specific MDAO model as reference in order to add all the Discipline blocks, its discipline variables and all the ports and connections between Disciplines.

First of all, it is necessary to import the profile defined so that all the stereotypes can be applied. Once imported, the following elements have to be stereotyped: the block (with *Discipline* stereotype), its properties or attributes (with *DisciplineVariable*), its ports (with *Artefact*) and the itemflows (with *VariablesFlow*), which represents the flow of variables between ports.

Figure 8 displays in red circles all these stereotypes in the Discipline block called Mission from our MDAO model. This discipline used the variables vit_eco and vit_max from the Driver (thus, there is a port called *Input mission-driver*) to compute the duration of the cruise flight (duree_crois). Then, it send the variable computed in it, duree_crois, and vit_max through the port *output mission* and these variables flow through the *Flow miss-mass* to other disciplines. Finally, it can be seen also that the stereotype *Artefact* from the *output mission* port contains these variables in the attribute *VariablesTransfered*.

C. Garcia-Rubio, K. Thanissaranon, J.-C. Chaudemar, N. Bartoli and T. Lefebvre
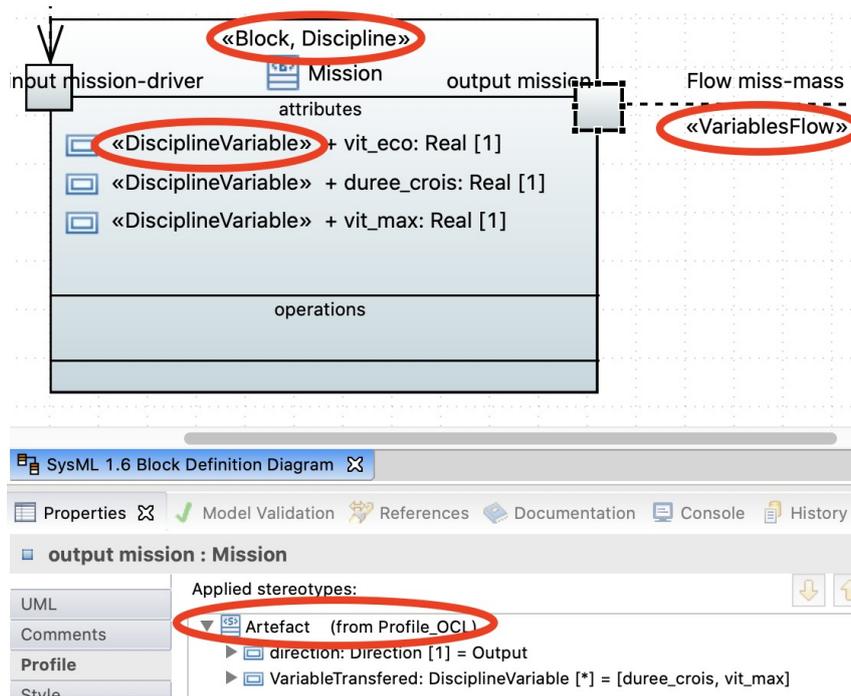
Figure 8: Example of Block in BDD with all the stereotypes for MDAO model.

By repeating the stereotype process as it has been done in Fig. 8, it is possible to implement an entire MDAO model in MBSE. Despite the fact that this could be already understood as a connection between the models, the process is not optimized. As it has been said, the models are built independently (the BDD or the MDAO are both built from scratch) and any improvement, where more elements have to be introduced, lead to a different change in each model. This is the reason for searching a real connection that allows to create the BDD and the OpenMDAO at the same time, reducing the time effort and improving the validation process.

3.3   MDAO-MBSE connection

This connection will be useful as an iterative process for going from one model to the other. In other words, when a change has to be introduced in one model (for example, a new discipline block in the BDD is needed to satisfy a new requirement or new variables are added in a MDAO discipline to optimize the computation value of an objective function), the other connected model added the new elements at the same time.

In order to achieve this connection, it was found that when building a Papyrus project, this tool creates an XML file containing all the information of all the elements from the model with their applied stereotypes. This file is not a read-only file, but it can be overwritten and the changes will appear in the model and diagrams as well. Therefore, the model can be changed or even created in this XML file. Furthermore, Python has two libraries which allow to parse XML files and modify them by adding new elements, changing the existing ones or eliminating them. As OpenMDAO is coded in Python, XML offers an interesting opportunity to establish the desired link.

C. Garcia-Rubio, K. Thanissaranon, J.-C. Chaudemar, N. Bartoli and T. Lefebvre

XML

Extensible Markup Language (XML) is a markup language that defines a set of rules for encoding documents in a format that is both human-readable and machine-readable. A further documentation can be found in [16], but, basically, XML documents are a string of characters, composed of elements and subelements. Each element or subelement begins with ¡ and ends with ¿ and is defined by a tag and its attribute. The tag can be seen as the name given for the element and the attribute consists of a set of name–value pairs that can be used to characterised the tag.

An example is given below in List 2 and represents the discipline variable vit_max from Fig. 8. This is a subelement of the element that defines the block Mission. Its tag is *ownedAttribute*, which means that it is an attribute owned by a package element (in this case the block Mission) and the attribute is the rest of the line contained between ¡ and ¿. In the attribute there are three name-value pairs: the first one specifies that this subelement type is a Property of the block; the second one is an id; and the third one is the name given to this owned attribute and displayed in the model. The second line is a subelement of the this *ownedAttribute*. It represents the value of the variable, which is going to be 15.8 m/s. Finally, the last line is the stereotype *Discipline Variable*.

```
<ownedAttribute xmi:type="uml:Property" xmi:id="TJL_xcP" name="vit_max">
    <defaultValue xmi:type="uml:LiteralReal" xmi:id="_5x4g" value="15.8"/>
</ownedAttribute>
<Profile_OCL:DisciplineVariable xmi:id="_zWCbD8" base_Property="TJL_xcP"/>
```

Listing 2: XML sample for vit_max variable

Just by observing in a same way as in List 2, the different elements in an XML file from an already built BDD, it is possible to identify all the discipline blocks, the discipline variables, the ports and the itemflows. It is easy to conclude that, knowing all the tags and attributes for each element of the diagram, it is only necessary to learn how to access or create those elements from an XML file using Python and, thereby, in the OpenMDAO model.

Luckily, Python has two libraries that parse XML files and allow to access the elements and subelements and, moreover, to create them. These libraries are called *minidom* and *ElementTree*.

Both libraries have similar features and functions to modify XML files. An interesting basic guide that explains them can be found in [17] and [18]. However, it seems that *minidom* is better to access existing elements and *ElementTree* eases the creation of new ones. This remark is really important because depending on which model should copy a new element added to the other model, one library or the other will be used.

When a new element is introduced in the BDD diagram from the MBSE model, the OpenMDAO model will have to add it as well. For this case, the element is automatically added to the XML file from the diagram. Hence, the OpenMDAO will just have to read it from the XML, so *minidom* is more comfortable to access the element and its attributes. For example, if a new discipline variable is added to a Discipline block, the OpenMDAO model will use its name and its default value attributes to specify the independent variable inside the discipline, its value and the connection, if necessary, with the variable in other disciplines.

For the other case where a new element or elements are introduced in the MDAO and, straightaway, to the BDD, they will be added manually in the Python code with the

C. Garcia-Rubio, K. Thanissaranon, J.-C. Chaudemar, N. Bartoli and T. Lefebvre

OpenMDAO model. For that purpose, *ElementTree* helps better to create the elements or subelements. It is essential to know which type of element is being upload to the XML file since the tag and attributes are defined in a different way. Looking at the XML sample described in List 2, it could have been created after the variable vit_max was defined in the OpenMDAO with a value of 15.8. Once the XML file is updated in Python, it can be imported in Papyrus and the variable will appear in the BDD diagram with the stereotype and the Default value as it can be seen in Fig. 9:
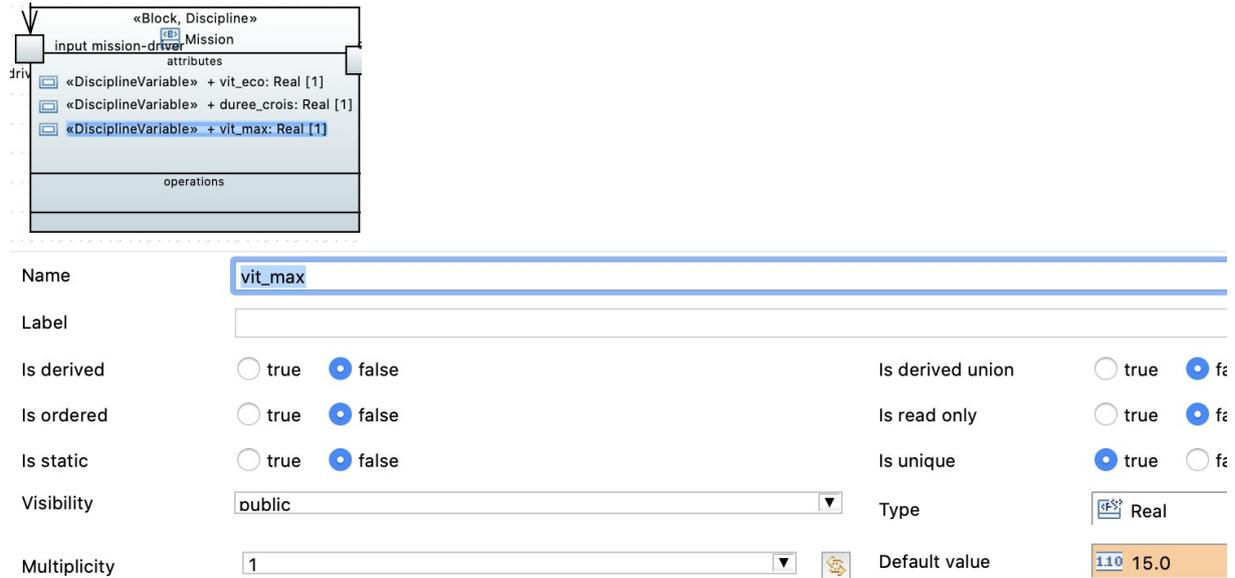
Figure 9: vit_max introduced to BDD using XML.

Both process with all their steps are explained in detail in [12]. Still, some of the functions from the libraries used need to be highlighted:

- *parse*: present in both libraries, this function is mandatory to be able to parse and modify the XML file.

- *getElementsByTagName()* and *getAttribute()*: only from *minidom*, the first function finds and creates a list of all the elements or subelements of the file that have the same tag name as the one defined in the brackets. The second function is used after the first one to access the value of the attribute name specified in brackets from one of the elements in the list previously built.

- *SubElement(parent, tag, attrib=)*: from *ElementTree*, this function creates an element instance, and appends it to an existing element (*parent*). *tag* is the subelement name and *attrib* is an optional dictionary, containing element attributes with their values. An example of how to create the XML lines in List 2 with this function is shown in List 3. In this list, firstly, it can be seen that the variable vit_max gets the value 27.8 in the MDAO model. Then three subelements are created: the first one specifies the *ownedAttribute* of the parent element, the Discipline block *Mission*; the second one is the applied stereotype *DisciplineVariable* from our Profile_OCL and is appended to App which is the first element of the XML and represents all the namespaces of the model; the third one is the default value (27.8) whose parent is, obviously, the first subelement created.

C. Garcia-Rubio, K. Thanissaranon, J.-C. Chaudemar, N. Bartoli and T. Lefebvre

- *write("Output.xml", xml_declaration=True, encoding= "UTF-8", method="xml")*: from *ElementTree*, writes the element tree to a XML output file with a UTF-8 output encoding. This XML file is the one with all the desirable modifications that will be imported to the Papyrus diagram.

```
top_1['p.vit_max']= 27.8
vitmax=str(top_1['p.vit_max']);
vitm=ET.SubElement(miss, 'ownedAttribute', attrib={'xmi:id' : vite_id, 'name' : "vit_max"
    , 'xmi:type' : "uml:Property"});
ET.SubElement(App, 'Profile_OCL:DisciplineVariable', attrib={'base_Property' : vite_id, '
    xmi:id' : vite_id2});
ET.SubElement(vitm, 'defaultValue', attrib={'xmi:id' : vite_value_id, 'xmi:type' : "uml:
    LiteralReal" , 'value' : vitmax});
```

Listing 3: Example code for creating the XML code of List 2 in Python

Taking into account all this information, it is possible to conclude that a link between model can be established. As it was explained before, it could be done by three different ways:

- Building firstly the MDAO model and, at the same time, building the XML in Python manually with *ElementTree* so that it will be imported to the MBSE model for the validation of the model itself and the requirements.

- Other way could be creating first a BDD diagram to see which block satisfies each requirement, so that the XML is automatically built and, next, accessing all the elements from that file with *minidom* for building the MDAO model to perform the analysis and optimization.

- Additionally, when both models have already been implemented, it is easier to change anything in one model and incorporate it to the other one without affecting the validation process.

In order to see the steps of these link processes, take a look at [12]. A final remark has to be done to explain the general structure of the XML file that Papyrus uses and is able to read and import. The principal element of this file is the group of namespaces used. In XML it is mandatory to have this namespaces registered every time the *ElementTree* library is used with the function *register_namespace()* as it is done in List 4. Furthermore, to be able to write correctly the namespaces in the output file, every namespace has to be referred with the second name given in the function *register_namespace*.

```
ET.register_namespace('xmi',"http://www.omg.org/spec/XMI/20131001");
ET.register_namespace('Blocks',"http://www.eclipse.org/papyrus/sysml/1.6/SysML/Blocks");
ET.register_namespace('Profile_OCL',"http://www.isae.fr/certification/1");
ET.register_namespace('uml',"http://www.eclipse.org/uml2/5.0.0/UML");
```

Listing 4: Python code for registering the namespaces

Therefore, the code in List 3 will not work correctly. It was displayed like that form to keep the same format of the previous XML in List 2. However, all the namespaces have to be changed. E.g. the *'xmi:id'* will be changed to the name given in *register_namespace*, *'http://www.omg.org/spec/XMI/20131001id'*, and the third line will be written like this:

```
vitm=ET.SubElement(miss, 'ownedAttribute', attrib={'{http://www.omg.org/spec/XMI
    /20131001}id' : vite_id, 'name' : "vit_max", '{http://www.omg.org/spec/XMI/20131001}
    type' : "uml:Property"});
```

C. Garcia-Rubio, K. Thanissaranon, J.-C. Chaudemar, N. Bartoli and T. Lefebvre

Appended to the namespaces element (called App in Python), there are several subelements. The first one and most important, is the uml package, where all the elements of the diagram have to be appended to, and after this element, all the stereotypes applied. Hence, when stereotyping in Python, the parent of the stereotype tag is not the variable to which the stereotype is applied, but the first element App.

4 RESULT AND ANALYSIS

As it was explained in the final part of the previous section, there are several ways to connect the models and perform a validation. During the project, although all ways were tested to see their viability, the main methodology used was to create a XML file in Python from an existing MDAO model due to the fact that several models were already available from last year research study. Hence, this process can be described as follows:
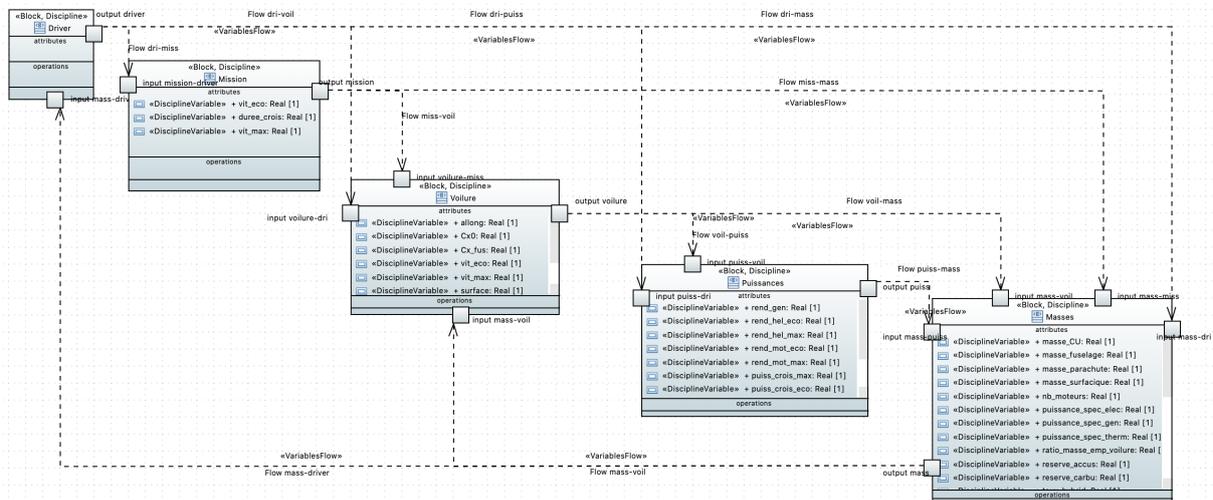
Figure 10: BDD result after importing the XML file created in MDAO.

1. In order to be able to import a correct XML file to Papyrus, the first step is to create an empty BDD in this tool and apply the *Profile_OCL* to use all their stereotypes. The XML file from this empty BDD will contain the first element with all the namespaces needed and the structure of the XML will be ready to be used in the MDAO model. It is important to highlight that to register the namespaces of the stereotyped profiles it is necessary to use them in one element of the empty BDD. Thus, it is necessary to create an empty block and stereotype it with *Discipline*.

2. The MDAO model used was the one from the mock-up in Fig. 10. In order to see results not too long this model is perfect. All the Python code was written in a Jupiter Notebook containing the model. The procedure was, after parsing the XML file created before from the empty BDD, writing the different elements in the XML file at the same time the OpenMDAO defined them. Thus, firstly, all the Discipline blocks were created, including the *Driver* with all the independent variables. Then, after modelling each discipline in MDAO, all the ports, variables and connections of them were added to XML.

3. Now the XML is already finished and, consequently, the BDD is built. It only remains to import the XML file in Papyrus and the model in MBSE is practically

C. Garcia-Rubio, K. Thanissaranon, J.-C. Chaudemar, N. Bartoli and T. Lefebvre

done. After importing the file, the model explorer will show that all the elements from MDAO have been added. However, the diagram console will not display them. This is not a problem because the elements exist in the model and the validation process of the OCL can be performed already. Just by dragging each element in the same order as in the XDSM of the MDAO model, it is possible to replicate it and the final result is shown in Fig. 10.

4. Afterwards, the OCL validation is performed to see the consistency of the model and to test any constraint that can be added to the profile to maybe fulfill the requirements in some variables or safety requirements. The validation in the BDD is really simple as by right clicking the diagram, there is a feature of OCL containing the validation bottom (see Fig. 11a). If any error is found in the model, it will be displayed in the model validation console as in Fig. 11b, along with the name of the OCL constraint violated and the variables that violate it. In Fig. 11b, it can be seen that two OCL were not satisfied correctly: the first one refers to *PortVariable-Type* and means that there is a variable in the port *input mission-driver* from the discipline *Mission* that has not the correct type; the second one refers to *FlowInput* and states that the itemFlow *Flow miss-voil* is sending a set of variables to an input port that does not contain that specific set.

5. Once the model has been validated, a final connection with the requirements can be done as in Fig. 5 to connect the Discipline blocks with the requirements. This is the last and most important step as it provides a connection between MDAO model and requirements.
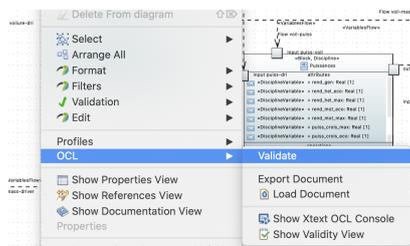
(a) OCL validation feature in BDD.   (b) Model validation console with OCL violated.
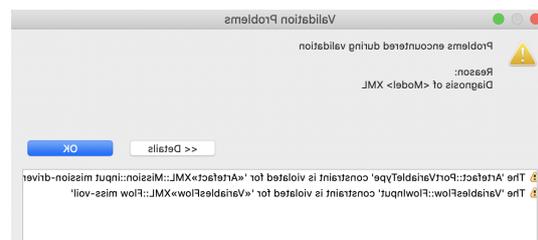
Figure 11: OCL validation

Comparing the BDD result in Fig. 10 with the initial MDAO model Fig. 1, it is possible to see the a lot of similarities between the models. The procedure leads to a good implementation of the MDAO in the BDD and the validation gave the good results expected.

It is necessary to highlight that for each discipline in the BDD, there is only one output port with all the variables that are sending from that discipline, regardless of the destiny of the variables.

Whereas it is not the same situation for the input ports, which only contain the variables sent through the *VariableFlow*, meaning that the origin of the variables has to be considered and, for each set of variables coming from a different discipline, one input port will be added. The reason is that, for the way the OCL language was defined for the *VariableFlow*, it checks that the set of variables in it and in the input port (*FlowInput*) has to be the same and, hence, no variables coming from other disciplines can be introduced.

C. Garcia-Rubio, K. Thanissaranon, J.-C. Chaudemar, N. Bartoli and T. Lefebvre

This could be changed by modifying the OCL and use the function *includesAll* as it was done with the output ports, so only one input port will be needed. But for the better understanding of the model and because of the convenience building the XML in Python, it was decided to build the model in this way. The validation process is no affected anyway.

Finally, once the method was finished, it was time to check in that all the design and performance requirements were satisfied by, at least, one discipline block looking at how the MDAO model was built and connecting them as in step 5). Then, it was perceived that some requirements were still not connected (for example one referring to a turn maneuver). That is why in Fig. 2, the discipline *Turn* was added. This step was not finished during the time of the research, but an idea of how to create the discipline can be concluded by looking at how it was explained the implementation of the XML in the MDAO using the *minidom* library.

5 CONCLUSION AND PERSPECTIVES

This link has been a first attempt to connect MDAO and MBSE and further investigation is needed to improve the efficiency of the connection, especially in terms of time effort (still, it is complicated and long to build the XML file in Python and there is no much time saved comparing with building the models independently). However, it is a good start and the validation process seems to work as expected.

More than one MDAO model was tested using this link and good results were obtained. In terms of effectiveness, if no model has been built, it is more pragmatic starting with the MDAO model in spite of the fact that the XML file has to be written manually. The main reason is that, if the BDD is built first, there is not much time saved reading the XML file with Python and the MDAO can be developed independently without using much more effort. However, if at the same time you are building the MDAO and the XML, the BDD will be automatically developed. Furthermore, [12] gives a guide to write the code for the XML and this process can be automated.

Even if the step 5) in the results section 4 provides a first link with requirements, the number and type of OCL constraints added to the model for a better connection to the MDAO model and the requirements is up to the user of this procedure. The profiles are available to be modified and add them, and a great variety of possibilities is offered. One example was given in List 1 to limit the value of a set of variables.

To conclude this paper some perspectives can be mentioned in order to keep developing these models and their connection:

1. Improve MDAO workflow especially on Mission accuracy (*Take-off*, *Landing* and *Climb*) and finalize *Turn* discpline.

2. Build other SysML diagrams for the MBSE model (Use case diagram and physical BDD were already developed, but there are other diagrams that may help to understand the model).

3. Investigate in the possibility of adding the OCL constraints directly in the BDD so that their context would be a specific discipline variable.

4. Make an OCL constraint work in the Requirements diagram so that the validation process takes into account that all requirements are satisfied by one or more discipline blocks. During the project the requirements profile was giving unexpected

error when trying to add any kind of OCL constraint. The idea is to introduce the constraint given below:

```
self.satisfiedBy−>notEmpty()
```

5. As it was explained in [8] and [9], finding a link with MBSA model is a really interesting research for many companies these days.

ACKNOWLEDGEMENTS

REFERENCES

[1] P. Choy and B. Danet. AVOCETTES UAV conceptual design tool. Technical report, ONERA, 2020.

[2] J. S. Gray, J. T. Hwang, J. R. Martins, K. T. Moore, and B. A. Naylor. Openmdao: An open-source framework for multidisciplinary design, analysis, and optimization. *Structural and Multidisciplinary Optimization*, 59(4):1075–1104, 2019.

[3] R. Lafage, S. Defoort, and T. Lefebvre. Whatsopt: a web application for multidisciplinary design analysis and optimization. In *AIAA Aviation 2019 Forum*, page 2990, 2019.

[4] A. B. Lambe and J. R. Martins. Extensions to the design structure matrix for the description of multidisciplinary design, analysis, and optimization processes. *Structural and Multidisciplinary Optimization*, 46(2):273–284, 2012.

[5] M. Hause et al. The sysml modelling language. In *Fifteenth European Systems Engineering Conference*, volume 9, pages 1–12, 2006.

[6] L. Delligatti. *SysML distilled: A brief guide to the systems modeling language*. Addison-Wesley, 2013.

[7] https://delair.aero/delair-commercial-drones/dt26x-surveillance/, 2020.

[8] K. Thanissaranon. Global model of aircraft design: from performance requirements towards architectures optimization. 2020.

[9] C. G. Rubio. Global model of aircraft design: from performance requirements towards architectures optimization. 2020.

[10] A. Essari. *Estimation of component design weights in conceptual design phase for tactical UAVs*. PhD thesis, Univerzitet u Beogradu-Mašinski fakultet, 2015.

[11] D. Raymer. *Aircraft design: a conceptual approach*. American Institute of Aeronautics and Astronautics, Inc., 2012.

C. Garcia-Rubio, K. Thanissaranon, J.-C. Chaudemar, N. Bartoli and T. Lefebvre

[12] C. G. Rubio and K. Thanissaranon. Supplementary document for global model of aircraft design: From performance requirements towards architectures optimization. 2021.

[13] Object constraint language. `https://www.omg.org/spec/OCL/2.4/PDF`, 2014.

[14] Acceleo/ocl operations reference. `https://wiki.eclipse.org/Acceleo/OCL_Operations_Reference`, 2019.

[15] L. Audibert. *UML 2: De l'apprentissage à la pratique*, volume 298. Ellipses, 2009.

[16] T. Bray, J. Paoli, C. M. Sperberg-McQueen, E. Maler, F. Yergeau, et al. Extensible markup language (xml) 1.0, 2000.

[17] The elementtree xml api. `https://docs.python.org/3/library/xml.etree.elementtree.html`, 2021.

[18] S. Robinson. Reading and writing xml files in python. `https://www.omg.org/spec/OCL/2.4/PDF`, 2021.

MULTIPLE UAV TRAJECTORY OPTIMISATION IN A FOREST FIRE DETECTION MISSION

Joaquim V.R. Sousa [1]*, and Pedro V. Gamboa [1]

1: Centre for Mechanical and Aerospace Science and Technologies (C-MAST-UBI)
Universidade da Beira Interior
6200-001 Covilhã
joaquim.sousa@ubi.pt, pgamboa@ubi.pt, http://www.ubi.pt

Abstract *This paper describes the work of UAVs trajectory optimisation in a possible fire detection mission context. The fire detection mission consists of using a team of UAVs to patrol a given search area here defined as a grid of equally spaced targets placed at a constant height above ground level. Each target is assigned with a score consisting of a count-up timer that starts from the mission beginning and resets every UAV visit. Each UAV is assumed to fly a 3D Dubins manoeuvre between two given targets and to have an electric propulsion system with a limited amount of onboard energy. The energy constraint prevents the entire search area from being covered in a single trip. The goal is to continuously optimise each new trajectory by determining the number and order of targets to visit that maximise the total trip score. The problem solution is found using the Variable Neighbourhood Search (VNS) metaheuristic, particularly the randomised variant of the VNS (RVNS). The trajectory optimisation algorithm is evaluated on a scenario where the team is composed of two fixed-wing aircraft and a multi-rotor. The proposed approach produces feasible results when generating optimised trajectories for a fire detection mission, ensuring the selection of targets that have not been visited more recently on future trajectories. The team was able to effectively patrol the search area with each target being visited every 550 seconds on average.*

Keywords: Fire detection, Trajectory optimisation, Unmanned Aerial Vehicle, Dubins airplane, Variable Neighbourhood Search, Remote Sensing

Joaquim V.R. Sousa and Pedro V. Gamboa

1. INTRODUCTION

Forest fires have been on the rise in recent years and are responsible for destroying millions of hectares of forest [1]. Climate change is cited as a major contributor to the global increase in the frequency of these occurrences. As average temperatures rise, forest fuels become drier, increasing the risk of wildfire [2]. Apart from destroying the local flora and fauna, these fires also destroy several infrastructures and, unfortunately, can result in human casualties among firefighting crews and civilians who may become accidentally engulfed in the smoke and fire. In this sense, early fire detection is an essential key that allows firefighting crews to devise more efficient combat strategies for controlling and extinguishing the fire at its early stages of development.

Recently, the use of Unmanned Aerial Vehicles (UAV) for fire detection missions has garnered considerable attention. These vehicles provide a more comprehensive and accurate perception of the fire's progression and are easily deployable in inaccessible or dangerous areas [3]. These vehicles also benefit from having a lower operating cost when compared to manned aircraft performing the same type of mission [4]. The current generation of unmanned aerial vehicle (UAV) fire detection systems rely heavily on image processing techniques to perform automatic fire segmentation from onboard video captured by visible spectrum or forward-looking infrared (FLIR) cameras [5–9]. Despite these systems' high detection sensitivity, each onboard sensor has a limited field of view (FOV), meaning that unless the camera is installed on a motorised gimbal and is capable of performing image magnification, a fire will be detected only when the UAV is flying directly above it. As a result, for UAVs equipped with a fixed focal length camera without a motorised gimbal, the patrol area must be divided into a grid of multiple targets. These targets should be spaced to cover the entire search area, considering the field of view (FOV) of the onboard sensors, the flight altitude, and the desired image resolution. In a fire detection mission, the fire ignition source can be located at any of the targets. Suppose ignition occurs at a target that has not been visited for an extended period of time. In that case, there is a high probability that the fire will spread to neighbour targets and become uncontrollable. As a result, to conduct an early fire detection, all targets must be visited continuously in the shortest amount of time possible.

This article discusses the use of a UAV team with varying flight capabilities to continuously patrol a given set of targets so that the time between each target visit is minimised. Each target has a score assigned to it. The target scoring is constantly updated throughout the mission execution and consists of a count-up timer that begins counting at the start of the mission and resets following each UAV target visit. This approach results in the highest scores for targets that have not been visited in a long time. The UAV team is composed of both fixed-wing and multi-rotor electric-powered UAVs with limited battery capacity. Due to the UAVs' limited onboard energy, it is impossible to visit all targets in a single trip. Therefore, each UAV trajectory is optimised accounting for their operational constraints such as airspeed, minimum turn radius, maximum allowable flight path angle, as well as energy requirements to ensure that the consumed energy does not exceed the battery capacity during each trip. The problem is to optimise each UAV trajectory by selecting the most rewarding targets that can be visited without exceeding the UAV's battery capacity.

The UAVs are assumed to fly a 3D curvature-constrained Dubins manoeuvre between successive targets to meet the minimum turn radius and maximum flight path angle constraints. The Dubins path consists of the shortest curvature-constrained path connecting two points in the two-dimensional Euclidean plane with prescribed initial and terminal headings and results from the combination of three segments [10]. These can be a maximum curvature left turn (L), a right turn (R) and a straight line (S). The Dubins path is frequently employed in UAV

Joaquim V.R. Sousa and Pedro V. Gamboa

applications to generate 2D trajectories where the flight altitude remains constant [11–15]. In [16], the 2D Dubins path is expanded to three dimensions. The three-dimensional model, referred to as Dubins Airplane, adds a climb-rate constraint to the 2D model. This addition allows generating trajectories between two given targets positioned at different heights. In [17], this model was modified to account for some practical considerations associated with its application on actual fixed-wing UAVs. The modifications include the addition of airspeed, flight-path angle and bank angle to the UAV equations of motion.

The Orienteering Problem (OP) is a routing problem that consists of determining a subset of targets to visit and respective visit order while maximising the total collected rewards without exceeding a given time or distance budget [18]. The OP for curvature constrained vehicles is addressed in [19]. This problem, known as Dubins Orienteering Problem (DOP), adds an extra variable to the OP. Besides determining the order and number of targets to visit, it is also required to determine the heading angle at each target. To solve the DOP, the authors proposed a solver algorithm based on the Variable Neighbourhood Search (VNS) metaheuristic, particularly the randomised variant of the VNS (RVNS). In their approach, a given target sequence is generated through the RVNS. Then, the vehicle heading is discretised into m uniformly sampled heading samples. At last, a feed-forward search is performed over all heading samples to determine which heading combination minimises the total travelled distance for that target sequence. The VNS algorithm consists of searching the solution space by systematically changing the neighbourhood structure [20]. Two different procedures allow the VNS algorithm to search across the solution space: Shake and Local Search. The Shake procedure diversifies the solution, preventing the convergence into a local minimum. The Local Search optimises the solution previously obtained with the Shake procedure using the given neighbourhood structures. The DOP was further extended to account for a climb-rate in addition to the turn-rate constraint in [21]. The authors took the same approach as in [19] by using the Randomised variant of the VNS (RVNS) combined with a feed-forward search over all heading samples. This problem was dubbed as Dubins Airplane Orienteering Problem (DA-OP).

In a real-world scenario, a travel budget based on the travelled distance might not produce feasible results. When flying a 3D Dubins path, the flight direction has a major role in the travel budget. If the UAV is in a climbing direction, more energy will be drawn from the battery, and the UAV might not be able to complete its trajectory. In this paper, we suggest modifying the DA-OP proposed in [21] to consider the total consumed energy as a travel budget instead of a travelled distance.

2. PROBLEM STATEMENT

The fire detection mission consists of using a team of UAVs to continuously patrol a given search area, here defined as a grid of n equally spaced targets placed at a constant height above ground level (AGL), $T = \{t_1, \dots, t_n\}, t_i \in \mathbb{R}^3$. Each target is assigned with a score that is directly proportional to the time elapsed since the last visit and is updated throughout the mission execution, $s_i \geq 0, \forall\, 1 < i < n$. The UAVs are assumed to fly a 3D Dubins manoeuvre between consecutive targets and to have an electric propulsion system with a limited amount of energy (E_{max}). At mission beginning, the first UAV trajectories are optimised from the lowest to the highest range UAV. This ensures that vehicles with a higher range select more distant targets instead of closer ones, thus preventing vehicles with a lower range from running out of targets to select in their trajectories planning. Subsequent trajectories are then optimised according to the arrival times, i.e., the following trajectory optimisation will take place for the UAV that first arrived at its destination. The UAVs are not allowed to select targets that are already in use by other UAVs. Therefore, it is first

Joaquim V.R. Sousa and Pedro V. Gamboa

required to check which targets from the total target list are available (T_{avail}). Additionally, it is not possible to have repeated targets in a single trip.

The trajectory optimisation consists of selecting a subset of k target locations from T_{avail} and determine the visit order described as the sequence $\sum_k = (\sigma_1, \dots, \sigma_k)$ that maximises the total collected score (S) without exceeding the available battery energy (E_{max}), where $1 \leq \sigma_i \leq n$, and σ_1 and σ_k are the departure and arrival locations, respectively. It is also required to determine the vehicle heading at each target from that sequence, $\psi_k = (\psi_{\sigma_1}, \dots, \psi_{\sigma_k})$. This optimisation problem can be formulated as:

$$maximize_{k, \sum_k, \psi_k} \qquad S = \sum_{i=1}^{k} s_{\sigma_i}$$

$$subject\ to: \qquad \sum_{i=1}^{k-1} E(q_i, q_{i+1}) \leq E_{max} \qquad (1)$$

$$q_i = (t_{\sigma_i}, \psi_{\sigma_i}, \gamma),$$
$$\sigma_1 = 1, \qquad \sigma_k = n,$$
$$\sigma_i \neq \sigma_j, \qquad \forall i, j: i \neq j$$

where $q(p, \psi, \gamma)$ represents the vehicle state given by its 3D location ($p \in \mathbb{R}^3$), vehicle heading ($\psi \in \mathbb{S}^1$), flight path angle ($\gamma \in \mathbb{S}^1$), and $E(q_i, q_{i+1})$ is the consumed battery energy while flying the 3D Dubins manoeuvre between two consecutive targets. Figure 1 shows the proposed modification to the DA-OP presented in [21] to account for multiple UAVs with limited onboard energy. The subsections that follow detail each aspect of the proposed algorithm.

Algorithm 1

Input: UAV_p, E_{max_p}, T, m
Output: $\sum_k$, Ψ_k, P

1. **for** *each UAV from* UAV_p **do**
2. | *calcDubinsPath(UAV_p)*
3. **end for**
4. **while** *in mission* **do**
5. | $i \leftarrow selectUAV(UAV_p)$
6. | $T_{avail} \leftarrow availableTargets(T, i)$
7. | $P \leftarrow generateInitialSol(T_{avail})$
8. | $\sum_k, \Psi_k \leftarrow selectTargets(P, m, E_{max\_i})$
9. | **while** *termination condition is not met* **do**
10. | $l \leftarrow 1$
11. | **while** $l \leq l_{max}$ **do**
12. | $P' \leftarrow shake(P, l)$
13. | $P'' \leftarrow localSearch(P', l)$
14. | $\sum''_k, \Psi''_k \leftarrow selectTargets(P'', m, E_{max\_i})$
15. | **if** $S(P'') > S(P)$ **and** *checkTerrain() = false* **then**
16. | $P \leftarrow P''$
17. | $\sum_k \leftarrow \sum''_k$
18. | $\Psi_k \leftarrow \Psi''_k$
19. | **else**
20. | $l \leftarrow l + 1$
21. | **end if**
22. | **end while**
23. | **end while**
24. | $s_{\sigma i} \leftarrow updateScores()$
25. **end while**

Figure 1. Trajectory Optimisation Algorithm

Joaquim V.R. Sousa and Pedro V. Gamboa

2.1. 3D Dubins manoeuvres

The initial step of the algorithm consists of computing all possible 3D Dubins manoeuvres between targets. The DA-OP discretises the vehicle's heading toward each target into *m* evenly sampled heading angles [21]; thus, between two random targets, there are m^2 possible trajectories resulting from the combination of different entry heading angles at each target.

In the proposed approach, the total consumed energy is considered as a travel budget. This means that different travelling directions result in different energy consumption levels, as the UAVs will consume more energy when climbing than descending. Therefore, the 3D Dubins manoeuvres must be computed in both travelling directions, leading to a total of $2m^2$ different trajectories between two given targets.

The 2D Dubins manoeuvre consists of the shortest curvature-constrained path connecting two given targets with prescribed initial and terminal headings. It results from the combination of a maximum curvature left turn (L), right turn (R) and a straight-line segment (S). These trajectories are classified as CSC and CCC, where "C" denotes curve and "S" denotes straight-line segment. RSR, RSL, LSR and LSL are all CSC trajectories. CSC trajectories are generated by drawing two minimum turning radius (r_{min}) circles tangent to the heading direction at both initial and terminal locations and finding all valid tangent lines between the circles, as shown in Fig.2(a). CSC trajectories are then created by connecting the circular arcs to the tangent lines, as depicted in Fig.2(b).

| (a) CSC tangent lines | (b) LSR trajectory example |
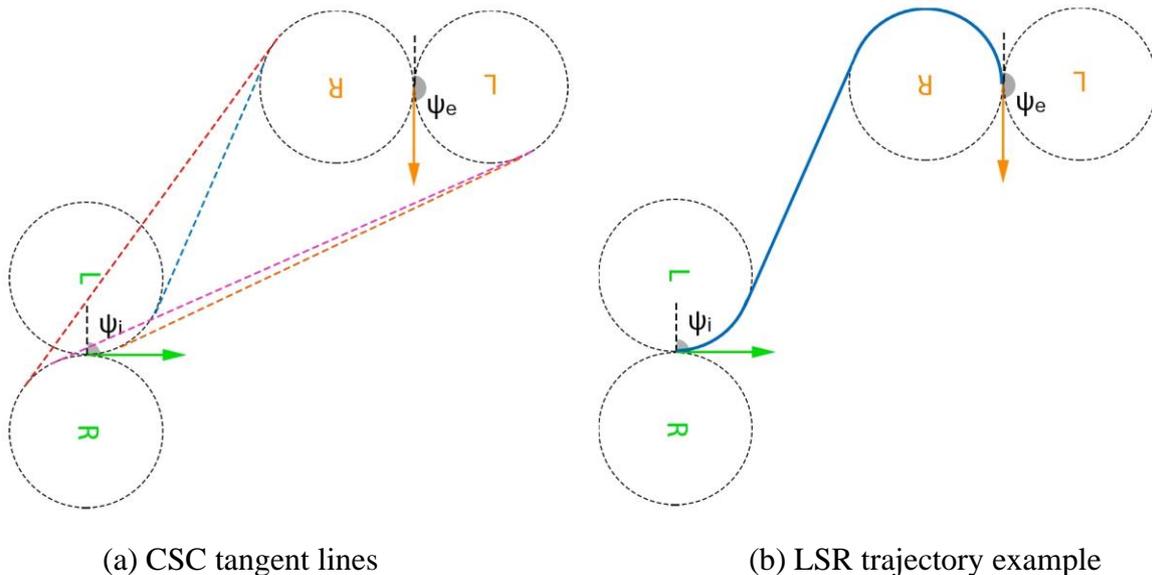
Figure 2. CSC trajectories generation

CCC trajectories include LRL and RLR trajectories and consist of three consecutive minimum turning radius curves in opposing directions. These trajectories are only valid when the distance between the initial and terminal locations is less than $4r_{min}$. CCC trajectories are generated by drawing two minimum turning radius (r_{min}) circles tangent to the heading direction at both initial and terminal locations, together with a third circle tangent to the previous ones. Finally, CCC trajectories are obtained by connecting the circular arcs up to the tangency points [10], [22], as shown in Fig.3.

Joaquim V.R. Sousa and Pedro V. Gamboa
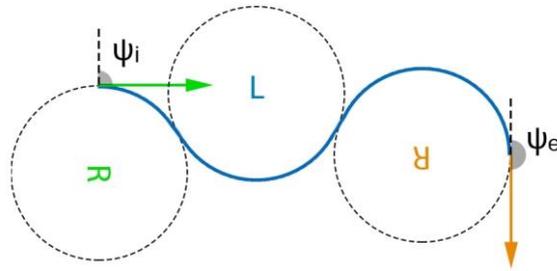
Figure 3. CCC trajectories generation

All CSC and CCC manoeuvres are computed for each pair of target locations, being the shortest distance manoeuvre selected as the optimal 2D Dubins path. The next step consists of expanding the 2D Dubins path to account for altitude differences between targets.

The 3D Dubins manoeuvres are classified according to the altitude difference between the initial and terminal targets in three categories: Low, Medium and High Altitude [16], [17]. Figure 4 illustrates the three different types of 3D Dubins manoeuvres.
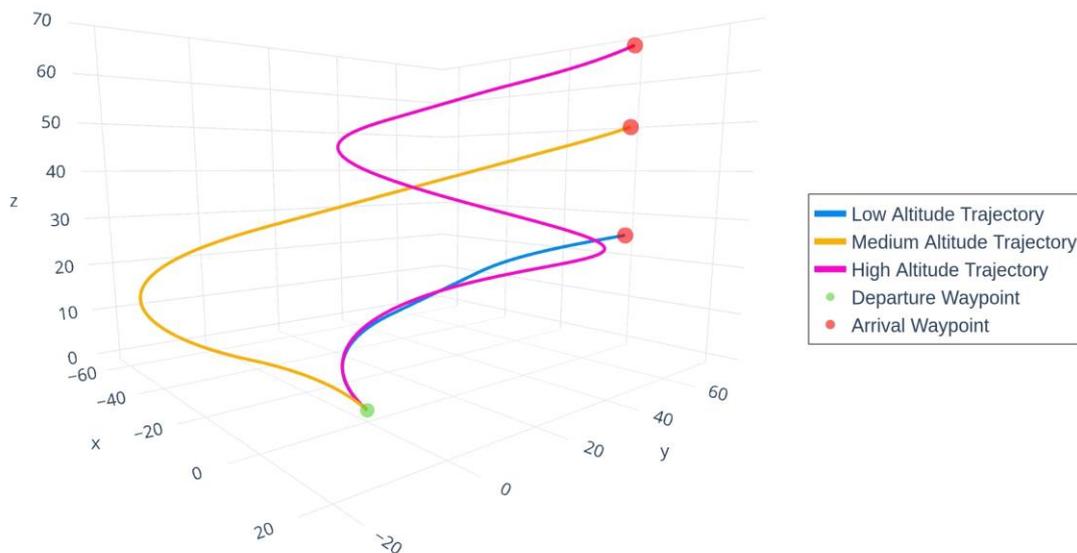
Figure 4. High, Medium and Low Altitude 3D Dubins trajectories

Low Altitude trajectories are suitable whenever the UAV is capable of flying the 2D Dubins path at a constant flight-path angle that is lower than the maximum allowed flight path angle constraint ($\pm\gamma_{max}$). In this scenario, the circular arcs are substituted with helical segments connected by a straight-line segment.

High Altitude trajectories are employed whenever it is not possible to reach the terminal location altitude while flying a 2D Dubins manoeuvre without exceeding the maximum allowed flight-path angle constraint. In these conditions, the trajectory is extended to include a given number of complete turns, and, if required, the turn radius might also be increased. The extra number of turns can be inserted on the path beginning, path end or even split between both. This paper considers the turns to be inserted at the path beginning when climbing and at the path end when descending. This ensures the UAVs have enough ground clearance before heading towards the terminal location, thus avoiding a potential ground collision.

Medium Altitude trajectories are an intermediate case between Low and High Altitude

Joaquim V.R. Sousa and Pedro V. Gamboa

trajectories. These trajectories are used whenever flying a 2D Dubins manoeuvre at the maximum flight-path angle constraint $(\pm\gamma_{max})$ is insufficient to produce the required altitude gain, or, when adding a full turn to the path exceeds the required altitude gain. In this case, an intermediate arc is inserted after the start helix or before the end helix [17].

2.2. UAV performance

The consumed energy calculation is performed for all computed 3D Dubins manoeuvres and is based on a static force analysis on each of the three segments that compose the trajectory. The total energy consumption results from the sum of the consumed energy in each segment of the trajectory.

2.2.1. Fixed-wing UAV

Figure 5 displays the diagram of forces acting on a fixed-wing UAV during flight.

(a) Side view   (b) Front view
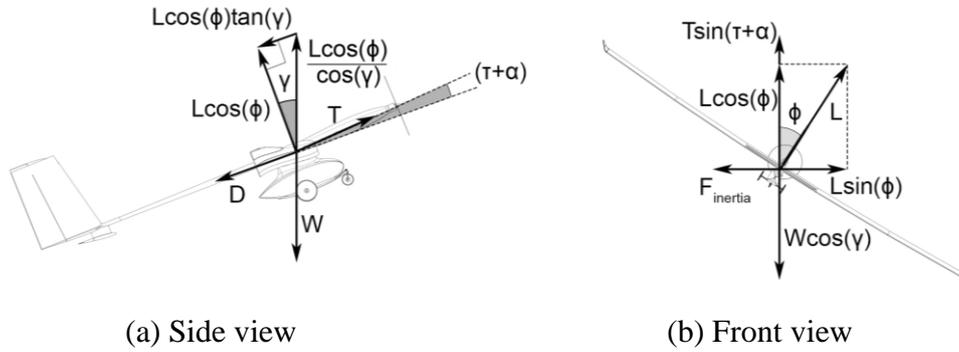
Figure 5. Static force analysis on a fixed-wing UAV

Considering that L is the lift, C_L the lift coefficient, D is the drag, C_D the drag coefficient, W the weight, T the thrust, R the turn radius, ϕ the bank angle, γ the flight-path angle, n the load factor, V the airspeed, $F_{inertia}$ the centrifugal inertia force, g the gravitational acceleration, α the angle-of-attack and τ the angle between the propulsive force and the fuselage axis, we can obtain the following system of equations:

$$
\begin{cases}
T = \dfrac{D + W\sin\gamma + \dfrac{W}{g}\dfrac{dV}{dt}}{cos(\tau + \alpha)} \\[4mm]
L = \dfrac{W\cos\gamma - T\sin(\tau + \alpha)}{\cos\phi} \\[4mm]
\dfrac{W}{g}\dfrac{V^2}{R} = L\sin\phi
\end{cases}
\tag{2}
$$

The airspeed should remain constant at each stage of the flight; therefore, *dV/dt*=0. Assuming now that the propulsive force is aligned with the fuselage axis and the angle of attack is relatively small $(\sin(\tau + \alpha) \cong 0)$, Eq.(2) can be further simplified to:

Joaquim V.R. Sousa and Pedro V. Gamboa

$$\begin{cases} T = D + W \sin \gamma \\ L = \dfrac{W \cos \gamma}{\cos \phi} \\ \dfrac{W}{g} \dfrac{V^2}{R} = L \sin \phi \end{cases} \tag{3}$$

The bank angle (ϕ) and load factor (n) can be derived from Eq.(3) and are given by:

$$\phi = \tan^{-1}\left(\frac{V^2}{gR \cos \gamma}\right) \tag{4}$$

$$n = \frac{\cos \gamma}{\cos \phi} \tag{5}$$

The lift coefficient (C_L) is determined using Eq.(6):

$$C_L = \frac{nW}{\dfrac{1}{2}\rho V^2 bc} \tag{6}$$

The drag polar expresses the variation of the drag coefficient with the corresponding lift coefficient. It can be experimentally obtained and fitted to a parabolic shape, as depicted in Fig.6.

$$C_D = 0.0903 - 0.1652C_L + 0.1988C_L{}^2$$
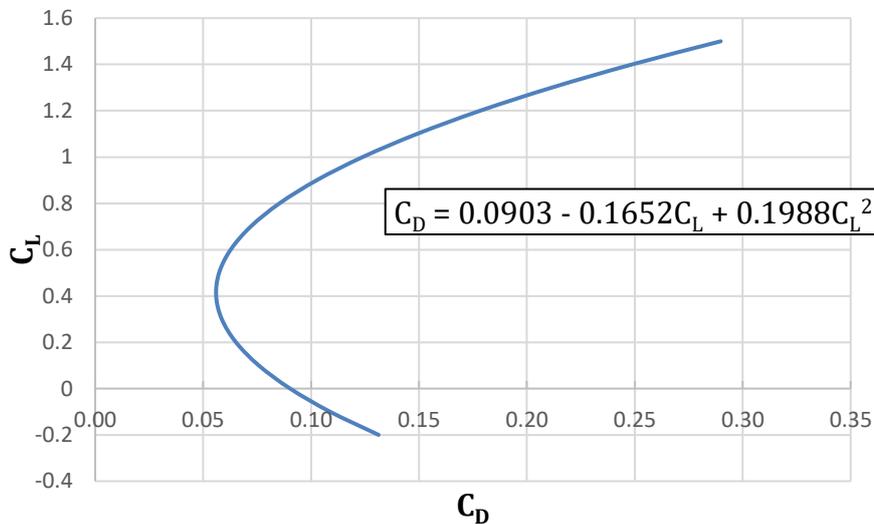
Figure 6. Fixed-wing UAV Drag Polar

The total drag (D) can now be determined with Eq.(7) by first finding the drag coefficient that matches the lift coefficient obtained with Eq.(6):

$$D = C_D \cdot \frac{1}{2}\rho V^2 \cdot bc \tag{7}$$

, where b and c are the wingspan and wing chord, respectively.

The required power (P_{req_W}) results from the multiplication of thrust by airspeed:

$$P_{req\_W} = T.V = (D + W \sin \gamma).V \qquad [W] \tag{8}$$

Joaquim V.R. Sousa and Pedro V. Gamboa

As for the required energy (E_{req_Wh}), it is given by the following equation:

$$E_{req\_Wh} = \frac{P_{req\_W} \cdot \Delta t}{3600} \quad [Wh] \tag{9}$$

, where Δt is the time in seconds required to complete the trajectory.

As expected, the total consumed energy (E_{cons_Wh}) is greater than the required energy (E_{req_Wh}). This can be explained due to losses that occur when converting electrical power into propulsive power. Given the propulsive system efficiency ($\eta_{propulsion}$), the total consumed energy can be expressed as:

$$E_{cons\_Wh} = \frac{E_{req\_Wh}}{\eta_{propulsion}} \quad [Wh] \tag{10}$$

The propulsive system efficiency is estimated using the propulsive system model developed in [23]. This model makes use of experimental wind-tunnel measurements and provides a polynomial approximation that allows us to estimate the propulsive system efficiency as a function of throttle setting (δ_{th}), air density (ρ), propeller pitch (p), propeller diameter (D), as well as motor specifications such as the speed constant (k_v), internal resistance (R), no load electric current (I_0) and maximum electric current (I_{max}).

Finally, the total consumed energy can be related to total consumed battery capacity (C_{batt_Ah}) using Eq.(11):

$$C_{batt\_Ah} = \frac{E_{cons\_Wh}}{v} \quad [Ah] \tag{11}$$

, where v is the battery nominal voltage.

2.2.2. Multi-rotor UAV

Figure 7 displays the diagram of forces acting on a multi-rotor UAV where point C is the turn centre, r_{min} the turn radius, $F_{inertia}$ is the centrifugal inertia force, m is the UAV mass, γ is the flight-path angle, V_∞ is the relative wind, W is the total weight, D is the total drag, T is the required thrust and T_x, T_y and T_z are the thrust components in the North-East-Down frame (NED). The NED frame has its origin on the surface of the geoid below the UAV's centre of mass, being the x-axis oriented to the north, the y-axis oriented east and the z-axis oriented down. The multi-rotor attitude is expressed in terms of three Euler angles: pitch (θ), roll (Φ), and yaw (ψ).
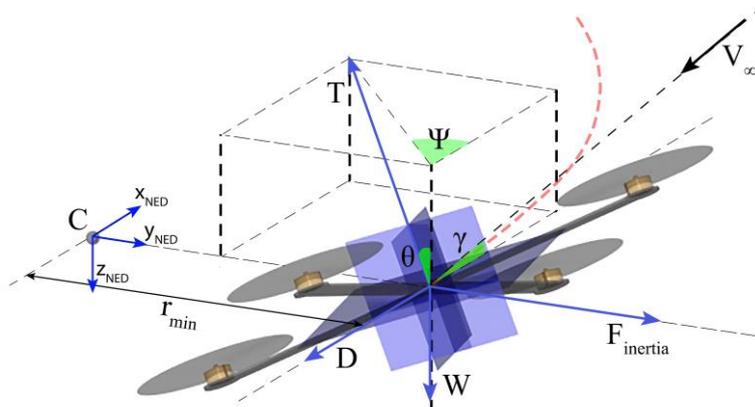
Figure 7. Static force analysis on a multi-rotor UAV

Joaquim V.R. Sousa and Pedro V. Gamboa

From a static force analysis, it is possible to obtain the following system of equations:

$$\begin{cases} T_x = D \cos \gamma \\ T_y = m \dfrac{V^2}{r} \\ T_z = W + D \sin \gamma \end{cases} \tag{12}$$

Equation (13) gives the total required thrust, T.

$$\mathrm{T} = \sqrt{T_x{}^2 + T_y{}^2 + T_z{}^2} \tag{13}$$

Despite having a multitude of Euler angles combinations producing the same thrust vector orientation, in this analysis, we consider the thrust vector orientation to be achieved only by the combination of pitch and yaw rotations. This assumption simplifies the Euler angles calculation for a given desired thrust vector orientation. The three Euler angles are given by:

$$\begin{cases} \theta = -\cos^{-1}\left(\dfrac{T_z}{T}\right) \\ \Phi = 0 \\ \psi = -\tan^{-1}\left(\dfrac{T_y}{T_z}\right) \end{cases} \tag{14}$$

For drag (D) calculation, the multi-rotor is modelled as three perpendicular plates centred at its centre of gravity. Then, the total area (A_{total}) results from merging the projections of these plates in a plane that is perpendicular to the relative wind, as shown in Fig.8.
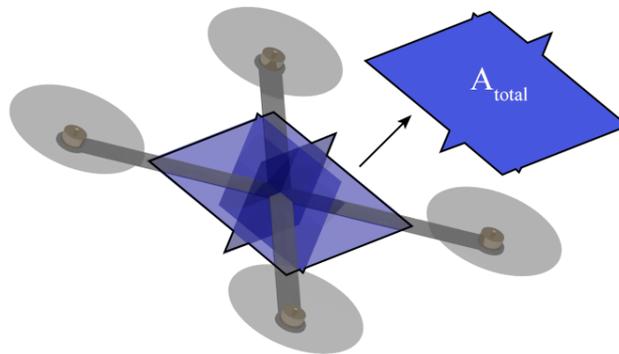
Figure 8. Flat plate Drag estimation

For a given area (A_{total}) and flat plate drag coefficient (C_D), the total drag (D) is determined using the following equation:

$$D = \frac{1}{2}\rho V^2 A_{total} C_D \tag{15}$$

Since drag (D) is a function of total area (A_{total}), and both are a function of the Euler Angles, the problem must be iteratively solved by assigning an initial guess to A_{total} and iterating it over a given number of iterations until a specified threshold is achieved.

For a multi-rotor equipped with a given number of motors (n_{motors}), each motor must produce the following thrust:

Joaquim V.R. Sousa and Pedro V. Gamboa

$$T_{motor} = \frac{T}{n_{motors}} \tag{16}$$

The required power per motor ($P_{req\_W/motor}$) results from the multiplication of T_{motor} by the airspeed component perpendicular to the rotor plane (V_{rotor}):

$$P_{req\_W/motor} = T_{motor} \cdot V_{rotor} \quad [W] \tag{17}$$

As for the required energy per motor ($E_{req\_Wh/motor}$), it is given by the following equation:

$$E_{req\_Wh/motor} = \frac{P_{req\_W/motor} \cdot \Delta t}{3600} \quad [Wh] \tag{18}$$

, where Δt is the time in seconds required to complete the trajectory.
The propulsive system efficiency is estimated using the same methodology presented in the previous section, and the consumed energy for a single motor is given by:

$$E_{cons\_Wh/motor} = \frac{E_{req\_Wh/motor}}{\eta_{propulsion}} \quad [Wh] \tag{19}$$

Finally, the total consumed energy and battery capacity are given by Eq.(20) and Eq.(21), respectively.

$$E_{cons\_Wh} = E_{cons\_Wh/motor} \cdot n_{motors} \quad [Wh] \tag{20}$$

$$C_{batt\_Ah} = \frac{E_{cons\_Wh}}{v} \quad [Ah] \tag{21}$$

2.3. Trajectory optimisation algorithm

Considering a team of p UAVs ($UAV = \{UAV_1, \dots, UAV_p\}$) with limited onboard energy ($E_{max} = \{E_{max\_1}, \dots, E_{max\_p}\}$), the trajectory optimisation algorithm begins by precomputing the 3D Dubins manoeuvres between all possible pair of targets for each UAV of the team, as shown in Fig.1. After this, the outer loop continuously optimises each trajectory until the mission ends. The optimisation cycle starts by selecting the current UAV, i, and determining which targets from the total target list are available (T_{avail}) to include in the trajectory. The *selectUAV()* function selects the current UAV according to the arrival order at the destination. Since all UAVs are launched simultaneously, for the first UAVs trajectories, this function selects the current UAV according to the increasing range, i.e., the trajectories are optimised from the lowest to the highest range UAV. The *availableTargets()* function provides the list of available targets (T_{avail}) by determining which targets are currently selected by other UAVs and removing them from the total target list.
In the DA-OP, the solution vector P consists of a sequence of all targets from (T_{avail}) without the initial and terminal locations, i.e., $P = (\sigma'_1, \sigma'_2, \dots, \sigma'_{n-2})$, where $\forall \sigma'_i \in P, \sigma'_1 \neq 1 \cap \sigma'_i \neq n$. An initial solution is first generated using the *generateInitialSol()* function. This function uses a greedy insertion technique in which targets are initially inserted into an empty vector P according to a convex combination of three ranks [24]. Since it is not possible to visit all targets in a single trip due to the onboard energy constraint, E_{max}, the problem solution consists of a subset of k targets from the solution vector P, i.e., $\sum_k = (\sigma_1, \sigma'_1, \sigma'_2, \dots, \sigma'_{k-2}, \sigma_k)$. The *selectTargets()* function iteratively adds targets from P to $\sum_k$, ensuring that the required battery energy does not exceed the total battery energy E_{max}. This function is also responsible

Joaquim V.R. Sousa and Pedro V. Gamboa

for determining the vehicle heading at each target from the sequence, $\psi_k = (\psi_{\sigma 1}, \ldots, \psi_{\sigma k})$. To do so, a feed-forward search over all heading samples is performed to determine which headings combination minimises the total consumed energy.

The initial solution is then improved by the VNS meta-heuristic method, in particular, the randomised variant of the VNS (RVNS). The VNS searches the solution space for new improved solutions by systematically changing the neighbourhood structure. The neighbourhood structures are ranked according to the maximum distance they can produce between two solutions, $N(l_1, \ldots, l_{max})$. In this paper, two neighbourhood structures ($l_{max} = 2$) are employed for shaking and local search procedures [19]. The shaking procedure diversifies the solution and prevents the convergence into a local minimum. It is used as a starting point for the local search and consists of the following procedures:

    1.   Path Insert:

This operation represents neighbourhood $l = 1$ and consists of selecting a random sub-sequence from P and inserting it at a randomly selected position of the solution vector.

    2.   Path Exchange:

It exchanges two randomly selected non-overlapping sub-sequences from P with the same length. This operation explores further away from the current solution and represents neighbourhood $l = 2$.

The local search procedure explores much closer solutions and optimises the solution previously obtained with the shaking procedure. In the randomised variant of the VNS, the local search procedure consists of performing n^2 local changes, being n the length of solution vector P. The local search encompasses the following operations:

    1.   Point Insert:

This operation represents neighbourhood $l = 1$ and consists of selecting a random element from P and inserting it in another randomly selected position of the vector.

    2.   Point Exchange:

This operation consists of selecting two random elements from P and swapping their position. It represents neighbourhood $l = 2$.

The *selectTargets( )* function is then called to determine the number of targets (k) to be inserted in the problem solution ($\sum_k$) as well as determining the corresponding heading angles at those targets ($\psi_k = (\psi_{\sigma 1}, \ldots, \psi_{\sigma k})$), at each sequence generated with the local search (P'').

Whenever an improved solution is found ($S(P'') > S(P)$), it becomes the new current solution as long as no terrain collision is detected. The *checkTerrain( )* function discretises the UAV trajectory into multiple points equally spaced by a given detection distance (d_{det}). Whenever those points' altitude is lower or equal to terrain, a ground collision is detected, and the function returns *True*. In this condition, the new solution is discarded, and the optimisation cycle continues. If no collision is detected, the *checkTerrain( )* function returns *False,* and the improved solution becomes the new current solution.

If the existing solution is not improved, the neighbourhood structure is increased to $l = 2$ to look further in the solution space. The VNS optimisation cycle is completed whenever the termination criterion is achieved. Maximum CPU processing time, a maximum number of iterations and a maximum number of iterations between successive improvements are the most common criteria used in optimisation [20].

The final step in the trajectory optimisation algorithm consists of using the *updateScores( )* function to update all targets score. Each target score is updated according to the elapsed time since the last UAV visit. With this approach, targets that are not visited for a long time have the highest score, thus are more likely to be chosen in subsequent trajectories.

Joaquim V.R. Sousa and Pedro V. Gamboa

3. RESULTS

3.1. Simulation parameters

The trajectory optimisation algorithm was evaluated for a team composed of two fixed-wing UAVs and a multi-rotor UAV. The fire detection mission consists of patrolling a search area given by a rectangular grid of 23 targets placed 600 m AGL with a 1200 m spacing. It is assumed that the UAVs must alternate between two base stations, BS1 and BS2, for charging or replacing batteries. Figure 9 displays the considered search area, as well as the base stations' location.
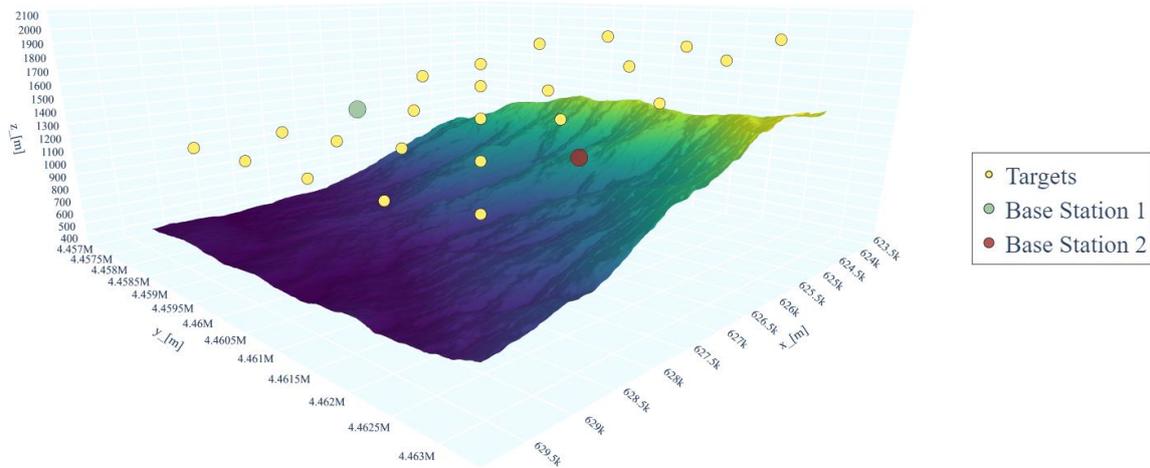
Figure 9. Target Grid (600 m AGL, 1200 m spacing)

Both fixed-wing UAVs are considered to be the same as shown in Fig.10. This UAV was developed and served as a testbed in [25] for evaluating the performance of a morphing wing prototype.

Figure 10. Fixed-wing UAV [25]

The main UAV specifications are presented in Tab.1.

Table 1. Fixed-wing UAV specifications

Airframe	
Wingspan, b	2.5 m
Wing chord, c	0.25 m
Takeoff weight, TOW	5.55 kg

Joaquim V.R. Sousa and Pedro V. Gamboa

Propeller	
Diameter, D	13 in
Pitch, p	12 in
Motor	
Speed constant, k_v	775
Internal resistance, R	0.02 Ω
No load current, I_0	1.61 A
Maximum current, I_{max}	65 A
Battery	
3S (11.1V) 4000 mAh Lithium-ion polymer battery (E_{batt} = 44.4Wh)	
Performance	
Drag polar	$C_D = 0.0903 - 0.1652C_L + 0.1988C_L^2$
Airspeed, V	16 m/s
Minimum Turn radius, r_{min}	22 m
Maximum flight-path angle, γ_{max}	$\pm 10^o$

The multi-rotor is considered to be equipped with four motors ($n_{motors} = 4$). Figure 11 displays the respective flat plate areas used when estimating the total drag (D), and Tab.2 presents the main UAV specifications.
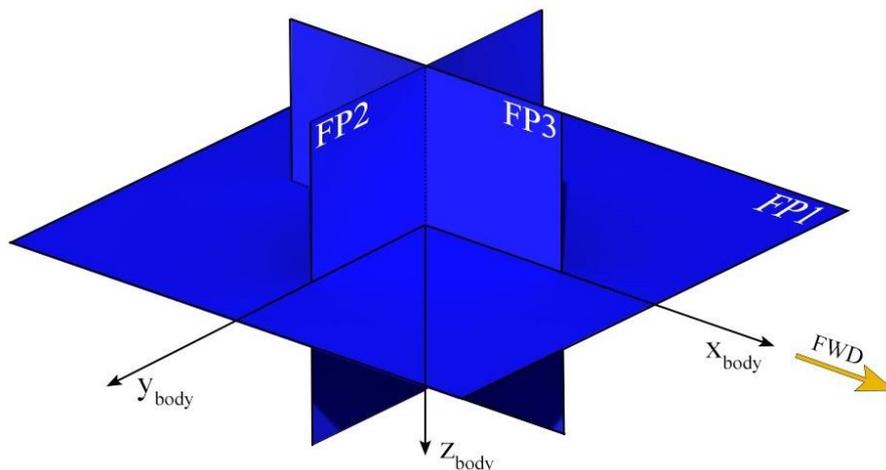
Figure 11. Multi-rotor flat plates model for drag estimation

Table 2. Multi-rotor UAV specifications

Airframe	
Flat plate 1 area, FP1	0.09 m²
Flat plate 2 area, FP2	0.0225 m²
Flat plate 3 area, FP3	0.0225 m²
Propeller	
Diameter, D	14 in
Pitch, p	10 in
Motor	
Number of motors, n_{motors}	4
Speed constant, k_v	775
Internal resistance, R	0.02 Ω
No load current, I_0	1.61 A
Maximum current, I_{max}	65 A

Joaquim V.R. Sousa and Pedro V. Gamboa

Battery	
3S (11.1V) 12000 mAh LiPo battery (E_{batt} = 133.2 Wh)	
Performance	
Airspeed, V	28 m/s
Minimum Turn radius, r_{min}	25 m
Maximum flight-path angle, γ_{max}	$\pm 10º$

A total of 9 trajectories were generated in this simulation; each trajectory optimised for 500 iterations. The number of sampled headings, m, has a direct effect on the solution's quality. Increasing sample size enhances the quality of the solution at the expense of increased computational cost. As a result, four heading samples ($m = 4$) were chosen as an acceptable trade-off between computational time and the solution quality. The trajectories were computed in an Intel Core i7-7700HQ CPU running at 2.8 GHz and took approximately 30 hours to complete.

3.2. Optimised trajectories

Figure 12 displays the first optimised trajectories for each UAV going from BS1 to BS2. The fixed-wing UAVs are labelled as UAV 1 and UAV 2, and the multi-rotor is labelled as UAV 3. At the mission beginning, all targets are assigned with a score of zero. Therefore, each trajectory is optimised to maximise the number of visited targets. The first trajectory is computed for UAV 3 since it is the lowest range UAV. UAV 3 completed its first trip in approximately 220 seconds and was able to visit a total of four targets. As expected, UAV 3 has visited targets that are almost aligned with a path connecting BS1 to BS2 directly. Since UAV 1 and UAV 2 have the same range, the following trajectories were optimised according to the increasing order of UAV's label. UAV 1 trajectory is depicted in orange colour. It was able to visit a total of seven targets located either above or below UAV 3 trajectory. UAV 2 visited a total of eight targets in 770 seconds, all targets placed in the upper part of the search area. Only four targets, located in the lower region of the search area, were not visited.
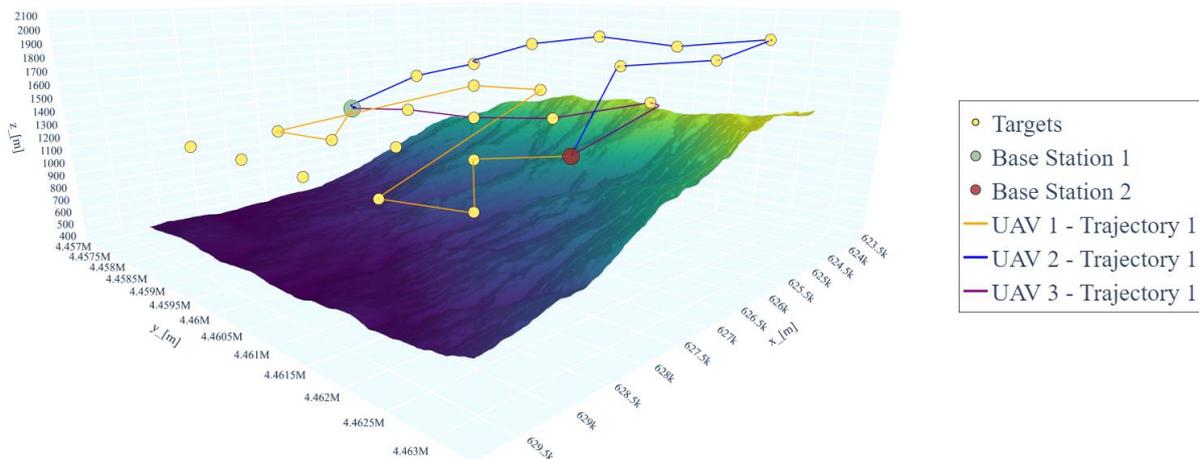
Figure 12. First optimised trajectories for UAV 1, 2 and 3

Figure 13 exhibits the optimised trajectories for each UAV returning from BS2 to BS1 (RTN). Since UAV 3 is both the lowest range and the highest airspeed UAV, it was able to perform three more trajectories than UAV 1 and 2 in the same time span. In Fig.3, only the first UAV 3 return trip is displayed to facilitate the trajectories visualisation. The remaining UAV 3

Joaquim V.R. Sousa and Pedro V. Gamboa

trajectories will be analysed in a separate plot.
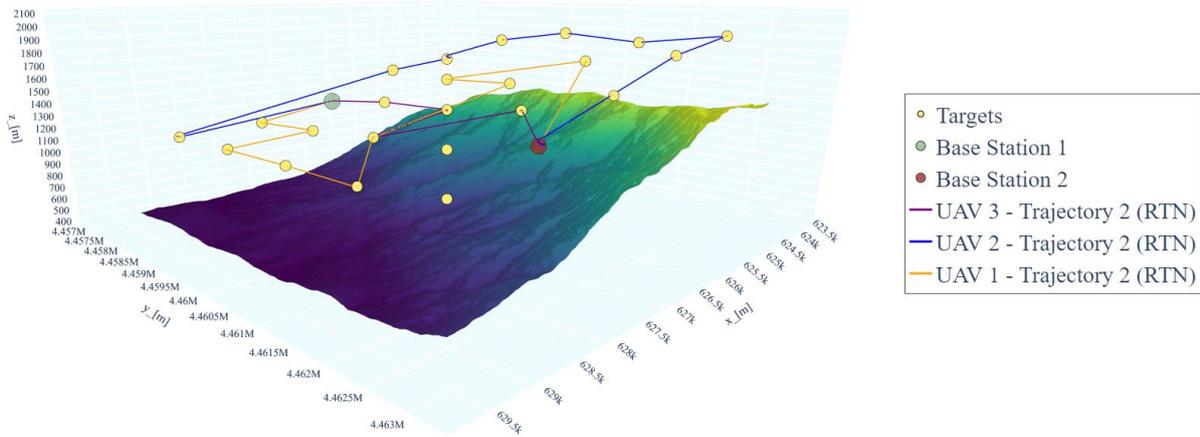
Figure 13. Optimised return trajectories for UAV 1, 2 and 3

The optimised trajectories returning from BS2 to BS1 follow the same pattern as the first generated trajectories. UAV 3 selects targets mainly located close to the direct path between BS1 and BS2. UAV 2 trajectory contains almost the same targets from its first trajectory and adds an extra target located in the lower side of the target grid that had not yet been visited. UAV 1 visits targets located both in the upper and lower region of the search area and visits the three remaining targets that were not visited on the first UAVs trajectories.
Figure 14 shows the additional trips made by UAV 3 during the fire detection mission.
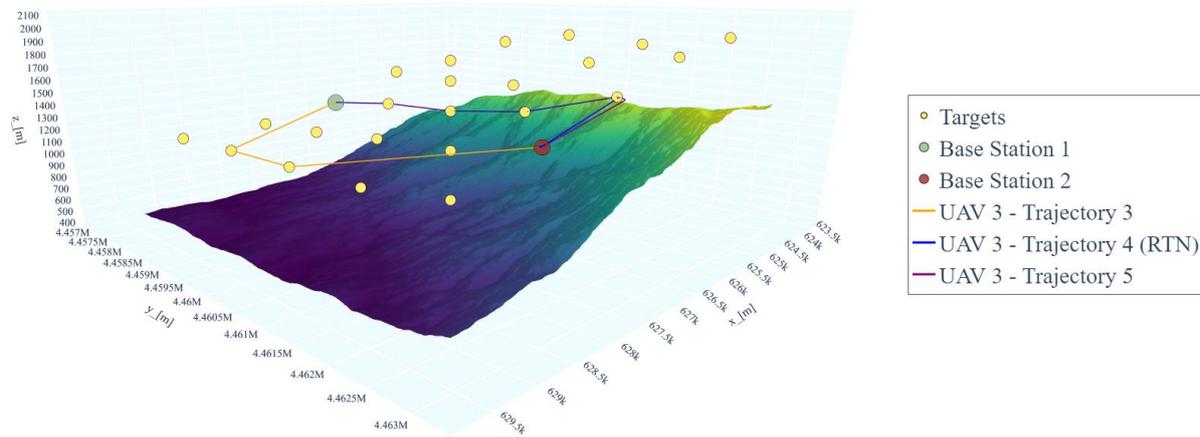
Figure 14. UAV 3 additional trajectories

The third trajectory of UAV 3 only includes two targets. This can happen because these targets are located further away from the direct path between BS1 and BS2. Trajectory 4 and trajectory 5 are almost identical, with the same targets being visited on both trips. The main difference relies on the selected heading angle at the nearest target from BS2. Trajectory 4, depicted in blue colour, is a return trajectory that has an initial climb from BS2 to the first target following a descent through the remaining targets up to BS1. As a result of the feed-forward search, the optimisation algorithm selects the heading combination that minimises the total consumed energy. In this case, the least energy-consuming trajectory consists of flying directly to the first target and only turning towards the following targets after passing it while descending. For

Joaquim V.R. Sousa and Pedro V. Gamboa

trajectory 5, the least energy-consuming path consists of flying almost directly up to the last target and then performing the turn towards BS2 after the last target visit, during the descent phase.

Table 3 displays all computed trajectories data such as number of visited targets, total distance, elapsed time, consumed energy and total collected score. The trajectories are listed following the computation order, i.e., according to the time of arrival at the destination.

Table 3. Optimised trajectories data

UAV/Trajectory	Targets number	Distance [m]	Time [s]	Consumed Energy [Wh]	Score
UAV 3 – Trajectory 1	4	6193.7	220.3	118.6	n/a
UAV 1 – Trajectory 1	7	14801.8	925.1	44.1	n/a
UAV 2 – Trajectory 1	8	12835.8	770.2	42.6	n/a
UAV 3 – Trajectory 2 (RTN)	4	7054.9	250.9	131.1	1065.2
UAV 3 – Trajectory 3	2	6589.4	234.4	128.5	1884.7
UAV 3 – Trajectory 4 (RTN)	4	6193.7	220.3	113.6	2966.8
UAV 2 – Trajectory 2 (RTN)	8	16211.8	979.9	44.1	5426.9
UAV 3 – Trajectory 5	4	6193.7	220.3	118.6	2279.6
UAV 1 – Trajectory 2 (RTN)	9	16590	999.6	42.3	6291

One way of assessing the team effectiveness in performing a fire detection mission is to measure the maximum average score as it reflects the average time elapsed between consecutive visits for a given target. Figure 15 shows how the average target score (S_{avg}) progresses over time.
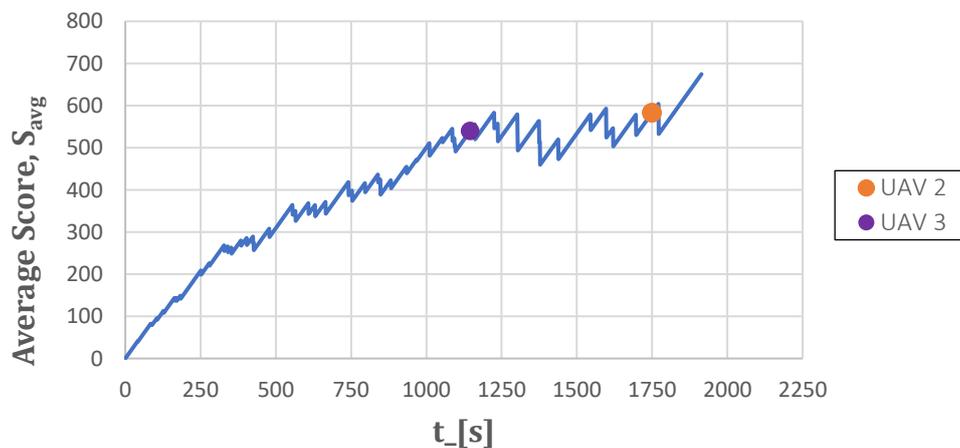
Figure 15. Average score as a function of mission time

Since only 9 trajectories were generated for this mission, it is expected each UAV to complete its trajectories at different mission times. The purple and orange dots depicted in Fig.15 indicate the time instant at which UAV 3 and UAV 2 completed their trajectories and stopped contributing to decreasing the average score. At mission beginning, the average score starts increasing almost linearly up to $t = 250$ s. As we move along time, the slope of the curve decreases towards zero, and the average score value tends to approximately 550. Since UAV 3 regularly visits the same targets, those targets score remains relatively low over time when compared to the remaining ones. Thus, no significant impact occurs in the average score curve at $t = 1146$ s when UAV 3 completes its trajectories. If more than nine trajectories were generated, one could expect UAV 3 to behave like a filter by decreasing the oscillation

Joaquim V.R. Sousa and Pedro V. Gamboa

amplitude that occurs from $t = 1146$ s. Once UAV 2 completes its trajectories, the average score starts increasing as a consequence of having only one UAV contributing to the average score decrease, UAV 1.

4. CONCLUSIONS

In this paper, we developed a trajectory optimisation algorithm that allows optimising the trajectory of a team of UAVs with different flight capabilities in a fire detection mission context. The proposed algorithm is based on the DA-OP [21] and accounts for the UAV's energy requirements when optimising each trajectory. This approach is driven by the fact that using a distance-based technique may result in infeasible paths, as the UAVs battery may lack the energy required to complete the generated trajectories. The trajectory optimisation algorithm was evaluated in a hypothetic scenario in which a team composed of two fixed-wing UAVs and one multi-rotor UAV were required to patrol a particular search area consisting of a grid of various targets set 600 m AGL with a 1200 m spacing. The results revealed that the team was able to patrol the search area with a maximum average score of 550. This means that each target is visited every 550 seconds on average. Despite the long computational time, the proposed algorithm yielded feasible results while generating optimised trajectories for a team of UAVs with limited onboard energy.

ACKNOWLEDGMENTS

REFERENCES

[1] J. R. Martinez-de Dios, B. C. Arrue, A. Ollero, L. Merino, and F. Gómez-Rodríguez, "Computer vision techniques for forest fire perception," Image and Vision Computing, vol. 26, no. 4, pp. 550–562, 2

[2] M. Turco, M.-C. Llasat, J. von Hardenberg, and A. Provenzale, "Climate change impacts on wildfires in a Mediterranean environment," Climatic Change, vol. 125, no. 3–4, pp. 369–380, Aug. 2014, doi: 10.1007/s10584-014-1183-3.

[3] L. Zhang, B. Wang, W. Peng, C. Li, Z. Lu, and Y. Guo, "Forest fire detection solution based on UAV aerial data," International Journal of Smart Home, vol. 9, no. 8, pp. 239–250, 2015, doi: 10.14257/ijsh.2015.9.8.25.

[4] B. R. Christensen, "Use of UAV or remotely piloted aircraft and forward-looking infrared in forest, rural and wildland fire management: evaluation using simple economic analysis," New Zealand Journal of Forestry Science, vol. 45, no. 16, 2015, doi: 10.1186/s40490-015-0044-9.

[5] J. V. R. Sousa and P. V. Gamboa, "Aerial Forest Fire Detection and Monitoring Using a Small UAV," in International Congress on Engineering — Engineering for Evolution, 2020, pp. 242–256. doi: 10.18502/keg.v5i6.7038.

[6] P. Chamoso, A. González-Briones, F. de La Prieta, and J. M. Corchado, "Computer vision system for fire detection and report using UAVs," in Robust Solutions for Fire Fighting (RSFF'18), 2018, vol. 2146, pp. 40–49. doi: 10.1017/cha.2017.1.

[7] S. Ma, Y. Zhang, J. Xin, Y. Yi, D. Liu, and H. Liu, "An Early Forest Fire Detection Method Based on Unmanned Aerial Vehicle Vision," in Proceedings of the 30th Chinese Control and Decision Conference, CCDC 2018, 2018, pp. 6344–6349. doi: 10.1109/CCDC.2018.8408244.

[8] C. Yuan, Z. Liu, and Y. Zhang, "Aerial Images-Based Forest Fire Detection for

Joaquim V.R. Sousa and Pedro V. Gamboa

Firefighting Using Optical Remote Sensing Techniques and Unmanned Aerial Vehicles," Journal of Intelligent and Robotic Systems: Theory and Applications, vol. 88, no. 2–4, pp. 635–654, 2017, doi: 10.1007/s10846-016-0464-7.

[9] V. Vipin, "Image Processing Based Forest Fire Detection," International Journal of Emerging Technology and Advanced Engineering, vol. 2, no. 2, pp. 87–95, 2014, doi: 10.1109/ICCPCT.2014.7054883.

[10] L. E. Dubins, "On Curves of Minimal Length with a Constraint on Average Curvature, and with Prescribed Initial and Terminal Positions and Tangents," American Journal of Mathematics, vol. 79, no. 3, p. 497, Jul. 1957, doi: 10.2307/2372560.

[11] S. Subchan, B. A. White, A. Tsourdos, M. Shanmugavel, and R. Żbikowski, "Dubins Path Planning of Multiple UAVs for Tracking Contaminant Cloud," in 17th IFAC World Congress, 2008, vol. 41, no. 2, pp. 5718–5723. doi: 10.3182/20080706-5-KR-1001.00964.

[12] P. B. Sujit, J. M. George, and R. W. Beard, "Multiple UAV coalition formation," in 2008 American Control Conference, Jun. 2008, pp. 2010–2015. doi: 10.1109/ACC.2008.4586788.

[13] A. Ismail, E. Tuyishimire, and A. Bagula, "Generating Dubins Path for Fixed Wing UAVs in Search Missions," in Lecture Notes in Computer Science, vol. 11277, N. Boudriga, MS. Alouini, S. Rekhis, E. Sabir, and S. Pollin, Eds. Springer International Publishing, 2018, pp. 347–358. doi: 10.1007/978-3-030-02849-7_31.

[14] Guang Yang and V. Kapila, "Optimal path planning for unmanned air vehicles with kinematic and tactical constraints," in Proceedings of the 41st IEEE Conference on Decision and Control, 2002., 2002, vol. 2, pp. 1301–1306. doi: 10.1109/CDC.2002.1184695.

[15] H. Yu and R. Beard, "A vision-based collision avoidance technique for micro air vehicles using local-level frame mapping and path planning," Autonomous Robots, vol. 34, no. 1–2, pp. 93–109, Jan. 2013, doi: 10.1007/s10514-012-9314-z.

[16] H. Chitsaz and S. M. LaValle, "Time-optimal paths for a Dubins airplane," in 2007 46th IEEE Conference on Decision and Control, 2007, pp. 2379–2384. doi: 10.1109/CDC.2007.4434966.

[17] M. Owen, R. Beard, and T. McLain, "Implementing Dubins Airplane Paths on Fixed-Wing UAVs," in Handbook of Unmanned Aerial Vehicles, K. P. Valavanis and G. J. Vachtsevanos, Eds. Springer, 2015, pp. 1677–1699. doi: 10.1007/978-90-481-9707-1.

[18] A. Gunawan, H. C. Lau, and P. Vansteenwegen, "Orienteering Problem: A survey of recent variants, solution approaches and applications," European Journal of Operational Research, vol. 255, no. 2, pp. 315–332, Dec. 2016, doi: 10.1016/j.ejor.2016.04.059.

[19] R. Penicka, J. Faigl, P. Vana, and M. Saska, "Dubins Orienteering Problem," IEEE Robotics and Automation Letters, vol. 2, no. 2, pp. 1210–1217, 2017, doi: 10.1109/LRA.2017.2666261.

[20] Z. Sevkli and F. E. Sevilgen, "Variable Neighborhood Search for the Orienteering Problem," in Levi A., Savaş E., Yenigün H., Balcısoy S., Saygın Y. (eds) Computer and Information Sciences – ISCIS 2006. ISCIS 2006. Lecture Notes in Computer Science, vol 4263, Springer, 2006, pp. 134–143. doi: 10.1007/11902140_16.

[21] P. Vana, J. Faigl, J. Slama, and R. Penicka, "Data collection planning with Dubins airplane model and limited travel budget," in 2017 European Conference on Mobile Robots (ECMR), 2017, no. 16, pp. 1–6. doi: 10.1109/ECMR.2017.8098715.

[22] A. Giese, "A Comprehensive, Step-by-Step Tutorial to Computing Dubin's Paths," 2012. https://gieseanw.wordpress.com/2012/10/21/a-comprehensive-step-by-step-tutorial-to-computing-dubins-paths/ (accessed Jun. 20, 2019).

Joaquim V.R. Sousa and Pedro V. Gamboa

[23] P. F. G. L. F. de Albuquerque, "Mission-Based Multidisciplinary Design Optimization Methodologies for Unmanned Aerial Vehicles with Morphing Technologies," PhD Thesis, Universidade da Beira Interior, 2017.

[24] B. L. Golden, L. Levy, and R. Vohra, "The orienteering problem," Naval Research Logistics, vol. 34, no. 3, pp. 307–318, Jun. 1987, doi: 10.1002/1520-6750(198706)34:3<307::AID-NAV3220340302>3.0.CO;2-D.

[25] P. Santos, J. Sousa, and P. Gamboa, "Variable-span wing development for improved flight performance," Journal of Intelligent Material Systems and Structures, vol. 28, no. 8, pp. 961–978, May 2017, doi: 10.1177/1045389X15595719.

DESIGN OPTIMIZATION OF ACTIVE HELICOPTER SEAT SYSTEM FOR FLIGHT TESTING

Yong Chen, Amin Fereidooni, Rene Laliberte, Viresh Wickramasinghe

Aerospace Research Centre
National Research Council Canada
K1A 0R6
Eric.Chen@nrc-cnrc.gc.ca, http://www.nrc.canada.ca

Abstract *Helicopter aircrew are exposed to high levels of whole-body vibration during fight, which can degrade their ride comfort and even contribute to health issues such as lower back pain and neck strain. A patented active seat mount technology has been developed to reduce aircrew whole-body vibration at the N/rev harmonic frequencies of the helicopter main rotor speed. This paper describes the prototype design that demonstrated significant whole body vibration reduction to the manikin occupant in mechanical shaker experiments. To demonstrate the performance through flight testing on the Bell-412 helicopter, re-design and optimization of the prototype active helicopter seat mount have been introduced. These include the structural modifications and improvements to the baseline actuation mechanism for integration within the helicopter cabin, as well as the need to satisfy airworthiness requirements for flight demonstration on the NRC Bell-412 helicopter testing platform.*

Keywords: helicopter seat mount, active vibration control, flight testing, design and testing

Yong Chen, Amin Fereidooni, Rene Laliberte, Viresh Wickramasinghe

1. INTRODUCTION

The helicopter is a versatile aerial platform widely used in military and civilian applications. However, the ride quality of most helicopters is relatively poor, mainly due to the harsh vibration and noise environment inside the cabin. During flight, helicopter floor vibration is transmitted from seat frame through seat cushions to the seated aircrew, exposing them to an environment known as whole-body vibration (WBV) exposure. In the short term, exposure to high levels of WBV can adversely affect their operational performance and situational awareness, leading to degraded ride comfort. Long term exposure to high WBV may contribute to aircrew health issues such as lower back pain and neck strain, which can result in loss of their flight status [1, 2].

Helicopter floor vibration is mainly related to the rotor aerodynamic and inertial loads at N/rev harmonic frequencies of the main rotor speed, where N is the number of main rotor blades [3]. The main rotor speed of most helicopters is relatively low, typically close to 5 Hz. ISO2631-1 standard indicates that human body response to the vibration excitation is prevalent within the low frequency range between 0.5 Hz and 80 Hz [4]. Especially, the frequency between 0.5 Hz and 12 Hz is the most sensitive range in the spine direction that introduces significant vibration impact on the human body. Since the dominant N/rev harmonics of the helicopter vibration are typically below 20 Hz, which is overlapped with the frequency range as outlined in ISO2631-1 standard, it is very important to control the vibration amplitudes at the lower frequency N/rev harmonics in order to effectively reduce the WBV exposure of the helicopter aircrew during flight operations.

Technologies to mitigate aircrew WBV typically fall into three categories, namely the passive, semi-active and fully-active solutions [5, 6]. Passive solutions such as passive seat cushions are effective in reducing vibrations at the high frequencies, but relatively less effective in the low frequency range that is most important for helicopter applications. Additionally, the impedance properties of the seat cushions are difficult to design in order to achieve satisfactory WBV reduction for varied aircrew and flight conditions. Thus relying solely on passive solutions is not sufficient to mitigate the aircrew exposure within the helicopter cabin. Semi-active solutions have been explored by many researchers for helicopter pilot vibration mitigation. These techniques often rely on functional materials or variable structures whereby the structural damping properties can be tuned for more effective energy dissipation. Wereley et al. [7] have tested a semi-active helicopter seat design where Magneto-rheological dampers are integrated in the vertical columns of the H-60 pilot seat frame. The semi-active seat design demonstrated significant reduction in high frequency vibration, but the performance in the lower frequency range, especially at the 1 and 2/rev harmonics of the helicopter main rotor speed, remained limited for aircrew WBV mitigation.

To provide more effective WBV mitigation to the helicopter aircrew, especially at the critical low N/rev frequencies, an active seat mount integrated with miniaturized actuators to provide adaptive cancellation forces has been developed. Active vibration mitigation of helicopter aircrew WBV was explored by Chen et al. [8, 9] using two parallel stacked piezo-stack actuators on a Bell-412 helicopter seat. Under representative Bell-412 vibration profiles, the seat provided effective reduction of vibration at most N/rev harmonics except for the 1/rev at 5.4 Hz frequency. This was due to the fact that the piezo-stack actuators cannot provide sufficient stroke required to reduce the 1/rev vibration. Despite this issue, this design demonstrated that an active control solution was more effective in the mitigation of WBV for helicopter aircrew.

This paper presents the prototype design and promising results of a multi-axis active

helicopter seat mount that acts as a vibration stabilized platform in order to reduce vibrations transmission to the seated helicopter occupant including the critical 1/rev harmonic frequency. To demonstrate the performance through flight testing on the Bell-412 helicopter, the need for re-design and optimization of the prototype active helicopter seat mount is also discussed. Modifications include the structural modifications as well as the improvement to baseline actuation mechanism for integration within the cabin of NRC Bell-412 helicopter test platform for flight demonstration.

2. PROTOTYPE MULTI-AXIS ACTIVE SEAT MOUNT DESIGN

The proof-of-concept multi-axis active seat mount was conceptually designed to retrofit the Bell-412 helicopter non-armored pilot seat. Since the Bell-412 pilot seat has two short horizontal supports that are locked to the floor rails inside helicopter cockpit, the prototype design introduced two identical active seat mount assemblies. The active seat mount assemblies are designed to install between the Bell-412 pilot seat frame and the floor rails, with the upper frame of each assembly was attached to one of the seat supports and acted as a vibration stabilized platform. This arrangement is expected to minimize the impact on helicopter seat crashworthiness requirement, and also allow for easy integration with other existing helicopter seat designs [10, 11]. One of the prototype assemblies is shown in Figure 1a, and the installation on a Bell-412 pilot seat is shown in Figure 1b.
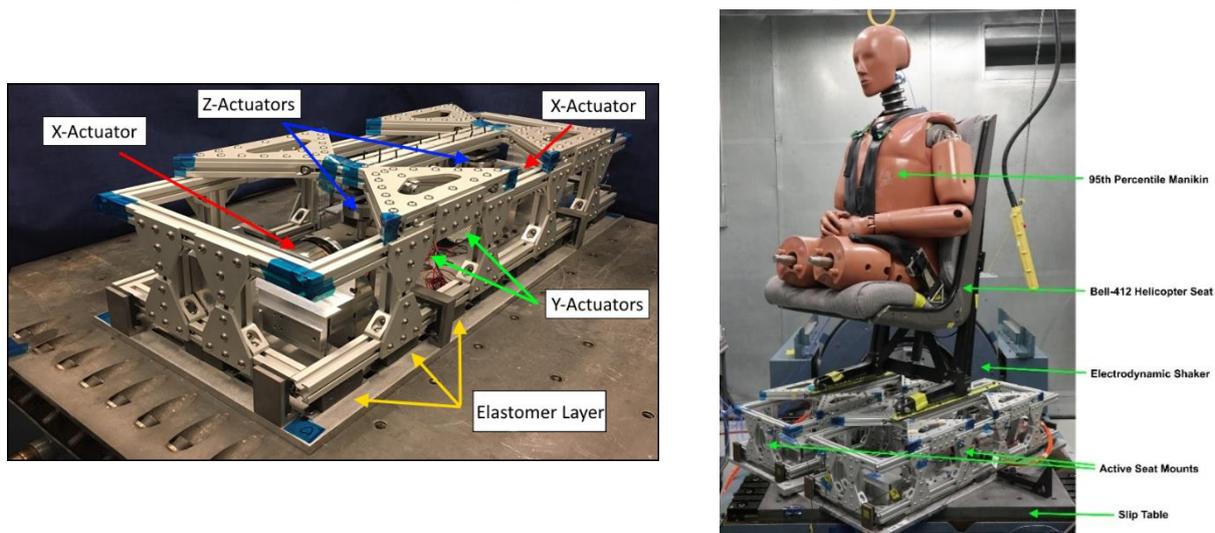
(a) active seat mount assembly (b) active seat mounts under Bell-412 pilot seat frame

Figure 1 Prototype multi-axis active seat mount

The active seat mount assembly is designed with two parallel load-carrying paths. The upper frame of the active seat mount assembly is attached to the base frame through two structural elements, and the base frame is fastened directly to the guide rails on the helicopter floor. First, the upper frame structure is attached to the seat mount base frame through a layer of soft elastomers which provide the baseline damping and stiffness for passive support of the pilot seat. Second, two actuators are connected between the upper frame and the seat mount base to provide multi-axis vibration control capability in parallel. In the proof-of-concept design, the compact GVCM 095-038-01 linear voice coil actuator was used, each has a continuous actuation force capacity of 100 N along with a stroke limit of 12.7 mm [12]. In the prototype active seat mount design, there are three groups of actuator to provide control authority in each orthogonal direction independently. Each group consists

of two miniature actuators, and is linked to the upper frame through a pair of stacked linear slides and a spherical ball joint, which together provide the active seat mount with 5 degrees-of-freedom (DOF). Therefore, this design allows for simultaneous and independent control of the actuator assemblies in three orthogonal directions.

3. ADAPTIVE CONTROL OF AIRCREW WHOLE BODY VIBRATION

3.1. FxLMS Algorithm

The prototype active seat mount design provides the capability of vibration control in three orthogonal directions independently. In each direction, the grouped actuators are controlled through an adaptive feed forward controller, implemented using the Filtered-x Least Mean Squares (FxLMS) algorithm [13, 14]. A block diagram of the FxLMS algorithm is shown in Figure 2.
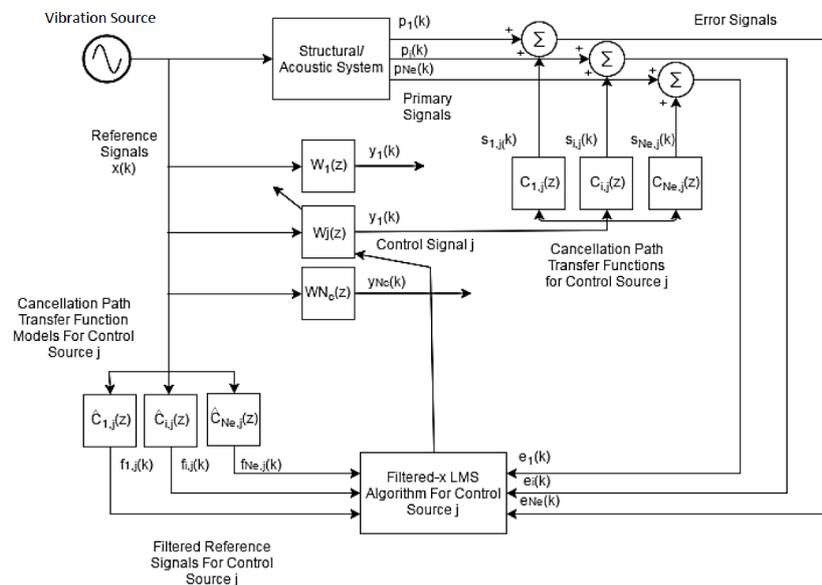
Figure 2 FxLMS algorithm block diagram

The FxLMS algorithm requires a reference signal that is correlated to the disturbance input in order to derive the control signal for cancellation of the vibration related to this disturbance input. Helicopter aircrew WBV is known to be related to the lower N/rev harmonics of the main rotor speed, which may vary depending on aircraft engine power settings in varied flight conditions. Therefore, an accelerometer was installed on the helicopter floor to measure the floor vibration. Since floor vibration also contains fuselage structural vibration responses, narrow band filters at the target N/rev harmonic frequencies and low frequency filters were applied to eliminate unrelated vibration components. The filtered vibration is then used as the reference signal to ensure convergence and stability of the FxLMS algorithm.

In this study, instrumented Hybrid III manikins were used as the occupant. Referencing to ISO 2631-1 standard, multiple accelerometers were installed at the seat cushion and occupant interfaces, as well as the occupant body locations, particularly at the head location with the objective to evaluate the neck load due to WBV exposure. The vibration levels at the seat cushion interfaces and manikin head location can be selected as the error signal for performance evaluation purposes.

Three parallel FxLMS controllers were implemented, each in a Single-Input Single-Output (SISO) configuration to control the group of four actuators in one direction as a single control path. This allows for the algorithm to account for variations in the dynamics of the actuators in each direction.

Compared to standard FxLMS algorithm, modification was made to include the weight functions as outlined in ISO 2631-1 standard to account for the frequency dependent sensitivity of the human body to WBV exposure. For example, ISO 2631-1 specifies the function Wk for human body vibration in the Z direction, which provides higher weighting between the frequency range of interest, nominally 3 and 12Hz. Therefore, this arrangement ensures effective WBV reduction for the Bell-412 helicopter aircrew because it encompasses the low N/rev harmonics of the helicopter main rotor speed.

3.2. Control Path Modeling

A total of three Hybrid III manikins were used as the occupants in this study: a 95th percentile male, a 50th percentile male and a 5th percentile female. For each occupant, control path models were derived independently in each orthogonal control direction through experimental identification techniques. In each direction, an upward sine sweep signal from 2 Hz to 80 Hz was applied to the four actuators in the target direction. The vibration responses of the seat and occupant were measured by accelerometers on the multi-axis seat mount and the selected locations on the manikin body. The transmissibility curves in three directions for the three Hybrid III manikins are shown in Figure 3.

(a)　X axis　　　　　　　　　　　(b)　　Z axis
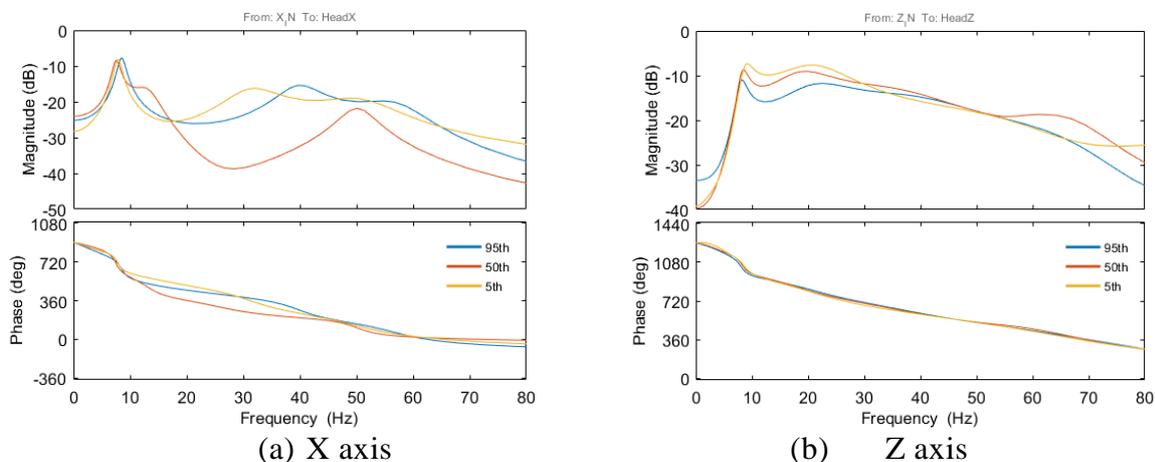
Figure 3 Transmissibility curves in the orthogonal directions

Within the frequency range of interest, it was noted that the identified control path models exhibited similar dynamics features. A resonant peak close to the 1/rev main rotor speed of the Bell-412 helicopter at 5.4 Hz was identified for each manikin. The frequency and amplitude of the transmissibility curves varied slightly depending on the weight and posture of the Hybrid III manikin mainly in the Z direction, with the 95th percentile manikin showed the lowest resonant frequency and lowest amplitude. This feature was related to the highest body weight of the 95th percentile manikin. In comparison, the transmissibility curves in the X and Y directions were generally similar. More importantly, it was noted that the phase characteristics of the transmissibility curves for the three manikins were very close. Since the convergence of the FxLMS algorithm was mainly determined by the phase features, the obtained transmissibility indicated that similar performance in convergence

can be expected for the three manikins. It also suggested that a "nominal control path model" may be used for WBV reduction without the need to identify control paths for each manikin, which would significantly reduce the complexity in the control law design.

4. ADAPTIVE CONTROL OF AIRCREW WHOLE BODY VIBRATION

In order to simulate the aircrew WBV environment inside the Bell-412 helicopter cabin for performance evaluation of the active seat mount technology, extensive tests were conducted on an Unholtz-Dickie 10,000 lb(f) electrodynamic shaker. The two multi-axis active seat mount assemblies were fastened to the shaker table, and a Bell-412 non-armored pilot seat was mounted on the upper frames of the two active seat mount assemblies through two helicopter floor rail sections. A Hybrid III manikin was seated on the Bell-412 pilot seat as the occupant, and secured using the built-in seat belts.

The experimental setup for simultaneous performance evaluation in X and Y directions is shown in Figure 1b. In this setup, the lower limbs of the manikin were removed to avoid the feet from impacting on the test apparatus. It was assumed that the weight of the lower legs would be supported by the helicopter floor, and thus the weight of the lower limbs would have insignificant impact on system dynamics.

The shaker was programmed to provide simulated vibration input to excite the active seat mount assemblies. The simulated vibration profile was derived by referencing to a Bell-412 floor vibration spectra. The profile included the first 8 N/rev harmonic peaks, with the amplitude of each peak scaled accordingly to match with the Bell-412 floor vibration spectrum at 120kts. In addition, a low level broadband random vibration between 3 and 50Hz was also incorporated to simulate aerodynamic excitations. The full vibration input level was 0.25 grms.

Closed-loop tests on the active seat mount system with a Hybrid III manikin as the occupant have been performed for performance evaluation purposes. The shaker table was controlled to provide consistent Bell-412 floor vibration spectrum in the test direction. First, the WBV responses of the manikin on the original Bell-412 seat were recorded and used as the baseline parameters. Then the FxLMS controllers were activated to control the active seat mount assemblies to reduce the WBV of the manikin occupant. The vibration responses of the manikin and active seat mount system were monitored and recorded throughout the experiment. When the controller converged, the vibration responses of the active mount and the manikin were compared with the baseline parameters to evaluate vibration mitigation performance.

4.1. Vertical Direction Test

In the helicopter cabin, the dominant aircrew WBV comes from the vertical Z direction [10]. Per ISO 2631-1, the vibration levels measured at the interfaces between the seat cushions and the human body were used as the metrics to determine the occupant WBV exposure levels, and the results on the 50th percentile manikin are shown in Figure 4.

With the shaker excitation input in the Z direction, the highest vibration level at the seat cushion interface was also in the Z direction, at a level of 0.17 g rms. Considerable level of vibration also existed in the X direction, which was introduced by the dynamic coupling between the tilted Bell-412 pilot seat frame and the seated manikin in the X and Z directions. Comparatively, the vibration level in the Y direction was relatively low, and the impact on the overall aircrew WBV was negligible. As expected, spectral analysis of the vibrations at the seat cushion interface indicated that the dominant vibration were related to the 1/rev, 2/rev and 4/rev harmonic frequencies. The vibrations due to other N/rev harmonics were

significantly lower.

With the adaptive control of the grouped actuators in the vertical direction, vibration level in the Z direction of the bottom seat cushion interface was reduced significantly. The peak vibration amplitudes at 1/rev, 2/rev and 4/rev were suppressed by 89.0%, 90.4% and 91.7%, respectively. The N/rev harmonic amplitudes in the X direction was also reduced simultaneously. As a result, the overall WBV of the 50th percentile male manikin was reduced by 36.0% and 26.5% in the X and Z directions, respectively. Per ISO 2631-1 metrics, the combined WBV was reduced by 26.6%.

(a) X direction   (b)   Z direction
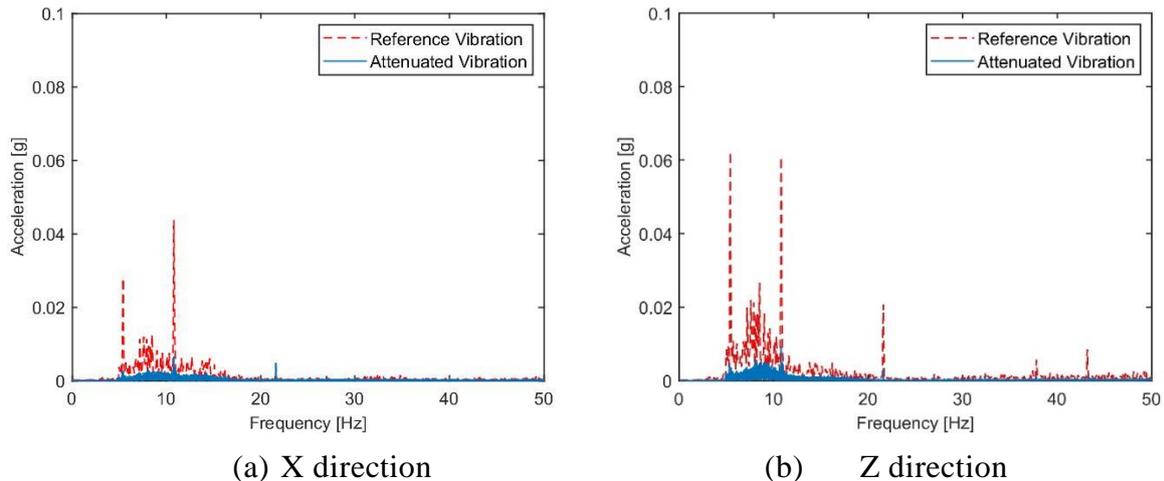
Figure 4 Vibration at seat cushion interface under vertical excitation

The aircrew WBV reduction not only improved the ride quality, but also extended the exposure time limit in helicopter flight missions. Based on ISO 2631-1, the active seat mount was expected to extend the aircrew exposure time limit significantly. Referencing to the Health Risk Likely Zone, the exposure time limit can be extended by 60% (equation B.1); the exposure limit for the Health Risk Caution Zone can be extended by 156% (equation B.2).

In addition to the direct evaluation of occupant WBV using ISO metrics, the vibration responses of the manikin body were also analyzed. Results are shown in Figure 5.

Head vibration level is a concern for helicopter aircrew because the aircrew are required to use flight helmets in flight operations, and the use of night vision goggles further increases the head mounted mass. The long durations of flight can contribute the aircrew neck strain and back injury issues, and high head vibration levels can further aggravate this problem. With the active seat mount system, it was noted that the vibration levels in the Z and X directions dominantly contributed to the overall vibration at the manikin head location. Test results demonstrated that the active seat mount was effective in mitigating manikin head vibration levels. In the Z direction, the vibration peaks at 1/rev, 2/rev and 4/rev were reduced by 87.2%, 84.0% and 93.9% respectively, which resulted in a reduction of 35.7% in terms of overall vibration level in the Z direction.

At the manikin spine location, the highest vibration came from the Z direction, and moderate vibration also existed in the X direction, possibly related to the dynamic coupling between X and Z directions of the pilot seat. The response in the Y direction was negligible. The vibration of the spine was also related to the peaks at the major N/rev harmonic frequencies such as the 1/rev, 2/rev and 4/rev. With the reduced vibration transmission of the active seat mount, the vibration level at the manikin spine location was reduced

effectively. For example, in the Z direction, the spine overall vibration level was reduced by 34.0%, with 86.1% reduction at 1/rev, 84.7% at 2/rev and 95.2% at 4/rev respectively.

(a) Head X direction   (b)   Head Y direction

(c) Spine X direction   (d)   Spine Z direction
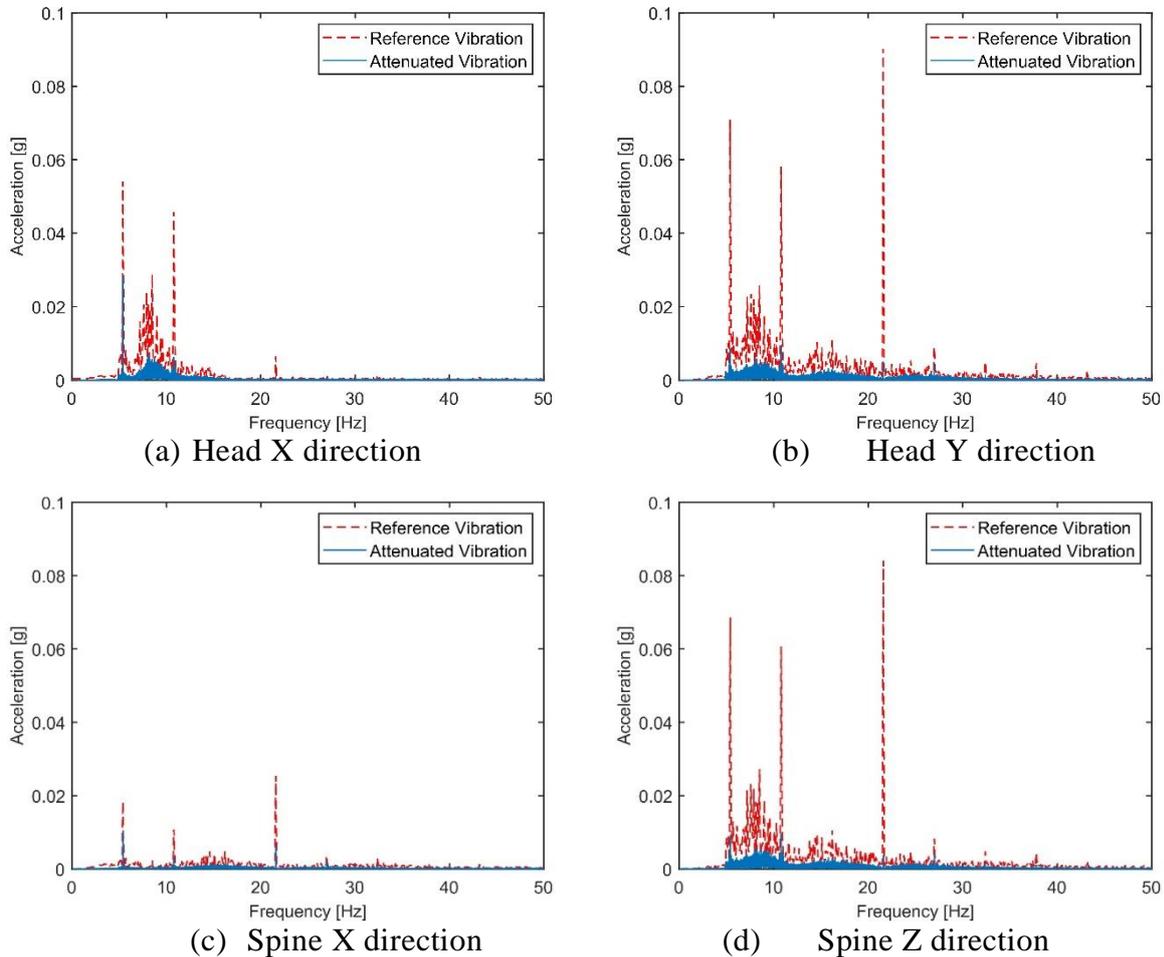
Figure 5 50th percentile manikin whole-body vibration under vertical excitation

This test case demonstrated that the active seat mount system was able to reduce the vibration levels at the pilot seat frame, seat cushion interface as well as the manikin body locations when excited in the Z direction and subjected to representative Bell-412 floor vibration profiles.

4.2. Combined Multiple Direction Test

The active seat mount assembly was also tested with combined vibration excitations in the X and Y directions simultaneously. In this case, the test setup was installed on the shaker slip table, and oriented at an angle of 45 degrees relative to the shaker vibration input direction. In the control scheme, the manikin vibration at the head location was used as the error signal, and the shaker table vibration input was used as the reference signal. Two parallel FxLMS controllers were activated to generate control signals for the actuator groups in the X and Y directions independently.

Test results on the 50th percentile male manikin are shown in Figure 6, where the red-dashed line represents the baseline vibration while the blue line indicates the attenuated vibration after the adaptive control converged. The plot legend shows the reduction of the first four N/rev harmonic frequecies. As shown by the baseline curves in this case, WBV

levels in the X and Y directions were much higher than that in the Z direction, indicating that the horizontal vibration input in X and Y directions did not lead to significant dynamic coupling with the vertical Z direction. Similar to the case of vibration input from Z direction, the manikin WBV was mainly related to the peaks at the 1/rev, 2/rev, and 4/rev harmonics while the amplitudes at other N/rev frequencies were significantly lower.

Examining the peak amplitudes at the 1/rev, 2/rev, and 4/rev frequencies in the X and Y directions, the active seat mount assembly was shown to reduce the major N/rev vibration peaks at the seat cushion interface by nearly 90% in both X and Y directions. With the suppression of the major N/rev peaks, the overall WBV level was reduced by 42.6% in the X direction and 50.2% in the Y direction.

(a) X direction   (b)   Y direction
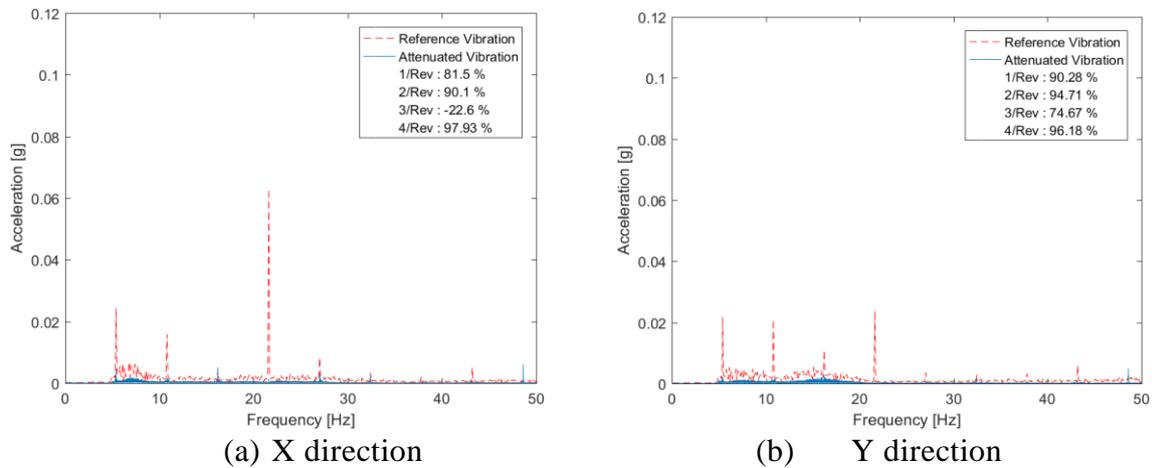
Figure 6 50th percentile manikin WBV under horizontal excitation

As shown in Figure 7, significant reduction was also achieved at the head and spine locations of the manikin. It was shown that the major N/rev peaks at the head and spine locations were reduced by nearly 85% in both X and Y directions. The overall vibration reduction at the spine location was 42.1% for X and 26.5% for Y directions, respectively. Similarly, 51.4% and 45.1% reduction for the X and Y directions at the head location.

This test case verified that the dynamic coupling among three orthogonal directions was not significant when actuated in the horizontal directions. The parallel controllers in the X and Y directions functioned independently, and achieved effective reduction to the manikin WBV in the X and Y directions simultaneously.

(a) Head X direction   (b)   Head Y direction

(c)   Spine X direction   (d)   Spine Y direction
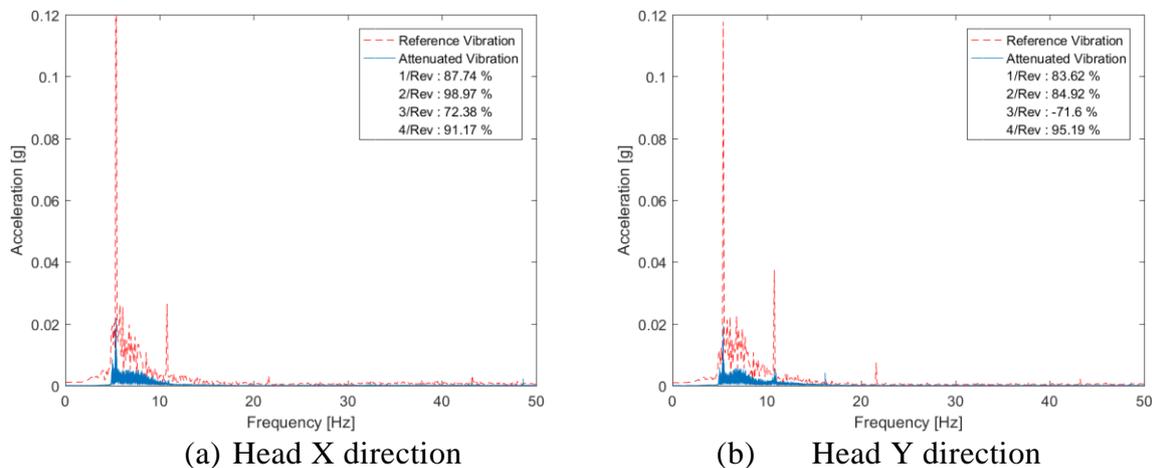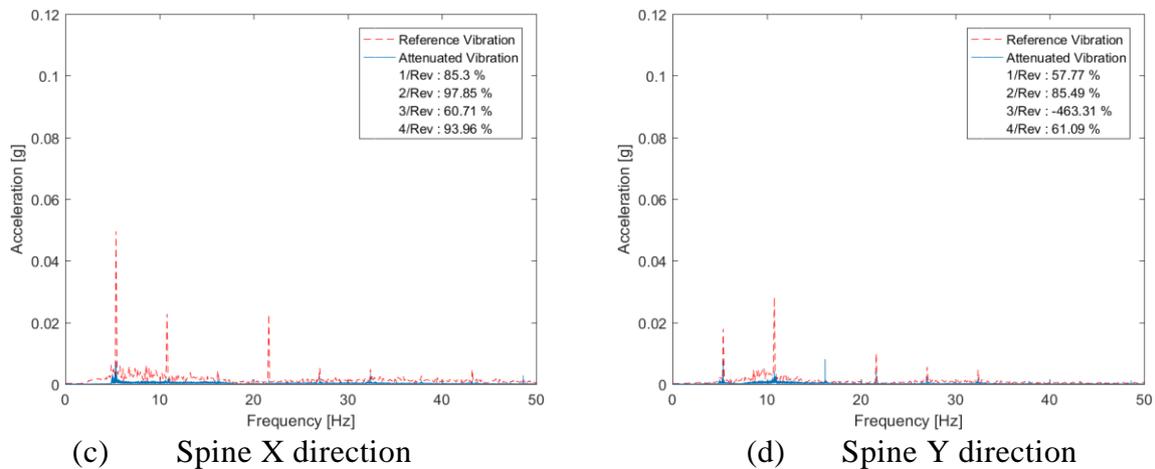
Figure 7 50th percentile manikin WBV vibrations under horizontal excitation

5. STRUCTURAL MODIFICATION FOR FLIGHT DEMONSTRATION

Inspired by the performance of the prototype active seat mount system to reduce helicopter aircrew WBV exposure related to the N/rev harmonic peaks, it was decided to explore the potential of the active seat mount technology through flight testing on the NRC Bell-412 helicopter testing platform using human or manikin occupants at representative flight conditions. Test conditions would include helicopter engine ground run, hovering in and out of ground effect heights, as well as level flights at various speed of the vehicle.

To achieve this objective, the two active seat mount assemblies need to be fully integrated within the Bell-412 helicopter cabin, and also to meet stringent airworthiness requirements while maintaining the full functionality of the prototype active seat mount design. Therefore, modification of the prototype design have been considered in order to satisfy multiple technical and airworthiness requirements. It is important to note that the current modifications mainly focus on the installation of the active seat mount assemblies inside the NRC Bell-412 helicopter cabin for flight demonstration, and it is reasonable to expect that additional structural modifications and further optimizations are required before the technology is matured for commercial product development.

The first requirement is to reduce the weight and dimension of the prototype active seat mount design in order to be fitted into the limited space of the Bell-412 helicopter cabin. The candidate installation locations include the cockpit or the rear cabin for demonstration purposes. Specifically, the height of the prototype active seat mounts need to be reduced in order for the human or ATD occupant to be seated in the Bell-412 helicopter cabin. In the original design, the two actuators grouped for vertical vibration control were positioned in the middle of the active seat mount assembly, which significantly increased the height of the active seat mount frame. Moreover, based on experimental results of the prototype design, the actuator rated force in the vertical direction is required to increase for control of higher vibration excitations from the vehicle at high speed. The larger height of the actuators further increases this challenge. In the improvement design, the two new and bigger actuators were relocated to the two ends of the active seat mount assembly to allow the top frame of the mount assembly be significantly lowered, which enabled the Bell-412 non-armored pilot seat frame to be installed and locked to the guide rails on the top of active seat mount assembly. These structural modifications are shown to reduce the height of the active seat mount assembly by 127 mm (5") at the seat rail sections, which provides the

Yong Chen, Amin Fereidooni, Rene Laliberte, Viresh Wickramasinghe

required vertical space for the Bell-412 non-armored pilot seat frame and occupant to be installed in the rear cabin, or the cockpit.

The prototype seat mount assembly was made of segmented metallic bars for proof-of-concept functionality demonstration. This simplified design does not meet airworthiness requirement for aircraft flight testing. Therefore, the metallic bar frames were replaced with 2024-T3 aluminum sheet metal structural components to satisfy flight testing requirement on the NRC Bell-412 helicopter. The high strength sheet metal structural design is shown to achieve greater strength and stiffness while reducing weight by 16 lbs.
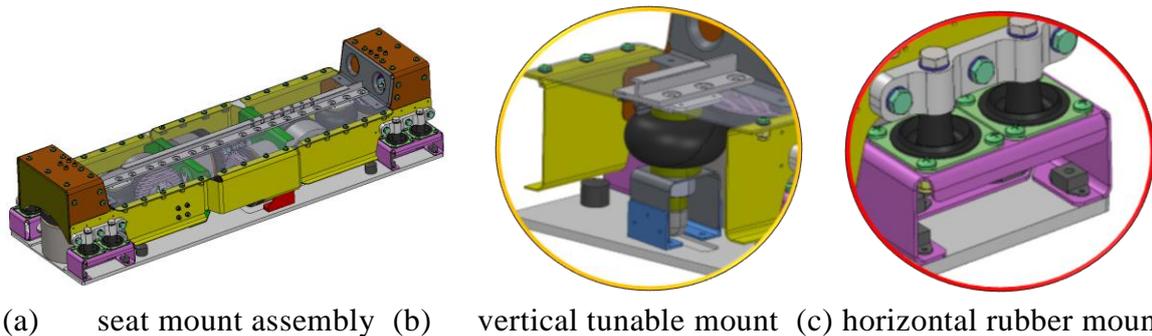
(a)   seat mount assembly (b)   vertical tunable mount (c) horizontal rubber mounts

Figure 8 redesigned active seat mount assembly

To avoid excessive displacement of the Bell-412 seat frame and occupant during aircraft flight maneuvers, the stiffness of the prototype active seat mount was redesigned in all three orthogonal directions. Two stiffness tunable vibration isolators were included to replace the original soft elastomeric supporting elements in the vertical direction. These pneumatic rubber isolators not only provide the required passive stiffness and damping for support in the vertical direction, but also offset the compressive displacement due to the static weight of the pilot seat and occupant. Similarly, the soft elastomeric supporting elements in the X and Y directions were also replaced with multiplane rubber isolators with equal stiffness rate. These off-the-shelf rubber isolators are expected to provide predictable and reliable vibration isolation to limit the displacement in horizontal directions. The redesigned active seat mount assembly and new isolators are schematically shown in Figure 8.
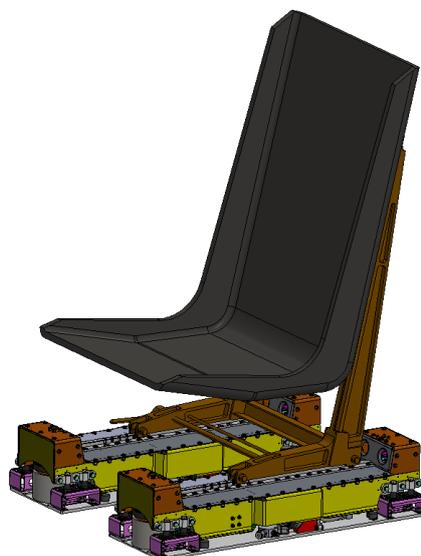
Figure 9 Bell-412 seat frame installed on the revised active seat mount assemblies

These structural modifications not only reduce the dimensions, but also reduce the weight of the prototype active mount system. The redesigned active seat mounts are shown to be able to fit into the NRC Bell-412 helicopter rear cabin for flight testing and demonstration purposes, and the assembly weight is reduced from 124 lbs to 51 lbs. The modified design of the active seat mount system installed with the Bell-412 non-armored pilot seat frame is shown in Figure 9. Preliminary assessment indicated that the crashworthiness compliance of the Bell-412 seat frame was not altered by the new active seat mount design. The incorporated design modifications are also shown to meet airworthiness requirements for permission of installation in the NRC Bell-412 helicopter platform for flight trails.

Currently, advanced structural analysis is being performed. Upon completion and pending on approval, components fabrication and system assembly will be pursued. The revised active seat mount system will be further tested to verify functionality for aircrew WBV mitigation on the mechanical shaker table. The flight test and demonstration phase on the NRC Bell-412 helicopter is planned for 2023.

5. CONCLUSION

The evaluation of a proof-of-concept multi-axis seat mount design to reduce helicopter aircrew whole body vibration is presented. The active seat mount assembly was integrated with a Bell-412 non-armored pilot seat, with Hybrid III manikins used as the occupants. Extensive tests have been completed on a large mechanical shaker table using simulated Bell-412 helicopter vibration profiles in the vertical and horizontal directions. Through the suppression of major N/rev harmonic peaks of the main rotor speed, the multi-axis active seat system was shown to reduce the seat frame vibration and manikin WBV levels simultaneously in accordance with ISO 2631-1 metrics. In addition, vibration levels at the occupant head and spine locations were also reduced significantly. These demonstrated that the multi-axis active seat mount system can effectively reduce aircrew whole-body vibrations in multiple directions.

Further structural modification and improvements have been introduced to enhance the prototype active seat mount design, which led to reduced dimension and height of the assembly. The modified active seat mount design has shown promising compliance of airworthiness requirements for installation and flight demonstration on the NRC Bell-412 helicopter. It is also acknowledged that further structural modifications and optimization will be needed before this technology is matured for commercial product development.

REFERENCES

[1] Bongers, P., Hulshof, C., Dljkstra, L., Boshuizen, H., Groenhout, H. and Valken, E., "Back pain and exposure to whole body vibration in helicopter pilots," *Ergonomics*, Vol. 33, No. 8, 1990, pp. 1007-1026.

[2] Branco, C., Rodriguez, E., "The Vibroacoustic Disease - An Emerging Pathology", *Aviation, space and environmental medicine*, Vol. 70, 1999, pp. A1-6.

[3] Seddon, J. M., and Newman, S., *Basic Helicopter Aerodynamics*, John Wiley & Sons,

West Sussex, UK, 2011.

[4]   International Standards Organization, Mechanical vibration and shock - Evaluation of human exposure to whole-body vibration - Part 1: General requirements, Geneva, Switzerland, 1997.

[5]   Harrer, K. L., Yniquez, D., Majar, M., Ellenbecker, D., Estrada, N. and Geiger, M., "Whole Body Vibration Exposure for MH-60S Pilots," Forty Third Annual SAFE Association Symposium, Crewell, OR, 2005.

[6]   Gan, Z., Hillis, A. J. and Darling, J., "Adaptive control of an active seat for occupant vibration reduction," *Journal of Sound and Vibration*, Vol. 349, 2015, pp. 39-55.

[7]   Hiemenz, G., Hu, W., and Wereley, N., "Semi-Active Magnetorheological Helicopter Crew Seat Suspension for Vibration Isolation", *Journal of Aircraft*, Vol. 45, 2008, pp. 945-953.

[8]   Chen, Y., Wickramasinghe,V., and Zimcik, D., "Development of Adaptive Seat Mounts for Helicopter Aircrew Body Vibration Reduction", *Journal of Vibration and Control*, Vol. 15, 2009, pp. 683-706.

[9]   Chen, Y., Wickramasinghe, V., and Zimcik, D. G., "Development of Adaptive Helicopter Seat for Aircrew Vibration Reduction," *Journal of Intelligent Material Systems and Structures*, Vol. 22, No. 5, 2011, pp. 489-502.

[10] Graham, S., Fereidooni, A., Chen, Y., and Wickramasinghe, V. K., "Investigation of a Parallel Active Vibration Isolation Mount for Mitigating N/Rev Helicopter Vibrations," 25th AIAA/AHS Adaptive Structures Conference, AIAA 2017-1441, 2017.

[11] Hadj-Moussa, F., Fereidooni, A., Chen, Y., and Wickramasinghe, V., "Development of a Multi-axis Active Seat Mount to Mitigate Vibration Transmission to Helicopter Aircrew," 2018 AIAA SciTech Forum, Kissimmee, Florida, January 8-12, 2018.

[12] Moticont website, http://www.pwr-con.com/gvcm-095-038-01.htm.

[13] Hansen, C., and Snyder, S., *Active Control of Noise and Vibration*, E & FN Spon, London, UK, 1997.

[14] Morgan, D. R. and Sanford, C., "A control theory approach to the stability and transient analysis of the filtered-X LMS adaptive notch filter," *IEEE Transactions on Signal Processing*, Vol. 40, No. 9, 1992, pp. 2341-2346.

AUTOMATIC SHAPE OPTIMIZATION OF A NON-PLANAR WING BASED ON DISCRETE ADJOINT AND RADIAL BASIS FUNCTION MESH DEFORMATION

Luca Abergo[1]*, Myles Morelli[2] and Alberto Guardone[3]

Department of Aerospace Science and Technologyr
Politecnico di Milano
Building B12, Via La Masa 34, Milano, MI 20156, Italy

1:Master Student, luca.abergo@mail.polimi.it
2: Postdoctoral Researcher, mylescarlo.morelli@polimi.it
3:Professor, alberto.guardone@polimi.it

Abstract. *The results obtained by an Automatic Shape Optimization tool are strongly effected by the mesh deformation method used. A computationally efficient Radial Basis Function (RBF) grid deformation is coded with two data reduction schemes: multi-level greedy surface point selection algorithms and volume point reduction methods. Following, it is combined with the discrete adjoint inside the open-source software SU2. The robustness of the method, the ability to handle complex shapes and apply large deformations makes possible to optimize also a non planar geometry like a wing provided with a winglet. The surface sensitivity, besides also the final value of the objective function, depends on how the grid is updated, since for the computation of the adjoint variables the process is differentiated by Automatic Differentiation. Finally, the gradient based algorithm "Sequential Least Squares Programming" drives the research of a new local minimum by gradually morphing the geometrical shape*

Keywords: discrete adjoint, design, optimization, mesh deformation, radial basis functions

Luca Abergo, Myles Morelli and Alberto Guardone

1 INTRODUCTION

Automatic Shape Optimization (ASO), based on Computational Fluid Dynamics (CFD) and guided by a gradient method, is becoming a powerful tool available to engineers for aircraft design. It can be applied to improve the aero-performance of airfoils, wings and rotors. The Optimization chain described in this paper is implemented in the open-source multiphysics solver SU2 [1], the several modulus needed are implemented in C++ and executed in the correct sequence by a python routine. The search of the optimal shape is driven by a gradient based algorithms named "Sequential Least Squares Programming" (SLSQP) [2], which has been proved to deliver the most robust solution [3]. In this context "optimal" is intended as a morphed form of the original body which provides a significant reduction of the objective function selected J, usually an aerodynamic coefficient or a combination of them. The general problem can be expressed as:

$$
\begin{aligned}
\min_{\alpha} \quad & J(U(\alpha), X(\alpha)) \\
\text{subject to} \quad & U(\alpha) = G(U(\alpha), X(\alpha)) \\
& X(\alpha) = M(\alpha) \, .
\end{aligned}
\tag{1}
$$

Where X is the computational grid which can be considered as sum of two different components $X = X_{\text{vol}} + X_{\text{surf}} = M(\alpha)$ where $X_{\text{vol}} = X_{\text{vol}}(X_{\text{surf}})$. It means that the volume grid depends explicitly on the wall mesh, that depends in a smooth way on the problem variables α. No assumptions on the structure of M are considered, except that is differentiable. Instead, U is the Reynolds Average Navier-Stokes (RANS) flow state that can be found solving the fixed point equation $U^{n+1} =: G(U^n)$. The local minimum found depends on the starting point and belongs to its close neighbour, besides the final value of J is linked to the amount of geometrical and aero-constraints and the number of design variables.

First, a mathematical description of the wall surface is needed, in this paper the interpolation method Free Form Deformation (FFD) is selected [4]. The body is immersed inside a plastic box, split in smaller bricks which vertices are selected as design variables α whose positions control the geometry. The displacement of the Design Variables (DVs) is obtained projecting into the design space the sensitivity of the target function with respect to the them. FFD can be applied to any kind of mesh and does not modify the connectivity. One the body is properly parametrize, the flow variables U and the current value of the objective function J must be computed, therefore Reynolds Averaged Navier-Stokes equations (RANS) are solved. Regarding this work, the one-equation Spalart Allmaras[5] turbulence model is used without wall functions. The following step is to determine how the objective function is going to change to a perturbation of one of the design variable, thus the surface sensitivity must be computed how it is done in SU2 is explained in Sec. 2. Once it is known how the body has to be morphed, the surface and fluid volume grid has to be adapted. This step is crucial for two reasons. First, the mesh deformation method selected is differentiated inside the process for computing the surface sensitivity therefore the direction of search in the design space is method dependent. Second, how the grid is updated, especially in case of large displacements and complex geometry, can generate a progressive lost in the quality of the mesh jeopardising the entire design process. Historically the first methods were based on an analogy to a continuum: springs or linear elasticity (ELA) [6, 7]. They both require the connectivity of the grid, they well handle

Luca Abergo, Myles Morelli and Alberto Guardone

only small deformations and are computationally expensive [8]. Therefore a method for morphing the grid based on interpolation is introduced and coupled with the adjoint, the technique is extensively described in Sec. 3. Concerning shape optimization, ELA is widely used also in SU2 [9–11], thus in this work it is used as comparison with the new optimization chain.

The design loop is repeated until the Karush-Kuhn-Tucker conditions (KKT) are respected or the maximum number of iterations is reached [12]. Most of the times the convergence history is not monotone, the maximum reduction of the objective function is reached before the last loop.
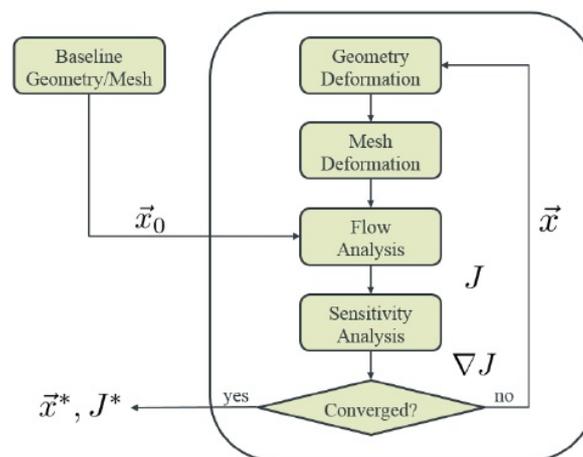
Figure 1: Optimization Design Loop

The comparison between the two ASO is made with the 3D commonly used planar wing the Onera M6 in Sec. 4.1. The cad is than modify to obtain a non planar wing to optimize in Sec. 4.3. The optimization histories are compared also the virtual memory consumption during the mesh deformation step is monitored.

2 SENSITIVITY COMPUTATION

Regarding SU2, $\frac{\mathrm{d}J}{\mathrm{d}\alpha}$ is computed through the discrete adjoint, which has been implemented by Albring, Saugeman and Gauge [13] with a state of art double system method [14]. The required Jacobians are constructed by Automatic Differentiation (AD), coded taking advantage of expression templates and operator overloading. This choice makes possible to differentiate viscous RANS equations with any turbulence model or easily extend the optimization problem to multiphysics pdes. Taking advantage of the library named CoDiPack [15], AD is implemented at statement-level, where the information that need to be stored are independent from the number of operations internally involved [16]. In particular "Reverse Mode" is used since it is attractive for all that kind of problems where a single or a small number of objective functions depend on a large set of variables. Discrete Adjoint is a perfect example since we need the sensitivity of J with respect to the long vector α. In contrast to the forward modality, a single output is selected and the first-order derivative with respect to each of the intermediate variables and the input variables is calculated in an unique process. Reverse AD, coded using expression templates, is 2.7-4 times slower than a direct simulation, making it comparable to the hand-written Jacobians. However, reverse AD requires a large amount of physical memory, some tech-

Luca Abergo, Myles Morelli and Alberto Guardone

niques as local preaccumulation and the usage of checkpoints can help to contain the ram consumption [17].

Discrete Adjoint provides the sensitivity with a computational cost scaling with the number of objective functions, therefore not with the length of α as finite difference, and without computing the volume mesh sensitivity.

$$\Lambda_f = \frac{\partial J^T}{\partial U} + \frac{\partial G^T}{\partial U}\Lambda_f$$
$$\Lambda_g = \frac{\partial J^T}{\partial X} + \frac{\partial G^T}{\partial X}\Lambda_f$$

(2)

where Λ_f represents the adjoint variables linked with the flow state, meanwhile Λ_g is a set of dual variables related to the grid movement problem.

It must be highlighted that the surface sensitivity still depends on the grid deformation method selected. Moreover, it strongly influence the ability to properly explore the design space, the complexity of the geometry manageable and the dimension of the displacements applied, resulting in a final value of the target function dependent on the method used. Mesh deformation algorithms can generate a slow degradation of the mesh quality which could cause the divergence of the RANS simulation thus even of the optimization process.

3 RADIAL BASIS FUNCTION

In this work, a Radial Basis Function technique, implemented by Morelli and Bellosta [18] for ice accretion prediction, is introduced in the ASO for its robustness and the ability to transfer a large displacement from the surface into the fluid grid. This helps to preserve the quality of the original grid and subsequently improve the robustness of the whole optimization process. As FFD it does not need the grid connectivity, therefore the described optimization chain can handle any type of mesh. It belongs to the class of interpolation methods, it takes as inputs a known boundary displacement field and a continuous base function $\phi(\mathbf{r}, \mathbf{r}_i) = \phi\left(\|\mathbf{r} - \mathbf{r}_i\|\right)$, where the distance corresponds to the radial basis centre, $\mathbf{r}_i$ between two nodes. A certain amounts of control points are selected then, the wall movement is interpolated and propagated in the whole fluid by a weighted sum of basis functions:

$$f(\mathbf{r}) = \sum_{i=1}^{N} \alpha_i \phi\left(\|\mathbf{r} - \mathbf{r}_i\|\right)$$

(3)

A linear system to obtain the weight coefficients need to be solved. This method requires the knowledge of the desired displacement of the entire surface grid. Concerning the optimization process implemented in SU2, from the adjoint solution projected into the design space the movement of the vertices of the FFD box is computed. Subsequently, with the free form deformation routine, which is also in this case an interpolation inside the control volume, the surface displacement is obtained. The vector ΔX collect the surface nodes movement which is underlined by the subscript "s", it is described by:

$$\Delta X_s = [\Delta x_{s_1}, \Delta x_{s_2}, \ldots, \Delta x_{N_s}]$$
$$\Delta Y_s = [\Delta y_{s_1}, \Delta y_{s_2}, \ldots, \Delta y_{N_s}]$$
$$\Delta Z_s = [\Delta z_{s_1}, \Delta z_{s_2}, \ldots, \Delta z_{N_s}]$$

(4)

Luca Abergo, Myles Morelli and Alberto Guardone

The three Cartesian directions can be combined in a more simplified formulation:

$$\Delta S = \Delta X_s \hat{x} + \Delta Y_s \hat{y} + \Delta Z_s \hat{z} \tag{5}$$

In analogy also the weight coefficients are collected in a vector:

$$\alpha_x = [\alpha_{x,s_1}, \alpha_{x,s_2}, \ldots, \alpha x, N_s]^T \tag{6}$$

The y and z coefficients are analogous. Following, the weights can be extracted by solving the linear system:

$$\Delta S = \Phi_{s,s} \alpha \tag{7}$$

where Φ is the universal basis matrix, it is generated with the radial basis function evaluated at each surface nodes, meaning that the matrix has size of N_s^2. The compact form of the universal basis function is expressed as:

$$\Phi_{s_j,s_i} = \phi||r_{s_i} - r_{s_j}|| \tag{8}$$

The next step is to compute the volume base matrix $\Phi_{v,s}$ of size $N_v \times N_s$, where "v" indicates a volume point. Finally, the volume displacement can be interpolated multiplying the above-mentioned matrix with the weights previously computed:

$$\Delta V = \Phi_{v,s} \alpha \tag{9}$$

RBF in the context of design optimization is not widely used due to the elevated computational cost. Even if its potential has been already highlighted by [19], there is no notion of RBF coupled with the discrete version of the adjoint and automatically differentiated. The SU2 versions becomes practicable since it introduces two data reduction schemes to increase the efficiency: multi-level greedy surface point selection algorithms [20] and volume point reduction methods [21]. To guide the greedy algorithm when selecting control points an error vector E is introduced, which is based on the difference between actual surface displacements and computed surface displacements:

$$\mathbf{E} = \Delta S - \mathbf{\Phi}_{s,c} \boldsymbol{\alpha} \tag{10}$$

The node with the largest error is selected as new control point. Denoting the control, surface, and volume points respectively by subscripts c, s, and v and the number of levels is described by the superscript l.Each time that a node is selected the linear system to obtain the weights must be solved. Therefore, the CPU cost of the greedy algorithm is of the order of N_c^4, where the final number of control points selected is the number of iterations of the process plus one. In the case of large displacement of complex geometry the computational cost of the simple greedy scheme becomes too large. The problem has been overtaken by introducing a multi-level subspace radial basis function interpolation, firstly introduced by Wang [20]. The object for the second level of interpolation is set equal to the error of the first step $E^{(0)}$. In a general form, it can be expressed as:

$$\Delta S_{l+1} = E^{(l)} \tag{11}$$

where the next step of the multi-level selection process is indicated by the subscript "$l+1$". The residual of Eq. 7 at the second level can be expressed as:

$$\Delta S^{(1)} = \Delta S^{(0)} - \Phi W^{(1)} = \Delta S - \Phi(\alpha^{(0)} + \alpha^{(1)}) \tag{12}$$

Luca Abergo, Myles Morelli and Alberto Guardone

the size of the displacement is strongly reduced $\Delta S_{l+1} << \Delta S_l$. The computational cost for the multilevel greedy algorithm is now of order of $N_l \times N_c^4$ instead of $(N_l \times N_c)^4$ for the single step. The multi-level selection process can be summarised as follows:

$$\Delta S = \sum_{i=0}^{i=N_l-1} \Delta S^{(i)} = \sum_{i=0}^{i=N_l-1} \mathbf{\Phi}_{s,c}^{(i)} \boldsymbol{\alpha}^{(i)} \tag{13}$$

$$\Delta V = \sum_{i=0}^{i=N_l-1} \Delta V^{(i)} = \sum_{i=0}^{i=N_l-1} \mathbf{\Phi}_{v,c}^{(i)} \boldsymbol{\alpha}^{(i)} \tag{14}$$

The CPU cost of the volume interpolation, after the multi greedy point selection, is now of the order of $N_l \times N_c \times N_v$. In the case of large scale geometry, it is of interest to find how to decrease N_v. One method was proposed by Xie and Liu [21]. They introduced a function which value is based on the distance from the closest wall:

$$\psi = \psi \left(\frac{d(r)}{D} \right). \tag{15}$$

where $d(r)$ is the space distance and D a support value imposed. We define the ratio between the two distances as ξ. The function decays in value when the distance increase and is zero outside the supported distance, so it is a compact support function. It can be expressed as:

$$\psi(\xi) = \begin{cases} (1 - \xi) & 0 \leq \xi < 1 \\ 0 & \xi \geq 1 \end{cases} \tag{16}$$

The value of support distance D depends on the maximum surface displacement multiplied for a volume reduction factor k imposed by the used. Mathematically it can be expressed as:

$$D = k(\Delta S_l)^{\max} \tag{17}$$

k in practice defines the range around the body inside which the flow nodes are going to be shifted, besides we are requiring that the elements outside this volume are not affected by the surface movement. It can be notice that is exactly the opposite behaviour respect to the linear elasticity analogy of the previous section where the higher stiffness of the grid's elements close to the wall boundary cases that the distortion is absorbed by the largest elements which are close to the farfield.

In the end the interpolation Eq. 3 is modified in order to include the wall distance correction:

$$f(r) = \psi \left(\frac{d(r)}{D} \right) \sum_{i=1}^{N} \alpha_i \varphi(||r - r_i||) \tag{18}$$

It is attractive the possibility to directly control the intrinsic interpolation error, the consumption of virtual memory and the wall time selecting the base function, the maximum amount of control points and the number of levels for the greedy algorithm.

4 RESULTS

In this section the old framework, with Ela as deformation mesh method, and the new one with RBF are compared. The optimization of a 3D planar wing is presented in Sec. 4.1. Moreover, to show the improved robustness of the new ASO the optimization of a full non planar wing is conducted in Sec. 4.3. Finally, the virtual memory allocation during the single deformation process is monitored and reported in Sec. 4.2

Luca Abergo, Myles Morelli and Alberto Guardone

4.1 ONERA M6

The ONERA M6 can be described as a swept, semi-span wing with no twist. The symmetric ONERA D section is used as an airfoil. It is a typical test case for turbulence flow over a transonic wing, widely adopted for CFD validation. Experimental data for the comparison of the pressure distribution are provided in [22]. The flight conditions are chosen to deal with a strong shock on the upper part of the wing collocated close to the 25% of the chord.

Mach	0.84
AoA	3.06
Re	$14.6E6$
Temperature	$300K$

Table 1: Free Stream Conditions Onera M6

Firstly, mesh convergence has been performed, four hybrid meshes are generated. The smallest one is used for optimization. This choice is dictated by the computational power available. The first three layers of the mesh have constant height than the growth ratio decrease from the coarse to the finer grid. The number of layers of the structured part has an opposite behaviour. Since the surface grid is almost everywhere structured, the number of points in the x,y direction are easily multiplied by a factor of 1.5 for the convergence. The following figures report the aerodynamic coefficients obtained and the relative error also the predicted value for an infinity dense mesh is marked. Moreover, the C_p distribution at four different stations is monitored.
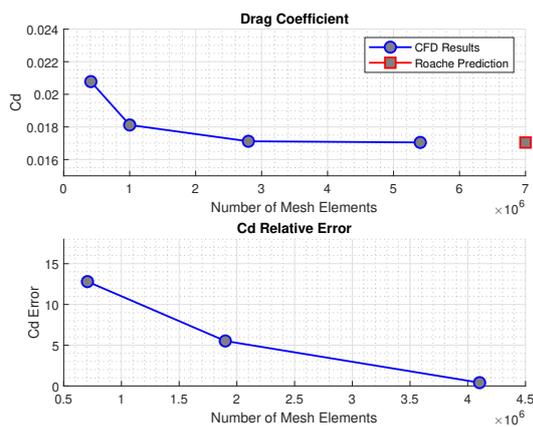
Figure 2: Onera M6: C_d Convergence
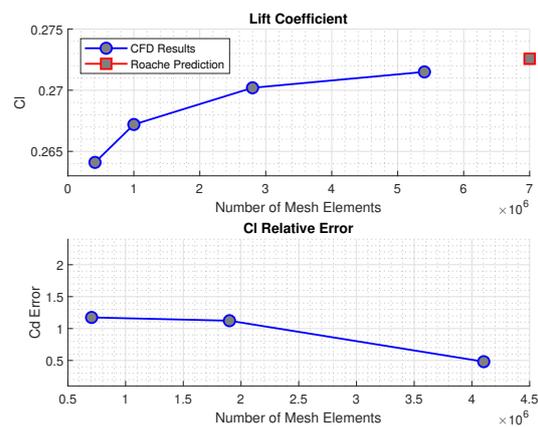
Figure 3: Onera M6: C_l Convergence

Luca Abergo, Myles Morelli and Alberto Guardone
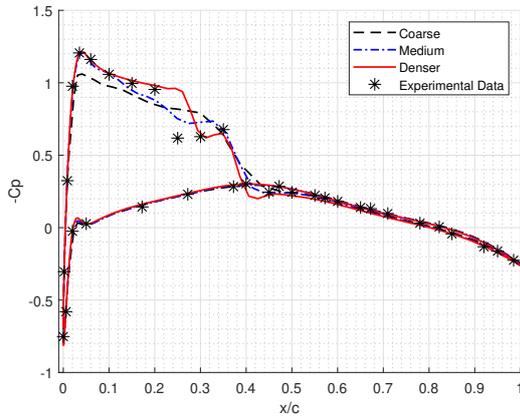
Figure 4: Onera M6: C_p Convergence y=80%b
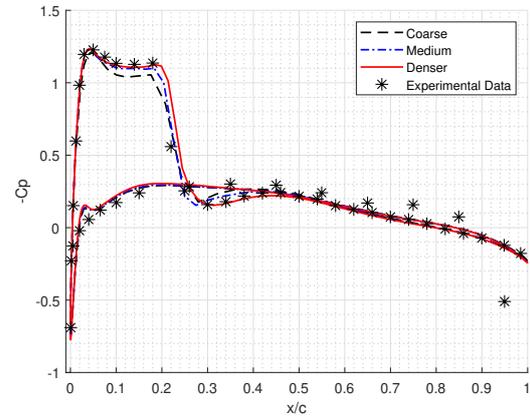
Figure 5: Onera M6: C_p Convergence y=95%b

The goal of the optimization is to reduce the drag without decreasing the lift and the volume of the body. The angle of attack is free to change, the variation of the torque moment is only monitored. Six geometrical constraints are imposed: the final maximum thickness at different span stations cannot be lower than the 75% of the initial value. The gradient based optimization using the SLSQP algorithm is performed once with RBF as mesh deformation method, then with ELA. Regarding RBF, the maximum number of control points selectable is the 10% of the surface's nodes, the volume reduction factor k is set at 5 and the Wendland $C0$ is selected as the interpolation function. This configuration makes RBF really robust, fast, and computationally cheap. Instead, considering ELA a final residual of $10^{(-10)}$ is required for the solution of the linear system and the stiffness of the cells is computed inversely with respect to their volume. Results are reported in the following figures:

Luca Abergo, Myles Morelli and Alberto Guardone
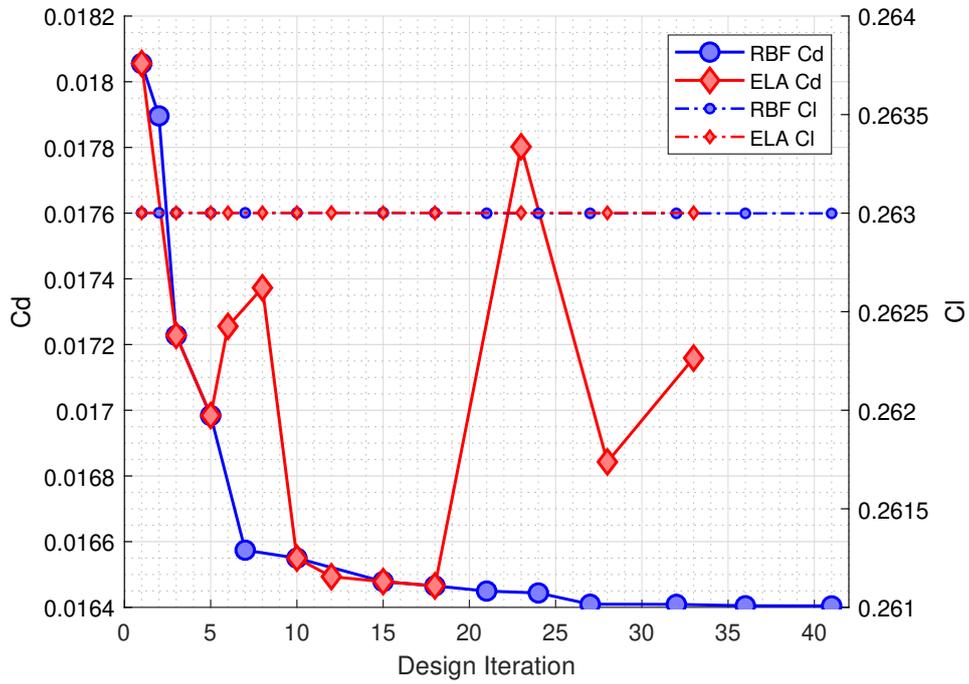
Figure 6: Onera M6: C_d Variation
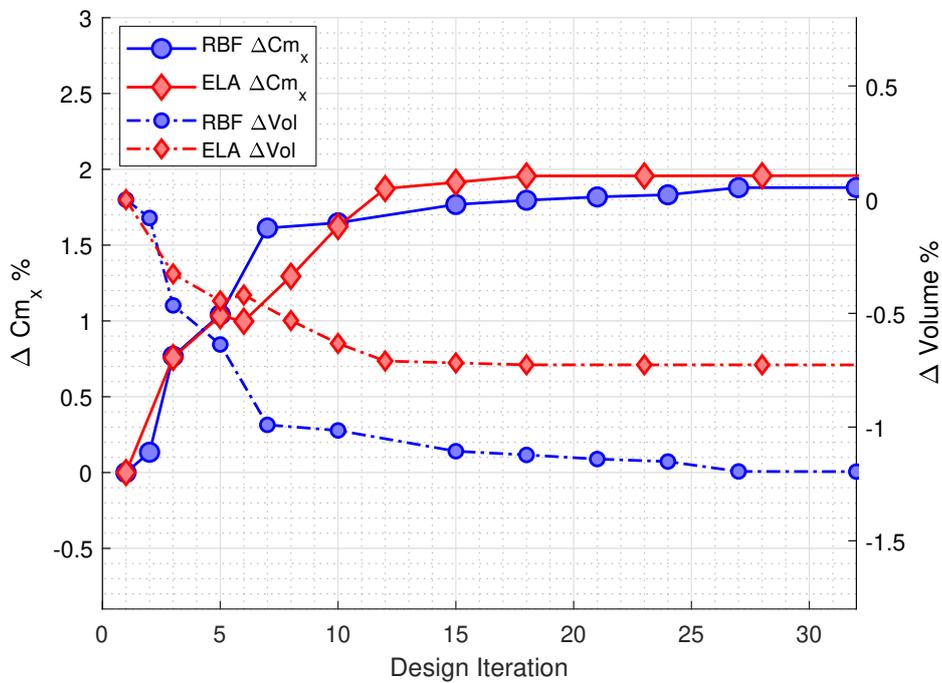
Figure 7: Onera M6: volume and torque variation

Fig 6 clearly shows that both methods are able to conserve the lift and reduce the drag, however the optimization history seems to be more robust using RBF with a more clear convergence. Regarding RBF, the overall drag reduction is around 9.15%, particularly the

Luca Abergo, Myles Morelli and Alberto Guardone

drag reduction between the last two loops is insignificant underlying the achievement of a minimum. Instead, ELA obtains a slightly smaller reduction of the C_d around 8.57%. The evolution of the drag with respect to the deformation loops is oscillating, this behaviour has been observed also by other researchers [23]. Further, the optimum is obtained at the $18th$ iteration than a big jump happens and this seems to be typical of the old SU2 optimization chain [24]. Both method increase the torque of the 2% and slightly reduce the volume even if a specific geometrical constraint is imposed. How the shape of the sections and thus the pressure distribution are modified after the optimization is shown in the next pics. The sections close to the root are more morphed, instead the tip of the wing is just more twisted. Especially close to the wing's tip, the peak of suction is decreased and this results in a less intense shock wave, accordingly a lower jump of pressure Fig. 10.
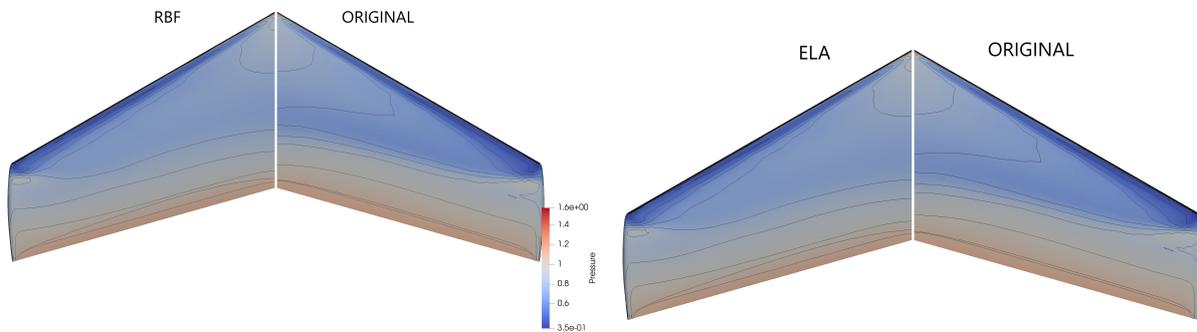
Figure 8: Onera M6: Isopressure Lines Upper Surface
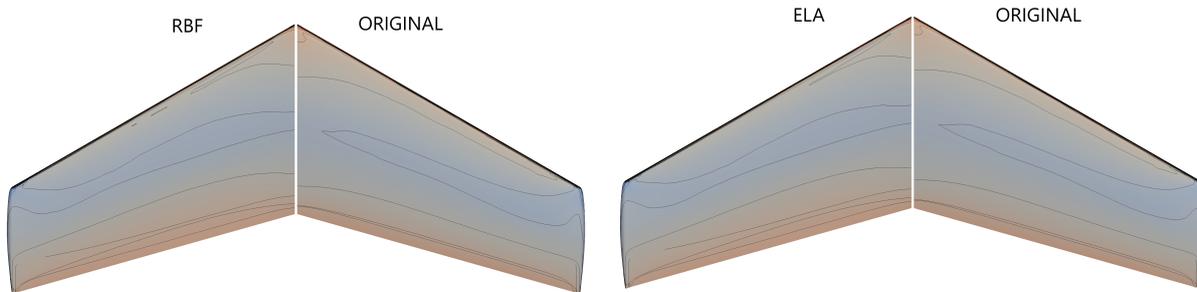
Figure 9: Onera M6: Isopressure Lines Bottom Surface

Luca Abergo, Myles Morelli and Alberto Guardone
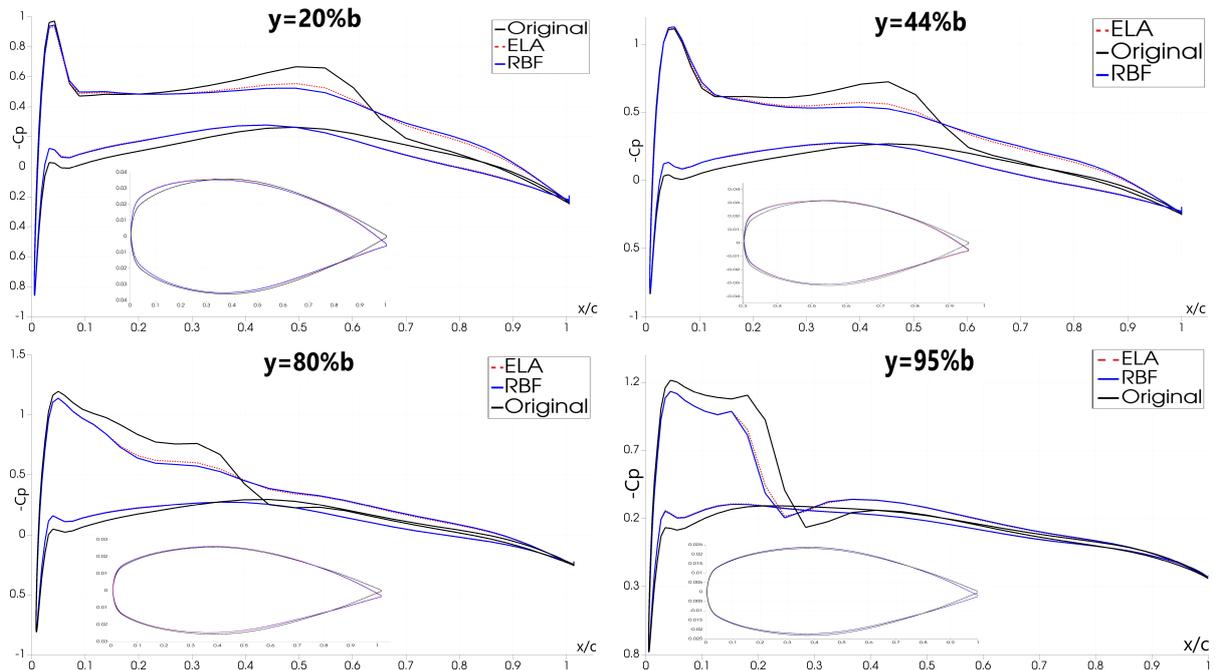
Figure 10: Onera M6: C_p Optimization

Moreover, Fig. 11 shows that the control points selected on the upper part of the wing, the distribution is strictly linked to the shape of the deformation wanted. In this case, the movement was the result of the first loop of optimization and it is evident that the tip is not touched instead the leading edge and the central part of the wing are more affected. The region of greater displacement should correspond to a zone of the surface with higher sensitive. It is confirmed by Fig. 12 where is shown the value of the adjoint variables for the last equation of the adjoint system and the magnitude of the three momentum equations combined.
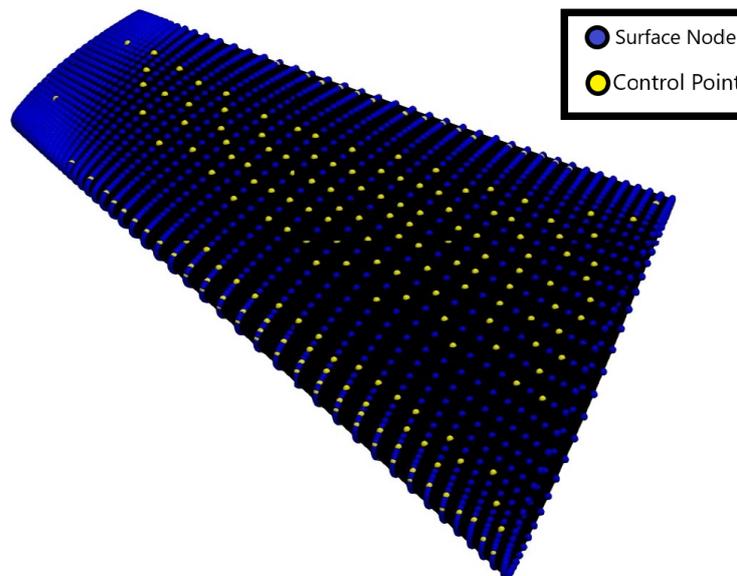
Figure 11: Onera M6: RBF Case 1 Control Points

Luca Abergo, Myles Morelli and Alberto Guardone
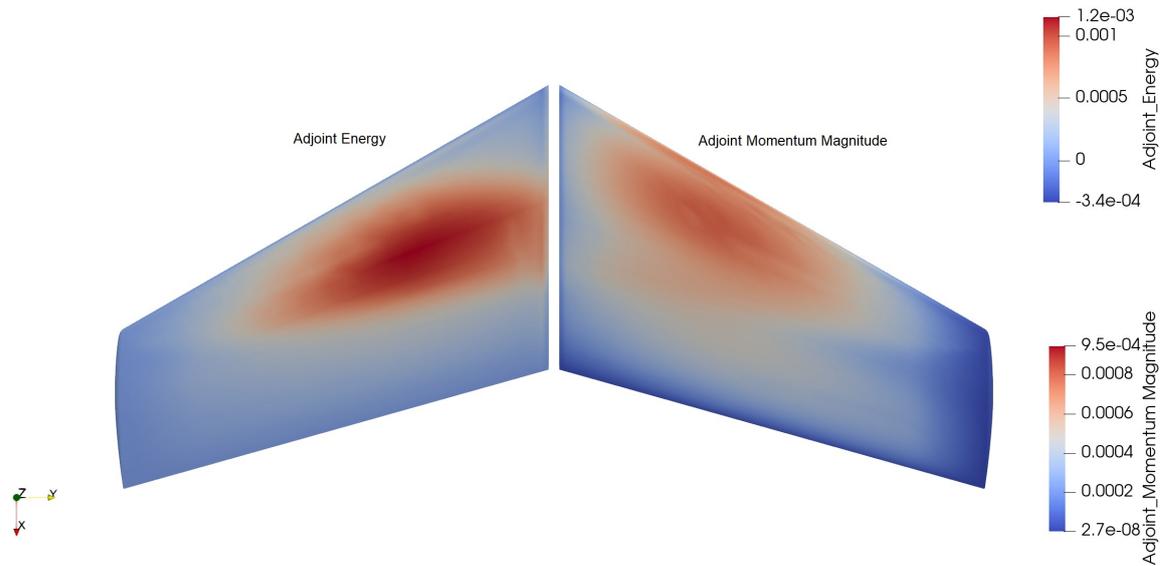
Figure 12: Onera M6: Adjoint Variable

4.2   MESH DEFORMATION PERFORMANCE

The Onera M6 test case has been used to compare the wall time and the ram consumption of the two mesh deformation considered in this text. The grid considered is hybrid, with 7319 surface nodes and 446685 cells. The performances of RBF are measured considering different settings: interpolation function, k, number of levels, amount of control points in percentage of the total surface nodes. The mesh deformation processes are executed on a single core of an AMD EPYC^{TM} of 2.4 GHz. The next table reports the combination of the parameters tested and the results obtained.

N.	Wendland	Control Points	K	N. Levels
0	$C0$	5%	5	one
1	$C0$	10%	5	one
2	$C0$	15%	5	one
3	$C0$	10%	10	one
4	$C0$	10%	5	two
5	$C2$	10%	5	one

Table 2: RBF Parameters

Three outputs are monitored: the maximum virtual memory allocated, the wall time excluded the deallocation of the data, and the error due to the surface interpolation. Regarding ELA, the stiffness of the cells is set with an inverse volume logical. The final linear system has to be solved with a final residual of $10^{(-10)}$ in maximum 800 iterations, this is the classical setting proposed in the SU2 tutorials. The results are reported in the next table:

Luca Abergo, Myles Morelli and Alberto Guardone

N.	RAM (G_b)	Interpolation Error	Cpu Time (min)
RBF.0	1.94	2.18%	1.81
RBF.1	2.55	1.07%	3.33
RBF.2	5.41	0.51%	7.89
RBF.3	2.55	0.98%	3.4
RBF.4	3.68	0.47%	6.46
RBF.5	2.74	0.15%	6.53
ELA	14.8	0%	13.66

Table 3: Performance Results

The comparison between ELA and the RBF number one, which is used for the optimization, shows remarkable results. The RAM usage is almost six times lower and the time employed is one quarter. Considering only RBF, in order to have a very low interpolation error maintaining excellent performance, the comparison shows that is better to increase the order of the interpolation function instead of the number of levels of the greedy algorithm. In every 3D optimization ELA has shown a better ability to conserve the volume of the wing, it could be linked to the interpolation error introduced using RBF. This underline the necessity to contain as much as possible the approximation introduced. The following figures show the allocation of the data in the virtual memory with respect to the cpu time. It can be noticed that the behavior of RBF and ELA are completely different, RBF is progressive, instead ELA quickly allocate all necessary information, then the ram consumption remains constant until the linear system is solved.
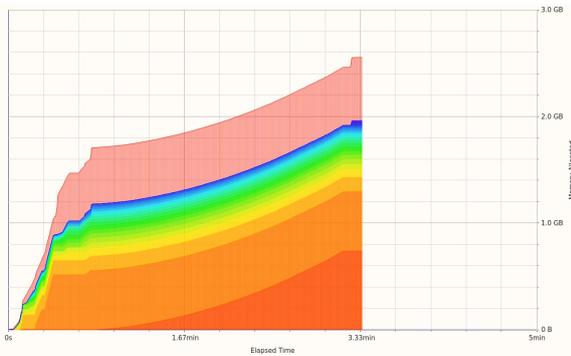
Figure 13: Onera M6: Case 1 Rbf
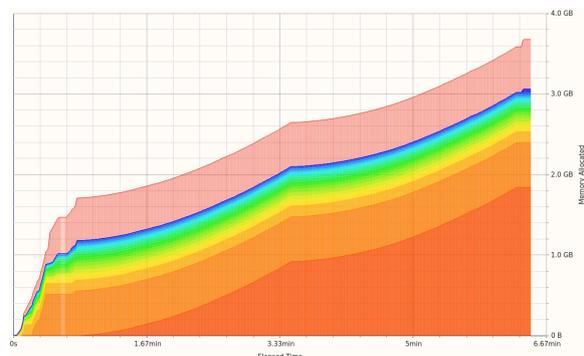
Figure 14: Onera M6: Case 4 Rbf
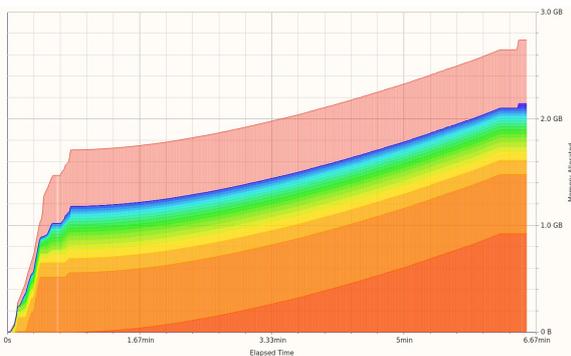
Figure 15: Onera M6: Case 5 Rbf
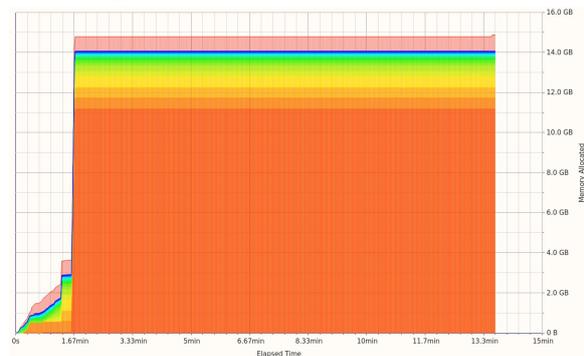
Figure 16: Onera M6: Performance Ela

4.3 ONERA M6 WITH WINGLET

The optimization of a non planar wing has been conducted in SU2 previously by Palacio in the project NERONE[25]. However, only Euler equations are solved and a new unstructured grid is generated at each iteration loop. In this section a RANS optimization is performed, with SA as turbulence model and RBF for updating the grid which can be of arbitrary topology. The winglet is obtained with a loft from the tip of the old planar configuration, generating a contraction of the final section.
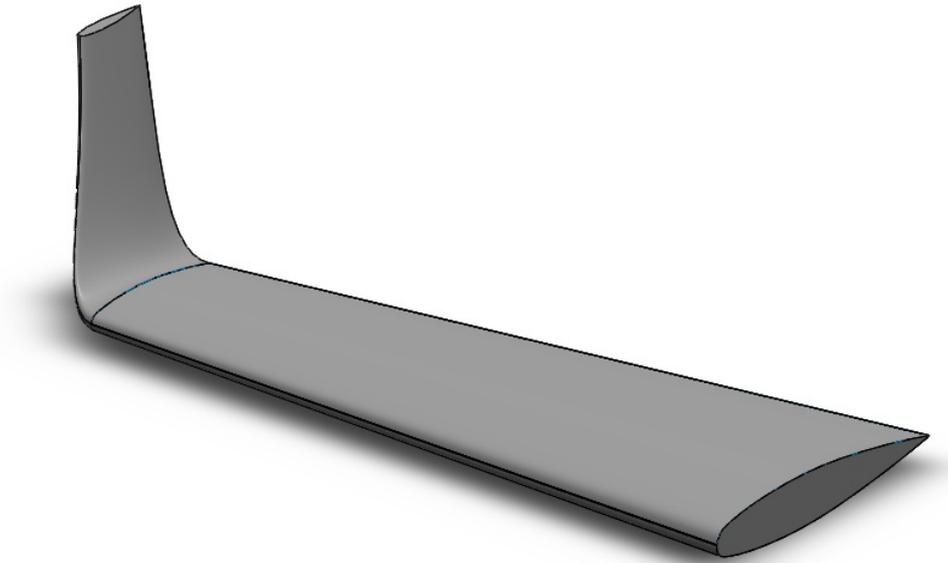
Figure 17: Onera M6 With Winglet Attached CAD

The free stream conditions and the target of the optimizations are the same of Sec. 4.1. The section constraints are imposed also for two station of the winglet so on two planes with z norm. With the same criteria previously used the convergence of the mesh is conducted at fixed C_l and the coarser one is used due to the limited computational resources available. The results has to be intended as the proof that the new framework is able to improve the aero-coefficient of a more complex geometry.

Luca Abergo, Myles Morelli and Alberto Guardone
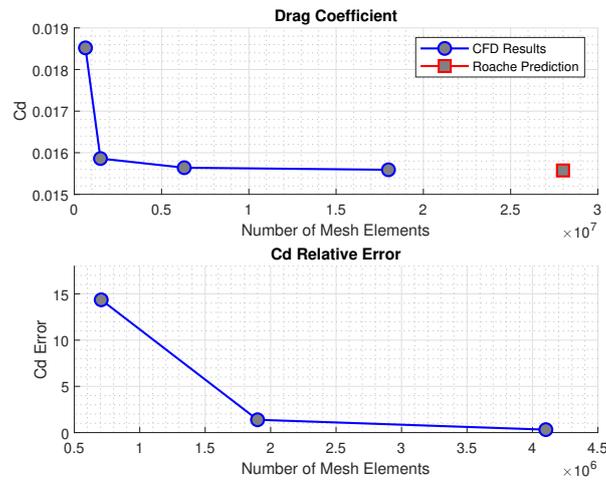
Figure 18: Onera M6 With Winglet Mesh Convergence

The design process is divided in two. At the start, two FFD boxes are selected, the first containing the planar part of the wing using 144 DVs free to translate only in z-direction and the second including only the winglet with 70 DVs that can shift in y,x direction. The sensitivity of the wing DVs is much higher, therefore in this phase the nodes of the planar part are shifted, the winglet is almost untouched. When the drag reduction becomes negligible, the optimization restarts from the last output grid but using only one FFD around the winglet. The DVs are increased to 160, in this phase the winglet is proper morphed and the final shape can be seen in Fig.19.
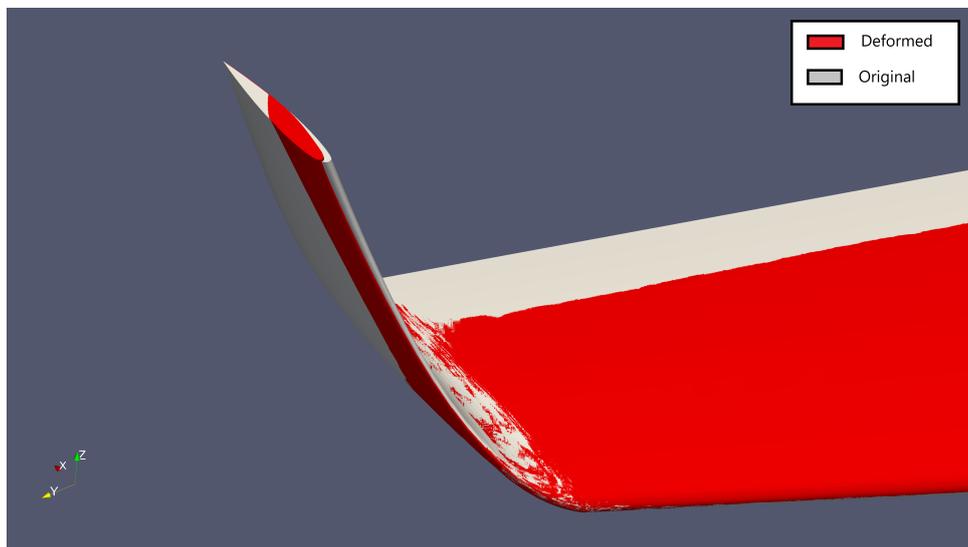
Figure 19: Onera M6 Original and Deformed Winglet

The history of the optimization is reported in Fig.20. A reduction of the drag from 185.34 counts to 163.43 is achieved, therefore the C_d is decreased of 11.82%. The lift and volume constraints are perfectly respected. It must be signaled that the y-momentum, which is not part of the optimization problem but only monitored, strongly increases from -0.112 to -0.148. Figs.21 shows how the C_p distribution and the shape section is modified for four locations, two concerning the winglet and two to the planar part.
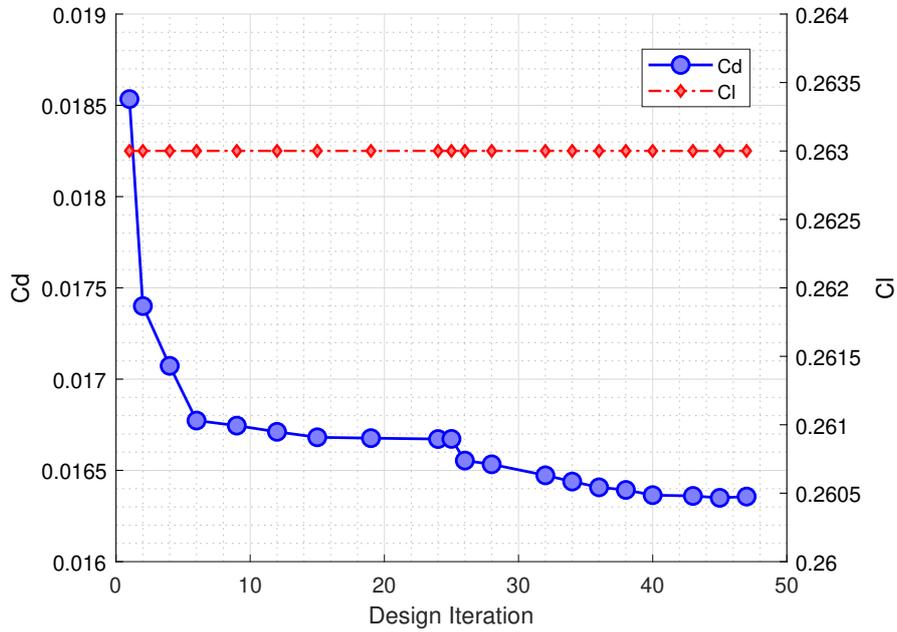
Figure 20: Onera M6 Winglet C_d Optimization
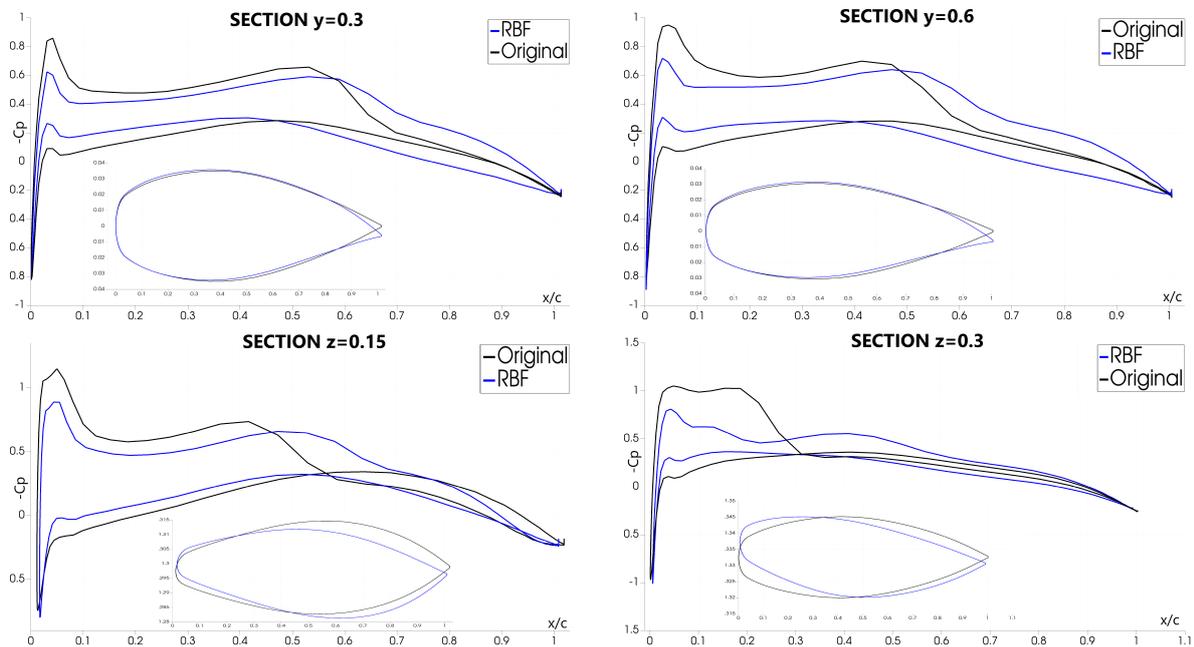
Figure 21: Onera Winglet: C_p Optimization

The optimization was possible only with RBF since it better preserves the quality of the mesh. It is tempted also with ELA where the stiffness is set with an inverse volume criteria. Two other criteria are, constant stiffness and wall distance are also tested, in these cases the lost of quality is more progressive and the design process is jeopardise only after some loops. In the next table it is only reported the orthogonality of the mesh after the first update of the grid.

Luca Abergo, Myles Morelli and Alberto Guardone

Method	N_c	N_v	Min Orthogonality
RBF C0	1100	392619	6.32
ELA inv volume	12676	645590	-43.92
ELA constant	12676	645590	6.21
ELA wall distance	12676	645590	6.28

Table 4: Mesh Orthogonality

5 CONCLUSIONS

The aim of this thesis was to increase the robustness and the possibility of the gradient based aerodynamic optimization chain implemented inside the open-source SU2. As optimization in this context it is intended the research of the body shape that provides a lower value of the objective function selected. Strictly concerning SU2 the optimizations using RBF with respects to ELA show a strong reduction of the virtual memory consumption, of the time needed and a better preserved orthogonality of the mesh. The reason is that the version of RBF implemented in SU2 includes two data reduction schemes: a multilevel greedy algorithms and a volume reduction system. Selecting the maximum number of the control points permitted, the levels and the base function it is possible to regulate the computational time and the virtual memory usage. This is extremely useful in case of scarce computational resource available.

The different value of the adjoint variables computed could drive the gradient based SLSQP to a complete different local minimum. RBF showed the possibility to obtain the same or even improve the drag reduction. The viscous optimization in transonic regime of a non planar wing, specifically an Onera M6 with a winglet attached, it is achieved only thanks to the combination of discrete adjoint and RBF, making a step forward respect to the work done in NERONE [25] where the optimization was done only solving Euler equations and regenerating the mesh from zero at each design loop.

REFERENCES

[1] F. Palacios, M. R. Colonno, A. C. Aranake, A. Campos, S. R. Copeland, T. D. Economon, A. K. Lonkar, T. W. Lukaczyk, T. W. Taylor, and J. J. Alonso. Stanford university unstructured (su2): An open-source integrated computational environment for multi-physics simulation and design. *AIAA paper*, 287:2013, 2013.

[2] T. A. Johansen, T. I. Fossen, and S. P. Berge. Constrained nonlinear control allocation with singularity avoidance using sequential quadratic programming. *IEEE Transactions on Control Systems Technology*, 12(1):211–216, 2004.

[3] Z. Lyu, Z. Xu, and J. Martins. Benchmarking optimization algorithms for wing aerodynamic design optimization. In *Proceedings of the 8th International Conference on Computational Fluid Dynamics, Chengdu, Sichuan, China*, volume 11. Citeseer, 2014.

[4] T. W. Sederberg and S. R. Parry. Free-form deformation of solid geometric models. In *Proceedings of the 13th annual conference on Computer graphics and interactive techniques*, pages 151–160, 1986.

[5] P. Spalart and S. Allmaras. A one-equation turbulence model for aerodynamic flows. In *30th aerospace sciences meeting and exhibit*, page 439, 1992.

[6] J. T. Batina. Unsteady euler airfoil solutions using unstructured dynamic meshes. *AIAA journal*, 28(8):1381–1388, 1990.

[7] R. P. Dwight. Robust mesh deformation using the linear elasticity equations. In *Computational fluid dynamics 2006*, pages 401–406. Springer, 2009.

[8] F. J. Blom. Considerations on the spring analogy. *International journal for numerical methods in fluids*, 32(6):647–668, 2000.

[9] A. H. Truong, C. A. Oldfield, and D. W. Zingg. Mesh movement for a discrete-adjoint newton-krylov algorithm for aerodynamic optimization. *AIAA journal*, 46 (7):1695–1704, 2008.

[10] C. Lee, D. Koo, K. Telidetzki, H. Buckley, H. Gagnon, and D. W. Zingg. Aerodynamic shape optimization of benchmark problems using jetstream. In *53rd AIAA Aerospace Sciences Meeting*, page 0262, 2015.

[11] G. Yang and A. Da Ronch. Aerodynamic shape optimisation of benchmark problems using su2. In *2018 AIAA/ASCE/AHS/ASC Structures, Structural Dynamics, and Materials Conference*, page 0412, 2018.

[12] H. W. Kuhn. Nonlinear programming: a historical view. In *Traces and Emergence of Nonlinear Programming*, pages 393–414. Springer, 2014.

[13] T. A. Albring, M. Sagebaum, and N. R. Gauger. Efficient aerodynamic design using the discrete adjoint method in su2. In *17th AIAA/ISSMO multidisciplinary analysis and optimization conference*, page 3518, 2016.

[14] E. J. Nielsen and M. A. Park. Using an adjoint approach to eliminate mesh sensitivities in computational design. *AIAA journal*, 44(5):948–953, 2006.

[15] M. Sagebaum, T. Albring, and N. R. Gauger. High-performance derivative computations using codipack. *ACM Transactions on Mathematical Software (TOMS)*, 45 (4):1–26, 2019.

[16] T. A. Albring, M. Sagebaum, and N. R. Gauger. Development of a consistent discrete adjoint solver in an evolving aerodynamic design framework. In *16th AIAA/ISSMO multidisciplinary analysis and optimization conference*, page 3240, 2015.

[17] A. Griewank and A. Walther. *Evaluating derivatives: principles and techniques of algorithmic differentiation*. SIAM, 2008.

[18] M. Morelli, T. Bellosta, and A. Guardone. Efficient radial basis function mesh deformation methods for aircraft icing. *Journal of Computational and Applied Mathematics*, page 113492, 2021.

[19] S. Jakobsson and O. Amoignon. Mesh deformation using radial basis functions for gradient-based aerodynamic shape optimization. *Computers & Fluids*, 36(6):1119–1136, 2007.

Luca Abergo, Myles Morelli and Alberto Guardone

[20] G. Wang, H. H. Mian, Z.-Y. Ye, and J.-D. Lee. Improved Point Selection Method for Hybrid-Unstructured Mesh Deformation Using Radial Basis Functions. *AIAA Journal*, 53(4):1016–1025, 2015. https://doi.org/10.2514/1.J053304.

[21] L. Xie and H. Liu. Efficient Mesh Motion Using Radial Basis Functions With Volume Grid Points Reduction Algorithm. *Journal of Computational Physics*, 348:401–415, 2017. https://doi.org/10.1016/j.jcp.2017.07.042.

[22] V. Schmitt. Pressure distributions on the onera m6-wing at transonic mach numbers, experimental data base for computer program assessment. *AGARD AR-138*, 1979.

[23] Y. Yu, Z. Lyu, Z. Xu, and J. R. Martins. On the influence of optimization algorithm and initial design on wing aerodynamic shape optimization. *Aerospace Science and Technology*, 75:183–199, 2018.

[24] F. Palacios, T. D. Economon, and J. J. Alonso. Large-scale aircraft design using su2. In *53rd AIAA aerospace sciences meeting*, page 1946, 2015.

[25] L. Pustina, R. Cavallaro, and G. Bernardini. Nerone: An open-source based tool for aerodynamic transonic optimization of nonplanar wings. *Aerotecnica Missili & Spazio*, 98(1):85–104, 2019.

SHAPE OPTIMIZATION OF NONPLANAR SOLID FOAM CORE WINGS WITH LARGE DEFORMATIONS

Cian Conlan-Smith[1]* and Casper Schousboe Andreasen[1]

1: Department of Mechanical Engineering
Section of Solid Mechanics
Technical University of Denmark
2800, Lyngby, Denmark
*: cicosm@mek.dtu.dk

Abstract

This work applies gradient-based shape optimization methods to the design of nonplanar wings with a solid foam core such as those commonly used on drones or model aircraft. A coupled aeroelastic model is used to capture the physics where the aerodynamics is modelled using a constant source-doublet 3D panel method with approximations for viscous drag, and the structural deformations are modelled using nonlinear co-rotating beam finite elements. The wings are parameterized based on the definitions of NACA 4-digit airfoils from which the majority of cross-sectional stiffness properties can be derived analytically. Approximations are introduced for the torsional stiffness and shear center location, which then yields expressions for the full cross-sectional stiffness matrix of a solid homogenous airfoil section without the need to conduct any cross-sectional analysis. Results are first presented to compare the differences between linear and nonlinear finite element models, which highlight the importance of capturing nonlinear deformations for coupled aeroelastic optimization problems. Finally, the aeroelastic behaviour of raised and drooped wings is investigated, where drooped wings are found to be beneficial due to an effective increase in wingspan as the wing deforms leading to a larger reduction in induced drag.

Keywords: Aeroelastic shape optimization, panel methods, co-rotating beam finite elements, analytic cross-sectional properties, drooped wings.

MULTI-POINT AERODYNAMIC SHAPE OPTIMIZATION OF AEROFOILS USING MODIFIED XOPTFOIL

Ricardo J.F. Palmeira[1]*, and Pedro V. Gamboa[1]

1: Centre for Mechanical and Aerospace Science and Technologies (C-MAST-UBI)
Faculdade de Engenharia
Universidade da Beira Interior
6200-001 Covilhã
ricardo.palmeira@ubi.pt, pgamboa@ubi.pt, http://www.ubi.pt

Abstract

Aerofoil shape has a significant influence on aircraft performance. Multiple methodologies can be applied, such as direct design, inverse design or performance design. With the improvement of computer technology there has been a continuing trend of automating this process by using performance-based methods and formal optimization algorithms. Parametrization formulations of aerofoils have continually advanced, some examplesare B-Spline, Class Shape Functions, Hicks-Henne functions and Bezier-PARSEC 3333. Main comparisons of parametrizations have focussed on morphology, design space and aerodynamic consistency. The parametrizations mentioned are applied and its results compared for different numbers of design variables.

A multi-point approach is used with an aggregated objective function using weights that are determined using the aircraft design data, to maximize the score for the competition Air Cargo Challenge (ACC), using XFOIL for aerodynamic analysis and particle swarm optimization (PSO) under a modified version of the program XOPTFOIL. The initial aerofoil was obtained by iterative inverse design during previous works, the optimization includes the flap chord and deflection angle for the different selected lift coefficient conditions as design variables. The initial population is bounded between maximum and minimum limits set by the initial aerofoil design variables and an initial perturbation.

The aerofoil is constrained by minimum and maximum thicknesses, a minimum trailing edge angle and a specified trailing edge thickness. Several additional restrictions are also imposed on the aerofoil to avoid unneeded analysis of a geometry with an expected non converged solution in XFOIL. These include the angles' maximum, minimum and difference values of the two points closest to the leading edge, the maximum angle between any three consecutive points and the number of curvature sign reversals at the upper surface and lower surface of the aerofoil. To deal with the constraints and restrictions a penalty function is used, each penalty being normalized by a maximum set value. To ensure that these do not unduly constrain the domain exploration of the optimization, a dynamic limit to the penalties is used. During the optimization, this limit decreases linearly with the iterations.

Keywords: Aerofoil design, aerodynamic shape optimization, particle swarm optimization, aerofoil parametrization methods, multi-point optimization

Ricardo J.F. Palmeira and Pedro V. Gamboa

1. INTRODUCTION

Historically, aerofoil design has been performed using direct design methodologies, then inverse design methodologies [1-3], single point and multi-point approaches. With the improvement of computer technology there has been a continuing trend of automating this process by using performance-based methods and formal optimization algorithms: gradient based algorithms [4] and stochastic algorithms [5]. Parametrization formulations of aerofoils have also been continually investigated. Several have been created or improved, such as NACA functions, PARSEC, B-Spline, Class Shape Functions, Hicks-Henne functions and Bezier-PARSEC 3333. Main comparisons of these have focussed on morphology, design space and aerodynamic consistency [6-7].

In this work, an aerofoil is optimized for conditions under the competition Air Cargo Challenge (ACC), using XFOIL [8] for aerodynamic analysis and particle swarm optimization (PSO) under a modified version of the program XOPTFOIL [9]. In the ACC competition, a remotely piloted air vehicle is designed, built, and flown to lift the most payload weight from a 60 m runway and fly as fast as possible for a given amount of time, subject to strict design constraints. Therefore, this leads to two opposing objectives: maximum lift coefficient and high lift-to-drag ratio during take-off and minimum drag coefficient during cruise.

Several aerofoil formulations: B-Spline, Class Shape Functions, Hicks-Henne functions and Bezier-PARSEC 3333 are used, and the results compared. The number of design variables are studied. Since the initial aerofoil was obtained by iterative inverse design during previous works, the difference in performance is analysed. Considering the new aerofoil is designed to use a plain flap, the optimization includes the flap chord and deflection angle as design variables for the different flight conditions.

The program XOPTFOIL was modified for use in this work. Several parametrizations were added, new design variables were introduced: plain flap hinge position and trailing edge thickness; XFOIL non convergence options added; constraints are now relative to original aerofoil; design radius function was changed; relative initial perturbation and constraint limit parameters were added; and maximum lift coefficient optimization type can now use a sequence of angles of attack.

2. MODIFIED XOPTFOIL PROGRAM

2.1. XOPTFOIL algorithm

This program minimizes an objective function given by a set of operating points under specified constrains. The implementation of this program is shown on Fig.1 and can be summarized as:

1. Read the input file, containing the initial aerofoil coordinates file location, operating points, constraints, parametrization options and optimization options;
2. From the initial aerofoil coordinates, transform the aerofoil so that it has a unitary chord length and zero angle of attack. Given a specified parametrization type, determine the design variables;
3. Employing the design variables, check the initial aerofoil constraint values and using XFOIL analyse the aerofoil at the operating points. Save the constraint values and aerodynamic values from the operating points as reference values;
4. Compute the initial design variables' upper and lower limits based on the reference values and an initial perturbation.
   a. Apply the particle swarm algorithm: calculate the population positions and

Ricardo J.F. Palmeira and Pedro V. Gamboa

speeds;
5. If population has converged or if iteration number limit has been reached stop the program, else continue to 6;
6. Compute the new aerofoil coordinates for the population according to the used parametrization;
7. Check the new aerofoil constraints and analyse its operating points using XFOIL. Calculate the objective function value from the constraints and aerodynamic analysis relative to the reference values. Return to step 4a.
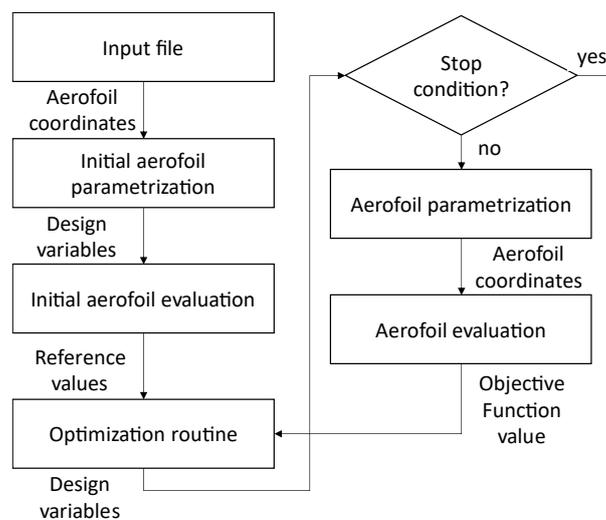

Figure 1. Modified XOPTFOIL program flowchart.

2.2. Aerofoil parametrization

Several aerofoil parametrizations are used in this work: B-Spline, Class Shape Functions, Hicks-Henne functions and Bezier-PARSEC 3333. B-Spline, Class Shape Functions and Bezier-PARSEC 3333 were added to the XOPTFOIL program in this work.

B-Splines are a subset of the non-uniform rational basis spline (NURBS), which are widely used in curve modelling. NURBS have additional degrees of freedom over the B-Splines, however this is undesired for the purpose of this study. B-Splines (BSP) are defined as the sum of all the products between the basis functions and control points [10].

In this work a cosine distribution is used for the distribution of control points in the chordwise direction (x), since the accuracy of the method depends mainly on the number of control points and not on degree [7], therefore all the B-Splines used have polynomial degree three.

In this work one B-Spline defines the upper surface and another the lower surface of the aerofoil. During the initial aerofoil parametrization, it is necessary to determine the distribution of control points normal to the chordwise direction (z) in each surface. To do so, the knot distribution (u) is calculated at each aerofoil x coordinate, and then the least squares method is used to calculate the z control point distribution from the z coordinates and u distribution for each surface.

Class Shape Functions (CSF) are defined as the product of a class function and a shape function [11-12]. While the class function can determine a wide range of bodies, in this work only the aerofoil class function is used. The shape function used is the linear

combination of Bernstein polynomials [12]. An additional term, known as leading edge modification [13] is also used since it increases the design space [7]. To determine all the coefficients, the least squares method is used for the upper and lower surfaces of the aerofoil.

Hicks-Henne (HH) functions are added to an existing aerofoil and consist of a linear combination of bump functions, which in turn are augmented sine functions, each with three variables [7, 14]. In this work all three variables are free.

Bezier-PARSEC 3333 (BPP) represents an aerofoil by four third degree Bezier curves and defines such curves by using twelve aerodynamic parameters: leading edge radius on thickness curve; maximum thickness value, position and curvature; trailing edge angle on thickness curve; trailing edge thickness; leading edge angle on camber curve; maximum camber value, position and curvature; trailing edge angle on camber curve; and trailing edge vertical position [15]. During the initial aerofoil parametrization, all these parameters are calculated.

The accuracy of the parametrized original aerofoil is measured against the original aerofoil using Eq.(1).

$$RMSE_{surface} = \sqrt{\frac{\sum_{i=1}^{n_{points}}\left(z_i - z_{original,i}\right)^2}{n_{points}}} \tag{1}$$

2.3. Aerofoil evaluation

The aerofoil is constrained by minimum and maximum thicknesses (*Thick*), a minimum trailing edge angle (*TEAngle*) and a specified trailing edge thickness. Several additional restrictions are also imposed on the aerofoil to avoid unneeded analysis of a geometry with an expected non converged solution in XFOIL. These include the angles' maximum, minimum and difference values of the two points closest to the leading edge (*LEAngles*), the maximum angle between any three consecutive points (*PAngle*) and the number of curvature sign reversals on the upper surface and on the lower surface of the aerofoil (*Curv*).

When an aerofoil is being evaluated most constraints are calculated before the XFOIL analysis. Each constraint (σ_j) is divided over its reference ($\sigma_{ref,j}$) to obtain the relative constraint ($\overline{\sigma}_j$). This value is compared to the constraint limit (δ) and if it exceeds the limit, the evaluation ends with Eq.(2).

$$Obj = 10^6\left(\overline{\sigma}_j\right), if\ \exists\left(\overline{\sigma}_j\right) > \delta \tag{2}$$

To ensure that the constraints do not unduly constrain the domain exploration of the optimization, a dynamic limit to the penalties is used. During the optimization, this limit decreases linearly with the iterations from δ_0 to δ_f.

If all relative constraints are under the limit, XFOIL analyses the operating points. An operating point is defined by an objective, sufficient aerodynamic properties to analyse (angle of attack or lift coefficient plus Reynolds number and Mach number) and a weight. The objectives used in this work are: maximum lift coefficient (Eq.(3)) and minimum drag coefficient (Eq.(4)). The sum of all operating points' weights is always equal to 1.

$$\varphi_i = \frac{1}{c_l} \tag{3}$$

Ricardo J.F. Palmeira and Pedro V. Gamboa

$$\varphi_i = C_d \tag{4}$$

Each aerodynamic objective (φ_i) is divided by its reference ($\varphi_{ref,i}$) to obtain the relative aerodynamic objective ($\overline{\varphi}_i$). The objective function (Obj) is the sum of the product between the weight ($\overline{w}_i$) and the relative aerodynamic objective ($\overline{\varphi}_i$) for each operating point (i) plus the sum of all relative constraints ($\overline{\sigma}_j$) for each constraint (j), Eq.(5).

$$Obj = \sum_{i=1}^{n}(\overline{w}_i\overline{\varphi}_i) + \sum_{j=1}^{m}(\overline{\sigma}_j), if \ \forall(\overline{\sigma}_j) \leq \delta \tag{5}$$

To safeguard against unrealistic values, the program reanalyses possible unrealistic operating points at a disturbed Reynolds number and compares the results between the two. The weakest results are kept. Additionally, if XFOIL does not converge, a single sequence of points (from a reference point up to the operating point) are analysed to help with convergence.

2.4. Optimization

Particle swarm optimization (PSO) with inertia weight was applied in this work. The upper (x_{max}) and lower (x_{min}) limits are functions of an absolute initial perturbation (ξ_{abs}), a relative initial perturbation (ξ_{rel}) and the initial design variables (x_{init}) in accordance with Eq.(6) and Eq.(7) for each element i from the design variables. The number of design variables is n_{var}.

$$x_{i,max} = x_{i,init} + x_{i,init} \cdot \xi_{rel} + \xi_{abs} \tag{6}$$
$$x_{i,min} = x_{i,init} - x_{i,init} \cdot \xi_{rel} - \xi_{abs} \tag{7}$$

The initial population position (X) and velocity (V) for each element j of the population are given by Eq.(8) and Eq.(9), respectively, for each matrix. *rand(a,b)* is a pseudo-random function that returns a number between a and b using a uniform distribution, while the speed limit (V_{max}) is a user input. The size of population is p_{size}.

$$X_{j,0} = (x_{max} - x_{min})rand(0,1) + x_{min} \tag{8}$$
$$V_{i,j,0} = V_{max} \ rand(-1,1) \tag{9}$$

During iteration (t), each position and velocity is updated using Eq.(10) and Eq.(11) for each element j of the population, while the inertia factor is calculated using Eq.(12). x_{best} is the design variables vector with lowest objective function value at each iteration. c_1, c_2, w_0, w_f and w_{rate} are user inputs.

$$X_{t,j} = X_{t-1,j} + V_{t-1,j} \tag{10}$$
$$V_{t,j} = w_t V_{t-1,j} + c_1(x_{best} - X_{t-1,j})rand(0,1) + c_2(x_{best} - X_{t-1,j})rand(0,1) \tag{11}$$
$$w_i = w_{i-1} - w_{rate}(w_{i-1} - w_f) \tag{12}$$

For the design variables that are constrained (i) between x_{max} and x_{min}, each overflow is solved using Eq.(13) to Eq.(16).

$$X_{t,j,i} = x_{min,i} \ if \ X_{t,j,i} < x_{min,i} \tag{13}$$

Ricardo J.F. Palmeira and Pedro V. Gamboa

$$V_{t,j,i} = -V_{t,j,i} rand(0,1) \text{ if } X_{t,j,i} < x_{min,i} \tag{14}$$

$$X_{t,j,i} = x_{max,i} \text{if } X_{t,j,i} > x_{max,i} \tag{15}$$

$$V_{t,j,i} = -V_{t,j,i} rand(0,1) \text{ if } X_{t,j,i} > x_{max,i} \tag{16}$$

Then, if the speed limit is exceeded the velocity vector (V_i) is calculated using Eq.(17).

$$V_{t,j} = \frac{V_{max}}{||V_{t,j}||} V_{t,j} \text{ if } ||V_{t,j}|| > V_{max} \tag{17}$$

One of the most important metrics during optimization is the design radius (r), which measures the diversity of the population. First the design variables are scaled between -1 and 1 for the entire population, Eq.(18).

$$\overline{X}_{j,i} = -1 + 2(X_{t,j,i} - x_{min,i})/(x_{max,i} - x_{min,i}) \tag{18}$$

Then the centroid ($\overline{x}_c$) for each design variable is computed, Eq.(19), p_{size} is the size of the population.

$$\overline{x}_{c,i} = \frac{\sum_{j=1}^{p_{size}} \overline{X}_{j,i}}{p_{size}} \tag{19}$$

Finally, the design radius of the population is computed, Eq.(20).

$$r = \frac{\sum_{j=1}^{p_{size}} \frac{||\overline{X}_j - \overline{x}_c||}{n_{var}}}{p_{size}} \tag{20}$$

3. AEROFOIL OPTIMIZATION CASE

3.1. Problem definition

The aim of this problem is to optimize the aerofoil used in the Air Cargo Challenge 2019, for the same conditions and restrictions so that it maximizes the competition score. The competition score is given by Equation (21), where m_{cargo} is the mass in kg of transported cargo, t_{flown} is the amount of time in seconds to fly 10 laps, a is a bonus for no parts lost during flight, b is a bonus for landing on the field, c is a bonus for landing within 60 meters, d is either 1 (valid flight) or 0 (invalid flight) and $Timebonus$ is related to the installation of the payload on the aircraft [16].

$$Score = \left(\frac{m_{cargo}}{t_{flown}} \cdot 2000 + a + b + c\right) \cdot d + Timebonus \tag{21}$$

Since neither a nor $Timebonus$ are related to the aerofoils, these are disregarded from the equation, Parameters b and c depend mostly on the landing gear and field, they may be disregarded, and d must have a value of 1, that is, the take-off distance must always be ensured to be at most the same as the runway length (60 m). This results in Eq.(22) as dependant on the aerofoil.

Ricardo J.F. Palmeira and Pedro V. Gamboa

$$Score = \frac{m_{cargo}}{t_{flown}} \cdot 2000 \tag{22}$$

At this point, the aerodynamic properties that influence $Score$ are $C_{l,max}$, C_l and C_d at take-off, C_d in the turn and C_d in the cruise, leading to Eq.(23).

$$\delta Score = w_1 C_{l,max,TO} + w_2\, C_{l,TO} + w_3 C_{d,TO} + w_4 C_{d,cruize} + w_5 C_{d,turn} \tag{23}$$

Since this aircraft was designed using a mission-based multidisciplinary optimization [17], the time flown is estimated, as is the cargo mass, the wing polars, the distances travelled and the aerofoil polars. Using these data, it is possible to determine all aerodynamic weights near the design solution, using Eq.(24) with γ_i being the respective aerodynamic property. These data are available in Tab.1. To simplify, consider that take-off aerodynamics only influences the cargo mass while turn and cruise only influences the time flown.

$$w_i = \frac{\partial Score}{\partial \gamma_i} \tag{24}$$

Table 1. Values of weights.

i	1	2	3	4	5
w_i	0.540	0.103	-0.060	-0.196	-0.031
$\overline{w_i}$	0.581	0.110	0.065	0.211	0.033

Upon analysing the weights, we can write the objective function that maximizes the Score when minimized, Eq.(25).

$$Obj = \overline{w_1}\frac{C_{l,max,TO,ref}}{C_{l,max,TO}} + \overline{w_2}\frac{C_{l,TO,ref}}{C_{l,TO}} + \overline{w_3}\frac{C_{d,TO}}{C_{d,TO,ref}} + \overline{w_4}\frac{C_{d,cruise}}{C_{d,cruise,ref}} + \overline{w_5}\frac{C_{d,turn}}{C_{d,turn,ref}} \tag{25}$$

with operating points:
1. Maximizing $C_{l,max}$ in take-off: sequence of angle of attack from 8 deg to 15 deg with a step of 1 deg with constant Reynolds number of 160,000, Mach number of 0.02 and weight of 0.581, flap hinge at 0.83 and deflection of 8 deg.
2. Maximizing C_l in take-off at an angle of attack of 1.5 deg with Reynolds number of 160,000, Mach number of 0.02 and weight of 0.110, flap hinge at 0.83 and deflection of 8 deg.
3. Minimizing C_d in take-off at an angle of attack of 1.5 deg with Reynolds number of 160,000, Mach number of 0.02 and weight of 0.065, flap hinge at 0.83 and deflection of 8 deg.
4. Minimizing C_d in cruise at a lift coefficient of 0.258 with Reynolds number of 571,300, Mach number of 0.08 and weight of 0.211, flap hinge at 0.83 and deflection of -8 deg.
5. Minimizing C_d in turn at a lift coefficient of 1.443 with Reynolds number of 348,500, Mach number of 0.05 and weight of 0.033, flap hinge at 0.83 and deflection of 0 deg.

subject to the constraints:
1. Lower value of maximum thickness at 0.1, no restriction on upper maximum thickness;
2. Minimum trailing edge angle of 40 deg;

3. Trailing edge thickness of 0.003;
4. Angles' maximum, minimum and difference values of the two points closest to the leading edge, of 89.99, 80.00 and 20.00 deg, respectively;
5. The maximum angle between any three consecutive points of 25 deg;
6. Number of curvature sign reversals at the upper surface and lower surface of the aerofoil of 4 each;
7. Flap hinge position between 0.7 and 0.9 in *x* on the lower surface of the aerofoil;
8. Flap deflection between -10 deg and 15 deg.

3.2. Optimization cases and conditions

The aerofoil optimization is executed at cases *a*, *b*, and *c* for each parametrization method, except for Bezier-PARSEC 3333 parametrization. From case *a* to *b*, the number of design variables for surface representation increases from 6 to 12 and from *b* to *c*, 12 to 24. Adding the 4 design variables for the flaps to the surface number of design variables, the total number of design variables for each case is calculated, Tab.2. There are 4 design variables for the flaps since there are three deflections, one for each flight condition ($defl_{TO}, defl_{cruise}, defl_{turn}$ and $hinge_x$), and a *x* hinge position to optimize. BPP has only ten design variables for the aerofoil shape since the trailing edge thickness and position are defined and constant.

Table 2. Total number of design variables used in each optimization case for each parametrization method.

Case	BSP	CSF	HH	BPP
A	10	10	10	14
B	16	16	16	-
C	28	28	28	-

Additionally, the initial perturbations vary depending on the parametrization, Tab.3. These were set to allow a comparable initial design space.

Table 3. Initial perturbations for each parametrization method.

	BSP	CSF	HH	BPP
ξ_{abs}	0.02	0.10	0.10	0.01
ξ_{rel}	0.50	0.50	0.00	0.50

The optimization constants can be consulted in Tab.4. While a population size (p_{size}) of 40 is not the most optimal for this algorithm [18], due to the number of design variables it is expected to perform adequately. The maximum number of iterations (i_{max}) of 500 was set so that in most of the cases the design radius would reach 0.005, meaning there is little diversity in the population.

Table 4. Optimization constants.

i_{max}	p_{size}	V_{max}	c_1	c_2	w_0	w_f	w_{rate}	δ_0	δ_f
500	40	0.025	1.4	1.0	1.8	0.8	0.02	0.1	0.0001

3.3. Results

The resulting aerofoils are shown in Fig.2 along with the original aerofoil. The trend shows a preference for a higher maximum thickness nearer to the leading edge and reduction in thickness on the lower surface, which in turn increases the maximum camber of the aerofoils. Table 5 presents these properties. In BSP case C, CSF case C and HH case C several curvature reversals are visible and significantly impact the aerofoil geometry. This is due to a higher number of design variables in these cases. Nonetheless, other cases also exhibit a higher number of curvature reversals when compared to the original aerofoil, increasing the optimization constraints would reduce these.

Table 5. Resulting aerofoil properties for each study case.

Case	$Thickness_{max}$	$x_{Thickness,max}$	$Camber_{max}$	$x_{Camber,max}$
Original	0.130	0.242	0.060	0.528
BSP case A	0.159	0.287	0.071	0.480
BSP case B	0.136	0.218	0.070	0.543
BSP case C	0.134	0.198	0.068	0.598
CSF case A	0.118	0.194	0.066	0.519
CSF case B	0.145	0.222	0.079	0.499
CSF case C	0.139	0.215	0.069	0.456
HH case A	0.125	0.215	0.068	0.493
HH case B	0.142	0.221	0.077	0.463
HH case C	0.135	0.201	0.079	0.510
BPP case A	0.148	0.227	0.070	0.529

The design variables variation and concentration from the first iteration up to the hundredth are shown in Fig.3. As previously mentioned, the initial perturbation parameters control this variation, naturally the higher concentrations are located near local minimums of *Obj*.

For the BPP case A, D1 to D5 on thickness surface correspond to leading edge radius, maximum thickness value, position and curvature and trailing edge angle in rad, respectively. While D1 to D5 on camber surface correspond to leading edge angle, maximum camber value, position and curvature and trailing edge angle in rad, respectively. The design variables variation decreases with iterations and presents the same behaviour of the design radius, per definition. The design radius for all iterations is presented in Fig.4. It is shown that the cases CSF case A and BPP case A have a much higher design radius of 0.0199 and 0.0517, respectively, than 0.005, meaning that 500 iterations are insufficient to reduce the diversity of the population. However, the number of iterations would be significantly higher than 500 if the behaviour of design radius stayed the same.

The count of optimization aerofoil evaluation types is present in Tab.6. *Thick, TEAngle, LEAngles, Curv* and *PAngle* are relative to the constraints with the same name and indicate that the aerofoil was not within the constraints, after the XFOIL analysis on the operating points there are two scenarios: all operating points have converged (*Conv*) or some point did not converge (*Non conv*). The higher count of *Thick* in BPP case A occurs because while the design variables have constraints for this case, the program does not check them until it tries to generate the aerofoil. If an invalid set of design variables is given, the aerofoil returned has no thickness nor camber, triggering the condition.

For the same optimization type, the number of *TEAngle* increases with the number of design variables, which is to be expected. The CSF is the exception to this behaviour. This is

Ricardo J.F. Palmeira and Pedro V. Gamboa

explained by the use of Bernstein polynomials in this parametrization which limit local changes on the aerofoil and trailing edge. This also explains the lower number of *Curv* for CSF.

Table 6. Count of the optimization evaluation type for each case study.

Case	Thick	TEAngle	LEAngles	Curv	PAngle	Non conv	Conv
BSP case A	216	989	15	0	4	2058	16718
BSP case B	244	990	72	0	4	726	17964
BSP case C	525	2430	110	1267	0	749	14919
CSF case A	271	2911	0	0	7	368	16443
CSF case B	348	1371	0	0	0	1206	17075
CSF case C	195	517	0	1	0	395	18892
HH case A	186	1157	4	49	42	237	18325
HH case B	380	1567	6	148	39	602	17258
HH case C	409	1968	23	228	8	332	17032
BPP case A	6988	8	0	0	352	460	12192

The resulting flap design variables are shown in Tab.7. In almost all cases the flap deflection during cruise is at the constraint minimum. This shows that if that constraint was altered it may have been possible to decrease the drag coefficient. The exception is the BPP case A, which increased the deflection when compared to the initial condition, probably due to an insufficient number of iterations. This is supported by the relative high design radius in Fig.4.

Table 7. Resulting flap design variables.

Case	$defl_{TO}$	$defl_{cruise}$	$defl_{turn}$	$hinge_x$
BSP case A	14.53	-10	2.45	0.817
BSP case B	10.88	-9.98	2.42	0.834
BSP case C	9.92	-9.75	1.53	0.855
CSF case A	13.4	-9.96	1.45	0.863
CSF case B	10.68	-9.97	0.11	0.809
CSF case C	11.48	-10	1.41	0.798
HH case A	12.36	-10	-0.01	0.833
HH case B	12.51	-10	-3.93	0.807
HH case C	8.83	-9.99	-0.36	0.799
BPP case A	10.05	-1.99	-4.64	0.802

Ricardo J.F. Palmeira and Pedro V. Gamboa

(a) BSP case A

(b) BSP case B

(c) BSP case C

(d) CSF case A

(e) CSF case B

(f) CSF case C

(g) HH case A

(h) HH case B

(i) HH case C

(j) BPP case A
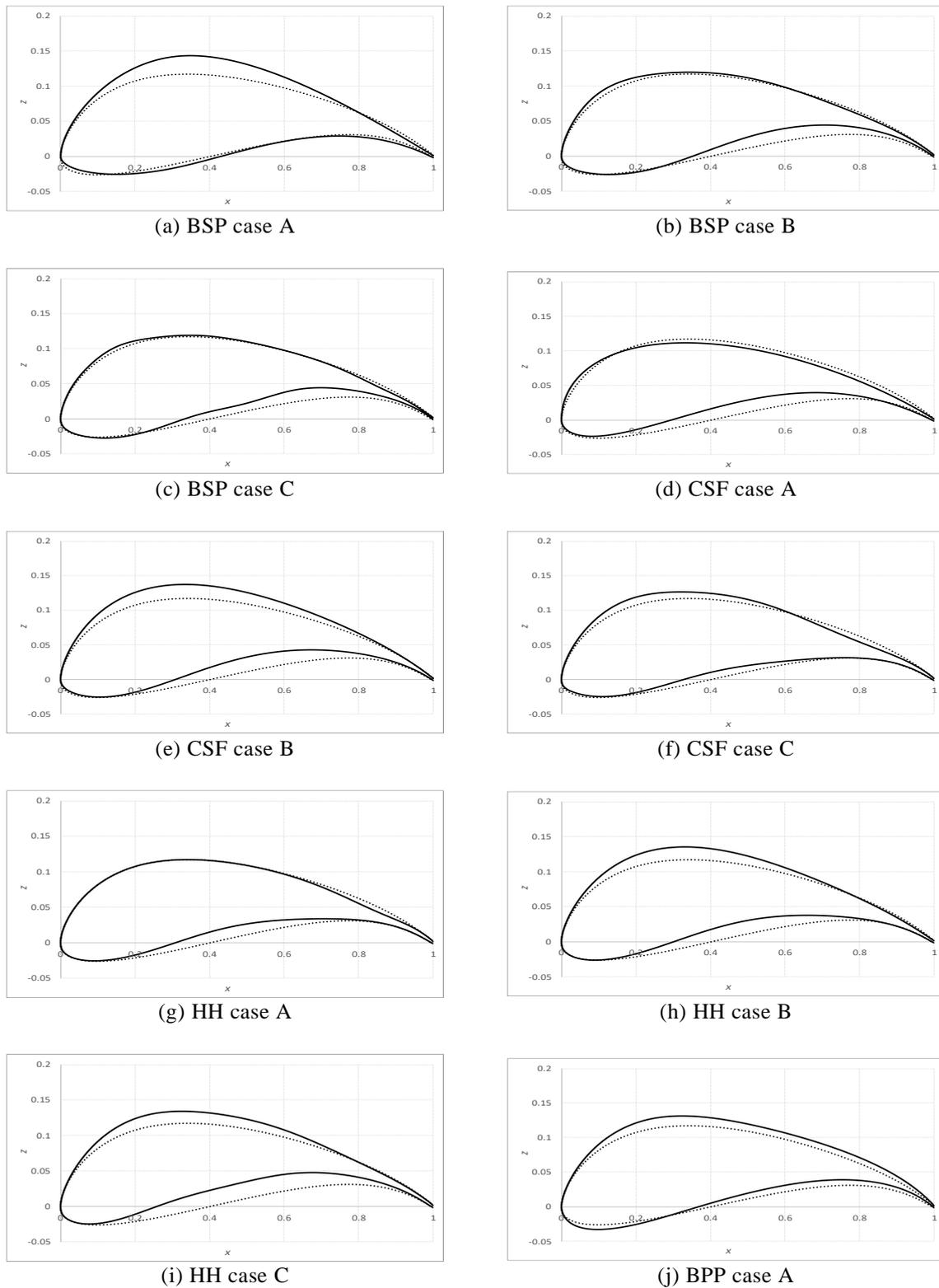
Figure 2. Optimised aerofoils (solid line) and original aerofoil (dashed line) for all study cases.

Ricardo J.F. Palmeira and Pedro V. Gamboa

(a) BSP case A

(b) BSP case B

BSP case C

(d) CSF case A

CSF case B

(f) CSF case C

HH case A

(h) HH case B

HH case C

(j) BPP case A
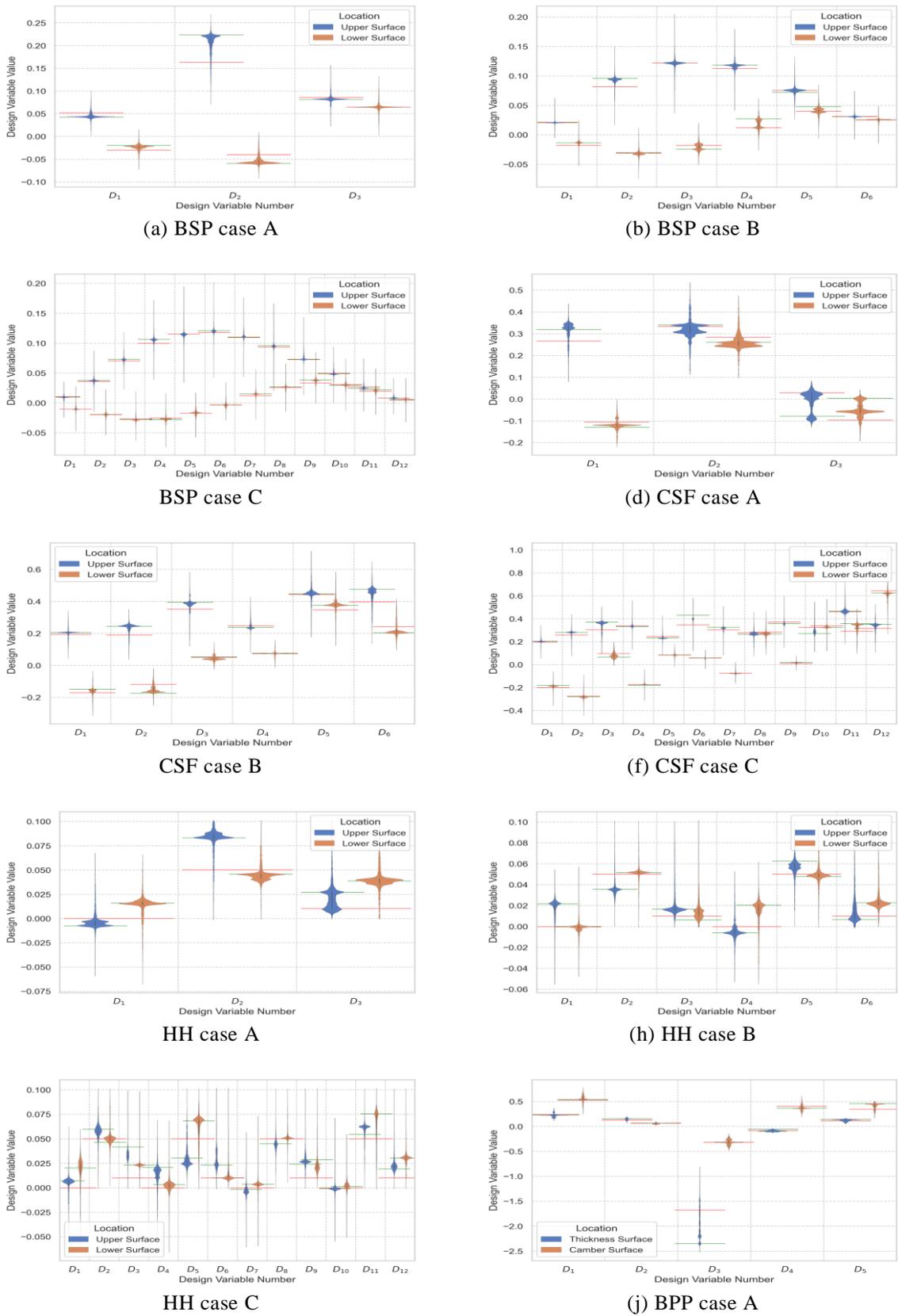
Figure 3. Violin graph of all design variables up to iteration 100. Red line marks initial variables and green line the best design variables at iteration 100.
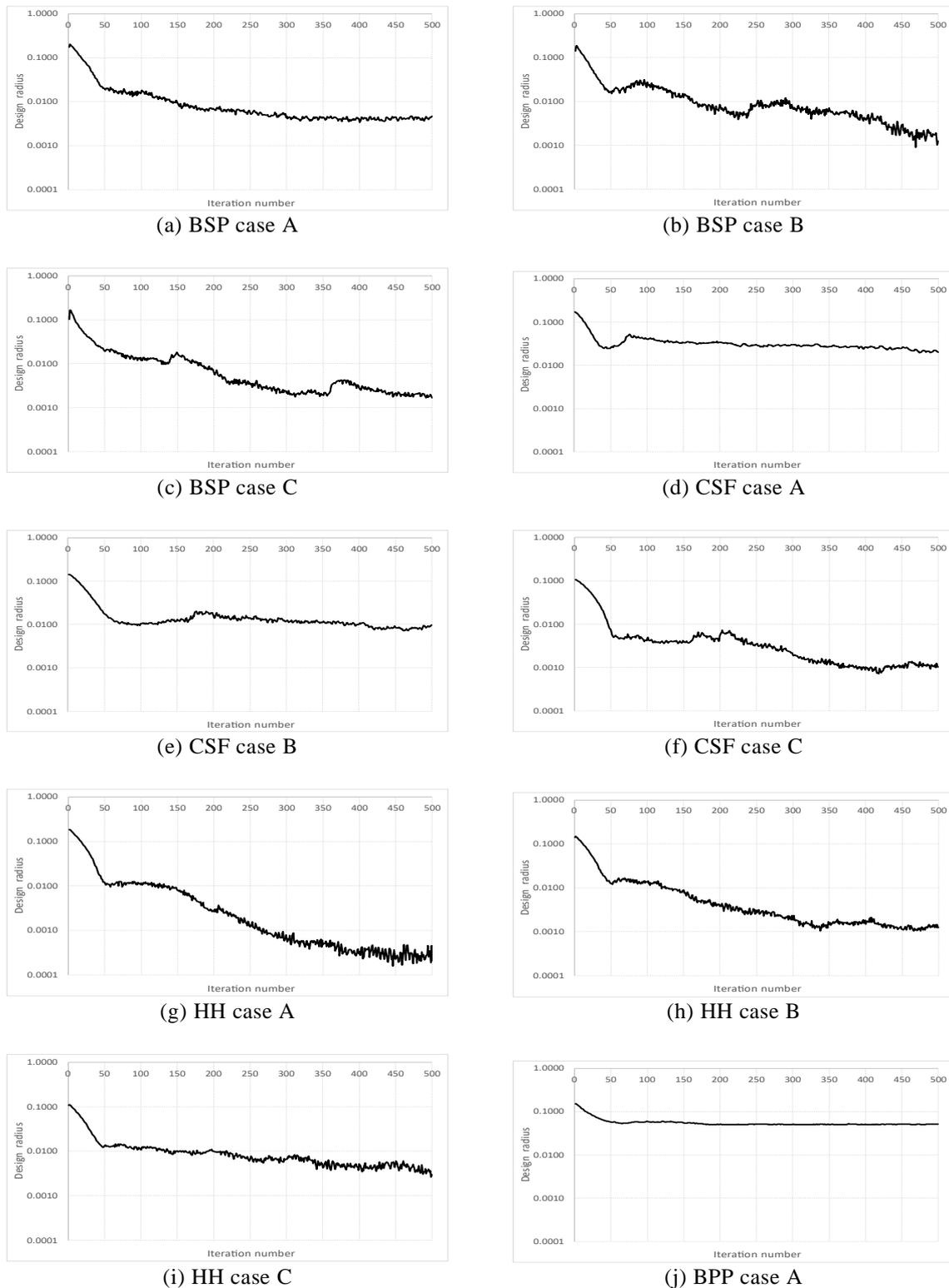
Figure 4. Design radius during optimization for all study cases.

The aerodynamic properties of the resulting aerofoils are shown in Tab.8, as well as the objective function (*Obj*) and an indicator of the improvement over the original aerofoil (1-*Obj*). The aerodynamic properties consistently improved are the maximum lift coeficient

Ricardo J.F. Palmeira and Pedro V. Gamboa

and lift coefficient during take-off which together account for almost seventy percent of the objective function.

The parametrization method with the lowest objective function is the B-Spline parametrization for all cases. The Class Shape Function and Hicks-Henne have similar results and the Bezier-PARSEC parametrization has the lowest improvement of all.

Table 8. Aerodynamic properties for the resulting aerofoil of each study case.

Case	$C_{l,max,TO}$	$C_{l,TO}$	$C_{d,TO}$	$C_{d,cruise}$	$C_{d,turn}$	Obj	$1-Obj$
Original	1.993	1.328	0.0183	0.0090	0.0150	1.0000	0.00%
BSP case A	2.244	1.680	0.0263	0.0094	0.0153	0.9509	4.91%
BSP case B	2.221	1.488	0.0218	0.0090	0.0165	0.9447	5.53%
BSP case C	2.234	1.455	0.0201	0.0086	0.0172	0.9312	6.88%
CSF case A	2.037	1.468	0.0200	0.0089	0.0149	0.9809	1.91%
CSF case B	2.258	1.602	0.0242	0.0097	0.0152	0.9512	4.88%
CSF case C	2.252	1.570	0.0215	0.0095	0.0153	0.9418	5.82%
HH case A	2.046	1.512	0.0195	0.0088	0.0139	0.9699	3.01%
HH case B	2.273	1.634	0.0244	0.0098	0.0149	0.9493	5.07%
HH case C	2.284	1.545	0.0214	0.0098	0.0152	0.9409	5.91%
BPP case A	2.246	1.509	0.0264	0.0103	0.0154	0.9823	1.77%

There is a correlation of 0.735 between 1-*Obj* and the number of design variables used. However, it is unclear which effect has had a higher influence: the original aerofoil parametrization accuracy or the design space.

Table 9. Accuracy of the parametrized original aerofoil.

Case	$RMSE_{upper}$	$RMSE_{lower}$
BSP case A	2.21×10^{-3}	1.79×10^{-3}
BSP case B	1.24×10^{-4}	3.35×10^{-4}
BSP case C	2.41×10^{-5}	6.04×10^{-5}
CSF case A	2.49×10^{-3}	2.13×10^{-3}
CSF case B	7.64×10^{-5}	2.49×10^{-4}
CSF case C	3.57×10^{-5}	6.30×10^{-5}
HH case A	0	0
HH case B	0	0
HH case C	0	0
BPP case A	4.64×10^{-3}	4.27×10^{-3}

A higher number of design variables increases the design space [7] and increases the accuracy of the parametrized original aerofoil, Tab.9, which is used to initialize the optimization. Since the initial optimization aerofoil is not the original aerofoil and the original aerofoil had good aerodynamic performance at the operating point, the initial optimization aerofoil has lower aerodynamic performance than the original. This means that each case starts at a different point of optimization, because the initial aerodynamic performance differs from case to case, depending on the accuracy of the parameterized original aerofoil.

The *BSP case C* has the lowest value of *Obj*, with a $C_{l,max,TO}$ of 2.234, 12% higher than the

original aerofoil, and a $C_{d,cruise}$ of 0.0086, 3% lower. To evaluate the aerofoil off-design performance, polars for each operating condition were calculated, as shown in Fig.5. The operating conditions are shown in Tab.10.

Table 10. Off-design conditions.

Case	Re	$Re\sqrt{C_l}$	M	$M\sqrt{C_l}$
Take-off	160,000	-	0.2	-
Cruise	-	290,000	-	0.04
Turn	-	420,000	-	0.06

(a) Lift coefficient for take-off

(b) Drag polar for take-off

(c) Lift coefficient for cruise

(d) Drag polar for cruise

(e) Lift coefficient for turn

(f) Drag polar for turn
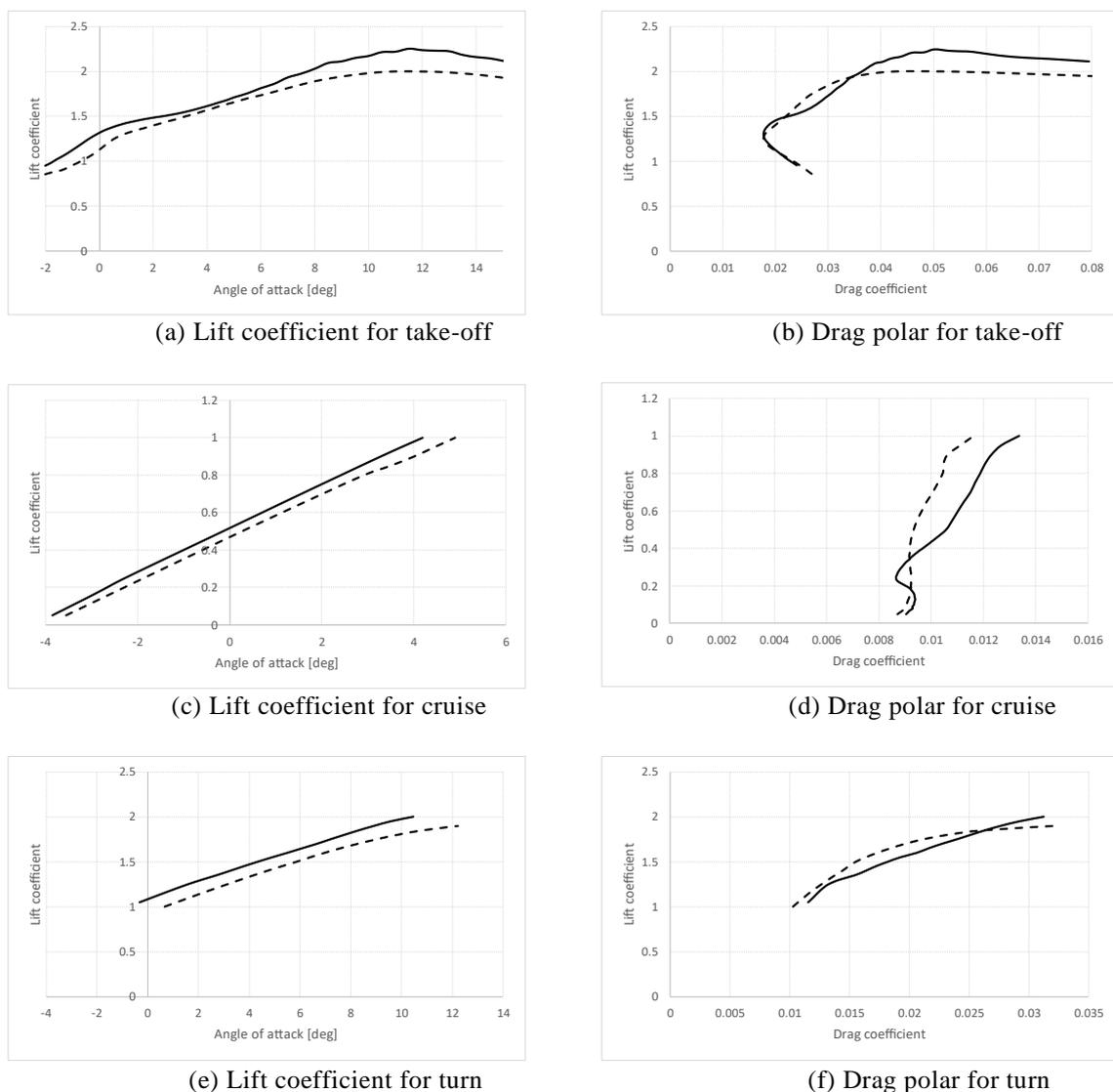
Figure 5. BSP case C polars (solid lines) and original aerofoil polars (dashed lines) for each operating condition near the operating point.

As expected, improved aerodynamic characteristics were obtained over the original aerofoil on the operating points. This is observed for take-off for operating points 2 and 3, where

Ricardo J.F. Palmeira and Pedro V. Gamboa

there is a lift coefficient increase and drag reduction near the angle of attack of 1.5 deg, Fig.5(a) and (b). as Also, for operating point 4, where there is a significant drag coefficient reduction near the lift coefficient of 0.258 is observed Fig.5(c) and (d). However, there is no improvement in the drag coefficient for operating point 5, Fig.5(e) and (f). This shows that from the optimization results an aerofoil with better aerodynamic performance near the optimization points was obtained.

4. CONCLUSIONS

For the purpose of this work, the program XOPTFOIL was modified. The parametrization methods B-Spline, Class Shape Functions and Bezier-PARSEC were added; plain flap hinge position and trailing edge thickness were introduced as design variables; XFOIL non convergence options were introduced; constraints became relative to the original aerofoil; design radius function was changed; relative initial perturbation and constraint limit parameters were added; and maximum lift coefficient optimization type can now use a sequence of angles of attack.

In this work, an aerofoil was optimized for the Air Cargo Challenge 2019 conditions using different aerofoil parametrizations and number of design variables.

From the results obtained in this study, it was shown that a higher number of design variables leads to higher aerodynamic performance in the resulting aerofoils The B-Spline parametrization results in higher performance, while Class Shape Functions and Hicks-Henne have similar results and Bezier-PARSEC the lowest. However, Class Shape Functions present less curvature reversals and trailing edge angle changes during optimization with higher numbers of design variables when compared to other parametrizations. It was also shown that the optimized aerofoil designs have higher aerodynamic performance than the original aerofoil near the operating points.

For future works it would be of interest to study the impact of initial perturbations, constraints limits and optimization parameters on the optimised aerofoils.

REFERENCES

[1]   M. Selig. Low Reynolds Number Airfoil Design Lecture Notes. https://m-selig.ae.illinois.edu/pubs/Selig-2003-VKI-LRN-Airfoil-Design-Lecture-Series.pdf, June 2020. University of Illinois at Urbana–Champaign.

[2]   M. Drela. Low-Reynolds-Number Airfoil Design for the M.LT. Daedalus Prototype: A Case Study. Journal of Aircraft, 25(8), 1987. doi: 10.2514/3.45650.

[3]   M. S. Selig and M. D. Maughmert. Multipoint Inverse Airfoil Design Method Based on Conformal Mapping. AIAA Journal, 30(5), 1992. doi: 10.2514/3.11046.

[4]   T. Ray and H. M. Tsai. Swarm Algorithm for Single- and Multiobjective Airfoil Design Optimization. AIAA Journal, 42(2): 366-373, 2004. doi: 10.2514/1.9099.

[5]   G. Carpentieri and M. J. L. van Tooren and B. Koren. Aerodynamic Shape Optimization by Means of Sequential Linear Programming Techniques. ECCOMAS CFD, 2006.

[6]   D. A. Masters and N. J. Taylor and T. C. S. Rendall and C. B. Allen and D. J. Poole. Review of Aerofoil Parameterisation Methods for Aerodynamic Shape Optimisation. AIAA 2015-076. doi:10.2514/6.2015-0761.

[7]   D. A. Masters and N. J. Taylor and T. C. S. Rendall and C. B. Allen and D. J. Poole. Geometric Comparison of Aerofoil Shape Parameterization Methods. AIAA Journal, 55(5), 2017. doi: 10.2514/1.J054943.

[8] M. Drela. XFOIL: An analysis and design system for low Reynolds number airfoils. T.J. Mueller (Ed.), Low Reynolds Number Aerodynamics. Lecture Notes in Engineering, Springer-Verlag, 1989. doi: 10.1007/978-3-642-84010-4_1.

[9] D. Prosser. XOPTFOIL. Version 1.11.1. Computer program. Retrieved from https://github.com/montagdude/Xoptfoil/tree/master, 21st of July 2020.

[10] L. Piegl ans W. Tiller. *The NURBS Book*. Springer, 1997. ISBN : 978-3-540-61545-3.

[11] B. M. Kulfan and J. E. Bussoletti. Fundamental Parametric Geometry Representations for Aircraft Component Shapes. 11th AIAA/ISSMO Multidisciplinary Analysis and Optimization Conference, AIAA Paper 2006-6948, Sept. 2006. doi:10.2514/6.2006-6948.

[12] B. M. Kulfan. Universal Parametric Geometry Representation Method. Journal of Aircraft, 45(1), 142–158, 2008. doi:10.2514/1.29958.

[13] B. M. Kulfan. Modfication of CST airfoil representaion methodology. http://www.brendakulfan.com/docs/CST8.pdf, July 2020.

[14] R. M. Hicks, and P. A. Henne. Wing design by numerical optimization. Journal of Aircraft, 15(7), 407-412, 1978. doi:10.2514/3.58379.

[15] R. W. Derksen and T. Rogalsky. Bezier-PARSEC: An optimized aerofoil parameterization for design. Advances in Engineering Software, 41(7), 923-930. 2010. doi: 10.1016/j.advengsoft.2010.05.002.

[16] Air Cargo Challenge 2019 in Stuttgart. Regulations for Air Cargo Challenge 2019 in Stuttgart.
http://www.euroavia.de/ACC/documents/regulation.pdf, Version 1.02, 5th of November 2018.

[17] P. F. Albuquerque and P. V. Gamboa, and M. A. Silvestre. Mission-Based Multidisciplinary Aircraft Design Optimization Methodology Tailored for Adaptive Technologies. Journal of Aircraft, 55(2), 755-770, 2018. doi: 10.2514/1.C034403.

[18] A. P. Piotrowski and J. J. Napiorkowski and A. E. Piotrowska. Population size in Particle Swarm Optimization. Swarm and Evolutionary Computation, 58, 100718, 2020. doi: 10.1016/j.swevo.2020.100718.

IMPACT OF THE DESIGN VARIABLES TYPE ON A FREEFORM WING OPTIMIZATION

Diego Bandeira de Melo Akel Thomaz[1], Pedro Tiago Silva Melo[1], Renata da Encarnacao Onety[2], Thiago Pontin Tancredi[3]

1: Mechanical Engineering / 2: Production Engineering
NEO - Nucleous of Engineering and Optimization / EST - Escola Superior de Tecnologia
UEA - Universidade do Estado do Amazonas
{dbdmat.eng16, ptsm.eng19, ronety}@uea.edu.br, http://www.uea.edu.br

3: TEG - Thermofluids Engineering Group / LabSin - Naval Simulation Lab
UFSC - Universidade Federal de Santa Catarina
thiago.tancredi@ufsc.br, http://ufsc.br/

Abstract. *This work discusses the impact of the variables choice on an optimization process. To exemplify this influence, the wing optimization of an aircraft is analyzed. Optimized geometry is defined by 3 sections that are described by 10 parameters. The first one refers to the section chord close to the aircraft fuselage. The other 9 parameters refer to the position, chord and offset of the three sections that control the wing geometry. In this model, the profile of each section is fixed and is not modified in the optimization. The aerodynamic performance is analyzed using the well-known AVL program. The objective function is the aircraft payload, which is calculated from the aerodynamic performance and an empirical model capable of estimating the aircraft weight. Once the work's focus is the influence of the choice of design variables on the optimization process, two optimization models are analyzed. The first model uses the absolute values of position, chord and offset for each section. The second one uses variations of these parameters as the design variables. The results showed that the model with relative variables had a considerably better performance for all evaluated metrics.*

Keywords: Optimization model, Wing, Shape optimization, Absolute variables, Relative variables.

Diego B. de M. A. Thomaz, Pedro T. S. Melo, Renata Onety and Thiago P. Tancredi

1 INTRODUCTION

The optimization of aircraft wings is one of the most important current topics about optimization applied to vehicle designs. The amount of recent works in the area is huge and covers different analysis techniques, optimization algorithms, geometric modeling strategies and objective functions. There are also a huge number of papers about the analysis and optimization of airfoil shapes.

Wings and airfoils can be represented as coordinates points. This method can be capable of representing a variety of forms and also allows local changes. However, it is very difficult to use a coordinate based method within an optimization process, because it involves enormous numbers of parameters with a high computation cost to explore the design space.

Among the main current works that discuss methods of parameterization of profiles and wings, it is important to cite [1], [2], [3], [4], [5] and [6]. In general, these works discuss different parameterization models, comparing the following techniques: mesh coordinates, Bezier Curves, NURBS, B-spline surfaces, Hicks-Henne bump functions, camber-line-thickness parameterization, Radial basis function domain element (RBF-DE) deformation, PARSEC and Class/Shape function transformation method (CST).

Most of these works concentrate efforts on single-objective optimization algorithms, such as SQP algorithm [7] and Adjunct method [3]. Regarding different models of parameterization to a wing (or profile), [8] highlights that such models should:

- have a compact number of design variables;

- have flexibility to cover the design space;

- represent of existing geometries with high accuracy;

- generate a smooth and realistic shapes.

In this work, we use a Genetic Algorithm, which, although slower, offers interesting metrics to evaluate the proposed parameterization models. For modeling, we use the mesh points technique, that, as demonstrated by [9] and [10], provide good results in all cases tested. The proposed approach is similar to the analysis and optimization methodologies that were used by [11]. However, this work focuses on the parameterization impact on the optimization process efficiency.

The objective is a conceptual discussion about the impact of the optimization model in each new engineering design. It is common to observe young researchers reflect few minutes on the optimization model and spend months to calibrate the analysis tools using a very high computational cost models to determine an optimized solution.

In this context, we propose an enlighten comparison using two types of parameterization to describe an aircraft wing. In the first, the classic control points coordinates approach (mesh points) is used. In the second, the coordinates of the points are described by parameters related to the points associated with the previous control section.

Although it is not a new technique, numerical metrics about the importance of this difference are presented, which can be applied to a large number of designs.

For example: In a ship design problem, it is common to use optimization models that incorporate the vessel length(L), beam(B) and draft (T). However, this model generates a

Diego B. de M. A. Thomaz, Pedro T. S. Melo, Renata Onety and Thiago P. Tancredi

large number of unfeasible solutions. It is close to absolute model studied in this article. On the other hand, if the relative variables L, L/B and B/T are used, the number of unfeasible solutions should drops suddenly, as demonstrated in this article.

2 CASE STUDY - CONCEPTUAL OPTIMIZATION MODEL

Two models are used to assess the impact of the parameterization model on the optimization process. Since the objective is to evaluate this influence, a small wing and an aerodynamic analysis tool based on vortex theory are used to reduce the computational cost, allowing a greater number of analyzes and comparisons.

2.1 Decision variables

The geometry proposed is defined by 10 parameters. The first one refers to the wing section chord close to the aircraft fuselage. The other 9 parameters refer to the position, chord and offset of the three sections that control the wing geometry (Figure 1).

| (a) Offset | (b) Span and chord |
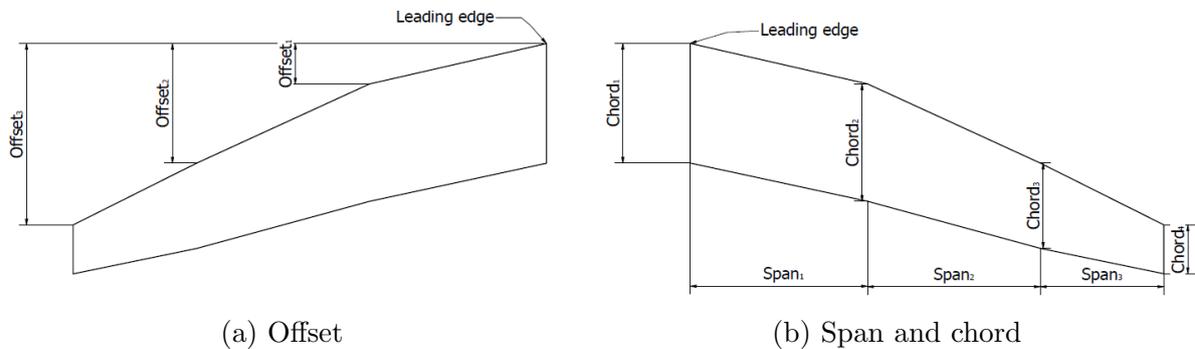
Figure 1: Wing surface parameters

It is important to highlight that the profile used in wing modeling is fixed, and it is always the profile whose characteristics are shown in Figure 2.

Features	Values
Thickness	12.60 [% of chord]
Camber	9.06 [% of chord]
Maximum thickness position	23.23 [% of chord]
Maximum camber position	40.40 [% of chord]
Stall angle	13.5°
Maximum C_L	2.290
Cruise C_L/C_D	96.754
Cruise C_M	0.265
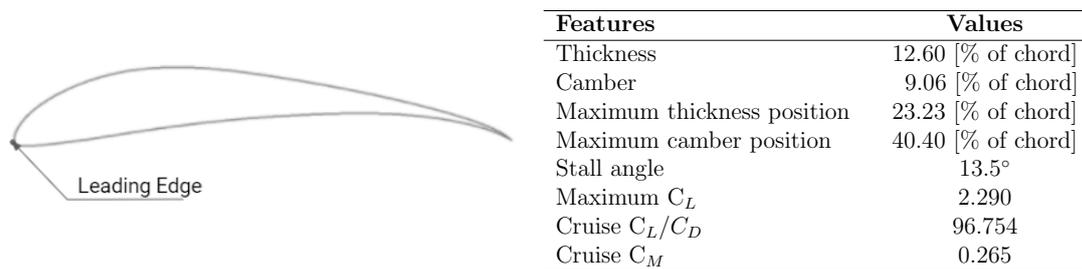
Figure 2: Wing profile characteristics

Finally, it is well-known that the wing with swept is more common in supersonic aircraft design. However, it was decided to include the offset variables in the optimization model, in order to increase the variability of the geometries, regarding that the analysis tool is capable of consider this characteristic.

2.2 Objective Function

The objective function aims at maximizing the aircraft payload, which is calculated from the aerodynamic performance and an empirical model capable of estimating the

aircraft weight (Equation 1).

$$F(\bar{X}) = Payload = W_{takeoff} - W_{aircraft} \tag{1}$$

Where $\bar{X}$ refers to the design variables vector and $W_{aircraft}$ refers to the empty aircraft mass, which is estimated based on the empirical model calculated using the area S referring to the total surface of the wings, measured in m^2 (Equation 2).

$$W_{aircraft} = 1.539331 * S^2 + 1.341043 * S \tag{2}$$

And $W_{takeoff}$ refers to the total mass that the aircraft is able to take off on a lane shorter than 90 meters and is calculated by Equation 3.

$$W_{takeoff} = \frac{L_{takeoff}}{g * F_s} \tag{3}$$

Where g refers to the acceleration of gravity (9.81 m/s^2) and F_s refers to a correction factor for the inclusion of the dynamic effects presented in the takeoff, with the value of 1.09 being arbitrated. The takeoff speed used was 1.2 times greater than the stall speed, as recommended by [12]. The lift and drag were calculated with 0.7 of this speed value, as recommended by [13].

$L_{takeoff}$ refers to the total lift generated by the wings at takeoff, which is determined based on the Algorithm 1, where at each iteration the aircraft mass increases 0.25 kg. The L_{lane} equation was developed in [14].

Algorithm 1: Takeoff Algorithm

Result: $L_{takeoff}$
$L_{lane} = 0$
$L_{takeoff} = 0$
while $L_{lane} < 90$ **do**

$\quad V = \sqrt[2]{\frac{2*L_{takeoff}}{\rho_{air}*S*C_L}} * 1.2 * 0.7$
$\quad T = a(0.7 * V)^2 + b * 0.7 * V + c$
$\quad D = 0.5 * C_D * S * \rho_{air} * V^2$
$\quad L = 0.5 * C_L * S * \rho_{air} * V^2$
$\quad L_{lane} = \frac{1.44*L_{takeoff}^2}{g*C_L*S*\rho_{air}*(T-D-\mu_{lane}*(L_{takeoff}-L))}$
$\quad$ **if** $L_{lane} < 90$ **then**
$\quad\quad |\quad L_{takeoff} = L_{takeoff} + 0.25 * g$
$\quad$ **end**

end

Where ρ_{air} refers to the specific mass of air (1.225 kg/m^3). μ_{lane} refers to the soil friction coefficient and according to [15], it is 0.025. The parameters [a, b, c] refer to the thrust curve, which were estimated in [-0.0126, -0.5248, 40.0248]. Finally, the coefficients C_D and C_L are obtained in the aerodynamic analysis of the modeled wing.

2.3 Constraints

As constraints of the problem, it was defined that the design space must be strictly the same for both models to ensure that they have the same optimization potential.

Diego B. de M. A. Thomaz, Pedro T. S. Melo, Renata Onety and Thiago P. Tancredi

Furthermore, the maximum wingspan allowed is 4.2 m and the aircraft needs to take off on a lane with a maximum of 90 m.

Regarding the wing geometry, the sections chords can never increase from a section closer to the fuselage to a section closer to the wing tip. Furthermore, the swept must always increase as it approaches the wing tip, preventing the forward swept wings.

3 OPTIMIZATION MODELS: ABSOLUTE VARIABLES AND RELATIVE VARIABLES

As already mentioned, the geometry is defined by 10 variables, which are called x_i and grouped in a vector $\bar{X}$:

$$[\bar{X}] = [x_1, x_2, x_3, x_4, x_5, x_6, x_7, x_8, x_9, x_{10}] \tag{4}$$

Once in the relative model the wing parameters are modeled by variables combinations, the Tab.1 shows the correspondence between the design parameters and the optimization variables in each of the studied models.

Table 1: Design variables in each optimization model

Geometric parameter	Absolute	Relative
$Span_1$	x_1	x_1
$Span_2$	x_2	$x_1 + x_2$
$Span_3$	x_3	$x_1 + x_2 + x_3$
$Chord_1$	x_4	x_4
$Chord_2$	x_5	$x_4 - x_5$
$Chord_3$	x_6	$x_4 - x_5 - x_6$
$Chord_4$	x_7	$x_4 - x_5 - x_6 - x_7$
$Offset_1$	x_8	x_8
$Offset_2$	x_9	$x_8 + x_8$
$Offset_3$	x_{10}	$x_8 + x_9 + x_{10}$

It is important to highlight that to maintain the same design space in both models, the limits of each variable must be carefully defined, as shown in Tab.2.

Table 2: The design space in each optimization model

Design Variable	Absolute		Relative	
	min value[m]	max value[m]	min value[m]	max value[m]
x_1	0.30	2.00	0.30	2.00
x_2	0.60	2.20	0.30	2.00
x_3	0.90	2.40	0.30	2.00
x_4	0.10	1.00	0.10	1.00
x_5	0.05	1.00	0.00	0.15
x_6	0.05	1.00	0.00	0.15
x_7	0.05	1.00	0.00	0.15
x_8	0.00	0.25	0.00	0.25
x_9	0.00	0.50	0.00	0.25
x_{10}	0.00	0.75	0.00	0.25

Each of the models received a set of constraints to satisfy the conceptual constraints described in section 2.3. The model with absolute variables requires 8 equations to satisfy the conceptual constraints, while the model with relative variables requires only 4 (Tab.3). The positions marked with an asterisk * in Tab.3 refer to conceptual constraints that are satisfied by the limitation of the design space.

Table 3: Constraints equations in each optimization model

Concept	Absolute	Relative
$2 * Span_3 < 4.2$	$x_3 < 2.1$	$x_1 + x_2 + x_3 < 2.1$
$Span_1 > 0.3$	*	*
$Span_2 - Span_1 > 0.3$	$x_2 - x_1 > 0.3$	*
$Span_3 - Span_2 > 0.3$	$x_3 - x_2 > 0.3$	*
$Chord_2 - Chord_1 < 0$	$x_5 - x_4 < 0$	*
$Chord_3 - Chord_2 < 0$	$x_6 - x_5 < 0$	*
$Chord_4 - Chord_3 < 0$	$x_7 - x_6 < 0$	*
$Offset_1 > 0$	*	*
$Offset_2 - Offset_1 > 0$	$x_9 - x_8 > 0$	*
$Offset_3 - Offset_2 > 0$	$x_{10} - x_9 > 0$	*
$Chord_1 > 0.05$	*	*
$Chord_2 > 0.05$	*	$x_4 - x_5 > 0.05$
$Chord_3 > 0.05$	*	$x_4 - x_5 - x_6 > 0.05$
$Chord_4 > 0.05$	*	$x_4 - x_5 - x_6 - x_7 > 0.05$

A single value of 10000 was adopted to penalize the objective function, since all constraints have the same magnitude order and there is only one objective function in the model.

4 METHODS AND TOOLS

4.1 Analysis

For the analysis, the Vortex Lattice Method was used with AVL (Athena Vortex Lattice) application. In this technique, the lift calculation uses an inviscid (non-viscosity) vortex of horseshoe type distributed over panels along the three-dimensional wing surface. Details about the solver are not relevant for this paper, but they can be seen in [16].

4.1.1 Verification of the numerical model

As the tool used in the aerodynamic analysis has a numerical approach, the mesh influence on the response quality must be evaluated. Therefore, a study case was done to identify the appropriated discretization for the studied geometry. The characteristics of the geometry used in mesh convergence study are shown in Figure 3.

The AVL program uses a discretization based on a number of elements in the chord direction and a number of elements in the wing span direction. Both parameters are set for each wing's segment defined between control sections. Initially, a parametric analysis was performed, varying the number of elements in chord direction from 1 to 30, always keeping the number of elements in span direction equal to 10 (Figure 4).

Diego B. de M. A. Thomaz, Pedro T. S. Melo, Renata Onety and Thiago P. Tancredi

Variable	Value [m]
$Span_1$	0.5
$Span_2$	0.9
$Span_3$	1.3
$Chord_1$	0.35
$Chord_2$	0.30
$Chord_3$	0.25
$Chord_4$	0.15
$Offset_1$	0.05
$Offset_2$	0.10
$Offset_3$	0.20
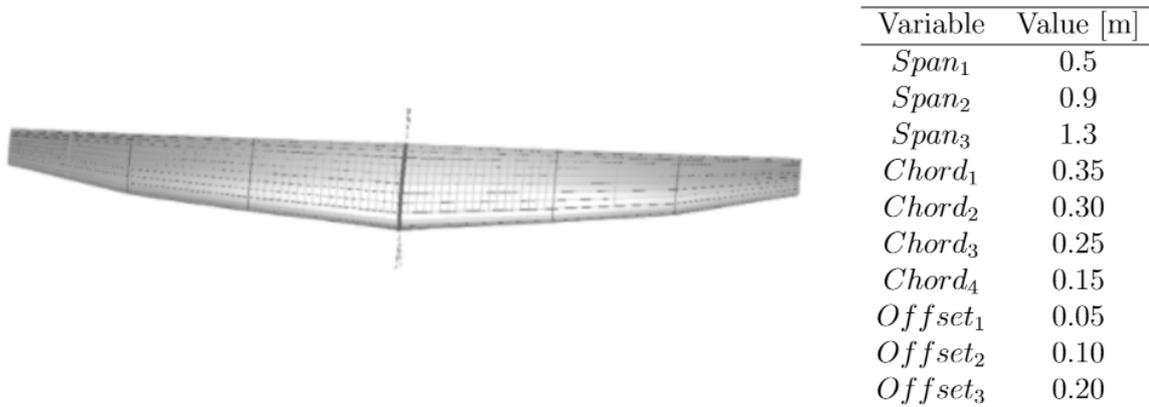
Figure 3: Geometry used in the mesh convergence study
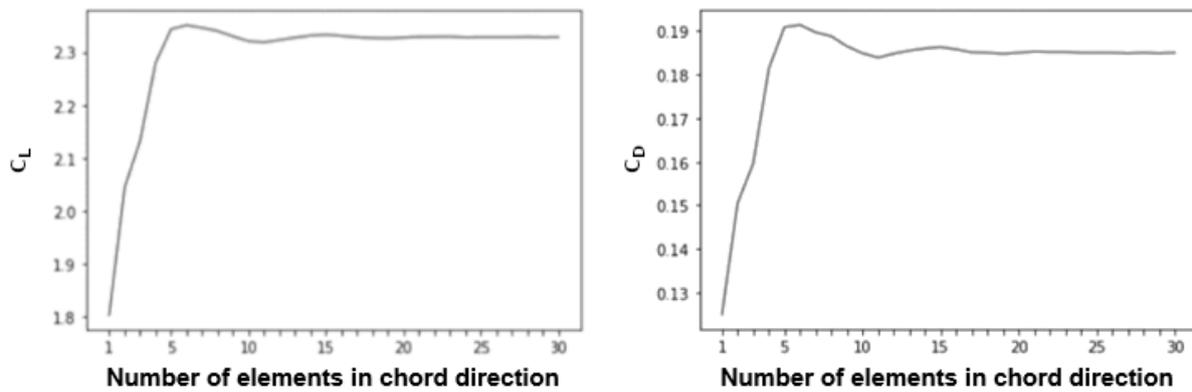
Figure 4: Mesh convergence study about number of elements in chord direction

As one observes, the analysis seems to reach convergence with about 22 elements in the chord direction. Then, a parametric analysis was performed, varying the number of elements in the span direction from 1 to 30, always keeping the number of elements in the chord direction equals to 22 (Figure 5).
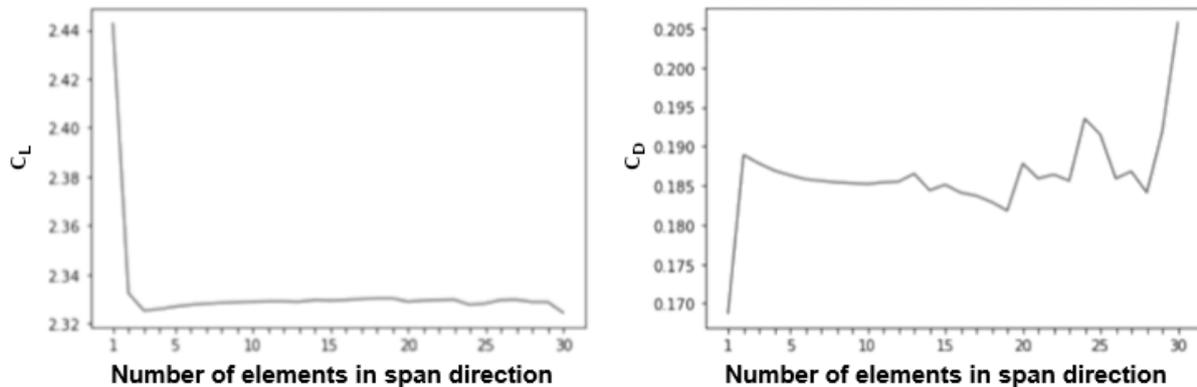
Figure 5: Mesh convergence study about number of elements in span direction

Diego B. de M. A. Thomaz, Pedro T. S. Melo, Renata Onety and Thiago P. Tancredi

It is evident that the region with more numerical stability is around 10 elements. However, it is important to note that the sections positions are design variables of optimization process. Once the segment's length can change significantly, the best approach is to define a typical element size and not a typical number of elements. As in the studied geometry the lengths of the segments are between 0.4m and 0.5m (Figure 3), a typical element size of 0.05m was defined. However, although the chords also can change, to keep a structured mesh it is a good approach to keep the number of elements in chord direction constant.

4.2 Optimization

The optimization process was conducted using a Genetic Algorithm implemented in Python in-house code. The algorithm uses a random initial population with 50% of feasibility. That is, random individuals are generated until the number of feasible solutions is equal to half of the population size.

The evolution process uses classical mutation and crossover operators, as described in [17]. Finally, an elitism operator is applied, keeping the population size constant, keeping the best individuals in each generation.

Each analysis performed consists of a population with 20 individuals, mutation rate of 4% and limit of 300 generations. All crossovers are done with a random percentage of genome cross.

The use of the maximum number of generations as the only criterion to finish the optimization, although inefficient, facilitates data processing and guarantees more uniform metrics for comparing results.

5 RESULTS

The optimization results of both parameterization models are presented below. To ensure a minimum of statistical reliability, each model was solved 5 times, always with a randomly initial populations. Figure 6 shows the evolution of the highest score obtained in each generation for each run of the models (only feasible individuals are considered).

(a) Relative (b) Absolute
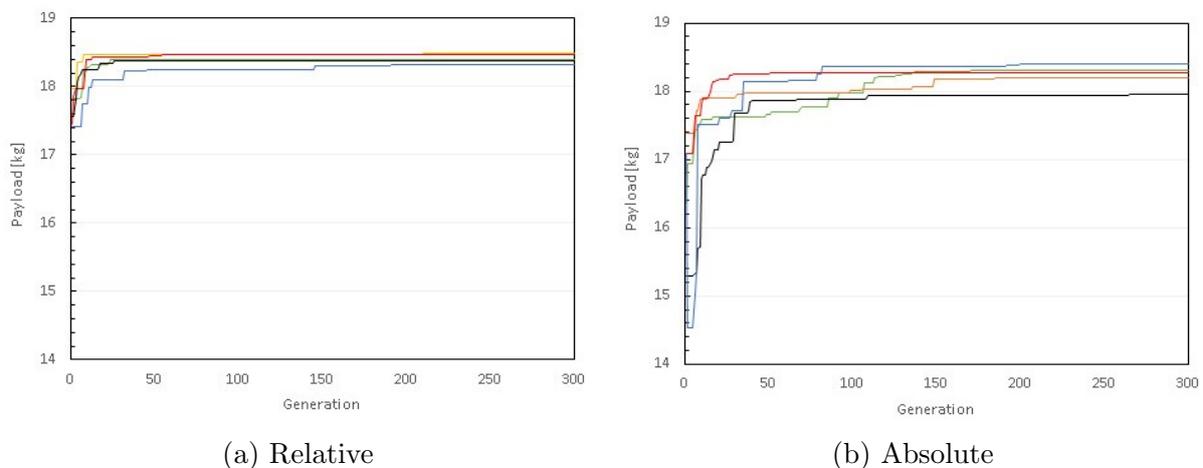
Figure 6: Maximum payload in each generation

Observing these results, it is possible to conclude that the absolute model has greater difficulty in generating promising solutions at the beginning of the process. On average, the highest payload obtained with this model in the initial generation is 5.7% smaller

than the average value obtained for the largest payload in the initial generation using the relative model.

Furthermore, it is notable that the absolute model has a slower convergence, requiring a greater number of generations to reach the optimal solution. On average, the number of generations required by the relative model is 42.2% lower than the number of generations required by the absolute model.

Finally, it is observed that the absolute model has a greater variability between different executions, requiring a greater number of repetitions to ensure an optimal solution.

The rash reader might imagine that the highest payload will result from the highest lift, which is resulted from a bigger wing surface. However, as noted in Figure 7, from a certain area value, the aircraft weight increases more than the lift gain. Thus there is an optimal area that will maximize the aircraft payload.

(a) Relative (b) Absolute
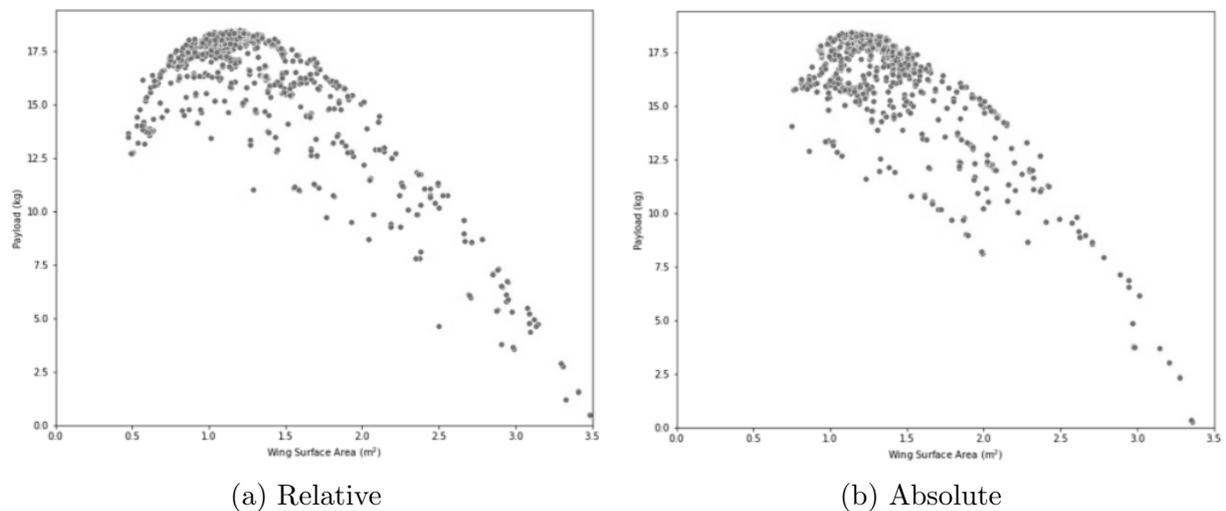
Figure 7: Payload in function of wing area

The existence of several payload values for the same wing area shows another important feature of the problem: not only the area is important but the geometric ratios as well. In order to better assess the impact of the parameterization on the efficiency of the optimization process, Tab.4 shows the number of evaluations of single solutions (feasible and non-feasible) performed along the optimization processes for each of the models.

It is noticed that, the average number of solutions evaluated during optimization using the absolute model is 6553, that is, almost 10 times the average number of evaluations performed by the relative model, which is 673 evaluations.

Furthermore, the probability of mutation or crossover to produce a feasible solution is about 10 times greater when using the relative model. That is because, in the absolute model, on average, only 6% of the solutions analyzed were feasible, while in the relative model, this number is close to 64%.

Finally, although it is not the focus of this research, Tab.5 and Tab.6 show the final solutions of each execution of the optimization processes for each studied model. The values of the optimization variables were converted to the wing's geometric parameters to facilitate the comparison and analysis of the results.

The results in Tab.4 show some interesting aspects. Firstly, the multi modal nature of the problem is observed, because there are different variables sets that result in a same

Diego B. de M. A. Thomaz, Pedro T. S. Melo, Renata Onety and Thiago P. Tancredi

Table 4: Single evaluations performed for each optimization process

Model	Run	Feasible	Non-Feasible	Total	%Feasible	%Non-feasible
Relative	1	350	232	582	60.1%	39.9%
Relative	2	416	272	688	60.5%	39.5%
Relative	3	495	207	7002	70.5%	29.5%
Relative	4	521	294	815	63.9%	36.1%
Relative	5	362	215	577	62.7%	37.3%
Absolute	1	320	6877	7197	4.4%	95.6%
Absolute	2	471	5465	5936	7.9%	92.1%
Absolute	3	405	4372	4777	8.5%	91.5%
Absolute	4	330	7856	8186	4.0%	96.0%
Absolute	5	369	6298	6667	5.5%	94.5%

Table 5: Geometric parameters of the optimum solutions

Model	Run	$Span_1$	$Span_2$	$Span_3$	$Chord_1$	$Chord_2$	$Chord_3$	$Chord_4$	$Offset_1$	$Offset_2$	$Offset_3$
		[m]	[m]	[m]	[m]	[m]	[m]	[m]	[m]	[m]	[m]
Relative	1	0.56	1.09	2.07	0.37	0.33	0.30	0.17	0.10	0.16	0.23
Relative	2	1.27	1.66	2.08	0.41	0.29	0.19	0.09	0.09	0.16	0.23
Relative	3	0.77	1.36	2.09	0.30	0.28	0.27	0.19	0.02	0.02	0.03
Relative	4	0.59	1.68	2.09	0.31	0.31	0.26	0.13	0.07	0.07	0.16
Relative	5	0.73	1.29	2.09	0.40	0.38	0.23	0.15	0.16	0.34	0.44
Absolute	1	1.03	1.52	2.04	0.39	0.30	0.29	0.08	0.08	0.13	0.14
Absolute	2	0.30	1.20	2.04	0.50	0.36	0.25	0.09	0.09	0.23	0.23
Absolute	3	0.31	0.88	2.03	0.65	0.41	0.35	0.11	0.22	0.41	0.55
Absolute	4	0.49	1.16	2.09	0.56	0.37	0.31	0.07	0.21	0.36	0.49
Absolute	5	0.30	1.08	2.08	0.40	0.33	0.29	0.14	0.09	0.16	0.46

Table 6: Performance attributes of the optimum solutions

Model	Run	Payload [kg]	Wingspan [m]	S [m^2]	C_L	C_D	$W_{aircraft}[kg]$
Relative	1	18.40	4.15	1.18	2.48	0.13	3.72
Relative	2	18.49	4.17	1.20	2.50	0.14	3.83
Relative	3	18.32	4.17	1.11	2.50	0.13	3.39
Relative	4	18.46	4.18	1.15	2.50	0.13	3.56
Relative	5	18.38	4.19	1.22	2.46	0.13	3.94
Absolute	1	18.30	4.09	1.20	2.48	0.14	3.82
Absolute	2	18.20	4.08	1.09	2.49	0.13	3.31
Absolute	3	17.95	4.06	1.29	2.39	0.14	4.28
Absolute	4	18.27	4.17	1.26	2.44	0.14	4.15
Absolute	5	18.40	4.15	1.14	2.49	0.13	3.51

objective function value. Notably, the optimal solution obtained in the fifth optimization of the absolute model has geometric parameters remarkably different from the parameters obtained in the first optimization of the relative model. However, both solutions have the same payload value.

Furthermore, it is observed that the average value of the objective function achieved

with the absolute model is 18.22 kg, which is 1% lower than the average value obtained with relative model, that is, 18.41 kg. Concerning the maximum value, the absolute model reached 18.40 kg, that is, 0.5% lower than the 18.49 kg reached by the relative model.

Since the maximum efficiency gain expected during an optimization process is around 5%, variations of 1% can be considered significant.

However, the most important observation is about the results dispersion. While the absolute model reached a standard deviation to the objective function of 0.15 kg, the standard deviation reached with the relative model was only 0.06 kg.

6 CONCLUSIONS

This paper presents a performance comparison of two parametrization models for an aircraft wing using the same design space and the same optimization algorithm. It was observed that the absolute model has greater difficulty in generating promising solutions at the beginning of the process, having a solution typically 5.7% smaller than the value typically obtained for the highest payload in the initial generation using the relative model.

During optimization, the relative model has a faster convergence, requiring 42.4% fewer generations than the absolute model. Furthermore, the absolute model has a greater variability between different executions, requiring a greater number of repetitions to ensure an optimal solution.

But the most important conclusion is that the average number of solutions evaluated during optimization using the absolute model was almost 10 times greater than the average number of evaluations performed by the relative model. And the probability of a mutation or crossover to produce a feasible solution is about 10 times greater when using the relative model.

Finally, it was observed that the relative model was able to obtain a solution 1% better with half of the variability when compared with the absolute model.

All of these features evidence that the relative model reaches a better result, with a smaller number of generations, evaluating a significantly smaller number of configurations with a smaller influence of the initial population.

Thus, instead of spending 10 minutes thinking about the optimization model and 1000 hours optimizing it, how about we think a little more about the optimization model?

ACKNOWLEDGEMENTS

REFERENCES

[1] I. Sadrehaghighi, J.A. Aircraft wing shape optimization. *Applied Sciences*, 2021. doi:https://www.researchgate.net/publication/318562320_Aircraft_Wing_Shape_Optimization.

[2] P. D. T. N. R. T. . A. C. Masters, Dominic A. Impact of shape parameterisation on aerodynamic optimisation of benchmark problem. *54th AIAA Aerospace Sciences Meeting [AIAA2016-1544] American Institute of Aeronautics and Astronautics Inc. (AIAA)*, 2016. doi:https://doi.org/10.2514/6.2016-1544.

Diego B. de M. A. Thomaz, Pedro T. S. Melo, Renata Onety and Thiago P. Tancredi

[3] M. J. A. George R. Anderson. Adaptive shape parameterization for aerodynamic design. *NAS Technical Report: NAS-2015-02*, 2015.

[4] K. Manohara Selvan. On the effect of shape parameterization on aerofoil shape optimization. *International Journal of Research in Engineering and Technology.*, 2015. doi:04. 123-133. 10.15623.

[5] M. P. Sripawadkul, V. and M.Guenov. A comparison of airfoil shape parameterization techniques for early design optimization. *AIAA-2010-9050*, 2010.

[6] R. D. D. Chauhan, Praveen Chandrashekarappa. Wing shape optimization using ffd and twist parameterization, bangalore, india. *12th Aerospace Society of India CFD Symposium*, 2010. doi:ffinria-00537316.

[7] M. W. Gill, P. E. and M. A. Saunders. Snopt: An sqp algorithm for large-scale constrained optimization. *SIAM journal on optimization*, 12(4):979–1006, 2002.

[8] J. Samareh. Survey of shape parameterization techniques for high-fidelity multidisciplinary shape optimization. *AIAA Journal*, 2001.

[9] P. Castonguay and S. Nadarajah. Effect of shape parameterization on aerodynamic shape optimization. *AIAA-2007-59*, 2007.

[10] C. P. Mousavi, A. and S. K. Nadarajah. Survey of shape parameterization techniques and its effect on three-dimensional aerodynamic shape optimization. *AIAA Computational Fluid Dynamics Conference*, 2007. doi:2007-3837.

[11] M. T. Akram and M.-H. Kim. Cfd analysis and shape optimization of airfoils using class shape transformation and genetic algorithm—part i. *Applied Sciences*, 11(9): 2049–2075, 2021. doi:10.3390/app11093791.

[12] F. A. Regulations. Part 23 airworthiness standards: Normal, utility, acrobatic and commuter category airplanes. *Washington DC, US Government Printing Office, Revised January*, 1989.

[13] J. D. Anderson Jr. *Fundamentos de engenharia aeronáutica*. AMGH Editora, 2015.

[14] F. A. Bortolete. Algoritmo de otimização aerodinâmica de asas voltadas auma aeronave de baixo numero de reynolds, "Aerodynamic Optimization Algorithm Of Low Reynolds Number Aircraft". Undergraduation Dissertation. Dept. Engenharia Mecânica, Universidade do Estado do Amazonas, Brasil, 2017.

[15] L. E. M. J. Rodrigues. Fundamentos da engenharia aeronáutica aplicações ao projeto sae-aerodesign. *NAS Technical Report: NAS-2015-02*, 1, 2011.

[16] H. Y. Mark Drela. Avl guide. `https://web.mit.edu/drela/Public/web/avl/`, 2004.

[17] A. A. S. M. T. Deb, K.; Pratap. A fast and elitist multiobjective genetic algorithm: Nsga-ii. ieee transactions on evolutionary computation. *SIAM journal on optimization*, 6(2), 2002.

DESIGN OF PRE-TWISTED TAPERED BEAMLIKE STRUCTURES VIA EFFICIENT YET ACCURATE MODELS AND FORMULAS

Giovanni Migliaccio

Department of Civil and Industrial Engineering,
University of Pisa,
Largo Lucio Lazzarino 2, 56122, Pisa, Italy,
giovanni.migliaccio.it@gmail.com

Abstract *Beamlike elements with tapered and pre-twisted cross-sections are widespread in engineering applications as their peculiar shape has long been exploited to optimize the mechanical behavior of many engineering structures, e.g. blades of helicopters and wind turbines just to mention some examples. Unfortunately, engineering methods and formulas commonly used to evaluate the stress and stain fields in prismatic beams provide incorrect results in tapered and pre-twisted cases because of the variable dimensions and orientations of their cross-sections which yield non-trivial stress and stain distributions absent in the prismatic case. Not to speak of the large displacements such structures may undergo, which further complicate the derivation of closed-form formulas for engineering design purposes. However, the design and optimization of the mechanical behaviour of such tapered and pre-twisted elements can be addressed via a modelling approach that is computationally efficient and accurate (with respect to nonlinear 3D-FEM approaches) and enables evaluating even analytically the effects of taper and pre-twist design parameters on the stress and strain fields, as is discussed in the present work.*

Keywords: non-prismatic beams, analytical results, structural design.

G. Migliaccio

1. INTRODUCTION

Many components of helicopters, aircraft, wind turbines, and other engineering structures, are beamlike and non-prismatic. Structures of this kind may be tapered, pre-twisted, and curved in their unstressed state, undergo large displacements and 3D cross-sectional warpings. Their mechanical modelling should be addressed via schematizations based on non-prismatic beam elements offering appropriate compromises between computational efficiency and accuracy, and accounting for the effects of geometric design features such as taper and pre-twist on their stress and strain fields via rigorous yet application-oriented models. Over the years several approaches have been proposed for beamlike bodies (e.g. [1-8]), reviews are also available in literature (such as [9-11]), but general non-prismatic cases still require investigation. In fact, engineering methods and formulas commonly used for prismatic beams provide incorrect results in non-prismatic cases because transverse cross-sections with variable dimensions and orientations produce stress and strain distributions, plus couplings among flexure, torsion and traction, absent in prismatic cases [12-15].

This paper discusses how the design and optimization of the aforementioned elements can be addressed via an approach that explicitly accounts for the effects of some geometric design parameters (related to taper and pre-twist) on the stress and strain fields. The general model is summarized in section 2. The results that allow analytical evaluations of the effects of the taper and pre-twist on stresses and strains are discussed in section 3. Numerical examples and comparisons with the outcomes of nonlinear 3D-FEM analyses are shown in section 4.

2. MECHANICAL MODEL

We begin recalling the main ingredients of our model, further details of which can be found in [13,15]. First of all, we consider a beamlike body as a collection of plane figures (transverse cross-sections) attached at a three-dimensional curve (beam's centre-line). The centre-line may undergo large displacements; the transverse cross-sections are fully deformable and may undergo warping displacements in and out of plane, as in Figure 1.
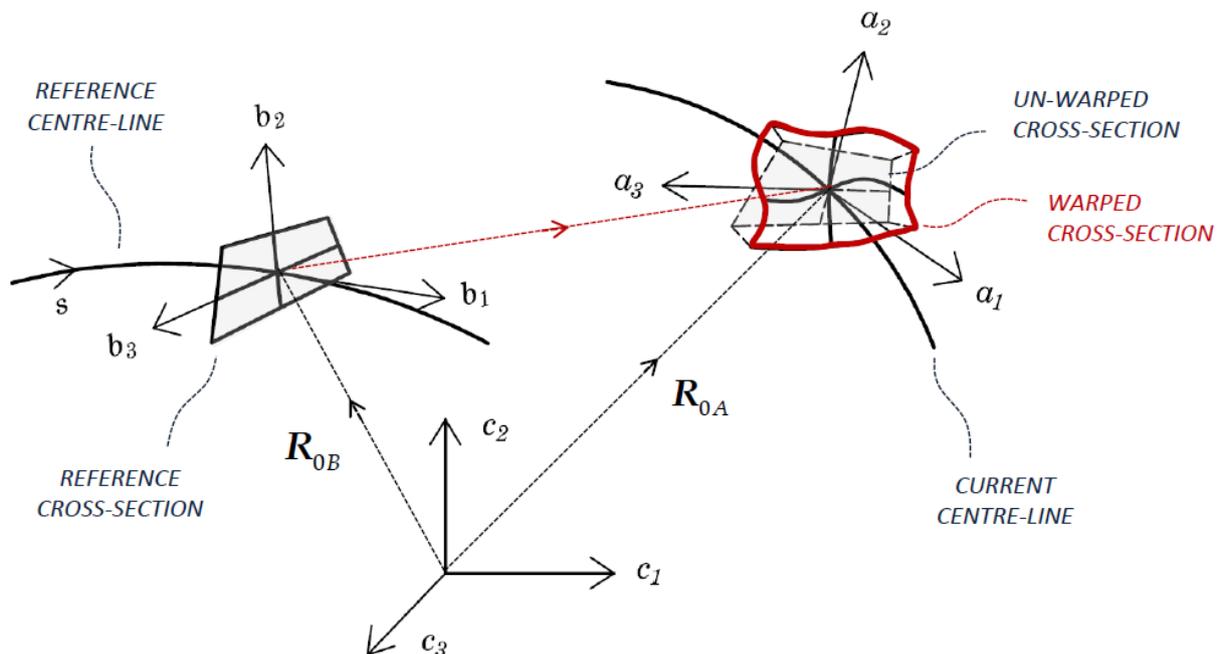
Figure 1. Schematic of current and reference centre-lines, cross-sections, and orthonormal triads.

G. Migliaccio

Two mapping functions identify the positions of the beam's points in their current and reference states. In particular, the reference mapping function, R_B, is defined by

$$R_B(z_i) = R_{0B}(z_1) + x_\alpha(z_i) b_\alpha(z_1) \tag{1}$$

where R_{0B} identifies the reference centre-line relative to triad c_i, x_α denote the cross-section's points relative to such line, and z_i are three mathematical variables, independent of time, with z_1 equal to the reference arc-length s, and z_α belonging to a bi-dimensional domain used to map the position, x_α, of the cross-section's points. Specifically, for the tapered and pre-twisted considered in this paper, we use the map $x_i = \Lambda_{ij} z_j$, with $\Lambda_{11} = 1$, $\Lambda_{22} = \Lambda_2(z_1)$, $\Lambda_{33} = \Lambda_3(z_1)$, while the others Λ_{ij} are zero. The current mapping function, R_A, is instead defined as follows

$$R_A(z_i, t) = R_{0A}(z_1, t) + x_\alpha(z_i) a_\alpha(z_1, t) + w_k(z_i, t) a_k(z_1, t) \tag{2}$$

where R_{0A} denotes the position of the centre-line's points in the current state, while w_k are the components of the warping displacement with respect to the current local triad a_k.

Note that throughout this paper, Greek indices range from 2 to 3, and Latin indices from 1 to 3, and repeated indices are summed over their range.

We now introduce vector and tensor fields used to describe the state of deformation of our beamlike body, starting with the vector fields k (related to the change in the beam's curvature between the current and reference states) and γ (related to the variation of the centre-line tangent vectors between the current and reference states), which are defined as

$$k = T^T k_A - k_B \tag{3}$$

$$\gamma = T^T R'_{0A} - R'_{0B} \tag{4}$$

where tensor field $T = a_i \otimes b_i$, $\otimes$ is the usual tensor (or dyadic) product, prime denotes the derivative with respect to s, and vectors k_A and k_B describe the beam's curvatures in the current and reference states, respectively (further details are, e.g., in [15]).

Vectors γ and k are referred to here as 1D strain measures, while the Green-Lagrange strain tensor E is referred to as 3D strain measure and is written in a form based on the assumptions of small strain and warping fields considered in this work. In particular, we assume that the reference cross-sectional dimension, *h*, is much smaller than the reference length, *L*, of the centre-line; the beam's curvatures are much smaller than *1/h*; the warping fields, w_k, are small in the sense that their maximum order of magnitude is *hε*, while the order of their derivative with respect to z_1 is at most *εh/L* (*ε* is a non-dimensional parameter much smaller than 1). In general, all strain components are considered small in the sense their order of magnitude is at most *ε*. The strain tensor E is then written (as in [13,15]) in the following form

$$E \simeq \frac{T^T H + H^T T}{2} - I \tag{5}$$

where H is the gradient of transformation between the reference and current states, that is, the derivative of the current map, R_A, with respect to the reference one, R_B.

The stress fields in our beam are now determined supposing it to be elastic, and expressing the second (symmetric) Piola-Kirchhoff stress tensor S in terms of E via the relation

$$S = \mathbb{C} E \tag{6}$$

where $\mathbb{C}$ is the classical elasticity tensor [3] characterizing the body's material behaviour, e.g. isotropic or not. For completeness, we also introduce the first Piola-Kirchhoff stress tensor P

G. Migliaccio

and Cauchy stress tensor C, which for our beamlike body are P=TS and C=TST$^{\text{T}}$ (as in [15]), plus cross-sectional stress resultants (force F and moment M) as follows

$$F = \int_{\Sigma} P_{i1} a_i$$
$$M = \int_{\Sigma} x_{\alpha} P_{i1}\, a_{\alpha} \wedge a_i$$

(7)

where Σ is the cross-sectional domain and $P_{ij} = P \cdot a_i \otimes b_j$.

We can now introduce the principle of expended power to derive balance equations for our beamlike body. To this end, its interactions with the external environment are quantified, for each velocity field attainable by the body, via the functional Π_e, called the external power

$$\Pi_e = \int_{\partial V} p \cdot v + \int_{V} b \cdot v$$

(8)

where b are body loads per unit body's reference volume V, p are surface actions per unit area of ∂V, and v is the time rate of the current positions of the body's points. Interactions among different parts of the body are instead quantified via the functional Π_i, the internal power

$$\Pi_i = \frac{d}{dt} \int_{V} \Phi$$

(9)

where Φ (body's energy density) is half the scalar product of tensors S and E, i.e. 2Φ=S·E.

Now, for any velocity field attainable by the body its interactions with the environment and among its parts have to be such that at any value of the evolution parameter *t* the total power vanishes (i.e. Π_e=Π_i). Such principle is commonly used in continuum mechanics to obtain balance equations in terms of the problem's unknowns (see, e.g., [3,7,15]). In our case, for instance, it enables writing balance equations for the stress resultants, F and M, in the form

$$F' + f = 0$$
$$M' + R'_{0A} \wedge F + m = 0$$

(10)

where f and m are the resultants of the body and contact actions per unit length of reference centre-line. The same principle also enables writing balance equations to determine the warping fields w_k. In particular, in the case the body loads and surface actions on the beam's lateral surface are neglected in calculating the warping fields, or vanish, it is possible to reduce the determination of such fields to those that meet the variational condition

$$\delta \int_{V} \Phi = 0$$

(11)

where δ denotes the variation of the energy function with respect to the warping fields. Note that warping fields satisfying (12) can be determined numerically or, in some cases, even analytically, as solutions of the corresponding Euler-Lagrange equations [16].

So far we have introduced the main ingredients of our modelling approach, by sketching the body's shape and defining the strain measures, stress measures, and balance equations we use to describe its behaviour. The resolution of our 3D nonlinear elasticity problem is now reduced to solving two problems: the first governs the cross-sectional warping motion and it's strong formulation can be given in terms of partial differential equations (PDEs) defined over a reference bi-dimensional domain (as in [13,15]); the second governs the centre-line motion and can be expressed in terms of a non-linear set of ordinary differential equations (ODEs) defined over a reference line (as, e.g., in [17-18]). The resulting model is computationally efficient and accurate with respect to nonlinear 3D-FEM approaches and, in addition, enables

analytical evaluations of the effects of important geometric features (e.g. taper and pre-twist) on the 3D stress and strain fields, as is discussed in the following.

3. ANALYTICAL RESULTS

Proceeding as in [15], we exploit the Euler-Lagrange equations that correspond to (12), keep terms up to order $\varepsilon h/L$, and write the PDEs problem the solution of which enables determining the components of E. In doing this, we choose the current local triads to be tangent to the centre-line and focus on tapered and pre-twisted beams the material properties of which are described in terms of two material constants only (the effects of material non-homogeneity, anisotropy, and centre-line curvature, are not considered here). The components E_{11}, E_{21}, E_{31} of E, related to the out-of-plane deformation of the cross-sections, are then given by

$$E_{11} = k_2 x_3 - k_3 x_2 + \gamma_1 + e_{1,1} + k_{B1}(x_3 e_{1,2} - x_2 e_{1,3})$$

$$2E_{21} = e_{1,2} - k_1 x_3 + e_2 + 2(1+\nu)(k_2 x_3 - k_3 x_2 + \gamma_1)(\Lambda_2^{-1}\Lambda_2' x_2 - k_{B1} x_3) \quad (12)$$

$$2E_{31} = e_{1,3} + k_1 x_2 + e_3 + 2(1+\nu)(k_2 x_3 - k_3 x_2 + \gamma_1)(\Lambda_3^{-1}\Lambda_3' x_3 + k_{B1} x_2)$$

In (13), $E_{ij} = E \cdot b_i \otimes b_j$, the subscript-comma denotes the derivative with respect to x_i, and the scalar fields e_1, e_2, e_3 are solutions of the PDEs problem below

$$e_{1,22} + e_{1,33} = 0 \quad in\ \Sigma$$

$$e_{2,2} + e_{3,3} = d_{k_3'} k_3' + d_{k_3} k_3 + d_{k_2'} k_2' + d_{k_2} k_2 \quad in\ \Sigma$$

$$e_{3,2} - e_{2,3} = g_{k_3'} k_3' + g_{k_3} k_3 + g_{k_2'} k_2' + g_{k_2} k_2 + g_{\gamma_1} \gamma_1 \quad in\ \Sigma \quad (13)$$

$$(e_{1,2} - k_1 x_3)n_2 + (e_{1,3} + k_1 x_2)n_3 = 0 \quad on\ \partial\Sigma$$

$$e_2 n_2 + e_3 n_3 = 0 \quad on\ \partial\Sigma$$

where Σ and $\partial\Sigma$ are the cross-sectional domain and its boundary, n_α are the components of the outward unit normal on $\partial\Sigma$, and coefficients "$d_{(\cdot)}$" and "$g_{(\cdot)}$" are given by

$$d_{k_3'} = 2(1+\nu)x_2$$

$$d_{k_3} = 2(1+\nu)\left(\Lambda_3^{-1}\Lambda_3' + 2\Lambda_2^{-1}\Lambda_2'\right)x_2$$

$$d_{k_2'} = -2(1+\nu)x_3$$

$$d_{k_2} = -2(1+\nu)\left(\Lambda_2^{-1}\Lambda_2' + 2\Lambda_3^{-1}\Lambda_3'\right)x_3$$

$$g_{\gamma_1} = 2k_{B1}(2+2\nu) \quad (14)$$

$$g_{k_3'} = -2\nu x_3$$

$$g_{k_3} = -2(1+\nu)\Lambda_3^{-1}\Lambda_3' x_3 - 2k_{B1}(3+2\nu)x_2$$

$$g_{k_2'} = -2\nu x_2$$

$$g_{k_2} = -2(1+\nu)\Lambda_2^{-1}\Lambda_2' x_2 + 2k_{B1}(3+2\nu)x_3$$

It is worth noting that PDEs problems as (14)-(15) can be solved in closed-form only for a few cases [19-20], but can always be solved numerically for all other cases as well. However, regarding our problem, it is apparent that its solution can be expressed as a linear combination of the 1D strains, γ_1 and k_i, their s-derivative, and application-oriented functions related to the

cross-sectional taper and pre-twist, Λ_α and k_{B1}. This result is very interesting as it allows us to consider even separately the effects of each 1D strain and geometric function on the 3D strain and stress fields, as is further discussed in the following.

Note that the approach used can also provide expressions for the strain fields E_{22}, E_{33}, E_{23}, related to the cross-sectional in-plane deformation. However, we do not provide details about this in the present paper, but focus on the determination of the scalar fields e_i and the study of the effects of the taper and pre-twist on the corresponding stress and strain fields.

3.5. Tapered beam with circular cross-sections

As anticipated in the foregoing, problem (14)-(15) admits closed-form analytical solutions in some cases. This holds, for example, for circularly cross-sectioned beams with taper functions $\Lambda_2 = \Lambda_3 = \Lambda$ and pre-twist coefficient $k_{B1} = 0$. In such case, in fact, our equations (14)-(15) are satisfied by $e_1 = 0$ and the expressions of e_2 and e_3 that follow

$$
\begin{aligned}
e_2 &= p_1 k_3' + p_2 k_2' + 2(1+\nu)\Lambda^{-1}\Lambda'\left[(x_2^2 - R^2)k_3 - x_2 x_3 k_2 \right] \\
e_3 &= q_1 k_2' + q_2 k_3' + 2(1+\nu)\Lambda^{-1}\Lambda'\left[(R^2 - x_3^2)k_2 + x_3 x_2 k_3 \right]
\end{aligned}
\tag{15}
$$

where R is the cross-sectional radius, and coefficients p_1, p_2, q_1, q_2, are given by

$$
\begin{aligned}
2p_1 &= (1-2\nu)x_3^2 + (3+2\nu)(x_2^2 - R^2) \\
p_2 &= -(1+2\nu)x_2 x_3 \\
2q_1 &= -(1-2\nu)x_2^2 - (3+2\nu)(x_3^2 - R^2) \\
q_2 &= (1+2\nu)x_3 x_2
\end{aligned}
\tag{16}
$$

Given the scalar fields e_i, we can also write closed-form expressions for the strain fields E_{11}, E_{21}, E_{31}, by combining equations (16)-(17) and (13). In this case, we get

$$
\begin{aligned}
E_{11} &= k_2 x_3 - k_3 x_2 + \gamma_1 \\
2E_{21} &= -k_1 x_3 + p_1 k_3' + p_2 k_2' + p_3 k_3 + p_4 \gamma_1 \\
2E_{31} &= +k_1 x_2 + q_1 k_2' + q_2 k_3' + q_3 k_2 + q_4 \gamma_1
\end{aligned}
\tag{17}
$$

where coefficients p_3, p_4, q_3, q_4, are given by

$$
\begin{aligned}
p_3 &= -2(1+\nu)\Lambda^{-1}\Lambda' R^2 \\
p_4 &= 2(1+\nu)\Lambda^{-1}\Lambda' x_2 \\
q_3 &= 2(1+\nu)\Lambda^{-1}\Lambda' R^2 \\
q_4 &= 2(1+\nu)\Lambda^{-1}\Lambda' x_3
\end{aligned}
\tag{18}
$$

As is apparent, the 3D strain fields obtained here, which explicitly depend on 1D strains, their s-derivative and geometric functions (e.g. Λ), reduce exactly to those of the linear theory of prismatic beams if Λ' vanishes and all displacements are small along with the strains (see e.g. [19-20]). Moreover, similar expressions can be obtained for other non-prismatic beams as well (as in [13,15]). However, what is most important is that the 3D strains can always be given in terms of linear combinations of 1D strains and their s-derivative, and the coefficients of such combinations can explicitly be expressed in terms of application-oriented functions

(e.g. taper and pre-twist functions) regardless of the solution procedure (i.e. analytical or numerical). In general, the difference between the result of this section (18) and that for a generic (tapered, pre-twisted) geometry is represented by the expressions of the coefficients of the aforementioned linear combinations (e.g. p_1-p_4), which are the functions of x_α to be found for each given geometry. Such functions, however, have to be computed only once for a given cross-sectional shape. This, in turn, helps to study analytically the effect of taper and pre-twist on the stress and strain fields and, at the same time, contributes to reduce the computational effort required to solve the problem, while producing accurate results compared to the results of nonlinear 3D-FEM approaches, as is shown in the following numerical examples.

4. NUMERICAL EXAMPLES

Hereafter we show some results obtainable by using our model, which we have implemented in a numerical code written in Matlab language and referred to here as 3D-BLM. The results of 3D-BLM in terms of displacement, strain and stress fields are also compared to those of nonlinear 3D-FEM analyses performed with the commercial software Ansys (based on a fine mesh of solid tetrahedral elements with ten nodes [21]).

The simulations regard a tapered beam like that treated analytically in section 3.1. In particular, the beam's centre-line is straight and 100m long; the radius of its root section is 2m and is scaled linearly up to the tip by 70%. The material properties are in terms of Young's modulus, 70GPa, and Poisson's ratio, 0.25. The beam is fixed at the root and loaded at the tip by a flapwise dead force, F, which is progressively increased as in Figure 2.

The simulation results are summarized hereafter. Specifically, Figure 2 shows the beam's un-deformed shape (F=0), its deformed shape for F=5000kN and F=10000kN from 3D-BML (left), and the deformed shape for F=5000kN given by nonlinear 3D-FEM (right).
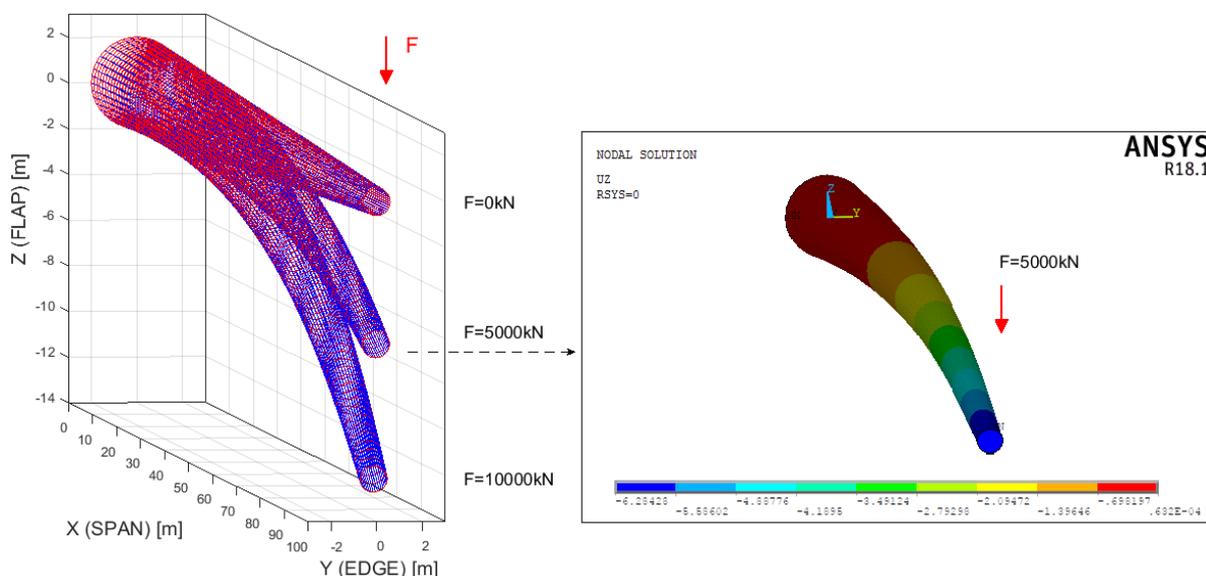
Figure 2. Beam's deflection using 3D-BLM for F increasing (left) and 3D-FEM (right) for F=5000kN

Figures 3 and 4, instead, provide comparisons between 3D-BLM and 3D-FEM in terms of centre-line's displacements and simulation times. As we can see, the simulation time required by 3D-BLM is much smaller than that required by the nonlinear 3D-FEM approach, while the accuracy of results obtained is almost the same.
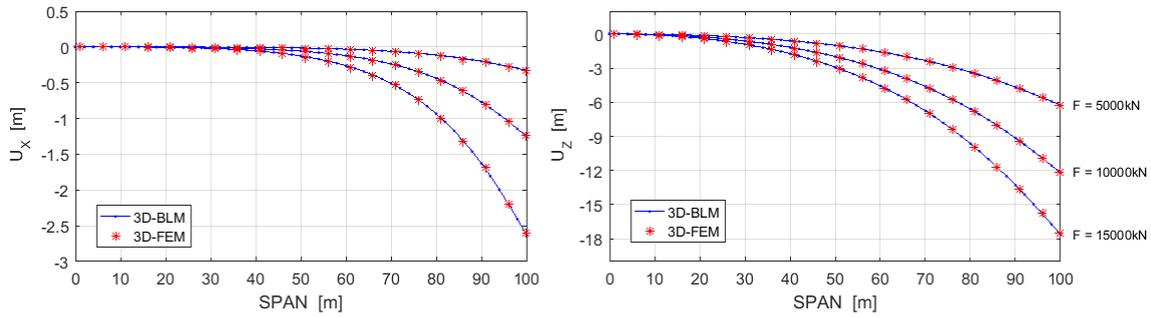
Figure 3. 3D-BLM versus 3D-FEM in terms of centre-line's displacements for F increasing
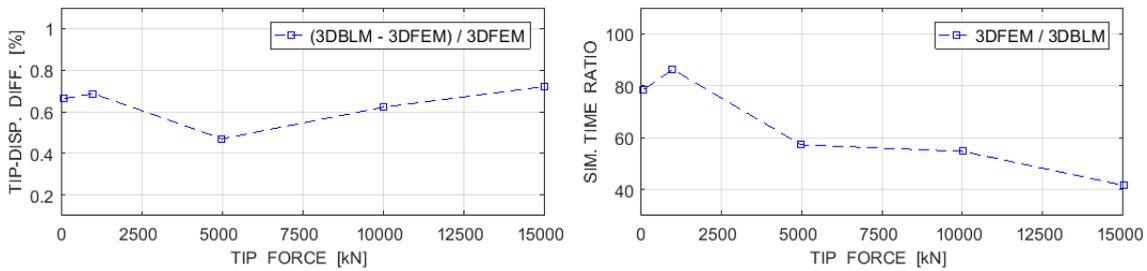
Figure 4. 3D-BLM versus 3D-FEM in terms of tip-displacements (left) and simulation times (right)

Moreover, 3D-BLM can furnish accurate results also in terms of other useful parameters related to the behaviour of our beam, e.g. local triad rotations, beam's curvature, 3D strains, and 3D stress fields as well. Figures 5-8, for instance, report comparisons between 3D-BLM and 3D-FEM in terms of Cauchy stresses for the present example: specifically, Figures 5 and 6 show the stress fields C_{XX} and C_{ZX} obtained for F=100kN at three reference cross-sections (30%, 50%, 70% span); Figures 7 and 8 report similar results for F=10000kN.
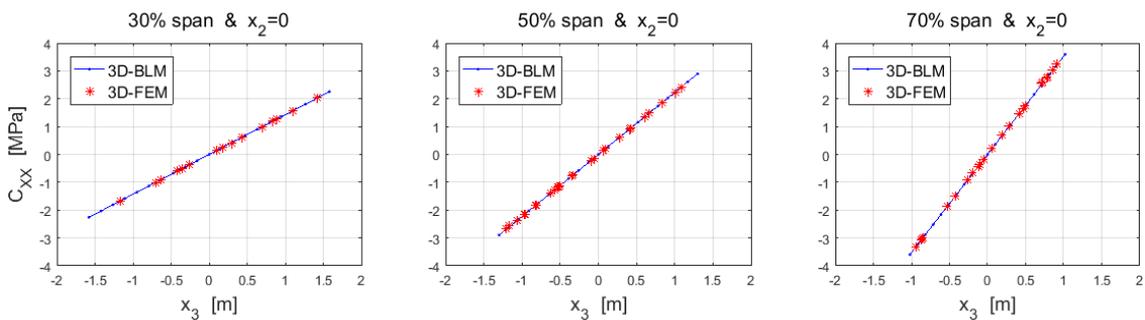
Figure 5. Stress field C_{XX} at different cross-sections (30%,50%,70%) for F=100kN
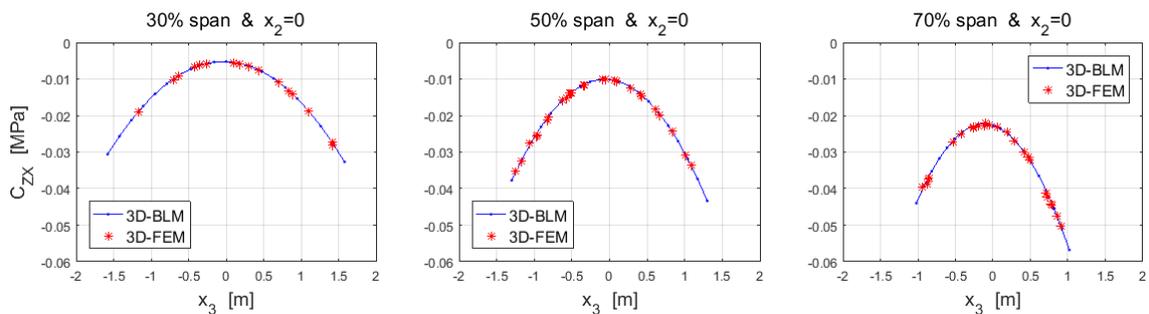
Figure 6. Stress field C_{ZX} at different cross-sections (30%,50%,70%) for F=100kN

G. Migliaccio
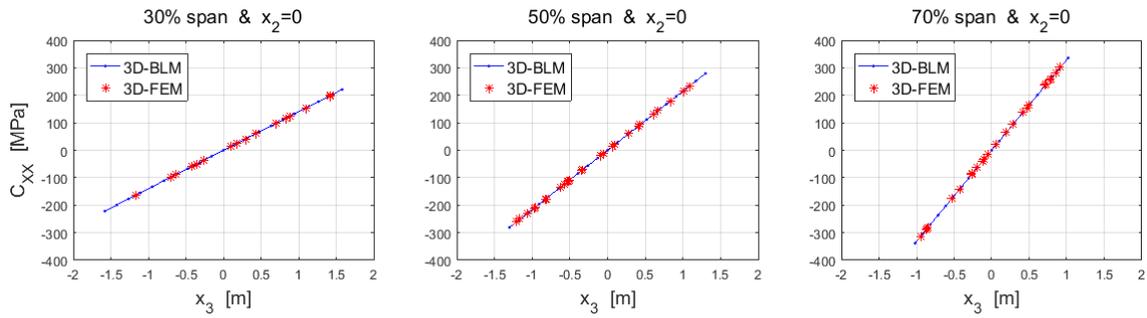
Figure 7. Stress field C_{XX} at different cross-sections (30%,50%,70%) for F=10000kN
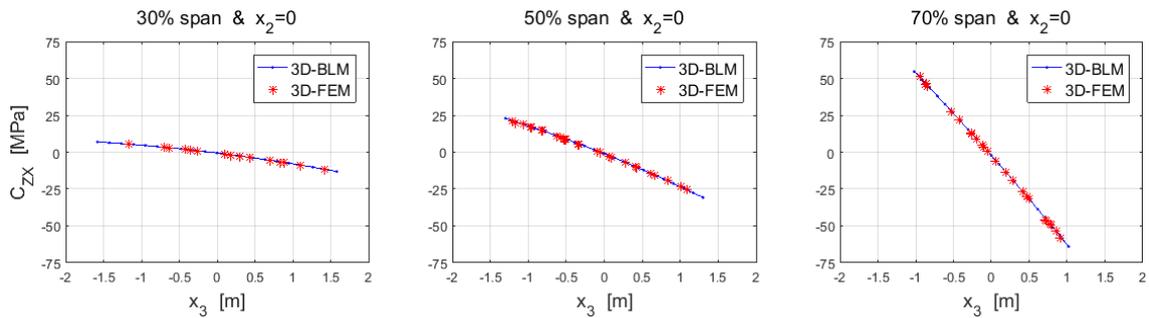
Figure 8. Stress field C_{ZX} at different cross-sections (30%,50%,70%) for F=10000kN

Taking a look at the results obtained, we note that the normal stresses follow a Navier-like distribution in each cross-section, while the shear stress distributions are quite different from those predictable by the linear theory of prismatic beams, as they do not do not vanish at the cross-section's boundary and change spanwise. Apart from qualitative remarks, the numerical results also confirm the effectiveness of our approach in terms of efficiency and accuracy with respect to nonlinear 3D-FEM. Other examples can also be found in [15,17,18].

5. CONCLUSIONS

Engineering methods and formulas used to evaluate the stress and strain fields in prismatic beams provide incorrect results in tapered, pre-twisted elements. However, the design of such elements, undergoing large displacements and small strains, can be addressed via a modelling approach that is efficient and accurate (with respect to nonlinear 3D-FEM) and, at the same time, enables evaluating analytically the effects of important geometric design parameters (e.g. taper and pre-twist) on the stress and strain fields. This work has illustrated such modelling approach, discussing how it can provide the 3D stress and strain fields in terms of linear combinations of 1D strain measures and geometric design parameters.

Analytical and numerical examples, including comparisons with nonlinear 3D-FEM, have also been presented to show how the model can be used and which results it can provide in practice. Apart from all theoretical outcomes of the model, it also appears to be very useful for the design and optimization of non-prismatic beams used in engineering: in fact, on the one hand, the formulas it enables obtaining can help an engineer since the preliminary design tasks; on the other hand, the numerical code implementing the model can be very suitable for multi-objective optimization tasks thanks to its computational efficiency and accuracy.

The results presented have addressed the cross-sectional out-of-plane deformations and the corresponding PDEs. Investigations about the in-plane deformations would also be important, along with studies about the effects of other geometric features (e.g. centre-line curvature) and material properties (e.g. non-homogeneity), and will be addressed in subsequent works.

REFERENCES

[1] Love A.E.H., *A treatise on the mathematical theory of elasticity*, 4th ed., Dover Publications, NY, 1944.

[2] Goodier G.N., and Griffin D.S., Elastic bending of pretwisted bars, *Int. J. Solids Structures*, 5, 1231-1245, 1969.

[3] Gurtin M.E., *An introduction to continuum mechanics*, Mathematics in Science and Engineering, 1st ed., Academic Press, 1981.

[4] Berdichevsky V.L., On the energy of an elastic rod, *J. Appl. Mathematics and Mechanics*, 45, 518-529, 1981.

[5] Rosen A., Theoretical and experimental investigation of the nonlinear torsion and extension of initially twisted bars, *J. Applied Mechanics*, 50, 321-326, 1983.

[6] Simo J.C., A finite strain beam formulation, the three-dimensional dynamic problem, part I, *Computer methods in applied mechanics and engineering*, 49, 55-70, 1985.

[7] Ruta G., Pignataro M., and Rizzi N., A direct one-dimensional beam model for the flexural-torsional buckling of thin-walled beams, *J. Mechanics of Materials and Structures*, 1, 1479-1496, 2006.

[8] Yu W., Hodges D.H., and Ho J.C., Variational asymptotic beam-sectional analysis - an updated version, *Int. J. Engineering Science*, 59, 40-64, 2012.

[9] Rosen A., Structural and dynamic behavior of pretwisted rods and beams, *American Society of Mechanical Engineers*, 44, 483-515, 1991.

[10] Kunz D.L., Survey and comparison of engineering beam theories for helicopter rotor blades, *J. of Aircraft*, 31, 473-479, 1994.

[11] Rafiee M., Nitzsche F., and Labrosse M., Dynamics, vibration and control of rotating composite beams and blades: a critical review, *Thin-walled structures*, 119, 795-819, 2017.

[12] Balduzzi G., Hochreiner G., and Füssl J., Stress recovery from one dimensional models for tapered bi-symmetric thin-walled I beams: deficiencies in modern engineering tools and procedures, *Thin-Walled Structures*, 119, 934-945, 2017.

[13] Migliaccio G., and Ruta G., The influence of an initial twisting on tapered beams undergoing large displacements, *Meccanica*, 1-15, https://doi.org/10.1007/s11012-021-01334-2, 2021.

[14] Mercuri V., Balduzzi G., et al., Structural analysis of non-prismatic beams: Critical issues, accurate stress recovery, and analytical definition of the finite element (FE) stiffness matrix, *Engineering Structures*, 213, 110252, 2020.

[15] Migliaccio G., Non-prismatic beamlike structures with 3D cross-sectional warping, *in the proc. of 14th World Congress in Computational Mechanics (WCCM) & ECCOMAS congress 2020*, Paris, France, 11-15 Jan. 2021.

[16] Courant R., and Hilbert D., *Methods of mathematical physics*, 1st ed., Interscience Publisher, 1953.

[17] Migliaccio G., Ruta G., et al., Beamlike models for the analyses of curved, twisted and tapered horizontal-axis wind turbine (HAWT) blades undergoing large displacements, *Wind Energy Science*, 5, 685-698, https://doi.org/10.5194/wes-5-685-2020, 2020.

[18] Migliaccio G., and Ruta G., Rotor blades as curved, twisted, and tapered beam-like structures subjected to large deflections, *Engineering Structures*, 222, 111089, 2020.

[19] Sokolnikoff I.S., *Mathematical theory of elasticity*, 1st ed., McGraw-Hill Inc., 1946.

[20] Timoshenko S.P., and Goodier J.N., *Theory of elasticity*, 2nd ed., McGraw-Hill, 1951.

[21] Madenci E., and Guven I., *The finite element method and applications in engineering using Ansys*, 2nd ed., Springer, 2015.

MULTIFIDELITY AEROELASTIC OPTIMIZATION APPLIED TO HAR WINGS

Yoann Le Lamer[1,2*], Giovanni Quaglia[1], Emmanuel Benard[1] and Joseph Morlier[2]

1: ISAE-Supaero
10 Avenue Edourd Belin, 31400 Toulouse, France
{yoann.le-lamer@isae-supaero.fr, giovanni.quaglia,
emmanuel.benard@isae-supaero.fr}@isae-supaero.fr

2: ICA, Université de Toulouse, ISAE-SUPAERO, MINES ALBI, UPS, INSA, CNRS,
Toulouse, France
joseph.morlier@isae-supaero.fr

Abstract. *As part of a global effort toward the reduction of CO2 emissions, the study of High Aspect Ratio wings is a particularly promising avenue of research. Considering this type of configuration at preliminary design stage is thus critical for optimization purposes. The use of multifidelity can help reduce computational costs by mainly running low-fidelity computations and only resorting to high-fidelity computations when necessary. The goal of this study is to develop a sufficiently accurate aero-structural model in order to fully exploit the drag reduction potential of HAR wings. The first step is to develop and apply a multifidelity approach on the CRM wing by creating a low-fidelity model. It is made sure that there is an adequate correlation between the structural modes of both high-fidelity and low-fidelity models. The so obtained low-fidelity structural model is then implemented within a in-house aeroelastic analysis and optimization framework. Afterwards, a modified version of the CRM wing with a higher aspect ratio (AR=13.5) is considered in order to apply the same methodology with the goal to reduce significantly computational costs.*

Keywords: Multifidelity, High Aspect Ratio wings, Aeroelasticity, Multidisciplinary Design Optimization

Yoann Le Lamer, Giovanni Quaglia, Emmanuel Benard, and Joseph Morlier

1   INTRODUCTION

Increasing the aspect ratio of wings is one promising way to reduce CO2 emissions by limiting induced drag. In order to benefit from the full potential of these aircraft configurations, it is necessary to resort to aerostructural optimization [1]. In particular, considering computational costs is critical to achieve this goal. Indeed, in the last century, complex mathematical models have been developed in order to simulate real systems in many areas of scientific research, but the main obstacle to an intensive exploitation of such models (visualization and analysis) is the computational cost which can easily become prohibitive even for simple cases [2]. This problem is crucial in the field of aerostructural design and optimization since many simulations are required and one single CFD run may require hours of CPU time. The challenge has been tackled by creating surrogate models, sometimes also referred to as meta-models, which are an approximation of the actual system based on a number of collected samples [3]. In recent years, multifidelity (MF) has been proposed as a valuable strategy to reduce computational time. With such an approach, the results employed to train and enrich surrogate models derive from sources of different precision and are balanced in order to reduce the overall cost. These sources can be seen as black-box functions [4] and are connected to each other in an optimization environment.

In the last decade, ONERA, in a joint effort with the university ISAE-Supaero, has developed the SEGOMOE (Super Efficient Global Optimization with Mixture Of Experts) framework [5]. It is a single-fidelity, surrogate-model based, Bayesian optimization tool, able to deal with high-dimensional problems with a large number of constraints. As a further progress, [6] exploited this technique as a benchmark to demonstrate the improvements offered by the use of a multifidelity approach in terms of computational time. In this research project, a subsonic airfoil with 15 variables has been designed using MFEGO (MultiFidelity Efficient Global Optimization). This work only considers unconstrained multifidelity optimization for now. Finally, [7] produced an aeroelastic black-box function, the aerostructure package [8], also used in [9], implemented in the OpenMDAO framework [10], which optimizes the NASA CRM (Common Research Model) wing using computationally cheap aerodynamic and structural solvers.

On the one hand, regarding aerodynamics, two levels of accuracy are currently represented by a CFD and a panels code. On the other hand, the subject of this article is the development of a low-fidelity version of the structural model. It features a reduced mesh resolution, a shorter analysis time but keeps a substantial correlation with respect to the original high-fidelity model. In particular, a *MATLAB* tool has been initially designed in order to produce a FEM mesh with a level of complexity fixed by the user. Later the model properties have been assessed through different tests.

In section 2, the different theoretical arguments are discussed, along with their mathematical formulation, to support the general framework. Section 3 presents the simplifications made on the original CRM model and how the low-fidelity structural model is created. In section 4, static and dynamic behaviours are validated and the model is tested on a simple unconstrained multifidelity optimization. Then, in section 5 an aeroelastic model for the HAR uCRM-13.5 wing is presented and first aeroelastic analysis results are provided. Lastly, section 6 reports the conclusions and lists the future objectives.

Yoann Le Lamer, Giovanni Quaglia, Emmanuel Benard, and Joseph Morlier

2 THEORETICAL FRAMEWORK

2.1 The aerostructural problem

During the design phase of an aircraft the focus is the enhancement of multiple objective functions, namely the QoI (Quantities of Interest), such as drag or fuel consumption under mass and maximum stress constraints. In the case of steady cruise flight, the QoI are computed as result of a static aeroelastic problem. In literature, two approaches to solve it can be found, the monolithic and the partitioned. The latter is the most applied nowadays and it consists in the coupling of two different solvers for the structural and fluid problems, such as a FEM and a CFD software. The theory is reported with the notation used in [11].

$$\mathbf{y} = \mathcal{F}(\mathbf{x}), \quad \mathbf{x} = S(\mathbf{y}) \tag{1}$$

Here, $\mathbf{x}$ and $\mathbf{y}$ are the vectors containing the structural and aerodynamic variables, namely the nodes displacements and the fluid pressure along the airfoil. S and $\mathcal{F}$ are the structural and fluid problems. The coupling can be expressed as:

$$\mathbf{x}^* = \arg \min_{\mathbf{x} \in \mathrm{IR}^{N^s}} \| \mathcal{R}(\mathbf{x}) \| \tag{2}$$

$$with \quad \mathcal{R}(\mathbf{x}) = S \circ \mathcal{F}(\mathbf{x}) - \mathbf{x} \tag{3}$$

Once the two software required by the disciplines are chosen, they are wrapped in a framework able to process the outputs in order to be provided as inputs one to the other. Given a set of design variable, the solver iterates until a predefined convergence criterion is reached, and finally the QoI and the constraints values are extracted. Hence, the ensemble can be seen as a black-box function as shown in figure 1.
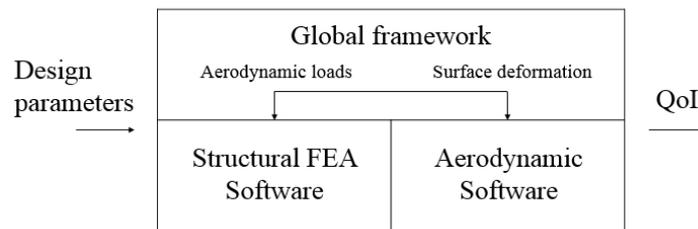
Figure 1: Black-box aeroelastic function diagram.

2.2 Multifidelity

The concept of multifidelity has already been introduced in the previous sections. When it is not possible to have more than few high-fidelity samples, the use of a cheaper solver allows to explore the variable design space. The large number of LF simulations permits to enrich the surrogate model and to address the optimum search. Moreover, the space of possible sources is huge. Samples used to train the model could come from experiments, software of different levels of modelling, such as CFD or panels codes in aerodynamics, a coarse and a fine mesh on the same problem or even a change in the convergence criteria

Yoann Le Lamer, Giovanni Quaglia, Emmanuel Benard, and Joseph Morlier

for an iterative algorithm [11]. Multifidelity is efficient if the accuracy of the optimum found is maintained while saving computational time performing less HF simulations. The main property required is the correlation between the results. The LF model must evolve in accordance with the HF one to correctly predict the behaviour of the objective function. Furthermore, the cheap code should be one or more orders of magnitude faster, allowing consistent scaling and time saving.

The theoretical background regarding MF methods is still ambiguous. While the results in terms of computational time are generally positive, it has been proven that the use of LF data can worsen the surrogate precision [12]. [13] delve into over 100 papers which make use of a MF approach. The research compared the studies in terms of levels of fidelity, disciplines, types of solvers, and data of correlation and time savings when made available. The conclusion is the absence of a clear pattern, able to determine whether or not it is convenient an MF implementation, and the lack of research in this direction.

3 DESIGN AND ANALYSIS OF A LOW FIDELITY STRUCTURAL MODEL

3.1 General framework

The focus in the current research is optimizing the NASA CRM wing in the SEGO framework enhanced by the use of multifidelity. First of all, the programming language of the SEGO optimization algorithm is python and, in this sense, the adoption of the OpenMDAO library results extremely useful. OpenMDAO is an open-source computing platform for multidisciplinary analysis and optimization. Its structure makes it well suited for wrapping the two disciplines solvers, creating an aeroelastic black-box function. In general OpenMDAO codes are written connecting components, which can be explicit or implicit, each of them representing a part of the problem. Every component has inputs and outputs which must all be connected in the main function. Once run, the solver iterates until also the implicit parts reach convergence.

One key part of this next step in the research is the OpenMDAO package *aerostructures* [7]. The framework is used for solving static and dynamic aeroelastic analysis and optimizations. The XDSM diagram 2 presents its functioning. Each block represents a component, one can find the two main disciplines which run at their interior Panair [14], an open-source aerodynamic panels code and Nastran95 [15], used for solving the structural problem. All the other boxes have linking scopes being the interpolation and the transfer of loads and displacements between the fluid and structural mesh.

Taking advantage of this package, setting up the new optimization framework has been straightforward. The MF-EGO/MF-SEGO environment can easily encapsulate *aerostructures* and creates two versions of the main function. The first type is directly the same as before, while in the other case Panair has been substituted by a component calling the execution of the CFD software ADFlow. In this way two levels of fidelity are available.

While this first version is currently being tested, one more step was needed to improve the multifidelity approach. In fact, both functions had as an input the original CRM FEM model, which is given with a high resolution mesh, weakening the possible advantages of MF. Finally, the scope of this work has been twofold. Firstly, the accuracy of the structural model has been reduced to allow faster simulations, secondly, the preserved correlation with the initial system has been analyzed. Figure 3 illustrates how the framework should resemble once this tasks have been achieved.

Yoann Le Lamer, Giovanni Quaglia, Emmanuel Benard, and Joseph Morlier
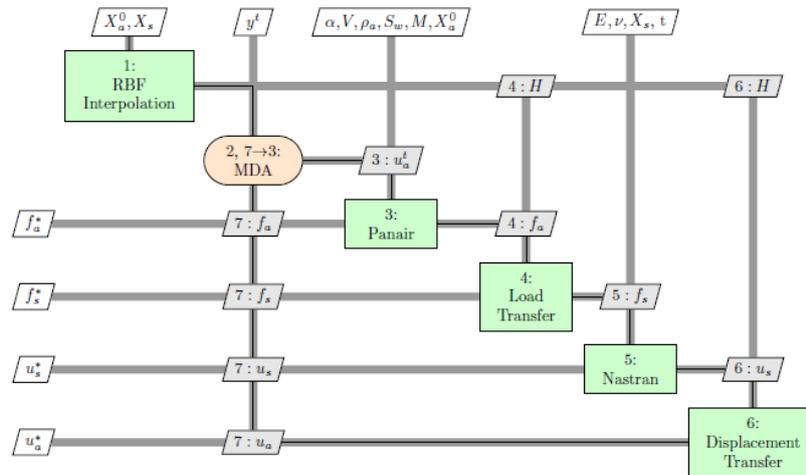
Figure 2: XDSM diagram of the static aeroelastic OpenMDAO LF solver [7].
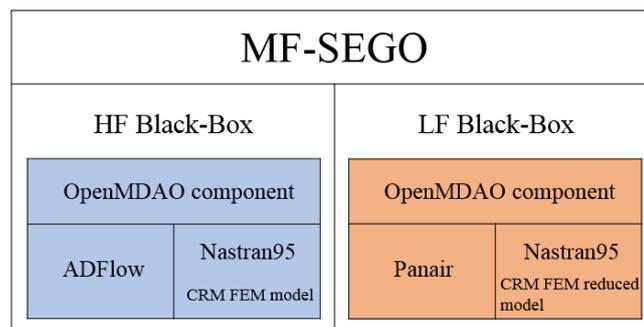
Figure 3: Diagram representing the current research framework.

3.2 The NASA CRM model

The Common Research Model is an attempt made by NASA to provide an experimental database for the validation of application of Computational Fluid Dynamics [16]. The related website is a repository of results from numerical and experimental analysis. In particular, some versions of different FEM models for the aircraft wing are released in Nastran language, one is drawn in figure 4. The one considered here has the following characteristics. The material is an aluminum alloy with $\rho = 2795.67$ and E $= 68.9$ GPa. The model consists of over 10500 nodes connected in 26600 elements. The structure is modelled as wing boxes delimited by 58 ribs closed by the upper and lower skins and with two spars at the leading and trailing edge. All this parts are explicitly represented by CQUAD4 elements depending on 12 PSHELL cards of different thickness. Moreover, ribs and skins are reinforced by stringers created with the CBAR class and with 6 different sections and principals of inertia.

3.3 Design phase

The first task of the project consisted in coding a routine able to receive as input the nastran *.bdf* file related to the original model and producing as outputs the reduced list of nodes and the new mesh description. As an additional objective it was planned to

Yoann Le Lamer, Giovanni Quaglia, Emmanuel Benard, and Joseph Morlier
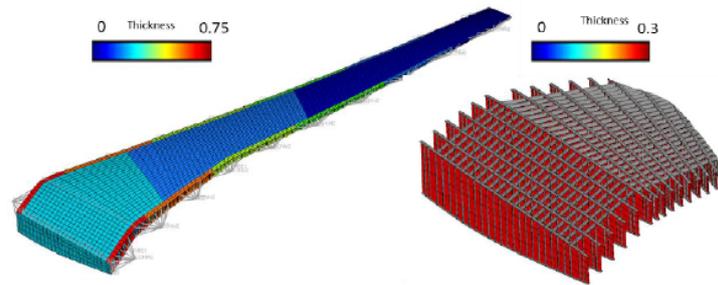
Figure 4: Illustration of the NASA CRM wing FEM model [16]

parametrise the code in order to allow choosing the desired complexity of the model. The environment used for coding the tool has been MATLAB. An early difficulty has been faced when dealing with the NASA input file. The list containing the nodes was given with no apparent order in the IDs so that it was impossible to find a mathematical law able to define their succession. As a consequence the problem as been split in writing two separate functions to order the nodes and to write the new mesh.

MainCreatePlanes.m is the first routine. One initial assumption has been made neglecting the intermediate nodes between two ribs with the outcome of having the elements representing skins and spars as long as each section. The removal of the additional rows of nodes in the cord direction diminishes the overall model flexibility with respect to the rotation around the body axis. As a result of such hypothesis the function operates with the following procedure. First, it reads a sub-list of the stringers elements inside the ribs and takes the two extreme points defining the first one. After that, it searches for a third node as the closest among the remaining and computes the 4 geometrical parameters of a plane passing through them. Finally, the node list is scanned, selecting and removing the entries whose distance from the plane is less than a fixed tolerance. The picked nodes are saved in a structure referring to a particular rib, and the process is iterated on the reduced file. As a final step, the 58 sections are sorted root to tip and the nodes belonging to each of them are locally enumerated. The result is presented in figure 5 where the initial chaotic cloud of points has been ordered.
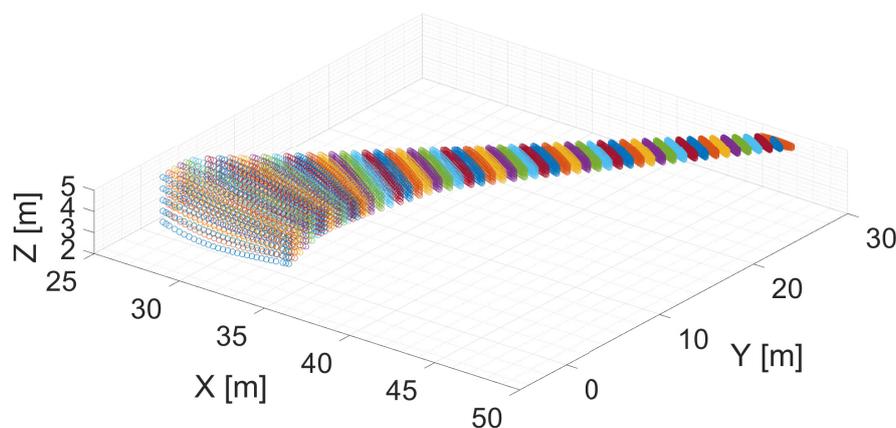
Figure 5: Matlab representation of the ordered nodes colored by rib section.

The second routine MainCreateMesh.m loads the structure containing the sorted nodes

Yoann Le Lamer, Giovanni Quaglia, Emmanuel Benard, and Joseph Morlier

and writes a new coarser model. At the beginning of the function two main parameters, L and V, are defined, as they set the number of points in the reduced mesh on the vertical and cord directions. One first sub-routine creates the list with the new nodes of the model. In order to accomplish this goal for each section the coordinates are transformed in a temporary reference frame so that the first two axes are in the rib plane and the third one is orthogonal to them. Then a spline interpolation is created for each row of nodes in the section, and it is evaluated in the number of points requested by L and V. The 57th rib has less nodes than the others and it is joint with the last one. Since the precise location of the intersection cannot be respected considering a coarser mesh, the function shifts all the points in the rib in order to place it as close as possible to the original.

Once created, the list with the new set of nodes is taken as database by a second sub-routine which has the scope of redefining all the elements as in the starting model. The last hypothesis regards the definition of the spars. In the original CRM model they are modelled explicitly by CQUAD4 elements in a I-beam. In the spirit of reducing the complexity of the system, the flanges were substituted with simple CROD elements as they are loaded only axially in first approximation. All the elements preserve the original properties, and in particular the V vectors are reassigned to the CBAR entries looking for the closest and identically oriented stringer.

One realization of the LF structural model is presented in figure 6 for the choices of L = 4 and V = 3.
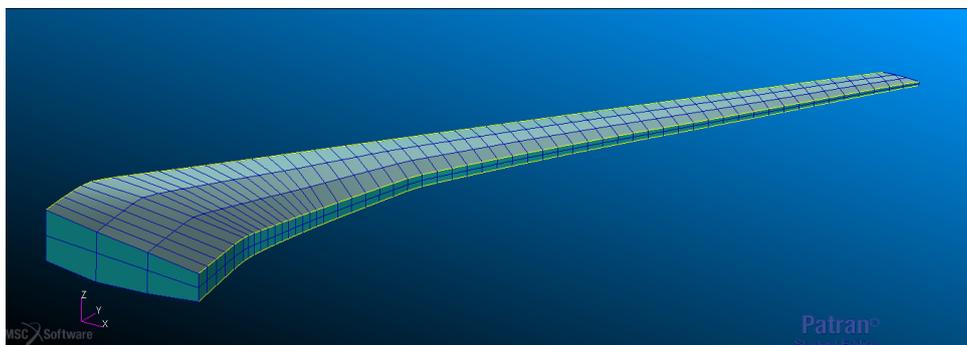
Figure 6: Low Fidelity structural model visualized in Patran for the choices of L = 4 and V = 3.

The last task during the design phase consisted in adapting the python *aerostructures* package to receive the same model with different mesh definitions. In fact the structure created by the MATLAB tool would have a decreased stiffness, due to the lower number of stringers, if the geometrical and inertial properties are kept as in the HF model. The problem was overcome providing to the main function the parameters L and V, the summation on all the stringer areas and principals of inertia as well as the size of the spar flanges. A new component is then added to the OpenMDAO group and it reassigns the properties according to the actual number of bars.

4 MODEL VALIDATION

4.1 Static analysis

In a preliminary phase of the validation process, all the simulations performed were static aeroelastic problems representing the aircraft in cruise condition. After computing the

Yoann Le Lamer, Giovanni Quaglia, Emmanuel Benard, and Joseph Morlier

converged solution in the OpenMDAO framework, Gmsh has been used to visualize the deformation of the wing subject to the aerodynamic loads along with the Von Mises stress distribution. As an example, figure 7 compares the solution of the original model with the one obtained with the L = 4 low fidelity structure. The standard geometrical values for wing surface, wing span and sweep angle were taken from the original NASA model [16], while the case parameters are reported in table 1. The QoI selected to be compared in the analysis have been the lift coefficient (Cl) and the induced drag (CDi) computed by Panair, and the tip vertical displacement (δ_{tip}) and the maximum Von Mises stress (VM$_{max}$) that come from the postprocessing of the Nastran95 output file.
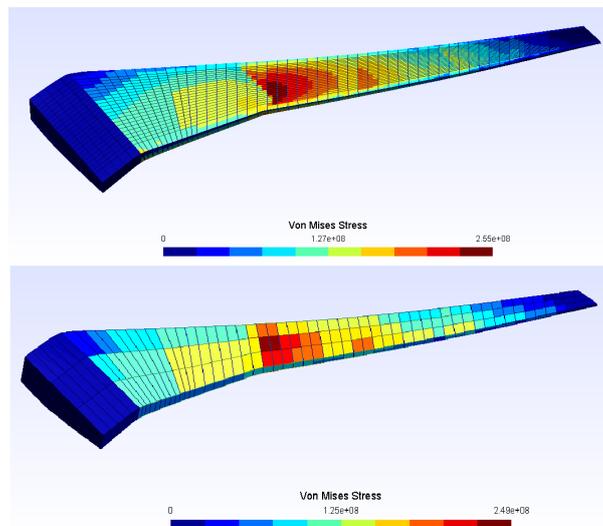
Figure 7: Gmsh visualizations of the converged solutions of the CRM wing for the HF case (up) and the L = 4 LF case (down).

Table 1: Aircraft cruise input parameters.

Name	Value
Flight speed	252.16168 [m/s]
Mach number	0.85
Air density	0.380580 [kg/m^3]
Wing incidence angle	1.34 [deg]

4.1.1 Mesh resolution influence

As a first step, the influence of the mesh resolution has been studied. The MATLAB tool designed was used to produce different FEM models for the parameter L varying in the interval [4-28]. The lower bound allows to have at least 2 stringers running along the wing span, while the upper bound reaches the same value of nodes in the cord direction as for the original model.

The computational cost is the major interest of MF, to this purpose, two timers, measuring the setup and run times of the OpenMDAO routine, were added to the main function . Figure 8 shows the results normalized by the values obtained running the full model. The

Yoann Le Lamer, Giovanni Quaglia, Emmanuel Benard, and Joseph Morlier

run time includes all the executions of Nastran95, hence it presents the greatest reduction. As expected, the line grows with a power trend due to the increasing number of elements for each node added. The key outcome is the ratio between the reference and the fastest simulation time (4), computed with L = 4. This is the maximum gain obtained and it can be called Fidelity Cost Ratio (FCR) and employed as an indicator, for example in the criterion for the next point fidelity.
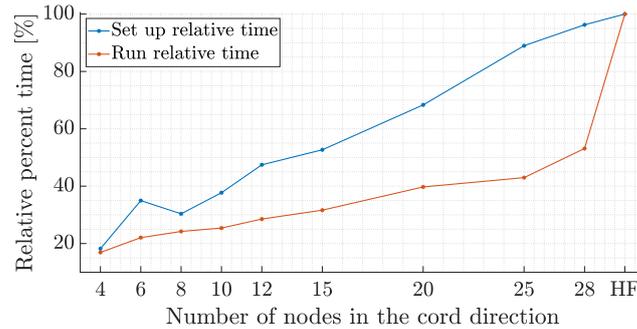
Figure 8: Setup and execution normalized timers as a function of the L parameter.

$$FCR = \frac{T_{run}^{L4}}{T_{run}^{HF}} = 16.9\% \tag{4}$$

Figure 9 shows the computed values of Cl depending on the L parameter along with the reference produced by the original model. The LF results have a general convergent trend, as the structure representation becomes more and more refined with the mesh, proving the coherent design of the model. The offset between the final values at L = 28 and the HF solution is the trade-off of a MF approach. It is caused by the simplifications assumed during the design phase, namely the removal of the rib intermediate nodes, the redefinition of spars and the shifting of the next to last rib.
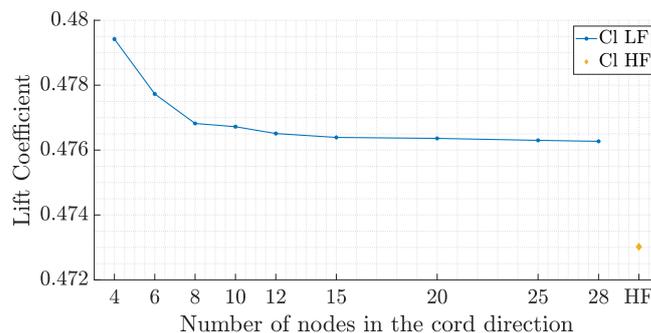
Figure 9: Lift coefficient as a function of the L parameter with reference HF value.

4.1.2 Multifidelity correlation analysis

Once the MATLAB tool has been validated and the FCR computed, it was possible to focus on the correlation analysis between the LF model with L = 4 and the HF original one. It is hopeful that the LF maintains the same offset found in the previous section even for other design variables inputs. For this reason maximum and minimum relative

variances must be always checked during the design space exploration. Moreover, the most important indicator is the correlation between the two fidelity, since it states if the LF can provide true information on the HF behaviour. This property has been tested in two cases, one with a random approach and one with predefined parameter steps.

In a first experiment the influence of a physical property of the structure has been analyzed. The vector containing the thickness of the 12 different PSHELL cards has been randomly modified changing its components independently inside the $\pm 40\%$ range. 10 different realizations of the properties have been considered, the 10th being the original one. The two fidelity have been tested on each configuration. The first outcome has been the representation of the four QoI values as a function of the scalar product between the modified and original thickness vectors normalized by themselves. This index is equal to 1 when the parameters are unchanged and it decreases expressing an overall distance in the variable design space. Figure 10 presents the two fidelity results for δ_{tip} and as well as the other graphs, it shows a perfect accordance in the results.
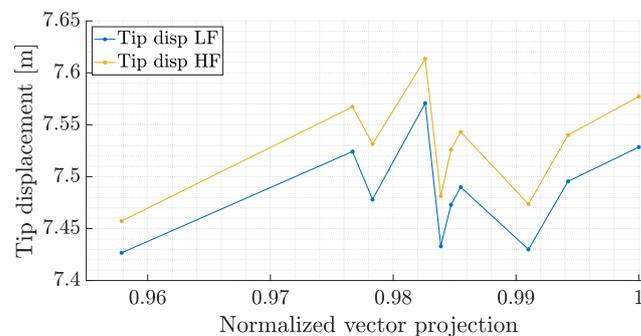
Figure 10: Tip vertical displacement as a function of the normalized projection of the shell elements thickness vectors onto the standard CRM property.

Moreover, the computation of the actual Pearson's correlation coefficient (PCC) between the HF and LF QoI validates the trend. Table 2 reports its values along with the relative percent variances with respect to the HF results.

Table 2: Comparative indices between HF and LF for different QoI, panels thickness case.

Indices:	Cl	CDi	δ_{tip}	$\mathbf{VM}_{max}$
PCC	0.9995	0.9987	0.9903	0.9849
Δ_{max}	1.365%	1.693%	0.704%	3.477%
Δ_{min}	1.126%	0.790%	0.404%	0.219%

The second experiment has focused on the effect of two geometrical properties, the wing span (b) and the sweep angle (φ). Their standard values were b = 58.7629 [m] and φ = 37.16, they were updated two times in both direction by a $\Delta b = 5$ [m] and $\Delta\varphi = 2.5$ step, resulting in 25 configuration cases. The main function was modified by the use of the *aerostructures* components able to deform the mesh according to a variation in those parameters. Figure 11 shows three realizations of the wing in the software Gmsh, the original and the two extreme cases.

In this second test the QoI has been represented on the Z axis of a 3D graph with the design variables on the XY plane. Figure 12 shows the surfaces for the VM_{max} quantity.

Yoann Le Lamer, Giovanni Quaglia, Emmanuel Benard, and Joseph Morlier
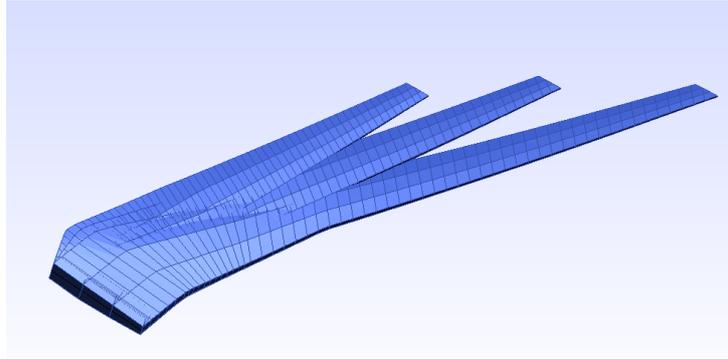
Figure 11: Gmsh visualization of the standard wing and of the two extreme configurations tested.

Once more the LF is able to correctly predict the behaviour of the HF. All the figures present a partial crossing of the surfaces for high values of the b parameter. Such long-span configuration could present some nonlinearity badly predicted by the aeroelastic function and should be object of further analysis. Finally the comparative indices, obtained from the matrices containing the QoI values, are reported in table 3.
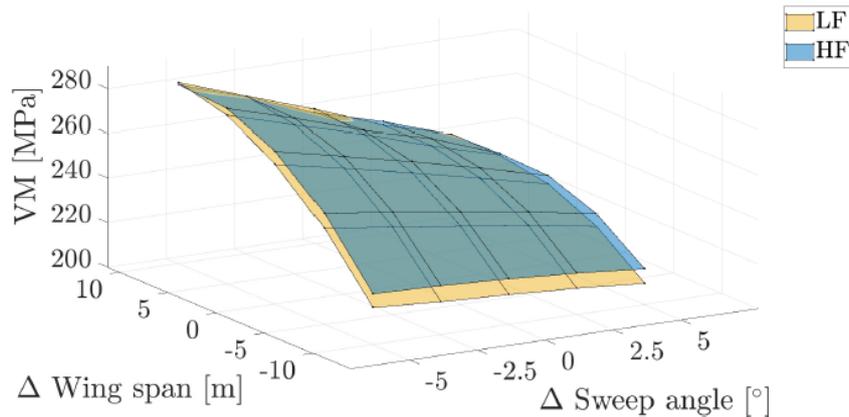
Figure 12: Maximum Von Mises stress as a function of the wing span and the sweep angle.

Table 3: Comparative indices between HF and LF for different QoI, 2 variables case.

Indices	**Cl**	**CDi**	δ_{tip}	**VM**$_{max}$
PCC	0.9998	0.9982	0.9997	0.9945
Δ_{max}	1.694%	1.547%	0.884%	2.841%
Δ_{min}	0.354%	0.119%	0.015%	0.118%

4.2 Dynamic analysis

The second phase of the validation has concerned the dynamic behaviour of the LF model. The objective has been the assessment of the correlation between the frequency response of the simplified structure and the original one. Nastran95 provides a solution for normal mode extraction even if it does not offer the same advanced options as in commercial releases. For example the standard Lanczos method is not available and thus a basic inverse

Yoann Le Lamer, Giovanni Quaglia, Emmanuel Benard, and Joseph Morlier

algorithm has been chosen for all the simulations. One common performance indicator for a dynamic comparison is the Modal Assurance Criterion (MAC) [17]. The Modal Assurance Criterion is a statistical indicator that is most sensitive to large differences and relatively insensitive to small differences in the mode shapes. When comparing two sets of eigenvectors in the same space, MAC indices are usually stacked in a matrix where a maximum value of 1 states full correlation, 0 being no correlation. Thus, the MAC matrix is calculated as the normalized scalar products of the two sets of vectors Φ_{HF} and Φ_{LF} as in (5).

$$MAC(i,j) = \frac{\left\|\Phi_{HF_i}^T \Phi_{LF_j}\right\|^2}{(\Phi_{HF_i}^T \Phi_{HF_i})(\Phi_{LF_j}^T \Phi_{LF_j})} \qquad (5)$$

Mode shapes must belong to the same space, therefore the HF ones are projected, through an interpolation, onto the LF subspace. Moreover, a good practice during the comparison is to apply a mode tracking algorithm able to find the most correlated modes regardless of their extraction order. Finally, this correlation criterion takes into account only eigenvectors while frequencies must be separately compared on a relative error basis.

The first result presented in table 4 is the FCR between a 10 modes extraction for the two fidelity.

Table 4: Computational cost of modal analysis.

HF extraction	LF extraction	FCR
840.53 s	21.44 s	2.55 %

The LF model gives a sharp decrease in the computational time while the FCR value can be use as a cost index in the multifidelity optimization.

Following the static validation, the fidelity correlation has been tested on the b and φ design variables with the same original values and variations. Since mode shapes might shift in order from one model to the other, the code extracts 10 eigenvectors from the HF and 30 from the LF, using mode tracking to find the best matches. From each analysis it is possible to compute the MAC matrix and a table of relative errors on the first 10 modes. Figure 13 and table 5 show the results for the CRM original values of the variables. Models are proven to have great dynamic correlation, in particular no mode tracking is needed since LF frequencies are ordered and the relative error is almost zero for the first three modes.

4.3 Multifidelity test case application

The final part of the validation process has consisted in a simple unconstrained optimization using the MFEGO algorithm. Both the static and dynamic HF behaviours are well represented by the LF model but the latter has been chosen as analysis type. The objective function to be minimize is the inverse of the distance between the first two frequencies, b and φ being taken as design variables in accordance with the tests made. Thus the problem is defined as in (6).

Yoann Le Lamer, Giovanni Quaglia, Emmanuel Benard, and Joseph Morlier
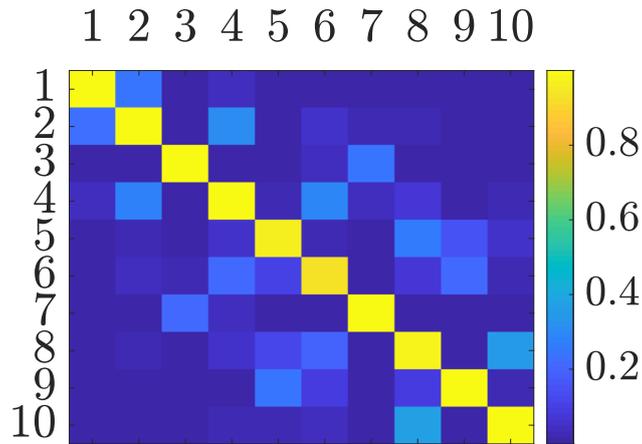
Figure 13: MAC matrix for the original values of b and φ.

Table 5: Frequencies [Hz] and relative error.

HF	LF	Relative error
1.9320	1.9398	-0.400
5.7476	5.7409	0.117
7.9694	7.9275	0.525
11.650	11.402	2.126
17.672	16.227	8.172
19.002	18.413	3.102
22.289	22.067	0.992
26.817	26.038	2.906
31.016	28.620	7.725
35.742	34.826	2.561

$$\begin{aligned}
\min_{b,\varphi} \quad & \frac{1}{f_2 - f_1} \\
\text{for} \quad & b \in [40m, 70m] \\
& \varphi \in [0°, 30°]
\end{aligned} \tag{6}$$

The MFEGO algorithm requires two black box functions, namely the LF and HF codes for normal modes extraction, the number of points used to initially train the Co-Kriging surrogate, 7 for each fidelity, and a cost evaluation. Based on the previous section the last vector is set to [0.01,1] and a budget of 15 is chosen. Each call of a function evaluation counts for a cost against the budget.

Figure 14 shows the initial LHS sampling of the design space. The same number of LF and HF points is chosen to train the first surrogate model.

Once the initial meta-model is obtained, the EGO algorithm successfully balances the exploration and exploitation of the design space choosing for each enrichment point the level of fidelity to be used. The final landscape is presented in figure 15 along with the location of the last point considered as optimum. Table 6 summarises the analysis results. [3]

Yoann Le Lamer, Giovanni Quaglia, Emmanuel Benard, and Joseph Morlier
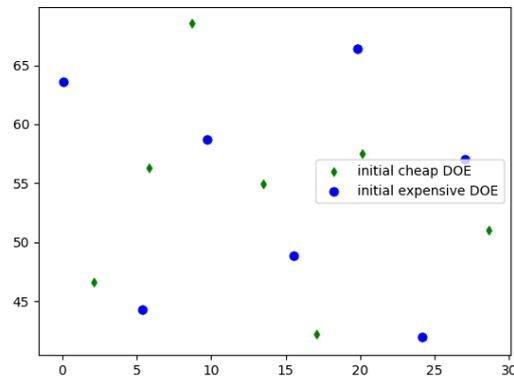
Figure 14:   Initial LHS sampling in the design space.
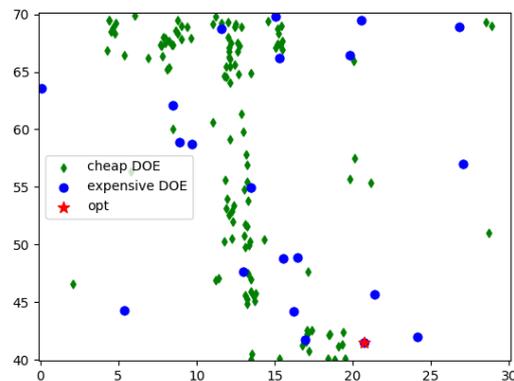
Figure 15:   Design space after the optimization.

Table 6: MFEGO test results.

LF calls	127
HF call	21
Total iterations	134
b solution	41.53 m
φ solution	20.69°
Objective function	3.393786858646402e-05

The simple test performed verifies the possibility to use the new LF in a multifidelity environment. The imposed cost ratio leads the algorithm to exploit three regions using many calls of the cheap code while the HF points are fewer and better spread. Nevertheless, the number of calls to the HF model is still consistent and a further reduction of the computational cost ratio would be an interesting development. The dynamic analysis is the first step towards flutter computing in the preliminary design loop.

Yoann Le Lamer, Giovanni Quaglia, Emmanuel Benard, and Joseph Morlier

5   APPLICATION TO HAR WING

From now on, we will consider the case of an HAR wing that will be refered to uCRM-13.5, that has been developed in [18] based on on the NASA CRM by mostly increasing overall span, also refered as uCRM-9.0 in [18].

5.1   Design phase of HAR wing structural model

A Python script has been written to automatically creates the different sections of the wingbox and the connections between them in a BDF file format to allow analysis using MSC Nastran solver. That is done by asking the user to specify the coordinates of leading edge and trailing edge of each section. This script is parametric and thus enables one to create different wing geometries.

This script has first been tuned/developed to be able to reproduce the properties of the original NASA CRM model

Therefore, thanks to the script being parametric, it has been used to create a new model with the geometric properties of uCRM-13.5, basically with an aspect ratio increased by 50%.

As for the design of the low-fidelity model, the same procedure than the one presented in subsection 3.3 is applied to the high-fidelity HAR wing model developed previously.

5.2   Aeroelastic static analysis

In this subsection HF and LF aeroelastic analysis were carried for uCRM-9.0 and uCRM-13.5 models in order to determine wingtip displacement for each case. Cruise parameters used in subsection 4.3 remain unchanged. As an example, figure 16 compares wing deformations of HF and LF models for uCRM-9.0 and uCRM-13.5. Also, table 7 compares wingtip displacements for the different cases.
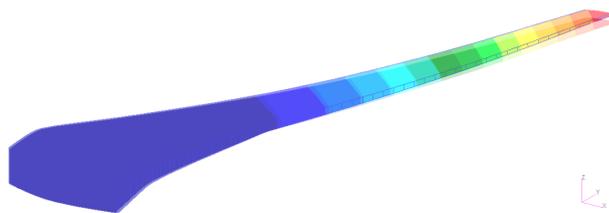
(a) Comparison of deformations of uCRM-9.0 wing for HF case (up) and LF case (down).
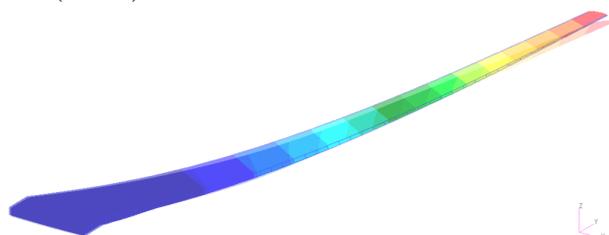
(b) Comparison of deformations of uCRM-13.5 wing for HF case (up) and LF case (down).

Figure 16: Comparison of deformations for uCRM-9.0 and uCRM-13.5 wings for HF and LF cases.

Yoann Le Lamer, Giovanni Quaglia, Emmanuel Benard, and Joseph Morlier

Table 7: Comparison of wingtip displacements between HF and LF models for uCRM-9.0 and uCRM-13.5 wings.

Model	HF model (m)	LF model (m)	Deviation (LF vs. HF in %)
uCRM-9.0	7.58	7.30	-3.69
uCRM-13.5	10.21	9.55	-6.46

As expected, higher deflections are observed for the high aspect ratio wing with regard to regular aspect ratio configuration.

The deviation of LF with regard to HF computation is satisfactory (below 5%) for uCRM-9.0 model. This deviation is higher for the high aspect ratio uCRM-13.5 model but remains reasonable (below 8%). That could be explained by the higher displacements, and the increased flexibility of HAR wing.

6   CONCLUSIONS

The first objectives of this research project have been achieved. First of all, the *MATLAB* tool developed in this paper is able to create a low-fidelity version of a high-fidelity wing model, whether it is the original NASA CRM model or the uCRM-13.5 model.
Static and dynamic validation results of the LF model are satisfactory in term of accuracy and correlation with regard to the HF model.
Then, we were able to develop a HF model of HAR wing uCRM-13.5, and the same simplification procedure was applied successfully. First results, show greater wingtip displacements than the original CRM as expected with reasonable deviation between HF and LF solutions.

Finally, the next step of this research project will be to accurately assess HAR wing performance while keeping reasonable computational costs for analysis and optimization. To be more specific, as higher aspect ratio wings show high rotations and displacements, structural geometrical non-linearities should be taken into account [19]. This will be done by using MSC Nastran SOL 400 non-linear solver.
Another goal will be the implementation of uCRM-13.5 wing structural model within the optimization framework in order to apply multifidelity to unconstrained, and then unconstrained optimization problems.

REFERENCES

[1] G. K. W. Kenway and J. R. R. A. Martins. Multipoint High-Fidelity Aerostructural Optimization of a Transport Aircraft Configuration. *Journal of Aircraft*, 51(1):144–160, Jan. 2014. doi:10.2514/1.C032150. URL `https://arc-aiaa-org.rev-doc.isae.fr/doi/10.2514/1.C032150`. Publisher: American Institute of Aeronautics and Astronautics.

[2] M. C. Kennedy and A. O'Hagan. Predicting the output from a complex computer code when fast approximations are available. *Biometrika*, 87(1):1–13, 2000. ISSN 00063444.

[3] D. R. Jones. A taxonomy of global optimization methods based on response surfaces. *Journal of Global Optimization*, 21(4):345–383, Dec 2001.

[4] D. R. Jones, M. Schonlau, and W. J. Welch. Efficient global optimization of expensive black-box functions. *Journal of Global Optimization*, 13(4):455–492, Dec 1998.

[5] N. Bartoli, I. Kurek, R. Lafage, T. Lefebvre, R. Priem, M. A. Bouhlel, J. Morlier, V. Stilz, and R. Regis. Improvement of efficient global optimization with mixture of experts: methodology developments and preliminary results in aircraft wing design. 06 2016.

[6] N. Bartoli, M. Meliani, J. Morlier, T. Lefebvre, M.-A. Bouhlel, and J. Martins. *Multi-fidelity efficient global optimization: Methodology and application to airfoil shape design*. 2019. doi:10.2514/6.2019-3236. URL `https://arc.aiaa.org/doi/abs/10.2514/6.2019-3236`.

[7] J. Mas-Colomer. *Aeroelastic Similarity of a Flight Demonstrator via Multidisciplinary Optimization*. PhD thesis, 12 2018.

[8] J. M. Colomer. Aerostructure package, 2019. URL `https://github.com/mid2SUPAERO/aerostructures`.

[9] G. R. Jiménez and J. M. J. Mas Colomer. Multifidelity aeroelastic optimization with application to a bwb. AIAA Aviation, 2021.

[10] openMDAO. Openmdao source docs, 2016. URL `http://openmdao.org/twodocs/versions/2.2.0/_srcdocs/index.html`.

[11] T. Scholcz. Multi-fidelity methods for fluid-structure interaction and uncertainty quantification. 09 2015.

[12] Z. Guo, L. Song, C. Park, J. Li, and R. T. Haftka. Analysis of dataset selection for multi-fidelity surrogates for a turbine problem. *Structural and Multidisciplinary Optimization*, 57(6):2127–2142, Jun 2018. ISSN 1615-1488. doi:10.1007/s00158-018-2001-8. URL `https://doi.org/10.1007/s00158-018-2001-8`.

[13] G. Fernandez, C. Park, N. Kim, and R. Haftka. Issues in deciding whether to use multifidelity surrogates. *AIAA Journal*, pages 1–16, 03 2019. doi:10.2514/1.J057750.

Yoann Le Lamer, Giovanni Quaglia, Emmanuel Benard, and Joseph Morlier

[14] Boeing. *A502I User's Guide-PAN AIR Technology Program for Solving Potential Flow about Arbitrary Configurations.* 02 1992.

[15] NASA. *The Nastran User's Manual.* 12 1980.

[16] NASA. Nasa common research model, 2017. URL `https://commonresearchmodel.larc.nasa.gov/`.

[17] M. Pástor, M. Binda, and T. Harčarik. Modal assurance criterion. *Procedia Engineering*, 48:543–548, 12 2012. doi:10.1016/j.proeng.2012.09.551.

[18] T. R. Brooks, G. K. Kenway, and J. R. R. A. Martins. Undeflected Common Research Model (uCRM): An Aerostructural Model for the Study of High Aspect Ratio Transport Aircraft Wings. In *35th AIAA Applied Aerodynamics Conference*. American Institute of Aeronautics and Astronautics. doi:10.2514/6.2017-4456.

[19] A. C. Gray and J. Martins. Geometrically Nonlinear High-fidelity Aerostructural Optimization for Highly Flexible Wings. In *AIAA Scitech 2021 Forum*, AIAA SciTech Forum. American Institute of Aeronautics and Astronautics, Jan. 2021. doi:10.2514/6.2021-0283.

AEROELASTIC IMPLICATIONS OF ACTIVE WINGLET CONCEPT AIMED TO IMPROVE CIVIL TRANSPORT AIRCRAFT PERFORMANCES

Martin Delavenne[1]*, Bernard Barriety[2], Fabio Vetrano[2], Valérie Ferrand[3] and Michel Salaün[4]

1: Aircraft Design Department
ISAE-Supaero
Univ. Toulouse
10 Av. Edouard Belin, Toulouse, France
martin.delavenne@isae-supaero.fr

2: Loads and Aeroelastic Department
Airbus Operations SAS
316 route de Bayonne, Toulouse, France

3: Aerodynamic and Propulsion Department
ISAE-Supaero

4: Structural Mechanics and Material Department
ISAE-Supaero

Abstract. *Reduction of aircraft environmental footprint has become over years a key objective for the industry. Particularly, for decades winglets have been proven to efficiently reduce drag and fuel consumption. However, the design of those wingtip extensions mainly relies on an aerodynamic shape optimisation for a given cruise condition resulting in suboptimal behaviour for the rest of the flight. Active winglet concept proposes to optimise the winglet cant angle along the flight to compensate the loss of efficiency inherent to fixed designs. The variation of winglet deflection impacts the lift distribution with repercussion on wing deformation that must be investigated. Besides, the presence of moving masses at the tip of the wing also has influence on dynamic response and particularly on flutter onset. This work proposes to evaluate those impacts through an aeroelastic analysis of both static and dynamic implications of active winglets combined with an aerodynamic performances optimisation. The XRF1, an Airbus provided industrial standard multi-disciplinary research test case representing a typical configuration for wide body long-range aircraft, is used as the baseline aircraft. Coupled CFD/CSM computations are performed to assess the evolution of wing shape with respect to winglets deflections and the consequences on mission performance optimisation. While a parametric flutter analysis is carried-out to highlight the dependence of critical flutter speed on winglet cant angle.*

Keywords: Active winglet, aeroelasticity, CFD/CSM, optimization

Martin Delavenne, Bernard Barriety, Fabio Vetrano, Valérie Ferrand and Michel Salaün

1   INTRODUCTION

In a context that urges aeronautical industry to reduce its environmental footprint, new solutions must be considered to improve aircraft performances. Historically, as illustrated in Fig.1 the increase of wings aspect ratio has been one of the preferred solution to improve the aerodynamic efficiency. Indeed, according to Prandtl's work [1] induced drag – that is responsible for more than one third of the total drag – is inversely proportional to the aspect ratio. However, this growth was limited by airports regulations on maximum span and the detrimental impact of high aspect ratio wings on structural weight. To overcome these limits winglets have been introduced in the 1970s and led to drag reduction by around 4% with limited impact on weight [2, 3]. More recently, the massive deployment of composite materials combined with folding wing-tips and loads alleviation devices (active or passive) allow for high aspect ratio wings without compromising ground operations nor structural weight [4–6].
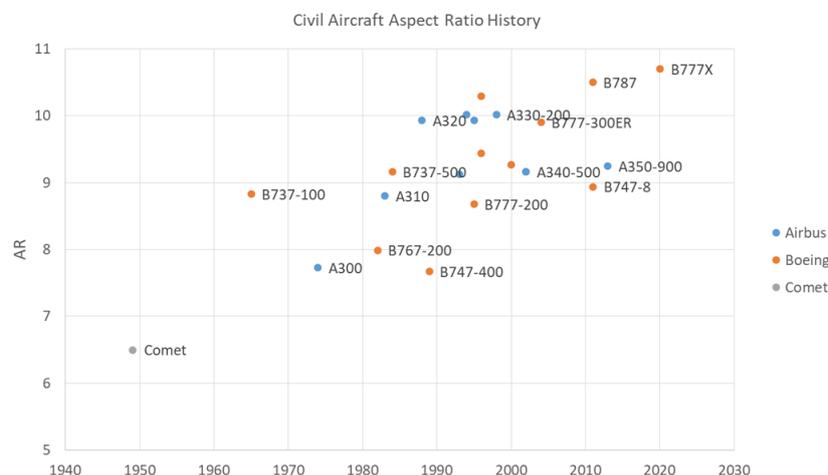
Figure 1: Aircraft aspect ratio constantly increases with years

However, the aerodynamic design approach that relies on fixed shapes optimised for a given flight condition must be challenged. Indeed, it can be shown that single point optimisation leads to suboptimal performances in the remaining of the flight domain with detrimental impact on fuel burnt [7]. The same source indicates that multipoint optimisation that considers static aeroelastic deformation is part of the solution to improve performances within the operational envelop but, as the wing shapes is still frozen at design stage, a slight overconsumption will persist. Morphing wing technologies [8] that relies on continuous shape adaptation appear as providential solutions. As Prandtl demonstrated in the 1920s [1], induced drag is directly related to the spanwise lift distribution. Its optimisation with active devices such as NASA's VCCTEF (Variable Camber Continuous Trailing Edge Flap) could lead to improvements of the aerodynamic efficiency by more than 5% [9, 10]. Additional gains are also to be expected from the loads alleviation and flutter control provided by these technologies. However, they may suffer from certification and maintenance issues as well as weight penalties from actuation system [11].

Active winglet patented by Airbus [12] consists in a winglet whose cant angle (δ) can change during the flight as illustrated in Fig.2. It takes advantage of higher aspect ratio wings and morphing technologies while limiting their downsides: It allows for higher span

Martin Delavenne, Bernard Barriety, Fabio Vetrano, Valérie Ferrand and Michel Salaün

Figure 2: Active winglet principle with variable cant angle.

without impact on ground operations and provides a mean to actively control the lift distribution with a simple actuation system. Loads alleviation capabilities have also been demonstrated and ensure a limited impact on structural weight [13]. First assessments of the benefits of the device have been carried out on the XRF1 – an Airbus provided industrial standard multidisciplinary research test case representing a typical configuration for wide body long range aircraft – equipped with retrofitted winglets [14, 15]. They highlighted the necessity to consider not only aerodynamic performances but also structural deformations through coupled approaches like CFD/CSM (Computational Fluid Dynamics / Computational Structural Mechanics) computations. It has indeed been shown that wing flexibility could drastically alter the efficiency of the device [14]. Consequently, fuel saving expectations are brought from 2% when only aerodynamics is considered [16] to less than 1% when coupled computations are carried out. In the present paper, surrogate-based mission analysis is extended to a XRF1 high aspect ratio wing configuration [17] and compared to the XRF1 with retrofitted optimised active winglets configuration [15]. The impact of the static aeroelastic deformations on the efficiency of the device perceived in [14] is detailed. Finally, the implications on flutter onset of moving masses at the tip of the wing are explored.

2   NUMERICAL METHODS

As mentioned in the introduction, the entire approach relies on coupled CFD/CSM computations aimed to assess the aerodynamic performances while considering wing deformations. This section provides details about both aerodynamic and structural models involved in the analysis. The surrogate model based mission analysis procedure is also presented.

2.1   XRF1 Test cases

Figure 3 presents the two test cases considered for this study: The XRF1 configuration with a retrofitted optimised winglet [15] and the high aspect ratio configuration equipped with a folding wing-tip. Hinges are respectively located at winglet root and at maximum span limit for this aircraft category i.e. 32m. The wing-tip size of the high aspect ratio configuration can be extended by moving the hinge inward down to 30m. Because of the wing size extension the maximum take-off weight (MTOW) and the operational weight empty (OWE) are increased by respectively 0.5% and 4.6% for the high aspect ratio configuration with respect to baseline XRF1. The wing reference surface also raises by almost 8%.

Martin Delavenne, Bernard Barriety, Fabio Vetrano, Valérie Ferrand and Michel Salaün

(a) XRF1 plus winglet configuration   (b) XRF1 high aspect ratio configuration
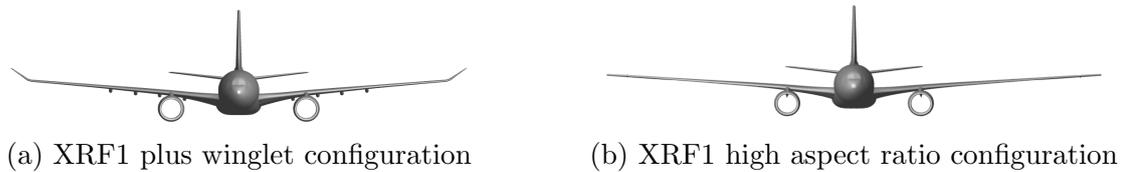
Figure 3: XRF1 configurations used in this study.

2.2 Aerodynamic computations

The aerodynamic performances are assessed using the DLR CFD code TAU [18]. RANS equations are solved for an unstructured mesh (Figure 4) of about 5 millions nodes with Menter-SST turbulence model. It can be shown [15] that the analysis of a simplified model only composed of the wing is sufficient to capture the effects of winglet cant variation on drag. This simplification is applied for the remainder of this study. For flutter assessment
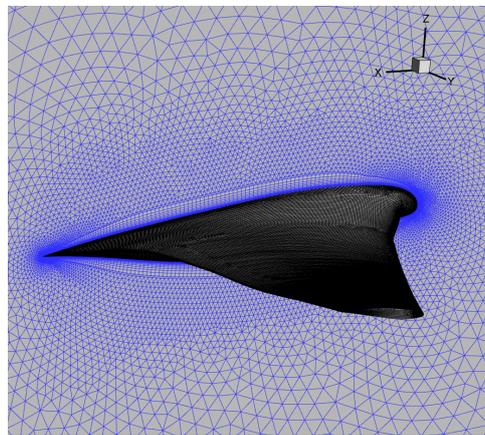
Figure 4: Example of unstructure mesh for the XRF1 wing

unsteady aerodynamics forces in the frequency domain must be considered. They are computed using Linearised Frequency Domain (LFD) method. The method relies on a linearisation of the RANS equations around a non-linear steady state considering small harmonic disturbances [19]. It allows to capture non-linearities such as shocks and flow separations and has been developed to capture flutter boundaries more accurately while maintaining a reasonable computational cost.

2.3 Structural computations

The structural displacements are computed with Finite Element Method. A wing model composed of approximately 300,000 degrees of freedom is considered as illustrated on Fig.5 for both XRF1 wing configurations. The wing is considered to be clamped at the root rib. The material is aluminium and the weight of non-structural elements such as fuel are taken into account through punctual masses distributed along the span. The weight of the actuation system is estimated to 140kg based on scaling of the Valkyrie folding wing-tip mechanism [20]. The stiffness of the actuation system is not considered and rigid links are assumed between the fixed part of the wing and the movable one. Both linear static and modal analyses are performed with MSC Nastran software [21] using respectively solutions SOL101 and SOL103 with a truncation to consider only the first 25 modes.

Martin Delavenne, Bernard Barriety, Fabio Vetrano, Valérie Ferrand and Michel Salaün

(a) XRF1 wing FEM

(b) XRF1 high aspect ratio FEM

Figure 5: Finite elements models for XRF1 test cases wings.

2.4 Flutter computations

In this study, the consequences of winglet cant angle (δ) deflections on flutter boundaries must be investigated. Indeed, changing significantly tip masses location is likely to have influence on flutter critical speed. To know whether this change increases or reduces margins is of first importance regarding aircraft safety. Flutter equation (1) must be solved for frequencies within the range of interest and every cant angle deflections.

$$-\mathbf{M}\omega^2 + i\mathbf{D}\omega + \mathbf{K} = \mathbf{Q} \tag{1}$$

The generalised aerodynamic forces $\mathbf{Q}$ are extracted from LFD computations. Because they depend on the frequency itself the eigenvalue problem must be solved iteratively. In this study, the *p-k* method is used [22]. The reduced frequencies k, that is computed from reference chord c and aircraft speed V such as $k = \frac{\omega c}{V}$, ranges from 0 to 4.0.

2.5 Surrogate based mission analysis

The evaluation of the mission performances relies on surrogate models built from CFD/CSM computations. A full-factorial design of experiment (DoE) composed of $n = 126$ samples ($\vec{x_i}$) is generated with aircraft mass, cruise altitude and cant deflection as parameters ($N = 3$). The range of each of them is indicated in Tab.1 with MZFW being the maximum zero fuel weight of the aircraft and MTOW its maximum take-off weight.

Table 1: Full-factorial design of experiment parameters ranges.

Param.	Lower Bound	Upper Bound
δ (deg)	-90	90
Altitude (ft)	30000	41000
Weight	MZFW	MTOW

Several surrogate models ($\hat{f}(\vec{x})$) have been tested to capture drag coefficient (C_D) and wing twist deformation ($\Delta\theta_{wing}$) evolutions with DoE parameters:

- Response Surface Model - RSM (p-polynomial)[23]:
  $\hat{f}(\vec{x}) = \beta_0 + \sum_{i_1=1}^{n} \beta_{i_1} x_{i_1} + \sum_{i_1=1}^{n} \sum_{i_2 \leq i_1}^{n} \beta_{i_1 i_2} x_{i_1} x_{i_2} + ... + \sum_{i_1=1}^{n} ... \sum_{i_p \leq i_{p-1}}^{n} \beta_{i_1...i_p} x_{i_1}...x_{i_p}$

- Gaussian Radial Basis Function - RBF [23]:
  $\hat{f}(\vec{x}) = \sum_{i=1}^{n} \beta_i \psi(\vec{x} - \vec{x_i})$ with $\psi(\vec{x}) = \exp(\frac{-||\vec{x}||^2}{2\sigma})$ – In this model σ is selected to minimize the cross-validation error.

- Ordinary Kriging [24]:
  $\hat{f}(\vec{x}) = \mu + \sum_{i=1}^{n} \beta_i \psi(\vec{x} - \vec{x_i})$ with $\psi(\vec{x} - \vec{x_i}) = exp[-\sum_{j=1}^{N} \theta_j |x_{,j} - x_{i,j}|^{p_j}]$ – In this model θ_j and p_j are parameters determine such that the model fit the sampling points.

The selection of the model is operated using cross-validation as detailed in [23]. The quality metrics Normalised Root Mean Square Error and the coefficient of determination R^2 are computed and compared for each model technique. Table 2 summarises the results of the cross-validation applied to the three pre-cited models and shows that kriging better performs and is the preferred choice.

Table 2: Validation and selection of drag and wing twist models

Model	NRMSE	R^2
C_D RSM	3.8×10^{-2}	0.972
C_D RBF	3.4×10^{-2}	0.982
C_D Kriging	**1.2×10^{-4}**	**0.999**
$\Delta\theta_{wing}$ RSM	4.87×10^{-2}	0.959
$\Delta\theta_{wing}$ RBF	2.02×10^{-2}	0.991
$\Delta\theta_{wing}$ Kriging	**6.6×10^{-3}**	**0.998**

Once the models have been built, the mission computation is performed. The cruise is cut in segments as illustrated in Fig.6. The drag on this segment (D_s) is computed and optimised from the model considering the weight and the altitude and changing winglet cant angle. The necessary thrust to maintain level flight is deduced and used to compute fuel consumption ($W_{fuel,s}$) and weight at the end of the segment. The process is iterated to ensure that starting weight fits with aircraft maximum take-off weight.
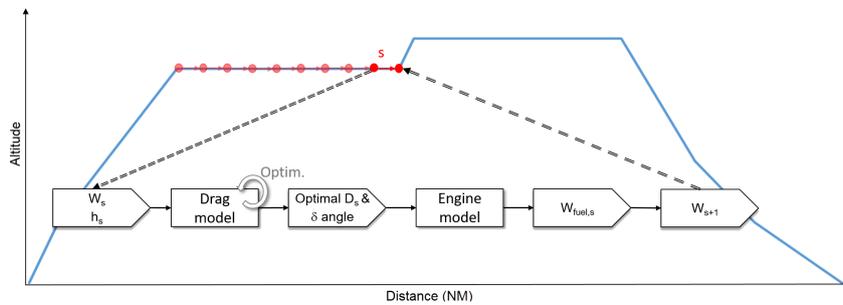
Figure 6: Mission cruise performance optimisation procedure.

3 STATIC AEROELASTIC DEFORMATIONS IMPACT ON PERFORMANCES

3.1 Active winglet efficiency

The active winglet efficiency is evaluated computing the reduction of fuel consumption for the two XRF1 test cases considering 500 different mission flight paths (range, altitudes) and payload combinations. The evolution of active winglet efficiency with mission range is presented in Fig.7a for both configurations. Figure 7b highlights its dependence on mean cruise altitude.

The first observation that can be drawn is the similarity between the two configurations. Despite the difference in term of wing design, the active winglet maximum efficiency seems to be roughly identical and does not exceed 1%. More difference appears when considering mean value, even small it reaches around 0.3% for high aspect ratio case while it is almost null for the configuration with retrofitted winglet. Indeed, negative

Martin Delavenne, Bernard Barriety, Fabio Vetrano, Valérie Ferrand and Michel Salaün

(a) Mission range   (b) Cruise mean altitude
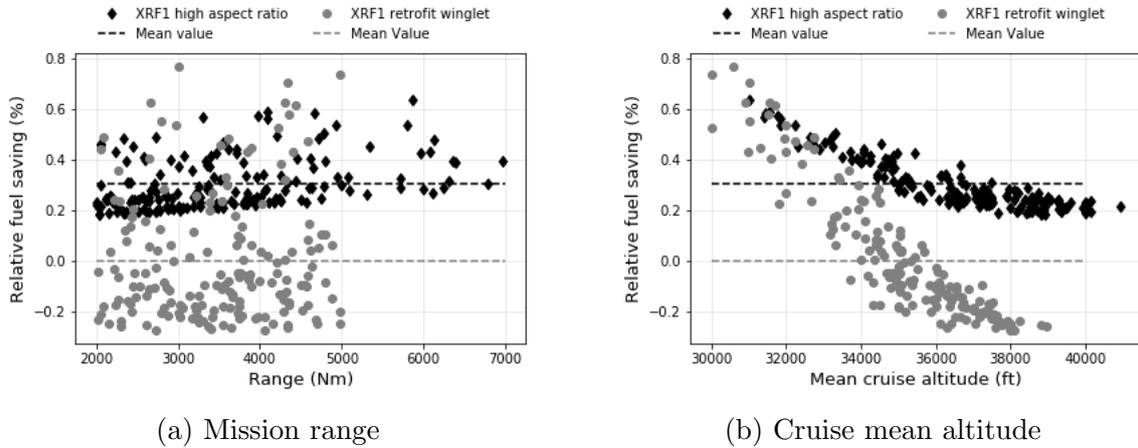
Figure 7: Mission fuel consumption reduction with active winglets depending on flight range and mean altitude.

fuel savings i.e. overconsumption are observed for this latter case. They originate from the additional weight of the actuation system. In the retrofitted case the reference for comparison is the XRF1 equipped with a fixed optimised winglet without any actuator. For the high aspect ratio the reference is the same wing but equipped with a folding wing-tip only active on ground (deployed in flight) therefore with an actuation system already existing. Computation without consideration about the actuation weight have been carried out and show positive average fuel savings [15].

Figure 7a shows little dependency of fuel savings on mission range. But, considering the variation with respect to mean flight altitude in Fig.7b a trend emerges: The lower the flight the larger the benefits of active winglets. More details about the phenomenon at stake are provided in next paragraph.

3.2 Influence of static aeroelastic deformation

Maximum values of active winglet efficiency demonstrated so far are distant from what could have been expected from the literature [16]. This major difference lies on the flexibility of the wing that produces antagonist effects and reduce drag sensitivity to winglet cant angle variation. To explain implications of static aeroelastic deformations on active winglet efficiency the dependence of local angle of attack (AoA) on the winglet on cant variation and wing deformation must be considered. It could be decomposed into two parts:

- A rigid part dependent on global angle of attack α_∞, wing dihedral angle δ_{wing}, winglet cant angle δ and winglet twist $\theta_{winglet}$:

$$\alpha_{winglet_r} = \alpha_\infty \cos(\delta + \delta_{wing}) + \theta_{winglet} \tag{2}$$

- A flexible part dependent on wing tip static aeroelastic twist deformation $\Delta\theta_{wing}(\eta = 1)$, wing dihedral angle δ_{wing} and winglet cant angle δ:

$$\alpha_{winglet_f} = \sin^{-1}[\sin(\Delta\theta_{wing}(\eta = 1))\cos(\delta + \delta_{wing})] \tag{3}$$

Rigorously, δ_{wing} contains a flexible part that results from the bending deformation. However, because the variation of dihedral angle due to wing deformation is small in front of cant angle variations its impact can be neglected.

Martin Delavenne, Bernard Barriety, Fabio Vetrano, Valérie Ferrand and Michel Salaün

Considering rigid wing, the lift distribution will only be affected by winglet folding. According to (2): $\lim_{|\delta| \to 90} \alpha_{winglet_r} \approx \theta_{winglet}$. Besides α_∞ tends to decrease with δ. Then, in cruise conditions because these two values are of the same order of magnitude the variation of local angle of attack on the winglet remains limited leading to similar loading on the winglet. Figure 8 illustrate this behaviour for a XRF1 wing that have been stiffened (Not perfectly rigid). The pressure contours evidence that winglet loading is marginally affected by cant deflection.
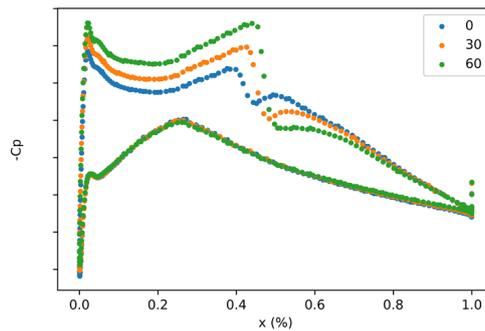
Figure 8: Pressure coefficient at 25% of winglet span for a rigid wing and three cant angles.

The consequence is that the normal force on the winglet barely changes while its orientation does. The lift it generates then drops, center of lift shifts inward and induced drag increases. This phenomenon is qualitatively illustrated in Fig.9a and the qualitative change in lift distribution is shown on Fig.9b for the stiffened XRF1 wing.
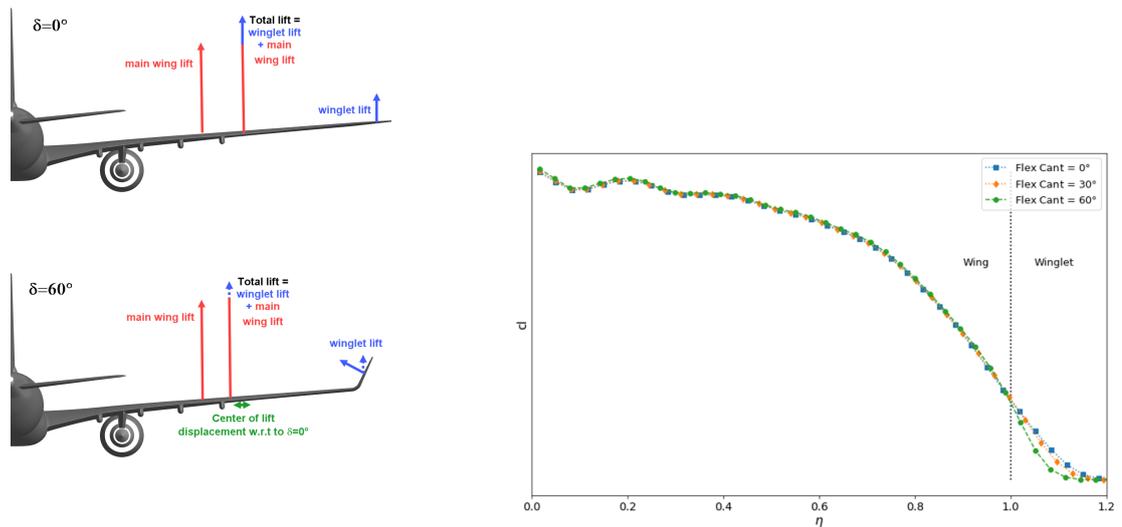
(a) Qualitative variation of winglet loading

(b) Quantitative variation of lift distribution

Figure 9: Qualitative and quantitative visualisation of winglet loading variation and impact on lift distribution for rigid wings.

Adding flexibility impacts drastically the variation of local AoA on the winglet and consequently the lift it generates. Indeed, in that case rigid effects (2) and flexible effects (3) act conjointly. For sweptback wings, wing twist deformation is negative (nose down)

Martin Delavenne, Bernard Barriety, Fabio Vetrano, Valérie Ferrand and Michel Salaün

and is propagated to the winglet reducing its local AoA for small cant values. When winglet folds up or down, flexible effect vanishes and only rigid one persists. Local AoA increases noticeably and so does the loads on the winglet as illustrated in Fig.10. Because flexible effect reduces the local AoA for small cant deflection it appears on pressure contours that the winglet generates almost no load for $\delta = 0 \deg$. On the contrary, from $\delta = 30 \deg$ to $\delta = 60 \deg$ it increases significantly.
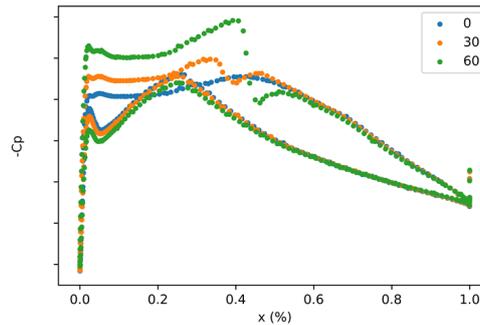
Figure 10: Pressure coefficient at 25% of winglet span for a flexible wing and three cant angles.

As winglet folds, the resultant aerodynamic force increases which compensates for the orientation change. Then lift remains the same within a range of cant variation. Once winglet loading increase is no more sufficient to balance force orientation modification the lift starts to drop. This phenomenon is illustrated in Fig.11a and Fig.11b. It clearly appears that until $\delta = 30 \deg$ the lift distribution barely change, then folding the winglet further has an impact on wing loading. As induced drag depends on lift distribution, its sensitivity to cant angle is reduced by flexible effects. The efficiency assessment of active winglet devices appears to be highly moderated by flexible effects and must be assessed using coupled approaches.
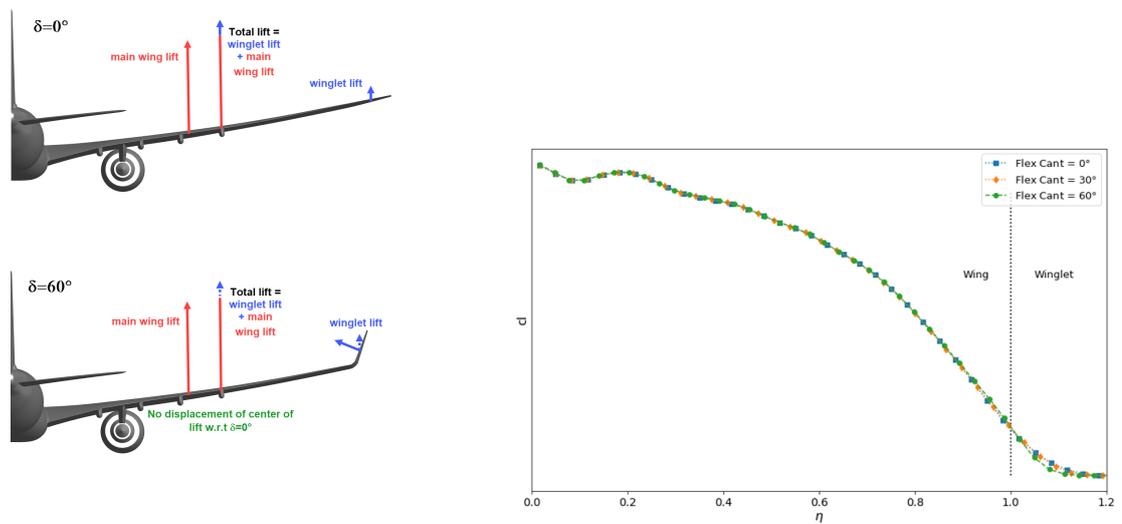
(a) Qualitative variation of winglet loading

(b) Quantitative variation of lift distribution

Figure 11: Qualitative and quantitative visualisation of winglet loading variation and impact on lift distribution for flexible wings.

Martin Delavenne, Bernard Barriety, Fabio Vetrano, Valérie Ferrand and Michel Salaün

A similar reasoning applies to explain the dependency of active winglet efficiency on mean flight altitude as highlighted in Fig.7b. For low flight levels and a given aircraft weight, AoA is lower than for high flight levels. Therefore, considering (2) + (3) the flexible effect dominates. Particularly, local AoA on winglet may increase by almost $2\,\mathrm{deg}$ when it folds as illustrated in Fig.12a. In Fig.12b this variation appears to be damped to around $0.8\,\mathrm{deg}$ for higher altitudes.

(a) Low cruise altitude.

(b) High cruise altitude
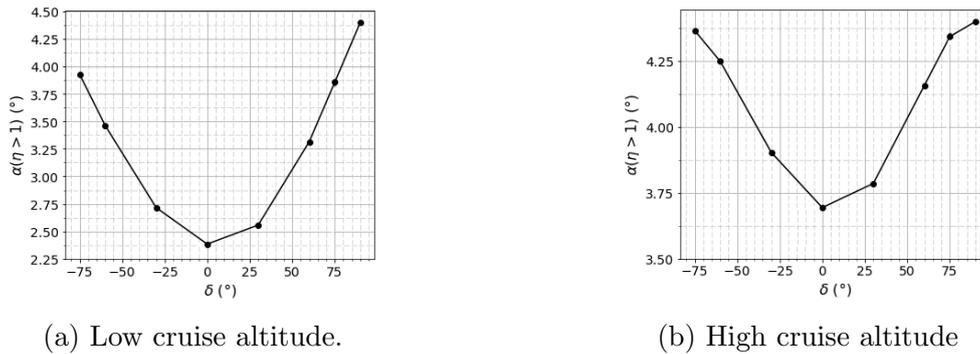
Figure 12: Evolution of local angle of attack at winglet tip with cant angle for different flight altitudes.

At low flight levels, as shown is Fig.13 the winglet barely generates lift independently of the XRF1 configuration considered. As cant angle absolute value increases, larger loads are observed on the winglets that are sufficient to make lift distribution shift outward as highlighted by Fig.15. The actuation of the winglet has beneficial implication on drag in that conditions.

(a) XRF1 retrofitted with winglets.

(b) XRF1 high aspect ratio
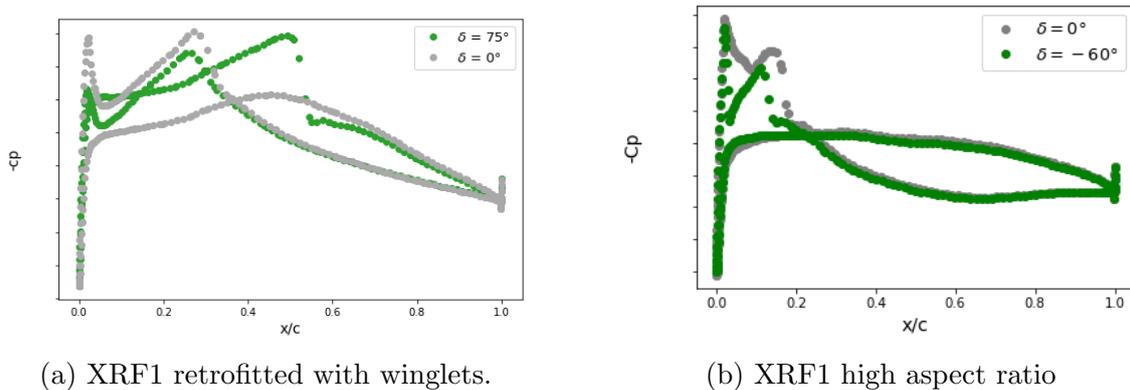
Figure 13: Winglet loading for two different cant deflections at low cruise altitude for the two XRF1 test cases.

Increasing the altitude means increasing $\alpha_{winglet_r}$ predominance in front of flexible effects. Loading on winglet keep on increasing as it folds as illustrated in Fig.15a but not sufficiently to compensate the change in resultant force orientation. The lift then shifts inward as in Fig.15b and optimal deflection lies in the vicinity of $\delta = 0\,\mathrm{deg}$. Small benefits are then expected from winglet actuation.

Martin Delavenne, Bernard Barriety, Fabio Vetrano, Valérie Ferrand and Michel Salaün

(a) XRF1 retrofitted with winglets.

(b) XRF1 high aspect ratio
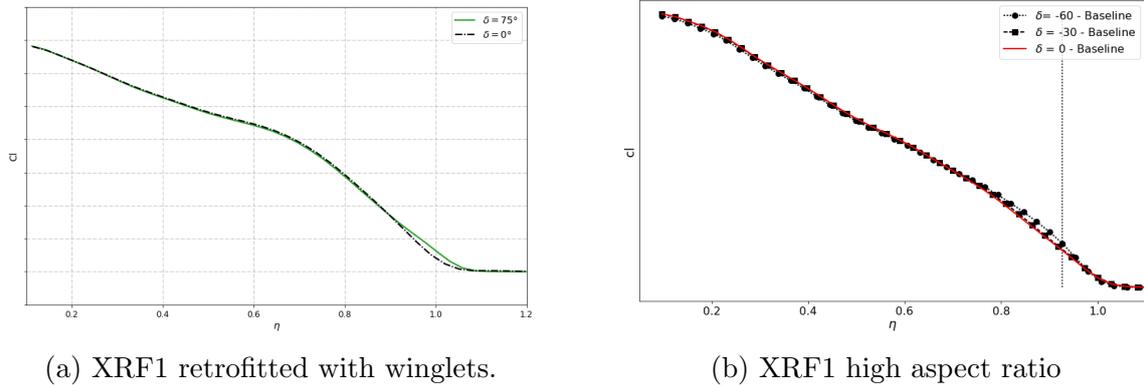
Figure 14: Lift distribution for two different cant deflections at low cruise altitude for the two XRF1 test cases.

(a) Pressure contour at 25% of winglet span

(b) Spanwise lift distribution
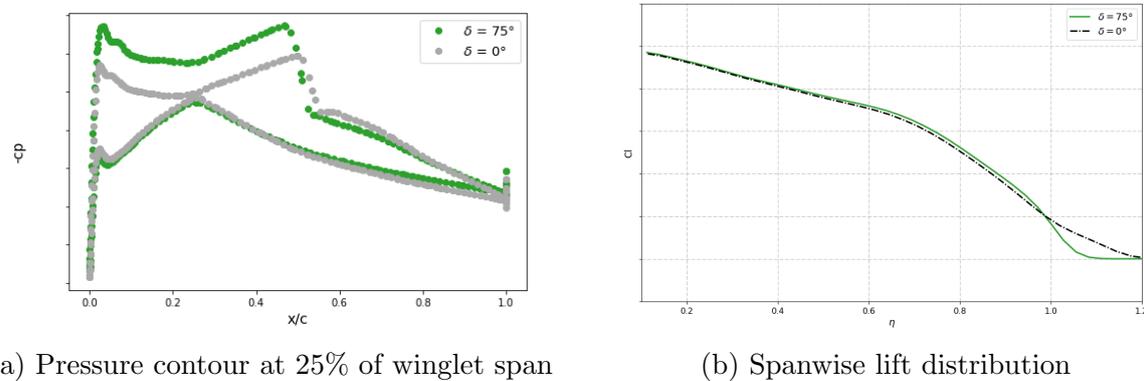
Figure 15: Pressure contour and lift distribution for high altitude flight illustrate effect of altitude on winglet loading and aircraft performances.

4 IMPLICATIONS ON FLUTTER BOUNDARIES

Moving masses at the tip of the wing may have consequences on the dynamic response of the structure and particularly on aeroelastic stability that must be assessed. It must be ensured that the flutter critical speed remains larger than the diving speed with a safety margin of 15% in the whole flight domain and whatever the winglet cant deflection.

4.1 Impact of cant variation on modes

First, a parametric modal analysis is performed for the XRF1 high aspect ratio wing. The configuration with retrofitted winglet is not presented here because it exhibits significant margins to flutter that could not be totally be erased by winglet actuation. Seven cant angles are analysed from $-90 \, \text{deg}$ to $90 \, \text{deg}$. The sensitivity to active winglet size is also considered by changing the hinge location. A winglet of 2m and a larger one of 4m are analysed.

The frequency evolution with cant angle of the six first structural modes is plotted in Fig.16a and in Fig.16b for the smaller and the larger winglet respectively.

From Fig.16a it can be noticed that mode 4, 5 and 6 frequencies vary by more than 5% when cant angle absolute value increases from $\delta = 0 \, \text{deg}$ to $\delta = 90 \, \text{deg}$. Particularly, larger variations occur above $|\delta| = 30 \, \text{deg}$. On the contrary the first three modes frequencies are less impacted by cant changes.

Martin Delavenne, Bernard Barriety, Fabio Vetrano, Valérie Ferrand and Michel Salaün
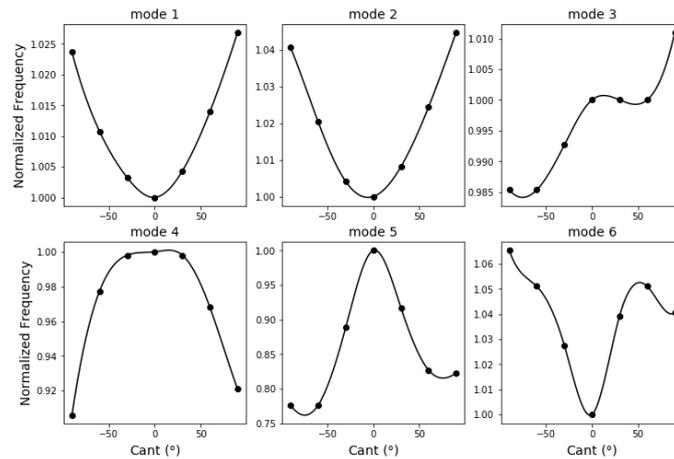
(a) Small winglet
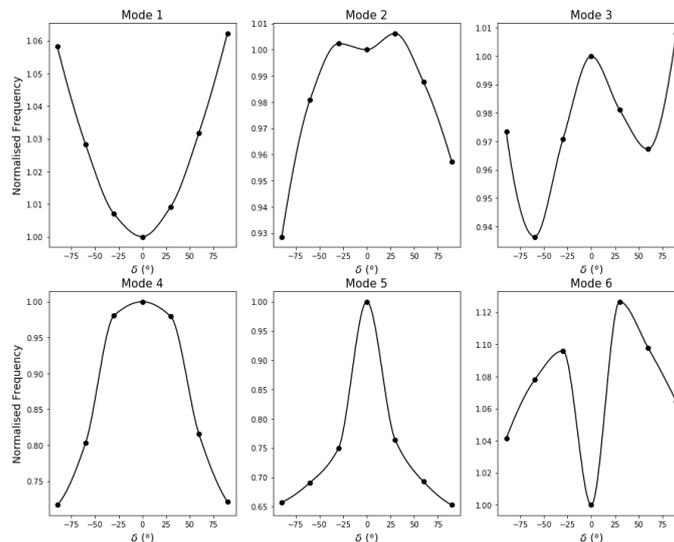
(b) Large winglet

Figure 16: First six structural modes frequency variations with cant angle for two winglet sizes.

Observing the evolutions for the larger winglet in Fig.16b shows that this behaviour is exacerbated and that all modes are impacted by large frequency variation with cant angle. Particularly, mode 2 frequency drops by 7%, mode 4 one by more than 25% and mode 5 by almost 35%.

The observation of the mode shapes for extreme cant deflections ($\delta = 0 \deg$ and $\delta = 90 \deg$) provides deeper insight into the phenomenon at stake. From Fig.17 it can be noticed that the nature of the three first modes remains unchanged. Namely, the 1 node bending, 2 nodes bending and 1 node fore-and-aft modes occur in first, second and third position respectively. On the other hand, the first torsion mode that appears in sixth position for $\delta = 0 \deg$ switches to fourth position when $\delta = 90 \deg$. In the meantime, the 3 nodes bending and 2 nodes fore-and-aft modes move backward respectively to fifth and sixth position. This alteration of the mode nature when cant angle varies is the cause for the modes frequencies to change abruptly.

The same occurs for the larger winglet but the change is even more pronounced. In-

Martin Delavenne, Bernard Barriety, Fabio Vetrano, Valérie Ferrand and Michel Salaün

| (a) Mode 1 | (b) Mode 2 | (c) Mode 3 |

| (d) Mode 4 | (e) Mode 5 | (f) Mode 6 |
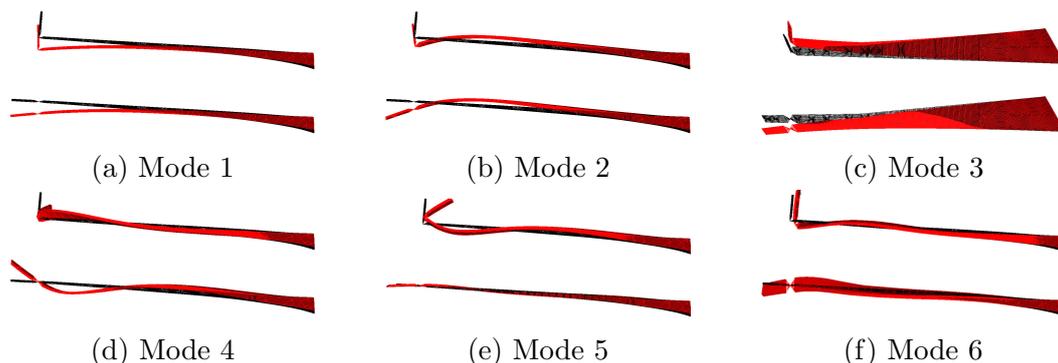
Figure 17: Small winglet first six structural mode shapes for $\delta = 0\,\text{deg}$ and $\delta = 90\,\text{deg}$.

deed, observing Fig.18 it appears that the first torsion mode switches from sixth position to second one when winglet folds passing through fourth position when $\delta \approx 30\,\text{deg}$ (not plotted here). Simultaneously the other modes move backward similarly to the observations made for the smaller winglet. This displacement of the first torsion mode within the mode sequence causes the fourth mode frequency to decrease slightly between $|\delta| = 0\,\text{deg}$ and $|\delta| = 30\,\text{deg}$ before to drop rapidly for further deflections. The second mode remains a bending mode till $|\delta| > 30\,\text{deg}$ then the frequency falls when it switches to torsion.

| (a) Mode 1 | (b) Mode 2 | (c) Mode 3 |

| (d) Mode 4 | (e) Mode 5 | (f) Mode 6 |
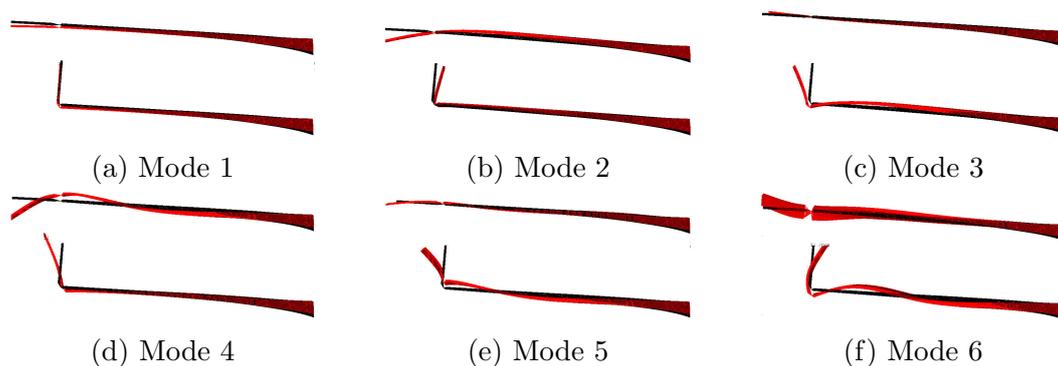
Figure 18: Large winglet first six structural mode shapes for $\delta = 0\,\text{deg}$ and $\delta = 90\,\text{deg}$.

4.2 Consequences on flutter onset

The alteration of the mode sequence that has just been evidenced is not without consequences on flutter onset. The instability occurs when torsion and bending modes couple. If torsion frequency falls while bending one increases slightly as it is figured in Fig.16 flutter is more prone to be triggered. As a results the flutter speed diminishes as winglet deflects upward or downward.

Figure 19 shows a reduction of almost 20% of the flutter critical speed for the smaller winglet and more than 35% for the larger one. The figure also highlights the modes involved in the coupling, it clearly shows that the change in the mode sequence is the main responsible for the dramatic degradation of flutter characteristics.

5 CONCLUSIONS

In this paper the active winglet efficiency is assessed for a high aspect ratio configuration of the XRF1 test case and compared to values from previous studies on XRF1 retrofitted

Martin Delavenne, Bernard Barriety, Fabio Vetrano, Valérie Ferrand and Michel Salaün

(a) Small winglet

(b) Large winglet
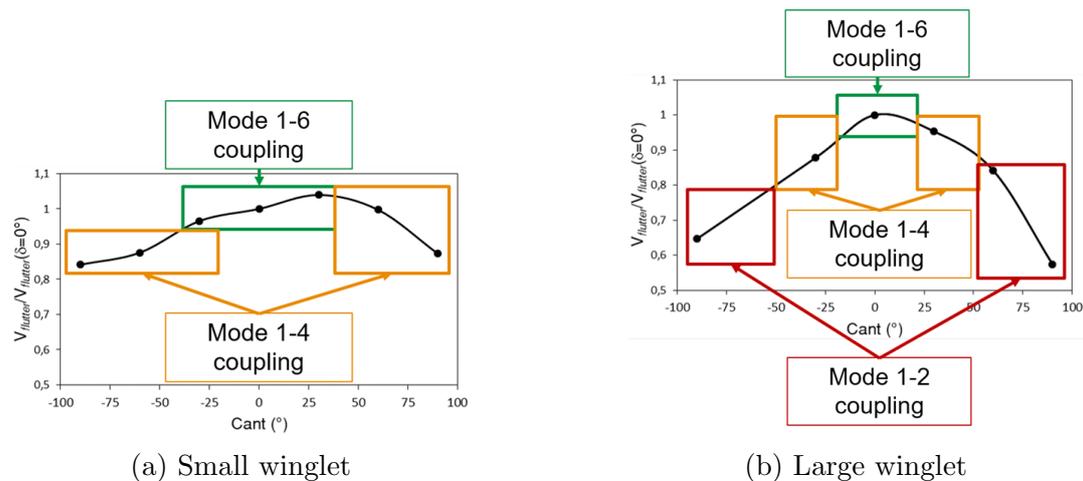
Figure 19: Flutter speed variation with cant angle for two active winglet sizes.

with optimised winglet. It reveals that the similar fuel savings are achievable with this technology independently of the configuration considered. This benefits are much lesser than those found in the literature so far. The explanation lies in the consideration of static aeroelastic deformation in this study while the technology was only assessed through aerodynamic computation. It is shown that wing deformation plays a center role in the variation of lift on the winglet and consequently on its distribution over the wing. Particularly it is demonstrated that for flexible wings winglet is less loaded for small cant angles than large ones leading small variation of lift when the winglet folds. The drag sensitivity to cant is then reduced and so does the device efficiency. This paper also analyses the implication of folding a winglet on flutter onset. It is shown that mode sequence is profoundly affected by the variation of winglet cant angle. It results that the torsion mode frequency drops as winglet folds. This favours coupling with bending modes and degrade the flutter stability. It is particularly shown that critical speed drops by 20 to more than 35% depending on the moveable part size.

REFERENCES

[1] L. Prandtl. Theory of lifting surfaces. Technical Note 9, NACA, 1920.

[2] R. Faye, R. Laprete, and M. Winter. Blended winglet for improved airplane performance. *Boeing Aero Magasin*, (17):16–31, 2002.

[3] R. T. Whitcomb. A design approach and selected wind-tunnel results at high subsonic speed for wing-tip mounted winglets. Technical Note 8260, NASA Langley Research Center, 1976.

[4] A. Castrichini, V. H. Siddaramaiah, D. E. Calderon, J. E. Cooper, T. Wilson, and Y. Lemmens. Preliminary investigations of use of flexible folding wing tips for static and dynamic load alleviation. *The Aeronautical Journal*, 121(1235):73–94, 2016. doi:10.1017/aer.2016.108.

[5] W. R. Kruger, J. Dillinger, R. D. Breuker, and K. Haydn. Investigations of passive wing technologies for load reduction. *CEAS Aeronautical Journal*, 10(4):77–93, 2019. doi:10.1007/s13272-019-00393-2.

Martin Delavenne, Bernard Barriety, Fabio Vetrano, Valérie Ferrand and Michel Salaün

[6] G. Moy, C. E. Jokisch, M. S. Good, M. J. Gardner, M. E. Renzelmann, and J. C. Houten. Folding wing system, 2017. US Patent 2017/0349296.

[7] R. P. Liem, G. K. W. Kenway, and J. R. R. A. Martins. Multimission aircraft fuel-burn minimization via multipoint aerostructural optimization. *AIAA Journal*, 53(1): 104–122, 2014. doi:10.2514/1.J052940.

[8] S. Vasista, L. Tong, and K. C. Wong. Realization of morphing wings: A multidisciplinary challenge. *Journal of Aircraft*, 49(1):11–28, 2012. doi:10.2514/1.C031060.

[9] D. A. Burdette, G. K. Kenway, and J. R. R. A. Martins. *Aerostructural design optimization of a continuous morphing trailing edge aircraft for improved mission performance.* 2016. doi:10.2514/6.2016-3209.

[10] N. Nguyen, U. Kaul, S. Lebofsky, E. Ting, D. Chaparro, and J. Urnes. *Development of Variable Camber Continuous Trailing Edge Flap for Performance Adaptive Aeroelastic Wing.* 2015. doi:10.2514/6.2016-3209.

[11] C. Concilio and L. Lecce. Historical background and current scenario. *Morphing Wing Technologies*, 49(1):3–84, 2012.

[12] B. Barriety. Aircraft with active control of the warping of its wings, 20104. US Patent 62827314B2.

[13] M. Delavenne, B. Barriety, F. Vetrano, V. Ferrand, and M. Salaun. *Parametric Analysis of an Active Winglet Concept for High Aspect Ratio Wing Using CFD/CSM Computations.* 2020. doi:10.2514/6.2020-2662.

[14] M. Delavenne, B. Barriety, F. Vetrano, V. Ferrand, and M. Salaun. *A Static Aeroelastic Analysis of an Active Winglet Concept for Aircraft Performances Improvement*, pages 77–82. Springer Singapore, Singapore, 2020. ISBN 978-981-33-4960-5.

[15] M. Delavenne, B. Barriety, F. Vetrano, V. Ferrand, and M. Salaun. Assessment of the efficiency of an active winglet concept for a long-range aircraft. *CEAS Aeronautical Journal*, 11(4):971–990, 2020. doi:10.1007/s13272-020-00465-8.

[16] J. E. Cooper, I. Chekkal, R. Cheung, C. Wales, N. J. Allen, S. Lawson, A. J. Peace, R. Cook, P. Standen, S. D. Hancock, and G. M. Carossa. Desing of a morphing wingtip. *Journal of Aircraft*, 52(5):1394–1403, 2015. doi:10.2514/1.C032861.

[17] G. K. W. Kenway and J. R. R. A. Martins. High fidelity aerostructural optimization of the airbus xrf1 aircraft configuration. Technical report, Airbus Operations SAS, 2016.

[18] *Technical documentation of the DLR TAU-Code release 2013.1.0.* Deutsches Zentrum fur Luft und Raumfhart, 2013.

[19] R. Thormann and M. Widhalm. Linear-frequency-domain predictions of dynamic-response data for viscous transonic flows. *AIAA Journal*, 51(11):2540–2557, 2013. doi:10.2514/1.J051896.

Martin Delavenne, Bernard Barriety, Fabio Vetrano, Valérie Ferrand and Michel Salaün

[20] G. X. Dussart, M. M. Lone, C. O'Rourke, and T. Wilson. *In-flight Folding Wingtip System: Inspiration from the XB-70 Valkyrie.* 2019. doi:10.2514/6.2019-1855.

[21] M. Software. Msc nastran, multidisciplinary structural analysis. Website, 2021. URL `https://www.mscsoftware.com/fr/product/msc-nastran`.

[22] H. J. Hassig. An approximate true damping solution of the flutter equation by determinant iteration. *Journal of Aircraft*, 8(11):885–889, 1971. doi:10.2514/3.44311.

[23] A. I. J. Forrester, A. Sóbester, and A. J. Keane. *Constructing a Surrogate*, chapter 2, pages 33–76. John Wiley & Sons, Ltd, 2008. doi:10.1002/9780470770801.ch2.

[24] D. R. Jones. A taxonomy of global optimization methods based on response surfaces. *journal of Global Optimization*, 21(4):345–383, 2001. doi:10.1023/A:10127710255751.

COMPUTATIONALLY EFFICIENT APPROXIMATE BUCKLING AND POSTBUCKLING ANALYSIS OF PRISMATIC COMPOSITE STRUCTURES

Jakob C. Schilling[1]* and Christian Mittelstedt[1]

1: Institute for Lightweight Construction and Design
Department of Mechanical Engineering
Technical University of Darmstadt
Otto-Berndt-Str. 2, 64287 Darmstadt, Germany
jakob.schilling@klub.tu-darmstadt.de, https://www.klub.tu-darmstadt.de

Abstract. *In order to optimize the design of structures of aircraft and space vehicles in preliminary stages, highly computationally efficient analysis methods are needed. Therefore, a closed-form approximate model is proposed that describes the stability behavior of prismatic composite structures. An example for such a structural element is an omega-stringer-stiffened panel that is currently used in the design of aircraft fuselages. The closed-form analysis is achieved by energy methods and aims to describe the stability behavior in the region of the bifurcation point approximately. The loadcase is limited to uniaxial compression. The results are compared to numerical methods. The introduced computational model offers the opportunity to fully utilize the potential of optimization by a highly efficient approximate analysis method.*

Keywords: Buckling, Composites, Postbuckling, Analytical, Computational model

Jakob C. Schilling and Christian Mittelstedt

1 INTRODUCTION

The design and analysis of lightweight structures is especially important for aerospace applications. Because the structural elements used are typically thin-walled, the analysis of the stability behaviour is a crucial factor. The lightweight potential is increasingly exploited by more suitable analysis methods in the context of preliminary design and advanced materials such as composites made of fibre reinforced plastics (FRP). During preliminary design, often optimization algorithms are utilized and numerous design configurations are analysed. Thus, the development of computationally highly efficient computational models for the stability analysis of thin-walled structures made of advanced materials is an important topic.

A typical representative of the mentioned structures is a stiffened composite panel, e.g. of an aircraft fuselage. The stiffened panels are usually prismatic structures, i.e. structures that are an assembly of flat plates. The stability analysis for these structural elements can be divided into the analysis of the linear buckling behaviour and the geometrically nonlinear postbuckling behaviour. A general overview of analysis methods is given by Ni et al. [1]. The present work is focussed on closed-from analytical computational models that approximate the postbuckling behaviour of composite panels. For single plates with different boundary conditions several works are available in literature that develop such closed-form solutions on the basis of different buckling shape functions [2–7]. The present computational method deals with a simplified omega-stringer-stiffened panel,
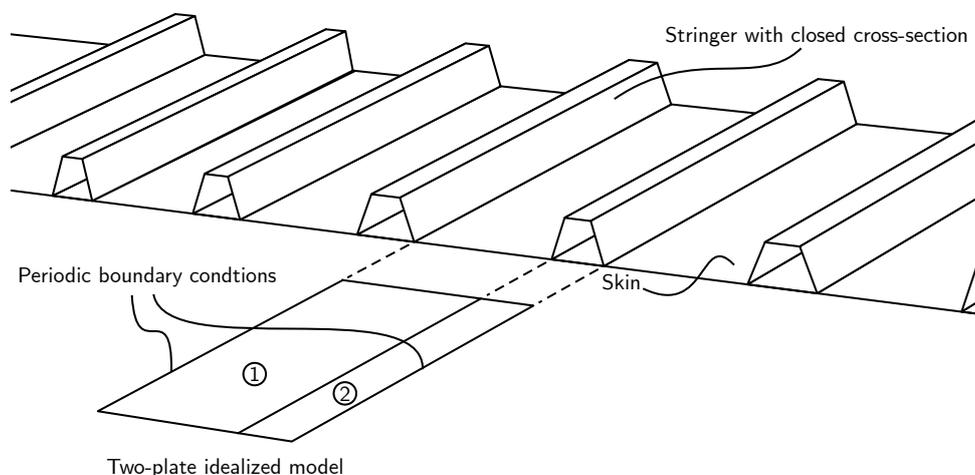
Figure 1: Omega-stringer-stiffened panel with periodic boundary conditions and the idealized two-plate model

that is reduced to an assembly of two adjacent plates with periodic boundary conditions as presented in Fig.1. Models so far usually approximate the behaviour by a single plate with elastic restraints along the longitudinal unloaded edges with spring stiffnesses representing the influence of the stringers [8]. Beerhorst extended the approach to an I-stringer stiffened panel consisting of two infinitely long plates [6]. The present approach allows to model the local buckling and postbuckling behaviour of the full skin of the omega-stringer-stiffened panel conservatively as the rotational restraint of the stringers is neglected. Thus, it allows the modelling of the problem of periodically repeating non-equidistant supports typical for panels reinforced with stringers with closed cross-sections. To address the lack of highly efficient computational models for prismatic plate assemblies the present model

Jakob C. Schilling and Christian Mittelstedt

is introduced.

The present closed-form analytical model consists of two parts. First the local linear buckling behaviour is analysed in order to obtain the bifurcation state of the structure. This is the foundation for the following postbuckling analysis. Both, the linear and nonlinear solution are derived based on energy methods. The total elastic potential of the plate assembly is computed and the critical buckling load and the postbuckling amplitude are formulated using the principle of the minimum of the potential energy. The postbuckling amplitude is hereby valid for low load proportionality factors, as the postbuckling mode is the buckling mode from the linear analysis and mode changes can not be modelled. Both steps are based on the constitutive law of the classical laminated plate theory. For the nonlinear problem van Kármán strains are incorporated. For these fundamentals, the reader is referred to suitable textbooks like Ref. [9–11]

The results obtained for the described model are compared to finite element analyses (FEA) and reveal good agreement for the desired field of application in preliminary design of lightweight structures. The new model is a promising first step in for the analysis of a full omega-stringer stiffened composite panel by highly computationally efficient closed-form analytical methods.

2 IDEALIZATION

The current model is an idealization of an omega-stringer-stiffened panel or other stiffened panels reinforced by stringers with closed cross-sections. The longitudinal edges of the unit cell shown in Fig.2 are modelled with periodic boundary conditions equating the moments $M_{yy,k}$ and rotations $\partial w / \partial y_k$. All edges are simply supported. The loadcase is uniaxial compression, that is controlled by the force N_{xx} in case of the linear buckling analysis in Sec. 3 and by the prescribed displacement U in the postbuckling analysis in Sec. 4. The coordinate system of each plate is located in the symmetry plane to enable
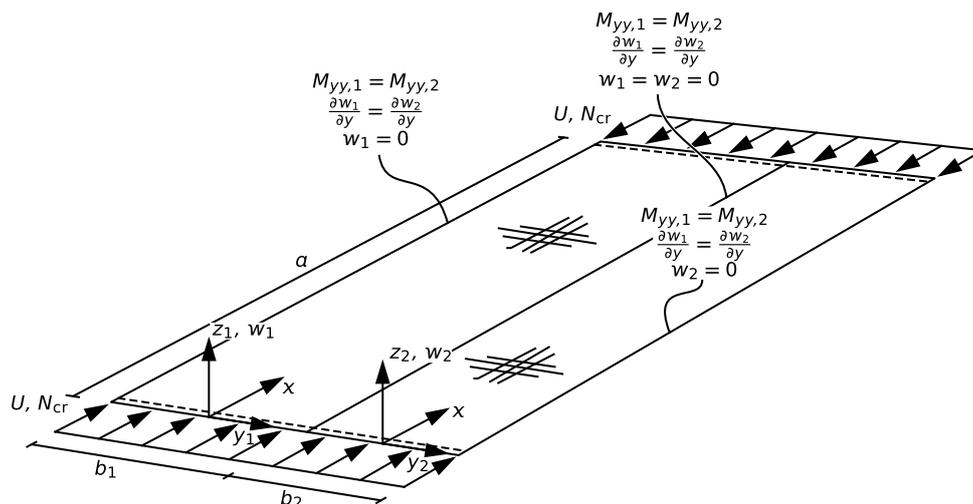
Figure 2: Example of figure.

shorter expressions especially in the postbuckling analysis. It simplifies the formulation of the airy stress function [8].

The boundary conditions of the longitudinal edges are needed in order to determine

Jakob C. Schilling and Christian Mittelstedt

suitable buckling shape functions. They are given in detail in Eq.(1).

$$w_k\left(x, y_k = \pm\frac{b_k}{2}\right) = 0$$

$$\left.\frac{\partial w_1}{\partial y_1}\right|_{y_1=\pm\frac{b_1}{2}} = \left.\frac{\partial w_2}{\partial y_2}\right|_{y_2=\mp\frac{b_2}{2}}$$

$$M_{yy,1}\left(x, y_1 = \pm\frac{b_1}{2}\right) = M_{yy,2}\left(x, y_2 = \mp\frac{b_2}{2}\right)$$

(1)

The loaded edges are simply supported as indicated in Fig.2 by the dashed lines.

3 LINEAR BUCKLING ANALYSIS

Before the postbuckling behaviour is investigated, a linear buckling analysis is performed. It will lead to an explicit closed-form expression for the critical buckling load N_{cr}, the critical half-wave number m and the ratio between the amplitudes of the two plates of the assembly.

3.1 Buckling shape functions

The buckling shape functions are assumed similar to the Ritz-method. The deflection of each plate is given by a combination of two terms that correspond to the Ritz-constants A and B expressed in Eq.(2). In contrast to the general Ritz-method, these constants are shared within the system of plates. For the current model only two constants are needed and the eigenvalue problem will be solvable in a closed-form fashion.

$$w_k = A\, w_{A,k}\left(x,\, y_k\right) + B\, w_{B,k}\left(x,\, y_k\right)$$

(2)

The buckling deformation is approximated using the polynomial functions w_{Ak} and w_{Bk} in Eq.(3).

$$w_{Ak} = \sin\left(\frac{\pi\, m\, x}{a}\right)\left(c_{A0k}\frac{{y_k}^4}{{b_k}^4} + c_{A1k}\frac{{y_k}^3}{{b_k}^3} + c_{A2k}\frac{{y_k}^2}{{b_k}^2} + c_{A3k}\frac{y_k}{b_k} + c_{A4k}\right)$$

$$w_{Bk} = \sin\left(\frac{\pi\, m\, x}{a}\right)\left(c_{B0k}\frac{{y_k}^4}{{b_k}^4} + c_{B1k}\frac{{y_k}^3}{{b_k}^3} + c_{B2k}\frac{{y_k}^2}{{b_k}^2} + c_{B3k}\frac{y_k}{b_k} + c_{B4k}\right)$$

(3)

The cofactors c_{Aik} and c_{Bik} are determined by inserting Eq.(2) into Eq.(1) and solving the resulting linear system of equations. Only the constants c_{A0k} and c_{B0k} are predetermined. In the present case c_{A0k} is $[1,0]$ and c_{B0k} is $[0,1]$. In the longitudinal direction the buckling deformation is described by the trigonometric term that fulfils the simply supported boundary conditions along the loaded edges.

3.2 Closed-form solution

With the fully defined buckling shape functions the total elastic potential is computed based on linear strains. For each of the two plates, the internal and external contribution to the potential energy is computed, as presented in Eq.(4) and Eq.(5) introducing the substitute variables X_k, Y_k, Z_k and U_k, V_k, W_k.

$$\Pi_{\mathrm{i},k} = A^2\, X_k + A\, B\, Y_k + B^2\, Z_k$$

(4)

$$\Pi_{\mathrm{e},k} = A^2\, N_{\mathrm{cr}}\, U_k + A\, B\, N_{\mathrm{cr}}\, V_k + B^2\, N_{\mathrm{cr}}\, W_k$$

(5)

Jakob C. Schilling and Christian Mittelstedt

where

$$
X_k = \int_0^a \int_{-\frac{b_k}{2}}^{\frac{b_k}{2}} \left\{ \frac{D_{11,k}}{2} \left(\frac{\partial^2 w_{A,k}}{\partial x^2} \right)^2 + 2\, D_{66,k} \left(\frac{\partial^2 w_{A,k}}{\partial y_k \partial x} \right)^2 \right.
$$
$$
\left. + \frac{D_{22,k}}{2} \left(\frac{\partial^2 w_{A,k}}{\partial y_k^2} \right)^2 + D_{12,k} \frac{\partial^2 w_{A,k}}{\partial y_k^2} \frac{\partial^2 w_{A,k}}{\partial x^2} \right\} \mathrm{d}y_k \, \mathrm{d}x
$$

$$
Y_k = \int_0^a \int_{-\frac{b_k}{2}}^{\frac{b_k}{2}} \left\{ D_{11,k} \frac{\partial^2 w_{B,k}}{\partial x^2} \frac{\partial^2 w_{A,k}}{\partial x^2} + D_{12,k} \frac{\partial^2 w_{B,k}}{\partial y_k^2} \frac{\partial^2 w_{A,k}}{\partial x^2} + D_{12,k} \frac{\partial^2 w_{A,k}}{\partial y_k^2} \frac{\partial^2 w_{A,k}}{\partial x^2} \right.
$$
$$
\left. + 4\, D_{66,k} \frac{\partial^2 w_{B,k}}{\partial y_k \partial x} \frac{\partial^2 w_{A,k}}{\partial y_k \partial x} + D_{22,k} \frac{\partial^2 w_{B,k}}{\partial y_k^2} \frac{\partial^2 w_{A,k}}{\partial y_k^2} \right\} \mathrm{d}y_k \, \mathrm{d}x
$$

$$
Z_k = \int_0^a \int_{-\frac{b_k}{2}}^{\frac{b_k}{2}} \left\{ \frac{D_{11,k}}{2} \left(\frac{\partial^2 w_{B,k}}{\partial x^2} \right)^2 + 2\, D_{66,k} \left(\frac{\partial^2 w_{B,k}}{\partial y_k \partial x} \right)^2 \right.
$$
$$
\left. + \frac{D_{22,k}}{2} \left(\frac{\partial^2 w_{B,k}}{\partial y_k^2} \right)^2 + D_{12,k} \frac{\partial^2 w_{B,k}}{\partial y_k^2} \frac{\partial^2 w_{B,k}}{\partial x^2} \right\} \mathrm{d}y_k \, \mathrm{d}x
$$

$$
U_k = \int_0^a \int_{-\frac{b_k}{2}}^{\frac{b_k}{2}} -\xi \frac{1}{2} \left(\frac{\partial w_{A,k}}{\partial x} \right)^2 \mathrm{d}y_k \, \mathrm{d}x \qquad W_k = \int_0^a \int_{-\frac{b_k}{2}}^{\frac{b_k}{2}} -\xi \frac{1}{2} \left(\frac{\partial w_{B,k}}{\partial x} \right)^2 \mathrm{d}y_k \, \mathrm{d}x
$$

$$
V_k = \int_0^a \int_{-\frac{b_k}{2}}^{\frac{b_k}{2}} -\xi \frac{\partial w_{A,k}}{\partial x} \frac{\partial w_{B,k}}{\partial x} \mathrm{d}y_k \, \mathrm{d}x
$$

Equation 6 shows the total elastic potential that is obtained adding the contributions of the individual plates.

$$
\Pi = \sum_{k=1}^2 (\Pi_{\mathrm{i},k} + \Pi_{\mathrm{e},k}) = A^2 \left(\sum_{k=1}^2 X_k + N_{\mathrm{cr}} \sum_{k=1}^2 U_k \right)
$$
$$
+ A\,B \left(\sum_{k=1}^2 Y_k + N_{\mathrm{cr}} \sum_{k=1}^2 V_k \right) + B^2 \left(\sum_{k=1}^2 Z_k + N_{\mathrm{cr}} \sum_{k=1}^2 W_k \right) \tag{6}
$$

The expression is further simplified by introducing the substitute variables $\Gamma_{1,2,3}$ and $\alpha_{1,2,3}$ leading to Eq.(7).

$$
\Pi = (\Gamma_1 + \alpha_1 N_{\mathrm{cr}})\, A^2 + (\Gamma_3 + \alpha_3 N_{\mathrm{cr}})\, A\,B + (\Gamma_2 + \alpha_2 N_{\mathrm{cr}})\, B^2 \tag{7}
$$

After using the principle of the minimum of the total elastic potential, which requires the first variation of the potential to vanish with respect to the Ritz-constants A and B, the eigenvalue problem can be solved explicitly for the critical buckling load N_{cr}. The simple closed-form solution is given in Eq.(8).

$$
N_{\mathrm{cr}} = \pm \frac{\Psi_2 + \sqrt{\Psi_2^2 - 4\,\Psi_1 \Psi_3}}{2\,\Psi_1} \qquad \text{with} \qquad
\begin{aligned}
\Psi_1 &= 4\,\alpha_1 \alpha_2 - \alpha_3^2 \\
\Psi_2 &= 4\,\Gamma_1 \alpha_2 + 4\,\Gamma_2 \alpha_1 - 2\,\Gamma_3 \alpha_3 \\
\Psi_3 &= 4\,\Gamma_1 \Gamma_2 - \Gamma_3^2
\end{aligned}
\tag{8}
$$

A more detailed description of the approach is available in Ref. [12]. Before the post-buckling analysis is derived in Sec.4, the quality of the linear buckling analysis is verified using a Lévy-type solution and FEA results.

Jakob C. Schilling and Christian Mittelstedt

3.3 Lévy-type solution

For the Lévy-type solution the buckling shape functions are exchanged. The expressions for w_1 and w_2 in Eq.(9) now represent the exact solution of the differential equation.

$$w_1\left(x, y_1\right) = \sin\left(\frac{\pi\, m\, x}{a}\right)\left(e^{\frac{\pi\, \lambda_{11}\, m\, y_1}{a}}\, C_1 + e^{\frac{\pi\, \lambda_{21}\, m\, y_1}{a}}\, C_2 + e^{\frac{\pi\, \lambda_{31}\, m\, y_1}{a}}\, C_3 + e^{\frac{\pi\, \lambda_{41}\, m\, y_1}{a}}\, C_4\right) \quad (9)$$

$$w_2\left(x, y_2\right) = \sin\left(\frac{\pi\, m\, x}{a}\right)\left(e^{\frac{\pi\, \lambda_{12}\, m\, y_2}{a}}\, C_5 + e^{\frac{\pi\, \lambda_{22}\, m\, y_2}{a}}\, C_6 + e^{\frac{\pi\, \lambda_{32}\, m\, y_2}{a}}\, C_7 + e^{\frac{\pi\, \lambda_{42}\, m\, y_2}{a}}\, C_8\right)$$

The new parameter λ_{ik} is defined for $i = 1, 2, 3, 4$ as given in Eq.(10).

$$\lambda_{ik} = \pm\sqrt{\frac{D_{12,k} + 2\,D_{66\,k} \pm \sqrt{\left(D_{12\,k} + 2\,D_{66\,k}\right)^2 - D_{22\,k}\left(D_{11\,k} - \frac{N_{11\,k}\,a^2\,\zeta_1}{m^2\,\pi^2}\right)}}{D_{22\,k}}} \quad (10)$$

The displacement functions are again inserted into the boundary conditions (Eq.(1)) and the linear system of equations in Eq.(11) is obtained with respect to the constants C_l.

$$\underline{\underline{M}}\,\underline{C} = 0 \qquad \text{with } \underline{C} = \begin{bmatrix} C_1 & C_2 & C_3 & C_4 & C_5 & C_6 & C_7 & C_8 \end{bmatrix}^T \qquad (11)$$

Now, the determinant of the coefficients matrix is evaluated and has to vanish for a non-trivial solution. This yields a function F that is implicitly depending on N_{cr}.

$$\det \underline{\underline{M}} = 0 \qquad\qquad F\left(N_{cr}\right) = 0 \qquad (12)$$

The critical buckling load can not be obtained explicitly. The implicit solution needs to be solved by a numerical strategy that involves the iteration of the critical buckling load in feasible regions.

3.4 Comparison to Lévy-type solution and FEA

The closed-form analytical solution for the linear buckling problem is in very good agreement with the Lévy-type solution and the FEA. The numerical results presented in Tab.1 reveal that the closed-form analytical method yields values with deviations below $0.2\,\%$ relative to the FEA. Furthermore, the Lévy-Solution confirms and verifies the obtained values. The verification of the linear buckling analysis supports the expectation

Table 1: Verification for a configuration with $a = 500\,\mathrm{mm}$, $b_1 + b_2 = 300\,\mathrm{mm}$ and an identical layup in both plates with the stacking sequence $[0°\ 90°\ 0°\ 90°]_\mathrm{s}$; $E_1 = 157000\,\mathrm{MPa}$; $E_2 = 8500\,\mathrm{MPa}$; $G_{12} = 4200\,\mathrm{MPa}$; $\nu_{12} = 0.35$; $t_\mathrm{ply} = 0.184\,\mathrm{mm}$

b_1/b_2	Closed-form		Lévy-type		FEA
	N_{cr}	Error	N_{cr}	Error	N_{cr}
-	Nmm^{-1}	%	Nmm^{-1}	%	Nmm^{-1}
0.25	14.903	0.179	14.884	0.0535	14.876
0.50	21.139	0.107	21.127	0.0512	21.116
0.75	14.903	0.179	14.884	0.0535	14.876

that a postbuckling analysis of the basis of the chosen buckling shape functions will yield good agreement with FEA for low load proportionality factors.

Jakob C. Schilling and Christian Mittelstedt

3.5 Results relevant for postbuckling analysis

For the following postbuckling analysis, the bifurcation state of the plate assembly is required. This includes the critical half-wave number m_{cr}, which is obtained by evaluating Eq.(8), and the ratio between the amplitudes of the deflection of the individual plates $\delta_{B/A}$. The latter is defined in Eq.(13) and will be called amplitude scaling factor in the following.

$$\delta_{B/A} = \frac{B}{A} = -\frac{(2\Gamma_1 + 2N_{\mathrm{cr}}\,\alpha_1)}{(\Gamma_3 + N_{\mathrm{cr}}\,\alpha_3)} \tag{13}$$

These two parameter describe the bifurcation state sufficiently for the postbuckling analysis of the present work.

4 POSTBUCKLING ANALYSIS

The postbuckling problem can be described for each of the two plates in the assembly by the following differential equations, that are obtained after the introduction of the Airy stress function ψ_k. Eq.(14) is describing the equilibrium state for a plate with imperfections $w_{k,\mathrm{i}}$.

$$D_{11}\frac{\partial^4 w_{k,0}}{\partial x^4} + D_{22}\frac{\partial^4 w_{k,0}}{\partial y^4} + (2\,D_{12} + 4\,D_{66})\frac{\partial^4 w_{k,0}}{\partial y^2 \partial x^2} - \left(\frac{\partial^2 w_{k,0}}{\partial x^2} + \frac{\partial^2 w_{k,\mathrm{i}}}{\partial x^2}\right)\frac{\partial^2 \psi}{\partial y^2}$$
$$+ 2\left(\frac{\partial^2 w_{k,0}}{\partial y \partial x} + \frac{\partial^2 w_{k,\mathrm{i}}}{\partial y \partial x}\right)\frac{\partial^2 \psi}{\partial x \partial y} - \left(\frac{\partial^2 w_{k,0}}{\partial y^2} + \frac{\partial^2 w_{k,\mathrm{i}}}{\partial y^2}\right)\frac{\partial^2 \psi}{\partial x^2} = 0 \tag{14}$$

The second differential equation (Eq.(15)) expresses the compatibility of the in-plane strains utilizing the inverse constitutive law, i.e. the inverted extensional stiffnesses $\bar{A}_{11}$, $\bar{A}_{22}$, $\bar{A}_{22}$, and $\bar{A}_{66}$.

$$\bar{A}_{22}\frac{\partial^4 \psi}{\partial x^4} + 2\,\bar{A}_{12}\frac{\partial^4 \psi}{\partial x^2 \partial y^2} + \bar{A}_{66}\frac{\partial^2 \psi}{\partial y^2 \partial x^2} + \bar{A}_{11}\frac{\partial^4 \psi}{\partial y^4} =$$
$$\left(\frac{\partial^2 w_{k,0}}{\partial x \partial y_k}\right)^2 - \frac{\partial^2 w_{k,0}}{\partial x^2}\frac{\partial^2 w_{k,0}}{\partial y^2} - \frac{\partial^2 w_{k,0}}{\partial x^2}\frac{\partial^2 w_{k,\mathrm{i}}}{\partial y^2} + 2\frac{\partial^2 w_{k,0}}{\partial x \partial y_k}\partial^2\frac{\partial^2 w_{k,\mathrm{i}}}{\partial x \partial y_k} - \frac{\partial^2 w_{k,\mathrm{i}}}{\partial x^2}\frac{\partial^2 w_{k,0}}{\partial y^2} \tag{15}$$

The Airy stress function ψ_k that allows the formulation of the problem with just two differential equation is introduced generally in Eq.(16). The approach fulfils the in-plane force equilibriums of the plates.

$$N_{xx} = \psi_{k,yy}\,(y,\,x)\,,\ N_{yy} = \psi_{k,xx}\,(y,\,x)\,,\ N_{xy} = -\psi_{k,xy}\,(y,\,x) \tag{16}$$

In order to obtain the desired closed-form analytical solution, the buckling shape functions are taken from the linear buckling analysis (Eq.(3)) and rewritten in the form of Eq.(17). As an initial imperfection $w_{k,\mathrm{i}}$ of the plates is taken into account for the analysis, it is introduced in the same form as the buckling shape function $w_{k,0}$ describing the deformation of a perfect plate.

$$w_{k,0} = A_0\,w_{A,k}\,(x,\,y_k) + B_0\,w_{B,k}\,(x,\,y_k) \tag{17}$$
$$w_{k,\mathrm{i}} = A_\mathrm{i}\,w_{A,k}\,(x,\,y_k) + B_\mathrm{i}\,w_{B,k}\,(x,\,y_k)$$

Consequently, the amplitudes A_0, B_0 and A_i, B_i are introduced. Before a solution for the postbuckling amplitude A_0 can be obtained by energy methods, the Airy stress function needs to be defined completely.

Jakob C. Schilling and Christian Mittelstedt

4.1 Airy stress function

The derivation of the Airy stress function involves the solution of the compatibility relationship expressed in Eq.(15). The solution of the problem is split in two homogeneous, $\psi_{h,1,k}$ and $\psi_{h,2,k}$, and one particular part, $\psi_{p,k}$, as given in Eq.(18).

$$\psi_k = \psi_{h,1,k} + \psi_{h,2,k} + \psi_{p,k} \tag{18}$$

Particular solution The particular solution starts with the evaluation of the right hand side of Eq.(15). Equations 17 are inserted and the simplified expression in Eq.(19) is obtained.

$$\left(\frac{\partial^2 w_{k,0}}{\partial x \partial y_k}\right)^2 - \frac{\partial^2 w_{k,0}}{\partial x^2}\frac{\partial^2 w_{k,0}}{\partial y^2} - \frac{\partial^2 w_{k,0}}{\partial x^2}\frac{\partial^2 w_{k,i}}{\partial y^2} + 2\frac{\partial^2 w_{k,0}}{\partial x \partial y_k}\frac{\partial^2 w_{k,i}}{\partial x \partial y_k} - \frac{\partial^2 w_{k,i}}{\partial x^2}\frac{\partial^2 w_{k,0}}{\partial y^2} =$$
$$= \left(A_0{}^2 + 2 A_0 A_i\right)\delta_{1k} + \left(A_0 B_0 + A_0 B_i + A_i B_0\right)\delta_{2k} + \left(B_0{}^2 + 2 B_0 B_i\right)\delta_{3k} \tag{19}$$

The substitute variables δ_{lk} for $l = 1, 2, 3$ are formulated as given in Eq.(20). The functions $O_{1,l,k}(y_k)$ and $O_{2,l,k}(y_k)$ are polynomials of various degrees.

$$\delta_{lk} = \cos\left(\frac{2\pi m x}{a}\right)[O_{1,l,k}(y_k)] + [O_{2,l,k}(y_k)] \tag{20}$$

Now, the left hand side of Eq.(15) is evaluated by introducing the following definition for the particular solution $\psi_{p,k}$ in Eq.(21).

$$\psi_{p,k} = \left(A_0{}^2 + 2 A_0 A_i\right)\omega_{1k} + \left(A_0 B_0 + A_0 B_i + A_i B_0\right)\omega_{2k} + \left(B_0{}^2 + 2 B_0 B_i\right)\omega_{3k} \tag{21}$$

The functions ω_{lk} are defined in dependency of the degree of the polynomials $O_{1,l,k}(y_k)$ and $O_{2,l,k}(y_k)$. The degree is substituted as $D_{1,l,k} = \deg(O_{1,l,k})$ and $D_{2,l,k} = \deg(O_{2,l,k})$.

$$\omega_{lk} = \cos\left(\frac{2\pi m x}{a}\right)\left[\sum_{n=0}^{D_{1,l,k}} F_{l,n+1,k}\, y_k^n\right] + \left[\sum_{n=0}^{D_{2,l,k}} F_{l,D_{1,l,k}+n+2,k}\, y_k^{n+4}\right] \tag{22}$$

Finally, the unknown cofactors F are determined by a comparison of coefficients for $l = 1, 2, 3$ using the relationship in Eq.(23).

$$\bar{A}_{22}\frac{\partial^4\omega_{lk}(x,y_k)}{\partial x^4} + \left(2\bar{A}_{12} + \bar{A}_{66}\right)\frac{\partial^2\omega_{lk}(x,y_k)}{\partial y_k^2 \partial x^2} + \bar{A}_{11}\frac{\partial^4\omega_{lk}(x,y_k)}{\partial y_k^4} = \delta_{lk}(x,y_k) \tag{23}$$

Homogeneous solution In the next step the homogeneous solution $\psi_{h,k} = \psi_{h,1,k} + \psi_{h,2,k}$ of Eq.(15) is obtained. Consequently, the problem is formulated as follows in Eq.(24).

$$\bar{A}_{22}\frac{\partial^4\psi_{h,k}}{\partial x^4} + 2\bar{A}_{12}\frac{\partial^4\psi_{h,k}}{\partial x^2\partial y^2} + \bar{A}_{66}\frac{\partial^2\psi_{h,k}}{\partial y^2\partial x^2} + \bar{A}_{11}\frac{\partial^4\psi_{h,k}}{\partial y^4} = 0 \tag{24}$$

It is solved with an exponential approach as described for example in Ref. [8] leading to the solution in Eq.(25) where only now the constants $C_{p,k}$ for $p = 1, 2, 3, 4$ need to be

Jakob C. Schilling and Christian Mittelstedt

determined by in-plane boundary conditions.

$$
\psi_{h,1,k}(x, y_k) = \cos\left(\frac{2\pi m x}{a}\right)\left(C_{1,k}\cosh(\lambda_{1,k}\, y_k) + C_{2,k}\sinh(\lambda_{1,k}\, y_k)\right.
$$
$$
\left. + C_{3,k}\cosh(\lambda_{2,k}\, y_k) + C_{4,k}\sinh(\lambda_{2,k}\, y_k)\right) \tag{25}
$$

where

$$
\lambda_{1,2,3,4,k} = \mp\frac{\pi\sqrt{2}\, m\sqrt{2\bar{A}_{12,2} + \bar{A}_{66,2} \pm \sqrt{-4\bar{A}_{11,2}\bar{A}_{22,2} + 4\bar{A}_{12,2}^2 + 4\bar{A}_{12,2}\bar{A}_{66,2} + \bar{A}_{66,2}^2}}}{\sqrt{\bar{A}_{11,2}}\, a}
$$

As this first part of the homogeneous solution is responsible for the load redistribution in the postbuckling behaviour of the structure, an additional part is needed to account for the equilibrium between externally applied constant displacements and the internal load. For this purpose $\psi_{h,2,k}$ is introduced in Eq.(26).

$$
\psi_{h,2,k}(x, y_k) = C_{5,k}\frac{y_k^2}{b_k^2} \tag{26}
$$

The constant $C_{5,k}$ is determined using the in-plane boundary condition in Eq.(27).

$$
u_k = U \qquad\qquad \text{for } x = 0, a \tag{27}
$$

The remaining necessary in-plane boundary conditions are given in Eq.(28).

$$
N_{xy}\left(x, y_k = \pm\frac{b_k}{2}\right) = 0 \qquad\qquad \left.\frac{\partial v}{\partial x}\right|_{y_k = \pm\frac{b_k}{2}} = 0 \tag{28}
$$

With the Airy stress function fully defined, the total elastic energy of the structure is computed in the next step.

4.2 Solution with the Ritz-method

The internal and external elastic potential $\Pi_{i,k}$ and $\Pi_{e,k}$ is computed for each plate individually according to Eq.(29) and Eq.(30).

$$
\Pi_{i,k} = \frac{1}{2}\int_0^a\int_{-\frac{b_k}{2}}^{\frac{b_k}{2}}\left\{\bar{A}_{22}\left(\frac{\partial^2\psi_k}{\partial x^2}\right)^2 + \bar{A}_{66}\left(\frac{\partial^2\psi_k}{\partial y_k\partial x}\right)^2 + \bar{A}_{11}\left(\frac{\partial^2\psi_k}{\partial y_k^2}\right)^2\right.
$$
$$
+ 2\bar{A}_{12}\frac{\partial^2\psi_k}{\partial x^2}\frac{\partial^2\psi_k}{\partial y_k^2} + D_{11}\left(\frac{\partial^2 w_{k,0}}{\partial x^2}\right)^2 + 4 D_{66}\left(\frac{\partial w_{k,0}}{\partial y_k\partial x}\right)^2 \tag{29}
$$
$$
\left. + D_{22}\left(\frac{\partial^2 w_{k,0}}{\partial y_k^2}\right)^2 + 2 D_{12}\frac{\partial^2 w_{k,0}}{\partial x^2}\frac{\partial^2 w_{k,0}}{\partial y_k^2}\right\}\mathrm{d}x\,\mathrm{d}y
$$

$$
\Pi_{e,k} = -U\frac{1}{b_k}\int_{-\frac{b_k}{2}}^{\frac{b_k}{2}}\frac{\partial^2\psi_k}{\partial y_k^2}\,\mathrm{d}x\,\mathrm{d}y \tag{30}
$$

Jakob C. Schilling and Christian Mittelstedt

The contributions to the total elastic potential Π are summarized (Eq.(31)).

$$\Pi = \sum_{k=1}^{2} \left\{ \Pi_{\mathrm{i},\,k} + \Pi_{\mathrm{e},\,k} \right\} \tag{31}$$

Now, the amplitudes B_0 and B_i are substituted in the total elastic potential using the amplitude scaling factor $\delta_{B/A}$ and its definition in Eq.(13). The expression is then derived with respect to A_0. This derivative yields the following expression in Eq.(32), that can be solved explicitly for A_0.

$$A_0{}^3 L_1 + A_0{}^2 A_\mathrm{i} L_2 + A_0 A_\mathrm{i}{}^2 L_3 + A_0 L_4 + A_\mathrm{i} L_5 = 0 \tag{32}$$

Here, the substitute variables L_o for $o = 1, 2, 3, 4, 5$ are introduced to simplify the expression.

5   RESULTS AND DISCUSSION

To give a first impression about the quality of the present closed-from analytical solution, load-deflection curves of both plates of the assembly are evaluated and compared to FEA results in Fig.3. The curves are given for the ratios b_1/b of 0.9, 0.75 and 0.5. The
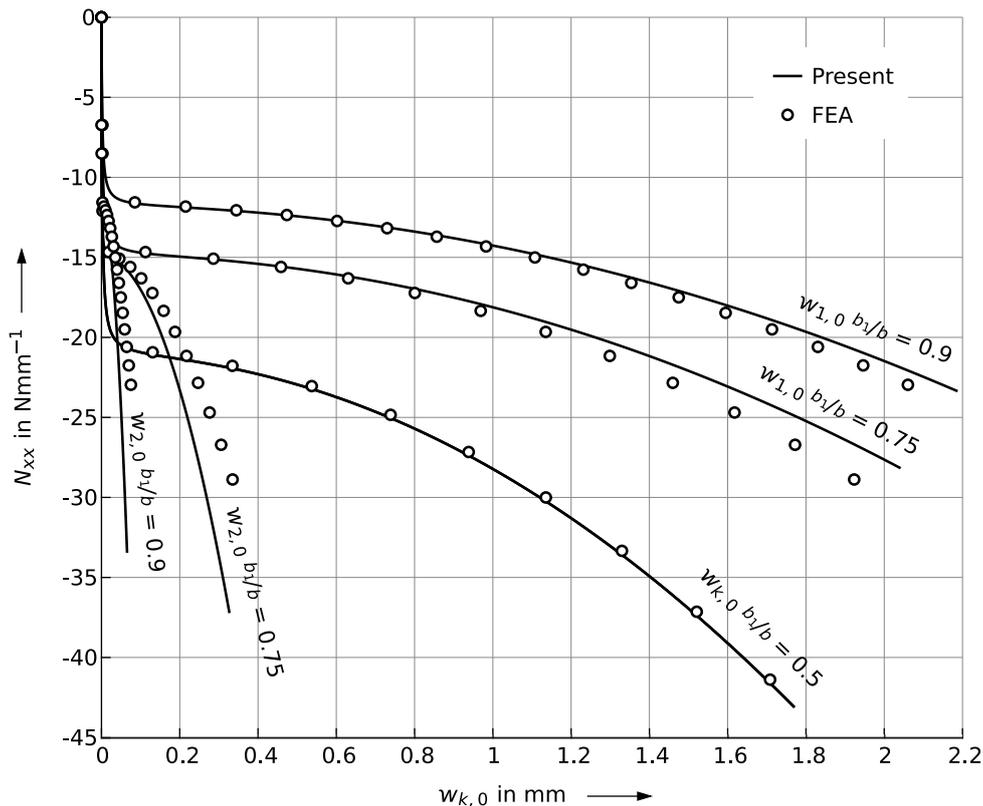
Figure 3: Postbuckling behaviour of investigated two-plate assembly for different ratios b_1/b with imperfections; $w_{k,\mathrm{i}} = 0.002$; lay-up $[0°90°0°90°]_s$; $a = 500\,\mathrm{mm}$; $b = b_1 + b_2 = 300\,\mathrm{mm}$, $E_1 = 157000\,\mathrm{MPa}$; $E_2 = 8500\,\mathrm{MPa}$; $G_{12} = 4200\,\mathrm{MPa}$; $\nu_{12} = 0.35$; $t_{\mathrm{ply}} = 0.184\,\mathrm{mm}$

last ratio equals a single plate with periodic boundary conditions. The imperfection is attributed with $w_{k,\mathrm{i}} = 0.002$ and the closed-form analytical model shows very good agreement in the area, where the imperfection is most relevant. The deviations grow with an

increasing load proportionality factor, as is to be expected in the present type of approximate analysis. Furthermore, the deviations are more distinguishable for the deflection of the smaller plate. The first results yield promising accuracy suitable for preliminary design. Nevertheless, more studies and the investigation of other parameters such as the effective width are necessary to provide more insight into the buckling behaviour and the quality of the model.

6 CONCLUSIONS

The presented computational models for the local buckling and postbuckling behaviour lead to the following conclusions.

- A new simple closed-form analytical model is successfully developed for local buckling and postbuckling analysis of a two-plate assembly with periodic boundary conditions.

- Due to their analytical nature, the new models provide a computationally efficient alternative to numerical methods with numerous degrees of freedom.

- The closed-form analytical solution for the linear buckling analysis is in very good agreement with FEA results and results of the derived Lévy-type solution.

- First results show a promising quality of the closed-form analytical model for the posbuckling behaviour in the range of low load proportionality factors.

- The quality of the postbuckling analysis needs further assessment that includes more parameter studies and the evaluation of postbuckling parameters such as the effective width.

- The results indicate that the new computational approximate models are very suitable for preliminary design.

It is planned that the approach of the postbuckling analysis is extended to the full omega-stringer-stiffened panel in future work.

ACKNOWLEDGEMENTS

REFERENCES

[1] X.-Y. Ni, B. G. Prusty, and A. K. Hellier. Buckling and Post-Buckling of Isotropic and Composite Stiffened Panels: A Review on Analysis and Experiment (2000-2012). *International Journal of Maritime Engineering*, 157:9–29, Mar. 2015. ISSN 1479-8751. doi:10.3940/rina.ijme.2015.a1.300. WOS:000370998100002.

[2] R. Chandra. Postbuckling analysis of crossply laminated plates. *AIAA Journal*, 13 (10):1388–1389, Oct. 1975. ISSN 0001-1452, 1533-385X. doi:10.2514/3.6995. URL https://arc.aiaa.org/doi/10.2514/3.6995.

[3] G. B. Chai, W. M. Banks, and J. Rhodes. The instability behaviour of laminated panels with elastically rotationally restrined edges. *Composite Structures*, 19(1):41–65, Jan. 1991. ISSN 0263-8223. doi:10.1016/0263-8223(91)90074-9. URL http://www.sciencedirect.com/science/article/pii/0263822391900749.

[4] C. Mittelstedt and K.-U. Schröder. Postbuckling of compressively loaded imperfect composite plates: closed-form approximate solutions. *International Journal of Structural Stability and Dynamics*, 10(04):761–778, Oct. 2010. ISSN 0219-4554. doi:10.1142/S0219455410003725. URL https://www.worldscientific.com/doi/abs/10.1142/S0219455410003725.

[5] M. Beerhorst, M. Seibel, and C. Mittelstedt. Fast analytical method describing the postbuckling behavior of long, symmetric, balanced laminated composite plates under biaxial compression and shear. *Composite Structures*, 94(6):2001–2009, May 2012. ISSN 02638223. doi:10.1016/j.compstruct.2012.01.026. URL https://linkinghub.elsevier.com/retrieve/pii/S0263822312000414.

[6] M. Beerhorst. *Entwicklung von hocheffizienten Berechnungsmethoden zur Beschreibung des Beul- und Nachbeulverhaltens von versteiften und unversteiften Flächentragwerken aus Faserverbundwerkstoffen.* PhD thesis, Technische Universität Berlin, Berlin, 2014.

[7] M. Quatmann and H.-G. Reimerdes. Preliminary design of composite fuselage structures using analytical rapid sizing methods. *CEAS Aeronautical Journal*, 2(1):231–241, Dec. 2011. ISSN 1869-5590. doi:10.1007/s13272-011-0025-5. URL https://doi.org/10.1007/s13272-011-0025-5.

[8] R. Vescovini and C. Bisagni. Single-mode solution for post-buckling analysis of composite panels with elastic restraints loaded in compression. *Composites Part B: Engineering*, 43(3):1258–1274, Apr. 2012. ISSN 1359-8368. doi:10.1016/j.compositesb.2011.08.029. URL http://www.sciencedirect.com/science/article/pii/S1359836811003635.

[9] R. M. Jones. *Mechanics of composite materials.* Taylor & Francis, Philadelphia, PA, 2nd ed edition, 1999. ISBN 978-1-56032-712-7.

[10] J. N. Reddy. *Mechanics of laminated composite plates and shells: theory and analysis.* CRC Press, Boca Raton, 2nd ed edition, 2004. ISBN 978-0-8493-1592-3.

[11] C. Mittelstedt and W. Becker. *Strukturmechanik ebener Laminate.* Studienbereich Mechanik, Technische Universität Darmstadt, Darmstadt, 1. auflage edition, 2016. ISBN 978-3-935868-99-0. OCLC: 969462101.

[12] J. C. Schilling and C. Mittelstedt. Local buckling analysis of omega-stringer-stiffened composite panels using a new closed-form analytical approximate solution. *Thin-Walled Structures*, 147:106534, Feb. 2020. ISSN 0263-8231. doi:10.1016/j.tws.2019.106534. URL http://www.sciencedirect.com/science/article/pii/S026382311931239X.

WINGBOX META-MODEL AND AERO-SERVO-ELASTIC OPTIMIZATION WITH NEOPT

Francesco Toffol[1]*, Sergio Ricci[1]

1: Department of Aerospace Science and Technology
Politecnico di Milano
Via La Masa 34, 20156, Milano, Italy
francesco.toffol@polimi.it, sergio.ricci@polimi.it
https://www.aero.polimi.it

Abstract *This work presents a new methodology for the description of the wingbox, suitable for the conceptual and preliminary design phases. Starting from few geometrical information, a semi-analytical model of the wingbox is realized. The wingbox is described with a stick model and its stiffness and mass properties are obtained with a cross-section finite element solver which manages isotropic and orthotropic materials. The beam properties are updated in the aero-elastic model (stick FE +VLM/DLM) which is used for the evaluation of dynamic and trim load envelopes. An optimization framework sizes the wingbox using as design variables its thicknesses, satisfying failure, buckling and flutter constraints.*
The framework is exploited to perform a sensitivity study on a long-haul aircraft, evaluating how different design choices affect the overall performances.

Keywords: Conceptual design, meta-model, multidisciplinary optimization, active control, aero-servo-elasticity

1. INTRODUCTION

Air transportation is an expanding market (+5% per year, pre COVID-19 era [1]), and with the same peace its related emissions are increasing too, recent studies foreseen an outpacing of the CO_2 emission prediction. In the context of an expanding market, aeronautic industries are asked to not only to reduce the greenhouse gases emission, but to invert their trends reaching a carbon neutral aviation by the 2050 [3]. To reach this goal, breakthrough configurations, innovative materials, biofuels and other disruptive solutions must be adopted. Concurrently, design tools must evolve to deal with these new technologies.

The aircraft's range, expressed through the Breguet's equation of Eq.(1), is a performance index which can be used to estimate the efficiency of an aircraft: extending the range with a fixed amount of fuel and payload is equivalent to fly the original range consuming less fuel, hence emitting less CO_2

$$R = \frac{V_{TAS}}{g} \left(\frac{L}{D}\right) \frac{1}{SFC} ln \left(\frac{W_{MTOW}}{W_{MTOW} - W_{FUEL}}\right) \tag{1}$$

Breguet's equation clearly identifies three areas that affect the performances of the aircraft and they are the aerodynamic efficiency L/D, the propulsive efficiency expressed through the specific fuel consumption (SFC) and a sort of structural efficiency term related to the initial aircraft mass (W_{MTOW}). Historically, the first improvement in fuel consumption [4] were achieved with the adoption of high bypass ratio (HBPR) engines on the B747 (late '60), in the '80 the diffusion of the computer and computer aided design (CAD) software, for examples in the CFD field [5], led to a new season of efficiency improvement. The latest structural improvements are reached with the adoption of composite materials (e.g. B787 and A350). Nowadays, materials and design methodologies are pushed to their limits, reaching a plateaux in the emissions reduction which can be overcome only adopting new structural configuration like the ultra-high aspect ratio wing (UHARW), the blended wing body (BWB) [6][7][8], the truss-braced wing (TBW) [9], the flying-V [10], the Prandltplane [11][12] and many other exotic ones.

The integrated nature of the aircraft design allows few configurations variation without incurring in multidisciplinary trade-offs, for example increasing the aspect ratio of the wing to achieve better aerodynamic efficiency by reducing the induced drag leads to higher bending moment which requires heavier structures to withstands the increased loads, this is reflected into a reduction of the structural efficiency. The aircraft design is a process where all the disciplines must be considered concurrently, optimizing the overall performance rather than finding the best solution for each field.

The design of a brand-new aircraft is a long and complex process and in the early design phases it is affected by a lot of uncertainty, the situation worsens when disruptive or extreme configurations are considered. The design tools must adapt to this situation, considering new technologies and materials in the design loop, discovering critical areas of the project in early design phases where it is simple and cheap to take mitigation and correction actions to the project, avoiding delay and extra costs.

Historically, the conceptual design tools are still based on statistical or analytical approach for the weight estimation, like the one proposed by Raymer [13] and Torenbeek [14]. These approaches are valid when considering classical tube-wing aluminium alloy configurations, but the spread of new composite materials, extreme configuration and active control technologies limits the validity of these methods.

In the last 15 years new design approaches to the conceptual design were developed:

PROTEUS is the toolbox implemented by TU-Delft [15], the procedure used by Bombardier is described in [16] and the one used by Gulfstresm (ATLASS) can be found in [17]. The Politecnico di Milano Department of Aerospace Science and Technology pioneered this field since the 2007, when it started the development of NeoCASS [18][19][20][21]: it is a Matlab based conceptual design environment, suitable to create low order and medium fidelity analysis models, sized with a physically based method.

NeoCASS performs a full-stress design of a stick FE model with a VLM/DLM aerodynamics, the loads used for the sizing come from aeroelastic trim manoeuvres. The design variables are the thicknesses of the components and through an analytical formulation the beams stiffness and mass matrices are computed. The secondary masses evaluation is performed on the base of statistical methods [22].

NeoCASS has some shortcomings that limit its validity: despite it implements a finite volume beam model [23] that allows to exploit the full beam stiffness matrix (6x6), it computes only the diagonal terms (EA,GA,GJ,EJ) and the extra diagonal terms due to the neutral axis and shear centre offsets with respect to the nodal line, this formulation loses its validity when composite materials are used and the coupling term introduced by them must be considered e.g. to account for the aeroelastic tailoring wash in/out effect.

Moreover, the wingbox's model used in the sizing process is rectangular and symmetric in term of material distribution. Lastly, the sizing is performed considering only static trim manoeuvres, neglecting the dynamic conditions (e.g. gust) and the flutter, which could jeopardize the aircraft safety.

The achievement of the last 70 years in the active control theory and application [25][26] shows how the structural efficiency can be improved by the usage of active technologies.

These aspects must be considered since the early design phases for two reasons: 1) the aero-servo-elastic criticalities must be investigated and faced in the early design phases, where the cost of implementing mitigation and correction actions is still low 2) active control technologies and composite materials must be exploited since this phase to fully take advantage of their potential.

This work proposes a novel aero-servo-elastic optimization framework, named NeOPT, which aims to bridge the gap of NeoCASS's shortcomings. Thanks to development of the wingbox's meta-model, the accuracy of the stick FEM is improved and implemented in an optimization loop able to manage multiple simulations (trim, flutter and dynamic gusts), exploiting composite materials and active control technologies.

2. THE WINGBOX META-MODEL

To provide a better description of the wingbox, the first improvement is related to its geometrical description: NeoCASS and other meta-models, for example the one used in [27], represent the structure with a rectangular section where the spars height is the mean value of the front and rear ones, moreover the skins curvature is not accounted in the properties and stress evaluation. To achieve a better geometrical description of the wingbox, its external surfaces is intersected with a set of planes normal to the beam axis as in Figure 1 (a), which represent the ribs. The obtained ribs outer limits are intersected once more with a set of planes identifying the stringers, which can be parallel to the front or rear spar, or parallel to the beam axis. The result of this intersection procedure is a cloud of 3D points that represents the connection points among the different structural elements as in Figure 1 (b) shows.

F.Toffol, S.Ricci

(a) Example of ribs planes   (b) Stringers and ribs skeleton
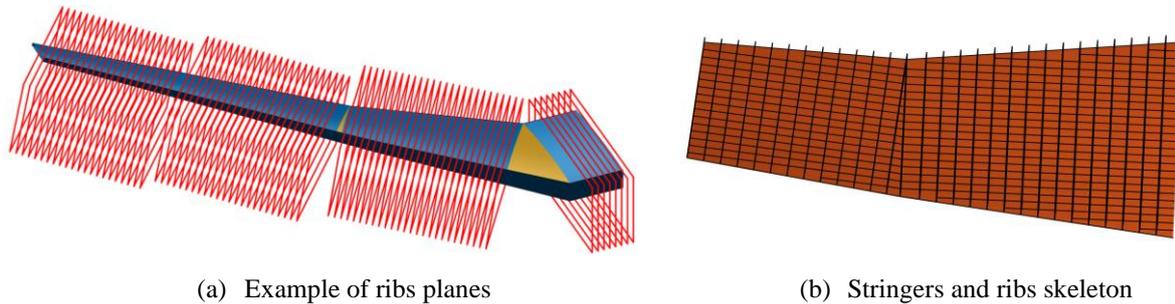
Figure 1: example of ribs planes and structural elements connection points

The connections among the intersection points identify the structural elements, and their structural properties in term of thickness and material are provided. In this way the wingbox is fully described with a semi-analytical representation called meta-model. The 3D points can be rearranged to obtain different analysis model e.g. by using the connectivity in chord-wise direction it is possible to generate a 2D sectional mesh used by a cross-sectional solver (Figure 2(a)), the overall connectivity generates a detailed 3D FE model of the wingbox with arbitrary mesh refinement along chord, span and spar height (Figure 2(b)).

(a) Cross-section 2D mesh   (b) Wingbox 3D FE
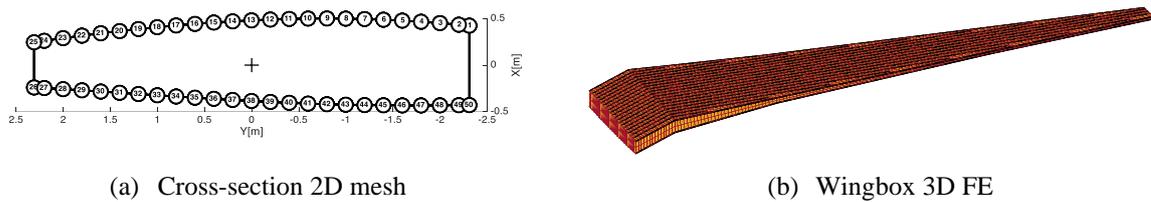
Figure 2: models generated by the metamodel.

Another model that can be generated by the meta-model is the CAD of the wingbox in IGES or CATIA format. The pivotal role of the meta-model with respect to the analysis models and results is represented by Figure 3, highlighting how it is more than a simple database of geometrical and structural information, it preserves the analytic connection between heterogenous model without losing information i.e. a modification of a structural properties is automatically mapped in all the domains.
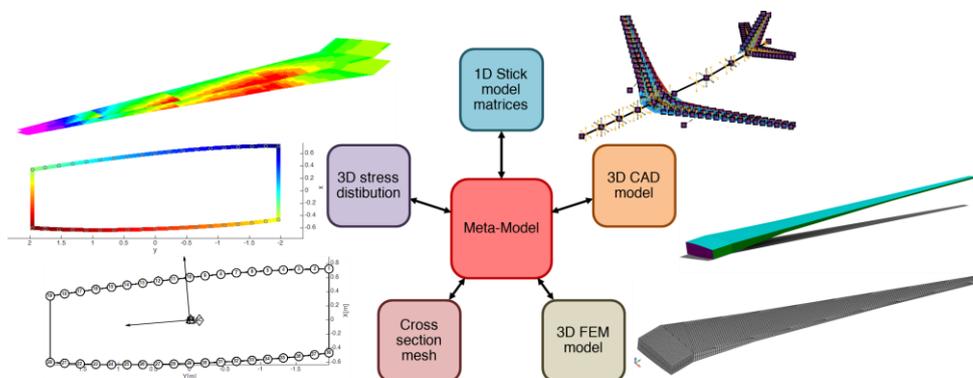
Figure 3: Pivotal role of the meta-model

2.1. NeoANBA

One of the shortcomings of NeoCASS is the lack of accuracy in the correct evaluation of the cross-sectional properties. The terms of the beam matrix are obtained multiplying the geometric properties of the section (A, J, J_t) by the elastic and shear modulus of the material.

$$K = \begin{bmatrix} G \times A_x & & & & & G \times A_x \times X_{SC} \\ & G \times A_y & & & & -G \times A_x \times X_{SC} \\ & & E \times A & -E \times A \times X_{NA} & E \times A \times Y_{NA} & \\ & & & E \times J_{xx} & & \\ & SYM & & & E \times J_{yy} & \\ & & & & & G \times J_t \end{bmatrix} \tag{2}$$

Since an analytic, efficient and accurate method for the evaluation of thin walled and orthotropic hollow section full stiffness matrix is not available, the adoption of a numerical procedure is required. The problem was faced back in the '80, when several models for the cross-section analysis were developed e.g. VABS [28] and ANBA [29], this work follows the approach proposed in the second formulation, calling the new version NeoANBA (NeoCASS + ANBA) [30]. It is a finite elements method cross-sectional solver which assumes that the displacement of a point is described by the sum of a reference line rigid displacement **r** and a warping term **g**, as shown in Figure 4 and described by Eq.(3).
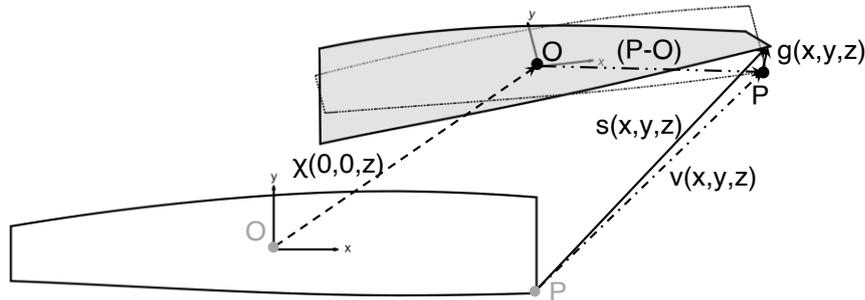
Figure 4: displacement components of a cross section arbitrary point

$$\boldsymbol{S}(x,y,z) = \boldsymbol{\chi}(z) + [(\boldsymbol{P} - \boldsymbol{O}) \times^T]\boldsymbol{\varphi}(z) + \boldsymbol{g}(x,y,z) = \boldsymbol{v}(z) + \boldsymbol{g}(x,y,z) \tag{3}$$

The finite element method is used to approximate the warping field, the unknowns become the warping of the nodes $g = \boldsymbol{Na}$. Exploiting the virtual work principle, it is possible to obtain the description of the internal and external work and to write a linear system which solution provides the cross-section stiffness matrix and the strains, hence stresses through the constitutive law, for unit loads. The current implementation of NeoANBA has only two type of elements: the stringer which considers only the axial stress and the flat panel which considers axial stress and transverse shear, these elements are sufficient to fully characterize the behaviour of a thin walled hollow section.

The full validation and mathematical description can be found in [30]. To demonstrate the capability of the tool, a comparison between the results obtained with a Nastran GFEM and the NeoCASS (meta-model + NeoANBA) is hereafter presented.

The composite rectangular wingbox of Figure 5 is fully realized in unidirectional CFRP and the upper and lower skin's panels have an anti-symmetric orientation of 30° with respect the

beam axis.
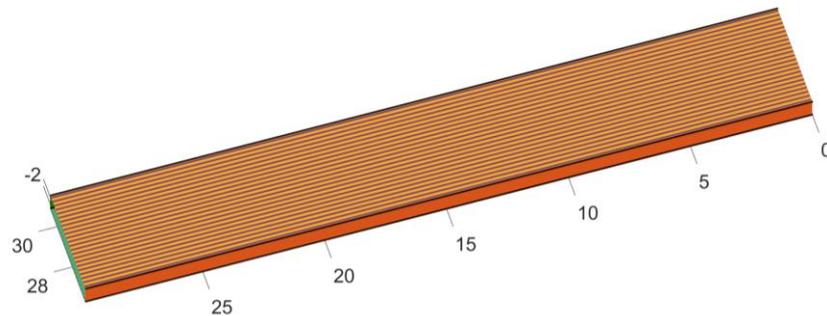
Figure 5: Rectangular wingbox

This kind of lamination creates a bending-torsion coupling, which means that an out of plane bending load, e.g. lift force, generates a torsion around the beam axis and vice-versa.

Figure 6 shows the results in term of displacement obtained for the two models: Figure 6(a) represents the out of plane displacement obtained for an out of plane load (z direction for both load and displacement) and the results obtained are similar, Figure 6(b) shows the rotation around the beam axis obtained for a force in out-of- plane direction (z direction for the force, rotation around y). In this case the discrepancies between the two models are concentrated at the wing root, where the constraints applied to the GFEM stiffen the structure reducing the torsion nearby the clamp, in the spanwise direction the offset between the two models is constant, meaning that the difference is due to a local phenomenon concentrated at the wing root.

(a) Out of plane displacement for out of plane force

(b) Torsion around beam axis for out of plane force
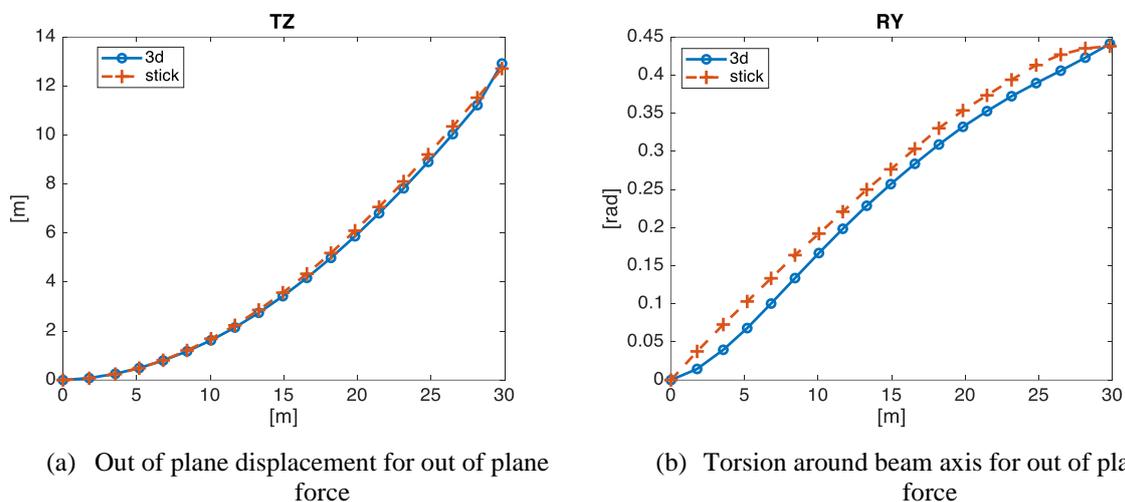
Figure 6: Bending-coupling effect introduced by anti-symmetric lamination of the skins.

Another quantity which can be recovered by both the models is the stress distribution, represented in Figure 7: the cross-cross section stress distribution obtained with NeoANBA, and expanded in 3D with the meta-model, well matches the one obtained with the GFEM.
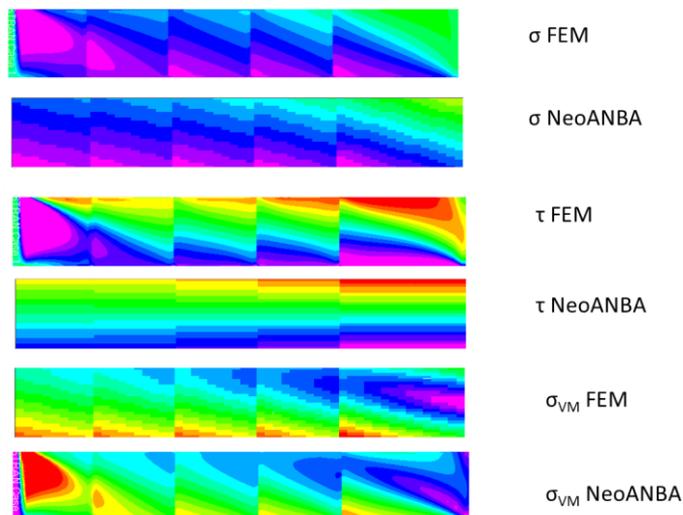
Figure 7: Comparison of the stress distribution

Since the panels used in NeoANBA consider only axial stress and transverse shear, only these components are compared. The global stress pattern is well matched, some discrepancies are present in the boundary regions (constraints and loads) and nearby the properties discontinuity. It must be pointed out that the GFEM is made of more than 20000 nodes while the stick model used by the meta-model has less than 20 nodes.

The proposed meta-model shows how it is possible to improve the characterization of the wingbox without increasing the complexity of the model, providing an improved description of the component which account for the effects introduced by orthotropic materials, exploiting their potential since the early design phases. Moreover, the automatic generation of the detailed 3D FE and CAD models, speeds up the design process providing higher fidelity and ready to use models to the next design phases, without losing the coherence with the stick representation of the aircraft which is still the reference model used for the load envelope computation and aeroelastic simulation.

3. ACTIVE CONTROL

Another important aspect that must be considered in the design process is the interaction between the structures, aerodynamics and control system. The holistic nature of the aero-servo-elasticity suggests that the control system must be designed concurrently to the structure, to fully consider their coupling and exploits possible benefits in term of loads reduction and mass saving. For this reason, an easy but robust and general procedure, suitable to be implemented in an optimization, must be developed. There is a whole literature of methods related to the control of flexible aircraft, but in the conceptual design phases is more important to evaluate the impact of a controller rather than achieve the best performance.

The control design method hereafter proposed is based on the Static Output Feedback structure [31], its simplicity makes this kind of regulator easy to be implemented. The control input $\mathbf{u}$ is a linear combination of the measure $\mathbf{y}$: $\boldsymbol{u} = -\boldsymbol{G}\boldsymbol{y}$, it is a sub-optimal method and there is not an analytical solution for the problem e.g. the Riccati equation for optimal control [32], for this reason the $\mathbf{G}$ gain matrix must be defined with a numerical procedure.

Among the solutions available in NeoCASS, there is the possibility to realize the State-Space model of the system and operate in continuous time domain [33][34], leading to the representation of Eq.(4).

F.Toffol, S.Ricci

$$
\begin{cases}
\dot{x} = Ax + B_u u + B_d d \\
y = C_y x + D_{yu} u + D_{yd} d \\
z = C_z x + D_{zu} u + D_{zd} d
\end{cases}
\tag{4}
$$

The gain matrix is obtained performing an optimization with the Matlab's fmincon, where the design variables are the elements of **G**, the objective function **f** is a weighted sum of the ratio between the closed and open loop performances **z** as in Eq.(5), and the constraints are the stability of the closed loop system and additional user defined and case-specific e.g. the technological limitation of the actuation system.

$$
f(x) = \sum_{i=1}^{N} \frac{max\ (|z_i(x,t)|)}{max\ (|z_{io}(x_0,t)|)}
\tag{5}
$$

The procedure can be exploited to design different controllers for different purposes, like for active flutter suppression (AFS) or a Gust Load Alleviation (GLA). Two applications of the methodology can be found in [30], one applied to the design of a GLA device and another one devoted to the AFS of a wind tunnel model. The results obtained show the soundness of the proposed approach.

4. THE OPTIMIZATION FRAMEWORK

The contents discussed in Sec.2 and Sec.3 enhance the analysis capability of NeoCASS. To fully exploit their potential, they are encompassed in an optimizer named NeOPT. This is a package that performs the refinement of the solution obtained with NeoCASS in the GUESS module, which is used as initial guess. The position of NeOPT inside NeoCASS is illustrated by Figure 8.

(a)   (b)
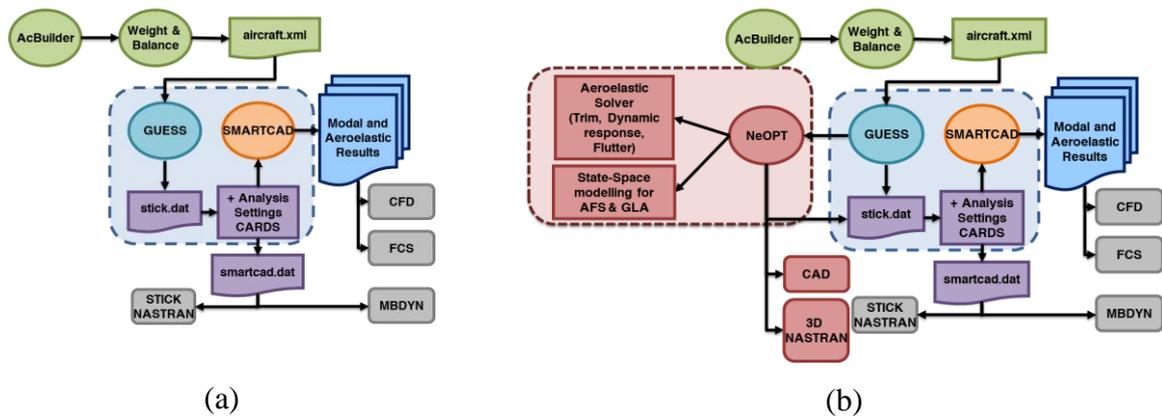
Figure 8: Difference between NeoCASS standard procedure and NeOPT

The optimizer exploits Matlab's fmincon [35], which is a gradient-based optimizer where the gradient is numerically computed.

The optimization flowchart of the procedure is shown in Figure 10, the design variables of are the thicknesses of the skins, spar webs, spar caps and stringers, the last two have a L and T shape with width and height proportional to the thickness. To limits the number of design variables. a two-level linking strategy is adopted. The first level acts on the cross section, where the user can choose the typology of the section, it can have from 4 to 12 variables: the simplest section has a symmetric distribution of the materials i.e. that the thickness of upper

F.Toffol, S.Ricci

and lower elements is equal, as well as the front and rear ones. With the increase of the design variables the symmetry is broken, decoupling the thicknesses of the elements. The second linking is performed in spanwise direction: the variables are constant on a user defined patch bounded by two ribs. The number of design variables for the optimization problem is the number of section variables multiplied by the number of patches.

When composite materials are considered, the stacking sequence in term of ply % thickness and orientation are user provided, the only parameters affected by the optimization are the thickness of the laminate and its global orientation with respect to the beam axis.

$\theta = +0.00°, \ thk = 0.15\%$

$\theta = +45.00°, \ thk = 0.15\%$

$\theta = -45.00°, \ thk = 0.15\%$

$\theta = +90.00°, \ thk = 0.05\%$
$\theta = +90.00°, \ thk = 0.05\%$

$\theta = -45.00°, \ thk = 0.15\%$

$\theta = +45.00°, \ thk = 0.15\%$

$\theta = +0.00°, \ thk = 0.15\%$
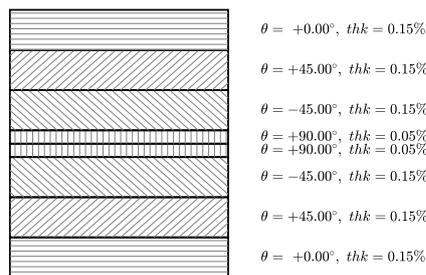
Figure 9: Example of stacking sequence
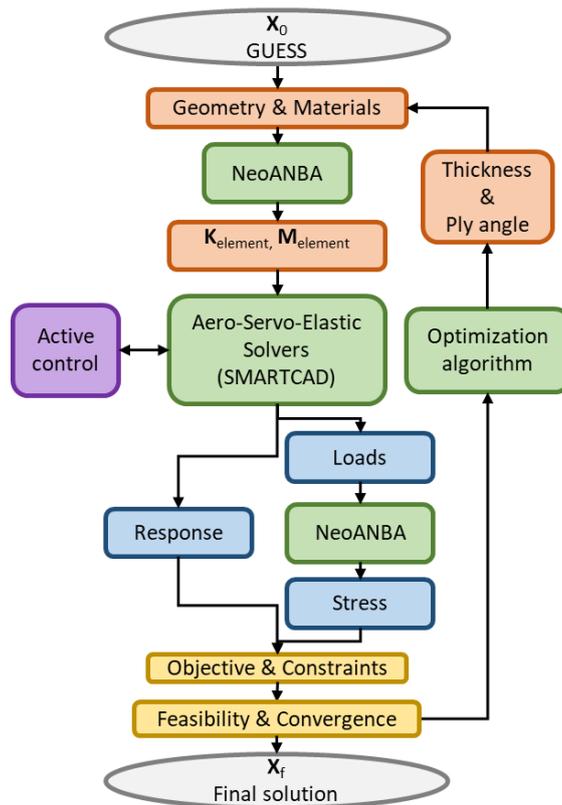
Figure 10: NeOPT flowchart

The constraints imposed to the optimizer are of two types: the first are structural the second are related to analysis response.

The structural constraints impose that no failure nor buckling affect the structure, for both the cases the internal forces obtained with aeroelastic analysis are translated into cross-sectional

F.Toffol, S.Ricci

stress distribution through the meta-model. The failure of each component is evaluated with the Von Mises criterion for isotropic materials and with the Tsai-Hill criterion for the laminates.

Four buckling mechanisms are considered: single panel buckling, stringer buckling, stringer web buckling and global panel buckling. The analytical approach used is the one described in [36][37] and it allows to deal with iso and orthotropic material in the same way.

Thanks to the opensource nature of the code and to its flexibility, it is possible to use whichever analysis response as objective or as constraint. Typical analysis responses used as constraints are the damping of the aero-elastic modes obtained with flutter solution, which is imposed to be positive across the flight envelope. Other examples of responses that can be considered are the aileron efficiency or the elevator deflection in levelled flight. The default objective function is the mass of the wingbox, but it can be easily modified in whichever available response.

The aeroelastic analyses which can be simultaneously considered in the optimization loop are: trim manoeuvres, flutter and dynamic excitation (gust, control surfaces, external load) with or without the active control.

5. APPLICATION OF NEOPT

The optimizer described in the previous chapter is here exploited to perform a sensitivity and trade-off study on a twin-aisle long-haul (TALH) aircraft, designed from scratch on the basis of the Airbus A330-300 public available data [38] reported in Table 1. The flight envelope consider is represented in Figure 11

Table 1 TAHL general data

Passengers	300
Wing Area	366.7 m^2
Aspect Ratio	9.17
Range 10200 km	(5500Nm)
Max cruise altitude	13100m (43kft)
Max Operative Mach	0.87
Max Operating Speed(EAS)	175m/s (340 kt)
Cabin Altitude	2440m (8000ft)
TAS cruise 38kft	244.91m/s
EAS cruise	127.5m/s
Max CL TO	2.1
Max CL LND	2.5
Clean MAx CL	1.75
Clean CL slope	5.7/rad
Flap TO	15°
Flap LND	25°
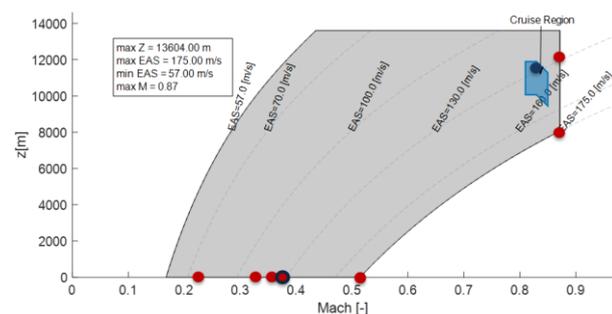
Figure 11 TAHL flight envelope

The objective of the study is to understand how different materials and aspect ratio affect the performance of the aircraft; the wing is stretched keeping fixed its surface to understand how much it is possible to improve the aerodynamic performance without paying too much from the structural point of view. The planar shapes considered and their span values are reported

in Figure 12 and Table 2
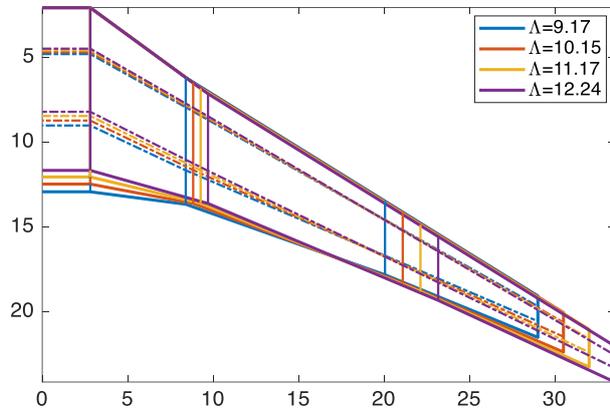
Figure 12: Wings planar shape

Table 2: Wings span and aspect ratio

Span [m]	Λ[-]
58	9.17
61	10.15
64	11.17
67	12.24

The sizing is performed considering 35 trim manoeuvres (push-up, pull down, roll, aileron and elevator deflection, sideslip, etc.) compliant with CS25 regulation and flutter constraints for three altitudes (sea level, corner point and cruise). The evolution of the wingbox mass with respect to the aspect ratio is illustrated in Figure 13 and reported in Table 3.
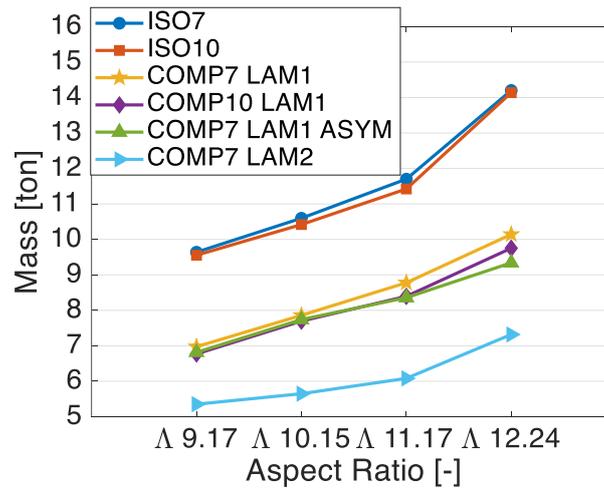
Figure 13: Half wingbox mass variation w.r.t. AR and materials

Table 3: Wingbox mass values

	9.17	10.15	11.17	12.24
ISO7	9639.55	10597.44	11700.06	14200.62
ISO10	9553.53	10418.53	11421.95	13594
COMP7 LAM1	6957.19	7858.91	8778.49	10141.52
COMP10	6770.72	7696.46	8394.62	9751.75
COMP7 LAM1 ASYM	6815.47	7739.76	8357.02	9340.36
COMP7 LAM2	5352.07	5648.47	6081.51	7318.4

The trend shows how a wingspan's increase leads to a heavier structure to withstand higher wing root bending moment, to evaluate if it is worth it an evaluation of the aircraft range and fuel consumption is performed. Both the performances are obtained solving the Breguet

equation, in the first case with a fixed amount of fuel in the second case on a prescribed route of 10000km.

$$R = \frac{V_{TAS}}{g} \frac{C_L}{C_{D0} + C_{Di}} \frac{1}{SFC} \ln \frac{W_1}{W_2} \tag{6}$$

The induced drag term is obtained with ALIS [39], a 3D panel method based on Morino's theory. The lift coefficient is the obtained considering a lift equal to the mean value between W_1 and W_2.

(a) Range   (b) Fuel consumption
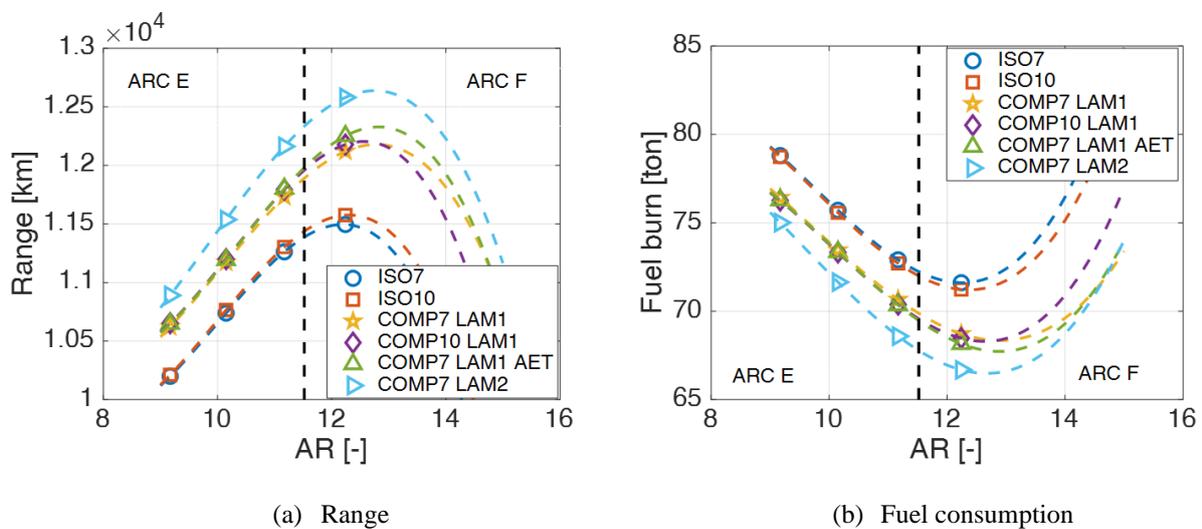
Figure 14: TAHL performances

The performances obtained show how, for this exercise, the increase of the aspect ratio is convenient for all the material considered, leading to lower fuel consumption. Anyway, some considerations must be done: the big advantage of the composite solution (LAM) is biased by the admissible stresses that are not reduced to consider local effects of fatigue and it may be too optimistic. The effect of aeroelastic tailoring can be noted in Figure 13 and Figure 14: the green triangle markers represent the solution obtained with the same stacking sequence of the yellow star markers, but in the first case (LAM ASYM) the laminate asymmetrical orientation is a design variable and the wash-out effect introduced by the bending-torsion coupling unload the external part of the wing. Figure 14 clearly shows that the AR increase has an optimum point depending on the material, in fact the fuel consumption in function of the AR has a convex shape which minimum can be estimated with a data fitting process. Another important consideration must be done on the span of the aircraft, wingspan larger than 65m requires a modification to the aerodrome reference code (ARC) of the aircraft, requiring different airport infrastructures.

6. CONCLUSIONS

This work proposes a novel aero-servo-elastic optimization toolbox which can be exploited in the early design phases to realize low-order medium fidelity aero-servo-elastic analysis models. The improvement achieved by the meta-model allows to describe the wingbox in a more detailed way, accounting for composite materials and aeroelastic tailoring since the

early design phases.

The proposed active control design methodology is intuitive but robust and it is encompassed in the aero-servo-elastic optimizer, which performs a concurrent optimization of both structure and active control law.

An application of the NeOPT shows a possible exploitation of the toolbox, which helps the designer to understand how design choices affect the overall performances of the aircraft, drawing trends and performing trade-off studies.

7. ACKNOWLEDGMENTS

REFERENCES

[1] https://www.iata.org/

[2] H. Tabuchi, "Worse than anyone expected: Air travel emissions vastly outpacepredictions." https://www.nytimes.com/2019/09/19/climate/air-travel-emissions.html, 2019.

[3] E. Commision, "Flightpath 2050 Europe's vision for aviation." https://ec.europa.eu/transport/sites/transport/files/modes/air/doc/flightpath2050.pdf, 2011.

[4] A. Kharina and D. Rutherford, "Fuel efficiency trends for new commercial jet aircraft: 1960 to 2014," 2015

[5] A. Jameson, "Re-engineering the design process through computation," Journal of Aircraft, vol. 36, no. 1, pp. 36–50, 1999.

[6] R. H. Liebeck, "Design of the blended wing body subsonic transport," Journal of aircraft, vol. 41, no. 1, pp. 10–25, 2004.

[7] Z. Lyu and J. R. Martins, "Aerodynamic design optimization studies of a blended-wing-body aircraft," Journal of Aircraft, vol. 51, no. 5, pp. 1604–1617, 2014.

[8] W. Su and C. E. Cesnik, "Nonlinear aeroelasticity of a very flexible blended-wing-body aircraft," Journal of Aircraft, vol. 47, no. 5, pp. 1539–1553, 2010.

[9] R. Jansen, C. Bowman, A. Jankovsky, R. Dyson, and J. Felder, "Overview of nasa electrified aircraft propulsion (eap) research for large subsonic transports," in 53rd AIAA/SAE/ASEE Joint Propulsion Conference, p. 4701, 2017.

[10] T. Delft, "Flying v." https://www.tudelft.nl/en/ae/flying-v/.

[11] A. Frediani, V. Cipolla, and E. Rizzo, "The prandtlplane configuration: overview on possible applications to civil aviation," Variational Analysis and Aerospace Engineering: Mathematical Challenges for Aerospace Design, pp. 179–210, 2012.

[12] R. Cavallaro, R. Bombardieri, L. Demasi, and A. Iannelli, "Prandtlplane joined wing: Body freedom flutter, limit cycle oscillation and freeplay studies," Journal of Fluids and Structures, vol. 59, pp. 57–84, 2015.

[13] D. Raymer, Aircraft design: a conceptual approach. American Institute of Aeronautics and Astronautics, Inc., 2012.

[14] E. Torenbeek, Synthesis of subsonic airplane design: an introduction to the preliminary design of subsonic general aviation and transport aircraft, with emphasis on layout, aerodynamic design, propulsion and performance. Springer Science & Business Media, 2013.

[15] N. Werter and R. De Breuker, "A novel dynamic aeroelastic framework for aeroelastic tailoring and structural optimisation," Composite Structures, vol. 158, pp. 369–386, 2016.

[16] P. Piperni, A. DeBlois, and R. Henderson, "Development of a multilevel multidisciplinaryoptimization capability for an industrial environment," AIAA journal, vol. 51, no. 10, pp. 2335–2352, 2013.

[17] B. A. Autry and D. Victorazzo, "Automated top level aircraft structural sizing tool (atlass): A framework for preliminary aircraft design and optimization," in AIAA Scitech 2019 Forum, p. 0550, 2019.

[18] L. Cavagna, S. Ricci, and L. Travaglini, "Neocass: an integrated tool for structural sizing, aeroelastic analysis and mdo at conceptual design level," Progress in Aerospace Sciences, vol. 47, no. 8, pp. 621–635, 2011.

[19] L. Cavagna, S. Ricci, and L. Travaglini, "Structural sizing and aeroelastic optimization in aircraft conceptual design using neocass suite," in 13th AIAA/ISSMO Multidisciplinary Analysis Optimization Conference, p. 9076, 2010.

[20] L. Cavagna, S. Ricci, and L. Riccobene, "A fast tool for structural sizing, aeroelastic analysis and optimization in aircraft conceptual design," in 50th AIAA/ASME/ASCE/AHS/ASC Structures, Structural Dynamics, and Materials Conference 17th AIAA/ASME/AHS Adaptive Structures Conference 11th AIAA No, p. 2571, 2009.

[21] L. Cavagna, S. Ricci, and L. Riccobene, "Structural sizing, aeroelastic analysis, and optimization in aircraft conceptual design," Journal of Aircraft, vol. 48, no. 6, pp. 1840–1855, 2011.

[22] Ardema, M. D., Chambers, M. C., Patron, A. P., Hahn, A. S., Miura, H., & Moore, M. D. (1996). Analytical fuselage and wing weight estimation of transport aircraft.

[23] G. L. Ghiringhelli, P. Masarati, and P. Mantegazza, "Multibody implementation of finite volume c beams," AIAA journal, vol. 38, no. 1, pp. 131–138, 2000.

[24] N. Harpur, "The effect of active control systems on structural design criteria," AGARD Active Control Systems for Load Alleviation, Flutter Suppression and Ride Control p 11-22(SEE N74-25550 15-02), 1974

[25] C. D. Regan and C. V. Jutte, "Survey of applications of active control technology for gust alleviation and new challenges for lighter-weight aircraft," 2012.

[26] E. Livne, "Aircraft active flutter suppression: State of the art and technology maturation needs," Journal of Aircraft, vol. 55, no. 1, pp. 410–452, 2018.

[27] G. Bindolino, G. Ghiringhelli, S. Ricci, and M. Terraneo, "Multilevel structural optimization for preliminary wing-box weight estimation," Journal of Aircraft, vol. 47,

no. 2, pp. 475–489, 2010.

[28] Cesnik, C. E., & Hodges, D. H. (1997). VABS: a new concept for composite rotor blade cross-sectional modeling. Journal of the American helicopter society, 42(1), 27-38.

[29] V. Giavotto, M. Borri, P. Mantegazza, G. Ghiringhelli, V. Carmaschi, G. Maffioli, and F. Mussi, "Anisotropic beam theory and applications," Computers & Structures, vol. 16, no. 1-4, pp. 403–413, 1983.

[30] Toffol, F. (2021). Aero-servo-elastic optimization in conceptual and preliminary design.

[31] V. L. Syrmos, C. T. Abdallah, P. Dorato, and K. Grigoriadis, "Static output feedback-a survey," Automatica, vol. 33, no. 2, pp. 125–137, 1997.

[32] Bittanti, S., Laub, A. J., & Willems, J. C. (Eds.). (2012). The Riccati Equation. Springer Science & Business Media.

[33] M. Ripepi and P. Mantegazza, "Improved matrix fraction approximation of aerodynamic transfer matrices," AIAA journal, vol. 51, no. 5, pp. 1156–1173, 2013.

[34] M. Ripepi, Model order reduction for computational aeroelasticity. PhD thesis, Italy, 2014.

[35] T. Mathworks, "Matlab optimization toolbox user's guide," Math Work, 2007.

[36] P. M. Weaver and M. P. Nemeth, "Bounds on flexural properties and buckling response for symmetrically laminated composite plates," Journal of engineering mechanics, vol. 133, no. 11, pp. 1178–1191, 2007.

[37] J. E. Herencia, P. M. Weaver, and M. I. Friswell, "Optimization of long anisotropic laminated fiber composite panels with t-shaped stiffeners," AIAA journal, vol. 45, no. 10, pp. 2497–2509, 2007.

[38] A330-300 triptych from web."
https://airbusa330300swissair.blogspot.com/2020/04/airbus-a330-300-technical-specifications.html.

[39] G. Bindolino, P. Mantegazza, and L. Visintini, "A comparison of panel methods for potential flow calculations," in VIII Congresso Nazionale AIDAA, pp. 23–27, 1985.

PRELIMINARY AIRCRAFT DESIGN INCORPORATING STRUCTURAL ENABLERS

Jonathan Cooper

University of Bristol, UK
cooper@bristol.uk, http://www.bristol.ac.uk/engineering/departments/aerospace/

Abstract. *Preliminary aircraft design is a key stage in the aircraft design process, where the conceptual configuration is optimised through consideration of the aerodynamics, structure and controls. Structural enablers are a broad range of technologies that can be used to facilitate improved aircraft performance through exploitation of the aeroelastic couplings and include morphing structures, aeroelastic tailoring, aeroservoelastic tailoring, folding wing-tips, vibration suppression devices, etc but there are few applications on current commercial jet aircraft. This presentation will show how incorporating structural enablers into a multi-disciplinary based approach can significantly improve preliminary aircraft designs in terms of the well-known Breguet Range Equation. The approach will be demonstrated upon high aspect ratio wing designs.*

Keywords: Morphing structures, Aeroelastic tailoring, Aeroservoelastic tailoring, Folding wing-tips, Vibration suppression devices

A MULTI-OBJECTIVE OPTIMIZATION APPROACH TO THE DESIGN OF A FREE-FLYER SPACE ROBOT FOR IN-ORBIT MANUFACTURING AND ASSEMBLY

João Vale[1]*, Alexandre Rocha[1], Marco Leite[2] and Rodrigo Ventura[1]

1: Instituto de Sistemas e Robótica
Instituto Superior Técnico
Universidade de Lisboa
Av. Rovisco Pais 1, 1049-001 Lisboa
{joao.luis.bruno.vale,alexandre.rocha,rodrigo.ventura}@tecnico.ulisboa.pt,
https://www.tecnico.ulisboa.pt

2: Instituto de Engenharia Mecânica
Instituto Superior Técnico Universidade de Lisboa
Av. Rovisco Pais 1, 1049-001 Lisboa
marcoleite@tecnico.ulisboa.pt, https://www.tecnico.ulisboa.pt

Abstract. *The growing need for larger assets in Space, ranging from commercial space stations to exploration beyond Earth orbit, will require the capability of manufacturing and assembling large structures in micro-gravity. Considering the use of autonomous space robots to perform these tasks, this paper studies the optimal design of a free-flyer robot for mobile manipulation with an emphasis on assembly and additive manufacturing. We propose a robot architecture comprising a dexterous six DoF parallel manipulator attached to a free-flyer robot body endowed with six DoF propulsion. The design methodology decouples the parallel manipulator from the robot body: For the parallel manipulator, we define performance metrics for work-space volume and accuracy. We employ multi-criteria optimization to determine the geometric parameters which best tradeoff defined metrics. For the robot body propulsion, we find which geometries result in maximum thrust and torque along all directions, in both force and torque space, thus maximizing maneuverability.*

Keywords: Space robotics, In-orbit manufacturing and assembly, Mobile manipulation, Multi-objective optimization

João Vale, Alexandre Rocha, Marco Leite and Rodrigo Ventura

1   INTRODUCTION

Space exploration is limited by current launching vehicles and systems: Constraints in mission design are imposed by the harsh launch conditions and limitations in payload volume and weight. The integration of in-orbit robotized manufacturing and assembly of parts, vehicles, and structures could be advantageous to mission design, reducing logistical requirements, launch system constraints, and Earth manufacturing constraints. With cooperative in-orbit manufacturing and assembly tasks in mind, this paper proposes the design of ACROBAT: an aerial free-flying robot for pressurized micro-gravity environments (e.g ISS). The nature of its propulsion system disallows the use of said system in vacuum. Instead, the intent is for this to be a steppingstone towards the design and development of spacecraft.

1.1   Free-Flying Robots

A Free-Flying robot can be defined as a vehicle capable of navigating and maneuvering the space with six DoF. Multiple aerial Free-Flying Robots have been tested in micro-gravity aboard the ISS: SPHERES [1] is a free-flying robot operated by NASA, designed as a testbed for formation flight. SPHERES uses twelve carbon-dioxide cold gas thrusters for its propulsion. Astrobee [2] is in some ways the successor of SPHERES, building on SPHERES's legacy and lessons learned. Astrobee's propulsion system is relatively simpler, comprised of two large fans inside it with twelve duct valves for control. The Astrobee is also equipped with a 2 DoF manipulator. Int-Ball [3] is a free-flying robot operated by JAXA, designed to be an autonomous mobile camera using twelve small, encapsulated fans for its propulsion.

Space CoBot [4] is a aerial robot designed for indoor micro-gravity environments. Its propulsion system is comprised of six propellers, similar to the ones employed in traditional Earth multi-rotors. Unlike Earth multi-rotors, the propellers are placed so that the kinematics are holonomic.

1.2   System Description

Figure 1 shows a CAD model of the first iteration of ACROBAT, which can be decoupled into two main components:

1. A robot body equipped with six propellers, displaced such that the kinematics are holonomic, meaning the robot can freely move with six DoF. Considering the target environment, propellers fans were chosen instead of other alternatives, such as cold gas thrusters. This is because they are simpler, faster to prototype, and easier to integrate into the design. The robot body will also house the main computer, batteries and required electronics and sensors (e.g IMU, camera). The CAD model of the robot body is depicted in Fig.2a, having a distance between two adjacent propellers of 19cm.

2. In isolation, the robot body has unbounded motion, but a low actuation bandwidth. The propeller's spin-up and spin-down time constrain the robot's fine movement capability which is detrimental for the targeted tasks. To enhance ACROBAT's manipulation capabilities, we attached a six DoF six Revolute-Spherical-Spherical

João Vale, Alexandre Rocha, Marco Leite and Rodrigo Ventura

(RSS) parallel manipulator, similar to HEXA [5] to the robot body, with a task dependent tool as the end-effector. Its CAD model can be seen in Fig.2b.
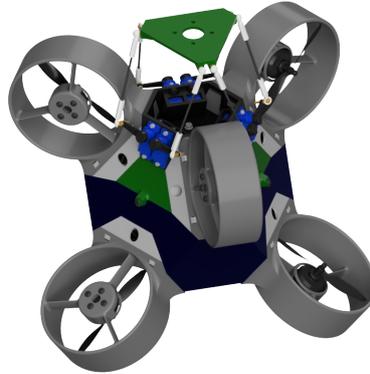
Figure 1: ACROBAT CAD model.
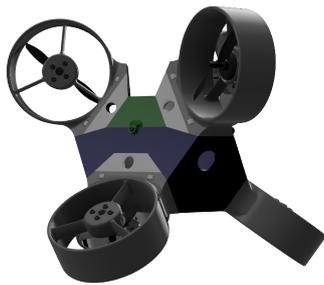
(a) Robot Body.
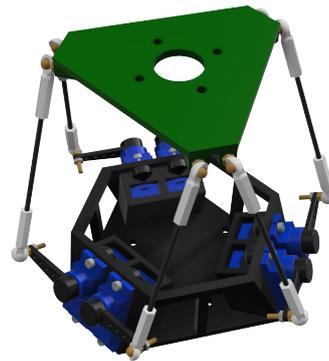
(b) Six RSS Manipulator.

Figure 2: CAD model of ACROBAT's components.

ACROBAT was designed to be modular, simplifying an iterative design and test approach. Figure 3 presents an adaptation for additive manufacturing. Two types of robots compose this example: a platform robot, equipped with a deposition platform as end-effector; and an extrusion robot, equipped with an extrusion head for material deposition as end-effector. Another possible adaptation is using ACROBAT for fine manipulation, by equipping the end-effector with a gripper.

1.3 Methodology

This paper aims to study how we should determine the geometric parameters of the proposed robotic system in order to maximize performance. To do so, we will decouple the manipulator from the robot body and treat each as an individual system. We will also compare the optimized designs with ACROBAT's first iteration presented in section 1.2.

The literature of parallel manipulator design optimization is vast. However, strategies often consist in defining performance metrics relevant to the application, and using an optimization methodology to find the design parameters which improve these metrics [6–9]. The need for a multi-objective methodology, arrives from the fact that the performance

João Vale, Alexandre Rocha, Marco Leite and Rodrigo Ventura
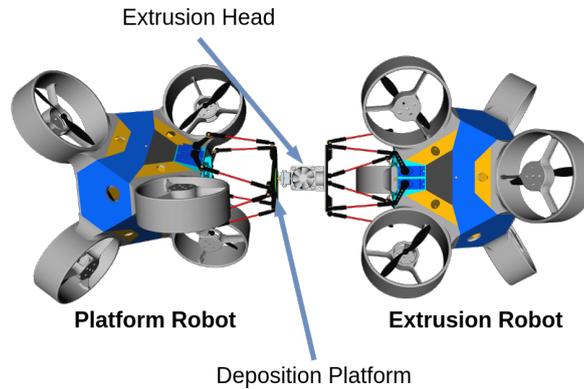
Figure 3: System adapted for additive manufacturing.

metrics can play opposing roles. For example, an increase in work-space volume can lead to a decrease in dexterity [10, 11].

2   ROBOT BODY DESIGN

2.1   Propulsion Model

A single propeller i, rigidly attached to the body frame $\mathcal{B}$ coincident with the Center of Mass (CoM), produces a thrust $\boldsymbol{F_i}$ and torque $\boldsymbol{M_i}$ on the vehicle body while rotating at speed n_i (in revolutions per second) [4]. $\boldsymbol{F_i}$ results directly from the propeller thrust

$$\boldsymbol{F_i} = f_i \boldsymbol{u_i} \qquad\qquad f_i = K_1 \left| n_i \right| n_i \qquad (1)$$

where $\boldsymbol{u_i}$ is a unit vector aligned with the propeller's axis of rotation and K_1 is a propeller constant. $\boldsymbol{M_i}$ is caused by the propeller non-central thrust $\boldsymbol{F_i}$ and reaction torque τ_i

$$\boldsymbol{M_i} = \boldsymbol{r_i} \times \boldsymbol{F_i} - \tau_i \boldsymbol{u_i} \qquad\qquad \tau_i = w_i K_2 \left| n_i \right| n_i \qquad (2)$$

where $\boldsymbol{r_i}$ is the propeller position relative to $\mathcal{B}$, w_i is, for a positive or forward thrust, -1 if the propeller rotates clockwise or 1 if it rotates anti-clockwise and K_2 is another propeller constant.
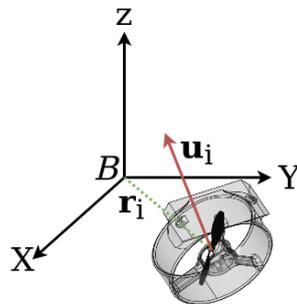
Figure 4: Notation of a single propeller, relative to the body's CoM.

Propeller constants K_1 and K_2 are given by

$$K_1 = \rho D^4 C_t \qquad\qquad K_2 = \frac{\rho D^5}{2\pi} C_P \qquad (3)$$

João Vale, Alexandre Rocha, Marco Leite and Rodrigo Ventura

where ρ is air density, D is propeller diameter, C_T is the thrust coefficient and C_P the power coefficient. C_T and C_P are blade dependent coefficients [12]. We assume that the propeller has similar K_1 and K_2 for both directions of rotation.

Consider an actuation signal vector $\boldsymbol{q}$, with i-th actuation signal following $q_i = |n_i|n_i$, resulting in

$$\begin{bmatrix} \boldsymbol{F_i} \\ \boldsymbol{M_i} \end{bmatrix} = \boldsymbol{a_i}q_i \tag{4}$$

where

$$\boldsymbol{a_i} = \begin{bmatrix} K_1\boldsymbol{u_i} \\ K_1\boldsymbol{r_i} \times \boldsymbol{u_i} - w_i K_2\boldsymbol{u_i} \end{bmatrix}. \tag{5}$$

To combine the effect of N propellers, resulting force $\boldsymbol{F}$ and torque $\boldsymbol{M}$ are given by the sum of Eq.(4), which can be written in matrix form as

$$\begin{bmatrix} \boldsymbol{F} \\ \boldsymbol{M} \end{bmatrix} = \begin{bmatrix} \boldsymbol{a_1} & \dots & \boldsymbol{a_6} \end{bmatrix} \begin{bmatrix} q_1 \\ \vdots \\ q_6 \end{bmatrix} = \boldsymbol{A}\boldsymbol{q} \tag{6}$$

where $\boldsymbol{A}$ is the actuation matrix. If $\boldsymbol{A}$ is a square matrix, meaning the robot is neither under nor over actuated, and $\boldsymbol{A}$ is full rank, meaning all propellers are non-redundant, $\boldsymbol{A}$ is invertible. As a result, it is possible to establish the following relationship

$$\boldsymbol{q} = \boldsymbol{A}^{-1} \begin{bmatrix} \boldsymbol{F} \\ \boldsymbol{M} \end{bmatrix}. \tag{7}$$

Matrix $\boldsymbol{A}^{-1}$ can be rewritten as a composition of matrices b and c

$$\boldsymbol{A}^{-1} = \begin{bmatrix} \boldsymbol{b}_1^T & \boldsymbol{c}_1^T \\ \vdots & \vdots \\ \boldsymbol{b}_6^T & \boldsymbol{c}_6^T \end{bmatrix} \qquad \text{with } \boldsymbol{b_i}, \boldsymbol{c_i} \in \mathbb{R}^3, \tag{8}$$

being possible to decouple torque and force and write $\boldsymbol{q}$ as

$$\boldsymbol{q} = \boldsymbol{b^T}\boldsymbol{F} + \boldsymbol{c^T}\boldsymbol{M}. \tag{9}$$

2.2 Parameterization

Considering the targeted 6 propellers, the actuation matrix described in Eq.(6) is a 6×6 matrix. $\boldsymbol{A}$ depends on propeller constants K_1 and K_2. To bypass this dependency, we divide Eq.(5) by K_1 resulting in

$$\boldsymbol{a'_i} = \begin{bmatrix} \boldsymbol{u_i} \\ \boldsymbol{r_i} \times \boldsymbol{u_i} - w_i \frac{K_2}{K_1}\boldsymbol{u_i} \end{bmatrix}. \tag{10}$$

Considering the size of the propellers that are expected to be used, around 4", the ratio $\frac{K_2}{K_1}$, takes values of magnitude 10^{-2}. Considering this, and for design purposes we will make the approximation of this term ($\frac{K_2}{K_1} = 0$), resulting in

$$\boldsymbol{a'_i} = \begin{bmatrix} \boldsymbol{u_i} \\ \boldsymbol{r_i} \times \boldsymbol{u_i} \end{bmatrix}. \tag{11}$$

João Vale, Alexandre Rocha, Marco Leite and Rodrigo Ventura

Despite this approximation, the methodology can be easily expanded to cover non-zero values of $\frac{K_2}{K_1}$.

The byproduct of Eq.(11) is a dimensionless actuation matrix. Now, to fully defineit, we need to specify each propeller position relative to the CoM $\boldsymbol{r_i}$ and thrust direction $\boldsymbol{u_i}$. Without loss of generality, let us assume that each propeller is located on a sphere of unit radius ($\|\boldsymbol{r_i}\| = 1$). Like depicted in Fig.5, $\boldsymbol{r_i}$ and $\boldsymbol{u_i}$ can be written as

$$\boldsymbol{r_i} = \begin{bmatrix} \cos(\theta_i)\sin(\gamma_i) \\ \sin(\theta_i)\sin(\gamma_i) \\ \cos(\gamma_i) \end{bmatrix} \qquad \text{with } \theta_i \in [0, \pi] \wedge \gamma_i \in [0, 2\pi) \qquad (12)$$

$$\boldsymbol{u_i} = \begin{bmatrix} \cos(\beta_i)\sin(\alpha_i) \\ \sin(\beta_i)\sin(\alpha_i) \\ \cos(\alpha_i) \end{bmatrix} \qquad \text{with } \beta_i \in [0, \pi] \wedge \alpha_i \in [0, 2\pi) \qquad (13)$$
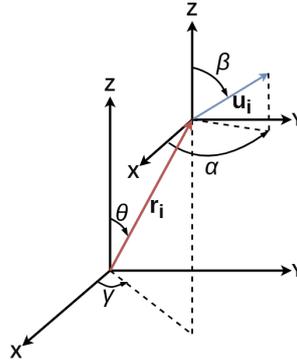
Figure 5: $\boldsymbol{r_i}$ and $\boldsymbol{u_i}$ description relative to the body's CoM.

Considering Eq.(12) and Eq.(13) expanded for the six propellers, the resulting vector of optimization variables $\boldsymbol{s}$ is given by $\boldsymbol{s} = (\gamma_1, \ldots, \gamma_6, \theta_1, \ldots, \theta_6, \beta_1, \ldots, \beta_6, \alpha_1, \ldots, \alpha_6)$.

2.3 Evaluation

To choose the $\boldsymbol{s}$ which results in the most apt robot body, we must define a performance evaluation criteria. One approach is to use the maximum force and torque possible in any direction [4]. Let us consider that the actuation signal $\boldsymbol{q}$ is bounded between -1 and 1, such that[1]

$$\|\boldsymbol{q}\|_\infty \leq 1. \qquad (14)$$

Let us also assume that $\boldsymbol{M} = 0$ and that $\boldsymbol{F} = F\boldsymbol{e}$ where $\boldsymbol{e}$ is the force direction. From Eq.(9) and Eq.(14) we get that

$$\|\boldsymbol{q}\|_\infty = \|F\boldsymbol{b}^T\boldsymbol{e}\|_\infty \leq 1, \qquad (15)$$

resulting in the upper bound of F given by

$$F \leq \frac{1}{\|\boldsymbol{b}^T\boldsymbol{e}\|_\infty}. \qquad (16)$$

---

[1]The infinity norm of $\boldsymbol{x}$ takes form $\|\boldsymbol{x}\|_\infty = \max\{|x_1|, \ldots, |x_n|\}$.

João Vale, Alexandre Rocha, Marco Leite and Rodrigo Ventura

in any direction $\boldsymbol{e}$. Likewise, the maximum force attainable along a given direction $\boldsymbol{e}$ is given by

$$F_{\boldsymbol{e}}^{max} = \frac{1}{\|\boldsymbol{b}^T \boldsymbol{e}\|_{\infty}}. \tag{17}$$

To obtain the maximum force attainable in any direction, we must minimize Eq.(17) in all directions. Considering that $\|\boldsymbol{b}^T \boldsymbol{e}\|_{\infty} = \max_i |\boldsymbol{b}_i^T \boldsymbol{e}|$ and $|\boldsymbol{b}^T \boldsymbol{e}| \leq \|\boldsymbol{b}_i\|$, maximum force in any direction is given by

$$F^{max} = \frac{1}{\max_i \|\boldsymbol{b}_i\|} = \min_i \frac{1}{\|\boldsymbol{b}_i\|} \qquad\qquad i \in \{1, \ldots, 6\}. \tag{18}$$

An analogous reasoning can be applied to obtain the maximum torque M^{max}, when $F = 0$, resulting in

$$M^{max} = \min_i \frac{1}{\|\boldsymbol{c}_i\|} \qquad\qquad i \in \{1, \ldots, 6\}. \tag{19}$$

2.4 Design Space

The parameterization described in section 2.2 has the drawback of leading to many symmetric designs, meaning that a given configuration can be redundantly described by different $\boldsymbol{s}$. For instance, switching a $\boldsymbol{r_i}$, $\boldsymbol{u_i}$ pair with other pair, leads to a different $\boldsymbol{s}$ that represents that same design. To avoid such cases, we shall constraint the propeller position $\boldsymbol{r_i}$ so that γ_i is ordered by increasing values of i:

$$\gamma_1 \leq \gamma_2 \leq \gamma_3 \leq \gamma_4 \leq \gamma_5 \leq \gamma_6 \tag{20}$$

Other types of symmetric designs can be obtained by choosing an arbitrary parameter vector $\boldsymbol{s}$, and rotating every $\boldsymbol{u_i}$ and $\boldsymbol{r_i}$ by an arbitrary rotation, arriving at a $\boldsymbol{s}$ which represents the same design, but has a different $\boldsymbol{s}$. To try mitigate the symmetric designs caused by rotations, we apply a few constraints to the design space. First, we set a fixed $\boldsymbol{r_1}$ ($\gamma_1 = 0$ and $\theta_1 = \frac{\pi}{2}$). A fixed $\boldsymbol{r_1}$ constrains the possible set of rotations causing symmetric designs to rotations around $\boldsymbol{r_1}$. To further constraint the symmetric designs, we will also set $\boldsymbol{r_2}$ so that $\boldsymbol{r_1}$ and $\boldsymbol{r_2}$ always belong to the same plain, no matter the $\boldsymbol{s}$. An easy way to do this, given the current parameterization, is to set $\theta_2 = \frac{\pi}{2}$ and let γ_2 be a free optimization variable. Considering this, we rewrite the vector of optimization variables $\boldsymbol{s}$ as $\boldsymbol{s} = (\gamma_2, \ldots, \gamma_6, \theta_3, \ldots, \theta_6, \beta_1, \ldots, \beta_6, \alpha_1, \ldots, \alpha_6)$.

Finally, given that the propellers are assumed to be bi-directional, we can set $\boldsymbol{u_i}$ to only one hemisphere given by: $\beta_i \in [0, \pi] \wedge \alpha_i \in [0, \pi]$ for $i \in \{1, \ldots, 6\}$. The resulting set of feasible designs $\mathcal{S}$ is a bounded box such that $\mathcal{S} = \{0 \leq \gamma_i \leq \pi, 0 \leq \theta_j \leq 2\pi, 0 \leq \beta_k \leq \pi, 0 \leq \alpha_k \leq \pi\}$ for $i \in \{2, \ldots, 6\}$, for $j \in \{3, \ldots, 6\}$, for $k \in \{1, \ldots, 6\}$.

2.5 Optimization

We wish to maximize both F^{max} and M^{max}, which can be translated into a minimization problem by considering their negative counterpart ($-F^{max}$ and $-M^{max}$). With the discussed bounds and constraints in mind, we can formulate the following multi-objective optimization problem:

João Vale, Alexandre Rocha, Marco Leite and Rodrigo Ventura

$$
\begin{aligned}
\text{Minimize} \quad & (-F^{max}, -M^{max}) \\
\text{w.r.t.} \quad & \boldsymbol{s} \in \mathcal{S} \\
\text{subject to} \quad & \gamma_2 \leq \gamma_3 \leq \gamma_4 \leq \gamma_5 \leq \gamma_6 \,.
\end{aligned}
\tag{21}
$$

Performance metrics F^{max} and M^{max} are calculated from $\boldsymbol{A}^{-1}$, which is numerically computed from $\boldsymbol{A}$, meaning they lack a closed-form solution. Consequently, their derivative is not available, making a derivative-free optimization methodology capable of addressing bounded problems with constraints necessary to estimate the Pareto front of the stated problem. Multiple algorithms have the capability of addressing this type of problem, namely evolutionary multi-objective approaches. However, based on our analysis we decided to use the Direct Multisearch for Multiobjective Optimization [13] algorithm.

2.6 Results

Point-wise approximation of the Pareto front can be found in Fig.6. The algorithm ran until a total of 4×10^5 objective function evaluations were generated starting from a random initialization. The Pareto front has a total of 447 non-dominated points.
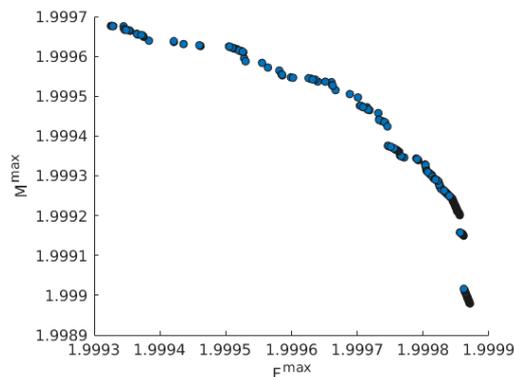
Figure 6: Point wise pareto-front approximation.

To check how the $\boldsymbol{s}$ that make the Pareto front in Fig.6 distribute over $\mathcal{S}$, we did the average and standard distribution of each optimization variable. The results are shown in Tab.1 and Tab.2. Observing the order of magnitude of the standard deviation presented by the solutions, 10^{-3}, and considering the range of values taken by the performance metrics in the Pareto front, one can assume that the set of solution is well represented by it's own average. In fact, the data in Fig.6 suggests that the Pareto front is comprised of a single point, being the dispersion justified in the algorithm's numeric nature. If so, it shows that there are solutions to the problem in Eq.(21) that are dominant in a way that maximize both F^{max} and M^{max}.

Table 1: Average and standard deviation of each design parameter relative to propeller position.

Variable	γ_2	γ_3	γ_4	γ_5	γ_6	θ_3	θ_4	θ_5	θ_6
Avg	1.603	3.202	4.694	4.701	4.785	0.134	3.108	1.577	0.013
Std (10^{-3})	3.252	12.80	5.106	3.642	0.945	2.771	2.717	16.04	110.1

João Vale, Alexandre Rocha, Marco Leite and Rodrigo Ventura

Table 2: Average and standard deviation of each design parameter relative to thrust direction.

Variable	α_1	α_2	α_3	α_4	α_5	α_6	β_1	β_2	β_3	β_4	β_5	β_6
Avg	1.593	1.558	1.560	0.025	1.627	0.058	1.549	3.123	1.582	0.872	0.019	1.582
Std (10^{-3})	2.981	3.791	0.607	1.785	1.645	1.159	1.677	1.068	3.370	1.972	1.520	0.682

Figure 7 shows a visual representation of propeller placement and thrust direction, between the robot body design presented in Tab.1 and Tab.2, and ACROBAT's first iteration (for comparison purposes, we will consider $\|\boldsymbol{r_i}\| = 1$ in both cases). The design obtained from the Pareto front has a performance vector of $(F^{max}, M^{max}) = (1.9996, 1.9994)$. For comparison, ACROBAT has a performance vector of $(F^{max}, M^{max}) = (2.0000, 2.0000)$. Performance-wise, both designs had similar results, which is not unexpected given that the problem defined in Eq.(21) can hold multiple solutions (different $\boldsymbol{s}$ can have the same performance vector). Considering this, we believe the design presented in section 1.2 to be optimal, given that it has the same performance has an optimal design.

(a) Design obtained from the Pareto front   (b) ACROBAT
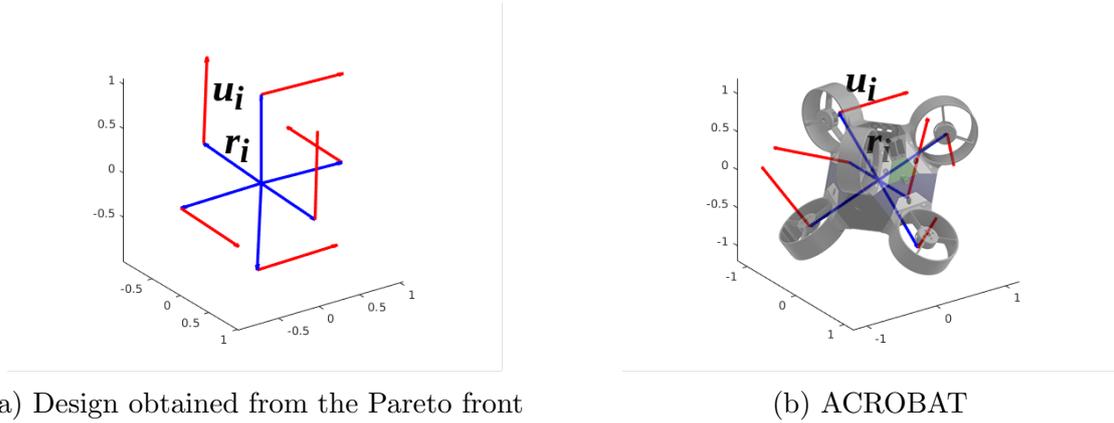
Figure 7: Representative diagram of the robot body.

3 MANIPULATOR DESIGN

3.1 Design Parameters

The manipulator is composed of a mobile platform, with origin ${}^p\mathcal{O}$, where the end-effector is located, and a fixed base, with origin ${}^b\mathcal{O}$. The k-th Revolute-Spherical-Spherical arm, with $k \in \{1, \ldots, 6\}$, closes the loop between the platforms, connecting base anchor $\boldsymbol{B_k}$ to the platform's anchor $\boldsymbol{M_k}$. As depicted in Fig.8, each anchor $\boldsymbol{B_k}$ is connected to each arm by an actuated revolute joint. A rigid link of length h connects $\boldsymbol{B_k}$ to $\boldsymbol{H_k}$, and a rigid link of length d connects $\boldsymbol{H_k}$ to $\boldsymbol{M_k}$. The joints located at $\boldsymbol{H_k}$ and $\boldsymbol{M_k}$ are passive spherical joints. From Fig.8a, we can obtain the following loop closure equation

$$\boldsymbol{i_k} = \boldsymbol{h_k} + \boldsymbol{d_k} = \boldsymbol{T} + \boldsymbol{R}\boldsymbol{m_k} - \boldsymbol{b_k}, \tag{22}$$

where $\boldsymbol{T} = \begin{bmatrix} x & y & z \end{bmatrix}^T$ is the translation and $\boldsymbol{R} \in \mathbb{R}^{3\times3}$ is the rotation matrix which define the mobile platform's pose $\boldsymbol{p} = \begin{bmatrix} x & y & z & \gamma & \theta & \psi \end{bmatrix}^T$. $\boldsymbol{R}$ can be described by three Euler angles (γ, θ, ψ), following the ZYZ convention

$$\boldsymbol{R}(\gamma, \theta, \psi) = \boldsymbol{R}(Z, \theta)\boldsymbol{R}(Y, \gamma)\boldsymbol{R}(Z, \psi). \tag{23}$$

João Vale, Alexandre Rocha, Marco Leite and Rodrigo Ventura

(a) Platform's dimensions.　　　　　(b) Manipulator diagram.
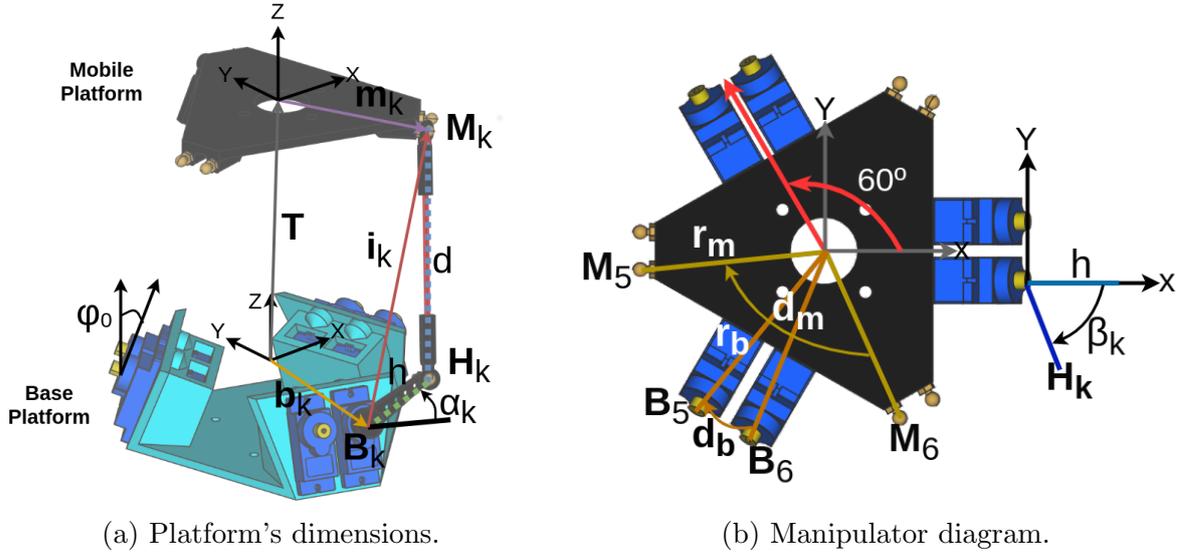
Figure 8: Parallel manipulator schematic.

According to Fig.8b, the base anchor arrangement is defined by vector $\boldsymbol{b_k}$

$$\boldsymbol{b_k} = \begin{bmatrix} r_b \cos(\theta_b) & r_b \sin(\theta_b) & 0 \end{bmatrix}^T \qquad \theta_b = \frac{2\pi \left\lfloor \frac{k+1}{2} \right\rfloor}{3} + (-1)^k d_b \qquad (24)$$

where d_b is the angle between the anchor pairing and r_b the base platform radius.

The mobile platform anchor arrangement is defined by vector $\boldsymbol{m_k}$

$$\boldsymbol{m_k} = \begin{bmatrix} r_m \cos(\theta_m) & r_m \sin(\theta_m) & 0 \end{bmatrix}^T \qquad \theta_m = \frac{2\pi \left\lfloor \frac{k+1}{2} \right\rfloor}{3} + (-1)^k d_m \qquad (25)$$

where d_m is the angle between the anchor pairing and r_m the mobile platform radius.

The k-th revolute joint arm orientation is defined by angles ϕ_k and β_k

$$\phi_k = (-1)^{k+1}\phi_0 \qquad \beta_k = \frac{2\pi \left\lfloor \frac{k+1}{2} \right\rfloor}{3} + (-1)^k \beta_0 \qquad (26)$$

where ϕ_0 and β_0 describe the revolute joint arm orientation in space.

In conclusion, to dimension the described manipulator, design parameters r_b, r_m, d_b, d_m, ϕ_0, β_0, d and h must be specified. The resulting vector of design parameters $\boldsymbol{s}$ is given by $\boldsymbol{s} = (r_b, r_m, d_b, d_m, \phi_0, \beta_0, d, h)$.

3.2 Kinematics

Inverse Kinematics

The inverse kinematics problem consists in computing the vector of actuated joints $\boldsymbol{\alpha}$ for a given pose $\boldsymbol{p}$ of the end effector: $\boldsymbol{\alpha} = f(\boldsymbol{p})$. As depicted in Fig.8, the k-th revolute joint arm $\boldsymbol{H_k}$ is obtained by first rotating the revolute joint arm by α_k along the Y axis, then rotating by ϕ_k along the X axis and finally rotating along the Z axis by β_k, resulting

João Vale, Alexandre Rocha, Marco Leite and Rodrigo Ventura

in

$$\boldsymbol{H_k} = \boldsymbol{B_k} + \boldsymbol{R}(Z, \beta_k)\boldsymbol{R}(X, \phi_k)\boldsymbol{R}(Y, -\alpha_k) \begin{bmatrix} h & 0 & 0 \end{bmatrix}^T \tag{27}$$

$$= \boldsymbol{B_k} + h \begin{bmatrix} \sin(\beta_k)\sin(\phi_k)\sin(\alpha_k) + \cos(\beta_k)\cos(\alpha_k) \\ -\cos(\beta_k)\sin(\phi_k)\sin(\alpha_K) + \sin(\beta_k)\cos(\alpha_k) \\ \cos(\phi_k)\sin(\alpha_k) \end{bmatrix} . \tag{28}$$

Using an alternative formulation, the k-th revolute joint arm $\boldsymbol{H_k}$ can be obtained by rotating $\boldsymbol{h_k}$ by $-\alpha_k$ around u_k, so that

$$\boldsymbol{H_k} = \boldsymbol{B_k} + \boldsymbol{R}(\boldsymbol{u_k}, -\alpha_0) \begin{bmatrix} h & 0 & 0 \end{bmatrix}^T \tag{29}$$

where u_k represents the revolute's joint axis of rotation given by

$$\boldsymbol{u_k} = \boldsymbol{R}(Z, \beta_k)\boldsymbol{R}(X, \phi_k) \begin{bmatrix} 1 & 0 & 0 \end{bmatrix}^T . \tag{30}$$

Considering the rigid links which make the platform's arms, the manipulator must obey the following constraints

$$d^2 = (\boldsymbol{M_k} - \boldsymbol{H_k})^T(\boldsymbol{M_k} - \boldsymbol{H_k}) \tag{31}$$

$$h^2 = (\boldsymbol{H_k} - \boldsymbol{B_k})^T(\boldsymbol{H_k} - \boldsymbol{B_k}) \tag{32}$$

Additionally, $\|\boldsymbol{i_k}\|^2$ can be calculated by

$$\|\boldsymbol{i_k}\|^2 = (\boldsymbol{M_k} - \boldsymbol{B_k})^T(\boldsymbol{M_k} - \boldsymbol{B_k}). \tag{33}$$

Combining and factorizing Eq.(31) and Eq.(33) [14]:

$$\|\boldsymbol{i_k}\|^2 - (d^2 - h^2) = 2\boldsymbol{B_k}^T\boldsymbol{B_k} - 2\boldsymbol{B_k}^T\boldsymbol{H_k} - 2\boldsymbol{B_k}^T\boldsymbol{M_k} + 2\boldsymbol{H_k}^T\boldsymbol{M_k} = 2(\boldsymbol{H_k} - \boldsymbol{B_k})^T(\boldsymbol{M_k} - \boldsymbol{B_k}). \tag{34}$$

Substituting $\boldsymbol{i_k}$ and $\boldsymbol{H_k}$ in Eq.(34) with Eq.(22) and Eq.(27), respectively, results in

$$\|\boldsymbol{i_k}\|^2 - (d^2 - h^2) = 2h \begin{bmatrix} \sin(\beta_k)\sin(\phi_k)\sin(\alpha_k) + \cos(\beta_k)\cos(\alpha_k) \\ -\cos(\beta_k)\sin(\phi_k)\sin(\alpha_K) + \sin(\beta_k)\cos(\alpha_k) \\ \cos(\phi_k)\sin(\alpha_k) \end{bmatrix}^T \boldsymbol{i_k}. \tag{35}$$

Rearranging Eq.(36)

$$\|\boldsymbol{i_k}\|^2 - (d^2 - h^2) = 2h(a_k\sin(\alpha_k) + b_k\cos(\alpha_k)) \tag{36}$$

$$a_k = \sin(\beta_k)\sin(\phi_k)\boldsymbol{i_k}^{(x)} - \cos(\beta_k)\sin(\phi_k)\boldsymbol{i_k}^{(y)} + \cos(\phi_k)\boldsymbol{i_k}^{(z)} \tag{37}$$

$$b_k = \cos(\beta_k)\boldsymbol{i_k}^{(x)} + \sin(\beta_k)\boldsymbol{i_k}^{(y)}. \tag{38}$$

Applying the trigonometric identity

$$a\sin(\alpha) + b\cos(\alpha) = \sqrt{a^2 + b^2}\sin(\alpha + \arctan 2(b, a)) \tag{39}$$

to Eq.(36) results in the following relation

$$\|\boldsymbol{i_k}\|^2 - (d^2 - h^2) = \sqrt{a_k^2 + b_k^2}\sin(\alpha + \arctan 2(b_k, a_k)) \tag{40}$$

$$\tag{41}$$

João Vale, Alexandre Rocha, Marco Leite and Rodrigo Ventura

therefore,

$$\alpha_k = \arcsin\left(\frac{\|\boldsymbol{i_k}\|^2 - (d^2 - h^2)}{\sqrt{a_k^2 + b_k^2}}\right) - \arctan 2(b_k, a_k). \tag{42}$$

The angle α_k of each revolute joint can be calculated using Eq.(42), solving the inverse kinematics problem. Given that there is a closed-form solution to the inverse kinematics, the manipulator can be fully described with only $\boldsymbol{p}$. In other words, the pose of all the joints can be derived with only knowing the end-effector pose $\boldsymbol{p}$.

Direct Kinematics

The direct kinematics problem consists in finding the vector of end effector pose $\boldsymbol{p}$ for a given vector of actuated joints $\boldsymbol{\alpha}$: $\boldsymbol{p} = g(\boldsymbol{\alpha})$. As the best of our knowledge, no closed form solution for the direct kinematics of this class of manipulators has been established.

However, a special case of the direct kinematics where $\alpha_k = 0$ for $k \in \{1, \ldots, 6\}$ exists. Given the platform geometry and symmetry, we can assume that in this case the end-effector has no rotation ($\boldsymbol{R} = \boldsymbol{I}$) and the translation is purely on the Z axis $\boldsymbol{T} = \begin{bmatrix} 0 & 0 & z \end{bmatrix}^T$. From Fig.8a we get

$$d^2 = (\boldsymbol{T} + \boldsymbol{C_k})^T(\boldsymbol{T} + \boldsymbol{C_k}) = \boldsymbol{T}^T\boldsymbol{T} + \boldsymbol{C_k}^T\boldsymbol{T} + \boldsymbol{T}^T\boldsymbol{C_k} + \boldsymbol{C_k}^T\boldsymbol{C_k} \tag{43}$$

where $\boldsymbol{C_k}$ is given by

$$\boldsymbol{C_k} = \boldsymbol{R}\boldsymbol{m_k} - \boldsymbol{H_k} = \boldsymbol{I}\boldsymbol{m_K} - \boldsymbol{B_k} + h\begin{bmatrix}\cos(\beta_k) \\ \sin(\beta_k) \\ 0\end{bmatrix} = \begin{bmatrix}r_m\cos(\theta_m) - r_b\cos(\theta_b) - h\cos(\beta_k) \\ r_m\sin(\theta_m) - r_b\sin(\theta_b) - h\sin(\beta_k) \\ 0\end{bmatrix} \tag{44}$$

substituting Eq.(44) and Eq.(43), and knowing that $\boldsymbol{C_k}^T\boldsymbol{T} = \boldsymbol{T}^T\boldsymbol{C_k} = 0$, we get

$$z = \pm\sqrt{d^2 - [r_m\cos(\theta_m) - r_b\cos(\theta_b) - h\cos(\beta_k)]^2 - [r_m\sin(\theta_m) - r_b\sin(\theta_b) - h\sin(\beta_k)]^2}. \tag{45}$$

Equation (45) holds two solutions, one for each working node of the manipulator. However, considering the defined working node, we will only consider $z \geq 0$.

3.3 Velocity Analysis

Consider an end-effector with twist $\boldsymbol{w} \in \mathbb{R}^6$. Let us assume that the end-effector has linear velocity $\boldsymbol{v}$ and angular velocity $\boldsymbol{\omega}$ so that $\boldsymbol{w} = \begin{bmatrix} \boldsymbol{v}^T & \boldsymbol{\omega}^T \end{bmatrix}^T$. The inverse kinematic Jacobian [15] is given by

$$\dot{\boldsymbol{\alpha}} = \boldsymbol{J}^{-1}(\boldsymbol{p})\boldsymbol{w}. \tag{46}$$

where $\dot{\boldsymbol{\alpha}}$ is the velocity vector of the actuated joints. The relation between the derivatives of the orientation representation described by three Euler angles (γ, θ, ψ) in Eq.(23) and the angular velocity $\boldsymbol{\omega}$ is given by matrix $\boldsymbol{H} \in \mathbb{R}^{3\times3}$ so that [15]

$$\boldsymbol{\omega} = \boldsymbol{H}(\gamma, \theta, \psi)\begin{bmatrix}\dot{\gamma} & \dot{\theta} & \dot{\psi}\end{bmatrix}^T, \tag{47}$$

where $\boldsymbol{H}$ depends on (γ, θ, ψ). On the other hand, we can establish that $\boldsymbol{v} = \dot{\boldsymbol{T}}$.

João Vale, Alexandre Rocha, Marco Leite and Rodrigo Ventura

Consider the loop-closure equation in Eq.(22). Differentiating relative to time, we get for each k that

$$\boldsymbol{w}_k^{R-S} \times \boldsymbol{h_k} + \boldsymbol{w}_k^{S-S} \times \boldsymbol{d_k} = \boldsymbol{v} + \boldsymbol{\omega} \times \boldsymbol{R}\boldsymbol{m_k} \tag{48}$$

where $\boldsymbol{w}_k^{R-S}$ is the twist of the R-S link and $\boldsymbol{w}_k^{S-S}$ the twist of the S-S link. To remove the $\boldsymbol{w}_k^{S-S}$ from the equation, we find the inner product of $\boldsymbol{d_k}$ on both sides resulting in

$$(\boldsymbol{w}_k^{R-S} \times \boldsymbol{h_k}) \cdot \boldsymbol{d_k} + (\boldsymbol{w}_k^{S-S} \times \boldsymbol{d_k}) \cdot \boldsymbol{d_k} = \boldsymbol{v} \cdot \boldsymbol{d_k} + (\boldsymbol{\omega} \times \boldsymbol{R}\boldsymbol{m_k}) \cdot \boldsymbol{d_k} \tag{49}$$

rearranging the terms and simplifying, we get

$$(\boldsymbol{h_k} \times \boldsymbol{d_k}) \cdot \boldsymbol{w}_k^{R-S} = \boldsymbol{d_k} \cdot \boldsymbol{v} + (\boldsymbol{R}\boldsymbol{m_k} \times \boldsymbol{d_k}) \cdot \boldsymbol{w} \tag{50}$$

putting in matrix form, and knowing that $\boldsymbol{w}_k^{R-S} = \boldsymbol{u_k}\dot{\alpha}_k$ we get

$$\dot{\alpha}_k = \left[\frac{\boldsymbol{d_k}}{(\boldsymbol{h_k} \times \boldsymbol{d_k}) \cdot \boldsymbol{u_k}} \quad \frac{\boldsymbol{R}\boldsymbol{m_k} \times \boldsymbol{d_k}}{(\boldsymbol{h_k} \times \boldsymbol{d_k}) \cdot \boldsymbol{u_k}} \right] \boldsymbol{w} \tag{51}$$

which corresponds to a line of $\boldsymbol{J^{-1}}$.

3.4 Work-space

The work-space $\mathcal{W}$ of a manipulator can be defined as the set of poses $\boldsymbol{p}$ the end effector can take while satisfying the constraints. Generally, three types of constraints restrict parallel manipulators: a) Constraints imposed by the actuators; b) constraints imposed by the passive joints; and c) constraints imposed by the mechanical interference of links. These constraints can be written as a system of kinematic equations

$$g(\boldsymbol{p}) = 0 \tag{52}$$

and kinematic inequations

$$h(\boldsymbol{p}) \leq 0 \tag{53}$$

imposed by the work-space constraints. A manipulator work-space can be defined in multiple ways: The reachable work-space $\mathcal{W}_R \in \mathbb{R}^6$ is the set of $\boldsymbol{p}$ that the end-effector can reach with at least one orientation $\mathcal{W}_R = \{\boldsymbol{p} : g(\boldsymbol{p}) = 0, h(\boldsymbol{p}) \leq 0\}$. The constant orientation works-space $\mathcal{W}_C \in \mathbb{R}^3$ is a subset of $\mathcal{W}_R$ where $\boldsymbol{p}$ has constant orientation. Because it is easier to represent and compute, it is commonly considered instead of the reachable work-space.

We will only consider constraints of type a), but the methodology can be easily expanded to other types of constraints. In the case of the manipulator presented here, for a $\boldsymbol{p}$ to belong to $\mathcal{W}$, it must hold a real solution to Eq.(42). Meaning that

$$-1 \leq \frac{\|\boldsymbol{i_k}\|^2 - (d^2 - h^2)}{\sqrt{a_k^2 + b_k^2}} \leq 1 \qquad\qquad k \in \{1, \ldots, 6\} \tag{54}$$

must hold, where each kinematic chain k imposes a constraint expressed in Eq.(54). Equation (54) can be rewritten as

$$h_k(\boldsymbol{p}) = [\|\boldsymbol{i_k}\|^2 - (d^2 - h^2)]^2 - (a_k^2 + b_k^2) \leq 0 \qquad\qquad k \in \{1, \ldots, 6\} \tag{55}$$

where i_k, a_k and b_k depend on $\boldsymbol{p}$ as shown in Eq.(22), Eq.(37) and Eq.(38) respectively.

João Vale, Alexandre Rocha, Marco Leite and Rodrigo Ventura

3.5 Evaluation

An important step for manipulator design is the choice of performance metrics to evaluate and compare different designs. Consider a vector of design parameters $\boldsymbol{s} \in \mathbb{R}^m$, a performance metric function f must evaluate $\boldsymbol{s}$ according to certain performance metric so that

$$L = f(\boldsymbol{s}) \tag{56}$$

where $L \in \mathbb{R}$ is the performance of $\boldsymbol{s}$ in a defined criterion. f can lack a closed-form solution, making methods to compute an approximate solution necessary.

The choice of metrics is heavily dependent on the tasks. Given the tasks at hand of assembly and additive manufacturing, we consider that both work-space volume and accuracy are desirable.

Work-space Volume

Work-space volume is a metric used to measure the size of a work-space. Work-space volume dimension depends on the type of work-space that is being measured. For instance, if the constant orientation work-space is considered, the work-space volume is a 3D volume. Formally, $V_{\mathcal{W}}$ is given by

$$V_{\mathcal{W}} = \int_{\mathcal{W}} d\mathcal{W} \tag{57}$$

where $\mathcal{W}$ is the targeted work-space.

Accuracy

A measure of accuracy must evaluate how a small displacement of the active joints $\delta\boldsymbol{\alpha}$ translates into a displacement of the end-effector pose $\delta\boldsymbol{p}$. These small active joint displacements may originate from the sensor noise, calibration errors or even thermal expansion and compression. Actuator displacement can be modeled by the kinematic Jacobian [15] such that

$$\delta\boldsymbol{p} = \boldsymbol{J}(\boldsymbol{p})\delta\boldsymbol{\alpha}. \tag{58}$$

Considering a actuator displacement bounded by a hyper-cube of side two

$$\|\delta\boldsymbol{\alpha}\|_\infty \leq 1, \tag{59}$$

if all actuated joints share a type (e.g. all actuated joints are revolute), the maximum displacement in translation $\sigma_{p,\infty}$ and the maximum displacement in rotation $\sigma_{r,\infty}$ is given by [16]

$$\sigma_{p,\infty} = \|\boldsymbol{J}_t\|_\infty \qquad\qquad \sigma_{r,\infty} = \|\boldsymbol{J}_r\|_\infty \tag{60}$$

where $\boldsymbol{J}_t$ and $\boldsymbol{J}_r$ are blocks of $\boldsymbol{J}$ such that $\boldsymbol{J} = [\boldsymbol{J}_t^T \boldsymbol{J}_r^T]^T$, obeying

$$\boldsymbol{v} = \boldsymbol{J}_t\dot{\boldsymbol{\alpha}} \qquad\qquad \boldsymbol{\omega} = \boldsymbol{J}_r\dot{\boldsymbol{\alpha}}. \tag{61}$$

Designwise, $\sigma_{p,\infty}$ and $\sigma_{r,\infty}$ measure translational and rotational sensitivity to actuator displacement and are representative of manipulator accuracy.

João Vale, Alexandre Rocha, Marco Leite and Rodrigo Ventura

The aforementioned metrics only evaluate the performance in a given pose. To evaluate the sensitivity of the manipulator over the entire work-space, we propose the GTSI and the GRSI, given by

$$GTSI = \frac{\int_{\mathcal{W}} \sigma_{t,\infty} \, d\mathcal{W}}{\int_{\mathcal{W}} d\mathcal{W}} \qquad\qquad GRSI = \frac{\int_{\mathcal{W}} \sigma_{r,\infty} \, d\mathcal{W}}{\int_{\mathcal{W}} d\mathcal{W}}, \qquad (62)$$

which must be minimized.

3.6 Design Space

Bounds

Let $\mathcal{S}$ be a bounded box, representing the feasible design parameter space. Given the bounds imposed by the parameterization context and application, we assume that $\mathcal{S}$ is bounded. For instance, consider the base radius r_b. Given that it must be large enough for the actuators to fit and small enough to fit the robot body, we consider that r_b must be larger than 0.01 meters and smaller than 0.06 meters. The same logic applies to the mobile platform radius r_m, which must be large enough for a tool to fit, so we assume that r_m must be larger than 0.01 meters and smaller than 0.06 meters. Considering manipulator geometry, the angle between mobile platform anchor pairings d_m and base platform pairings d_b is defined to be between 0 and $\frac{\pi}{3}$. However, given the platform's symmetry, these bounds would produce redundant designs (The manipulator with $d_m = d_b = 0$ is the same as $d_m = d_b = \frac{\pi}{3}$), so we set the maximum d_b at $\frac{\pi}{6}$. Likewise, we define define ϕ_0 to be between $-\frac{\pi}{3}$ and $\frac{\pi}{3}$ and β_0 to be between 0 and π.

In conclusion, $\mathcal{S}$ is a bounded box so that $\mathcal{S} = \{0.01 \leq r_b \leq 0.06, 0.01 \leq r_m \leq 0.06, 0 \leq d_b \leq \frac{\pi}{3}, 0 \leq d_m \leq \frac{\pi}{3}, -\frac{\pi}{3} \leq \phi_0 \leq \frac{\pi}{3}, 0 \leq \beta_0 \leq \pi, 0.01 \leq d \leq 0.2, 0.01 \leq h \leq 0.2\}$.

Constraints

However, not all $\boldsymbol{s}$ inside the bounded box $\mathcal{S}$ produce feasible manipulators. Two types of constraints still apply: *a)* $\boldsymbol{s}$ which lead to kinematically impossible manipulators; and *b)* $\boldsymbol{s}$ which lead to kinematically legal manipulators but is physically impossible given inter-link interference.

Let us start by addressing the first case. A way to verify if $\boldsymbol{s}$ represents a possible manipulator is to ascertain if Eq.(45) has any real solutions. If it has no real solution, $\boldsymbol{s}$ leads to a manipulator which either has a void work-space or has non-void work-space but there is no pose where $\alpha_k = 0$ for $k \in \{1, \ldots, 6\}$. For Eq.(45) to hold a real solution, the following constraint must hold

$$C_1(\boldsymbol{s}) = [r_p \cos(d_p) - r_b \cos(d_b) - h \cos(\beta_0)]^2 + [r_p \sin(d_p) - r_b \sin(d_b) - h \sin(\beta_k)]^2 - d^2 \leq 0. \qquad (63)$$

The second case is shown in Fig.9. An important class of designs to discard is the $\boldsymbol{s}$ which lead to manipulators with links described by $\boldsymbol{H_k}$ cross paths. Considering the plane in which $\boldsymbol{H_k}$ takes positions, and given that all points $\boldsymbol{B_k}$ share the same plane, we can say that if two links represented by $\boldsymbol{H_j}$ and $\boldsymbol{H_i}$ do not cross paths with $\alpha_k = 0$ for $k \in \{1, \ldots, 6\}$, they will not cross for in any other value of α_k, leading us to consider the scenario where $\alpha_k = 0$. Considering points $\boldsymbol{H_1}$ and $\boldsymbol{H_2}$, given that the R joint axis of rotation is located at $\boldsymbol{B_1}$ and $\boldsymbol{B_2}$ respectively, and by construction, we know that

João Vale, Alexandre Rocha, Marco Leite and Rodrigo Ventura

$\boldsymbol{B_1^{(y)}} - \boldsymbol{B_2^{(y)}} \leq 0$, we can guarantee that the links represented by points $\boldsymbol{H_1}$ and $\boldsymbol{H_2}$ do not cross paths if

$$C_2(\boldsymbol{s}) = \boldsymbol{H_1^{(y)}} - \boldsymbol{H_2^{(y)}} = [r_b \sin(-d_b) + h\sin(-\beta_0))] - [r_b\sin(d_b) + h\sin(\beta_0))] \leq 0. \quad (64)$$

As depicted in Fig.9, an analogous relation can be applied to the interlink interference between links represented by points $\boldsymbol{H_1}$ and $\boldsymbol{H_3}$:

$$C_3(\boldsymbol{s}) = \boldsymbol{H_3^{(y)}} - \boldsymbol{H_1^{(y)}} = [r_b\sin(\frac{4\pi}{3} + d_b) + h\sin(\frac{4\pi}{3} + \beta_0)] - [r_b\sin(-d_b) + h\sin(-\beta_0)] \leq 0 \quad (65)$$
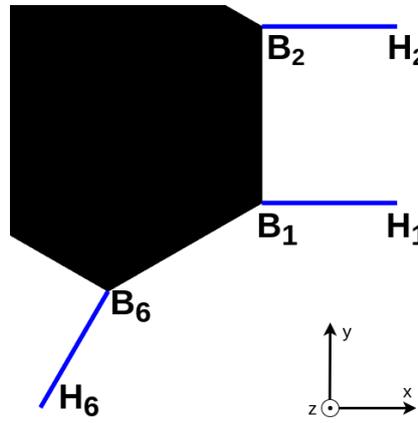
Figure 9: Diagram of link pose when $\alpha_k = 0$ for $k \in \{1, 2, 6\}$, based on Fig.8. The black patch represents the fixed base, connecting all anchors $\boldsymbol{B_k}$. The blue lines represent the R-S links, starting at $\boldsymbol{B_k}$ and ending at $\boldsymbol{H_k}$.

Given the manipulator symmetry, we do not need to check all $\boldsymbol{H_k}$ pairs for inter-link interference, and the relations presented in Eq.(64) and Eq.(65) will suffice.

3.7 Optimization

Given the antagonic nature of work-space volume and accuracy, we wish to find the set of $\boldsymbol{s}$ which best compromise those criteria. Considering this, we consider necessary to employ a multi-objective optimization methodology. Specifically, we wish to maximize the work-space volume ($V_\mathcal{W}$) while minimizing the global translational sensitivity $GTSI$ and global rotational sensitivity $GRSI$. We can easily translate the problem into an all-minimization problem by considering the work-space volume symmetric ($-V_\mathcal{W}$).

With this considerations in mind, we can formulate the following multi-objective optimization problem:

$$\begin{aligned} \text{Minimize} \quad & (-V_{\mathcal{W}_D}, GTSI, GRSI) \\ \text{w.r.t.} \quad & \boldsymbol{s} \in \mathcal{S} \\ \text{subject to} \quad & C_1(\boldsymbol{s}) \leq 0 \\ & C_2(\boldsymbol{s}) \leq 0 \\ & C_3(\boldsymbol{s}) \leq 0 \,. \end{aligned} \quad (66)$$

João Vale, Alexandre Rocha, Marco Leite and Rodrigo Ventura

As far as we know, the performance metric functions presented in Eq.(57) and Eq.(62) lack a closed-form solution, so we will approximate their value by discretizing the work-space. In our implementation, we will use a constant orientation work-space (meaning that $\boldsymbol{R} = \boldsymbol{I}$), but the methodology can be easily expanded to consider the reachable work-space, at the cost of a heavier computational burden.

To compute a point-wise approximation of the Pareto front of the optimization problem formulated in Eq.(66), we will use the Direct Multisearch for Multiobjective Optimization [13] algorithm. Given that Eq.(57) and Eq.(62) lack a closed-form solution, their derivative also has no close-form solution, so a derivative-free method was chosen.

3.8 Results

The point-wise approximation of the Pareto front can be found in Fig.10 with a total of 1822 non-dominated points found after the algorithm completed a total of 10^5 objective function evaluations.

(a) Volume - GTSI.

(b) Volume - GRSI.

(c) GTSI - GRSI.

(d) Prespective.
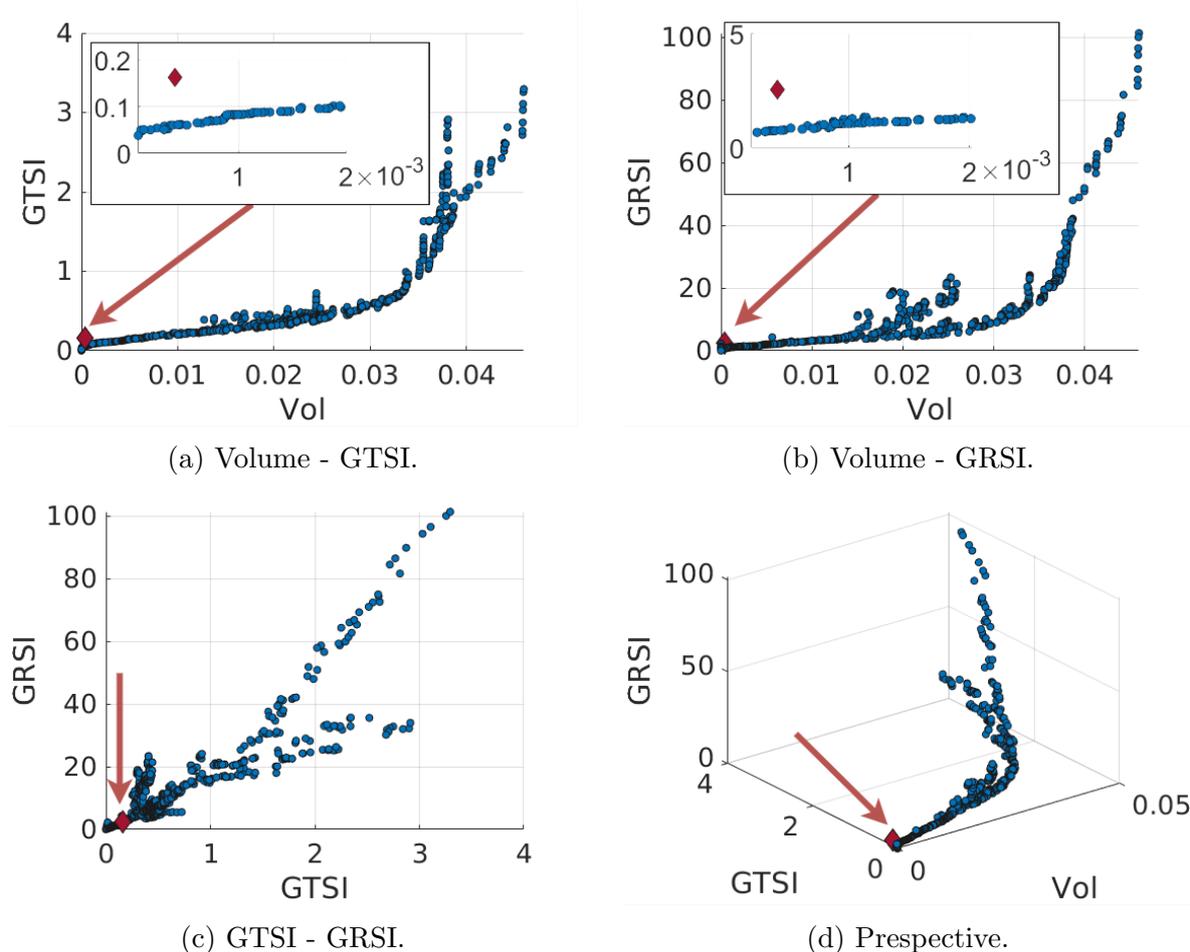
Figure 10: Point-wise Pareto Front Approximation. The red diamond represents ACRO-BAT's first iteration manipulator. A high volume but low GTSI and GRSI is desired.

From these results, we found that as the volume increases, both the rotational and translational sensitivity to actuator displacement also increase, resulting in a decrease in accuracy.

João Vale, Alexandre Rocha, Marco Leite and Rodrigo Ventura

To choose a final design we searched the Pareto set to find the solution with GTSI closer to ACROBAT's sub-optimal manipulator. Table 3 compares the design parameters and performance between both designs and Fig.11 presents a visual representation of the joint placement. The optimized design has a substantial increase in work-space volume while maintaining the same accuracy.

Table 3: Design parameters and performance of ACROBAT's first iteration manipulator and the optimized manipulator taken from Fig.10.

Design	r_b	r_m	d_b	d_m	d	h	ϕ_0	β_0	Vol (10^{-3})	GTSI	GRTS
ACROBAT	52.57	48.14	0.148	0.964	117.50	27.00	0.349	1.571	0.408	0.163	2.539
Opt	60.00	60.00	0.4932	0.0167	200.00	45.43	0.0562	1.2812	6.510	0.162	2.353
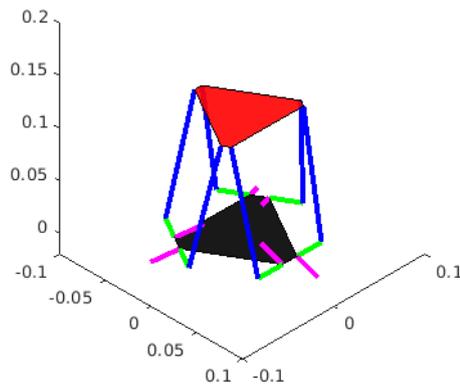
(a) ACROBAT's manipulator.
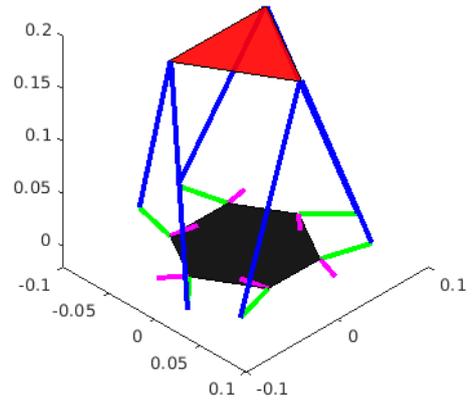
(b) Optimized design.

Figure 11: Joint representation of ACROBAT's first iteration manipulator and the optimized manipulator. The color scheme goes as follows: The red patch is the mobile platform, the black patch the fixed platform, the purple line-segment the actuated joint axis of rotation u_k and the green and blue line-segment are rigid links of size h and d, respectively.

Given the increase in performance shown here, we will substitute ACROBAT's first iteration manipulator by its optimized version.

4 CONCLUSIONS

In conclusion, a methodology for optimal design of an areal robot for in-orbit construction and assembly was presented. The methodology was aimed at propeller based robots but can be easily expanded to other types of propulsion, like cold gas thrusters, needing only to define a fitting parameterization of the actuation matrix. Our approach was to favor maximum force and torque in any direction, considering the type of tasks we intend to complete. However, an alternative approach is to, instead of considering the maximum force and torque in any direction, to consider some directions to be more important than others. This alternative approach might be advantageous if we know a priori which force

and torque directions are more desired in the targeted application. A methodology for parallel manipulator design based on maximizing work-space volume and accuracy was presented and a Pareto front successfully estimated. Multiple approaches can be used to chose the final from the Pareto front. For instance, the task dependent maximum actuator displacement can be provided and the final design chosen accordingly. The presented methodology can also be easily expanded to deal with different types of manipulators and performance metrics.

ACKNOWLEDGEMENTS

REFERENCES

[1] D. Miller, A. Saenz-Otero, J. Wertz, A. Chen, G. Berkowski, C. Brodel, S. Carlson, D. Carpenter, S. Chen, S. Cheng, D. Feller, S. Jackson, B. Pitts, F. Perez, and J. Szuminski. Spheres: A testbed for long duration satellite formation flying in micro-gravity conditions. *Advances in the Astronautical Sciences*, 105 I:167–179, 2000. ISSN 00653438.

[2] M. Bualat, J. Barlow, T. Fong, C. Provencher, T. Smith, and A. Zuniga. Astrobee: Developing a free-flying robot for the international space station. *AIAA SPACE 2015 Conference and Exposition*, pages 1–10, 2015. doi:10.2514/6.2015-4643.

[3] S. Mitani, M. Goto, R. Konomura, Y. Shoji, K. Hagiwara, S. Shigeto, and N. Tanishima. Int-Ball: Crew-Supportive Autonomous Mobile Camera Robot on ISS/JEM. *IEEE Aerospace Conference Proceedings*, 2019-March:1–15, 2019. ISSN 1095323X. doi:10.1109/AERO.2019.8741689.

[4] P. Roque and R. Ventura. Space CoBot: Modular design of an holonomic aerial robot for indoor microgravity environments. *IEEE International Conference on Intelligent Robots and Systems*, 2016-Novem:4383–4390, 2016. ISSN 21530866. doi:10.1109/IROS.2016.7759645.

[5] F. Pierrot, P. Dauchez, and A. Fournier. HEXA: a fast six-DOF fully-parallel robot. In *Fifth International Conference on Advanced Robotics 'Robots in Unstructured Environments*. IEEE, 1991. ISBN 0-7803-0078-5. doi:10.1109/ICAR.1991.240399.

[6] R. E. Stamper, L. W. Tsai, and G. C. Walsh. Optimization of a three DOF translational platform for well-conditioned workspace. *Proceedings - IEEE International Conference on Robotics and Automation*, 4(April):3250–3255, 1997. ISSN 10504729. doi:10.1109/robot.1997.606784.

[7] Y. Lou, G. Liu, and Z. Li. Randomized optimal design of parallel manipulators. *IEEE Transactions on Automation Science and Engineering*, 5(2):223–233, 2008. ISSN 15455955. doi:10.1109/TASE.2007.909446.

João Vale, Alexandre Rocha, Marco Leite and Rodrigo Ventura

[8] Z. Gao, D. Zhang, and Y. Ge. Design optimization of a spatial six degree-of-freedom parallel manipulator based on artificial intelligence approaches. *Robotics and Computer-Integrated Manufacturing*, 26(2):180–189, 2010. ISSN 07365845. doi:10.1016/j.rcim.2009.07.002. URL `http://dx.doi.org/10.1016/j.rcim.2009.07.002`.

[9] K. Tanakitkorn. Design Optimisation of a 6-RSS Parallel Manipulator via Surrogate Modelling. *IOP Conference Series: Materials Science and Engineering*, 501(1), 2019. ISSN 1757899X. doi:10.1088/1757-899X/501/1/012020.

[10] F. Hao and J. P. Merlet. Multi-criteria optimal design of parallel manipulators based on interval analysis. *Mechanism and Machine Theory*, 40(2):157–171, 2005. ISSN 0094114X. doi:10.1016/j.mechmachtheory.2004.07.002.

[11] R. Badora. Stability properties of some functional equations. *Springer Optimization and Its Applications*, 52:3–13, 2012. ISSN 19316836. doi:10.1007/978-1-4614-0055-4_1.

[12] B. McCormick. *Aerodynamics, Aeronautics, and Flight Mechanics*. Wiley, 1994. ISBN 9780471575061.

[13] C. P. Brás and A. L. Custódio. On the use of polynomial models in multiobjective directional direct search. *Comput. Optim. Appl.*, 77:897–918, 2020.

[14] F. Szufnarowski. Stewart platform with fixed rotary actuators : a low cost design study. *Faculty of Technology, Bielefeld University, Germany*, 2013. ISSN 0094114X.

[15] J. P. Merlet. *Parallel Robots*. Springer Publishing Company, Incorporated, 2nd edition, 2010. ISBN 9048170532.

[16] P. Cardou, S. Bouchard, and C. Gosselin. Kinematic-sensitivity indices for dimensionally nonhomogeneous jacobian matrices. *IEEE Transactions on Robotics*, 26(1):166–173, 2010. ISSN 15523098. doi:10.1109/TRO.2009.2037252.

SIZING OF HIGH ASPECT RATIO WINGS INCORPORATING FOLDING WINGTIP

H. Gu[1*], F. Healy[1], and J.E.Cooper[1]

Dept of Aerospace Engineering
Faculty of Engineering
University of Bristol
Email address
huaiyuan.gu@bristol.ac.uk

Abstract. *There is currently much interest in the development of high Aspect Ratio Wings due to the inherent reduction in induced drag that they provide; however, there are a number of potential problems including the increased structural weight and the limits on the wingspan imposed by the airport gate sizes. The use of floating folding wingtips has been shown to not only enable the aircraft to meet with the operational conditions in the airports, but also to reduce loads imposed on the wing. In this work, a comprehensive sizing of aircraft models is performed for a range of aspect ratios and incorporating a folding wing tip device with semi-aeroelastic hinge. The hinge is locked during cruise allowing the optimum aerodynamic performance to be obtained, while releasing it during gust and manoeuvres to achieve effective load alleviation. It was found that the wing-box mass reduces linearly with increasing proportions of the folding wingtip. A 30% reduction in wing weight can be achieved by extending the folding wingtip up to 40% of the wingspan, leading to an improved performances at the overall system level.*

Keywords: High Aspect Ratio Wings, Folding Wing tips, Preliminary Aircraft Design

H. Gu, F. Healy, and J.E.Cooper

1 INTRODUCTION

The wing aspect ratios used in current commercial aircraft are far below the optimum [1], leading to a strong drive to implement higher aspect ratio wings in the next generation of aircraft, reducing induced drag during flight. However, there are a number of challenges in the design of high aspect ratio wings. Chief among these is the limitations imposed by the operational conditions in the airports such as the gate, runway and taxiway separation. Therefore, folding wingtips have become an attractive solution to many aircraft designers as it would allow the wingspan to be reduced on the ground, enabling the aircraft to to meet operational requirements. High aspect ratio wings often leads to penalties in structural weight due to the increase in the bending moment, which led to work investigating the ability of the hinged wingtip device to reduce the bending load by allowing it to fold in-flight. Recent studies suggest that the folding wingtip devices can also be exploited in flight to reduce both static and aerodynamic loads [2–4]. However, it is unclear what the impact of the load alleviation achieved by the folding wingtip devices is upon the weight of the wing-box and the benefit attained at the overall system level.

Figure 1 shows a schematic drawing of the folding wingtip device where the hinge line is at an angle to the oncoming flow direction, known as the flare angle,Λ. With this configuration, the local angle of attack on the folding wingtip reduces with the fold angle,θ. When the hinge is released in flight, the wingtip folds towards to a particular fold angle known as the coast angle, at which the aerodynamic and gravitational moments about the hinge balance, and the system is statically stable. At small fold angle, the change in the local angle of attack can be related to the fold angle,θ, as

$$\Delta\alpha = -\arctan(\sin\Lambda\tan\theta) \tag{1}$$

The influence of the flare angle upon the load alleviation has been reported [2] [5]. It was shown that a better load alleviation can be obtained by increasing the flare angle,Λ, and reducing the overall mass of the wingtip.

In this paper, sizing analysis has been performed on aircraft models created with varying wing aspect ratios (AR) and folding wingtip configurations. First, the aeroelastic models are described including the wing-box and planform properties, and analysis methods, where an A321-like aircraft was chosen as the baseline model. A sizing framework is then presented which introduces a detailed methodology for evaluating the wing-box weight. Finally, a comparison has been made between the sizing results of the different aircraft models, where the results have been used to calculate the range of the aircraft for a given mission.

2 AIRCRAFT MODEL

An A321-like aircraft model was built as the baseline model, and the wing configurations including the leading edge(LE) sweep angles, trailing edge (TE) sweep angles, dihedral, taper ratio, and thickness to chord ratios were listed in Table 1 where the data were sourced from the CeRAS CSR-01 technical report[5]. To investigate the performances of the folding wingtip device on different aspect ratio wings, a number of new model configurations, with increased aspect ratios were built by stretching the wingspan of the baseline model. During this process the surface area, leading-edge sweep angle, taper ratio and engine position were kept constant as illustrated in Figure 3. The second
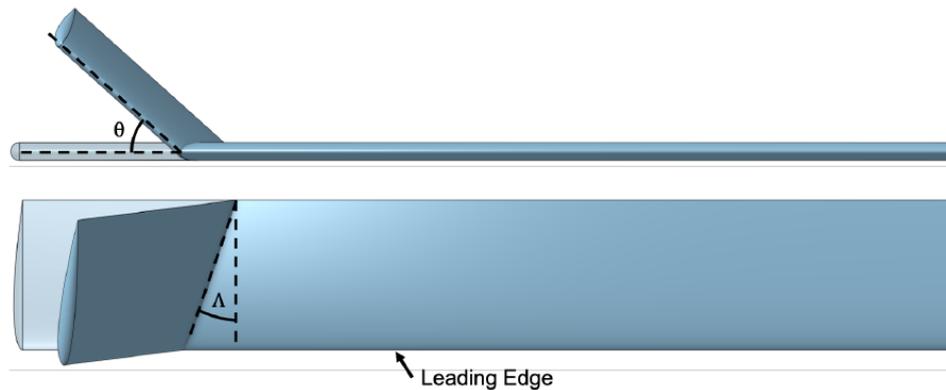
Figure 1: Schematic drawing of the folding wing tip device with a flare angle of Λ and fold angle,θ.

part of the Table 1 shows the mass configuration defined on the baseline model. It was assumed that the mass of the aircraft minus the mass of the wings, was a constant value for all model configurations.

Figure 2 shows the aeroelastic model that has been implemented in this study. The structure was created with beam elements (element code CBEAM in Nastran) and the material properties were chosen based on Aluminium 7075 with modulus of 70 GPa and yield strength of 520 MPa. The payload, fuel and secondary mass were modelled as lumped masses distributed across the structure (element code CONM2 in Nastran). The Aerodynamic forces were computed using the Double Lattice Method (DLM) implemented in MSC. Nastran. A beam spline was defined which generates interpolation between the aerodynamic mesh and the structural nodes, allowing for the aerodynamic forces to be transferred to the structure and change with respect to the displacement of the structural nodes. Note that the aerodynamic panels were only assigned to the wings and tailplane. The aerodynamic forces produced by the fuselage and engine nacelles were neglected.

(a) structural model (b) aerodynamic model
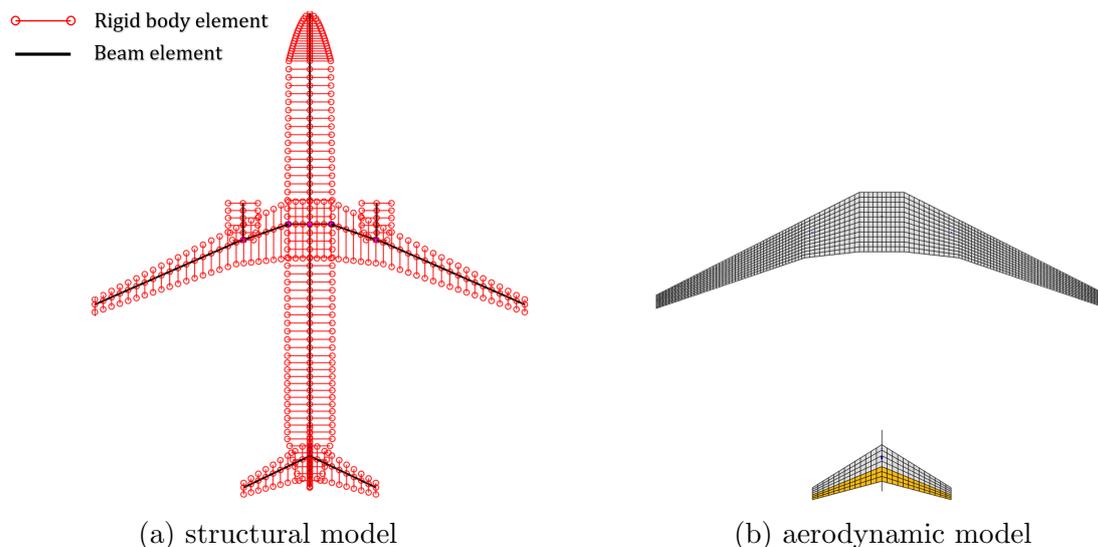
Figure 2: Aeroelastic model used in the analysis

Folding wingtips were implemented on each aircraft model as separate bodies, with the relative motion of the inner wing and wingtip constrained at two coincident nodes along the hinge line, only allowing for the relative rotation about the hinge line as shown in Figure 4. Each wing-box model consists of 36 beam elements, with 25 elements inboard of the hinge line and 11 elements along the folding wingtip. An active hinge control system was considered in the present study, where the hinge will be locked during cruise to obtain the optimum aerodynamic efficiency, and released during manoeuvres or gust to reduce the loads carried by the wing, leading to a reduced structural weight. The hinge flare angle was held constant at 25°, whereas the proportion of the wings devoted to the folding wingtips, η, was ranged from 10% up to 40% of the wingspan.

Table 1: Summary of the baseline aircraft model (A321).

Wing plan form Parameters	Value		
Span position(m)	2	6.37	17.5
LE sweep angle(°)	0	27	27
TE sweep angle(°)	0	0	16.5
Dihedral(°)	0	5	5
Thickness ratio	0.15	0.12	0.11
Front spar	0.15	0.15	0.15
Rear spar	0.65	0.65	0.65
Mass configurations	**Mass (kg)**		
Payload	25000		
Max.take off weight (MTOW)	97000		
Operating weight empty (OWE)	47800		
Max. fuel weight	25860		
Engine mass	7362		
Pylon	1630		
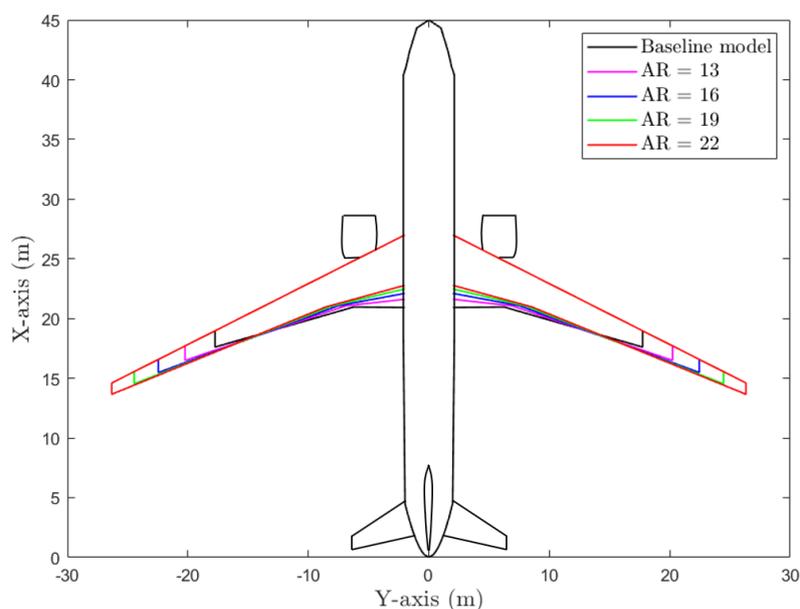
Figure 3: Stretched aircraft models.

H. Gu, F. Healy, and J.E.Cooper
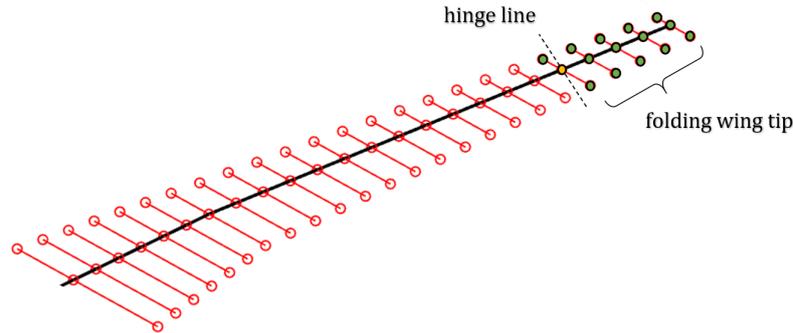
Figure 4: Structural model of the wing with folding wingtip.

3 SIZING FRAMEWORK

Sizing framework was established shown in Figure 5 to determine the structural mass of the wing-box for each aircraft configuration described in section 2. After setting up the planform, lumped masses were assigned to the beam nodes to represent the payload, fuel mass, secondary mass, engine and pylon. The maximum take-off mass of each model was assumed to be 97,000 kg, which was then used for estimating the secondary structural mass of the wing including the high-lifting devices on the leading and trailing edge using the empirical formulas given in the work of Torenbeek[6]. The sum of the secondary mass and fuel mass were then distributed along the wing span based on the internal volume of each section.

The wing structure was assumed to be a box-beam as shown in Figure 6, where the stiffness and strength were determined by the thickness of individual component i.e. spar, skin and stringers. For each sizing iteration, optimisation of the aerodynamic twist was performed to ensure an elliptical lift distribution was achieved along the wingspan when the hinge was locked, to maximise the aerodynamic efficiency.

On each design iteration the internal stresses were then computed at a range of load cases including both static manoeuvres and gust encounters, as Table 2. The variables spar thickness, t_{spr} , skin thickness, t_{skn}, and stringer area, A_{strg} were then adjusted based upon the the ratio of the internal stresses to their corresponding critical values. When the ratio is greater than one, indicating the structure failures will occur. Therefore, a higher thickness will be applied to the model for the next sizing iteration and vice versa. The whole iterative process ends when the internal stresses in the spar, skin and stringers converge towards their critical stresses where a safety factor of 1.5 was applied throughout the internal stress computation.

3.1 Beam model formulation

The wing-box was first discretised into consecutive sections and each section was represented by a symmetrical box with $z-$stringers attached to the upper and lower skin as shown in Figure 6. The box width was determined based upon the relative spar location. which were assumed to be located at 15% and 65% of the chord. The box height was equal to 79% of the maximum thickness of the wing to account for the effect of the airfoil curvatures, where the reduction factor was derived to ensure the wing-box fit with a NACA 4-digits airfoil profile[7]. The stringer pitch was 0.24 metres, and the stringer number was determined based on the wing-box width at each section. The stringer dimensions were

fully characterised by its area, A_{strg}, where $A_{strg} = 3d_s t_s$ and $t_s = 0.12d_s$. The initial guess of the spar thickness, t_{spr0}, skin thickness, t_{skn0}, and stringer area, A_{strg0}, were given to each section to allows for the computation of an initial stiffness matrix for the beam, which was then used for the formulation of 1D beam model. A new set of stiffness values will be assigned to the beam model based on the updated thickness variables i.e. t_{spr}, t_{skin} and A_{strg}.
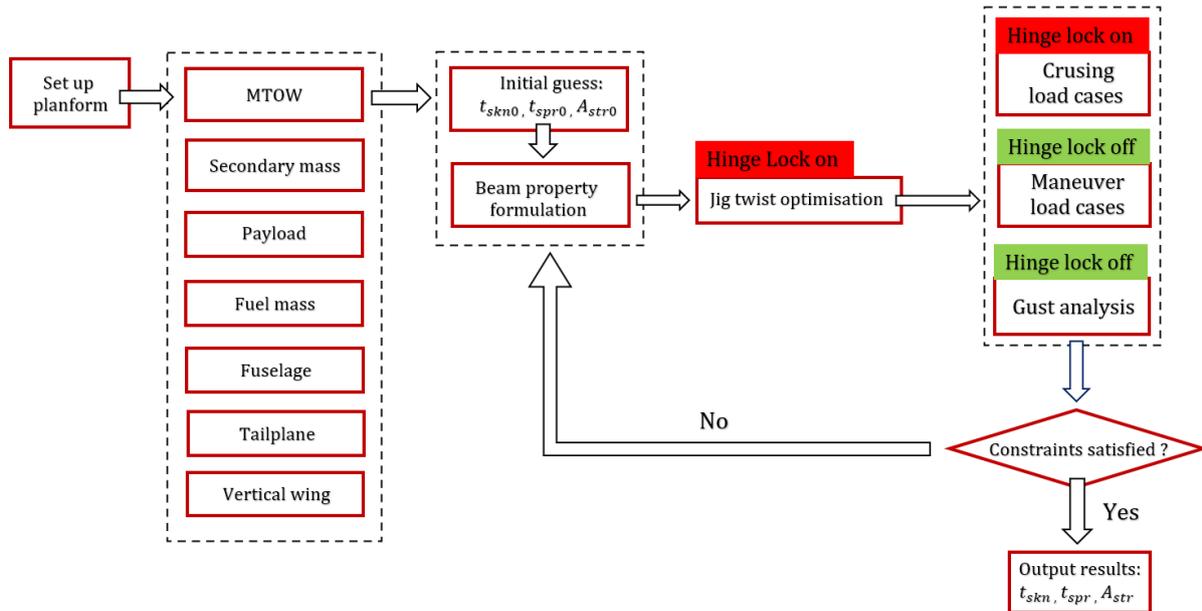
Figure 5: Sizing frameworks for wing-box mass estimation.
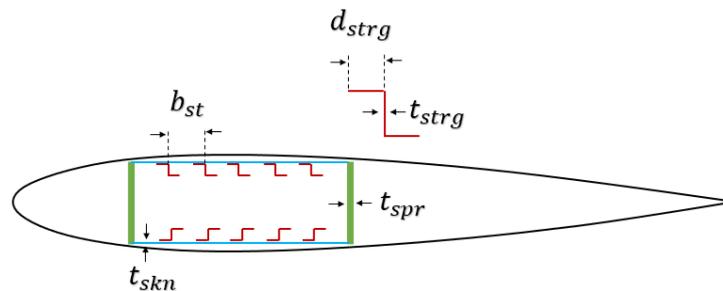
Figure 6: Wing-box cross section.

3.2   Load cases

The load case 1-3 presented in the Table 2 were considered with the aircraft manoeuvring at different altitudes where the hinge of the wingtip was released. The cruise condition was examined in the load case 4 in which the hinge was locked in the trim. The load cases 5-8 evaluated the gust response of the aircraft during level flight at different altitudes with hinge lock off. In this study, the aircraft was assumed to be subjected to a family of discrete gusts in the form of one minus cosine (1MC), where the gust length, L_g, was ranged from 18 to 214 metres according to CS-25 certification specifications [8]. The gust profile was defined as,

Table 2: Load cases considered in the sizing.

Load case	Load factor (g)	Gust length (m)	Gust type	March No.	Altitude (ft)
1	2.5	NA	NA	0.78	36000
2	2.5	NA	NA	0.48	3000
3	-1	NA	NA	0.48	3000
4	1	NA	NA	0.78	3000
5	1	18–214	± 1MC	0.78	36000
6	1	18–214	± 1MC	0.6	20000
7	1	18–214	± 1MC	0.48	3000

$$w_g(t) = \frac{U_{ds}}{2}(1 - \cos\frac{2\pi Vt}{L_g}) \tag{2}$$

where V is the true air speed (TAS) and U_{ds} is the peak gust velocity, which is calculated as,

$$U_{ds} = U_{ref}F_g(\frac{H}{106.17})^{\frac{1}{6}} \tag{3}$$

F_g is the load alleviation factor which is taken as 1. U_{ref} is the reference gust velocity determined based on the CS-25 certification specifications, which varies linearly from 13.4 m/s at an altitude of 15,000 ft to 7.9 m/s at an altitude of 50,000 ft.

3.3 Internal stresses

Tensile yield

It is assumed that the vertical shear force, V_z, is predominantly carried by the spars, and the bending loads are taken by the skin and stringers, as shown in Figure 7, whereas the shear flow produced by the torque,T_x, is distributed across the skins and spars. Hence, the normal stress in the skin can be calculated as,

$$\sigma_{skn} = \frac{M_y}{I_{yy}}(\frac{h_b}{2} - \frac{t_{skn}}{2}) \tag{4}$$

The shear stresses in the spar and skin are related to the vertical shear force and torque as,

$$\tau_{skn} = \frac{T_x}{2A_b t_{skn}} \quad \text{and} \quad \tau_{spr} = \frac{T_x}{2A_b t_{spr}} + \frac{V_z Q}{I_{yy} t_{spr}} \tag{5}$$

where V_z is the vertical shear force, Q is the first moment of area with respect to the horizontal neutral axis. I_{yy} is the moment of inertia. The critical stress for the tensile failure is determined by the Von Mise yield criterion [9], where the equivalent tensile stresses in the skin and spar can be calculated as,

$$\sigma_{skn}^{von} = \sqrt{\sigma_{skn}^2 + 3\tau_{skn}^2} \quad \text{and} \quad \sigma_{spr}^{von} = \sqrt{\sigma_{spr}^2 + 3\tau_{spr}^2} \tag{6}$$

Hence, the sizing constraints for tensile failure can be expressed as,

$$\frac{\sigma_{skn}^{von}}{\sigma_y} \leq 1 \quad \text{and} \quad \frac{\sigma_{spr}^{von}}{\sigma_y} \leq 1 \tag{7}$$

Skin buckling

Compressive failure has also been considered in the sizing routine to avoid compressive yielding and buckling of the skin and stringers. According to Niu [10], the critical buckling stresses of the skin under compression and shear load are,

$$\sigma_{skn}^{b} = \frac{k_c \pi^2 E}{12(1-v^2)} \frac{t_{skn}}{b_{st}} \quad \text{and} \quad \tau_{skn}^{b} = \frac{k_s \pi^2 E}{12(1-v^2)} \frac{t_{skn}}{b_{st}} \tag{8}$$

where b_{st} is the stringer pitch. k_c and k_s are the buckling coefficient for the compression and shear loads which are equal to 4 and 5.6 respectively. This leads to the sizing constraint,

$$\frac{\sigma_{skn}^{p}}{\sigma_{skn}^{b}} \leq 1 \quad \text{and} \quad \frac{\sigma_{spr}^{max}}{\tau_{skn}^{b}} \leq 1 \tag{9}$$

σ_{skn}^{p} and σ_{spr}^{max} are the compressive principal stress and the maximum shear stress on the skin which can be related to σ_{skn} and τ_{skn} as,

$$\sigma_{skn}^{p} = \frac{\sigma_{skn}}{2} + \sqrt{(\frac{\sigma_{skn}}{2})^2 + \tau_{skn}^2} \quad \text{and} \quad \tau_{skn}^{max} = \sqrt{(\frac{\sigma_{skn}}{2})^2 + \tau_{skn}^2} \tag{10}$$

Stringer crippling

The stringer was sized to avoid local instability i.e. crippling. The general solution of the allowable crippling stress for stringer was given by Niu[10] as,

$$\frac{\sigma_{cc}}{\sigma_{cy}} = B(\sqrt{\frac{\sigma_{cy}}{E}(\frac{d_{strg}}{t_{strg}})})^A \tag{11}$$

where σ_{cy} and E are the compressive yield stress and the modulus of the material. The coefficients A and B for each segment of the $z-$stringer are given by -0.79 and 0.62 for segment 1 and 3 as shown in Figure 7. For segment 2 with no free edge, the coefficients are -0.80 and 1.21 respectively. The allowable crippling stress for the entire section of the z-stringer is obtained by calculating the weight average of σ_{cc} for each segment,

$$\sigma_{cc}^{*} = \frac{\sum d_{strg}^{n} t_{strg}^{n} \sigma_{cc}^{n}}{\sum d_{strg}^{n} t_{strg}^{n}} \tag{12}$$

This leads to the sizing constraint,

$$\frac{\sigma_{strg}}{\sigma_{cc}^{*}} \leq 1 \tag{13}$$

H. Gu, F. Healy, and J.E.Cooper

Column buckling

The buckling stress of the skin-stringer panel was related to the slenderness ratio, K, which is defined as,

$$K = \frac{L}{\rho\sqrt{c}} \tag{14}$$

where L is equal to the rib pitch. The end rigidity coefficient, c, is taken as 1. ρ is the least radius of gyration of the column cross-section which can be calculated as,

$$\rho = \sqrt{\frac{1}{A_{eff} + A_{strg}}} \quad \text{and} \quad A_{eff} = 1.7t_{skn}^2\sqrt{\frac{E}{\sigma_{strg}}} \tag{15}$$

For columns with high slenderness ratio, the buckling stress is well characterised by the classical Euler equation,

$$\sigma_{col}^E = \frac{\pi^2 E}{K^2} \tag{16}$$

For low or intermediate slenderness ratio, the failure is predominantly due to local crippling or compressive yielding where the critical stress is calculated based on the Johnson-Euler equation,

$$\sigma_{col}^J = \sigma_{cc}^*(1 - \frac{\sigma_{cc}^* K^2}{4\pi^2 E}) \tag{17}$$

Hence the column buckling stress is expressed,

$$\sigma_{col} = \min(\sigma_{col}^E, \sigma_{col}^J) \tag{18}$$

The constraint for skin-stringer panel failure can therefore written as,

$$\frac{\sigma_{strg}}{\sigma_{col}} \leq 1 \tag{19}$$
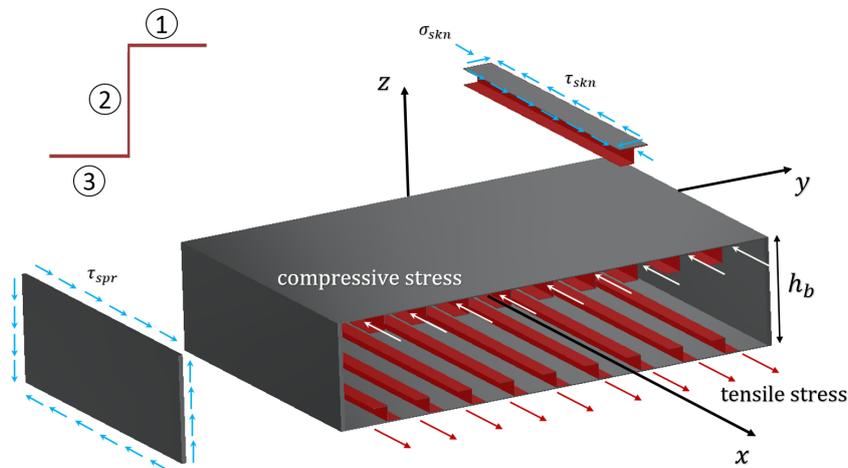
Figure 7: Wing-box stress.

H. Gu, F. Healy, and J.E.Cooper

4 RESULTS

4.1 Coast angle

The sizing analysis has been performed on the aircraft models with a wing aspect ratio ranging between 10 and 22 as described in section 2. Folding wingtips with active hinge lock were implemented on each model, where the relative size of the wingtip with respect to the overall wingspan, denoted as, η, was increased from 10% to 40%. Figure 8 shows the wing deflection of an aircraft model with, $AR = 16, \eta = 30\%$, during cruise (with hinge lock on) and maneuverer (free hinge). The coast angle denoted as θ_c, reduces almost linearly with increasing η, as shown in Figure 9 which is associated with the variation in mass, centre of mass and the centre of aerodynamic pressure on the folding wingtip.

(a)

(b)
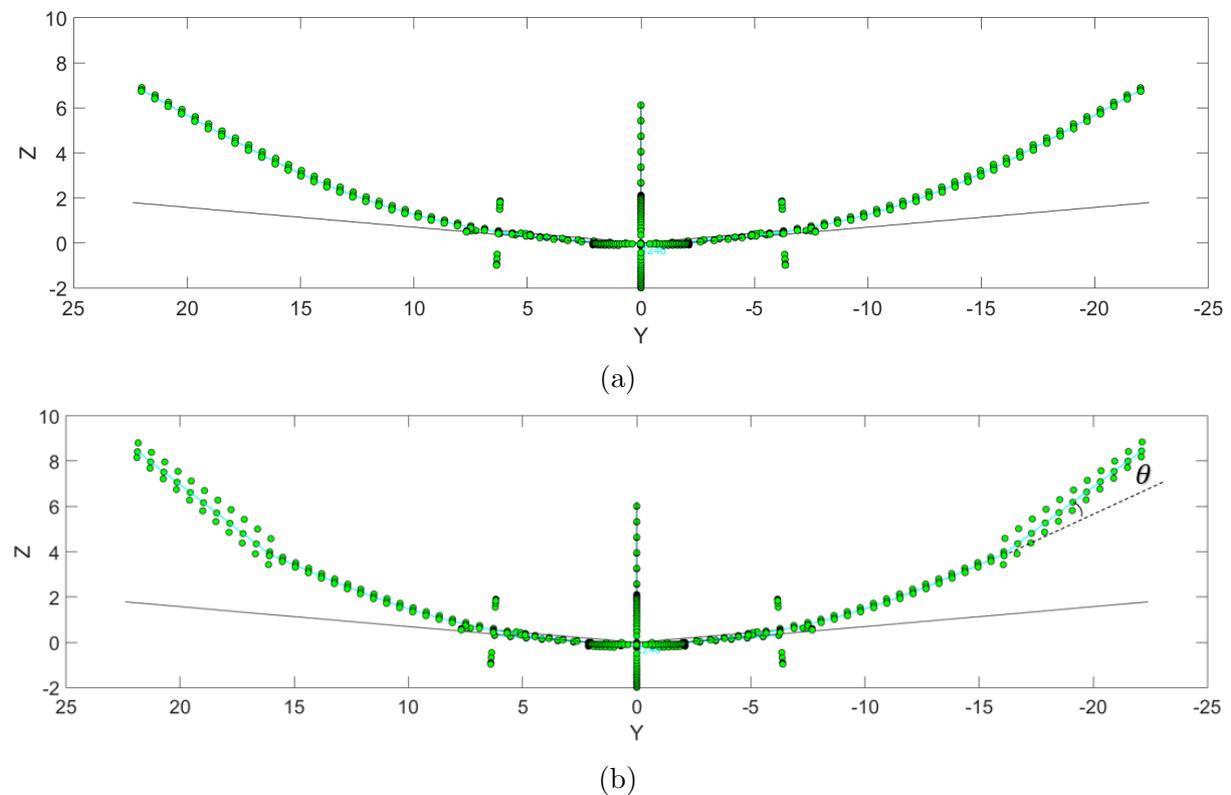
Figure 8: . Wing deflection of the aircraft model with $AR = 16$ and $\eta = 30\%$, during (a)cruise (b)manoeuvre.

4.2 Load distribution

Figure 10 compares the incremental gust loads including, bending moment, vertical shear force and torque on the model created with varying hinge positions (leading to the varying size of the folding wingtip). The results represent the upper bound of the loads calculated from the predefined gust families described in the section 3. It was found that the incremental bending moment, ΔM, reduces with increasing folding wingtip size,η, as a higher lift was generated from the in-board section with reduced average moment arm with respected to the wing root. The incremental vertical shear forces, ΔV, were predominantly distributed on the inboard section, although there is a small amount of shear force taken up by the folding wing tip. There is no obvious effect of the wingtip

H. Gu, F. Healy, and J.E.Cooper
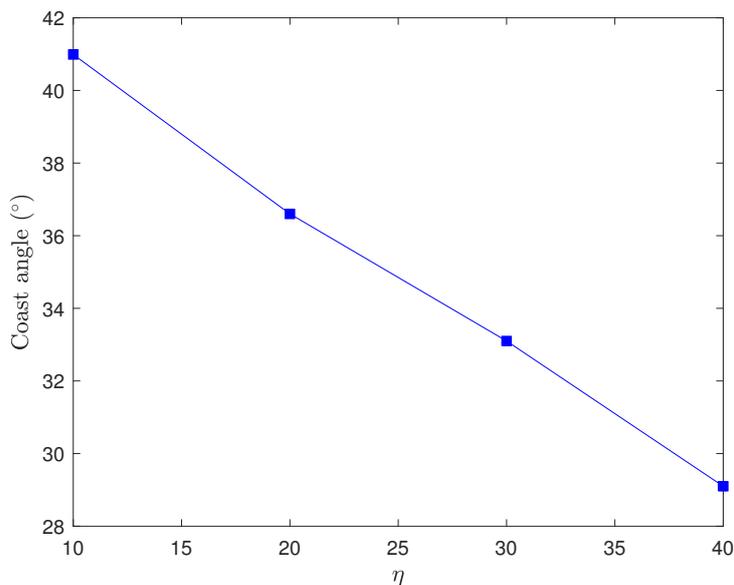
Figure 9: Coast angle of AR 16 model with changing size the folding wingtip.

size upon the magnitude of the incremental vertical shear forces particularly at the wing root. It shows that the increase in the folding proportion results in an increased torque at the wing root. This is attributed to the increased oscillating motion of the engine caused by the increased lifting forces applied to the inboard wing, leading to a higher vertical acceleration on the wing sections.

Figure 11 shows the distribution of external forces including the out of plane bending moment, vertical shear force and torque on an aircraft model with $AR = 16$, subjected to the load case 1 described in the Table 2, It was found that the bending moment reduces significantly with the increasing size of the folding wingtip, particularly for $\eta > 20\%$. There are no clear correlations between the vertical shear force and η when $\eta < 20\%$. However, an obvious reduction in the shear force is seen for $\eta > 30\%$, which is associated with the change in the bending moment distribution as the magnitude of the shear force is proportion to the derivative of the bending moment, dM/dx. With a significant reduction in the bending moment,M, its derivative respect to the spanwise distance, x, is also decreased. However, there are no clear relationship between η and torque observed from the results.

4.3   Wing-box mass

The reduced external loads applied on the wing-box due to the folding wingtip resulted in a lower thickness of the spar, skin, and smaller area of stringers in the sizing results. Figure 12 presents the distribution of the bending stiffness of the sized wing-box, where the required stiffness reduces with increasing η. A more significant impact has been seen on the wing-box weight as shown in Figure 13. It was found that the folding wingtip resulted in a higher percentage of the weight reductions of the wing-box with higher aspect ratios. Reducing the wing-box mass by approximately 30% when $\eta = 40\%$.
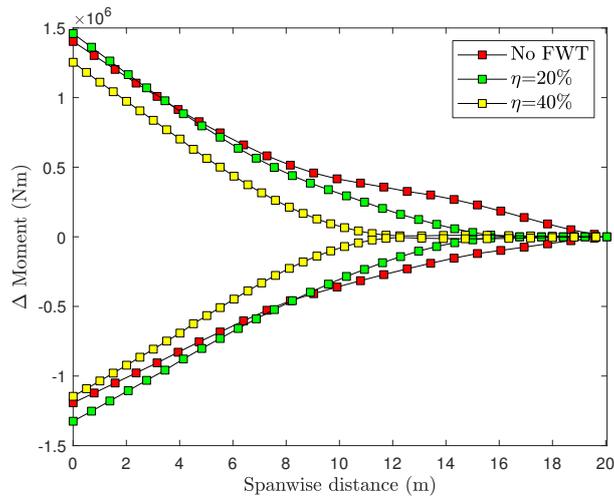
(a)
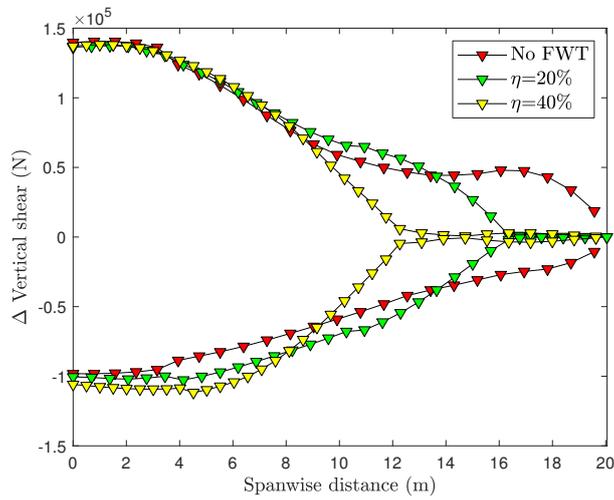
(b)
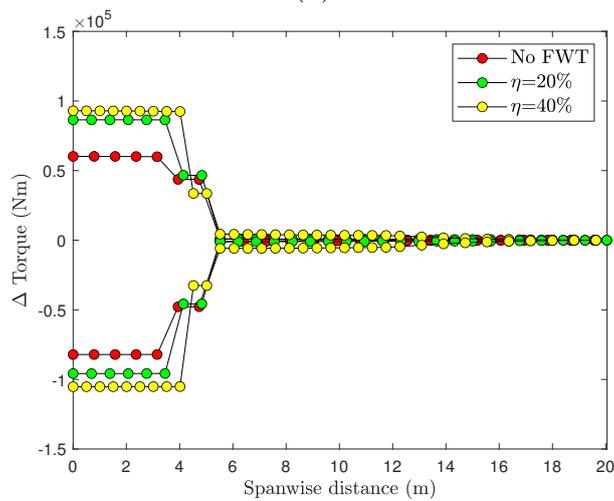
(c)

Figure 10: Incremental gust load of AR 16 model with changing η, (a)out of plane bending moment (b)vertical shear (c)torque.

H. Gu, F. Healy, and J.E.Cooper
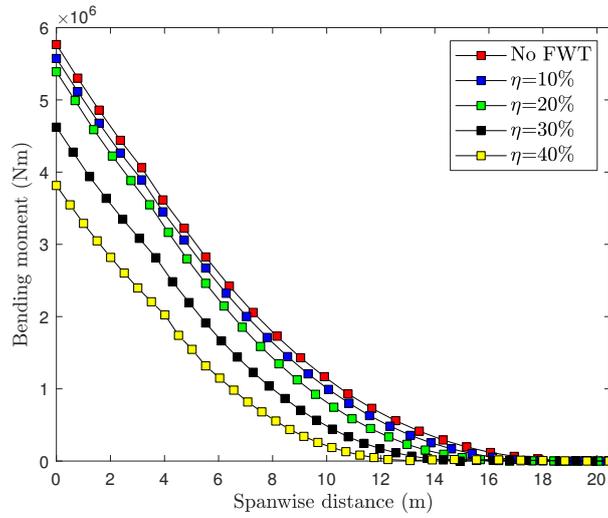
(a)
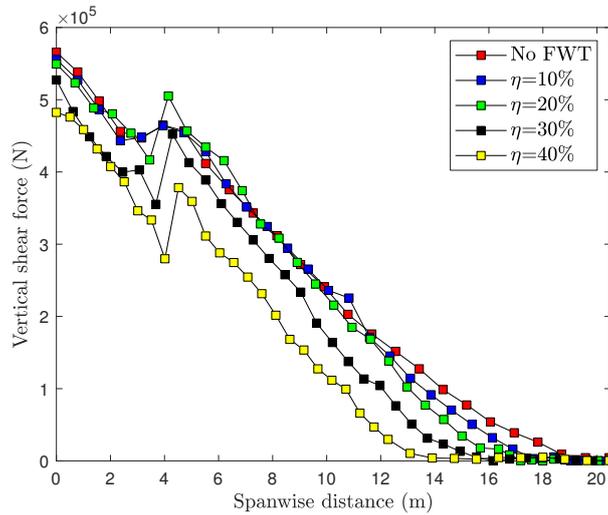
(b)
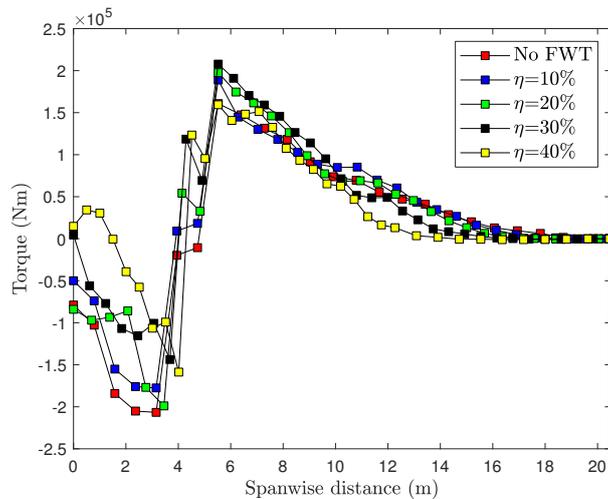
(c)

Figure 11: Incremental gust load of AR 16 model with changing η, (a)bending moment (b)vertical shear (c)torque.

(a)

(b)
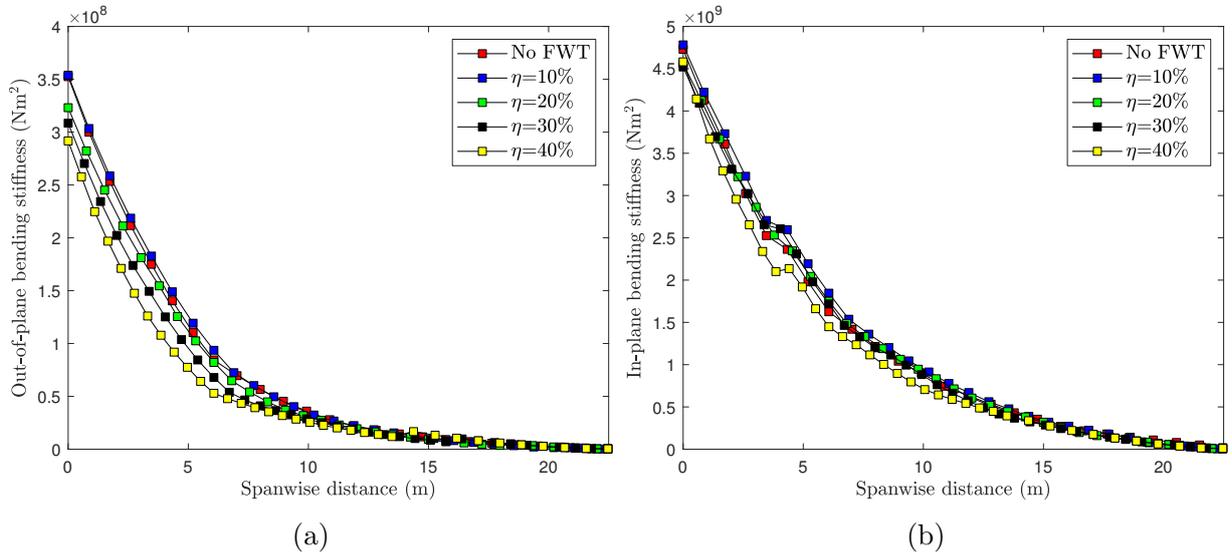
Figure 12: (a)Out-of-plane and (b)In-plane bending stiffness of the sized wing-box.
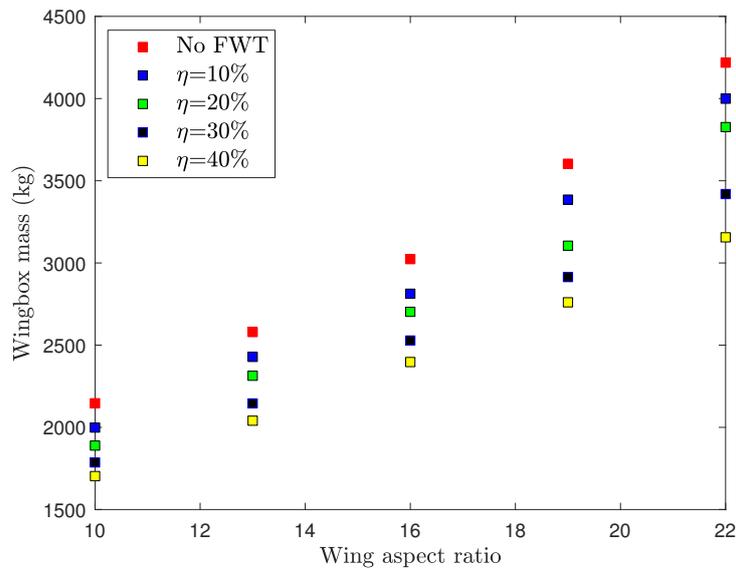
Figure 13: Variation in the wing-box mass of the sized aircraft model, with varying aspect ratio and folding wingtip size.

4.4 Breguet range

The range of the aircraft was calculated for the cruise condition using the Breguet range equation [11] with full payload (25,000 kg) and half fuel tank (12,930 kg). The induced drag was estimated based upon the lift distribution where the detailed computation is described in the work of Kalman et.al. [12]. The zero-lift drag was estimated by sum up the contributions of individual components including the fuselage, wings, and nacelle by [13],

$$C_{D0} = \frac{\sum C_{fc} FF_c Q_c S_{wetc}}{S_{ref}} \tag{20}$$

where C_f is the skin friction drag coefficient, FF is the form factor which takes into account drag components due to pressure drag. The factor Q is associated with the interference drag. S_{wet} and S_{ref} are the wetted area and reference area of the wing, respectively. Figure 14 shows the calculated drag polar for the aircraft models across different aspect ratios, from which the lift to drag ratio, L/D, for the given mission can be calculated, as shown in Figure 15. Hence the range of the aircraft models can be estimated as,

$$Range = \frac{V}{SFC\ g} \frac{L}{D} \ln(\frac{W_i}{W_f}) \tag{21}$$

where the specific fuel consumption, SFC, is taken as 16.03 $(g/s)/kN$, V is the cruise velocity which assumed to be 230 m/s, W_i and W_f are the initial and final weight of the aircraft. The calculated results are presented in Figure 16, where it shows the range can be increased significantly with increasing aspect ratio, while an additional improvement is obtained by introducing the folding wingtip to the models. With an increase in the folding proportion, η , more weight can be reduced from the wing-box, leading to a better efficiency and higher range for a given mission.
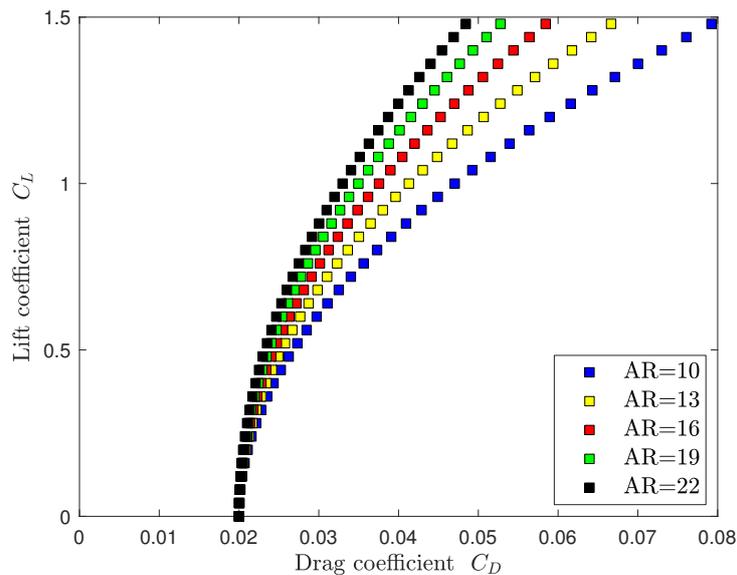
Figure 14: Drag polar of the aircraft models created with different wing aspect ratios.

H. Gu, F. Healy, and J.E.Cooper
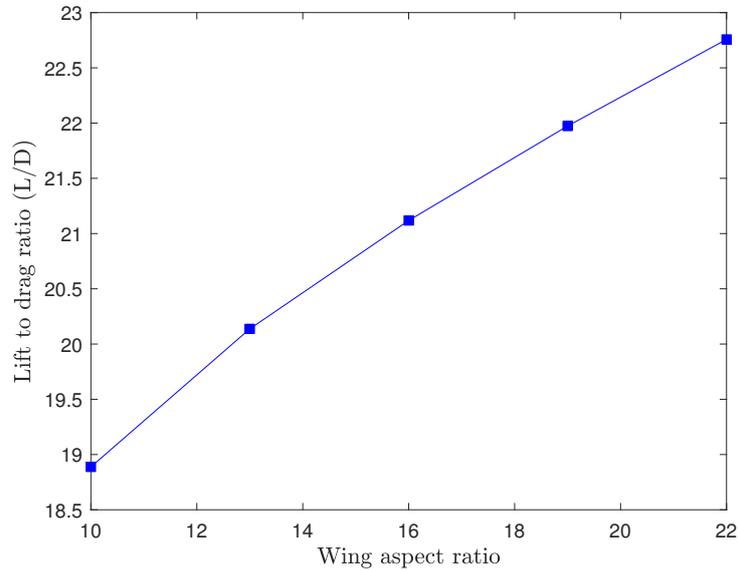
Figure 15: Lift to drag ratio of the aircraft models subjected to the predefined mission.
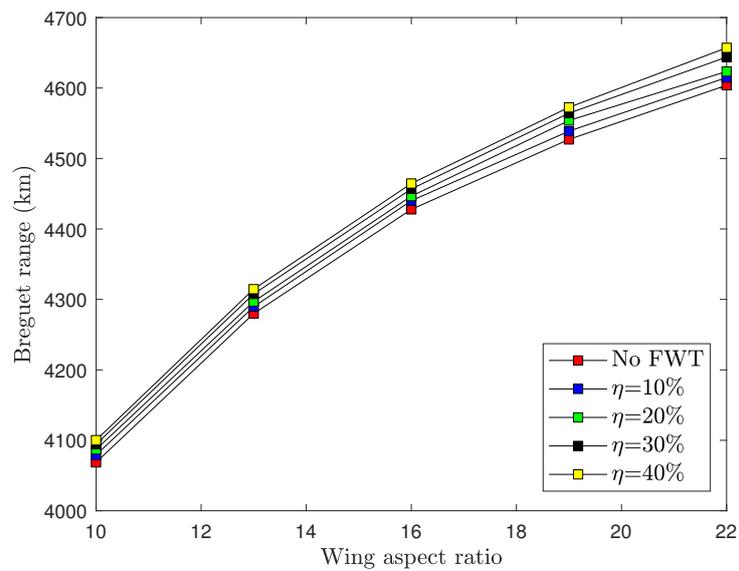
Figure 16: Breguet range of the aircraft models with different wing aspect ratios and folding wing tip proportions.

5   CONCLUSIONS

In this paper, aircraft models with varying wing aspect ratios were sized with changing folding wingtip configurations. The influence of using folding wingtip as a load alleviation device upon the wing-box weight and aircraft range was examined. From the static and gust analysis, it was observed that the bending moment in the wing was significantly reduced with increasing the size of the folding wingtip, η, leading to a reduced wing-box weight. A 30% reduction of the wing-box weight were found when the size of the folding wingtip was increased up to 40% of the wingspan, resulting in an increased range. By applying the Breguet range equation, it was found that the range of the aircraft model with AR of 22 was increased by approximately 1.5% with the folding wingtip device. A higher percentage of the improvement in range is expected to be seen when the wing aspect ratio increases further, where the wing weight takes up a greater proportion of the overall structural weight. The investigation of the 'sweet spot' for the optimum aspect ratio with its corresponding folding wingtip configuration is to be carried out in the next stage of the study.

ACKNOWLEDGMENTS

REFERENCES

[1] D. E. Calderon, J. E. Cooper, M. Lowenberg, S. A. Neild, and E. B. Coetzee. Sizing high-aspect-ratio wings with a geometrically nonlinear beam model. *Journal of Aircraft*, 56(4):1455–1470, 2019. doi:10.2514/1.C035296.

[2] A. Castrichini, V. Hodigere Siddaramaiah, D. E. Calderon, J. E. Cooper, T. Wilson, and Y. Lemmens. Nonlinear folding wing tips for gust loads alleviation. *Journal of Aircraft*, 53(5):1391–1399, 2016. doi:10.2514/1.C033474.

[3] A. Castrichini, V. H. Siddaramaiah, D. Calderon, J. Cooper, T. Wilson, and Y. Lemmens. Preliminary investigation of use of flexible folding wing tips for static and dynamic load alleviation. *The Aeronautical Journal*, 121(1235):73–94, 2017. doi:10.1017/aer.2016.108.

[4] J. E. Cheung. R. C. M., Rezgui. D. Cooper and W. T. Testing of a hinged wingtip device for gust loads alleviation. *Journal of Aircraft*, 55(5):2050–2067, 2018. doi:10.2514/1.C034811.

[5] K. Risse. Ilr micado design of ceras csr-01 technical report. *Institute of Aerospace Systems (ILR), RWTH Aachen University*, 2014.

[6] E. Torenbeek. Development and application of a comprehensive, design-sensitive weight prediction method for wing structures of transport category aircraft. *Delft Univ. of Technology Rept*, 1992.

[7] G. Chiozzotto. A modular implementation of aircraft simplified loads methods for conceptual design and variable fidelity processes. *In: Proceedings 62nd Deutscher Luft- und Raumfahrtkongress*, 2013.

[8] Cs-25 certification specifications for large aeroplanes. *European Aviation Safety Agency (EASA)*, 2003.

[9] J.R.Barber. *Intermediate Mechanics of Materials*. Springer, Dordrecht, 2nd edition, 2011. ISBN 978-94-007-0295-0.

[10] M. C. Niu. *Airframe Stress Analysis and Sizing*. Adaso/Adastra Engineering Center, 3rd edition, 2011. ISBN 978-9627128120.

[11] D. R. Lloyd R Jenkinson, Paul Simpkin. *Civil jet aircraft design*. American Institute of Aeronautics and Astronautics, 1999. ISBN 978-0340741528.

[12] K. T. P., G. J. P., and R. W. P. Spanwise distribution of induced drag in subsonic flow by the vortexlattice metho. *Journal of Aircraft*, 7(6):574–576, 1970. doi:10.2514/3.44219.

[13] D. P. Raymer. *Aircraft Design: A Conceptual Approach*. AIAA Education Series, 5th edition, 2012. ISBN 9781600869112.

CONSTRAINED BAYESIAN OPTIMIZATION OVER MIXED CATEGORICAL VARIABLES, WITH APPLICATION TO AIRCRAFT DESIGN

Paul Saves[1,2], Nathalie Bartoli[2], Youssef Diouane[1], Thierry Lefebvre[2], Joseph Morlier[3], Christophe David[2], Eric Nguyen Van[2] and Sébastien Defoort[2]

1: ISAE-SUPAERO, Université de Toulouse, Toulouse, France
{paul.saves2,youssef.diouane}@isae-supaero.fr

2: ONERA/DTIS, Université de Toulouse Toulouse, France
{nathalie.bartoli,thierry.lefebvre,christophe.david,eric.nguyen_van,sebastien.defoort}@onera.fr

3: ICA, Université de Toulouse, ISAE-SUPAERO, MINES ALBI, UPS, INSA, CNRS, Toulouse, France
joseph.morlier@isae-supaero.fr

Abstract. *Multidisciplinary Design Optimization (MDO) methods aim at adapting numerical optimization techniques to the design of engineering systems involving multiple disciplines or components. Among MDO architectures, various ones are considering the resolution of the Multidisciplinary Design Analysis (MDA). In our study, the system of interest being an aircraft, the resolution of the MDA will be provided by the Future Aircraft Sizing Tool with Overall Aircraft Design (FAST-OAD), a point mass approach that estimates the required fuel and energy consumption for a given set of top-level aircraft requirements. In this context, a large number of mixed continuous, integer and categorical variables that arise from aircraft design has to be tackled by the optimization process.*

Recently, there has been a growing interest in mixed variables constrained Bayesian optimization based on Gaussian process surrogate models. In this setting, most existing approaches severely increase the dimension of the covariance matrix related to the surrogate. In fact, the construction of the Gaussian process model may not be scalable to practical applications involving a large number of mixed variables.

In this paper, we address this issue by constructing a covariance kernel for the surrogate model that depends on only a few hyperparameters. The new kernel is constructed based on the information obtained from the partial least squares method. The obtained numerical results lead to interesting results for the optimization of a baseline aircraft and to reduce the fuel consumption of "DRAGON", a new hybrid electric propulsion aircraft, with a high number of mixed variables and for a small budget of time-consuming evaluations.

Keywords: Green Aircraft, Future Aircraft, Multidisciplinary Design Optimization, Bayesian Optimization, Surrogate-based Optimization, Gaussian Process

P. Saves, N. Bartoli, Y. Diouane, Th. Lefebvre, J. Morlier, C. David, E. Nguyen Van and S. Defoort

1   INTRODUCTION

New aircraft configurations with a lower footprint on the environment (also known as Eco-aircraft design) have seen a resurgence of interest [1]. In this context, one targets to minimize the footprint on the environment of the aircraft using a *Multidisciplinary Design Analysis* (MDA) [2–4] with dedicated disciplines such as emissions, noise, ... The process of finding the best configuration, known as *Multidisciplinary Design Optimization* (MDO), is formulated as a minimization constrained problem where the objective and the constraints functions are typically expensive-to-evaluate and their derivatives are not available.

In the context of aircraft design, the MDO process generally involves mixed continuous-categorical design variables. For instance, the size of aircraft structural parts can be described using continuous variables; in case of thin-sheet stiffened sizing, they represent panel thicknesses and stiffening cross-sectional areas. The set of discrete variables can encompass design variables such as the number of panels, the list of cross sectional areas or the material choices. Thus, the regarded optimization problem is of the following form:

$$\min_{w=(x,z,c)\in\Omega\times S\times\mathbb{F}^l}\{f(w) \text{ s.t. } g(w)\leq 0 \text{ and } h(w)=0\} \tag{1}$$

where $\Omega\subset\mathbb{R}^n$ represents the bounded continuous design set for the n continuous variables; $S\subset\mathbb{Z}^m$ represents the bounded integer set where $L_1,...,L_m$ are the numbers of levels of the m quantitative integer variables on which we can define an order relation and $\mathbb{F}^l=\{1,\ldots,L_1\}\times\{1,\ldots,L_2\}\times\ldots\times\{1,\ldots,L_l\}$ is the design space for l categorical qualitative variables with their respective $L_1,...,L_l$ levels.

$f:\mathbb{R}^n\times\mathbb{Z}^m\times\mathbb{F}^l\mapsto\mathbb{R}$ is the objective function, $g:\mathbb{R}^n\times\mathbb{Z}^m\times\mathbb{F}^l\mapsto\mathbb{R}^{n_g}$ gives the inequality constraints, and $h:\mathbb{R}^n\times\mathbb{Z}^m\times\mathbb{F}^l\mapsto\mathbb{R}^{n_h}$ returns the equality constraints. The functions f, g, and h are typically expensive-to-evaluate simulations with no exploitable derivative information.

When only continuous design variables are optimized (i.e., $S\times\mathbb{F}^l$ is reduced to a single choice), *Bayesian optimization* (BO) is shown to be a powerful strategy for solving problem (1) [5]. BO uses *Gaussian processes* (GPs) [6–10] to define response surfaces, the sequential enrichment is performed by maximizing a given acquisition function [6]. The latter is meant to model a compromise between exploration of new zones in the design space and exploitation (i.e. minimization) of the GPs. For general mixed integer problems, several modeling strategies to build GPs have been proposed [11, 12]. Based on these GPs models, a trade-off acquisition function was adapted for optimization [13]. Some other modelling strategies consist in computing a continuous model for each category [14], either by continuously relaxing the design variables [15], by using a multi-armed bandit strategy to handle the categorical choices [16] or by considering a Gower distance to model simultaneously the proximity over categorical and continuous variables [17]. Recently, a continuous relaxation BO based method [18] to tackle mixed integer variables has been shown to solve efficiently expensive-to-evaluate optimization problems. In fact, using continuous relaxation within BO leads to better results. However, the relaxation of the categorical design variables increases the number of the hyperparameters needed (to be tuned) associated with the GP model. This in particular constrained the method in [18] to be used only for small dimensional optimization problems. Since, the construction of the GP model may not be scalable to practical applications involving a large number of mixed variables.

P. Saves, N. Bartoli, Y. Diouane, Th. Lefebvre, J. Morlier, C. David, E. Nguyen Van and S. Defoort

In this work, we show how to reduce the computational cost related to the construction of the mixed categorical GP model as proposed in [15]. Our proposed approach allows in particular to solve higher dimensional mixed integer MDO problems. The method relies on combining continuous relaxation and the use of principle components analysis to reduce the number of the hyperparameters (known as KPLS [19, 20], Kriging model with Partial Least Squares). The good potential of the proposed approach is showed over a set of analytical test cases.

The performance of the proposed approach is also confirmed on two MDO applications from the FAST-OAD framework [21]: "CERAS" and "DRAGON". FAST-OAD is an open-source Python framework that provides a flexible way to build and solve the Overall Aircraft Design problems by assembling discipline models from various sources: FAST-OAD currently comes with some bundled, quick and simple, models dedicated to commercial aircraft. In this paper, FAST-OAD will resolve an MDA problem that mainly: (a) sizes the geometry of main aircraft components, (b) computes mass and centers of gravity of aircraft parts, (c) estimates the aerodynamics and propulsion along the computed mission, and (d) return the fuel consumption related to the mission. These estimated quantities will be used to define the objective and the constraints of our two optimization problems.

The outline of the paper is as follows. In Section 2, a detailed review of the Bayesian optimization framework is given. The continuous relaxation as well as the use of the KPLS technique are detailed in Section 3. Section 4 presents our academical tests as well as the obtained results on the two regarded MDO test cases. Conclusions and perspectives are finally drawn in Section 5.

2   CONTINUOUS CONSTRAINED BAYESIAN OPTIMIZATION

In this section, we will only consider that all the design variables are continuous in problem (1). Namely, the design space will be restricted to $\Omega \subset \mathbb{R}^n$; hence $w = x$ in the optimization problem (1). The Efficient Global Optimization (EGO) framework [6] suggests to use the GP model to find the global minimum of an expensive-to-evaluate black-box objective function (based on the preliminary results of Močkus [7]). In general, a GP is used to fit a response surface model from an initial set of points known as the Design of Experiments (DoE) [8, 9, 22]. The GP provides a mean response hypersurface as well as a pointwise estimation of its variance. Thereafter, we will consider that our unknown black-box objective function f is a realization of an underlying distribution of mean $\hat{f}$ and of standard deviation s^f such that $f(.) \sim GP(\hat{f}(.), [s^f]^2(.))$.

Let n_t be the number of already evaluated points in $\mathbb{R}^n$ of the deterministic function f and $\forall i \in \{1, .., n_t\}$, let $x^i = (x^i_1, ..., x^i_n) \in \mathbb{R}^n$ be the ith point with its respective n continuous variables values, we can define the known data as (x, y^f). The stochastic model [23] writes as: $f(x^i) = \mu(x^i) + \epsilon^i \in \mathbb{R}$ with ϵ^i the error term between f and the model approximation $\mu(x)$. The errors terms are considered *iid* of variance σ^2.

Let R be the error correlation matrix between the inputs points $R_{ij} = Corr(\epsilon(x^i), \epsilon(x^j))$. The correlation function $Corr$ is computed using a kernel function k that relies on n hyperparameters θ estimated typically using maximum likelihood estimator (MLE) [24]. Let $r_i(x^*) = Corr(\epsilon(x^*), \epsilon(x^i))$ for a given x^*, then

$$\hat{f}(x^*) = \hat{\mu}^f + r(x^*)^T R^{-1}(y^f - \mathbb{1}\hat{\mu}^f), \tag{2}$$

P. Saves, N. Bartoli, Y. Diouane, Th. Lefebvre, J. Morlier, C. David, E. Nguyen Van and S. Defoort

and

$$[s^f]^2(x^*) = [\hat{\sigma}^f]^2 \left[1 - r(x^*)^T R^{-1} r(x^*) + \frac{(1 - \mathbb{1}^T R^{-1} r(x^*))^2}{\mathbb{1}^T R^{-1} \mathbb{1}} \right], \tag{3}$$

where $\hat{\mu}^f$ and $\hat{\sigma}^f$, respectively, are the maximum likelihood estimator of μ and σ given the data set (x, y^f).

Within EGO, at a given iteration t, a GP surrogate, referred as Kriging, model of the black-box f is computed from the current DoE. Henceforth, one wants to estimate the best new point to evaluate, as it is costly, by taking into account all the available information to converge as fast as possible to the real optimum of the black-box. The point that we will evaluate next is the one that gives the best improvement *a priori* according to an acquisition function like the Expected Improvement (EI). The objective value as this new point will then be evaluated and used to enrich the surrogate database. The hyperparameters that characterize and define the model are updated at each iteration until convergence. The Bayesian optimization process is thus made from these GPs in an iterative manner.

To tackle constrained Bayesian optimization, EGO was extended to Super-Efficient Global Optimization (SEGO) method [10]. SEGO uses surrogate models of the constraints to give an estimation of the search space Ω_f. The latter was enhanced to tackle multi-modal and equality constraints with the Upper Trust Bound (UTB) criterion [25, 26].

The acquisition function that we use is the $WB2s$ (Watson and Barnes 2nd criterion with scaling) [26] that is known to be more robust than the Expected improvement (EI) criterion; especially in high dimension. $WB2s$ can be seen as smooth version compared to the $WB2$ [10] criterion and is less multimodal compared to EI. Algorithm 1 details the SEGO optimization procedure.

Algorithm 1: SEGO for continuous inputs.

Result: Solution of the problem (1) over the continuous design space Ω.

Inputs: Initial DoE $\mathscr{D}_0$ and set $t = 0$. The search space Ω.

while *the stopping criterion is not satisfied* **do**

1. Build the surrogate model of the objective to obtain the mean and standard deviation prediction at a given point: $(\hat{f}, s^f)$ from the DoE $\mathscr{D}_t$.

2. Build the surrogate model for each constraint i,j: $(\hat{g}_i, s_i^g)$, $(\hat{h}_j, s_j^h)$ from the DoE $\mathscr{D}_t$ and compute an estimation of the search space Ω_f.

3. Construct the acquisition function $WB2s$.

4. Maximize the acquisition function $WB2s$ over Ω_f: $x_t = \underset{x \in \Omega_f}{\arg\max}\, WB2s(x)$.

5. Add $x_t, f(x_t), g(x_t), h(x_t)$ to the DoE $\mathscr{D}_{t+1}$. Increment t.

end

---

3   MIXED CATEGORICAL CONSTRAINED BAYESIAN OPTIMIZATION

To handle mixed categorical design variables, we propose to use the continuous relaxation method that has been recently shown to be well-suited for expensive discrete problems [15, 18]. The main drawback of such method is that it enlarges the dimension of the design space according to the size of the categorical space. To overcome such issue,

P. Saves, N. Bartoli, Y. Diouane, Th. Lefebvre, J. Morlier, C. David, E. Nguyen Van and S. Defoort

we propose to combine continuous relaxation with the well-known partial least-square procedure [20] to reduce the number of the GP hyperparameters.

For mixed categorical design variables, the proposed treatment relies on continuous relaxation. The design space $\Omega \times S \times \mathbb{F}^l$ is relaxed to a continuous space Ω' constructed on the following way:

- $\forall i \in \{1, \ldots, m\}$, the variable z_i is relaxed within its bounds and treated as continuous.

- $\forall j \in \{1, \ldots, l\}$, we use a relaxed one-hot encoding [27] for c_j and add L_j new continuous dimensions into Ω'.

Therefore, we get, after relaxation, a new design space $\Omega' \subseteq \mathbb{R}^{n'}$ where $n' = n + m + \sum_{j=1}^{l} L_j > n + m + l$.

The nature of the variables should be respected when evaluating a point in the relaxed space so we define the inverse operator $Project$ that projects a point $X \in \Omega'$ to its closer point w^X in $\Omega \times S \times \mathbb{F}^l$. Namely, $Project$ rounds the value of an integer variable z_i to the closer value among its L_i levels and, for a categorical variable c_j, $Project$ selects the level which corresponding dimension value is the highest.

In this work, when building the Kriging model, the error correlation will be estimated using a squared exponential (or Gaussian) correlation kernel over the relaxed design space. We denote by $X^{w_i} = Relax(w^i)$ the relaxation in Ω' of a point $w^i \in \Omega \times S \times \mathbb{F}^l$. The mixed categorical kernel is

$$k(X^{w^i}, X^{w^j}) = \prod_{p=1}^{n'} \exp\left(-\theta_p \left(X_p^{w_i} - X_p^{w_j}\right)^2\right), \theta_p \in \mathbb{R}^+ \tag{4}$$

This kernel relies on n' hyperparameters θ_p estimated by maximum of likelihood such that the more the number of variables n' for the problem, the more the number of hyperparameters to optimize. Reducing this number leads to a better estimation for the hyperparameters, a more convenient optimization of the likelihood and makes the model scalable for high-dimensional problems. To do so, the Partial Least Squares (PLS) method [28] searches the direction that maximizes the variance between the input and output variables. This is done by a projection into a smaller space spanned by the so-called principal components. The number of principal components d that corresponds to the new number of hyperparameters for KPLS is chosen to be much lower than n'. The resulting PLS squared exponential kernel is given by

$$k(X^{w^i}, X^{w^j}) = \prod_{q=1}^{d} \prod_{p=1}^{n'} \exp\left(-\theta_q \left(b_{*p}^q X_p^{w_i} - b_{*p}^q X_p^{w_j}\right)^2\right), \forall\, \theta_q \in \mathbb{R}^+ \tag{5}$$

where $[b_{*p}^q]_{p,q}$ are scalars that measure the influence of the input variables on the output y^f. Combining this model construction with SEGO gives the method described in Algorithm 2.

P. Saves, N. Bartoli, Y. Diouane, Th. Lefebvre, J. Morlier, C. David, E. Nguyen Van and S. Defoort

---

Algorithm 2: SEGO for mixed categorical inputs using KPLS

Result: Solution of the problem (1) over the mixed categorical design space $\Omega \times S \times \mathbb{F}^l$.

Inputs: Initial DoE $\mathscr{D}_0$ and set $t = 0$. The search space $\Omega \times S \times \mathbb{F}^l$.

while *the stopping criterion is not satisfied* **do**

1. Relax continuously integer and categorical input variables to a real bounded space Ω' of dimension $n' = n + m + \sum_{j=1}^{l} L_j$. Namely, we continuously relax the mixed categorical DoE $\mathscr{D}_t = \{w^i\}_i \in (\Omega \times S \times \mathbb{F}^l)^{n_t}$ to a continuous DoE $\mathscr{D}'_t = \{X^{w^i}\}_i \in (\Omega')^{n_t}$ using the relaxation procedure *Relax*.

2. Use PLS to reduce the number of the hyperparameters from n' to d $(d << n')$, during the construction of the GP models (for the objective function f and the constraints g and h) related to the DoE $\mathscr{D}'_t$.

3. Build an estimation of the feasible domain $\Omega'_f \subset \Omega'$ with the criterion UTB and construct the acquisition function $WB2s$.

4. Maximize the acquisition function $WB2s$ over Ω'_f:
   $X_t = \underset{X \in \Omega'_f}{\arg\max} \, WB2s(X)$.

5. Project the obtained continuous solution over $\Omega \times S \times \mathbb{F}^l$:
   $w_t = Project(X_t)$.

6. Add $w_t, f(w_t), g(w_t), h(w_t)$ to the DoE $\mathscr{D}_{t+1}$. Increment t.

end

---

4 RESULTS

In this section, we carry out experiments for unconstrained and constrained test cases, with several number of variables and an increasing complexity. We optimize analytical test cases as a benchmark study and then we solve aircraft design optimization problems as a validation and application of the present work.

4.1 Implementation choices

In order to compare, we used several optimization algorithms detailed hereafter: Bandit-BO, NSGA2, SEGO with Kriging, SEGO with Gower distance and the proposed method, SEGO coupling Kriging and PLS.

The Bandit-BO implementation used is the one by Nguyen et al. [16], we are not considering parallelization or batch evaluations. Bandit-BO creates a GP model for each arm, so it requires at least $2 \times N_c$ initial points, N_c being the number of categorical possibilities for the problem inputs. If we are not using Bandit-BO, for constrained optimization, we are using a continuous relaxed Latin hypercube sampling and then we project the output points to obtain the mixed integer DoE.

The NSGA2 [29] algorithm used is the implementation from the toolbox pymoo [30] with the default parameters (probability of crossover $= 1$, eta $= 3$). Fronts are not relevant in our study as we are considering single-objective optimization.

The optimization with SEGO is made from SEGOMOE [26] for both constrained and

P. Saves, N. Bartoli, Y. Diouane, Th. Lefebvre, J. Morlier, C. David, E. Nguyen Van and S. Defoort

unconstrained cases. For SEGO using Gower distance [17] (denoted by SEGO+GD), we are considering the implementation of the Surrogate Modeling Toolbox (SMT) [31], an open-source python toolbox where some computations associated to the present work have been done. The same holds for SEGO and Kriging coupled with PLS to reduce to d the number of hyperparameters (denoted SEGO+KPLS_dD). As the PLS could potentially lead to numerical instabilities, we are using the homoscedastic noise that maximizes the likelihood as a so-called nugget. For SEGO using Kriging (denoted by SEGO+KRG), we also use the implementation from the toolbox SMT. For the constrained analytical test cases, we are using the UTB criterion [25]. Some adaptions have been done to Bandit-BO and NSGA2 to consider both integer and categorical variables. As NSGA2 can only consider integer variables, categorical variables are treated as integer ones. Contrarily, Bandit-BO can treat only categorical variables so integer variables are treated as categorical ones. For Kriging, Kriging with PLS or Gower distance, the hyperparameters are optimized with COBYLA [32] and the chosen model regression is constant. When optimizing with SEGO, the acquisition function is maximized using ISRES [33] to find some interesting starting points and SNOPT [34] to finalize the process based on these starting points. The squared exponential kernel is the only one considered for these methods.

In order to compute some statistical data (median and variance), we are doing 20 repetitions of the optimization process for a given method and an initial DoE size. We consider that a constraint is respected if the constraint violation is smaller than the threshold value 10^{-4}.

4.2 Benchmark test cases including unconstrained and constrained optimization problems

In this section, a benchmark of different problems is proposed in order to compare the efficiency of the proposed algorithm with some state-of-the-art methods. The first ten are analytical cases, with or without constraints in order to provide some data profiles and the last two concern some more complex applications for aircraft conceptual design.

4.2.1 Unconstrained optimization

To begin with, we validate our method on unconstrained problems up to 14 dimensions. The first analytical test case is a modified Branin function [14], denoted by "Branin 5", where the first variable is an integer $x_1 \in \{-5, -4, \ldots, 9, 10\}$ and the second one $x_2 \in [0, 10]$ is a continuous variable. As this problem is only 2-dimensional, SEGO-KRG is considered without the coupling with the PLS technique. For Bandit-BO, we represent x_1 as a bandit with 16 arms associated to the 16 integer values from 0 to 15. Therefore, an initial DoE of at least 32 points is required for Bandit-BO. A smaller initial DoE is also considered for NSGA2 and SEGO-KRG in order to compare the convergence according to the DoE size: 5 points or 32 points. For a given DoE size (5 or 32), 20 different initial DoE are obtained via Latin hypercube sampling in order to compute some statistical data (median and variance) about the convergence results. In Fig.1a, the medians and the associated quartiles (25% and 75%) of the 20 runs are illustrated for each of the three algorithms. The initial DoE is shown before the black dotted line. For the DoE with 32 initial points, we are doing 50 iterations of the methods Bandit-BO and SEGO-

P. Saves, N. Bartoli, Y. Diouane, Th. Lefebvre, J. Morlier, C. David, E. Nguyen Van and S. Defoort

KRG, for a total of 82 evaluations. For NSGA2, 200 iterations are performed. When the DoE size is reduced to 5 points, 200 iterations of SEGO-KRG are made and compared to 300 evaluations for NSGA2. These comparisons show that SEGO-KRG outperforms BANDIT-BO and NSGA2 in terms of convergence. Moreover, we find that a smaller initial DoE performs better for SEGO, that is a known result [35].

To compare the dispersion of the best results over the 20 runs, Fig.1b shows the boxplots for SEGO-KRG, Bandit-BO and NSGA2 after 50 iterations associated to a initial DoE of 32 points. These plots show that, not only SEGO-KRG converges better in median but also it is the only method to converge for every of the 20 initial DoE. However, Bandit-BO converges better than NSGA2 on this test case.

(a) Convergence curves. (b) Boxplot with a DoE of 32 points.
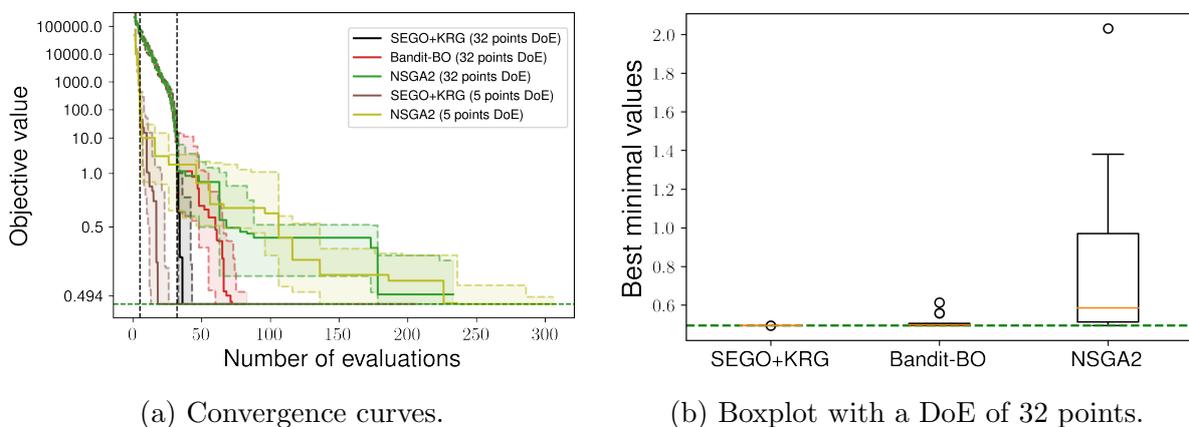
Figure 1: "`Branin 5`" obtained optimization results. The Boxplots are generated, after 50 iterations, using the 20 best points.

The second analytical test case is a toy function that consists in the choice between a set of 10 1-dimensional continuous functions [13], denoted by "`Set 1`", where the first variable is a categorical variable $x_1 \in \{0, 1, \ldots, 9\}$ and the second one $x_2 \in [0, 1]$ is a continuous variable. This problem only has 2 variables but, as the relaxed space is in dimension 11, SEGO with KPLS is then considered to compare with SEGO with Kriging such that we can see how reducing the number of spatial correlations from 11 to 5 in the model can impact the optimization process. For Bandit-BO, we represent x_1 as a bandit with 10 arms from 0 to 9 and an initial DoE with a minimum of 20 points is required. As previously for NSGA2 and SEGO-KRG, two initial DoE sizes are considered with 5 points and 20 points. For a given DoE size, 20 different initial DoE are obtained to compute statistics on the convergence results. In Fig.2, the medians and the associated quartiles (25% and 75%) of the 20 runs are illustrated for each of the four algorithms. The initial DoE is shown before the black dotted line. For the DoE with 20 initial points in Fig.2b, 50 iterations of the methods Bandit-BO, SEGO+KPLS_5D and, SEGO-KRG are performed for a total of 70 evaluations and for NSGA2 200 iterations are performed. When the DoE size is reduced to 5 points in Fig.2a, 200 iterations of SEGO-KRG are done and compared to 300 evaluations for NSGA2. These convergence plots show that the smaller the DoE, the faster the convergence. Also, KPLS slows the convergence at the start but this dimension reduction does not change the convergence overall and the incumbent is even better at the end with KPLS than without. On this test case, Bandit-BO method does not perform well. To compare the dispersion of the best results

over the 20 runs, Fig.2c shows the boxplots for SEGO-KRG, Bandit-BO, NSGA2 and, SEGO+KPLS_5D after 50 iterations associated to a initial DoE of 20 points. These plots show that SEGO+KPLS does not converge properly because 2 runs are outliers that did not have converged whereas with NSGA2 and SEGO-KRG, there is only one outlier. Nevertheless, NSGA2 is not as precise as SEGO-KRG on average.
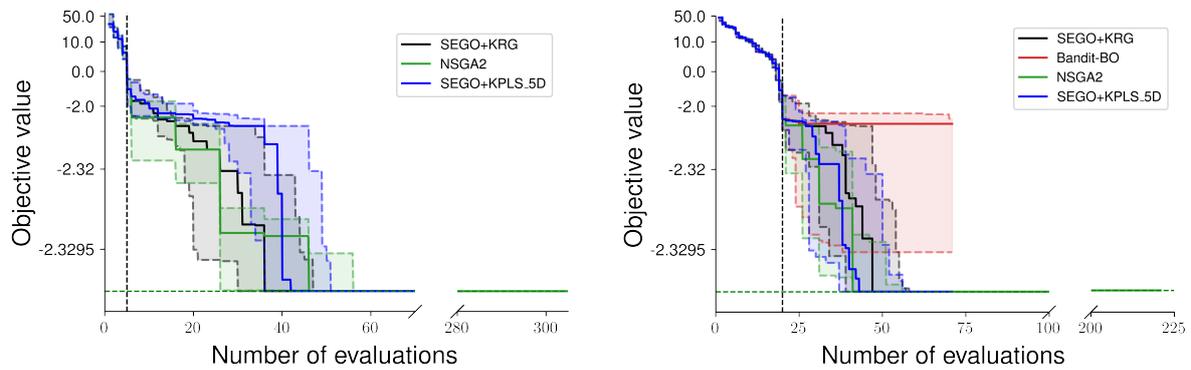
(a) Convergence curves using 5 points initial DoE

(b) Convergence curves using 20 points initial DoE.
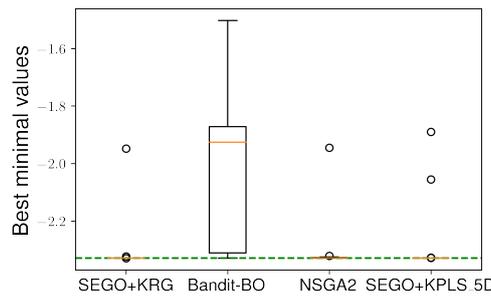
(c) Boxplots with a DoE of 20 points.

Figure 2: "Set 1" obtained optimization results.

4.2.2 Constrained optimization

For constrained optimization, Bandit-BO can not be considered as it can not deal with constraints, so SEGO is only compared to NSGA2. The first constrained test case is a modified Branin function [11] with one constraint, denoted by "Branin 3", where the two first variables are categorical variables with 2 levels each such that there is 4 possible Branin function variations and the two last variables are the continuous ones.

This problem has 4 variables in the initial space and 6 in the relaxed one, so SEGO with Kriging is applied without any dimension reduction technique. According to the previous experiments, a small initial DoE with 5 points is considered in order to obtain better results for a given number of evaluations. In Fig.3a, the medians and the associated quartiles (25% and 75%) of the 20 runs are illustrated for NSGA2 and SEGO-KRG. The initial DoE is shown before the black dotted line, then 50 iterations of SEGO-KRG are performed and compared with 200 iterations of NSGA2. To compare the dispersion of the best results over the 20 runs, Fig.3b shows the boxplots for SEGO-KRG and NSGA2 after 50 iterations. On this low-dimension constrained case, the mixed integer version of

P. Saves, N. Bartoli, Y. Diouane, Th. Lefebvre, J. Morlier, C. David, E. Nguyen Van and S. Defoort

SEGO with Kriging is shown to perform well and be adapted to the constrained mixed optimization.

(a) Convergence curves.   (b) Boxplots.
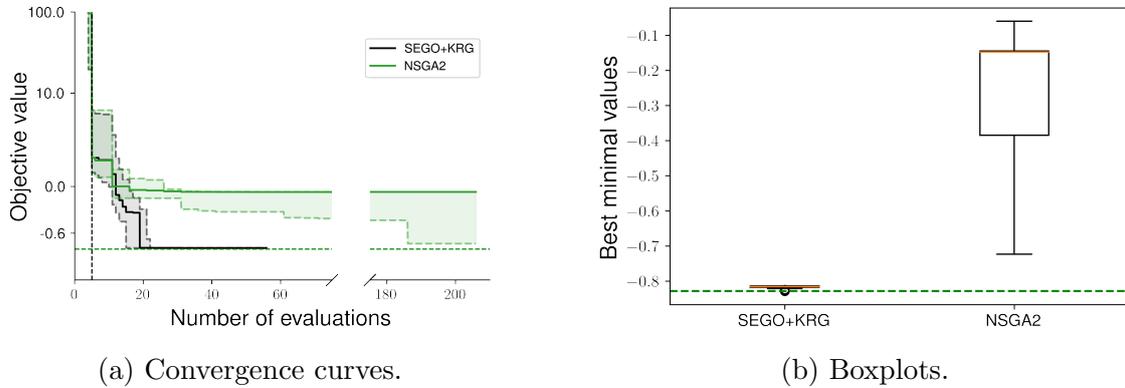
Figure 3: "`Branin 3`" optimization results.

The second constrained test case is an augmented dimension modified Branin function [11] with one constraint, denoted by "`Branin 4`". The firsts two variables are categorical with 2 levels each and the 10 last variables are continuous. Therefore, we can see the test case as a set of 4 continuous augmented 10-dimensional Branin functions. This problem has 12 variables in the initial space and 14 in the relaxed space. SEGO with KPLS is considered with 2 principal components for the PLS technique to compare the dimension reduction with SEGO-KRG. As previously an initial DoE with 5 points is chosen and shown before the dotted line in Fig.4a. The medians and the associated quartiles (25% and 75%) of the 20 runs are illustrated for NSGA2 and SEGO. On this graph, 50 iterations of SEGO-KRG are compared with 200 iterations of NSGA2. To compare the dispersion of the best results over the 20 runs, Fig.4b shows the boxplots for SEGO-KRG, SEGO-KPLS_2D and NSGA2 after 50 iterations. On this high-dimension constrained case, our method is still efficient.

(a) Convergence curves.   (b) Boxplots.
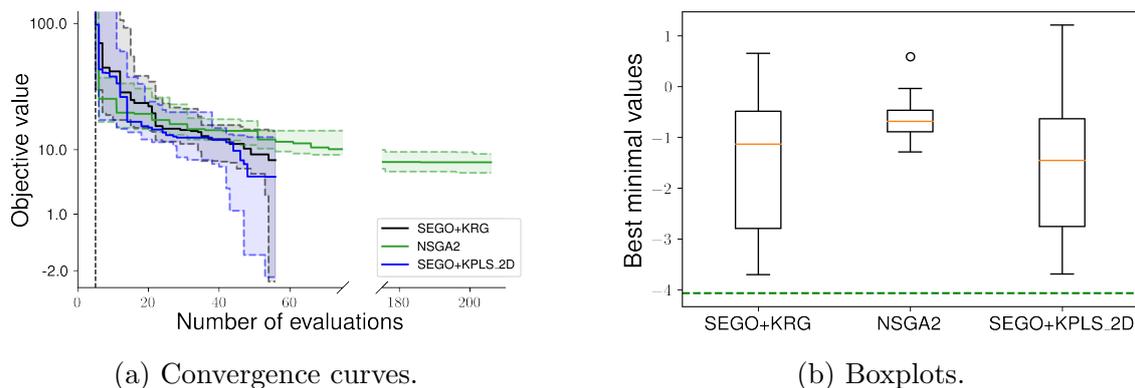
Figure 4: "`Branin 4`" optimization results.

These four analytical cases have shown that SEGO performs better than both Bandit-BO for mixed integer Bayesian Optimization and NSGA2 for constrained optimization. It has been shown that the PLS technique allows the method to be scalable for high-dimension and even to give better results than Kriging by carrying favor to the most relevant space.

P. Saves, N. Bartoli, Y. Diouane, Th. Lefebvre, J. Morlier, C. David, E. Nguyen Van and S. Defoort

4.2.3   Overall benchmark results

For 10 different test cases (3 constrained and 7 unconstrained) we are considering 20 runs with differents DoE sampled by Latin hypercube sampling for a total of 200 instances. The resulting percentages of instances that have converged after a given budget for every method are plotted on Fig.5. For unconstrained test cases, in order to compare with Bandit-BO, the size of the initial DoE is given by $\min\{5, 2 \times N_c\}$ where N_c is the number of categorical possibilities and for constrained test cases, we took 5 points for the initial DoE size. This allow us to compare Bandit-BO, SEGO, SEGO with Gower Distance, SEGO with KPLS and NSGA2. Some tests are in dimension 2, so in order to compare with the same number of hyperparameters for all tests, we had to choose between 1 or 2 principal components for KPLS. As the number of points increases, the projected points are really closed to each other, so, to insure a certain stability, we choose KPLS with 2 principal components and noise evaluation, denoted by KPLS_2D in the following.

These 10 test cases were extracted from several state-of-the-art papers [11–14, 17, 36, 37] from dimension 2 to 12, with integer, continuous and/or categorical variables. For constrained case, we keep only the inputs that gives a constraint violation smaller than 10^{-4}. A problem is considered solved if the error to the known solution is smaller than 2% on Fig.5a and smaller than 0.5% on Fig.5b. The mean error after the 50 iterations can be found in Tab.1. SEGO with PLS gives the smaller errors on constrained test cases but, for unconstrained ones, SEGO-KRG performs the best. As we can see on the data profiles, SEGO-KRG and SEGO+KPLS_2D are similar and outperform the three others methods. However, SEGO with PLS being less efficient on unconstrained test cases, SEGO-KRG gives better results over all tests. These preliminary results are promising and some more realistic applications are considered in the next section.
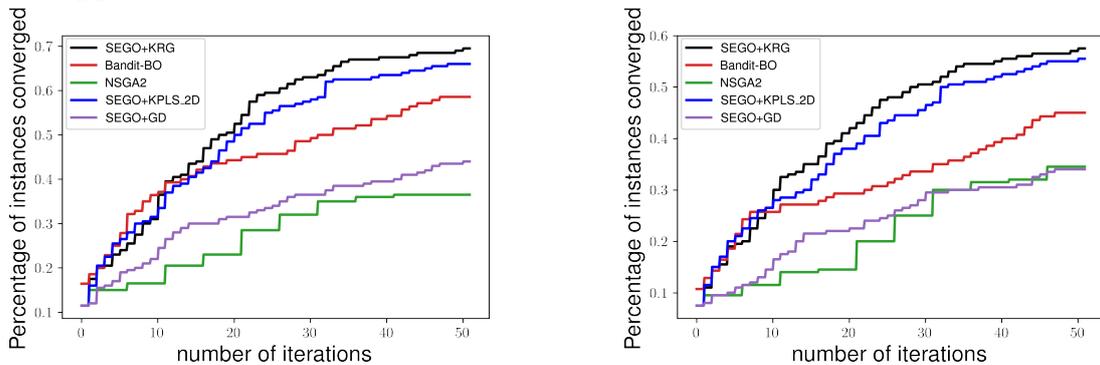
(a) Data profiles for a tolerance of 2%   (b) Data profiles for a tolerance of 0.5%

Figure 5: Data profiles generated using 10 analytical test cases

Table 1: Mean errors of each method after 50 iterations.

ERRORS	NSGA2	Bandit-BO	SEGO+KRG	SEGO+KPLS_2D	SEGO+GD
Unconstrained test cases	14.29%	5.84%	2.27%	5.74%	8.41%
Constrained test cases	58.27%	-	27.61%	25.41%	47.83%

P. Saves, N. Bartoli, Y. Diouane, Th. Lefebvre, J. Morlier, C. David, E. Nguyen Van and S. Defoort

4.3   Aircraft design test cases

For the core MDO application, we apply FAST-OAD on two different aircraft design problems. The first one named "CERAS" is a classic well-known aircraft and the second "DRAGON" is a more innovative new one that is currently under development. This time, as the evaluations are expensive, we are doing only 10 runs instead of 20. For each run, we draw a random starting DoE of 5 points. As we have no equality constraint and a small budget, we will not force the constraints to be as large as possible and we will use only the mean prediction of the constraint models and not the UTB criterion [25]. Also, to have realistic results, the constraints violation will be forced to be less than 10^{-3}.

4.3.1   CERAS

To validate the results of section 4.2 on a real test case, we are considering the data from the CEntral Reference Aircraft System ("CERAS") based on an Airbus A320 aircraft. The problem to solve is a constrained optimization problem with 6 continuous design variables, 2 categorical variables and 2 integer ones, for a total of 10 design variables. The presented version of SEGO (with or without the PLS technique) is used as an optimizer in a Multidisciplinary feasible (MDF) architecture where the MDA is computed with FAST-OAD. The optimization problem is described in Tab.2 where the total number of variables is reported using the relaxation technique.

Table 2: Definition of the "CERAS" optimization problem.

	Function/variable	Nature	Quantity	Range
Minimize	Fuel mass	cont	1	
with respect to	x position of MAC	cont	1	$[16., 18.]$ (m)
	Wing aspect ratio	cont	1	$[5., 11.]$
	Vertical tail aspect ratio	cont	1	$[1.5, 6.]$
	Horizontal tail aspect ratio	cont	1	$[1.5, 6.]$
	Wing taper aspect ratio	cont	1	$[0., 1.]$
	Angle for swept wing	cont	1	$[20., 30.]$ $(°)$
	Total continuous variables		6	
	Cruise altitude	discrete	1	$\{30k,32k,34k,36k\}$ (ft)
	Number of engines	discrete	1	$\{2,3,4\}$
	Total discrete variables		2	
	Tail geometry	cat	2 levels	$\{$T-tail, no T-tail$\}$
	Engine position	cat	2 levels	$\{$front or rear engines$\}$
	Total categorical variables		2	
	Total relaxed variables		**12**	
subject to	$0.05 <$ Static margin < 0.1	cont	2	
	Total constraints		**2**	

We are testing 3 methods, NSGA2, SEGO with Kriging and SEGO with KPLS over 10 DoEs and 200 iterations. As for the analytical test cases, Fig.6a shows that PLS method speeds up the optimization process at the start. However, the boxplots of the final results on Fig.6b show that, at the end, the KPLS and Kriging versions give similar results while KPLS uses 3 times less correlation length hyperparameters. The Kriging version starts slower but catches up with KPLS quickly and for every given budget Kriging gives better results than NSGA2. The best configuration is obtained after a SEGO+KPLS_4D optimization, the optimal result is given in Tab.3. The optimal aircraft geometries obtained

P. Saves, N. Bartoli, Y. Diouane, Th. Lefebvre, J. Morlier, C. David, E. Nguyen Van and S. Defoort

using each of the three methods and the baseline are plotted in Fig.7. As SEGO with Kriging is almost the same as the best, SEGO+KRG and SEGO+KPLS are grouped on the geometries. With KPLS we obtain a constraint margin of 0.500 and an objective of 16722.73 kg.
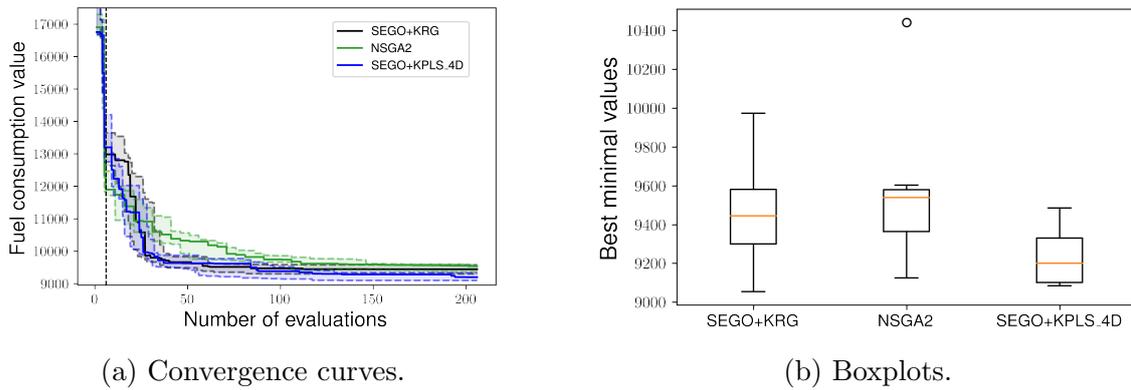

| (a) Convergence curves. | (b) Boxplots. |
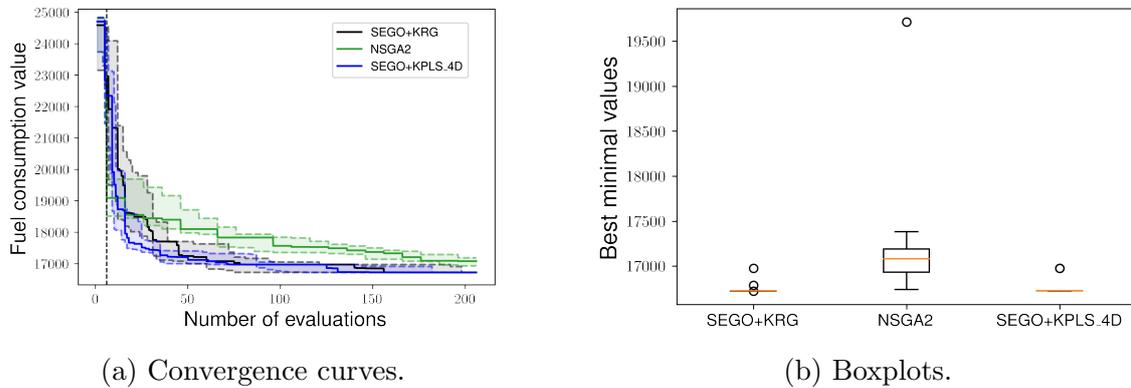
Figure 6: "`CERAS`" optimization results using a DoE of 5 points. The Boxplots are generated, after 200 iterations, using the 10 best points.

Table 3: "`CERAS`" Optimal aircraft configuration.

Name	Nature	Value
Fuel mass	cont	16722.55 kg
static margin	cont	0.0495
x position of MAC	cont	16.2825 m
Wing aspect ratio	cont	11
VT aspect ratio	cont	6
HT aspect ratio	cont	6
Wing taper ratio	cont	0.5099
Wing sweep angle	cont	30.0 °
Cruise altitude	discrete	36,000 ft
Tail geometry	cat	T-tail
Engine position	cat	Front engine
Number of engines	discrete	2

From an aircraft design point of view, the obtained optimized values can be surprising for some parameters, but are logical given the limits of current models in FAST-OAD:

- as the flight ceilings (buffeting, aerodynamics, ...) are not computed, the algorithm logically goes toward high altitudes,

- the mass of a strongly swept wing is not properly computed, and does not bring enough penalty on such configuration,

- similarly, the models do not compute the additional mass that should be required for a T-tail with such a large aspect ratio on vertical tail.

However, the capabilities of the proposed algorithm are very promising for a conceptual design stage where a lot of architecture choices are still undetermined, leading to a large

combinatorial problem. In that perspective, the ability of the method to capture the right trends regarding number of engines (integer) and their position (categorical) is a good perspective, that needs to be confirmed with an even more complex design case using many categorical and integer variables. The "DRAGON" hybrid aircraft case described below provides this feature.
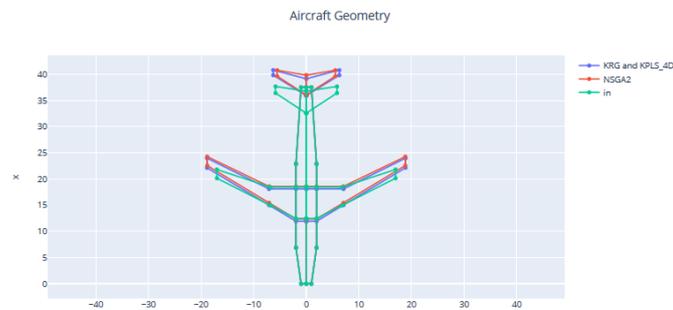
Figure 7: "CERAS" best configurations geometries.

4.3.2 DRAGON

The "DRAGON" aircraft concept in Fig.8 has been introduced by ONERA in 2019 [38] within the scope of the European CleanSky 2 program [1] which sets the objective of 30% reduction of CO2 emissions by 2035 with respect to 2014 state of the art. ONERA responded to this objective by proposing a distributed electric propulsion aircraft that improves the aircraft fuel consumption essentially by increasing the propulsive efficiency. Such efficiency increase is obtained through improvement of the bypass ratio by distributing a large number of small electric fans on the pressure side on the wing rather than having large diameter turbofans. This design choice avoids the problem associated with large under-wing turbofans and at the same time allows the aircraft to travel at transonic speed. Thus the design mission set for "DRAGON" is 150 passengers over 2750 Nautical Miles at Mach 0.78.

Figure 8: "DRAGON" aircraft concept.

The employment of a distributed propulsion comes at a certain cost; a turbo-electric propulsive chain is necessary to power the electric fans which brings additional complexity and weight. Typically, turboshafts coupled to electric generators are generating the electrical power on board the aircraft. The power is then carried to the electric fans through an electric architecture ensuring robustness to single component failure. This safety feature is obtained with redundant components as depicted in Fig.9. The baseline configuration

---

[1] https://www.cleansky.eu/technology-evaluator

P. Saves, N. Bartoli, Y. Diouane, Th. Lefebvre, J. Morlier, C. David, E. Nguyen Van and S. Defoort

is two turboshafts, four generators, four propulsion buses with cross-feed and forty fans. This configuration was selected for an initial study as it satisfies the safety criterion. However it was not designed to optimize aircraft weight. The turboelectric propulsive chain being an important weight penalty, it is of particular interest to optimize the chain and particularly the number and type of each component, characterized by some discrete or particular values.
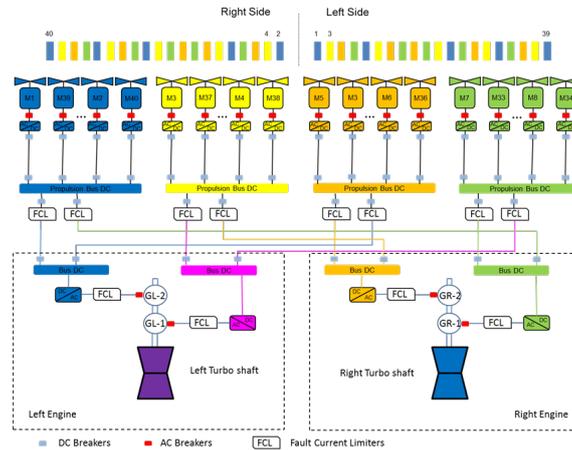
Figure 9: "DRAGON" turboelectric propulsive architecture.

To know how optimizing the fuel mass will impact the aircraft design, we are considering the problem described in Tab.4 where the Mean Average Chord is referred as MAC and the Takeoff Field Length as TOFL. We consider this problem as a test case involving a large number of mixed integer variables and four constraints. The problem to solve is a constrained optimization problem with 8 continuous design variables and 4 integer ones, for a total of 12 design variables.

Table 4: Definition of the "DRAGON" optimization problem.

	Function/variable	Nature	Quantity	Range
Minimize	Fuel mass	cont	1	
with respect to	Cruise Mach number	cont	1	$[0.6, 0.8]$
	TOFL for sizing	cont	1	$[1800., 2500.]$ (m)
	Climb reserve for sizing	cont	1	$[300., 800.](ft/min)$
	Fan operating pressure ratio	cont	1	$[1.05, 1.45]$
	Span	cont	1	$[30., 36.]$ (m)
	Angle for swept wing	cont	1	$[20., 40.]$ $(°)$
	Wing taper aspect ratio	cont	1	$[0.2, 0.5]$
	Engine length to diameter ratio	cont	1	$[1., 5.]$
	Total continuous variables		8	
	Electric motors and fan number	discrete	1	$\{16,24,32,40\}$
	Electric cores number	discrete	1	$\{2,4,6,8\}$
	Generators per turbomachine	discrete	1	$\{1,2,4,8\}$
	Turbomachines number	discrete	1	$\{2,3,4\}$
	Total discrete variables		4	
	Total relaxed variables		**12**	
subject to	Climb time < 29 (s)	cont	1	
	TOFL < 2200 (m)	cont	1	
	Climb reserve > 500 (ft/min)	cont	1	
	Fan radius < 0.1 MAC (m)	cont	1	
	Total constraints		**4**	

P. Saves, N. Bartoli, Y. Diouane, Th. Lefebvre, J. Morlier, C. David, E. Nguyen Van and S. Defoort

To validate our method, we are comparing, in Fig.10, SEGO with KPLS (4 hyperparameters) with its more expensive version using Kriging and with NSGA2. The best method after 50 iterations is the proposed one involving PLS regression as shown in the boxplots in Fig.10b. In Fig.10a, after 200 iterations, we still find that SEGO is better than NSGA2 and that the PLS helps for the convergence. After 50 iterations, SEGO seems to have almost converged whereas NSGA2 takes twice the number of iterations.

Like for "CERAS", we find that the best configuration found with SEGO and Kriging with and without PLS regression are almost the same. The best configuration found is described in Tab.5.

| (a) Convergence curves. | (b) Boxplots. |

Figure 10: "DRAGON" optimization results using a DoE of 5 points. The Boxplots are generated, after 200 iterations, using the 10 best points.

Table 5: "DRAGON" Optimal aircraft configuration.

Name	Nature	Value
Fuel mass	cont	9055 kg
Climb time	cont	28.95 s
TOFL	cont	1865.67 m
Climb reserve at beginning of cruise	cont	583.165 ft/min
fan radius	cont	0.1 MAC
Cruise Mach number	cont	0.7233
TOFL for sizing	cont	2091.72 m
Climb reserve for sizing	cont	572.12 ft/min
Fan operating pressure ratio	cont	1.099
Span	cont	36.0 m
Angle for swept wing	cont	20.0°
Wing taper aspect ratio	cont	0.298
Engine length to diameter ratio	cont	5.0
Electric motors and fan number	discrete	40
Electric cores number	discrete	6
Generators per turbomachine	discrete	1
Turbomachines number	discrete	2

The observation of the optimization results from an aircraft design point of view leads to surprising conclusions, ultimately resulting in questioning the validity of the models utilized for the design. Among which:

- The optimal fan operating pressure ratio slightly less than 1.1 reveals a default in the coarse drag model used to assess the additional installation drag of distributed

P. Saves, N. Bartoli, Y. Diouane, Th. Lefebvre, J. Morlier, C. David, E. Nguyen Van and S. Defoort

electric propulsion.

- The sizing rules of the architecture is based on the default architecture and do not apply as easily to this new arrangement. Specifically connecting 40 motors to 6 cores of equal power is not straight forward.

- Additionally the safety analysis and cabling design for this new architecture have to be performed offline and may not be satisfying. Especially since the generator redundancy is removed by the optimization.

However, we can notice the clear direction taken by the optimizer to use the maximum number of motors with a low fan operating pressure ratio and constrained fan diameter. This also drives the motor length to diameter ratio to high values giving a clear indication for the choice of electric motor technology. A trade off is being made between propulsion efficiency, installation drag and space limitation which represents one of the challenge of DRAGON. The fact that such a trade off with continuous and discrete variables can be made is a great advantage for the study of aircraft with distributed electric propulsion. In future work, the flexibility of the optimization could allows us to view the architecture not only defined with discrete variables but provide a selection of architectures as categorical variables. This can help identify the most efficient architecture and most important redundancy or interconnection to install.

5 CONCLUSION AND PERSPECTIVES

To conclude, we have observed on both analytical and industrial cases than SEGO with KPLS is well-suited and efficient for a mixed integer high-dimensional constrained efficient global optimization problem. We have seen that continuous relaxation allows straightforward use of continuous GP but can be impractical as it increases the computational effort required to build the surrogate model. By using the PLS regression, it is possible to reduce the computational cost and makes the continuous relaxation affordable in practical contexts. This method has been applied to aircraft design optimization and contributed to the development of an MDA tool designing future aircraft configurations.

Future works will involve mixed integer Gaussian kernels for high-dimensional black-box problems to compare with this method. The number of components for PLS should be chosen from a global strategy and not beforehand and we expect KPLS to be useful for mixed integer Gaussian Kernels dimension reduction. For the Aircraft Design, the MDA for the "DRAGON" concept will soon be treated through overall aircraft design within FAST-OAD. The FAST-OAD Tool is still in development and will be made even more flexible and general.

REFERENCES

[1] E. Duriez and J. Morlier. Hale multidisciplinary design optimization with a focus on eco-material selection. In *Aerospace Europe Conference*, 2020.

[2] A. Lambe and J. R. R. A. Martins. A unified description of mdo architectures. In *9th World Congress on Structural and Multidisciplinary Optimization*, 2011.

[3] A. Lambe and J. R. R. A. Martins. Extensions to the design structure matrix for the description of multidisciplinary design, analysis, and optimization processes. *Structural and Multidisciplinary Optimization*, 46:273–284, 2012.

[4] J. R. R. A. Martins and A. Lambe. Multidisciplinary design optimization: A survey of architectures. *AIAA Journal*, 51:2049–2075, 2013.

[5] J. Mockus. *Bayesian approach to global optimization: theory and applications*, volume 37. Springer Science & Business Media, 2012.

[6] D. R. Jones, M. Schonlau, and W. J. Welch. Efficient global optimization of expensive black-box functions. *Journal of Global Optimization*, 13:455–492, 1998.

[7] J. Močkus. On bayesian methods for seeking the extremum. In *Optimization Techniques IFIP Technical Conference Novosibirsk*, 1974.

[8] C. E. Rasmussen and J. Quiñonero-Candela. A unifying view of sparse approximate gaussian process regression. *Journal of Machine Learning Research*, 6:1939–1959, 2005.

[9] A. Forrester, A. Sobester, and A. Keane. *Engineering Design via Surrogate Modelling: A Practical Guide*. Wiley, 2008. ISBN 9780470770795.

[10] M. J. Sasena, P. Papalambros, and P. Goovaerts. Exploration of metamodeling sampling criteria for constrained global optimization. *Engineering Optimization*, 34: 263–278, 2002.

[11] J. Pelamatti, L. Brevault, M. Balesdent, E.-G. Talbi, and Y. Guerin. Efficient global optimization of constrained mixed variable problems. *Journal of Global Optimization*, 73:583–613, 2019. doi:10.1007/s10898-018-0715-1.

[12] O. Roustant, E. Padonou, Y. Deville, A. Clément, G. Perrin, J. Giorla, and H. Wynn. Group kernels for gaussian process metamodels with categorical inputs. *arXiv e-prints*, 2018.

[13] M. M. Zuniga and D. Sinoquet. Global optimization for mixed categorical-continuous variables based on gaussian process models with a randomized categorical space exploration step. *INFOR: Information Systems and Operational Research*, 58:1–32, 2020. doi:10.1080/03155986.2020.1730677.

[14] S. Roy, W. A. Crossley, B. K. Stanford, K. T. Moore, and J. S. Gray. A mixed integer efficient global optimization algorithm with multiple infill strategy - applied to a wing topology optimization problem. In *AIAA Scitech 2019 Forum*, 2019. doi:10.2514/6.2019-2356.

[15] E. C. Garrido-Merchán and D. Hernández-Lobato. Dealing with categorical and integer-valued variables in bayesian optimization with gaussian processes. *Neurocomputing*, 380:20–35, 2020.

[16] D. Nguyen, S. Gupta, S. Rana, A. Shilto, and S. Venkatesh. Bayesian optimization for categorical and category-specific continuous inputs. In *AAAI-20 Technical Tracks*, 2020. doi:10.1609/aaai.v34i04.5971.

[17] M. Halstrup. *Black-Box Optimization of Mixed Discrete-Continuous Optimization Problems*. PhD thesis, TU Dortmund, 2016.

[18] R. Karlsson, L. Bliek, S. Verwer, and M. de Weerdt. Continuous surrogate-based optimization algorithms are well-suited for expensive discrete problems. *arXiv e-prints*, 2020.

[19] M. Bouhlel, N. Bartoli, R. Regis, A. Otsmane, and J. Morlier. Efficient global optimization for high-dimensional constrained problems by using the kriging models combined with the partial least squares method. *Engineering Optimization*, 50:2038–2053, 2018.

[20] A. M. Bouhlel, N. Bartoli, A. Otsmane, and J. Morlier. Improving kriging surrogates of high-dimensional design models by partial least squares dimension reduction. *Structural and Multidisciplinary Optimization*, 53:935–952, 2016.

[21] C. David, S. Delbecq, S. Defoort, P. Schmollgruber, E. Benard, and V. Pommier-Budinger. From FAST to FAST-OAD: An open source framework for rapid overall aircraft design. *IOP Conference Series: Materials Science and Engineering*, 1024:012062, jan 2021. doi:10.1088/1757-899x/1024/1/012062.

[22] S. H. Kim and F. Boukouvala. Surrogate-based optimization for mixed-integer nonlinear problems. *Computers & Chemical Engineering*, 140, 2020.

[23] D. Duvenaud. *Automatic model construction with Gaussian processes*. PhD thesis, University of Cambridge, 2014.

[24] R. J. Rossi. *Mathematical statistics: an introduction to likelihood based inference*. John Wiley & Sons, 2018.

[25] R. Priem, N. Bartoli, Y. Diouane, and A. Sgueglia. Upper trust bound feasibility criterion for mixed constrained bayesian optimization with application to aircraft design. *Aerospace Science and Technology*, 105:105980, 2020.

[26] N. Bartoli, T. Lefebvre, S. Dubreuil, R. Olivanti, R. Priem, N. Bons, J. R. R. A. Martins, and J. Morlier. Adaptive modeling strategy for constrained global optimization with application to aerodynamic wing design. *Aerospace Science and technology*, 90:85–102, 2019.

[27] D. Golovin, B. Solnik, S. Moitra, G. Kochanski, J. Karro, and D. Sculley. Google vizier: A service for black-box optimization. In *Proceedings of the 23rd ACM SIGKDD International Conference on Knowledge Discovery and Data Mining*, page 1487–1495, New York, NY, USA, 2017. Association for Computing Machinery. doi:10.1145/3097983.3098043. URL https://doi.org/10.1145/3097983.3098043.

[28] H. Wold. Soft modelling by latent variables: The non-linear iterative partial least squares (nipals) approach. *Journal of Applied Probability*, 12:117–142, 1975.

[29] K. Deb, A. Pratap, S. Agarwal, and T. Meyarivan. A fast and elitist multiobjective genetic algorithm: Nsga-ii. *IEEE Transactions on Evolutionary Computation*, 6: 182–197, 2002.

[30] J. Blank and K. Deb. Pymoo: Multi-objective optimization in python. *IEEE Access*, 8:89497–89509, 2020.

[31] M. A. Bouhlel, J. T. Hwang, N. Bartoli, R. Lafage, J. Morlier, and J. R. R. A. Martins. A python surrogate modeling framework with derivatives. *Advances in Engineering Software*, 135, 2019. doi:10.1016/j.advengsoft.2019.03.005.

[32] M. J. D. Powell. *A Direct Search Optimization Method That Models the Objective and Constraint Functions by Linear Interpolation*, pages 51–67. Springer Netherlands, 1994.

[33] T. P. Runarsson and X. Yao. Search biases in constrained evolutionary optimization. *IEEE Transactions on Systems, Man, and Cybernetics, Part C (Applications and Reviews)*, 35:233–243, 2005.

[34] P. E. Gill, W. Murray, and M. A. Saunders. Snopt: An sqp algorithm for large-scale constrained optimization. *SIAM Review*, 47:99–131, 2005.

[35] R. L. Riche and V. Picheny. Revisiting bayesian optimization in the light of the coco benchmark. 2021.

[36] J. Pelamatti, L. Brevault, M. Balesdent, E.-G. Talbi, and Y. Guerin. *High-Performance Simulation-Based Optimization*, chapter Overview and Comparison of Gaussian Process-Based Surrogate Models for Mixed Continuous and Discrete Variables: Application on Aerospace Design Problems, pages 189–224. Springer International Publishing, 2020.

[37] C. Vanaret. A global method for mixed categorical optimization with catalogs. *arXiv e-prints*, 2021.

[38] P. Schmollgruber, C. Döll, J. Hermetz, R. Liaboeuf, M. Ridel, I. Cafarelli, O. Atinault, C. François, and B. Paluch. Multidisciplinary Exploration of DRAGON: an ONERA Hybrid Electric Distributed Propulsion Concept. In *AIAA Scitech 2019*, 2019.

INVESTIGATING THE INFLUENCE OF UNCERTAINTY IN NOVEL AIRFRAME TECHNOLOGIES ON REALIZING ULTRA-HIGH ASPECT RATIO WINGS

Yiyuan Ma[1]*, Edmondo Minisci[2] and Ali Elham[1]

1: Institute of Aircraft Design and Lightweight Structures
Faculty of Mechanical Engineering
Technische Universität Braunschweig
35 Hermann-Blenk Street, 38108, Braunschweig, Germany
{Yiyuan.Ma, a.elham}@tu-braunschweig.de, https://www.tu-braunschweig.de/ifl

2: Intelligent Computational Engineering Laboratory
Faculty of Engineering
University of Strathclyde
75 Montrose Street, G1 1XJ, Glasgow, UK
edmondo.minisci@strath.ac.uk https://www.strath.ac.uk/staff/minisciedmondodr/

Abstract *This work studies the influence of uncertainty analysis on the unconventional aircraft conceptual design outcomes. The SBW and TF configurations are considered for the Short-Range (SR), Mid-Range (MR) and Long-Range (LR) missions, respectively. Conceptual design and analysis methodologies for the SBW and TF configurations are developed. Besides, the uncertainty analysis, constrained optimisation and global sensitivity analysis methodologies are presented. The proposed conceptual design methods are used to design an SBW and a TF aircraft for each mission, respectively, and the best-in-class configuration for each mission is initially obtained. Then the main uncertainties of each aircraft are identified and constrained optimisation is applied to find the best-case configuration with the objective function of the fuel weight. Moreover, a surrogate-based cut-HDMR method is used for the global sensitivity analysis to identify the most critical uncertainties and quantify their influences on the objective function. The results showed that according to the conceptual design results, the SBW configuration is the best-case for the SR mission, while the TF configuration is the best-case configuration for the MR and LR missions. Six main uncertainties, including four technologies-related and two mission-related parameters, are identified. The performed uncertainty analyses point out that, while there is not appreciable difference in terms of robustness against the operative and technology uncertainties for the SR mission configurations, the TF configuration is also more robust for MR and LR missions. Moreover, the sensitivity analyses assists in understanding which are the main uncertain drivers for each configuration and mission.*

Keywords: Uncertainty analysis, conceptual design, constrained optimisation, global sensitivity analysis, configuration comparative study

Yiyuan Ma, Edmondo Minisci and Ali Elham

1. INTRODUCTION

Making future air transportation more sustainable and energy-efficient, the European Commission and NASA have put forward challenging goals for future-generation aircraft and funded numerous advanced technologies and projects to facilitate the early realization of these goals [1, 2]. The Ultra-High Aspect Ratio Wing (UHARW) configuration is one of the most promising approaches to improve aircraft fuel efficiency and reduce emissions.

For the UHARW concept application, some strategies need to be proposed to reduce the huge bending moment and shear force in the wing structure. Strut-Braced Wing (SBW) and Twin-Fuselage (TF) concepts are two promising aircraft configurations for the UHARW design, which could significantly reduce the wing bending moment through the strut support or the off-centreline located fuselages with their payloads. There have been many studies on the SBW configuration and the TF configuration. For example, the Subsonic Ultra Green Aircraft Research (SUGAR) project, carried out by NASA, Boeing and the Georgia Institute of Technology, has comprehensively researched the SBW configuration for the next-generation mid-range transport mission [1]. Hosseini et al. [3] investigated the application potential of the SBW concept in regional jet aircraft. Virginia Polytechnic and State University carried out the conceptual design and optimization of a long-range SBW passenger aircraft [4]. However, comprehensive research on the SBW configuration for different missions, including uncertainty analysis for the novel airframe technologies and operating parameters, is still lacking. Many different kinds of TF aircraft have been designed, developed and flight-tested, such as WhiteKnightTwo [5], a general aircraft HY4 [6] and a TF Unmanned Aerial Vehicle (UAV) [7] and so on. However, there is little published research on the TF passenger aircraft, which probably due to airport infrastructure constraints (e.g., runway width and terminal access).

Due to the scarcity of data during the conceptual design phase, expert knowledge elicitation can be used to quantify subjective judgements and use this information to properly characterize the uncertainties. Since during the conceptual design phase there are not enough elements to characterise the model uncertainties through "precise" probability functions the interval approach or the evidence theory can be used to model and propagate both aleatory and epistemic uncertainties expressed as a set of intervals or imprecise probability distributions. Based on the characterised uncertainties, the best and worst performance response as a function of the considered uncertainties, can be obtained through a minimization process (best) and a maximization optimization process (worst). Moreover, optimization under uncertainties can be performed, and best- and worst-case configurations can be obtained through a min-min optimization process (best case) and a min-max optimization process (worst case) on both design and uncertain parameters, as well as configurations giving the best trade-off in terms of belief, through a multi-objective optimization process.

Robust- and sustainable-by-design ultra-higH aspEct ratio wing and Airframe (RHEA) is a Europe Union-funded project within the Clean Sky 2 Joint Undertaking (https://www.rhea-cleansky2.org/). The RHEA research team, composed of TU Braunschweig (DE), University of Strathclyde (UK), Imperial College (UK), DNW Wind Tunnels (NL) and IRT-Saint Exupery (FR), aims to design future-generation passenger aircraft with ultra-high aspect ratio wings and associated airframe to improve aircraft fuel efficiency. To this end, the overarching objective of RHEA is to improve the aerostructural design and efficiency of UHARW by combining advanced numerical and experimental methods for Multidisciplinary Design and Optimisation (MDO). Eventually, Short-Range (SR), Medium-Range (MR) and Long-Range (LR) missions will be addressed by RHEA and a paradigm shift towards robust design methods will be introduced.

This paper combines aircraft conceptual design methodology and uncertainty analysis at the conceptual design phase to study the effect of novel airframe technologies on the aircraft conceptual design outcomes. The conceptual design methodology of unconventional aircraft configurations, including SBW and TF concepts, and the uncertainty parameter analysis methodology, are introduced. Six aircraft configurations are designed based on the unconventional aircraft conceptual design process, and uncertainty analysis and global sensitivity analysis are performed for each of the six aircraft. Finally, referring to the uncertainty analysis results, the best-case and worst-case configurations and the configuration giving the best trade-off in terms of belief are obtained for each mission.

2. METHODOLOGY

This section presents the unconventional aircraft conceptual design and analysis methodology used in this research which involves uncertainty analysis and sensitivity analysis.

2.1. Conceptual design methodology

2.1.1. Conceptual design and analysis environment

Since this project addresses the future-generation passenger aircraft, several novel airframe technologies, including Hybrid Laminar Flow Control (HLFC), advanced materials and structure concept and active load alleviation, are assumed to be available in the Entry Into Service (EIS) timeframe of the aircraft studied in this paper, i.e., 2040.

Natural Laminar Flow (NLF) can significantly reduce the viscous wing drag for subsonic aircraft [8]. However, mid-range and long-range passenger aircraft operating in the transonic region require high wing sweep angles to reduce wave drag, making it challenging to maintain a wide range of NLF on the wing. Therefore, the HLFC technology will be applied to RHEA aircraft. In recent years, composites have gradually replaced metallic material in aircraft structures. For the RHEA aircraft, advanced materials and structures, such as tow-steered composite material [9] and thin ply materials for Composite Fibre-Reinforced Polymers (CFRP) structures, will be considered with respect to the structural weight saving at the conceptual design stage. Besides, aircraft structures need to be sized according to the worst-case operating condition, which can be represented by load factors. If the maximum load factors can be reduced to +1.5g and -0.5g by using advanced active load alleviation technologies for future-generation passenger aircraft, the wing weight saving can even reach 45% [10]. However, an aircraft design considering these new technologies includes a considerable level of uncertainties. The influence of these uncertainties on the outcome of the aircraft design is addressed in this work and the uncertainty analysis method used in this paper is presented in the next section.

Since unconventional aircraft configurations, including SBW and TF, are studied in this work, the traditional aircraft conceptual design methodologies and tools need to be extended, making them feasible for unconventional aircraft concepts involved in this work. In this research, the open-source aircraft design environment Stanford University Aerospace Vehicle Environment (SUAVE) [11] is used for the multi-fidelity analysis of aircraft performance and missions. The conceptual design methods of SBW and TF configurations, especially weight estimation methods and the above-mentioned novel technologies' influences on the initial sizing, are developed and added to SUAVE, making SUAVE feasible for the unconventional aircraft configurations investigated in this project. An in-house initial aircraft sizing tool PyInit [12], which was developed by the authors, is used for the initial aircraft sizing and

preliminary performance analysis. Besides, OpenVSP is used for aircraft geometric modeling and visualisation.

2.1.2. SBW sizing methodology

In this module, the required thrust-to-weight/power-to-weight ratio and wing loading are first estimated, and then the components' initial sizing and preliminary aerodynamic analysis (a semi-empirical method) are carried out by using the modified PyInit. Then the initially sized aircraft is input into the SUAVE for the weight breakdown and missions iteration analysis.

As mentioned above, SUAVE needs to be extended for the SBW aircraft configuration in this study, especially the weight estimation module. A semi-empirical wing weight estimation method for SBW configuration developed by Chiozzotto [13] is used in this paper, which was developed from structural sizing analysis and could capture the influences of the strut reaction and the design features of the high aspect ratio wing. Besides, this wing weight estimation method also considers the aeroelastic phenomena. The total wing weight of SBW configuration, including wing and strut, is estimated by:

$$m_w = k_{ail}\left(m_{covers} + m_{web+ribs}\right) + m_{sec} + m_{strut} \tag{1}$$

where m_w is the total wing weight, k_{ail} is the weight penalty factor due to the aileron efficiency constraints, m_{covers} is the wing box covers mass, $m_{web+ribs}$ is the wing cox spar webs and ribs mass, m_{sec} is the wing secondary structure mass and m_{strut} is the strut mass. m_{covers} . $m_{web+ribs}$ and m_{strut} are estimated by using a regression formula. More detailed information on this wing weight estimation method can be found in Ref. [13]. In addition, it should be noted that this method has been validated by several conventional aircraft [13] and an SBW passenger aircraft [3].

Since the other components of the SBW aircraft, including fuselage, tails, engines, landing gears and so on, are similar to those of conventional aircraft, the Flight Optimization System (FLOPS) [14] is used for these components' mass estimation.

2.1.3. TF sizing methodology

Similar to the SBW sizing methodology, the required thrust-to-weight/power-to-weight ratio and wing loading are first estimated, and then the components' initial sizing and preliminary aerodynamic analysis are carried out by PyInit. It should be noted that the fuselage of the TF aircraft needs to be sized especially. In this paper, the fuselage sizing method presented by Torenbeek [15] is used, i.e., each fuselage's length and equivalent width equal to that of the reference fuselage multiplied by $\sqrt{2}$, which ensures the TF aircraft and the reference conventional aircraft have the same total cabin floor area, i.e., the same passenger capacity.

The weight estimation method for TF configuration is integrated into the SUAVE as well. A semi-analytical wing mass estimation method for TF aircraft developed by Udin [16] is used, which estimates the TF aircraft wing mass according to the wing spanwise load distribution, including aerodynamic load, fuel mass, wing structural mass and concentrated load. The TF aircraft wing structural mass is expressed as

$$m_s = k_{sl}k_{tw}k_{man}\left(m_M + m_Q\right) + m_{rib} + m_{ail} + m_{sk} + m_{flap} \tag{2}$$

where m_{rib}, m_{ail}, m_{sk} and m_{flap} are the secondary structure mass, k_{sl} is the service life factor, k_{tw} is the twist moment factor, k_{man} is the manufacturing factor and m_M and m_Q are the wing structural mass required to carry the bending moment and shear force, respectively, which are

shown in Figure 1. The detailed derivation process and integral calculations of this method can be referred to Ref. [16].
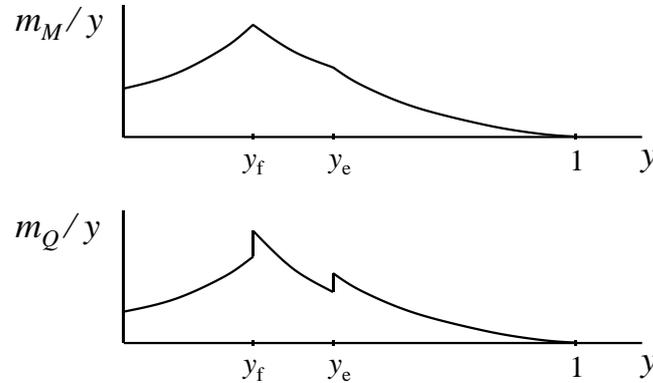
Figure 1. Spanwise distribution of relative wing mass [16].

Other components of TF aircraft, such as fuselage, tails, engines and so on, are similar to those of the conventional configuration, and the FLOPS method is used for these components' mass estimation.

2.2. Uncertainty analysis methodology

Six main uncertainties, four technologies related and two mission-related ones, have been identified. They include the achievable area of laminar flow over the wing, the achievable level of load reduction, the amount of structural weight reduction by using new materials and structures, the weight penalties on the wing due to folding mechanisms and the uncertainties on aircraft cruise Mach number and cruise altitude.

A file-based I/O process is implemented to interface the conceptual design tool with optimisers and sensitivity analysis codes and tools. The considered uncertainty inputs are:

- Cruise altitude, H_c
- Cruise Mach, M_c
- Vehicle range, R
- Maximum positive load factor, $n_{+,max}$
- Laminar transition (main wing), T_{Lw}
- Weight reduction factor (main wing), W_{Rw}
- Weight reduction factor (stabilizer), W_{Rs}
- Weight reduction factor (fuselage), W_{Rf}
- Wing weight penalty (due to the folding mechanisms), W_{Iw}

The conceptual design module has been interfaced with derivative-based and non-derivative-based search algorithms to explore the variability of the response W_f. The optimizer-conceptual design module coupling considers that the conceptual design module solves an internal constrained optimisation process to find the best sizing subject to a constraint on the payload weight, W_P.

- To estimate the variability of W_f due to the uncertainties, two optimisation processes have been performed for each tested configuration:
$$\min_{U} W_f \text{ (best case scenario)}$$
- and
$$\max_{U} W_f \text{ (worst case scenario)}$$

- where $U=\{\ H_c\ ,\ M_c\ ,\ R,\ n_{+,max}\ ,\ T_{Lw}\ ,\ W_{Rw}\ ,\ W_{Rs}\ ,\ W_{Rf}\ ,\ W_{Iw}\}$.

To perform the sensitivity analysis and following ranking, the adaptive cut-High Dimensional Model Representation (A-cut-HDMR) [17,18,19] approach (a non-intrusive method similar to the Analysis Of Variance, ANOVA, decomposition) has been used. The A-cut-HDMR approach decomposes the general function response, $f(U)$, in a sum of the contributions given by each uncertainty variable and each one of their interactions through the model, considered as increments with the respect to the response in the anchor point (not necessarily the nominal response), f_c:

$$f\left(U\right) = f_c + \sum_{i=1}^{n_u} F_i\left(U_i\right) + \sum_{i \leq i < j \leq n_u} F_{i,j}\left(U_i, U_j\right) + \ldots + F_{1,2,\ldots,n_u}\left(U_1, U_2, \ldots, U_{n_u}\right) \tag{3}$$

where n_u is the number of variables, and F_i, $i=1,\ldots,n_u$, are the orthogonal incremental contributions of every single uncertain parameter, $F_{i,j}$, $1 \leq i < j \leq n_u$, are the incremental contributions of each pair of uncertain parameters, and $F_{1,2,\ldots,n_u}$ is the incremental contribution of the interaction of all the uncertain parameters.

A surrogate model representation can be independently generated for each incremental contribution and only for the non-zero elements, thus greatly reducing the complexity of sampling and building the model. Moreover, the contribution of each term of the sum to the global response can be quantified independently so that higher-order interactions with low or zero contribution can be neglected already by analysing the lower-order terms.

This particular approach can be used to propagate any known standard distribution, from the classic Gaussian and uniform to Gumbell and Landau ones, and also non-standard distributions, as those deriving from the sum of kernels. The only assumption is the independence of the input uncertainties.

Not only is the output of this method the distribution of the quantity of interest, but also the quantification of the global contribution of each term of the sum to the global response. This feature allows for a complete analysis of the sensitivity of the response with respect to each of the stochastic variables, as well as their interactions. Moreover, in the case that the output function of interest is given by a black-box model, the analysis of the single contributions can give an insight into the structure of the response function.

The A-cut-HDMR is adaptive in terms of sampling and truncation of terms in Eq. (3). The adaptive sampling takes into account the shape of the underlying response and also the input probability distributions, leading to an efficient distribution of samples for the considered uncertainties and combination of uncertainties. The adaptive truncation removes the interactions that give a contribution to the overall response lower than a predefined threshold. The implemented heuristics for additivity have been demonstrated to be robust and efficient on a broad range of engineering cases.

2.3. Conceptual design and uncertainty analysis structure

The conceptual design and uncertainty analysis framework developed in this paper is shown in Figure 2. Firstly, PyInit is used to determine the constraint diagrams and size the aircraft dimensions, and then the initially sized aircraft and its operating conditions are input into the modified SUAVE for performance analysis. If the aircraft performance meets the design requirements, the initially designed aircraft will be transferred to the uncertainty analysis module. Otherwise, the design parameters will be adjusted in PyInit until the conceptual design process converges.

Constrained optimisation approaches are applied to find the best-case and worst-case configurations when the objective function is the fuel weight and the constraint on the

payload weight is implicitly imposed in the conceptual design module. Moreover, a surrogate-based cut-High Dimensional Model Representation (cut-HDMR) based approach, [19], is used to perform a global sensitivity analysis aimed at identifying the most critical uncertainties and quantifying their influence on the considered objective function.
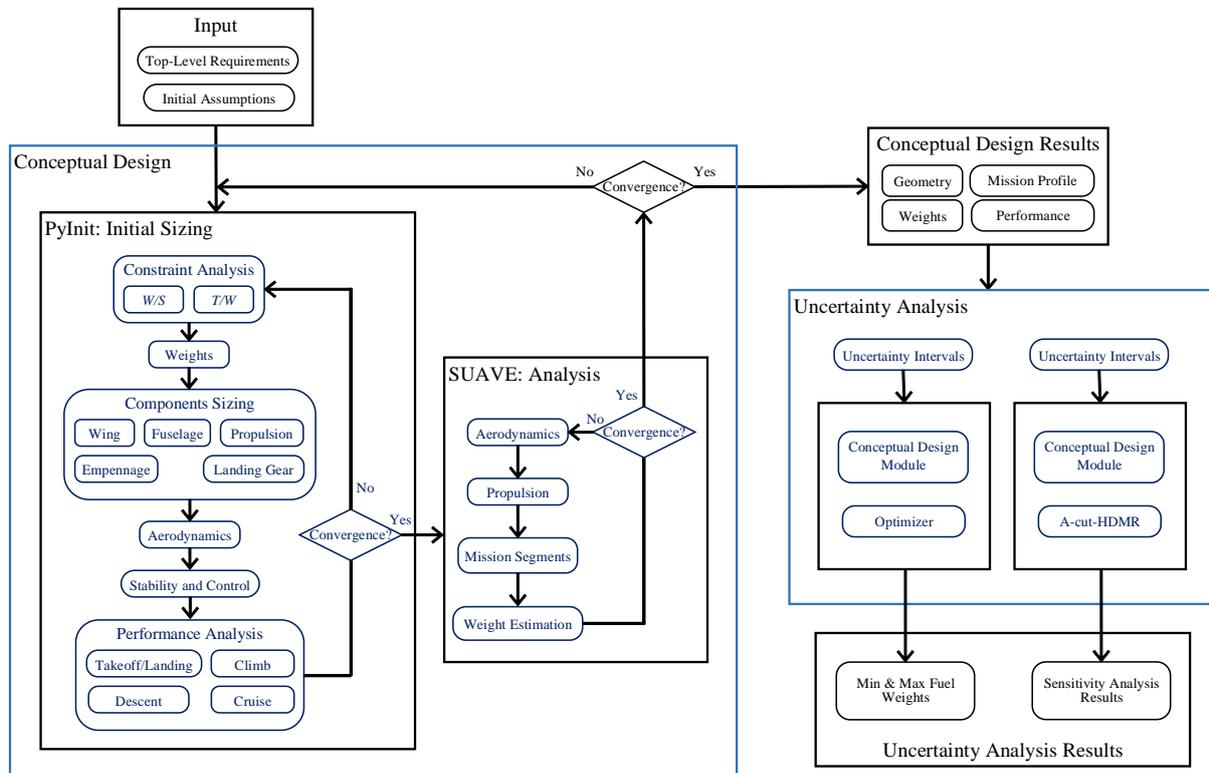
Figure 2. Conceptual design and uncertainty analysis structure.

3. AIRCRAFT CONCEPTUAL DESIGN AND UNCERTAINTY ANALYSIS

A total of six aircraft for the three missions are designed and studied in this section using the developed aircraft conceptual design and uncertainty analysis framework. According to the combination of aircraft performance analysis results and uncertainty analysis results, the best-case configuration of each mission is determined, and a comparison is conducted to study how the determination of the best-case and worst-case configurations is influenced by the uncertainty analysis. Besides, corresponding to the identified uncertainties, constrained optimisation is carried out to compare the SBW and TF aircraft for each mission. Then, the cut-HDMR method is used for the global sensitivity analysis of each aircraft to analyse the uncertainty characteristics.

3.1. Overview of the RHEA aircraft design requirements

The EIS of RHEA aircraft is taken as the year 2040, and RHEA aircraft is designed to comply with CS-25 certificate regulations [20]. The RHEA aircraft mission profile is shown in Figure 3. The entire mission is divided into several segments, including a main mission and a reserve phase. As the RHEA project aims at investigating the UHARW, the aircraft wing aspect ratio is initially taken as 25 in the conceptual design stage, which will be optimised in the later optimisation research phase. Besides, it should be noted that since the RHEA aircraft is designed with the UHARW concept, the wing may need to be designed to be foldable due to

airport facilities constraints.
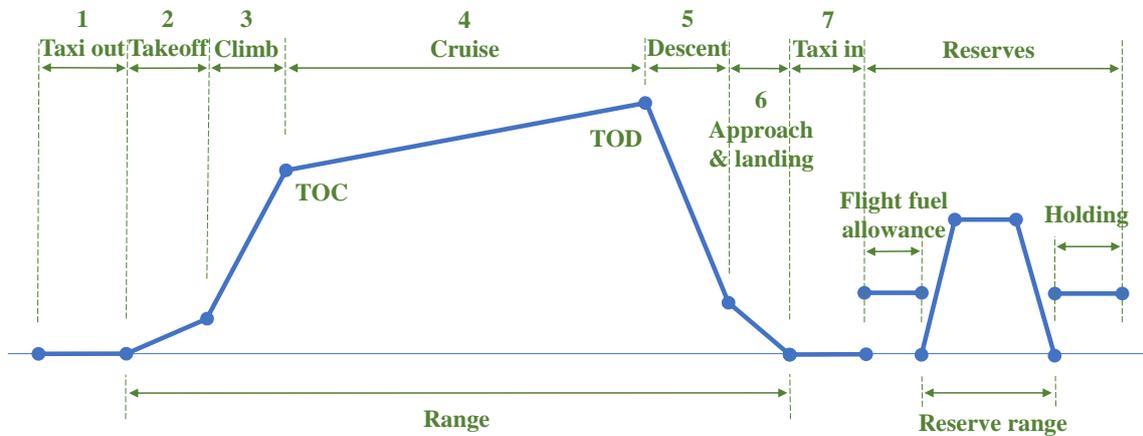
Figure 3. RHEA aircraft mission profile.

As described in Section 2.1, several novel airframe technologies for the next-generation passenger aircraft are considered in the RHEA aircraft design, including HLFC, load alleviation and advanced materials and structures. Assumptions for these novel technologies for different missions and different configurations are given in Table 1.

Table 1. Assumptions of novel airframe technologies.

Configuration		HLFC (Percentage of laminar flow area on the wing and tailplane)	Load alleviation (load factors)	Advanced materials & structures
Short-range	SBW	65%	+1.5g and -0.5g	20% structural weight reduction
	TF	70%		
Mid-range	SBW	50%	+1.5g and -0.5g	20% structural weight reduction
	TF	55%		
Long-range	SBW	50%	+1.5g and -0.5g	20% structural weight reduction
	TF	55%		

3.2. RHEA aircraft conceptual design

According to the top-level aircraft requirements proposed in each subsection and the novel technologies assumed in Table 1, an SBW configuration and a TF configuration are initially sized by PyInit and analysed by SUAVE for each mission, respectively.

3.2.1. RHEA short-range aircraft

ATR 72-600 was selected as the reference aircraft for the SR mission. The top-level aircraft requirements of RHEA-SR aircraft are listed in Table 2. The RHEA-SR aircraft will operate at ICAO Class C airports, which requires that the aircraft wingspan should not exceed 36 meters and the main landing gear span should not exceed 9 meters (active constraint in the SR-TF aircraft configuration sizing).

Table 2. Top-level aircraft requirements of RHEA-SR aircraft.

Parameter	Unit	RHEA-SR

Yiyuan Ma, Edmondo Minisci and Ali Elham

Reference aircraft		—	ATR 72-600
Propulsion concept		—	Turboprop
Cruise Mach number		—	0.42
Max. Mach number		—	0.457
Passengers		—	72
Range		nm	825
Reserves	Contingency fuel	—	3%
	Divert segment	nm	87
	Hold (at 1500 ft)	min	10
Cruise altitude		ft	20000
Service ceiling		ft	25000
Take-off field length		ft	4373
Landing distance		ft	3002
Approach speed		kt	113
Airport (ICAO C)	Wingspan	m	36
	Main landing gear span	m	9

The high-wing configuration with two turboprop engines was chosen for the RHEA-SR aircraft, and the wing was designed foldable with the folding position at 36 meters of the wingspan. NACA 65-618 and NACA 65-613 were chosen for the wing roots and wingtips to maximize the laminar flow range. The initially sized SR-SBW and SR-TF aircraft by PyInit are shown in Figure 4

SBW

TF
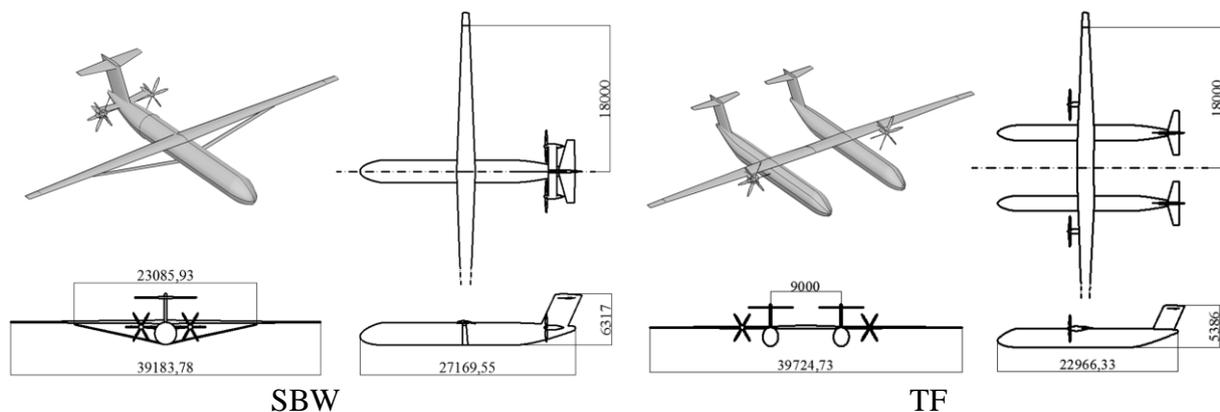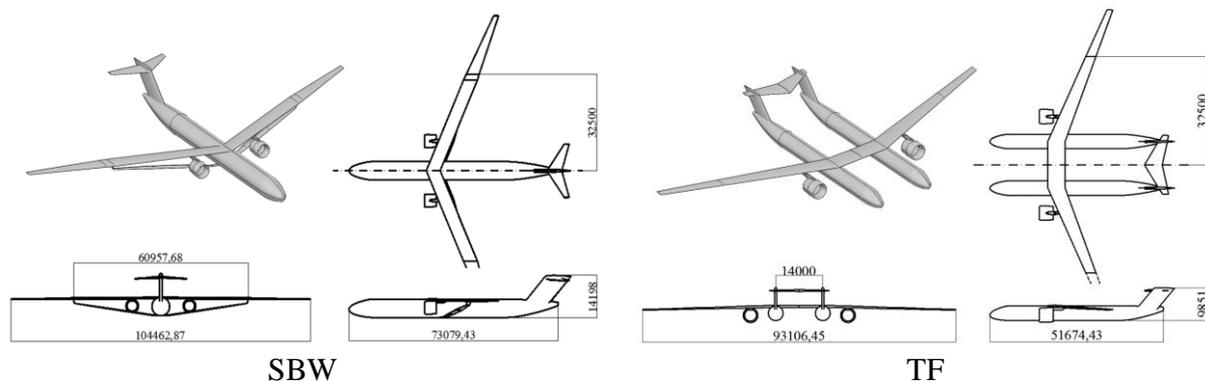
Figure 4. Three-view dimensions of RHEA-SR aircraft.

The fuselage of ATR 72-600 was used for the SR-SBW aircraft and was taken as the reference fuselage for the SR-TF aircraft, and both the SR-SBW and SR-TF aircraft were designed to have the same 72-seat capacity as the ATR 72-600. The SR-SBW aircraft uses the same fuselage interior arrangement as that of ATR 72-600, and the cabin interior arrangement of SR-TF aircraft is shown in Figure 5. It should be noted that the TF aircraft fuselage width was manually reduced to include a 2-abreast seating arrangement and the fuselage cross-section's height was slightly increased to the same height as the reference fuselage. In particular, two super-first-class seats are arranged at the non-cockpit fuselage nose with the best view, making full use of the fuselage space and providing more profits for airliners.

Yiyuan Ma, Edmondo Minisci and Ali Elham
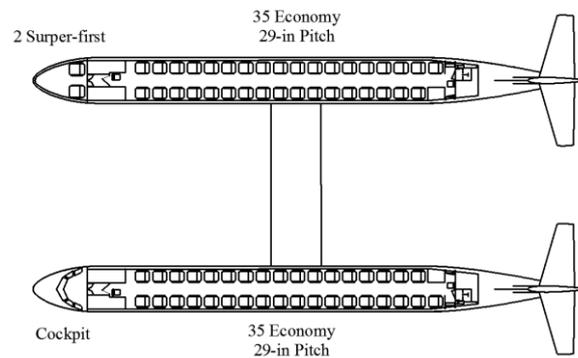
Figure 5. SR-TF aircraft interior arrangement.

Then the flight conditions and the initially sized SR-SBW and SR-TF aircraft were input into the modified SUAVE for performance analysis through iterative calculations. The SUAVE analysis results of the SR aircraft and the key weight data of the reference aircraft ATR 72-600 [21] are given in Table 3.

Table 3. Weight breakdown of short-range aircraft

Group	SR-SBW	SR-TF	ATR 72-600 [21]
MTOW, kg	22229	24028	22800
Fuel weight, kg	1432	2191	2000
Empty weight, kg	12821	13860	13500
Empty weight breakdown			
Wing, kg	2103	1556	
Fuselages, kg	2497	3052	
Propulsion, kg	1019	1094	
Nacelles, kg	269	287	
Landing gear, kg	643	690	
Horizontal tail, kg	201	414	
Vertical tail, kg	312	349	
Paint, kg	199	250	
Systems, kg	5579	6167	

Therefore, according to the aircraft dimensions in Figure 4 and the weight comparisons in Table 3, the SBW configuration outperforms the TF configuration in the SR mission because of its better fuel efficiency, lighter takeoff weight and smaller wingspan.

3.2.2. RHEA mid-range aircraft

A320neo was selected as the reference aircraft for the MR mission. The top-level aircraft requirements of RHEA-MR aircraft are listed in Table 4. The RHEA-MR aircraft will also operate at ICAO Class C airports.

Table 4. Top-level aircraft requirements of RHEA-MR aircraft.

Parameter	Unit	RHEA-MR
Reference aircraft	—	A320neo

Yiyuan Ma, Edmondo Minisci and Ali Elham

Cruise Mach number		—	0.78
Max. Mach number		—	0.82
Passengers (1 class)		—	186
Passengers (2 class)		—	150
Range		nm	3400
Reserves	Contingency fuel	—	3%
	Divert segment	nm	200
	Hold (at 1500 ft)	min	10
Cruise altitude		ft	33000
Service ceiling		ft	38500
Takeoff field length		ft	<6400
Landing distance		ft	<4500
Approach speed		kt	136
Airport (ICAO C)	Wingspan	m	36
	Main landing gear span	m	9

Similar to the SR aircraft design, considering the UHARW concept, both the MR-SBW and MR-TF aircraft feature a high-wing configuration with two wing-mounted high bypass ratio turbofan engines, and the wings are designed to be foldable with the folding position at 36 meters of the wingspan. As the RHEA-MR aircraft will operate at the transonic region, the supercritical airfoils NASA SC(2)-0412 and NASA SC(2)-0410 were adopted for the wing root and wingtip airfoils, respectively, and NASA SC(2)-0010 was used for the tail airfoils. Besides, the wing sweep angle ($0.25c$) was taken as 12.5 deg to facilitate the laminar flow on the wing surface. OpenVSP was used for the aircraft visualization, and the initially sized MR-SBW and MR-TF aircraft are shown in Figure 6.
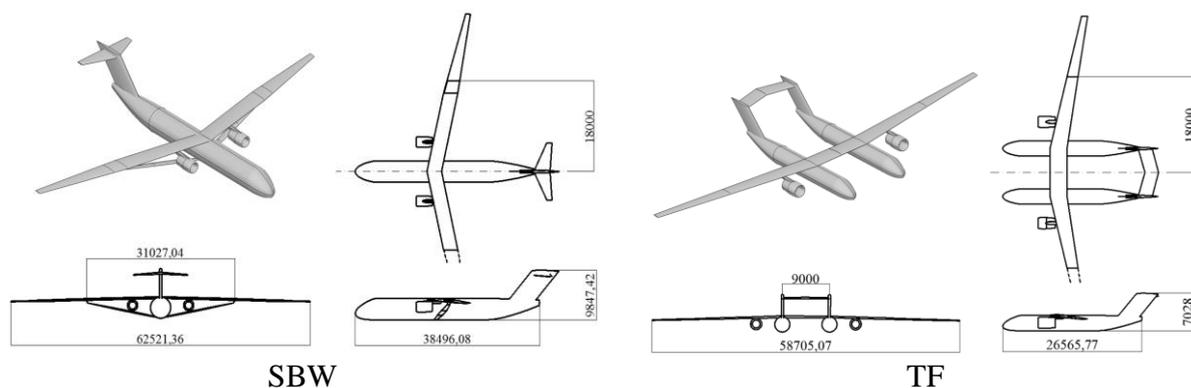
Figure 6. Three-view dimensions of RHEA-MR aircraft.

The fuselage of the A320neo was used for the MR-SBW aircraft and was taken as the reference for the MR-TF aircraft fuselage sizing, and both the MR-SBW and MR-TF aircraft were designed to have the same 150-seat arrangement as the A320neo. The MR-TF aircraft features a 4-abreast seating arrangement that meets the cabin parameter design requirements. In contrast, the reference A320neo has a 6-abreast seating arrangement in economy class. The cabin interior arrangement of the MR-TF aircraft is shown in Figure 7. Similar to the SR-TF aircraft design, two super-first-class seats are arranged in the non-cockpit fuselage nose.
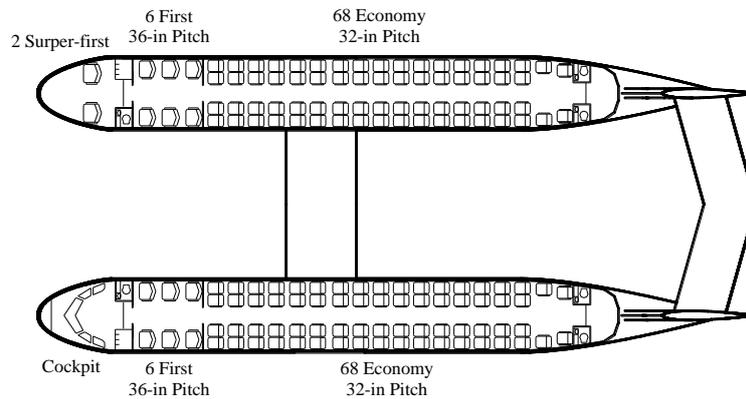
Figure 7. MR-TF aircraft interior arrangement.

Then the modified SUAVE was used to converge the aircraft weights while satisfying the required flight missions. The flight conditions and initially sized aircraft configurations of the MR-SBW and MR-TF aircraft obtained by PyInit were input into SUAVE for iterative calculations, respectively. The SUAVE analysis results of the MR aircraft and the key weight data of the reference aircraft A320neo [22] are listed in Table 5.

Table 5. Weight breakdown of mid-range aircraft

Group	MR-SBW	MR-TF	A320neo [22]
MTOW, kg	67929	57777	79000
Fuel weight, kg	16127	13328	20980
Empty weight, kg	37582	30229	44300
Empty weight breakdown			
Wing, kg	9393	4631	
Fuselages, kg	7066	5241	
Propulsion, kg	4493	3710	
Nacelles, kg	527	490	
Landing gear, kg	2292	1976	
Horizontal tail, kg	414	772	
Vertical tail, kg	902	844	
Paint, kg	447	415	
Systems, kg	12049	12151	

As given in Table 5, both SBW and TF configurations with the novel airframe technologies have significant advantages over the A320neo for the proposed mid-range mission. The MR-TF aircraft has significantly better fuel efficiency than that of MR-SBW aircraft, which is mainly due to the lighter operating empty weight. Besides, it is worth noting that the MR-TF aircraft's wing weight is significantly lighter than that of MR-SBW aircraft because of its better wing spanwise load distribution. Therefore, corresponding to the weight comparison in Table 5 and the aircraft dimensions in Figure 6, the TF configuration is the best-case configuration in the MR mission proposed in this paper.

3.2.3. RHEA long-range aircraft

B777-300ER was selected as the reference aircraft for the RHEA-LR mission. The top-level

aircraft requirements of RHEA-LR aircraft are listed in Table 6.

Table 6. Top-level aircraft requirements of RHEA-LR aircraft.

Parameter		Unit	RHEA-LR
Reference aircraft		—	B777-300ER
Cruise Mach number		—	0.84
Max. Mach number		—	0.89
Passengers (2 class)		—	350
Range		nm	7500
Reserves	Contingency fuel	3%	3%
	Divert segment	200	200
	Hold (at 1500 ft)	10	10
Cruise altitude		ft	35000
Service ceiling		ft	40000
Takeoff field length		ft	9000
Landing distance		ft	9000
Approach speed		kt	140
Airport (ICAO C)	Wingspan	m	65
	Main landing gear span	m	14

Due to the UHARW design, the high-wing configuration with two wing-mounted high bypass ratio turbofan engines was used for both the LR-SBW and LR-TF aircraft. The LR aircraft wings are designed to be foldable with the folding position at 65 meters of the wingspan. The supercritical airfoils NASA SC(2)-0412 and NASA SC(2)-0410 were adopted for the wing root and wingtip airfoils, respectively. A wing sweep angle ($0.25c$) of 23 deg was chosen as a trade-off between the wave drag and the laminar flow on the wing surface. OpenVSP was used for the aircraft visualisation, and the initially sized LR-SBW and LR-TF aircraft are shown in Figure 8.

Figure 8. Three-view dimensions of RHEA-LR aircraft.

The fuselage of the reference aircraft B777-300ER was used for the LR-SBW aircraft and was taken as the reference for the LR-TF aircraft fuselage sizing. The LR-SBW and LR-TF aircraft were designed to have the same number of first- and economy-class seats. The reference aircraft B777-300ER and the LR-SBW aircraft feature a 6-abreast and 9-abreast

seating arrangement for the first-class and economy-class, respectively, while a 4-abreast first-class and 6-abreast economy-class seating arrangement was chosen for the sized LR-TF aircraft cabin, as shown in Figure 9. Besides, similar to the above-mentioned designs, the non-cockpit fuselage nose was arranged with two super-first-class seats.
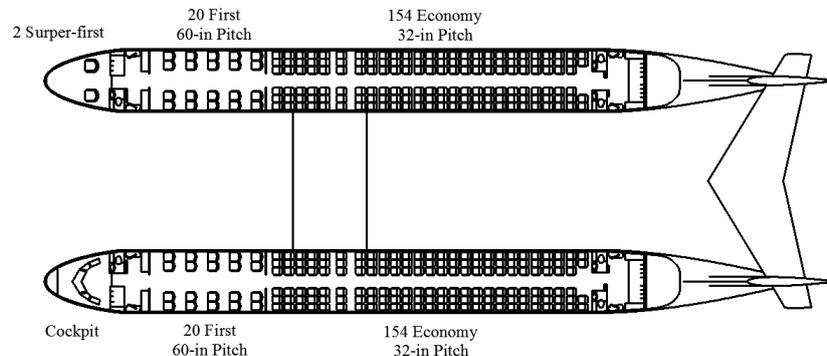
Figure 9. LR-TF aircraft interior arrangement.

The flight conditions and aircraft configurations of the LR-SBW and LR-TF aircraft obtained during the initial sizing by PyInit were input into the modified SUAVE for iterative calculations, respectively. The SUAVE analysis results of the LR aircraft and the key weight data of the reference aircraft B777-300ER [23] are tabulated in Table 7. Both SBW and TF configurations with the novel airframe technologies have significant advantages over the B777-300ER for the long-range mission. Due to the load distribution on the TF aircraft wings is more optimal than that of the SBW aircraft because the large centrally positioned fuselage weight is replaced by two outboard positioned weights, the TF aircraft wing weight is significantly lighter than that of the LR-SBW aircraft.

Table 7. Weight breakdown of long-range aircraft

Group	LR-SBW	LR-TF	B777-300ER [23]
MTOW, kg	262962	207105	351535
Fuel weight, kg	89716	79428	145538
Empty weight, kg	140066	94496	167829
Empty weight breakdown			
Wing, kg	47401	13687	
Fuselages, kg	25757	20596	
Propulsion, kg	18650	14774	
Nacelles, kg	2460	2255	
Landing gear, kg	7023	5639	
Horizontal tail, kg	1483	1515	
Vertical tail, kg	2923	2436	
Paint, kg	1237	1151	
Systems, kg	33133	32444	

As listed in Table 7, the LR-TF aircraft has a significantly better fuel efficiency than that of the LR-SBW aircraft. Therefore, the TF configuration is the best-case configuration in the LR mission due to its obvious performance advantages and its smaller size.

A summary of the RHEA aircraft conceptual design and initial comparison results are shown

in Figure 10, which will be further studied by uncertainty analysis in the next section.
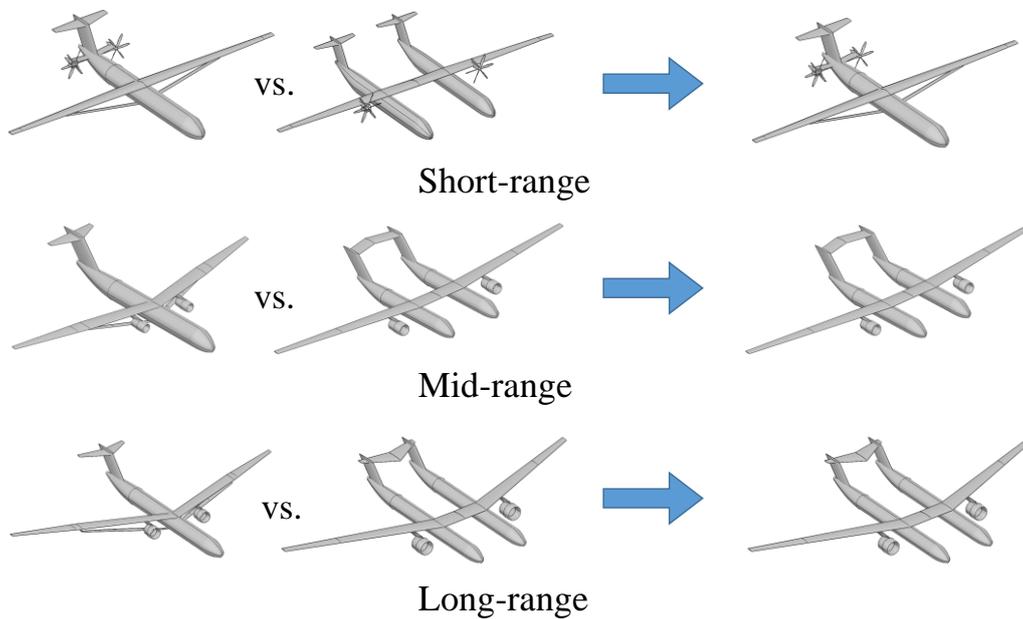
Figure 10. RHEA aircraft conceptual design results.

3.3. RHEA aircraft uncertainty analysis

Given the iterative process of the conceptual design module, the $W_f(U)$ function is very noisy, and to find the minima and maxima a combination of gradient-based and pattern search algorithms has been used. All the considered algorithms are part of the MATLAB optimization toolboxes.

3.3.1. Short-range configurations

For both cases (SBW and TF) the considered uncertainty bounds have been set as in Table 8 (**Lb** and **Ub** values). The corresponding values for max and min of the performance function, W_f, are reported in the same table too.

The pursuit of the SBW best case scenario (minimisation process) brings to a sizing that allows $W_f = 1302\ kg$. The pursuit of the best-case scenario (maximisation process) brings to a sizing with $W_f = 1912\ kg$. The pursuit of the best-case scenario (minimisation process) brings to a sizing that allows $W_f = 2028\ kg$. The pursuit of the best-case scenario (maximisation process) brings to a sizing with $W_f = 2682\ kg$. It can be seen that from Table 8, for both configurations, the minimum value of W_f is obtained when the lower bound of H_c is considered, and, vice versa, then the maximum value is obtained when the upper bound of H_c is considered. The technology-related uncertainties play a role in accordance with a priori expectations. It is interesting to note that M_c does not play a role in this case, and this is also confirmed by the sensitivity analysis presented in Sec. 3.4.1

Table 8. Short-Rage: Lower and upper bounds (**Lb** and **Ub**, respectively) of the uncertain parameters, and values of uncertainty parameters giving the best case (min W_f) and the worst case (max W_f) sizings for the SBW and TF configurations.

ID	Uncertain parameters	*Lb*	*Ub*	Min W_f SBW	Max W_f SBW	Min W_f TF	Max W_f TF

1	H_c [km]	6.096	8.534	6.096	8.534	6.096	8.534
2	M_c	0.4	0.45	0.4	0.4	0.4	0.4
3	R [nm]	800	850	800	850	800	850
4	n_{+max} [g]	1.5	2.5	1.5	2.5	1.5	2.5
5	T_{Lw} [%]	0.5	0.5	0.75	0.5	0.75	0.5
6	W_{Rw} [%]	0.1	0.25	0.25	0.1	0.25	0.1
7	W_{Rs} [%]	0.1	0.25	0.25	0.1	0.25	0.1
8	W_{Rf} [%]	0.1	0.25	0.25	0.1	0.25	0.1
9	W_{Iw} [%]	0.05	0.1	0.05	0.1	0.05	0.1

3.3.2. Mid-range configurations

For both cases (SBW and TF) the considered uncertainty bounds and the corresponding values for max and min of the performance function, W_f, are reported in Table 9.

The pursuit of the SBW best case scenario (minimisation process) brings to a sizing that allows $W_f = 10617\ kg$. The pursuit of the best-case scenario (maximisation process) brings to sizing with $W_f = 17872\ kg$, which is very similar to the conservative nominal sizing.

The pursuit of the best-case scenario (minimisation process) brings to a sizing that allows $W_f = 9877\ kg$. The pursuit of the best-case scenario (maximisation process) brings to a sizing with $W_f = 15229\ kg$, which is again very similar to the conservative nominal sizing. It can be seen that in this case the H_c plays differently and the minimum value of W_f can be obtained for high cruise altitudes (vice versa for the maximum value). The cruise Mach now plays a more important role, and the achievable W_f increases in accordance with M_c.

Table 9. Mid-Rage: Lower and upper bounds (***Lb*** and ***Ub***, respectively) of the uncertain parameters, and values of uncertainty parameters giving the best case (min W_f) and the worst case (max W_f) sizings for the SBW and TF configurations.

ID	Uncertain parameters	*Lb*	*Ub*	Min W_f SBW	Max W_f SBW	Min W_f TF	Max W_f TF
1	H_c [km]	8.53	13.716	13.04	8.53	13.61	8.53
2	M_c	0.71	0.78	0.736	0.78	0.748	0.78
3	R [nm]	3300	3500	3457	3300	3300	3322
4	n_{+max} [g]	1.5	2.5	1.5	2.5	1.5	2.5
5	T_{Lw} [%]	0.5	0.75	0.75	0.5	0.75	0.5
6	W_{Rw} [%]	0.1	0.25	0.25	0.1	0.25	0.1
7	W_{Rs} [%]	0.1	0.25	0.25	0.1	0.25	0.1
8	W_{Rf} [%]	0.1	0.25	0.25	0.1	0.25	0.1
9	W_{Iw} [%]	0.05	0.1	0.1	0.1	0.1	0.1

3.3.3. Long-range configurations

For both cases (SBW and TF) the considered uncertainty bounds and the corresponding values for max and min of the performance function, W_f, are reported in Table 10.

The pursuit of the SBW best case scenario (minimisation process) brings to a sizing that allows $W_f = 58815\ kg$. The pursuit of the best case scenario (maximisation process) brings to a sizing with $W_f = 121820\ kg$. The pursuit of the best case scenario (minimisation process)

brings to a sizing that allows $W_f = 56971\ kg$. The pursuit of the best-case scenario (maximisation process) brings to a sizing with $W_f = 94946\ kg$. As for the short-range case, again W_f decreases with the cruise altitude and increases with the cruise Mach.

Table 10. Long-Rage: Lower and upper bounds (***Lb*** and ***Ub***, respectively) of the uncertain parameters, and values of uncertainty parameters giving the best case (min W_f) and the worst case (max W_f) sizings for the SBW and TF configurations.

ID	Uncertain parameters	*Lb*	*Ub*	Min W_f SBW	Max W_f SBW	Min W_f TF	Max W_f TF
1	H_c [km]	9.144	13.716	12.104	9.144	12.602	9.144
2	M_c	0.75	0.85	0.75313	0.813	0.76875	0.837
3	R [nm]	7400	7600	7600	7400	7600	7400
4	n_{+max} [g]	1.5	2.5	1.5	2.4375	1.5	2.5
5	T_{Lw} [%]	0.5	0.75	.75	0.5	0.75	0.5
6	W_{Rw} [%]	0.1	0.25	.2375	0.1	0.2375	0.1
7	W_{Rs} [%]	0.1	0.25	.25	0.1	0.175	0.1
8	W_{Rf} [%]	0.1	0.25	.2375	0.1	0.2375	0.1
9	W_{Iw} [%]	0.05	0.10	0.05	0.1	0.075	0.1

3.4. Influence of uncertainties on the conceptual design outcomes

For this work, even if there are no data to properly characterise the distribution of input uncertainties, the A-cut-HDMR approach had been used considering uniform input distributions with the same bounds presented in tables included in Sec. 3.3 to perform the sensitivity analysis and rank the contributions of the single uncertainties as well as the possible contributions of the interactions. For each case, the tables in this section present the main contributions of the increment functions in absolute terms (6sigma, i.e. six times the standard deviation of each increment function) and relative terms (sensitivity variance, an index of relative ranking).

3.4.1. Sensitivity analysis for the short-range configurations

The adaptive sampling and related adaptive detection of important contributions bring to sensitivity analysis in terms of mean and variance sensitivity as shown in Table 11. The most important uncertainty contributions (measured as contribution to variance) for the SBW configuration, given the value of $f_c = 1563$ kg, are H_c (increment function 1) and T_{Lw} (increment function 5), followed by n_{+max}, (increment function 4) and M_c (increment function 2). The most important uncertainty contributions for the TF configuration, given the value of $f_c = 2317$ kg, are, again, H_c (increment function 1) and T_{Lw} (increment function 5), followed by M_c (increment function 2) and n_{+max}, (increment function 4).

Since short-range mission aircraft operate at low Mach numbers and aircraft performance is not very sensitive to compressive drag, the effect of cruise Mach number (i.e., *2* in Table 11) on both SR-SBW and SR-TF aircraft is minimal among the studied parameters. Mainly due to the high sensitivity of the turboprop engine performance to the operating altitude, this parameter has a significant impact on both SR-SBW and SR-TF aircraft. It is noteworthy that the cruise Mach number has the greatest effect on both configurations studied in this paper. Therefore, researchers should pay more attention to the cruise altitude when designing such aircraft. Besides, the laminar transition also plays an important role, which is consistent with a

previous preliminary estimation for an aircraft that features extended laminar flow along the airframes demonstrated a significant reduction (up to 50%) in overall drag [24]. And this impact on the TF configuration is significantly higher than that of the SBW configuration, which is due to the TF configuration has a shorter fuselage, so the TF configuration's tail area is larger than that of the SBW configuration. It is interesting to note that the maximum positive load factor $n_{+,max}$ has a more pronounced effect on the SBW configuration than the TF configuration, which may be due to the fact that the TF configuration has a better wing unloading effect than the SBW configuration, so that the $n_{+,max}$ has less effect on the TF configuration, and this phenomenon can also be observed in the MR and LR cases.

Table 11. Sensitivity analysis via A-cut-HDMR: main increment functions contributing to the variance of W_f for the SR-SBW configuration (left), and the SR-TF configuration (right)

Increment functions SBW	Partial 6sigma for SWB [kg]	Sens. Variance SBW		Increment functions TF	Partial 6sigma for TF [kg]	Sens. Variance TF
1	500	0.70229		*1*	444	0.4995
2	23	0.015		2	65	0.0105
4	145	0.0567		4	64	0.0103
5	287	0.2306		5	428	0.46325
8	35	0.0035		8	57	0.0082

3.4.2. Sensitivity analysis for the mid-range configurations

The adaptive sampling and related adaptive detection of important contributions bring to sensitivity analysis in terms of mean and variance sensitivity as shown in Table 12. The most important uncertainty contributions (measured as contribution to variance) for the SBW configuration, given the value of f_c = 12884 kg, are T_{Lw} (increment function 5) and H_c (increment function 1), followed by M_c (increment function 2) and n_{+max}, (increment function 4). The most important uncertainty contributions for the TF configuration, given the value of f_c = 11594 kg, are, again, T_{Lw} (increment function 5) and H_c (increment function 1), followed by M_c (increment function 2) and n_{+max}, (increment function 4).

Since the cruise phase of the MR mission accounts for a significant proportion in the whole mission, the laminar flow contributes the most to the aircraft performance due to the significant drag reduction. The most important contribution in the SR mission, i.e., the cruise altitude, also plays an important role in the MR mission, especially for the TF configuration. As explained in the sensitivity analysis for the SR mission (in Sec. 3.4.1), the contribution of the maximum positive load factor is more pronounced for the SBW configuration than for the TF configuration. As listed in Table 9, the Mach number's bounds considered for the MR mission were [0.71, 0.78], and the compressive drag in this range is not significant enough, so the sensitivity of the Mach number is relatively smaller than the others.

Table 12. Sensitivity analysis via A-cut-HDMR: main contributing increments functions for the MR-SBW configuration (left), and the MR-TF configuration (right)

Increment functions SBW	Partial 6sigma for SWB [kg]	Sens. Variance SBW		Increment functions TF	Partial 6sigma for TF [kg]	Sens. Variance TF
1	3145	0.24035		*1*	2917	0.35187

Yiyuan Ma, Edmondo Minisci and Ali Elham

2	835	0.016947		*2*	813	0.027303
4	1886	0.086361		*4*	709	0.020773
5	5102	0.63224		*5*	3744	0.57959
1.2	739	0.013265		*1.2*	481	0.0095483

3.4.3. Sensitivity analysis for the Long-Range Configurations

The adaptive sampling and related adaptive detection of important contributions bring to sensitivity analysis in terms of mean and variance sensitivity as shown in Table 13. The most important uncertainty contributions (measured as contribution to variance) for the SBW configuration, given the value of f_c = 73021 kg, are n_{+max}, (increment function 4) and T_{Lw} (increment function 5), followed by M_c (increment function 2) and H_c (increment function 1). The most important uncertainty contributions for the TF configuration, given the value of f_c = 68033 kg, are, T_{Lw} (increment function 5) and M_c (increment function 2), followed by H_c (increment function 1), and, very marginally this time, by and n_{+max}, (increment function 4).

For the SR and MR missions, the distribution of the parameter sensitivity variances is essentially consistent with the two configurations. However, the sensitivity contributions of the parameters for the LR mission are significantly different between the SBW and TF configurations. According to the partial 6sigma values given in Table 13, it can be observed that this difference is mainly due to the different performance of the maximum positive load factor for these two configurations. As described in Sec. 3.4.1, because of the off-centreline located fuselages of the TF configuration, the wing unloading effect of this configuration is better than that of the SBW configuration, so the sensitivity contribution of the TF configuration's maximum positive load factor is smaller than that of the SBW configuration, and the difference in this contribution between these two configurations is greater than for the SR and MR missions since the off-centreline located fuselages are heavier in the LR mission, which is consistent with the weight breakdown data given in Table 7. Besides, similar to the MR mission, the laminar flow transition also has a significant impact on the SBW and TF configurations of the LR mission due to the large proportion of the cruise phase in the whole mission. The partial 6sigma results show that the cruise Mach's absolute influence value is similar for both configurations, while the cruise Mach's sensitivity variance of the TF configuration is much higher than for the SBW configuration due to the less contribution of the maximum positive load factor for the TF configuration. Finally, it should be noted that the cruise altitude is observed plays a more important role for the TF configuration than the SBW configuration.

Table 13. Sensitivity analysis via A-cut-HDMR: main contributing increments functions for the LR-SBW configuration (left), and the LR-TF configuration (right)

Increment functions SBW	Partial 6sigma for SWB [kg]	Sens. Variance SBW		Increment functions TF	Partial 6sigma for TF [kg]	Sens. Variance TF
1	6356	0.0183		*1*	13640	0.2064
2	13433	0.0818		*2*	14212	0.224
4	35971	0.5864		*4*	5867	0.0382
5	25988	0.3061		*5*	21457	0.5107
6	3081	0.0043		*6*	1682	0.0031
8	2578	0.003		*8*	2030	0.0046

				1.2	3406	0.0129

4. CONCLUSION

This paper addressed the influence of uncertainty analysis on the unconventional aircraft conceptual design outcomes. The SBW configuration and TF configuration were considered with respect to SR, MR and LR missions, respectively. Conceptual design and analysis methodologies for the SBW configuration and the TF configuration were first proposed. Six aircraft were preliminary designed by using the proposed methods and the best-in-class configuration of each mission was initially determined corresponding to the obtained performance analysis results. Then six main uncertainties, including four novel airframe technology parameters and two operating parameters, were identified and constrained optimisation approaches were applied to search for the best-in-class configuration. In addition, a surrogate-based cut-HDMR method was used to perform a global sensitivity analysis aimed at identifying the most critical uncertainties and quantifying their influences on the objective function. Finally, the best-case and worst-case configurations for each mission identified through uncertainty analysis and optimisation were compared with the initial conceptual design results, and the influence of uncertainties on the conceptual design outcomes was analysed.

Corresponding to the proposed top-level aircraft design requirements and novel technologies, an SBW configuration and a TF configuration aircraft were design for each mission, respectively, and their performance was analysed by using PyInit and SUAVE. The best-in-class configuration of each mission was obtained by comparing the fuel weight, takeoff weight and aircraft dimensions, i.e., the SBW configuration for the SR mission and the TF configuration for MR and LR missions.

The performed uncertainty analyses confirm the ranking of the different configurations and highlight which are the most critical aspects among the building technologies and the operative conditions that should be considered in the future design phases for each configuration, or at least for the configurations that will proceed further. In particular, the sensitivity analyses pointed out that: 1) while there is not appreciable difference in terms of robustness (measured here as difference between max and min W_f) against the operative and technology uncertainties for the SR mission configurations, the TF configuration is more robust for MR and LR missions; 2) the technology uncertainty that is always a major player, even if with different weights, for all the configurations is that related to the laminar to turbulence transition extension; 3) the operative conditions, i.e., cruise Mach and altitude, play a different role for each of the configurations and missions, and this should be taken into account for the next design phases.

ACKNOWLEDGMENTS

REFERENCES

[1] Greitzer, E. M., Bonnefoy, P. A., De la Rosa Blanco, E., Dorbian, C. S., Drela, M., Hall, D. K., ... and Mody, P., N+3 Aircraft Concept Designs and Trade Studies, Final Report. NASA/CR-2010-216794/VOL1, 2010.

[2] Anon., Realising Europe's Vision for Aviation: Strategic Research & Innovation Agenda, Vol. 1. Advisory Council for Aviation Research and Innovation in Europe, 2012.

[3] Hosseini, S., Ali Vaziri-Zanjani, M. and Reza Ovesy, H., Conceptual design and analysis of an affordable truss-braced wing regional jet aircraft. *Proceedings of the Institution of Mechanical Engineers, Part G: Journal of Aerospace Engineering*, 0954410020923060, 2020. doi: 10.1177/0954410020923060.

[4] Khan, K. H., Mallik, W., Kapania, R. K. and Schetz, J. A., Distributed Design Optimization of Large Aspect Ratio Wing Aircraft with Rapid Transonic Flutter Analysis in Linux. AIAA Paper 2021-1354, Jan. 2021. doi: 10.2514/6.2021-1354.

[5] Guerster, M. and Crawley, E. F. Dominant Suborbital Space Tourism Architectures, *Journal of Spacecraft and Rockets*, 56(5): 1580-1592, 2019. doi: 10.2514/1.A34385.

[6] Kallo, J., DLR Leads HY4 Project for Four-Seater Fuel Cell Aircraft. *Fuel Cells Bulletin*, 2015(11): 13, 2015. doi: 10.1016/S1464-2859(15)30362-X.

[7] Ma, Y., Zhang, W., Zhang, Y., Zhang, X. and Zhong, Y., Sizing Method and Sensitivity Analysis for Distributed Electric Propulsion Aircraft. *Journal of Aircraft*, 57(4): 730-741, 2020. doi: 10.2514/1.C035581.

[8] Beck, N., Landa, T., Seitz, A., Boermans, L., Liu, Y. and Radespiel, R., Drag Reduction by Laminar Flow Control. *Energies*, 11(1), 2018.

[9] Brooks, T. R., Martins, J. R. and Kennedy, G. J., High-Fidelity Aerostructural Optimisation of Tow-Steered Composite Wings. *Journal of Fluids and Structures*, 88: 122-147, 2019.

[10] Rossow, C., Geyr, H. and Hepperle, M., The 1g-Wing, Visionary Concept or Naive Solution? *DLR-IB-AS-BS-2016-121*, 2016.

[11] Lukaczyk, T. W., Wendorff, A. D., Colonno, M., Economon, T. D., Alonso, J. J., Orra, T. H. and Ilario, C., SUAVE: An Open-Source Environment for Multi-Fidelity Conceptual Vehicle Design. AIAA Paper 2015-3087, Jun. 2015.

[12] Karpuk, S. and Elham, A., Conceptual design trade study for an energy-efficient mid-range aircraft with novel technologies. *AIAA Scitech 2021 Forum*, January 2021. doi: 10.2514/6.2021-0013.

[13] P. Chiozzotto, G., Initial weight estimate of advanced transport aircraft concepts considering aeroelastic effects. AIAA Paper 2017-0009, Jan. 2015. doi: 10.2514/6.2017-0009.

[14] Wells, D. P., Horvath, B. L. and McCullers, L. A., The flight optimization system weights estimation method, NASA/TM-2017-219627/Volume I, 2017.

[15] Torenbeek, E., *Advanced aircraft design: conceptual design, analysis and optimization of subsonic civil airplanes*, John Wiley and Sons Ltd, West Sussex, 2013.

[16] Udin, S. V. and Anderson, W. J., Wing mass formula for twin fuselage aircraft, *Journal of Aircraft*. 29 (5): 907-914, 1992. doi: 10.2514/3.46261.

[17] Mehta, P.M., Kubicek, M., Minisci, E., Vasile, M., Sensitivity Analysis and Probabilistic Re-entry Modeling for Debris using High Dimensional Model Representation based Uncertainty Treatment, *Advances in Space Research*, Vol.59, Issue 1, pp 193–211, January 2017.

[18] Kubicek, M., High Dimensional Uncertainty Propagation for Hypersonic Flows and Entry Propagation, PhD Thesis, University of Strathclyde, 2018.

[19] Kubicek, M., Minisci, E. and Cisternino, M., High dimensional sensitivity analysis using surrogate modeling and High Dimensional Model Representation. *International Journal for Uncertainty Quantification*, 5(5): 393–414, 2015

Yiyuan Ma, Edmondo Minisci and Ali Elham

[20] Certification Specifications and Acceptable Means of Compliance for Large Aeroplanes CS-25. June, 2020. URL https://www.easa.europa.eu/document-library/certification-specifications/cs-25-amendment-25.

[21] ATR-72 Series 600 Brochure. 2014. URL http://www.atraircraft.com/products_app/media/pdf/Brochure-ATR-600-Series_2014.pdf.

[22] Airbus S.A.S., A320 Aircraft Characteristics Airport and Maintenance Planning. Issue: 30 Sept. 1985, Rev: 1 April 2020.

[23] Airplanes, B. C. 2015. 777-200LR/-300ER/-freighter airplane characteristics for airport planning, Document Number D6-58329-2. URL http://www. boeing. com/assets/pdf/commercial/airports/acaps/777_2lr3er.pdf.

[24] Beck, N., Landa, T., Seitz, A., Boermans, L., Liu, Y. and Radespiel, R., Drag Reduction by Laminar Flow Control. *Energies*, 11(1), pp 252, 2018.

PERFORMANCE OF HYBRID OPTIMIZATION METHODS APPLIED TO ACTIVE FLOW CONTROL DEVICES

Martí Coma[1,2]*, Navid M. Tousi[1], Jordi Pons-Prats[1,2], Josep M. Bergadà[1] and Gabriel Bugeda[1,2]

1: Universitat Politècnica de Catalunya. Barcelona Tech (UPC)
Edificio C1, Gran Capitan, 08034
Gran Capitan, 08034, Barcelona, Spain
Tel. (+34) 934016494 / Fax. (+34) 934016894
e-mail:
marti.coma,navid.monshi.tousi,jordi.pons-prats,josep.m.bergada,gabriel.bugeda@upc.edu,
http://www.upc.edu

2: Centre Internacional de Mètodes Numèrics a l'Enginyeria (CIMNE)
Edificio C1, Gran Capitan, 08034
Barcelona, Spain. Tel. (+34) 932057016 / Fax. (+34) 934016517
e-mail: mcoma, jpons, bugeda@cimne.upc.edu, http://www.cimne.com

Abstract. *Genetic Algorithms (GA) are optimization methods that are usually very robust but have a slow convergence to the exact minimum. On the other hand, Gradient Based methods which converge better, are not so robust, and can get stuck in local minimums or flat areas. In this article a Hybrid optimization method is presented and its performance is compared against a Gradient Based method and a Genetic Algorithm. The comparison is established with a Gradient Based method, which is a Conjugate Gradient, and a Genetic Algorithm, based on a $\mu + \lambda$ strategy. The Hybrid methods combine the two above-mentioned methods. Each Hybrid implementation is composed of a GA and a Conjugate Gradient which share information at each iteration, to try overcome individual-method limitations and achieve a better performance. The strategy used for sharing information among each method is based on games theory, more specifically Nash Games. The use of a coupling based on competitive players enhances the overall performance of the method pushing each one with the improvements of the other one. This enables an efficient management of the individuals, and the optimum ones, ensuring a good balance when dealing with elite individuals. A performance comparison is done with the optimization of an Active Flow Control (AFC) over a 2D Selig-Donovan 7003 (SD7003) airfoil at Reynolds number 6×10^4 and 14 degrees of attack. Five design variables are considered: jet position, jet width, momentum coefficient, forcing frequency and jet inclination angle. The fluid flow problem is solved using Computational Fluid Dynamics (CFD) with the Spalart-Allmaras turbulent model. The motivation behind the current study is to evaluate the performance of the Hybrid methods in a physical problem with a computationally expensive objective function.*

Keywords: Hybrid Optimization Methods, Optimization, Population-based Methods, Gradient-based Methods, Evolutionary Techniques, Active Flow Control, Synthetic Jet

Martí Coma, Navid M. Tousi, Jordi Pons-Prats, Josep M. Bergadà and Gabriel Bugeda

1 INTRODUCTION

Optimization methods search for a good trade-of between exploration and exploitation. These two aspects are usually associated with different optimization techniques and approaches. For example, Evolutionary Algorithms are usually very robust and have great exploration capabilities, but they lack precision to find the exact minimum efficiently. On the other hand, Gradient Based methods are very efficient exploiting minimums, assuming function continuity, differentiability and convexity.

In order to mitigate the drawbacks of each method, different hybridizations have been proposed. At least three main strategies can be found in the literature. The first strategy is the definition of new operators, similar to the traditional genetic operators (namely selection, crossover and mutation), but with improved local search capabilities. The second group combines two optimization methods, ideally one with great exploration capabilities and the other focused on exploitation. Both methods share information to increase the performance. The last group is composed by multi-population strategies.

An example of hybridization on Genetic Algorithms can be found at Cheng et al. [1]. The article describes the hybridization of genetic operators (crossover and mutation) combining global and local methods. Another example is Wang et al. [2], which defines a new selection operator, a new mutation operator and local search operators. Other examples of operator hybridization can be found in Weare et al. [3], Valls et al. [4] and Ho et al. [5].

Regarding the combination of two methods, Kelly Jr and Davis [6] combines a Genetic Algorithm with k-nearest neighbors classification algorithm, as hybridization and Genetic Algorithms are not only used in optimization. In the vehicle routing field, Jih and Hsu [7] uses Genetic Algorithms hybridized with Dynamic Programming. The Dynamic Programming algorithm produces a first approach to the solution, and the Genetic Algorithm starts from those results. Another example of hybridization combining different methods is the work of El-Mihoub et al. [8], which presents an hybridization of a Genetic Algorithm with other local search algorithms. The assessed ones are Lamarckian learning, Baldwinian Learning, and an hybrid Lamarckian-Baldwinian model. The work treats the balancing and communication between the different methods.

Regarding the strategy, which defines multiple populations working in parallel and sharing genetic information, there are different approaches. For example, Ho et al. [5] defines an hybrid Genetic Algorithm with multiple population, applied to Vehicle routing problem, with each population using different operators. Another approach is presented by Berger and Barkaoui [9] who splits the objective functions in one population and the restrictions in another, and shares the information between them. The work of Lee et al. [10] propose an hybrid Genetic Algorithms based on the Nash Games, splits the problem (objective functions and design variables) into two different populations, and a third one which deals with the overall problem, receiving information back and forth with the two others.

2 PROPOSED HYBRID METHOD AND REFERENCE OPTIMIZATION METHODS

In this section the proposed Hybrid Method is presented, as well as the used Genetic Algorithm and the Gradient Method. The performance comparison has been done with the two methods that the hybrid method combines, but running separately.

2.1 Proposed hybrid method description

The proposed Hybrid Method consists of a combination of two optimization algorithms, called players. According to the classification of hybridization types presented in the *Sec. 1 Introduction*, this falls into the second type. The first player, mainly, dedicated to exploration is a Genetic Algorithm, explained in detail in *Sec. 2.2 Genetic Algorithm*. The second player, dedicated to exploitation is a Conjugate Gradient, explained in detail in *Sec. 2.3 Conjugate Gradient*. Both players run sequentially, one after the other. The players pause its progression after each iteration. At this moment a *Migration Epoch* occurs, and both algorithms share information. This is inspired in the evolution of the species, where different populations exchange individuals at some point, and then continue its own evolution on its own after another migration occurs.

The fittest individual found by the Genetic Algorithm player migrates to the Conjugate Gradient one. On the other side, the best individual from the Genetic Algorithm player migrates to the Conjugate Gradient one.

The Genetic Algorithm player receives the individual substituting the less fitted individual in its current population with the one that comes from the Conjugate Gradient one. On the other hand, the Conjugate Gradient player treats the individual from the Genetic Algorithm one as a new seed and starts to optimize from there.

After some testing on the Hybrid Method, the Conjugate Gradient was modified to overcome some instabilities when running inside the Hybrid Method as a player. The step size is the distance increased during the line search in the design variables space. During the line search process the step size is recomputed using the Brent Method [11]. In case of the step size becomes zero, the iteration is considered finished and the default step size value is set. Then, the player is ready for the next seed, that will arrive from the Genetic Algorithm.

2.2 Genetic Algorithm

Genetic Algorithms were initially proposed by Holland [12], further developed by Goldberg and Holland [13] and more recently evolved by Deb et al. [14] which proposes different new operators. The methodology of Genetic Algorithm mimics the natural evolution process, which selects the best fitted individuals to generate new offspring, which tend to be better fitted than its predecessors.

The Genetic Algorithm used as a reference in this study is based on the NSGAII implementation developed by Deb et al. [14]. The main algorithm and operators are the same as the original published by the authors, but some modifications have been included, mainly to parallelize the evaluation of the objective functions. The *Selection()* operator employs a $\mu + \lambda$ strategy with a Crowded-Comparison Operator, proposed by Deb et al. [14]. For the *Crossover()* operator, a Simulated Binary Crossover (SBX) operator, also proposed by Deb and Agrawal [15] is used and the *Mutation()* operator is performed with Polynomial Mutation proposed by Deb [16]. The values of the configuration of the different operators are presented in the Tab.1.

2.3 Conjugate Gradient

A Conjugate Gradient, which is explained in detail by Shewchuk et al. [17], has been used. The Conjugate Gradient has been coded with the capability to compute the nec-

Martí Coma, Navid M. Tousi, Jordi Pons-Prats, Josep M. Bergadà and Gabriel Bugeda

Table 1: Parameters of the Genetic Algorithm.

Parameter	Value
Population size	20
Probability of crossover	0.9
Probability of mutation	0.1

essary individuals to obtain the gradient approximation in parallel. It needs the values of the design variables corresponding to the current individual, and a $\pm\epsilon$ for each one in order to approximate the value of the gradient using a finite differences scheme. This defines different sets of design variables corresponding to different designs whose objective functions can be computed in parallel, as they are independent between them. After the gradient is computed, the minimum in this direction is found using a line search method. This method needs information about the objective function at certain points, but it generates the points one by one, after the evaluation of the objective function of the previous point is computed. Because of that, the evaluations of the individuals can not be run in parallel. Tab.2 presents the configuration for the Conjugate Gradient.

Table 2: Parameters of the Conjugate Gradient.

Parameter	Value
Search Direction Method	Fletcher Reeves [18]
Optimal Step Size Method	Brent Method [11]
Epsilon for numerical differentiation	10^{-6}
Optimal step size tolerance	10^{-3}

3 CASE OF STUDY

We have proceed to make a comparison between the different algorithms by solving the optimization of the parameters of an Active Flow Control (AFC) device over a 2D Selig-Donovan 7003 (SD7003). The Reynolds number of the free stream is set to 6×10^{-4} and the angle of attack is 14 degrees.

Five design variables are taken into account for the optimization of the AFC. These are, the jet position x/C, jet width h/C, momentum coefficient C_μ, forcing frequency F^+ and jet inclination angle $\theta°$. The fluid is solved using Computational Fluid Dynamics (CFD) with the Spalart-Allmaras turbulent model. A complete explanation of the AFC case used in this study can be found at Tousi et al. [19]. The case computed in the paper differs from the original one in the mesh size and the number of objective functions which is now set to 1. As the goal of this study is to compare the performance of different optimization methods, and not the flow structure of the AFC, the mesh size has been enlarged to reduce the computational time at each iteration. The mesh size is about 36000 cells. A new mesh is generated for each individual as some of the design variables affect the geometry of the AFC device location.

The boundaries for the design variables are presented at Tab.3.

The objective of the optimization problem is to maximize the lift coefficient C_l. The implementation of the optimizer always treats the optimization as a minimization problem,

Martí Coma, Navid M. Tousi, Jordi Pons-Prats, Josep M. Bergadà and Gabriel Bugeda

Table 3: AFC Design variables and their evaluation ranges.

F^+	C_μ	$\theta°$	x/C	h/C
$[0.1\,,10]$	$[0.0001\,,0.02]$	$[5\,,175]$	$[0.001\,,0.3]$	$[0.005\,,0.015]$

the objective function f is set to $-C_l$.

$$f = -C_l \tag{1}$$

4   RESULTS

In this section, the results obtained for the three different optimization methods are presented. The Genetic Algorithm and the Hybrid Method have been run twice with different random seeds, in order to evaluate the robustness of the methods, as both methods have a stochastic component due to the Genetic Algorithm operators (Mutation and Crossover). The Conjugate Gradient has been run 6 times with different initial individuals (the first 6 individuals from the first generation of one of the Genetic Algorithms have been used). The Conjugate Gradient does not have a random behavior, but is highly dependent on the initial seed if the objective space has local minimums. To extract relevant statistical data, more runs with different seeds are needed, but as the study case is computationally very expensive, the results are evaluated looking at the tendency of the convergence graphs.

The convergence as a function of the number of evaluations of the CFD problem is presented in Fig.1. In this case, the performance of the convergence of the Hybrid Method is better than the Genetic Algorithm, and in addition it is more robust. The results of both runs of the Hybrid Method are better and more consistent than the Genetic Algorithm ones. The Hybrid Method took advantage of the internal Conjugate Gradient player to converge much faster to better results. On the other hand, analyzing the results of the Conjugate Gradient alone, one of the runs got stuck at a local minimum at the beginning of the analysis. Another one spent about 80 evaluation without improving the initial seed. And four of them were able to improve the initial seeds, but after around 100 iterations got stuck achieving better results than the Genetic Algorithm (at the same number of evaluations). Finally, comparing the Hybrid method against the Conjugate Gradient, the Hybrid Method has a convergence speed similar to the Conjugate Gradient, but does not get stuck and at around 150 evaluations reaches its best results.

As explained in *Sec. 2.1 Proposed hybrid method description*, the three methods are capable of parallelizing the evaluations of the individuals in some parts of the algorithm. The level of parallelization that can be achieved is not the same for each algorithm. The evaluation of all the individuals belonging to the same population can be performed in parallel whereas the line search method is not parallelized because each design is obtained sequentially after the evaluation of the previous one. This makes that the improvement on the performance of the different algorithms when using parallel capabilities is not the same. In order to take into account this phenomena two additional graphics are presented. These graphics shows the convergence with a different x axis, which takes into account the speedup of each algorithm due to the parallelization capabilities. The graphics consider that all evaluations of the objective functions takes the same amount of time, which is not always true. It depends on the solver used to evaluate the objective function (for

Martí Coma, Navid M. Tousi, Jordi Pons-Prats, Josep M. Bergadà and Gabriel Bugeda
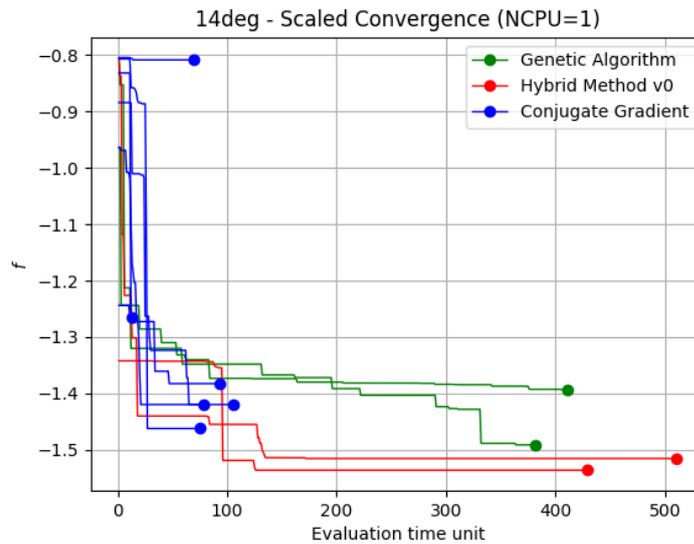
Figure 1: Convergence with 1 CPU.

example, an iterative process inside the objective function evaluation may take more or less iterations, and thus time, depending on the exact condition, i. e. design variables), but it gives a clear idea of the parallelization capabilities of each optimization algorithm. 11 CPU is the maximum number of CPU that the Conjugate Gradient can take advantage for five design variables, as it can only compute in parallel the objective functions needed to calculate the gradient, twice the number of design variables plus the current point. And 20 CPU is the maximum number of CPU that the Genetic Algorithm can use with a population of 20 individuals, as no assynchronization strategy is implemented and it needs the whole population computed before generating a new offspring.

The graphics in Fig.2 and Fig.3 shows the scaled convergence for 11 and 20 CPU, respectively. The algorithm that most benefits from the availability of CPU is the Genetic Algorithm, as it can parallelize all evaluations in chunks of the population size. The Conjugate Gradient is the algorithm that benefits less of the availability of the results, as the line search is not parallelized. The Hybrid Method also takes advantage of the parallelization, but the improvement is mainly noticed up to 11 CPU, as the Conjugate Gradient player can not benefit from more CPU, defines the bottleneck.

The Genetic Algorithm should run additional iterations in order to clearly identify the converged solution when using 11 and 20 CPU. It is currently still running, but the problem is computationally high demanding and this are the results so far.

Martí Coma, Navid M. Tousi, Jordi Pons-Prats, Josep M. Bergadà and Gabriel Bugeda
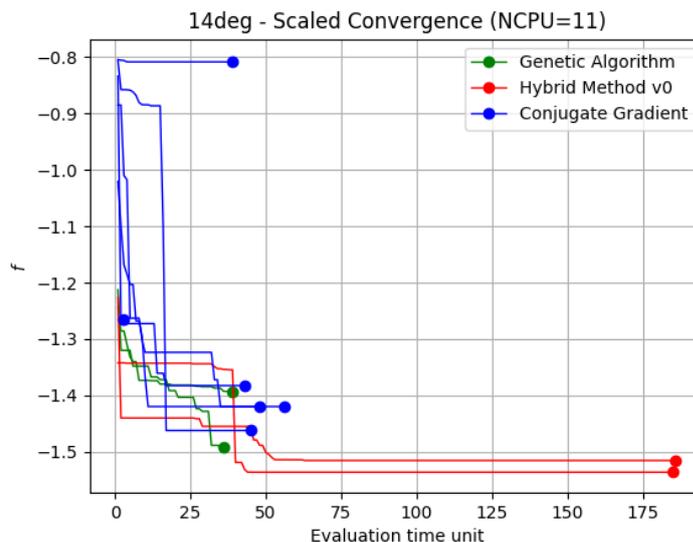
Figure 2: Convergence with 11 CPU.
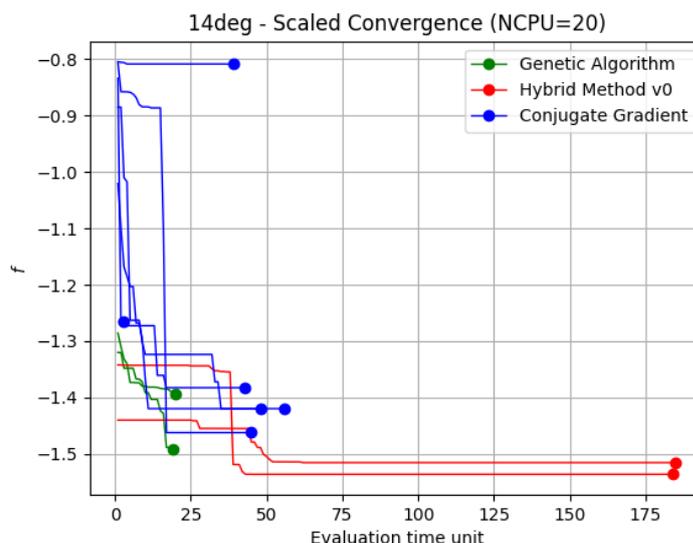
Figure 3: Convergence with 20 CPU.

5   CONCLUSIONS

The present article describes the application of three different optimization strategies to a complex and high-demanding problem. Although the problem definition has been simplified, as described in the 1, each individual evaluation of the objective function is taking around 12 hours, making the whole optimization analysis a costly process. Due to the computational cost, the aim of the proposed methods is to speed up the analysis while keeping the robustness on the solution, as well as its convergence to the accurate optimum.

The proposed Hybrid Algorithm has demonstrated a general better performance than the traditional Genetic Algorithm and Conjugate Gradient methods. The algorithm suc-

Martí Coma, Navid M. Tousi, Jordi Pons-Prats, Josep M. Bergadà and Gabriel Bugeda

cessfully takes advantage of the strengths of each player. Each of them contributes to analyze the search space from the global and local search point of view, and the shared information along the process facilitates the speed up of each individual player. The result of this cooperation is reflected on the general behavior of the method. The Conjugate Gradient needs a good seed, close to the minimum which requires previous knowledge in the problem, which is not always available. This seed-dependence could greatly affects the final performance of the method.

When considering the availability of a large number of computational resources, the Genetic Algorithm has an advantage, and could outperform the Hybrid Method. What could determine if the Genetic Algorithm outperforms the Hybrid Method is the fact that the multiple CPU graphs are showing the ideal case that all evaluations of the objective functions takes the same amount of time. If that is not the case, the benefits of increasing the number of CPU are less than the shown by the presented results.

The planned future work is to evaluate better the performance of the algorithms with regards to the number of CPU. The optimizations should be run with different number of CPU in order to compare the real time, and not only applying a scale factor considering that all individuals take the same amount of time to evaluate. The main issue with this tests is to obtain enough computational resources.

Another future work is to evaluate the performance of the Hybrid Method when dealing with multi objective functions. It has not been stated before but the Hybrid Method is extended to multi objective problems, and will be tested using the same problem described by Tousi et al. [19].

ACKNOWLEDGEMENTS

REFERENCES

[1] R. Cheng, M. Gen, and Y. Tsujimura. A tutorial survey of job-shop scheduling problems using genetic algorithms, part ii: hybrid genetic search strategies. *Computers & Industrial Engineering*, 36(2):343–364, 1999.

[2] Y. Wang et al. A new hybrid genetic algorithm for job shop scheduling problem. *Computers & Operations Research*, 39(10):2291–2299, 2012.

[3] R. Weare, E. Burke, and D. Elliman. A hybrid genetic algorithm for highly constrained timetabling problems. *Department of Computer Science*, 1995.

[4] V. Valls, F. Ballestin, and S. Quintanilla. A hybrid genetic algorithm for the resource-constrained project scheduling problem. *European Journal of Operational Research*, 185(2):495–508, 2008.

[5] W. Ho, G. T. Ho, P. Ji, and H. C. Lau. A hybrid genetic algorithm for the multi-depot vehicle routing problem. *Engineering Applications of Artificial Intelligence*, 21 (4):548–557, 2008.

[6] J. D. Kelly Jr and L. Davis. A hybrid genetic algorithm for classification. In *IJCAI*, volume 91, pages 645–650, 1991.

[7] W.-R. Jih and J. Y.-J. Hsu. Dynamic vehicle routing using hybrid genetic algorithms. In *Proceedings 1999 IEEE International Conference on Robotics and Automation (Cat. No. 99CH36288C)*, volume 1, pages 453–458. IEEE, 1999.

[8] T. A. El-Mihoub, A. A. Hopgood, L. Nolle, and A. Battersby. Hybrid genetic algorithms: A review. *Engineering Letters*, 13(2):124–137, 2006.

[9] J. Berger and M. Barkaoui. A parallel hybrid genetic algorithm for the vehicle routing problem with time windows. *Computers & Operations Research*, 31(10):2037–2053, 2004.

[10] D. Lee, J. Periaux, J. Pons-Prats, G. Bugeda, and E. Oñate. Double shock control bump design optimization using hybridised evolutionary algorithms. In *Evolutionary Computation (CEC), 2010 IEEE Congress on*, pages 1–8. IEEE, 2010.

[11] R. P. Brent. *Algorithms for minimization without derivatives.* Courier Corporation, 2013.

[12] J. H. Holland. *Adaptation in natural and artificial systems: an introductory analysis with applications to biology, control, and artificial intelligence.* MIT Press, Cambridge, Massachusetts, Jan. 1992.

[13] D. E. Goldberg and J. H. Holland. Genetic algorithms and machine learning. *Machine Learning*, 3:95–99, 1988. doi:10.1023/A:1022602019183.

[14] K. Deb, A. Pratap, S. Agarwal, and T. Meyarivan. A fast and elitist multiobjective genetic algorithm: NSGA-II. *Evolutionary Computation, IEEE Transactions on*, 6 (2):182–197, Apr 2002. ISSN 1089-778X. doi:10.1109/4235.996017.

[15] K. Deb and R. B. Agrawal. Simulated binary crossover for continuous search space. *Complex systems*, 9(2):115–148, 1995.

[16] K. Deb. *Multi-objective optimization using evolutionary algorithms*, volume 16. John Wiley & Sons, Chichester, UK, 2001.

[17] J. R. Shewchuk et al. An introduction to the conjugate gradient method without the agonizing pain, 1994.

[18] R. Fletcher. *Practical methods of optimization.* John Wiley & Sons, 2013.

[19] N. Tousi, M. Coma, J. Bergadà, J. Pons-Prats, F. Mellibovsky, and G. Bugeda. Active flow control optimisation on sd7003 airfoil at pre and post-stall angles of attack using synthetic jets. *Applied Mathematical Modelling*, 98:435–464, 2021. ISSN 0307-904X. doi:https://doi.org/10.1016/j.apm.2021.05.016. URL https://www.sciencedirect.com/science/article/pii/S0307904X21002614.

STUDY OF DISTRIBUTED ARCHITECTURES FOR MULTI-DISCIPLINARY OPTIMIZATION USING OpenMDAO

Shantanu S. Gulawani[1]*, K. M. Kiran Babu[1] and Rajkumar S. Pant[1]

Department of Aerospace Engineering,
Indian Institute of Technology Bombay, Mumbai
{shantanusg, kiranbabu, rpant}@iitb.ac.in, http://www.aero.iitb.ac.in/

Abstract *Multidisciplinary Optimization (MDO) is the approach of solving a problem to arrive at an optimum solution by considering all the significant disciplines that simultaneously influence the design. Many opensource and commercial MDO architectures are available, each having its own unique capabilities and benefits, such as OpenMDAO, which is an open-source MDO framework developed by NASA. With the use of MDO architectures, a largescale multi-disciplinary optimization problem can be transformed into a series of optimization sub-problems. In this study, an attempt is made to study and implement Collaborative Optimization (CO), Enhanced Collaborative Optimization (ECO) and MDO of Independent system (MDOIS) in OpenMDAO framework. The two test problems implemented in this study are Sellar's analytical problem and a Two-bar truss problem. Sellar's problem is solved by CO; the results are then compared with monolithic architectures. The two-bar truss design problem is formulated as a multi-level structural optimization problem and solved with CO, ECO and MDOIS. The implementation of nested optimization problems allowed the formulation of various distributed architectures.*

Keywords: Multi-Level Optimization, Collaborative Optimization, Distributed Architectures, Gradient-Based Optimization, Multi-Disciplinary Analysis

1. INTRODUCTION

Multi-disciplinary Design Optimization (MDO) is a field of engineering design optimization that involves analyses of multiple coupled disciplines. Optimizing multiple disciplines simultaneously, as done in MDO, can reduce the design time significantly as opposed to optimizing the disciplines sequentially. The optimization time involved in an MDO problem is not only driven by the complexity of disciplinary analysis modules, but also the nature of coupling among them. A fundamental method of solving such problems involves carrying out Multi-disciplinary Analysis (MDA) in every step of the optimization process. This procedure is known as Multi-disciplinary Feasible (MDF) MDO architecture. From the architecture used in a problem, one can get the information about the optimization process, coupling of disciplines and disciplinary analysis methodology. Hence, solving the same problem through different architectures conserves the problem characteristics, but the solution algorithm is different. Two categories of these algorithms are Monolithic and Distributed. In a Monolithic approach, a single optimization problem is solved, whereas in a Distributed approach, the same problem is partitioned into multiple sub-problems of optimization containing small subsets of the variables and constraints.

The optimization of multidisciplinary engineering systems was first discussed in detail by Haftka et al. [1] from the standpoint of the computational alternatives available to the designer. The formulation of the analysis process involved in such problems, solution techniques were discussed for sample optimization test problems. Cramer et al. [2] discussed various concepts of MDO, monolithic architectures like Multidisciplinary Feasible (MDF), All-in-Once (AiO) and Individual Disciplinary Feasible (IDF), MDA process followed by importance of feasibility of disciplinary analysis and derivative requirements of MDO. Kodiyalam [3] compared results by MDF, IDF, AiO and Collaborative Optimization (CO) on various test problems in MDO. Kodiyalam and Yuan [4] discussed the implementation of Bi-Level Integrated System Synthesis (BLISS) and its variants on industrial MDO problems.

Braun et al. [5] have compared CO with other architectures, examined the details of the formulation and commented on some aspects of their performance. Alexandrov and Lewis [6] discussed criteria by which one can classify, analyze, and evaluate approaches to solving MDO problems. Besides proposing a solution methodology for the problem formulation, they also made some general remarks for comparison of MDO architectures.

Martins and Lambe [7] provided a detailed review of both Monolithic and Distributed architectures that have been developed to date. Their study involved systematic classification of the MDO architectures based on their problem formulations and solution algorithms. Along with the decomposition of problems, an Extended Design Structure Matrix (XDSM) diagram is also provided. Finally, the issues related to benchmarking MDO algorithms are reported. Application of distributed MDO architectures to Multi-level structural optimization problems was discussed by de Wit and van Keulen [8]. The multi-level problems are formed by decomposing the optimization problems into separate levels of the system. The subcomponents are identical to disciplines in MDO problems. Therefore, a vast range of multilevel structural optimization problems present an opportunity to test MDO architectures in detail. Multilevel structural optimization problems are scalable which help in benchmarking of the architectures.

Sobieski et al. [9] have shown how in a two-level approach, the optimization problem can be decomposed into a single problem at the assembled structure level (system level) and multiple subproblems (subsystem level), one for each finite element, at the lower level. Sobeiski et al. [10] have also developed and analysed the strategy for three-level decomposition. It was demonstrated using a structure of beams for which the top level is analysis of the assembled structure, intermediate level of individual beams as a box which is deposed as stiffened plates

in the bottom level. The scheme for multilevel structuring is shown in Figure 1, where the case of two-level problem corresponds to the upper two levels of the Figure, and further substructures of the second level define the physical meaning of individual elements.
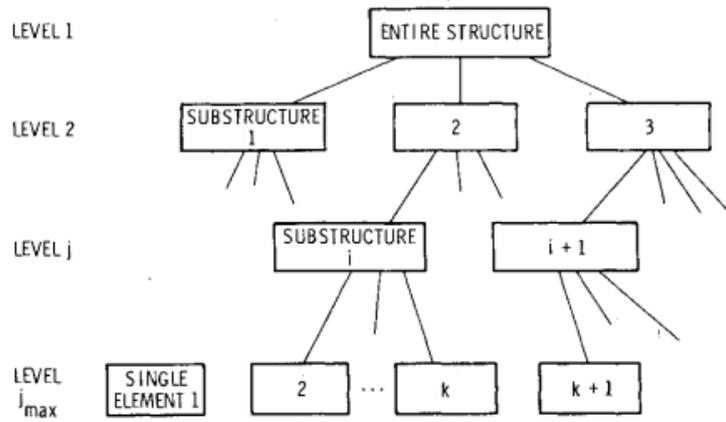
Figure 1. Multilevel Decomposition of Problem. [9]

An and Huang [11] have presented a two-level multipoint approximation strategy for mixed-variable problems using Genetic Algorithms. For calculation of fitness function, a second-level approximation is provided with the cross sections of structural members. The performance of this methodology is demonstrated for integrated topology and frame structure optimization.

The layout of this paper is as follows. Section 2 describes the test problems used for the study. Section 3 provide details of some MDO architectures, and shows how two test problems can be formulated in them. The implementation of test problems is carried out in *OpenMDAO*, an open-source MDO library [12]. Results of the implementation in *OpenMDAO* are discussed in Section 4.

2. TEST PROBLEMS

This section outlines MDF formulation of test problems chosen for the study. It includes Sellar's problem and Two-bar truss problem. The notations used for optimization, and the optimal solutions are also listed.

2.1 The Sellar's Problem [13]

Sellar et al. [13] have proposed a two-discipline analytical problem of constrained optimization, commonly referred as Seller's problem. Outputs of the disciplines are fed into each other, which form a system of coupled model that need to be solved using nonlinear solvers.

Problem Formulation:

$$\text{min. } f = x_1{}^2 + z_1 + y_1 + e^{-y_2}$$
$$\text{w.r.t} \quad x_1, z_1, z_2$$
$$\text{s.t.} \quad 3.16 - y_1 \le 0$$
$$y_2 - 24.0 \le 0$$

(1)

Disciplinary Governing Equations:

$$\text{Discipline \#1: } y_1 = z_1{}^2 + z_2 + x_1 - 0.2y_2$$
$$\text{Discipline \#2: } y_2 = \sqrt{y_1} + z_1 + z_2$$

$$\text{Design Variables: } x_1: 0 \leq x_1 \leq 10,$$
$$z_1: 0 \leq z_1 \leq 10$$
$$z_2: 0 \leq z_2 \leq 10$$

(2)

Solution:

$$x^*_1 = 0.0, z^* = 1.9776, 0$$
$$f^* = 3.18339$$

where x_1: Local design variable of discipline 1
$z = [z_1, z_2]$: Global design variable
$y = [y_1, y_2]$: Disciplinary response variables

2.2 Two-Bar Truss

Kirsch [14] has proposed a two-bar truss problem, in which the objective is to minimize the total volume of the truss, subjected to a single vertical load of 100 KN at node 1, as shown in Fig 2.
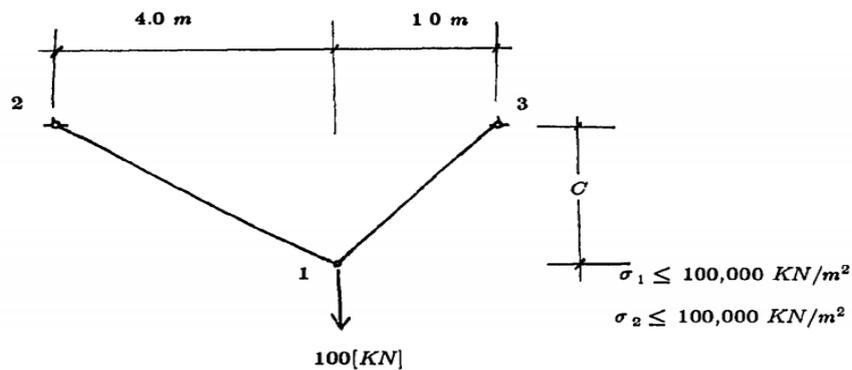
Figure 2. Two Bar Truss Problem [14].

The design variables are the cross-sectional areas of bars D1, D2, and C, i.e., the vertical coordinate of node 1. Stress constraints are imposed on the stress developed in each of the truss members, which need to have a positive value of cross-sectional areas. In addition, geometrical constraints are imposed on the magnitude of C, which is constrained to take any values within a specified range.

Problem Formulation:

$$\text{min. } f = f_1 + f_2$$
$$\text{w.r.t. } C$$
$$\text{s.t. } 1.0 \leq C \leq 3.0$$
$$D_1, D_2 \geq 0.0$$

(3)

Disciplinary Analysis

Discipline #1: $f_1 = min \, D_1\sqrt{16 + C^2}$
 w.r.t. D_1
s.t. $20\sqrt{16 + C^2} \, / \, CD_1 \leq 100,000$ (Stress in Element 1)
Discipline #2: $f_2 = min \, D_2\sqrt{1 + C^2}$

$$\text{w.r.t} \quad D_2$$
$$\text{s.t.} \quad 80\sqrt{1 + C^2} \,/\, CD_2 \leq 100{,}000 \quad \text{(Stress in Element 2)}$$

$$(4)$$

$$\text{Solution } C^* = 2.0 \ m, D_1 = 4.48e - 4 \ m^2, D_2 = 8.96e - 4 \ m^2$$
$$f^* = 4.0e - 3 \ m^3$$

3. MDO ARCHITECTURES

OpenMDAO is an open-source project by NASA developed in the Python language. It is developed with support for modular problem structure, multi-disciplinary analysis capabilities, parallel computations of the disciplinary analysis and gradient-based solution strategy based on Unified Derivatives architecture. The *Problem Class* in *OpenMDAO* holds various components of the optimization setup together, as shown in Fig 3 [12].
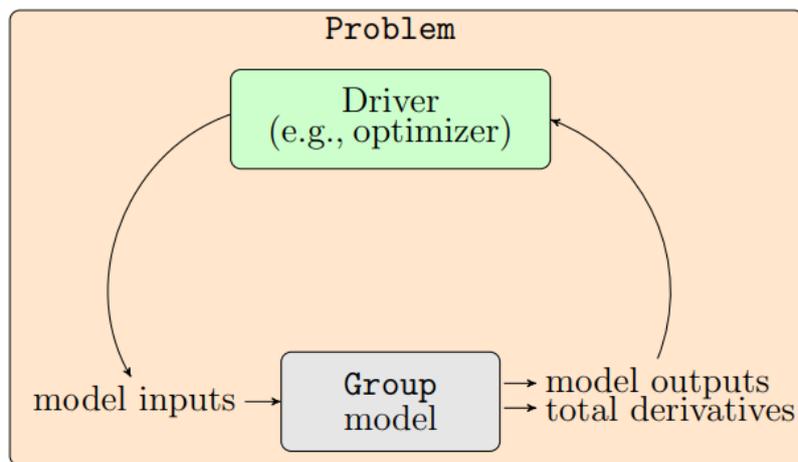
Figure 3. *Problem Class* in *OpenMDAO* [12].

The model of a problem is an instance of *Group Class* in which various disciplinary modules are imported and solved using MDA. Finally, the driver carries out the optimization of the model. It supports analytical, finite-differences and complex step methods for derivative calculation both at the discipline level and also at model level. [12]

In this section, we discuss the distributed MDO architectures and formulations for test problems described in Section 2. These architectures are implemented as per the algorithms described by Martins and Lambe [7] and Kirsch [14]. As an illustration, Collaborative Optimization (CO), Enhanced Collaborative Optimization (ECO) and MDO of Independent Systems (MDOIS) were chosen.

3.1 Collaborative Optimization (CO)

Collaborative Optimization is a distributed version of IDF architecture. It consists of a system level optimization problem that solves the design objective, and discipline level optimization problems that solve system consistency. The system level constraints include a global constraint vector, a single consistency constraint (also called system feasibility) for the l^2- norm (denoted by J) of difference in design variables and discipline's response variables with their respective

Shantanu Gulawani, K M Kiran Babu and Rajkumar S Pant

targets (targets denoted by "^"). At the discipline-level, the objective is to satisfy the discipline-level system feasibility. The formulation of Sellar's problem in CO is given below.

System Level:
$$min\ f = \hat{x}_1{}^2 + z_1 + \hat{y}_1 + e^{-\hat{y}_2}$$
$$w.r.t\ z = [z_1, z_2], x_1, \hat{x}_1, \hat{y} = [\ \hat{y}_1, \hat{y}_2]$$
$$s.t.J^* = \left|\left|z - \hat{z}_1\right|\right|^2 + ||z - \hat{z}_2||^2 + ||y_1 - \hat{y}_1||^2 + ||y_2 - \hat{y}_2||^2 + ||x_1 - \hat{x}_1||^2 = 0$$
$$(5)$$

Subproblem 1:
$$min\ J_1(\hat{z}, x_1, y_1)$$
$$w.r.t\ \hat{z} = [\ \hat{z}_1, \hat{z}_2], x_1$$
$$s.t.\ 3.16 - y_1 \leq 0$$
$$(6)$$

Subproblem 2:
$$min\ J_2(\hat{z}, y_2)$$
$$w.r.t\ \hat{z} = [\ \hat{z}_1, \hat{z}_2]$$
$$s.t.\ y_2 - 24 \leq 0$$
$$(7)$$

The disciplinary analysis for both Discipline 1 and 2 is the same as in original formulation except that it is done with copies of coupling variables, global design variables and local design variables.

The formulation of Two bar truss in CO is as follows:

System Level:
$$min\ f = \hat{f}_1 + \hat{f}_2$$
$$w.r.t\ C, D_1, D_2, \hat{D}_1, \hat{D}_2$$
$$s.t.J^* = ||C - \hat{C}_1||^2 + ||C - \hat{C}_2||^2 + ||D - \hat{D}_1||^2 + ||D - \hat{D}_2||^2 = 0$$
$$(8)$$

Subproblem 1:
$$min\ J_1(\hat{C}, D_1)$$
$$w.r.t\ \hat{C}, D_1$$
$$(9)$$

Subproblem 2:
$$min\ J_2(\hat{C}, D_2)$$
$$w.r.t\ \hat{C}, D_2$$
$$(10)$$

As in the Sellar's Problem formulation, D_1, D_2 are computed from disciplinary analysis explained in Section 2.

3.2 Enhanced Collaborative Optimization (ECO)

In Enhanced Collaborative Optimization (ECO), the system feasibility becomes the system level objective function and the global objective function are minimized at the disciplinary level through copies of coupling variables and global design variables. In addition to the objective of

discipline's subproblem, a penalty as a function of system feasibility and for nonlocal design constraints are added, in contrast to CO.

The two-bar truss problem described in Section 2 can be is posed in ECO as follows:

System Level:
$$min\ J^* = ||C - \hat{C}_1||^2 + ||C - \hat{C}_2||^2 + ||D - \widehat{D}_1||^2 + ||D - \widehat{D}_2||^2$$
$$w.r.t\ C, \widehat{D}_1, \widehat{D}_2 \tag{11}$$

Subproblem 1:
$$min\ w_{c1} \cdot J_1(\hat{C}, D_1)$$
$$w.r.t\ \hat{C}, D_1 \tag{12}$$

Subproblem 2:
$$min\ w_{c2} \cdot J_2(\hat{C}, D_2)$$
$$w.r.t\ \hat{C}, D_2 \tag{13}$$

3.3 Multi-Disciplinary Optimization of Independent System (MDOIS)

The MDO of independent system architecture is applicable for problems with no global objective function and only disciplinary design variables. To implement it, the two-bar truss problem was selected with global design variable $C = 2.0\ m$. Hence, the discipline's subproblems are separable with the coupling variables, as follows:

Subproblem 1:
$$min\ f_1 = D_1\sqrt{16 + C^2}$$
$$\text{w.r.t}\quad D_1$$
$$\text{s.t.}\quad 20\sqrt{16 + C^2}\ /\ CD_1 \leq 100,000$$
$$\tag{14}$$

Subproblem 2:
$$min\ f_2 = min\ D_2\sqrt{1 + C^2}$$
$$\text{w.r.t}\quad D_2$$
$$\text{s.t.}\quad 80\sqrt{1 + C^2}\ /\ CD_2 \leq 100,000$$
$$\tag{15}$$

4. RESULTS AND DISCUSSION

The test problems were implemented in the *OpenMDAO* framework V3.8, and this section reports convergence history of the objective function and design variables.

4.1. Monolithic Formulations of Sellar's Problem

This problem was solved using MDF, IDF, SAND monolithic architectures and CO and ECO distributed architectures. The convergence history is shown in Figure 4. The MDA solver used was Newton's solver and the optimizer was SciPy's SLSQP, a sequential least squares programming algorithm which uses the Han–Powell quasi–Newton method. The partial and total derivatives were calculated using default finite differences.

Shantanu Gulawani, K M Kiran Babu and Rajkumar S Pant
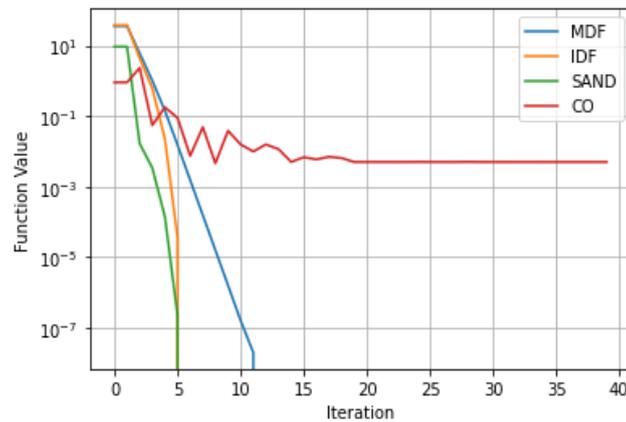
Figure 4. Convergence of Sellar's Problem

The implementation of monolithic architecture was done following the formulation described by Martins and Lambe [7]. The results showed satisfactory convergence. For CO, the consistency constraint was modeled as an inequality constraint with an upper limit of 0.0005. The values of design variable, objective function and coupling variables are listed in Table 1 for different architectures.

Table 1: Results of Sellar's Problem

Architecture	x	z	y	f
MDF	~0	1.977638, 0	3.16, 3.75527	3.18339
IDF	~0	1.977638, 0	3.16, 3.75527	3.18339
SAND	~0	1.977638, 0	3.16, 3.75527	3.18339
CO	1.32 e-10	1.977757, 0	3.16, 3.75431	3.17842

4.2. Multi-level MDO Formulations of Two-bar Truss Problem

The results of distributed architectures are shown in Figure 5.
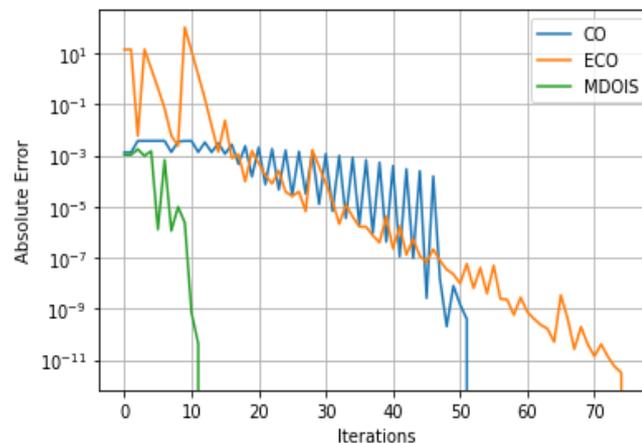
Figure 5. Convergence of Two-bar Truss Problem.

The uniqueness of this problem was the nested use of the optimization problem class for the disciplinary level. This modular capability also made it possible to implement CO and ECO. MDOIS was implemented keeping global design variables equal to optimum value. The oscillations in the convergence are likely because of nested optimization formulation of the problem. The reason being that similar oscillations were not observed in case of CO on Sellar's problem. A similar trend is found in variation of local design variables as depicted in Figure 6.
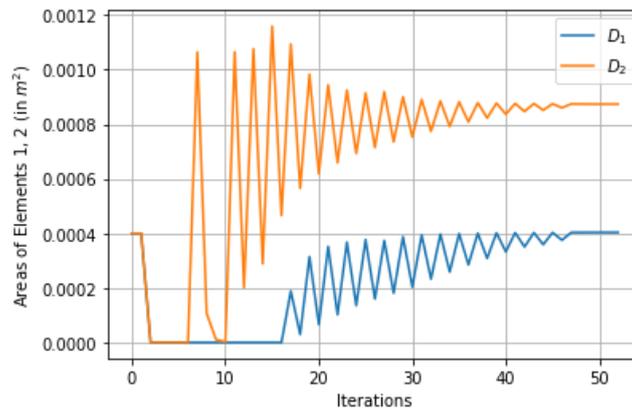
Figure 6. Areas of Elements 1 & 2 (CO architecture).

The variation of global design variable is shown in Figure 7, which is not oscillatory, as expected.
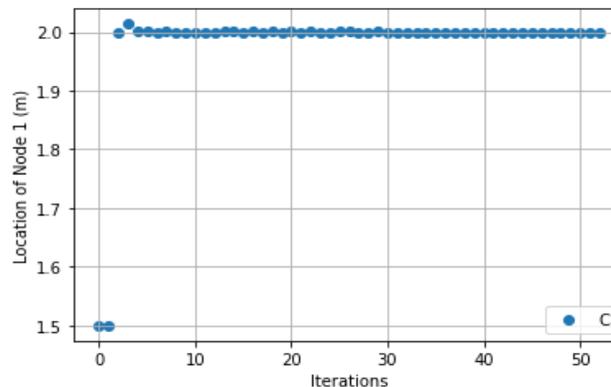
Figure 7. Distance of node C (CO architecture).

5. CONCLUSIONS

This study reports the implementation of a set of distributed architectures, namely CO, ECO and MDOIS, which were analysed on two differentiable, non-discrete, single objective optimization problems taken from literature. The first, viz., the Sellar's problem, was implemented in CO and monolithic architectures. The second, viz., the two-bar truss problem, was analysed in CO, ECO and MDOIS architectures. The MDOIS formulation of the problem required elimination of global design variables to be set to optimal value. The truss problem was modeled as a multi-level structural optimization problem. This class of problems forms an excellent test cases for MDO problems as those are characterized by complex inter-disciplinary coupling yet analytical expressions for analysis. Besides, they also provide scalability for benchmarking studies. All the MDO architectures which were investigated converged, however it was observed that the convergence of CO was susceptible to the tolerance used.

ACKNOWLEDGMENTS

REFERENCES

1. R. T. Haftka, J. Sobieszczanski-Sobieski and S. L. Padula. On options for interdisciplinary analysis and design optimization. *Structural optimization*, 4(2), 65-74, 1992. doi:10.1007/BF01759919

2. E. J. Cramer, Jr. J. E. Dennis, P. D. Frank, R. M. Lewis and G. R. Shubin. Problem formulation for multidisciplinary optimization. *SIAM Journal on Optimization*, 4(4), 754-776, 1994. doi:10.1137/0804044

3. S. Kodiyalam. Evaluation of methods for multidisciplinary design optimization (MDO), Phase I. National Aeronautics and Space Administration, Langley Research Center, 1998.

4. S. Kodiyalam and C. Yuan. Evaluation of methods for multidisciplinary design optimization (MDO), Phase II. National Aeronautics and Space Administration, Langley Research Center, 2000.

5. R. Braun, P. Gage, I. Kross and I. Sobieski. Implementation and performance issues in collaborative optimization. *In 6th symposium on multidisciplinary analysis and optimization,* p. no. 4017, 1996. doi:10.2514/6.1996-4017

6. N. M. Alexandrov, and R. M. Lewis. Comparative properties of collaborative optimization and other approaches to MDO. *ICASE Report* No. 99-24, NASA 1996.

7. J. R. R. A. Martins and A. B. Lambe. Multidisciplinary design optimization: A survey of architectures. *AIAA Journal*, 51(9):2049-2075, 2013. doi:10.2514/1.J051895.

8. A. de Wit, and F. van Keulen. Numerical comparison of multi-level optimization techniques. *In 48th AIAA/ASME/ASCE/AHS/ASC Structures, Structural Dynamics, and Materials Conference* p. no. 1895, 2012. doi:10.2514/6.2007-1895

9. J. Sobieszczanski-Sobieski, B. J. Benjamin and R. D. Augustine. Structural optimization by multilevel decomposition. *AIAA Journal*, 23(11), 1775-1782, 1985. doi: 10.2514/3.9165

10. J. Sobieszczanski-Sobieski, B. B. James and M. F. Riley. Structural sizing by generalized, multilevel optimization. *AIAA Journal*, 25(1), 139-145, 1987.

11. H. An and H. Huang. Topology and sizing optimization for frame structures with a two-level approximation method. *AIAA Journal*, 55(3), 1044-1057, 2017. doi:10.2514/1.J055020

12. J. S. Gray, J. T. Hwang, J. R. R. A. Martins, K. T. Moore and B. A. Naylor. OpenMDAO: An open-source framework for multidisciplinary design, analysis, and optimization. *Structural and Multidisciplinary Optimization*, 59(4), 1075-1104, 2019. doi:10.1007/s00158-019-02211-z

13. R. S. Sellar, S. M. Batill and J. E. Renaud, Response Surface Based, Concurrent Subspace Optimization for Multidisciplinary System Design. *Proceedings References 79 of the 34th AIAA Aerospace Sciences Meeting and Exhibit, Reno, NV*. 1996.

14. U. Kirsch. Multilevel approach to optimum structural design. *Journal of the Structural Division*, 101(4), 957-974, 1975. doi:10.1061/JSDEAG.0004043

WING AEROSTRUCTURAL OPTIMIZATION WITH ACTIVE FLOW CONTROL AND ACTIVE LOAD ALLEVIATION

Valerio Mosca[1*], Ali Elham[2]

1: Cluster of Excellence SE[2]A – Sustainable and Energy-Efficient Aviation
Institute of Aircraft Design and Lightweight Structures
Technische Universität Braunschweig
Braunschweig, Germany, 38108
v.mosca@tu-braunschweig.de, https://www.tu-braunschweig.de/ifl/cad

2: Cluster of Excellence SE[2]A – Sustainable and Energy-Efficient Aviation
Institute of Aircraft Design and Lightweight Structures
Technische Universität Braunschweig
Braunschweig, Germany, 38108
a.elham@tu-braunschweig.de, https://www.tu-braunschweig.de/ifl/cad

Abstract. *A medium-fidelity but physics-based analysis is performed to investigate advantages of novel technologies on the energy efficiency of a mid-range passenger aircraft. The framework intends to obtain accurate results, while keeping the computational cost lower than high-fidelity analysis and optimization. For this purpose, the coupled-adjoint aerostructural analysis and optimization tool FEMWET is modified to consider the effect of active flow control and active load alleviation on the outcome of a wing aerostructural optimization and consequently, on the overall aircraft fuel efficiency. Different test cases were studied, varying the maximum load factors reachable during flight and portion of laminar flow on the wing. Both technologies are found to be beneficial for fuel weight reduction. Best results are obtained considering the use of load alleviation, hence for n_{max} 2 and 1.5 and for a wing with 80% laminar flow. The reduction is about 8.3% of the fuel weight while the wing drag may be reduced up to 22.5%.*

Keywords: Sustainable aviation, novel technologies, aircraft design, medium-fidelity analysis, aerostructural optimization

V. Mosca, A. Elham

1   INTRODUCTION

During the last century, Europe has been facing different challenges such as globalization, various financial crises, climate change, and an increasing scarcity of resources. Governments started being worried about the necessity of innovation and of a common strategy to keep Europe's competitiveness in a long-term vision. The growing demand for the movement of goods and people, foreseen for the future, needs to be seen as a new opportunity for job positions but as a challenge for environmental impact. Flightpath 2050 [1] sets promising but challenging goals for the new aircraft generation, like reducing 75% and 90% of CO2 and NOx emission, respectively, and a 65% noise reduction. The Cluster of Excellence SE^{2}A (Sustainable and Energy Efficient Aviation) [2] is an interdisciplinary research center developed in Germany to pursue the above-mentioned objectives by investigating the technologies required for a sustainable and eco-friendly air transport system. Scientists from different universities and research centers are working on reducing emissions and noise, as well as life-cycle concepts for structures and potential improvements in air traffic management. In particular, the following technologies are considered to fulfill the SE^{2}A goals: hybrid laminar flow control, load alleviation, boundary layer ingestion, advanced structures, and ultra-high bypass ratio turbofan engines. To investigate the potentials of the novel technologies understudy in the SE^{2}A project, a series of reference aircraft equipped with those technologies is designed. A multi-layer framework is considered for aircraft conceptual design and multidisciplinary optimization. The first layer is mainly represented by aircraft conceptual design at low fidelity level but useful to obtain general outputs like aircraft geometry, weight breakdown, and energy consumption. A second layer is used as a link between more advanced analysis and low fidelity data using a surrogate modeling toolbox. The last two layers are characterized by medium and high-level analysis and optimization respectively. In particular, high fidelity analysis is applied when the main configuration parameters are known, and the effect of advanced technologies on selected dominant aircraft components is the subject of the investigation with a high level of accuracy. High fidelity analysis can be applied for aircraft lifting surfaces and structure design through the use of Computational Fluid Dynamics (CFD) and Finite Element Analysis (FEA) products. However, this approach implies high computational power and cost. For these reasons, the use of medium-fidelity but physics-based analysis methods represents a promising approach between a low-fidelity design with low computational power and the most advanced analysis, which cost may not be affordable. One of the reference aircraft considered in the SE^{2}A project is a mid-range passenger aircraft that complies with CS-25 regulations. The top-level requirements are set similar to the Airbus A320 aircraft. The aircraft initial sizing has been performed using an in-house tool PyInit. The software SUAVE [3] is then used for the mission analysis in an iterative process computing the new configuration and constraint diagram. The cycle is stopped once the tolerance on the maximum take-off mass is reached. Finally, performance parameters are obtained. The details of the initial sizing and conceptual design of this aircraft are presented in [4]. This research aims to present the next step in the design of this aircraft, where a medium-fidelity but physics-based analysis and optimization framework for wing aerostructural optimization is developed and applied to investigate the advantages of the mentioned novel technologies on aircraft energy efficiency.

2   SE²A MID-RANGE AIRCRAFT

Inside the Cluster of Excellence, a mid-range aircraft with novel technologies for future aviation has been designed [4]. Top level requirements were selected similar to the reference A320 and are summarized in Tab.1.

Table 1: SE²A Mid-range aircraft Top-level Requirements

Parameter	Value	Units
Design range for maximum payload	3981	km
Maximum number of passengers	186	
Maximum payload weight	19625	kg
Cruise Mach number	0.78	
Climb rate at Top-of-Climb	3.00	m/s
Sustained turn angle at the cruise altitude	15	deg
Range with maximum payload	3982	km
Take-off field length	2000	m
Landing field length	1530	m
Certification	CS-25	

The aircraft is equipped with Boundary Layer Suction (BLS), passive and active load alleviation as well as novel materials and structures. Load alleviation is used to achieve a more favorable wing load distribution and hence reduce the wing bending moment. The BLS technology is the key element for the laminarization of the wing flow, acting to delay transition at different chord position according to the scenario studied. Empennage only features NLF if the wing sweep permits, while the fuselage is laminar until the wing-fuselage junction completely using BLS. High bypass ratio turbofan engines with Boundary Layer Ingestion (BLI) were also considered. Two engines are located above the wing for noise reduction and one engine is located at the fuselage to maximize BLI benefits. Two configurations were considered: the forward- and backward-swept aircraft (Fig.1). Both wing configurations have constraints of the leading edge sweep of 17 degrees. DLR F15 airfoils were selected for the initial design. The wing thickness distribution was selected similar to the A320 to avoid potential early design issues related to low thickness and insufficient space for the landing gear. The initial designs also used single-slotted Fowler flaps and no leading-edge devices to enable natural laminar flow capabilities. The designed aircraft is then refined with an optimization process to reduce fuel weight (W_f). The current research is based on the backward swept configuration, the forward one will be analyzed in future with new developments of the FEMWET tool. The reference geometric data are shown in Tab.2.

3   AEROSTRUCTURAL ANALYSIS

The aerostructural analysis is performed by the coupled-adjoint aerostructural analysis and optimization tool FEMWET [5]. FEMWET consists of a quasi-three-dimensional aerodynamic analysis and a finite beam element structural solver, coupled together using the Newton method. The tool is modified to consider the effect of active flow control and active load alleviation on the outcome of a wing aerostructural optimization and consequently, on the overall aircraft fuel efficiency.

V. Mosca, A. Elham
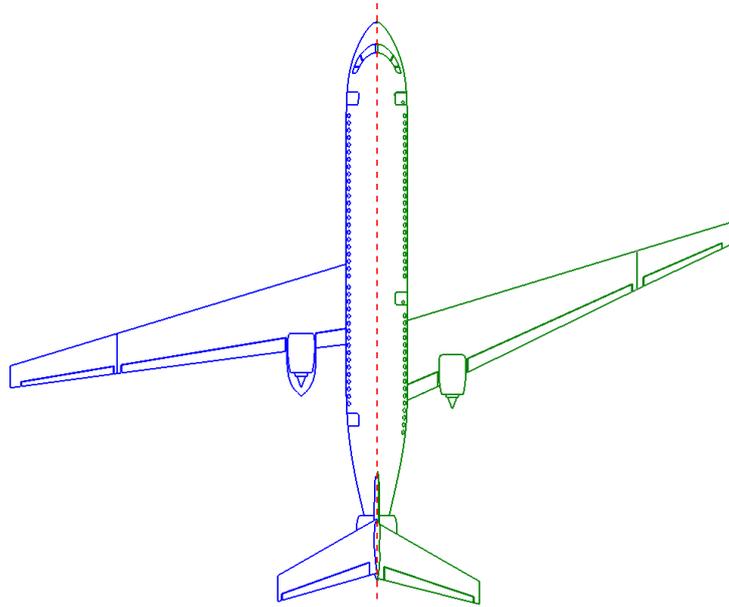
Figure 1: Configuration layouts for the mid-range aircraft [4].

Table 2: SE^{2}A Mid-range aircraft reference data

Parameter	Value	Units
Span	50.9	m
Choord root	5.7	m
Taper ratio	0.27	
Cruise Mach number	0.78	
Kink position (respect to span)	25%	
Dihedral angle	4	deg
Sweep angle (leading edge)	17	deg
Twist angle (root)	0	deg
Twist angle (tip)	0	deg
Airfoil	DLR F15	
Root thickness	12%	
Tip thickness	10%	

3.1 Structural module

The FEMWET tool represents the core of the structural analysis [5]. From a structural point of view, the elastic wing is modeled as a finite beam placed at its elastic axis. The use of a beam model is preferred with respect to a shell one because the possible increment of accuracy, estimated in literature as about 5%, does not compensate for the consequent increase of computational power [6]. The finite beam is characterized by the generation of nodes placed at the shear centers of each section. Besides, these nodes are determined by the structural properties of the wing box sections. The thicknesses of the wing box equivalent panels represent the input of the tool. The element stiffness, mass, and force matrices are computed and built thanks to the consistent shape functions for a 3D Timoshenko beam. The structural governing equation (1) is solved to obtain the displacement vector U.

V. Mosca, A. Elham

$$KU = F \qquad (1)$$

In fact, the force vector F is known and the stiffness matrix K can be constructed once the wing box properties such as EA, EI, GJ, are computed at each node, considering the geometry, material and structural properties of the *real wing box* (more detail in [7]). Once U is determined, the stress distribution in the wingbox structure can be calculated. These stresses are used to determine the failure criteria due to material yield and to structural buckling. In detail, the stiffened panel efficiency method [8] is used for the stiffened panels such as the upper and lower equivalent panels. The shear buckling load failure is applied for the spars webs. The wing total weight computation is based on the equation from Kennedy and Martins [9], in which the weight is characterized by two terms (Eq. 2): the optimum wingbox weight from finite element analysis with a correction factor to take into account for weights not modeled in FEM, the secondary weight representing weights for leading edge, trailing edge, flaps, slats etc.

$$W_{wing} = 1.5 W_{wingbox}^{FE} + 15 S_{wing} \qquad (2)$$

Due to the use of novel materials and structures, the 80% of the previous wing weight estimation is considered during the optimization of the Mid-range aircraft analyzed in this paper.

3.2   Aerodynamic module

The aerodynamic analysis is based on the Quasi-Three-Dimensional (Q3D) [10] aerodynamic solver, with some modifications to connect the structural with the aerodynamic module inside the optimization framework. The lift distribution on the wing is computed using a Vortex Lattice Method (VLM), based on the methodology developed by Katz and Plotkin [11] and the strip theory [12] to calculate viscous drag at different spanwise positions. The VLM is used to calculate the wing lift distribution, the wing lift coefficient C_L, and the wing induced drag coefficient C_{Di}. C_{Di} is calculated using Trefftz plane analysis [13]. In particular, from the wing geoemetry and the angle of attack, the Aerodynamic Influence Coefficients (AIC) matrix and the Right Hand Side (RHS) vector are computed. Considering the governing equation:

$$AIC\ \Gamma = RHS \qquad (3)$$

The strengths of the vortex rings (Γ) can be calculated and consequently the wing lift distribution by the Kutta-Joukowski theorem. At high Mach numbers the Prandtl-Glauert compressibility correction is used. The lift coefficient is interpolated to find C_L at a given spanwise section. Sweep theory is applied to obtain C_L, Mach number and velocity, normal to the sweep line. Considering that pressure drag acts perpendicularly to the shock wave line, a sweep line coinciding with the shock wave [14, 15], for transonic regime analysis, is chosen. Hence, a half-chord sweep angle is used. The effective velocity and Reynolds are then evaluated and become the input of MSES to compute the effective angle of attack and effective drag parameters. MSES is an interactive viscous/inviscid Euler method, the software aids in the analysis and design for single and multi-element airfoils at low Reynolds numbers and transonic Mach numbers. In addition, it can predict local flow features such as boundary layer separation and transition, investigate effects of geometry

changes [16]. In this research, the Chebychev polynomials are used to parameterize the airfoil geometry. MSES is able to compute the derivatives of the output like lift or drag, respect to the input, such as angle of attack, Mach number and Reynolds number. This characteristic is very useful for the computation of the wing drag respect to the wing geometry. Finally, the profile drag coefficient is obtained in the streamwise direction. The wing total profile drag (Eq.(4)) is calculated by integrating the parasite drag coefficient of the 2D sections over the span, and from its sum with the induced drag, wing total drag is obtained (Eq.(5)).

$$C_{D_{\text{parasite}}} = \frac{2}{S_w} \int_0^{b/2} C_{d_{\text{parasite}}} c \, dy \tag{4}$$

$$C_D = C_{D_{\text{parasite}}} + C_{D_{\text{i}}} \tag{5}$$

Three general sources of instabilities may occur on the wing during flight: 1) Tollmien – Schlichting Instabilities (TSI), 2) Cross-flow Instabilities (CSI), and 3) Attachment line Instabilities (ALI). Flow transitions from laminar to turbulent flow due to the amplification of these instabilities. Boundary layer suction is an approach towards dampening the growth of these instabilities, in particular the transition to turbulent flow is delayed by removing a small portion of the boundary layer near the wall. One way to simulate the boundary layer suction, is to modify the boundary layer equations in MSES similar to the work of [17]. However, due to our limited license of MSES, which does not allow us applying modification to the source code, we used a simplified approach to consider the effect of boundary layer suction on the wing drag. In this approach, the aerodynamic model explained has been modified to take into account drag penalties for different drag components. In fact, MSES runs with transition of the upper and lower airfoil surface fixed at 3% of the chord to simulate full turbulent flow over the airfoil. Then, a series of coefficients is applied to different drag components calculated using the full turbulent case to simulate drag reduction by active flow control. Hence, the drag computation obtained by Q3D is based on the penalty model, as the calculation of derivatives necessary for the gradient based optimization. In particular, four different penalties are studied: friction drag, wave drag, form drag (pressure with no wave drag) and finally induced drag. Hence, Eq.5 is modified to consider the respective penalty coefficients:

$$C_D = K_f C_{D_{\text{f}}} + K_{p-w} C_{D_{\text{p-w}}} + K_w C_{D_{\text{w}}} + K_i C_{D_{\text{i}}} \tag{6}$$

A campaign of simulation using MSES has been performed to identify proper values for the correction factors in Eq. 6. Different supercritical airfoil such as DLR F15 and RAE2822 have been analysed for an average Cl of 0.4 at different Mach and Reynolds number for a range of (forced) boundary layer transition. Figure 2 represents an example of the analysis performed, in which the DLR F15 at Cl=0.4 with a Mach number 0.8 with Reynolds number changing from 10 M to 30 M. Two components are calculated fixing the transition at different chord position: friction drag and pressure drag without the portion of wave drag. A linear model is then implemented to predict drag values of the airfoil experiencing the desired portion of laminar flow. The model can be considered as a low-fidelity approximation, but it gives anyhow a good understanding of the benefits in the use of novel technologies for future aircraft design. In particular, conservative values are selected, in this way the aerostructural adjoint optimization results in promising

outputs. Penalties used for this research are shown in Fig.3. The K_{p-w} parameter has been introduced to give the possibility to apply corrections to drag estimation without influencing the wave drag. In fact, this extra drag component is generated due to the compressibility effect typical of transonic regime flights and so it should not be involved in the simulation of boundary layer suction. At the present moment, research activities with higher fidelity aerodynamic models are done inside the SE^{2}A Cluster to fully understand the interaction between all the components of drag for active flow control application. It can been noticed that the same value of K_{p-w} is established for the two scenarios of 80% and 70% of laminar flow and so the drag prediction of BLS acts on the friction component only. In fact, a small difference is expected and the current design choice avoids quite optimistic results. No penalties are applied for wave and induced drag.
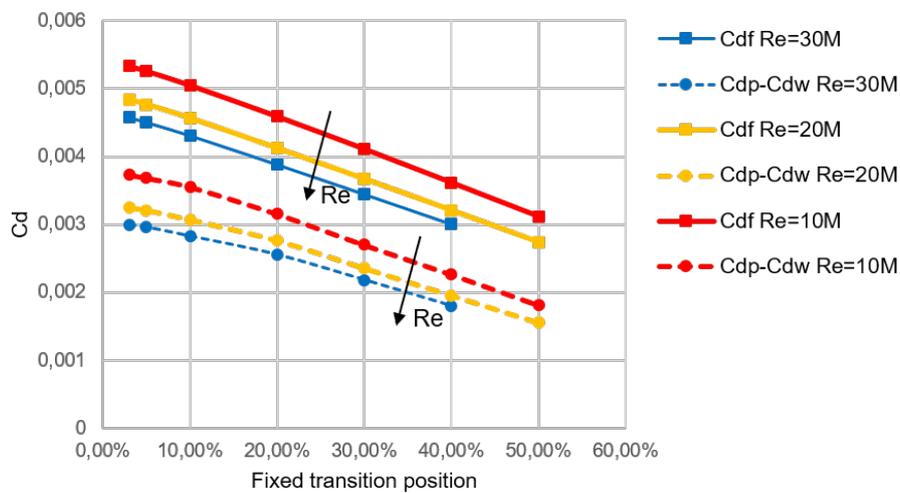
Figure 2: DLR F15 simulations for Cl=0.4 and M=0.8.

	80% laminar flow	70% laminar flow	60% laminar flow
K_f	33,00%	40,00%	50,00%
K_p-w	20,00%	20,00%	33,00%
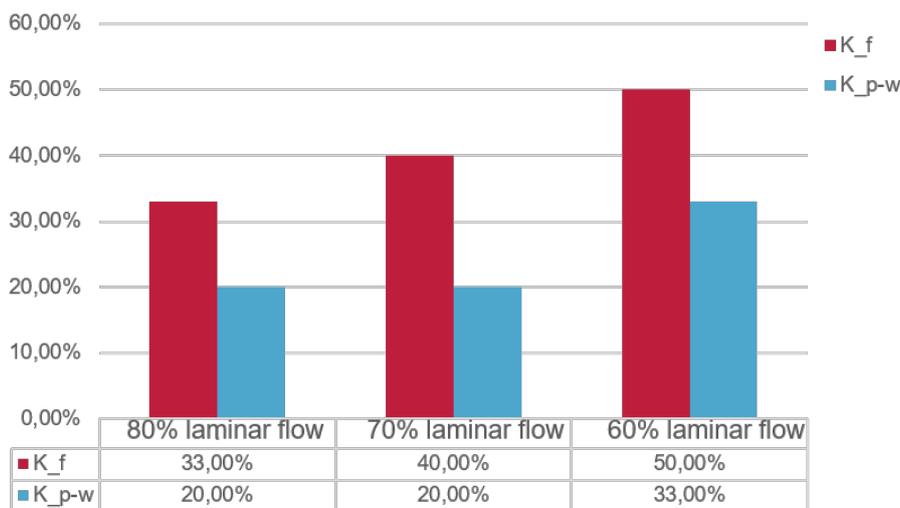
Figure 3: Drag penalties for different laminar flow conditions.

Drag estimation for a mid-range aircraft for different laminar flow conditions have been studied by Beck et al. [18]. Data obtained for the DLR F15 airfoil, at Cl=0.5, M=0.7 and

Re=30M are compared with the estimation of drag reduction coming from the penalty drag model implemented in this research. Results showed in Beck's work represent the profile drag reduction through BLS at different position of the end of suction. Figure 4 shows the comparison of drag reduction between the two models, the reader should notice that data presented in [18] are referred to different portion of end suction, then an estimation of transition position is applied. According to Beck et al. the end of suction located at 80% of the choord delays transition at 85%, hence, at least a conservative extra 5% should be considered at the end of suction location to predict transition. In some cases, transition can be delayed for values close to 10%. The drag penalty model is characterized by similar values but keeping a conservative attitude with lower drag estimation. The validity is well established especially considering two factors: the first related to the prediction of the transition which needs to consider an extra portion of choord length from the end of suction (unless the simulation is performed with fixed transition) bringing the two curves closer, and finally because the outputs in [18] are obtained through XFOILSUC [17, 19]. In fact, the solver represents a modified version of XFOIL [20] with the integration of a full e^N method, hence is not able to predict wave drag portion at transonic regime. At the opposite, MSES computes the wave drag contribute, even if its value for M=0.7 is limited. As a consequence, the shifting of the drag penalty model for lower profile drag reduction keeps a reliable justification with a safety margin.
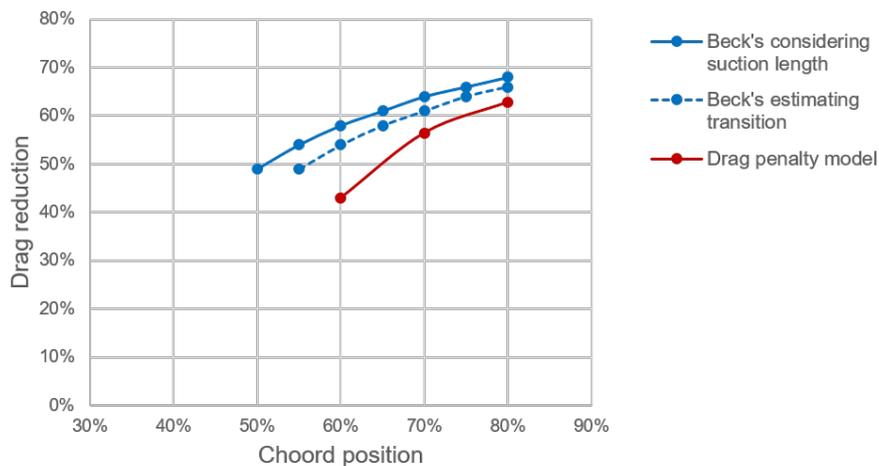
Figure 4: Drag reduction comparison with Beck's et al. for DLR F15 Cl=0.5, M=0.7, Re=30M

3.3 Aerostructural coupled system

The aerodynamic module characterized by the Q3D application is integrated with FEMWET. The wing drag is considered as negligible and hence neglected for the the computing of wing structural deformation. At the opposite, this component becomes relevant for the wing drag calculation. The aileron effectiveness, defined as the ratio of elastic to rigid roll moment of the wing due to an aileron deflection, represents a constraint for the wing aerostructural optimization.

V. Mosca, A. Elham

$$\eta_a = \frac{L_{\delta elastic}}{L_{\delta rigid}} \tag{7}$$

The aerostructural system is characterized by the following four systems of governing equations:

$$R_1(X, \Gamma, U, \alpha) = AIC(X, U)\Gamma - RHS(X, U, \alpha) = 0 \tag{8}$$

$$R_2(X, \Gamma, U) = K(X)U - F(X, \Gamma) = 0 \tag{9}$$

$$R_3(X, \Gamma) = L(X, \Gamma) - nWdes = 0 \tag{10}$$

$$R_4(X, \Gamma, U, \alpha, \alpha_i) = Cl_{2d}(X, U, \alpha, \alpha_i) - Cl_\perp(X, \Gamma) = 0 \tag{11}$$

In particular, Eq.(8) represents the governing equation of the VLM. Equation (9) is linked to the structural finite element model. The third one relates the total lift as equal to the design weight ($W_{des} = \sqrt{MTOW(MTOW - W_f)}$) considering a proper design load factor. The last equation indicates that the sectional lift calculated by the drag tool as MSES needs to be equal to the lift evaluated by the VLM. The coupled system is solved using the Newton numerical method.

3.4 Sensitivity analysis

The Newton numerical iterative method needs the computation of the partial derivatives of the governing equations with respect to the state variables. The framework presents a gradient based optimization, hence sensitivities of any function of interest are required. The tool calculates all the needed derivatives by the use of coupled-adjoint method, Automatic Differentiation (AD) and chain rule of differentiation. The total derivative of a function of interest I with respect to a design variable x is computed as:

$$\frac{dI}{dx} = \frac{\delta I}{\delta x} - \lambda_1^{\mathrm{T}}(\frac{\delta R_1}{\delta x}) - \lambda_2^{\mathrm{T}}(\frac{\delta R_2}{\delta x}) - \lambda_3^{\mathrm{T}}(\frac{\delta R_3}{\delta x}) - \lambda_4^{\mathrm{T}}(\frac{\delta R_4}{\delta x}) \tag{12}$$

where the adjoint vector is represented by:

$$\lambda = [\lambda_1 \ \lambda_2 \ \lambda_3 \ \lambda_4]^T \tag{13}$$

More deep explanations about the calculation can be found in [5].

3.5 Performance module

The fuel weight necessary for the mission is evaluated through the methodology presented by Roskam [21]. In details, the required fuel for the cruise is calculated using the Breguet equation and some statistical factors for the estimation of the fuel weight of the other segments of the flight mission. The total fuel weight fraction M_{ff} represents the consumed fuel as the ratio between the total aircraft weight at the end of the mission and at the beginning. The fuel weight (W_F) includes a 5% of the total fuel weight as reserve fuel, it is computed by Eq.(14).

$$W_F = 1.05(1 - M_{ff})MTOW \tag{14}$$

The module needs the computation of the lift over drag ratio. In particular, the drag is computed considering two terms: wing drag and drag of the rest of the aircraft. The rest

drag is kept constant because the optimization involves the wing only. Hence, the cruise drag is computed at a first step considering the initial L/D obtained from preliminary design, from its value the wing drag obtained from a single run of FEMWET is subtracted to obtain the rest drag. The aircraft range, cruise Mach number and altitude and the engine parameters are assumed to be constant.

3.6 Validation

The FEMEWET tool has been validated considering three different aspects: accuracy of the wing drag computation, estimation of the wing deformation and verification of the adjoint sensitivity analysis. The validation has been performed in [5]. The good accuracy of Q3D in the drag prediction is shown using a higher fidelity CFD tool: MATRICS-V code [22]. The tool is based on fully conservative full potential outer flow in quasi-simultaneous interaction with an integral boundary layer method on the wing. The code uses a far field analysis method for drag prediction in transonic regime [23]. Considering data about wing twist under 1g load of A320-200 aircraft in [24], FEMWET presents an error of -0.12% in the wing weight calculation, considering an aeroelastic optimization that provides the thickness of the equivalent panels. The optimization presents a minimization of the wing weight subjected to constraints on wing failure under different load cases and aileron effectiveness. Evaluating the deformation of the same aircraft at 1g load case, it shows a maximum error of 8.5% at wing tip. The validity of the use of the adjoint method, used for the gradient based optimization, is explained in details in [5], in which different derivatives of functions of interest with respect to design variables are computed and compared respect to the finite difference method. Considering the new modified drag model, introduced in the aerodynamic module to take into account penalties in drag computation for the estimation of the active flow control, a sensitivity analysis, comparing the adjoint and finite difference methods is implemented. Figure 5 shows the good accordance of the two methodologies, using a step lenght of 10^{-4}.
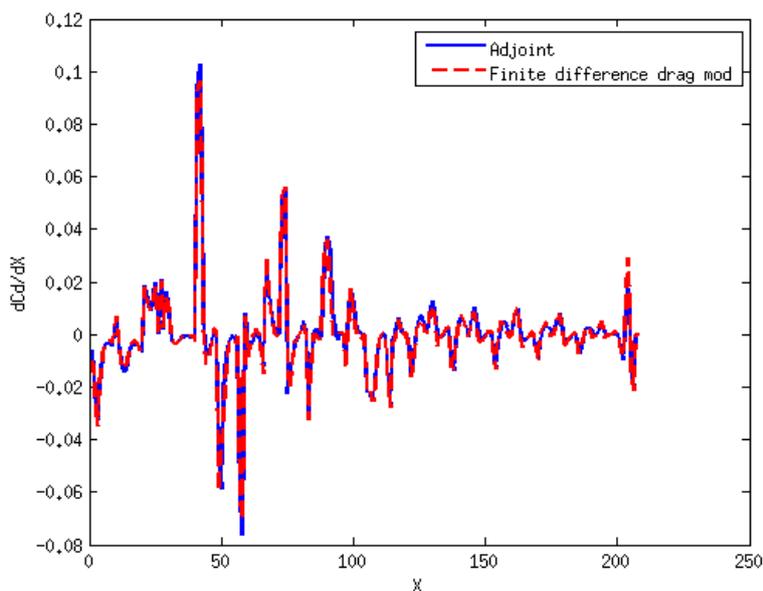
Figure 5: Sensitivity comparison for different design variables.

V. Mosca, A. Elham

4   MULTIDISCIPLINARY DESIGN OPTIMIZATION

As already stated in the paper, a gradient based optimization is performed to minimize the fuel weight of the SE^{2}A Mid-range aircraft. The multidisciplinary design problem can be defined as:

$$
\begin{aligned}
\text{Minimize} \quad & W_{fuel_s}(X) \\
\text{w.r.t.} \quad & X \\
\text{subject to} \quad & Failure_k \leq 0 \\
& \frac{L_{\delta 0}}{L_\delta} - 1 \leq 0 \\
& \frac{MTOW/S_w}{MTOW_0/S_{w0}} - 1 \leq 0 \\
& \frac{W_{fuel}}{W_{fuel_s}} - 1 = 0 \\
& \frac{MTOW}{MTOW_s} - 1 = 0 \\
& X_{lower} \leq X \leq X_{upper}
\end{aligned}
\tag{15}
$$

The design vector is:

$$
X = [t_{ui}, t_{li}, t_{fsi}, t_{rsi}, G_j, C_r, \lambda, b, \gamma, \epsilon_{kink}, \epsilon_{tip}, W_{fuels}, MTOW_s]
\tag{16}
$$

The first 4 components represent the thicknesses of the upper and lower equivalent panel, thicknesses of the front and rear spar, all defined in different 10 spanwise positions from root to tip, for a total of 40 variables. The G vector consists of the modes used for the Chebyschev plynomials to parametrize airfoil shapes. 10 modes are used for the upper surface and 10 modes for the lower one, for a total of 160 variables taking into account 8 different sections. The wing geometry is defined through the choord root, taper ratio, span, sweep angle at leading edge, twist angle at kink and tip. The kink position is fixed at 25% of the span. Finally two surrogate variables are introduced, fuel weight and maximum take-off weight, used to avoid iterations during aeroelastic analysis.

Prior to start the full aerostructural optimizations, a series of aeroelastic optimization (fixed wing shape and only optimizing structural variables) is executed for different maximum load factor (n_{max}), to initialize the values of the thicknesses of the equivalent panel and the consequent reduction in the wing weight. Hence, depending on the values of n_{max}, a fast gradient based optimization with only the first 4 components of the design vector X is performed for minimizing W_w. Both the aerostructural and aeroelastic problem are characterized by several constraints. The first group consists of constraints on the structure failure, including tensile, compressive and buckling failure criteria.

For this reason, five different load cases are evaluated (Tab.3): two pull up maneuver cases at maximum load factor (n_{max}), varying depending on the load alleviation rate considered, a -1g push over maneuver, a 1.3g gust load to simulate the fatigue of the wing lower panel and a roll maneuver to compute the aileron effectiveness. Finally, obviously the cruise flight condition is also evaluated, necessary for the performance estimation. All these conditions are determined based on flight envelope and load diagram studied in preliminary aircraft design of the aircraft [4].

V. Mosca, A. Elham

Table 3: SE^{2}A Mid-Range Load cases

Load case	Type	Aircraft weight	H [m]	M	n [g]
1	pull-up	MTOW	7500	0.89	n_{max}
2	pull-up	MTOW	0	0.58	n_{max}
3	push-over	MTOW	7500	0.89	-1
4	gust	ZFW	7500	0.89	1.3
5	roll	W_{des}	4000	0.82	1
6	cruise	W_{des}	10600	0.78	1

The aileron effectiveness, defined as the ratio of the elastic to the rigid roll moment of the wing due to an aileron deflection, represents a constraint to satisfy the requirements on the roll performance. The roll performance is not only a function of the aircraft roll moment but also of the aircraft moment of inertia. In particular, during the aerostructural optimization, the planform geometry will change and so changing the two variables. Considering that the reference aircraft is based initially on the characteristic of the A320 and with a similar MTOW, the rigid roll moment of the A320 is computed and from this the minimum roll moment representing the constraint for the elastic roll moment for an aileron effectiveness of 0.5, the value is basd on [25]. Last constraint is given by the wing loading (MTOW/S) lower or equal to its initial value. In this way, the aircraft can satisfy the take-off and landing requirements. In total, 3 different aeroelastic optimizations are performed, for different maximum load factor to minimize wing weight varying the thicknesses of the wing-box panels. These, are the inputs of 9 different aerostructural optimizations (3 optimization for each maximum load factor), which objective function is represented by fuel weight and all the characteristics shown in Eq.15 and Eq.16. The whole optimizations framework is clarified in Fig.6.
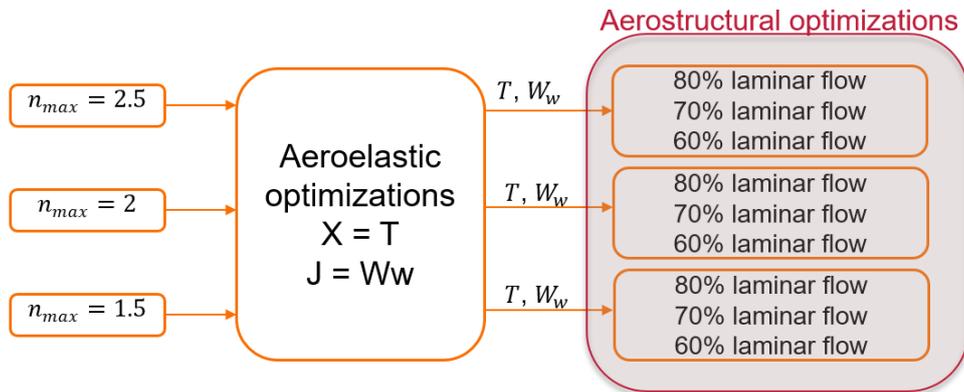
Figure 6: MDO problem.

5 RESULTS

Figure 7 shows the fuel weight reduction for different maximum load factor and portion of laminar flow. In particular, best results are achieved with the maximum use of boundary layer suction, which is for 80% laminar flow. Precisely for $n_{max} = 2.5$, W_f can be reduced by 7.1%, while for $n_{max} = 2$ the fuel weight is reduced of 7.9%, finally with $n_{max} = 1.5$, it is possible to achieve the highest reduction: 8.3%. Detailed values of the optimizations are shown in Tab.4. The final weights are presented and values of lift and drag coefficient

during cruise mission. Reference data represent values obtained for the reference SE^{2}A Mid-range (back-swept) aircraft (Tab.2) for $n_{max} = 2$ and 70% laminar flow, according to the last updated hypotheses inside the Cluster. As expected, at the condition of maximum laminar flow, the highest reduction on the wing drag is obtained. Detailed variations of each component of wing drag are reported in Tab.5. A slightly augmentation of the $C_{D_{wing}}$ is obtained for 60% laminar flow, in fact, as mentioned reference data presents laminar flow until the 70% of the chord. In these cases, weights are optimized thanks to a different distribution of thicknesses of the equivalent panels and hence stiffness of the wing. Augmenting the active flow control action and hence lowering maximum load factor, highest saving of fuel weight is achievable. In fact, this condition favours a more flexibility of the wing, reducing the wing weight for transition simulated at 80%. For the other two conditions of laminar flow, a limited augmentation of wing weight is reached. In fact, Fig.8 shows higher distribution of panels thicknesses from root to tip. The different values obtained are given considering that they represent respectively thickness of the upper and lower panel, then front and rear spar at 10 different spanwise positions. The higher thickness is mainly observable for the lower panel (Fig.8b) and the rear spar (Fig.8d).
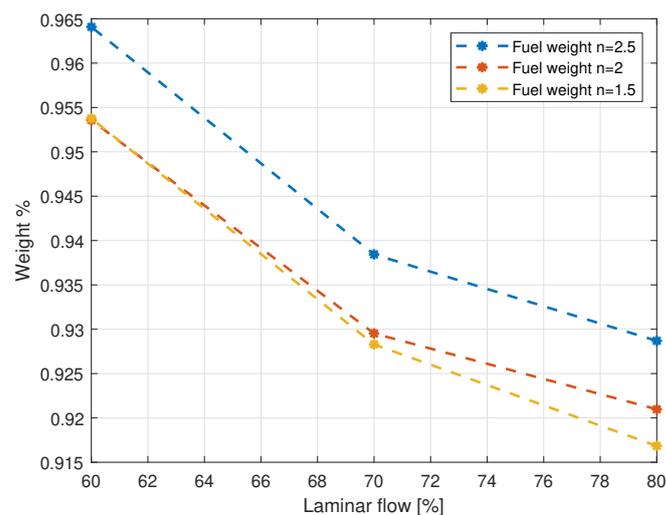
Figure 7: Fuel weight reduction.

Figure 9 shows the different wing planform configurations for different maximum load factor and portion of laminar flow.

All configurations present a lower sweep angle. A strong reduction of the wave drag, as stated in Tab.5 is mainly reached by the weakening of shock waves, as can be seen in Fig.10 and Fig.11.

Generally, for 80% and 70% laminar flow the wing geometry is almost overlapped. An exception occurs for n=1.5, making the wing being optimized mainly for wave drag reduction. The distribution of the lift coefficient, respect to the span, is visible in Fig.12. Considering the reference case being characterized by a maximum load factor of 2 for pull-up maneuver and 70% laminar flow, the case has been compared with the optimized for the same conditions in Fig.12b. The optimized configurations reach a more efficient distribution of CC_l leading to an almost triangular distribution.

The SE^{2}A reference aircraft reaches a maximum of bending displacement of 2.2 m at

V. Mosca, A. Elham

(a) Upper panel.

(b) Lower panel.

(c) Front spar.

(d) Rear spar.
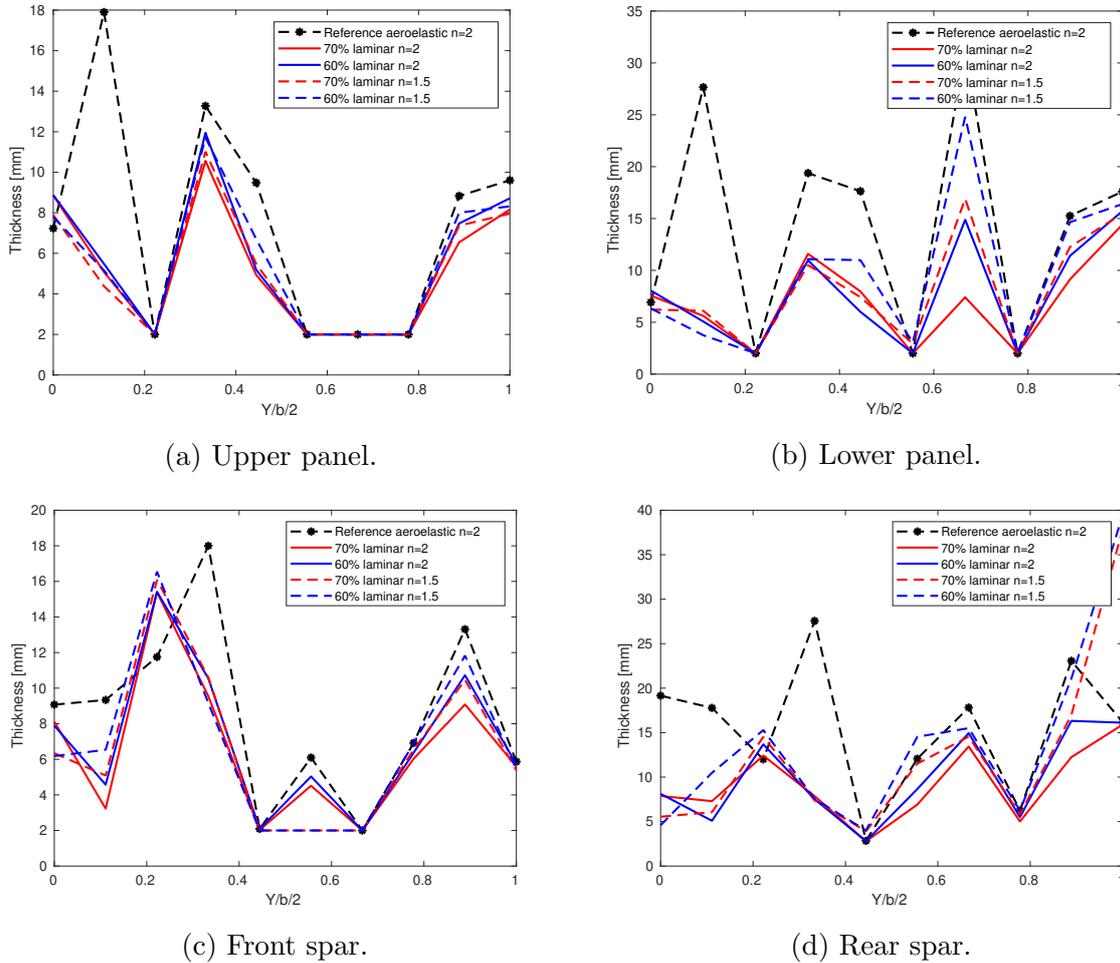
Figure 8: Distribution of thicknesses of the wing box along the span.

Table 4: Optimizations results.

		MTOW [kg]	W_{fuel} [kg]	W_{wing} [kg]	C_L	C_D
Reference		72102	9808	11661	0.397	0.00622
n=2.5	80%	66958	9109	7216	0.393	0.00516
	70%	67172	9204	7335	0.394	0.00548
	60%	67933	9456	7844	0.396	0.00629
n=2	80%	66394	9033	6728	0.379	0.00486
	70%	66313	9117	6563	0.379	0.00524
	60%	66432	9353	6446	0.395	0.00637
n=1.5	80%	65932	8992	6306	0.374	0.00482
	70%	66382	9105	6644	0.377	0.00512
	60%	66590	9354	6602	0.396	0.00633

tip and in the same location -2.2 deg of maximum twist angle, considering 1-g cruise mission. Depending on the laminarization strategy chosen and on the aerostructural optimization with its maximum load factor used for the optimization constraints, highest values of bending displacements (at tip) are between 2.5 m and 3.2 m. The lowest twist angle (at tip) reached is between -2.8 deg and -2.6 deg. Hence optimized configurations

Table 5: Drag relative variation.

		C_D	C_{Di}	C_{Df}	C_{Dp}	C_{Dw}
Reference		0.00622	0.00332	0.00200	0.00090	4.01E-04
n=2.5	80%	-17.1%	-11.2%	-18.7%	-35.5%	-94.3%
	70%	-11.8%	-11.0%	-1.6%	-37.8%	-94.1%
	60%	+1.0%	-11.0%	+23.9%	-5.4%	-94.2%
n=2	80%	-21.9%	-19.1%	-19.0%	-39.1%	-97.3%
	70%	-15.8%	-17.6%	-1.7%	-40.7%	-95.5%
	60%	+2.4%	-6.1%	+22.6%	-11.3%	-99.5%
n=1.5	80%	-22.5%	-22.4%	-19.0%	-30.5%	-82.1%
	70%	-17.6%	-20.8%	-1.6%	-41.8%	-95.6%
	60%	+1.8%	-8.7%	+23.4%	-7.5%	-98.4%
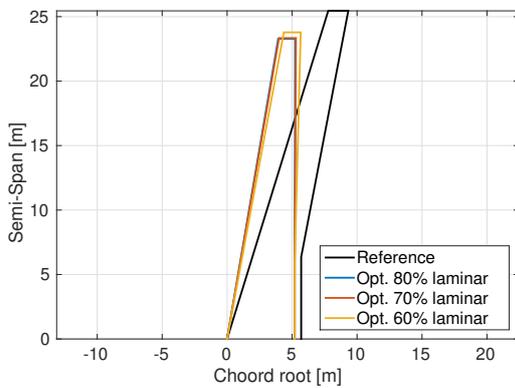
(a) Wing planform for n=2.5.
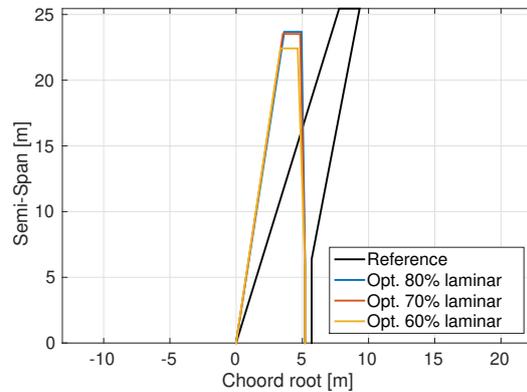
(b) Wing planform for n=2.
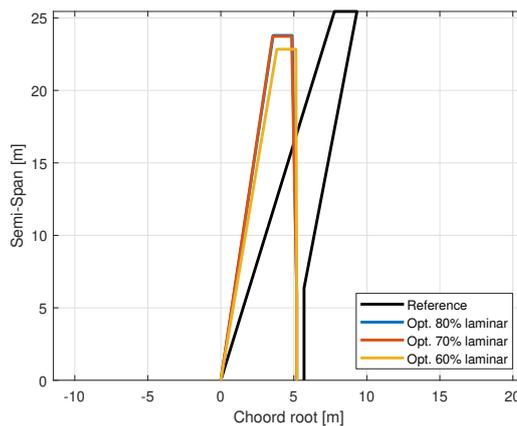
(c) Wing planform for n=1.5.

Figure 9: Wing geometry at different load factor and portion of laminar flow.

are more flexible. The higher flexibility respect to the reference case is clearly visible in Fig.13, comparing the reference wing and the optimized one at the highest reduction of load factor and equal portion of laminar flow (70%). During optimizations, a minimum rolling moment for the flexible wing needs to be satisfied (as explained in Sec.4), therefore the aileron effectiveness may vary in case the new optimized wing is able to perform

(a) Section 1.

(b) Section 2.

(c) Section 3.

(d) Section 4.

(e) Section 5.

(f) Section 6.

(g) Section 7.
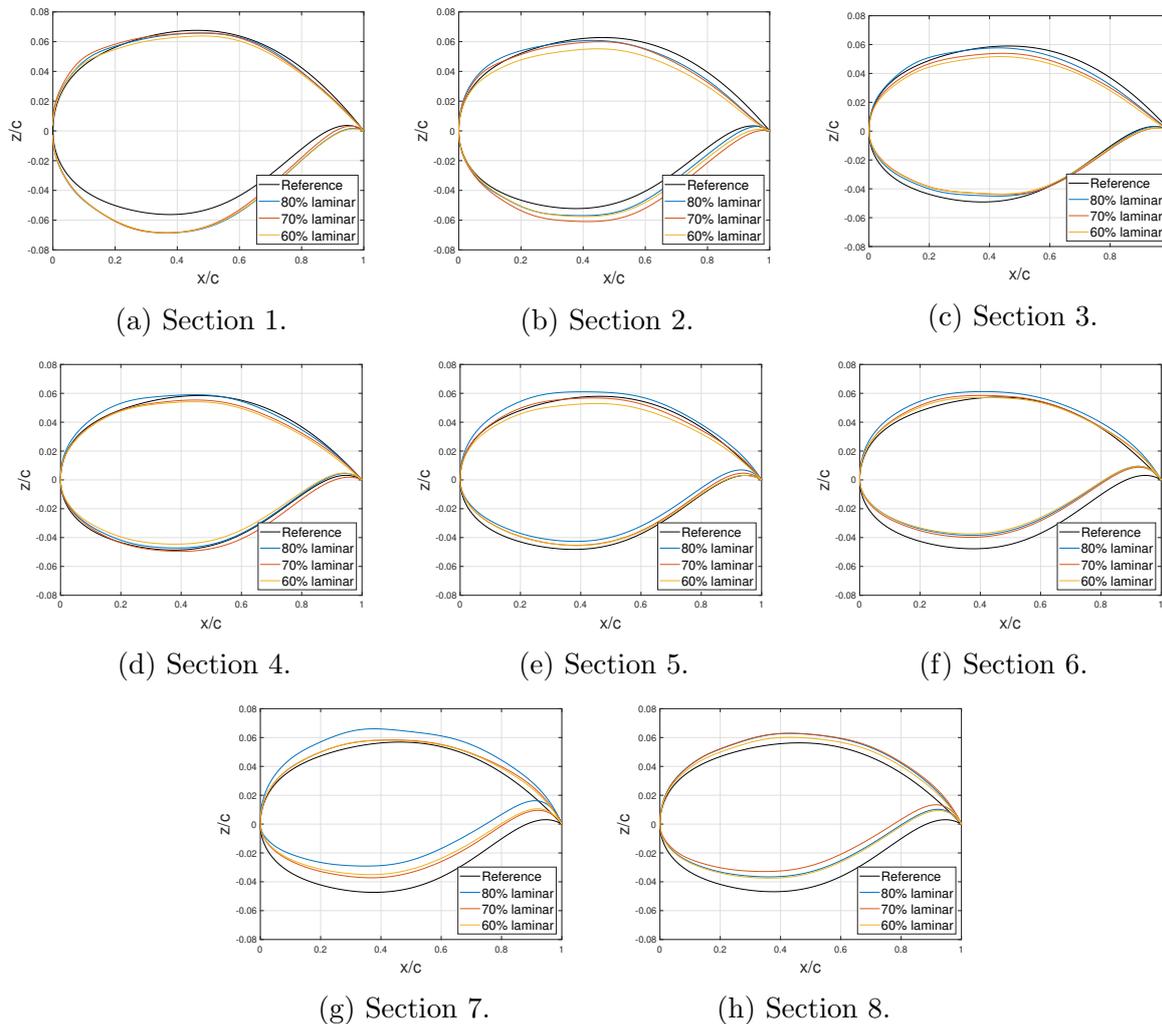
(h) Section 8.

Figure 10: Airfoil of sections perpendicular to the sweep line for several wing spanwise positions, case with $n_{max} = 2$.

with higher flexibility. As a consequence, the reference η_a=0.5 is mostly halved for the optimized results.

6 CONCLUSIONS

An aerostructural optimization framework with active flow control and load alleviation was presented. The use of novel materials and structures is also taken into account thanks to a predicted reduction of the wing weight. In total, three different aeroelastic optimizations are conducted, to minimize wing weight varying thicknesses of the panels of the wing boxes. They consider the three different maximum load factors achieved during pull-up maneuver: 2.5, 2.0, 1.5. The thicknesses and wing weight obtained become input of nine aerostructural optimizations in which the optimizer tries to reduce fuel weight considering thickness of the wing panels, airfoil shapes, wing geometry. Each optimization simulates a different use of the BLS by mean of drag penalty coefficients applied to full turbulent cases evaluated by MSES tool. Three different scenarios are studied: 80%, 70% and 60% of laminar flow. All the 2D data are then applied properly considering a finite wing configuration thanks to Q3D. The FEMWET tool integrates this aerodynamic

V. Mosca, A. Elham

(a) Section 1.

(b) Section 2.

(c) Section 3.

(d) Section 4.

(e) Section 5.

(f) Section 6.

(g) Section 7.
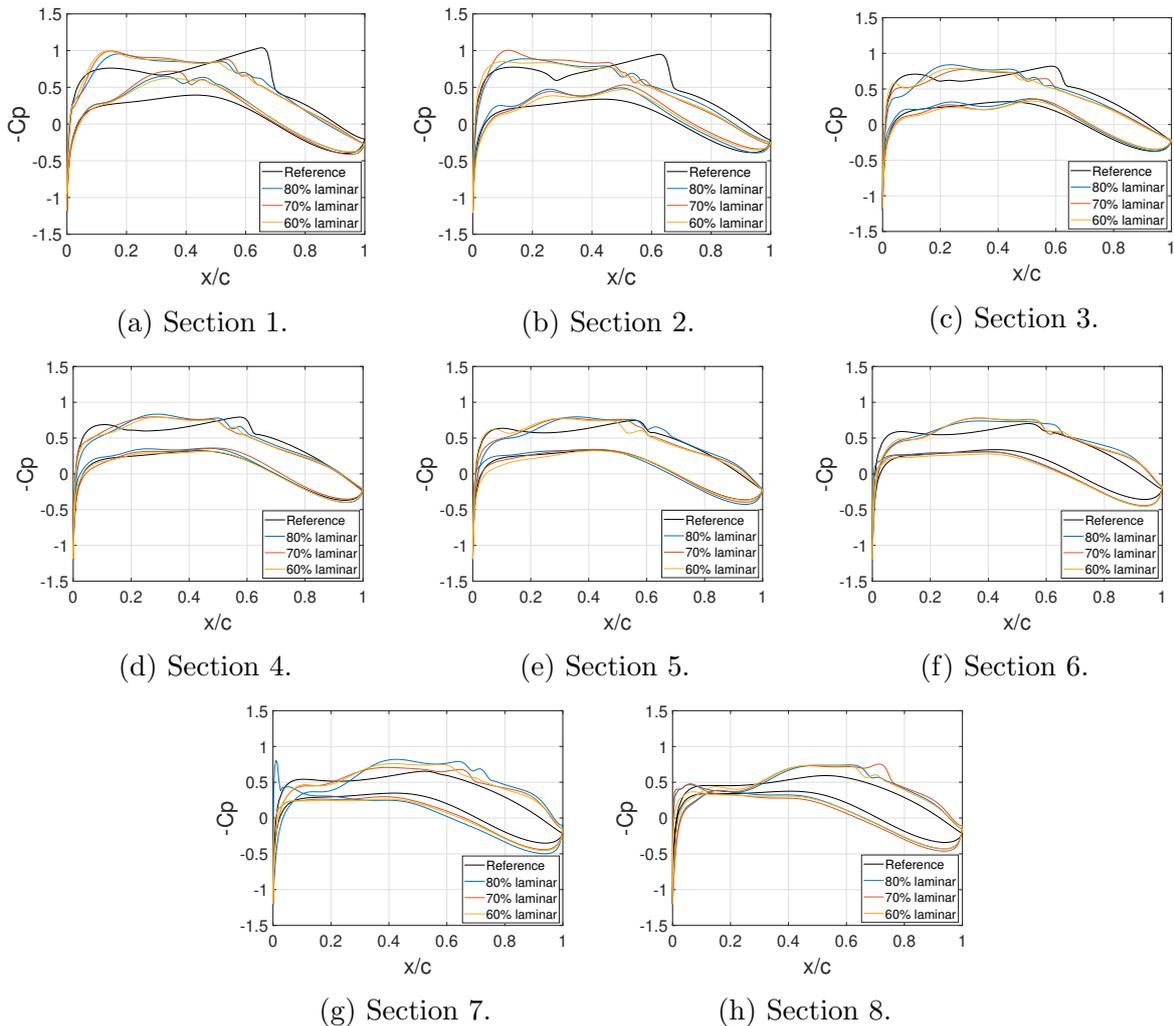
(h) Section 8.

Figure 11: Pressure distribution on sections perpendicular to the sweep line in different wing spanwise positions, case with $n_{max} = 2$.

analysis with a structural study, considering the wing approximated as a flexible beam and real section properties applied at different node positions. The research is applied to the SE^{2}A back-swept mid-range aircraft. The highest benefits are obtained considering the maximum application of load alleviation technology, used to reduce the maximum load factor achievable to 1.5 and for 80% laminar flow: more than 8% of fuel weight is reduced, with a drag reduction of 22.5%. Novel technologies are indeed fundamental to reduce environmental impact keeping or improving flight performance for future aviation, their use needs to be further studied considering possible aeroelastic effect with composite structures and use of forward-configuration for transonic flights.

(a) CC_l for n=2.5.

(b) CC_l for n=2.

(c) CC_l for n=1.5.
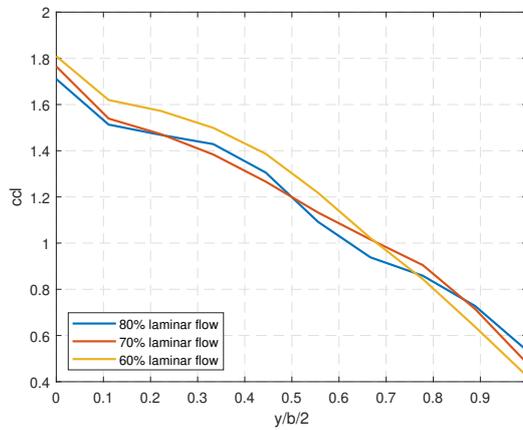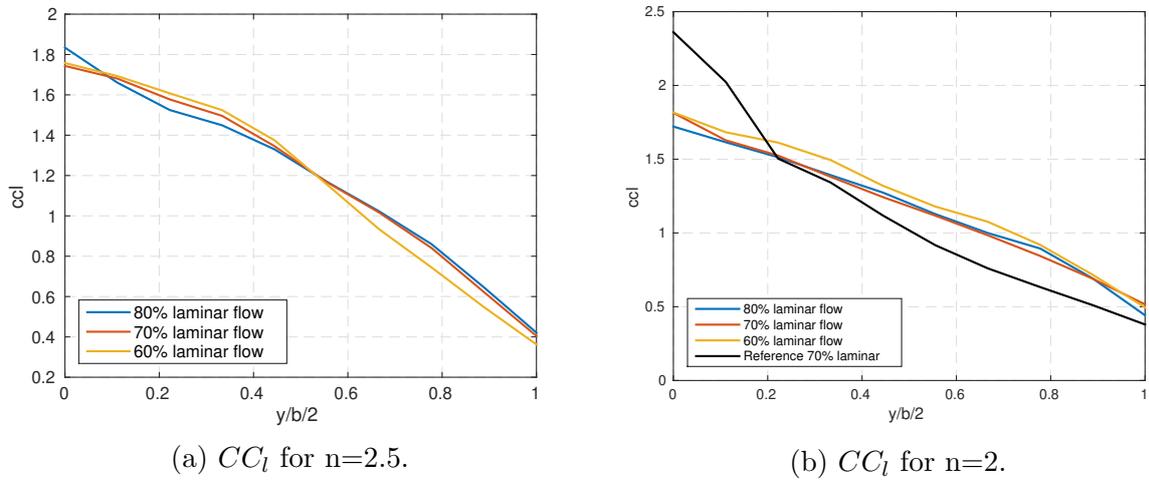
Figure 12: CC_l distribution.

(a) Reference wing.

(b) Optimized case: $n_{max} = 1.5$ and 70% laminar flow.
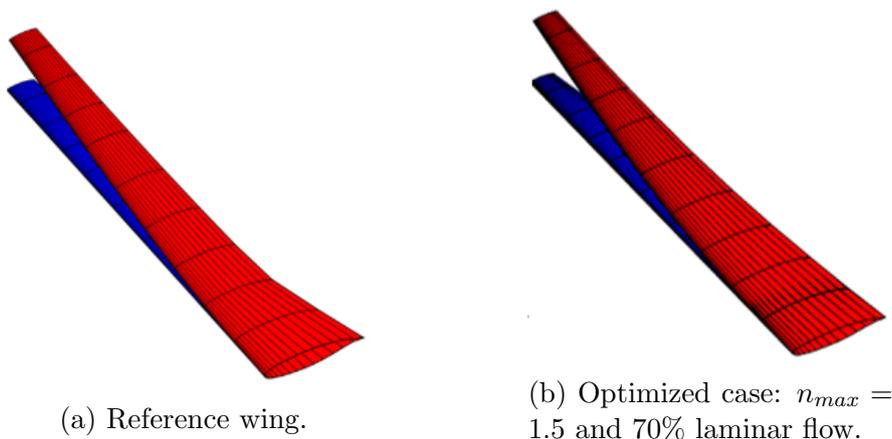
Figure 13: Wing deformations at cruise.

ACKNOWLEDGEMENTS

REFERENCES

[1] Flightpath 2050-europe's vision for aviation: Advisory council for aeronautics research in europe, 2011.

[2] P. Horst, A. Elham, and R. Radespiel. Reduction of aircraft drag, loads and mass for energy transition in aeronautics. *Deutsche Gesellschaft für Luft- und Raumfahrt - Lilienthal-Oberth e.V.*, 2021. doi:10.25967/530164.

[3] T. Lukaczyk, A. Wendroff, M. Colonno, T. Economon, J. Alonso, T. Orra, and C. Ilario. Suave: An open-source environment for multi-fidelity conceptual vehicle design. *16th AIAA/ISSMO Multidisciplinary Analysis and Optimization Conference*, 2015. doi:10.2514/6.2015-3087.

[4] S. Karpuk and A. Elham. Conceptual design trade study for an energy-efficient mid-range aircraft with novel technologies. *AIAA Scitech 2021 Forum.* doi:10.2514/6.2021-0013.

[5] A. Elham and M. J. van Tooren. Coupled adjoint aerostructural wing optimization using quasi-three-dimensional aerodynamic analysis. *Structural and Multidisciplinary Optimization*, 54(4):889–906, 2016. doi:10.1007/s00158-016-1447-9.

[6] F. Dorbath, B. Nagel, and V. Gollnick. Comparison of beam and shell theory for mass estimation in preliminary wing design. 10 2010.

[7] A. Elham and M. J. Van Tooren. Tool for preliminary structural sizing, weight estimation, and aeroelastic optimization of lifting surfaces. *Proceedings of the Institution of Mechanical Engineers, Part G: Journal of Aerospace Engineering*, 230(2):280–295, 2016. doi:10.1177/0954410015591045.

[8] M. Niu. *Airframe stress analysis and sizing.* Conmilit Press Ltd., Hong Kong.

[9] G. Kennedy and J. Martins. A parallel aerostructural optimization framework for aircraft design studies. *Struct Multidisc Optim*, 50:1079–1101, 2014. doi:10.1007/s00158-014-1108-9.

[10] J. Mariens, A. Elham, and M. J. Van Tooren. Quasi-three-dimensional aerodynamic solver for multidisciplinary design optimization of lifting surfaces. *Journal of Aircraft*, 51(2):547–558, 2014. doi:10.2514/1.C032261.

[11] J. Katz and A. Plotkin. *Low speed aerodynamics.* Cambridge University Press, Cambridge, UK.

[12] G. A. Flandro, H. M. McMahon, and R. L. Roach. *Basic aerodynamics: Incompressible flow.* Cambridge University Press, New York.

[13] M. Meheut and D. Bailly. Drag-breakdown methods from wake measurements. *AIAA Journal*, 2008.

[14] M. Drela. Simultaneous Optimization of the Airframe, Powerplant, and Operation of Transport Aircraft. *Proceedings of the 2nd Aircraft Structural Design Conference*, 2010.

[15] M. Drela. N+3 Aircraft Concept Designs and Trade Studies, vol. 2 (Appendices): Design Methodologies for Aerodynamics, Structures, Weight, and Thermodynamic Cycles (Appendix A: TASOPT Transport Aircraft System OPTimization). *Proceedings of the 2nd Aircraft Structural Design Conference*, 2010.

[16] M. Drela and M. B. Giles. Viscous-inviscid analysis of transonic and low reynolds number airfoils. *AIAA Journal*, 25(10):1347–1355, 1987. doi:10.2514/3.9789.

[17] C. Ferreira. Implementation of boundary layer suction in xfoil and application of suction powered by solar cells at high performance sailplanes. *Master's Thesis, TU Delft*, 2002.

[18] N. Beck, T. Landa, A. Seitz, L. Boermans, Y. Liu, and R. Radespiel. Drag reduction by laminar flow control. *Energies*, 11(1):89–127, 2018. doi:10.3390/en11010252.

[19] J. Bongers. Implementation of a new transition prediction method in xfoil. *Master's Thesis, TU Delft*, 2006.

[20] M. Drela. Xfoil: An analysis and design system for low reynolds number airfoils. In T. J. Mueller, editor, *Low Reynolds Number Aerodynamics*, pages 1–12, Berlin, Heidelberg, 1989. Springer Berlin Heidelberg.

[21] J. Roskam. *Airplane design, Part, I: Preliminary sizing of airplanes.* DARcorporation, Lawrence Kansas.

[22] A. van der Wees, J. J. van Muijden, and J. van der Vooren. A fast and robust viscous-inviscid interaction solver for transonic flow about wing/body configurations on the basis of full potential theory. *23rd Fluid Dynamics, Plasmadynamics, and Lasers Conference*, page 1993–3026, 1993. doi:10.2514/6.1993-3026.

[23] J. van der Vooren and A. J. van der Wees. Inviscid drag prediction for transonic transport wings using a full-potential method. *Journal of Aircraft*, 28(12):869–875, 1991. doi:10.2514/3.46111.

[24] E. Obert. *Aerodynamic design of transport aircraft.* OS press, Amsterdam.

[25] BDM. Boeing design manual bdm 6001. Chicago, IL, 1989. The Boeing Company.

UNCERTAINTY QUANTIFICATION OF AEROELASTIC SYSTEMS USING ACTIVE LEARNING GAUSSIAN PROCESS

Sihmehmet Yildiz[1], Enes Cakmak[2], Emre Kara[2] and Melike Nikbay[3]

1: Research Assistant, Faculty of Aeronautics and Astronautics
Istanbul Technical University, Maslak, Istanbul, 34469, Turkey
yildizsih@itu.edu.tr

2: Research Scholar, AeroMDO Lab, Faculty of Aeronautics and Astronautics
Istanbul Technical University, Maslak, Istanbul, 34469, Turkey
cakmake19@itu.edu.tr
karae16@itu.edu.tr

3: Professor, Faculty of Aeronautics and Astronautics
Istanbul Technical University, Maslak, Istanbul, 34469, Turkey
nikbay@itu.edu.tr

Abstract.   *This paper presents an uncertainty quantification study for the aeroelastic analysis of the High Reynolds Number Aerostructural Dynamics (HIRENASD) wing. The computational aeroelastic analysis employs an open-source multi-physics suite SU2 with a fully-coupled fluid-structure interaction capability. The surrogate model which is used for the uncertainty quantification study is constructed by integrating an Active Learning procedure into the Gaussian Process Regression Method for improving efficiency and accuracy. The current Active Learning assisted uncertainty quantification approach is assessed with respect to the conventional uncertainty analyses which are based on surrogates generated with Polynomial Chaos Expansion, Kriging, and Polynomial Chaos-based Kriging metamodel methods. The root mean square error and maximum absolute error verification metrics demonstrated that the Active Learning assisted Gaussian Process method provided more successful results than other methods in capturing both global and local features during this aeroelastic uncertainty quantification study.*

Keywords: Aeroelasticity, Uncertainty Quantification, Gaussian Process, Active Learning, Adaptive Sampling, HIRENASD

Sihmehmet Yildiz, Enes Cakmak, Emre Kara and Melike Nikbay

1 INTRODUCTION

Fulfilling reliability and robustness requirements of aerospace engineering systems is a critical design challenge while developing successful air vehicles. Development of reliable and robust systems is only possible by incorporating and quantifying uncertainties inherent in geometry, materials and operating conditions during the early design phases. Thus, uncertainty quantification (UQ) methods propagate effects of uncertain input variables to the performance of overall system. Probabilistic methods can be used for UQ if sufficient information is available about the probability distribution of uncertain variables. However, if a large number of uncertain parameters exists in the input set, efficiency of UQ becomes an important factor in the implementation. Therefore, the motivation of this study is to explore applicability of efficient uncertainty analysis methods for a multi-physics problem such as aeroelasticity.

Aeroelastic systems are more prone to randomnesses because of the interaction between two physics; aerodynamics and structure. Many uncertainties may not be considered simultaneously during modelling, analysis and experiments of aeroelastic systems. Beran et al. [1] presented a comprehensive review of UQ in traditional aeroelasticity, UQ in computational aeroelasticity, and aeroelastic optimization under uncertainty. UQ in flutter is specifically investigated to assure aeroelastic stability inside the flight envelope within a 15% equivalent airspeed margin rule regulated by Naval Air Systems Command [2]. Most of the UQ in flutter studies draw on reduced order models as polynomial chaos expansion (PCE), proper orthogonal decomposition (POD). By using the results obtained as a result of the coupling of computational fluid dynamics (CFD) and computational structural dynamics (CSD), reduced-order models are established and using these reduced order models, sampling-based uncertainty analysis is performed with various sampling methods as Monte Carlo sampling (MCS), Latin hypercube sampling (LHS). Danowsky et al. [3] investigated different methodologies for aeroelastic UQ where an accurate approximated model of the system is provided by Design of Experiment and Response Surface Method (DOE/RSM) and robust stability of the system is computed with Structured Singular Value (μ) method. Various studies focused on UQ in static aeroelasticity. Cunningham and Holman [4] performed a static aeroelastic analysis on the S4T model with NONLI-NAE where DAKOTA software is used for uncertainty analysis. Nikbay and Heeg [5] used Euler flow based ZEUS solver for static aeroelastic analysis where modal analysis was provided by MSC NASTRAN package. They stated that a linear relation between inputs and outputs was observed in statistical distributions. Studies of Cunningham and Holman [4], and Nikbay and Heeg [5] were done as a part of the NATO Science and Technology Organization AVT-191 Task group. Nikbay et al. [6] investigated the effects of aeroelastic uncertainties on sonic boom signature and ground noise for commercial supersonic transport. FUN3D tool was used for the aeroelastic analysis and sBOOM was used for the aeroacoustic analysis. Phillips and West [7] focused on integrating a robust evaluation of uncertainties into present low-boom aircraft configurations. They used MSC NASTRAN for the static aeroelastic analysis and Cart3D for the aeroacoustic analysis. The common point of these four studies is the use of similar methodologies for UQ. The MCS, LHS and PCE methods were used in all of them. Additionally, POD was used in the study of Cunningham and Holman [4].

Optimization and UQ studies using high-fidelity engineering analyses frequently result with significant computational burden. In such design studies, optimization and uncer-

tainty analyses are performed by establishing surrogate models [8–10] and reduced-order models [5, 11, 12] which represent expensive computational models much more efficiently. However, depending on the number of random variables in the study, the efficiency of metamodeling methods becomes an important parameter in the implementation [13]. In the literature, orthogonal polynomial-based surrogate modelling methods such as PCE are frequently used because they are successful in capturing the global behaviour in uncertainty analyses. The authors of [13] proposed the Point Collocation Non-Intrusive PCE method for efficient UQ studies and used it in aeroelastic uncertainty analysis for a transonic wing geometry. However, the number of simulations required to construct the surrogate models based on orthogonal polynomials often increases in a factorial relationship with the degree of polynomials and the number of design variables [14]. In contrast to the methods based on orthogonal polynomials, kernel-based surrogate models such as the Gaussian Process (GP) (also called as Kriging) are more suitable for problems with limited sample sizes [15]. In addition, these models have the ability to capture the local behaviour of the physical models due to the nature of kernel functions. However, it can not achieve the global behavior properly in cases where little data is used. The polynomial chaos based Kriging (PC-K) method has been developed to combine the advantages of orthogonal polynomials and kernel-based models [14]. On the other hand, there are few studies where accurate and efficient surrogate models are created with less simulation data with the Active Learning algorithms [16, 17].

In this study, we aim to perform an aeroelastic UQ study by creating an accurate surrogate model in capturing both global and local features efficiently. For this purpose, the Gaussian Process method is implemented with an Active Learning (AL) method and an aeroelastic uncertainty analysis is performed using this approach. The current results are compared with different conventional surrogate modelling methods to show the benefit of the Active Learning approach used in this study. Section 2 presents the aeroelastic analysis framework and the mathematical descriptions of the surrogate modelling methods. In Section 3, the application process related to the uncertainty analysis processes is explained. Finally, Section 4 provides an overview and assessment of the current study.

2 METHODOLOGY

In this section, we describe the methodology followed in the study. Firstly, the aeroelastic analysis process is introduced. Then, the analytical background of the surrogate modelling methods used in the study is presented. Finally, the sampling procedure with and without the active learning procedure is explained. In addition, the evaluation metrics used to test the accuracy of surrogate models are described.

2.1 Aeroelasticity

Accurate computation of wing-tip displacement is crucial for static aeroelasticity. Therefore, computational methods for coupled fluid and structure analysis, are mainly used for predicting the wing-tip displacement and investigating Fluid-Structure Interaction (FSI). In this study, the open-source SU2 multi-physic suite [18] is employed for high-fidelity FSI analysis. For the current study, a nonlinear structural model and a compressible Navier-Stokes flow solver are coupled simultaneously within SU2 as explained in [19, 20].

For flow analysis, compressible Reynolds-Averaged Navier-Stokes (RANS) equations are the governing equations. Finite volume method (FVM) with a standard edge-based

data structure on a dual grid with vertex-based scheme is used to discretize RANS equations in space. At the midpoint of an edge, the convective and viscous fluxes are calculated. The Roe method is used for calculation of convective fluxes.

FSI requires moving boundaries and deformation of grids. Therefore, a mesh movement problem must be defined to track the deformation of mesh. In mesh problem, fictitious stiffness matrix multiplied with vector of nodal mesh displacements will be equal to fictitious forces that enforce the displacements of the boundary. The fluid problem is updated counting for the mesh deformation. Thus, the governing equation is updated by using Arbitrary Lagrangian-Eulerian (ALE) framework for fluid domain.

The full discrete structural non-linear problem will be the governing equation for structural analysis. The governing equation is solved with linearization and an iterative solution with a Newton method. The structural problem must be updated by considering the mesh deformation and inertia. The inertial force term is included and surface force is modified.

FSI interface is intersection of flow domain and structural domain. Partitioned approach is adopted for FSI. Therefore, compatibility and continuity conditions are required at the FSI interface. For continuity condition, equilibrium of tractions over the interface is required.

Governing equations of the coupled FSI problem are composed of the structural, fluid, and fluid mesh equations. Governing equations of the coupled FSI problem will be written as a function of problem state variables. FSI problems and coupled problems in general, are non-linear. Applying Newton-Raphson methods, coupled solutions can be achieved. The Block-Gauss-Seidel (BGS) strategy is used for avoiding complexity in the Jacobian of the problem. BGS iteratively solves of linearized problem until convergence.

2.2 Surrogate Modeling Techniques

In this study, we aim to assess the success of the Gaussian Process Metamodels by integration of Active Learning (Adaptive Sampling) method for better capturing the local and global features of the physical problem with less simulation. In order to show the benefits of the proposed method, a comparative process with conventional surrogate modelling methods is also conducted. In the following sections, the background for some conventional surrogate models and our current approach based on Active Learning assisted Gaussian process (AL-GP) method will be presented.

2.2.1 Polynomial Chaos Expansion

The PCE method is a stochastic metamodel method developed by Wiener [21] in 1938. There are 2 different types of PCE as intrusive and non-intrusive. In order to use the intrusive PCE method, existing governing equations need to be modified. Although it seems simple in theory, the operations can be difficult to implement. On the contrary, the non-intrusive PCE method uses the program as a black box and only deals with the input and output values of the analysis program. There are approaches such as quadrature-based and point-collocation for the non-intrusive PCE method. In this study, a python code is developed for the point-collocation non-intrusive PCE method, which is frequently used in flight simulations and CFD problems. The computational model $M(\mathbf{X})$ is expressed

Sihmehmet Yildiz, Enes Cakmak, Emre Kara and Melike Nikbay

by the PCE method as a combination of orthogonal polynomials as in Eq. (1).

$$M(\mathbf{X}) = \sum_{i=1}^{\infty} \alpha_i \Psi_i(\mathbf{X}) \tag{1}$$

where $\mathbf{X}$ is a random input vector of size n. In this equation, $\Psi(\mathbf{X})$ represents the multivariate orthogonal polynomials basis, and $\boldsymbol{\alpha}$ represents the expansion coefficients corresponding to the basis functions. For the polynomial basis, Hermite polynomials are used for the normal distribution and Legendre polynomials are used for the uniform distribution. In Eq. (1), the computational model is expressed as the sum of an infinite number of orthogonal polynomials, and the sum of these orthogonal polynomials for computation has to be truncated somewhere. Therefore, a truncated PCE form is used as in Eq. (2).

$$M(\mathbf{X}) \approx M^{PCE}(\mathbf{X}) + \epsilon \equiv \sum_{i=1}^{P} \alpha_i \Psi_i(\mathbf{X}) + \epsilon \tag{2}$$

$M^{PCE}(\mathbf{X})$ in Eq. (2) is the approximate PCE model. The computational model is expressed as the sum of the approximate PCE model and a zero-mean residual. The unknown $\boldsymbol{\alpha}$ expansion coefficients are obtained by minimizing the residual between the approximate model and the computational model at the data points used to train the surrogate model. The unknown $\boldsymbol{\alpha}$ parameters are obtained by solving the least square minimization problem defined in Eq. (3).

$$\hat{\alpha} = \arg\min_{\alpha} \mathbb{E}\left[\boldsymbol{\alpha}^T \Psi(\mathbf{X}) - M(\mathbf{X})\right] \tag{3}$$

By solving the unknown $\boldsymbol{\alpha}$ parameters, the PCE approximate model is obtained. The minimum number of parameters required to obtain unknown $\boldsymbol{\alpha}$ parameters in the approximate model is expressed as in Eq. (4).

$$P = \frac{(p+n)!}{p!\, n!} \tag{4}$$

In this equation, p represents the degree of PCE, and n represents the number of random input parameters.

2.2.2 Kriging - Gaussian Process

Kriging is a statistical interpolation method proposed by Krige in 1951, in which interpolation values are modeled with a Gaussian operation [22]. There are versions of the Kriging method with different trend function definitions such as simple, ordinary, and universal Kriging. In the simple Kriging method, the model is considered to have a constant and known mean, while in the ordinary Kriging method, the model is considered to have a constant but unknown mean. In both of these methods, a surrogate model is created by modelling the deviations of the model from the constant mean in the design space. Unlike these two methods, the universal Kriging method assumes changing and unknown mean in the design space instead of a fixed mean-variance. Due to the addition of spatial dependence to the surrogate modelling, the universal Kriging method better

Sihmehmet Yildiz, Enes Cakmak, Emre Kara and Melike Nikbay

models the functions where sudden changes are observed. Due to this feature, the universal Kriging method is used in this study. This method is also called the Gaussian process (GP) method.

The universal Kriging method is a stochastic interpolation method, and an $M(\mathbf{X})$ computational model is tried to be modeled as in Eq. (5).

$$M(\mathbf{X}) \approx M^K(\mathbf{X}) = \boldsymbol{\beta}^T f(\mathbf{X}) + \sigma^2 Z(\mathbf{X}) \tag{5}$$

The $\boldsymbol{\beta}^T f(\mathbf{X})$ term in this equation represents the mean value of the model called the trend function. The $f(\mathbf{X})$ and $\boldsymbol{\beta}$ vectors in the trend function expression represent the coefficients corresponding to the regression functions and the regression coefficients, respectively. σ^2 represents the Gaussian process variance, and $Z(\mathbf{X})$ represents the zero-mean unit-variance stationary Gaussian process. Thus, $Z(\mathbf{X})$ shows the deviation from the trend function of the surrogate model to be established.

Correlation functions measure the correlation between input variables and are determined depending on the distance between two sampling points. In this study, the Gaussian correlation equation is used and the equation is expressed as in Eq. (6).

$$r\left(x, x'; \theta\right) = \exp\left[-\frac{1}{2}\left(\frac{\mid x - x' \mid}{\theta}\right)^2\right] \tag{6}$$

The x and x' in this equation represent two points in the training set of size N_{tr}, also θ is the length-scale and is the unknown hyperparameter. $R_{N_{tr} \times N_{tr}}$ correlation matrix is obtained by using the correlation value between the points in the whole training dataset ($R_{ij} = r(x_i, x_j; \theta)$; $i, j = 1 \dots N_{tr}$). By using the correlation matrix, analytically optimal β and σ parameters are expressed as Eq. (7) and (8).

$$\hat{\boldsymbol{\beta}} = \left(\mathbf{F}^T\mathbf{R}^{-1}\mathbf{F}\right)^{-1} \mathbf{F}^T\mathbf{R}^{-1}\mathbf{Y_{tr}} \tag{7}$$

$$\hat{\sigma}^2 = 1/N_{\text{tr}} \left(\mathbf{Y_{tr}} - \mathbf{F}\hat{\boldsymbol{\beta}}\right)^T \mathbf{R}^{-1} \left(\mathbf{Y_{tr}} - \mathbf{F}\hat{\boldsymbol{\beta}}\right) \tag{8}$$

$\mathbf{Y_{tr}}$ in these equations is the analysis result corresponding to the $\mathbf{X_{tr}}$ points, and the matrix F ($F_{ij} = f_j(x(i))$) is the Vendermonde matrix. These equations depend on the θ hyperparameter and are obtained by minimizing the negative maximum likelihood function given in Eq. (9).

$$\hat{\theta} = \arg\min\left(\frac{1}{2}\log(\det(\mathbf{R})) + \frac{N_{\text{tr}}}{2}\log\left(2\pi\sigma^2\right) + N_{\text{tr}}/2\right) \tag{9}$$

Using the obtained hyperparameter, the mean and estimated variance value of a new point x is obtained using Eq. 10 and 11, respectively.

$$\hat{y}(\boldsymbol{x}) = \boldsymbol{f}(\boldsymbol{x})^\top\boldsymbol{\beta} + \boldsymbol{r}(\boldsymbol{x})^\top\mathbf{R}^{-1}(Y - \mathbf{F}\boldsymbol{\beta}) \tag{10}$$

$$\sigma_{\hat{y}}^2(\boldsymbol{x}) = \sigma^2\left(1 - \langle\boldsymbol{f}(\boldsymbol{x})^\top\boldsymbol{r}(\boldsymbol{x})^\top\rangle \begin{bmatrix} \mathbf{0} & \mathbf{F^T} \\ \mathbf{F} & \mathbf{R} \end{bmatrix}^{-1} \begin{bmatrix} \boldsymbol{f}(\boldsymbol{x}) \\ \boldsymbol{r}(\boldsymbol{x}) \end{bmatrix}\right) \tag{11}$$

The Active Learning procedure is based on adding a new sample to the maximum value of the estimated variance value given in Eq.(11) in the design space.

2.3 Polynomial Chaos based Kriging

Kriging method is successful in capturing local features, PCE method is successful in capturing the global behaviour of the computational model. The Polynomial Chaos based Kriging (PC-K) is a metamodelling method developed by combining the PCE and universal Kriging to combine the success of these two methods in capturing local and global features. The general equation used for PC-K is given in Eq. (12).

$$M(\mathbf{X}) \approx M^{PCK}(\mathbf{X}) = \boldsymbol{\alpha}^T \boldsymbol{\Psi}(\mathbf{X}) + \sigma^2 Z(\mathbf{X}) \tag{12}$$

The $\boldsymbol{\alpha}^T \boldsymbol{\Psi}(\mathbf{X})$ term in this equation is the truncated PCE expression given in Eq. (2). This term is used to obtain the general behaviour of the computational model. The $\sigma^2 Z(\mathbf{X})$ expression in the equation represents the deviation of the computational model from the trend function calculated in universal Kriging. This term is used to capture the local features of the model.

2.4 Sampling Procedure and Verification Metrics

In this section, sampling methodology and surrogate model verification metrics are defined. Firstly, the Active-Learning method will be introduced. Then, the conventional sampling methodology (without the active learning method) will be described. Finally, the verification metrics used to verify the accuracy of the surrogate models are defined.

2.4.1 Active Learning Methodology

Active learning is an iterative data selection method to improve model accuracy with limited training data. This process is called adaptive sampling in the statistical field [23]. Settles [24] published a literature review on Active Learning and classified its strategies as pool-based sampling, query synthesis, stream-based selective sampling. The pool-based sampling strategy is used in this study.

The pool-based sampling strategy is the process of guiding the sampling process by actively selecting the most informative candidates from a large sample pool that has not been analyzed. The dataset used to establish the current surrogate model and the information obtained from the surrogate model are used to select the most informative candidates. Gaussian process predictive variance equation is very suitable for variance-based active learning implementation. In this study, Gaussian process variance equation is used to define the next sampling point as in Eq.(13).

$$\boldsymbol{x}^{(m+1)} = \arg \max_{\boldsymbol{x} \in \mathcal{X}} \sigma_{\hat{y}}^2(\boldsymbol{x}) \tag{13}$$

2.4.2 Sampling Procedure

Positions of the sampling points used while establishing the surrogate model greatly affect success of the surrogate model. Therefore, in order to make a fair comparison between the methods which are assisted by the active learning procedure and not assisted, an appropriate sampling procedure should be selected. For this purpose, some sampling methods used in the literature are evaluated. A certain number of sampling is made with Monte Carlo sampling (MCS), Latin hypercube sampling (LHS), Halton sequence

Sihmehmet Yildiz, Enes Cakmak, Emre Kara and Melike Nikbay

sampling, optimized LHS methods and the distribution of the samples in the design space are shown in Fig 1.
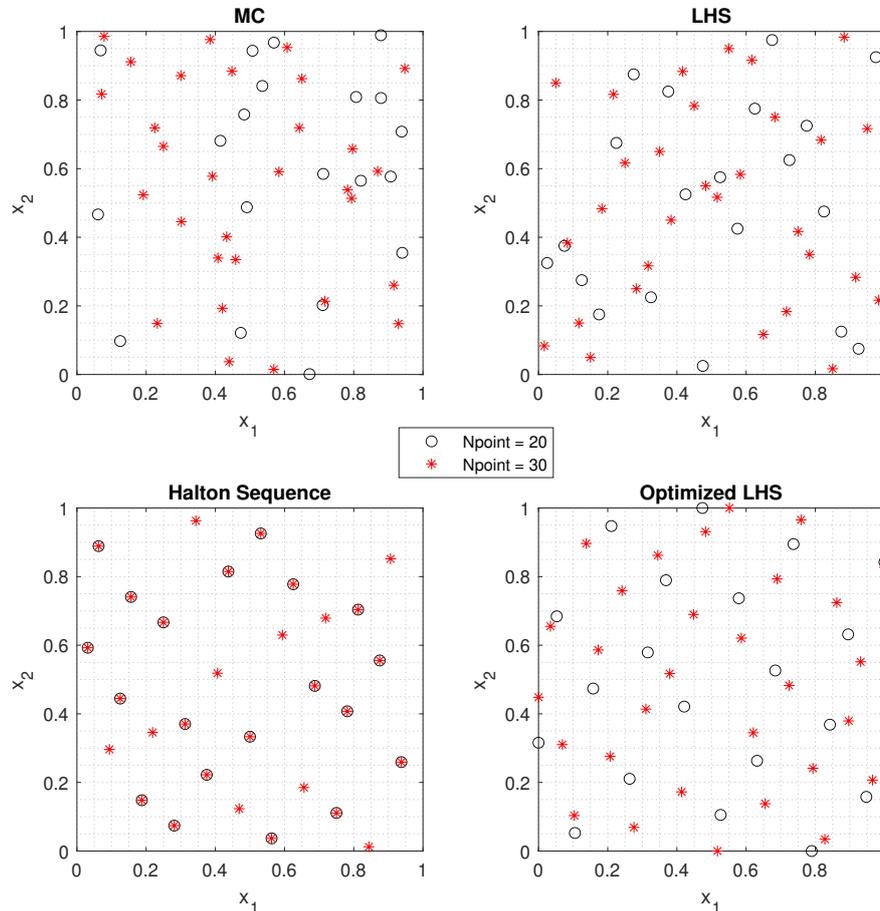
Figure 1: Comparison of sampling methods.

The MCS method, also called the pseudo-random sampling method, was developed by Metropolis and Ulam [25]. The MCS method attempts to fill the design space by determining the sampling points with random actions for a variable with a certain distribution. However, in studies where limited sampling is used, as in Fig. 1, it may cause clusters and gaps in some parts of the design space. The LHS method was developed by McKay et al. in 1979 [26]. Unlike the MCS method, the LHS method generates random data based on the cumulative distributions of the variables in order to fill the design space better. However, due to the random selection of the cumulative distribution intervals of the variables to be sampled in the multidimensional sampling process, it may not provide suitable space filling [22]. The optimized LHS method combines the space-filling criterion and the optimization algorithm to increase the efficiency of the LHS method [27]. As can be seen in Fig. 1, the optimized-LHS method is quite successful in the space-filling of the design space compared to other sampling methods. The Halton sequence method was first introduced in the 1960s, and the method generalizes the Van der Corput sequence to identify sampling points [28]. Despite the sequences are deterministic, the Halton sequences are of

low discrepancy and the sampling points appear randomly distributed. The most prominent difference of the Halton sequence method than the other methods is as seen in Fig. 1 when two separate samplings are made with the Halton sequence method, low-number sampling constitutes a subset of high-number sampling. Therefore, here in applications where the Active Learning algorithm is not used, the Halton sequence method is used to add to the existing sampling points without compromising the space-filling criterion.

2.4.3 Verification Metric

Various verification metrics have been defined in the literature [29] to test the accuracy of surrogate models constructed with few data in a large design space. In this study, two verification metrics are used because it is desired to test both the accuracy of the global and local behavior of the methods. In this study, the root mean square error (RMSE) metric is used to measure the global behavior of the surrogate model, and a maximum absolute error metric (MaxAE) is defined to measure the local behavior. Formulation of the RMSE and MaxAE metrics are given in Eq.(14) and (15), respectively.

$$\text{RMSE} = \sqrt{\frac{1}{N_{\text{test}}} \sum_{i=1}^{N_{\text{rest}}} (y_i - \hat{y}_i)^2} \tag{14}$$

$$\text{MaxAE} = \max\left(|y_i - \hat{y}_i|\right) \quad (i = 1, 2, \ldots, N_{\text{test}}) \tag{15}$$

3 APPLICATION

This section introduces the application of aeroelastic uncertainty quantification for the High Reynolds Number Aerostructural Dynamics (HIRENASD) wing geometry. The HIRENASD wing is one of the test cases which were presented in the 1st AIAA Aeroelastic Prediction Workshop (AePW-1) held in Honolulu in April 2012 to validate aeroelastic capabilities [30]. Here, the aeroelastic case and computations are introduced in the following section with the validation results. Then, the results of the sensitivity analysis performed to determine the important variable parameters are explained. Next, an aeroelastic UQ study is performed using the Active Learning assisted Gaussian Process method and finally the achieved results are demonstrated along with the conventional surrogate methods.

3.1 Validation of the Aeroelastic Analysis

In the following section, aeroelastic capabilities are validated for the HIRENASD wing model using the FSI capability within the open source software SU2. The initial focus of the study is to validate the aerodynamic part, then also using SU2's multi-physics capabilities, FSI analysis is performed.

3.1.1 Analysis Setup

The HIRENASD project was initiated at RWTH Aachen University in 2004 in order to analyze aeroelastic experiments in transonic regime with an elastic wing. The wind tunnel model of HIRENASD was tested in the European Transonic Windtunnel (ETW) in 2006. The planform of the HIRENASD wind tunnel model, which is a semi-span, the

SFB 401 clean wing configuration with a 34 degree of backward sweep angle is given in Fig. 2.
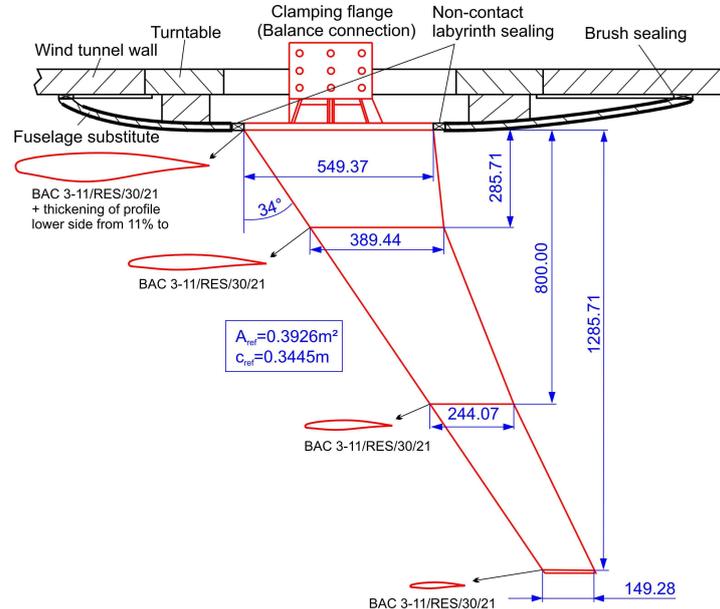
Figure 2: Planform of the HIRENASD wind tunnel model [31]

The aerodynamic model of the HIRENASD wing is provided by NASA for the 1st AIAA Aeroelastic Prediction Workshop. Since the Computational Fluid Dynamics (CFD) analysis is performed using the RANS solver, unstructured tetrahedral grids with prism elements in the boundary layer were used in this model. The flow mesh used is shared in Fig. 3 and consists of 7.8 million mesh elements.
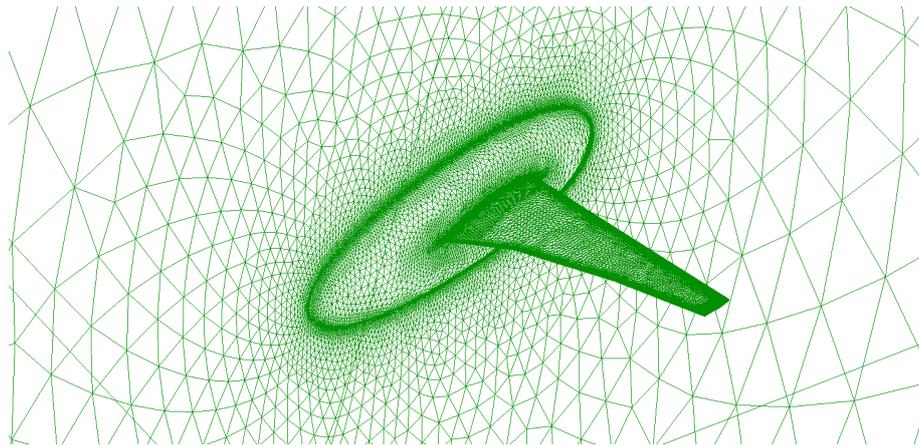
Figure 3: Aerodynamic Mesh for the HIRENASD Wing

There are two different finite element models in Nastran for the wing structure on the HIRENASD website [32]. One of them has hexagonal elements, the other one has tetrahedral elements. Since SU2 can not run the Nastran mesh file, a different mesh was generated here. The new model has 134 thousand elements including quad and triangular element as shown in Fig. 4.

Sihmehmet Yildiz, Enes Cakmak, Emre Kara and Melike Nikbay
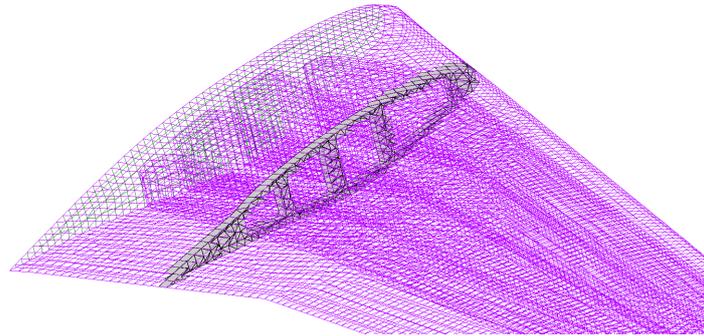
Figure 4: Finite Element Model of HIRENASD Wing

The static aeroelastic analysis is performed using the multi-physics solver in SU2 which can combine fluid and structural solvers. Nikbay and Acar [33] stated that ZEUS Euler solution with boundary layer coupling provides good approximation with experiments and RANS solutions, and computional time is shorter. However, it does not model viscous effects with high fidelity. Therefore, a Finite-Volume Method based RANS is used as a fluid solver with FGMRES (Flexible Generalized Minimum Residual). CFD analyses were performed for three different angles of attack (0.5, 1.5 and 2.5) for the flight conditions specified in Table 1.

Table 1: SU2 Fluid solver parameters for the HIRENASD Wing

Parameter	
Turbulence model	Spalart–Allmaras
Mach number	0.8
Temperature (K)	279
Reynolds number	7×10^6

The structural solver that is implemented in this work is the finite element-based elasticity. The implementation allows for static structural analysis using large-deformations problem with compressible Neo-Hookean material model, which is embraced in order to add material non-linearities into the problem. As a linear solver, Conjugate Gradient which is used only for elasticity problems is selected. SU2 allows only three inputs for material properties. In the HIRENASD project, 18 Nickel Maraging Steels whose mechanical properties are shown in Table 2 is used as structure material.

Table 2: 18 Nickel Maraging Steels Mechanical Properties

Parameter	
Elasticity modulus (Pa)	1.81×10^{11}
Poisson ratio	0.264
Density (kg/m^3)	7920

After the fluid and structural solvers inputs are prepared, coupled calculations are performed with the Block Gauss-Seidel method, which is widely used for the resolution of the strong coupling in the computational simulation of FSI.

Sihmehmet Yildiz, Enes Cakmak, Emre Kara and Melike Nikbay

3.1.2   Results of the Aeroelastic Analysis

Aeroelastic analyses are performed at 3 different angles of attack to validate the analyses results. The wing tip deflections for three different angles of attack are shown in Fig. 5. These aeroelastic analyses are performed using a workstation with 32-core 2.4GHz processors. Convergence is observed after 100 iterations in approximately 6 hours.
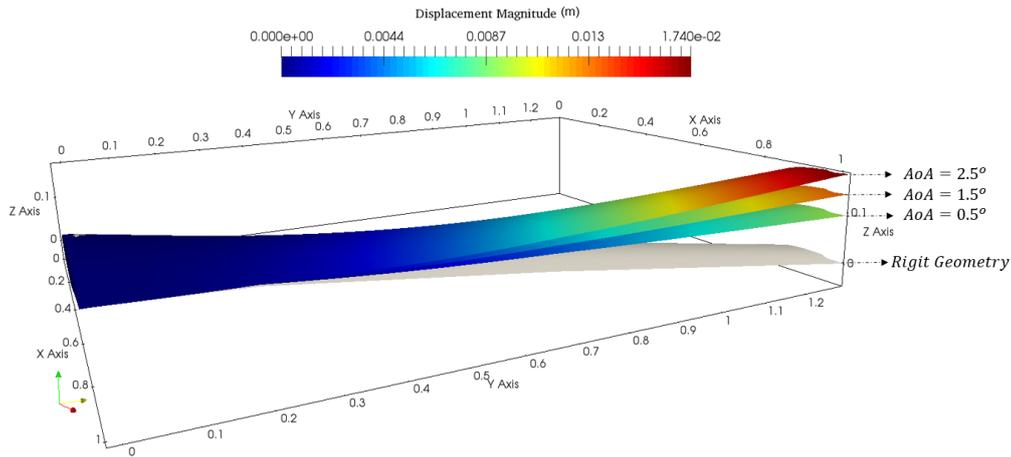
Figure 5: Deformation of the HIRENASD wing for different angle of attack

.

In order to validate the results obtained, the pressure coefficient values on the geometry and displacement values are compared with the experimental results [34]. The pressure distributions obtained in certain sections along the span on the wing are shown in Fig. 6.
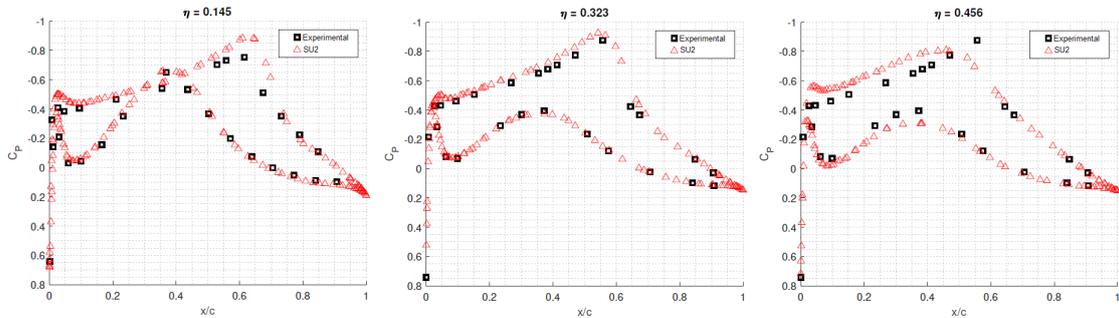
Figure 6: Comparison of pressure coefficient distributions at $M = 0.80$, $Re = 7 \times 10^6$ and $AoA = 1.5^o$.

The maximum wing tip displacement values on geometry obtained with the SU2 are compared with the experimental data [34]. The results are shown in Fig. 7.

Sihmehmet Yildiz, Enes Cakmak, Emre Kara and Melike Nikbay
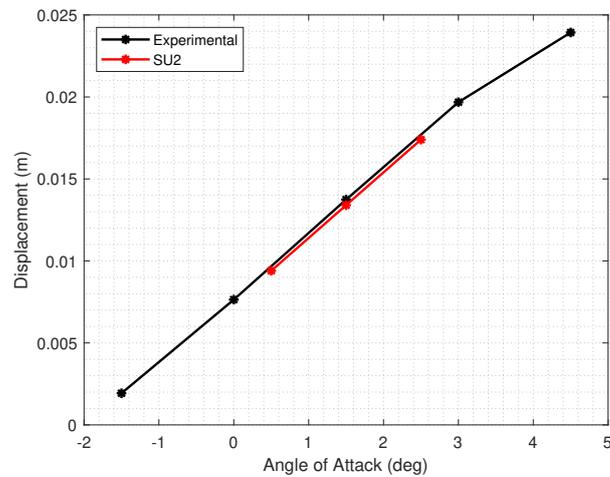
Figure 7: Comparison of maximum displacements between SU2 and experimental data
.

When Fig. 6 and 7 are examined, it is seen that the obtained results agree well with the experimental results. These results confirm that the performed aerolastic analysis can be used for the UQ study.

3.2 Uncertainty Quantification of Aeroelastic Systems

In this subsection, aeroelastic UQ study is explained. Firstly, the dominant uncertain variables are determined by a sensitivity analysis. Then, using the dominant variables, the UQ study is carried out with different surrogate models.

3.2.1 Sensitivity Analysis

Although the required number of analyses varies depending on the surrogate modelling methods, the computational cost is usually exponentially dependent on the number of random parameters. For this reason, global sensitivity analysis is performed to identify important uncertain parameters for the aeroelastic behaviour of the HIRENASD wing. Statistical properties of uncertain variables used in the sensitivity analysis are given in Table 3.

Table 3: Statistics of uncertain variable.

Uncertain Variable	Distribution	Mean	Standard Deviation
Mach	Normal	0.8	0.0016
Angle of Attack (°)	Normal	1.5	0.0750
Elasticity Module (Pa)	Normal	1.81×10^{11}	7.24×10^9
Material Density (kg/m^3)	Normal	7920	316.8
Poisson Ratio	Normal	0.264	0.0025

The aim is to identify important uncertainty variables and the precision of the results is not critical. Therefore, analysis is performed for 40 different variable value combinations in the SU2 program with low convergence criterion (10^{-6}) and fluid-structure iteration (10) number. With the displacement values obtained from the analysis results, surrogate

Sihmehmet Yildiz, Enes Cakmak, Emre Kara and Melike Nikbay

models are established with Kriging, PCE and PC-K methods. First-order Sobol indices are calculated with 10^6 sampling using the established surrogate models.
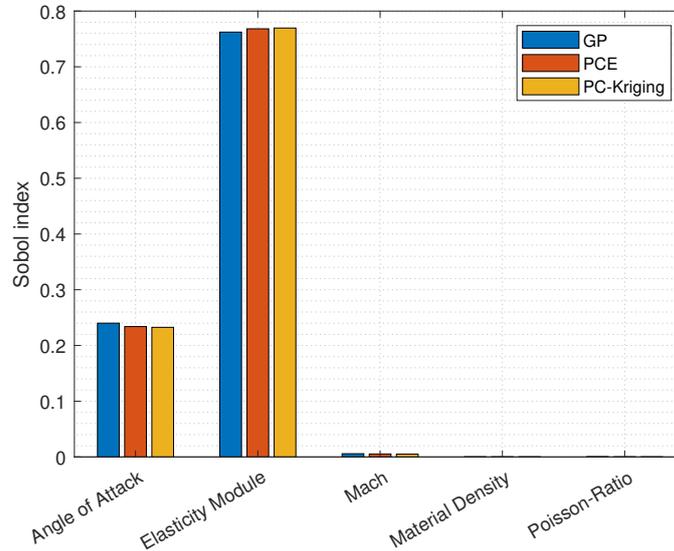
Figure 8: Global sensitivity index of uncertain variables

The values of the first Sobol indices obtained as a result of the sensitivity analysis are shown in Fig. 8. The Sobol indices obtained with different surrogate models give similar results. It is seen that the effect of material density and Poisson ratio on displacement values is negligible. Therefore, uncertainty analyses will be performed using elasticity module, angle of attack, and Mach number parameters, which are relatively important relative to other parameters, as uncertain variables.

3.3 Aeroelastic Uncertainty Quantification

In this section, aeroelastic uncertainty analysis is performed for the HIRENASD geometry using the random parameters determined as a result of the sensitivity analysis. Firstly, a surrogate model for maximum wing displacement values is established using the AL-GP method. The process of creating a surrogate model with AL-GP started with 5 training data. Aeroelastic analysis is performed at the design point where the estimated variance value was maximum in each iteration, and the results were added to the training set. This process continued until the maximum estimated variance value in the design space was less than 10^{-3}. The AL-GP method terminated at the end of the 13th iteration, and the surrogate model is established with 18 analysis results for 3 variables. In this process, 15 test data randomly determined in the design space are used to observe the change in the global and local success of the surrogate model. At these test points, $RMSE$ and $MaxAE$ values are calculated at each iteration. The results are depicted in Fig. 9.

Sihmehmet Yildiz, Enes Cakmak, Emre Kara and Melike Nikbay
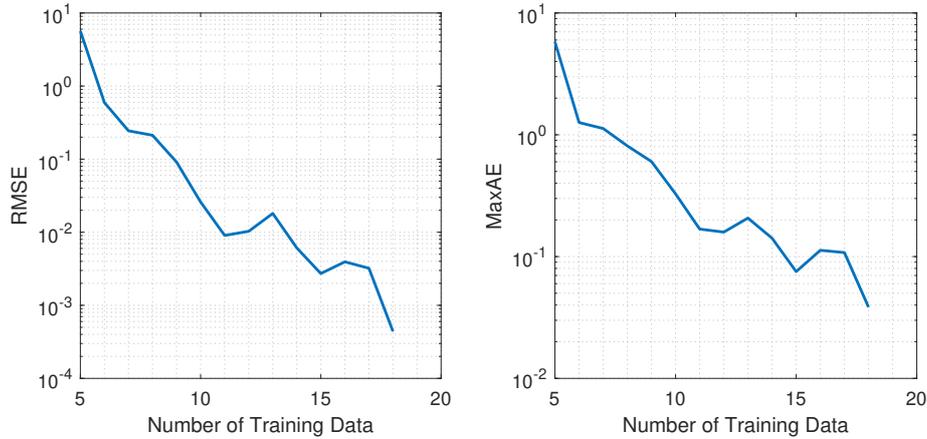
Figure 9: The change of the values of verification metrics in the Active Learning process.

In order to take the benefit of the Active Learning procedure, surrogate models are built using different metamodeling methods that did not use the AL procedure, and verification metrics were calculated. Two separate training datasets are created for the surrogate modelling methods to be used in the comparison.

- Dataset 1: Training dataset with 18 data determined by Halton sequence sampling method

- Dataset 2: Training dataset with 36 data determined by Halton sequence sampling method

Using the two training datasets, surrogate models are built and verification metrics are calculated. The results are listed in Table 4.

Table 4: Comparison of verification metrics of surrogate models

	AL-GP	**Kriging**	**Kriging**	**PCE**	**PCE**	**PC-K**	**PC-K**
Dataset		1	2	1	2	1	2
N_{train}	18	18	36	18	36	18	36
$RMSE_{train}$	3.65E-12	2.17E-13	2.80E-14	0.0038	0.0031	5.61E-07	2.27E-05
$RMSE_{test}$	4.39E-04	0.0082	0.0075	0.0060	0.0036	0.0021	0.0012
$MaxAE_{train}$	5.78E-06	1.48E-06	7.44E-07	0.0588	0.1366	2.30E-03	2.63E-02
$MaxAE_{test}$	3.84E-02	0.1844	0.1477	0.1520	0.1358	0.0838	0.0753
Max Error Test Point(%)	0.3417	1.6805	1.3154	0.9707	0.726	1.0416	0.4618

To observe the regression and prediction capabilities of the methods, the verification metrics are calculated for the train and test data, respectively. The results are listed in Table 4. As stated in the literature, it is expected that the Kriging method is more successful in capturing local features and the PCE method is more successful in capturing global features. When the verification metrics of the PC-K method are examined, it is observed that it is better than the Kriging and PCE methods in capturing local and global features. Additionally, it is observed that the AL-GP method gives the most accurate results among all compared methods. This situation reveals the importance of

Sihmehmet Yildiz, Enes Cakmak, Emre Kara and Melike Nikbay

the positioning of the samples in surrogate modelling. Uncertainty analysis is carried out with the 10^7 realization points using the constructed surrogate models. Obtained results are given in Table 5.

Table 5: Results of the uncertainty quantification study with different surrogate models

	AL-GP	**Kriging**	**Kriging**	**PCE**	**PCE**	**PC-K**	**PC-K**
Dataset		1	2	1	2	1	2
N_{train}	18	18	36	18	36	18	36
Mean (mm)	13.5413	13.5414	13.5628	13.5752	13.5712	13.5433	13.5555
Standart Deviation (mm)	0.5937	0.5954	0.5933	0.6097	0.6149	0.5874	0.5922
Skewness	0.2063	0.1977	0.2004	0.2076	0.1942	0.1917	0.1995
Kurtosis	3.0798	3.1027	3.0879	3.0734	3.0564	3.0899	3.0854

Maximum wing tip displacement probability distribution obtained for AL-GP method and boxplots obtained for different methods are presented in Fig. 10.
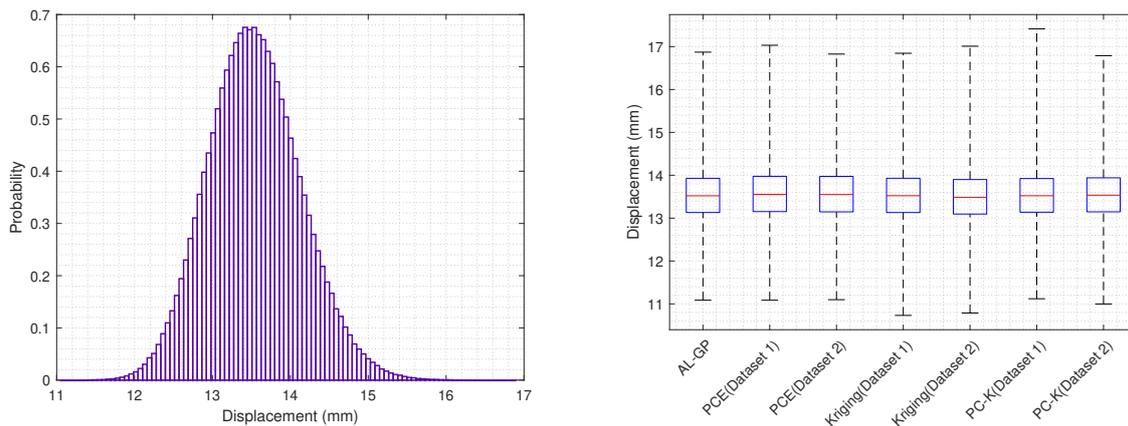
Figure 10: Probability distribution of maximum win tip displacement AL-GP, and box plots of max displacement based on different surrogate modelling.

When the uncertainty analysis results performed with different surrogate models as shown in Table 5 are examined, it is seen that the results of the methods are close to each other. There are slight differences between the results, mainly due to the accuracy of the established surrogate models. When the box plot graph given in Fig. 10 is examined, it is observed that there are differences between the minimum and maximum values obtained from the surrogate models. When the verification metrics are examined, it shows that the most accurate model is the surrogate model established with AL-GP. In this case, it can be stated that AL-GP results are more reliable than the results obtained by other methods.

4 CONCLUSIONS AND DISCUSSION

The goal of this paper was to establish an efficient and accurate surrogate model for high-fidelity aeroelastic analyses to be used in an uncertainty quantification study. For this, the Gaussian process method is assisted with an Active Learning method. The

Sihmehmet Yildiz, Enes Cakmak, Emre Kara and Melike Nikbay

Gaussian process estimated variance equation is used as an Active Learning information source. The approach is demonstrated on the HIRENASD wing geometry from 1st AIAA Aeroelastic Prediction Workshop. Before the uncertainty analysis, uncertain variables that have a significant effect on wing tip displacement were determined by the global sensitivity analysis. As a result of the sensitivity analysis, it is determined that the elasticity modulus, angle of attack and Mach number parameters had a significant effect on the wing tip displacement. Using these uncertain parameters, a surrogate model was established using the AL-GP method with 18 analyses results. In order to demonstrate the efficiency and accuracy of the established surrogate model by the AL-GP method, surrogate models were established with the PCE, Kriging and PC-K methods using training sets with 18 and 36 analyses determined by the Halton sequence method. The reason why these surrogate models are preferred for comparison is that the Kriging method is good at capturing local properties, the PCE method is good at capturing global properties, and the PC-K method is good at capturing both local and global properties. We aimed to determine the success of the AL-GP method for capturing both local and global features by comparing the surrogate model with these three methods. As a result of the $RMSE$ and $MaxAE$ verification metrics calculated using the test dataset, it is observed that the AL-GP method was more successful than other methods in capturing both global and local features. We conclude that an aeroelastic UQ analysis is performed using the AL-GP surrogate model for the HIRENASD geometry efficiently.

As future work, we plan to further integrate Active Learning algorithms into PCE and PC-Kriging methods and investigate the feasibility of these methods for multifidelity UQ studies. We would like to perform an aeroelastic UQ study for static displacement and flutter speeds of the NASA-CRM wing using multifidelity techniques.

ACKNOWLEDGEMENTS

REFERENCES

[1] P. Beran, B. Stanford, and C. Schrock. Uncertainty quantification in aeroelasticity. *Annual Review of Fluid Mechanics*, 49(1):361–386, Jan. 2017. doi:10.1146/annurev-fluid-122414-034441. URL `https://doi.org/10.1146/annurev-fluid-122414-034441`.

[2] N. A. S. Command. Airplane strength and rigidity, vibration, flutter, and divergence. In *Mil. Specif. MIL-A-8870C*. Nav. Air Syst. Command, Dep. Navy, 1993.

[3] B. Danowsky, J. Chrstos, D. Klyde, C. Farhat, and M. Brenner. Application of multiple methods for aeroelastic uncertainty analysis. In *AIAA Atmospheric Flight Mechanics Conference and Exhibit*. American Institute of Aeronautics and Astronautics, June 2008. doi:10.2514/6.2008-6371. URL `https://doi.org/10.2514/6.2008-6371`.

[4] A. M. Cunningham and R. J. Holman. Studies of aeroelastic uncertainty quan-

tification for a wind tunnel model and test program - overview and static aeroelastic analysis. In *55th AIAA Aerospace Sciences Meeting*. American Institute of Aeronautics and Astronautics, Jan. 2017. doi:10.2514/6.2017-1651. URL `https://doi.org/10.2514/6.2017-1651`.

[5] M. Nikbay and J. Heeg. Aeroelastic uncertainty quantification studies using the s4t wind tunnel model. In *55th AIAA Aerospace Sciences Meeting*. American Institute of Aeronautics and Astronautics, Jan. 2017. doi:10.2514/6.2017-1652. URL `https://doi.org/10.2514/6.2017-1652`.

[6] M. Nikbay, B. Stanford, T. K. West, and S. K. Rallabhandi. Impact of aeroelastic uncertainties on sonic boom signature of a commercial supersonic transport configuration. In *55th AIAA Aerospace Sciences Meeting*. American Institute of Aeronautics and Astronautics, Jan. 2017. doi:10.2514/6.2017-0040. URL `https://doi.org/10.2514/6.2017-0040`.

[7] B. D. Phillips and T. K. West. Aeroelastic uncertainty quantification of a low-boom aircraft configuration. In *2018 AIAA Aerospace Sciences Meeting*. American Institute of Aeronautics and Astronautics, Jan. 2018. doi:10.2514/6.2018-0333. URL `https://doi.org/10.2514/6.2018-0333`.

[8] S. Kawai and K. Shimoyama. Kriging-model-based uncertainty quantification in computational fluid dynamics. In *32nd AIAA Applied Aerodynamics Conference*. American Institute of Aeronautics and Astronautics, June 2014. doi:10.2514/6.2014-2737. URL `https://doi.org/10.2514/6.2014-2737`.

[9] P. S. Palar, K. Zakaria, L. R. Zuhal, K. Shimoyama, and R. P. Liem. Gaussian processes and support vector regression for uncertainty quantification in aerodynamics. In *AIAA Scitech 2021 Forum*. American Institute of Aeronautics and Astronautics, Jan. 2021. doi:10.2514/6.2021-0181. URL `https://doi.org/10.2514/6.2021-0181`.

[10] J. Weinmeister, X. Gao, and S. Roy. Analysis of a polynomial chaos-kriging metamodel for uncertainty quantification in aerodynamics. *AIAA Journal*, 57(6): 2280–2296, June 2019. doi:10.2514/1.j057527. URL `https://doi.org/10.2514/1.j057527`.

[11] I. Tartaruga, J. E. Cooper, G. Georgiou, and H. Khodaparast. Flutter uncertainty quantification for the s4t model. In *55th AIAA Aerospace Sciences Meeting*. American Institute of Aeronautics and Astronautics, Jan. 2017. doi:10.2514/6.2017-1653. URL `https://doi.org/10.2514/6.2017-1653`.

[12] M. Nikbay and P. Acar. Reduced order modelling for static and dynamic aeroelastic predictions with multidisciplinary approach. *CEAS Aeronautical Journal*, 6(3):455–469, Apr. 2015. doi:10.1007/s13272-015-0154-3. URL `https://doi.org/10.1007/s13272-015-0154-3`.

[13] S. Hosder, R. Walters, and M. Balch. Efficient uncertainty quantification applied to the aeroelastic analysis of a transonic wing. In *46th AIAA Aerospace Sciences*

Meeting and Exhibit. American Institute of Aeronautics and Astronautics, Jan. 2008. doi:10.2514/6.2008-729. URL `https://doi.org/10.2514/6.2008-729`.

[14] J. Weinmeister, N. Xie, X. Gao, A. K. Prasad, and S. Roy. Analysis of a polynomial chaos-kriging metamodel for uncertainty quantification in aerospace applications. In *2018 AIAA/ASCE/AHS/ASC Structures, Structural Dynamics, and Materials Conference.* American Institute of Aeronautics and Astronautics, Jan. 2018. doi:10.2514/6.2018-0911. URL `https://doi.org/10.2514/6.2018-0911`.

[15] P. S. Palar, K. Zakaria, L. R. Zuhal, K. Shimoyama, and R. P. Liem. Gaussian processes and support vector regression for uncertainty quantification in aerodynamics. In *AIAA Scitech 2021 Forum.* American Institute of Aeronautics and Astronautics, Jan. 2021. doi:10.2514/6.2021-0181. URL `https://doi.org/10.2514/6.2021-0181`.

[16] E. Pasolli and F. Melgani. Gaussian process regression within an active learning scheme. In *2011 IEEE International Geoscience and Remote Sensing Symposium.* IEEE, July 2011. doi:10.1109/igarss.2011.6049994. URL `https://doi.org/10.1109/igarss.2011.6049994`.

[17] X. Yue, Y. Wen, J. H. Hunt, and J. Shi. Active learning for gaussian process considering uncertainties with application to shape control of composite fuselage. *IEEE Transactions on Automation Science and Engineering*, 18(1):36–46, Jan. 2021. doi:10.1109/tase.2020.2990401. URL `https://doi.org/10.1109/tase.2020.2990401`.

[18] T. D. Economon, F. Palacios, S. R. Copeland, T. W. Lukaczyk, and J. J. Alonso. SU2: An open-source suite for multiphysics simulation and design. *AIAA Journal*, 54(3):828–846, Mar. 2016. doi:10.2514/1.j053813. URL `https://doi.org/10.2514/1.j053813`.

[19] *https : //su2code.github.io/docs_v7/Theory/*. Stanford University, Jan. 2012.

[20] R. Sanchez Fernandez. A coupled adjoint method for optimal design in fluid-structure interaction problems with large displacements. 2017. doi:10.25560/58882. URL `http://spiral.imperial.ac.uk/handle/10044/1/58882`.

[21] N. Wiener. The homogeneous chaos. *American Journal of Mathematics*, 60(4): 897–936, 1938. ISSN 00029327, 10806377. URL `http://www.jstor.org/stable/2371268`.

[22] A. I. J. Forrester, A. Sóbester, and A. J. Keane. *Engineering Design via Surrogate Modelling.* Wiley, July 2008. doi:10.1002/9780470770801. URL `https://doi.org/10.1002/9780470770801`.

[23] X. Yue, Y. Wen, J. H. Hunt, and J. Shi. Active learning for gaussian process considering uncertainties with application to shape control of composite fuselage. *IEEE Transactions on Automation Science and Engineering*, 18(1):36–46, 2021. doi:10.1109/TASE.2020.2990401.

[24] B. Settles. Active learning. *Synthesis Lectures on Artificial Intelligence and Machine Learning*, 6(1):1–114, June 2012. doi:10.2200/s00429ed1v01y201207aim018. URL `https://doi.org/10.2200/s00429ed1v01y201207aim018`.

[25] M. D. Morris and T. J. Mitchell. Exploratory designs for computational experiments. *Journal of Statistical Planning and Inference*, 43(3):381–402, Feb. 1995. doi:10.1016/0378-3758(94)00035-t. URL `https://doi.org/10.1016/0378-3758(94)00035-t`.

[26] M. D. McKay, R. J. Beckman, and W. J. Conover. A comparison of three methods for selecting values of input variables in the analysis of output from a computer code. *Technometrics*, 21(2):239, May 1979. doi:10.2307/1268522. URL `https://doi.org/10.2307/1268522`.

[27] M. M. Rajabi, B. Ataie-Ashtiani, and H. Janssen. Efficiency enhancement of optimized latin hypercube sampling strategies: Application to monte carlo uncertainty analysis and meta-modeling. *Advances in Water Resources*, 76:127–139, Feb. 2015. doi:10.1016/j.advwatres.2014.12.008. URL `https://doi.org/10.1016/j.advwatres.2014.12.008`.

[28] L. Kocis and W. J. Whiten. Computational investigations of low-discrepancy sequences. *ACM Transactions on Mathematical Software*, 23(2):266–294, June 1997. doi:10.1145/264029.264064. URL `https://doi.org/10.1145/264029.264064`.

[29] P. Jiang, Q. Zhou, and X. Shao. *Surrogate Model-Based Engineering Design and Optimization*. Springer Singapore, 2020. doi:10.1007/978-981-15-0731-1. URL `https://doi.org/10.1007/978-981-15-0731-1`.

[30] J. Heeg, P. Chwalowski, J. P. Florance, C. D. Wieseman, D. M. Schuster, and B. Perry. Overview of the aeroelastic prediction workshop. In *51st AIAA Aerospace Sciences Meeting including the New Horizons Forum and Aerospace Exposition*. American Institute of Aeronautics and Astronautics, Jan. 2013. doi:10.2514/6.2013-783. URL `https://doi.org/10.2514/6.2013-783`.

[31] P. Acar and M. Nikbay. Steady and unsteady aeroelastic computations of HIRENASD wing for low and high reynolds numbers. In *54th AIAA/ASME/ASCE/AHS/ASC Structures, Structural Dynamics, and Materials Conference*. American Institute of Aeronautics and Astronautics, Apr. 2013. doi:10.2514/6.2013-1800. URL `https://doi.org/10.2514/6.2013-1800`.

[32] https://heinrich.lufmech.rwth aachen.de/en/. Aachen University, June 2010.

[33] M. Nikbay and P. Acar. Aeroelastic predictions for steady and unsteady flow characteristics of the HIRENASD wing. *Progress in Computational Fluid Dynamics, An International Journal*, 16(1):26, 2016. doi:10.1504/pcfd.2016.074253. URL `https://doi.org/10.1504/pcfd.2016.074253`.

[34] P. Chwalowski, J. P. Florance, J. Heeg, C. D. Wieseman, and B. Perry. Preliminary computational analysis of the HIRENASD configuration in preparation for the aeroelastic prediction workshop. In *International Forum on Aeroelasticity and Structural Dynamics IFASD*, IFASD 2011-108, Paris, France, June 2011.

ROBUST DESIGN OF AIRCRAFT WING SIZING INCLUDING JIG TWIST SHAPE

L. Liu[1]*, C. Scarth[2] and J.E. Cooper[1]

[1] Dept of Aerospace Engineering
Faculty of Engineering
University of Bristol
University Walk, Bristol, BS81TR
long.liu@bristol.ac.uk
[2] Dept of Mechanical Engineering
University of Bath

Abstract *The aim of aircraft structural design is to produce a structure that enables the aircraft to meet all of the design requirements - range, performance, payload - whilst meeting all structural and aeroelastic constraints. Recent optimization approaches to achieve this goal have considered robust and reliable designs whereby uncertainties in the manufacturing, material and operating conditions are taken into consideration. This work will consider the effect that uncertainties in the jig (i.e manufactured shape on the ground) twist shape have upon design aerodynamic and aeroelastic performance. Robust design strategy is evaluated on a simple wing box model and compared to deterministic (i.e. no uncertainty) solutions to minimize wing weight, maximize lift over drag and maximize flight range. It is shown how it is important to consider jig shape uncertainties in the design optimization in order to produce viable practical solutions.*

Keywords: Jig Twist Shape, Aeroelastic performance, MDO, Robust and Reliable Optimisation

L. Liu, C. Scarth and J.E. Cooper

1. INTRODUCTION

The aircraft industry is searching for environmental friendly designs that not only reduce the environmental impact but also improve flight performance. Wing design is a very important part of aircraft structural design and several techniques have been proposed to tackle these contradictory requirements by improving flight efficiency and reducing fuel burn. One popular trend is the introduction of high aspect ratio wings (HARW) that can provide higher lift-to-drag ratios and longer ranges by reducing the induced drag [1, 2]. As the flight shape has an important influence on the aerodynamic drag acting, and it can be affected by the jig shape, it is significant to determine the jig shape required to achieve the desired flight shape for minimum weight when subjected to a range of constraints.

In order to further improve both weight and aerodynamic characteristics, the aeroelasticity optimization design method has been developed as a typical application of multi-disciplinary design optimization (MDO), which can overcome barriers between different discipline groups while reducing the design cycle time [3, 4]. Optimization techniques can be used to achieve significant improvements in the performance of structures, however, the effects of uncertainty can result in considerable degradation in performance in practice [5]. Traditional deterministic optimization methods are used with a safety factor to minimize the wing weight whilst satisfying different constrains, but it is believed that deterministic optimization approaches which cannot account for uncertainties in material and structural parameters in design process can result in an overly conservative solution. In actual applications, uncertainties related to geometry, material properties and the manufacturing process exist widely. As such, it can be desirable to incorporate uncertainty into the design process, which may be achieved using different approaches that can be broadly categorized as Reliability-Based Design Optimization (RBDO) [6] and Robust Design Optimization (RDO) [7]. Hence, the interest in reliable and robust design optimization methods is growing for an optimum wing design [8-13].

To consider the effect of uncertainties in the design process, effective uncertainty quantification approaches are required as the conventional Monte Carlo Simulation (MCS) method [14, 15] is highly computationally expensive and not practical for solving a robust and reliable design optimization problem. Gaussian Process Emulator is one kind of surrogate model that can conduct uncertainty quantification at a low computational cost [16-18]. Combined with constrained genetic algorithms [19], a robust optimization method assisted by surrogate models can be developed to produce an optimal design subjected to constraints with a good robustness.

In this paper, the thickness distribution of the leading and trailing edge spars and jig twist distribution are used as design parameters to explore the effect of uncertainties on high aspect ratio wing designs. By considering the uncertainty of these two kinds of parameters in design process, a robust wing box optimization example is presented to find the optimal spar sizes and jig twist angle distributions that lead to the minimum wing weight, maximum lift over drag and maximum Breguet range under aeroelastic constraints according to different optimization strategies. Finally, the effect of coefficient of variations on the optimal solution is discussed.

L. Liu, C. Scarth and J.E. Cooper

2. WING MODEL AND ANALYSIS METHOS

2.1 WING MODEL

As shown in Figure 1, one detailed Finite Element (FE) model for a high aspect ratio wing box is used for the analyses presented in this paper. In this model, there are two skin panels (upper skin and lower skin), two spars (leading edge (LE) and trailing edge (TE)), one stringer panel from the root midline to the tip midline and 21 ribs uniformly distributed from the root to tip. In this paper, the jig twist shape is determined by three parameters, namely the twist angle at the root, mid-span and tip. The wing jig twist is varied at mid-span and tip, and the jig twist angle at the root is assumed as zero. The changes between these locations are linearly interpolated, as is shown in Figure 2, and more information on the simple wing box model is shown in Table 1.

(a) Wing box along the wing span

(b) Wing box cross section
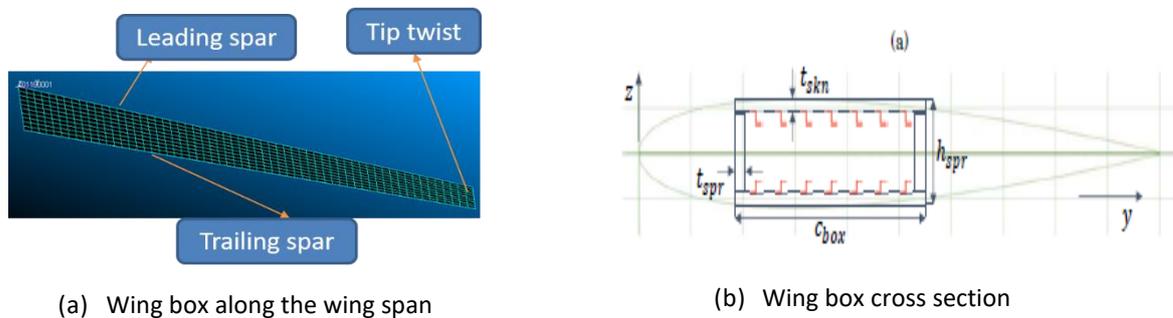
Figure 1 Simple wing-box model

Table 1 Basic parameter information of the simple wing box model

Parameter	Value
Wing span	20 m
Sweep angle Λ	20 degrees
Root chord length	1 m
Tip chord length	0.5 m
Upper and lower skin thickness	2 mm
Rib thickness	20 mm
Stringer thickness	10 mm
Angle of attack	5 degrees
Spar width	15 cm

L. Liu, C. Scarth and J.E. Cooper
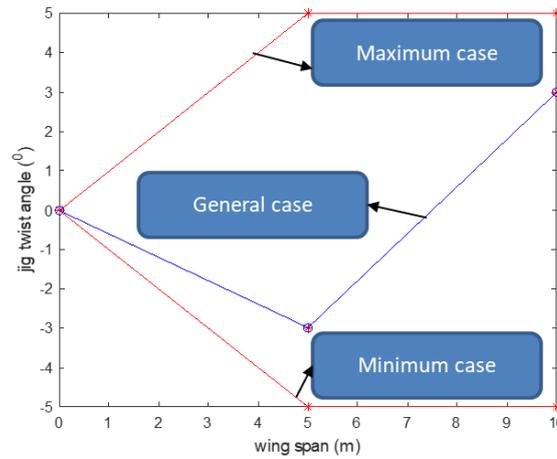
Figure 2 Jig twist shape variations

As is shown in Figure 3, five shape functions are used to define the thickness distribution of each spar, reducing the number of parameters required to describe the thickness distribution of two spars. The formulation of these five shape functions are, for wing semi-span L

$$y_1 = 1 \tag{1}$$

$$y_2 = \frac{x}{L} \tag{2}$$

$$y_3 = 1 - \frac{x}{L} \tag{3}$$

$$y_4 = 1 - \left(\frac{x}{L}\right)^2 \tag{4}$$

$$y_5 = \left(\frac{x}{L}\right)^2 \tag{5}$$

where x represents the location along the wing. Based on these five shape functions, the thickness distribution of two spars can be constructed using

$$\begin{aligned} y_{tl} &= a_1 y_1 + a_2 y_2 + a_3 y_3 + a_4 y_4 + a_5 y_5 \\ &= (a_5 - a_4)\left(\frac{x}{L}\right)^2 + (a_2 - a_3)\left(\frac{x}{L}\right) + a_1 + a_3 + a_4 \end{aligned} \tag{6}$$

$$\begin{aligned} y_{tt} &= a_6 y_1 + a_7 y_2 + a_8 y_3 + a_9 y_4 + a_{10} y_5 \\ &= (a_{10} - a_9)\left(\frac{x}{L}\right)^2 + (a_7 - a_8)\left(\frac{x}{L}\right) + a_6 + a_8 + a_9 \end{aligned} \tag{7}$$

where y_{tl} and y_{tt} are the thickness distribution of leading spar and trailing spar respectively, and $a_i (i = 1, 2, ..., 10)$ are ten thickness parameters describing the thickness distribution of two spars. In this way, the thickness of two spars at each location can be represented by ten thickness parameters. It can be seen that the thickness of two spars at each location is 60 mm at the thickest case, and the thinnest case is 3mm. Adding two jig twist parameters to describe the wing jig shape then there are a total of twelve design parameters, namely ten thickness

L. Liu, C. Scarth and J.E. Cooper

parameters and two twist parameters, whose variation range and uncertainty covariance are shown in Table 2 (assuming all the design parameters are distributed with Gaussian distributions whose coefficient of variations is 0.1. A base value of 0.1 degrees is added on the covariance of tip twist parameter to prevent the jig twist angle uncertainty being zero when the mean value is zero).

Table 2 Variation range and covariance for twelve design parameters

Design parameter	Variation range	Covariance
Ten thickness parameter $a_i (i = 1, 2, ..., 10)$	[1,20]	0.1* mean
Tip twist angle	[-5, 5] degrees	0.1+0.1* mean
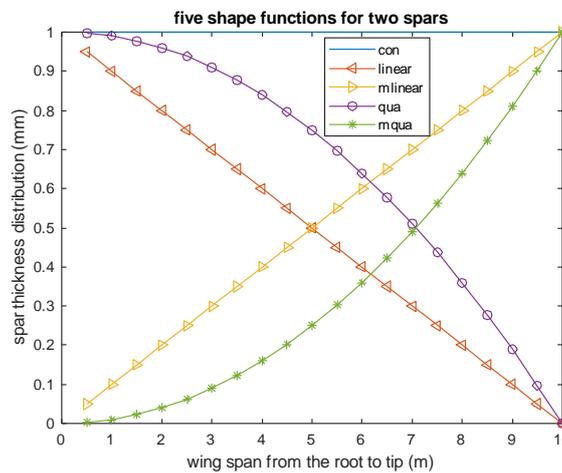
Figure 3 Five shape functions to construct spar thickness distribution

2.2 AEROELASTIC CONSTRAINTS AND DESIGN REQUIREMENTS

In the aircraft design process, consideration of aeroelasticity is one of the critical design criteria towards completing the certification process. In this model, trimmed analysis, aeroelastic instabilities and discrete gust loads are considered. The trimmed analysis involves the calculation of the static response, including loads and stresses in the structures at different flight conditions which is necessary for wing structural design. In this model, the lift is always the same no matter how we change the spar thickness distribution and the jig shape. The static aeroelastic analysis is modelled in MSC. Nastran with SOL 144. The aeroelastic stability is assessed using MSC Nastran SOL 145, which employs the frequency matching 'p-k' method to predict the flutter speed.

For discrete gust load, the gust velocity varies in deterministic manner which is represented using '1-cosine' gust profile. The expression governing the '1-cosine' gust is given by

$$w_g(t) = \frac{w_{g0}}{2}(1 - \cos\frac{2\pi V}{L_g}t) \tag{8}$$

where V is the flight speed, L_g is the gust length, w_{g0} is obtained by

L. Liu, C. Scarth and J.E. Cooper

$$w_{g0} = U_{ref} F_g \left(\frac{H}{107} \right)^{\frac{1}{6}} \tag{9}$$

where U_{ref} is the reference gust velocity which is assumed as 13.41m/s, H is gust gradient distance which equals to half the gust length, F_g is the flight profile alleviation factor which is assumed as 1. In this paper, the flight speed is set to 230m/s. The gust length L_g is chosen to vary from 18m to 216m. MSC Nastran is used to evaluate the discrete gust response with SOL 146. Based on the time history curves for 6 different gust length, the maximum and minimum gust response for each gust length can be obtained and then the plot of the maximum and minimum gust responses for different gust length can be obtained. Further details can be found in [20]. In this paper, the flutter speed, the maximum stress at three locations, maximum tip twist angle, maximum tip displacement, root bending moment and root torque are set as aeroelastic constraints.

In this paper, three design requirements are discussed, namely minmizing wing weigh, maximizing lift/drag, maximizing range. For wing weight, it can be determined by the thickness distribution of spars as the mass of all the other parts are constant. For the calculation of lift/drag, lift coefficient CL is obtained by the lift distribution from MSC Nastran. The induced drag coefficient CDi is calculated according to the lift distribution based on lifting line theory [21] and in this study it is assumed that CDi/CD=0.4 in cruise (CD is total drag coefficient), then CL/CD can be translated to the calculation of CL/CDi. According to Breguet range function [4], the cruise range can be obtained based on CL/CD and wing weight. More details on these computations are provided in Section 3.

2.3 SURROGATE MODEL

For reasons of the computational cost arising from the effects of random parameters variations in optimisation algorithms, surrogate models are used to approximate the outputs quickly. Gaussian Process Emulator (GPE) assumes that the model output y is distributed with a Gaussian probability distribution rather than a determined value given arbitrary input vector **x**. Thus the GPE can be determined by finding the mean and covariance function of the Gaussian Process. Firstly, training points are assumed given as the output matrix **y** corresponding to a number of n training data points $(\mathbf{x}_1, \mathbf{x}_2, ..., \mathbf{x}_n)$ can be obtained by experiments. Then some inferences including the mean and covariance function can be obtained based on training points. Assume the mean function as

$$E\{f(x) | \boldsymbol{\beta}\} = \mathbf{h}^T(\mathbf{x}) \boldsymbol{\beta} \tag{10}$$

where **h(x)** is the basis function and $\mathbf{h}(\mathbf{x}) = (1, \mathbf{x}^T)$, and it can be seen that the mean function is conditional on the weight parameter **β** which can be determined by training points. Generally, the output can be represented as a smooth function which means the output value for a point x is close to that for a point near x. Thus the covariance function can be assumed as

$$\text{cov}\{f(\mathbf{x}), f(\mathbf{x}') | \sigma^2, B\} = \sigma^2 c(\mathbf{x}, \mathbf{x}') \tag{11}$$

where

$$c(\mathbf{x}, \mathbf{x}') = \exp\{-(\mathbf{x} - \mathbf{x}')^T B(\mathbf{x} - \mathbf{x}')\} \tag{12}$$

the scaling factor σ^2 and roughness matrix B will be approximated based on training points.

Based on Eqs. (10)-(12), the output corresponding to arbitrary test points can be determined as

$$[f(\mathbf{x})|\mathbf{y}, \sigma^2, B, \boldsymbol{\beta}] \sim GP(m^*(x), c^*(x, x')) \tag{13}$$

where

$$m^*(\mathbf{x}) = \boldsymbol{\beta}^T[\mathrm{h}(\mathbf{x}) - H^T A^{-1}\mathbf{t}(\mathbf{x})] + \mathbf{y}^T A^{-1}\mathbf{t}(\mathbf{x}) \tag{14}$$

$$c^*(\mathbf{x}, \mathbf{x}') = c(\mathbf{x}, \mathbf{x}') - \mathbf{t}^T(\mathbf{x}) A^{-1}\mathbf{t}(\mathbf{x}) \tag{15}$$

$$\mathbf{t}^T(\mathbf{x}) = [c(\mathbf{x}, \mathbf{x}_1), ..., c(\mathbf{x}, \mathbf{x}_n)] \tag{16}$$

$$H^T = [h^T(\mathbf{x}_1), ..., h^T(\mathbf{x}_n)] \tag{17}$$

$$A = \begin{bmatrix} 1 & c(\mathbf{x}_1, \mathbf{x}_2) & ... & c(\mathbf{x}_1, \mathbf{x}_n) \\ c(\mathbf{x}_2, \mathbf{x}_1) & 1 & & \vdots \\ \vdots & & \ddots & \\ c(\mathbf{x}_n, \mathbf{x}_1) & \cdots & & 1 \end{bmatrix} \tag{18}$$

x is the test point, $(\mathrm{f}(\mathbf{x}_1), \mathrm{f}(\mathbf{x}_2), ..., \mathrm{f}(\mathbf{x}_n))$ are the outputs corresponding to training points $(\mathbf{x}_1, \mathbf{x}_2, ..., \mathbf{x}_n)$. It can be seen that Eq. (13) is still conditional on σ^2, B and $\boldsymbol{\beta}$ that are determined by using Maximum Likelihood Estimation (MLE), and more specific process can refer to [18]. Commonly, the mean function m*(x) in Eq. (14) is used to predict the output matching arbitrary input vector approximately and the covariance function in Eq. (15) is assumed to represent the prediction error.

3. OPTIMIZATION FRAMEWORK

3.1 MULTIDISCIPLINARY DESIGN OPTIMIZATION

Multidisciplinary design optimization (MDO) is very crucial for the conceptual design of the aircraft as the aircraft design entails multiple conflicting performance criteria related to different disciplines. In this study, the robust optimization challenge consists of optimizing the wing jig shape and spar thickness distribution to balance the confidence of achieving aerodynamic or structural performance and satisfying load constraints. The problem consists of three different disciplinary analyses:

(1) Aerodynamic performance analysis which can be represented by lift over drag
(2) Structural performance analysis which can be represented by wing weight
(3) Loads calculations which can be presented by the aeroelastic constraints

In order to perform an optimization that considers simultaneously both structural and aerodynamic performances, the objective function must combine the wing aerodynamic and structural properties. In this study, the aircraft Breguet range function [4], commonly used in aircraft design is chosen such that

$$R = \frac{V}{g} \frac{1}{SFC} \frac{L}{D} \ln\left(\frac{W_{initial}}{W_{final}}\right) \tag{19}$$

where R is the range, V is the flight speed, g is the acceleration of gravity, SFC represents specific fuel consumption and they are assumed as constant parameters in this question, L/D means lift over drag, $W_{initial}$ represents initial weight of the aircraft W_{final} represents the aircraft final weight.

In this equation, L/D represents the aerodynamic performance while $W_{initial}/W_{final}$ represents the structural optimization term. According to several formulation transformations, the aircraft range evaluation can be reduced to a function of the wing weight and the lift-to-drag ratio as

$$R = f(L/D, W_w) \tag{20}$$

and therefore the range maximization yields a trade-off between W_w minimization and L/D maximization.

3.2 DETERMINISTIC OPTIMIZATION

A general deterministic optimization problem is introduced in order to illustrate the necessity to conduct the robust design strategy. A general deterministic optimization problem is expressed as:

$$\min_x f(\mathbf{x})$$
$$s.t. g(\mathbf{x}) \le 0 \tag{21}$$
$$\mathbf{x}_L \le \mathbf{x} \le \mathbf{x}_U$$

where $f(\mathbf{x})$ is the objective, $g(\mathbf{x})$ the aeroelastic constraints, and $\mathbf{x}$ the design variable vector whose lower and upper bounds is denoted as $\mathbf{x}_L$ and $\mathbf{x}_U$ respectively. In this paper, there are twelve design parameters, which can be expressed as:

$$\mathbf{x} = [t_1, t_2, t_3, t_4, t_5, t_6, t_7, t_8, t_9, t_{10}, \theta_1, \theta_2] \tag{22}$$

where $t_i (i=1,2,...,10)$ represents thickness parameters to describe the spar thickness distribution, and $\theta_i (i=1,2)$ is the jig twist angle relative to the root in degrees.

3.3 ROBUST DESIGN OPTIMIZATION

For robust design optimization, the uncertainty of input parameters needs to be considered in the design process and the objective function changes to be one combination of mean value and standard deviation. A robust design optimization problem can be expressed as:

$$\min_x F(\mu(f(\mathbf{x})), \sigma(f(\mathbf{x})))$$
$$s.t. P(g(\mathbf{x}) \le g_{cri}) \ge P_{cri} \tag{23}$$
$$\mathbf{x}_L \le \mathbf{x} \le \mathbf{x}_U$$

In this study, P_{cri} =99.74% and the constraints are added into the objective function in the form of penalty function. The optimization process can be formed as following, as is shown in Figure 4:

Step 1: Use Nastran to compute the aeroelastic constraints (stress, tip displacement, tip twist, root bending moment, root torque, flutter speed) given 200 input samples generated by LHS for training the surrogate models.

Step 2: Use Nastran to compute the stress, tip displacement, tip twist, root bending moment, flutter speed given 60 input samples generated by Latin Hypercube Sampling (LHS) [22] for validating the accuracy of the surrogate models (error within 2%)

Step 3: Generate multiple populations for the first generation.

Step 4: For each population, generate 10000 samples around it according to the uncertainties defined. Based on the surrogate models constructed, calculate the aeroelastic constraints, lift/drag, wing weight and flight range.

Step 5: According to different optimization objective, calculate the fitness function (such as the mean value or standard deviation of flight range)

Step 6: Check whether the optimization converged or the maximum generation achieved. If yes, output the optimal solution and end. If no, generate new generations based on the information collected (through selection, mutation and crossover) and go back to Step 4 until convergence.
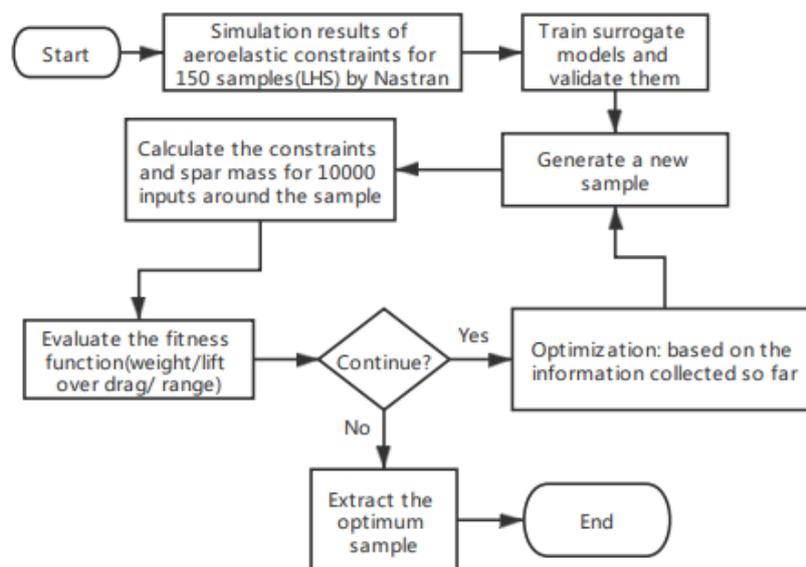
Figure 4 Robust optimization flowchart

4. RESULTS AND DISCUSSION

In this paper, the optimization problem is separated into two single questions first, namely maximizing aero dynamic performance objectives and minimizing the wing weight. Finally, the two objectives are integrated as a flight range driven design optimization question with the help of Breguet function, by means of which the jig twist parameters that match a good aerodynamic performance as well as weight performance is found.

4.1. Optimization on wing weight

To minimize the wing weight, three optimization strategies are conducted. Firstly, deterministic is used to minimize the wing weight subjected to aeroelastic constraints. The optimal spar thickness distribution and jig twist shape are shown in Figure 5. It was found that the leading spar thickness is thinner than that of trailing spar. The optimal jig twist shape is

the minimum case. However, if we consider the uncertainty of design parameters, the optimal solution will violate stress constraints, as is shown in Figure 6. It can be found that the tip displacement and tip twist angle can violate the critical value with a big probability. Therefore, it is not safe to use deterministic optimal solutions as the optimization result. There are two ways to solve this effect. One is to add a safety factor when using deterministic optimization, the other one is to consider parameter uncertainties in the design process.

(a) Deterministic optimal spar thickness distribution   (b) Deterministic optimal jig shape
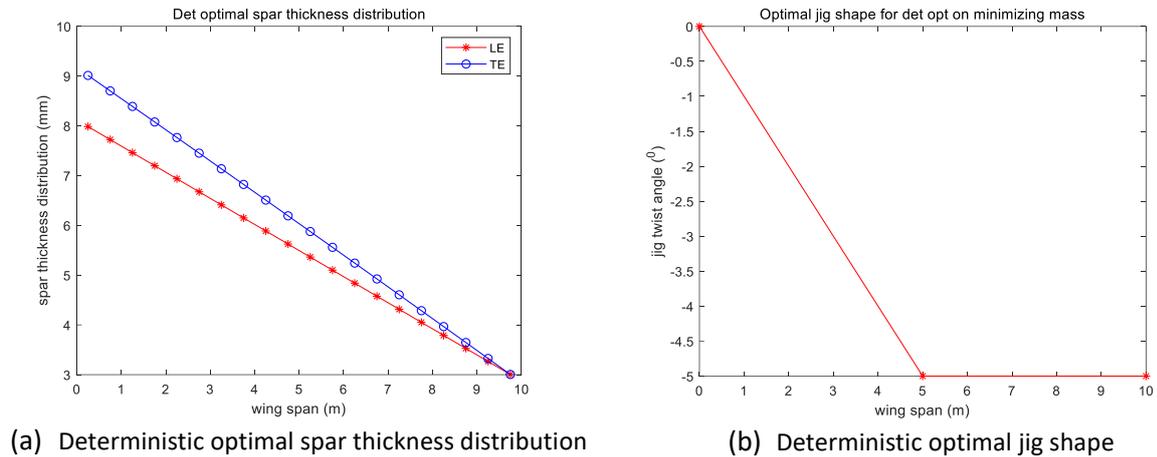
Figure 5 Deterministic optimal spar thickness distribution and jig twist shape
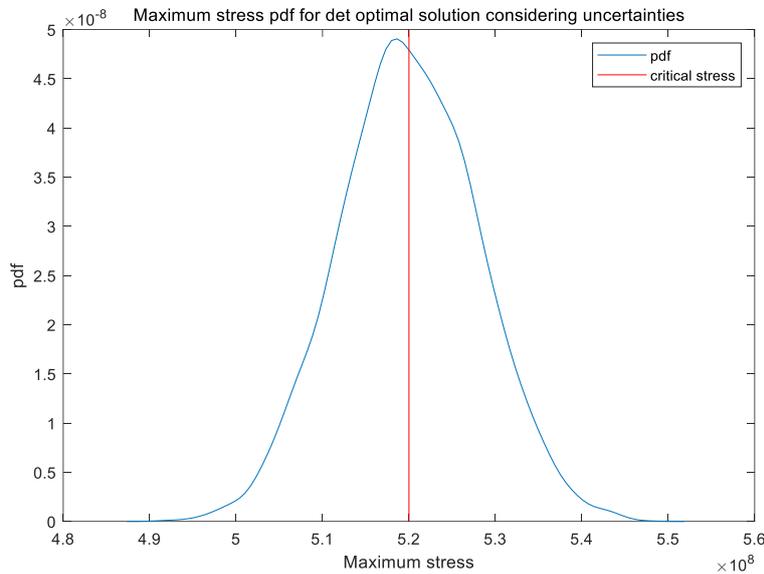
Figure 6 pdfs of the maximum stress for deterministic optimal solution considering uncertainties

To consider the uncertainties in the optimization process, robust optimization is conducted and the optimal solution is compared with that of deterministic optimization with or without a safety factor, as is shown in Figure 7. It can be found that the spar mass obtained by the deterministic optimal solution is thinnest, but it is not safe as illustrated before. The optimal solution from deterministic optimization with a safety facor is much heavier than those of robust and deterministic optimization, which means it is too conservative. Thus, it is necessary to consider parameter uncertainties in the design process to achieve a good weight performance. For robust optimization and deterministic optimization with a safety factor of

1.5, all the constraints satisfy the critical values with a probability larger than 99.74%. The pdfs of maximum stress for these three optimal solutions on minimizing wing weight are shown in Figure 8.
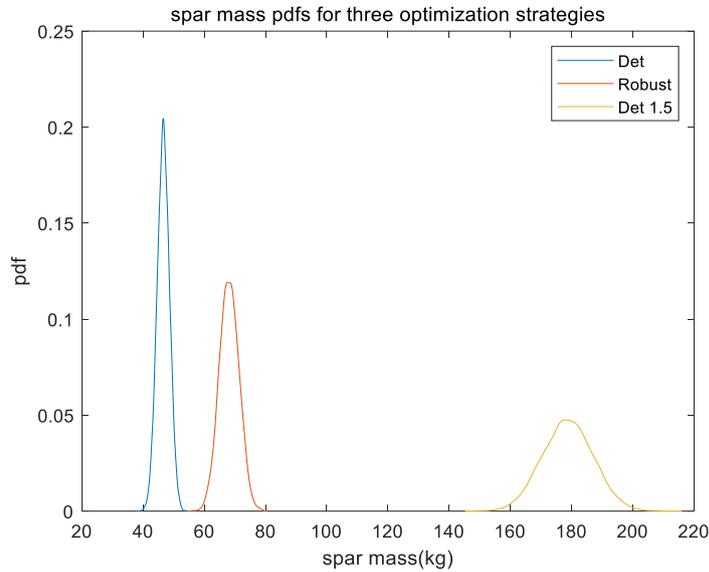
Figure 7 Optimization results on wing weight for three optimization strategies
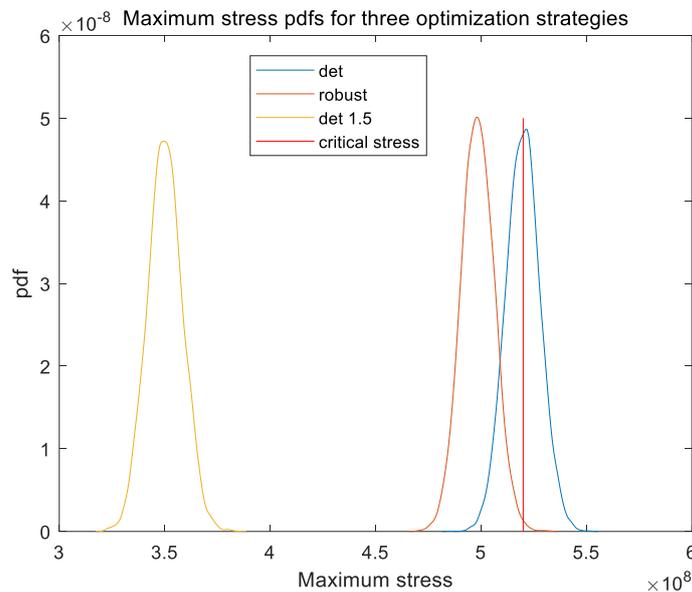
Figure 8 pdfs of the maximum stress for three optimal solutions minimizing wing weight

4.2. Optimization on lift over drag

Similarly, three optimization strategies are conducted to maximize lift over drag. The pdfs of lift/drag for three optimal solutions are shown in Figure 9. The optimal jig twists for these three optimization strategies are shown in Figure 10. It can be found that more outboard load will be added if we want to maximize the mean value of CL/CD.
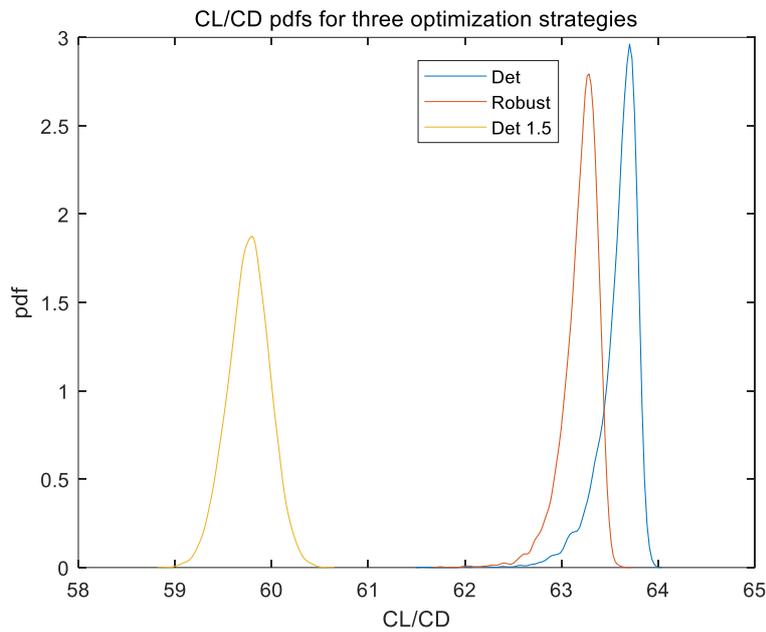
Figure 9 Optimization results on CL/CD for three optimization strategies
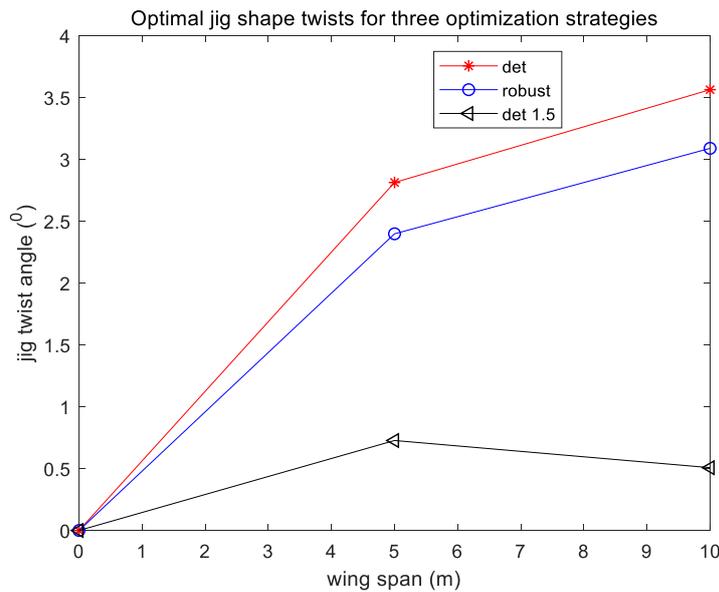
Figure 10 Optimal jig twist shape for three optimization strategies on CL/CD

4.3 OPTIMIZATION ON FLIGHT RANGE

For flight range optimization, four optimization strategies are conducted first and the result is shown in Figure 11. It can be found that the average range from minimizing range standard deviation is even smaller than that of deterministic optimization (with a safety factor of 0.5) results. It means the average range will be smaller if the standard deviation needs to be minimized. Robustness is achieved at the expense of weight. The balance between range mean value and standard deviation will be determined in practice according to optimization aims. What is clear from Figure 11 is that the reliable optimization strategy "min mean" provides near as good estimates as the deterministic answers. As is shown in Figure 12, the

optimal jig shape angle for four optimization strategies are compared. It can be found that the optimal jig twist shapes for minimizing range standard deviation are almost zero along the wing. The reason is the uncertainties of jig twist parameters are minimum when the coefficient of variations is zero. The uncertainties of jig twist parameters will increase with the increase of jig twist parameter absolute values, which leads to the increase of standard deviation for outputs.
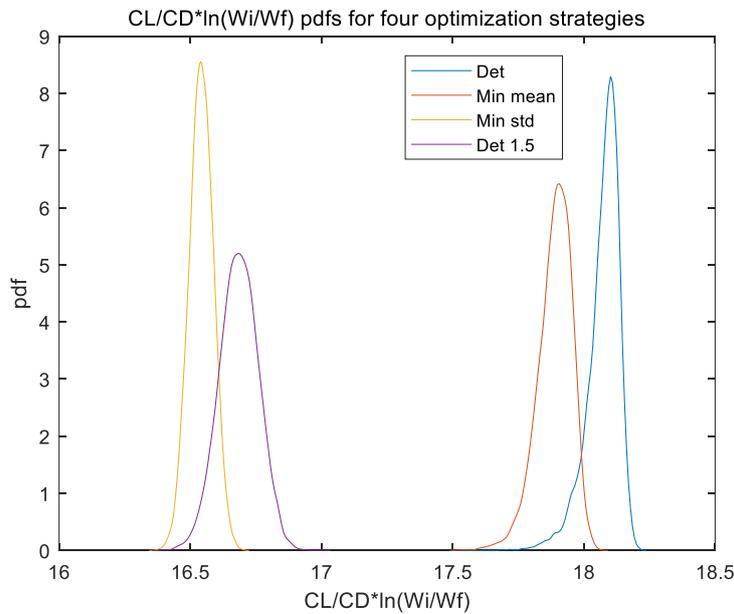
Figure 11 Optimization results on flight range for three optimization strategies
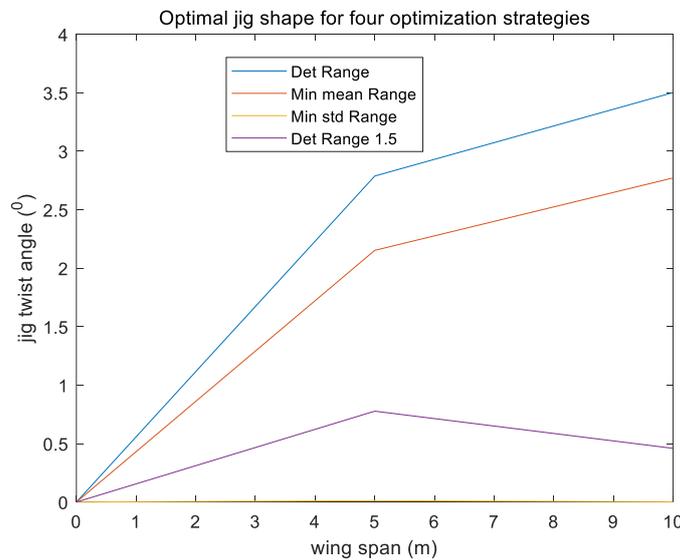
Figre 12 Optimal jig twist angle for four optimization strategies

As is shown in Figure 13, the optimal jig twist angle for three optimization objectives are compared. It can be found that the jig twist angle for maximizing CL/CD is the largest to provide more outboard load. The optimal jig twist for minimizing wing mass is the smallest. It adds a minus jig twist along the wing to minimize the wing weight. The optimal jig twist for maximizing range is between those two optimal jig twist to make a balance between these

L. Liu, C. Scarth and J.E. Cooper

two objectives. The optimal jig shapes for maximizing range and maximizing CL/CD are similar.
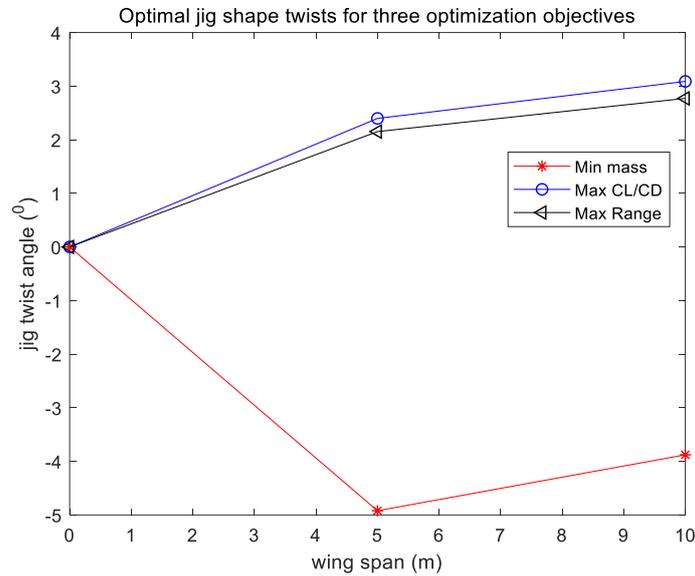
Figure 13 Optimal jig twist angle for three optimization objectives

Although the optimal jig twist shapes for maximizing CL/CD and maximizing range are similar, the spar thickness distribution is different, as is shown in Figure 14. It can be found that the spar weight for maximizing range is a little heavier than that of maximizing CL/CD.
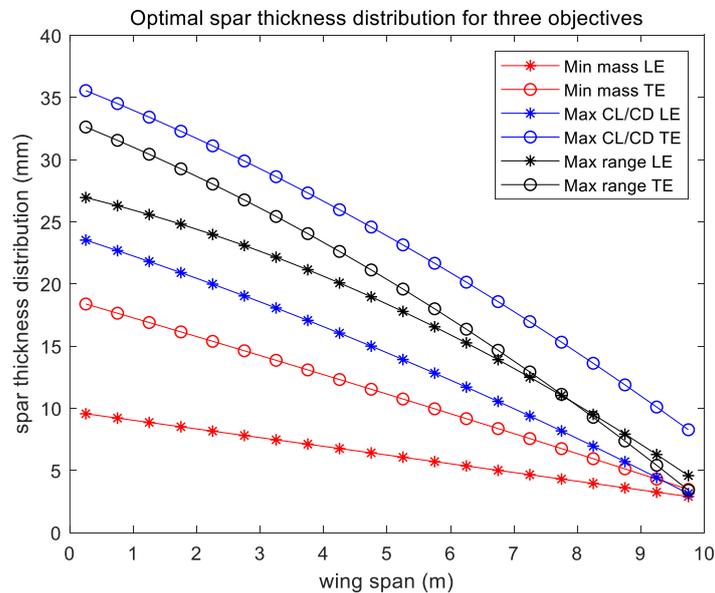
Figure 14 Optimal spar thickness distribution for three optimization objectives

5. CONCLUSIONS

A robust design optimisation approach is presented on a simple wing box model to incorporate design parameter uncertainty into the design process. The optimisation objective is to minimise weight/maximise lift over drag/maximise range subject to multiple aeroelastic constraints, including stress, tip displacement, tip displacement and flutter margin. The procedure accounts for stochastic variations in spar thickness and jig twist parameters. Based

L. Liu, C. Scarth and J.E. Cooper

on grounds of computational cost, a Gaussian Process Emulator is used for the quantification of the effect of uncertainties on structural weight and lift/drag. The results presented in this paper support the following conclusions:

The optimal solutions for deterministic and robust optimization are different. The deterministic optimal solution can violate the constraints with a big probability when considering the design parameter uncertainties, while the robust optimal solution will always satisfy the constraints with a designed probability.

Optimising for robustness successfully reduces the design sensitivity to stocastic variations at the cost of additional weight/lift over drag.

The optimal jig shape for maximizing lift/drag and maximizing range is almost the same, but the optimal spar thickness distribution is different, where the optimal spar weight for maximizing range is a little larger than that of maximizing lift/drag.

For different optimization objectives, the optimal jig twist shape and spar thickness distribution can be rather different, so it is needed to make a balance when several optimization objectives needs to be considered simultaneously.

ACKNOWLEDGMENTS

REFERENCES

1. Afonso, F., Vale, J., Oliveira, É., Lau, F., and Suleman, A. "A review on non-linear aeroelasticity of high aspect-ratio wings," *Progress in Aerospace Sciences* Vol. 89, 2017, pp. 40-57.
doi: https://doi.org/10.1016/j.paerosci.2016.12.004
2. Abbas, A., de Vicente, J., and Valero, E. "Aerodynamic technologies to improve aircraft performance," *Aerospace Science and Technology* Vol. 28, No. 1, 2013, pp. 100-132.
doi: https://doi.org/10.1016/j.ast.2012.10.008
3. Mastroddi, F., Tozzi, M., and Capannolo, V. "On the use of geometry design variables in the MDO analysis of wing structures with aeroelastic constraints on stability and response," *Aerospace Science and Technology* Vol. 15, No. 3, 2011, pp. 196-206.
doi: https://doi.org/10.1016/j.ast.2010.11.003
4. Benaouali, A., and Kachel, S. "Multidisciplinary design optimization of aircraft wing using commercial software integration," *Aerospace Science and Technology* Vol. 92, 2019, pp. 766-776.
doi: https://doi.org/10.1016/j.ast.2019.06.040
5. Kuttenkeuler, J., and Ringertz, U. "Aeroelastic tailoring considering uncertainties in material properties," *Structural optimization* Vol. 15, No. 3, 1998, pp. 157-162.
doi: 10.1007/BF01203526
6. Frangopol, D. M., and Maute, K. "Life-cycle reliability-based optimization of civil and aerospace structures," *Computers & Structures* Vol. 81, No. 7, 2003, pp. 397-410.
doi: https://doi.org/10.1016/S0045-7949(03)00020-8
7. Padulo, M., Forth, S. A., and Guenov, M. D. "Robust Aircraft Conceptual Design Using Automatic Differentiation in Matlab." Springer Berlin Heidelberg, Berlin, Heidelberg, 2008, pp. 271-280.
8. Othman, M. F., Silva, G. H. C., Cabral, P. H., Prado, A. P., Pirrera, A., and Cooper, J. E. "A robust and reliability-based aeroelastic tailoring framework for composite aircraft wings," *Composite Structures* Vol. 208, 2019, pp. 101-113.
doi: https://doi.org/10.1016/j.compstruct.2018.09.086
9. Paiva, R. M., Crawford, C., and Suleman, A. "Robust and Reliability-Based Design Optimization Framework for Wing Design," *AIAA Journal* Vol. 52, No. 4, 2014, pp. 711-724.
doi: 10.2514/1.j052161
10. Scarth, C., Sartor, P. N., Cooper, J. E., Weaver, P. M., and Silva, G. H. C. "Robust and Reliability-Based Aeroelastic Design of Composite Plate Wings," *AIAA Journal* Vol. 55, No. 10, 2017, pp. 3539-3552.
doi: 10.2514/1.j055829
11. Liang, Y., Cheng, X.-q., Li, Z.-n., and Xiang, J.-w. "Robust Multi-Objective Wing Design Optimization Via CFD Approximation Model," *Engineering Applications of Computational Fluid Mechanics* Vol. 5, No. 2, 2011, pp. 286-300.
doi: 10.1080/19942060.2011.11015371
12. Manan, A., and Cooper, J. "Design of Composite Wings Including Uncertainties: A Probabilistic Approach," *Journal of Aircraft* Vol. 46, No. 2, 2009, pp. 601-607.
doi: 10.2514/1.39138

13. Nikbay, M., and Kuru, M. N. "Reliability Based Multidisciplinary Optimization of Aeroelastic Systems with Structural and Aerodynamic Uncertainties," *Journal of Aircraft* Vol. 50, No. 3, 2013, pp. 708-715.

doi: 10.2514/1.C031693

14. Kim, T.-U., and Hwang, I. H. "Optimal design of composite wing subjected to gust loads," *Computers & Structures* Vol. 83, No. 19, 2005, pp. 1546-1554.

doi: https://doi.org/10.1016/j.compstruc.2005.02.002

15. Touran, A., and Wiser, E. P. "Monte Carlo Technique with Correlated Random Variables," *Journal of Construction Engineering and Management* Vol. 118, No. 2, 1992, pp. 258-272.

doi: doi:10.1061/(ASCE)0733-9364(1992)118:2(258)

16. Fricker, T. E., Oakley, J. E., Sims, N. D., and Worden, K. "Probabilistic uncertainty analysis of an FRF of a structure using a Gaussian process emulator," *Mechanical Systems and Signal Processing* Vol. 25, No. 8, 2011, pp. 2962-2975.

doi: https://doi.org/10.1016/j.ymssp.2011.06.013

17. Marrel, A., Iooss, B., Laurent, B., and Roustant, O. "Calculations of Sobol indices for the Gaussian process metamodel," *Reliability Engineering & System Safety* Vol. 94, No. 3, 2009, pp. 742-751.

doi: https://doi.org/10.1016/j.ress.2008.07.008

18. O'Hagan, A. "Bayesian analysis of computer code outputs: A tutorial," *Reliability Engineering & System Safety* Vol. 91, No. 10, 2006, pp. 1290-1300.

doi: https://doi.org/10.1016/j.ress.2005.11.025

19. Yeniay, Ö. "Penalty Function Methods for Constrained Optimization with Genetic Algorithms," *Mathematical and Computational Applications* Vol. 10, No. 1, 2005, pp. 45-56.

20. Wright, J. R., and Cooper, J. E. *Introduction to aircraft aeroelasticity and loads*: John Wiley & Sons, 2008.

21. Houghton, E. L., Carpenter, P. W., Collicott, S. H., and Valentine, D. T. "Aerodynamics for engineering students." Seventh edition / ed., Butterworth-Heinemann, Kidlington, United Kingdom, 2017.

22. Sheikholeslami, R., and Razavi, S. "Progressive Latin Hypercube Sampling: An efficient approach for robust sampling-based analysis of environmental models," *Environmental Modelling & Software* Vol. 93, 2017, pp. 109-126.

doi: https://doi.org/10.1016/j.envsoft.2017.03.010

MODELLING VARIABILITY IN ADDITIVELY MANUFACTURED MATERIAL FOR TOPOLOGY OPTIMIZATION

Daniel D Pepler[1*] and Craig A Steeves[1]

1: Advanced Aerospace Structures Laboratory
Institute for Aerospace Studies
University of Toronto
4925 Dufferin St, North York, ON, Canada
d.pepler@mail.utoronto.ca, csteeves@utias.utoronto.ca

Abstract. *Topology optimization is a powerful optimization technique for efficiently generating optimal structures that can be very intricate, far beyond what a human designer could conceive. Additive manufacturing (AM) is one of the few manufacturing approaches that can be employed to construct such designs. However, the layering common to all additive manufacturing systems creates both anisotropic and stochastic material properties. If these material properties are not considered during the topology optimization, heavy manual post processing is required to ensure a robust design. This paper discusses the uncertainty expected in AM materials, and how the uncertainty can be measured using digital image correlation, quantified and incorporated in a numerical model. This employs a novel layered finite element that explicitly models the inherent morphology of AM materials. It is ideal for use in density-based topology optimization, because it enables modelling both the anisotropic and stochastic material properties simultaneously. The results indicate that the observable variation in the properties of AM materials can be modelled using layered elements.*

Keywords: Uncertainty, Quantification, Topology, Optimization, Additive, Manufacturing

Daniel D Pepler and Craig A Steeves

1 INTRODUCTION

Topology optimization is an optimization tool that finds material configurations that maximize chosen performance metrics. Structural topology optimization complements additive manufacturing because it often produces complex structures and the layer-by-layer additive manufacturing approach is capable of printing these structures [1]. Additionally, additive manufacturing has the potential to waste less material and operate in a small production facility. However, additive manufacturing techniques are not regularly being implemented in industry because of inconsistency in the properties of the printed material [2, 3].

It is difficult to model or directly measure variability in the material properties because the layer fusion process is highly non-linear and localized [2, 3]. The fusion processes include phenomena such as metal grain growth or polymer entanglement, which are computationally prohibitive to predict at the scale necessary to model additive manufacturing. There are also process induced defects which cause local material variation, which is difficult to measure because conventional testing techniques give spatially averaged values and more advanced testing techniques are not well suited to additively manufactured material. For example, atomic force microscopy can measure local Young's modulus, but it requires a smooth surfaces for Young's modulus determination. While in theory the surface of an additively manufactured material could be polished, the heating from the polishing can change the fusion characteristics near the surface. This may make the measured properties at the surface unrepresentative of the rest of the material. Since Young's modulus cannot be measured directly, an indirect measurement coupled to a data analysis technique is required.

The overall goal of this paper is to present an integrated process where simple experiments can be performed to collect relevant data for the determination of spatial fields of Young's modulus in additively manufactured material for use in finite element analysis. This process begins by performing a tensile test using digital image correlation (DIC) to collect the surface strain field data. The strain data are transformed into the Young's modulus field. The necessary random field properties can be calculated using the Young's modulus field, and then integrated into a novel finite element model for additively manufactured material. Finally, the random field properties and the novel finite element model enable stochastic finite element analysis to be performed for any given structure, a necessity for any robust topology optimization algorithm. Developing the experimental techniques, data reduction process and numerical methods simultaneously ensures that there is a seamless pipeline from experimentation to computational design.

1.1 Additive Manufacturing

Additive manufacturing processes use a layer-by-layer manufacturing method. In general, these approaches require a 3D CAD model that is 'sliced' into layers. Each layer is built sequentially from the base to the top of the part. This layering process introduces unique material properties which depend on how the layers are constructed. In general, all additively manufactured material exhibits anisotropy caused by fusion of the layers. When considering different additive manufacturing processes, the major sources of variation are caused by differences in the material and the fusion process. When considering variation within the same additive manufacturing process, the major sources of variation are related to in-fill pattern, material choice, and processing conditions. This

Daniel D Pepler and Craig A Steeves

variation in material properties is difficult to control or predict, and as a result additively manufactured material properties exhibit apparently random spatial variability.

Currently, a major focus of additive manufacturing research is improving the consistency of additively manufactured material by reducing the uncertainty and anisotropy of the printed material [1, 3]. In contrast, the research described here will focus on a method to measure and manage the spatial variation in the properties of existing materials. This paper uses fused filament fabrication (FFF) as exemplary of the physical phenomena which could cause observed variation in material properties. FFF was chosen because it is the most common additive manufacturing method [4] and has known process-induced defects. While this paper focuses on FFF, the method is not inherently limited to FFF material and could be used to control the impact of local variation for any additively manufactured material.

In polymer FFF, a molten filament is deposited based on a computer generated in-fill pattern one layer at a time, creating the 3D structure [5]. As the molten filament is placed on the previous layer its heat locally remelts the previous layer allowing the filaments to fuse [5]. The heat from the molten filament allows the polymer chains in the previous layer to entangle with the polymer chains in the molten filament; this entanglement process is called 'fusion' [6]. This thin region connecting printed filaments will be referred to as the fusion layer, while all other material will be referred to as the bulk layer. The weld layer is typically indented, and can be measured using an optical microscope.

The amount of fusion between the molten filament and the previous layer depends on the ambient temperature, the air gap and the melt temperature [5]. Additionally, vibrations can cause print head movement, which results in local misalignment of the filaments. Overall, the balance of parameters is difficult to optimize, and the fusion region typically exhibits less stiffness and strength compared with bulk material properties [6, 7]. This variation in material properties causes material anisotropy, and a bulk orthotropic composite model can be used to describe FFF material [8–14]. Additionally, composite failure models [15, 16] can be used to predict failure in FFF material [17–20]. While composite models work well in some cases, there are significant differences between conventional composites, such as carbon-fibre reinforced epoxy, and FFF printed material.

Process induced defects like voids, unmelted material, and misalignment of layers cause variations in local material properties. All of these defects decrease the fused surface area, the consequences of which can be modelled by a stochastic Young's modulus. For voids or unmelted material the reduction in stiffness is localized, and should only affect a small area around the defect. Assuming that defects in one layer do not affect the presence of defects in another layer, correlation only exists along the printed path. This allows the effect of defects to be described using a series of 1D correlated random fields.

1.2 Density Based Topology Optimization

Topology optimization, popularized by Bendsoe and Sigmund [21] with the solid isotropic material with penalization (SIMP) method, can very efficiently and simply solve the structural optimization problem, as demonstrated by Sigmund's 99-line MATLAB code [22]. This efficiency comes from the use of a fixed mesh and allowing material to have intermediate density between solid and void. The continuous density enables the use of gradient based optimization. However, intermediate density holds little physical meaning so, to limit the prevalence of intermediate densities, they are penalized by a power greater than

one. This penalized density is used in the calculation of the Young's modulus, which is separable from the integral for the element stiffness matrix. By maintaining this separability, sensitivities with respect to the density can readily be determined. If the Young's modulus is described by a random distribution, the separation of the Young's modulus from the integral for the element stiffness matrix also separates the random variable, which simplifies the calculation of the statistical moments of the material stiffness.

In robust topology optimization algorithms the statistical moments of the stiffness matrix are used to calculate the statistical moments of the displacement. These statistical moments of displacement are necessary for calculating quantities of interest, such as the mean and standard deviation of compliance. In Section 4 it will be shown that the measured Young's modulus distribution is well suited for determining the random field properties required for performing stochastic finite element analysis, and hence to serve as the underlying physical model necessary for robust topology optimization.

2 EXPERIMENTAL METHODS AND RESULTS

The purpose of the experiments is to collect empirical data on the spatial variation of the elastic properties of the FFF material. As discussed in the introduction, it is difficult to measure local variation in the Young's modulus directly. However, DIC can be used to measure local variation in surface strain, which is related to the local Young's modulus. Using the simple assumption that the relationship between the strain and the Young's modulus is inversely linear enables the development of a model to infer the Young's modulus based on strain data. In Section 3 it will be shown how this Young's modulus data will be used calculate the necessary random field properties; specifically, the mean Young's modulus, its standard deviation, and a correlation length are required.

2.1 Material Testing Method

A rectangular sheet of FFF printed polylactic acid (PLA) of length, width, and thickness 260 mm, 280 mm, and 3.5 mm was used for the specimens. To isolate the material properties orthogonal to the printing direction, all layers had the same unidirectional printing direction, as shown in Fig.1. The layer height was 0.2 mm and the machine accuracy was reported as 0.05 mm. The print speed was set to 50 mm/sec, while the print and bed temperature were set to 200°C and 50°C, respectively.
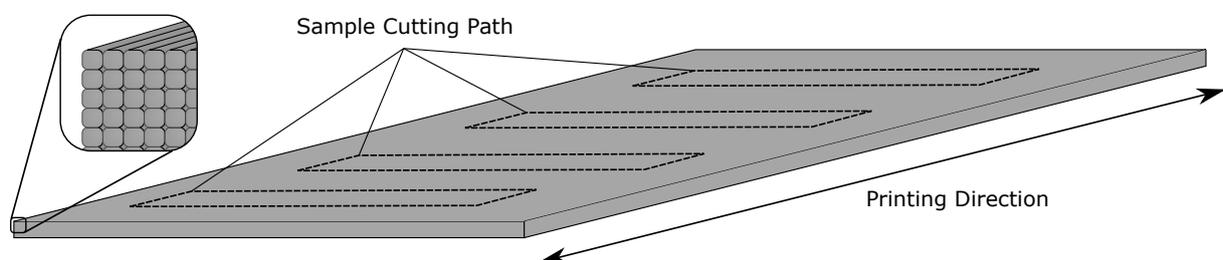
Figure 1: A sketch of a plate of FFF printed material, showing the orientation of the printed filaments and the orientation of the rectangular tensile samples.

Four rectangular tensile samples 20 mm x 180 mm x 3.5 mm were cut from a plate of FFF printed PLA. The specimens were oriented such that the long edge was perpendicular to the printing path, as shown in Fig.1. A black and white speckle pattern was applied

to each specimen using an airbrush. Each speckle pattern was analysed to ensure that the ratio of black to white was within 10% of a 1:1 ratio. Additionally, care was taken to ensure that the speckle size was between 10 μm and 40 μm, and that the distribution of speckles appeared sufficiently random. These factors are important for achieving the desired resolution and accuracy in the DIC analysis. A controlled tensile force was applied using an MTS load frame. Each sample was secured such that there was at least 4 cm of material within each grip. The load frame piston displacement rate was 0.1 mm/sec.

Images were captured using a FLIR camera with square pixels to simplify the DIC analysis. A Tamron macro lens was used to achieve the desired pixel physical size of 10 μm. Five images were collected every 0.5 mm of piston displacement. While the images were being captured, the load frame was held stationary. Each set of five images images was averaged to limit the effect of static noise when capturing images. Limiting the noise is important as the DIC radius must be relatively small (200 μm to 400 μm).

The open source 2D Ncorr MATLAB software was used for DIC analysis. When setting up the DIC analysis a subset radius of 20 pixels and a subset spacing of 1 pixels were used. For the convergence criteria the norm of the difference vector cutoff and maximum number of iterations were set to the defaults of 1×10^{-6} and 50, respectively. A radius of 10 pixels was used to calculate strain. Only the axial strains are reported here because that was the only direction that showed any significant variation in strain, as was expected given the direction of the load.

Two of the four samples were sanded to determine if the surface roughness, caused by the 3D printing process, had any effect on the DIC analysis. Additionally, when the specimens were tested, a second test was performed on the same specimen rotated 180°. The results of these experiments verified, to the authors' satisfaction, that the observed variation in strain corresponds with variation in the Young's modulus and is not an artifact of the testing procedure.

2.2 Tensile Experiment Results

The first sample was strained to failure due to fracture, following a different image capturing procedure than the one outlined in the methods section. The images were captured every 0.1 mm of cross-head displacement (1 s) during the continuous displacement of the sample. Figure 2 shows a specimen after 2.6 mm displacement, overlaid with the axial strain field calculated using DIC. The alternating horizontal lines of low and high strain correspond to the bulk layers and fusion layers of the material, indicating a difference in elastic properties in the two layers. An inadvertent pre-existing flaw on the side of the specimen, indicated by the yellow arrow, is associated with a line of very high strain. The specimen eventually failed along this line.

2.3 Measurement of Layer Spacing

The DIC calculations on the strained sample indicate a distinct horizontal layering of the strain. These layers are correspond to the alternating bulk and fusion layers in the material. This can be corroborated through other measurements: if the layers of high strain correspond to fusion layers, the distance between strain peaks should correspond to layer spacing measured optically. For the optical measurements, a microscope was used to image the surface of four samples. For each sample image, five total layer thickness and five fusion layer thickness measurements were manually made (40 measurements total). A

Daniel D Pepler and Craig A Steeves
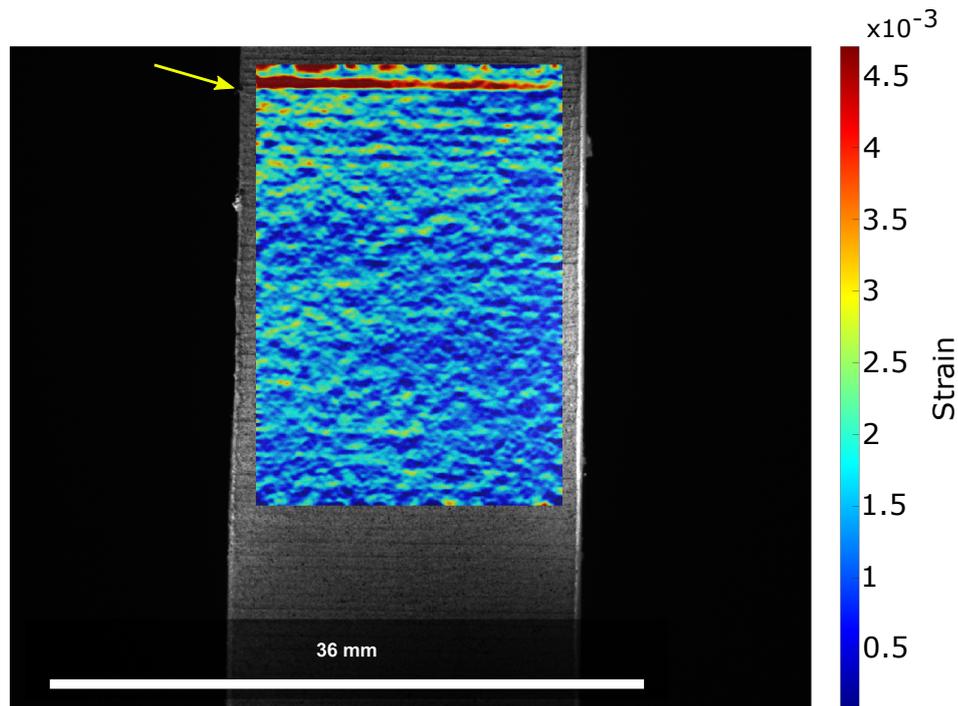
Figure 2: The specimen image and DIC strain field overlay, at 2.6 mm of cross-head displacement. The yellow arrow shows a pre-existing flaw which resulted in a line of higher strain in the fusion layer, and ultimately was the location were the sample fractured.

total layer includes both one bulk layer and one fusion layer. Representative measurements are shown in Fig.3(A). The optical microscope measurements were confirmed using the reference images captured for DIC, shown in Fig.3(B), and using the DIC results shown in Fig.4.

The mean and standard deviation of the optical measurements of the total layer thickness were 0.408 mm and 0.078 mm, respectively. The standard deviation of 0.078 mm was greater than the reported machine precision (0.05 mm), but is still within a reasonable margin. The fusion layer thickness measured optically required more user judgement because the beginning and end of the fusion layer must be selected manually. The mean and standard deviation of the fusion layer thickness were 0.045 mm and 0.016 mm, respectively. These measurements are used when constructing the mesh for finite element analysis.

Figure 4(A) is a plot of the mean of the strain for each horizontal line of pixels and Fig.4(B) displays contours of the strain field. The mean strain was used to confirm the optical microscope measurements. The total layer thickness is the distance between local maxima in the mean strain plot. Using this method, the mean and standard deviation of the total layer thickness were calculated as 0.412 mm and 0.068 mm, respectively. These measurements are within 1% of the optical microscope measurements. The crucial observation is that the spacing of the DIC strain peaks and troughs is consistent with the layer spacing of the FFF printed material. This is evidence that there is a difference in the material properties in the fusion layer and the bulk layer, specifically that the fusion layer corresponds to lower average Young's modulus, and that this difference can be measured using DIC.

Daniel D Pepler and Craig A Steeves
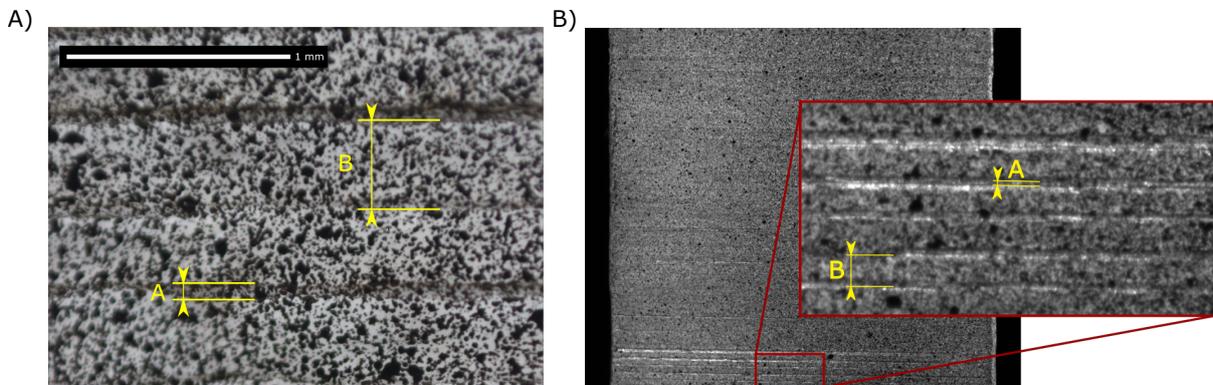
Figure 3: Layer thickness measurements using optical images. 'A' shows a sample measurement for the fusion layer thickness, and 'B' shows a sample measurement for the total layer thickness. (A) Microscope image of the tensile sample used for DIC analysis. (B) Reference image of the tensile sample used for DIC analysis.
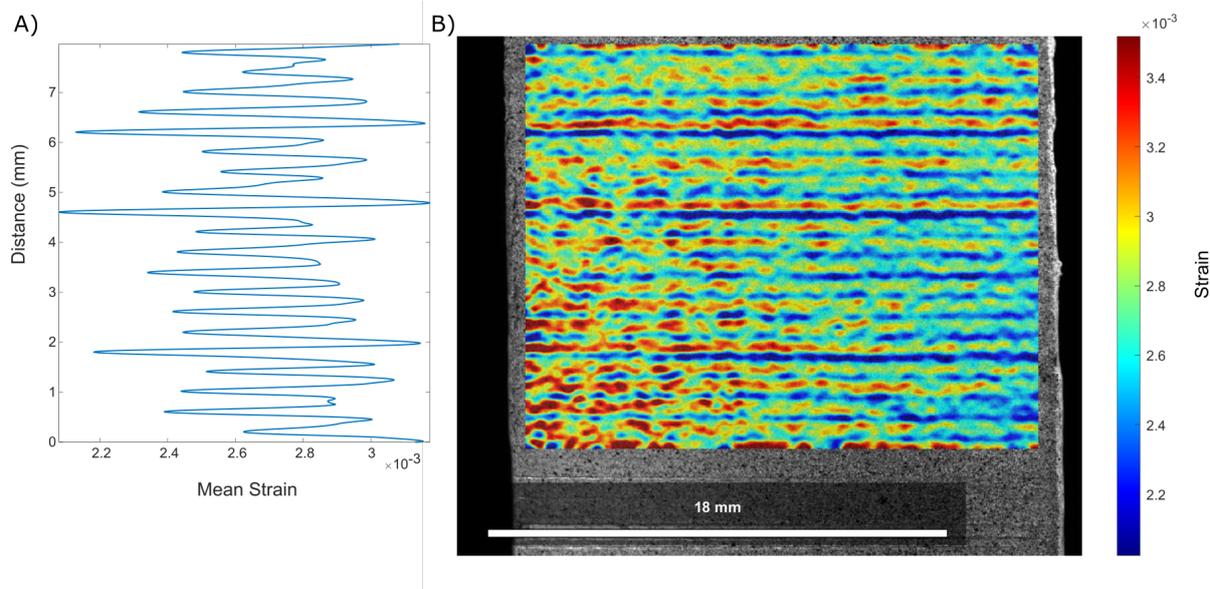
Figure 4: (A) The mean of the strain for each row of pixels. (B) DIC plot of the 2D surface strain.

Daniel D Pepler and Craig A Steeves

3 CHARACTERIZING YOUNG'S MODULUS FROM EXPERIMENTAL DATA

The goal of the material testing was to assemble relevant measured data that allow the inference of spatial fields of varying Young's modulus, from which the statistical properties of the field can be extracted. The following sections describe how the experimental results are used to generate a description of the field of elastic properties for use with finite element calculations. Numerical simulations show that the results are qualitatively consistent with the experimental data.

3.1 Inferring the Young's Modulus Field

The next step is to extract the Young's modulus field from the strain field. In order to convert the strain data to a Young's modulus field, a very simple linear relationship is assumed based upon Hooke's Law. This implies that there is no influence of horizontally adjacent material on the local behaviour of a material point. Given the known stress, σ, applied to the specimen during the experiment, the Young's modulus, E, for a given pixel is:

$$E = \frac{\sigma}{\epsilon} \tag{1}$$

where ϵ is the strain measured through DIC. The results of this transformation from strain to Young's modulus are displayed on Fig.5.
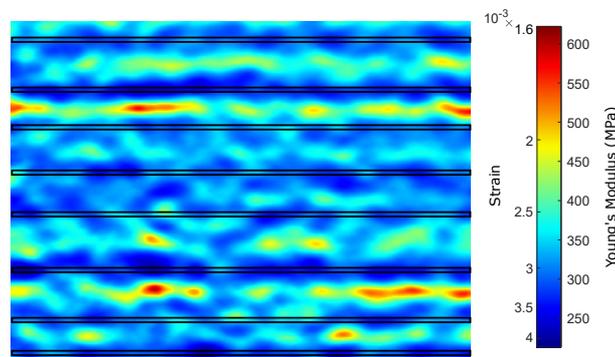
Figure 5: An example defining eight fusion layers based on strain maxima locations for a sample strain field. The inferred Young's modulus field is also shown with the same contours. The fusion layers are shown by the black rectangles, where the thickness of the rectangles is determined by the optically measured fusion layer thickness. Any data not within a black rectangle is considered part of the bulk layer.

The strain data are associated with either the bulk or fusion layers based on physical location, with one strain value for each pixel in the images. As shown in Section 2.3, the fusion layers are associated with the strain maxima and the locations of the strain maxima are considered the centres of fusion layers. The thickness of the fusion layer is set based on the measurements performed in Section 2.3 and the remainder of the region is considered as part of the bulk layers. An example of grouping the Young's modulus data into the two regions is also shown in Fig.5.

Daniel D Pepler and Craig A Steeves

3.2 Random Field Properties

Once the measured strain data have been converted into a Young's modulus field, the random field properties of the grouped bulk and fusion layer Young's modulus data from Section 3.1 are calculated. This includes calculating the mean and the standard deviation, as well as approximating the correlation length of the Young's modulus field for 1D fields. The mean and standard deviation are calculated using the standard operators,

$$E_{mean} = \sum_{e=1}^{N} E_e/N, \tag{2}$$

$$E_{std} = \sum_{e=1}^{N} \frac{(E_e - E_{mean})^2}{N}, \tag{3}$$

where E_{mean} is the mean of the Young's modulus data, E_{std} is the standard deviation of the Young's modulus data, N is the number of data points, and E_e refers to the eth Young's modulus data point. These calculations are performed separately on the bulk and fusion layer Young's modulus data.

The Young's modulus for the bulk layers has a mean and standard deviation of 353 MPa and 24 MPa, respectively, and the Young's modulus for the fusion layers has a mean and standard deviation of 314 MPa and 33 MPa, respectively. It was determined that these two regions had significantly different distributions by a two-sample Kolmogrorov-Smirnov test, which is a special form of a p-test used for non-Gaussian distributions. This test rejected that the distribution of the two regions came from the same distribution with a 0.1% significance level, and a p-value of zero. This confirms that separating the regions into bulk and fusion layers is more likely to reflect the actual nature of the material than assuming that the material is homogeneous and orthotropic, as a would be the case for a conventional fibre composite model. The p-value is zero, rather than a very small number, because of the large sample size. Figure 6 shows both the histogram and random field distributions for both the fusion and bulk layers.

A fundamental assumption in the determination of the correlation length is that there is correlation only in the horizontal direction, along the filaments, and not in the axial direction, perpendicular to the filaments. There is not a standard method for calculating correlation lengths, so the correlation length selected relies upon the judgment of the authors. Additionally, there appears to be both short-range and long-range correlation, further complicating the calculation of the correlation length. For this reason, in the determination of the correlation length it is assumed that there are two correlation lengths.

For the correlation lengths for 1D fields, it is estimated that, for both the bulk and fusion layers, the short-range correlation length is 80 μm and the long-range correlation length is 2500 μm. Both the bulk and fusion regions were assumed to have the same correlation lengths because there was no obvious difference between the two regions, other than the mean and standard deviation. This could suggest that either similar phenomena are causing the local variation in material properties in both the bulk and fusion regions or that there is not enough physical distance between these two regions to separate the local variation completely. That is, defects in the fusion region are causing variation in the bulk region strain, which are not captured by the simple model. Further research is required to develop a method which can map specific types of physical defects onto quantitative correlation lengths.

Daniel D Pepler and Craig A Steeves
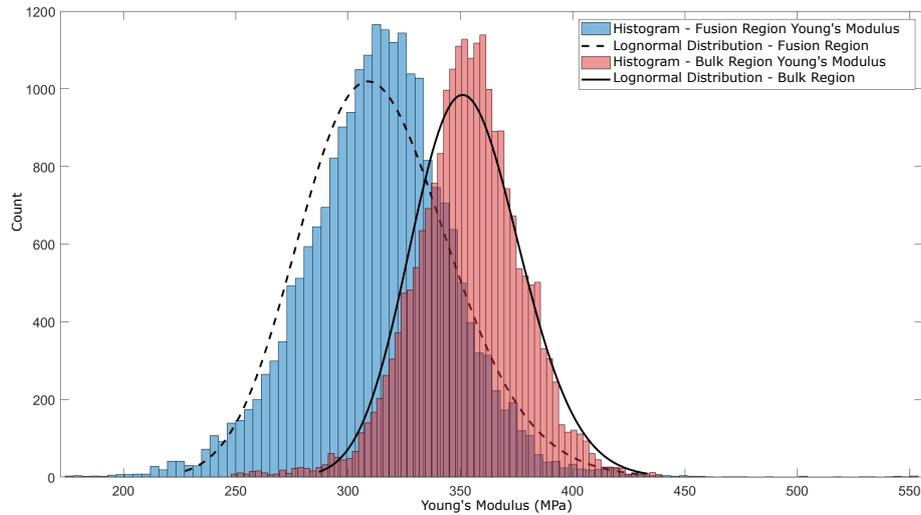
Figure 6: Histograms of both the fusion layer and bulk layer Young's modulus, each with a 100 equally sized bins from the minimum to maximum Young's modulus value. Transparent blue bars show the count of fusion layer Young's modulus and the transparent red bars show the count of bulk layer Young's modulus. The fitted lognormal distributions of each are shown by the black lines.

3.3 Numerical Verification

If the process used to calculate the statistical parameters of the distribution of Young's modulus is correct, then it should be possible to recover strain fields similar to the measured field through numerical simulations, which would provide some verification that the method performs as intended. Finite element analysis (FEA) is used to calculate strain fields based on simulated Young's modulus fields. Because of the assumption that correlation was only in the direction of the filaments, it is necessary only to calculate one dimensional fields based on the measured Young's modulus data. Two 1D Young's modulus fields are needed for each layer, one for the bulk material and one for the fusion material. These 1D fields can be calculated by taking the mean of the Young's modulus for each horizontal position within a layer. This process is illustrated in Fig.7.
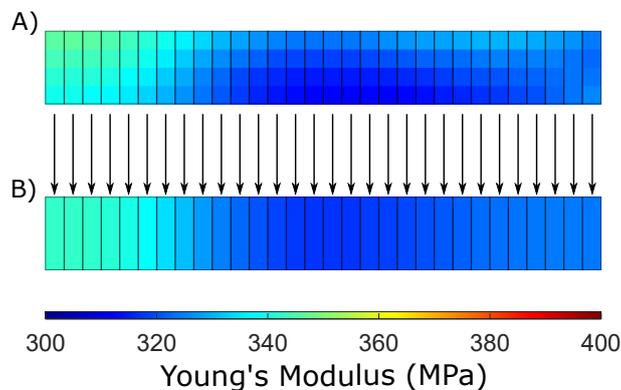
Figure 7: An example of 30 horizontal sections for a fusion layer. In (A) the Young's modulus data varies in two dimensions. The levels in (B) are calculated by taking the mean of Young's modulus for each horizontal location in (A). The horizontal groups of data are shown by the black rectangles, and the arrows show the calculations performed.

Daniel D Pepler and Craig A Steeves

The calculated 1D Young's modulus fields are used in custom anisotropic elements that separate the fusion and the bulk layers. These elements enable the separation of material properties between the two types of layers while minimizing the number of elements. Maintaining the separation of material properties is important because it allows variable fusion layer characteristics to be modelled. Figure 8 shows a sample finite element for a section of printed filament, in which the white region represents the bulk layer and the grey region represents the fusion layer. The elements are grouped in this way because fusion material cannot exist without the bulk material, a feature that is particularly important for topology optimization. Also, calculating the bulk layer and fusion layer Young's moduli, E_b and E_f, in terms of a base Young's modulus, E, allows for the separation of the base Young's modulus from the calculation of the stiffness matrix integral. The degree of variation, d_b and d_f, can be a function of a random variable, and allows for separate distributions for the bulk and the fusion layers.
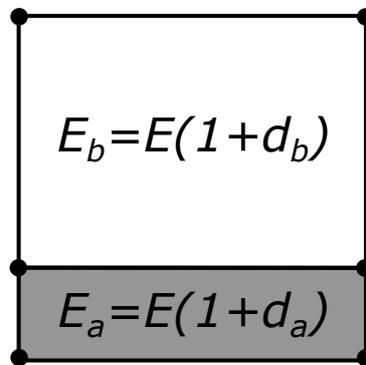
Figure 8: An example of a layered finite element for use in topology optimization, showing how the base Young's modulus E is separable.

Assembling these elements into a finite element mesh results in a meshing structure as given in Fig.9. In this model it is assumed that each layer is independent, so a one dimensional random field is used to describe the Young's modulus values along each layer. A series of one dimensional fields allows for the full two dimensional random field to be realized, although without any correlation in the second dimension.
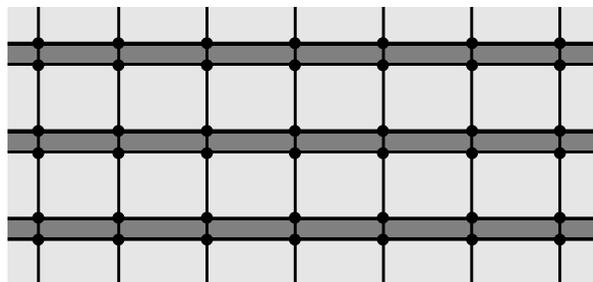
Figure 9: A representative anisotropic finite element mesh which is used to model additively manufactured material. Light grey represents bulk layers and dark grey represents fusion layers.

An example of these one dimensional Young's modulus fields are shown in Fig.10. The measured Young's modulus data used to calculate the one dimensional fields is shown in Fig.10(A). In Fig.10(B), a small portion of the assembled mesh is shown for visual clarity.

Daniel D Pepler and Craig A Steeves
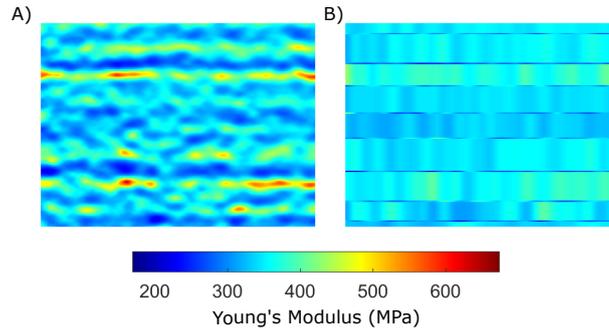
Figure 10: An sample section of: A - the measured Young's modulus data and B- the calculated one dimensional Young's modulus fields for use in the anisotropic mesh.

To provide further verification that this method produces plausible fields of Young's modulus, the simulated displacement at the top edge of the specimen and strain fields are compared with the measured DIC data. Figure 11 gives a plot of the simulated top edge displacements and the measured DIC top edge displacement. In general, the simulated displacement follows the same displacement trends as the measured displacement: having a slowly reducing displacement from a low to high horizontal position. Local displacement variations were also captured in the simulated displacement field. Of note, at a horizontal position 1 mm there is a local increase in the measured displacement that was captured by the simulated displacement. Additionally, from a horizontal position of 7 mm to 10 mm, the simulated displacements matches the uniform displacement observed in the measured displacement data. Near the right edge of the sample, horizontal position 20 mm, the simulated displacement is consistently lower than the measured displacement; however, the absolute displacement values are very small, and overall the simulated displacement is able to match the measured displacement.
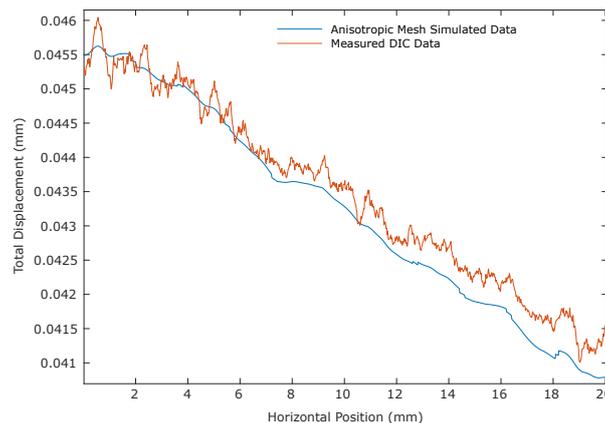
Figure 11: Comparison of the simulated top edge displacement and the measured DIC top edge displacement for every horizontal position.

Figure 12 shows the measured DIC strain field and the simulated strain field using the layered mesh. Qualitatively comparing the simulated strain field to the measured DIC strain field, the simulated strain field looks like a simplified version of the measured strain field. Upon close inspection, the simulated strain values are slightly higher on the left side of the figure and slightly lower on the right side compared with the measured strain data, which is consistent with the displacement results. It can also be seen that most of the local

Daniel D Pepler and Craig A Steeves

minima and maxima in the measured strain data are captured by the simulated strain data. Based on the comparison of the strain and the displacement results, it appears that the layered mesh is suitable for modelling the measured variation.
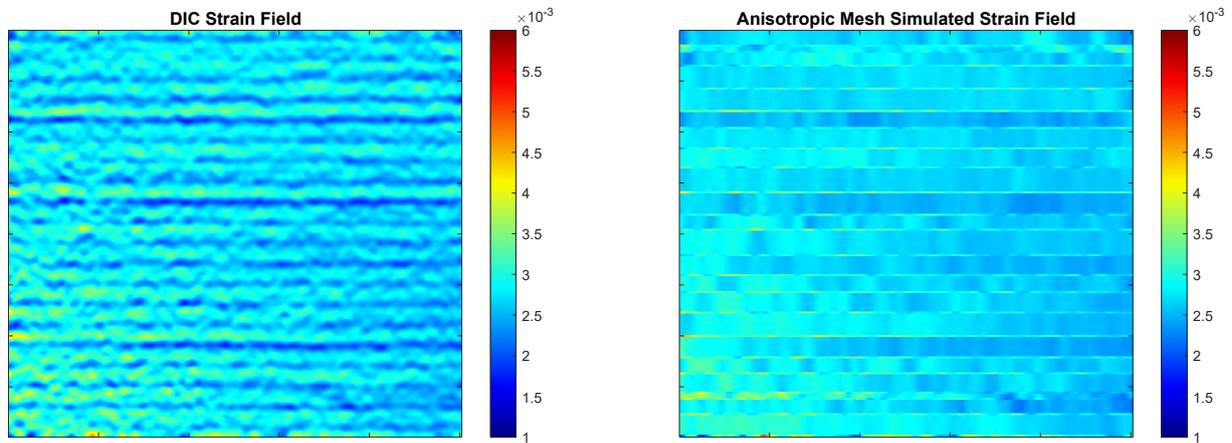
Figure 12: Comparison of the measured DIC strain field and the simulated strain field using the layered mesh.

4 STOCHASTIC FINITE ELEMENT MODEL

The random field statistics for the fusion and bulk regions, determined in Section 3.2, can be used to describe the Young's modulus in any arbitrary structure. In this section it will be used to perform stochastic finite element analysis of a cantilever beam system, shown in Fig.13. Finite element analysis of this nature is essential for robust topology optimization. The cantilever beam is 16 mm in height and 40 mm in width, with each layer being 40 μm in height. The left boundary is fixed and the load is applied to the top right corner. The cumulative distribution of the output displacement will be determined at the bottom right corner, point A.

Figure 13: Cantilever beam system where The left boundary is fixed and the force is shown by the red arrow f. The point at which the displacement will be evaluated is labelled A.

In this example, the Young's modulus field is described using a polynomial chaos (PC) expansion of the lognormal distribution and a Karhunen-Loeve (KL) expansion of the covariance function. This method is described in detail by Ghanem [23] and is applied to topology optimization by Tootkaboni et al. [24]. When using a PC expansion to describe an input parameter (the Young's modulus), the output parameter (displacement)

is also expressed in terms of a PC expansion. The displacement PC expansion is solved using a stochastic Galerkin method, and the linear system of equations is solved using a pre-conditioned conjugate gradient method. The inverse of the mean stiffness matrix is the pre-conditioner. The cumulative distribution function of the displacement can be directly evaluated using the PC expansion expression. The resulting cumulative distribution function for both the x and y displacement at point A are shown in Fig.14. While these displacements are for a solid cantilever beam, this illustrates that the stochastic finite element method can be applied using the calculated random field properties, a necessary step in any robust topology optimization algorithm.
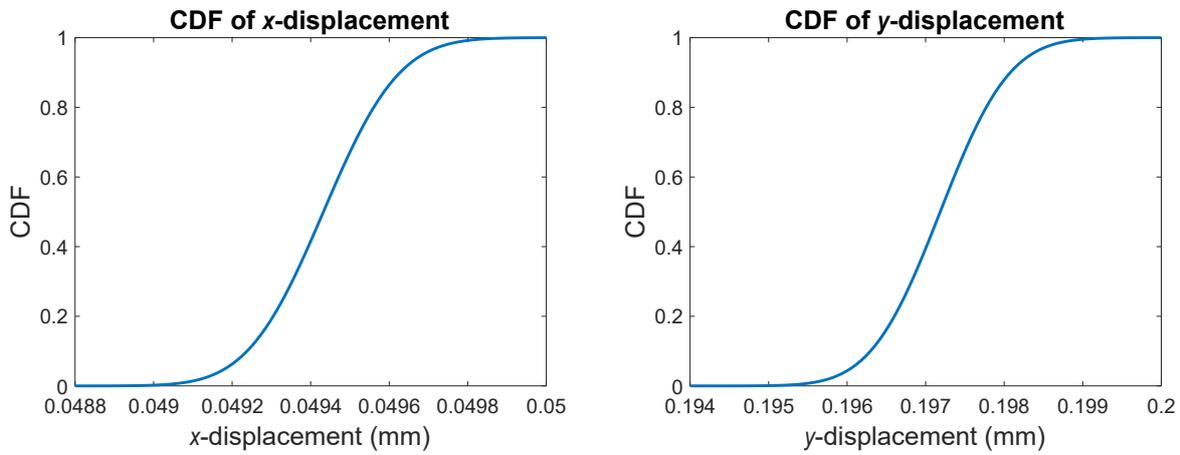
(a) The cumulative distribution function for the x-displacement.

(b) The cumulative distribution function for the y-displacement.

Figure 14: The cumulative distribution functions for the displacement at point A in the cantilever beam

5 CONCLUDING COMMENTS

This paper has described a process which can be followed to determine the stochastic properties of additively manufactured material for robust topology optimization. This includes the sample preparation and experimental procedures required for DIC, which enables the measurement of the varying surface strain field. Based upon the strain data, the varying Young's modulus field was calculated and analyzed to determine the relevant statistical properties. The measured elastic properties were used in a novel finite element model, designed to capture the characteristic layered properties of additively manufactured material. There is good agreement between the measured data and the simulations using finite element analysis with the calculated Young's modulus fields, demonstrating that the approach produces realistic results. The measured and calculated data is essential for stochastic finite element analysis of additively manufactured material, a necessity for performing robust topology optimization.

REFERENCES

[1] J. Liu, A. T. Gaynor, S. Chen, Z. Kang, K. Suresh, A. Takezawa, L. Li, J. Kato, J. Tang, C. C. Wang, et al. Current and future trends in topology optimization for additive manufacturing. *Structural and Multidisciplinary Optimization*, 57(6): 2457–2483, 2018.

[2] W. Gao, Y. Zhang, D. Ramanujan, K. Ramani, Y. Chen, C. B. Williams, C. C. Wang, Y. C. Shin, S. Zhang, and P. D. Zavattieri. The status, challenges, and future of additive manufacturing in engineering. *Computer-Aided Design*, 69:65–89, 2015.

[3] T. D. Ngo, A. Kashani, G. Imbalzano, K. T. Nguyen, and D. Hui. Additive manufacturing (3d printing): A review of materials, methods, applications and challenges. *Composites Part B: Engineering*, 143:172–196, 2018.

[4] Sculpteo. The state of 3d printing report: 2020. https://www.sculpteo.com/en/ebooks/state-of-3d-printing-report-2020. Accessed: 2021-02-23.

[5] B. Mueller. Additive manufacturing technologies–rapid prototyping to direct digital manufacturing. *Assembly Automation*, 32(2), 2012.

[6] C. Bellehumeur, L. Li, Q. Sun, and P. Gu. Modeling of bond formation between polymer filaments in the fused deposition modeling process. *Journal of Manufacturing Processes*, 6(2):170–178, 2004.

[7] B. N. Turner, R. Strong, and S. A. Gold. A review of melt extrusion additive manufacturing processes: I. process design and modeling. *Rapid Prototyping Journal*, 2014.

[8] A. Bellini and S. Güçeri. Mechanical characterization of parts fabricated using fused deposition modeling. *Rapid Prototyping Journal*, 2003.

[9] R. Zou, Y. Xia, S. Liu, P. Hu, W. Hou, Q. Hu, and C. Shan. Isotropic and anisotropic elasticity and yielding of 3d printed material. *Composites Part B: Engineering*, 99: 506–513, 2016.

[10] R. Hernandez, D. Slaughter, D. Whaley, J. Tate, and B. Asiabanpour. Analyzing the tensile, compressive, and flexural properties of 3d printed abs p430 plastic based on printing orientation using fused deposition modeling. In *27th Annual International Solid Freeform Fabrication Symposium, Austin, TX*, pages 939–950, 2016.

[11] C. Casavola, A. Cazzato, V. Moramarco, and C. Pappalettere. Orthotropic mechanical properties of fused deposition modelling parts described by classical laminate theory. *Materials & design*, 90:453–458, 2016.

[12] M. Domingo-Espin, J. M. Puigoriol-Forcada, A.-A. Garcia-Granada, J. Llumà, S. Borros, and G. Reyes. Mechanical property characterization and simulation of fused deposition modeling polycarbonate parts. *Materials & Design*, 83:670–677, 2015.

Daniel D Pepler and Craig A Steeves

[13] L. Li, Q. Sun, C. Bellehumeur, and P. Gu. Composite modeling and analysis for fabrication of fdm prototypes with locally controlled properties. *Journal of manufacturing processes*, 4(2):129–141, 2002.

[14] J. T. Cantrell, S. Rohde, D. Damiani, R. Gurnani, L. DiSandro, J. Anton, A. Young, A. Jerez, D. Steinbach, C. Kroese, et al. Experimental characterization of the mechanical properties of 3d-printed abs and polycarbonate parts. *Rapid Prototyping Journal*, 2017.

[15] V. Azzi and S. Tsai. Anisotropic strength of composites. *Experimental mechanics*, 5 (9):283–288, 1965.

[16] P. K. Mallick. *Fiber-reinforced composites: materials, manufacturing, and design.* CRC press, 2007.

[17] J. Karlsson, T. Sjögren, A. Snis, H. Engqvist, and J. Lausmaa. Digital image correlation analysis of local strain fields on ti6al4v manufactured by electron beam melting. *Materials Science and Engineering: A*, 618:456–461, 2014.

[18] T. Yao, J. Ye, Z. Deng, K. Zhang, Y. Ma, and H. Ouyang. Tensile failure strength and separation angle of fdm 3d printing pla material: Experimental and theoretical analyses. *Composites Part B: Engineering*, 188:107894, 2020.

[19] J. Martínez, J. Diéguez, E. Ares, A. Pereira, P. Hernández, and J. Pérez. Comparative between fem models for fdm parts and their approach to a real mechanical behaviour. *Procedia Engineering*, 63:878–884, 2013.

[20] Y. Zhao, Y. Chen, and Y. Zhou. Novel mechanical models of tensile strength and elastic property of fdm am pla materials: Experimental and theoretical analyses. *Materials & Design*, 181:108089, 2019.

[21] M. Bendsoe and O. Sigmund. *Topology Optimization: Theory, Methods, and Applications.* Springer, 2003.

[22] O. Sigmund. A 99 line topology optimization code written in Matlab. *Structural Multidisciplinary Optimization*, pages 120–127, 2001.

[23] R. Ghanem. Stochastic finite elements with multiple random non-gaussian properties. *Journal of Engineering Mechanics*, 125(1):26–40, 1999.

[24] M. Tootkaboni, A. Asadpoure, and J. K. Guest. Topology optimization of continuum structures under uncertainty–a polynomial chaos approach. *Computer Methods in Applied Mechanics and Engineering*, 201:263–275, 2012.

ACTIVE CONTROL OF DIGITAL MORPHING AIRFOILS USING DEEP LEARNING

Raul Carreira Rufato [1*] and Joseph Morlier[2]

1: Institut Supérieur de l'Aéronautique et de l'Espace (ISAE-SUPAERO)
Université de Toulouse
31055 Toulouse, FRANCE
raulc.rufato@hotmail.com

2: ICA, Université de Toulouse, ISAE-SUPAERO, MINES ALBI, UPS, INSA, CNRS, France
Université de Toulouse
31055 Toulouse, FRANCE
joseph.morlier@isae-supaero.fr

Abstract. *Detect and prevent an aircraft instability condition is extremely important, especially for flight control, and morphing airfoils can be used for this purpose. This work proposes the determination of a digital morphing airfoil, using a deep learning approach, to avoid an unstable aeroelastic condition in a 2D wing model. To parametrize the airfoil's geometry, Bezier – Parsec 3434 parametrization was used and some of the parameters were determined by an optimization process based on a Genetic Algorithm. The airfoil's geometric C_g position, c_l, c_d and c_m distributions for some angles of attack were used to train a deep neural network, capable to estimate the desired BP3434 parameters. Finally, this trained machine learning model was then coupled to the 2D aeroelastic model of a wing to change the airfoil's curvature when it faced an instability. The trained deep learning algorithm had an excellent Person's coefficient of 0.919 when predicting a new geometry. Our methodology permits to automatically detect and avoid instability using digital morphing techniques coupled with AI, using only one sensor, monitoring the dynamic behaviour of the airfoil.*

Keywords: Digital morphing airfoils, deep neural networks, Bezier-Parsec parameterization, 2D aeroelastic instabilities

Raul Carreira Rufato and Joseph Morlier

LIST OF SYMBOLS

c_l	lift coefficient
c_d	drag coefficient
c_m	moment coefficient
C_g	center of gravity
EA	elastic axis
ODE	ordinary differential equation
MSE	mean square error
ANN	artificial neural networks

1   INTRODUCTION

Historically, the study of airfoils has always been extremely important in the aeronautical industry [1]. Airfoils are also essential in describing the aeroelastic characteristics of a wing, so studying and improving their performance is highly necessary. In this context, morphing airfoils are being studied, due to their ability to adapt to a given flight requirement, as this technology is aimed at very efficient aerodynamic and structural designs during flight, contributing to the performance of an aircraft [2]. The impact of this new technology, as well as simple modelling of this type of airfoil was better described in [3].

In an aircraft, several situations that occurs during flight can alter the global center of gravity and even that of the wing, such as jettisoning and fuel consumption, which can instantly bring the aircraft into an unstable condition. Therefore, using airfoils with variable geometry allows the optimization of their shape, hence returning the aircraft to a stable position. Due to the high non-linearity of this process, it is interesting to use deep neural networks, which are viable computational models aimed at a wide variety of problems, including optimization, nonlinear system modelling and control [4], seeking to represent the way the human brain works, with neurons and connections between them. This modelling is one of the most modern ways to optimize high complex systems and obtain acceptable results. This work links the study of the aeroelastic characteristics of morphing airfoils with the deep neural network tool.

Despite a 2D aeroelastic model of a wing, with a reduced number of degrees of freedom, being simplistic, a few problems can occur, as in [5]:

• For the construction of the database there is the need to carry out an optimization to determine some parameters, therefore, it can be computationally expensive to build a large dataset.

• To guarantee the training of a neural network with high accuracy and low loss function, a high number of airfoils and their respective parametrization is necessary, which further increases the time of the process.

• Difficulty in coupling the neural network model with the aeroelastic model. Consequently, this work neglects the transient changes in the geometry of the airfoil

Despite these problems that can occur, this research aims to develop a simplified model, although being very representative for this case study.

2 STATE OF ART

Determining an optimal geometry for the morphing airfoil consists of a high complex optimization problem as well-known airfoils are described by many points as in [6]. However, using a form of parameterization through Bezier-Parsec curves as described in [7], it is possible to parameterize the geometric characteristics of an airfoil's geometry through a reduced number of parameters. It is possible to say that Bezier's formulation is more directly related to airflow than the formulation presented by Parsec, where the parameters are more aerodynamically oriented. The Bezier-Parsec (BP) parameterization uses Parsec variables as parameters, which in turn define four separate Bezier curves. These curves describe the leading and trailing portions of the camber line, and the leading and trailing regions of the thickness distributions [8].

Using the BP parameterization it is possible to train a neural network as in [5], for a desired input vector capable to predict these parameters. In this work, we chose to use the same idea to train a deep neural network using the Keras package in Python [9]. Additionally, there will be a coupling with a 2D aeroelastic simulation, in which an airfoil undergoes a sudden change on its geometric C_g, taking it to an unstable condition of flutter. For the modeling of this condition, an algorithm developed by ALTRAN was used [10]. The neural network will then be able to predict a new airfoil (through BP3434 parameters) and return the C_g to a stable condition, maintaining the same aerodynamic characteristics as the current profile. The construction of the database to train the neural network will be done using the Matlab software and the Xfoil code. Then the neural network and the aeroelastic code will be coupled in Python language.

The background section (Section 3) presents a basic review of the concepts used in the development of the work. Then, the methodology section (Section 4) shows how these concepts were put together to model the behavior of the desired digital morphing airfoil. The results section (Section 5) shows the results obtained. Finally, a general conclusion (Section 6) about the work is made.

3 BACKGROUND

3.1 Artificial neural networks

Artificial neural networks (ANN) are computational models designed to simulate mathematically how the human brain analyses and processes information. Such systems learn to perform tasks by learning from examples (supervised learning algorithm) and they are formed by a set nodes called neurons. After some mathematical transformations, each neuron propagates an output value y_j. The network consists of connections between these neurons, each connection providing an output which is then an input to another neuron. For each of these connections a weight w_{ij}, that represents its relative importance as well as the effect of the neuron i on neuron j, is assigned [11]. Each neuron also has an external input (bias) b_j that shifts the value up and down. Then, the product input-weight and the bias are added up and passed through a function called "activation function", to model the non-linear behaviors. Most frequently the form of the propagation rule is given in [5].

$$y_j(t) = \sum_{i=1}^{N} w_{ij}(t)x_j(t) + b_j(t) \qquad (1)$$

Next, an activation function $f(\bullet)$ is given and it then determines the new level of

Raul Carreira Rufato and Joseph Morlier

---

activation based on the effective input $x_j(t)$ (Figure 1):
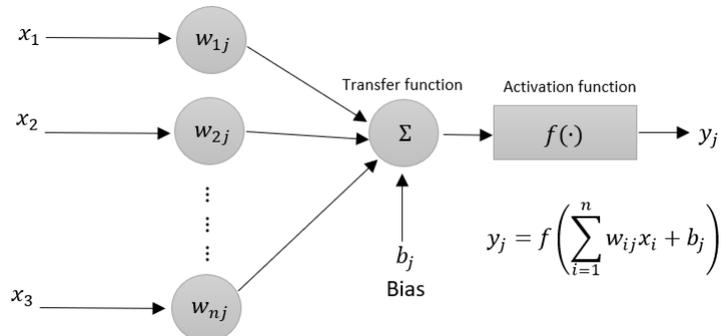
Figure 1: Structure of one neuron

Thus, each neuron receives an input from its neighbours and uses this to compute an output value, which is propagated to another neuron. The connections between them build the deep neural network (called "deep" because it has some intermediate columns called layers) as can be seen in Fig.2. The second step is to adjust the weights w_{ij} and the bias b_j through a learning method, which consists basically in an optimization process, that can be done by a simple gradient descent method (although other complex methods could be used). The objective function for this optimization is called "Loss function" and it measures the distance between the desired output $y_j^{desired}$ and the obtained y_j for each step.
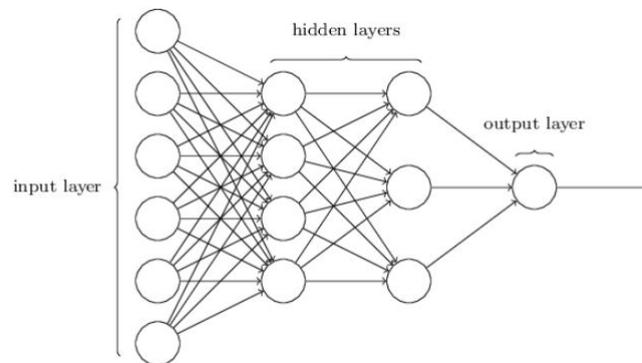
Figure 2: Structure of an ANN

Moreover, it is important to select the correct activation function as it performs the non-linear transformation in the input data, making it possible to learn and perform more complex tasks. The aim of this work is to predict the BP parameters given the aerodynamic coefficients and the C_g position as inputs, resulting in a regression task. There are several types of activation functions, such as Linear, Sigmoide, Tanh, ReLU, Leaky ReLU, Softmax, in which Leaky ReLU was selected for this work. However, it is first necessary to define the ReLU function, which is the rectified linear unit. The ReLU function is defined in Eq.2:

$$f(x) = max(0, x) \tag{2}$$

Raul Carreira Rufato and Joseph Morlier

It is the most used activation function when designing neural networks. The ReLU function is non-linear, which means that it can easily copy the errors back and have multiple layers of neurons activated by the ReLU function. The main advantage of using the ReLU function over other activation functions is that it does not activate all neurons at the same time. However, in the ReLU function, the gradient is 0 to $x < 0$, which causes neurons to "die" from activations in that region. Hence the use of Leaky ReLU, which helps to solve this problem. The Leaky ReLU function is defined in Eq.3:

$$
\begin{aligned}
f(x) &= ax, \ x < 0 \\
f(x) &= x, \ x \geq 0
\end{aligned}
\tag{3}
$$

so the ReLU graph ends up having a small slope and avoiding null values for the gradient during the optimization process.

3.2 Genetic algorithms

The genetic algorithm is a method for solving both constrained and unconstrained optimization problems that is based on a genetic natural selection [5]. This optimization algorithm is interesting because there is no need to know the function or even its derivative to be able to do the desired optimization. Its convergence is not proved mathematically although it always converges to an optimal value.

At each step, the genetic algorithm selects the best individuals from the current population and combines their characteristics randomly to produce the new generation of candidates. The first population is generated randomly but after several iterations, the population evolves to an optimal solution. The algorithm uses three main rules to evaluate and generate its population: the selection rule chooses the best individuals to propagate their characteristics to the next generation; the crossover rule combines the characteristics of these individuals to generate the children and the mutation rule applies random changes from parents to children.

In this work, the genetic algorithm was used to optimize some parameters of the BP curves from the airfoil points, consequently to generate the training and test databases for the neural network. This optimization was used because the function of this transformation was not known.

3.3 Bezier curves

A Bezier curve of degree n is defined by $n + 1$ points of a polygon. To describe the airfoil four Bezier curves were used, two for the camber line and two for the thickness distribution. The general expression for one curve with degree n is Eq.4:

$$
P(u) = \sum_{i=0}^{n} P_i \frac{n!}{i!(n-i)!} u^i (1-u)^{n-i}
\tag{4}
$$

Where P_i represents a control point. The parameter u goes from 0 to 1 with 0 at the P_0 control point and 1 at the P_n control point.

This work will use a third degree curve and a fourth degree curve that will be later explained. A third order Bezier curve is given by the following equations (Eq.5):

Raul Carreira Rufato and Joseph Morlier

$$x(u) = x_0(1-u)^3 + 3x_1u(1-u)^2 + 3x_2u^2(1-u) + x_3u^3$$
$$y(u) = y_0(1-u)^3 + 3y_1u(1-u)^2 + 3y_2u^2(1-u) + y_3u^3$$
(5)

And a fourth order Bezier curve is given by the following equations (Eq.6):

$$x(u) = x_0(1-u)^4 + 4x_1u(1-u)^3 + 6x_2u^2(1-u)^2 + 4x_3u^3(1-u) + x_4u^4$$
$$y(u) = y_0(1-u)^4 + 4y_1u(1-u)^3 + 6y_2u^2(1-u)^2 + 4y_3u^3(1-u) + y_4u^4$$
(6)

An airfoil can be described by the Bezier curves, however the problem with this parametrization is that it does not establish a proper relationship with the airfoil's aerodynamic parameters.

3.4 Parsec parameters

The Parsec method is a very common method of airfoil parameterization. It uses eleven parameters to define the aerofoil shape which are the leading edge radius, upper crest location, lower crest location, upper and lower curvature, trailing edge coordinate and direction, trailing edge wedge angle and thickness [7]. This method incorporates the parameters that have a physical relevance to the airfoil shape.

The problem is that the Parsec parametrization does not provide sufficient control over the trailing edge shape, because it fits a smooth curve between the maximum thickness point and the trailing edge, making changes difficult at this location, better described in [12]. For this reason, the couple with the Bezier parameters is interesting.

3.5 Bezier–Parsec parameterization

Combining both methods described before, the Bezier-Parsec can parametrize a given airfoil with parameters that are related to its aerodynamic and geometrical characteristics. The detailed development of this method is given by [13]. As said in [7], Oyama et al. [14] showed that Bezier-Parsec parametrization increased the robustness and convergence speed for aerodynamic optimization using genetic algorithms. It has a lot of advantages and in this work it will be used to parametrize the airfoil shape, building the database to train the neural network architecture. Other parameterizations could be used as the one presented in [15].

The Berzier-Parsec parametrization uses the Parsec variables as parameters, which in turn define four separated Bezier curves, two curves to describe the leading edge of the thickness curve & camber curve and two to describe the trailing edge for both of them. In this work a BP3434 parametrization will be used. As in the name, both leading edge curves have polynomials of third degree while both the trailing edge curves have the polynomials of fourth degree. In Fig.3 these curves can be seen as well as the Bezier control points and the ten Parsec parameters. The parametrization assumes a unitary chord for the airfoil.

The parameters in Eq.5 and Eq.6 can be determined by the control points for each section as follows:

Leading edge thickness curve: Equation 7

Raul Carreira Rufato and Joseph Morlier
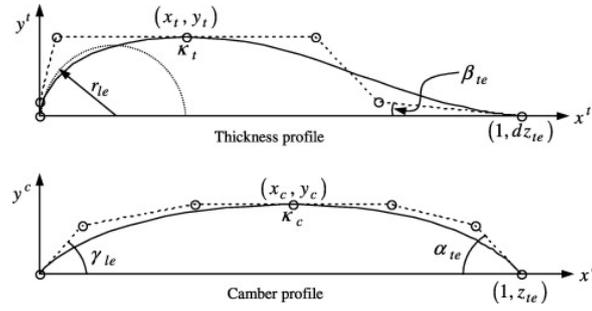
Figure 3: BP 3434 airfoil geometry and Bezier control points defined by ten aerodynamic and five Bezier parameters [7]

$$
\begin{aligned}
(x_0, y_0) &= (0,0); \\
(x_1, y_1) &= (0, b_8); \\
(x_2, y_2) &= (\frac{-3b_8^2}{2r_{le}}, y_t); \\
(x_3, y_3) &= (x_t, yt);
\end{aligned}
\tag{7}
$$

In which b_8 is between $0 < b_8 < min(y_t, \sqrt{\frac{-2r_{le}x_t}{3}})$

Trailing edge thickness curve: Equation 8

$$
\begin{aligned}
(x_0, y_0) &= (x_t, y_t); \\
(x_1, y_1) &= (\frac{7x_t + 9b_8^2}{8r_{le}}, y_t); \\
(x_2, y_2) &= (3x_t + \frac{15b_8^2}{4r_{le}}, \frac{y_t + b_8}{2}); \\
(x_3, y_3) &= (b_{15}, dz_{te} + (1 - b_15)tan(\beta_{te})); \\
(x_4, y_4) &= (1, dz_{te});
\end{aligned}
\tag{8}
$$

Leading edge camber curve: Equation 9

$$
\begin{aligned}
(x_0, y_0) &= (0,0); \\
(x_1, y_1) &= (b_0, b_0 tan(\lambda_{le})); \\
(x_2, y_2) &= (b_2, y_c); \\
(x_3, y_3) &= (x_c, y_c);
\end{aligned}
\tag{9}
$$

Trailing edge camber curve: Equation 10

Raul Carreira Rufato and Joseph Morlier

$$
\begin{aligned}
(x_0, y_0) &= (x_c, y_c); \\
(x_1, y_1) &= (\frac{3x_c - y_c cot(\lambda_{le})}{2}, y_c); \\
(x_2, y_2) &= (\frac{-8y_c cot(\lambda_{le}) + 13x_c}{6}, \frac{5y_c}{6}); \\
(x_3, y_3) &= (b_{17}, z_{te} - (1 - b_{17})tan(\alpha_{te})); \\
(x_4, y_4) &= (1, z_{te});
\end{aligned}
\tag{10}
$$

3.6   Aeroelastic Model

The aeroelastic model chosen in this work is a simplified model of an airfoil with two degrees of freedom: Translation and rotation. A schematic representation of the system can be seen in Fig.4.
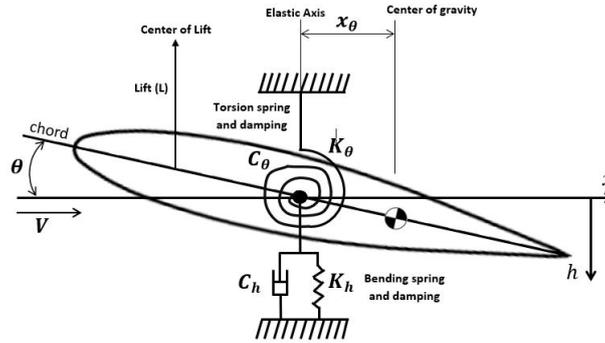
Figure 4: Modeled system

The airfoil has a damping and stiffness system in both degrees of freedom, therefore it is possible to model the system as in [16]. Knowing that x is measured along the chord and it is not a generalized coordinate, it cannot undergo virtual change. The generalized coordinates can be described as in Eq.11.

$$
\{q_1 = h, \ q_2 = \theta\}
\tag{11}
$$

And the displacement of any point in the airfoil is (Eq.12).

$$
\overrightarrow{r} = u \overrightarrow{i} + z \overrightarrow{k}
\tag{12}
$$

Where u is the horizontal displacement component and z is the vertical displacement component. From the geometric characteristics it can be said (Eq.13):

$$
\theta \ll 1 \rightarrow \begin{cases} u = x[cos\theta - 1] \approx 0 \\ z = -h - xsin\theta \approx -h - x\theta \end{cases}
\tag{13}
$$

Hence, the kinetic energy is calculated as Eq.14:

Raul Carreira Rufato and Joseph Morlier

$$T = \frac{1}{2} \int [(\frac{dz}{dt})^2 + (\frac{du}{dt})^2]\rho dx$$

$$\simeq \frac{1}{2} \int (\frac{dz}{dt})^2 \rho dx$$

$$= \frac{1}{2} \int (-\dot{h} - \dot{\theta}x)^2 \rho dx \qquad (14)$$

$$= \frac{1}{2}\dot{h}^2 \int \rho dx + \dot{h}\dot{\theta} \int x\rho dx + \frac{1}{2}\dot{\theta}^2 \int x^2 \rho dx$$

$$= \frac{1}{2}\dot{h}^2 m + \dot{h}\dot{\theta}x_\theta m + \frac{1}{2}\dot{\theta}^2 I_\theta$$

Where $m = \int \rho dx$ is the total mass; $I_\theta = \int \rho x^2 dx$ is the moment of inertia and ρ is the mass per unit chord length.

The potential energy is Eq.15:

$$U = \frac{1}{2}K_h h^2 + \frac{1}{2}K_\theta \theta^2 \qquad (15)$$

where K_h and K_θ are the spring stiffness. Then, calculating the generalized forces and using the Lagrange's equations, with the right algebraic arrangement, it is possible to obtain the equation of motion that describes the model (Eq.16):

$$\begin{bmatrix} m & mx_\theta \\ mx_\theta & I_\theta \end{bmatrix} \times \begin{bmatrix} \ddot{h} \\ \ddot{\theta} \end{bmatrix} + \begin{bmatrix} C_h & 0 \\ 0 & C_\theta \end{bmatrix} \times \begin{bmatrix} \dot{h} \\ \dot{\theta} \end{bmatrix} +$$
$$\begin{bmatrix} K_h & 0 \\ 0 & K_\theta \end{bmatrix} \times \begin{bmatrix} h \\ \theta \end{bmatrix} = \begin{bmatrix} F \\ M \end{bmatrix} \qquad (16)$$

In which m represents the mass of the airfoil; x_θ represents the distance between the C_g (center of gravity) and the elastic axis and $I_\theta = I_0 + mx_\theta^2$ is the moment of inertia displaced from the C_g; $h(t)$ is the degree of freedom plunge and $\theta(t)$ is the degree of freedom in torsion, both measured from the static equilibrium position.

Considering this a dynamic aeroelasticity problem, it was used an aerodynamic model to describe the flow. Thus, the panel method was used to determine the aerodynamic loads during the time simulation. Because aerodynamic and structural models have different requirements, it is necessary to use different approaches for the discretization of the modelled geometry, consequently , the aerodynamic and structural meshes are different, containing an interface which provides the communication between them. The solution for the interface used, provided by ALTRAN, uses a Radial-Basis-Function (RBF), a method for spatial interpolation in 2D, which transfers the loads from the structural mesh to the aerodynamic mesh.

4 METHODOLOGY

The diagram that represents the order of development of the work can be seen in Fig.5.

The work began with the construction of the airfoil database and its respective parameters, to train the neural network. In parallel to this process, the aeroelastic code

Raul Carreira Rufato and Joseph Morlier
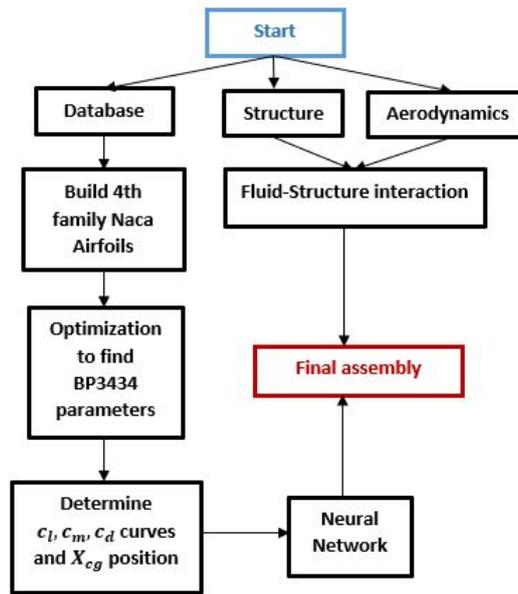
Figure 5: Project main scheme

was developed implementing the described system, as well as the possibility of changing the center of gravity to an unstable position. Then, after analysing the validity of the results for both models, it was possible to train the neural network and couple it with the fluid-structure interface. The validations of each step are presented in the following sections.

4.1 Construction and validation of the database

The research development started by building the database, which is important for training the neural network. First, the x and y coordinates were determined for the airfoil points of the 4th NACA Family, varying: maximum thickness, maximum camber and location of maximum camber, where a thousand different airfoils of the same family were built. An optimization was then performed to determine the parameters of Bezier-Parsec 3434 that would be able to describe them. However, in order to reduce the number of optimization parameters, it was possible to determine seven of them analytically (d_{zte}, z_{te}, r_{le}, x_c, y_c, x_t and y_t), because they are geometric characteristics of each profile, such as the maximum thickness and maximum camber. The remaining eight parameters have been optimized, using the differential evolution (DE) algorithm of Rainer Storn [17], in MATLAB through parallel simulation processing. The characteristics of the optimization can be seen in Tab.1.

Finally, it was possible to determine the control points of the airfoil and estimate its curve using the relationships between camber and thickness lines. The results of this approach can be seen in Fig.6, for the NACA 0012 airfoil.

It is possible to see through Fig.6a that the curve adjustment was satisfactory given the number of points that describes the airfoil. Figure 6b shows the control points to describe the thickness and camber lines, determined by the Bezier-Parsec parameters.

The curves of c_l, c_m, c_d (for angles of attack from $1deg$ to $11deg$) and the position of X_{cg} for each airfoil were determined using the code Xfoil [18]. In possession of the aerodynamic curves and the Bezier-Parsec parameters of each profile, the necessary database for the

Raul Carreira Rufato and Joseph Morlier

Table 1: Optimization characteristics

Objective Function	Square error (real and fitted)
Bounds	Constrained
Type	Without derivate
Number of members of the population	120
Desirable value for objective function	1e-6
Number of variables to optimize	8
Crossover probability	0.8
Maximum number of iterations (generations)	50
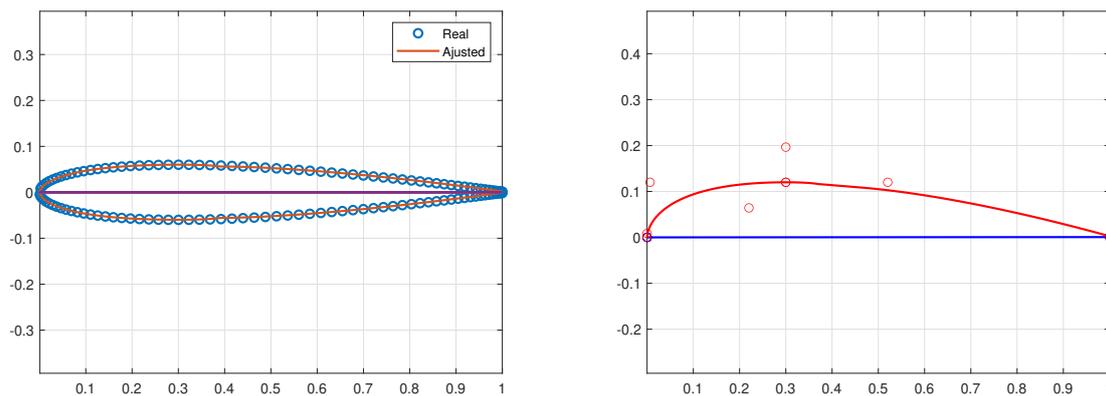
Figure 6: NACA 0012 airfoil geometry aproximation using Bezier-Parsec 3434 parameters. In the right figure the thickness line is represented in red, camber line in blue and the points represent the control points of the parametrization

training of the neural network was built.

4.2 Neural network training

Using the built database, the problem to be solved by the neural network consists of predicting the 15 parameters for a Bezier-Parsec 3434 parametrization, given c_l, c_m and c_d curves and the X_{cg} of an unknown airfoil, therefore it is a regression problem.

For the construction of this neural network, the Keras library was used in python [9], generating a Deep Feed Forward (DFF) type architecture. The DFF is basically an artificial neural network in which connections between the nodes do not form a cycle [19]. This is the simplest type of neural network, as the information moves unidirectionally, from the input layer - through the hidden layers, if any - to the output layer, with no loops or cycles, where all neurons in one layer are fully connected with those in the next layer. The information on the neural network implemented in this work is described in Tab.2.

Table 2: Deep Feed Forward (DFF)

Layers	3
Hidden layers	LeakyReLU
Architecture	500-100-50-15
Output layer	No activation function
Optimizer	Adam (learning rate=0.001)
Loss	MSE
Data division	Training 80% ; Test 20%

Three hidden layers with 500,100 and 50 neurons respectively were used, all of them with the LeakyReLU activation function explained previously in Section 3.1. The Output layer must not have any activation function, as it is a regression task, in which the values must be predicted and not classified. The Adam optimizer with a low learning rate [20] was used to train the network and determine the optimal weights for each connection. The loss function chosen was the Mean Square Error (MSE) function, described by Eq.17:

$$MSE = \frac{1}{n} \sum_{i=1}^{n} (y_i - \widetilde{y}_i)^2 \qquad (17)$$

The database was used for two different reasons, being 80% for training the neural network and 20% for testing. Using a database of 1000 4th NACA family airfoils and their respective parameters, it was possible to train the neural network and test it. Additionally, its quality was analyzed using the K-fold cross-validation method, which is a resampling procedure used to evaluate machine learning models on a limited data sample. It is really usefull to verify and avoid overfitting. The procedure has a single parameter called k that refers to the number of groups that a given data sample is to be split into. As such, the procedure is often called k-fold cross-validation [21]. The validation process is also described at [21].

Using $k = 10$ number of splits in the dataset, an average result equal to -0.02 and standard deviation equal to 0.004, representing a satisfactory result for this data set. Therefore, by training the neural network, it was possible to test it. The results can be

seen in Fig.7a, Fig.7b and Fig.7c.

(a) Test

(b) Mean square error during epochs

(c) Prediction exemple
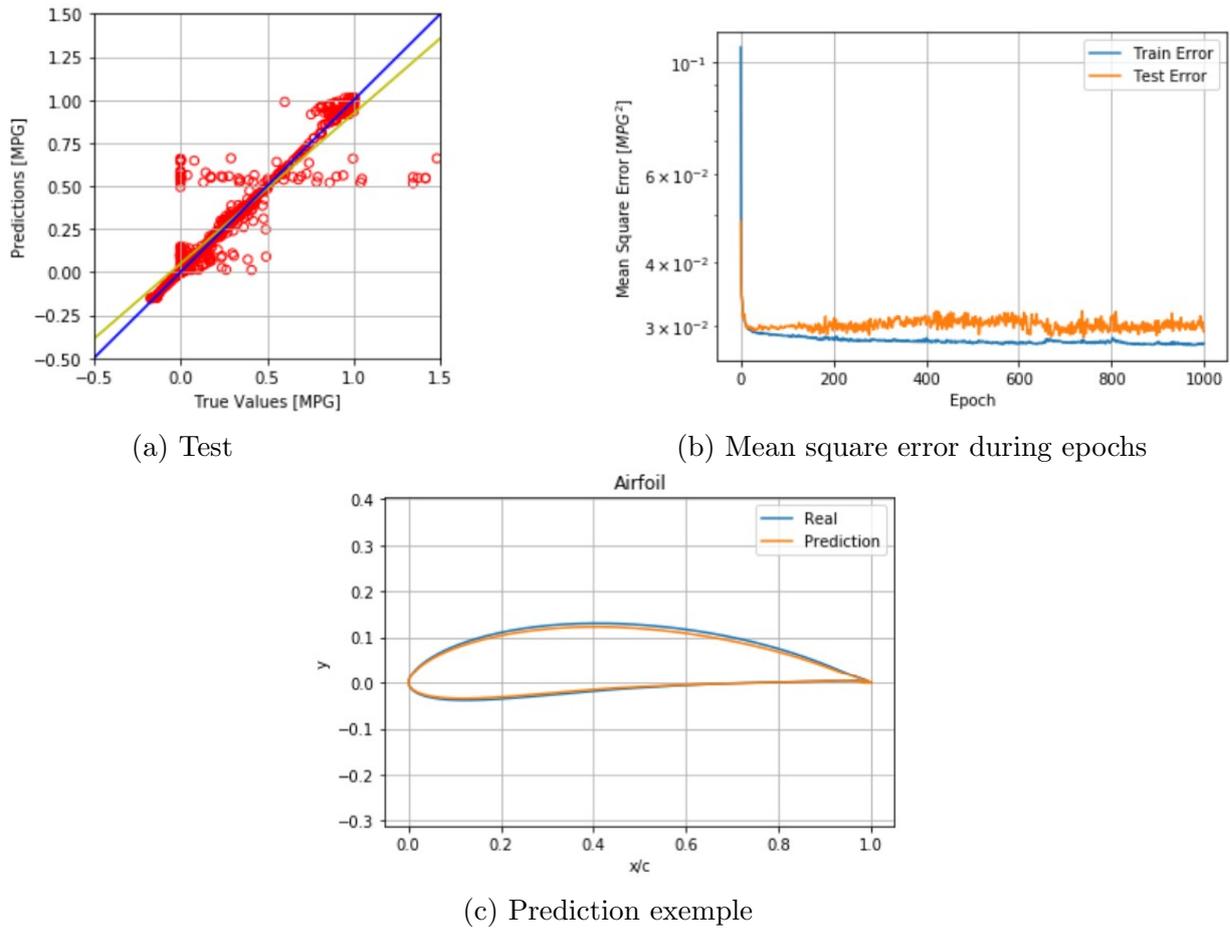
Figure 7: Prediction results

In Fig.7a the blue line represents the points for which the predicted values are equal to the real values ($y = 1.0x + 0.0$) and the yellow line represents the best regression of the points obtained by the code ($y = 0.88x + 0.04$). Pearson's coefficient, which is a parameter that measures linear correlation between X and Y, was also calculated, and the value found was equal to 0.919. Hence, with the straight lines very close and the high correlation, it is possible to say that the model was well trained, despite the existence of some poorly predicted values. A result of the prediction can be seen in Fig.7c which shows a desired airfoil and the one found by the neural network, concluding that the neural network has been trained and validated, despite its limitation in predicting only airfoils of the 4th NACA family.

4.3 Aeroelastic solution

Based on the system described in Section 3.6 it was possible to build a structural module, an aerodynamic module and the connection interface between them. This code was provided by ALTRAN [10] and adapted for the purpose of this work.

The structural sector is responsible for transforming the loads by applying them at the reference point, in this case the elastic axis, together with the delivery of the displacements from each point of the mesh to the interface. It is also the place where the equation of

motion is solved using Euler's numerical integration method. To explain this method, suppose that you want to approximate the solution to a problem of initial value (Eq.18):

$$y'(t) = f(t, y(t)); \quad y(t_0) = y_0 \tag{18}$$

Choosing a value for the time step Δt and assigning each step a point within the range, we have $t_n = t_0 + n\Delta t$. In this, the next step t_{n+1} from the previous t_n is defined as $t_{n+1} = t_n + \Delta t$, so Euler's method consists of determining y_{n+1} via Eq.19:

$$y_{n+1} = y_n + \Delta t f(t_n, y_n) \tag{19}$$

In which y_n is an approximation of the ODE solution at the point $t_n : y_n \approx y(t_n)$, therefore consisting of an explicit method of integration.

By using this method with the state vector $y = [h \;\; \dot{h} \;\; \theta \;\; \dot{\theta}]^T$ it is possible to obtain an approximation for the solution of Eq.16 at each time step Δt. Also using the acceleration values calculated for each iteration described by:

$$\begin{cases} \ddot{h}_t = \frac{I_\theta(F - C_h \dot{h}_t - K_h h_t) - m x_\theta(F - C_\theta \dot{\theta}_t - K_\theta \theta_t)}{m I_\theta - m^2 x_\theta^2} \\ \ddot{\theta}_t = \frac{-m x_\theta(F - C_h \dot{h}_t - K_h h_t) + m(F - C_\theta \dot{\theta}_t - K_\theta \theta_t)}{m I_\theta - m^2 x_\theta^2} \end{cases} \tag{20}$$

It is the responsibility of the aerodynamic module to calculate the loads introduced by the fluid. The code developed by ALTRAN using the 2D panel method was used in this work, basically consisting of a solution technique applicable to the potential flow theory, in which the mathematical equation governing the method is the Laplace equation, given by the following expression (Eq.21):

$$\triangledown^2 \phi = 0 \tag{21}$$

The Eq.21 is valid for a stationary, incompressible and irrotational flow (so consisting of a perfect flow). There are several ways to solve this equation, but the method used in this work is through singularities as sources, dipoles and vortices. Since the equation is linear, it is possible to use an overlap of singularities to obtain the solution for a given flow. The complete formulation of the method is described in [22].

Therefore, in possession of the aerodynamic and structural module and the interface, it is possible to carry out experiments for a given initial airfoil geometry. A simulation was performed for a system with the characteristics present in Table 3. The results are shown in Fig.8.

It is possible to notice the increase in the amplitude of the oscillations over time, therefore, it is identified an unstable flow called Aeroelastic Flutter. It is defined as "an unstable, self-excited structural oscillation at a definite frequency where energy is extracted from the airstream by the motion of the structure" [23]. It represents a type of flow in which the frequencies of the two modes of the system are equal, exciting each other and increasing energy to the flow, which can result in catastrophic situations. The exponential growth envelope of this system can be approximated by an exponential interpolation curve through the signal amplitude peaks, thus used in this work to predict the appearance of instability. The results of this modelling were satisfactory in the system description.

Raul Carreira Rufato and Joseph Morlier

Table 3: Characteristics

Mass	$7.0kg$
I_0	$7.0kg.m^2$
X_{cg}	0.4
X_{EA}	0.35
V	$6m/s$
ρ	$1.225kg/m^3$
K_h	$30.0N/m$
K_θ	$50.0N/rad$
C_h	$2.0N/m/s^2$
C_θ	$6.0N/m/s^2$
dt	$0.1s$
Number of steps	$100s$
Airfoil	NACA-3412
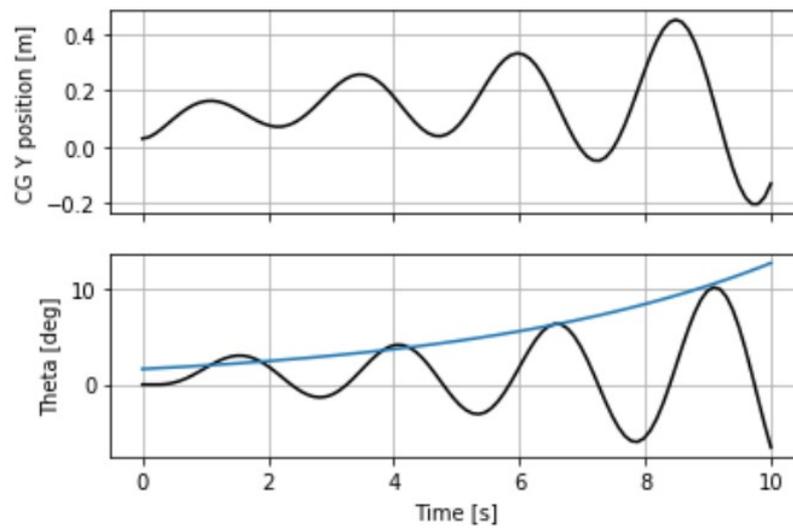
Figure 8: Aeroelasticity simulation

703

Raul Carreira Rufato and Joseph Morlier

5 RESULTS OF FINAL COUPLING

Using the described modelling, after all validations, it was possible to couple the codes of the neural network and the fluid-structure, expecting the code to modify the geometry of the airfoil as soon as an instability arises over time. To verify the appearance of instability, the characteristic of its exponential envelope was analysed, whether it was growing or decreasing during the flight simulation. Then, in order to verify the results, the characteristics of the new desired airfoil (after instability) were pre-determined using an airfoil of the 4th NACA family, using its geometric X_{cg}. Additionally, the aim was to alter the profile's center of gravity, which may have been modified in some way (such as jettisoning or fuel consumption) for a region that would cause instability to arise. To make this sudden change in the center of gravity, a change in the positioning of X_{cg} in relation to X_{EA} was made artificially in the simulation at a certain time.

A simulation was performed with the same characteristics of Tab.3, however it started with $X_{cg} = 0.3$ and $X_{EA} = 0.4$, since it is a stable system, as the center of gravity would be in front of the elastic axis according to Pines [24] theory. At eight seconds of real time, the value of X_{cg} was abruptly changed to 0.5, bringing the system to a region of instability and at ten seconds the code was able to detect the increase in energy in the system and the increase in the oscillation amplitudes of the model, thus changing the geometry of the airfoil and advancing the position of the center of gravity, returning the system to a stable position. In Fig.9a the temporal response of the simulation is observed, showing that until eight seconds the amplitudes are reducing in time, in sequence, from eight to ten seconds, the amplitudes start to increase, but after ten seconds (change of geometry and advance of the C_g) the system becomes damped again. To return the system to a stable position, the neural network generated a new airfoil, different from the previous one, which can be seen in Fig.9b.

| (a) Time simulation | (b) Airfoil comparison |
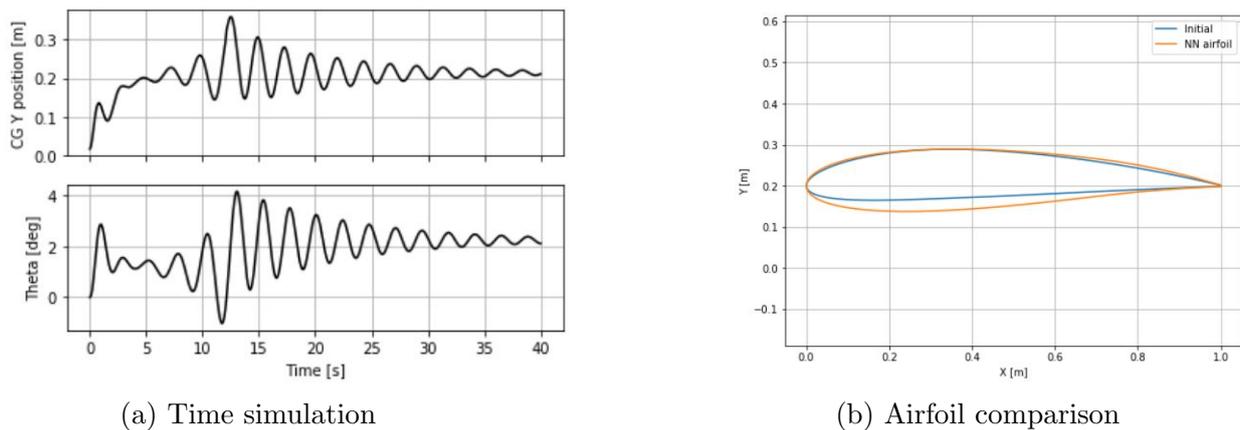
Figure 9: Results for a given case

It can be seen that the code was able to predict instability and change the airfoil by correcting and dampening the system.

A problem that was found was the high sensitivity of the neural network when choosing the curves of the desired airfoil. With each simulation in which the neural network was trained, it was possible to obtain different results, which perhaps, were not satisfactory, even with the same training database. This fact occurs due to the random choice of the neural network between the training and test data, therefore requiring an increase in the

robustness of this network, such as change the neural network architecture.

6 CONCLUSION

This work showed the implementation and validation of methods used in the modelling of an aeroelastic system and a neural network capable of changing the geometry of an airfoil and stabilizing an unstable system. The following tools were used: Bezier-Parsec 3434 parametrization, genetic algorithm, construction of neural network, solution of 2D aeroelastic problem with dynamic alteration of the C_g and final coupling. It is observed through the validation of the codes and the results obtained that the proposed model was well implemented. Figure 9a also shows the correct prevention of the instability that was initiated, thus demonstrating its validity.

However, the problems foreseen in the introduction occurred and the greatest difficulty encountered was the construction of the database, a process that required significant time and computational power. The deficiencies of this work were the simplicity of the aeroelastic model, the inability of the neural network to predict different families of airfoils, the sudden change in profile geometry, due to its impossibility in reality, and also the delay in building the database necessary for the training of this network architecture. The main problem was the instability of the neural network's code, because it can generate different results depending on the database used for training.

As possible future works, it is necessary to try to correct these problems: the neural network can be improved, making it more generic and powerful; the aeroelastic model and the method of solving the equation of motion can be more accurate and closer to reality. Finally, it is also possible to add new capabilities to the model, such as the introduction of a flap mechanism as a way of controlling instabilities.

ACKNOWLEDGEMENTS

REFERENCES

[1] D. Raymer. Aircraft design: A conceptual approach. *4th edn., AIAA Education Series, AIAA*, 2006.

[2] N. Tsushima, K. Soneda, T. Yokozeki, T. Imamura, H. Arizono, and W. Su. Structural and aerodynamic models for aeroelastic analysis of corrugated morphing wings. *AIAA SciTech Forum*, Jan 2020.

[3] J. Bowman, M. B. Sanders, and D. T. Weisshaar. Evaluating the impact of morphing technologies on aircraft performance. *43rd AIAA/ASME/ASCE/AHS/ASC Structures, Structural Dynamics, and Materials Conference, No. AIAA-2002- 1631*, April 2002.

[4] M. H. Hassoun. Fundamentals of artificial neural networks. *MIT press Cambridge, Massachusetts, London*, 1995.

Raul Carreira Rufato and Joseph Morlier

[5] A. Kharal and A. Saleem. Neural networks based airfoil generation for a given cp using bezier–parsec parameterization. *Aerospace Science and Technology*, 23:330–344, 2012.

[6] M. S. Selig. `http://www.ae.illinois.edu/m-selig/ads/coord_database.html`. [Online; accessed on 20 May 2020].

[7] N. P. Salunke, J. A. R. A., and S. Channiwala. Airfoil parameterization techniques: A review. *American Journal of Mechanical Engineering*, 2:99–102, no. 4 (2014).

[8] R. Derksen and T. Rogalsky. Bezier-parsec: An optimized aerofoil parameterization for design. *Advances in Engineering Software*, 41:923–930, 2010.

[9] F. Chollet et al. Keras. 2015. URL `https://github.com/fchollet/keras`.

[10] V. T. Nagaraj and D. J. Johns. Flutter analysis of a wing with concentrated inertias by a direct matrix method. *Symposium on structural dynamics paper No. E.5*, 1975.

[11] A. Zell. Simulation neuronaler netze [simulation of neural networks] (in german) (1st ed.). *Addison-Wesley.Chapter 5.2.*, 2003.

[12] A. J. Ava Shahrokhi. Airfoil shape parameterization for optimum navier–stokes design with genetic algorithm. *Aerospace Science and Technology 11 443- 450*, 2007.

[13] R. T. Acceleration of differential evolution for aerodynamic design. ph.d. thesis. *University of Manitoba*, 2004.

[14] N. K. Oyama A, Obayashi S. Fractional factorial design of genetic coding for aerodynamic optimization. *AIAA Paper 99 - 3298*, 1999.

[15] M. A. Bouhlel, S. HE, and J. Martins. msann model benchmarks. *Mendeley Data, V1*, 2019. doi:doi: 10.17632/ngpd634smf.1.

[16] E. H. Dowell. *A Modern Course in Aeroelasticity*. Springer, fifth revised and enlarged edition edition, 1999.

[17] R. Storn. `http://www.icsi.berkeley.edu/~storn/code.html`. [Online; accessed on 01 May 2020].

[18] M. Drela. `https://web.mit.edu/drela/Public/web/xfoil/`. [Online; accessed on 21 June 2020].

[19] A. Zell. *Simulation Neuronaler Netze [Simulation of Neural Networks] (in German)*. Addison-Wesley. p. 73. ISBN 3-89319-554-8, 1 edition, 1994.

[20] J. B. Diederik P. Kingma. Adam: A method for stochastic optimization. *3rd International Conference for Learning Representations*, 2015.

[21] J. Brownlee. `https://machinelearningmastery.com/k-fold-cross-validation/`.

Raul Carreira Rufato and Joseph Morlier

[22] J. D. Anderson. *Fundamentals of aerodynamics.* McGraw-Hill, 5th edition, Feb. 2011. ISBN 9780073398105.

[23] R. Mittal. `https://engineering.jhu.edu/fsag/research/aeroelastic-flutter/#:~:text=Aeroelastic%20Flutter,wide%20range%20of%20engineering%20fields`.

[24] P. S. An elementary explanation of the flutter mechanism. *Proceedings nature specialists meeting on dynamics and aeroelasticity, Institute of the Aeronautical Sciences, Ft.Worth, Texas, pp 52–58*, 1958.

A FINITE-ELEMENT TRANSONIC POTENTIAL SOLVER WITH AN EMBEDDED WAKE APPROACH FOR AIRCRAFT AEROELASTIC OPTIMIZATION

Iñigo López[1]*, Marc Núñez[2], Armin Geiser[1], Riccardo Rossi[2], Roland Wüchner[1] and Kai-Uwe Bletzinger[1]

1: Chair of Structural Analysis
Department of Civil, Geo and Environmental Engineering
Technical University of Munich
Arcisstr. 21, 80333, Munich, Germany
inigo.lopez@tum.de, armin.geiser@tum.de, wuechner@tum.de, kub@tum.de,
https://www.bgu.tum.de/en/st/forschung/

2: Kratos Multiphysics Group
International Center for Numerical Methods in Engineering
Polytecnic University of Catalonia
C/ Gran Capità s/n Campus Nord UPC, 08024, Barcelona, Spain
mnunez@cimne.upc.edu, rrossi@cimne.upc.edu, https://www.cimne.com

Abstract. *An embedded wake approach for the effective use of potential transonic solvers in the context of aircraft aeroelastic optimization is presented. To support a jump in the potential across the wake, cut elements are disconnected across wake surfaces by enriching the finite element space with additional degrees of freedom. The wake boundary conditions are then applied with the additional equations that stem from the discretization. Representing the wake implicitly within the domain saves modeling time and allows performing aircraft aeroelastic optimization, where the position of the wake may change due to the structural response or due to the geometry's evolutionary steps. Using embedding techniques can potentially lead to ill-conditioned systems due to the so-called small cut cell problem. To ensure robustness and avoid large condition numbers, a full-integration technique is presented. The wake surface can be automatically generated by shedding it from the trailing edge in the freestream velocity direction. A robust and accurate capturing of the potential jump across the wake is achieved by automatically refining the mesh with a metric-based technique. An artificial compressibility method is used to stabilize the problem in supersonic flow regions preventing the Jacobian from becoming singular and allowing to capture shock waves. To validate the method, the transonic flow solution over the ONERA M6 wing is compared with wind tunnel data and reference solutions from other codes. The solver is implemented in KRATOS Multiphysics and is available under a BSD license.*

Keywords: Embedded wake surfaces, full potential equation, finite element method, aeroelastic optimization, transonic flow

Iñigo López, Marc Núñez, Armin Geiser, Riccardo Rossi, Roland Wüchner and Kai-Uwe Bletzinger

1 INTRODUCTION

Despite the increase of computational power and the advances in high-fidelity methods in the last decades, potential linear solvers, typically panel or vortex lattice solvers, are still widely used in the industry for aircraft aeroelastic optimization at the early stages of design. In the early design stages, many configurations have to be explored, ensuring the structural integrity for a large number of flight conditions. Therefore, the required number of fluid evaluations scales with the number of configurations, the number of optimization steps, and the number of aeroelastic iterations needed in each optimization step. This yields a number that ranges from a couple of hundreds to a couple of thousands of fluid evaluations. Fast solvers are thus still required for practical applications. However, it is often attempted to shift the use of high-fidelity solvers to early design stages to detect design flaws as soon as possible, saving time and money. The full-potential equation offers an appealing trade-off, allowing to obtain fast solutions while enlarging the range of application to capture transonic nonlinear compressibility effects.

Nevertheless, to support a jump in the potential across the wake, standard full-potential solvers require modeling a gap in the mesh, adapting the model to the wake's topology [1, 2]. This hinders the effective use of such solvers for aeroelastic optimization, where the wake's position may change due to the structural response and the geometry's evolutionary steps. To achieve efficiency, an embedded wake approach for potential transonic solvers is proposed. The solver is implemented in KRATOS Multiphysics. KRATOS is an open-source finite-element framework for building parallel, multi-disciplinary simulation software [3].

2 METHOD

2.1 Full-potential equation

The full-potential equation expresses conservation of mass in terms of density ρ and velocity $\boldsymbol{u}$:

$$\nabla \cdot (\rho \boldsymbol{u}) = 0 \tag{1}$$

where, assuming irrotational flow, the velocity can be expressed using the freestream velocity $\boldsymbol{u}_\infty$ and the gradient of the scalar potential ϕ as:

$$\boldsymbol{u} = \boldsymbol{u}_\infty + \nabla \phi \tag{2}$$

Assuming isentropic flow, the density may be derived from the energy equation:

$$\rho = \rho_\infty \left[1 + \frac{\gamma - 1}{2} \frac{u_\infty^2}{a_\infty^2} \left(1 - \frac{u^2}{u_\infty^2} \right) \right]^{\frac{1}{\gamma - 1}} \tag{3}$$

where ρ_∞ and a_∞ are the freestream density and speed of sound respectively [4]. The constant γ is the heat capacity ratio, which is 1.4 for air.

2.2 Boundary conditions

Figure 1 illustrates the fluid domain and its boundaries. Eqs. (4) to (7) are the boundary conditions.

Iñigo López, Marc Núñez, Armin Geiser, Riccardo Rossi, Roland Wüchner and Kai-Uwe Bletzinger
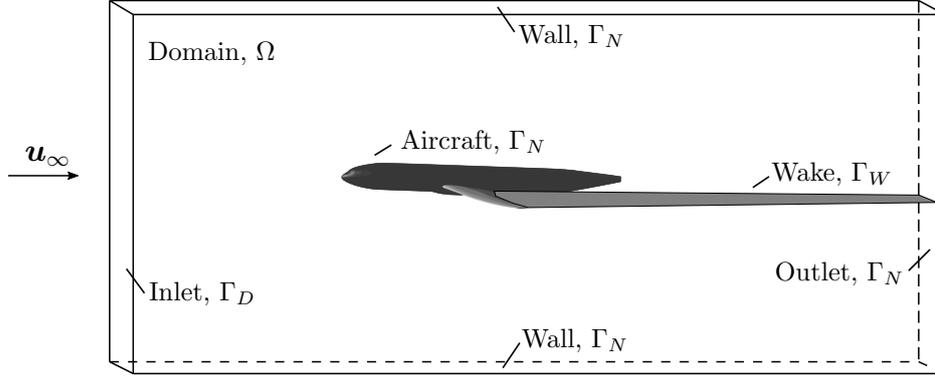
Figure 1: Fluid domain and its boundaries.

$$\phi = \phi_\infty \qquad \text{on } \Gamma_D \qquad (4)$$

$$\mathbf{n} \cdot (\rho \boldsymbol{u}) = g \qquad \text{on } \Gamma_N \qquad (5)$$

$$\mathbf{n} \cdot (\rho_\mathrm{u} \boldsymbol{u}_\mathrm{u} - \rho_\mathrm{l} \boldsymbol{u}_\mathrm{l}) = 0 \qquad \text{on } \Gamma_W \qquad (6)$$

$$|\boldsymbol{u}_\mathrm{u}|^2 - |\boldsymbol{u}_\mathrm{l}|^2 = 0 \qquad \text{on } \Gamma_W \qquad (7)$$

Equation (4) is a Dirichlet condition, where ϕ_∞ is an arbitrary value specified along the domain's Γ_D boundary. This condition is necessary because the full-potential equation and the remaining boundary conditions are only defined in terms of the potential's derivatives.

Because the wake intersects the outlet, and there is a jump in the potential across the wake, a Dirichlet condition cannot be applied at the outlet. Instead, the freestream velocity is specified at the outlet as a Neumann condition using Eq. (5) and setting $g = \boldsymbol{n} \cdot (\rho \boldsymbol{u}_\infty)$. On the airfoil and walls, a slip condition is applied ($g = 0$).

The wake is modeled as a straight surface in the freestream direction. To relax this assumption, mass flux is allowed across the wake. Eq. (6) enforces the conservation of mass flux across the wake, where the subscripts $( )_\mathrm{u}$ and $( )_\mathrm{l}$ stand for the upper and lower wake. Because the wake is thin, it cannot support pressure jumps. The pressure equality condition is imposed in Eq. (7).

2.3 Finite element discretization

Equation (1) is discretized using a standard Galerkin approach. Here unstructured meshes with linear triangular and tetrahedral elements are used. Weighting Eq. (1) with the test function N and discretizing into finite elements results in:

$$\sum_e \int_{\Omega_e} N \nabla \cdot (\rho \boldsymbol{u}) \, d\Omega_e = 0 \qquad (8)$$

being Ω_e each element's domain. Using integration by parts, applying the divergence theorem, and inserting Eq. (5) yields:

$$\sum_e \int_{\Omega_e} \nabla N \cdot (\rho \boldsymbol{u}) \, d\Omega_e = \sum_c \int_{\Gamma_c} N g \, d\Gamma_c \qquad (9)$$

Iñigo López, Marc Núñez, Armin Geiser, Riccardo Rossi, Roland Wüchner and Kai-Uwe Bletzinger

where Γ_c is the boundary of element c. Equation (9) can be rewritten in residual form using Einstein notation as:

$$R^i = \sum_e \int_{\Omega_e} \frac{\partial N^i}{\partial x^a} \rho u^a \, d\Omega_e - \sum_c \int_{\Gamma_c} N^i g \, d\Gamma_c = 0 \tag{10}$$

where R^i is the residual at each node. Equation (10) is solved using Newton's method:

$$J^{ij} \Delta \phi^j = -R^i \tag{11}$$

being $\Delta \phi^j$ the solution update and J^{ij} the corresponding Jacobian, which is defined as:

$$J^{ij} = \frac{\partial R^i}{\partial \phi^j} = \sum_e \int_{\Omega_e} \frac{\partial N^i}{\partial x^a} \left(\rho \frac{\partial u^a}{\partial \phi^j} + \frac{\partial \rho}{\partial \phi^j} u^a \right) d\Omega_e \tag{12}$$

2.4 Artificial compressibility

To stabilize the problem in supersonic flow regions an artificial compressibility method is employed [5]. This prevents the Jacobian from becoming singular and allows capturing shock waves. In this method, an upwind scheme is used to compute the density:

$$\tilde{\rho} = \rho - \mu \left(\frac{\partial \rho}{\partial s} \right) \Delta s \approx \rho - \mu(\rho - \rho_{\text{up}}) \tag{13}$$

where ρ_{up} is the upstream element's density and μ is the upwinding factor, which is defined as the following switching function:

$$\mu = \mu_c \max(0, \mu, \mu_{\text{up}}) \tag{14}$$
$$\mu = 1 - \frac{M_{\text{crit}}^2}{M^2}$$

where μ_c is the upwinding factor constant, and M_{crit} is the critical Mach number. These factors control the amount of artificial dissipation introduced into the system. Eq. (13) replaces ρ in Eqs. (10) and (12). To avoid reaching vacuum conditions, the fluid variables and their derivatives are clamped to a maximum Mach number squared of $M^2 = 3.0$.

2.5 Embedded wake approach

To support a jump in the potential, elements cut by the wake are enriched with auxiliary degrees of freedom and disconnected across the wake so that wake elements are present twice. This is illustrated in Figure 2, where the auxiliary degrees of freedom are denoted by ϕ^i_{aux}. Note that the separation between upper and lower mesh presented in Figure 2 is only for visualization purposes; in practice, there is only one mesh, and the separation is achieved via the element formulation proposed in this section.

As shown in Figure 2, the degrees of freedom ϕ^i_{u} and ϕ^i_{l} corresponding respectively to the upper and lower wake elements are:

$$\phi^i_{\text{u}} = \begin{cases} \phi^i & \text{if } i^{\text{th}} \text{ node above the wake} \\ \phi^i_{\text{aux}} & \text{if } i^{\text{th}} \text{ node below the wake} \end{cases} \qquad \phi^i_{\text{l}} = \begin{cases} \phi^i_{\text{aux}} & \text{if } i^{\text{th}} \text{ node above the wake} \\ \phi^i & \text{if } i^{\text{th}} \text{ node below the wake} \end{cases} \tag{15}$$

Iñigo López, Marc Núñez, Armin Geiser, Riccardo Rossi, Roland Wüchner and Kai-Uwe Bletzinger

(a) Mesh around the trailing edge.

(b) Elements above the wake.   (c) Elements below the wake.
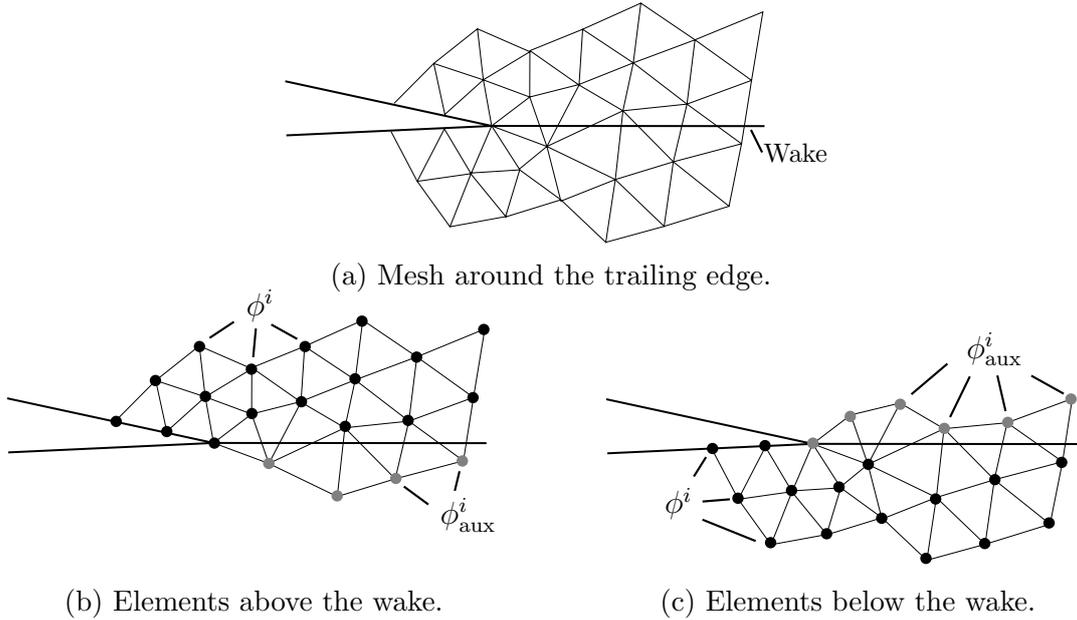
Figure 2: Elements are disconnected across the wake to support a jump in ϕ.

The additional equations stemming from these auxiliary degrees of freedom are then used to apply the wake boundary conditions (Eqs. (6) and (7)). In the current implementation, first, Eq. (6) is linearized by substituting the freestream density ρ_∞ for ρ_u and ρ_l, which yields:

$$g_1 = \mathbf{n} \cdot (\boldsymbol{u}_\mathrm{u} - \boldsymbol{u}_\mathrm{l}) = 0 \qquad \text{on } \Omega_W \tag{16}$$

where $\mathbf{n}$ is the normal vector to the wake defined upwards, and Ω_W is the domain covered by the wake elements. Second, approximating the average wake sheet velocity with the freestream velocity allows linearazing Eq. (7) as:

$$g_2 = \hat{\boldsymbol{u}}_\infty \cdot (\boldsymbol{u}_\mathrm{u} - \boldsymbol{u}_\mathrm{l}) = 0 \qquad \text{on } \Omega_W \tag{17}$$

where $\hat{\boldsymbol{u}}_\infty$ is a unit vector defined as $\hat{\boldsymbol{u}}_\infty = \boldsymbol{u}_\infty / u_\infty$. Eq. (17) is a homogeneous linear convection equation for the potential jump across the wake. It states that the potential jump is constant along the freestream sheet streamlines. Applying a least squares finite element approach on Eqs. (16) and (17), yields the following residual energy functional:

$$\Pi = \frac{1}{2} \int_{\Omega_W} g_1^2 + g_2^2 \ d\Omega_W \tag{18}$$

Deriving with respect to the degrees of freedom results in the upper and lower wake conditions' residuals:

$$R_\mathrm{u}^i = \frac{\partial \Pi}{\partial \phi_\mathrm{u}^i} = \sum_{W_\mathrm{u}} \int_{\Omega_{W_\mathrm{u}}} \frac{\partial N_\mathrm{u}^i}{\partial x^b} \left(\hat{n}^b g_1 + \hat{u}_\infty^b g_2 \right) \ d\Omega_{W_\mathrm{u}} \tag{19}$$

$$R_\mathrm{l}^i = \frac{\partial \Pi}{\partial \phi_\mathrm{l}^i} = \sum_{W_\mathrm{l}} \int_{\Omega_{W_\mathrm{l}}} \frac{\partial N_\mathrm{l}^i}{\partial x^b} \left(\hat{n}^b g_1 + \hat{u}_\infty^b g_2 \right) \ d\Omega_{W_\mathrm{l}} \tag{20}$$

Iñigo López, Marc Núñez, Armin Geiser, Riccardo Rossi, Roland Wüchner and Kai-Uwe Bletzinger

and their corresponding Jacobians:

$$J_{\text{uu}}^{ij} = \frac{\partial R_{\text{u}}^i}{\partial \phi_{\text{u}}^j} = \sum_{W_{\text{u}}} \int_{\Omega_{W_{\text{u}}}} \frac{\partial N_{\text{u}}^i}{\partial x^b} \left(\hat{n}^b \hat{n}^a + \hat{u}_\infty^b \hat{u}_\infty^a \right) \frac{\partial N_{\text{u}}^j}{\partial x^a} \, d\Omega_{W_{\text{u}}} \tag{21}$$

$$J_{\text{ul}}^{ij} = \frac{\partial R_{\text{u}}^i}{\partial \phi_{\text{l}}^j} = -\sum_{W_{\text{u}}} \int_{\Omega_{W_{\text{u}}}} \frac{\partial N_{\text{u}}^i}{\partial x^b} \left(\hat{n}^b \hat{n}^a + \hat{u}_\infty^b \hat{u}_\infty^a \right) \frac{\partial N_{\text{l}}^j}{\partial x^a} \, d\Omega_{W_{\text{u}}} \tag{22}$$

$$J_{\text{lu}}^{ij} = \frac{\partial R_{\text{l}}^i}{\partial \phi_{\text{u}}^j} = -\sum_{W_{\text{l}}} \int_{\Omega_{W_{\text{l}}}} \frac{\partial N_{\text{l}}^i}{\partial x^b} \left(\hat{n}^b \hat{n}^a + \hat{u}_\infty^b \hat{u}_\infty^a \right) \frac{\partial N_{\text{u}}^j}{\partial x^a} \, d\Omega_{W_{\text{l}}} \tag{23}$$

$$J_{\text{ll}}^{ij} = \frac{\partial R_{\text{l}}^i}{\partial \phi_{\text{l}}^j} = \sum_{W_{\text{l}}} \int_{\Omega_{W_{\text{l}}}} \frac{\partial N_{\text{l}}^i}{\partial x^b} \left(\hat{n}^b \hat{n}^a + \hat{u}_\infty^b \hat{u}_\infty^a \right) \frac{\partial N_{\text{l}}^j}{\partial x^a} \, d\Omega_{W_{\text{l}}} \tag{24}$$

Eqs. (19) to (24) are assembled in the global equation system together with Eqs. (10) and (12). The wake surface can be automatically generated by shedding it from the trailing edge in the freestream velocity direction. A robust and accurate capturing of the potential jump across the wake can be achieved by automatically refining the mesh with a metric-based technique [6]. This implicit representation of the wake within the domain saves modeling time and allows to perform aeroelastic optimization in practical applications efficiently.

3   3D ONERA M6 WING TRANSONIC VALIDATION CASE

This section presents the validation and verification of the three-dimensional potential transonic solver using the proposed embedded wake approach. To do so, the flow solution over the ONERA M6 wing is compared with wind tunnel test data and with reference solutions from other solvers using different fluid fidelity levels. The Onera M6 wing has become a standard CFD validation case for external transonic flows because it is challenging to reproduce the complex double shock appearing on the upper surface and the underlying local supersonic flow. In this case, the wing is at an angle of attack of $\alpha = 3.06°$ and a freestream Mach number of $M_\infty = 0.84$, corresponding to the conditions of the wind tunnel test 2308 described in [7].

3.1   Wing's geometry and mesh

Onera M6 is a swept, semi-span wing with no twist. The wing's surface is constructed via conical generation from the symmetrical ONERA-D airfoil, i.e., all airfoil sections are homothetic. Figure 3 presents the parameters describing the wing's planform geometry. The numbers 1 to 6 indicate the position of the sections where the pressure coefficient distribution is analyzed. The exact sections' position is presented in a table in Figure 3. The reference area for the computation of the aerodynamic coefficients is $A_{\text{ref}} = 0.7532 \, \text{m}^2$. The ONERA-D airfoil coordinates can be found in [7], where it can be seen that the trailing edge has a finite thickness. For the purposes of this study, the CAD geometry is taken from [8], where the trailing edge has been made sharp, as described in [9]. Figure 4 shows the wind tunnel and CAD models.

Salome is used to generate a volumetric domain of 25 m around the wing's surface. The domain is then discretized using a tetrahedral mesh with the NETGEN algorithm

Iñigo López, Marc Núñez, Armin Geiser, Riccardo Rossi, Roland Wüchner and Kai-Uwe Bletzinger

Parameter	Value
Span b	1.1963 m
Mean aerodynamic chord $\bar{c}$	0.64607 m
Aspect ratio Λ	3.8
Taper ratio λ	0.562
Sweep angle φ_{25}	26.7°
Leading edge sweep	30.0°
Trailing edge sweep	15.8°

Sections	
N	y/b
1	0.20
2	0.44
3	0.65
4	0.80
5	0.90
6	0.95
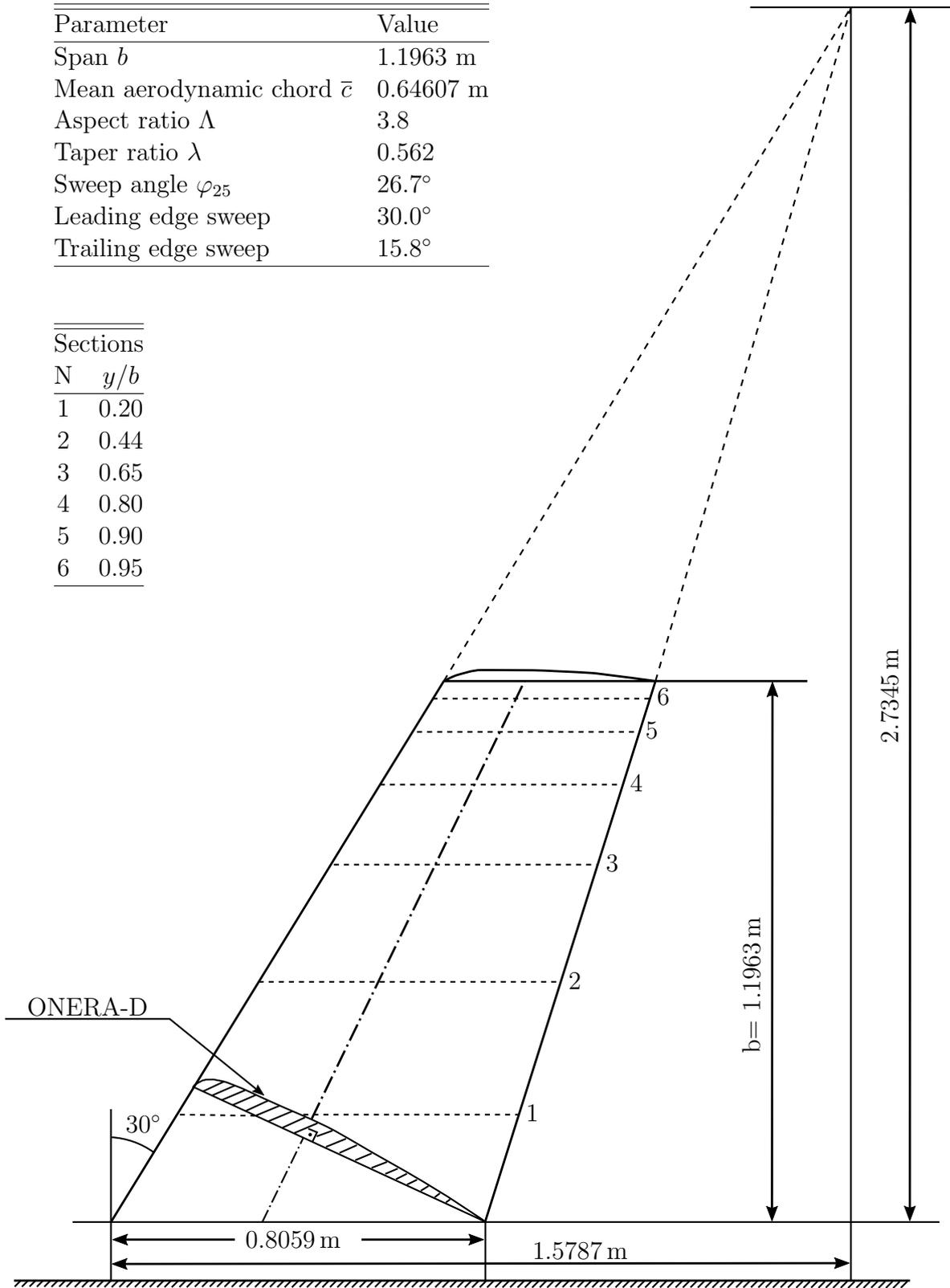
Figure 3: ONERA M6 planform layout [7].

Iñigo López, Marc Núñez, Armin Geiser, Riccardo Rossi, Roland Wüchner and Kai-Uwe Bletzinger

(a) Wind tunnel model [7].　　　　　　(b) CAD model [9]
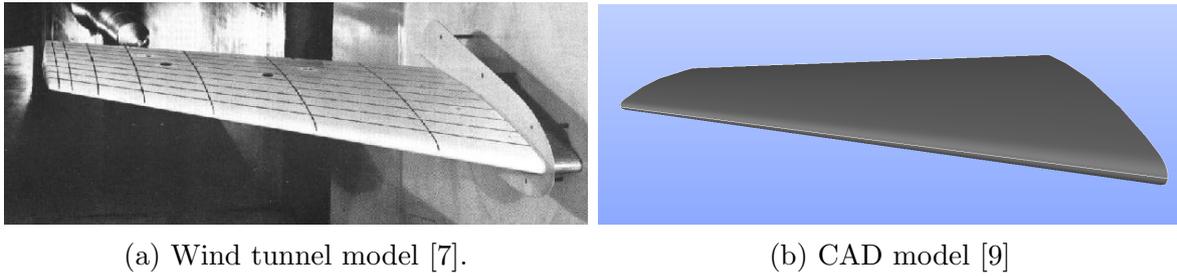
Figure 4: ONERA M6 models.

[10]. To capture the solution gradients, the meshes are refined towards the leading and trailing edge. This refinement also accurately captures the geometry at the leading edge, where the radius of curvature is smallest. The main parameters defining the mesh are the minimum element size at the leading and trailing edges (0.002 m), the maximum element size at the inlet, outlet and walls (1.25 m), and the surface and volume growth rates (0.2), which are the maximum ratios by which two adjacent elements can differ (e.g. a growth rate of 0.2 means that the linear dimensions of two adjacent elements can differ by 20%). Figure 5 shows the wing's surface mesh in blue together with a cut of the tetrahedral volume mesh along $y/b = 0.2$ in green. Transparent black triangles indicate the embedded wake surface. The volume mesh has a total of $1.7 \cdot 10^5$ degrees of freedom and $8.7 \cdot 10^5$ elements. The wing's surface mesh has $2.7 \cdot 10^4$ nodes and $5.4 \cdot 10^4$ triangular conditions. Note the substantial benefit of using an embedded approach, where the wake does not have to be explicitly represented in the mesh.
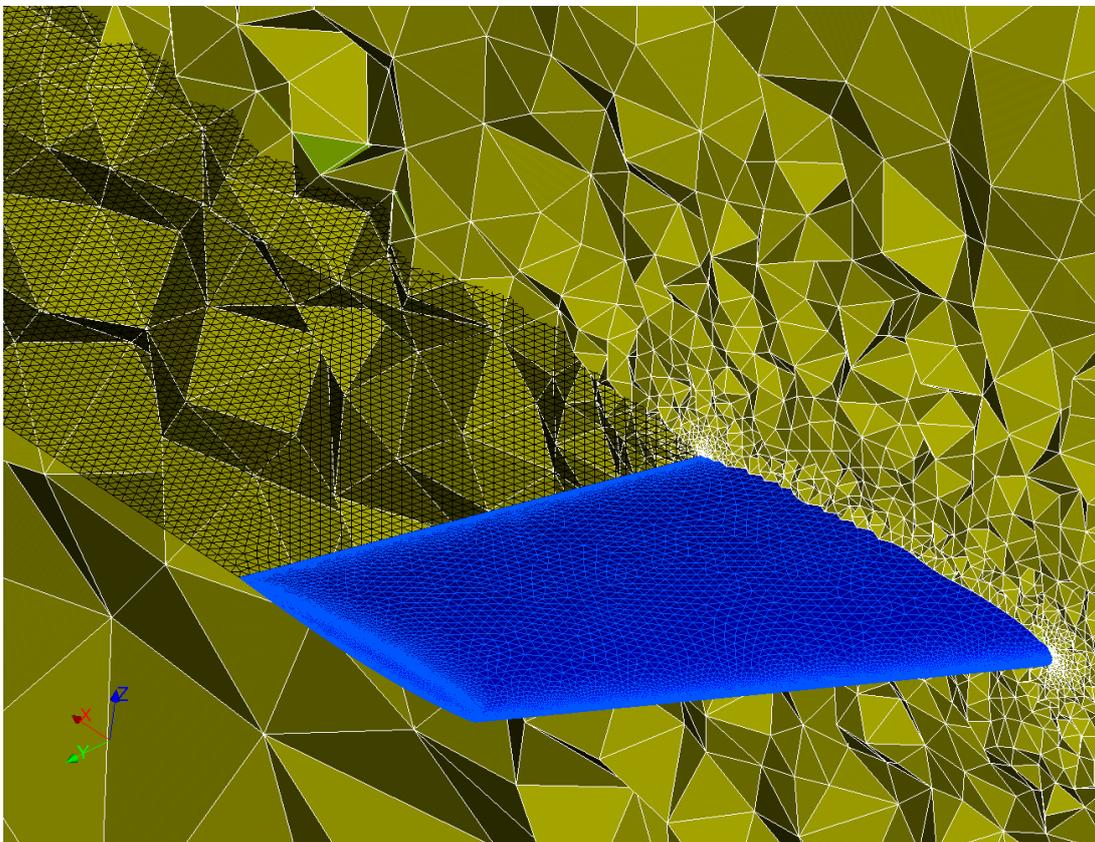
Figure 5: Meshes of the ONERA M6 wing, tetrahedral volume, and embedded wake.

Iñigo López, Marc Núñez, Armin Geiser, Riccardo Rossi, Roland Wüchner and Kai-Uwe Bletzinger

3.2 Pressure coefficient validation and verification

Figure 7 compares the pressure coefficient distribution at the sections indicated in Figure 3 with the finite volume potential transonic solution from [11], the RANS reference solution from [12], and the wind tunnel data from [7]. The accuracy of the wind tunnel data is +/-0.02. The critical pressure coefficient is indicated with a dashed line to quickly identify the regions where the flow is locally supersonic. All data predict the appearance of a double-shock pattern on the upper surface. In general, the solution is close to the RANS data, except in the vicinity of the shock wave in sections 1 to 4. In these sections, the computed shock wave position is closer to the other full potential solution, and both full potential solutions predict a shock that is stronger and located after compared to the RANS and wind tunnel data. In sections 5 and 6 the solution predicted by Kratos matches with the RANS and wind tunnel data better than the other potential solution, even regarding the shock's strength and position. It seems that the other potential solution has too much artificial dissipation, which would explain why this curve appears below the rest in the supersonic region, and why the shock is not as sharply captured as for the rest of the solutions. Note that the proposed potential solver with an embedded wake approach successfully captures the pressure gradients and the pressure equality condition in the vicinity of the trailing edge.

As a general rule, the RANS solution lies closer to the wind tunnel data than the full-potential solutions. In fact, the C_p predicted by RANS matches with the wind tunnel data, except in section 1, where the shock appears to be stronger and after, and in section 4, where RANS predicts the coalescence of the two shocks, whereas for the wind tunnel measurements this coalescence happens at a further spanwise location.

Figure 6 presents the pressure coefficient and Mach contour distributions on the wing's upper surface. Both distributions capture the three-dimensional lambda-type shock structure formed by the double-shock pattern on top of the wing.

(a) Pressure coefficient.   (b) Mach number.
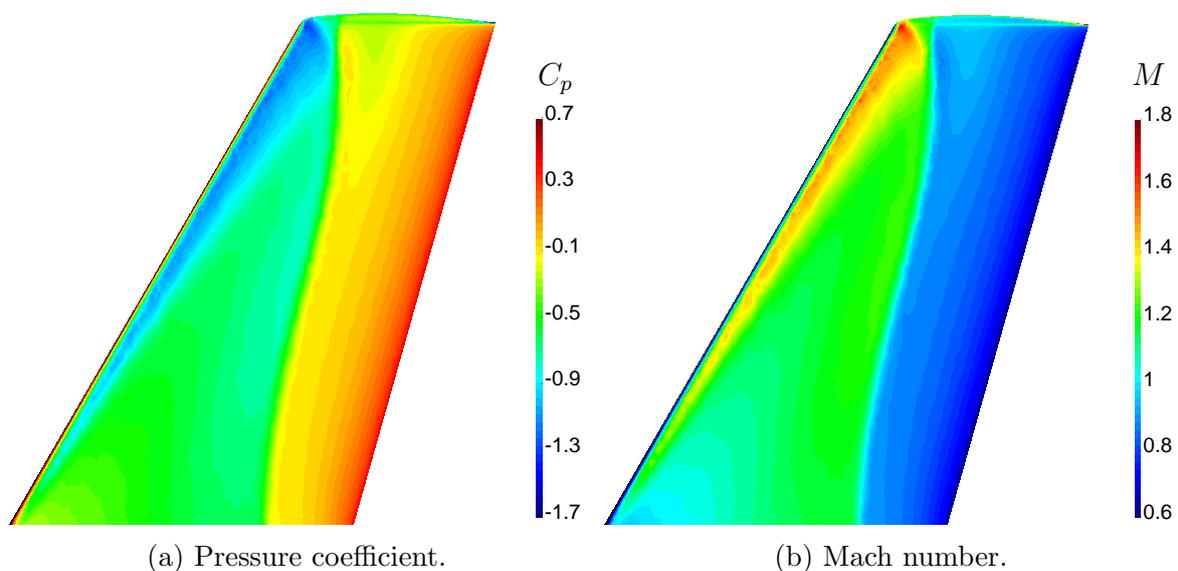
Figure 6: Contour plots over ONERA M6.

Iñigo López, Marc Núñez, Armin Geiser, Riccardo Rossi, Roland Wüchner and Kai-Uwe Bletzinger
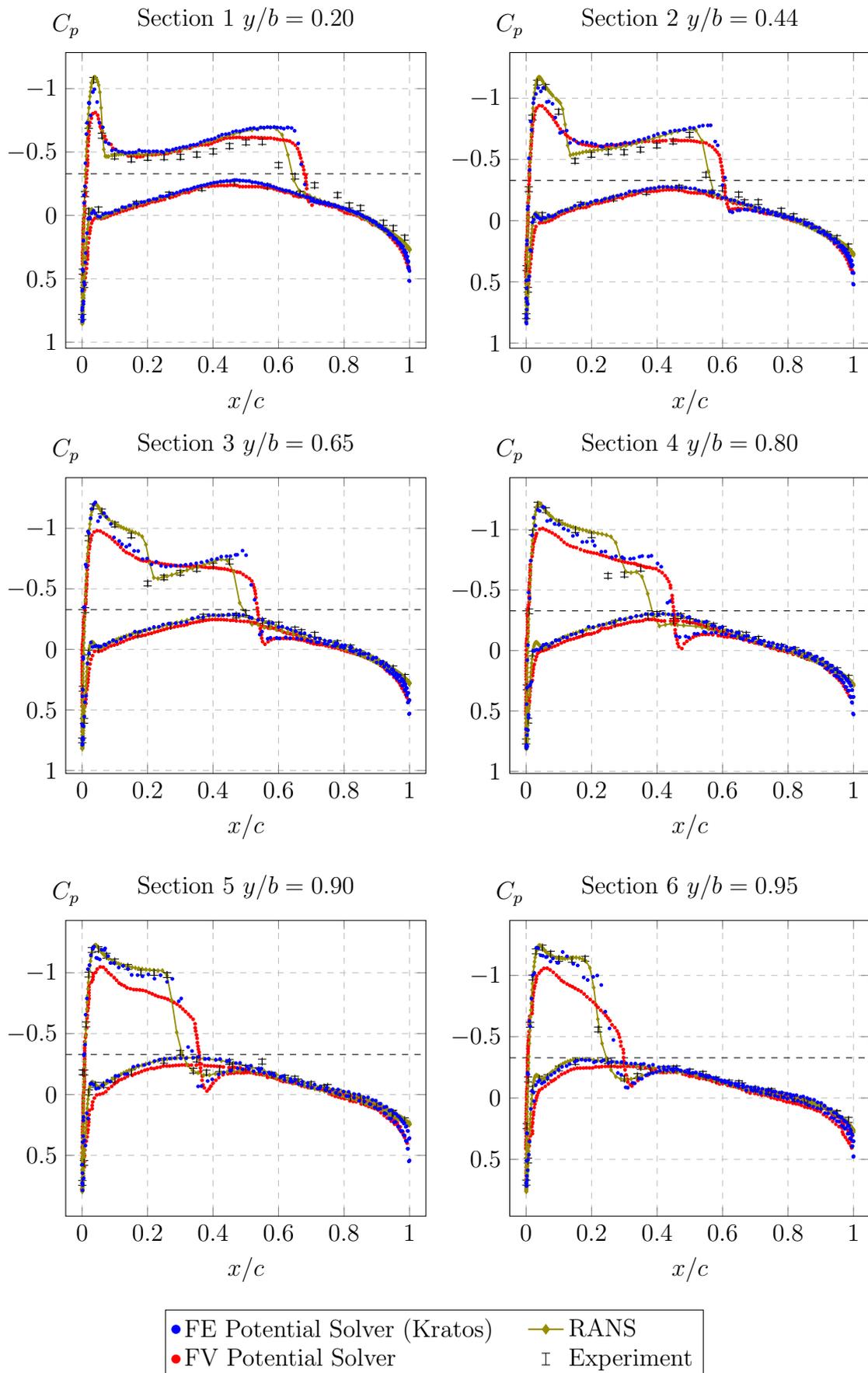
Figure 7: Pressure coefficient distribution at different wing sections.

Iñigo López, Marc Núñez, Armin Geiser, Riccardo Rossi, Roland Wüchner and Kai-Uwe Bletzinger

3.3 Aerodynamic loads verification

Crovato et al. provide a rigorous study on the impact of the aerodynamic fidelity level used in preliminary aircraft design [13]. Following their results, the solution obtained with the proposed embedded wake approach is compared to the reference data from five other solvers, including five fidelity levels. Table 1 presents the naming convention used to refer to the fidelity levels, the corresponding software packages, and the aerodynamic coefficients resulting from the pressure coefficient integration over the wing. The reference point for the computation of the moment coefficient is taken at the root's chord leading edge. Note that Kratos accurately matches the solution predicted by Tranair. The lift coefficient is the same up to the precision used, and the drag and moment coefficients relative errors lay within 1% and 2%, respectively.

Compared with the other models, the linear inviscid solvers (PAN and NAS) underestimate the lift and moment coefficients. The drag coefficient predicted by Panair is very small because it cannot capture the wave drag. Correcting NAS solution with Euler (NASC) yields results closer to the nonlinear inviscid models. The nonlinear inviscid solvers (TRN, KRATOS, FLO and SU2) overestimate the lift and moment coefficients and underestimate the drag coefficient compared to the viscous solvers (TRNV and SU2V) because they do not solve the boundary layer, which changes the pressure coefficient distribution and includes the skin friction drag effect [13].

Model	Solver	Aerodynamic fidelity level	C_L	C_D	C_M
PAN	Panair	Linear Potential	0.247	0.0047	-0.181
NAS	NASTRAN	Linear Potential	0.248		-0.181
NASC	NASTRAN	Linear Potential corrected by Euler	0.271		-0.201
TRN	Tranair	Full Potential	0.288	0.0111	-0.212
KRATOS	Kratos	Full Potential with Embedded Wake	0.288	0.0112	-0.208
FLO	Flow	Full Potential	0.294	0.0110	-0.217
SU2	SU2	Euler	0.286	0.0130	-0.212
TRNV	Tranair	Full Potential and Boundary Layer	0.255	0.0161	-0.181
SU2V	SU2	Reynolds-Averaged Navier-Stokes	0.272	0.0181	-0.196

Table 1: Naming convention and aerodynamic coefficients obtained with different levels of fidelity for the Onera M6 wing ($\alpha = 3.06°$, $M_\infty = 0.84$) [13].

3.4 Performance comparison

To compare the computational cost of the proposed approach with other solvers, the wall-clock and CPU times required to obtain the solutions presented in Section 3.3 are given in Table 2 along with the mesh sizes. Kratos was run in serial in a desktop machine fitted with an Intel Xeon E5-1650 processor (3.5 GHz), SU2 was run on a cluster with Intel Xeon X5650 processors (2.7 GHz), and the rest of the solvers were run in serial on a laptop equipped with an Intel Core i7-7700HQ processor (2.8GHz). According to Table 2, KRATOS performs slightly faster than FLO and slightly slower than TRN. Note that the comparison is not entirely fair since the solvers were run in different machines. However, this comparison allows assessing that the time required by KRATOS, TRN, and FLOW is of the same order of magnitude. This shows that the capability of embedding the wake does not come at the cost of increasing the computational time nor losing accuracy.

Iñigo López, Marc Núñez, Armin Geiser, Riccardo Rossi, Roland Wüchner and Kai-Uwe Bletzinger

Model	n. Cells [1]	n. Threads	Wall-Clock Time	Cpu Time
PAN	$1.0 \cdot 10^3$	1	10 s	10 s
NAS	$5.0 \cdot 10^2$	1	20 s	20 s
NASC	$5.0 \cdot 10^2$	1	20 s	20 s
TRN	$5.0 \cdot 10^5$	1	7 min	7 min
KRATOS	$8.7 \cdot 10^5$	1	10 min	10 min
FLO	$5.9 \cdot 10^5$	1	13 min	13 min
SU2	$5.1 \cdot 10^5$	12	14 min	3 h
TRNV	$5.0 \cdot 10^5$	1	15 min	15 min
SU2V	$1.5 \cdot 10^6$	36	24 h	36 d

Table 2: Models mesh sizes and computational times [13].

Table 2 shows that the linear inviscid solvers provide a much faster solution than the other solvers. This is because they only solve a comparatively small linear system of equations once, whereas the nonlinear inviscid solvers require finer meshes and several Newton iterations. The highest fidelity solvers (SU2 and SU2V) need more time because they have more degrees of freedom per cell (corresponding to the 5 and 6 equations models) compared to the potential solvers, which only solve for one degree of freedom per cell (corresponding to the scalar potential equation).

3.5 Wake potential jump condition and wingtip vortex

Figure 8 shows the potential jump contour plot over the wake surface. Note that the potential jump is constant along the freestream sheet streamlines, which means that Eq. (17) is applied correctly with the proposed embedded wake approach. This is also shown in Figure 9, where the potential jump at the trailing edge and the intersection between the wake and a Trefftz plane positioned at the outlet is plotted over the dimensionless spanwise location. The largest disagreements occur in the vicinity of the wake tips at the outlet, where the mesh is too coarse and cannot capture the largest solution gradients. As the potential jump tends to zero towards the wake tips, the error introduced by the lack of conformity between elements can be neglected. Four different perspectives of the wingtip vortex behind the ONERA M6 wing are shown in Figure 10 to demonstrate that the proposed embedded wake approach can also capture the wingtip vortices. The top right figure also shows the pressure coefficient contour plot at the plane $x = 1.2 \, \text{m}$, where the low-pressure core of the vortex can be identified. This low-pressure core is related to the high-speed spin reached in the vortex center.
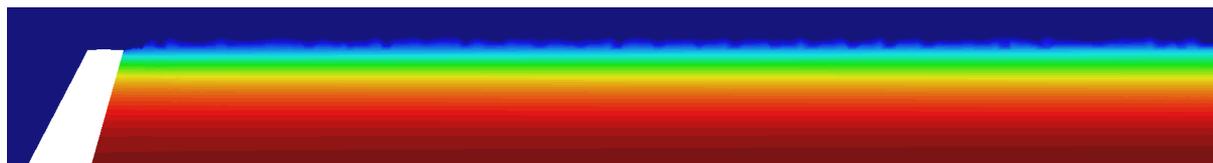
Figure 8: Potential jump contour plot over the wake surface.

---

[1] For Kratos it is number of elements.

Iñigo López, Marc Núñez, Armin Geiser, Riccardo Rossi, Roland Wüchner and Kai-Uwe Bletzinger
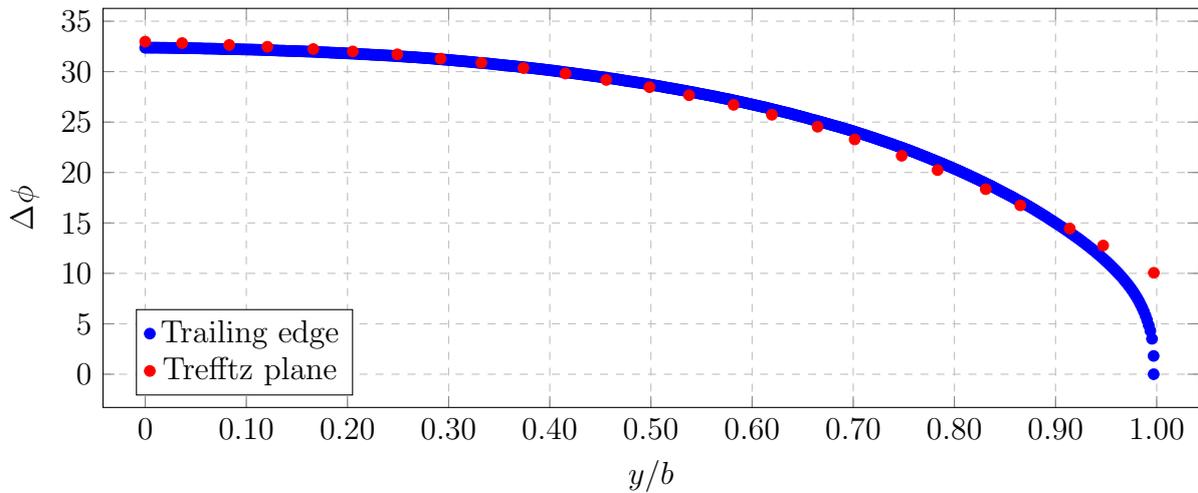
Figure 9: Potential jump spanwise distribution.
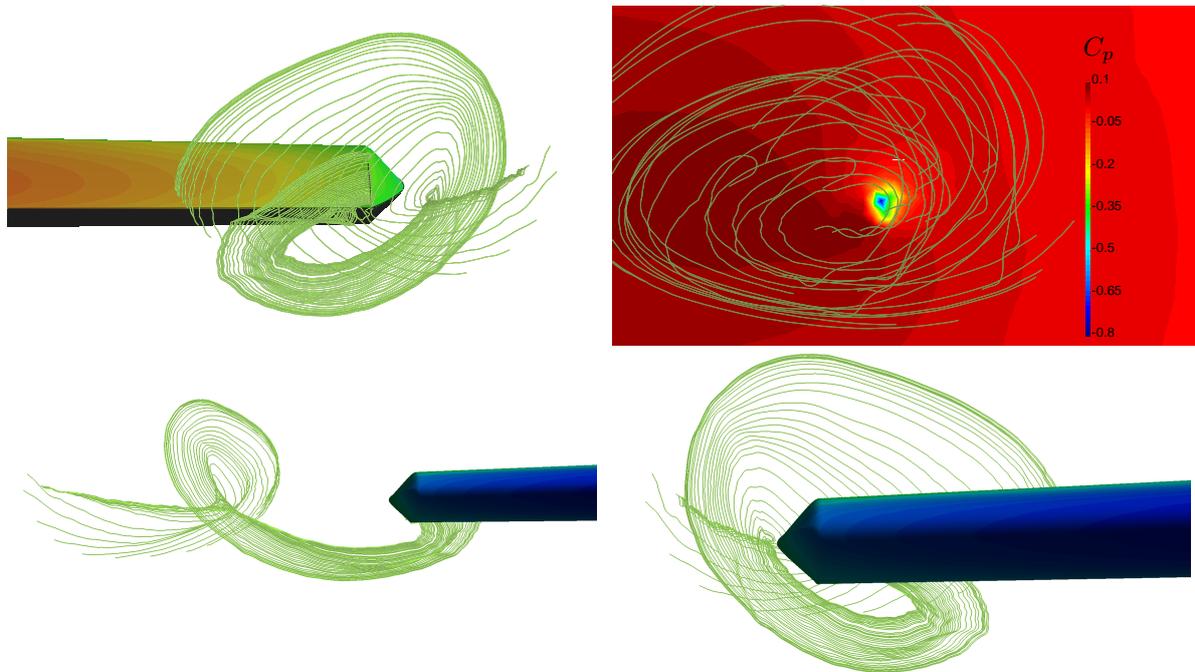
Figure 10: Four different perspectives of the wingtip vortex behind the ONERA M6 wing rolling up from the trailed vorticity sheet.

4   CONCLUSIONS

An embedded wake approach for a potential transonic solver is presented. This approach allows reducing the modeling time significantly. Furthermore, the method's robustness is demonstrated in a three-dimensional example, where the reference data is accurately reproduced without requiring an extra mesh refinement towards the wake compared to a wake body-fitted approach. Describing the wake implicitly within the mesh allows to effectively perform aeroelastic optimization, where the wake's position may change due to the structural response and the geometry's evolutionary steps. In the future, an adjoint approach will be implemented to compute the coupled sensitivities and perform aeroelastic optimization.

Iñigo López, Marc Núñez, Armin Geiser, Riccardo Rossi, Roland Wüchner and Kai-Uwe Bletzinger

ACKNOWLEDGEMENTS

REFERENCES

[1] D. Eller. Fast, Unstructured-Mesh Finite-Element Method for Nonlinear Subsonic Flow. *Journal of Aircraft*, 49(5):1471–1479, sep 2012. ISSN 0021-8669. doi:10.2514/1.c031738.

[2] B. Nishida. Fully simultaneous coupling of the full potential equation and the integral boundary layer equations in three dimensions. 1996.

[3] P. Dadvand, R. Rossi, and E. Oñate. An object-oriented environment for developing finite element codes for multi-disciplinary applications. *Archives of Computational Methods in Engineering*, 17(3):253–297, jul 2010. ISSN 11343060. doi:10.1007/s11831-010-9045-2. URL `https://github.com/KratosMultiphysics`.

[4] M. Drela. *Flight Vehicle Aerodynamics*. 2013. ISBN 9780262526449.

[5] M. Hafez, J. South, and E. Murman. Artificial compressibility methods for numerical solutions of transonic full potential equation. *AIAA Journal*, 17(8):838–844, 1979. doi:10.2514/3.61235.

[6] V. Mataix. *Innovative mathematical and numerical models for studying the deformation of shells during industrial forming processes with the Finite Element Method*. PhD thesis, Universitat Politècnica de Catalunya, 2020. URL `http://hdl.handle.net/2117/328952`.

[7] V. Schmitt and F. Charpin. Pressure distributions on the onera-m6-wing at transonic mach numbers, experimental data base for computer program assessment. Technical report, Report of the Fluid Dynamics Panel Working Group 04, AGARD AR 138, 1979.

[8] C. Rumsey. 3d onera m6 wing validation case. `https://turbmodels.larc.nasa.gov/onerawingnumerics_val.html`, 2018. Accessed: 2021-03-30.

[9] J. Mayeur, A. Dumont, V. Gleize, and D. Destarac. *RANS simulations on TMR 3D test cases with the Onera ¡italic¿elsA¡/italic¿ flow solver*. doi:10.2514/6.2016-1357. URL `https://arc.aiaa.org/doi/abs/10.2514/6.2016-1357`.

[10] J. Schoeberl. Netgen an advancing front 2d/3d-mesh generator based on abstract rules. *Computing and Visualization in Science*, 1:41–52, 07 1997. doi:10.1007/s007910050004.

[11] F. LYU, T. XIAO, and X. YU. A fast and automatic full-potential finite volume solver on cartesian grids for unconventional configurations. *Chinese Journal of Aeronautics*, 30(3):951–963, 2017. ISSN 1000-9361. doi:https://doi.org/10.1016/j.cja.2017.03.001. URL `https://www.sciencedirect.com/science/article/pii/S1000936117300730`.

Iñigo López, Marc Núñez, Armin Geiser, Riccardo Rossi, Roland Wüchner and Kai-Uwe Bletzinger

[12] B. Diskin, W. K. Anderson, M. J. Pandya, C. L. Rumsey, J. Thomas, Y. Liu, and H. Nishikawa. *Grid Convergence for Three Dimensional Benchmark Turbulent Flows.* doi:10.2514/6.2018-1102. URL `https://arc.aiaa.org/doi/abs/10.2514/6.2018-1102`.

[13] A. Crovato, H. S. Almeida, G. Vio, G. H. Silva, A. P. Prado, C. Breviglieri, H. Guner, P. H. Cabral, R. Boman, V. E. Terrapon, and G. Dimitriadis. Effect of levels of fidelity on steady aerodynamic and static aeroelastic computations. *Aerospace*, 7(4), 2020. ISSN 2226-4310. doi:10.3390/aerospace7040042. URL `https://www.mdpi.com/2226-4310/7/4/42`.

INTERACTIVE AIRFOIL DESIGN USING ARTIFICIAL INTELLIGENCE

Martin Eizinger[1], Markus Trenker[1] and Werner Toplak[2]

1: Aerospace Engineering
Fachhochschule Wiener Neustadt
Johannes-Gutenberg-Straße 3, 2700 Wiener Neustadt, Austria
martin.eizinger@gmx.at, markus.trenker@fhwn.ac.at

2: TopLab - Toplak Laboratory e.U.
dr.toplak@toplab.at

Abstract. *Aerodynamic shape design has a long history of extensive and detailed development, including different methods of optimization based on the various technologies that have been made available over the years, ranging from simple manual iteration to numerical inverse design. As artificial intelligence sees increasing popularity, it has also penetrated the field of fluid dynamics. We present a machine learning workflow for developing an artificial neural network that predicts the two-dimensional distribution of the coefficient of pressure along the perimeter of parameterized airfoils in variable steady-state subsonic high-Reynolds flow conditions. The data set is obtained from computational fluid dynamics simulations of pseudo-randomly generated parameter sets comprising of profile shape parameters and flow conditions. Several artificial neural networks are trained and ranked by performance, based on methods and quality metrics commonly used in machine learning. The highest-ranking network is further validated using several methods, including comparison to theory and experimental data. A software implementation of the neural network including a graphical user interface achieves real-time prediction and display of the distribution of the coefficient of pressure in response to variations of the shape and flow parameters. Other software features have been implemented, including interfaces to numeric solvers that can verify predicted results by executing the same automated workflow that has been used for creating the training data. The developed prototype toolbox has the potential to contribute in industry - in both optimization and conceptual design - as well as in education of professionals and students by providing a means to analyze in detail how the flow responds to a shape variation.*

Keywords: machine learning, airfoil optimization, computational fluid dynamics

Martin Eizinger, Markus Trenker and Werner Toplak

1 INTRODUCTION

The design of airfoil shapes has been a subject of interest for more than a century [1]. During this time the way new airfoils have been developed has been under severe changes. It started out with a purely experimental approach in a trial and error manner, building up a knowledge base on how an airfoil should be shaped to produce a favorable pressure distribution. Prandtl's thin airfoil theory [2] marks one of the first milestones in developing a mathematical model providing a closed solution on how the shape of an airfoil is connected to global parameters such as lift. This theory was the basis for the development of the well known NACA 4 series of airfoils. Developing this theory to also cover arbitrary airfoil shapes leads to challenging mathematics, not generally applicable for practical aerodynamic engineers in industry. Joukowski's idea of transforming the problem into the complex plane and mapping the problem to the flowfield around a cylinder was constricted to a certain family of airfoils. This theory was further developed by A. Betz and others [3].

With the increase in available computer resources, numerical tools capable of calculating the flow around airfoils have been developed, which are more generally known as computational fluid dynamics codes (CFD codes). Available computing power was the basis for new design methods especially for transonic speeds. Most notable in this respect are design methods for shock-free transonic airfoils developed by Korn [4], Garabedian [5] and Sobieczky [6] and others. Another idea was put into practice which is referred to as inverse methods: Here a prescribed pressure distribution serves as input and an algorithm calculates the airfoil producing this pressure distribution. With computing power becoming affordable for a wide range of applications, also optimization methods found their way into airfoil design through CFD-codes. One of the latest optimization methods is based on the adjoint equation method, which dramatically reduces the number of iterations for an optimized airfoil, shown by Jameson [7]. These optimization methods gave rise to new airfoil shapes and found their way into practical applications, especially for applications that have particularly high computational demands, such as multi-point optimization. Most of these methods, some of them combined with others, and experiments, are currently applied in research and the industry.

Despite all methods and CFD-codes available, the process of designing an airfoil for a certain application can be a cumbersome task, sometimes still performed in a trial and error manner. This is time consuming and also expensive, especially when it comes to experiments. Many of the commonly known design methods still lack an interactivity between the actual airfoil shape and its pressure distribution due to a time consuming workflow consisting of preprocessing, meshing, the actual flow calculation and postprocessing of the data. For the understanding and validation of how certain local changes of the airfoil's shape influence the pressure distribution and on the other hand how to change an airfoil shape locally to achieve certain desired changes in the pressure distribution, a fast and interactive workflow is crucial. Certainly some dedicated engineers working in the field for years have gained lots of experience, however some tool providing an interactive airfoil design process is highly desirable. Also from an educational point of view, some software capable of delivering the pressure distribution for a given airfoil on the fly together with an access to airfoil shaping parameters would be an enrichment for an applied aerospace engineering education.

In this contribution the method for setting up and training an ANN (artificial neural network) for the prediction of the pressure distribution of airfoils is presented. The concept of artificial intelligence dates back to the 1950s, and in some aspects truly earlier. The principle of connectionism is that information is processed by very simple processor units (PUs), which are interconnected within a network structure. With biological neural networks (BNNs) in scope, first ANN topologies originated in the late 1950s. Today a few dozen specific ANN architectures are known, which vary in the type of neurons or PUs, the type of interconnection (network structure) and the type of layers in which neurons are more or less hierarchically organized. Each PU behaves according to a given activity function. Since about 2012, ANNs are strongly related to terms like machine learning (ML), deep learning (DL), or deep neural networks (DNNs).

Bai and Zhou [8] have succeeded in the prediction of pressure distributions for turbine blade cross-sections. Their use of a convolutional artificial neural network, which strongly resembles approaches used in image recognition, yields results with a great accuracy, albeit low resolution. Similarly, Timnak et al. used an innovative approach for designing a neural network that was used for a genetic algorithm to iteratively optimize the lift-to-drag-ratio of airfoils [9].

The approach presented in this contribution is tailored to airfoils that are parameterized using a polynomial function [10]. The resulting tool provides a means for intuitive design of airfoils using a graphical user interface, where airfoil shaping parameters are set in a visual manner while the corresponding pressure distribution on the airfoil's upper and lower side is predicted by the neural network and displayed immediately. This approach can greatly shorten the design process of airfoils. It can support the work of practical aircraft designers in industry as well as students of aerospace engineering to understand the influence of local airfoil shape modifications on the pressure distribution and subsequently on global parameters such as lift and moment coefficient.

2 METHODS

The following presents all the methods applied to implement an interactive airfoil design tool with an underlying neural network.

2.1 Airfoil definition

Many different approaches for mathematical descirptions of airfoil shapes exist in the literature (see e.g. [11, 12]). For this application, the PARSEC-method [10] is used since it defines airfoils by means of a set of parameters that are closely connected to the actual shape of the airfoil. The airfoil's upper and lower side are each defined by the polynomial

$$Z = \sum_{n=1}^{6} a_n \cdot X^{n-1/2}, \quad \text{for } 0 < X < 1 \tag{1}$$

with X the dimensionless position on the airfoil chord and coefficients a_n, which are defined by geometric properties of the airfoil and have a familiar meaning to aerodynamic design engineers. These parameters are the leading edge radius r_{LE}, position of thickness maximum X_u, X_l, the maximum thickness Z_u, Z_l, the curvature at the location of

maximum thickness Z_{xxu}, Z_{xxl}, the trailing edge opening angle β_{TE}, the trailing edge direction angle γ_{TE}, the vertical position of the trailing edge Z_{TE} and the thickness of the trailing edge t_{TE}, shown in Fig.1. Eq.(1) is applied to the airfoil's upper and lower side and connected at the leading edge, reducing the number of coefficients to 11.
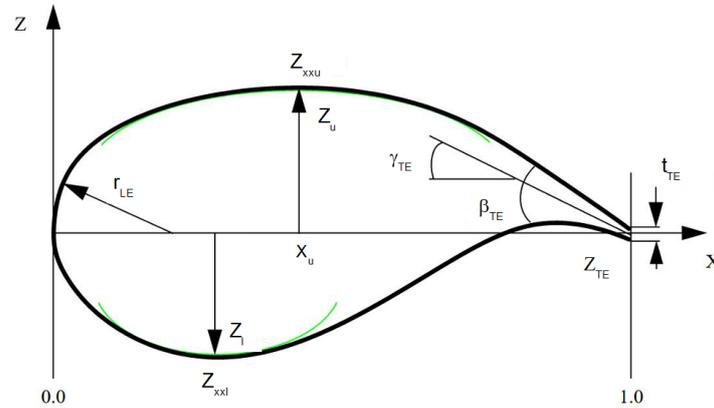
Figure 1: PARSEC parameters for the definition of airfoils, scaled z axis

In the following, the airfoils are defined using 301 points, which are clustered at the leading and trailing edge for improved mesh resolution.

2.2 Mesh generation

For the generation of the training database for the ANN, the flowfield for a number of airfoils has to be calculated. The mesh generation for these simulations is performed using GMSH [13], an open-source unstructured mesh generator. The tool is custom-scripted to generate refinement regions and structured layers close to the airfoil to resolve the strong flow gradients in the boundary layer. The mesh resolves the boundary layer with a $y^+ < 1$, omitting the use of wall functions. This requires knowledge about the boundary layer thickness, which cannot be known prior to performing the simulation. In order to avoid the need to recalculate the same simulation with multiple meshes - while making the mesh as coarse as possible to reduce computation time -, the skin friction coefficient and boundary layer thickness are estimated beforehand using a flat plate approximation and Schlichting's skin friction correlation [14], respectively. This allows to determine the maximum thickness of the first cell for achieving a $y^+ < 1$. A mesh for an exemplary airfoil is shown in Fig.2.

Martin Eizinger, Markus Trenker and Werner Toplak
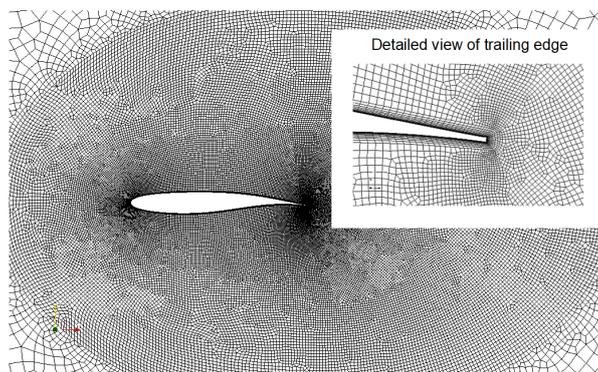
Figure 2: The unstructured mesh with structured layers for resolving the boundary layer together with a detailed view of the mesh at the trailing edge

The quality of a sample set of meshes produced by the fully automatic algorithm is determined based on cell aspect ratio, skewness, smoothness, cell-orthogonality, and mesh-orthogonality. Furthermore, using a scaling variable that affects the mesh resolution of both the structured and unstructured regions, a mesh independence study is performed to show that (1) the mesh quality of the meshes produced by the algorithm does not depend on size, and (2) the simulation result does not depend on the mesh resolution (i.e. the mesh is fine enough to resolve flow phenomena).

2.3 Flow solver

The work at hand implements two different flow solvers for calculating the pressure distribution. XFOIL, [15], is a fast two-dimensional potential flow solver that is based on high-order panel methods coupled with viscous methods for the boundary layer. The second code available is SU2, [16], solving the three-dimensional, Reynolds averaged Navier-Stokes equations in a finite volume approach. Several state-of-the-art turbulence models are implemented. For this application, the model by Spalart-Allmaras is used.

2.4 Design of experiments

For training the neural network, a database has to be generated, consisting of shape and aerodynamic parameters and output data of the flow solver, in this case the pressure distribution of the airfoil stored as the local pressure coefficient at every point defining the airfoil. The airfoils are generated inside the following limits of PARSEC-parameters, where all distance related values are given in percentage of the chord length c:

Martin Eizinger, Markus Trenker and Werner Toplak

Table 1: Limits for PARSEC parameters

parameter	description	lower bound	upper bound
r_{LE}	leading edge radius	0.2 %	2.8 %
X_u	location of upper crest	20 %	60 %
Z_u	upper crest	4 %	15 %
Z_{xxu}	upper curvature	−75 %	−2 %
X_l	location of lower crest	25 %	50 %
Z_l	lower crest	−15 %	−4 %
Z_{xxl}	lower curvature	10 %	100 %
Z_{TE}	trailing edge coordinate	−3 %	3 %
γ_{TE}	trailing edge direction angle	−8°	8°
t_{TE}	trailing edge thickness	0.01 %	0.3 %
β_{TE}	trailing edge wedge angle	2°	20°

To extend the applicability of the design method also the freestream conditions may vary according to Tab.2 and are therefore included in the input parameters.

Table 2: Limits for Mach number, angle of attack and Reynolds number

parameter	description	lower bound	upper bound
M	Mach number	0.2	0.7
α	angle of attack	−5°	10°
Re	Reynolds number	10^6	$8 \cdot 10^6$

The selection of data sets from this parameter space can be seen from the view of the design of experiments (DOE) to generate a representative set of data which covers the complete parameter space in the most efficient way. For this purpose, the Latin Hypercube Sampling (LHS), [17], is implemented, which is a statistical method for the generation of a pseudo-random sample of parameter values from a multidimensional distribution, wherein each parameter is selected at random from a subspace of its full range while ensuring that the subspaces of all parameters are shuffled. This aims to decrease the probability that several samples share similar combinations of parameters, which in turn means that samples tend to be more different from one another.

2.5 Artificial neural network

An ANN can be seen as some transfer function f mapping an input parameter space (in this case $\mathbb{R}^{14}$) to an output parameter space (in this case $\mathbb{R}^{301}$),

$$f : \ \mathbb{R}^{14} \mapsto \mathbb{R}^{301}$$

where the tuning parameters of this transfer function are to be found by training. For this specific application, the input parameter space holds the PARSEC-parameters, the Mach number, the angle of attack and the Reynolds number, such that the set of input parameters for one sample of the database can be written as

$$S_{\text{inp}} = \{r_{LE}, \ X_u, \ Z_u, \ Z_{xxu}, \ X_l, \ Z_l, \ Z_{xxl}, \ Z_{TE}, \ \gamma_{TE}, \ t_{TE}, \ \beta_{TE}, \ M, \ \alpha, \ Re\} \quad (2)$$

Martin Eizinger, Markus Trenker and Werner Toplak

Similarly, we can consider one set of outputs S_{out} as the values describing the pressure distribution:

$$S_{\text{out}} = \{c_{p_1}, \ \ldots, c_{p_{NP}}\} \tag{3}$$

with $NP = 301$ the number of points describing the airfoil contour.
Note that the respective locations of these coefficients of pressure are not trained, as they are deliberately invariant.

A neural network consists of cells, also called neurons, and connectors. Each cell holds a value, which can be thought of as a continuous measure of how "active" it is - a notion vaguely based on biology.
The process of utilizing an ANN can be summarized as follows:

- **Generating a database**
  Using LHS, approximately[1] 7000 airfoils are generated within the limits given in Tab.1. A flow simulation is carried out for every airfoil for an angle of attack, Mach number and Reynolds number selected by the LHS within the limits given in Tab.2. All other values that are necessary for performing the flow simulation with the selected code are set to standard air conditions. Once converged, the pressure distribution is stored for every airfoil in the form of a list of local values distributed on the perimeter of the airfoil. Not all combinations of PARSEC parameters lead to physically valid airfoil designs suitable for the database generation. Corresponding parallel plots of valid and invalid patterns are shown in Fig.3 and Fig.4. For illustrating the high variety in the parameter space, blue patterns are those where a certain parameter lies in some small range (magenta lines). Gray patterns do not belong to the selection set. Besides using the valid patterns for pressure prediction, all the patterns - valid and invalid ones - can be used for clustering and classification of validity for generating further patterns for higher granularity.

---

[1]the algorithm automatically stops after a predefined number of successful simulations, i.e. 2500

Martin Eizinger, Markus Trenker and Werner Toplak
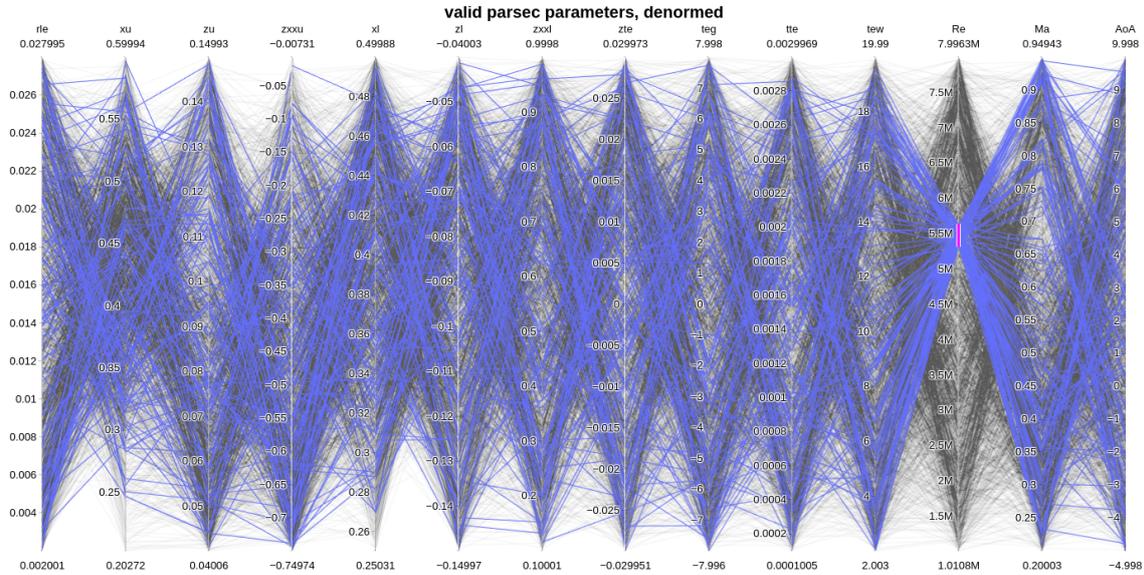
Figure 3: Parallel plot of valid normed PARSEC parameter patterns
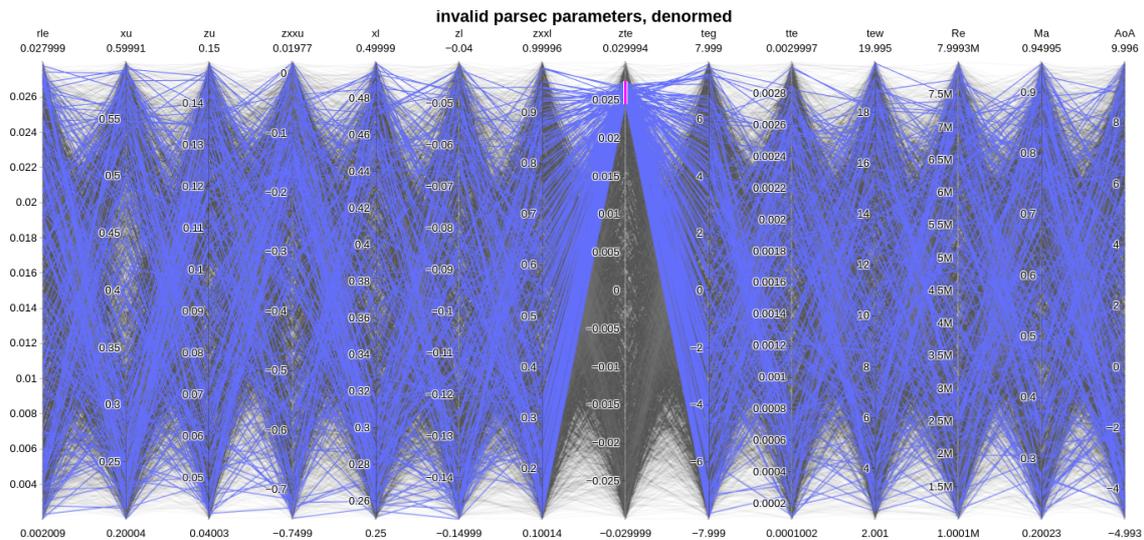
Figure 4: Parallel plot of invalid normed PARSEC parameter patterns

- **Choosing an ANN model**

  Available ANN topologies can be highly customized regarding their architecture (e.g. neurons, layers, interconnection structure, self-reference). There are also many methods from ML that can be applied to a given ANN for training with simulation data. The multi-layer perceptron (MLP) - a common nonlinear classifier and predictor - is widely used as a multi purpose network (e.g. [18]). Here, it serves to investigate the potential of a basic stack for a machine learning process specialized on airfoil design optimization. The network is trained by supervised learning, which adapts connection weights according to given input and output patterns in a way that minimizes the error of the network's output. Within the presented work

Martin Eizinger, Markus Trenker and Werner Toplak

a nonlinear feed-forward input-output (IO) system is defined, mapping the airfoil's PARSEC and freestream condition parameters to the pressure distribution. In such a structure, the numerical value of a cell is determined from (1) the input, i.e. all neurons that are connected to its input side and the strength of their respective connections, and (2) its own activation bias and activation function. This is also generally the order in which the value is determined: the value of the relevant input cells are multiplied by the values associated with their connectors, all contributions are summed, a bias is added, and an activation function is applied. Activation functions are non-linear and as such add complexity to the network that allows it to be fit to non-linear problems. Common activation functions are the rectified linear unit (ReLU) and sigmoid functions [19].

The physical system described via simulation parameters and simulation results is expected to be nonlinear, so the neural network is modelled accordingly: all cells use the sigmoid function

$$\sigma(x) = \frac{1}{1 + e^{-x}}, \tag{4}$$

as a nonlinear activation function with Euler's number e. Fig.5 shows the sigmoid function in a subdomain.
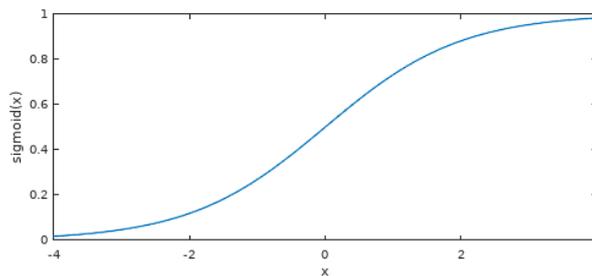
Figure 5: A plot of the sigmoid Eq.(4) in the interval [-4, 4]

Because the network is nonlinear, several layers can be used[2]. For this application, three hidden layers have been inserted between input and output layer. Fig.6 shows a schematic sketch of the ANN together with inputs and outputs.

---

[2]Linear systems - even if originally modelled with several layers - can always mathematically be reduced to one layer.
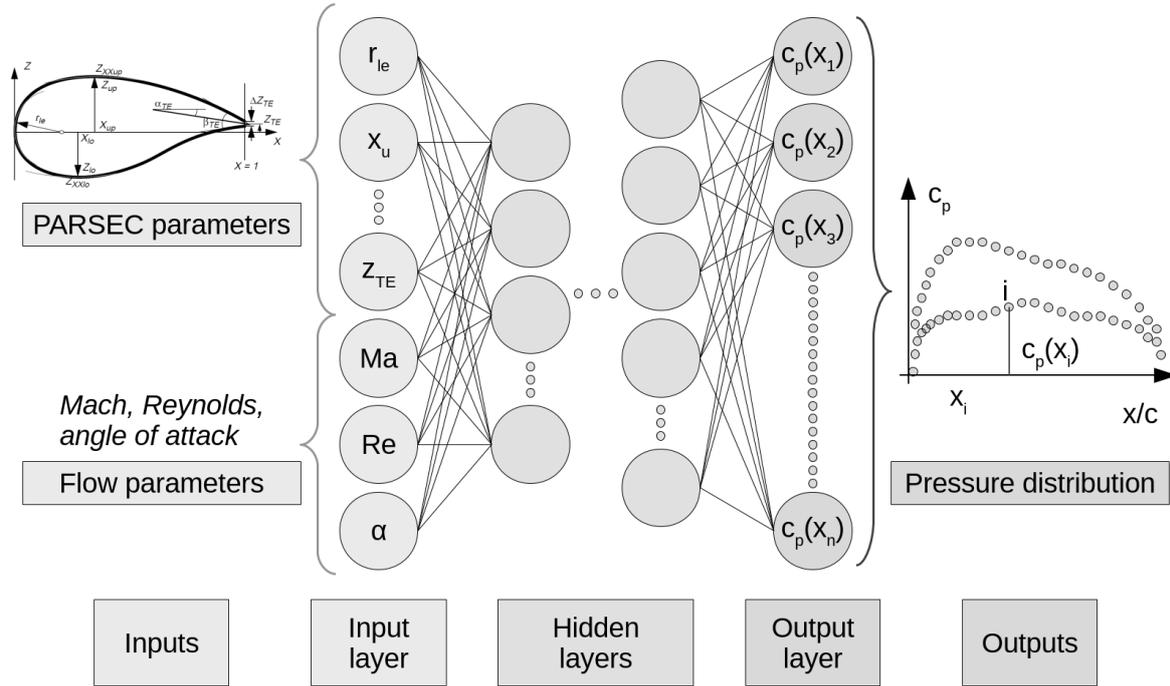
Figure 6: The ANN model for manual, intuitive airfoil optimisation and design. Left: the input PARSEC and flow parameters. Center: the ANN, a processing unit. Right: the local pressure coefficient as output.

The output of such an ANN can be written as the mathematical function $\boldsymbol{y} = \boldsymbol{f}(\boldsymbol{B}, \boldsymbol{W}, \boldsymbol{x})$ with $\boldsymbol{B}$ the biases, $\boldsymbol{W}$ the weights, $\boldsymbol{x}$ the parameters of the input space and $\boldsymbol{y}$ the parameters of the output space.

- **Training and loss function**
  In supervised learning, both $\boldsymbol{x}$ and $\boldsymbol{y}$ in the notation above are known. Instead of calculating $\boldsymbol{y}$ with constants $\boldsymbol{B}$ and $\boldsymbol{W}$, as done in prediction, the bias vectors and weight matrices are variables during the training phase. They are initialized as $\boldsymbol{B_0}$ and $\boldsymbol{W_0}$ [20]. A prediction is computed for the first training sample $j = 1$ according to the general prediction formula

$$\boldsymbol{y}_{C,j} = \boldsymbol{f}(\boldsymbol{B}_{j-1}, \boldsymbol{W}_{j-1}, \boldsymbol{x}_j)$$

with $\boldsymbol{y}_{C,j}$ the output of the ANN calculated from the previous weights and biases. Using the actual result $\boldsymbol{y}_{R,j}$, which, for the data set, is known from the CFD solver, we define the loss function Λ as the mean square error

$$\Lambda = \frac{1}{n} \cdot \sum_{i=1}^{n} \left(y_{R_i} - y_{C_i} \right)^2 \tag{5}$$

with n the number of output cells. Λ is a measure of the quality for a specific combination of bias vectors and weight matrices. If it is high, the ANN is far from

modelling the system accurately. A wide variety of loss functions have seen conventional use [21].

After determining the loss for some number of cases (batch size), the weights and biases are adjusted to minimise Λ. This process is repeated with every sample of the data set, usually several times (number of epochs).

A common rule of thumb is to split available data samples in a 70:20:10 manner (70% training, 20% cross-validation, 10% testing). For this proof of concept, 95% of the samples are used for training due to the low number of physically valid simulation results. The selection is made using a Hammersley-set, which has been researched for ANN training sampling in the context of structural design [22].

- **Optimization**
  Optimization is used to minimize the value of the loss function. Out of many possible minimization algorithms, a few have proven themselves in the field of ANNs, most notably the gradient descent (GD) method. This method again has a multitude of implementations and variations [23]. One aspect by which these methods are distinguishable is the batch size, i.e. the number of samples which are taken into account before updating the function. The step size of the optimization method is defined by the learning rate.
  The essence of GD algorithms is to iteratively calculate the loss function and to minimise it by moving in the opposite direction of its gradient, which is defined as the change of the loss function with respect to all of the network's weights and biases.

- **Cross-Validation**
  To avoid overfitting, cross-validation is performed with 3.75% of the samples. The trainer logs the evolution of the loss function by frequently performing predictions using an intermediate development stage of the ANN and evaluating the loss function of the predictions. This cross-validation is done in batches of 5 to reduce the impact of unusually poorly performing samples. During training, the process is paused in regular intervals and the intermediate state of the ANN is used to predict the output for the samples. The loss function is computed for all five, and their median is taken as the cross-validation value of this intermediate ANN. In addition, the weights and biases are stored whenever cross-validation is performed. At the end of the training process, the weights and biases of the ANN associated with the lowest recorded median is selected. This somewhat peculiar approach to cross-validation arises from the typically observed behaviour of a learning curve of the study at hand shown in Fig.7.

Martin Eizinger, Markus Trenker and Werner Toplak
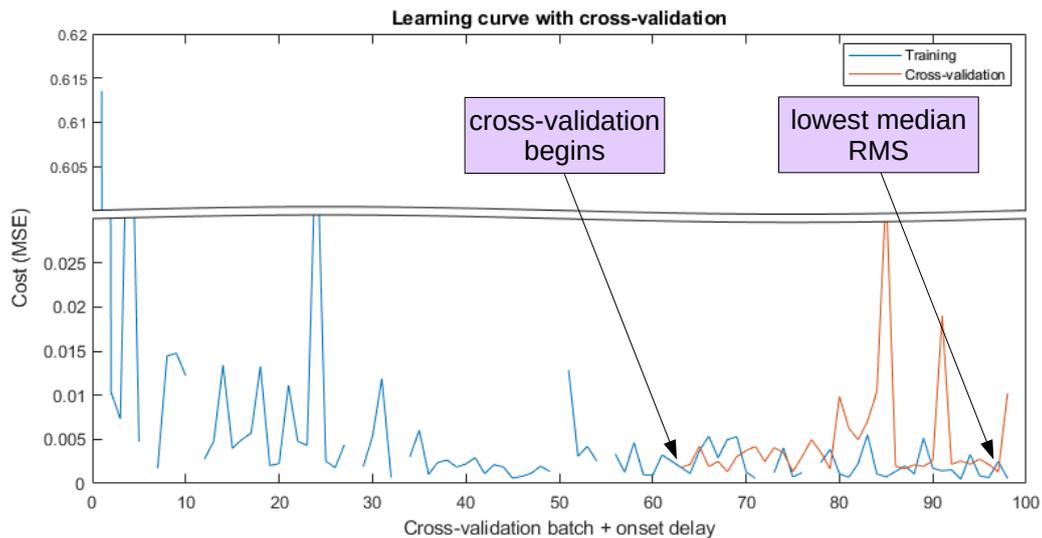
Figure 7: A typically observed learning curve of the training progress: mean-squared-error versus cross-validation batch

- **Testing**
  The remaining 1.25% of the available samples are initially set aside for final testing. This provides a method of measuring the final quality of the prediction.

- **Hyperparameter tuning**
  Through manual execution of various training cycles, the following set of hyperparameters has proven to be suitable for the regression problem based on results using SU2 for the flow simulation.

  - Learning rate: 0.0008
  - Batch size: 1
  - Epochs: between 220 and 500, based on cross-validation
  - Structure: MLP with 3 hidden layers of size 50, 120, and 190

- **Prediction**
  For an efficient practical usage of the trained ANN an interactive program is developed in MATLAB: a graphical user interface enables an interactive work-flow by selecting PARSEC parameters in a visual way. Together with chosen Mach number, angle of attack and Reynolds number, the trained ANN predicts a pressure distribution for the generated airfoil. Fig.8 shows the graphical user interface as a prototype programmed in MATLAB. The two highlighted areas contain the main input and output data: the airfoil parameters and free stream conditions (left) and the actual airfoil shape, defined by the parameter set, along with its pressure distribution (right).

Martin Eizinger, Markus Trenker and Werner Toplak
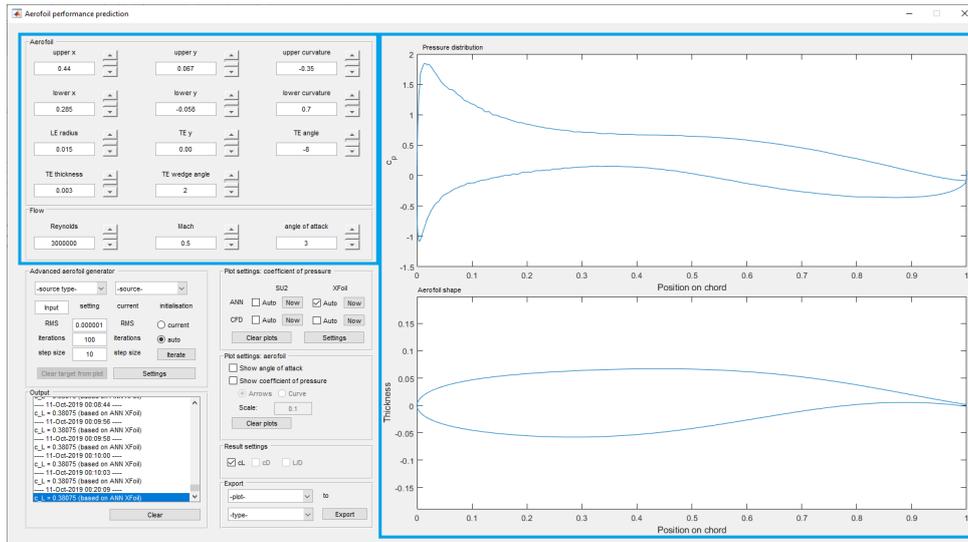
Figure 8: A graphical user interface developed for the purpose of making the artificial neural network readily accessible, with the two main areas highlighted in blue

3   RESULTS

The method presented is validated exemplarily by predicting the pressure distribution for the NACA 0012 at two different angles of attack and comparing the result to experimental data given by [24] for a free stream Mach number of M=0.3 and a Reynolds number of $6 \cdot 10^6$.

Since the automated workflow can only process PARSEC parameters, not direct airfoil shape coordinates, an approximation of the NACA0012 is generated using the PARSEC function by means of least-square fitting, resulting in the PARSEC parameters in Tab.3.

Table 3: PARSEC parameters for NACA 0012 fit

r_{LE}	X_u	Z_u	Z_{xxu}	X_l	Z_l	Z_{xxl}	Z_{TE}	γ_{TE}	t_{TE}	β_{TE}
0.0157	0.3	0.06	-0.4	0.3	-0.06	0.4	0	0	0.00252	15.945

The original airfoil and the PARSEC fit are shown in Fig.9.
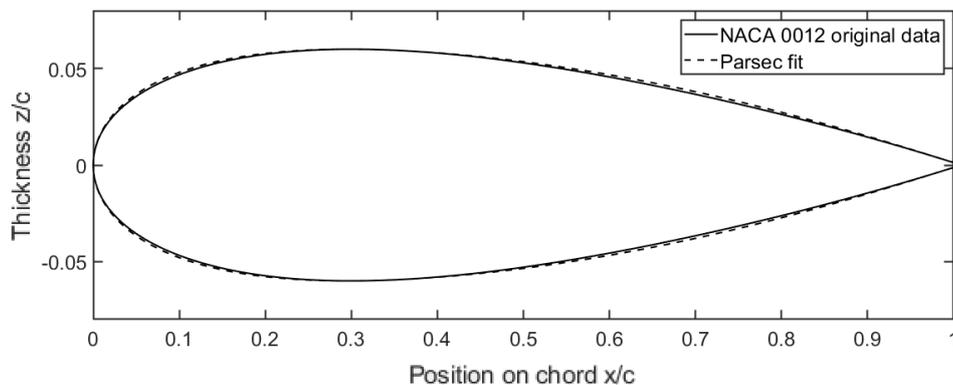
Figure 9: Comparison original NACA 0012 and PARSEC fit

Martin Eizinger, Markus Trenker and Werner Toplak

Fig.10 shows comparisons of the pressure distributions at 0° and 10° angle of attack.
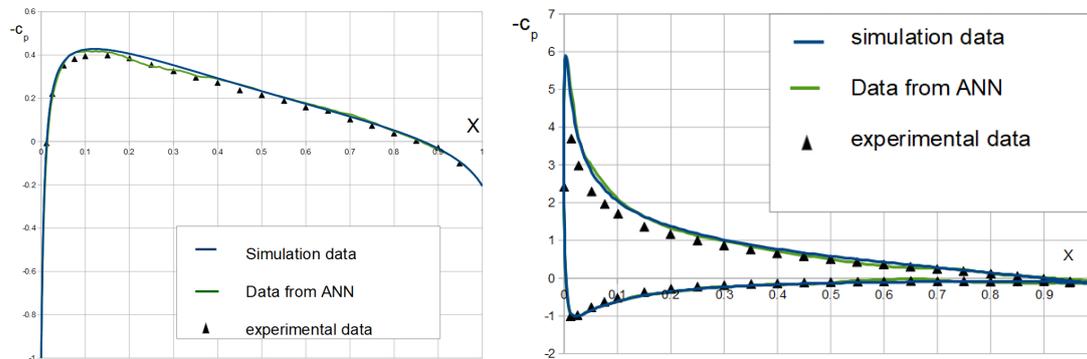
Figure 10: Comparison of pressure distributions for the NACA 0012: experimental data from [24], numerically obtained data from SU2, and prediction from the trained ANN

As a proof of concept, methods for calling CFD codes directly from this GUI for the actual airfoil are also implemented. This enables verification of the pressure distribution produced by the ANN, by performing an isolated flow simulation for the airfoil and comparing this pressure distribution to the one which was found by the ANN. This comparison is shown in Fig.11 for the XFOIL solver and in Fig.12 for the SU2 solver. Red lines correspond to the pressure distribution found by the AI (ANN values) whereas the blue lines result from a CFD calculation for this airfoil.
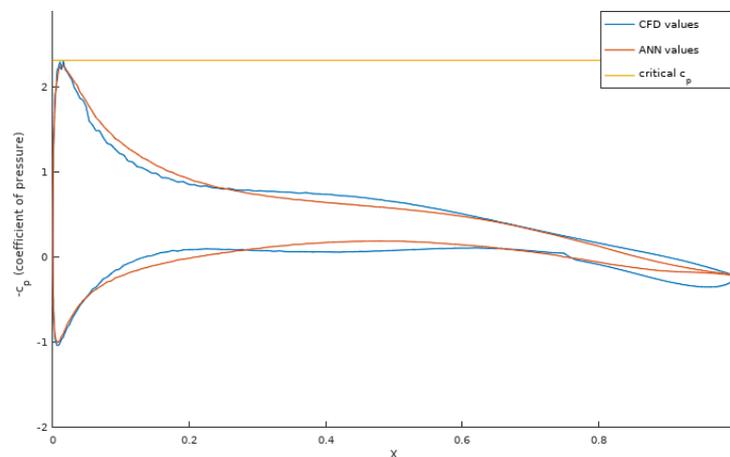
Figure 11: Distribution of the pressure coefficient over the chord of a random airfoil at M = 0.48, Re = 6·10^6, angle of attack = 5°, based on the panel method solver XFOIL

The pressure distributions are displayed over the dimensionless chord length from 0 to 1. As the ordinate shows the negative pressure coefficient, upper curves correspond to the airfoils' upper sides.

Martin Eizinger, Markus Trenker and Werner Toplak
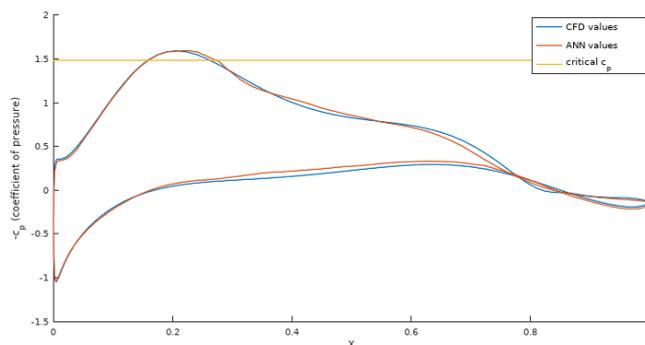
Figure 12: Distribution of the pressure coefficient over the chord of a random airfoil at M = 0.57, Re = 1.5·10^6, angle of attack = 4.35°, based on the CFD-solver SU2

4 CONCLUSION AND OUTLOOK

In this contribution it was shown that artificial intelligence can be effectively used as a design tool for two-dimensional wing cross-sections. Several numerical tools already available were coupled to generate a work flow which automatically produces a database for training artificial neural networks. Training sets include the parameters for the definition of airfoils using PARSEC and additional parameters for defining the free stream conditions. A prototype was implemented in MATLAB showing the huge potential of AI for airfoil design and verification. This approach of intuitive airfoil design not only targets industry-related projects but also supports teaching since the influence of airfoil parameters on the pressure distribution can be shown in realtime with the omittance of flow simulations in favor of artificial intelligence. In future the prototype will be developed further, with focus on performance improvement and moving away from proprietary software. Some variations in the machine learning algorithm will be investigated, such as alternative activation functions and loss functions. The number of valid patterns has to be increased with a richer database of simulations. On the ML and ANN side the search for robust and adequate ANN configurations will be in focus. An additional neural network using unsupervised learning like a Self Organizing Map (MAP) can be used to cluster physically valid and invalid patterns as well. This can improve the training step and allows for designers to receive direct feedback if certain CFD parameters are likely to give unfeasible results.

REFERENCES

[1] J. Anderson. *Fundamentals of Aerodynamics*. McGraw-Hill Education, 2010. ISBN 9780073398105. URL `https://books.google.nl/books?id=xwY8PgAACAAJ`.

[2] L. Prandtl. *Tragflügeltheorie: 1918*. Number v. 1. 1918. URL `https://books.google.nl/books?id=Bq68NAEACAAJ`.

[3] A. Betz. *Konforme Abbildung*. Springer, 1964.

[4] D. Korn, C. I. of Mathematical Sciences, and U. A. E. Commission. *Computation of Shock-free Transonic Flows for Airfoil Design*. AEC research and development report. New York University, Courant Institute of Mathematical Sciences, 1969. URL `https://books.google.nl/books?id=H4u1FMA3SIkC`.

[5] P. R. Garabedian and D. G. Korn. Analysis of transonic airfoils. *Communications on Pure and Applied Mathematics*, 24(6):841–851, 1971. doi:https://doi.org/10.1002/cpa.3160240608. URL `https://onlinelibrary.wiley.com/doi/abs/10.1002/cpa.3160240608`.

[6] H. Sobieczky. *Verfahren für die Entwurfsaerodynamik moderner Transportflugzeuge*. Deutsche Forschungs-und Versuchsanstalt für Luft-und Raumfahrt, 1985.

[7] A. Jameson, L. Martinelli, and N. Pierce. Optimum aerodynamic design using the navier–stokes equations. *Theoretical and Computational Fluid Dynamics*, 10:213–237, 01 1998. doi:10.1007/s001620050060.

[8] C. Bai and C. Zhou. Pressure predictions of turbine blades with deep learning. *CoRR*, abs/1806.06940, 2018. URL `http://arxiv.org/abs/1806.06940`.

[9] N. Timnak, A. Jahangirian, and S. Seyyedsalehi. An optimum neural network for evolutionary aerodynamic shape design. *Scientia Iranica*, 24, 08 2017. doi:10.24200/sci.2017.4308.

[10] H. Sobieczky. Parametric airfoils and wings. In *Recent development of aerodynamic design methodologies*, pages 71–87. Springer, 1999.

[11] R. Bilstein, U. S. N. Aeronautics, S. A. O. of Management, U. S. N. Aeronautics, S. A. Scientific, and T. I. Division. *Orders of Magnitude: A History of the NACA and NASA, 1915-1990*. NASA SP. National Aeronautics and Space Administration, Office of Management, Scientific and Technical Information Division, 1989. ISBN 9780160042591. URL `https://books.google.nl/books?id=7zACAAAAIAAJ`.

[12] J. A. Samareh. A survey of shape parameterization techniques. In *NASA Conference Publication*, pages 333–344. Citeseer, 1999.

[13] C. Geuzaine and J.-F. Remacle. A three-dimensional finite element mesh generator with built-in pre- and post-processing facilities. `http://gmsh.info`.

[14] H. Schlichting and K. Gersten. Boundary-layer theory, (2000). *International Journal of Aerospace Engineering Hindawi www. hindawi. com*, 2018, 1979.

[15] M. Drela. Xfoil subsonic airfoil development system. `https://web.mit.edu/drela/Public/web/xfoil/`.

[16] T. Economon, F. Palacios, S. Copeland, T. Lukaczyk, and J. Alonso. Su2: An open-source suite for multiphysics simulation and design. *AIAA Journal*, 54:1–19, 12 2015. doi:10.2514/1.J053813.

[17] M. D. McKay, R. J. Beckman, and W. J. Conover. A comparison of three methods for selecting values of input variables in the analysis of output from a computer code. *Technometrics*, 21(2):239–245, 1979. ISSN 00401706. URL `http://www.jstor.org/stable/1268522`.

[18] *Artificial Intelligence enhancing a CFD Snow Deposition Approach for the Use in Infrastructure Management, Maintenance and Virtual Reality*, 2012.

Martin Eizinger, Markus Trenker and Werner Toplak

[19] S. Haykin. *Neural Networks A Comprehensive Foundation.* Pearson Education, Inc., 2 edition, 1999. ISBN 81-7808-300-0.

[20] G. Dreyfus. *Neural Networks Methodology and Applications.* Springer, 2 edition, 2004.

[21] G. Bonaccorso. *Mastering machine learning algorithms: expert techniques to implement popular machine learning algorithms and fine-tune your models.* Packt Publishing Ltd, 2018.

[22] F. Tong and X. Liu. Samples selection for artificial neural network training in preliminary structural design. *Tsinghua Science and Technology*, 10(2):233–239, 2005.

[23] S. Ruder. An overview of gradient descent optimization algorithms. *arXiv preprint arXiv : 1609.04747*, 2016.

[24] C. L. Ladson, A. S. Hill, and W. G. Johnson Jr. Pressure distributions from high reynolds number transonic tests of an naca 0012 airfoil in the langley 0.3-meter transonic cryogenic tunnel. 1987.

A COMPARATIVE STUDY ON MULTI-FIDELITY SONIC BOOM PREDICTION FOR A SUPERSONIC AIRCRAFT

Yusuf Demiroglu[1] and Melike Nikbay[2]

1:Research Assistant, Faculty of Aeronautics and Astronautics
Istanbul Technical University, Maslak, Istanbul, 34469, Turkey
demirogluy@itu.edu.tr

2:Professor, Faculty of Aeronautics and Astronautics
Istanbul Technical University, Maslak, Istanbul, 34469, Turkey
nikbay@itu.edu.tr

Abstract. *Sonic boom signature prediction is a primary criterion for low-boom commercial supersonic aircraft design and requires a multidisciplinary analysis framework. Due to high computational time required in multidisciplinary optimization processes, we study sonic boom prediction within a multi-fidelity approach. In this study, sonic boom loudness is computed by employing multi-fidelity aerodynamic and acoustics solvers. First, PANAIR panel code is used to determine the aerodynamic characteristics and the near-field pressure signature with low-fidelity. Meanwhile, at high-fidelity, SU2 multi-physics solver is employed to solve for the near-field flow region around the aircraft. As a high-fidelity acoustic solver, NASA's sBOOM code is coupled with the SU2 code via a Python script to automate the aerodynamic and acoustic solution processes sequentially. Various wing-body combinations and several test cases were analyzed with both low- and high-fidelity solvers in our former studies. Here, the near-field pressure signature and sonic boom ground signature of a complete low-boom aircraft configuration are studied with more focus to get a better understanding of the physical and geometrical limitations of the combined low-fidelity solution methods. This study aims to address the low-fidelity sonic boom prediction methods with respect to high-fidelity solutions in support of multi-fidelity design exploration and multidisciplinary optimization studies for supersonic aircraft design.*

Keywords: Sonic Boom Prediction, CFD, Panel Methods, Supersonic Flight, Acoustics

Yusuf Demiroglu and Melike Nikbay

1 INTRODUCTION

Regulations and policies which require low-boom civil transport technologies mandate the most demanding requirements for supersonic aircraft design in the aerospace industry. In order to meet the market demand in the future of the aviation industry, researchers are challenged to develop quieter and more efficient aircraft designs. As the computational power has increased and become more available over the last decades, high-fidelity analysis methods have been employed for the low-boom aircraft design optimization studies. However, this computational cost still may not be affordable for most optimization and uncertainty quantification (UQ) studies in the aerospace industry, especially for those that require high-fidelity flow solutions. Therefore, multi-fidelity methods that leverage utilization of both low and high-fidelity methods have been developed by researchers [1] using reduced order modeling (ROM) techniques. Combining data from different levels of fidelity and sources, these multi-fidelity ROM methods can be used to construct a surrogate model to be further used in optimization studies [2]. Furthermore, deep learning algorithms such as convolutional neural networks have been used with multi-fidelity data to predict the aerodynamics characteristics. In this regard, accurate and rapid prediction of the aerodynamic characteristics with low-fidelity methods is still a significant concern in aircraft design studies. Therefore, in this study, a low-fidelity prediction capability is assessed via comparisons with high-fidelity results for a low-boom supersonic aircraft geometry.

From the aerodynamics point of view, computational fluid dynamics (CFD) is currently available as the most accurate method to be used for high-fidelity analysis. SU2, an open-source multi-physics solver developed by Stanford University ADL [3], is employed in this study for flow solution. A finite volume solver with unstructured mesh can be used for the discretization of governing equations in SU2. For the low-fidelity flow solution, A502 program, known as PANAIR [4], is integrated into the multi-fidelity prediction framework. PANAIR was developed to solve potential flow around bodies with several boundary conditions. Its supersonic flow solution capability makes PANAIR a preferred code over other panel codes for supersonic aircraft design studies [2, 5–7]. Also, PANAIR can be obtained as an open-source code written in the Fortran language. A supersonic solution in PANAIR is only valid for slender geometries at moderate angles of attack. Since low-boom aircraft geometries meet these requirements, it is acceptable to use the results obtained from PANAIR in a multi-fidelity analysis for a low-boom aircraft.

After obtaining solutions from the aerodynamic analyses, an acoustic analysis must be performed to predict and examine loudness on the ground caused by an aircraft when it flies in the supersonic regime. The aerodynamic analysis covers only the solution of the near-field region around the aircraft. However, the concerned region for the loudness calculation is related to the region between the aircraft and the ground. Since modeling of this region is not feasible with flow solvers, acoustics methods for sonic boom propagation are developed since the beginning of the supersonic flight. Whitham [8] first proposed a linear method called the F-function method based on the modified linear theory. Researchers used this linear method or a modified version for decades [9–12]. Then, non-linear sonic boom propagation methods are developed for more accurate results with a real atmosphere assumption. In 2011, Rallabhandi [13] explained the sBOOM code which is developed at NASA Langley Research Center. In this study, the sBOOM code is integrated into a multidisciplinary framework to predict the sonic boom loudness on the

Yusuf Demiroglu and Melike Nikbay

ground for the high-fidelity sonic boom prediction.

This paper is organized as follows: first, methodologies used for both aerodynamic and acoustic solutions are explained in Section 2. Then, the multi-fidelity framework is presented in Section 3. Application cases on different geometries are assessed with both high and low-fidelity solutions. Finally, a geometric parametric study is performed and presented in Section 3 for a selected configuration.

2 METHODOLOGY

First, high- and low-fidelity methods that provide the near-field flow solution are demonstrated. Then, the acoustics methods employed in this study are explained.

2.1 Near-Field Flow Solution

The SU2 open-source multi-physics solver developed by Stanford University ADL is employed in this study with steady inviscid flow conditions. SU2 has been used in our previous studies [2] for the accurate prediction of the near-field pressure signature. Acceptable convergence rates have been obtained in our studies. Therefore, SU2 is considered as a validation and reference tool for the low-fidelity predictions in this study. For the governing equations of the high-fidelity solution, Euler equations are solved. Euler equations in a conservative form are shown in Eq. (1).

$$\frac{\partial Q}{\partial t} + \nabla \cdot \bar{F}_c(Q) = 0 \tag{1}$$

where Q is the conservative state vector and F_c is the convective flux vector. Q and F_c are given by

$$Q = \left\{ \begin{array}{c} \rho \\ \rho\bar{V} \\ \rho E \end{array} \right\} \quad \bar{F}_c = \left\{ \begin{array}{c} \rho\bar{V} \\ \rho\bar{V} \otimes \bar{V} + \bar{\bar{I}}p \\ \rho E\bar{V} + p\bar{V} \end{array} \right\} \tag{2}$$

In these equations, ρ, E, p, $\bar{V}$, and $\bar{I}$ represent density, energy per mass, thermodynamic pressure, velocity vector and identity matrix. In SU2, discretization can be made by a finite volume method based on a vertex-based data structure. Jameson-Schmidt-Turkel (JST) scheme is selected for the computation of convective fluxes. Since SU2 can be used with unstructured meshes, a mixed mesh which consists of both structured and unstructured regions is used in the SU2 analyses.

PANAIR is integrated for the near-field solution from a low-fidelity solver. PANAIR solves the linear potential equation provided in Eq.(3) on the surface of the aircraft.

$$\beta^2\phi_{xx} + \phi_{yy} + \phi_{zz} = 0 \tag{3}$$

where $\beta = \sqrt{1 - M_\infty^2}$ and ϕ is the perturbation velocity potential. For discretization, aircraft surfaces are divided into quadrilateral elements called panels. Surface singularities which depend on the boundary conditions are solved by Neumann boundary condition for the velocity potential function. In this study, all cases are solved with supersonic solid surface boundary condition which is represented by $kt = 11$. kt indicates boundary condition type of a network in PANAIR such as solid surface, wake, and inlet. PANAIR solution runs on a single core and lasts under 10 minutes. Also, a near-field pressure signal on a predefined line in the flow region can be extracted from the PANAIR program. This

makes PANAIR more suitable as a code to be combined with a sonic boom propagation code. However, large oscillations occur in these pressure signatures as explained in Section 3 and this should be cured.

2.2 Far-Field Acoustics Solution

The sBOOM code is integrated into our multi-fidelity prediction framework as an acoustical solver. The augmented Burger Equations shown in Eq. (4) are solved in a ray tube coordinate system by sBOOM. First, a near-field pressure signature is obtained from a near-field flow solution. These pressure signatures is taken on a line aligned with the free-stream direction at typically 2 or 3 body lengths away from the aircraft axis. Also, this 2 or 3 body lengths requirement mostly determines the size of the domain for the high-fidelity flow solution. Then, this near-field pressure signature can be used as a initial wave signal for acoustical calculation. By using the ray-tracing technique, propagation of this initial wave is simulated in ray tubes to the ground [13]. During the propagation, molecular relaxation and thermo-viscous effects are taken into account as seen in Eq. (4).

$$\frac{\partial p}{\partial x} = \frac{\beta p}{\rho_0 c_0^3} \frac{\partial p}{\partial t'} + \frac{\delta}{2c_0^3} \frac{\partial^2 p}{\partial t'^2} + \sum_\nu \frac{c_\nu'}{c_0^2} \int_{-\infty}^{t'} \frac{\partial^2 p}{\partial y^2} e^{-(t'-y)/t_\nu} dy \qquad (4)$$

The effects of a stratified atmosphere such as the wind profile is taken into account by courtesy of ray tracing technique. sBOOM generates a ground signature signal and A-weighted and C-weighted loudness values. However, USU Aero Lab's PyLdB code [14] based on Stevens' Mark VII algorithm [15] is integrated in our framework to calculate the perceived level loudness from the ground signature signal. The general concept of the sonic boom loudness calculation process is illustrated in Fig. 1.
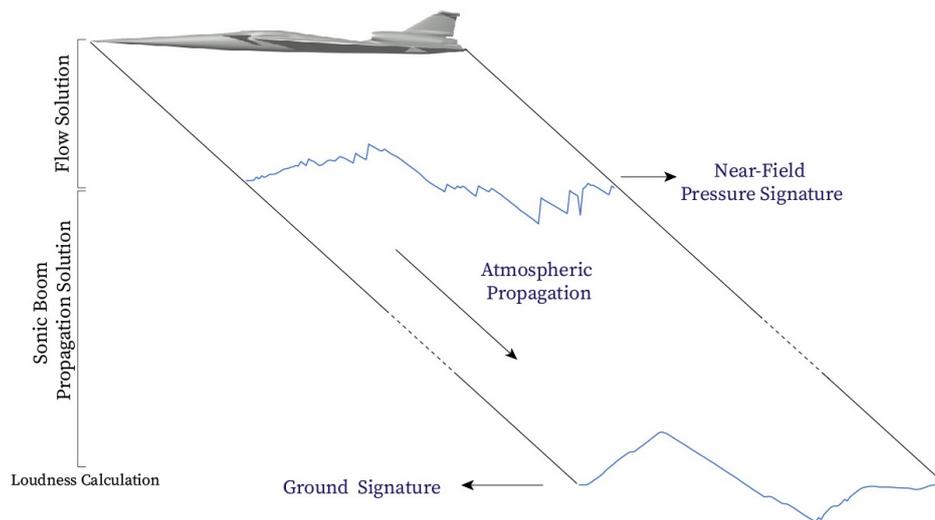
Figure 1: Sonic boom loudness calculation process

3 APPLICATION

This section introduces several application cases for multi-fidelity sonic boom prediction studies. First, the computer program developed to automate the analysis process is explained. Then, benchmark geometries from AIAA Second Sonic Boom Prediction

Workshop are presented with the applied solutions and results. Next, a supersonic airliner model is introduced for high- and low-fidelity solutions. Finally, a study that investigates low-fidelity prediction capability with varying several geometry parameters is presented.

3.1 The Computational Framework

A multi-fidelity design and optimization framework for sonic boom prediction is developed at ITU AeroMDO (Aerospace Multidisciplinary Design Optimization) Lab. In this study, the flow solution and acoustic propagation are already presented. In this framework, first a geometric definition is required. A sample geometry can be imported into the analysis in IGS format or OpenVSP format which allows parameterization of the geometry to produce new geometries. Next, the meshing scripts which execute the external mesh software are run by the driver code. Then, the generated structured surface mesh is transformed into the PANAIR network format. Also, volume mesh is saved with "*.su2" format. Both PANAIR and SU2 require a case description file called the input file. This input file is generated by the driver code according to the input parameters and the boundary conditions such as Mach number. Next, PANAIR and SU2 are called to execute both high- and low-fidelity analyses.
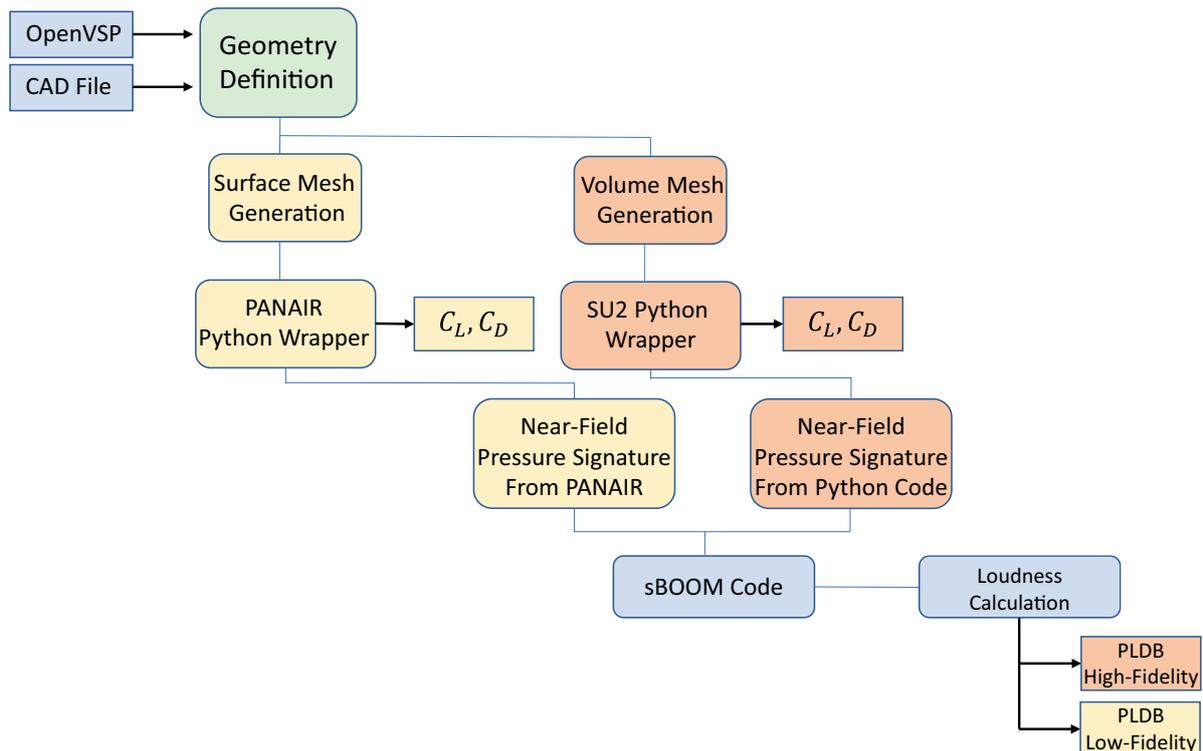
Figure 2: Flow diagram of the multi-fidelity calculation process

SU2 can be run with parallel computation while PANAIR can only be used on a single core. In the post-process phase of the flow solution, the files generated by SU2 and PANAIR are read by the driver code. SU2 generates a volume result file in the VTK file format. However, PANIAR generates several output files to be processed. In the Python wrapper section developed for PANAIR, USU Aero Lab [7] Python code is utilized and modified to be integrated into our framework. The driver program for PANAIR also can

Yusuf Demiroglu and Melike Nikbay

create a near-field pressure signature if specified by the user. However, a Python script is written to take a near-pressure signature from the SU2 volume output file. Then, sBOOM code provided by NASA Langley Research Center is integrated for sonic boom calculation. sBOOM requires two input files; analysis definition and near-field signal. Therefore, the driver program creates these files according to the defined conditions by the user to run sBOOM. After sBOOM solution is obtained, ground signature data is generated to be used in loudness calculation. As mentioned before, USU Aero Lab's PyLdB code [14] based on Stevens' Mark VII algorithm is called to obtain the perceived level loudness value. The overall process is illustrated in Fig.2. This program is called in an iterative process by the multi-fidelity framework to perform optimization and UQ studies.

3.2 Application to Sonic Boom Prediction Workshop Models

To begin a comparative study on a multi-fidelity supersonic flow calculations, the analysis process is applied to several geometries with increasing complexity from simple to complex models. Therefore, AIAA Sonic Boom Prediction [16, 17] (SBPW) models are preferred for the beginning of the study. First, an axisymmetrical model called Seeb ALR is considered for the comparison. Then, a delta wing model with a symmetrical diamond airfoil section is analyzed. After, a wing-body configuration called JAXA Wing-Body (JWB) [18] is used for several conditions to investigate the capability of low-fidelity. Finally, a full configuration supersonic airliner is generated and analyzed to compare.

3.2.1 The Seeb ALR Axisymmetrical Model

The Seeb ALR model is provided in 1st sonic boom prediction workshop to the participants. The Seeb ALR model is an axisymmetrical model which has 17.667 inches length with a 0.006 scale factor. The analysis is performed for 1.6 Mach number at an altitude of 55000 ft [16]. Since the geometry is provided by the workshop, only surface and volume discretizations are made. An unstructured mesh that has 8 million elements is generated for the SU2 analysis. Besides, three different surface grids which have 300, 600, and 1000 elements are generated for PANAIR analysis to examine the effect of the panel number. Obtained results are illustrated in Fig. 3 with surface pressure coefficient distribution from PANAIR and Mach number distribution on symmetry plane from SU2.
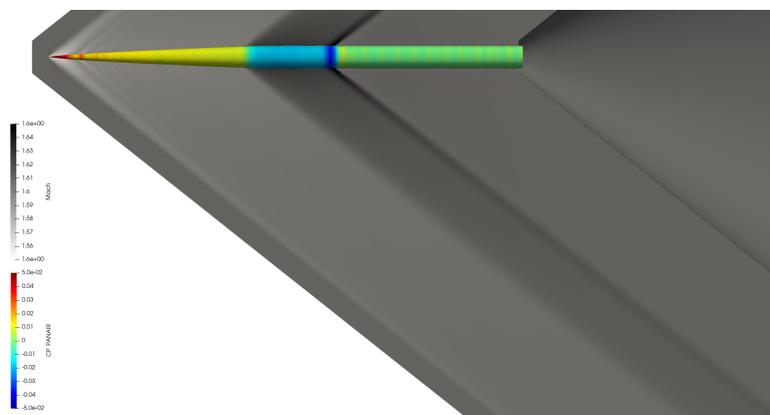
Figure 3: Surface pressure coefficient distribution and Mach number distribution on symmetry plane

Yusuf Demiroglu and Melike Nikbay

Near-field pressure signatures and ground signatures are provided in Fig. 4 for three different PANAIR cases with different grids and SU2 case.
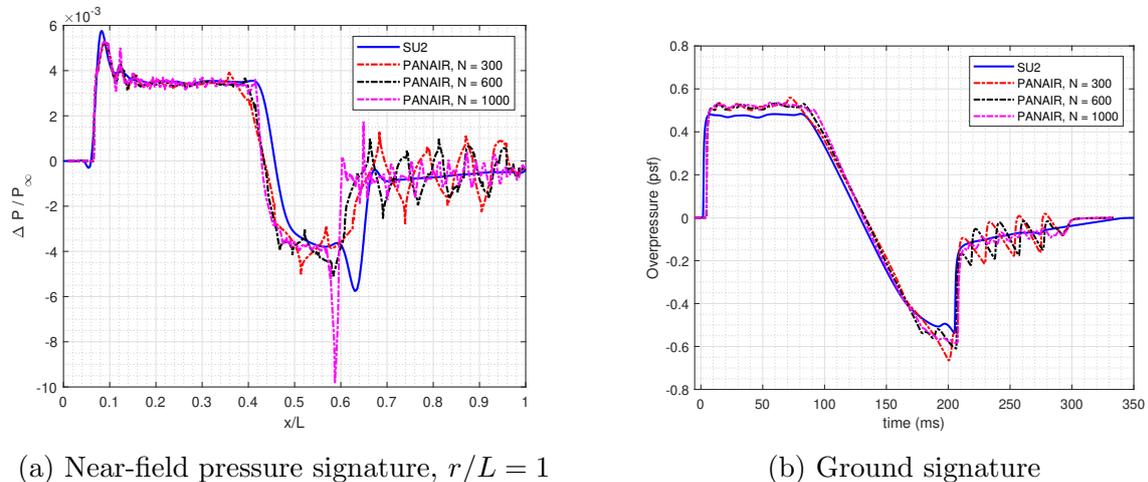
(a) Near-field pressure signature, $r/L = 1$ (b) Ground signature

Figure 4: The Seeb ALR model near-field pressure signature comparison, PANAIR and SU2

From Fig. 4, it can be observed that oscillations occur in PANAIR solution for three different grids. However, lots of these oscillations are damped in the ground signature. Loudness values are provided in Tab. 1.

Table 1: Loudness values

	PLDB	Percentage Error
SU2	89.92457	-
PANAIR, $N = 300$	93.25187	3.70010497
PANAIR, $N = 600$	93.4718	3.944679226
PANAIR, $N = 1000$	92.20473	2.535640552

3.2.2 The Delta Wing Model

The second model for validation study is the 69° Delta Wing geometry from First Sonic Boom Prediction Workshop. The delta Wing model is a symmetrical geometry with respect to the horizontal plane. Mach number of the analysis is set to 1.7 with atmospheric conditions at 55000 ft. An unstructured mesh is created with 14 million elements for the SU2 analysis. For the PANAIR analysis, 2 different surface grids are generated. Both of these grids have 3550 elements, however, panel distribution along the span-wise direction is different. A uniform panel distribution and a cosine distribution which results in a clustering region near the tip of the wing are created to examine the effect of panel distribution over the wing. Also, two different near-field locations such as 2 and 3 body lengths away are selected to investigate the effect of near-field pressure signature location. In Fig. 5, surface pressure coefficient distribution is given for both SU2 and PANAIR results. Near-field pressure signatures and ground signatures are shown in Fig. 6 and Fig.7 for $2L$ and $3L$ cases, respectively.

Yusuf Demiroglu and Melike Nikbay
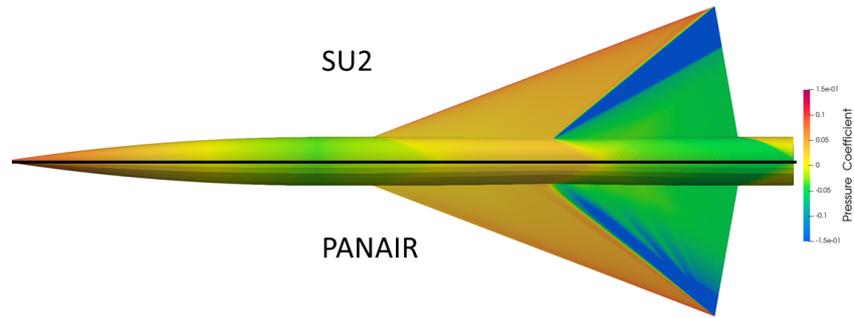
Figure 5: Surface pressure coefficient distribution comparison
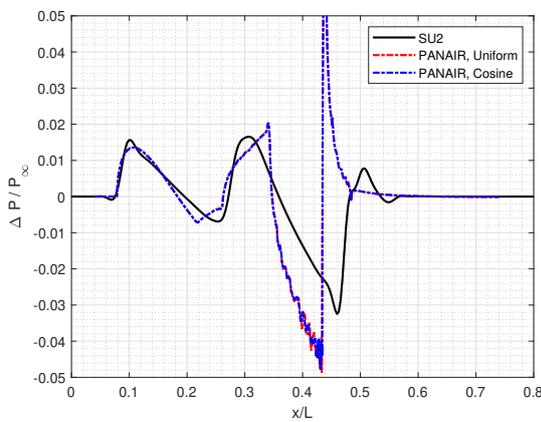
(a) Near-field pressure signature
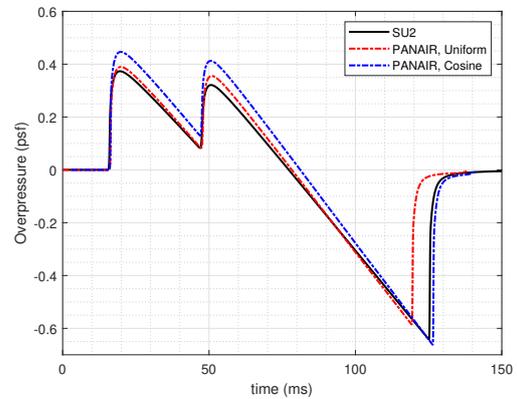
(b) Ground signature

Figure 6: Signature comparison at $r/L = 2$
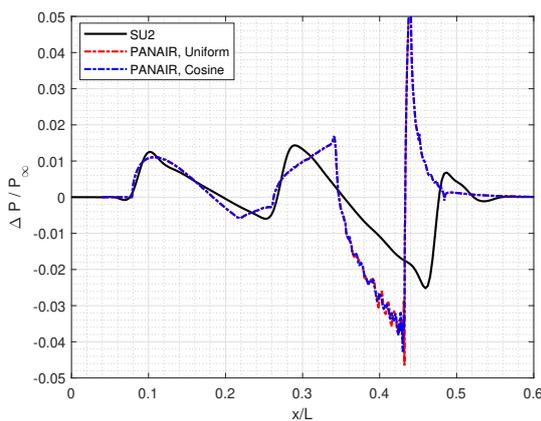
(a) Near-field pressure signature
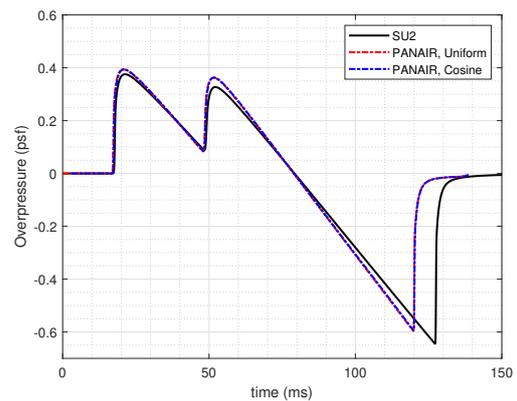
(b) Ground signature

Figure 7: Signature comparison at $r/L = 3$

From the ground pressure signature graph, it is concluded that cosine distribution gives better results for $2L$. However, as the vertical distance of the near-field pressure signature increases, the effect of distribution decreases in terms of sonic boom calculations. Also, resulting loudness values are provided in Tab. 2.

Table 2: Loudness values of different cases

	Distribution	Signature Position	PLDB	Percentage Error
SU2 Case 1	-	$2L$	94.23364	-
SU2 Case 2	-	$3L$	94.27574	-
PANAIR Case 1	Uniform	$2L$	93.93793	0.31380
PANAIR Case 2	Cosine	$2L$	95.49605	1.29440
PANAIR Case 3	Uniform	$3L$	94.10798	0.13334
PANAIR Case 4	Cosine	$3L$	94.13695	0.14721

3.2.3 The JAXA Wing Body Model

Finally, a sonic boom analysis is applied to the JWB model from Second Sonic Boom Prediction Workshop. The JWB model has the same equivalent area distribution with the NASA C25D low-boom aircraft with only a wing-body configuration [18]. Flow conditions of the JWB model are taken from the workshop [17] as 1.6 Mach number with 52000 ft altitude. For the SU2 analysis, an unstructured volume mesh with 13 million elements is generated. Size of the solution domain for the CFD analysis determined by the near-field pressure signature location as 2 body lengths away from the aircraft in the radial direction. Then, a surface mesh is generated for the PANAIR analysis with approximately 4500 elements. The surface grid of the JWB model for the PANAIR analysis is illustrated in Fig. 8. As a result of the previous example, a finer mesh region is used near the tip of the wing.
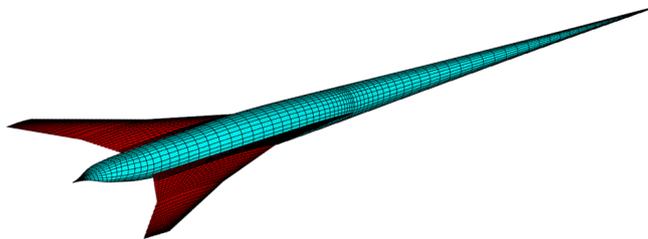
Figure 8: JWB model surface discretization for PANAIR

A PANAIR solution takes approximately 10 minutes on a single core while an SU2 solution lasts 1.5 hours with a parallel run on 36 cores. Resulting pressure signature distributions from both SU2 and PANAIR analyses are compared in Fig. 9.
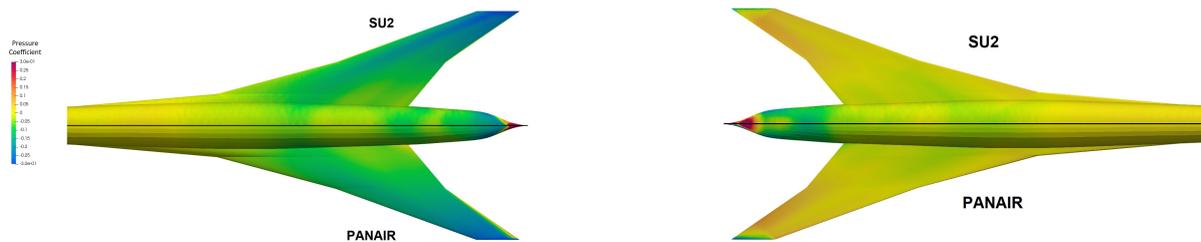
(a) C_p distribution on the upper surface
(b) C_p distribution on the lower surface

Figure 9: Pressure coefficient distribution comparison on the surface, PANAIR and SU2

Yusuf Demiroglu and Melike Nikbay

Pressure signature comparisons are demonstrated in Fig. 10 for both near-field and ground signatures. Likewise in the Delta Wing model, oscillations are observed with a lifting case. In addition, the linear solution gives a non-physical pressure distribution at the tip of the wing.

(a) Near-field pressure signatures

(b) Ground signatures
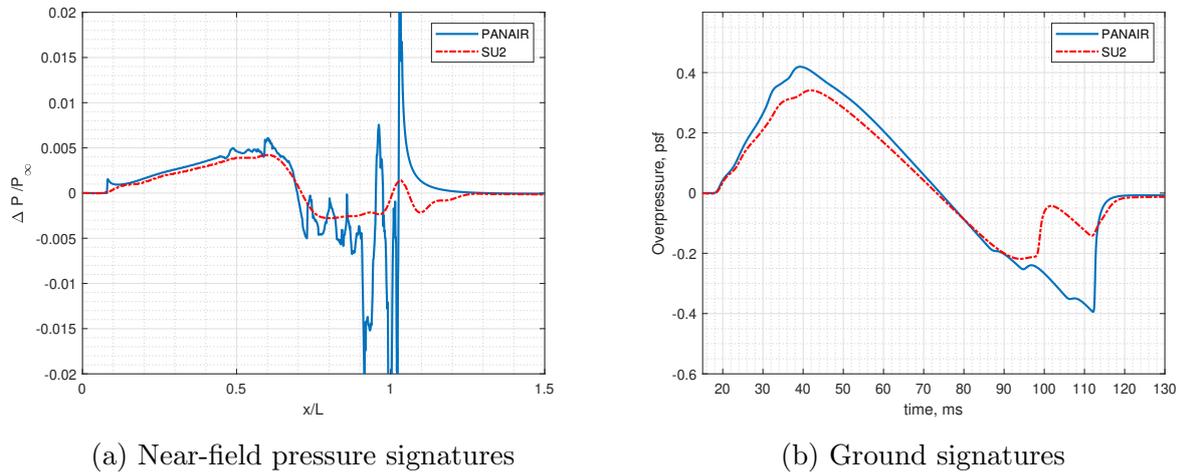
Figure 10: Pressure signature comparison

The lift and drag coefficients with loudness values are presented in Tab. 3. It is seen that PANAIR can be used for multi-fidelity design phases due to the agreeable aerodynamic prediction capability in the supersonic regime.

Table 3: Aerodynamic coefficients and loudness values

	C_L	C_D	Loudness (PLdB)
SU2	0.07702	0.00693	79.11894
PANAIR	0.07227	0.00641	87.08112
Percentage Error	6.16560	7.51906	10.06356

For a further examination of the capability of PANAIR solution, the JWB model is analyzed at different angles of attacks and Mach numbers. Three different Mach numbers such as 1.5, 1.6, and 1.8 are used at 10 different angle of attacks varying between -5 and 5 degrees. Obtained results are illustrated in Fig. 11 for the perceived loudness and Fig. 12-14 for the lift and drag coefficients.

(a) PLdB, $M = 1.5$

(b) PLdB, $M = 1.6$

(c) PLdB, $M = 1.8$
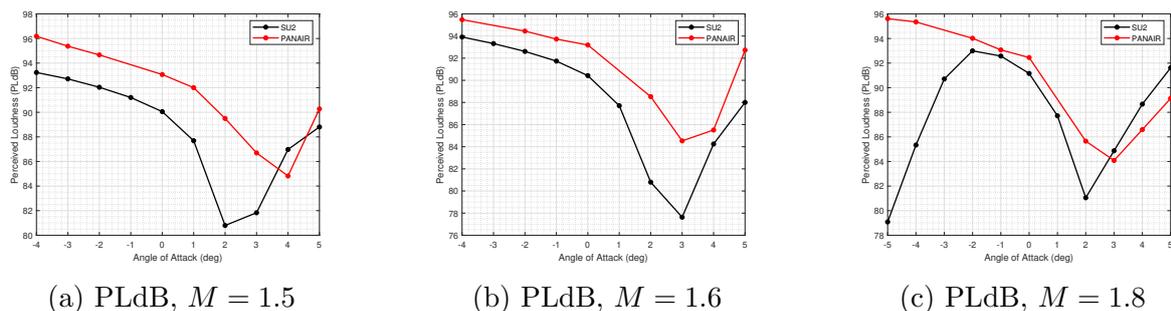
Figure 11: Perceived loudness values for different Mach numbers

Yusuf Demiroglu and Melike Nikbay
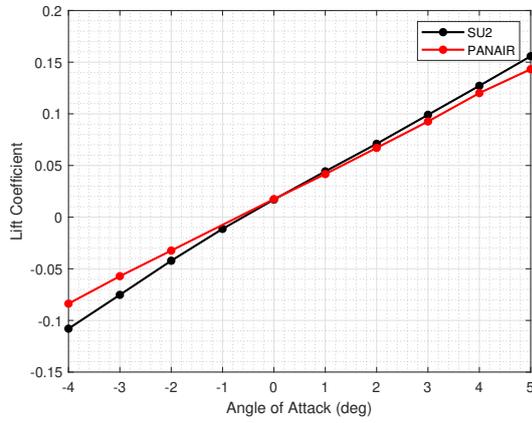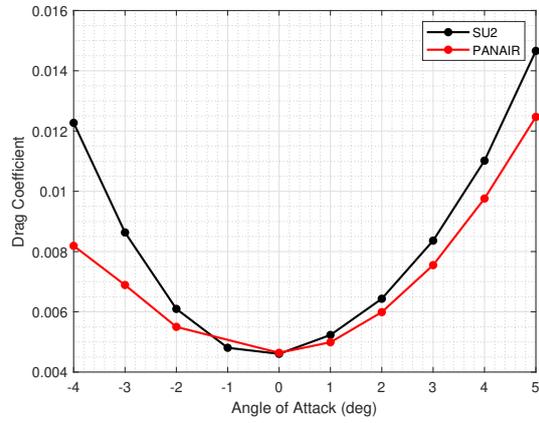
(a) Lift coefficient

(b) Drag coefficient

Figure 12: Aerodynamic coefficients, $M = 1.5$
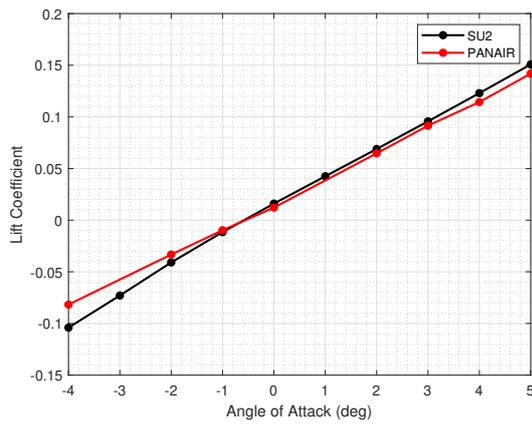
(a) Lift coefficient
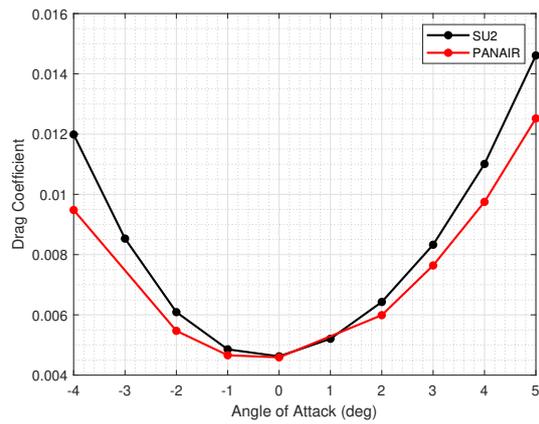
(b) Drag coefficient

Figure 13: Aerodynamic coefficients, $M = 1.6$
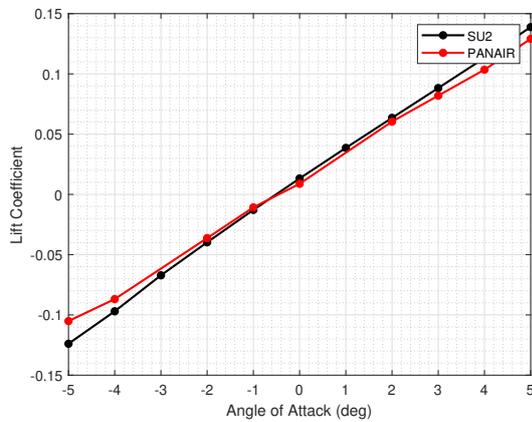
(a) Lift coefficient
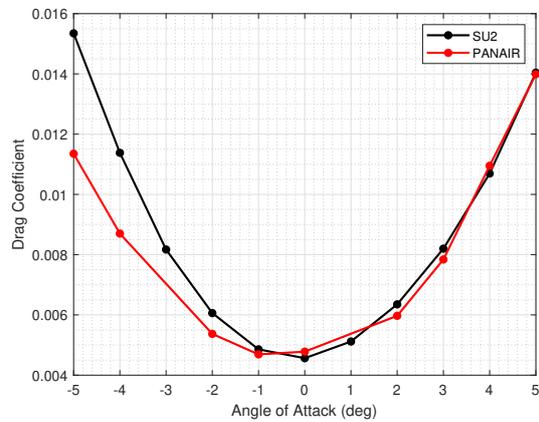
(b) Drag coefficient

Figure 14: Aerodynamic coefficients, $M = 1.8$

We can state that PANAIR can provide acceptable results for small angles of attack, especially for aerodynamic coefficients. However, errors in perceived loudness increase dramatically at $M = 1.8$ for the negative angles of attack.

3.3 Supersonic Airliner Configuration

After performing analysis on AIAA workshop models, a new full configuration aircraft model is generated for further comparative study. First, an aircraft geometry that has wing, horizontal and vertical tail, and engine nacelle is generated using OpenVSP for the baseline model. Therefore, an approximate geometry is created by using the planform information from Li and Geiselhart [19]. The OpenVSP view of the airline model is provided in Fig. 15.
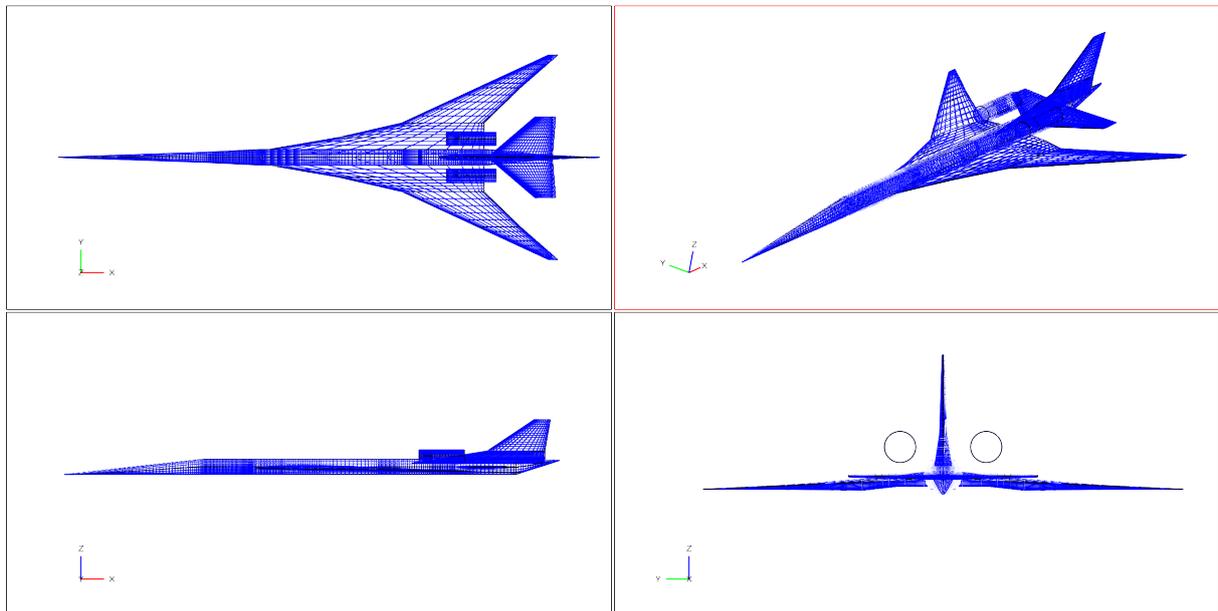
Figure 15: OpenVSP view of the airliner model

This model has a 242 ft long fuselage and a wing that has 98 ft wingspan. The analysis condition is set to 1.8 Mach number at an altitude of 60000 ft. An unstructured mesh with 15 million elements is created to be solved by the SU2 analysis. Besides, a surface grid is generated with 5400 quadrilateral elements for the PANAIR analysis. The surface grid of the supersonic airliner model is illustrated in Fig.16. It is seen that engine nacelle is modeled as an ellipsoid for the low-fidelity analysis. However, other components are modeled the same as the high-fidelity model. OpenVSP can calculate intersection curves of the component of the aircraft model. This allows generating the surface grids much easier for PANAIR. In addition to surface grids which are called solid boundary networks, wake networks are generated starting from the trailing edge of the lifting surface such as the wing and the horizontal tail.

The SU2 solution converged to 10^{-7} residual for RMS density in 1.5 hours by using Intel 2.4 GHz processors with 36 cores. On the other hand, PANAIR solution is completed approximately in 10 minutes with the supersonic solid boundary condition on a single core.

Yusuf Demiroglu and Melike Nikbay
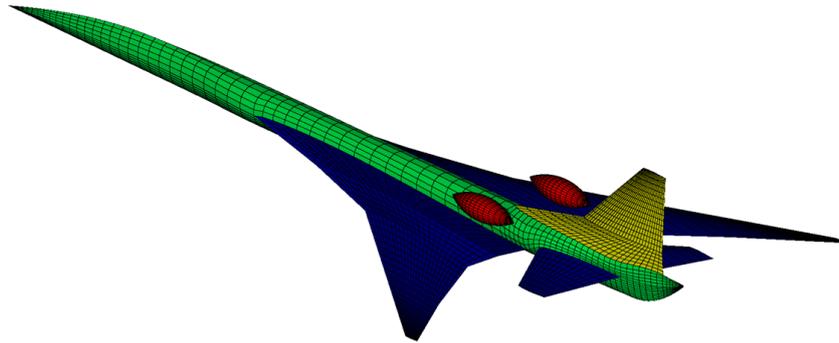
Figure 16: Surface grid of supersonic airliner model for PANAIR

Figure 17 shows Mach number distribution on the symmetry plane and pressure distribution on the surface of the aircraft from the SU2 solution. Also, the surface pressure coefficient distribution on the surface of the aircraft is compared in Fig. 18 for both upper and lower surfaces.
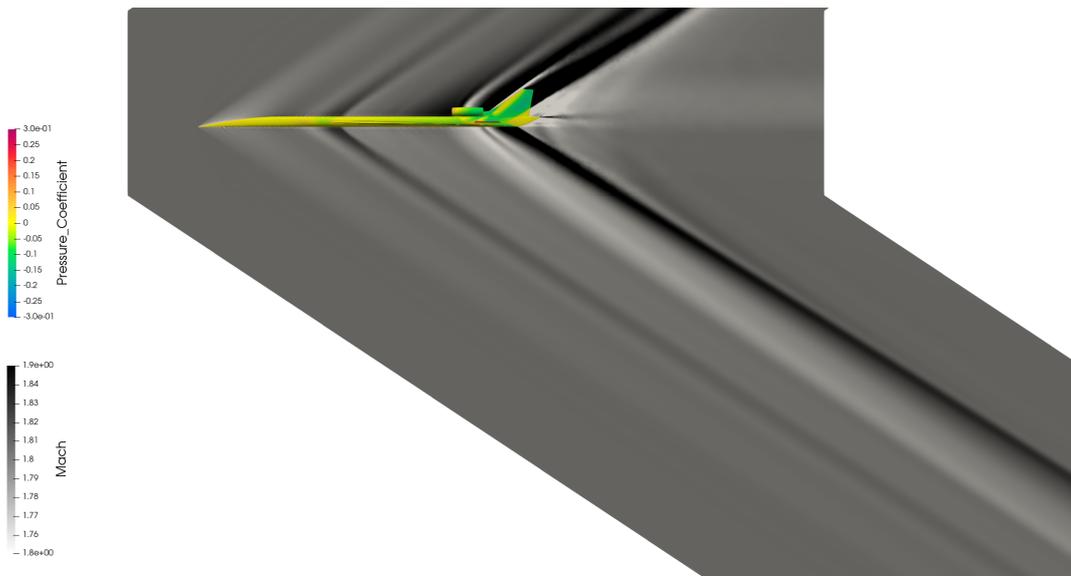
Figure 17: Mach number and surface pressure coefficient distribution

(a) Upper surface   (b) Lower surface
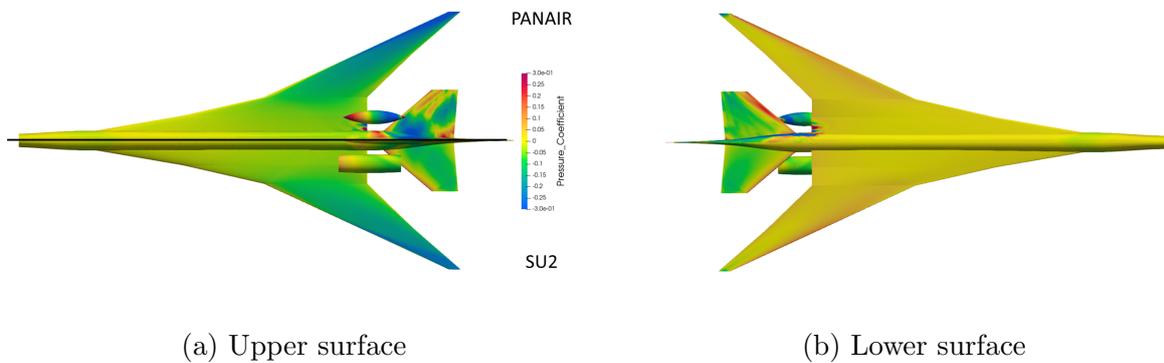
Figure 18: Comparison of surface pressure coefficient distribution, SU2 and PANAIR

Yusuf Demiroglu and Melike Nikbay

Surface pressure coefficient distributions of the two fidelities are very close to each other on the wing and fuselage. However, non-physical oscillations are observed on the horizontal tail and aft-body where the engine nacelle is located. Table 4 shows aerodynamic coefficients and loudness values for both solutions. A very close agreement is obtained for lift coefficient and loudness values. However, the drag coefficient prediction from the PANAIR solution is not sufficiently close for the supersonic airliner configuration. Also, it should be noticed that the loudness value is higher than expected for a low-boom geometry. This error may result from geometry generation which has small differences from the reference study as the exact reference geometry was not available in public domain.

Table 4: Aerodynamic Coefficients and Loudness

	C_L	C_D	PLdB
SU2	0.08541	0.00743	97.08555
PANAIR	0.08171	0.01181	97.81347
Percentage Error	4.33204	58.95020	0.74977

Next, a near-field pressure signature is taken from 2 body length away and a ground signature comparison is presented in Fig. 19. Since large oscillations occur in the near-field pressure signature, a low-pass filter is applied to obtain more realistic pressure signature and eliminate the non-physical peak points.

(a) Near-field pressure signatures   (b) Ground signatures
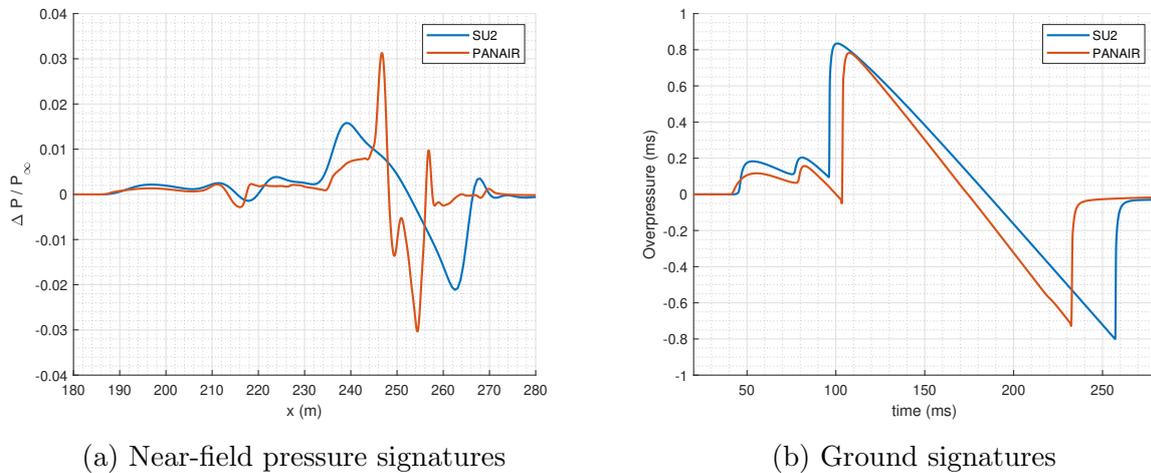
Figure 19: Pressure signature comparison, SU2 and PANAIR

After obtaining solutions for the supersonic airliner, a study is performed to investigate the effect of several parameters such as wing sweep angle and engine location for the prediction capability of the low-fidelity method.

3.3.1   Wing Sweep Angle Study

The wing of the aircraft model consist of two partitions; inboard and outboard. Three different wings are created with varying sweep angles for the outboard partition of the wing as illustrated in Fig. 20. The sweep angles are measured from the trailing edge of the wing partition.

Yusuf Demiroglu and Melike Nikbay
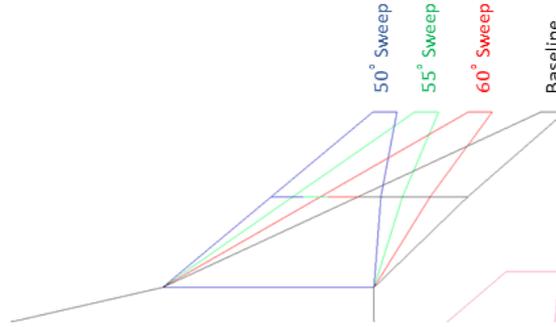
Figure 20: Wing geometries with various sweep angles

Table 5 shows results obtained for three different configurations. It is seen that very good agreement is obtained for the lift coefficient and the loudness value, however, while as the wing sweep angle increases, the error between SU2 and PANAIR solution increases. Unfortunately, the drag coefficient agreement is not obtained.

Table 5: Aerodynamic coefficients and loudness values for various wing sweep angles

	50° Degree Sweep	55° Degree Sweep	60° Degree Sweep
C_L, SU2	0.07923	0.08120	0.08345
C_L, PANAIR	0.08412	0.08763	0.09123
Percentage Error	6.17197	7.91780	9.31501
C_D, SU2	0.00801	0.00779	0.00762
C_D, PANAIR	0.01429	0.01481	0.01117
Percentage Error	78.3786	89.96145	46.61956
PLdB, SU2	98.54318	98.85438	97.22028
PLdB, PANAIR	97.79447	98.129648	98.31980
Percentage Error	0.75977	0.73313	1.13096

Pressure signature comparisons are provided in Fig. 21 by using a low-pass filter for the PANAIR results.
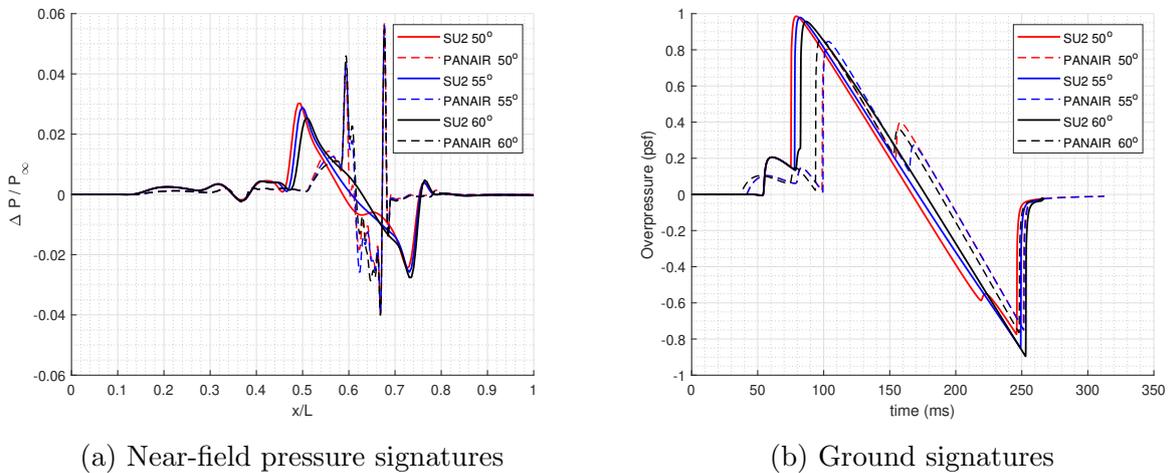
(a) Near-field pressure signatures

(b) Ground signatures

Figure 21: Pressure signature comparison for various wing sweep angles

3.3.2 Engine Nacelle Location Study

The effect of engine nacelle location on sonic boom prediction capability is examined. Four different engine locations are selected and illustrated in Fig. 22. Main reason for the nacelle position study is to observe nacelle-fuselage and nacelle-wing interaction and observe its impact on the sonic boom prediction.
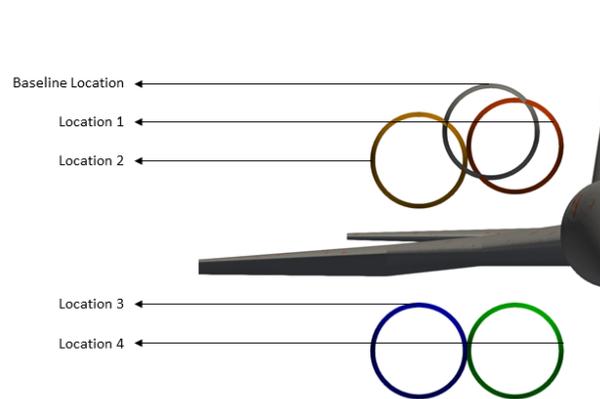
Figure 22: Locations of different nacelle configurations

The results are presented in Tab. 6. From this table, it is concluded that error in the lift coefficient increases when the nacelle is placed under the wing. However, the best near-field signature is obtained for location 4 where the lift coefficient has the maximum error.

Table 6: Aerodynamic coefficients and loudness values for various engine locations

	Location 1	Location 2	Location 3	Location 4
C_L, SU2	0.08582	0.08284	0.09289	0.08759
C_L, PANAIR	0.08713	0.08069	0.10003	0.07301
Percentage Error	1.515	2.603	7.676	16.65
C_D, SU2	0.00730	0.00719	0.00789	0.00752
C_D, PANAIR	0.01102	0.01214	0.01379	0.01290
Percentage Error	50.755	68.788	74.737	71.622
PLdB, SU2	97.0581	96.8775	96.5955	96.9046
PLdB, PANAIR	93.6779	94.8763	95.8018	96.7939
Percentage Error	3.482	2.065	0.821	0.114

Pressure signature comparisons are given in Fig. 23. For locations 3 and 4 where the nacelle is located under the wing, peak points in the signature is too high when compared to others. This behavior is expected due to the shocks from the nacelle itself.

(a) Near-field pressure signatures

(b) Ground signatures
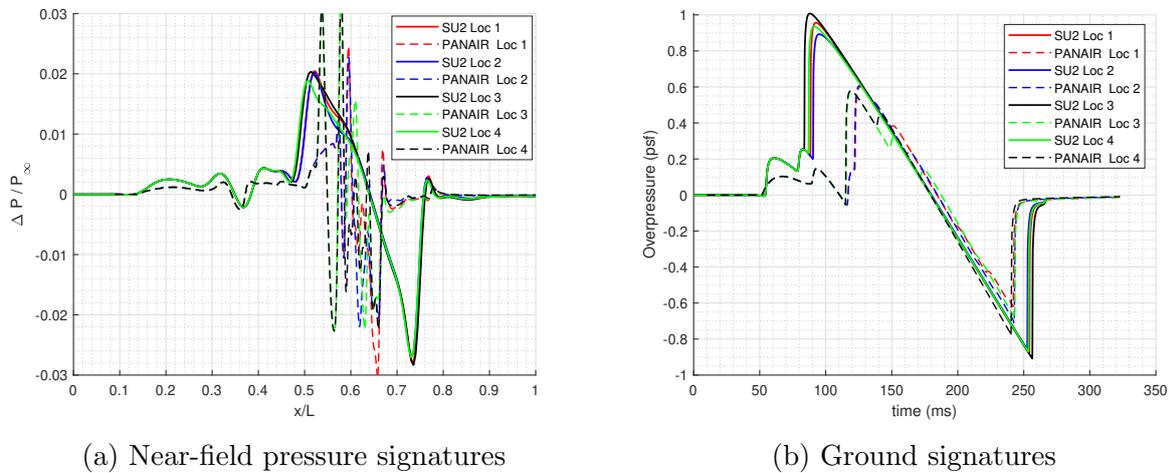
Figure 23: Pressure signature comparison for various nacelle locations

4 CONCLUSION

In this study, the capability of a low-fidelity solver PANAIR for the low-boom supersonic aircraft design is investigated. For small angles of attack, a sufficient agreement is obtained in terms of aerodynamic coefficients and sonic boom loudness value. However, error in the low-fidelity solution increases as the angle of attack exceeds $\pm 5^o$. Therefore, low fidelity tools can be used for design space explorations for cruise conditions. For complex geometries where large oscillations occur in the surface pressure distribution, several geometric simplifications should be performed such that replacing the engine nacelle with an ellipsoid. Prediction of the lift coefficient and near-field pressure signature is in the acceptable range with the low-fidelity solutions. However, the drag coefficient prediction is not in the acceptable range to be used in optimization studies for a full configuration supersonic aircraft. The various low-fidelity solutions examined and the experience gained in this study give enough confidence to employ PANAIR solutions for generation of surrogate models within multi-fidelity analysis, uncertainty quantification and optimization studies. Furthermore, machine learning techniques can be employed to generate a framework where low-fidelity flow analyses can be corrected and processed with the assistance of high-fidelity training data for sonic boom prediction and sonic boom minimization purposes.

As future work of this study, an in-house code for linear and nonlinear sonic boom calculations will be implemented by using the equivalent area distribution-based sonic boom theories which will use directly the surface pressure distribution on the aircraft obtained by the PANAIR code.

ACKNOWLEDGEMENTS

Propagation Code". The second author would like to thank NASA Langley Research Center for distributing sBOOM sonic boom prediction code internationally for academic research.

REFERENCES

[1] L. Brevault, M. Balesdent, and A. Hebbal. Overview of gaussian process based multi-fidelity techniques with variable relationship between fidelities, application to aerospace systems. *Aerospace Science and Technology*, 107:106339, Dec. 2020. doi:10.1016/j.ast.2020.106339.

[2] Y. Demiroglu, S. Yildiz, and M. Nikbay. Multi-fidelity sonic boom minimization of a supersonic aircraft by parametric wing shape design. In *AIAA Scitech 2021 Forum*. American Institute of Aeronautics and Astronautics, Jan. 2021. doi:10.2514/6.2021-1009. URL `https://doi.org/10.2514/6.2021-1009`.

[3] T. D. Economon, F. Palacios, S. R. Copeland, T. W. Lukaczyk, and J. J. Alonso. SU2: An open-source suite for multiphysics simulation and design. *AIAA Journal*, 54(3):828–846, Mar. 2016. doi:10.2514/1.j053813. URL `https://doi.org/10.2514/1.j053813`.

[4] R. CARMICHAEL and L. ERICKSON. PAN AIR - a higher order panel method for predicting subsonic or supersonic linear potential flows about arbitrary configurations. In *14th Fluid and Plasma Dynamics Conference*. American Institute of Aeronautics and Astronautics, June 1981. doi:10.2514/6.1981-1255. URL `https://doi.org/10.2514/6.1981-1255`.

[5] S. Choi, J. J. Alonso, I. M. Kroo, and M. Wintzer. Multifidelity design optimization of low-boom supersonic jets. *Journal of Aircraft*, 45(1):106–118, Jan. 2008. doi:10.2514/1.28948. URL `https://doi.org/10.2514/1.28948`.

[6] I. Kroo, K. Willcox, A. March, A. Hass, D. Rajnarayan, and C. Kays. Multifidelity Analysis and Optimization for Supersonic Design. Technical Report CR–2010–216874, NASA CONTRACTOR REPORT, 2010.

[7] F. L. Carpenter, P. Cizmas, C. R. Bolander, T. N. Giblette, and D. F. Hunsaker. A multi-fidelity prediction of aerodynamic and sonic boom characteristics of the JAXA wing body. In *AIAA Aviation 2019 Forum*. American Institute of Aeronautics and Astronautics, June 2019. doi:10.2514/6.2019-3237. URL `https://doi.org/10.2514/6.2019-3237`.

[8] G. B. Whitham. The flow pattern of a supersonic projectile. *Communications on Pure and Applied Mathematics*, 5(3):301–348, aug 1952. ISSN 00103640. doi:10.1002/cpa.3160050305. URL `http://doi.wiley.com/10.1002/cpa.3160050305`.

[9] B. Argrow, K. Maute, C. Farhat, and M. Nikbay. F-function lobe balancing for sonic boom minimization. *Computational Fluid Dynamics Journal*, 17(4):221–234, 2009.

Yusuf Demiroglu and Melike Nikbay

[10] K. Maute, C. Farhat, B. Argrow, and M. Nikbay. Sonic boom mitigation via shape optimization using an adjoint method and application to a supersonic fighter aircraft. *European Journal of Computational Mechanics*, 17(1-2):217–243, Jan. 2008. doi:10.3166/remn.17.217-243.

[11] C. Farhat, K. Maute, B. Argrow, and M. Nikbay. Shape optimization methodology for reducing the sonic boom initial pressure rise. *AIAA Journal*, 45(5):1007–1018, May 2007. doi:10.2514/1.27607.

[12] C. Farhat, B. Argrow, M. Nikbay, and K. Maute. Shape optimization with f-function balancing for reducing the sonic boom initial shock pressure rise. *International Journal of Aeroacoustics*, 3(4):361–377, Oct. 2004. doi:10.1260/1475472043499281.

[13] S. K. Rallabhandi. Advanced sonic boom prediction using the augmented burgers equation. *Journal of Aircraft*, 48(4):1245–1253, July 2011. doi:10.2514/1.c031248.

[14] C. R. Bolander, D. F. Hunsaker, H. Shen, and F. L. Carpenter. Procedure for the calculation of the perceived loudness of sonic booms. In *AIAA Scitech 2019 Forum*. American Institute of Aeronautics and Astronautics, Jan. 2019. doi:10.2514/6.2019-2091. URL https://doi.org/10.2514/6.2019-2091.

[15] S. S. Stevens. Perceived level of noise by mark VII and decibels (e). *The Journal of the Acoustical Society of America*, 51(2B):575–601, Feb. 1972. doi:10.1121/1.1912880.

[16] M. A. Park and J. M. Morgenstern. Summary and statistical analysis of the first AIAA sonic boom prediction workshop. In *32nd AIAA Applied Aerodynamics Conference*. American Institute of Aeronautics and Astronautics, June 2014. doi:10.2514/6.2014-2006. URL https://doi.org/10.2514/6.2014-2006.

[17] M. A. Park and M. Nemec. Nearfield summary and statistical analysis of the second AIAA sonic boom prediction workshop. *Journal of Aircraft*, 56(3):851–875, May 2019. doi:10.2514/1.c034866. URL https://doi.org/10.2514/1.c034866.

[18] A. Ueno, M. Kanamori, and Y. Makino. Multi-fidelity low-boom design based on near-field pressure signature. In *54th AIAA Aerospace Sciences Meeting*. American Institute of Aeronautics and Astronautics, Jan. 2016. doi:10.2514/6.2016-2033. URL https://doi.org/10.2514/6.2016-2033.

[19] W. Li and K. Geiselhart. Multidisciplinary design optimization of low-boom supersonic aircraft with mission constraints. In *AIAA Scitech 2020 Forum*. American Institute of Aeronautics and Astronautics, Jan. 2020. doi:10.2514/6.2020-0664. URL https://doi.org/10.2514/6.2020-0664.
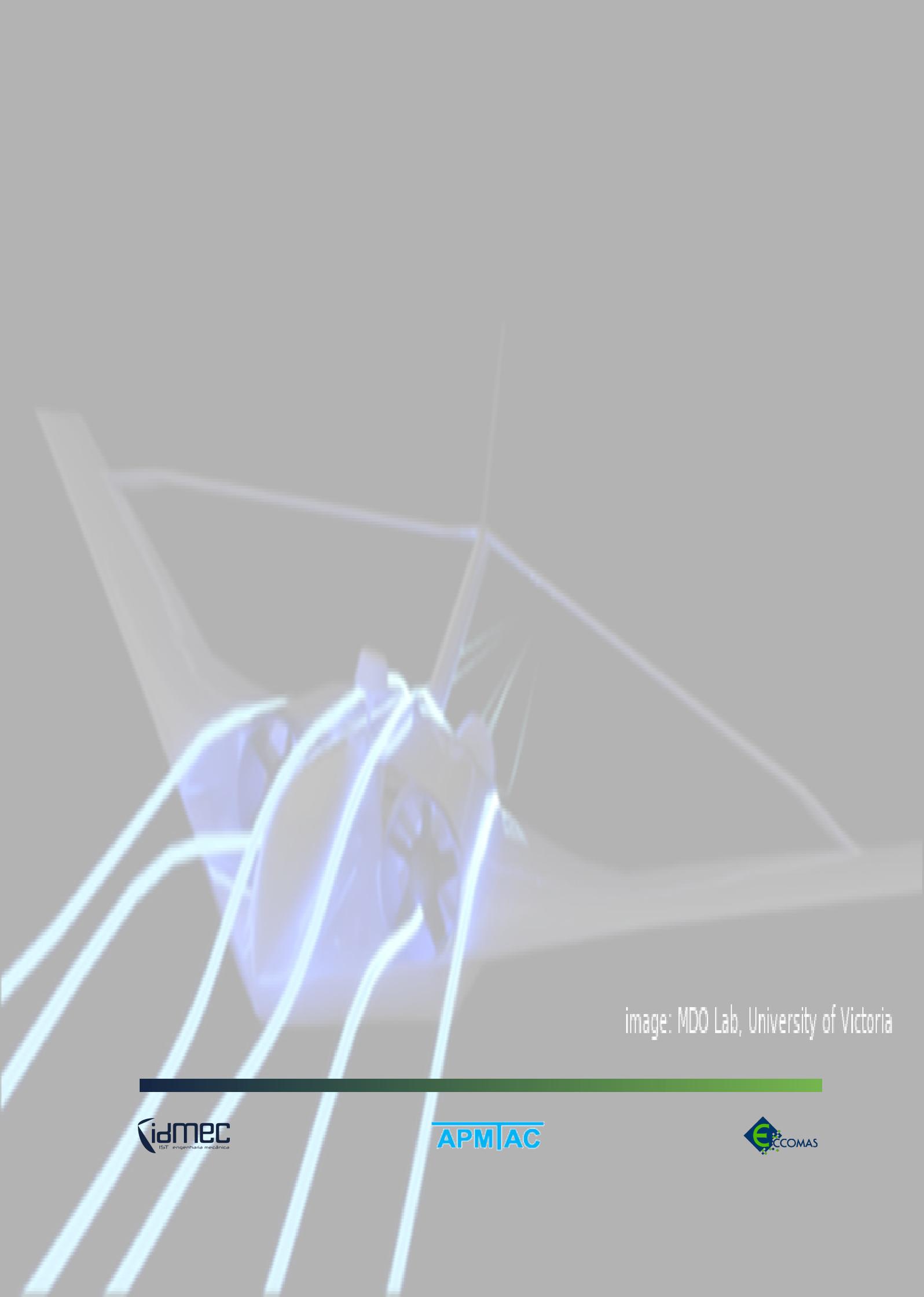
Index of Authors

image: MDO Lab, University of Victoria